DEPARTMENT OF PHYSICS & ASTROPHYSICS
UNIVERSITY OF DELHI
DELHI-110 007
INDIA

Ph. H.O.D:
+ 91-11 27667793
27666796/7155
27667725/1354
Admn. Office:
27667725/1256-8
Fax: 27667061
e-mail:head@physics.du.ac.in

This is to state that the research outcomes published in different reputed national/international journals are considered to be the main achievement of the collaborative works as far as basic research is concerned. Therefore the publications from our faculty in different journals (national/international) in collaboration with different institutes/universities/industry in India and abroad are evidences for linkage with different institutes/universities/industry.

Head of the Department

MEMORANDUM OF UNDERSTANDING
(MOU)

UNIVERSITY OF DELHI

DEFENCE RESEARCH &
DEVELOPMENT ORGANISATION
(DRDO)

JOINT COLLABORATION
ON
RESEARCH AND DEVELOPMENT

1. This memorandum of understanding entered into on the 23 day of January, Two thousand and twelve (2012) between the University of Delhi (hereinafter referred to as DU) and Defence Research and Development Organization (hereinafter referred to as DRDO) at New Delhi with the desire to promote academic and research interaction and cooperation between the two organizations.

2. University of Delhi (DU)

2.1 University of Delhi (DU) is a premier university of the country known for its high standards in teaching and research, having eminent scholars as faculty members and it attracts the very best students across the globe. It was established in 1922 as a unitary, teaching and residential university by an Act of the then Central Legislative Assembly. At present, there are 14 faculties, 86 academic departments and 79 colleges spread all over the city, with about 2,20,000 students. The University currently has 15 libraries besides two Central Instrument facilities (CIFs) equipped with a number of state-of-the-art research instruments which are used by several departments of the University and by other institutions in Delhi and elsewhere. The South Campus of the University has developed a Biotech Centre for Research and Development (R&D). The University has been recognized by the Department of Science and Technology as India's leading university in research and has been awarded PURSE grant for three years by DST to strengthen the academic activities in the University.

3. Defence Research and Development Organization (DRDO)

3.1 Defence Research and Development Organization (DRDO) works under the Department of Defence Research and Development of Ministry of Defence. DRDO is working towards enhancing self-reliance in Defence systems and undertakes design and development leading to production of world class weapon systems in accordance with expressed needs and requirements of the three services. DRDO has the mission to design, develop and produce state-of-art sensors, weapon systems, platforms and allied equipment for our defence services. DRDO is committed to provide technological solutions to the Services to optimize combat effectiveness and to promote well-being of the troops. DRDO is also involved with developing infrastructure and has committed quality manpower to build strong indigenous technology base in India.

3.2 Today, DRDO is a network of more than 50 laboratories which are deeply engaged in developing defence technologies covering disciplines like aeronautics, armaments, electronics, combat vehicles, instrumentation engineering systems, missiles, advanced computing, simulation, special materials, naval systems, life sciences, psychology, human resources development, information systems and agriculture. Presently, the organization is backed by over 7000 scientists and around 23000 other scientific, technical and supporting personnel.

3.3 To fulfil the mandate of DRDO, the organization is committed to closely working with academic institutions, Research and Development (R&D) centres and production agencies of Ministries/Departments of Science and Technology (S&T) universities and in the industry, to gainfully harness the talent present in the cooperation (but not limited to) based on the following guidelines. The two organizations would seek to undertake

4. **Presently, DRDO - University of Delhi interactions are through the following mechanisms.**

(a) Grants-in-Aid projects awarded to University of Delhi through the Dte of ER&IPR and the Research Boards.

(b) CARS awarded to University of Delhi from DRDO Labs.

(c) Ad-Hoc grants to conferences/seminars/workshop organised by the various Departments of University of Delhi.

Through these mechanisms a formal interaction between DRDO & University of Delhi exists, promoting research and academic collaboration.

5. Guidelines

5.1 DU would grant recognition to certain number of senior scientists (Scientist 'E' and above) of following DRDO HQ and co-located laboratories as adjunct faculty in various departments of DU:

i) Centre for Fire, Explosive & Environment Safety

ii) Centre for Personnel Talent Management

iii) Defence Institute of Physiology & Allied Sciences

iv) Defence Institute of Psychological Research

v) Defence Scientific Information & Documentation Centre

vi) Defence Terrain Research Laboratory

vii) Institute of Nuclear Medicine & Allied Sciences

viii) Institute for Systems Studies & Analysis

ix) LASER Science & Technology Centre

x) Scientific Analysis Group

xi) Solid State Physics Laboratory

5.2 These adjunct faculties could register limited number of students (Two for scientist 'E' and four for scientist 'F' and above) for Ph.D. supervision from DU provided their names are duly forwarded by the Director of their parent institutions. Recognition of the scientists as supervisors would be granted by the concerned DRC, Delhi University, after due evaluation on a case by case basis, taking publications in International Journals of repute and/or International/National patents as one of the main criteria. DRDO 'Scientists' registering for Ph.D. program has to show the residency of period (as per DU requirement) in the parent DRDO institute. The Supervisor would have to ascertain/ testify their presence. All other conditions, pertaining to students will be followed according to the Ordinance VI B of the University.

5.3 DU would also grant recognition to certain numbers of Senior Scientists of DRDO as Guest faculty/part time faculty. Guest faculty or part time faculty of DRDO laboratories would be accorded all non-financial privileges of DU including (but not limited to) library and computing facilities and DU faculty will have reciprocation of the same.

5.4 The Junior and Senior Research Fellows (JRF/SRF) in DRDO labs will be allowed to have similar status of JRF/SRF of CSIR-UGC fellows for registering for Ph.D. program at DU.

5.5 DU and DRDO shall actively initiate a process to identify core technology research areas of mutual interest and work on to establish centre of excellence (CoE) at DU through appropriate funding from Defence Research and Development Organisation preferably within a time frame of 3 years.

5.6 Due acknowledgement/credit to DU be given by the faculty/ scientists/ students of DRDO laboratories for the research work carried out during Ph.D. program from DU. The authorship must be shared according to terms that are mutually agreed upon at the time of the registration/commencement of their Ph.D. programme.

5.7 Senior scientists of DRDO laboratories (Scientist 'E' and above) who have been granted the status of Guest faculty/part time faculty by DU and who have been accorded status of Ph.D. guide(s), may be involved in active teaching of postgraduate programmes of DU. Such scientists will be paid as guest faculty of the university as per DU regulation.

5.8 Scientists of DRDO laboratories and faculty of DU may collaborate jointly in the Research and Development programmes of DRDO in the scientific areas mentioned above and also in other areas mutually agreed upon. Joint sponsored projects may be undertaken with both long-term and short-term goals, keeping in view the interest and philosophies of the respective institutions.

5.9 DRDO laboratories would make their state-of-the-art facilities accessible for the faculty and students of DU on requirement basis.

6. General Points

6.1 This MOU shall come into force on the date of its signature and shall be in force for a period of five years initially and can be extended for such further period as may be mutually decided upon by the parties. The MOU can be terminated by either party by a written communication addressed to the other party six months in advance. Early termination of MOU shall in no way affect the conclusion of the activities initiated prior to such termination.

6.2 Issues arising during the course of implementation of the MOU shall be dealt by a Monitoring & Assessment Committee duly constituted by the Vice

Chancellor, Delhi University, consisting of members from both the organisations. The meeting of this Committee should be held at least once a year.

6.3 This MoU is made in duplicate and signed on this 23 day of January, 2012 at Development Enclave, DRDO, New Delhi each party retaining one.

Dr. V K Saraswat
Scientific Advisor to Raksha Mantri &
Secretary, Dept. of Defence R&D &
Director General, R&D
Defence R&D Organisation (DRDO)

Prof. Dinesh Singh
Vice Chancellor
University of Delhi

Witnesses

Dr. A K Singh
Director, Human Resource Development
Defence R&D Organisation (DRDO)

Mr. R K Sinha, IAS
Registrar
University of Delhi

Langmuir
Article
pubs.acs.org/Langmuir

Structure and Activity of Lysozyme on Binding to ZnO Nanoparticles

Soumyananda Chakraborti,[†] Tanaya Chatterjee,[†] Prachi Joshi,[‡] Asim Poddar,[†] Bhabatarak Bhattacharyya,[†] Surinder P. Singh,[§] Vinay Gupta,[‖] and Pinak Chakrabarti*[,†]

[†]Department of Biochemistry, Bose Institute, P-1/12 CIT Scheme VIIM, Kolkata 700054, India, [‡]National Physical Laboratory, New Delhi 110012, India, [§]Department of Engineering Sciences and Materials, University of Puerto Rico, Mayaguez, Puerto Rico 00681-9000, and [‖]Department of Physics and Astrophysics, University of Delhi, New Delhi 110007, India

Received August 21, 2009. Revised Manuscript Received November 23, 2009

The interaction between ZnO nanoparticles (NPs) and lysozyme has been studied using calorimetric as well as spectrophotometric techniques, and interpreted in terms of the three-dimensional structure. The circular dichroism spectroscopic data show an increase in α-helical content on interaction with ZnO NPs. Glutaraldehyde cross-linking studies indicate that the monomeric form occurs to a greater extent than the dimer when lysozyme is conjugated with ZnO NPs. The enthalpy-driven binding between lysozyme and ZnO possibly involves the region encompassing the active site in the molecule, which is also the site for the dimer formation in a homologous structure. The enzyme retains high fraction of its native structure with negligible effect on its activity upon attachment to NPs. Compared to the free protein, lysozyme−ZnO conjugates are more stable in the presence of chaotropic agents (guanidine hydrochloride and urea) and also at elevated temperatures. The possible site of binding of NP to lysozyme has been proposed to explain these observations. The stability and the retention of a higher level of activity in the presence of the denaturing agent of the NP-conjugated protein may find useful applications in biotechnology ranging from diagnostic to drug delivery.

Introduction

Adsorption of proteins on inorganic surfaces may lead to structural and functional changes[1,2] that are dependent on both the nature of the adsorbed proteins and the physicochemical properties of the inorganic surfaces.[3,4] Protein surface recognition offers a powerful tool in understanding protein−protein interaction,[5] which is a key aspect of many complex cellular functions.[6] Nanoparticles (NPs), because of their small size, have distinct properties compared to the bulk form of the same material, thus offering many new developments in the fields of biosensors, biomedicine, and bionanotechnology. The adsorption of protein on NPs and its consequence on the structure and function are strongly dependent on the size and shape of the NPs.[7]

Chicken egg white lysozyme (molecular weight (MW) = 14.6 kDa) is a small globular protein, consisting of 129 amino acid residues with four disulfide bonds. The importance of lysozyme relies on its extensive use as a model system to understand the underlying principles of protein structure, function, dynamics, and folding through theoretical and experimental studies.[8,9] High natural abundance is also one of the reasons for choosing lysozyme as a model protein for studying protein−NP interaction. Another important aspect of lysozyme is its ability to carry drug.[10] According to the X-ray crystal structure, lysozyme possesses a relatively rigid structure.[11] It contains six tryptophan (Trp) residues. Three of them are located in the substrate binding site, two are located in the core hydrophobic region, and one is separated from all other residues. Trp62 and Trp108 are the most dominant fluorophores.[12]

NPs have been widely explored for a wide range of biotechnological applications from sensing to drug delivery. In the past few years, there has been a great deal of work to identify the interaction of lysozyme with silica and single-walled carbon nanotubes of varying shape and size.[13,14] It is reported that lysozyme retains a considerable amount of native-like secondary and tertiary structure when adsorbed on small hydrophilic silica NPs as compared to that on larger NPs. The fact that NPs with greater surface area cause higher degrees of perturbation of structure and function of the protein has also been shown by studying the effect of the increasing size of silica NPs on the thermodynamic stability and enzymatic activity of RNase A.[15] Despite all these studies, little is known about the fundamental role of NPs in governing protein structure and function, and the region on the protein surface where NPs bind still remains nebulous. Zinc oxide (ZnO), with wide band gap (3.3 eV) and high excitonic binding energy (60 MeV), is a potential nanomaterial for biomedical application because of its biocompatibility

*Corresponding author. E-mail: pinak@boseinst.ernet.in.

(1) Larsericsdotter, H.; Oscarsson, S.; Buijs, J. *J. Colloid Interface Sci.* **2001**, *237*, 98–103.
(2) Billsten, P.; Carlsson, U.; Jonsson, B. H.; Olofsson, G.; Hook, F.; Elwing, H. *Langmuir* **1999**, *15*, 6395–6399.
(3) Hobora, D.; Imabayashi, S.-I.; Kakiuchi, T. *Nano Lett.* **2002**, *2*, 1021–1025.
(4) Roach, P.; Farrar, D.; Perry, C. C. *J. Am. Chem. Soc.* **2005**, *127*, 8168–8173.
(5) Janin, J.; Bahadur, R. P.; Chakrabarti, P. *Q. Rev. Biophys.* **2008**, *41*, 133–180.
(6) Degterev, A.; Lugovskoy, A.; Cardone, M.; Mulley, B.; Wagner, G.; Mitchison, T.; Yuan, J. Y. *Nat. Cell Biol.* **2001**, *3*, 173–182.
(7) Shang, W.; Nuffer, J. H.; Muniz-Papandrea, V. A.; Colon, W.; Siegel, R. W.; Dordick, J. S. *Small* **2009**, *5*, 470–476.
(8) Buck, M.; Schwalbe, H.; Dobson, C. M. *Biochemistry* **1995**, *34*, 13219–13232.
(9) Ghosh, A.; Brinda, K. V.; Vishveshwara, S. *Biophys. J.* **2007**, *92*, 2523–2535.
(10) Zhang, Z.; Zheng, Q.; Han, J.; Gao, J.; Liu, J.; Gong, T.; Gu, Z.; Huang, Y.; Sun, X.; He, Q. *Biomaterial* **2009**, *30*, 1372–1381.
(11) Blake, C. C. F.; Koenig, D. F.; Mair, G. A.; North, A. C. T.; Phillips, D. C.; Sarma, V. R. *Nature* **1965**, *206*, 757–761.
(12) Imoto, T.; Foster, L. S.; Ruoley, J. A.; Tanaka, F. *Proc. Natl. Acad. Sci.U. S.A.* **1972**, *69*, 1151–1155.
(13) Asuri, P.; Bale, S. S.; Pangule, R. C.; Shah, D. A.; Kane, R. S.; Dordick, J. S. *Langmuir* **2007**, *23*, 12318–12321.
(14) Vertegal, A. A.; Siegel, R. W.; Dordick, J. S. *Langmuir* **2004**, *20*, 6800–6807.
(15) Shang, W.; Nuffer, J. H.; Dordick, J. S.; Siegel, R. W. *Nano Lett.* **2007**, *7*, 1991–1995.

and high stability.[16−18] It has been reported that ZnO nanowires get solubilized in biofluids after a survival time of a few hours, which may find applications in drug delivery.[19]

In the present paper, we show that lysozyme, when bound to ZnO NPs of 7 nm diameter at pH 7.4, takes on a more regular structure in comparison to its free form. Isothermal calorimetry (ITC) has been used to quantify the interaction. When conjugated to NP, lysozyme undergoes a lesser degree of unfolding induced by guanidine hydrochloride (GdnHCl) and urea, and as a result, some residual activity is retained in the presence of denaturing agent. A molten globule intermediate can be detected in the urea-induced unfolding of the protein in the presence of NPs. ZnO possibly binds around the active site of lysozyme and prevents the dimerization of the molecule.

Experimental Section

Materials. Chicken egg white lysozyme and *Micrococcus lysodeikticus* cells were purchased from Sigma (St. Louis, MO) as salt-free, dry powders and were used without further purification. GdnHCl, urea, glutaraldehyde, and all other chemicals were purchased from Merck, India, and used as received. All other reagents were of analytical grade, and double-distilled water was used throughout the experiment.

NP Preparation. ZnO quantum dots (QDs) were prepared by wet chemical route,[20] using zinc nitrate hexahydrate ($Zn(NO_3)_2 \cdot 6H_2O$) as a precursor. Ten millimolars of the compound was sonicated in water to get a clear solution. Twenty millimolar NaOH was also sonicated in water and added dropwise to the zinc nitrate solution with stirring. The solution was allowed to stir for 4−5 h. The precipitate was centrifuged, washed three to four times, and collected after drying at 70 °C.

Sample Preparation. A buffer solution, consisting of 0.1 mM sodium phosphate at pH 7.4, was used in all the experiments. Protein solution (concentration 10 μM) was exhaustively dialyzed; using membrane (Spectra biotech membrane; molecular weight cutoff (MWCO) = 3500, Spectrum Laboratories, Compton, CA) against buffer solution at 4 °C. For studying NP−lysozyme interaction a fixed amount of the NP solution was added to the protein solution, mixed by vortexing, and incubated at room temperature for overnight. Longer incubation time did not alter the spectroscopic results. For unfolding studies, urea solution was prepared immediately before use. Commercially available GdnHCl powder was used for preparing 10 M GdnHCl solution. Different amounts of the stock solution of urea or GdnHCL were used to obtain samples with 0−8 M concentration of urea and 0−6 M GdnHCl, but maintaining the same protein concentration. A fixed amount (0.01 M of dithiotheritol (DTT) was used for reducing the disulfide bonds.

Circular Dichroism (CD) Spectropolarimetry. We measure the far-UV CD spectra to evaluate the structural change of lysozyme induced by the addition of ZnO NP. The CD spectra were obtained using a JASCO-810 spectropolarimeter equipped with a thermostatically controlled cell holder. Protein concentration was 10 μM for all the experiments. The far UV region was scanned between 200 and 260 nm with an average of three scans and also a bandwidth of 5 nm at 25, 70, and 80 °C, respectively. The final spectra were obtained by subtracting the buffer contribution from the original protein spectra. The CD results were expressed in terms of mean residual ellipticity (MRE) in $deg \cdot cm^2 \cdot dmol^{-1}$ according to the following equation:

$$\mathrm{MRE} = \{\text{observed CD in (m deg)}\}/C_p nl \qquad (1)$$

C_p is the molar concentration of protein, n is the number of amino acid residues (129), and l is the path length (0.1 cm). Deconvolution of the far-UV CD spectra to determine percentage composition of the different secondary structural elements was done with CDNN (http://bioinformatik.biochemtech.uni-halle.de/cd-spec/cdnn).

Fourier Transform Infrared (FT-IR) Spectroscopy. Ten milligrams of lyophilized lysozyme powder was added to a solution containing 0.1 mg of ZnO NPs and made (using SPEED VAC, Savant, Inc.) into a dry powder (protein/NP ratio of 100:1). Protein FT-IR spectra were recorded on a Perkin-Elmer spectrometer equipped with a DTGS KBr detector and a KBr beam splitter. All the spectra were taken via the absorbance mode with constant nitrogen purging. Spectra were obtained at 4 cm^{-1} resolution with 50 scans. Spectra of background were collected and subtracted from the original protein spectra. If not specifically mentioned, all the spectra were collected in the range of 1400−1800 cm^{-1}.

Fluorescence Spectroscopy. Fluorescence spectroscopy was used to monitor the tertiary structural change in lysozyme induced by ZnO NP. All measurements were carried out using a Hitachi F3000 spectrofluorimeter with 10 μM protein concentration. The slits were 5 nm for excitation and emission scans. Fluorescence was measured by excitation at 295 nm and emission at 310−430 nm. Unfolding of lysozyme was monitored by noting the changes of Fluorescence λ_{max} as a function of GdnHCl concentration. The signals were fitted to an equation describing a two-state model of unfolding.[21] 8-Anilinonaphthalene-1-sulfonic acid (ANS), a hydrophobic fluorescence dye, is popularly used to monitor the exposure and/or disruption of hydrophobic patches of protein during its unfolding/folding process.[22] We also used ANS fluorescence to study ANS binding; the excitation wavelength was set at 340 nm, and the emission spectra were recorded in the range of 440−600 nm.

For fluorescence quenching measurements, ZnO NP was added to the protein from a 500 μM stock solution. The fluorescence intensities were determined at the λ_{max} and inner filter correction, and data analysis was done using the Stern−Volmer equation:[23]

$$F_O/F_C = 1 + K_{SV} \times [\mathrm{NP}] = 1 + K_q \tau_0 [\mathrm{NP}] \qquad (2)$$

F_o and F_c denote the steady-state fluorescence intensities in the absence and in the presence of a quencher (ZnO NP), respectively; K_{SV} is the Stern−Volmer quenching constant, and [NP] is the concentration of quencher. K_q is the bimolecular quenching constant, and τ_0 is the lifetime of fluorophore. Equation 2 was used for determining K_{SV}.

ITC. ITC measurement was performed on a VP-ITC calorimeter (Microcal Inc., Northampton, MA). Lysozyme was dialyzed extensively against 0.1 M sodium phosphate buffer, and the ligand (ZnO NPs) was dissolved in the last dialysate. A typical titration involved 12 injections of the NPs (20 μL aliquot per injection from a 400 μM stock solution) at 5 min intervals into the sample cell (volume 1.4359 mL) containing lysozyme (concentration, 35 μM). The titration cell was stirred continuously at 310 rpm. The heat of the ligand dilution in the buffer alone was subtracted from the titration data for each experiment. The data were analyzed to determine the binding stoichiometry (N), affinity constant (K_a), and other thermodynamic parameters[24] of the

(16) (a) Singh, S. P.; Arya, S. K.; Pandey, P.; Malhotra, B. D.; Saha, S.; Sreenivas, K.; Gupta, V. *Appl. Phys. Lett.* **2007**, *91*, 063901.

(17) Wu, Y. L.; Lim, C. S.; Fu, S.; Tok, A. I. K.; Lau, H. M.; Boey, F. C.; Zeng, X. T. *Nanotechnology* **2007**, *18*, 215604.

(18) Kumar, A. S.; Chen, M. S. *Anal. Lett.* **2008**, *41*, 141–158.

(19) Guo, D.; Wu, C.; Jiang, H.; Li, Q.; Wang, X.; Chen, B. *J. Photochem. Photobiol. B* **2008**, *93*, 119–126.

(20) Joshi, P.; Chakraborti, S.; Chakrbarti, P.; Haranath, D.; Shanker, V.; Ansari, Z. A.; Singh, S. P.; Gupta, V. *J. Nanosci. Nanotechnol.* **2009**, *9*, 6427–6433.

(21) Pace, C. N. *Methods Enzymol.* **1986**, *13*, 266.

(22) Semisotonov, G. V.; Rodionova, N. A.; Kutysheno, V. P.; Elbert, B.; Blank, J.; Pitiqyn, O. B. *FEBS Lett.* **1987**, *224*, 9–13.

(23) Lakowicz, J. R. *Principle of Fluorescence Spectroscopy*, 3rd ed.; Springer: New York, 2006; 278−285.

(24) Goobes, G.; Goobes, R.; Shaw, J. W.; Gibson, M. J.; Long, R. J.; Raghunathan, V.; Schueler-Furman, O.; Popham, M. J.; Baker, D.; Campbell, T. C.; Stayton, S. P.; Drobny, G. P. *Magn. Reson. Chem.* **2007**, *45*, S32–S47.

reaction using Origin software. Calorimetric titration of lysozyme with ZnO NPs was carried out at 25 °C. The reported thermodynamic quantities were the average of two parallel experiments.

Glutaraldehyde Cross-Linking. A glutaraldehyde cross-linking experiment was carried out to monitor the oligomeric status of lysozyme in the presence of ZnO NPs. Ten micromolars of protein was treated with 0.1 and 0.2% glutaraldehyde and incubated at room temperature for different time period. The reaction was then terminated by the addition of 1 M Tris-HCl (pH 8.0) and 1X sodium dodecyl sulfate polyacrylamide gel electrophoresis (SDS-PAGE) gel loading buffer. After being boiled in a water bath,[25] samples were loaded on 10% tris-glycine SDS-PAGE along with a molecular weight marker from Bio-Rad. The bands were subjected to densitometry analysis (using the MOLECULAR ANALYST software (Bio-Rad, USA) for determining the dimer/monomer ratio.

Lytic Activity of Lysozyme. The rate of lysis of *Micrococcus lysodeikticus* (*M. luteus*) by lysozyme was measured as reported.[26] The lytic activity was monitored turbidometrically at 450 nm at pH 7 and 30 °C. To a 1 mL suspension of *M. luteus* in 0.1 mM of sodium phosphate buffer, 50 μL lysozyme solution was added. Change in the turbidity at 450 nm was recorded per minute using a Shimadzu UV-2401 spectrophotometer with a thermostatically controlled cell holder. One unit is equal to a decrease in turbidity of 0.001 per minute at 450 nm at pH 7.0 and 30 °C under the specified conditions. The formulas used to obtain the activity are given below.

$$\text{Units/mg} = (\Delta A_{450/\text{minute}} \times 1000)/(\text{mg enzyme in reaction mixture}) \quad (3)$$

$$M_g P/\text{mL} = A_{280} \times 0.39 \quad (4)$$

Determination of Binding Stoichiometry between Lysozyme and ZnO NPs by UV Spectroscopy. In this experiment, 10 μM of lysozyme in phosphate buffer was equilibrated for 4 h at 37 °C with varying protein/NP ratios, that ranged from 5:1 to 1:4. After exposure, this suspension was centrifuged at 8000 rpm, and the protein concentration in the supernatant was determined from UV absorbance at 280 nm using a Shimadzu UV-2401 spectrophotometer. The difference between the initial and final concentration of the protein, i.e., the amount of adsorbed lysozyme, was normalized to the milligram of protein adsorbed per unit area of ZnO NP and plotted against the mole fraction of the NP. The stoichiometry of the protein−NP complex was determined by the molar-ratio method using a Jobs plot. The breakpoint in the plot corresponds to the mole fraction of the NP in its protein complex, giving the binding stoichiometry.[27]

Structural Analysis. The three-dimensional coordinates of hen egg white lysozyme (code: 2 VB1, determined at a resolution of 0.65 Å)[28] were obtained from the Protein Data Bank (PDB).[29] As a representative of dimeric form of the molecule, we used *Tapes japonica* lysozyme (code: 2DQA, resolution 1.6 Å).[30] The structures were superimposed using the DALI server,[31] and the residues in the equivalent positions were used to make a sequence alignment (Figure S1, Supporting Information). The residues forming the dimeric interface in 2DQA were identified using PROFACE[32] and were mapped into 2 VB1, thus identifying the putative interface for the hen egg white lysozyme that may exist in solution. The surface potential of the molecule was calculated using GRASP.[33] Pockets and cavities in lysozyme were identified using the CASTp (Computed Atlas of Surface Topography of proteins) server[34] located at http://cast.engr.uic.edu with the default probe radius of 1.4 Å. PyMol[35] was used to make molecular diagrams.

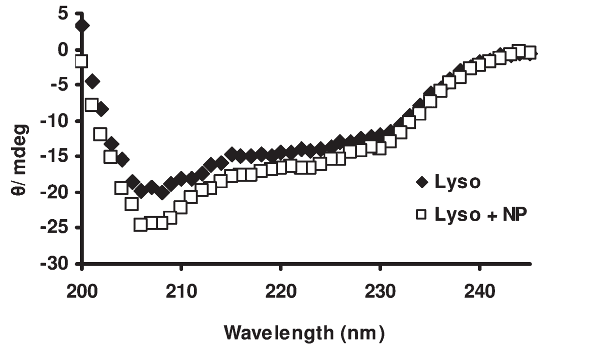

Figure 1. Far-UV CD spectra of lysozyme (10 μM in 0.1 M sodium phosphate buffer) in the absence and presence of ZnO NPs.

Results

Properties of ZnO NPs. For all the experiments, colloidal ZnO NPs were used. ZnO NPs are spherical in shape, as confirmed by transmission electron microscopy (TEM) measurements, with size ranging from 4 to 7 nm.[20] The isoelectric point, pI, of ZnO has been reported to be ~9.5.[18] However, as there may be some differences depending on the method of synthesis, and there could be some residual nitrate anions adsorbed on surface of our ZnO NPs,[20] we also determined the zeta potential at different pH values (Figure S2), and the isoelectric point (9) was found to be quite close. Thus the ZnO NPs are slightly positively charged under the experimental conditions. Dynamic light scattering data showed that the NPs have a natural tendency to form aggregates in solution (data not shown). To prevent aggregation, prolonged sonication was done to achieve a monodisperse solution of ZnO NPs.

Secondary Structure of Lysozyme in the Presence of NPs. Far-UV CD analysis provides information regarding the change in secondary structures, at pH 7.4 with the addition of ZnO NPs (Figure 1). The bands at 208 and 222 nm, characteristics of an α-helical structure, become more negative, indicating an increase in the helical content of lysozyme at the expense of the coil region (Table S1, Supporting Information) with the addition of NPs. Thus NPs induce the protein to acquire a more regular conformation. Even when lysozyme is unfolded in the presence of NPs, the helical content is more as compared to the unfolding of the free form of the protein by urea or GdnHCl (Table S2). Also, when we compare the free and NP-conjugated forms of lysozyme, the latter seems to have a higher helical content when the temperature is increased (Figure S3).

The decrease in the random coil content of lysozyme induced by NP conjugation is also revealed using FT-IR spectroscopy (Figure 2). Among the different bands of protein, the amide I in

(25) Wang, Y.; Guo, C. H. *J. Biol. Chem.* **2003**, *278*, 3210–3219.
(26) Shugar, D. *Biochim. Biophys. Acta* **1952**, *8*, 302–309.
(27) Ghosh, K. S.; Maiti, T. K.; Mandal, A.; Dasgupta, S. *FEBS Lett.* **2006**, *580*, 4703–4708.
(28) Wang, J.; Dauter, M.; Alkire, R.; Joachimiak, A.; Dauter, M *Acta Crystallogr. D* **2007**, *63*, 1254–1268.
(29) Berman, H. M.; Westbrook, J.; Feng, Z.; Gilliland, G.; Bhat, T. N.; Weissig, H.; Shindyalov, N.; Bourne, P. E. *Nucleic Acids Res.* **2000**, *28*, 235–242.
(30) Goto, T.; Abe, Y.; Kakuta, Y.; Takeshita, K.; Imoto, T.; Ueda, T. *J. Biol. Chem.* **2006**, *282*, 27459–27467.
(31) Holm, L.; Kaariainen, S.; Rosenstrom, P.; Schenkel, A. *Bioinformatics* **2008**, *24*, 2780–2781.
(32) Saha, R. P.; Bahadur, R. P.; Pal, A.; Mandal, S.; Chakrabarti, P. *BMC Struct. Biol.* **2006**, *6*, 11.
(33) Nicholls, A.; Sharp, K. A.; Honig, B. *Proteins: Struct., Funct., Genet.* **1991**, *11*, 281–296.
(34) Binkowski, T. A.; Naghibzadeh, S.; Liang, J. *Nucleic Acids Res.* **2003**, *31*, 3352–3355.
(35) DeLano, W. L. *The PyMOL Molecular Graphics System*; Delano Scientific: Palo Alto, CA, **2002**; http://www.pymol.org.

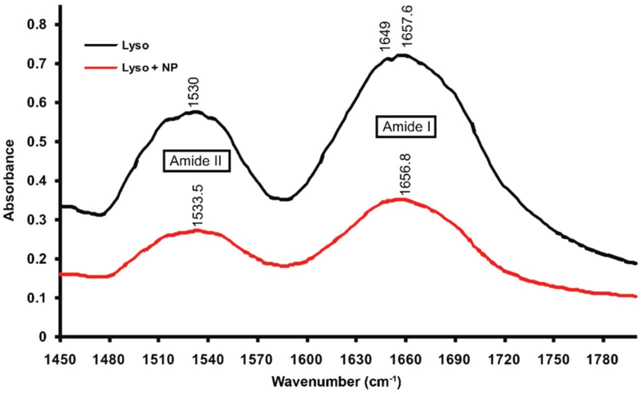

Figure 2. FT-IR spectra of lysozyme in 0.1 M sodium phosphate buffer (pH 7.4) and treated with ZnO NPs.

the region 1600−1700 cm^{-1} (mainly C═O stretch) has a relationship with the secondary structure of protein, whereas the absorbance intensity of the amide II band in the region 1500−1600 cm^{-1} (C−N stretch coupled with N−H bending mode) has been reported to be proportional to the amount of the protein absorbed on a surface.[36] A shift in the amide II band from 1530 to 1533.5 cm^{-1} with a loss of intensity indicates absorption of lysozyme on the NP surface. Different regions of the amide I band are contributed by different secondary structural elements: 1620−1645 cm^{-1} by β-sheet, 1645−1652 cm^{-1} by random coil, 1652−1662 cm^{-1} by α-helix, and 1662−1690 cm^{-1} by turns.[37] A small peak around 1649 cm^{-1}, observed for free lysozyme, disappears completely when it is bound to the ZnO NP, indicating a loss in the nonregular structural region in the protein. Further a shift from 1657.6 to 1656.8 cm^{-1} is suggestive of small alterations in the helical structure of lysozyme in the presence of the ZnO NP.

Unfolding of Lysozyme in the Presence of Urea and GdnHCl. The effect of NPs on the unfolding of lysozyme was studied using Trp fluorescence. Eight molar urea and 6 M GdnHCl were used as denaturing agents. The effect of NP is more on the urea-treated sample (Figure 3); while the protein alone has a λ_{max} at 340 nm in the folded form, which moves to 349 nm in the presence of 8 M urea, the shift is only to 346 nm when NP is present. Thus the protein is not completely unfolded, and is possibly trapped in a molten globule-like intermediate due to the presence of NPs (elaborated on in the next section). No such intermediate is apparent when the unfolding is caused by GdnHCl. Moreover, there is no significant difference in the unfolding transition monitored by CD and fluorescence spectroscopy (Figure S4). As such, the unfolding induced by GdnHCl (Figure 4) was fitted with a two state model (N ↔ U) and the parameters are presented in Table 1. On the basis of the unfolding free energy (ΔG_{NU}), ZnO NPs stabilize the folded form of lysozyme by 0.3 kcal/mol. Also the unfolding transition midpoint is shifted by ~0.2 M to higher GdnHCl concentration.

ANS Binding Studies. As the data given in the previous section suggested that the presence of an intermediate when lysozyme is unfolded in the presence of NP, we characterized it using the fluorescence spectra of ANS−lysozyme complex in the 440−600 nm wavelength range (Figure 5). At 5 M urea, there is a substantial enhancement of the fluorescence intensity, likely to be caused by exposure of hydrophobic residues. Although there is a reduction in the ANS fluorescence intensity when the urea

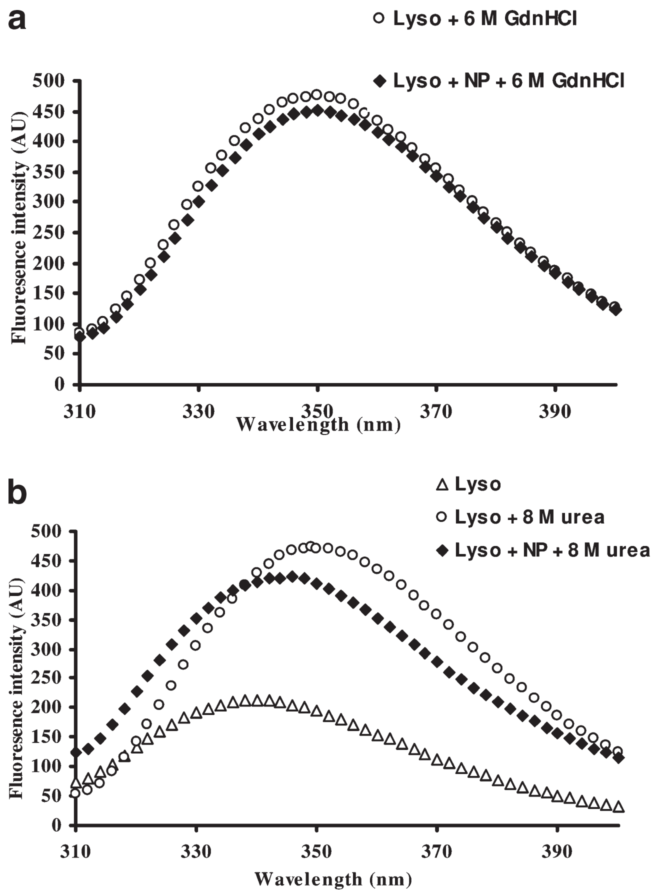

Figure 3. Fluorescence spectra (λ_{ex} = 295) of lysozyme in the presence and absence of ZnO NPs on being treated with (a) 6 M GdnHCl and (b) 8 M urea.

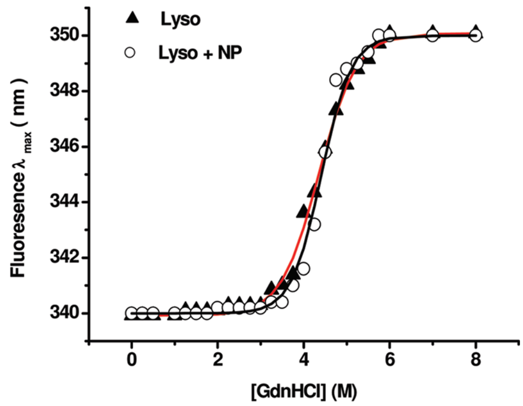

Figure 4. Shift in λ_{max} of the fluorescence spectrum (λ_{ex} = 295 nm) of free and NP-treated lysozyme as a function of GdnHCl concentration. Data were fitted with a two-state model, and the parameters obtained are shown in Table 1.

Table 1. GdnHCl-Induced Unfolding of Lysozyme: Two-State Analysis Using Fluorescence Data[a]

Λ_{max}-monitored data	lysozyme	NP-conjugated lysozyme
S_N	340	340.0
S_U	351	350.0
ΔG_{NU} (kcal/mol)	5.86 ± 0.25	6.16 ± 0.15
m_{NU} (kcal/mol/M)	1.35 ± 0.06	1.36 ± 0.09

[a] Based on data shown in Figure 4.

concentration is increased to 8 M, it is still substantial. The unfolding of free lysozyme does not cause any change in ANS

(36) Surewicz, W. K.; Mantsch, H. H.; Chapman, D. *Biochemistry* **1993**, *32*, 389–394.
(37) Speare, J. O.; Rush, T. S., III. *Biopolymer* **2003**, *72*, 193–204.

 DOI: 10.1021/la903118c

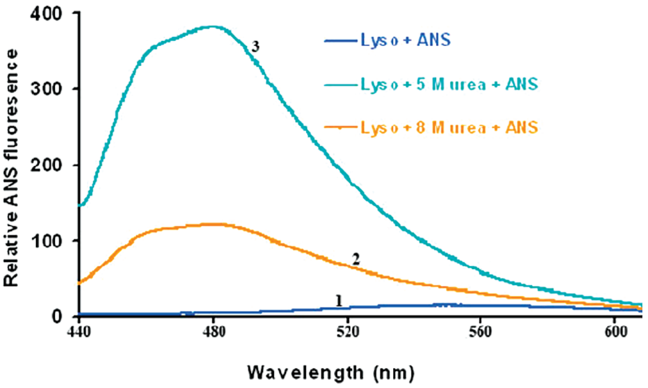

Figure 5. Fluorescence emission spectra (λ_{ex} = 340) of ANS bound to NP-conjugated lysozyme (curve 1), and on being treated with 8 M (curve 2), and 5 M (curve 3) urea. The 2.5 M urea-treated sample shows same fluorescence intensity as curve 1.

fluorescence intensity (data not shown). ANS does not normally bind to the native or fully unfolded protein, both the forms being devoid of sufficiently organized, exposed hydrophobic patches that can constitute a binding site for the dye.[38] The binding of ANS indicates the existence of a molten globule-like intermediate when the unfolding of lysozyme by urea is carried out in the presence of ZnO NPs.

Quenching of Trp Fluorescence by ZnO NP. To study the proximity of the NP binding sites on lysozyme to the location of Trp residues in the protein structure, we analyzed the change in intrinsic fluorescence spectra with increasing NP concentrations (0−26 μM). Figure 6 indicates a steady reduction in the fluorescence signal from lysozyme. Mechanisms of fluorescence quenching are usually based on dynamic or static processes. However, it has been reported that ZnO NPs form a ground-state complex with Trp,[39] and it is quite likely that the quenching of the intrinsic fluorescence of lysozyme results from a complex formation between the protein and the NP. The analysis of the Stern−Volmer plot provides a value of 2×10^4 M^{-1} as the K_{SV} constant.

Thermodynamic Data on Lysozyme−NP Interaction. We used ITC to investigate protein−NP interaction. The raw data of the binding of the ZnO NPs to lysozyme at 25 °C is shown at the top of Figure 7, while at the bottom is shown a plot of the heat flow per mole of the titrant (NP) versus the molar ratio (NP: lysozyme) at each injection, after subtraction of the background titration. The addition of ZnO NPs exhibits an exothermic ligand binding event, the various parameters for which are shown in Table 2. The values of ΔG and K_a indicate moderate binding between the two components. Although there is some reduction in entropy (and the CD data do indicate a slight increase in helical content at the expense of nonregular structure), this gets adequately compensated by the enthalpy, and overall the binding reaction is enthalpically driven. Although the data have been presented for 7 nm particles, very similar results are observed for smaller (4 nm) particles also (data not shown).

According to the fitted parameters for the ITC measurements (Table 2) two protein molecules interact with one ZnO NP. However, as the calorimetric results do not always coincide with the biding isotherm data,[24] a plot (Figure S5) showing the adsorption isotherm for lysozyme onto the NP surface has also been made using the protocol discribed in the Experimental Section. This indicates a binding ratio of 1:1, i.e., a lesser surface coverage of NPs by lysozyme molecules as compared to the ITC data.

(38) Mukherjee, D.; Saha, R. P.; Chakrabarti, P. *Biochim. Biophys. Acta* **2009**, *1794*, 1134–1141.
(39) Mondal, G.; Bhattacharya, S.; Ganguly, T. *Chem. Phys. Lett.* **2009**, *472*, 128–133.

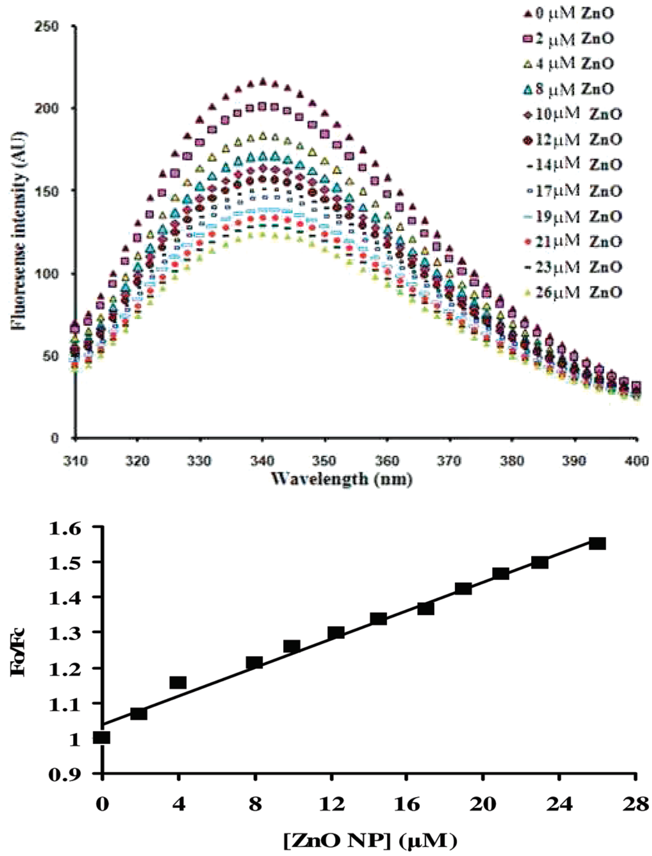

Figure 6. Quenching of Trp fluorescence of lysozyme in the presence of varying concentrations of ZnO NPs. The corresponding Stern−Volmer plot is shown below; the equation of the fitted line is $F_o/F_c = 1 + 0.0201 \times [NP]$ ($R^2 = 0.988$).

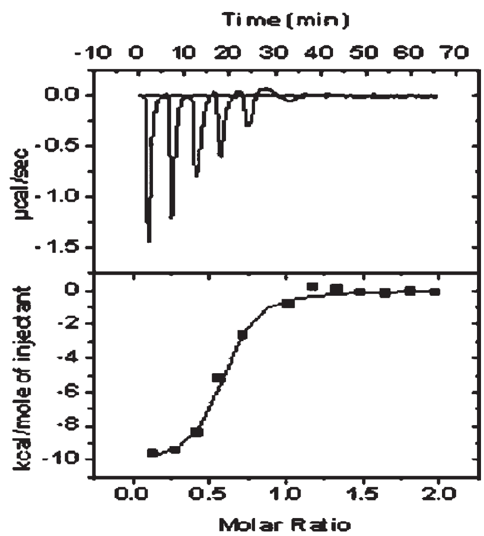

Figure 7. ITC data from the titration of 35 μM lysozyme in the presence of 0.4 mM ZnO NPs. Heat flow versus time during the injection of ZnO NPs at 25 °C and heat evolved per mole of added NPs (corrected for the heat of ZnO NP dilution) against the molar ratio (NP to lysozyme) for each injection, shown at the top and bottom, respectively. The data were fitted to a standard model.

Table 2. Thermodynamics Parameters Involved in the Binding between Lysozyme and ZnO NP, Derived from ITC Measurements

parameter	value (standard deviation)
N (NP: protein stoichiometry)	0.54 ± 0.01
K_a (binding constant, M^{-1})	$1.03 \times 10^6 \pm 0.2$
ΔH (binding enthalpy, kcal/mol)	-10.3 ± 0.3
ΔS (entropy change, cal/mol.K)	-6.38
ΔG (free energy change, kcal/mol)	-8.37

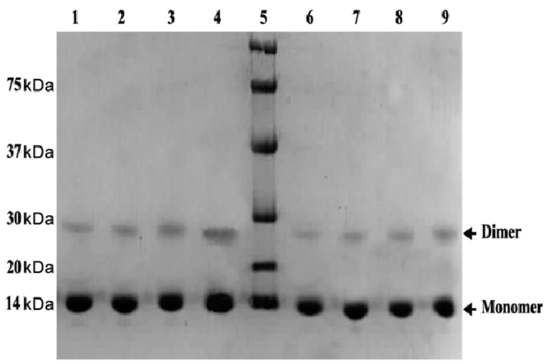

Figure 8. Glutaraldehyde cross-linking of lysozyme. SDS-PAGE of glutaraldehyde cross-linked samples of lysozyme, untreated (lanes 1−4) and treated with ZnO NPs (lanes 6−9). Lane 5 shows the protein marker. Concentration and incubation period of glutaraldehyde for various samples are as follows. Lane 1: 0.1%, 1 min; 2: 0.2%, 1 min; 3: 0.1%, 3 min; 4: 0.2%, 3 min; 6: 0.1%, 1 min; 7: 0.2%, 1 min; 8: 0.1%, 3 min; 9: 0.2%, 3 min.

Table 3. Dimer-to-Monomer Ratio of Lysozyme in the Presence of Different Concentrations of Glutaraldehyde at pH 7.4

sample	glutaraldehyde concentration (%)	time of incubation (min)	ratio[a] (dimer/ monomer)
lysozyme	0.1	1	0.11
lysozyme	0.2	3	0.19
lysozyme + NP	0.1	1	0.07
lysozyme + NP	0.2	3	0.1

[a] From densitometry analysis of the bands in Figure 8.

Glutaraldehyde Cross-Linking. Lysozyme from hen egg has a tendency to form a weak dimer.[40] Glutaraldehyde cross-linking experiments carried out at physiological pH confirmed the existence of both monomer and dimer forms of lysozyme (Figure 8), but in the presence of NP the relative content of the dimeric form was reduced (Table 3). The dimer-to-monomer ratio is 0.11 when lysozyme is incubated with 0.1% glutaraldehyde for 1 min (lane 1), which increases to 0.19 with 0.2% glutaraldehyde and 3 min incubation (lane 4). In the presence of NPs, the corresponding ratios are 0.07 (lane 6) and 0.1 (lane 9), respectively. This may possibly indicate that the association between two lysozyme chains is hindered by the direct binding of NPs at the same region that is involved in the dimer formation, or that the interference is caused indirectly by the perturbation brought about in the structure by NP binding.

Lysozyme Activity. To test whether adsorption of lysozyme to a ZnO NP has any role in the enzymatic activity, we examined the activity of the protein adsorbed on the ZnO NP surface relative to that of the free protein (Figure 9). Even when the lysozyme/NP ratio is 1:500, the enzyme retains about 90% of its activity. We also tested the activity under denaturing conditions. While only 8% of the activity is retained when lysozyme is treated with 8 M urea, it is 14% when the protein is in the conjugated form. Incubated with 6 M GdnHCl, there is drastic reduction in the activity, but still the NP treated protein showed 3% higher activity over the untreated protein. These results indicate that ZnO NP stabilizes the integrity of the active site in the presence of chaotropic agents.

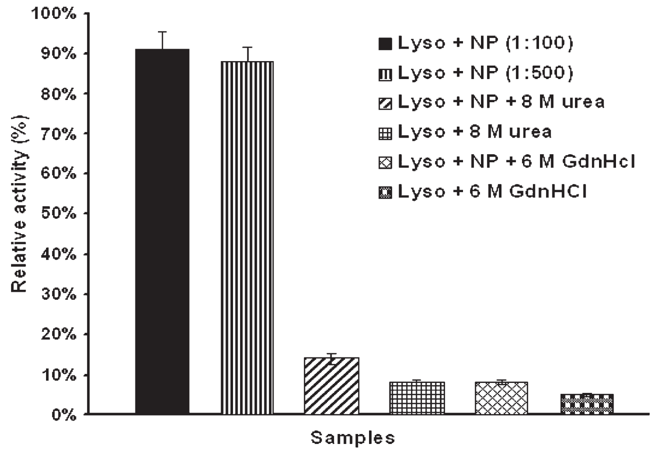

Figure 9. The relative activity (%) (with respect to the free enzyme) of lysozyme with varying concentration of NPs (the first two bars) and of unfolded lysozyme (with 8 M urea, middle two bars, and 6 M GdnHCl, the last two bars) treated with fixed concentration of NPs.

Discussion

Effect of ZnO NP on the Secondary Structure Content of Lysozyme. There is an approximately 4% increase of the helical content (at the expense of random coil structures) of lysozyme in the presence of NPs, as can be seen from the CD and IR data (Figures 1 and 2, and Table S1). Interestingly, ZnO NPs have also been reported to bring about a very similar change in the α-helical content of glucose oxidase.[41] Lysozyme as well as horseradish peroxidase and subtilisin Carlsberg, when covalently attached to single-walled carbon nanotubes, were found to retain a high fraction of their native structure and activity, and were more stable in the presence of GdnHCl and at elevated temperature relative to the free enzyme.[13] Bovine serum albumin when conjugated to gold NPs underwent substantial conformational changes, i.e., a decrease in helical structures and an increase in β-sheet structure, becoming more flexible.[42] On the other hand, chymotrypsin was denatured completely by functionalized mixed-monolayer protected gold clusters[43] and single-walled carbon nanotubes.[44] Similarly, nano-TiO_2 induced transition of α-helix into β-sheet, resulting in a substantial inactivation of lysozyme.[45] It is likely that the hydrophobic/hydrophilic nature of the NP, its size, and surface curvature, the charge distribution on the protein, and so forth would have consequences on the site of binding on the protein surface and how the binding of NP affects the structure of the protein.[14,15] Although the existing data on the details of NP−protein interactions are rather meager, the discussion below provides some insight into the possible binding site of ZnO NPs on lysozyme.

(40) Onuma, K.; Inaka, K. *J. Crystal Growth.* **2008**, *310*, 1174–1181.

(41) Ren, X.; Chen, D.; Meng, X.; Fangqiong, T.; Hou, X.; Han, D.; Zhang, L. *J. Colloid Interface Sci.* **2009**, *334*, 183–187.

(42) Shang, L.; Wang, Y.; Jiang, J.; Dong, S. *Langmuir* **2007**, *23*, 2714–2721.

(43) Fischer, N. O.; McIntosh, C. M.; Simard, J. M.; Rotello, V. M. *Proc. Natl. Acad. Sci.U.S.A.* **2002**, *99*, 5018–5023.

(44) Karajanagi, S. S.; Vertegel, A. A.; Kane, R. S.; Dordick, J. S. *Langmuir* **2004**, *20*, 11594–11599.

(45) Xu, Z.; Liu, X. W.; Ma Y. S.; Gao, H. W. *Environ. Sci. Pollut. Res.* [Online early access]. DOI: 10.1007/s11356-009-0153-1. Published on the web: April 2009.

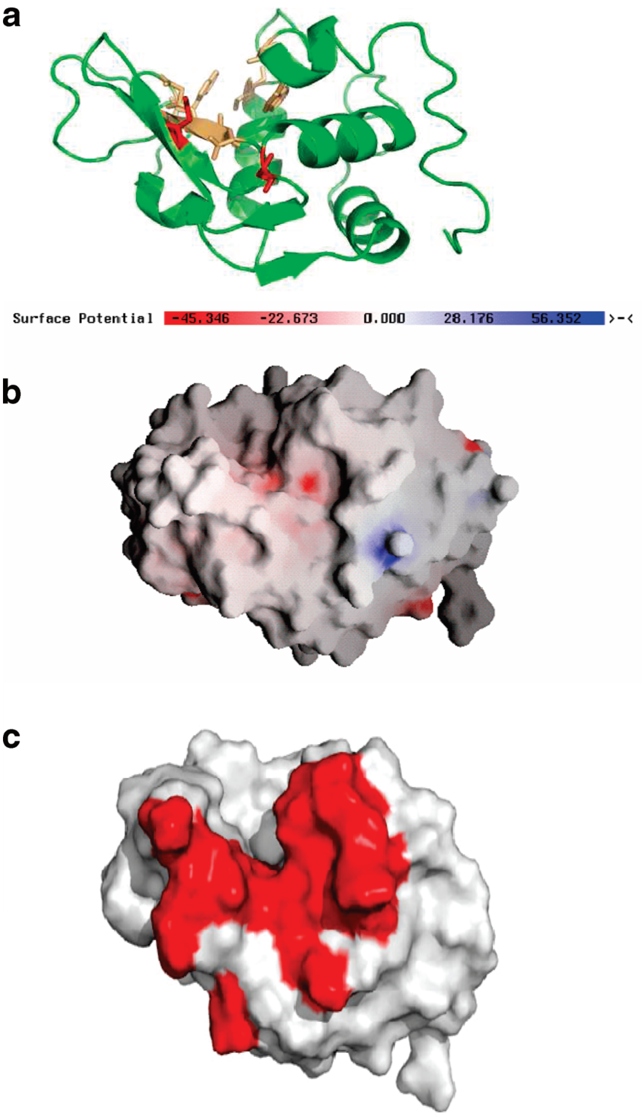

Figure 10. Cartoon and surface representations of the structure of hen egg white lysozyme showing the largest pocket on the surface. (a) The active site pocket with the catalytic residues (Glu35 and Asp52) in red and the other residues in the binding site (Gln57, Ile58, Asn59, Trp63, Ile98, Ala107, Trp108) in light orange. (b) Surface potential of the molecule with the scale shown on top. (c) The putative dimeric interface of the molecule is shown in red. The orientations of the molecules in b and c are roughly the same and approximately 90° rotated about a horizontal axis relative to that in a.

Putative Binding Site of ZnO NPs on Lysozyme and Its Consequence. The catalytic residues, Glu35 and Asp52, lie in a cleft that is contiguous to the largest pocket (with a volume of 84 $Å^3$ and molecular surface area of 73 $Å^2$) harboring the binding site (Figure 10a). This largest depression on the protein surface would allow a close approach by NPs providing the maximum contact surface area. The interaction would also be facilitated by the electrostatic charge distribution (Figure 10b), a negative potential at the active site; at pH below 9.5, the surface of ZnO NPs becomes positively charged by absorption of surrounding H^+.[18] As the entropy contribution to binding is not large (Table 2), there may not be much change in the conformation and water structure around the active site induced by the binding. Because of this, binding the integrity of the active site would be preserved, even at higher concentrations of urea, explaining the residual catalytic activity (Figure 9). Moreover, as the binding constant is not very large (Table 2), NPs can be replaced by the substrate, and the enzyme can still function at the 90% level in the presence of NPs.

The active site of lysozyme contains two Trp residues that are important for substrate binding (Figure 10a). Our conjecture of this is that the NP binding site is also supported by the fluorescence quenching data (Figure 6), as this position would bring ZnO particle in close proximity to the two Trp residues. From the equilibrium adsorption isotherm (Figure S5), one protein molecule interacts with one NP. For a proper perspective of the geometry of binding, the distance between the opposite tips of the pocket in Figure 10a is ~21 Å (= 0.21 nm). Interestingly, the increase in the helical content of lysozyme brought about by the binding of NP at the active site has also been observed during the binding of a drug molecule, menadione at the same site.[46]

ZnO NP Binding and the Oligometric State of Lysozyme. A dimeric form of lysozyme is also known to exist in solution.[40] However, as there is no known crystal structure of hen egg white lysozyme in this oligomeric form, we used the dimeric structure of *Tapes japonica*[30] to model the possible interface region of the putative dimer. Although the C-terminal region of the molecules from the two organisms differ considerably (Figure S1), the structures are similar enough to enable us to transfer information on dimerization from one molecule to the other. Comparison of panels b and c in Figure 10b shows that there is considerable overlap between the active site and the interface regions, indicating that NPs bound to the former would prevent the formation of the dimer, as has been indicated by cross-linking studies (Figure 8 and Table 3).

Urea-Induced Unfolding of Lysozyme in the Presence of ZnO NPs. The Trp fluorescence did not indicate a complete unfolding of lysozyme by 8 M urea (Figure 3b). The existence of a molten globule intermediate in the unfolding pathway is indicated by the binding and consequent enhancement of ANS fluorescence, which persisted even at 8 M concentration of urea (Figure 5). Molten globule-like structures have also been reported during the unfolding of lysozyme adsorbed on silica NPs,[47] as also for free lysozyme under various denaturing conditions.[48,49] The exposure of hydrophobic patches with consequent ANS-binding has also been observed during the unfolding of β-lactoglobulin adsorbed on silica NP surfaces.[50]

Conclusions

In conclusion, using lysozyme as a model protein, we have shown that NPs are capable of disrupting protein−protein association. ZnO NPs bind to the largest cleft on the protein surface, thereby helping it to retain the secondary structures to a greater degree and exhibit enzymatic activity even under denaturing conditions. There have been promising applications of ZnO-based nanomaterials in biosensors even at elevated temperatures.[16−18] The stabilizing influence of ZnO NPs on lysozyme and the mode of interaction elucidated in this article would be useful for the fruitful application of NPs in biotechnology.

Acknowledgment. We thank Dr. K. Chattopadhyay for his help in zeta potential measurement. T.C. and P.C. are supported

(46) Banerjee, S.; Choudhury, D. S.; Dasgupta, S.; Basu, S. *J. Lumin.* **2008**, *128*, 437–444.
(47) Wu, X.; Narsimhan, G. *Biochim. Biophys. Acta* **2008**, *1784*, 1694–1701.
(48) Hameed, M.; Ahmed, B.; Fazili, K. M.; Andrabi, K.; Khan, R. H. *J. Biochem.* **2007**, *141*, 573–583.
(49) Bhattacharjya, S.; Balaram, P. *Protein Sci.* **1997**, *6*, 1065–1073.
(50) Wu, X.; Narsimhan, G. *Langmuir* **2008**, *24*, 4888–4893.

by grants from the Department of Science and Technology. S.P. acknowledges the funding from IFN-EPSCoR.

Supporting Information Available: Two tables (Tables S1 and S2) describing data on the secondary structural content of lysozyme (at different temperatures and in the presence of denaturants) based on CD spectra, and five figures (Figures S1−S5) showing temperature-dependent CD spectra, overlay of unfolding of lysozyme monitored by CD and fluorescence spectroscopy, the sequence alignment of two homologues of lysozyme, the adsorption pattern of lysozyme on the NP surface, and measurement of zeta potential of ZnO NP at different pH values. This material is available free of charge via the Internet at http://pubs.acs.org.

Monthly Notices of the ROYAL ASTRONOMICAL SOCIETY
MNRAS **451,** 2–16 (2015) doi:10.1093/mnras/stv931

The evolution of disc galaxies with and without classical bulges since $z \sim 1$

Sonali Sachdeva,[1]★ Dimitri A. Gadotti,[2]★ Kanak Saha[3]★ and Harinder P. Singh[1]

[1] *Department of Physics and Astrophysics, University of Delhi, Delhi 110007, India*
[2] *European Southern Observatory, Alonso de Cordova 3107, Vitacura, Casilla 19001, Santiago, Chile*
[3] *Inter-University Centre for Astronomy and Astrophysics, Pune 411007, India*

Accepted 2015 April 23. Received 2015 April 22; in original form 2014 December 29

ABSTRACT

Establishing relative role of internally and externally driven mechanisms responsible for disc and bulge growth is essential to understand the evolution of disc galaxies. In this context, we have studied the physical properties of disc galaxies without classical bulges in comparison to those with classical bulges since $z \sim 0.9$. Using images from the *Hubble Space Telescope* and Sloan Digital Sky Survey, we have computed both parametric and non-parametric measures, and examined the evolution in size, concentration, stellar mass, effective stellar mass density and asymmetry. We find that both disc galaxies with and without classical bulges have gained more than 50 per cent of their present stellar mass over the last ∼8 Gyr. Also, the increase in disc size is found to be peripheral. While the average total (Petrosian) radius almost doubles from $z \sim 0.9$ to $z \sim 0$, the average effective radius undergoes a marginal increase in comparison. Additionally, increase in the density of the inner region is evident through the evolution of both concentration and effective stellar mass density. We find that the asymmetry index falls from higher to lower redshifts, but this is more pronounced for the bulgeless disc sample. Also, asymmetry correlates with the global effective radius, and concentration correlates with the global Sérsic index, but better so for higher redshifts only. The substantial increase in mass and size indicates that accretion of external material has been a dominant mode of galaxy growth, where the circumgalactic environment plays a significant role.

Key words: galaxies: bulges – galaxies: evolution – galaxies: high-redshift – galaxies: interactions – galaxies: structure.

1 INTRODUCTION

One of the major challenges linked to the morphological evolution of disc galaxies is to understand the formation and evolution of their bulge component. The bulge of a disc galaxy, observationally, is the central component which contains all the light that is in excess of an inward extrapolation of a constant scale-length exponential disc (Wyse, Gilmore & Franx 1997; Buta 2013). Internal and external mechanisms can explain the growth of bulges in disc galaxies.

Externally driven bulge growth in discs can occur through major mergers, multiple minor mergers and accretion of small components or satellites (Kauffmann, White & Guiderdoni 1993; Baugh, Cole & Frenk 1996; Aguerri, Balcells & Peletier 2001; Bournaud, Jog & Combes 2007; Hopkins et al. 2010). The fraction of baryons which lose angular momentum due to the dynamical friction produced in these mergers and accretion processes fall to the centre of the galaxy to form the bulge component (Parry, Eke & Frenk 2009; Governato et al. 2010; Brook et al. 2011, see also recent review by Brooks & Christensen 2015).

In terms of internally driven, there can be two bulge-building mechanisms. The first one is known as secular evolution. In this mechanism, slow, internally created processes contribute to the rearrangement of angular momentum and mass inside disc galaxies, leading to the growth of pseudo-bulges, which have properties similar to discs (Binney & Tremaine 1987; Combes 2001; Kormendy & Kennicutt 2004; Kormendy et al. 2010; Saha & Gerhard 2013). In the second mechanism, the coalescence of giant star-forming clumps, due to internal gravitational instabilities, leads to bulge formation in discs (Elmegreen, Bournaud & Elmegreen 2008, see recent review by Bournaud 2015). The relative importance of these mechanisms in forming present day discs with varied bulge properties is as yet not quantitatively known (see discussion in Kormendy 2015).

One of the most prominent unresolved issues associated with bulge evolution is the conspicuous presence of a large number of bulgeless galaxies (disc galaxies without classical bulges) in the local Universe. This is because, naively, a relatively low number of disc galaxies, formed as per the Λ cold dark matter (ΛCDM)

★ E-mail: sonali.com@gmail.com (SS); dgadotti@eso.org (DAG); kanak@iucaa.ernet.in (KS)

Published by Oxford University Press on behalf of the Royal Astronomical Society

structure formation scenario, are expected to survive without forming a classical bulge in the centre. The intense amount of merger violence associated with hierarchical clustering is expected to destroy the fragile thin disc of stars. Thus, their presence is a huge challenge as emphasized through observations (Kautsch et al. 2006; Kautsch 2009; Kormendy et al. 2010), models (Hopkins et al. 2009; Governato et al. 2010), simulations (Scannapieco et al. 2009; Zavala et al. 2012) and detailed in reviews (Baugh 2006; Benson 2010; Peebles & Nusser 2010; Kormendy 2013).

Observational evidence is required to pin down the relative role of various mechanisms in bulge growth and understand the formation of discs without bulges. The constraint involved is that for distant galaxies only the very basics of structure and morphology can be investigated. However, recent developments in observational facilities and in parametric and non-parametric measurements of galaxy structure (Conselice 2014, and references therein) have enabled us to use galaxy structure to measure fundamental properties of distant galaxies. These properties can then be compared with those of nearby galaxies to determine bulge–disc evolution.

There has been some progress in this regard. Gadotti (2009) found an overlap in the structural properties of pseudo- and classical bulges indicating that the different processes for bulge growth might have happened concomitantly. Parry et al. (2009) studied the models based on ΛCDM cosmology and found that most spiral bulges acquire their stellar mass through minor mergers and disc instabilities. Mo, van den Bosch & White (2010) explained the formation of bulges through mergers, secular internal processes and misaligned/perturbed infalling gas. Watson et al. (2011) studied the neutral hydrogen properties of 20 bulgeless galaxies to compare the role of mergers versus internal processes in bulge formation. They report that even though some of the discs have distinct outer components indicating recent interaction, the discs remain bulgeless. Zavala et al. (2012) examined the impact of mergers on the growth of bulges using simulated data. They found that the main channels of bulge mass assembly are stars from infalling satellites, and stars transferred from primary discs due to merger-induced perturbations. Pérez et al. (2013) showed through simulations that strong disc instabilities at high redshifts lead to classical bulge formation, which cannot be prevented by even the most energetic supernova feedback. Bruce et al. (2014) found that from redshift 3 to 1, galaxies move from disc-dominated to increasingly bulge-dominated morphology.

Although these works have given us considerable insight into disc structural evolution, the relative role of internal and external mechanisms in the formation and evolution of discs of varied bulge types is as yet not established. To achieve this, it will be insightful to examine the evolution in the inner region properties of disc galaxies of different bulge types in a relative manner. The crucial aspect in that direction is that the separation of disc galaxies according to their bulge type has to be achieved in a quantitative and robust manner.

Thus, in this paper, we undertake a comparative study of the evolution of disc galaxies with and without classical bulges. Disc galaxies without classical bulges are, by definition, labelled as 'bulgeless' and those with classical bulges are labelled as 'normal'. The two morphological types are separated using both Sérsic index and Kormendy relation criteria (Gadotti 2009). This work is a follow-up to Sachdeva (2013), such that the galaxy sample is the same and we also utilize the parametric measures (through Sérsic function fitting) derived in that paper. Here we derive the non-parametric measures (Petrosian radius, concentration, asymmetry) along with rest-frame colours, total stellar mass and effective stellar mass density. The evolution in the inner region properties is thus examined through both parametric as well as non-parametric measures.

The study is done since $z \sim 1$, when the galaxies have just formed a familiar Hubble sequence structure (Conselice et al. 2011; Mortlock et al. 2013), to the present epoch, where they have developed and settled into few distinctly identifiable categories (Gadotti 2009; Buta 2013; Graham 2013). This time interval has the potential to reveal the major processes involved in bulge and disc evolution.

For distant galaxies we make use of deep imaging from the Great Observatories Origins Deep Survey (GOODS) obtained using *Hubble Space Telescope* (*HST*)[1]-Advanced Camera for Surveys (ACS) in the *Chandra Deep Field*-South (CDF-S; Giavalisco et al. 2004). For local galaxies, images are from the NASA–Sloan Atlas,[2] based on the Sloan Digital Sky Survey (SDSS; Blanton et al. 2005b). We obtain the parametric and non-parametric measures for bright ($M_B \le -20$) disc-dominated (Sérsic index $n < 2.5$) galaxies in three redshift ranges ($0.77 \le z < 1.0$, $0.4 \le z < 0.77$ and $0.02 \le z < 0.05$) for rest-frame B band. We then examine the evolution of the inner-region properties of the bulgeless disc galaxies in comparison to the normal disc galaxies over the three redshift ranges.

We consider a flat Λ-dominated Universe with $\Omega_\Lambda = 0.73$, $\Omega_m = 0.27$, $H_0 = 71\,\mathrm{km\,s^{-1}\,Mpc^{-1}}$. In Section 2, we describe our data in terms of sample selection, preparation of images, defining and computation of various parameters. In Section 3, we present the results obtained by examining the evolution of size, concentration, stellar density and asymmetry. We also report the correlation seen between various parameters. In Section 4, we list the primary results of this work and discuss their implications in the light of previous studies.

2 DATA

2.1 Sérsic parameters

In a previous work (Sachdeva 2013), images taken from *HST*-ACS in V (*F606W*), i (*F775W*) and z (*F850LP*) filters were used to obtain the rest-frame B-band properties of the galaxies lying in the CDF-S with redshift ranging from 0.4 to 1.0. First, SExtractor (Bertin & Arnouts 1996) was used to identify the sources in the z-band image. Then, single Sérsic (Sersic 1968) components were fit (using GALFIT; Peng et al. 2002) on all the three filter images. The Sérsic profile for the variation of a galaxy's surface brightness from its centre is given as

$$I(r) = I_e \exp\left[-b_n\left(\left(\frac{r}{r_e}\right)^{1/n} - 1\right)\right], \quad (1)$$

where n (the Sérsic index) controls the degree of curvature of the profile, I_e is the surface brightness at r_e and b_n is a constant such that r_e is the half-light radius for a given value of n. We thus obtained parameters such as apparent total magnitude, half-light radius and Sérsic index for all the galaxies in the three filters.

Redshifts were obtained from the Classifying Objects by Medium-Band Observations in 17 filters (COMBO-17) survey

[1] Based on observations obtained with the NASA/ESA *Hubble Space Telescope*, which is operated by the Association of Universities for Research in Astronomy, Inc. (AURA) under NASA contract NAS 5-26555.

[2] http://www.nsatlas.org. Funding for the NASA–Sloan Atlas has been provided by the NASA Astrophysics Data Analysis Program (08-ADP08-0072) and the NSF (AST-1211644).

(Wolf et al. 2004). The *V* filter provides rest-frame *B*-band properties for galaxies lying in the redshift range of 0.4–0.6. The *z* filter provides the same for the redshift range of 0.8–1.0. For the redshift range of 0.6–0.8, both *i* and *z* filters can be used and thus an average of the properties obtained using both the filters was employed. The parameters were thus obtained for 4124 sources in the rest-frame *B* band for the full redshift range (0.4–1.0).

Using the redshifts and accepted cosmological parameters, we then computed absolute magnitude, half-light radius in kpc and surface brightness in mag arcsec^{-2}. The absolute magnitude, M, for the galaxies is calculated using the relation

$$M = m - 5\,\log_{10}(D_L \times 10^5) - K, \tag{2}$$

where D_L is the luminosity distance in Mpc and K is the K-correction term that accounts for the difference between the observed band and rest-frame band. It depends on the object's spectral energy distribution (Oke & Sandage 1968; Hogg et al. 2002) and, for a power-law continuum, it is given by the relation

$$K_{\rm cont} = -2.5(1+\alpha_\nu)\log(1+z), \tag{3}$$

where α_ν is the slope of the continuum and has a canonical value of -0.5 (Richards et al. 2006). Therefore

$$M_B = m - 5\,\log(D_L \times 10^5) + 2.5\,\log(\sqrt{(1+z)}). \tag{4}$$

The half-light radius of the galaxies that we obtain from Sérsic component fitting is in pixels. They were converted into arcseconds according to the plate-scale of the telescope and then into radians. The intrinsic half-light radius in kpc was then calculated using the relation

$$R_{\rm e} = D_{\rm A} \times 1000 \times \Delta\Theta, \tag{5}$$

where $D_{\rm A}$ is the angular diameter distance in Mpc and $\Delta\Theta$ is the radians covered on the detector by the half-light radius.

The redshift–magnitude distribution of the galaxies was examined in the 0.4–1.0 redshift range for galaxies with $M_B > -20$ and $M_B \le -20$ (shown in Fig. 1 of Sachdeva 2013). For $M_B > -20$, galaxies with lower luminosities were not seen at high-redshift ranges at all. However, for $M_B \le -20$, the number of galaxies was seen to be evenly distributed. Also, the number of galaxies in two equal comoving volume redshift bins (0.4–0.77 and 0.77–1.0) was found to be almost the same for $M_B \le -20$. Additionally, the magnitude limit for a reliable redshift estimate from COMBO-17 is $m_Z \sim 23.5$, which for our upper redshift limit of $z = 1.0$ corresponds to $M_B \sim -20$. Based on the depth of *HST* imaging, and the redshift accuracy limit of COMBO-17, a magnitude cut of -20 was applied on the sample. We, thus, obtained 727 sources in the rest-frame *B* band ($0.4 \le z < 1.0$) with $M_B \le -20$ (elaborated in Sachdeva 2013).

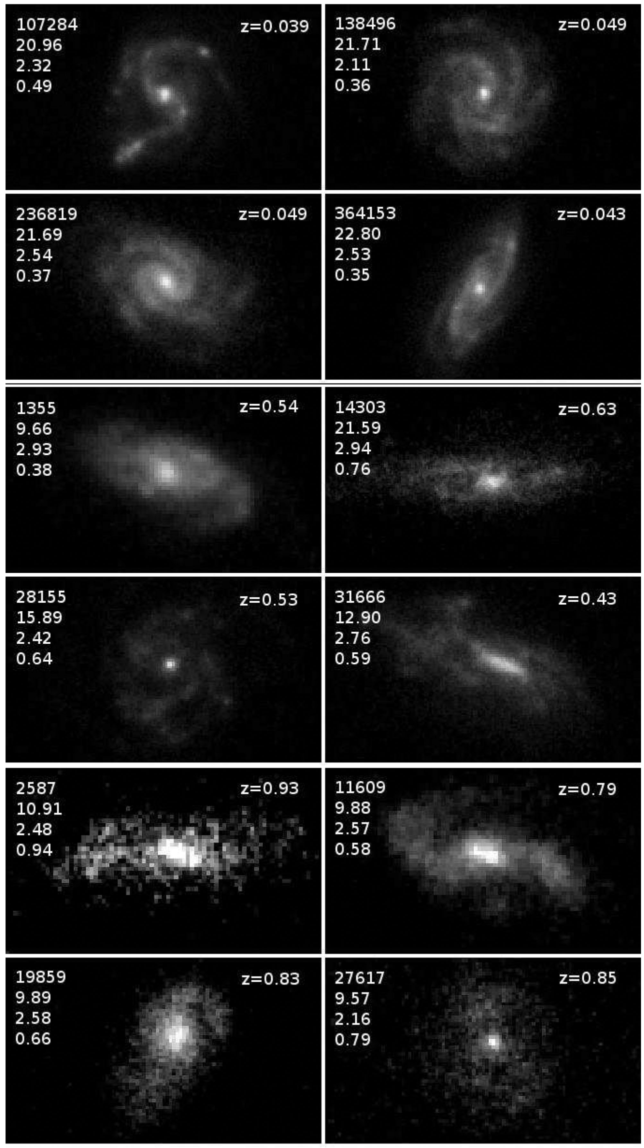

Figure 1. Some of the bulgeless disc galaxies lying in the three redshift ranges (0.02–0.05, 0.4–0.77 and 0.77–1.0) are shown. The non-parametric measures computed for each source are shown at the top left-hand corner. They are in this particular order: ID (as per the NYU-VAGC and GOODS *HST*-ACS catalogues), Petrosian radius, concentration and asymmetry. Precise positional information of the galaxies is provided in Table 1. *HST*-ACS galaxies cover ~7 arcsec (out of the 10 arcsec image cutout) and SDSS galaxy images cover ~2 arcmin (out of the 3 arcmin image cutout).

2.1.1 *Separating bulgeless disc and normal disc galaxies*

The Sérsic index value of 2.5 is employed in numerous studies to separate early-type ($n > 2.5$) and late-type ($n < 2.5$) galaxies (e.g. Ravindranath et al. 2004; Barden et al. 2005; van der Wel 2008). We used these criteria to obtain 496 late-type (or disc-dominated) ($n < 2.5$), bright ($M_B \le -20$) galaxies in the rest-frame *B* band.

The bulgeless disc galaxies include disc galaxies without bulges and those with pseudo-bulges. Pseudo-bulges are the bulges which have a higher ratio of ordered motion to random motion. Since they exhibit nearly exponential brightness profiles, disc galaxies with pseudo-bulges are, therefore, considered as bulgeless (Kormendy & Kennicutt 2004; Kormendy et al. 2010). Thus, to separate bulgeless disc and normal disc galaxies, we separated discs with no-bulge or pseudo-bulge from discs with classical bulge in our disc-dominated sample.

The Sérsic index values ranging from 1.7 to 2.0 have been suggested by many studies for the separation of classical bulges from pseudo-bulges (e.g. Shen et al. 2003; Laurikainen et al. 2007; Fisher & Drory 2008). To obtain a Sérsic index limit for our sample, we divided the entire sample (i.e. without the magnitude cut, 4124 sources) into three ranges ($0.8 > n$, $0.8 \le n < 1.7$, $1.7 \le n$) with each range getting almost equal number of sources. We then examined the distribution of the mean half-light radius against

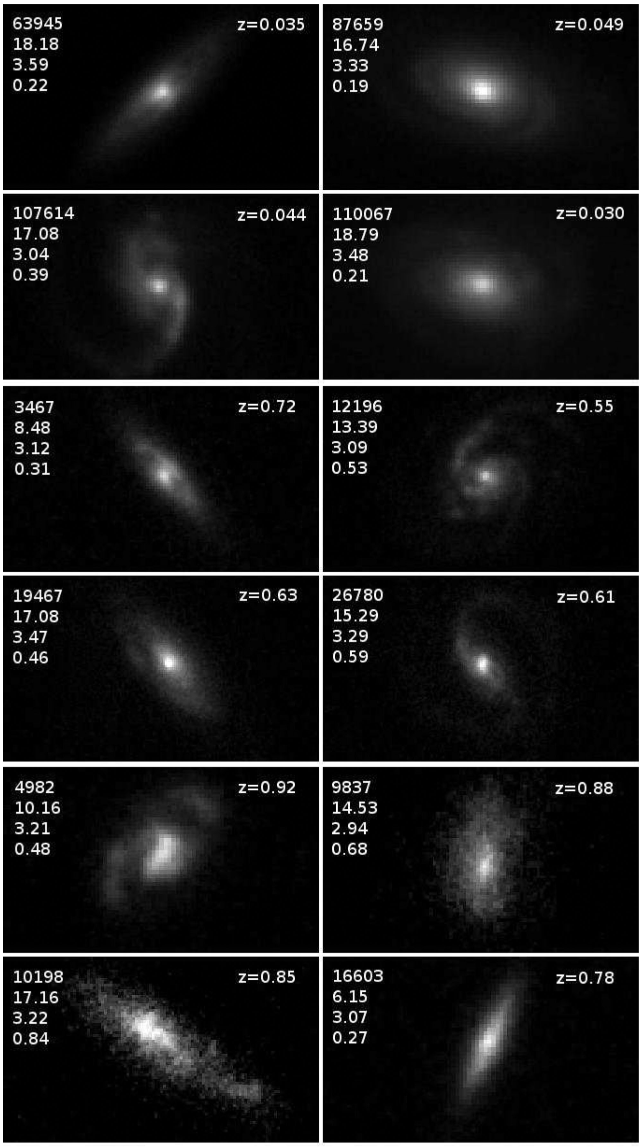

Figure 2. Some of the normal disc galaxies lying in the three redshift ranges (0.02–0.05, 0.4–0.77 and 0.77–1.0) are shown. The non-parametric measures computed for the source are shown at the top left-hand corner. They are in this particular order: ID (as per the NYU-VAGC and GOODS *HST*-ACS catalogues), Petrosian radius, concentration and ssymmetry. Precise positional information of the galaxies is provided in Table 1. *HST*-ACS galaxy images cover ~7 arcsec (out of the 10 arcsec image cutout) and SDSS galaxy images cover ~2 arcmin (out of the 3 arcmin image cutout).

the absolute magnitude bins for different Sérsic index ranges (see Fig. 2 of Sachdeva 2013).

We found that a value of $n \sim 1.7$ divides galaxies into two groups where each group follows a particular half-light radius–magnitude ($\overline{R}$–M) relation, independent of n (shown in Fig. 2 of Sachdeva 2013). This is in striking agreement with Shen et al. (2003), who found the same value based on SDSS data, and claimed that the cut separates galaxies with exponential surface brightness profile (Sb/Sc) from the galaxies which do not have such profiles.

In addition to applying the Sérsic index limit of $n \sim 1.7$, we have applied the Kormendy relation (Kormendy 1977) to ascertain the separation of bulgeless disc and normal disc galaxies. This is based on the fact that, since the Kormendy relation is followed by elliptical

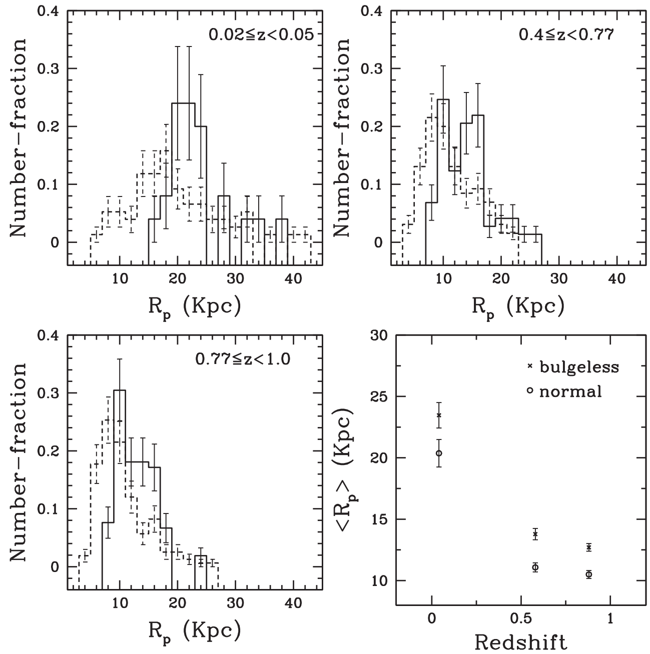

Figure 3. Distributions of Petrosian radius for bulgeless disc (solid lines) and normal disc (dashed lines) galaxies for the three redshift ranges. The distribution of the means of the two samples with redshift is also shown. There is a significant increase in sizes for both samples with time.

galaxies, galaxies which are bulgeless should show themselves as outliers to the relation (see Gadotti 2009, for details).

To achieve this, we fitted a linear relation to the surface brightness versus log-size data of elliptical galaxies in our sample, i.e. those with $2.8 \leq n < 4.5$ from the 727 sources ($0.4 \leq z < 1.0$, $M_B \leq -20$). Those disc galaxies ($n < 2.5$) which were lying below the $\pm 3\sigma$ value of the zero-point (with fixed slope) were taken as outliers. The outliers obey the following relations:

$$\mu_{\mathrm{e},B} > 19.36 + 2.92\ \log(R_{\mathrm{e},B}), \quad 0.4 \leq z < 0.77 \tag{6}$$

and

$$\mu_{\mathrm{e},B} > 19.32 + 2.92\ \log(R_{\mathrm{e},B}), \quad 0.77 \leq z < 1.0. \tag{7}$$

More than 80 per cent of the disc galaxies which were found to be bulgeless according to these relations were also seen to have $n < 1.7$. The two criteria are thus complementary to each other. Only those galaxies which satisfied both criteria, i.e. had Sérsic index less than 1.7 and were outliers to the Kormendy relation, were chosen to be bulgeless (Fig. 3 of Sachdeva 2013). The bulge/total light ratio was found to be less than 0.2 (or 20 per cent) for our bulgeless sample. This process of morphological determination was found to separate the galaxies in a similar manner in the infrared as they do in the optical (Sachdeva 2013).

2.1.2 *Overall sample obtained*

We obtained Sérsic parameters in rest-frame *B* band for 496 bright, disc-dominated galaxies separated into 186 bulgeless disc galaxies and 310 normal disc galaxies, in two equal comoving volume redshift ranges ($0.77 \leq z < 1.0$ and $0.4 \leq z < 0.77$).

In addition to this, a low-redshift ($0.02 \leq z < 0.05$) catalogue of disc-dominated galaxies was taken from the New York University Value-Added Galaxy Catalog (NYU-VAGC; Blanton et al. 2005a,b) to establish a local sample. We obtained rest-frame B-band parameters from the single Sérsic fit parameters in g and r filters. Their AB magnitudes are galactic extinction corrected (Schlegel, Finkbeiner & Davis 1998) and also K-corrected (Blanton et al. 2003) to the rest-frame bandpasses. We used relations from Fukugita et al. (1996) and Jester et al. (2005) to obtain the absolute magnitude in rest-frame B band:

$$g' = V + 0.56(B - V) - 0.12, \tag{8}$$

$$r' = V - 0.49(B - V) + 0.11. \tag{9}$$

Using those two equations we get

$$B = 1.419\, g' - 0.419\, r' + 0.216. \tag{10}$$

The Sérsic half-light radii of the g and r bands were converted from arcseconds to kpc according to their redshift. The relations given by Barden et al. (2005), that were found using the de Jong (1996) data, were used to obtain half-light radii in the rest-frame B band. Using the NYU-VAGC catalogue, they studied the ratio of half-light sizes in the five SDSS bands to the size measured in one band as a function of wavelength. The results were accurately described by a linear fit (only ± 3 per cent correction factor) and were in striking agreement with the fit found for the de Jong (1996) data. The slope gives average corrections to obtain the rest-frame sizes:

$$R_{\rm e}(V) = 1.011\, R_{\rm e}(r), \tag{11}$$

$$R_{\rm e}(B) = 1.017\, R_{\rm e}(V). \tag{12}$$

Using those two we get

$$R_{\rm e}(B) = 1.017 \times 1.011\, R_{\rm e}(r). \tag{13}$$

We obtained the final local catalogue of 764 galaxies in rest-frame B band, in the redshift range $0.02 \le z < 0.05$ with $M_B \le -20$. After that we applied the Sérsic index criteria to separate disc galaxies. Then disc galaxies were further separated into a sample of bulgeless disc and normal disc galaxies using both the Sérsic index and Kormendy relation criteria, as described for the main sample.

Overall, we obtained Sérsic parameters in rest-frame B band for 597 bright disc galaxies separated into 211 bulgeless disc and 386 normal disc galaxies over three redshift ranges ($0.77 \le z < 1.0$, $0.4 \le z < 0.77$ and $0.02 \le z < 0.05$). For details and the catalogue please consult Sachdeva (2013).

2.2 Obtaining and cleaning the images

To probe the formation and evolution of bulges in disc galaxies with time, it is required to do image analysis and compute parameters like concentration and asymmetry of stellar light in each individual galaxy of this sample.

For the main sample ($0.4 \le z < 1.0$), a 10-arcsec cutout is downloaded from the *HST*-ACS data archive and for the local sample ($0.02 \le z < 0.05$), a 3-arcmin cutout is downloaded from the NASA–Sloan Atlas data archive. Since the aim is to do the study in rest-frame B band, the filter chosen for obtaining the galaxy image is according to the redshift of the galaxy. The images are thus taken in V, i, z and g filters for redshifts 0.4–0.6, 0.6–0.8, 0.8–1.0 and 0.02–0.05, respectively. The cutout is such that the centre of the galaxy (brightest pixel) is at the centre of the image and an average-size galaxy covers not more than 60 per cent of the total area.

Out of 597 downloaded images, 27 source images are not taken up for analysis. This is because 12 of these galaxies are only partially imaged and the rest of the 15 galaxies have a highly fragmented light distribution which in part appears to be due to multiple overlapping sources. For the latter galaxies, it is difficult to determine and study their isolated light distribution. Also, since there is a lack of proper structure and there is a degeneracy of bright patches, there is no clear area from where the initial central pixel value can be selected which is crucial for the computation of radius, concentration and asymmetry. Out of these 15 sources, three are in the high-redshift range (0.77–1.0) of the bulgeless disc category constituting ∼1 per cent of this sample. Five are in the middle-redshift range (0.4–0.77) of the normal disc category constituting less than ∼4 per cent of this sample. The rest of the 15 are in the high-redshift range (0.77–1.0) of the normal disc category and they also constitute ∼4 per cent of this sample. All these galaxies cover a large range of luminosity, Sérsic index and half-light radius values. Their small fractions and even distribution in terms of redshift and parameter values indicate that their removal from the total sample should not affect the statistical estimations.

The major task involved now is to clean or decontaminate the 570 galaxy images, i.e. to remove the neighbouring sources. These images are final in the sense of flat-fielding, bias subtraction, cosmic ray removal, etc. To clean the images, each galaxy image is taken up separately and the value of the pixels covered by a neighbouring source is replaced with the average value of the sky pixels surrounding that source. The neighbouring sources are recognized through the use of SExtractor's catalogue and segmentation map. Along with all the individual object coordinates, the SExtractor also provides an estimation of the radius of the object that contains more than 90 per cent of its light. The replacing of pixels is done using the Image Reduction and Analysis Facility (IRAF) IMEDIT task, which creates a circular annulus of a chosen radius around the selected central coordinates of the source and replaces the pixels within the inner circle with the average value of the pixels inside the annulus. We have tried to ensure that the masking process in each of the galaxy images does not strongly affect the light distribution of the outer parts of the main source.

Next important thing is to remove the background flux from all the galaxy images. To estimate the background flux, a blank patch (i.e. which even without masking is devoid of any light sources) is selected near the galaxy. The patch is chosen in such a way that it is small and far enough from the source, so as not to have any diffuse light, and yet large and near enough to give a reasonable estimate. The *HST* object mosaics have an area of 333 × 333 pixels (10 arcsec^2, 0.03 arcsec pixel^{-1}) and the selected background patch in each mosaic covers an area of 30 × 30 pixels. The SDSS object mosaics have an area of 440 × 440 pixels (3 arcmin^2, 0.396 arcsec pixel^{-1}) and the selected background patch in each mosaic covers an area of 40 × 40 pixels. The mean flux per pixel is then estimated from this patch and subtracted out from the image. The stability of the process is ascertained by selecting a large number of blank patches for some of the galaxy images. It is seen that they provide consistent background flux values. After cleaning and background flux subtraction, the images are ready for the computation of various parameters.

2.3 Computing Petrosian radii

The total radius of a disc galaxy is difficult to be determined in a reproducible manner due to difficulties regarding its extent in terms of the dark matter halo. Also, to measure the optical or stellar extent, use of a fixed isophotal value of brightness is not optimal, due to the vast range of surface brightnesses in which galaxies exist. However, it is important to be determined in such a way that sizes and the associated parameters can be compared for galaxies of different luminosities and distances.

In that regard, the Petrosian radius (Petrosian 1976) is considered an effective way of measuring galaxy sizes (Bershady, Jangren & Conselice 2000; Graham et al. 2005). This radius is determined by tracking the ratio of surface brightness at each successively increasing radius to that averaged inside the radius. When the ratio ($\eta = I(r)/\langle I(<r)\rangle$) falls to a chosen small fraction (we take 0.2), that radius is multiplied by a factor (we take 1.5) to obtain the Petrosian radius. The values 0.2 and 1.5 are determined to be most appropriate (Conselice 2003; Lotz, Primack & Madau 2004). For our sample, we first determine the centre accurately using the IRAF task IMCENTROID and then measure the surface brightness at and inside successively increasing radii. Then, using

$$\eta(r_{\mathrm{p}}) = \frac{I(r_{\mathrm{p}})}{\langle I(< r_{\mathrm{p}})\rangle} = 0.2, \tag{14}$$

$$R_{\mathrm{P}} = 1.5(r_{\mathrm{p}}), \tag{15}$$

we measure R_{P} (the Petrosian radius) in rest-frame B band for all the galaxies. This radius is in pixels and converted into kpc according to the redshift and chosen cosmology.

2.4 Computing concentration

For the well-resolved low-redshift galaxies, the bulge prominence is quantified and studied through e.g. bulge/disc decompositions (e.g. Gadotti 2008; Simard et al. 2011). However, for high redshifts, single/global Sérsic indices are commonly used to obtain a quantitative assessment of the bulge component (e.g. Buitrago et al. 2013; Mosleh, Williams & Franx 2013, and references therein). We have global Sérsic index values for all the galaxies in our sample, obtained earlier from Sérsic function fitting (Sachdeva 2013). We now compute concentration, which is considered a more robust parameter in terms of surface brightness dimming (detailed in Graham et al. 2005) and a better estimator of the bulge-to-total ratio (Gadotti 2009).

To compute concentration, we first measure the total flux (or total counts) inside the Petrosian radius, i.e. the full flux from the source. Then, the number of counts in successively increasing radii, from the centre, is computed for each galaxy. When the number of counts is 20 per cent of the total number of counts, that radius is taken as the 'inner radius'. When it is 80 per cent, that radius is taken as the 'outer radius'. Concentration of the source is defined as (Bershady et al. 2000; Conselice 2003; Graham et al. 2005)

$$C = 5\log_{10}\left(\frac{r_{80\,\mathrm{per\,cent}}}{r_{20\,\mathrm{per\,cent}}}\right). \tag{16}$$

Concentration of stellar light, in rest-frame B band, is thus computed for all the galaxies in the sample. The higher this measure, the larger is the fraction of total light contained in the central region.

2.5 Computing asymmetry

Asymmetry in the stellar light of disc galaxies arises from features like bars, star-forming clumps, spiral arms, rings, etc. It is also observed to be higher for galaxies which are going through interactions or mergers with companion galaxies or accreting satellites (or non-virialized baryonic matter) from the intergalactic medium (Conselice 2003; Lotz et al. 2008; Reichard et al. 2008). Since the presence of these features, as well as interactions and mergers, is the expected cause of bulge formation and evolution, tracking the evolution of the asymmetry measure and its relationship with other parameters is of utmost importance.

To compute asymmetry of stellar light in a disc galaxy, we follow the procedure given in Conselice, Bershady & Jangren (2000). We take the cutout galaxy image and rotate it around its centre by 180°. The extraction radius for rotation is given as the Petrosian radius. The rotated image is then subtracted from the main image to get the residual image. The flux from this residual image is a measure of the flux from the asymmetric features of the galaxy. This flux is normalized with respect to the total flux from the main image to get the asymmetry parameter.

For the asymmetry parameter to be meaningfully comparable for the range of disc galaxies, all the sources of probable biases need to be removed (Conselice 2003). The first concern is that the extraction radius should be bias-free, and thus, we choose the Petrosian radius. The second concern is the centre for rotation, which can produce spurious results if not chosen properly. To minimize this effect, the centre for rotation is found in an iterative manner: it is the position for which the asymmetry of the source attains a global minimum.

Another concern is noise, in terms of the background asymmetry. To take that into account, the asymmetry must also be computed from an empty background patch and subtracted from the source's asymmetry. The difficulty with estimating the background asymmetry value is that even if there is a small amount of diffuse light which is more concentrated on one side of the background patch, the asymmetry value increases by a considerable amount. To avoid this issue, we identify relatively clear background patches from a number of galaxy images which are chosen such that they cover a wide range of RA and Dec. The asymmetry is computed on all such patches according to the procedure described above. The mean of these values is then used as the background asymmetry. This procedure is done separately for the galaxy samples in the three redshift ranges.

The asymmetry of the stellar light distribution of the galaxies, in rest-frame B band, is thus computed for our sample.

2.6 Computing effective stellar mass densities

The stellar mass density of a galaxy is seen to be correlated with its integrated colour, Sérsic index, concentration, environmental density, as well as star formation rate (Kauffmann et al. 2003; Brinchmann et al. 2004; Baldry et al. 2006; Driver et al. 2006; Bamford et al. 2009). The stellar mass density inside the effective radius (termed here as effective stellar mass density, ESMD), being highly correlated with the bulge properties of the disc galaxy, is a useful parameter to be examined.

To compute this parameter, the first thing is to obtain the stellar mass. For that, we need to multiply total luminosity in a given band with the corresponding stellar mass-to-light ratio of the galaxy. Total luminosity (L) is obtained in units of solar luminosity from the earlier computed absolute magnitudes of the galaxies:

$$M_B = -2.5\log_{10}\left(\frac{L}{\mathrm{L}_{\odot}}\right) + 5.38, \tag{17}$$

where $\mathrm{L}_{\odot}$ is the solar luminosity and 5.38 is solar absolute magnitude in rest-frame B band. The luminosity inside the effective radius (or half-light radius) is, by definition, half of the total luminosity.

The next step is to obtain the stellar mass-to-light ratio which is known to strongly correlate with the integrated colours (Bell &

de Jong 2001). To obtain the rest-frame colours, we employ EAZY, which is a photometric redshift code that provides estimates for rest-frame colour indices (Brammer, van Dokkum & Coppi 2008). It compares photometric data to the synthetic photometry of a large range of template spectra and outputs the best match. The important feature of this code is that if the redshift of the source is known with reasonable accuracy, it can be given as a prior or held fixed. Also, the template spectra are based on semi-analytical models and not on empirical spectroscopic samples, which are usually highly biased (Brammer et al. 2008). Note that there are other codes similar to EAZY, e.g. FAST (Kriek et al. 2009) and LEPHARE (Arnouts & Ilbert 2011).

The stellar mass-to-light ratio is then computed from the rest-frame $B - V$ colour, using values from Bell & de Jong (2001) for the mass-dependent galaxy formation model with bursts (Cole et al. 2000). We chose this model because mass dependence is the common feature of the presently acceptable galaxy formation scenarios (Benson 2010, and references therein). Also, Bell & de Jong (2001) selected this model as their default model claiming that this model reproduces the trends in age and metallicity with respect to surface brightness with the least scatter for local spiral galaxies.

We, thus, obtain the total stellar mass for each galaxy in our sample using the stellar mass-to-light ratio computed above. This method of obtaining stellar masses is extensively used in extragalactic studies where well-resolved spectral data are not available. The concern is that we are not taking the galaxy colour gradient into account by opting for its global colour. This may lead to an underestimation of mass, however, it should not affect our analysis of relative increase in mass and density.

The stellar mass inside effective radius is half of the total stellar mass. This mass is then divided by the area within the effective radius to obtain stellar mass density inside the effective radius (or ESMD) in units of solar mass per square kpc.

2.7 Checking for accuracy and error computation

The working of the overall procedure/code written to compute Petrosian radii, concentrations and asymmetries of the sources was tested using artificially created images and real images with known parameters.

The artificial images are created using GALFIT's Sérsic component. First, we fix the Sérsic index (at $n = 1$) and create images with varying half-light radius, i.e. $r_e = 40$, 50, 60, 62, 65 and 70 pixels. Since the Sérsic index is fixed, the Petrosian radius is expected to increase with the increase in half-light radius. This is indeed seen as the Petrosian radius for these images is computed to be 98.46(±4.92), 122.74(±6.14), 146.65(±7.33), 151.47(±7.57), 158.44(±7.92) and 169.91(±8.49) pixels, respectively.

Similarly, for fixed half-light radius (at $r_e = 50$ pixels), we create images with varying Sérsic index, i.e. $n = 0.8$, 1.2, 1.6, 2.0 and 2.4. Here, since the radius containing half of the light is held fixed, the concentration of the galaxy is expected to increase with the increase in its Sérsic index. This is indeed reported as the concentration index for these images is computed to be 2.65(±0.07), 3.01(±0.08), 3.29(±0.09), 3.52(±0.09) and 3.71(±0.10), respectively.

Next, we create images with different levels of asymmetry. This is done by keeping all the parameters (apparent magnitude, half-light radius, Sérsic index) fixed and adding Fourier modes. A detailed discussion of the representation of various asymmetric galactic features with Fourier modes is provided in Peng et al. (2010). We add the first Fourier mode of varying amplitudes, i.e. 0.07, 0.09, 0.11, 0.13, 0.15, 0.17 and 0.19. The asymmetry measure responds favourably such that it increases with the increasing amount of the Fourier mode amplitude. It is computed to be 0.080, 0.103, 0.125, 0.147, 0.169, 0.191 and 0.213, respectively, with error in the range of ±0.045–0.048. The procedure, thus, reproduces the measures with reasonable accuracy, responding well to the small shifts produced in the structural properties.

A concern relating to the accurate computation of these parameters at high redshift is the cosmological surface brightness dimming, which may lead to the non-detectability of faint features. However, the surface brightness evolution, reported to be 1–1.5 mag since $z = 1$ (Barden et al. 2005; Melbourne et al. 2007; Sachdeva 2013) is expected to counter this dimming. Another concern is that of low resolution of galaxies at high redshift. It should not affect our study (till $z \sim 1$) because the images are from overlapping five-orbit depth GOODS survey using *HST*-ACS, which provides a resolution of 0.03 arcsec pixel^{-1}. This is verified in a quantitative way by Conselice (2003). He simulated the local bright galaxies to higher redshifts as per how these galaxies would be imaged by various surveys. Then they compared the values measured at $z \sim 0$ to the values measured at various redshifts. For $z = 1$ (for GOODS *HST*-ACS), they report a marginal change of 0.10 ± 0.18 in the concentration measure and a change of -0.03 ± 0.07 in the asymmetry measure. Thus, the indices are highly reproducible with negligible scatter.

The error bars in the measurement of these parameters stem from the uncertainties involved in determining the total flux associated with the pixels of interest and also in the selection of the pixels of interest. The error associated with the measurement of flux using the aperture photometry package APPHOT of IRAF is calculated using

$$\begin{aligned} \text{error} = \sqrt{(}&\text{counts/gain} + \text{area} \times \text{stdev}^2 \\ &+ \text{area}^2 \times \text{stdev}^2/\text{nsky}), \end{aligned} \tag{18}$$

where gain is in electrons per analog-to-digital unit (ADU) and area (of the aperture) in pixels^2, stdev is the standard deviation of the sky counts and nsky is the number of sky pixels.

Out of the total sample of 570 galaxies, the algorithm/procedure did not converge to give the parameter values for three galaxies, reporting a floating point zero error. This is an extreme case caused for sources with central point of such high brightness that the inner radius goes to zero.

2.8 Overall data sample

We obtained parameters for overall 567 bright ($M_B \le -20$) bulgeless (i.e. without classical bulge) and normal (i.e. with classical bulge) disc-dominated galaxies in the three redshift ranges (263 in $0.77 \le z < 1.0$, 203 in $0.4 \le z < 0.77$, 101 in $0.02 \le z < 0.05$) in rest-frame B band. We have their redshifts, absolute magnitudes, half-light radii in kpc and Sérsic index from Sachdeva (2013). We have now computed their Petrosian radii in kpc, concentration, asymmetry, total stellar mass and effective stellar mass density. Some of the bulgeless and normal disc galaxy images from the sample are shown in Figs 1 and 2 for the three redshift ranges. The computed parameters along with the associated errors for these images are provided in Table 1. In the next section, we present the results that provide insights into bulge formation and evolution occurring in disc galaxies, by examining the evolution and relationships of these parameters.

3 RESULTS

The formation and evolution of bulges in disc galaxies can be probed by examining the mutual evolution and relationship of those

Table 1. Parameters for galaxies shown in Figs 1 and 2.

Source	ID	RA (J2000) (°)	Dec. (J2000) (°)	z	C	C-err	A	A-err	R_{P} (kpc)	R_{P}-err (kpc)
SDSS	107284	18.182632	15.70782	0.039	2.318	0.118	0.492	0.026	20.962	1.048
SDSS	138496	140.67966	57.51786	0.049	2.106	0.128	0.359	0.036	21.709	1.085
SDSS	236819	318.44444	− 5.8170589	0.049	2.543	0.157	0.367	0.034	21.686	1.084
SDSS	364153	148.98351	53.693652	0.044	2.531	0.127	0.356	0.027	22.805	1.140
SDSS	63945	226.72858	0.1863334	0.035	3.586	0.182	0.222	0.016	18.186	0.909
SDSS	87659	231.89702	0.28918961	0.049	3.333	0.254	0.192	0.009	16.739	0.837
SDSS	107614	28.966593	14.940272	0.044	3.042	0.203	0.397	0.018	17.078	0.854
SDSS	110067	42.326159	− 8.1749502	0.030	3.485	0.156	0.211	0.008	18.788	0.939
HST-ACS	1355	53.0167785	− 27.7189942	0.538	2.93	0.192	0.376	0.034	9.661	0.483
HST-ACS	14303	53.1091768	− 27.8529078	0.629	2.937	0.096	0.759	0.119	21.586	1.079
HST-ACS	28155	53.190166	− 27.7349438	0.530	2.417	0.104	0.643	0.077	15.897	0.795
HST-ACS	31666	53.2226372	− 27.8475767	0.432	2.755	0.121	0.598	0.058	12.901	0.645
HST-ACS	2587	53.0311719	− 27.7357189	0.935	2.483	0.209	0.937	0.197	10.912	0.546
HST-ACS	11609	53.093944	− 27.8727229	0.789	2.573	0.202	0.581	0.074	9.875	0.494
HST-ACS	19859	53.1384525	− 27.6806527	0.828	2.581	0.207	0.657	0.111	9.887	0.494
HST-ACS	27617	53.1859173	− 27.7756062	0.848	2.155	0.186	0.791	0.16	9.571	0.478
HST-ACS	3467	53.0391609	− 27.7100294	0.716	3.12	0.276	0.312	0.036	8.484	0.424
HST-ACS	12196	53.0975165	− 27.7212663	0.551	3.09	0.156	0.531	0.048	13.391	0.669
HST-ACS	19467	53.1361845	− 27.836454	0.633	3.466	0.139	0.46	0.05	17.084	0.854
HST-ACS	26780	53.179339	− 27.9235978	0.615	3.296	0.151	0.596	0.07	15.290	0.764
HST-ACS	4982	53.050917	− 27.7724075	0.924	3.211	0.246	0.482	0.043	10.156	0.508
HST-ACS	9837	53.0831774	− 27.7471694	0.883	2.937	0.163	0.678	0.108	14.526	0.726
HST-ACS	10198	53.0854551	− 27.6830331	0.847	3.224	0.138	0.837	0.129	17.162	0.858
HST-ACS	16603	53.120832	− 27.8230569	0.783	3.067	0.367	0.272	0.033	6.149	0.307

Table 2. Mean and median values of Petrosian radius and half-light radius.

Redshift range	Disc type	No. of sources	Mean of Petrosian radius $\langle R_{\mathrm{P}}\rangle$ (kpc)	Std. dev. of R_{P} σ	Median of R_{P}	Mean of half-light radius $\langle R_{\mathrm{e}}\rangle$ (kpc)	Std. dev. of R_{e} σ	Median of R_{e}
0.77–1.0	Bulgeless	105	12.706(±0.317)	3.246	12.249(±0.397)	5.429(±0.179)	1.844	4.902(±0.224)
0.77–1.0	Normal	158	10.498(±0.325)	4.087	9.411(±0.407)	3.725(±0.149)	1.885	3.170(±0.187)
0.4–0.77	Bulgeless	73	13.787(±0.459)	3.922	13.871(±0.575)	5.947(±0.251)	2.148	5.539(±0.314)
0.4–0.77	Normal	130	11.075(±0.368)	4.194	10.507(±0.461)	4.446(±0.193)	2.208	4.080(±0.242)
0.02–0.05	Bulgeless	25	23.464(±1.035)	5.177	22.395(±1.297)	6.972(±0.500)	2.504	6.508(±0.626)
0.02–0.05	Normal	76	20.373(±1.119)	9.761	18.244(±1.402)	4.552(±0.147)	1.280	4.368(±0.184)

parameters whose measure is associated with bulge properties. We, thus, examine the evolution of size, concentration, inner stellar density and asymmetry.

3.1 Size evolution

The sizes of the massive disc galaxies in the Universe are seen to undergo a dramatic increase with time (e.g. Trujillo et al. 2007; Buitrago et al. 2008; Carrasco, Conselice & Trujillo 2010; van Dokkum et al. 2010; Cassata et al. 2013). Some studies have attempted to explain this increase through inside-out processes, major mergers, minor mergers, accretion, active galactic nucleus (AGN) processes, etc. (Hopkins et al. 2009; Kaviraj et al. 2009; Bluck et al. 2012; Ownsworth et al. 2012; McLure et al. 2013).

The mechanisms that lead to the overall increase in disc length are also expected to produce variations in the inner region. For example, secular evolution driven by various asymmetric structures causes galactic discs to expand on the outside and contract on the inside (Tremaine 1989; van Dokkum et al. 2010; Kormendy 2013). To understand the relative role of the mechanisms in disc growth, the increase in the total optical extent should be tracked with the change in the inner region properties.

We, therefore, examine the increase in the Petrosian radius of the galaxy relative to the increase in its half-light radius. This relative increase will be seen separately for discs with and without classical bulges at the three redshift ranges (0.02–0.05, 0.4–0.77, 0.77–1.0).

The distribution of the Petrosian radius for bulgeless and normal disc galaxies is shown in Fig. 3 for the three redshift ranges. For the bulgeless disc galaxies it increases by 85(±4) per cent (from 12.71 to 23.46 kpc) from $z \sim 0.9$ to the present epoch. Over the same time range, for the normal disc sample, it increases by 94(±6) per cent (from 10.50 to 20.37 kpc) (see Table 2).

Thus, both morphological types show a significant increase in size. However, the evolution is faster and leads to a more effective increase in size for the normal disc galaxies. Nevertheless, it is interesting to note that bulgeless disc galaxies are larger than the normal disc galaxies, on average, at all redshift bins.

In contrast to the Petrosian radius, the half-light radius for both bulgeless and normal disc samples shows a minor increase of 28(±2) per cent (from 5.43 to 6.97 kpc) and 22(±1) per cent (from 3.72 to 4.55 kpc), respectively, from $z \sim 0.9$ to the present epoch (Table 2).

If we see the relative quantity, i.e. the ratio of Petrosian radius to half-light radius, it increases from 2.34 to 3.36 from $z \sim 0.9$

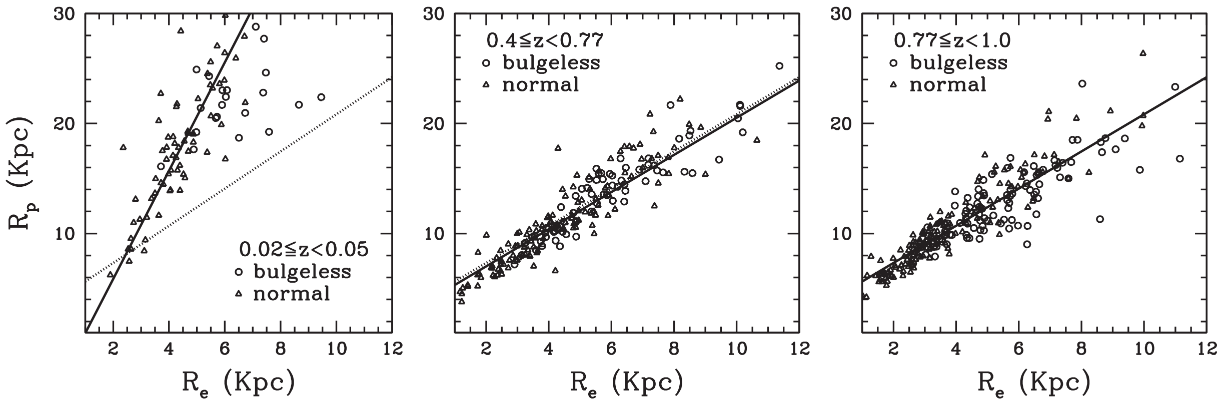

Figure 4. Petrosian radius is plotted against half-light radius for bulgeless and normal disc galaxies in the three redshift ranges. The solid line in each graph marks the linear relation followed by the full sample at that redshift range. The highest redshift range (0.77–1.0) relation is shown on the two lower redshift range (0.4–0.77, 0.02–0.05) plots with dotted lines. It is seen to almost overlap the intermediate-redshift range (0.4–0.77) relation. However, for the local sample (0.02–0.05), the slope is entirely different. There the half-light radius is seen to be a much smaller fraction of the Petrosian radius. For the Petrosian radius, the error scales with the value and is seen to be in the range of ±5 per cent. For half light radius, the typical error is of ±0.2 kpc.

to the present epoch for bulgeless disc galaxies. However, the increase is larger, from 2.82 to 4.48, for the normal disc galaxies. For these galaxies, their total radius becomes ∼4.5 times their half-light radius, as we reach the present epoch.

The two sizes (half-light radius and Petrosian radius), though computed in totally different ways (parametrically and non-parametrically), are found to be highly correlated in our galaxy sample, as seen in Fig. 4. The linear fit relation found for the highest redshift range (0.77–1.0) almost overlaps the relation found for the intermediate-redshift range (0.4–0.77). However, the slope changes drastically for the local redshift range (0.02–0.05):

$$R_{\rm P} = 1.69(\pm 0.06)R_{\rm e} + 3.62(\pm 0.31); \quad 0.4 \le z < 1.0, \tag{19}$$

$$R_{\rm P} = 4.92(\pm 0.68)R_{\rm e} - 2.04(\pm 0.59); \quad 0.02 \le z < 0.05. \tag{20}$$

The change of slope further signifies that the half-light radius reduces to a much smaller fraction of the Petrosian radius as we reach the present epoch.

Overall, we find that while the total extent of our discs almost doubles with time, the radius containing half the stellar light increases marginally in comparison. This suggests significant peripheral increase, which is seen to be somewhat more pronounced for the normal disc sample.

3.2 Concentration evolution

The Sérsic index is extensively used not just for morphological characterization of galaxies but also to study their structural evolution (Shen et al. 2003; Blanton et al. 2005b; Fisher & Drory 2008; Conselice et al. 2011; Bruce et al. 2012; Buitrago et al. 2013). Being related to the steepness of the intensity profile, it is a measure of the prominence of the bulge component (Sersic 1968; Peng et al. 2002). The concentration parameter, however, is seen to be a better estimator of the bulge presence for low-redshift galaxies (Conselice 2003; Graham et al. 2005; Gadotti 2009).

Our full (disc-dominated) sample is separated on the basis of Sérsic index (along with the Kormendy relation). We now examine the evolution in their concentration value. The distribution of the concentration for bulgeless and normal disc galaxies is studied for the three redshift ranges (0.02–0.05, 0.4–0.77, 0.77–1.0). The mean concentration of the bulgeless disc galaxies shows a statistically insignificant increase from $z \sim 0.9$ to the present epoch (Table 3). However, for the normal disc sample it increases by 12.3(±0.3) per cent (from 2.77 to 3.11), over the same time range (Table 3).

Thus, while the average bulgeless disc galaxy concentration remains almost similar over the three redshift ranges, there is a significant (albeit admittedly small) increase in average normal disc galaxy concentration.

While the Sérsic index has been obtained parametrically, i.e. by fitting a function to the surface brightness profile, the concentration is based on total count ratios, i.e. non-parametrically. We examine the relationship of the two parameters for the full sample (Fig. 5) in the three redshift ranges. The two quantities are seen to be well correlated for both morphological types and follow a single relation for both the higher (0.77–1.0) and intermediate (0.4–0.77) redshift ranges:

$$C = 0.38(\pm 0.03)n + 2.32(\pm 0.04), \quad 0.4 \le z < 1.0. \tag{21}$$

The two quantities appear to provide a similar estimate of the bulge component. Thus, according to our study they are equally well deserving to be chosen at high redshifts for morphological determination.

However, the correlation is absent for the local redshift range (0.02–0.05). This lack of correlation at local redshifts is also reported by Gadotti (2009). We speculate that for highly resolved local galaxies the intensity gradient between the bulge and the disc is enhanced, leading to poorer fits when only a single function is used to fit the entire galaxy.

3.3 Stellar density evolution

Total stellar mass is one of the most significant properties of a galaxy and is seen to be correlated with not just the overall concentration but also the star formation rate of the galaxy (Caon, Capaccioli & D'Onofrio 1993; Conselice 2003; Noeske et al. 2007; Disney et al. 2008; Bauer et al. 2011). Recent studies have found that close to half of the present stellar mass of the galaxies assembled by $z \sim 1$ (Bundy, Ellis & Conselice 2005; Mortlock et al. 2011; Marchesini et al. 2014; Ownsworth et al. 2014). We first examine the growth in the stellar mass for our full sample from $z \sim 0.9$ to the present epoch (Fig. 6).

Table 3. Mean and median values of concentration and asymmetry.

Redshift range	Disc type	No. of sources	Mean of concentration ⟨C⟩	Std. dev. of C σ	Median of C	Mean of asymmetry ⟨A⟩	Std. dev. of A σ	Median of A
0.77–1.0	Bulgeless	105	2.748(±0.027)	0.278	2.772(±0.034)	0.827(±0.014)	0.145	0.831(±0.017)
0.77–1.0	Normal	158	2.767(±0.030)	0.382	2.784(±0.037)	0.568(±0.014)	0.181	0.559(±0.017)
0.4–0.77	Bulgeless	73	2.726(±0.037)	0.317	2.677(±0.046)	0.719(±0.019)	0.159	0.718(±0.024)
0.4–0.77	Normal	130	2.819(±0.034)	0.391	2.776(±0.042)	0.515(±0.016)	0.188	0.494(±0.020)
0.02–0.05	Bulgeless	25	2.791(±0.067)	0.448	2.674(±0.084)	0.412(±0.023)	0.115	0.394(±0.029)
0.02–0.05	Normal	76	3.107(±0.064)	0.560	3.010(±0.080)	0.308(±0.015)	0.131	0.280(±0.019)

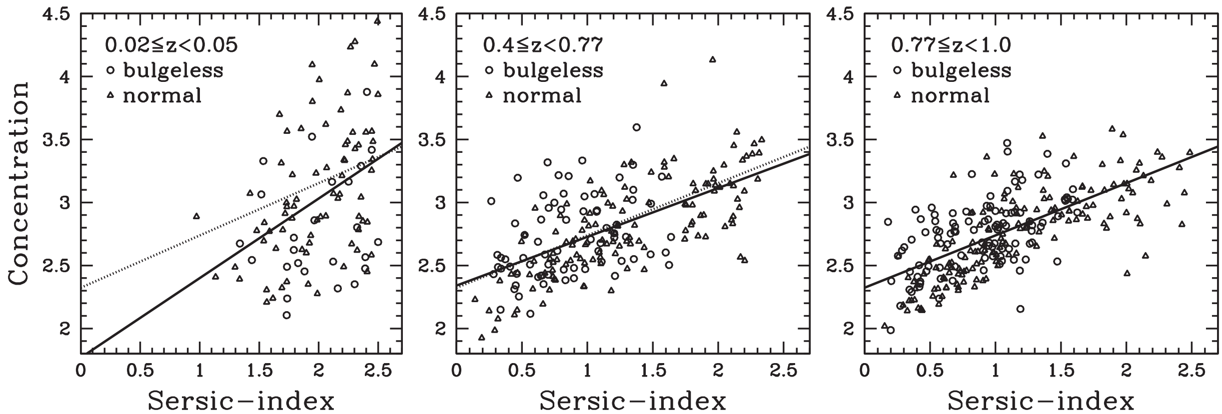

Figure 5. Concentration is plotted against Sérsic index, n, for bulgeless and normal disc galaxies in the three redshift ranges. The solid line in each graph marks the linear relation followed by the full sample at that redshift range. The highest redshift range (0.77–1.0) relation is shown on the two lower redshift range (0.4–0.77, 0.02–0.05) plots with dotted lines. The two parameters are seen to be highly correlated and the relation almost overlaps for the two high-redshift ranges (0.77–1.0, 0.4–0.77). However, the local sample shows a lack of correlation in the two values. For concentration, typical error on the value is ±0.17 and for Sérsic index it is ±0.05.

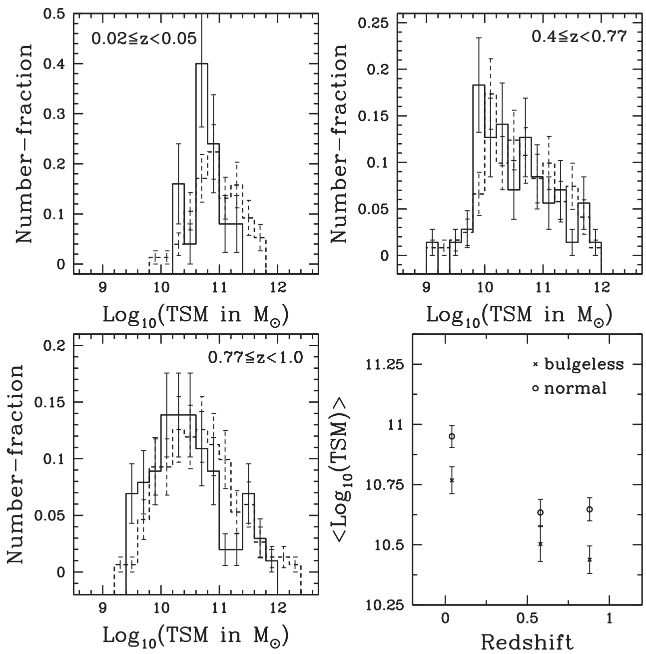

Figure 6. Distribution of log of total stellar mass (in units of $M_{\odot}$) is shown in the three redshift ranges for bulgeless disc (solid lines) and normal disc (dashed lines) galaxies. The distribution of their mean values with redshift is also shown. Since it is on log scale, even a slight shift corresponds to a huge increase in the mass of the galaxy. A shift towards higher mass can be seen for both morphological types. Their stellar mass at $z \sim 0$ is more than double of that at $z \sim 0.9$.

The mean values of the log of total stellar mass (in units of solar mass, $M_{\odot}$) are given in the three redshift ranges in Table 4. The bulgeless disc galaxies witness an increase of 3.1×10^{10} $M_{\odot}$ (from 2.7 to 5.8×10^{10} $M_{\odot}$) from $z \sim 0.9$ to the present epoch. Over the same time range, the normal disc galaxies witness an increase of 4.5×10^{10} $M_{\odot}$ (from 4.4 to 8.9×10^{10} $M_{\odot}$).

Thus, we find that both the morphological types have gained more than 50(±6) per cent of their present stellar mass since $z \sim 0.9$. The interesting part is that the increase in the total stellar mass of a normal disc galaxy is ∼1.5 times more than that seen for a bulgeless disc galaxy over the last ∼8 Gyr, on average. The difference in the average total stellar mass of the two morphological types almost doubles (from 1.7 to 3.1×10^{10} $M_{\odot}$) from $z \sim 0.9$ to the present epoch.

Next we examine the growth of stellar mass density in the inner region, i.e. the effective stellar mass density. The distribution of the effective stellar mass density on the log-scale is shown in Fig. 7 for bulgeless and normal disc galaxies in the three redshift ranges.

Examining the mean values from $z \sim 0.9$ to the present epoch (Table 4), we find an increase of 4.7×10^7 $M_{\odot}$ kpc^{-2} (from 1.6 to 2.1×10^8 $M_{\odot}$ kpc^{-2}), on average, for the effective stellar mass density of bulgeless disc galaxies; and of 8.8×10^7 $M_{\odot}$ kpc^{-2} (from 6.6 to 7.4×10^8 $M_{\odot}$ kpc^{-2}), on average, for the normal disc galaxies.

While the normal disc galaxies witness an increase of 13(±5) per cent in their effective stellar mass density, this is more prominent for the bulgeless disc galaxies, namely 30(±1) per cent. However, in absolute terms, the increase for the average normal disc galaxy is ∼1.8 times that seen for a bulgeless disc galaxy over the last

Table 4. Mean values of log of total stellar mass (LTSM) and log of effective stellar mass density (LESMD).

Redshift range	Disc type	No. of sources	Mean of LTSM ⟨LTSM⟩	Std. dev. of LTSM σ	Median of LTSM	Mean of LESMD ⟨LESMD⟩	Std. dev. of LESMD σ	Median of LESMD
0.77–1.0	Bulgeless	101	10.438(±0.057)	0.574	10.381(±0.071)	8.214(±0.058)	0.584	8.219(±0.073)
0.77–1.0	Normal	151	10.647(±0.048)	0.593	10.610(±0.060)	8.817(±0.049)	0.598	8.795(±0.061)
0.4–0.77	Bulgeless	71	10.503(±0.072)	0.603	10.386(±0.090)	8.211(±0.064)	0.544	8.178(±0.080)
0.4–0.77	Normal	121	10.634(±0.055)	0.609	10.562(±0.069)	8.654(±0.062)	0.682	8.575(±0.078)
0.02–0.05	Bulgeless	25	10.768(±0.056)	0.280	10.755(±0.070)	8.324(±0.049)	0.248	8.339(±0.061)
0.02–0.05	Normal	76	10.950(±0.045)	0.391	10.943(±0.056)	8.872(±0.043)	0.377	8.854(±0.054)

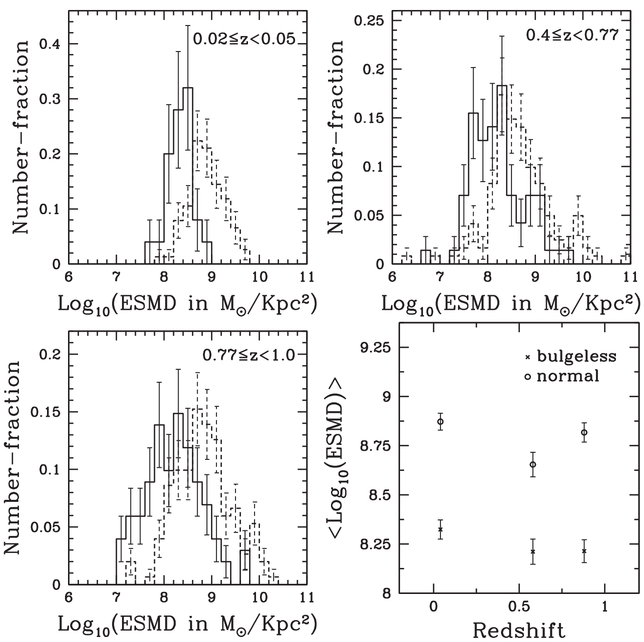

Figure 7. Distribution of log of effective stellar mass density is shown in the three redshift ranges for bulgeless disc (solid lines) and normal disc (dashed lines) galaxies. The distribution of their mean values with redshift is also shown. Since it is on log scale, even a slight shift corresponds to a huge increase in the mass density of the galaxy. The normal sample shows fluctuation, however, the density at $z \sim 0$ is more than that at $z \sim 0.9$ for both morphological types.

$\sim$8 Gyr. Thus, for both total stellar mass and effective stellar mass density, the increase seen for the normal disc sample is considerably more than that seen for the bulgeless disc sample.

In addition, we note that the effective stellar mass density can be a better indicator of galaxy morphology than concentration. This is seen using the Kolmogorov–Smirnov (KS) test which is considered an efficient mathematical tool for determining the significance of the difference of two distributions. We use this test to compare the bulgeless and normal disc galaxy samples with respect to concentration and effective mass density in three redshift ranges (Table 5).

The null hypothesis is that the two distributions are from the same parent set and this test quantifies a probability for this null hypothesis. For that, we compute the distance (D-observed) between the empirical cumulative distribution functions of the two samples. Based on this distance and the sample size, the probability for the null hypothesis is found (Table 5). In the case of concentration, this probability is not convincingly low for the two distributions to be considered significantly different. However, it is found to be negligible at all redshift ranges in the case of effective stellar mass density.

Table 5. KS-test D-observed and probability values.

Parameter	Redshift range	D-observed	Probability
Conc	0.02–0.05	0.337	0.021
Log-EMD	0.02–0.05	0.709	3.4e-09
Conc	0.40–0.77	0.178	0.092
Log-EMD	0.40–0.77	0.395	9.7e-07
Conc	0.77–1.00	0.132	0.204
Log-EMD	0.77–1.00	0.414	8.9e-10

3.4 Correlations with asymmetry

The asymmetric features in the disc galaxy, created by both internally and externally driven processes, lead to the formation of pseudo- and classical bulges in disc galaxies (Khochfar & Silk 2006; Elmegreen et al. 2008; Jogee et al. 2009; Hopkins et al. 2010; Kormendy et al. 2010; Conselice 2014). Thus, it is imperative to analyse the evolution of asymmetry and its relationship with other parameters of disc galaxies.

The distribution of the asymmetry for bulgeless and normal disc galaxies is shown in Fig. 8 for the three redshift ranges. The mean asymmetry for bulgeless disc galaxies falls by 50(±3) per cent (from 0.83 to 0.41) from $z \sim 0.9$ to the present epoch (Table 3). Over the same time range, the mean asymmetry for the normal disc sample falls by 45(±2) per cent (from 0.57 to 0.31; Table 3).

Both bulgeless and normal disc galaxies show a huge decline in their asymmetry value with time, indicating the disappearance of asymmetric features. The bulgeless disc sample is more asymmetric than the normal disc sample at all redshift ranges (Fig. 8). However, due to the more significant fall seen in the average asymmetry value of the bulgeless disc sample, it reaches closer to the average asymmetry value of the normal disc sample.

The asymmetry parameter shows a correlation with half-light radius (Fig. 9). Bulgeless disc galaxies, having larger half-light radii than the normal disc galaxies, have higher asymmetries. At fixed radii, bulgeless disc galaxies are found to be more asymmetric than normal disc galaxies, on average.

The asymmetry parameter shows an anticorrelation with effective stellar mass density, as explored in Fig. 10 for both morphological types. There is a steep fall in the asymmetry with the increase in effective stellar mass density for all the redshift ranges. The slope for $0.4 \le z < 1.0$ is

$$A = -0.21(\pm 0.02)\log(\mathrm{EMD}) + 2.47(\pm 0.13). \quad (22)$$

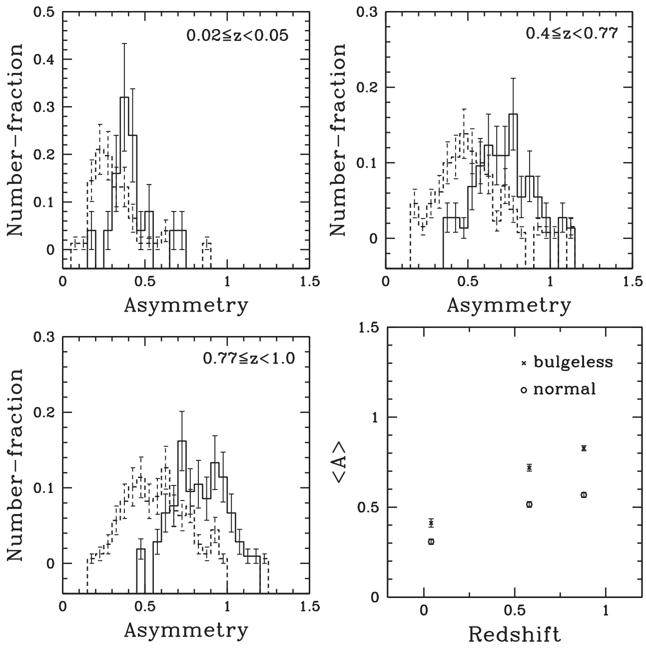

Figure 8. Distribution of asymmetry for bulgeless disc (solid lines) and normal disc (dashed lines) galaxies is shown for the three redshift ranges. The distribution of the means with redshift is also shown. Reduction in the scatter of the parameter value with time is apparent. The fall in the mean value of asymmetry is more significant for the bulgeless disc sample.

Bulgeless disc galaxies being more asymmetric and less dense as compared to normal disc galaxies are on the higher end of the slope in all three redshift ranges.

4 DISCUSSION

We have a total sample of 567 disc-dominated galaxies separated into bulgeless (without classical bulge) discs and normal (with classical bulge) discs in three redshift ranges ($0.77 \leq z < 1.0$, $0.4 \leq z < 0.77$ and $0.02 \leq z < 0.05$). We have examined the evolution in size, concentration, effective stellar mass density and asymmetry of these two samples. We first list our major findings and then discuss the implications.

(i) Both morphological types show a significant increase [94(±6) per cent for the normal disc sample] in total optical extent since $z \sim 0.9$. The half-light radius of the galaxies witnesses a much smaller increase [22(±1) per cent for the normal disc sample] in comparison. This peripheral size evolution is more evident for the normal disc sample in which the outer radius becomes ∼5 times the inner radius by $z \sim 0$.

(ii) The mean concentration of stellar light undergoes a significant increase ($\Delta C = 0.34$) for the normal disc sample as compared to the bulgeless disc sample ($\Delta C = 0.04$) since $z \sim 0.9$. The concentration parameter of the galaxy is seen to be well correlated with its global Sérsic index value for both morphological types at higher redshift ranges (0.44–0.77, 0.77–1.0). However, the correlation is absent for the local sample (0.02–0.05).

(iii) Both morphological types have gained more than half of their present stellar mass since $z \sim 0.9$. In absolute terms, the increase in the total stellar mass as well as effective stellar mass density is significantly more important (∼1.5 and 1.8 times, respectively) for the normal disc sample.

(iv) The bulgeless disc sample is more asymmetric than the normal disc sample at all redshift ranges. Both samples witness a fall in their mean asymmetry value from $z \sim 0.9$ to ∼0, the fall being more drastic [∼50(±3) per cent] for the bulgeless disc sample. Asymmetry is found to be correlated with the half-light radius, and anticorrelated with the effective stellar mass density of the galaxy.

4.1 Impact of internal evolution

In our sample, from $z \sim 0.9$ to ∼0, the Petrosian radius increases more significantly than the effective radius. In other words, the strong increase in the total radius of the full sample is not reflected in its half-light radius. This peripheral increase appears to provide evidence in support of internal secular evolution in which, due to the outward transfer of angular momentum, galaxy discs are expected to expand on the outside and get more concentrated on the inside (Tremaine 1989; Combes 2001; Kormendy & Kennicutt 2004). However, there are complexities with this explanation.

The asymmetric features such as spiral arms and bars that induce and speed up internal secular evolution (Kormendy & Kennicutt 2004; Jogee 2006; Coelho & Gadotti 2011; Sheth et al. 2012; Cheung et al. 2013) are known to be present in the bulgeless disc galaxies with greater propensity (Buta 2013). In our study also the

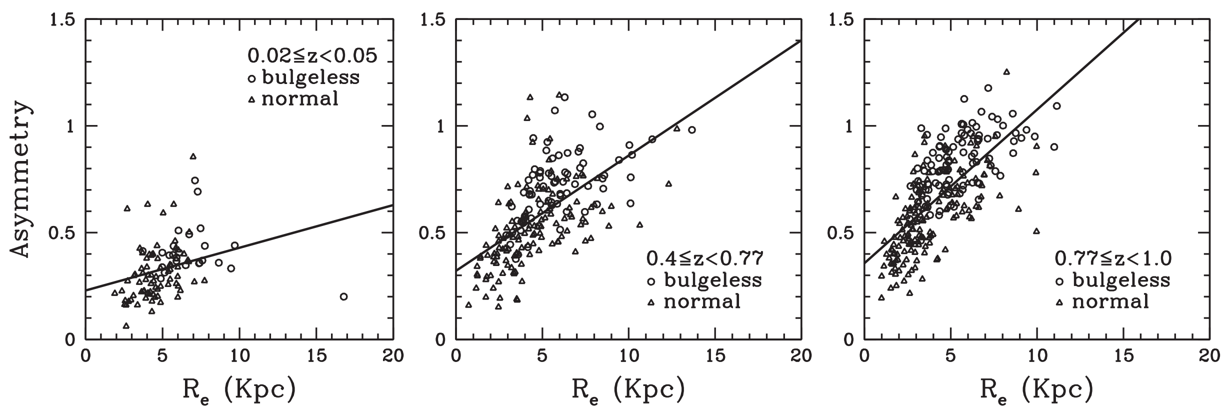

Figure 9. Asymmetry is plotted against half-light radius for bulgeless disc and normal disc galaxies in the three redshift ranges. The solid line in each graph marks the linear relation followed by the full sample at that redshift range. The larger the radius, the greater is seen to be the asymmetry value of the galaxy. Sources from the bulgeless disc sample, having on an average larger half-light radii, are found to have higher asymmetry values. The typical error on the asymmetry value is ±0.08 and for the half-light radius it is ±0.2 kpc.

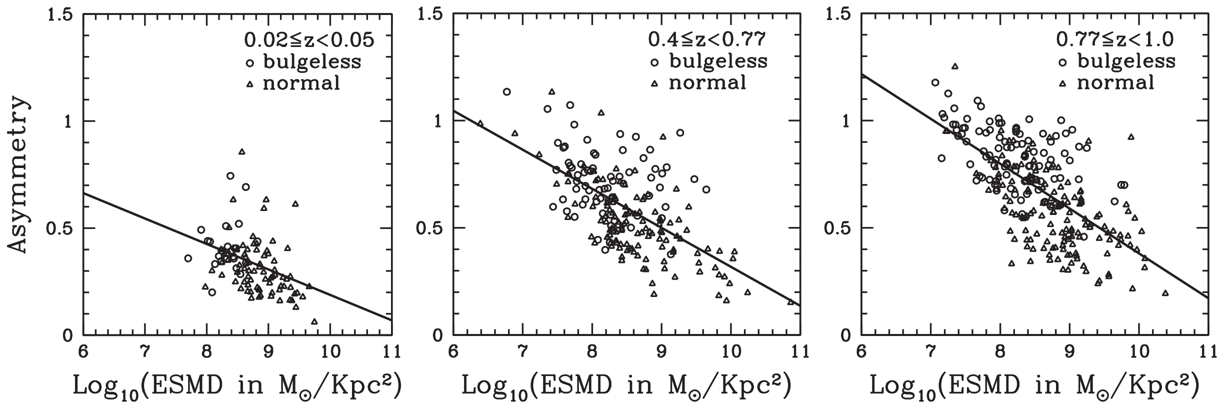

Figure 10. Asymmetry is plotted against log of effective stellar mass density for bulgeless disc and normal disc galaxies in the three redshift ranges. The solid line in each graph marks the linear relation followed by the full sample at that redshift range. The two parameters are seen to be highly correlated for both morphological types. The higher the galaxy's stellar mass density inside its effective radius, the lower is the asymmetry of its stellar light distribution. The typical error on the asymmetry value is ±0.08 and for the log of effective stellar mass density it is ±0.05.

bulgeless disc sample is found to be more asymmetric than the normal disc sample at all three redshift ranges. This in turn might favour the build-up of central concentration and eventual fading of the asymmetric features with time (Kormendy & Kennicutt 2004; Athanassoula 2005) in bulgeless galaxies. This can be the probable cause for a relatively steeper decrease in the asymmetry value of our bulgeless disc sample.

Naively, thus, internal secular evolution is expected to be more efficient for the bulgeless disc sample. However, we find that the evolution in terms of size and increase in the density of the inner region, as seen through concentration and effective stellar mass density, in absolute terms, is considerably more for the normal disc sample. This gives us an indication that internal secular processes are not the only evolution determining forces.

In addition to that, it is known through simulations and observations that the huge increase in disc galaxies' total optical extent is occurring due to stellar mass build up in the outer regions of these galaxies (Cappellari et al. 2009; Newman et al. 2010). We also report growth in stellar masses by a factor of 2 since $z \sim 1$ for both the morphological samples.

This increase in size in terms of stellar mass build-up as well as the increase in internal density cannot be achieved only through the rearrangement of mass and angular momentum. Thus, in addition to the internal secular evolution, there might be other processes causing the disc evolution from $z \sim 0.9$ to the present epoch. We argue that such inside-out growth might be driven by the transfer of matter from the circumgalactic environment to the galaxy, in the next section.

4.2 Impact of external evolution

Our findings that discs have grown by such large factors from $z \sim 1$ to now argues that stellar discs are robust structures, difficult to be destroyed, and that catastrophic mergers are rather rare at the second half of the age of the Universe. This is in agreement with recent studies, based on simulations and observations, which report a significant decline in the major merger rate with time (Conselice, Yang & Bluck 2009; Jogee et al. 2009; Bluck et al. 2012).

However, there is continuous accretion of matter from the intergalactic medium, and minor mergers are also frequent (Parry et al. 2009; Kaviraj 2010; López-Sanjuan et al. 2011; Bluck et al. 2012). We do observe that both bulgeless and normal disc galaxies have gained more than 50 per cent of their total stellar mass in the past ∼8 Gyr. Although star formation within the galaxy can also lead to the increase in its stellar mass, its contribution is measured to be much less compared to that from minor mergers and accretion (Ownsworth et al. 2012, 2014; Madau & Dickinson 2014).

During the last ∼8 Gyr, galaxies are predicted to suffer a period of intense bombardment by minor satellites (Khochfar & Silk 2006; Hopkins et al. 2009; Feldmann et al. 2010; Oser et al. 2010; Quilis & Trujillo 2012). These bombardments are expected to bring morphological changes in the disc population by building classical bulges and also giving rise to spheroidal galaxies (Hopkins et al. 2010; Oesch et al. 2010; Cameron et al. 2011; van der Wel et al. 2011; Weinzirl et al. 2011; Law et al. 2012; Buitrago et al. 2013). For the full sample studied, we report a considerable increase in the density of the inner region through the measures of Sérsic index, concentration and the effective stellar mass density for the past ∼8 Gyr.

This increase is also observed in the fact that the fraction of disc galaxies with classical bulges are increasing from $z \sim 0.9$ to the present epoch. It increases from 60 per cent at the highest redshift range (0.77–1.0) to 64 per cent at the intermediate-redshift range (0.4–0.77) and finally to 75 per cent at the local redshift range (0.02–0.05), indicating that some of the bulgeless discs are growing a classical bulge with time. Although internal secular mechanisms driven by disc instabilities also lead to the increase in inner density, these methods can only lead to the formation of pseudo-bulges (Binney & Tremaine 1987; Kormendy & Kennicutt 2004; Kormendy et al. 2010; Saha & Gerhard 2013). The evidence, thus, suggests that minor mergers and accretion are playing a significant role from $z \sim 0.9$ to the present epoch.

There is substantial literature that establishes the dependence of galaxy properties on local environmental density such that the higher the density of the local environment, the more massive, dense, early-type and non-star forming is the galaxy (Dressler 1984; Gómez et al. 2003; Blanton & Moustakas 2009; Scoville et al. 2013). In the specific case of discs, discs with classical bulges are rarely found in low-density environments (Kormendy et al. 2010). Also, discs without classical bulges are expected to keep this way by being in more isolated environments (Peebles & Nusser 2010). By that argument, at $z \sim 1$, normal disc galaxies supporting a classical bulge and being denser, more massive and less star forming are expected to be placed in denser environments as compared to the bulgeless disc galaxies.

There is observational evidence that galaxies in denser environments show a more rapid increase of galaxy size with redshift (Cooper et al. 2012; Lani et al. 2013). Our results are in agreement, such that, normal disc galaxies show faster size evolution as compared to the bulgeless galaxies. Dense environments should also facilitate a stronger evolution in the inner region of galaxies as they are expected to undergo an increased amount of accretion and interaction with satellites (Conselice 2014, and references therein). In our study also, in absolute terms, the increase in the inner density is observed to be more prominent in the case of the normal disc sample. Thus, environment appears to have strongly affected bulge growth over the past ∼8 Gyr.

Overall, we have found that both internal and external mechanisms are involved in disc and bulge evolution. External processes, in the form of minor mergers and accretion, appear to be playing a more effective role in growing classical bulges in relatively denser environments.

Examining the inner region properties through both parametric and non-parametric measures provides considerable insight into the relative role of the processes involved in disc evolution. Further understanding can perhaps be obtained from studies in other wavelengths, especially the infrared region, in which dust effects are minimized.

ACKNOWLEDGEMENTS

We are thankful to Christopher J. Conselice, Michael Blanton and Knud Jahnke for providing useful inputs. SS is thankful to receive senior research fellowship (09/045(0972)/2010-EMR-I) from Council of Scientific and Industrial Research (CSIR), India. SS also acknowledges the grant received as a DGDF-2014 project student at ESO, Chile. SS is thankful to Ranjeev Misra, Ajit Kembhavi and Yogesh Wadadekar for useful discussions. Lastly, SS would like to thank IUCAA, India, and ESO, Chile, for the local hospitality provided during the course of this work. We are highly grateful to the referee for providing detailed and insightful comments, which has improved the presentation of the work.

REFERENCES

Aguerri J. A. L., Balcells M., Peletier R. F., 2001, A&A, 367, 428
Arnouts S., Ilbert O., 2011, LePHARE: Photometric Analysis for Redshift Estimate. Astrophysics Source Code Library, record ascl:1108.009
Athanassoula E., 2005, MNRAS, 358, 1477
Baldry I. K., Balogh M. L., Bower R. G., Glazebrook K., Nichol R. C., Bamford S. P., Budavari T., 2006, MNRAS, 373, 469
Bamford S. P. et al., 2009, MNRAS, 393, 1324
Barden M. et al., 2005, ApJ, 635, 959
Bauer A. E., Conselice C. J., Pérez-González P. G., Grützbauch R., Bluck A. F. L., Buitrago F., Mortlock A., 2011, MNRAS, 417, 289
Baugh C. M., 2006, Rep. Progress Phys., 69, 3101
Baugh C. M., Cole S., Frenk C. S., 1996, MNRAS, 283, 1361
Bell E. F., de Jong R. S., 2001, ApJ, 550, 212
Benson A. J., 2010, Phys. Rep., 495, 33
Bershady M. A., Jangren A., Conselice C. J., 2000, AJ, 119, 2645
Bertin E., Arnouts S., 1996, A&AS, 117, 393
Binney J., Tremaine S., 1987, Nature, 326, 219
Blanton M. R., Moustakas J., 2009, ARA&A, 47, 159
Blanton M. R. et al., 2003, AJ, 125, 2348
Blanton M. R., Lupton R. H., Schlegel D. J., Strauss M. A., Brinkmann J., Fukugita M., Loveday J., 2005a, ApJ, 631, 208
Blanton M. R. et al., 2005b, AJ, 129, 2562
Bluck A. F. L., Conselice C. J., Buitrago F., Grützbauch R., Hoyos C., Mortlock A., Bauer A. E., 2012, ApJ, 747, 34
Bournaud F., 2015, in Laurikainen E., Peletier R., Gadotti D. A., eds, Galactic Bulges. Springer-Verlag, New York, in press
Bournaud F., Jog C. J., Combes F., 2007, A&A, 476, 1179
Brammer G. B., van Dokkum P. G., Coppi P., 2008, ApJ, 686, 1503
Brinchmann J., Charlot S., White S. D. M., Tremonti C., Kauffmann G., Heckman T., Brinkmann J., 2004, MNRAS, 351, 1151
Brook C. B. et al., 2011, MNRAS, 415, 1051
Brooks A. M., Christensen C., 2015, in Laurikainen E., Peletier R., Gadotti D. A., eds, Galactic Bulges. Springer-Verlag, New York, in press
Bruce V. A. et al., 2012, MNRAS, 427, 1666
Bruce V. A. et al., 2014, MNRAS, 444, 1001
Buitrago F., Trujillo I., Conselice C. J., Bouwens R. J., Dickinson M., Yan H., 2008, ApJ, 687, L61
Buitrago F., Trujillo I., Conselice C. J., Häußler B., 2013, MNRAS, 428, 1460
Bundy K., Ellis R. S., Conselice C. J., 2005, ApJ, 625, 621
Buta R. J., 2013, in Oswalt T. D., Keel W. C., eds, Planets, Stars and Stellar Systems. Springer Science+Business Media, Dordrecht, Vol. 6, p. 1
Cameron E., Carollo C. M., Oesch P. A., Bouwens R. J., Illingworth G. D., Trenti M., Labbé I., Magee D., 2011, ApJ, 743, 146
Caon N., Capaccioli M., D'Onofrio M., 1993, MNRAS, 265, 1013
Cappellari M. et al., 2009, ApJ, 704, L34
Carrasco E. R., Conselice C. J., Trujillo I., 2010, MNRAS, 405, 2253
Cassata P. et al., 2013, ApJ, 775, 106
Cheung E. et al., 2013, ApJ, 779, 162
Coelho P., Gadotti D. A., 2011, ApJ, 743, L13
Cole S., Lacey C. G., Baugh C. M., Frenk C. S., 2000, MNRAS, 319, 168
Combes F., 2001, in Aretxaga I., Kunth D., Mújica R., eds, Advanced Lectures on the Starburst-AGN Connection. World Scientific, Singapore, p. 223
Conselice C. J., 2003, ApJS, 147, 1
Conselice C. J., 2014, ARA&A, 52, 291
Conselice C. J., Bershady M. A., Jangren A., 2000, ApJ, 529, 886
Conselice C. J., Yang C., Bluck A. F. L., 2009, MNRAS, 394, 1956
Conselice C. J., Bluck A. F. L., Ravindranath S., Mortlock A., Koekemoer A. M., Buitrago F., Grützbauch R., Penny S. J., 2011, MNRAS, 417, 2770
Cooper M. C. et al., 2012, MNRAS, 419, 3018
de Jong R. S., 1996, A&AS, 118, 557
Disney M. J., Romano J. D., Garcia-Appadoo D. A., West A. A., Dalcanton J. J., Cortese L., 2008, Nature, 455, 1082
Dressler A., 1984, ARA&A, 22, 185
Driver S. P. et al., 2006, MNRAS, 368, 414
Elmegreen B. G., Bournaud F., Elmegreen D. M., 2008, ApJ, 688, 67
Feldmann R., Carollo C. M., Mayer L., Renzini A., Lake G., Quinn T., Stinson G. S., Yepes G., 2010, ApJ, 709, 218
Fisher D. B., Drory N., 2008, AJ, 136, 773
Fukugita M., Ichikawa T., Gunn J. E., Doi M., Shimasaku K., Schneider D. P., 1996, AJ, 111, 1748
Gadotti D. A., 2008, MNRAS, 384, 420
Gadotti D. A., 2009, MNRAS, 393, 1531
Giavalisco M. et al., 2004, ApJ, 600, L93
Gómez P. L. et al., 2003, ApJ, 584, 210
Governato F. et al., 2010, Nature, 463, 203
Graham A. W., 2013, in Oswalt T. D., Keel W. C., eds, Planets, Stars and Stellar Systems. Springer Science+Business Media, Dordrecht, Vol. 6, p. 91
Graham A. W., Driver S. P., Petrosian V., Conselice C. J., Bershady M. A., Crawford S. M., Goto T., 2005, AJ, 130, 1535
Hogg D. W., Baldry I. K., Blanton M. R., Eisenstein D. J., 2002, arXiv Astrophysics e-prints
Hopkins P. F., Cox T. J., Younger J. D., Hernquist L., 2009, ApJ, 691, 1168
Hopkins P. F. et al., 2010, ApJ, 715, 202
Jester S. et al., 2005, AJ, 130, 873

Jogee S., 2006, in Alloin D., Johnson R., Lira P., eds, Lecture Notes in Physics, Vol. 693, Physics of Active Galactic Nuclei at All Scales. Springer-Verlag, Berlin, p. 143
Jogee S. et al., 2009, ApJ, 697, 1971
Kauffmann G., White S. D. M., Guiderdoni B., 1993, MNRAS, 264, 201
Kauffmann G. et al., 2003, MNRAS, 341, 54
Kautsch S. J., 2009, PASP, 121, 1297
Kautsch S. J., Grebel E. K., Barazza F. D., Gallagher J. S., III, 2006, A&A, 445, 765
Kaviraj S., 2010, MNRAS, 406, 382
Kaviraj S., Peirani S., Khochfar S., Silk J., Kay S., 2009, MNRAS, 394, 1713
Khochfar S., Silk J., 2006, MNRAS, 370, 902
Kormendy J., 1977, ApJ, 218, 333
Kormendy J., 2013, in Falcón-Barroso J., Knapen J. H., eds, Secular Evolution of Galaxies. Cambridge Univ. Press, Cambridge, p. 1
Kormendy J., 2015, in Laurikainen E., Peletier R., Gadotti D. A., eds, Galactic Bulges. Springer-Verlag, New York, in press
Kormendy J., Kennicutt R. C., Jr, 2004, ARA&A, 42, 603
Kormendy J., Drory N., Bender R., Cornell M. E., 2010, ApJ, 723, 54
Kriek M., van Dokkum P. G., Labbé I., Franx M., Illingworth G. D., Marchesini D., Quadri R. F., 2009, ApJ, 700, 221
Lani C. et al., 2013, MNRAS, 435, 207
Laurikainen E., Salo H., Buta R., Knapen J. H., 2007, MNRAS, 381, 401
Law D. R., Steidel C. C., Shapley A. E., Nagy S. R., Reddy N. A., Erb D. K., 2012, ApJ, 759, 29
López-Sanjuan C. et al., 2011, A&A, 530, A20
Lotz J. M., Primack J., Madau P., 2004, AJ, 128, 163
Lotz J. M. et al., 2008, ApJ, 672, 177
McLure R. J. et al., 2013, MNRAS, 428, 1088
Madau P., Dickinson M., 2014, ARA&A, 52, 415
Marchesini D. et al., 2014, ApJ, 794, 65
Melbourne J., Phillips A. C., Harker J., Novak G., Koo D. C., Faber S. M., 2007, ApJ, 660, 81
Mo H., van den Bosch F. C., White S., 2010, Galaxy Formation and Evolution. Cambridge Univ. Press, Cambridge
Mortlock A., Conselice C. J., Bluck A. F. L., Bauer A. E., Grützbauch R., Buitrago F., Ownsworth J., 2011, MNRAS, 413, 2845
Mortlock A. et al., 2013, MNRAS, 433, 1185
Mosleh M., Williams R. J., Franx M., 2013, ApJ, 777, 117
Newman A. B., Ellis R. S., Treu T., Bundy K., 2010, ApJ, 717, L103
Noeske K. G. et al., 2007, ApJ, 660, L47
Oesch P. A. et al., 2010, ApJ, 714, L47
Oke J. B., Sandage A., 1968, ApJ, 154, 21
Oser L., Ostriker J. P., Naab T., Johansson P. H., Burkert A., 2010, ApJ, 725, 2312
Ownsworth J. R., Conselice C. J., Mortlock A., Hartley W. G., Buitrago F., 2012, MNRAS, 426, 764
Ownsworth J. R., Conselice C. J., Mortlock A., Hartley W. G., Almaini O., Duncan K., Mundy C. J., 2014, MNRAS, 445, 2198
Parry O. H., Eke V. R., Frenk C. S., 2009, MNRAS, 396, 1972
Peebles P. J. E., Nusser A., 2010, Nature, 465, 565
Peng C. Y., Ho L. C., Impey C. D., Rix H.-W., 2002, AJ, 124, 266
Peng C. Y., Ho L. C., Impey C. D., Rix H.-W., 2010, AJ, 139, 2097
Pérez E. et al., 2013, ApJ, 764, L1
Petrosian V., 1976, ApJ, 209, L1
Quilis V., Trujillo I., 2012, ApJ, 752, L19
Ravindranath S. et al., 2004, ApJ, 604, L9
Reichard T. A., Heckman T. M., Rudnick G., Brinchmann J., Kauffmann G., 2008, ApJ, 677, 186
Richards G. T. et al., 2006, AJ, 131, 2766
Sachdeva S., 2013, MNRAS, 435, 1186
Saha K., Gerhard O., 2013, MNRAS, 430, 2039
Scannapieco C., White S. D. M., Springel V., Tissera P. B., 2009, MNRAS, 396, 696
Schlegel D. J., Finkbeiner D. P., Davis M., 1998, ApJ, 500, 525
Scoville N. et al., 2013, ApJS, 206, 3
Sersic J. L., 1968, Atlas de Galaxias Australes. Observatorio Astronomico, Cordoba, Argentina
Shen S., Mo H. J., White S. D. M., Blanton M. R., Kauffmann G., Voges W., Brinkmann J., Csabai I., 2003, MNRAS, 343, 978
Sheth K., Melbourne J., Elmegreen D. M., Elmegreen B. G., Athanassoula E., Abraham R. G., Weiner B. J., 2012, ApJ, 758, 136
Simard L., Mendel J. T., Patton D. R., Ellison S. L., McConnachie A. W., 2011, ApJS, 196, 11
Tremaine S., 1989, in Sellwood J. A., ed., Dynamics of Astrophysical Discs. Cambridge Univ. Press, Cambridge, p. 231
Trujillo I., Conselice C. J., Bundy K., Cooper M. C., Eisenhardt P., Ellis R. S., 2007, MNRAS, 382, 109
van der Wel A., 2008, ApJ, 675, L13
van der Wel A. et al., 2011, ApJ, 730, 38
van Dokkum P. G. et al., 2010, ApJ, 709, 1018
Watson L. C., Schinnerer E., Martini P., Böker T., Lisenfeld U., 2011, ApJS, 194, 36
Weinzirl T. et al., 2011, ApJ, 743, 87
Wolf C. et al., 2004, A&A, 421, 913
Wyse R. F. G., Gilmore G., Franx M., 1997, ARA&A, 35, 637
Zavala J., Avila-Reese V., Firmani C., Boylan-Kolchin M., 2012, MNRAS, 427, 1503

This paper has been typeset from a TEX/LATEX file prepared by the author.

Antireflection properties of graphene layers on planar and textured silicon surfaces

Nanotechnology **24** (2013) 165402 (8pp) doi:10.1088/0957-4484/24/16/165402

Antireflection properties of graphene layers on planar and textured silicon surfaces

Rakesh Kumar[1], A K Sharma[1], Mehar Bhatnagar[1], B R Mehta[1] and Shyama Rath[2]

[1] Thin Film Laboratory, Department of Physics, Indian Institute of Technology Delhi, Hauz Khas, New Delhi 110016, India
[2] Department of Physics and Astrophysics, University of Delhi, Delhi 110007, India

E-mail: brmehta@physics.iitd.ernet.in

Received 29 December 2012, in final form 20 February 2013
Published 27 March 2013
Online at stacks.iop.org/Nano/24/165402

Abstract
In this study, theoretical and experimental investigations have been carried out to explore the suitability of graphene layers as an antireflection coating. Microwave plasma enhanced chemical vapor deposition and chemically grown graphene layers deposited on polished and textured silicon surfaces show that graphene deposition results in a large decrease in reflectance in the wavelength range of 300–650 nm, especially in the case of polished silicon. A Si_3N_4/textured silicon reference antireflection coating and graphene deposited polished and textured silicon exhibit similar reflectance values, with the graphene/Si surface showing lower reflectance in the 300–400 nm range. Comparison of experimental results with the finite difference time domain calculations shows that the graphene along with a SiO_2 surface layer results in a decrease in reflectance in the 300–650 nm range, with a reflectance value of <5% for the case of graphene deposited textured silicon surfaces. The monolayer and inert character along with the high transmittance of graphene make it an ideal surface layer. The results of the present study show its suitability as an antireflection coating in solar cell and UV detector applications.

(Some figures may appear in colour only in the online journal)

1. Introduction

Graphene with its two-dimensional honeycomb lattice of tightly packed carbon atoms has attracted phenomenal interest due to its new physics and unique electronic, electrical, mechanical and optical properties. The mobility of charge carriers in suspended graphene samples goes up to 200 000 $cm^2\ V^{-1}\ s^{-1}$ for carrier densities below $5 \times 10^9\ cm^{-2}$ at temperatures near absolute zero [1, 2]. The experimentally measured values of thermal conductivity (at room temperature) and the thermoelectric power of graphene are 3000–5000 W mK^{-1} [3] and 50–100 $\mu V\ K^{-1}$ [4, 5], respectively. Recent experiments have established graphene as the strongest material with second-, third-order elastic stiffness and intrinsic strength for monolayer graphene of $340 \pm 50\ N\ m^{-1}$, $-690 \pm 120\ N\ m^{-1}$ and $42 \pm 4\ N\ m^{-1}$, respectively, corresponding to a Young's modulus of 1.0 ± 0.1 TPa [6]. Startlingly low absorption with high transmittance of 96–98% in the UV–visible region has been estimated for monolayer graphene [7, 8]. High electron mobility and high optical transmittance make it inherently attractive as a transparent electrode in optoelectronic devices and it has been used or proposed in a number of optical and electronic devices. A graphene–Si Schottky junction [9] has shown a photovoltaic conversion efficiency of 8.6% [10]. Graphene layers have also been used to modify the interface properties of a Ti–CuO–Cu junction where the introduction of multilayer graphene (MLG) in between CuO–Cu leads to the observation of bipolar resistive switching [11]. Due to its remarkable optoelectronic properties, a number of reviews have highlighted that graphene is likely to benefit photovoltaics devices as a near transparent electrode and antireflection coating [12–17]. This study is a first attempt to examine the suitability of few-layer graphene as an antireflection coating on polished and textured silicon, which are commonly used in solar cell structures.

An antireflection coating (ARC) is an integral part of optoelectronic device fabrication technology. For a fixed wavelength, the phase relationship condition requires the optical thickness of the layer (the refractive index multiplied by the physical thickness) to be equal to a quarter the wavelength of the incoming wave and the refractive index to be the geometric mean of the refractive index of the semiconductor and air. For photovoltaic applications, the reflectance is minimized for a wavelength of 0.6 μm which is close to the maximum power point of the solar spectrum. By increasing the number of layers of different refractive index and thickness, the reflectance can be decreased over a wider spectral range. In silicon solar cell technology, texturing of the silicon surface using chemical etchants and subsequent coating of silicon nitride (Si_3N_4) is commonly used to reduce the reflection losses from 40–58% for polished Si to 5–15% [18]. The monolayer character of a graphene layer makes it an ideal surface layer which can adhere well to a planar, textured or corrugated surface.

We report the antireflection properties of graphene films on polished surface (PS) and chemically textured surface (TS) commonly used in Si solar cell technology. Graphene layers formed by microwave plasma enhanced chemical vapor deposition (MPCVD) and chemical methods (chemically prepared graphene, RGO) are dispersed on silicon surfaces and reflectance was measured in the wavelength range 300–650 nm. The experimental results are compared with those for a standard Si_3N_4 ARC used in silicon solar cell technology. The optical properties of graphene layers having different configurations on silicon surfaces were studied using the finite difference time domain (FDTD) simulation [19]. The measured reflectance for both types of graphene deposited substrates was compared with simulated results.

2. Experimental details

Two types of graphene layers (i) prepared using the MPCVD technique (designated as 'G1') and (ii) prepared using a chemical route (RGO) procured from ACS Materials USA (designated as 'G2') were used in this study.

The graphene films were grown on 25 μm thick Cu foil (99.98%, Sigma Aldrich, item no. 349208) using the MPCVD technique with CH_4, H_2 and Ar as the precursor forming gases. Before deposition, Cu foil was cleaned in acetic acid followed by de-ionized water and isopropyl alcohol to remove the copper oxide present at the surface. Keeping the copper foil substrate at a temperature of about 750 °C, a plasma was created by using H_2 (400 sccm) and Ar (30 sccm) at a gas pressure of 30 Torr with a microwave (2.45 GHz) power of 1.5 kW. After annealing the Cu foil for about 20 min, CH_4 (10 sccm) was introduced and a graphene layer was deposited for 5 min. The substrate was allowed to cool down naturally. Flow of all the gases was stopped as the temperature reached close to room temperature.

To study the deposition and optical properties of graphene deposition of Si, the graphene from the Cu foil was transferred onto a Si substrate. The transfer process involved several steps [20]. In the first step, polymethylmethacrylate (PMMA) (Sigma Aldrich, average $M_W \sim 996\,000$, item no. 182265, 6 wt% in anisole) was spin coated on one side of the Cu foil. The other side of the Cu foil was exposed to O_2 plasma to remove graphene from that side since graphene growth is known to take place on both sides of Cu foil. In a second step, Cu foil was etched out using $FeCl_3$ (10%, wt/vol.) for 3–4 h and subsequently PMMA/graphene film was cleaned several times in a bath of de-ionized water and carefully transferred to a quartz and silicon substrate. Thereafter, the sample was allowed to dry for 12 h and then PMMA was removed using acetone for 5 h at a temperature of 50 °C. The sample was further treated for 5 h in a H_2 (200 sccm) and Ar (30 sccm) environment at a temperature of 450 °C to remove the remaining traces of PMMA [20, 21].

Chemically prepared graphene films (containing ~92% carbon, <8% oxygen) produced via thermal exfoliation reduction and hydrogen reduction of single-layer graphene oxide was obtained from ACS Material USA and was also used for studying the deposition and optical properties of graphene deposition on Si substrate. The 2 mg of as-obtained graphene powder was dispersed in 5 ml of *N*, *N*-dimethylformamide (DMF) organic solvent, which exhibited long-term dispersion stability, using ultra-sonication and further spin coated on the desired substrate [22].

Raman spectroscopic measurements were carried out in backscattering geometry using the 514.5 nm line of the Ar^+ laser for excitation. The scattered light was analyzed with a Renishaw spectrometer and a charged couple device was employed for detection. A Quanta 3D FEI field emission scanning electron microscope (FESEM) was used to ascertain the morphology of the graphene films. Atomic force microscopy (AFM) was done in contact mode using a Nanoscope IIIa instrument from Digital Instruments, USA. All the optical spectra were recorded on a Perkin–Elmer Lambda 35 UV/Vis spectrophotometer.

As already mentioned, polished planar and anisotropically etched textured silicon surface substrates are used in the present study. A chemically and mechanically polished p-type Czochralski silicon wafer substrate (⟨100⟩ oriented, 300 μm thick, textured Si substrate having a pyramid structure of height 8–12 μm) was used for the study. A polished Si substrate as obtained from the supplier was used in the present study without removing native oxide. In textured Si samples, the final step of oxide removal after texturing the Si was also not carried out. The textured Si substrate reduces the net reflection of visible light and thereby increases optical absorption in silicon. As silicon nitride (Si_3N_4) is widely used in the industrial manufacture of Si solar cells as an ARC we chose a plasma enhanced chemical vapor deposited Si_3N_4 of thickness ~80 nm coating as a reference to compare the antireflection properties of graphene deposited on planar and textured silicon surfaces.

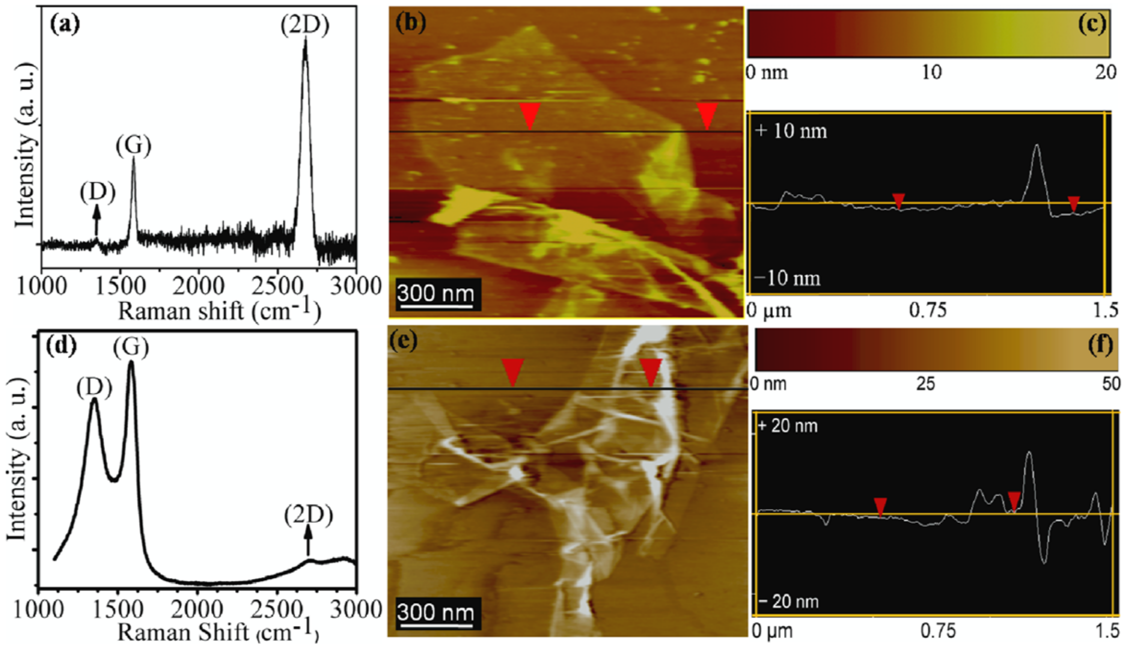

Figure 1. The Raman spectra, AFM micrograph and section profile are shown in (a), (b) and (c) for G1; and (d), (e) and (f) for G2, respectively.

3. Result and discussion

3.1. Elemental and morphological characterization of graphene films

Figure 1(a) shows the Raman spectra of graphene deposited on Cu foil using the MPCVD method. As is well known, the three most prominent features of graphene, corresponding to the D peak at ~1350 cm^{-1}, the G peak at ~1580 cm^{-1} and the 2D peak at ~2680 cm^{-1}, are observed [23]. The D peak is a defect-induced Raman feature observed due to disorder or defects at the edge of the graphene. The G peak is known to be an indication of the sp^2 carbon networks in the sample. In our sample, the intensity of the D peak is quite small which indicates defect-free growth of the graphene film. The 2D peak originates from a second-order Raman process and can be used to determine the thickness of graphene. The intensity ratio (I_{2D}/I_G) higher than 1.9 indicates the formation of single-layer graphene in the presented sample [24]. The thickness of graphene was further confirmed by using section profile analysis of the AFM image. Figure 1(b) shows the AFM image of the graphene layer on the Si substrate. Some wrinkles may be seen in the graphene film. The thickness of the graphene film calculated from the section profile analysis, as shown in figure 1(c), has been observed to be 0.352 nm, which indicates the presence of a single layer of graphene [25]. This is in good agreement with the results obtained from the intensity ratio of the 2D peak to the G peak in Raman spectra.

Figure 1(d) shows the Raman spectra of chemically prepared graphene (RGO). The dominance of the D peak in the Raman spectra indicates the presence of disorder in the RGO film. This may be due to the presence of folding as well as the residual oxygen and point defects in the RGO film. Figures 1(e) and (f) show the AFM and section profile images of RGO film, respectively. Some wrinkles and folding in the RGO film could be clearly seen. The thickness of the RGO film calculated from the section profile analysis, as shown in figure 1(f), has been observed to be 1.21 nm. At some points, the thickness seems to be higher due to the presence of the folding and wrinkles in the RGO film. The presence of functional groups, structural defects and adsorbed water molecules is known to result in a greater thickness of the RGO monolayer compared to monolayer graphene prepared by the MPCVD method [25–27].

Figure 2 shows a FESEM micrograph of graphene layers deposited on silicon surfaces of polished samples G1–PS (figure 2(a)) and G2–PS (figure 2(c)) and textured samples G1–TS (figure 2(b)) and G2–TS (figure 2(d)). In sample G1–PS, graphene with some wrinkles is observed to follow most of the specimen surface. In sample G1–TS, graphene appears to be well settled on the pyramids. In sample G2–PS, graphene layers are non-uniformly deposited and seem to be agglomerated in comparison to sample G1–PS. In sample G2–TS, graphene seems to be unattached to the pyramids at a number of points.

3.2. Optical characterization of graphene films

Figure 3(a) illustrates the transmittance spectra of graphene film G1 on quartz glass (sample G1–Q), showing 88–97% transmittance in the 300–650 nm wavelength range. This is considered to fulfil the provision of a transparent coating in solar cell and other optoelectronic devices [28]. The reflectance spectra show that the graphene overlayer on the polished Si surface on sample G1–PS results in a drastic

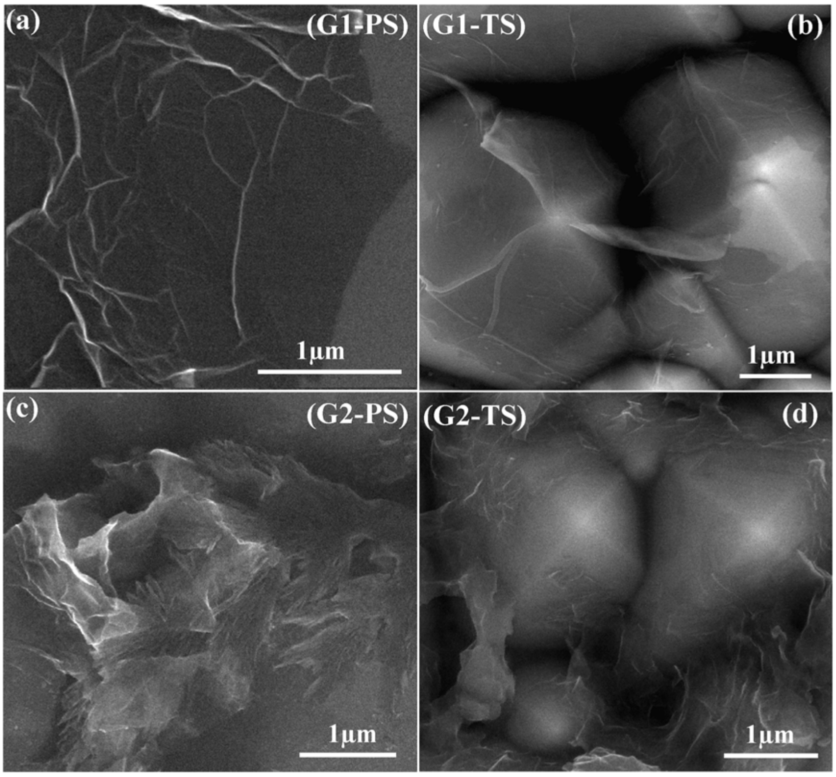

Figure 2. FESEM micrograph of MPCVD prepared graphene film G1 transferred on (a) polished Si (G1–PS) and (b) textured Si (G1–TS) substrate and chemically prepared graphene film G2 spin coated on (c) polished Si (G2–PS) and (d) textured Si (G2–TS) substrate, respectively.

reduction in the reflectance value from 88–43% to 17–11% in the 300–650 nm wavelength range. In the case of the graphene layer on a textured Si surface in sample G1–TS, a reduction in reflectance from 19–15% to 8–14% in the 300–650 nm wavelength range is observed. It may be noted that although the reflectance of sample G1–TS is 8% lower than that of sample G1–PS (17%), reduction in the reflectance value on graphene deposition is more in G1–PS than in G1–TS, with respect to the PS and TS samples without a graphene layer.

Figure 3(b) shows the transmittance spectra of graphene film G2 on quartz glass (sample G2–Q) and shows 82–92% transmittance in the 300–650 nm wavelength range. The transmittance value of sample G2–Q is lower than that of sample G1–Q. This may be due to the difference in the quality and thickness of the RGO monolayer from that of the graphene layer prepared by MPCVD [25]. Graphene deposition on the polished Si surface sample G2–PS reduces the reflectance value from 88–43% to 77–35%, higher than that obtained for sample G1–PS in the 300–650 nm range. The reason for such a difference in the reflectance values may be attributed to the different morphology of graphene deposited on samples G1–PS and G2–PS, particularly noticeable in figures 2(a) and (c) respectively. This observation indicates the decisive role of graphene deposition morphology, and thereby of the deposition scheme, to exploit the antireflection characteristics of graphene. In the case of graphene deposition on the textured Si surface sample G2–TS the percentage reflectance decreases from 19–15% to 15–7% almost the same as that obtained for sample G1–TS in the 300–650 nm range.

Figure 3(c) illustrates a comparison of the reflectance spectra of MPCVD prepared graphene on a textured Si substrate (sample G1–TS) and chemically prepared graphene on a textured Si substrate (sample G2–TS) with the reference antireflection coating of silicon nitride (Si_3N_4) on a textured Si substrate (sample SN–TS) in the 300–650 nm wavelength range. It is important to note that the reflectance spectrum of sample SN–TS is about 30–9% in the 300–650 nm wavelength range with a peak value of 35% at 330 nm. The graphene overlayer on textured Si in sample G1–TS shows reflectance values of 8–13% in the 300–430 nm range, well below the reflectance values of SN–TS substrate in same range. In the wavelength range 440–650 nm, the reflectance value of 14% for the G1–TS sample is $\sim$4% more than the reflectance values of the SN–TS sample. In sample G2–TS, the reflectance values of 14–7% are better than the reflectance values for SN–TS in the 300–650 nm wavelength range.

In summary: (i) G1–TS and G2–TS respond with very similar reflectance values $<$15% in the 300–650 nm wavelength range; (ii) the G1–TS and G2–TS samples more or less follow the reference ARC sample SN–TS in the 450–650 nm range and are somewhat better in 300–400 nm wavelength range. The reflectance response of graphene deposited samples in the 300–400 nm UV region make them promising candidates for nanoscale ultraviolet

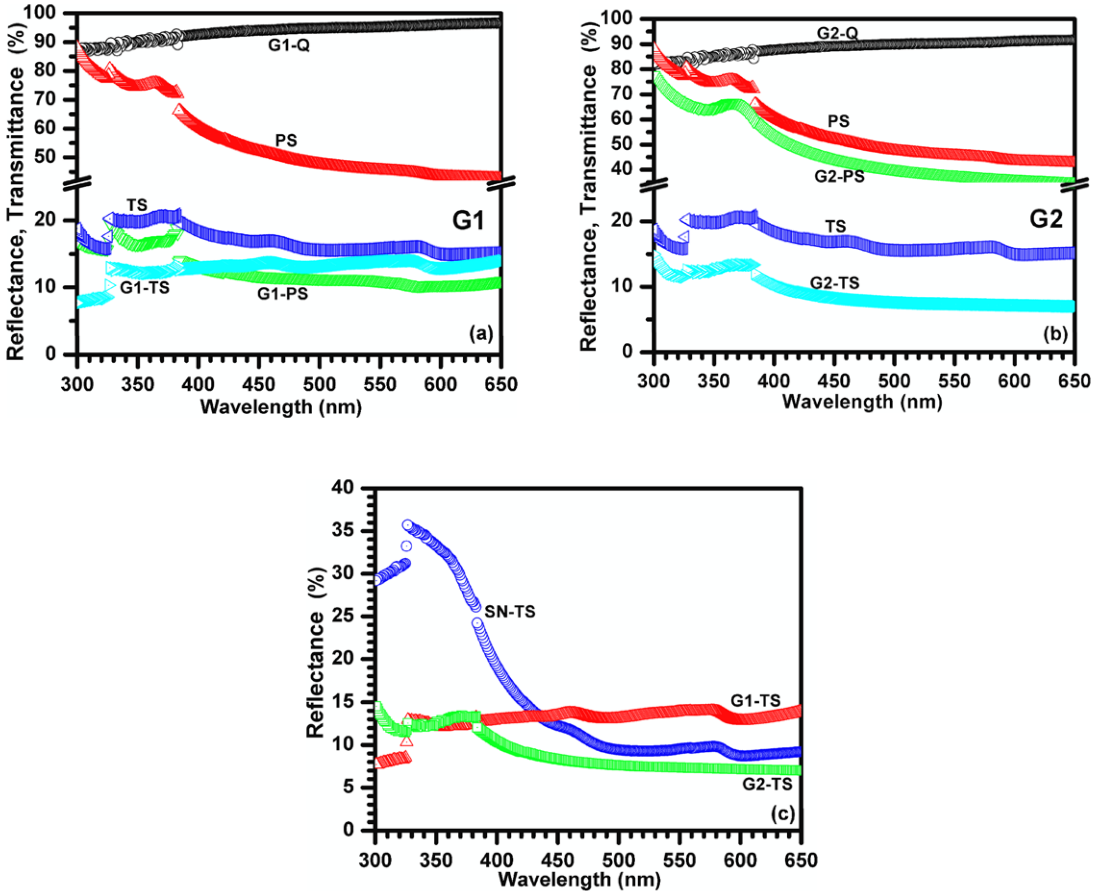

Figure 3. (a) Measured transmittance and reflectance as a function of wavelength of a MPCVD prepared graphene layer (G1) deposited on quartz glass (G1–Q) and polished Si (G1–PS) textured Si substrate (G1–TS), respectively. (b) Measured transmittance and reflectance as a function of wavelength of a chemically prepared graphene layer (G2) deposited on quartz glass (G2–Q) and polished Si (G2–PS) textured Si substrate (G2–TS), respectively. (c) Measured reflectance as a function of wavelength of reference silicon nitride ARC on textured Si (SN–TS) MPCVD prepared graphene layer (G1) and chemically prepared graphene layer (G2) deposited on textured Si substrate.

photo-detectors and other UV sensitive photo-electronic devices [29].

3.3. Reflectance spectra of different model configurations using FDTD simulation

The effect of graphene deposition on the reflectance of polished and textured Si surfaces was also evaluated using FDTD simulation via the Lumerical package [19]. A plane light wave was launched normally to the substrate. Perfectly matched layer (PML) conduction was used for the boundary of the simulation window, which absorbs the energy without inducing any reflection. An override mesh of 0.5 nm was used to resolve the graphene film. In this simulation, graphene of thickness 1 nm with optical constants taken from [30, 31] was used in the simulation models. The simulation models are as follows: I, polished Si (PS); II, polished Si with two graphene layers (PS + G + G); III, polished Si with SiO_2 (PS + SO); IV, polished Si with SiO_2 layer and two graphene layers (PS + SO + G + G); V, textured Si (TS); VI, textured Si with two graphene layers (TS + G + G); VII, textured Si with SiO_2 (TS + SO); VIII, textured Si with SiO_2 layer and two graphene layers (TS + SO + G + G). In this simulation, graphene is assumed to be a normal bulk material with the thickness of each layer being 1 nm, the thickness of SiO_2 40 nm and the pyramid height of the textured Si surface 1 μm. As already mentioned in the experimental section, the native oxide on Si samples (PS and TS) was not etched out. Therefore, the 40 nm thickness of SiO_2 assumed in the FDTD simulation corresponds to the native oxide.

Figure 4(a) shows the reflectance spectra of model configuration (I–IV) in the case of a polished Si (PS) surface in the 300–650 nm wavelength range. The reflectance of a bare polished Si substrate without graphene or SiO_2 overlayers is calculated as 60–34%. On assuming two graphene layers on polished Si the reflectance drops to 47–32% in the 300–650 nm wavelength range. The presence of a SiO_2 overlayer on polished Si significantly affects the reflectance value. With a 40 nm thick SiO_2 layer the reflectance value reduced to 38–28% on polished silicon. Subsequently, an addition of two graphene layers of thickness 1 nm each reflectance was found to reduce 20–24% in the 300–650 nm wavelength range.

Figure 4(b) shows the reflectance spectra of model configurations (V–VIII) in the case of a textured Si (TS) surface in the 300–650 nm wavelength range. Reflectance of a

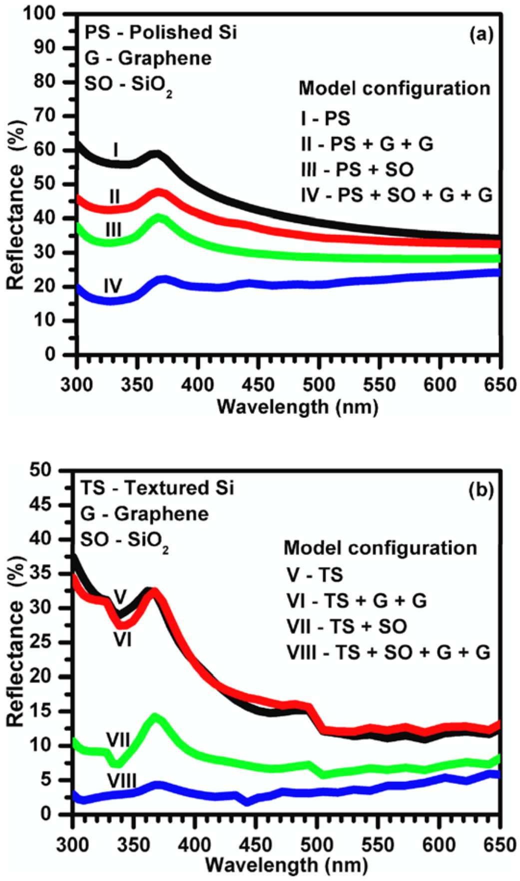

Figure 4. Calculated reflectance as a function of wavelength of different model configurations: (a) I, polished Si (PS); II, polished Si with two graphene layers of thickness 1 nm each (PS + G + G); III, polished Si with 40 nm thick SiO_2 (PS + SO); IV, polished Si with 40 nm thick SiO_2 and then two graphene layers of thickness 1 nm each (PS + SO + G + G); (b) V, textured Si (TS), textured Si with two graphene layer of 1 nm thickness each (TS + G + G); VI, textured Si with 40 nm thick SiO_2 (TS + SO); and VII, textured Si with 40 nm thick SiO_2 and then two graphene layer of thickness 1 nm each (TS + SO + G + G).

bare textured Si substrate without graphene or SiO_2 overlayers is 37–12%. The difference in the reflectance value from the experimentally measured 19–15% in the 300–650 nm wavelength range may be due to difference between pyramids height of the experimental textured Si substrate and the theoretically assumed values. On assuming two graphene layers on a textured Si surface, no significant change was observed in reflectance values. With a SiO_2 overlayer on a textured Si surface the reflectance attains 10–8% in the 300–650 nm wavelength range. Subsequent addition of two graphene layers of thickness 1 nm causes the reflectance to drop to 3–6% in the 300–650 nm wavelength range.

3.4. Electric field intensity distribution of different model configurations using FDTD simulation

In order to see the light trapping effect via the electric field intensity distribution inside and around the Si material for different model configurations of polished Si and textured Si surfaces at wavelengths of 300 and 600 nm, two-dimensional FDTD simulation [19] was carried out. The model configurations assumed for this are: (i) textured Si with silicon nitride (TS + SN) as reference antireflection model configuration; (ii) polished Si with SiO_2 and then two graphene layers (PS + SO + G + G) and (iii) textured Si with SiO_2 and then two graphene layers (TS + SO + G + G). These model configurations will be referred as M1, M2 and M3, respectively. Here again we assume graphene to be a normal bulk material with the thickness of each layer being 1 nm, the thickness of silicon nitride is 80 nm, the thickness of SiO_2 is 40 nm and the pyramid height of textured Si surface is 1 μm.

From figures 5(a)–(c), at 300 nm, the electric field intensity distribution for the reference antireflection model configuration M1 shows that the light in not well trapped inside the Si pyramidal structure and the magnitude of intensity is lower outside Si for model configurations M2 and M3. This observation states that the reflectance is less for model configurations M2 and M3 in comparison with M1. This is consistent with the experimental results of lower reflectance for sample G1–PS and G1–TS shown in figure 3(a). At 600 nm, the electric field intensity distribution of the reference antireflection model configuration M1 shows weak intensity outside the Si pyramidal structure, also followed by model configurations M2 and M3, consistent with its antireflection properties at this wavelength value shown in figure 3(c). The electric field intensity distribution shown in figure 5(c) implies that the model configuration M3 has lower reflectance than the reference antireflection model configuration M1 at 300 nm and almost the same reflectance at 600 nm.

The comparison of experimental and simulated results shows that the presence of SiO_2 and a graphene layer, on both PS and TS substrates, results in a significant reduction in reflectance values throughout the UV–visible spectral range. Both PS and TS substrates used in the experimental investigation are expected to have 20–40 nm of SiO_2. The assumption of a 1 nm thick graphene layer in the calculation was done keeping in mind the two to three monolayer graphene, especially in case of the chemically prepared sample G2. It is important to note that without the presence of SiO_2 layer, inclusion of two to three graphene layers in the model configuration did not result in a significant reduction in reflectance. It is worth noting that graphene transferred onto silicon substrates has some wrinkles and defects. Especially in the case of textured Si (as shown in figures 2(b) and (d)), poor adhesion seems to have resulted in locally suspended and loosely adherent graphene. This can significantly affect the transmittance value.

It is clear that a SiO_2 overlayer is essential to realize the antireflection properties of graphene. Similar inferences have been drawn in a study on the identification of graphene by the total color difference method, which shows that a 72 nm thick Al_2O_3 film is most suited for this purpose [32]. Normally SiO_2 or Si_3N_4 films are used for graphene identification [33]. These results indicate that the dielectric thickness and number of graphene layers can be the control parameters to reduce the reflectance of the silicon substrate in a particular wavelength range. Near field enhancement of plasmonic nanostructures

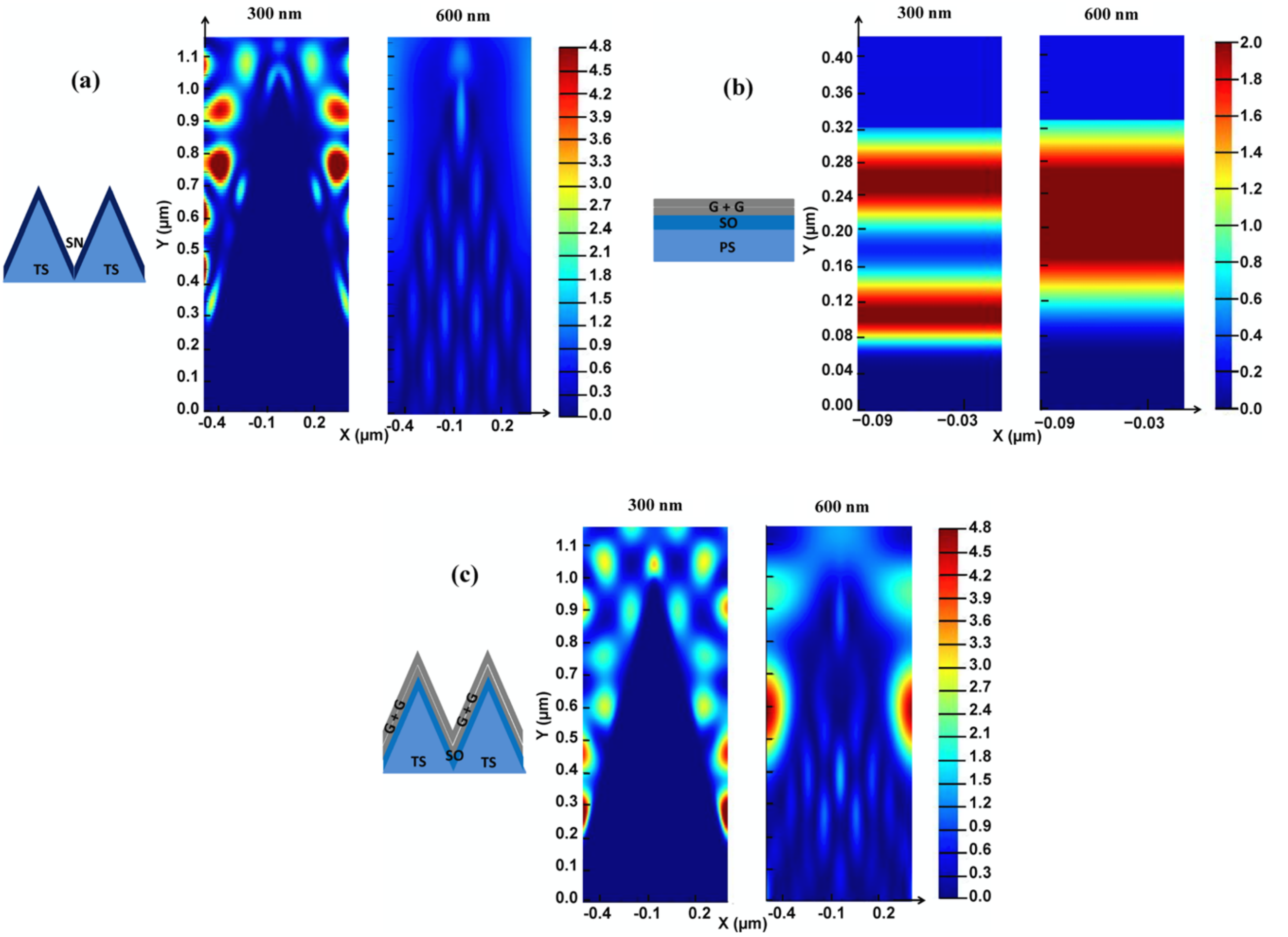

Figure 5. FDTD simulated electric field intensity distribution for different model configurations: (a) M1, silicon nitride reference antireflection coating on textured Si (TS + SN); (b) M2, polished Si with SiO_2 and then two graphene layers (PS + SO + G + G); and (c) M3, textured Si with SiO_2 and then two graphene layers (TS + SO + G + G). The vertical scale Y (μm) is the silicon to source stack height and the horizontal scale X (μm) is material width.

has been used to explain the spectral selectivity of graphene layers [34]. A combination of high Fermi velocity in graphene and the presence of high electric field at the graphene–silicon interface has been proposed to explain the high quantum efficiency of graphene-layer-based photovoltaic cells [35]. An increased degree of field enhancement and interaction strength has been proposed in graphene layers having 2D, 1D and 0D confinement [36]. In addition to refractive index matching, the above effects may also influence the reflectance and the antireflection properties of graphene layers deposited on a silicon surface. The inert nature of the graphene layer may be an additional advantage in antireflection applications. It may be interesting to explore the passivation properties of graphene on silicon surfaces.

4. Conclusion

We have studied the optical reflectance of few-layer MPCVD and chemically grown graphene deposited on polished and textured silicon surfaces and compared these results with the Si_3N_4/textured silicon reference ARC. The results of the present study show that the graphene overlayers result in a large decrease in reflectance in the wavelength range of 300–650 nm, with an enormous decrease in case of polished silicon. Si_3N_4 reference antireflection coating and graphene deposited polished and textured silicon is observed to have similar reflectance values in the 450–650 nm range. In the 300–400 nm range, graphene/Si surfaces show significantly lower reflectance values (8–10% in comparison to about 30% in the case of Si_3N_4). The FDTD calculations show that the presence of a SiO_2 intermediate layer is an important requirement for the observed decrease in reflectance in the 300–650 nm range. It is conjectured that thickness of SiO_2 and the number of graphene layers can be varied to achieve low reflectance in a desired wavelength range. Deposition of graphene onto large areas seems to be important for exploiting its antireflection properties for photovoltaic and other optoelectronic applications.

Acknowledgments

The authors thank Ms Pratha Jhawar, Mr S Ravi and Mr Saji Salkalachen from the Semiconductor Device and Photovoltaic Department, BHEL, Bangalore, for discussion related to this work.

References

[1] Du X, Skachko I, Barker A and Andrei E Y 2008 Approaching ballistic transport in suspended graphene *Nature Nanotechnology* **3** 491–5

[2] Pati S K, Enoki T and Rao C N R (ed) 2011 *Graphene and its Fascinating Attributes* (Singapore: World Scientific)

[3] Balandin A A 2011 Thermal properties of graphene and nanostructured carbon materials *Nature Mater.* **10** 569–81

[4] Wei P, Bao W, Pu Y, Lau C N and Shi J 2009 Anomalous thermoelectric transport of dirac particles in graphene *Phys. Rev. Lett.* **102** 166808

[5] Checkelsky J G and Ong N P 2009 Thermopower and Nernst effect in graphene in a magnetic field *Phys. Rev.* B **80** 081413

[6] Lee C, Wei X, Kysar J W and Hone J 2008 Measurement of the elastic properties and intrinsic strength of monolayer graphene *Science* **321** 385–8

[7] Nair R R, Blake P, Grigorenko A N, Novoselov K S, Booth T J, Stauber T, Peres N M R and Geim A K 2008 Fine structure constant defines visual transparency of graphene *Science* **320** 1308

[8] Lee C, Kim J Y, Bae S, Kim K S, Hong B H and Choi E J 2011 Optical response of large scale single layer graphene *Appl. Phys. Lett.* **98** 071905

[9] Li X, Zhu H, Wang K, Cao A, Wei J, Li C, Jia Y, Li Z, Li X and Wu D 2010 Graphene-on-silicon Schottky junction solar cells *Adv. Mater.* **22** 2743–8

[10] Miao X, Tongay S, Petterson M K, Berke K, Rinzler A G, Appleton B R and Hebard A F 2012 High efficiency graphene solar cells by chemical doping *Nano Lett.* **12** 2745–50

[11] Singh B, Mehta B R, Govind, Feng X and Mullen K 2011 Electronic interaction and bipolar resistive switching in copper oxide–multilayer graphene hybrid interface: graphene as an oxygen ion storage and blocking layer *Appl. Phys. Lett.* **99** 222109

[12] Bae S *et al* 2010 Roll-to-roll production of 30-inch graphene films for transparent electrodes *Nature Nanotechnology* **5** 574–8

[13] Weber C M *et al* 2010 Graphene-based optically transparent electrodes for spectroelectrochemistry in the UV–vis region *Small* **6** 184–9

[14] Wu J, Agrawal M, Becerril H A, Bao Z, Liu Z, Chen Y and Peumans P 2009 Organic light-emitting diodes on solution-processed graphene transparent electrodes *ACS Nano* **4** 43–8

[15] He M, Jung J, Qiu F and Lin Z 2012 Graphene-based transparent flexible electrodes for polymer solar cells *J. Mater. Chem.* **22** 24254–64

[16] Won R 2010 Photovoltaics: graphene–silicon solar cells *Nature Photon.* **4** 411

[17] Cooper D R *et al* 2012 Experimental review of graphene *ISRN Condens. Matter Phys.* **2012** 56

[18] Singh P K, Kumar R, Lal M, Singh S N and Das B K 2001 Effectiveness of anisotropic etching of silicon in aqueous alkaline solutions *Sol. Energy Mater. Sol. Cells* **70** 103–13

[19] Lumerical FDTD Solutions. www.lumerical.com

[20] van der Zande A M, Barton R A, Alden J S, Ruiz-Vargas C S, Whitney W S, Pham P H Q, Park J, Parpia J M, Craighead H G and McEuen P L 2010 Large-scale arrays of single-layer graphene resonators *Nano Lett.* **10** 4869–73

[21] Li X *et al* 2009 Large-area synthesis of high-quality and uniform graphene films on copper foils *Science* **324** 1312–4

[22] Paredes J I, Villar-Rodil S, Martínez-Alonso A and Tascón J M D 2008 Graphene oxide dispersions in organic solvents *Langmuir* **24** 10560–4

[23] Ferrari A C *et al* 2006 Raman spectrum of graphene and graphene layers *Phys. Rev. Lett.* **97** 187401

[24] Ferrari A C 2007 Raman spectroscopy of graphene and graphite: disorder, electron–phonon coupling, doping and nonadiabatic effects *Solid State Commun.* **143** 47–57

[25] Eda G, Fanchini G and Chhowalla M 2008 Large-area ultrathin films of reduced graphene oxide as a transparent and flexible electronic material *Nature Nanotechnology* **3** 270–4

[26] McAllister M J *et al* 2007 Single sheet functionalized graphene by oxidation and thermal expansion of graphite *Chem. Mater.* **19** 4396–04

[27] Stankovich S, Dikin D A, Piner R D, Kohlhaas K A, Kleinhammes A, Jia Y, Wu Y, Nguyen T S and Ruoff S R 2007 Synthesis of graphene-based nanosheets via chemical reduction of exfoliated graphite oxide *Carbon* **45** 1558–65

[28] Wang S J, Geng Y, Zheng Q and Kim J-K 2010 Fabrication of highly conducting and transparent graphene films *Carbon* **48** 1815–23

[29] Chitara B, Krupanidhi S B and Rao C N R 2011 Solution processed reduced graphene oxide ultraviolet detector *Appl. Phys. Lett.* **99** 113114

[30] Weber J W, Calado V E and van de Sanden M C M 2010 Optical constants of graphene measured by spectroscopic ellipsometry *Appl. Phys. Lett.* **97** 091904

[31] Bruna M and Borini S 2009 Optical constants of graphene layers in the visible range *Appl. Phys. Lett.* **94** 031901

[32] Gao L, Ren W, Li F and Cheng H-M 2008 Total color difference for rapid and accurate identification of graphene *ACS Nano* **2** 1625–33

[33] Jung I, Rhyee J-S, Son J Y, Ruoff R S and Rhee K-Y 2012 Colors of graphene and graphene-oxide multilayers on various substrates *Nanotechnology* **23** 025708

[34] Liu Y, Cheng R, Liao L, Zhou H, Bai J, Liu G, Liu L, Huang Y and Duan X 2011 Plasmon resonance enhanced multicolour photodetection by graphene *Nature Commun.* **2** 579

[35] Grigorenko A N, Polini M and Novoselov K S 2012 Graphene plasmonics *Nature Photon.* **6** 749–58

[36] Koppens F H L, Chang D E and García de Abajo F J 2011 Graphene plasmonics: a platform for strong light–matter interactions *Nano Lett.* **11** 3370–7

Applied Surface Science 256 (2010) 7091–7095

Contents lists available at ScienceDirect

Applied Surface Science

journal homepage: www.elsevier.com/locate/apsusc

Growth dynamics of pulsed laser deposited indium oxide thin films: a substrate dependent study

Neeti Tripathi[a,*], Shyama Rath[a], V. Ganesan[b], R.J. Choudhary[b]

[a] Department of Physics & Astrophysics, University of Delhi, Delhi 110007, India
[b] UGC-DAE Consortium for Scientific Research, University Campus, Khandwa Road, Indore 452017, India

ARTICLE INFO

Article history:
Received 2 April 2010
Received in revised form 3 May 2010
Accepted 3 May 2010
Available online 15 May 2010

Keywords:
Indium oxide
Pulsed laser deposition
XRD
Raman spectroscopy
AFM
Power spectral density

ABSTRACT

Indium oxide films are deposited by pulsed laser deposition in the presence of oxygen atmosphere, on different substrates, namely GaAs, Si, quartz, and glass. The structural, morphological, and interface characteristics are studied. Cubic In_2O_3 phase is confirmed by high resolution X-ray diffraction measurements. While the films on Si, glass, and quartz substrates are polycrystalline, the films on GaAs exhibit a preferred orientation along (2 2 2) plane. The structure and crystalline nature of the films are also confirmed by Raman spectroscopy. Furthermore, Raman spectra show the appearance of gallium oxide modes arising due to Ga diffusion from the substrate. The morphology of the films deposited on different substrates is studied by atomic force microscopy and *rms* roughness values are obtained. A two-dimensional power spectral density analysis has been used to calculate the growth exponent (α). A value of $\alpha > 1$ ($\alpha < 1$) for films grown on GaAs/Si (quartz/glass) substrates suggests that the growth on crystalline substrates is governed by the linear diffusion model, whereas the growth on amorphous substrates follows the dynamic scaling behaviour. UV–visible study shows a high optical transmittance of >90% and a band gap value of 3.64 and 3.79 eV for the films deposited on quartz and glass substrates, respectively.

1. Introduction

In_2O_3, belonging to the family of transparent conducting oxides (TCOs), has a remarkable combination of low electrical resistivity and high optical transmittance for visible light. It has potential applications in solar cells [1], large area display [2], and gas sensors [3]. In particular, for solar cells, apart from the optical and electrical requirements, an appropriate surface texturing is required for light scattering [4,5]. In order to achieve these conditions, a wide range of deposition techniques such as sputtering [6], molecular beam epitaxy [7], thermal evaporation [8], sol–gel [9], spray-pyrolysis [10], spin coating [11], and pulsed laser deposition [12] have been explored for the fabrication of In_2O_3 thin films. With each technique, a variety of surface morphologies could be realized. Pulsed laser deposition (PLD) is an attractive technique for the growth of high quality metal-oxide semiconductor films, in which a precise control over the electrical properties can be achieved by controlling the oxygen flux during deposition, which is difficult to maintain by any other methods. Moreover, PLD is recognized as a single step method since no further treatment such as post-annealing, which is commonly required in most other techniques, is necessary here. With these advantages, an appropriate selection of the substrate, which affects the crystallographic orientation, grain-size distribution, and its texture properties, is an important factor. Huang et al. [13] studied the effect of oxygen flow and bias voltage on the morphology of indium tin oxide (ITO) films and found that the grain size increased and surface roughness decreased with the increase of oxygen flow. Adurodija et al. [14] investigated the effect of substrate temperature on the electrical, microsctructural, and optical properties of pulsed laser deposited In_2O_3 thin films. They observed that films became smoother above 200 °C, whereas textured growth occurred for substrate temperatures between 50 and 150 °C. Ghosh et al. [15] studied the effect of substrate-induced strain on the growth of polycrystalline ZnO film fabricated by sol–gel process. ZnO films deposited on sapphire, glass, quartz, and Si show polycrystalline growth, whereas *c*-axis oriented growth occurred on GaN substrates due to minimum substrate-induced strain. However, the substrate dependence of the growth processes and the ensuing variations in surface morphology have not been investigated in any detail in TCOs.

The aim of our present work is to investigate the growth behaviour and microsctructural properties of pulsed laser deposited In_2O_3 films on GaAs ⟨1 1 1⟩, Si ⟨1 0 0⟩, quartz, and glass by atomic fore microscopy (AFM). Power spectral density (PSD) analysis is used to get a better insight into the mechanism involved in the growth process by calculating the scaling exponent. The crystal orientations of the deposited thin films are influenced by the substrate,

* Corresponding author. Fax: +91 11 27667061.
E-mail addresses: neetidtripathi@gmail.com, ntripathi@physics.du.ac.in (N. Tripathi).

0169-4332/$ – see front matter © 2010 Elsevier B.V. All rights reserved.
doi:10.1016/j.apsusc.2010.05.033

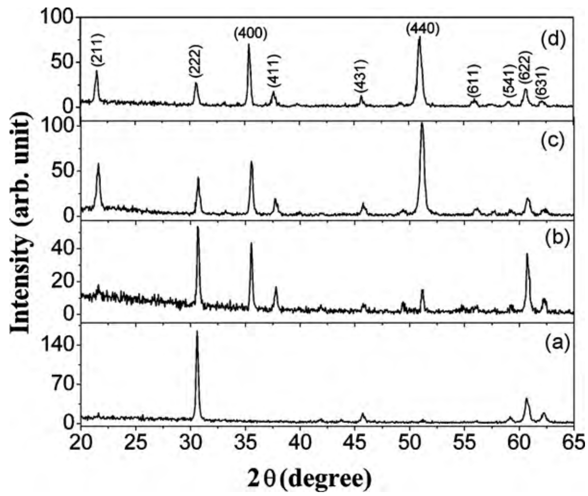

Fig. 1. XRD pattern of (a) In_2O_3/GaAs, (b) In_2O_3/Si, (c) In_2O_3/quartz, and (d) In_2O_3/glass.

as observed in the high resolution X-ray diffraction (HR-XRD). The nature of the interface is also revealed in the Raman spectra. Optical characteristics are investigated by UV–visible spectroscopy.

2. Experimental

In_2O_3 films were deposited by PLD on four different substrates (GaAs, Si, quartz, and glass). A KrF (248 nm) excimer laser operating at a repetition rate 10 Hz and an energy 220 mJ was used for deposition. A 1.5 cm diameter sintered In_2O_3 (Sigma–Aldrich, 99.99% In_2O_3 powder) pellet was used as a target. The target was mounted on a circular holder rotating with a speed of 15 rpm. The target to substrate distance was kept at 5 cm. The laser beam emerging from KrF excimer laser source is rectangular of dimensions ~12 mm × 12 mm [16]. It is focused onto the target using a lens placed outside of the deposition chamber. The energy density measured at target surface is ~1.8 J/cm^2. The total deposition area of the substrate was 1 cm× 1 cm. The deposition was performed in vacuum with a base pressure of 1.065×10^{-2} Pa. Substrate temperature was maintained at 450 °C and deposition carried out for 20 min. During deposition, oxygen pressure was maintained at 0.133 Pa by a mass flow controller. The thickness of the deposited films, as measured using a stylus profilometer, was around 200 ± 20 nm. HR-XRD patterns were recorded with a glancing angle of 1° using Cu K_α radiation (λ = 0.154 nm). Raman spectra were recorded at room temperature using the 488 nm excitation of an Ar ion laser. The scattered light was analysed with a Jobin Yvon Horiba LABRAM HR800 single monochromator and detected with a Peltier-cooled charge coupled device. The thin film morphology on a wide range of scan lengths (10, 5, 2, and 1 μm) was investigated by atomic force microscopy (AFM). The AFM measurements were performed using Nanoscope-E from Digital Instruments, USA. A 100 μm Si_3N_4 cantilever with a spring constant of ~0.57 N/m was used and the images taken in contact mode. The optical properties were measured by a Hitachi U-3300UV-VIS spectrophotometer.

3. Results and discussion

Fig. 1 shows the HR-XRD pattern of In_2O_3 film on different substrates. Peaks observed from the film can be indexed to bcc-cubic structure of In_2O_3 (JCPDS #71-2194). It is observed that the films on Si, glass, and quartz exhibit a polycrystalline nature showing random orientations along (2 1 1), (2 2 2), (4 0 0), (4 1 1), (4 3 1), (4 4 0), (6 1 1), (5 4 1), (6 2 2), and (6 3 1) planes. However, the XRD pattern on the GaAs ⟨1 1 1⟩ substrate shows the peak at a 2θ position 30.62° corresponding to the (2 2 2) plane is much more intense as compared to the other peaks corresponding to (4 3 1), (5 4 1), (6 2 2), and (6 3 1) planes. Prominent peaks from (2 1 1), (4 0 0), and (4 4 0) orientations on the Si, glass, and quartz substrates are however absent in GaAs. Recently, Liu et al. studied the growth of indium oxide on GaAs ⟨1 1 1⟩ substrate and inferred that the growth direction is limited by the orientation of the substrate, allowing the film to grow only parallel to the substrate orientation [17]. However, in general, the nucleation and crystal growth occurred throughout the films without being initiated exclusively on the substrate surface. This shows randomly oriented growth on Si, quartz, and glass. The biaxial strain in In_2O_3 film is calculated using the relation [18]:

Table 1
Lattice constant and biaxial strain values, calculated from XRD data.

Sample	Lattice constant (Å)	Strain (%)
In_2O_3/GaAs ⟨1 1 1⟩	10.1079 ± 0.0008	−0.14
In_2O_3/Si ⟨1 0 0>	10.0916 ± 0.0015	−0.25
In_2O_3/quartz	10.0846 ± 0.0007	−0.36
In_2O_3/glass	10.1226 ± 0.0011	+0.01

$$\varepsilon = \frac{c - c_0}{c_0} \times 100\% \qquad (1)$$

where c is the lattice parameter of strained film, calculated from XRD data, and c_0 is the lattice parameter of bulk In_2O_3 (JCPDS #71-2194). Estimated strain values for different substrates are given in Table 1. The strain is compressive for GaAs, Si, and quartz substrates, and almost negligible for glass substrate.

Fig. 2(a)–(d) shows the Raman spectra of In_2O_3 films on GaAs, Si, quartz, and glass substrates along with the Raman spectra of the bare substrates (dashed lines). In_2O_3 film shows the presence of five modes at the positions 132, 307, 366, and 496 cm^{-1}, and 625 cm^{-1}. The Raman spectrum of the films grown on Si substrate is masked by those of the Si substrate and only the sharp mode at 132 cm^{-1} is observed. In_2O_3 belongs to cubic C-type rare-earth oxide structure. The factor group analysis predicts $4A_g$ (Raman) + $4E_g$ (Raman) + $14T_g$ (Raman) + $5A_u$ (inactive) + $5E_u$ (inactive) + $16T_u$ (IR) modes [19]. The modes observed here correspond to bcc-In_2O_3, agreeing well with the values reported in the literature [20,21]. In general, the peak positions and widths of the Raman

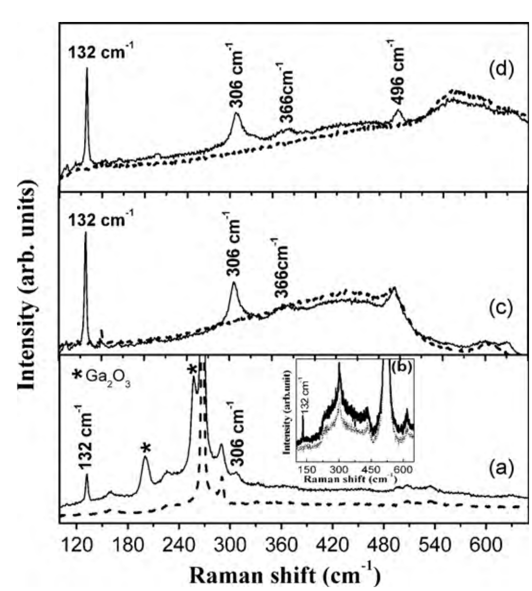

Fig. 2. Raman spectra of (a) In_2O_3/GaAs, (b)In_2O_3/Si, (c)In_2O_3/quartz, and (d) In_2O_3/glass.

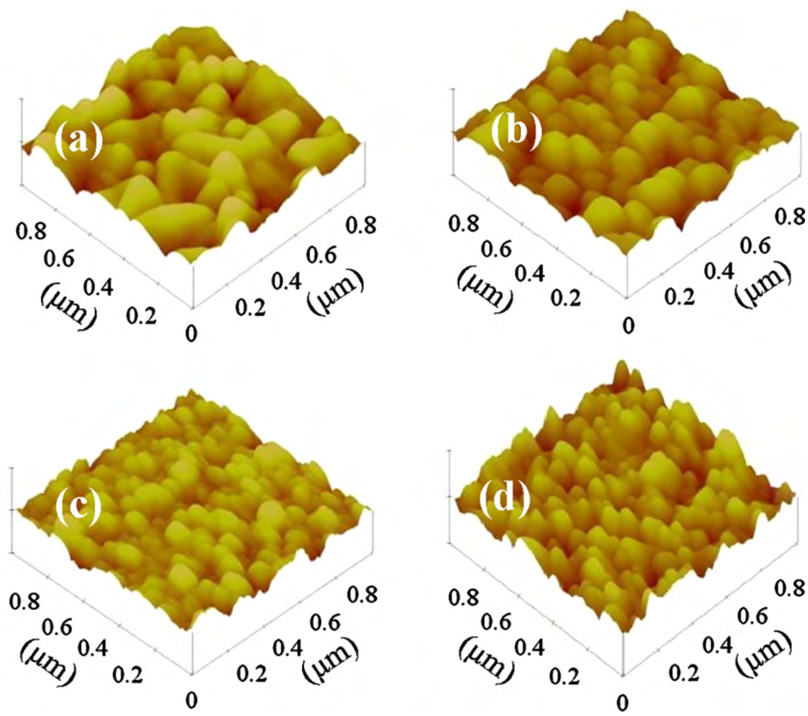

Fig. 3. AFM images of (a) In_2O_3/GaAs, (b) In_2O_3/Si, (c) In_2O_3/quartz, and (d) In_2O_3/glass.

modes for In_2O_3 phase in all the films indicate good quality crystalline nature of the films irrespective of the substrate used. The film deposited on GaAs substrate also shows a number of extra peaks at 200 and 253 cm^{-1} that are attributed to the Gallium oxide phase [22]. Gallium has a high affinity for oxygen and hence oxide formation at the interface is expected due to diffused Ga from the substrate interacting with the oxygen. Such a strong signal of the interface layer that is buried roughly 200 nm deep is a surprising result and shows the capability of Raman spectroscopy in thin film characterisation.

AFM images, depicting the surface morphologies of the In_2O_3 thin films resulting from growth on different substrates, are illustrated in Fig. 3(a)–(d). Films grown on GaAs and Si substrates consist of clusters of size 100–130 nm, whereas those on quartz and glass show comparatively smaller clusters of size 60–80 nm. Liu et al. suggested that excess oxygen partial pressure led to an increase of oxygen adatoms on the growing surface, which decreased the surface mobility of the indium adatoms and hence suppressed the process of clustering. But, in our case, oxygen partial pressure is maintained as a constant value for all depositions, and the difference is in the substrates used. This indicates that, apart from the oxygen partial pressure, film growth is also affected by the nature of the substrate. Most commonly, surface properties are characterized in terms of average roughness. The root mean square (*rms*) roughness is applied to characterize the vertical dimensions and defined as [23]:

$$\sigma = \sqrt{\frac{1}{n}\sum_{i=1}^{n}(s(x_i) - s_{av})^2} \tag{2}$$

where $s(x)$ is the surface height at point x on the surface profile and s_{av} is the average surface height. The *rms* roughness values for GaAs is ~6 nm, Si substrate ~12 nm, quartz ~6 nm, and glass ~6 nm. However, the *rms* roughness only gives an indication on the vertical dimensions of surfaces and not entire information of topography. It can be seen from the figures that lateral sizes are different. Therefore a spectral analysis is required to provide both the lateral as well as vertical information. A surface scaling analysis using PSD is used to determine the growth process determining the surface evolution. The PSD function describes the surface by several sinusoidal profiles with different periodic lengths and is related to the *rms* roughness in the simplified form by equation:

$$\sigma^2 = \int s(\omega) d\,\omega = \mathrm{PSD}_{\mathrm{total}} \tag{3}$$

Here $s(\omega)$ is the PSD frequency distribution given by [24],

$$s(\omega) = \frac{1}{L}\left|\int dx e^{i\omega x} zx\right|^2 \tag{4}$$

where ω is the frequency in the range from $1/L$ to $(N/2)/L$, where L is the scan length, N is the number of sample points and $z(x)$ is the line profile. Various kinds of surfaces have been analysed from the PSD spectra using scaling behaviour [25]. It is based on the Fast Fourier Transform (FFT) of individual line scans that comprise an area scan, squaring the amplitude of the Fourier coefficients to determine the "power" and averaging the 256 individual line scan powers at each frequency to generate PSD. Stated simply, the PSD shows the contribution to an image of different frequency features. It can be used to analyse the scaling behaviour according to

$$\mathrm{PSD}(k) \propto k^{-\gamma} \tag{5}$$

where k corresponds to the spatial frequency, the exponent γ is related to the height correlation exponent $\alpha = (\gamma - d)/2$, and d is the line scan dimension [26]. For our analysis $d = 2$, since the PSD curve is two-dimensional. The linear slope in PSD curve provides the scaling exponent (α). The two-dimensional PSD curve obtained from the AFM data is shown in Fig. 4. It consists of two distinct regions: the low frequency region representing the uncorrelated white noise and the high frequency region (straight line) representing the correlated surface features. The scaling exponents were extracted for all the samples from the linear region of the plots beyond the saturation seen. The estimated values of the scaling exponent for films

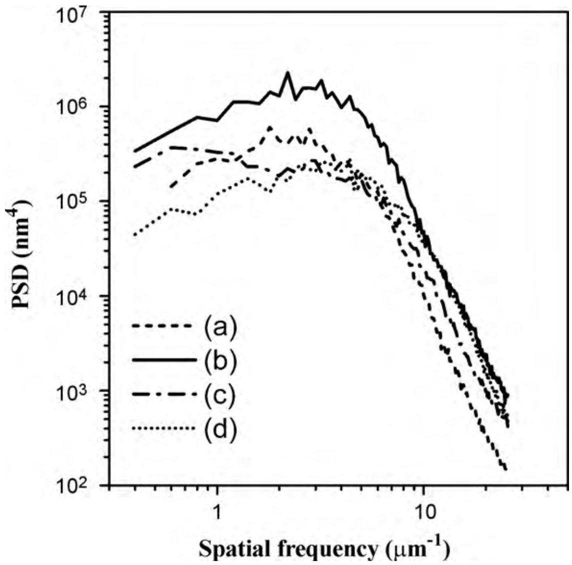

Fig. 4. PSD curves of (a) In_2O_3/GaAs, (b) In_2O_3/Si, (c) In_2O_3/quartz, and (d) In_2O_3/glass.

on GaAs, Si, quartz, and glass substrates are 1.09, 1.15, 0.24, and 0.23, respectively. Depending on the values of scaling exponent (α), different kinds of growth models, local and nonlocal, have been proposed [26–29]. For local models, the growth rate described by the nonlinear Kardar–Parisi–Zhang (KPZ) model [27,28] depends predominantly on the local properties of the interface. These models usually give a growth exponent $0 < \alpha < 1$. This behaviour has been described as a balance between the roughening mechanisms and smoothing processes such as surface diffusion so that the local structure remains unchanged.

For nonlocal models, the growth rate depends not only on the local properties of the interface, but also on the surrounding environment. In this situation, the roughening fluctuations and the smoothing effect cannot quite reach a balance. This type of behaviour is anomalous scaling, which give $\alpha \geq 1$ [29,30]. These scaling exponents suggest that the growth of In_2O_3 thin film on crystalline GaAs and Si substrates is governed by theoretical results that explained anomalous scaling behaviour dominated by the surface diffusion, whereas growth of the In_2O_3 thin film on the amorphous quartz and glass substrates corresponds to the KPZ dynamic scaling behaviour.

Fig. 5 shows the optical transmission spectra of In_2O_3 thin films on quartz and glass substrates. The average transmission of the In_2O_3 thin film over the wavelength range of 200–800 nm is high at T = 96%. The inset shows the dependence between $(\alpha h\nu)^2$, (α is the absorption coefficient) and the photon energy, $h\nu$, which indicates that the electronic transitions are direct across the band gap of the film. The optical band gap of the In_2O_3 thin films was estimated from the Tauc's relation

$$(\alpha h\nu)^2 = A(h\nu - E_g) \quad (6)$$

where E_g is the optical band gap and A is a constant. The extrapolation of the linear part of the curve onto the energy axis gives the optical band gap values of 3.64 and 3.79 eV for quartz and glass substrates, respectively, and is in good agreement with previous studies [31]. These values are well above the required values for optoelectronic applications of TCOs [5]. The resistivity was also measured using four-probe technique and was also reasonably low at around 10^{-3} Ω-cm for all the samples.

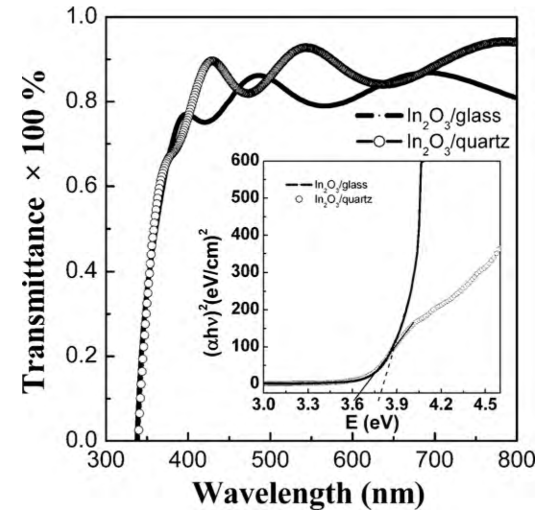

Fig. 5. Transmission spectra of In_2O_3 thin film deposited on glass and quartz substrates (inset shows the $(\alpha h\nu)^2$ vs $h\nu$ plot for extracting band gap).

4. Conclusions

High quality In_2O_3 films have been deposited by PLD without any post-deposition treatment. A moderate substrate temperature was sufficient to obtain crystalline films with high optical transparency. A combination of XRD, Raman, and AFM was used to study the structure and topographical variations of In_2O_3 films on different substrates. Polycrystalline growth of In_2O_3 films is observed on Si, quartz, and glass substrate, whereas highly oriented growth along (2 2 2) plane, parallel to the substrate orientation, is observed on GaAs ⟨1 1 1⟩ substrate. The Raman spectra further confirmed the structure and crystallinity. In addition, the spectrum on GaAs shows gallium oxide phonon modes due to gallium diffusion from the substrate. AFM images reveal that the film on each substrate realizes a different topography. Using a detailed analysis based on scaling behaviour of power spectral density function, it is proposed that the growth mechanism on the quartz and glass substrate is governed by the KPZ dynamic scaling behaviour, while on Si and GaAs substrates, it is dominated by the surface diffusion. Results of this work suggest that, while maintaining a high transparency and conductivity, a variety of textured surface of In_2O_3 films can be achieved by changing the substrate.

Acknowledgements

We are grateful to Prof. Ajay Gupta for access to the experimental facilities at IUC, Indore, India and for useful discussions. We thank Ms. Deepti Jain and Mr. Mohan Gangrade for their assistance in AFM measurements, and Mr. Manoj Kumar and Mr. Anil Gome for their technical support in PLD and HR-XRD, respectively. This work was supported by research funding under the UFUP scheme (Project Code No. 43301) of the Inter-University Accelerator Centre, New Delhi, and Delhi University R&D grant.

References

[1] G. Golan, A. Axelevitch, B. Gorenstein, A. Peled, Appl. Surf. Sci. 253 (2007) 6608–6611.
[2] A.M.E. Raj, K.C. Lalithambika, V.S. Vidhya, G. Rajagopal, A. Thayumanavand, M. Jayachandran, C. Sanjeevirajae, Physica B 403 (2008) 544–554.
[3] M. Suchea, N. Katsarakis, S. Christoulakis, S. Nikolopoulou, G. Kiriakidis, Sens. Actuators B 118 (2006) 135–141.
[4] S. Calnan, A.N. Tiwari, Thin Solid Films 518 (2010) 1839–1849.
[5] S. Prathiban, V. Gokulakrishnan, K. Ramamurthi, E. Elangovan, R. Martins, E. Fortunato, R. Ganesan, Solar Energy Mater. Solar Cells 93 (2009) 92–97.

[6] G.Q. Ding, W.Z. Shen, M.J. Zheng, Z.B. Zhou, Appl. Phys. Lett. 89 (2006) 063113–63123.
[7] E.H. Morales, Y. He, M. Vinnichenko, B. Delley, U. Diebold, New J. Phys. 10 (2008) 125030.
[8] V. Senthilkumar, P. Vickraman, Curr. Appl. Phys. 10 (2010) 880–885.
[9] M.A. Flores-Mendoza, R. Castanedo-Perez, G. Torres-Delgado, J. Márquez Marín, O. Zelaya-Angel, Thin Solid Films 517 (2008) 681–685.
[10] P. Pratap, G.G. Devi, Y.P.V. Subbaiah, K.T. Ramakrishna Reddy, V. Ganesan, Curr. Appl. Phys. 8 (2008) 120–127.
[11] L. Francioso, M. Russo, A.M. Taurino, P. Siciliano, Sens. Actuators B 119 (2006) 159–166.
[12] P.F. Xing, Y.X. Chen, S.-S. Yan, G.L. Liu, L.M. Mei, K. Wang, X.D. Han, Z. Zhang, Appl. Phys. Lett. 92 (2008) 022513–22523.
[13] J.Y. Huang, Y.-T. Jah, B.-S. Yau, C.-Y. Chen, H.-H. Lu, Thin Solid Films 370 (2000) 33–37.
[14] F.O. Adurodija, H. Izumi, T. Ishihara, H. Yoshioka, M. Motoyama, K. Murai, J. Vac. Sci. Technol. A 18 (3) (2000) 814–818.
[15] R. Ghosh, D. Basak, S. Fujihara, J. Appl. Phys. 96 (2004) 2689–2692.
[16] D.B. Chrisey, G.H. Hubler (Eds.), Pulsed Laser Deposition of Thin Films, Wiley Interscience, New York, 1994.
[17] H.F. Liu, G.X. Hu, H. Gong, J. Cryst. Growth 311 (2009) 268–271.
[18] K.J. Lethy, D. Beena, V.P.M. Pillai, V. Ganesan, J. Appl. Phys. 104 (2008) 033515–33611.
[19] O.M. Berengue, A.D. Rodrigues, C.J. Dalmaschio, A.J.C. Lanfredi, E.R. Leite, A.J. Chiquito, J. Phys. D: Appl. Phys. 43 (2010) 045401–45404.
[20] D. Liu, W.W. Lei, B. Zou, S.D. Yu, J. Hao, K. Wang, B.B. Liu, Q.L. Cui, G.T. Zou, J. Appl. Phys. 104 (2008) 083506–83515.
[21] M. Seethaa, S. Bharathia, A. Dhayal Raja, D. Mangalarajb, D. Nataraja, Mater. Charact. 60 (2009) 1578–1582.
[22] J. Zhang, F. Jiang, Chem. Phys. 289 (2003) 243–249.
[23] E. Marken, G. Maurstad, B.T. Stokke, Thin Solid Films 516 (2008) 7770–7776.
[24] R. Edrei, E.N. Shauly, A. Hoffman, J. Vac. Sci. Technol. B 18 (1) (2000) 41–47.
[25] D.C. Agarwal, R.S. Chauhan, D.K. Avasthi, S.A. Khan, D. Kabiraj, I. Sulania, J. Appl. Phys. 104 (2008) 024304–24308.
[26] N.K. Sahoo, S. Thakur, R.B. Tokas, Thin Solid Films 503 (2006) 85–95.
[27] D. Aurongzeb, M. Holtz, L. Menon, Appl. Phys. Lett. 89 (2006) 092501–92503.
[28] Z.-W. Lai, S.D. Sharma, Phys. Rev. Lett. 66 (1991) 2348–2351.
[29] D. Aurongzeb, M. Holtz, Latika Menon, Appl. Phys. Lett. 89 (2006) 092501–92503.
[30] A.E. Lita, J.E. Sanchez, J. Appl. Phys. 85 (1999) 876–882.
[31] N. Novkovski, A. Tanuševski, Semicond. Sci. Technol. 23 (2008) 095012–95014.

Interaction of zinc peroxide nanoparticle with fibroblast cell

Conference Paper · March 2016

4 authors:

Bharti Sharma
Kuruksheta University

Nahar Singh
Council of Scientific and Industrial Research (C...

R. P. Tandon
University of Delhi

Ajit Kumar Mahapatro
University of Delhi

Interaction of zinc peroxide nanoparticle with fibroblast cell

Bharti Sharma[1], Nahar Singh[2], Ram P. Tandon[1], Ajit K. Mahapatro[1*]

[1]*Department of Physics and Astrophysics, University of Delhi, Delhi, 110007, India*
[2]*Analytical Chemistry Division, CSIR-National Physical Laboratory, Dr. K. S. Krishnan Marg, New Delhi, 110012, India*

[*]Corresponding author: E-mail: amahapatro@physics.du.ac.in; Tel: (+91) 9871074984

Received: 09 April 2016, Revised: 23 August 2016 and Accepted: 17 April 2017

DOI: 10.5185/amp.2017/708
www.vbripress.com/amp

Abstract

This work demonstrates the structural interaction of the as-synthesized zinc peroxide (ZnO_2) nanoparticles with fibroblast cells (FBC). The ZnO_2 nanoparticles (ZNP) of desired sizes (10-20 nm) are synthesized, and the purity and structural confirmations are studied using various imaging and spectroscopic techniques. FBC (buffalo) lines are cultured in Dulbecco's modified Eagle's medium (DMEM) supplemented with 10% fetal bovine serum and penicillin (100 µg/mL), and with non-essential amino acid and vitamin as additional ingredients, followed by incubation at 37°C with continuous purging of the chamber using 5% CO_2. The fluorescent microscopic images are captured for the initial healthy and cultured FBCs, and after pouring the nanoparticles in the cultured FBCs. Healthy cell-growth is noticed during the cell culture process suggesting the formation of ZNP-FBC complexes without contamination and coagulation. After allowing the interaction of ZNPs with the FBCs, the presence of ZNPs only on the cell sites are observed without coagulation of ZNPs in the cell areas, suggesting the selective interference of ZNPs on the surface of the grown cell. The understanding of the interaction process of the ZNPs with the living cell, would provide the practical utilization of the ZNPs in nanomedicine and nano-drug delivery.

Keywords: Zinc peroxide (ZnO_2) nanoparticle (ZNP), fibroblast cell (FBC), ZNP-FBC interaction, cell metabolism, nano-drug delivery.

Introduction

The gain in knowledge on the interaction of nanomaterials with living cell could provide information about the possible accessibility to interfere with the living cell machinery without potentially triggering the side effects and toxicity. The nanoparticle and cell interaction is a crucial issue in nanomedicine and nanotoxicology. The ability of the molecular sized nanoparticles to invade the living cells through the cellular endocytosis machinery is an interesting aspect for identifying targeting cells and transporting essential drugs into the biological entity through nanoparticle processing. Utilization of nanoparticles in therapeutic and/or diagnostic agents for biomedical applications and for intracellular targets, it is requires the nanomaterials to enter the living cell. The advantages of the nanoparticles are their small size with unique size dependent properties, high reactivity and large surface area that allow them to interact with cell components.

The currently available diagnostic tools in clinical practice including magnetic resonance imaging, ultrasound, radio imaging, X-ray imaging, optical imaging, etc., do not facilitate comprehensive diagnostic visualization about a diseased cell/tissue/organ **[1-3]**. Investigation for understanding the interaction between the nanomaterials and living cell could lead to practical biomedical applications of nanomaterials. The mechanisms involved at the nano–bio interface comprises of the dynamic physicochemical interactions, kinetics and thermodynamic exchanges between nanomaterial surfaces and the surfaces of biological components including proteins, membranes, phospholipids, endocytic vesicles, organelles, DNA, and biological fluids. The factors describing the dynamical interaction includes, (i) the nanoparticle surface with physicochemical compositions, (ii) stress at the nanoparticle-cell interface due to the changes during the particle interaction with the surrounding medium, and (iii) interaction of nanoparticle and substrate at the contact zone of the biological entity.

The physico-chemical features of the nanoparticles are the determining factors for the nanoparticle-living cell interactions and consequently influence cell behaviour. The size and shape of the nanomaterials and chemical functionalities on the surface play a critical role in binding the nanomaterials to cell membrane and subsequent cellular uptake **[4-6]**. This motivates pursuing research towards the biological interference of nanoparticles and development of multi-model diagnostic probes that could facilitate the combination dignostics, preferably covering both the anatomical and physiological aspect of various disease **[7-8]** including the deadly cancer.

The advantage of nanoparticles such as ultra-small size, ease in synthesis, and biocompatibility are suitable for a variety of medical applications **[9-11]**. Nanoparticles present ideal platform for the fabrication of multimodal agents [12-13]. The structural nanoparticles, such as silica, biodegradable polymers, etc., which provide a matrix for hosting one or multiple active agents, including smaller functional nanoparticles with unique physical parameters defined in metallic and inorganic nanoparticles, quantum dots, etc. The surface of the nanomaterials can be aptly functionalized to enhance their circulation in the blood and targeting specificity **[14-16]**. Various kind of functional nanoparticles available, zinc oxide, iron oxide which have the most promising application in the field of medicine **[17-20].**

In a given medium, the most important nanoparticle characteristics that determine the surface properties are the material's chemical composition, surface functionalization, shape and angle of curvature, porosity and surface crystalinity, heterogeneity, roughness, and hydrophobicity or hydrophilicity **[21-23]**. Other quantifiable properties, such as effective surface charge (zetapotential), particle aggregation, state of dispersion, stability/biodegradability, dissolution characteristics, hydration and valence of the surface layer, are determined by the characteristics of the suspending media, including the ionic strength, pH, temperature and the presence of large organic molecule **[24]**. The media and bio-entity could also induce large scale changes in the nanomaterials properties including nanoparticle dissolution, ion leaching, phase transformation and agglomeration. The zinc peroxide nanoparticles have broad antibacterial activities against bacteria and fungus with biocompatible and non-toxic.

In this work, we have synthesized highly pure zinc peroxide (ZnO_2) nanoparticles (ZNPs) and demonstrated the interaction of the ZNPs with the Fibroblast cells (FBCs). The high purity of the ZNPs are characterized using advanced imaging and spectroscopic tools.

Experimental

Materials

The required chemicals zinc acetate, zinc nitrate, zinc sulphate, zinc chloride, sodium hydroxide, hydrogen peroxide, glycerol, polyvinaylpyrrilodone (PVP), tetra ethylamine (TEA), 3- mercaptopropoinic acid (MPA), acetone, methanol, ethanol etc. used in the synthesis of ZnO_2 of analytical grade and are purchased from E. Merck. Hydrochloric acid (35%) of GR Grade used after purify through sub–boiling distillation quartz glass device. De-ionized water used of 18.2 MΩ resistivity for all experimental work is prepared with Millipore milli-Q element water purification system, USA. The 1µg/ml standard stock solution of ZnO_2 is prepared in DMEM media. The pipettes, beakers, volumetric flask of various capacities used are of Borosil glass works India limited. The pipettes and volumetric flasks were calibrated prior to analysis following international standard procedure and protocol **[25]**. All the wet chemical digestion and dilution work is carried out in a laminar flow clean bench.

Synthesis of ZnO_2 nanoparticles

10 gm of zinc salt was dissolved in dilute ammonia solution and further diluted to 200 ml in 1:1 ratio of methanol and water. Varying quantity of PVP is added to this solution achieve desired particles size of ZnO_2. Further dilute hydrogen peroxide solution is added upto complete precipitation in solution is achieved maintain the pH of 9-11 at 50-55 °C temperature and stirred on magnetic stirrer for 1 hour. The precipitate formed is centrifuged at 8000 rpm followed by washing with de-ionized water and methanol for several time. Finally, the precipitate is dried at 105 ºC in an oven upto complete dryness **[26]**.

Cell culture and counting

The cell lines from different origins of tissues are utilized. Fibrobalast cell is grown in Dulbecco's modified Eagle's medium (DMEM) supplemented with 10% fetal bovine serum (FBS) and 1% penicillin/streptomycin. Cell suspension is added to 25 cm^2 vials and transferred into an incubator at 37 °C with 5% CO_2. After incubation, the cells trypsinized with 1% trypsin solution and rushed down from the bottom of 25 cm^2 vials when they are in a semi confluent state and still in log phase of growth. For analyzing the cell stability with various nanoparticles the cell was trypsinized and resuspended in fresh media, one day prior to treatment, 100000 cells per 1mL fresh media are added to each well of a sterilized 24-well plate, and transferred to the incubator for attachment and overnight growth. The next day, three different dosages of the various samples are added to the cells at a confluency of 70-80% and swirl mixed, transferred back to the incubator. After three days of incubation, the plate is taken out, and the cells in each well are washed three times with sterile PBS.

The density of cell is estimated by counting the numbers using hemocytometer.

Characterization

The ZnO_2 nanoparticles are characterized for the crystallographic phases by X-ray diffraction, XRD, (Bruker) model AXS D8 Advance Diffractometer. The data collection and analysis are carried out using Diffrac^{plus} software, while the diffractogram is rerecorded using CuKα radiation with a graphite monochromator in the diffracted beam. The shape and size of nanoparticlesare characterized using transmission electron microscopy, FEI, Netherland make, model F-30 G2 STWI. The cells are visualized under a fluorescent inverted microscope and photographed using a Nikon DIGITAL SIGHT DS-F11 Camera, NikonTS-100 (Nikon, Japan).

Results and discussion

The surface morphology of the ZnO_2 nanoparticle is imaged by using LEO 440 scanning electron microscope (SEM) at 5 kX magnifications and is shown in **Fig. 1**, which shows hexagonal morphologies of the as-synthesized ZNPs.

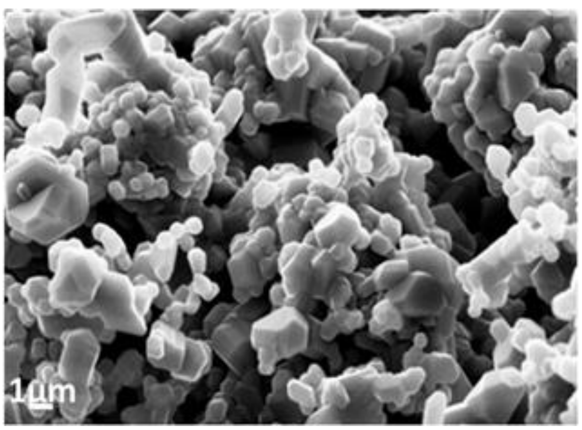

Fig. 1. SEM image of the as-synthesized ZnO_2nanocomposite

The EDX measurements, as represented in **Fig. 2**, recodes the contents of O and Zn of synthesized samples. The table in the inset of **Fig. 2**, shows the composition of the elemental O and Zn content present in the synthesized ZnO_2 nanocomposites, confirming the stoichiometric ratio of 1:2.

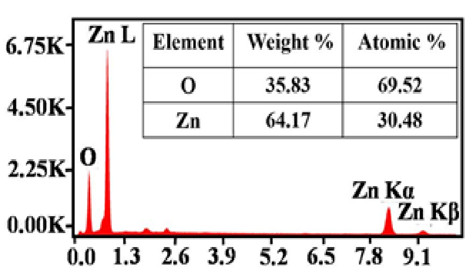

Fig. 2. Energy dispersive X-ray (EDX) spectroscopy for synthesized ZnO_2 nanocomposite. The table in the inset shows the composition of the elemental O and Zn content present in the synthesized nanocomposites.

The crystallography study of ZNPs is recorded using XRD patterns and a representative XRD pattern of the as-synthesized ZnO_2nanoparticles 2θ in the range of 20° to 80°is shown in **Fig. 3**. The observed diffraction pattern agrees well with the JCPDS data PDF # 13-0311, confirms the formation of a single-phase ZnO_2 nanoparticle. The crystallite size of 6±2 nm is estimated for the currently developed as-synthesized ZNPs using Scherrer's equation [**27**]. ZNP pellets are formed by the KBr Pellet technique of gentle mixing of ZnO_2 species with 300mg of KBr powder and compressed into discs at a force of 13kN for 5min using a manual tablet presser.

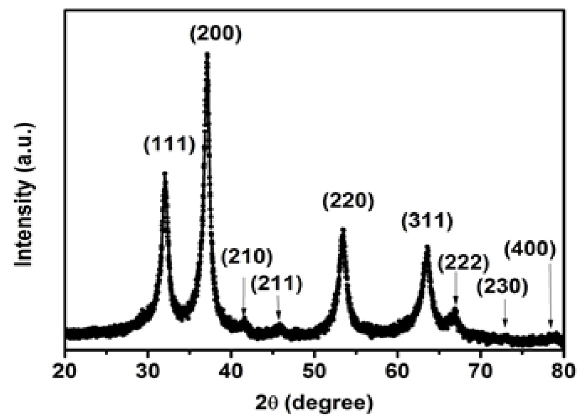

Fig. 3. XRD pattern of the as-synthesized ZnO_2nanocomposites having crystallite size 6±2 nm.

FTIR spectra of the resulting ZNP is recorded at room temperature and is plotted in **Fig. 4.** This shows the characteristic peak ZnO_2 absorption at 435–445cm^{-1} for the ZNPs. The peaks at 1040–1070cm^{-1}, 3200–3600cm^{-1}, and 1630–1660 cm^{-1} are originated from the O–O bands, water O–H stretching vibration mode, and OH bending of water, respectively. This indicates the presence of small amount of water adsorbed on the nanoparticles surface. Also, the existence of CO_2 molecule in the ambient air, there is FTIR peak at around 2360cm^{-1}.

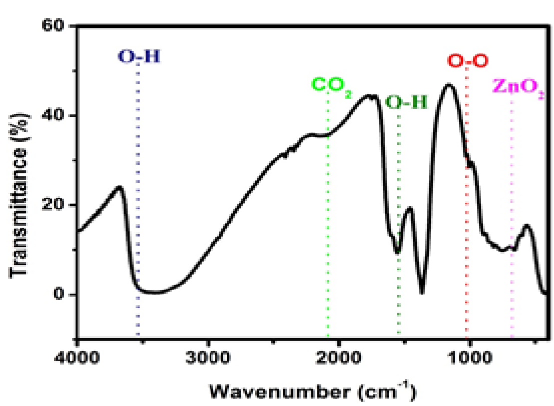

Fig. 4. FTIR spectra of the as-synthesized ZnO_2nanoparticles absorbed at 435–445cm^{-1}

The phase contrast images of living cells interaction with ZnO_2 NPs. are captured using fluorescent microscopy. The fibrobalast cells are visualized as growing and reproducing after the ZNPs are directly in contact with FBCs (**Fig. 5**). These contrast images are divided in two part (a) is cell grown in media without nanoparticles, which represent in squre box, (b) ZNPs nanoparticle are attached with the surface of the grown cells after pouring of the ZnO_2 nanoparticles in culture FBCs that interact with the cell without coagulation and without bacterial infection, after one day the ZNPs are remaining in the same position of the cell surface, which shows the cell growth with the ZNPs nanoparticles are evenly directly contact which marked in circle).

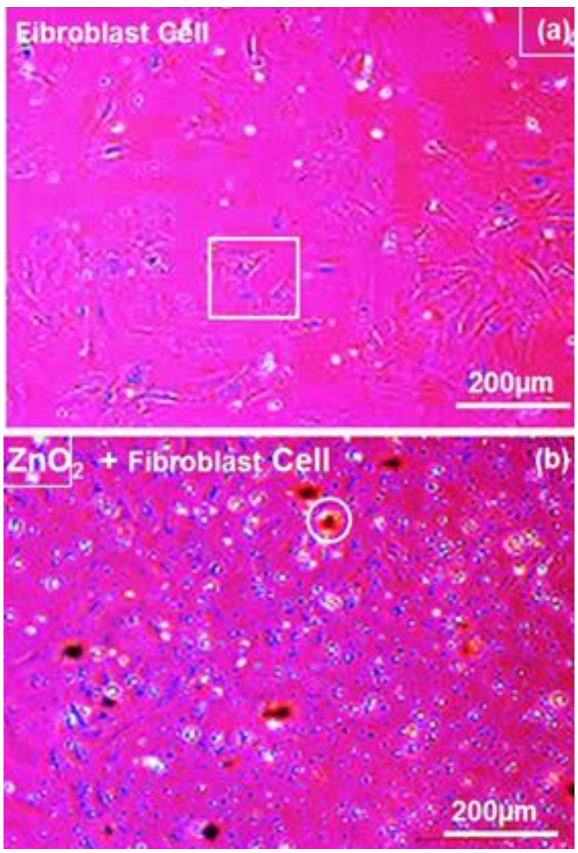

Fig. 5. Fluorescent Microscopic images of (a) fibroblast cell (b) ZnO_2+ fibrobalast cell.

This suggests that the ZnO_2 nanoparticles are biocompatible and biosafe for the FBC cell lines. We have reported the first cellular level study on the biocompatibility and biosafety of ZnO_2 NPs and second is attachment with the cells. Fibarobalast cell line showed complete biocompatible to ZnO_2 nanostructures at low concentration.

Conclusion

This work demonstrates the initial cellular level study on the biocompatibility and biosafety of as-synthesized ZnO_2 nanoparticles. Cell lines from different origins of tissues are utilized to study the interaction of ZNP with the live cells. The Fibarobalast cell lines show stable and complete biocompatibility to the ZnO_2 nanostructures interaction. This study shows the ZNPs could be applied in vivo biomedical science and engineering applications at normal concentration range.

Acknowledgements

The authors are grateful to Prem Singh Yadav of CIRB, Hisar, India,for encouragement and providing permission to pursue the cell culture experiments in the institute. The authors would like to thank the Life Science Reserch Board of Defence Research and Development Organization (DRDO), Delhi, India, for providing fellowship to BS and for allocating extramural research funding to pursue this research work.

References

1. Prasad, P. N.; Nanotechnology for Biophotonics: Bionanophotonics. Introduction to Bionanophotonics; John Wiley & Sons: Hoboken, NJ, USA, **2004**; 520.
   DOI: 10.1002/0471465380.ch15
2. James, M. L.; Gambhir, S.S.; *Physiol. Rev*. **2012**, *92*, 897.
   DOI: 10.1152/physrev.00049.2010
3. Higgins, L .J.; Pomper, M.G.; *Semin. Oncol*. **2011**, *38*, 3.
   DOI: 10.1016/j.ejca.2014.01.004
4. Verma, A.; Stellacci, F.; *Small Weinh. Bergstr. Ger*. **2010,** *6*, 12.
   DOI: 10.1016/j.nantod.2015.07.002
5. Shang, L.; Nienhaus, K.,; Nienhaus, G.U.; *J. Nanobiotechnol*. **2014**, *12*, 5.
   DOI: 10.1186/1477-3155-12-5
6. Zhao, F.; Zhao, Y.; Liu, Y.; Chang, X.; Chen, C.; Zhao, Y.; *Small Weinh. Bergstr. Ger*. **2011**, *7*, 1322.
   DOI: 10.1155/2015/961208
7. Lee, D. E.; Koo, H.; Sun, I. C.; Ryu, J. H.; Kim, K.; Kwon, I. C.; *Chem. Soc. Rev*. **2012**, *41*, 2656.
   DOI: 10.1039/C2CS15261D
8. Swierczewska, M.; Lee, S.; Chen, X.; *Mol. Imaging*. **2011**, *10*, 3.
   DOI: NIHMS454982
9. Koo, Y. E.; Fan ,W.; Hah, H.; Xu, H.; Orringer, D.; Ross, B.; Rehemtulla, A.; Phillbert, M. A.; kopelman, R.; *Appl. Opt*. **2007,** *46*, 1924.
   DOI: 10.1039/c4ra00331d
10. Doane, T. L.; Burda, C. Chem.Soc.Rev. **2012**, *41*, 2885.
    DOI: 10.1039/C3CC47124A
11. Sharma, P.; Singh, A.; Brown, S. C.; Bengtsson, N.; Walter, G. A.; Grobmyer, S. R.; Lwakuma.; Santra, S.; Scott, E.W.; Moudgil, B. M.; + **2010**, *624*, 67.
    DOI: 10.1039/C3TB20859A
12. Yong, K.T.; Roy, I.; Swihart, M. T.; Prasad, P.N.; *J. Matter. Chem*. **2009**, *19*, 4655
    DOI: 10.1021/nn8008933
13. Parveen, S.; Misra, R.; Sahoo, S. K.; *Nanomedicine*. **2012**, *8*, 147
    DOI: 10.1016/j.nano.2011.05.016.
14. Davis, S. S.; *Trends Biotechnol*.. **1997**, *15*, 217
    DOI: 9183864 [PubMed]
15. Ruoslahti, E.S.; Bhatia N.; Sailor, M. J.; *J. Cell Biol*. **2010**, *188*, 759.
    DOI: 10.1083/jcb.200910104
16. Gong, Y. K..; Winnik, F. M.; *Nanoscale*. **2012**, *4*, 360.
    DOI: 10.1039/c1nr11297j
17. Vasir, J. K., Labhasetwar, V.; *Technol. Cancer Res. Treat*. **2005**, *4*, 363.
    DOI: 16029056 [PubMed]
18. Li, Z.;, Yang, R.; Yu, M.; Bai, F.; Li, C.; Wang, Z. L.; *J. Phys. Chem. C*. **2008**, *112*, 20114.
    DOI: 10.1021/jp808878p
19. Gupta, A. K., Gupta, M.; *Biomaterials*, **2005**, *26*, 3995.

DOI: 10.1016/j.biomaterials.2004.10.012

20. MeCarthy, J. R.; Weissleder R.; *Adv. Drug Delivery Rev.* **2008**, *60*, 1241.
DOI: 10.1016/j.addr.2008.03.014
21. Nel, A.; Xia, T.; Madler, L.; Li, N. *Science*. **2006**, *311*, 622–627**.**
DOI: 10.1186/1743-8977-2-8
22. Oberdorster, G. *et al*.; *Part. Fibre Toxicol.***, 2005,** *2*, 8
DOI: 10.1186/1743-8977-2-8
23. Vertegel, A. A.; Siegel, R. W.; *Langmuir,* **2004,** *20*, 6800–6807**.**
DOI: 10.1021/la0497200 PMID:15274588
24. Sigmund, W.; Pyrgiotakis, G.; Daga, A. *Chemical Processing of Ceramics* (CRC, **2005**).
DOI: ISBN- 1574446487
25. Singh, N et al, *Chalcogenide Lett.*, **2010**, *4*, 7.
26. Singh, N.; Rashmi.; Singh,S.; Pasricha, R.; Gupta, P.K.; Soni, D.; Patent Application; Publication Number US 8715612 B2, May 6, **2014**.
27. Cullity, B. D.; Stock S. R.; Elements of X-ray Diffraction, 3rd edition, Prentice Hall, **2001.**
DOI: 10.1098/rsif.2013.0319

High-spin states in ^{133}Cs and the shell model description

S. Biswas,[1] R. Palit,[1,*] J. Sethi,[1] S. Saha,[1] A. Raghav,[2] U. Garg,[3] Md. S. R. Laskar,[1] F. S. Babra,[1] Z. Naik,[1] S. Sharma,[1] A. Y. Deo,[1,4] V. V. Parkar,[1,5] B. S. Naidu,[1] R. Donthi,[1] S. Jadhav,[1] H. C. Jain,[1] P. K. Joshi,[6] S. Sihotra,[7] S. Kumar,[8] D. Mehta,[7] G. Mukherjee,[9,10] A. Goswami,[11] and P. C. Srivastava[4]

[1]*Department of Nuclear and Atomic Physics, Tata Institute of Fundamental Research, Mumbai 400005, India*
[2]*Department of Physics, University of Mumbai, Mumbai 400098, India*
[3]*Department of Physics, University of Notre Dame, Notre Dame, Indiana 46556, USA*
[4]*Department of Physics, Indian Institute of Technology Roorkee, Roorkee 247667, India*
[5]*Bhabha Atomic Research Centre, Mumbai 400085, India*
[6]*HBCSE, Tata Institute of Fundamental Research, Mumbai 400088, India*
[7]*Department of Physics, Panjab University, Chandigarh 160014, India*
[8]*Department of Physics, Delhi University, New Delhi 110007, India*
[9]*Physics Group, Variable Energy Cyclotron Centre, 1/AF Bidhan Nagar, Kolkata 700064, India*
[10]*Homi Bhabha National Institute, Training School Complex, Anushaktinagar, Mumbai 400094, India*
[11]*Nuclear Physics Division, Saha Institute of Nuclear Physics, Kolkata 700064, India*

(Received 13 February 2017; revised manuscript received 17 April 2017; published 22 June 2017)

The high-spin states in ^{133}Cs, populated using the reaction ^{130}Te(^{7}Li,4n) with 45-MeV beam energy, have been extended up to an excitation energy of 5.265 MeV using the Indian National Gamma Array. The observed one- and three-quasiparticle bands in ^{133}Cs, built on the $\pi h_{11/2}$, $\pi g_{7/2}$, $\pi d_{5/2}$; and $(\pi g_{7/2}\pi d_{5/2})^1 \otimes \nu h_{11/2}^{-2}$ configurations, respectively, have similar structure as seen in the lighter odd-A Cs isotopes. The experimental level scheme has been compared with the large-scale shell model calculation without truncation using the $jj55pna$ interaction, showing a good agreement for both positive- and negative-parity states.

DOI: 10.1103/PhysRevC.95.064320

I. INTRODUCTION

The study of high-spin states of Cs isotopes with proton particles beyond $Z = 50$ and neutron holes below $N = 82$ continues to provide information on a variety of nuclear structure phenomena such as signature inversion [1] and chirality [2]. The heavier Cs isotopes near the $N = 82$ closed shell are the testing ground of continuously evolving shell model calculations based on the effective interactions [3,4]. With the increasing neutron number, the finite-range liquid-drop model predicts an evolution of ground state shape from deformed to spherical while going from ^{121}Cs to ^{137}Cs [5]. Here, the active orbitals for the neutrons are $h_{11/2}$, $s_{1/2}$, and $d_{3/2}$, and that of protons are $h_{11/2}$, $g_{7/2}$, $d_{5/2}$, and $g_{9/2}$. Cesium isotopes are the best examples in this mass region which show four distinct one-quasiparticle collective features [6–11]: (i) a series of $\Delta I = 2$ bands built on the $11/2^-$ state in $^{119-131}$Cs, (ii) a series of $\Delta I = 2$ bands built on the $7/2^+$ state in $^{125-133}$Cs, (iii) a series of $\Delta I = 2$ bands built on the $5/2^+$ state in $^{129-131}$Cs, and (iv) a series of $\Delta I = 1$ bands built on the $9/2^+$ state in $^{119-127}$Cs. The ^{135}Cs isotope, being very close to the shell closure, has a spherical structure, and shell model calculations compare favorably with the observed level scheme [3].

In a recent shell model calculation [4], excited states of ^{131,133,135,137}Cs isotopes were studied and compared with the experimental states. While the calculation provided an overall good description of the excited positive-parity medium-spin states, discrepancies between theory and experiment were noted for the relative ordering of low-spin positive-parity states. In this calculation, because the two-body interactions which affect the negative-parity states were introduced, large inconsistencies for the negative-parity states were observed. The calculation also pointed out its limitation in explaining the states associated with neutron and proton interaction.

The ^{133}Cs isotope lies in between the deformed ^{131}Cs and the spherical ^{135}Cs, and is the subject of the present investigation. Previously, the low-lying excited states in ^{133}Cs were studied via the reaction ^{130}Te$(\alpha,n)^{133}$Xe which in turn β-decays to ^{133}Cs [12], and from the decay of ^{133}Ba [13]. The high-spin states of ^{133}Cs were populated up to an excitation energy of 2.833 MeV using the reaction ^{130}Te(^{6}Li,3n)^{133}Cs [11]. In the present work, the high-spin states were investigated using the reaction ^{130}Te(^{7}Li,4n)^{133}Cs up to an excitation energy of 5.265 MeV. An extension of the available level structure of ^{133}Cs up to high spin for both positive- and negative-parity states was required to see how its high-spin states compare with those of the lighter odd-A Cs isotopes which have regular band structures as well as the heavier isotopes, i.e., ^{135,137}Cs, which show shell model like excitation. This chain of nuclei would provide a good testing ground for various theoretical models. We have restricted the present study to a comparison with the large-scale shell model (LSSM) calculations without truncation, which is possible up to the ^{133}Cs isotope below $N = 82$. The comparison of the measured level structure up to high spin for ^{133}Cs with LSSM calculations without truncation will test the effective interaction used in the shell model calculation and provide guidance for the interpretation of the excited states.

*Corresponding author: palit@tifr.res.in

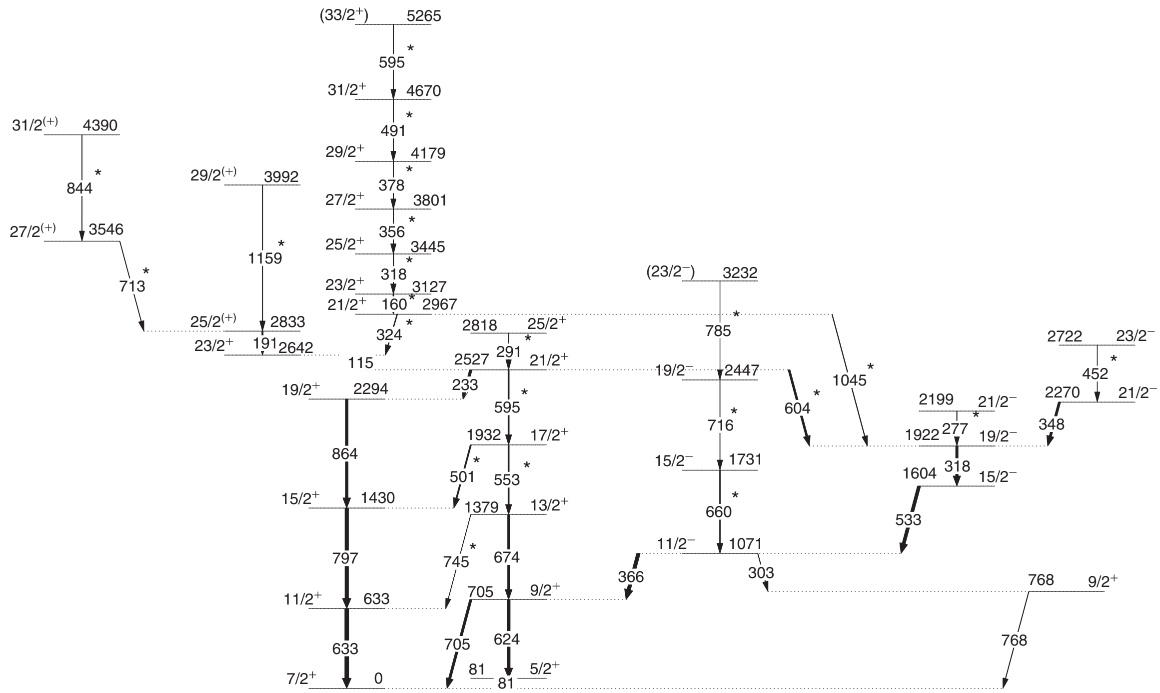

FIG. 1. Level scheme of ^{133}Cs. Transitions marked with an asterisk are new.

The current paper is organized as follows: The experimental details are given in Sec. II. Section III discusses the experimental results. Section IV shows the systematics of Cs isotopes and the comparison between the experimental observations and theoretical calculations with LSSM. Section V briefly summarizes the work reported in the paper.

II. EXPERIMENTAL DETAILS

The experiment was carried out with the Indian National Gamma Array (INGA) at Tata Institute of Fundamental Research (TIFR), Mumbai, using the reaction ^{130}Te(^{7}Li,4n)^{133}Cs. A ^{7}Li beam with 45-MeV energy was bombarded on a 5-mg/cm^2 ^{130}Te target backed with 2-mg/cm^2 Al. During the experiment, there were 15 Compton suppressed high purity germanium (HPGe) clover detectors in the array. The detectors were placed in rings at angles (number of detectors) 40° (2), 65° (2), 115° (2), 140° (2), 157° (3), and 90° (4) with respect to the beam direction. γ rays emitted from the deexciting residual nuclei were detected in the array and stored with a digital data acquisition (DDAQ) system, based on Pixie-16 modules of XIA LLC [14], in two-fold coincidence mode.

The time stamped data were processed on an event by event basis into γ-γ matrices and γ-γ-γ cubes for subsequent analysis using the multiparameter coincidence search program developed at TIFR [15]. There were about 1.06×10^8 events in the γ-γ-γ cube, which was analyzed using the RADWARE package [16] to obtain the coincidences among the different γ rays to construct the level scheme. The spin of the levels were obtained using directional correlation from oriented states (DCO), using the detectors at 90° and 157°, defined by the following relation [17]:

$$R_{\mathrm{DCO}} = \frac{I_{\gamma_1}(\text{measured at } 157^\circ;\text{ gated by } \gamma_2 \text{ at } 90^\circ)}{I_{\gamma_1}(\text{measured at } 90^\circ;\text{ gated by } \gamma_2 \text{ at } 157^\circ)}.$$

The DCO ratios of stretched dipole and quadrupole transitions are ~0.5 (1.0) and ~1.0 (2.0), respectively, for a pure quadrupole (dipole) gate.

The parities of the states were obtained by measuring the polarization asymmetry Δ defined as in Ref. [18]:

$$\Delta = \frac{a(E_\gamma)N_\perp - N_\parallel}{a(E_\gamma)N_\perp + N_\parallel},$$

using the clover detectors as a polarimeter, for which all four 90° detectors were used [19]. Here, $N_\parallel(N_\perp)$ is the number of γ transitions scattered parallel (perpendicular) to the reaction plane and $a(E_\gamma)$ is a correction factor for the parallel to perpendicular scattering asymmetry within the crystals of a clover. In the present experiment, for the four clovers kept at 90° with respect to the beam direction, $a(E_\gamma)$ was measured as 1.00(1) from the ^{133}Ba and ^{152}Eu sources. Using the integrated polarization direction correlation method [18], the polarization asymmetry values of the γ transitions were extracted. For this analysis, two asymmetric matrices were constructed with coincident events corresponding to parallel or perpendicular scattered γ rays at 90° detectors with another γ ray detected at any other angle. In the case of unmixed stretched transition, a positive (negative) value of the polarization asymmetry indicates the electric (magnetic) nature of the transitions [20].

III. EXPERIMENTAL RESULTS

The level scheme of ^{133}Cs established in this work is shown in Fig. 1. In the present work, 22 new transitions have been

TABLE I. Level energies (E_i), γ-ray energies (E_γ), initial and final spins and parities of the levels ($I_i^\pi \rightarrow I_f^\pi$), relative intensities (I_γ), DCO ratios (R_{DCO}), and polarization asymmetry (Δ) values for ^{133}Cs arranged in order of increasing excitation energies. The uncertainties in the energies of γ rays are 0.5 keV for intense peaks and 0.7 keV for weak peaks.

E_i (keV)	E_γ (keV)	$I_i^\pi \rightarrow I_f^\pi$	I_γ	R_{DCO}	Δ	Assignment
81	80.8	$5/2^+ \longrightarrow 7/2^+$	318(22)	0.58(9)		$M1$
633	632.7	$11/2^+ \longrightarrow 7/2^+$	100	1.00(15)	0.112(19)	$E2$
705	623.9	$9/2^+ \longrightarrow 5/2^+$	96(5)	0.98(14)	0.089(13)	$E2$
705	705.4	$9/2^+ \longrightarrow 7/2^+$	22(4)	0.53(10)	− 0.059(12)	$M1$
768	767.6	$9/2^+ \longrightarrow 7/2^+$	7.3(7)	0.58(9)	− 0.041(27)	$M1$
1071	303.4	$11/2^- \longrightarrow 9/2^+$	5.6(8)	0.55(9)	0.048(28)	$E1$
1071	366.3	$11/2^- \longrightarrow 9/2^+$	53(4)	0.61(10)	0.118(33)	$E1$
1379	674.4	$13/2^+ \longrightarrow 9/2^+$	39(3)	1.03(16)	0.169(25)	$E2$
1379	745.4	$13/2^+ \longrightarrow 11/2^+$	0.3(1)			$M1$
1430	796.7	$15/2^+ \longrightarrow 11/2^+$	86(5)	0.96(15)	0.057(13)	$E2$
1604	533.4	$15/2^- \longrightarrow 11/2^-$	48(4)	1.02(15)	0.084(19)	$E2$
1731	659.7	$15/2^- \longrightarrow 11/2^-$	9(1)	1.09(25)	0.068(34)	$E2$
1922	318.2	$19/2^- \longrightarrow 15/2^-$	35(4)	0.95(14)	0.055(12)	$E2$
1932	501.4	$17/2^+ \longrightarrow 15/2^+$	21(3)	0.46(10)	− 0.078(27)	$M1$
1932	552.6	$17/2^+ \longrightarrow 13/2^+$	18(3)	0.81(13)	0.156(77)	$E2$
2199	277.2	$21/2^- \longrightarrow 19/2^-$	4.2(8)	0.54(15)	− 0.032(13)	$M1$
2270	347.6	$21/2^- \longrightarrow 19/2^-$	8(2)	0.44(12)	− 0.038(13)	$M1$
2294	864.3	$19/2^+ \longrightarrow 15/2^+$	57(5)	0.95(15)	0.074(12)	$E2$
2447	715.8	$19/2^- \longrightarrow 15/2^-$	3.1(4)	0.85(11)	0.167(23)	$E2$
2527	233.0	$21/2^+ \longrightarrow 19/2^+$	39(4)	0.61(10)	− 0.086(28)	$M1$
2527	595.4	$21/2^+ \longrightarrow 17/2^+$	9(2)			$E2$
2527	604.1	$21/2^+ \longrightarrow 19/2^-$	12(3)	0.62(18)	0.034(17)	$E1$
2642	114.7	$23/2^+ \longrightarrow 21/2^+$	37(6)	0.62(9)		$M1$
2722	452.2	$23/2^- \longrightarrow 21/2^-$	2.5(5)	0.54(10)	− 0.043(12)	$M1$
2818	290.7	$25/2^+ \longrightarrow 21/2^+$	4.8(8)	0.93(17)	0.114(42)	$E2$
2833	190.7	$25/2^{(+)} \longrightarrow 23/2^+$	7.5(9)	0.60(9)		
2967	324.2	$21/2^+ \longrightarrow 23/2^+$	25(5)	0.57(11)	− 0.048(15)	$M1$
2967	1044.7	$21/2^+ \longrightarrow 19/2^-$	5.1(7)	0.59(10)	0.132(70)	$E1$
3127	160.3	$23/2^+ \longrightarrow 21/2^+$	23(4)	0.51(12)		
3232	785.2	$(23/2^-) \longrightarrow 19/2^-$	0.5(2)			
3445	318.2	$25/2^+ \longrightarrow 23/2^+$	18(3)	0.64(10)	− 0.045(24)	$M1$
3546	713.2	$27/2^{(+)} \longrightarrow 25/2^{(+)}$	2.9(6)	0.50(11)	− 0.042(21)	$M1$
3801	355.6	$27/2^+ \longrightarrow 25/2^+$	12(2)	0.51(10)	− 0.127(31)	$M1$
3992	1158.9	$29/2^{(+)} \longrightarrow 25/2^{(+)}$	2.1(4)	1.06(20)	0.058(23)	$E2$
4179	377.8	$29/2^+ \longrightarrow 27/2^+$	8.9(9)	0.69(12)	− 0.030(15)	$M1$
4390	844.4	$31/2^{(+)} \longrightarrow 27/2^{(+)}$	2.3(3)	0.89(12)	0.103(35)	$E2$
4670	490.7	$31/2^+ \longrightarrow 29/2^+$	3.3(5)	0.67(10)	− 0.117(33)	$M1$
5265	595.3	$(33/2^+) \longrightarrow 31/2^+$	0.8(3)			

identified both in the positive-parity and the negative-parity bands. The new transitions have been marked with an asterisk in Fig. 1. Table I lists the level energies (E_i), γ-ray energies (E_γ), initial and final spins along with the parities of the levels ($I_i^\pi \rightarrow I_f^\pi$), relative intensities (I_γ), DCO ratios (R_{DCO}), and polarization asymmetry (Δ) values. Multipolarities of most of the transitions are extracted from the stretched $\Delta I = 2$ transitions with 533-, 624-, 633-, 674-, and 797-keV energies.

1. Positive-parity states

In the level scheme of ^{133}Cs reported in Ref. [11], positive-parity states have been observed up to $I^\pi = 19/2^+$ at an excitation energy of 2.295 MeV. Three more transitions extending up to spin (25/2) above the $19/2^+$ state were identified in that reference, but the parities of those states had not been identified.

In the present work, the positive-parity band has been extended to $I^\pi = (33/2^+)$ with an excitation energy of 5.265 MeV. A strong $\Delta I = 2$ band, consisting of 633-, 797-, and 864-keV transitions built on the $7/2^+$ state, has been observed which is consistent with the previous work. The 233-, 115-, and 191-keV transitions, which were identified as dipole transitions in the previous work, have also been observed in the present work as evident from the measured values of R_{DCO} in the 633-keV gate. The parity of the 2.527-MeV state, which deexcites by the 233-keV transition was confirmed by the R_{DCO} and Δ values for the 604-keV transition. A sum of double gates of 191/L and 324/L with L denoting the list gate of 633-, 797-, 864-, 233-, and 115-keV transitions, is

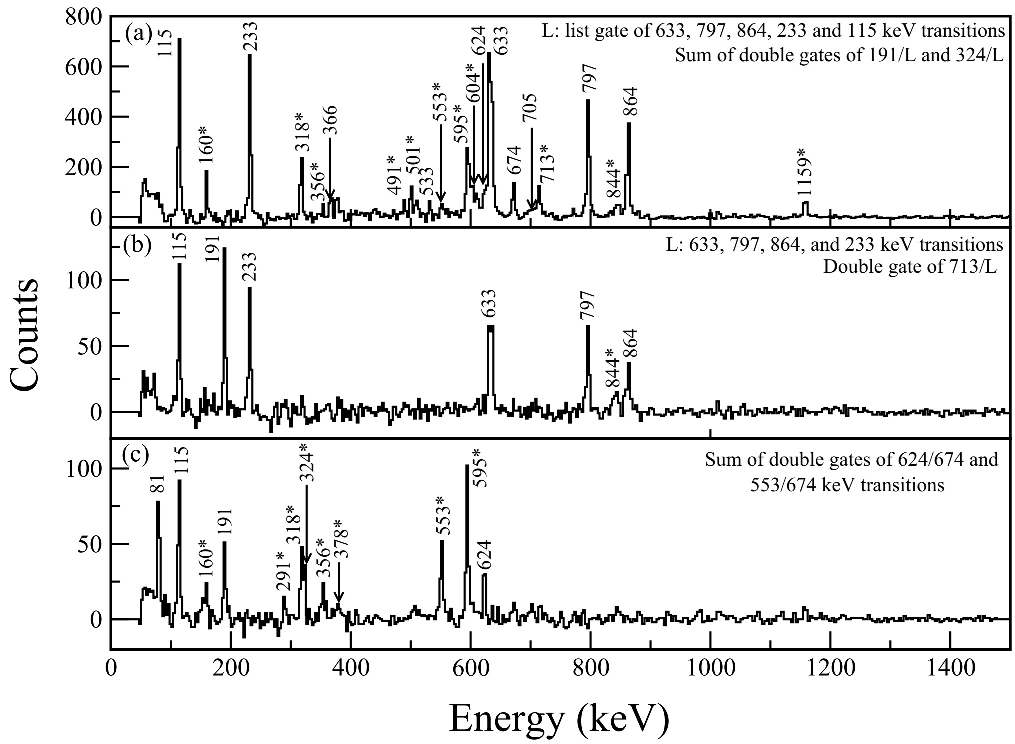

FIG. 2. Spectra obtained by (a) sum of double gates of 191/L and 324/L keV, L depicting the list gate of transitions as shown; (b) double gating on 713/L; and (c) sum of double gates on the transitions shown. The newly observed transitions have been marked with an asterisk.

shown in Fig. 2(a). This spectrum shows many of the new transitions, namely, the 160, 318, 356, 378, 491, 501, 553, 595, 604, 713, 844, and 1159 keV and have been marked with asterisks. The 501-keV interconnecting transition has a $\Delta I = 1, M1$ character. The other interconnecting transition, namely, the 745-keV transition (shown in the level scheme), is not seen in this spectrum as it is very weak, but confirmed in the double gate of 633- and 553-keV transitions. The spin and parity of the 2.967-MeV state, which is populated by the 160-keV transition, is fixed by the 324- and 1045-keV transitions. With the measured R_{DCO} in the 633-keV gate and Δ values, the 318-, 356-, 378-, and 491-keV transitions have been assigned as forming a $\Delta I = 1$ band with $M1$ transitions. The R_{DCO} of the 160-keV transition in the 633-keV gate suggests a $\Delta I = 1$ nature and since it has been observed in coincidence with the 318-, 356-, 378-, 491-, and 595-keV transitions and further assuming its magnetic nature (due to the similarity with the lower-A Cs isotopes), this cascade of $\Delta I = 1$ γ-ray transitions has been designated as an $M1$ band. The newly identified 1159-keV transition has been assigned as a $\Delta I = 2$, $E2$ transition from the measured R_{DCO} in the 633-keV gate and Δ value. With a double gate on 713/L with L being the list gate of 633-, 797-, 864-, and 233-keV transitions, a new 844-keV transition is observed in addition to the known 115-, 191-, 233-, 633-, 797-, and 864-keV transitions, as shown in Fig. 2(b). This 844-keV transition has been identified as a $\Delta I = 2$, $E2$ transition.

Another new $\Delta I = 2$ cascade of 624-, 674-, 553-, 595-, and 291-keV γ-rays built on the $5/2^+$ state has been observed in the present work. Though the 624-keV transition was already established in the previous work [11], this 674-keV transition was placed in the negative-parity band in coincidence with the 366- and 624-keV transitions. However, with a double gate on 624- and 366-keV transitions, the 674-keV transition has not been observed. Figure 2(c) shows the spectrum obtained by the sum of double gates of 624/674- and 553/674-keV transitions. This spectrum shows the 81-, 115-, 160-, 191-, 291-, 318-, 324-, 356-, 378-, 553-, 595-, and 624-keV coincident transitions. The newly observed 553-, 595-, and 291-keV transitions are $\Delta I = 2$ transitions.

2. *Negative-parity states*

In the previous work [11], the negative-parity states were reported up to $I^\pi = (15/2^-)$ at an excitation energy of 1.604 MeV. Two more transitions of 318 and 348 keV were identified above this $(15/2^-)$ state in that reference, and the corresponding states with excitation energies 1.923 and 1.952 MeV were assigned the spins (19/2) and (17/2), respectively, but the parities were not measured.

In the present work, the negative-parity band has been extended up to $I^\pi = (23/2^-)$ with an excitation energy of 3.232 MeV. To obtain the γ-ray transitions at higher spins, a spectrum was obtained by the sum of double gates of 366/624-, 366/705-, and 533/366-keV transitions as depicted in Fig. 3(a). New γ-ray 160-, 277-, 318-, 324-, 356-, 378-, 452-, 491-, 595-, 604-, 660-, 713-, 716-, 844-, and 1045-keV transitions are observed in coincidence. The 160-, 318-, 324-, 356-, 378-, 491-, 595-, 713-, and 844-keV transitions have already been observed in the positive-parity band, with 318-keV being

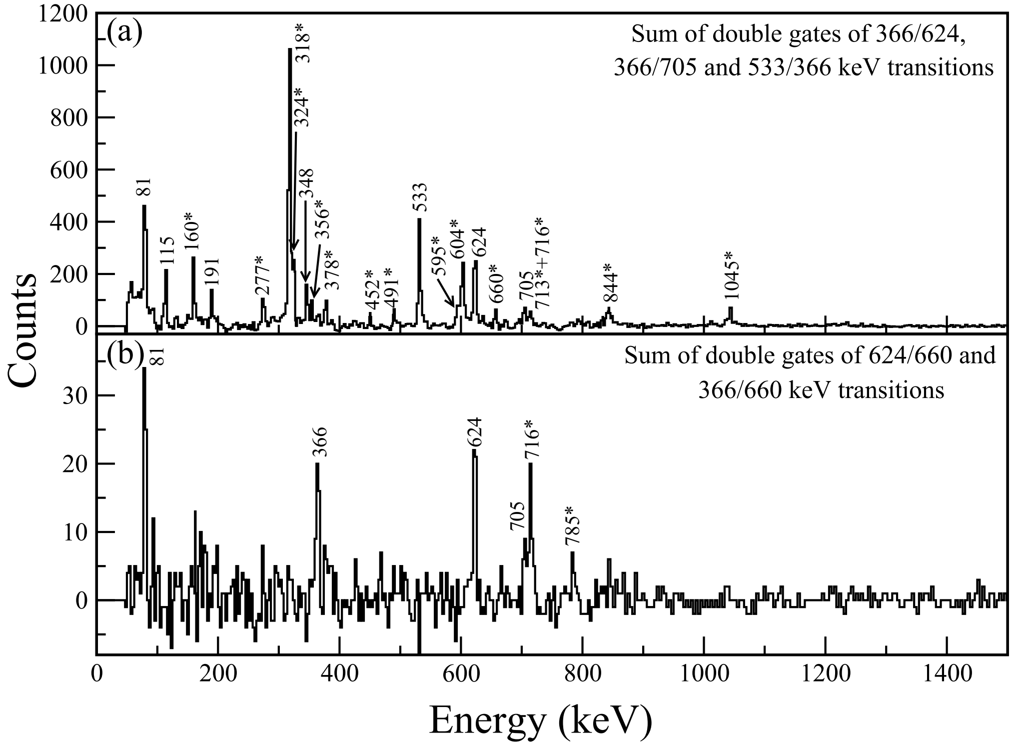

FIG. 3. Spectra obtained by sum of double gates on various transitions.

a doublet. Out of the remaining transitions, the measured R_{DCO} in the 624-keV gate and Δ values show that the 604-, and 1045-keV transitions have a $\Delta I = 1$, $E1$ character. The positive-parity band is connected to the negative-parity states by these two transitions. A newly observed $M1$ transition, 277 keV, is in coincidence with the 533- and 366-keV transitions. Also, the 452-keV $M1$ transition is in coincidence with the 348-keV transition. In addition, 660- and 716-keV $E2$ transitions have been observed in coincidence. In order to see higher spin states above the 660- and 716-keV transitions, a spectrum was obtained by the sum of double gates of 624/660- and 366/660-keV transitions as shown in Fig. 3(b). Newly identified 716-keV $E2$ transition and 785-keV transition have been observed in coincidence in this spectrum.

IV. CALCULATIONS AND DISCUSSION

1. Energy systematics

One- and three-quasiparticle bands similar to those observed in $^{127-131}$Cs [6–11] have also been observed in ^{133}Cs. Three distinct one-quasiparticle band structures have been observed in ^{133}Cs: (i) a $\Delta I = 2$ band built over the $5/2^+$ state, (ii) a $\Delta I = 2$ band built over the $7/2^+$ state, and (iii) a $\Delta I = 2$ band built over the $11/2^-$ state.

The evolution of bandhead energies as a function of neutron number [$N = 72$ (black), 74 (blue), 76 (green), 78 (magenta), 80 (indigo), and 82 (maroon)] corresponding to the isotopes ^{127,129,131,133,135,137}Cs, respectively, is shown in Fig. 4(a) [3,8,21–23]. As can be seen from Fig. 4(a), there is a decrease in the bandhead energy of the $5/2^+$ state till $N = 76$ and again increases at $N = 78$. Also, the bandhead energy of the $7/2^+$ state decreases as a function of N, in contrary to that for the $11/2^-$ state, showing that the $7/2^+$ band becomes highly yrast and the $11/2^-$ band becomes nonyrast as N increases from 72 to 78. Systematics of the two positive-parity (built on $5/2^+$ and $7/2^+$ states) and negative-parity (built on $11/2^-$ state) one-quasiparticle band structures in odd-A $^{127-137}$Cs are shown in Figs. 4(b)–4(d). The relative excitation energies of the excited states of the $5/2^+$ band [Fig. 4(b)] increases till spin $13/2^+$ with increasing N, but decreases above that in the case of ^{133}Cs, showing a structural change of this band in ^{133}Cs. Also, the increase in the relative excitation energies of the $7/2^+$ band with increasing N [Fig. 4(c)] shows that the deformation decreases as N increases. Again the increase in the relative excitation energies of the $11/2^-$ band with increasing N [Fig. 4(d)] shows that the deformation decreases from $N = 72$ to 78. These band structures have also been compared with the yrast bands of respective even-even Xe isotopes to probe the evolution of collectivity in odd-A Cs. The evolution of the three bands matches quite well with that of the even-even Xe isotopes. This shows that the valance proton occupancy in odd Cs doesn't have a strong influence on the evolution of deformation of odd-Cs isotopes. The positive-parity three-quasiparticle band structures in odd-A $^{127-133}$Cs have also been studied and they follow the systematics as well (see Fig. 5) [8,22,24].

2. LSSM calculations

The wave functions for the excited states in ^{133}Cs can be understood microscopically by comparing with the large-scale shell model (LSSM) calculations, carried out using the code NUSHELLX [25,26], without any truncation. The orbitals $0g_{7/2}$,

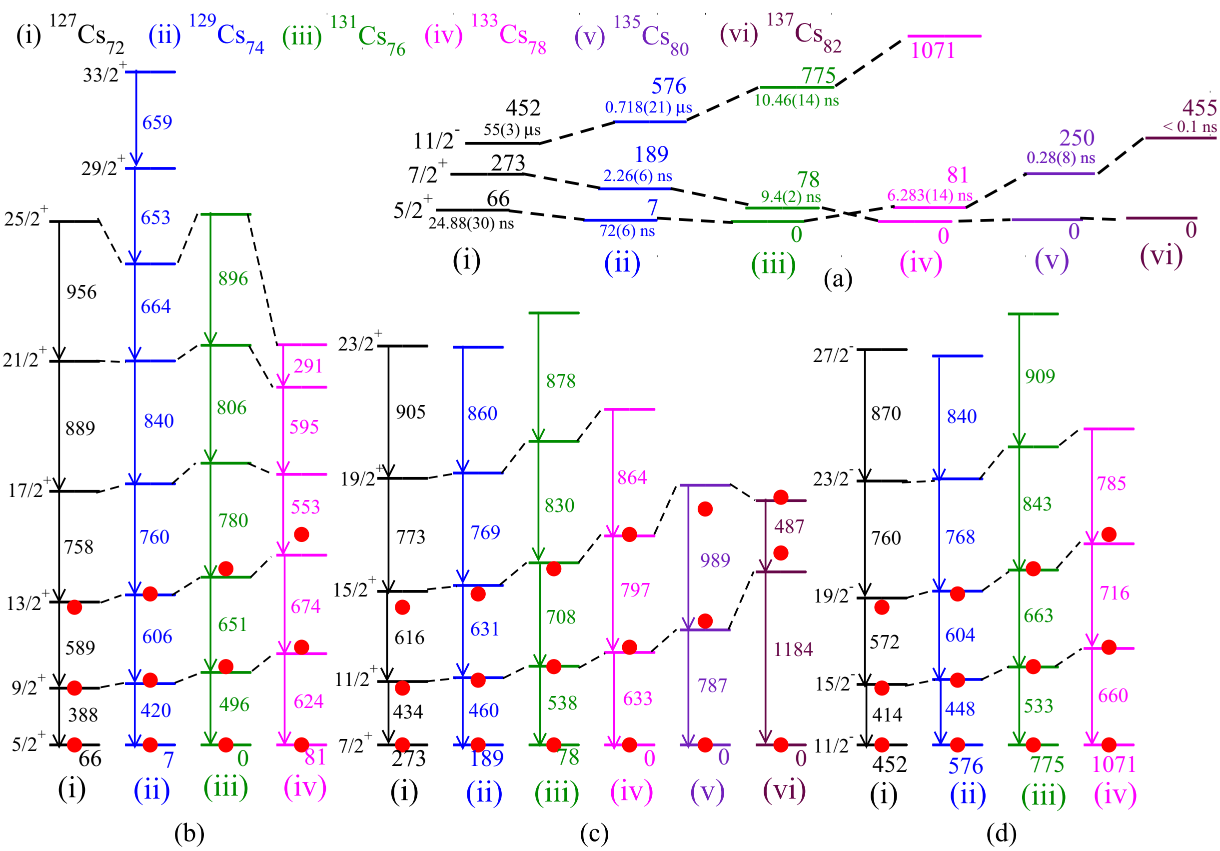

FIG. 4. (a) Evolution of the $5/2^+$, $7/2^+$, and $11/2^-$ bandheads as a function of neutron number for the odd-A $^{127-137}$Cs isotopes denoted by indices (i)–(vi): (i) ^{127}Cs$_{72}$, (ii) ^{129}Cs$_{74}$, (iii) ^{131}Cs$_{76}$, (iv) ^{133}Cs$_{78}$, (v) ^{135}Cs$_{80}$, and (vi) ^{137}Cs$_{82}$. The bandhead energies and their half-life (wherever known) are also quoted. Comparison is given of the bands built on (b) $5/2^+$, (c) $7/2^+$, and (d) $11/2^-$ states in the same isotopes [3,8,21–23]. The excitation energies corresponding to $J^\pi = 0^+$, 2^+, and 4^+ states of even-A $^{126-136}$Xe isotopes are shown by red circles.

$1d_{5/2}$, $1d_{3/2}$, $2s_{1/2}$, and $0h_{11/2}$ outside of the ^{100}Sn core were used as the valence space for both protons and neutrons. The single-particle energies used with the *jj55pna* interaction [27] are 0.80720 ($\pi 0g_{7/2}$), 1.56230 ($\pi 1d_{5/2}$), 3.31600 ($\pi 1d_{3/2}$), 3.22380 ($\pi 2s_{1/2}$), 3.60510 ($\pi 0h_{11/2}$), −10.60890 ($\nu 0g_{7/2}$), −10.28930 ($\nu 1d_{5/2}$), −8.71670 ($\nu 1d_{3/2}$), −8.69440 ($\nu 2s_{1/2}$), and −8.81520 ($\nu 0h_{11/2}$) MeV. The single-particle energies of these orbitals were chosen so as to reproduce the excited states in ^{133}Sb and ^{131}Sn. The residual two-body matrix elements for the *jj55pna* interaction were obtained starting with a G matrix derived from the CD-Bonn nucleon-nucleon potential [28]. The *n-n* interaction strength for the *jj55pna* interaction was reduced by a factor of 0.9 to better reproduce the levels in ^{130}Sn [27]. This interaction has been used to explain the excited states in $^{119-126}$Sn [29,30], $^{124-132}$Te [31,32], and $N = 82$ isotones ^{136}Xe, ^{137}Cs, ^{138}Ba, ^{139}La, and ^{140}Ce [33].

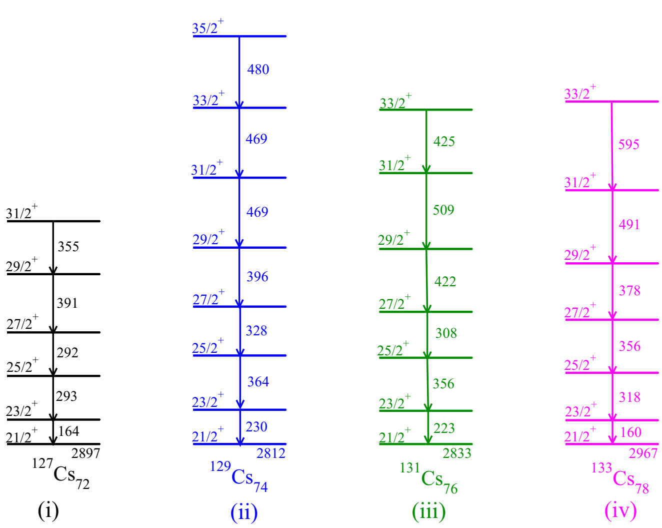

FIG. 5. Evolution of the dipole band as a function of neutron number for the odd-A $^{127-133}$Cs isotopes denoted by indices (i-iv): (i) ^{127}Cs$_{72}$ [8], (ii) ^{129}Cs$_{74}$ [24], (iii) ^{131}Cs$_{76}$ [22], and (iv) ^{133}Cs$_{78}$ (present work).

Figure 6 compares the experimentally obtained positive-parity yrast, dipole, and negative-parity bands with those obtained from shell model calculations. Previously in Ref. [4], the same model space was used but with the inclusion of an extended pairing plus quadrupole-quadrupole effective interaction to calculate the excited states of Sn, Sb, Te, I, Xe, Cs, and Ba isotopes. In the case of ^{133}Cs, the ordering of $7/2^+$ and $5/2^+$ states was reversed. Also, they did not obtain good agreement for the negative-parity states. It is evident from this figure that the shell model predicts quite well the positive- and negative-parity $E2$ bands within ∼150keV for most spins, but ∼350keV for the $21/2^+_1 - 25/2^+_1$ states.

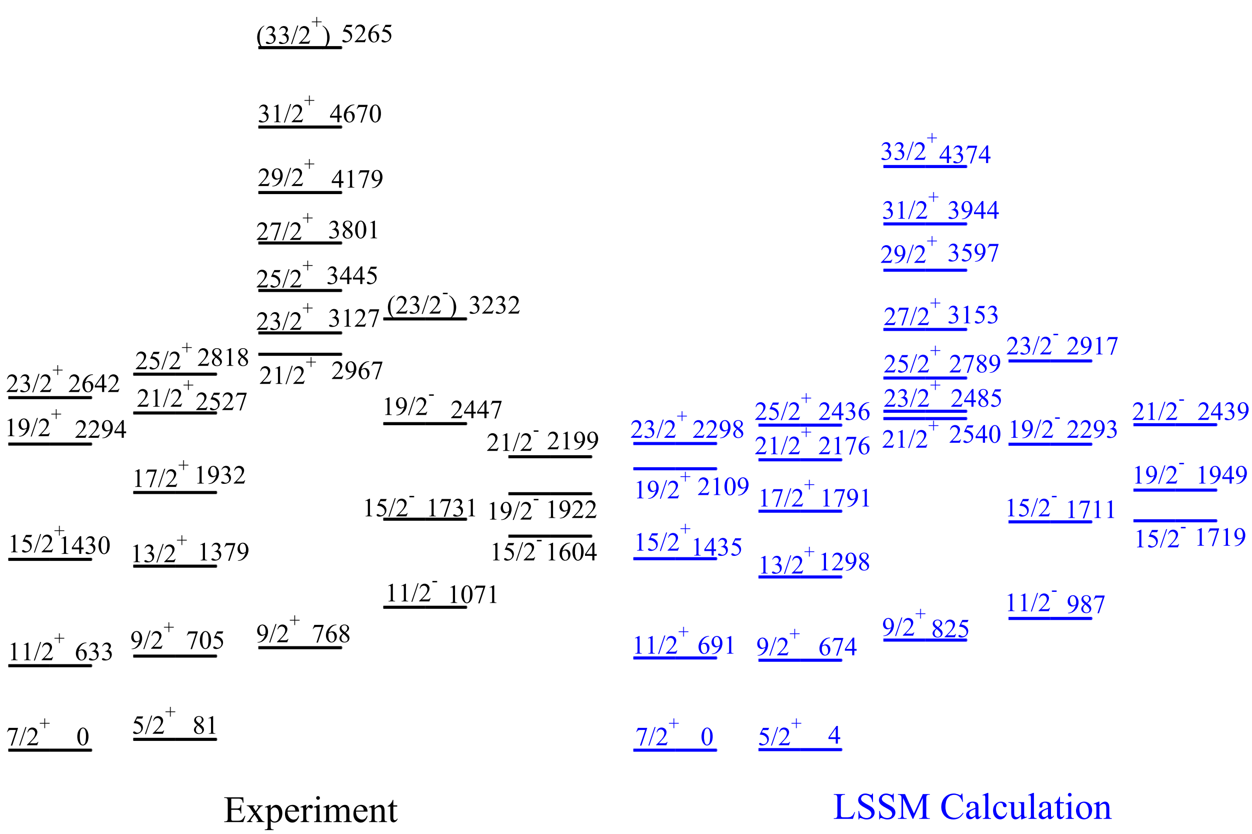

FIG. 6. Comparison between experiment and shell model calculations for the positive-parity yrast, dipole, and negative-parity bands in ^{133}Cs.

However it underestimates the energies of the dipole band by ∼800keV. There are a few features which are well reproduced in the calculations and are thus worth mentioning: (i) the ordering of the $7/2^+$ and $5/2^+$ states is correctly predicted with the energy difference being 4 keV, (ii) the second $9/2^+$ state lies just above the first $9/2^+$ state with the difference being 151 (63) keV for the shell model (experimental) case, (iii) the $21/2_2^+$ state in the dipole band is located above the first $25/2^+$ state with the difference being 104 (149) keV for the shell model (experimental) case, and (iv) the position of the $11/2^-$ state agrees with the experimental observation within ∼80keV.

Table II lists the decomposition of angular momenta for protons and neutrons ($I_\pi \otimes I_\nu$) (with probabilities greater than 10%) and the corresponding dominant wave functions along with their probabilities for the positive-parity $g_{7/2}$, $d_{5/2}$, and dipole bands, and the two negative-parity bands due to proton and neutron holes in the $h_{11/2}$ orbital. As is evident from the wave functions in Table II, the positive-parity $g_{7/2}$ band is mainly based on three proton particles in $g_{7/2}$ and two proton particles in the $d_{5/2}$ orbital. In addition, there are two neutron holes in the $d_{3/2}$ and $h_{11/2}$ orbitals. Thus in the ground state, the valence proton particle in the $g_{7/2}$ orbital is responsible for the spin $7/2^+$ and the neutron holes are coupled to an angular momentum of 0^+, which has the most dominant decomposition angular momentum probability (57.36%). As the spin increases, the neutron-hole pair in the $h_{11/2}$ orbital aligns completely, giving rise to an angular momentum of 10^+ in the $23/2^+$ state with 28.18% decomposition probability. For the case of the positive-parity $d_{5/2}$ band, there is one proton particle in the $d_{5/2}$ orbital and four proton particles in the $g_{7/2}$ orbital. Similar to the $g_{7/2}$ band, here there are two neutron holes in the $d_{3/2}$ and $h_{11/2}$ orbitals. The valence proton particle in the $d_{5/2}$ orbital is responsible for the spin $5/2^+$ for the lowest state of this band, and the neutron holes are coupled to an angular momentum of 0^+, which has the most dominant decomposition probability (51.06%). Again, as the spin increases, the neutron-hole pair in the $h_{11/2}$ orbital breaks giving rise to an angular momentum of 10^+ in the $21/2^+$ state with 42.64% probability. The $25/2^+$ state, however, has a 44.58% (19.63%) angular momentum decomposition probability from protons coupled to $7/2^+$ ($5/2^+$) and neutrons coupled to 10^+. In the case of the dipole band, the $21/2_2^+$ state has a proton configuration $g_{7/2}^3 d_{5/2}^2$ but for the higher spins this changes to $g_{7/2}^4 d_{5/2}^1$, indicating that the valence proton lies mostly in the $d_{5/2}$ orbital. Here also, the dominant neutron configuration is $d_{3/2}^{-2} h_{11/2}^{-2}$. But for the excited states in the dipole band, the neutron pair in the $h_{11/2}$ orbital is completely aligned with probabilities 17.93% ($21/2_2^+$), 43.96% ($23/2_2^+$), 22.91% ($25/2_2^+$), and 18.81 ($27/2_2^+$) showing that the shell model agrees with the three-quasiparticle nature of this dipole band. In addition, for the $25/2_2^+$ and $27/2_2^+$ states, there are contributions from the neutron configuration $d_{3/2}^{-1} s_{1/2}^{-1} h_{11/2}^{-2}$, giving a neutron angular momentum coupling of 12^+. For the remaining higher spin states ($29/2_2^+$ to $33/2_2^+$),

TABLE II. Decomposition of angular momenta of protons and neutrons (with probabilities greater than 10%) and the corresponding dominant partition of wave functions for the positive-parity $g_{7/2}$, $d_{5/2}$, dipole bands; and the two negative-parity bands, due to proton and neutron holes in the $h_{11/2}$ orbital, in ^{133}Cs using the *jj55pna* interaction.

I	$I_\pi \otimes I_\nu$ (probability)	Wave function (probability)
$7/2^+$	$7/2^+_\pi \otimes 0^+_\nu$ (57.36)	$(g^3_{7/2}d^2_{5/2})_\pi \otimes (d^{-2}_{3/2}h^{-2}_{11/2})_\nu$ (21.67)
	$5/2^+_\pi \otimes 4^+_\nu$ (14.03)	$(g^3_{7/2}d^2_{5/2})_\pi \otimes (d^{-2}_{3/2}h^{-2}_{11/2})_\nu$ (4.93)
$11/2^+$	$7/2^+_\pi \otimes 2^+_\nu$ (38.40)	$(g^3_{7/2}d^2_{5/2})_\pi \otimes (d^{-2}_{3/2}h^{-2}_{11/2})_\nu$ (15.34)
	$11/2^+_\pi \otimes 0^+_\nu$ (29.07)	$(g^3_{7/2}d^2_{5/2})_\pi \otimes (d^{-2}_{3/2}h^{-2}_{11/2})_\nu$ (12.30)
$15/2^+$	$11/2^+_\pi \otimes 2^+_\nu$ (30.72)	$(g^3_{7/2}d^2_{5/2})_\pi \otimes (d^{-2}_{3/2}h^{-2}_{11/2})_\nu$ (14.28)
	$15/2^+_\pi \otimes 0^+_\nu$ (21.64)	$(g^3_{7/2}d^2_{5/2})_\pi \otimes (d^{-2}_{3/2}h^{-2}_{11/2})_\nu$ (11.81)
	$7/2^+_\pi \otimes 4^+_\nu$ (18.49)	$(g^3_{7/2}d^2_{5/2})_\pi \otimes (d^{-2}_{3/2}h^{-2}_{11/2})_\nu$ (7.86)
$19/2^+$	$7/2^+_\pi \otimes 6^+_\nu$ (18.89)	$(g^3_{7/2}d^2_{5/2})_\pi \otimes (d^{-2}_{3/2}h^{-2}_{11/2})_\nu$ (8.97)
	$11/2^+_\pi \otimes 4^+_\nu$ (16.46)	$(g^3_{7/2}d^2_{5/2})_\pi \otimes (d^{-2}_{3/2}h^{-2}_{11/2})_\nu$ (8.04)
	$5/2^+_\pi \otimes 8^+_\nu$ (10.77)	$(g^3_{7/2}d^2_{5/2})_\pi \otimes (d^{-2}_{3/2}h^{-2}_{11/2})_\nu$ (5.63)
	$15/2^+_\pi \otimes 2^+_\nu$ (10.00)	$(g^3_{7/2}d^2_{5/2})_\pi \otimes (d^{-2}_{3/2}h^{-2}_{11/2})_\nu$ (5.43)
$23/2^+$	$7/2^+_\pi \otimes 10^+_\nu$ (28.18)	$(g^3_{7/2}d^2_{5/2})_\pi \otimes (d^{-2}_{3/2}h^{-2}_{11/2})_\nu$ (14.34)
	$5/2^+_\pi \otimes 10^+_\nu$ (20.50)	$(g^3_{7/2}d^2_{5/2})_\pi \otimes (d^{-2}_{3/2}h^{-2}_{11/2})_\nu$ (9.74)
$5/2^+$	$5/2^+_\pi \otimes 0^+_\nu$ (51.06)	$(g^4_{7/2}d^1_{5/2})_\pi \otimes (d^{-2}_{3/2}h^{-2}_{11/2})_\nu$ (29.99)
	$5/2^+_\pi \otimes 2^+_\nu$ (15.49)	$(g^4_{7/2}d^1_{5/2})_\pi \otimes (d^{-2}_{3/2}h^{-2}_{11/2})_\nu$ (9.34)
$9/2^+$	$5/2^+_\pi \otimes 2^+_\nu$ (31.40)	$(g^4_{7/2}d^1_{5/2})_\pi \otimes (d^{-2}_{3/2}h^{-2}_{11/2})_\nu$ (16.54)
	$9/2^+_\pi \otimes 0^+_\nu$ (29.69)	$(g^4_{7/2}d^1_{5/2})_\pi \otimes (d^{-2}_{3/2}h^{-2}_{11/2})_\nu$ (16.25)
$13/2^+$	$13/2^+_\pi \otimes 0^+_\nu$ (29.28)	$(g^4_{7/2}d^1_{5/2})_\pi \otimes (d^{-2}_{3/2}h^{-2}_{11/2})_\nu$ (19.71)
	$9/2^+_\pi \otimes 2^+_\nu$ (25.95)	$(g^4_{7/2}d^1_{5/2})_\pi \otimes (d^{-2}_{3/2}h^{-2}_{11/2})_\nu$ (13.67)
	$5/2^+_\pi \otimes 4^+_\nu$ (10.37)	$(g^4_{7/2}d^1_{5/2})_\pi \otimes (d^{-2}_{3/2}h^{-2}_{11/2})_\nu$ (4.72)
	$13/2^+_\pi \otimes 2^+_\nu$ (10.23)	$(g^4_{7/2}d^1_{5/2})_\pi \otimes (d^{-2}_{3/2}h^{-2}_{11/2})_\nu$ (6.57)
$17/2^+$	$17/2^+_\pi \otimes 0^+_\nu$ (39.41)	$(g^4_{7/2}d^1_{5/2})_\pi \otimes (d^{-2}_{3/2}h^{-2}_{11/2})_\nu$ (29.54)
	$13/2^+_\pi \otimes 2^+_\nu$ (22.52)	$(g^4_{7/2}d^1_{5/2})_\pi \otimes (d^{-2}_{3/2}h^{-2}_{11/2})_\nu$ (12.53)
$21/2^+$	$5/2^+_\pi \otimes 10^+_\nu$ (42.64)	$(g^4_{7/2}d^1_{5/2})_\pi \otimes (d^{-2}_{3/2}h^{-2}_{11/2})_\nu$ (23.98)
$25/2^+$	$7/2^+_\pi \otimes 10^+_\nu$ (44.58)	$(g^3_{7/2}d^2_{5/2})_\pi \otimes (d^{-2}_{3/2}h^{-2}_{11/2})_\nu$ (18.04)
	$5/2^+_\pi \otimes 10^+_\nu$ (19.63)	$(g^5_{7/2})_\pi \otimes (d^{-2}_{3/2}h^{-2}_{11/2})_\nu$ (5.65)
$21/2^+_2$	$7/2^+_\pi \otimes 8^+_\nu$ (25.74)	$(g^3_{7/2}d^2_{5/2})_\pi \otimes (d^{-2}_{3/2}h^{-2}_{11/2})_\nu$ (10.52)
	$7/2^+_\pi \otimes 10^+_\nu$ (17.93)	$(g^3_{7/2}d^2_{5/2})_\pi \otimes (d^{-2}_{3/2}h^{-2}_{11/2})_\nu$ (7.58)
	$5/2^+_\pi \otimes 8^+_\nu$ (10.01)	$(g^3_{7/2}d^2_{5/2})_\pi \otimes (d^{-2}_{3/2}h^{-2}_{11/2})_\nu$ (3.62)
$23/2^+_2$	$5/2^+_\pi \otimes 10^+_\nu$ (43.96)	$(g^4_{7/2}d^1_{5/2})_\pi \otimes (d^{-2}_{3/2}h^{-2}_{11/2})_\nu$ (22.90)
	$9/2^+_\pi \otimes 10^+_\nu$ (11.54)	$(g^4_{7/2}d^1_{5/2})_\pi \otimes (d^{-2}_{3/2}h^{-2}_{11/2})_\nu$ (5.79)
$25/2^+_2$	$5/2^+_\pi \otimes 10^+_\nu$ (22.91)	$(g^4_{7/2}d^1_{5/2})_\pi \otimes (d^{-2}_{3/2}h^{-2}_{11/2})_\nu$ (11.13)
	$5/2^+_\pi \otimes 12^+_\nu$ (22.87)	$(g^4_{7/2}d^1_{5/2})_\pi \otimes (d^{-1}_{3/2}s^{-1}_{1/2}h^{-2}_{11/2})_\nu$ (14.89)
	$7/2^+_\pi \otimes 10^+_\nu$ (16.52)	$(g^4_{7/2}d^1_{5/2})_\pi \otimes (d^{-2}_{3/2}h^{-2}_{11/2})_\nu$ (9.14)
$27/2^+_2$	$5/2^+_\pi \otimes 12^+_\nu$ (21.38)	$(g^4_{7/2}d^1_{5/2})_\pi \otimes (d^{-2}_{3/2}s^{-1}_{1/2}h^{-2}_{11/2})_\nu$ (11.66)
	$7/2^+_\pi \otimes 10^+_\nu$ (18.81)	$(g^5_{7/2})_\pi \otimes (d^{-2}_{3/2}h^{-2}_{11/2})_\nu$ (5.14)
$29/2^+_2$	$9/2^+_\pi \otimes 10^+_\nu$ (18.99)	$(g^4_{7/2}d^1_{5/2})_\pi \otimes (d^{-2}_{3/2}h^{-2}_{11/2})_\nu$ (10.76)
	$5/2^+_\pi \otimes 12^+_\nu$ (18.32)	$(g^4_{7/2}d^1_{5/2})_\pi \otimes (d^{-1}_{3/2}s^{-1}_{1/2}h^{-2}_{11/2})_\nu$ (7.23)
	$7/2^+_\pi \otimes 12^+_\nu$ (15.43)	$(g^4_{7/2}d^1_{5/2})_\pi \otimes (d^{-1}_{3/2}s^{-1}_{1/2}h^{-2}_{11/2})_\nu$ (7.28)
$31/2^+_2$	$11/2^+_\pi \otimes 10^+_\nu$ (21.38)	$(g^4_{7/2}d^1_{5/2})_\pi \otimes (d^{-2}_{3/2}h^{-2}_{11/2})_\nu$ (13.77)
	$13/2^+_\pi \otimes 10^+_\nu$ (19.04)	$(g^4_{7/2}d^1_{5/2})_\pi \otimes (d^{-2}_{3/2}h^{-2}_{11/2})_\nu$ (12.97)
	$7/2^+_\pi \otimes 12^+_\nu$ (15.12)	$(g^5_{7/2})_\pi \otimes (d^{-1}_{3/2}s^{-1}_{1/2}h^{-2}_{11/2})_\nu$ (4.88)
$33/2^+_2$	$13/2^+_\pi \otimes 10^+_\nu$ (25.39)	$(g^4_{7/2}d^1_{5/2})_\pi \otimes (d^{-2}_{3/2}h^{-2}_{11/2})_\nu$ (15.64)
	$17/2^+_\pi \otimes 10^+_\nu$ (24.09)	$(g^4_{7/2}d^1_{5/2})_\pi \otimes (d^{-2}_{3/2}h^{-2}_{11/2})_\nu$ (17.64)
	$15/2^+_\pi \otimes 10^+_\nu$ (12.82)	$(g^4_{7/2}d^1_{5/2})_\pi \otimes (d^{-2}_{3/2}h^{-2}_{11/2})_\nu$ (7.14)
$11/2^-$	$11/2^-_\pi \otimes 0^+_\nu$ (47.28)	$(g^4_{7/2}h^1_{11/2})_\pi \otimes (d^{-2}_{3/2}h^{-2}_{11/2})_\nu$ (26.57)
	$11/2^-_\pi \otimes 2^+_\nu$ (27.93)	$(g^4_{7/2}h^1_{11/2})_\pi \otimes (d^{-2}_{3/2}h^{-2}_{11/2})_\nu$ (15.28)
$15/2^-$	$11/2^-_\pi \otimes 2^+_\nu$ (34.01)	$(g^4_{7/2}h^1_{11/2})_\pi \otimes (d^{-2}_{3/2}h^{-2}_{11/2})_\nu$ (17.86)
	$15/2^-_\pi \otimes 0^+_\nu$ (24.95)	$(g^4_{7/2}h^1_{11/2})_\pi \otimes (d^{-2}_{3/2}h^{-2}_{11/2})_\nu$ (12.69)
	$15/2^-_\pi \otimes 2^+_\nu$ (11.53)	$(g^4_{7/2}h^1_{11/2})_\pi \otimes (d^{-2}_{3/2}h^{-2}_{11/2})_\nu$ (4.78)
$19/2^-$	$19/2^-_\pi \otimes 0^+_\nu$ (34.60)	$(g^4_{7/2}h^1_{11/2})_\pi \otimes (d^{-2}_{3/2}h^{-2}_{11/2})_\nu$ (22.43)
	$19/2^-_\pi \otimes 2^+_\nu$ (24.49)	$(g^4_{7/2}h^1_{11/2})_\pi \otimes (d^{-2}_{3/2}h^{-2}_{11/2})_\nu$ (14.94)
	$15/2^-_\pi \otimes 2^+_\nu$ (17.72)	$(g^4_{7/2}h^1_{11/2})_\pi \otimes (d^{-2}_{3/2}h^{-2}_{11/2})_\nu$ (9.36)
$23/2^-$	$23/2^-_\pi \otimes 0^+_\nu$ (34.17)	$(g^3_{7/2}d^1_{5/2}h^1_{11/2})_\pi \otimes (d^{-2}_{3/2}h^{-2}_{11/2})_\nu$ (13.85)
	$23/2^-_\pi \otimes 2^+_\nu$ (17.58)	$(g^3_{7/2}d^1_{5/2}h^1_{11/2})_\pi \otimes (d^{-2}_{3/2}h^{-2}_{11/2})_\nu$ (8.01)
	$19/2^-_\pi \otimes 2^+_\nu$ (13.44)	$(g^4_{7/2}h^1_{11/2})_\pi \otimes (d^{-2}_{3/2}h^{-2}_{11/2})_\nu$ (5.43)
$15/2^-_2$	$7/2^+_\pi \otimes 5^-_\nu$ (40.58)	$(g^5_{7/2})_\pi \otimes (d^{-2}_{3/2}s^{-1}_{1/2}h^{-1}_{11/2})_\nu$ (15.94)
	$5/2^+_\pi \otimes 5^-_\nu$ (24.16)	$(g^5_{7/2})_\pi \otimes (d^{-2}_{3/2}s^{-1}_{1/2}h^{-1}_{11/2})_\nu$ (11.10)
$19/2^-_2$	$7/2^+_\pi \otimes 7^-_\nu$ (44.75)	$(g^5_{7/2})_\pi \otimes (d^{-1}_{3/2}h^{-1}_{11/2})_\nu$ (16.53)
	$5/2^+_\pi \otimes 7^-_\nu$ (24.91)	$(g^5_{7/2})_\pi \otimes (d^{-1}_{3/2}h^{-1}_{11/2})_\nu$ (10.92)
$21/2^-_2$	$7/2^+_\pi \otimes 7^-_\nu$ (53.56)	$(g^5_{7/2})_\pi \otimes (d^{-1}_{3/2}h^{-1}_{11/2})_\nu$ (22.24)

the proton-particle pair in $g_{7/2}$ breaks giving rise to dominant proton angular momentum coupling of $9/2^+$ (18.99%), $11/2^+$ (21.38%), and $13/2^+$ (25.39%), respectively.

The negative-parity bands as shown in Table II have two different origins: (i) due to the presence of a proton particle in the $h_{11/2}$ orbital ($\pi g^4_{7/2}h^1_{11/2}$) and (ii) due to a neutron hole in the $s_{1/2}$ or $d_{3/2}$ and $h_{11/2}$ orbitals ($\nu d^{-2}_{3/2}s^{-1}_{1/2}h^{-1}_{11/2}$ or $\nu d^{-1}_{3/2}h^{-1}_{11/2}$). Bands arising from these two structures have been observed in the present experiment. Similar bands have also been observed in ^{135}La as given in Refs. [34,35]. The first set of negative-parity bands ($11/2^-$,$15/2^-$,$19/2^-$, and $23/2^-$) have a dominant wave function with four proton particles in the $g_{7/2}$ orbital and one proton particle in the $h_{11/2}$ orbital. There are two neutron holes in the $d_{3/2}$ and $h_{11/2}$ orbitals, similar to the case of positive-parity states. The valence proton particle in the $h_{11/2}$ orbital is responsible for the spin $11/2^-$ and the neutron holes are coupled to an angular momentum of 0^+ for the lowest state of this band, which is the most dominant decomposition probability (47.28%). For the $15/2^-$ state, the maximum contribution (34.01%) comes from the decomposition $I_\pi \otimes I_\nu = 11/2^-_\pi \otimes 2^+_\nu$, with additional contribution from a proton pair breaking in the $g_{7/2}$ orbital giving rise to $15/2^-_\pi$ and neutrons coupled to 0^+. For the $19/2^-$ and $23/2^-$ states, the governing contributions are from neutrons coupled to 0^+ and protons coupled to $19/2^-$ (34.60%) and $23/2^-$ (34.17%), respectively. The second set of negative-parity states ($15/2^-_2$,$19/2^-_2$, and $21/2^-_2$) have a dominant wave function with all five proton particles in the $g_{7/2}$ orbital and neutron configuration $\nu d^{-2}_{3/2}s^{-1}_{1/2}h^{-1}_{11/2}$ for $15/2^-_2$ and $d^{-1}_{3/2}h^{-1}_{11/2}$ for $19/2^-_2$ and $21/2^-_2$ states. The valence

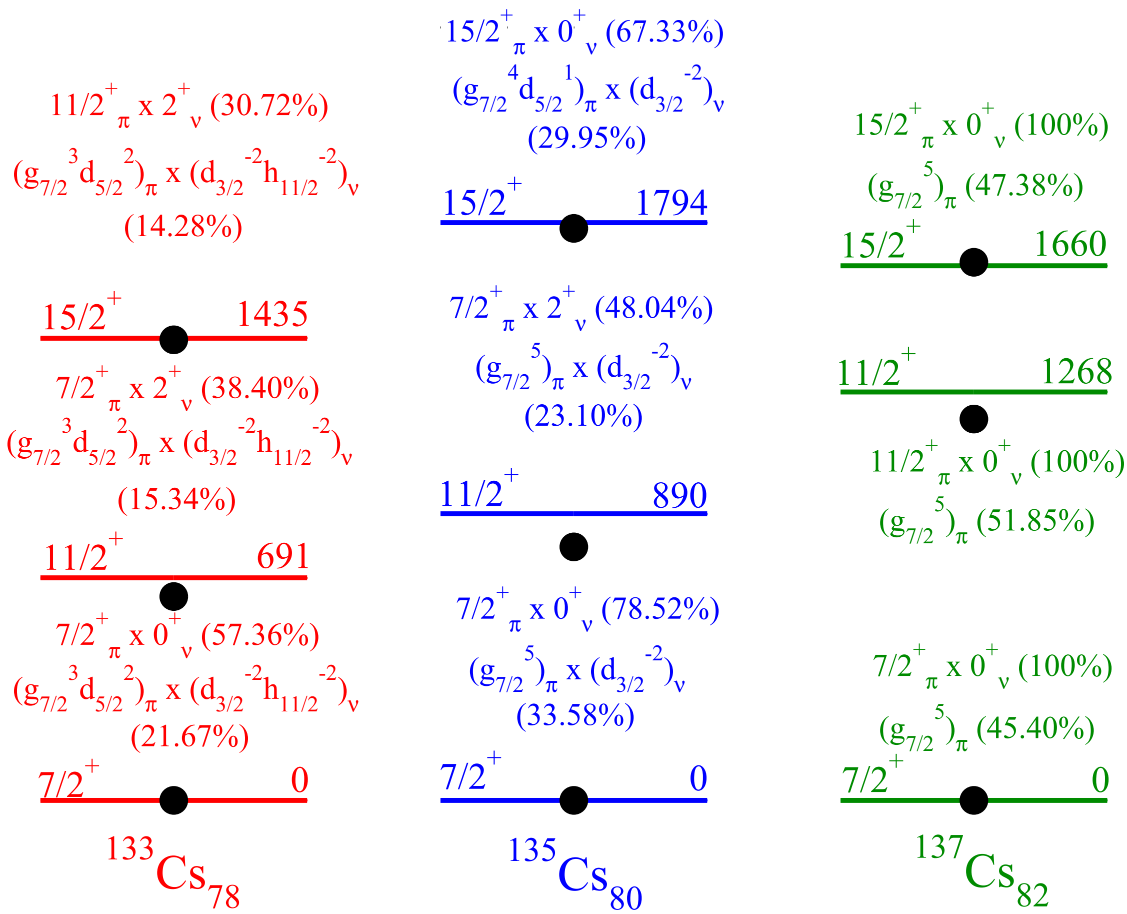

FIG. 7. Comparison between experiment (black filled circles) and shell model calculations for the $7/2^+$, $11/2^+$, and $15/2^+$ states of the positive-parity yrast bands in ^{133,135,137}Cs. There are two expressions for each state: the first expression shows the dominant angular momentum decomposition and the second expression shows the largest wave-function partition corresponding to the dominant angular momentum decomposition. A detailed explanation of these expressions is given in the text.

proton particle in the $g_{7/2}$ orbital and one neutron hole each in $s_{1/2}$ and $h_{11/2}$ orbitals is responsible for the spin $15/2^-_2$ state of this band, which has a maximum decomposition probability (40.58%). The maximum contributions for the $19/2^-_2$ and $21/2^-_2$ states come from $I_\pi = 7/2^+$ and $I_\nu = 7^-$ with probabilities 44.75% and 53.56%, respectively.

LSSM calculations without truncation for ^{135,137}Cs isotopes when compared with the experimental results give an overall good description of the level structure for the positive- as well as negative-parity states [33,36]. However, some deviation has been observed for the negative-parity states with higher spins. Comparison between experiment (black filled circles) and shell model calculations for the $7/2^+$, $11/2^+$, and $15/2^+$ states of the positive-parity yrast bands in ^{133,135,137}Cs are shown in the Fig. 7. The dominant angular momentum decomposition and the corresponding largest wave-function partition (the most dominant configuration) are also shown. For the ground state ($7/2^+$) in ^{137}Cs, the first expression depicts the angular momentum decomposition due to protons (π) and neutrons (ν), respectively: $7/2^+_\pi \times 0^+_\nu$ (100%). The neutrons do not participate in the excitation because the shell is completely filled. The five valence proton particles thus couple to generate an angular momentum of 7/2 and this leads to the angular momentum decomposition probability being 100%. However, this angular momentum decomposition does not convey the exact configuration of the valence proton particles in the different valence orbitals, and hence a knowledge of the wave function is required. The wave function (configuration) of the $7/2^+$ state corresponding to the angular momentum decomposition $7/2^+_\pi \times 0^+_\nu$ is given in the second expression. The LSSM calculations give the following wave function partitions, which add to 96.65% (< 100%): (i) $(g^5_{7/2})_\pi$ (45.40%), (ii) $(g^3_{7/2}d^2_{5/2})_\pi$ (29.89%), (iii) $(g^3_{7/2}h^2_{11/2})_\pi$ (11.46%), (iv) $(g^3_{7/2}d^2_{3/2})_\pi$ (4.16%), (v) $(g^1_{7/2}d^2_{5/2}h^2_{11/2})_\pi$ (2.23%), (vi) $(g^1_{7/2}d^4_{5/2})_\pi$ (1.87%), and (vii) $(g^3_{7/2}s^2_{1/2})_\pi$ (1.64%). In Fig. 7, only the most dominant wave-function partition is shown.

The angular momentum decomposition for the ground state ($7/2^+$) in ^{135}Cs is also shown in the first expression: $7/2^+_\pi \times 0^+_\nu$ (78.52%). Here, the neutrons also participate in excitations and hence the angular momentum decomposition probability is not 100% (contrary to ^{137}Cs). LSSM also gives other decompositions such as $5/2^+_\pi \times 2^+_\nu$ (7.60%), $11/2^+_\pi \times 2^+_\nu$ (5.33%), $9/2^+_\pi \times 2^+_\nu$ (2.87%), $3/2^+_\pi \times 2^+_\nu$ (2.05%), and $7/2^+_\pi \times 2^+_\nu$ (1.38%). The sum of all these probabilities gives

97.75% (<100%). Only the dominant angular momentum decomposition is shown in Fig. 7. The second expression depicts the wave function of the $7/2^+$ state corresponding to the dominant angular momentum decomposition, $7/2^+_\pi \times 0^+_\nu$ (78.52%). The shell model again gives a number of wave-function partitions: $(g^5_{7/2})_\pi \times (d^{-2}_{3/2})_\nu$ (33.58%), $(g^3_{7/2}d^2_{5/2})_\pi \times (d^{-2}_{3/2})_\nu$ (23.78%), $(g^3_{7/2}h^2_{11/2})_\pi \times (d^{-2}_{3/2})_\nu$ (9.48%), etc. The sum of probabilities for all these partitions add to 66.84% (< 78.52%).

The analysis of the wave functions indicates that the amplitude of the most dominant configuration for the $15/2^+$ state reduces from 47.38% for ^{137}Cs to 14.28% for ^{133}Cs. This demonstrates the increase in the mixing of configurations when one goes away from the $N = 82$ shell gap. Shell model calculations with a truncated model space, i.e., a model space consisting of proton $g_{7/2}$, $d_{5/2}$ orbitals and neutron $g_{7/2}$, $d_{5/2}$, $d_{3/2}$, $s_{1/2}$, and $h_{11/2}$ orbitals have also been used to calculate the positive-parity energy levels in $^{129-133}$Cs. However, the energy levels obtained from such calculations are very much compressed. This shows that a full model space is required to explain the excited states in odd-A Cs isotopes.

V. SUMMARY AND CONCLUSIONS

High-spin states in ^{133}Cs have been studied using the heavy-ion-induced fusion evaporation reaction ^{130}Te(^{7}Li,4n)^{133}Cs. The new data on the high-spin states in ^{133}Cs are important additions to the systematics of odd-A Cs isotopes, i.e., ^{127,129,131,135,137}Cs. Three different band structures, also seen in other odd-A Cs nuclei, viz. bands built on the $7/2^+$, $5/2^+$, and $11/2^-$ states, have been identified in ^{133}Cs. The proton $h_{11/2}$ band reported in the present work fits nicely with the systematics. The excitation energy of this bandhead increases with mass number for odd-A Cs isotopes, making it nonyrast and therefore difficult to observe for heavier odd-A Cs isotopes. The evolution of collectivity for these bands in odd Cs looks similar to that of their even-even Xe cores. Additionally, a dipole band arising from a three-quasiparticle structure has also been observed. Large-scale shell model calculations using the $jj55pna$ interaction have been used to compare the experimental levels of ^{133}Cs with the calculated ones. This comparison of the measured levels with the results of the shell model calculations provided a way for the interpretation of the various excited states in ^{133}Cs. The energy levels from the shell model calculations match remarkably well with the experimental data for the two sets of positive- and negative-parity states as has been observed for the measured levels in ^{135,137}Cs isotopes. In the case of ^{133}Cs, the shell model calculation has been carried out without truncation of the model space. Therefore, the present comparison really tests the predictive power of the interaction used in the calculation. It will be interesting to test the predictive power of the same model for the lighter odd-A Cs isotopes. However, with the present resources it is difficult to perform calculations for the lighter Cs isotopes without truncation. It is important to note that there is scope for improvements of the calculations to understand the observed discrepancies with the measurements for the dipole band which is underestimated. Interestingly, from the analysis of the LSM wave functions of certain positive-parity states in ^{133,135,137}Cs, it has been demonstrated that the mixing of configurations increases when one goes away from the $N = 82$ shell gap. It is important to carry out future measurements of lifetimes of excited states and compare the measured transition strengths with the prediction of the shell model calculation to probe the nature of collectivity of these states.

ACKNOWLEDGMENTS

The authors acknowledge the TIFR-BARC Pelletron Linac Facility for providing a good quality beam. The help and cooperation of the INGA Collaboration in setting up the array is acknowledged. This work has been partially funded by the Department of Science and Technology, Government of India (No. IR/S2/PF-03/2003-II) and the U.S. National Science Foundation (Grant No. PHY-1419765).

[1] R. Kumar, D. Mehta, N. Singh, H. Kaur, A. Görgen, S. Chmel, R. P. Singh, and S. Murlithar, Eur. Phys. J. A **11**, 5 (2001).
[2] E. Grodner, J. Srebrny, A. A. Pasternak, I. Zalewska, T. Morek, C. Droste, J. Mierzejewski, M. Kowalczyk, J. Kownacki, M. Kisieliński *et al.*, Phys. Rev. Lett. **97**, 172501 (2006).
[3] N. Fotiades, J. A. Cizewski, K. Higashiyama, N. Yoshinaga, E. Teruya, R. Krücken, R. M. Clark, P. Fallon, I. Y. Lee, A. O. Machiavelli *et al.*, Phys. Rev. C **88**, 064315 (2013).
[4] E. Teruya, N. Yoshinaga, K. Higashiyama, and A. Odahara, Phys. Rev. C **92**, 034320 (2015).
[5] P. Möller, A. J. Sierk, R. Bengtsson, H. Sagawa, and T. Ichikawa, At. Data Nucl. Data Tables **98**, 149 (2012).
[6] F. Lidén, B. Cederwall, P. Ahonen, D. W. Banes, B. Fant, J. Gascon, L. Hildingsson, A. Johnson, S. Juutinen, A. Kirwan *et al.*, Nucl. Phys. A **550**, 365 (1992).
[7] U. Garg, T. P. Sjoreen, and D. B. Fossan, Phys. Rev. C **19**, 217 (1979).
[8] Y. Liang, R. Ma, E. S. Paul, N. Xu, D. B. Fossan, and R. A. Wyss, Phys. Rev. C **42**, 890 (1990).
[9] L. Hildingsson, W. Klamra, T. Lindblad, F. Lidén, Y. Liang, R. Ma, E. S. Paul, N. Xu, D. B. Fossan, and J. Gascon, Z. Phys. A **340**, 29 (1991).
[10] R. Kumar, K. Singh, D. Mehta, N. Singh, S. S. Malik, E. S. Paul, A. Görgen, S. Chmel, R. P. Singh, and S. Muralithar, Eur. Phys. J. A **24**, 13 (2005).
[11] U. Garg, T. P. Sjoreen, and D. B. Fossan, Phys. Rev. C **19**, 207 (1979).
[12] P. Alexander and J. P. Lau, Nucl. Phys. A **121**, 612 (1968).
[13] S. Törnkvist, L. Hasselgren, S. Ström, J.-E. Thun, and S. Antman, Nucl. Phys. A **142**, 238 (1970).
[14] H. Tan *et al.*, in *Proceedings of the IEEE Nuclear Science Symposium and Medical Imaging Conference* (2008NSS/MIC) Dresdan (IEEE, New York, 2009), p. 2471.
[15] R. Palit, S. Saha, J. Sethi, T. Trivedi, S. Sharma, B. S. Naidu, S. Jadhav, R. Donthi, P. B. Chavan, H. Tan *et al.*, Nucl. Instrum. Methods Phys. Res. Sect. A **680**, 90 (2012).

[16] D. C. Radford, Nucl. Instrum. Methods Phys. Res. Sect. A **361**, 297 (1995).
[17] A. Krämer-Flecken, T. Morek, R. M. Lieder, W. Gast, G. Hebbinghaus, H. M. Jäger, and W. Urban, Nucl. Instrum. Methods Phys. Res. Sect. A **275**, 333 (1989).
[18] K. Starosta, T. Morek, C. Droste, S. G. Rohoziński, J. Srebrny, A. Wierzchucka, M. Bergström, B. Herskind, E. Melby, T. Czosnyka *et al.*, Nucl. Instrum. Methods Phys. Res. Sect. A **423**, 16 (1999).
[19] R. Palit, H. C. Jain, P. K. Joshi, S. Nagaraj, B. V. T. Rao, S. N. Chintalapudi, and S. S. Ghugre, Pramana **54**, 347 (2000).
[20] Y. Zheng, G. deFrance, E. Clement, A. Dijon, B. Cederwall, R. Wadsworth, T. Back, F. GhaziMoradi, G. Jaworski, B. M. Nyako, J. Nyberg, M. Palacz, H. Al-Azri, G. deAngelis, A. Atac, O. Aktas, S. Bhattacharyya, T. Brock, P. J. Davies, A. DiNitto, Z. Dombradi, A. Gadea, J. Gal, P. Joshi, K. Juhasz, R. Julin, A. Jungclaus, G. Kalinka, J. Kownacki, G. LaRana, S. M. Lenzi, J. Molnar, R. Moro, D. R. Napoli, B. S. NaraSingh, A. Persson, F. Recchia, M. Sandzelius, J. N. Scheurer, G. Sletten, D. Sohler, P. A. Soderstrom, M. J. Taylor, J. Timar, J. J. Valiente-Dobon, and E. Vardaci, Phys. Rev. C **87**, 044328 (2013).
[21] W. Lie-Lin, Z. Li-Hua, L. Jing-Bin, W. Xiao-Guang, L. Guang-Sheng, H. Xin, Z. Yun, H. Chuang-Ye, W. Lei, L. Xue-Qin *et al.*, Chin. Phys. Lett. **27**, 022101 (2010)
[22] S. Sihotra, R. Palit, Z. Naik, K. Singh, P. K. Joshi, A. Y. Deo, J. Goswamy, S. S. Malik, D. Mehta, C. R. Praharaj *et al.*, Phys. Rev. C **78**, 034313 (2008).
[23] A. Astier, M.-G. Porquet, T. Venkova, D. Verney, C. Theisen, G. Duchêne, F. Azaiez, G. Barreau, D. Curien, I. Deloncle *et al.*, Phys. Rev. C **85**, 064316 (2012).
[24] S. Sihotra, K. Singh, S. S. Malik, J. Goswamy, R. Palit, Z. Naik, D. Mehta, N. Singh, R. Kumar, R. P. Singh, and S. Muralithar, Phys. Rev. C **79**, 044317 (2009).
[25] B. A. Brown and W. D. M. Rae, Nucl. Data Sheets **120**, 115 (2014).
[26] W. D. M. Rae, NUSHELLX, http://www.garsington.eclipse.co.uk.
[27] B. A. Brown, N. J. Stone, J. R. Stone, I. S. Towner, and M. Hjorth-Jensen, Phys. Rev. C **71**, 044317 (2005).
[28] R. Machleidt, F. Sammarruca, and Y. Song, Phys. Rev. C **53**, R1483 (1996).
[29] A. Astier, M.-G. Porquet, C. Theisen, D. Verney, I. Deloncle, M. Houry, R. Lucas, F. Azaiez, G. Barreau, D. Curien *et al.*, Phys. Rev. C **85**, 054316 (2012).
[30] Ł. W. Iskra, R. Broda, R. V. F. Janssens, J. Wrzesiński, B. Szpak, C. J. Chiara, M. P. Carpenter, B. Fornal, N. Hoteling, and F. G. Kondev *et al.*, Phys. Rev. C **89**, 044324 (2014).
[31] A. Astier, M.-G. Porquet, T. Venkova, C. Theisen, G. Duchêne, F. Azaiez, G. Barreau, D. Curien, I. Deloncle, O. Dorvaux *et al.*, Eur. Phys. J. A **50**, 2 (2014).
[32] S. Biswas, R. Palit, A. Navin, M. Rejmund, A. Bisoi, M. S. Sarkar, S. Sarkar, S. Bhattacharya, D. C. Biswas, M. Caamaño *et al.*, Phys. Rev. C **93**, 034324 (2016).
[33] P. C. Srivastava, M. J. Ermamatov, and Irving O. Morales, J. Phys. G: Nucl. Part. Phys. **40**, 035106 (2013).
[34] Ritika Garg, S. Kumar, M. Saxena, S. Goyal, D. Siwal, S. Verma, R. Palit, S. Saha, J. Sethi, S. K. Sharma *et al.*, Phys. Rev. C **87**, 034317 (2013).
[35] R. Leguillon, H. Nishibata, Y. Ito, C. M. Petrache, A. Odahara, T. Shimoda, N. Hamatani, K. Tajiri, J. Takatsu, R. Yokoyama *et al.*, Phys. Rev. C **88**, 044309 (2013).
[36] S. Biswas *et al.* (unpublished).

Available online at www.sciencedirect.com

ScienceDirect

Nuclear Data Sheets 114 (2013) 2023–2078

Nuclear Data Sheets

www.elsevier.com/locate/nds

Nuclear Data Sheets for A = 215

Principal Author and Coordinator:
Balraj Singh (McMaster Univ, Hamilton, Canada)
Author and Coordinator:
Gopal Mukherjee (Variable Energy Cyclotron Centre (VECC), Kolkata, India)
Authors:
Daniel Abriola (International Atomic Energy Agency (IAEA), Vienna, Austria)
Swapan Kumar Basu (VECC, Kolkata, India)
Paraskevi Demetriou (IAEA, Vienna, Austria)
Ashok Jain (Indian Institute of Technology (IIT), Roorkee, India)
Suresh Kumar (Delhi University, Delhi, India)
Sukhjeet Singh (M.M. University, Mullana, Ambala, India)
Jagdish Tuli (Brookhaven National Laboratory (NNDC,BNL), Upton, NY, USA)
Reviewer:
Edgardo Browne (NNDC,BNL, Upton, NY, USA)
Trainees:
Srijit Bhattacharya (Barasat Government College, Kolkata, India)
Sudeb Bhattacharya (Saha Institute of Nuclear Physics, Kolkata, India)
Shinjinee Dasgupta (VECC, Kolkata, India)
A. De (Raniganj Girls' College, Burdwan, India)
R. Gowrishankar (S.S. Institute of Higher Learning (SSIHL), Prasanthi Nilayam, India)
Navneet Kaur (Panjab University, Chandigarh, India)
S. Lakshmi (IIT, Roorkee, India)
Jeong-Yeon Lee (Sejong Univ, Seoul, Korea)
Bhoomika Maheshwari (IIT, Roorkee, India)
Debasish Mondal (VECC, Kolkata, India)
Aman Rohilla (Delhi University, Delhi, India)
K. Rojeeta Devi (Delhi University, Delhi, India)
K. Vijay Sai (SSIHL, Prasanthi Nilayam, India)

(Received April 18, 2013; Revised October 22, 2013)

Abstract: The evaluated spectroscopic data are presented for 12 known nuclides of mass 215 (Hg, Tl, Pb, Bi, Po, At, Rn, Fr, Ra, Ac, Th, Pa). For ^{215}Hg, ^{215}Tl, ^{215}Pb, and ^{215}Pa nuclei, no excited states are known. The decay characteristics of ^{215}Hg and ^{215}Tl are unknown. The decay scheme of ^{215}Pb is considered as incomplete. Ordering of γ cascades in the decay of 36.9-s isomer of ^{215}Bi and for high-spin states above 2251 keV in ^{215}Fr are not established. High-spin excitations, including several isomeric states, are well known in ^{215}Bi, ^{215}Po, ^{215}Rn, ^{215}Fr, ^{215}Ra, and ^{215}Ac. No particle-transfer reaction data are available for any of the A=215 nuclei.

The rms charge radii for ^{215}Pb, ^{215}Bi, ^{215}Po, ^{215}Rn, ^{215}Fr and ^{215}Ra have been evaluated by Daniel Abriola, from extrapolation or interpolation of available evaluated data in 2013An02 for radii of respective Z chains using formula 9 in 2004An14.

This evaluation was carried out as part of ENSDD-workshop at VECC, Kolkata for Nuclear Structure and Decay Data, organized and hosted by VECC and Board of Research in Nuclear Sciences (BRNS) in Kolkata, India, November 26-29, 2012. This work supersedes the previous A=215 evaluation (2001Br31) published by E. Browne which covered literature prior to May 2001.

Cutoff Date: All data received prior to October 22, 2013 have been considered. Main source of bibliographic search was Nuclear Science References (NSR) database (2011Pr03) available at www.nndc.bnl.gov webpage.

General Policies and Organization of Material: See the January issue of the *Nuclear Data Sheets* or http://www.nndc.bnl.gov/nds/NDSPolicies.pdf.

Acknowledgments: We thank JoAnn Totans (NNDC, BNL) for access to several articles, and Marion Blennau (NNDC, BNL) for preparation of printed version from ENSDF-formatted data files submitted by the evaluators.

This work was supported by VECC and BRNS, India; and the Office of Science, US Department of Energy.

General Comments: All Q values are from 2012Wa38. All theoretical conversion coefficients are from the computer code BrIcc (2008Ki07). A general uncertainty of 1.4% is assumed in the quoted values of these coefficients. When weighted average of a set of data is taken, the assigned uncertainty is assumed not lower than the lowest experimental uncertainty in the set.

http://dx.doi.org/10.1016/j.nds.2013.11.003

Index for A = 215

Skeleton Scheme for A=215

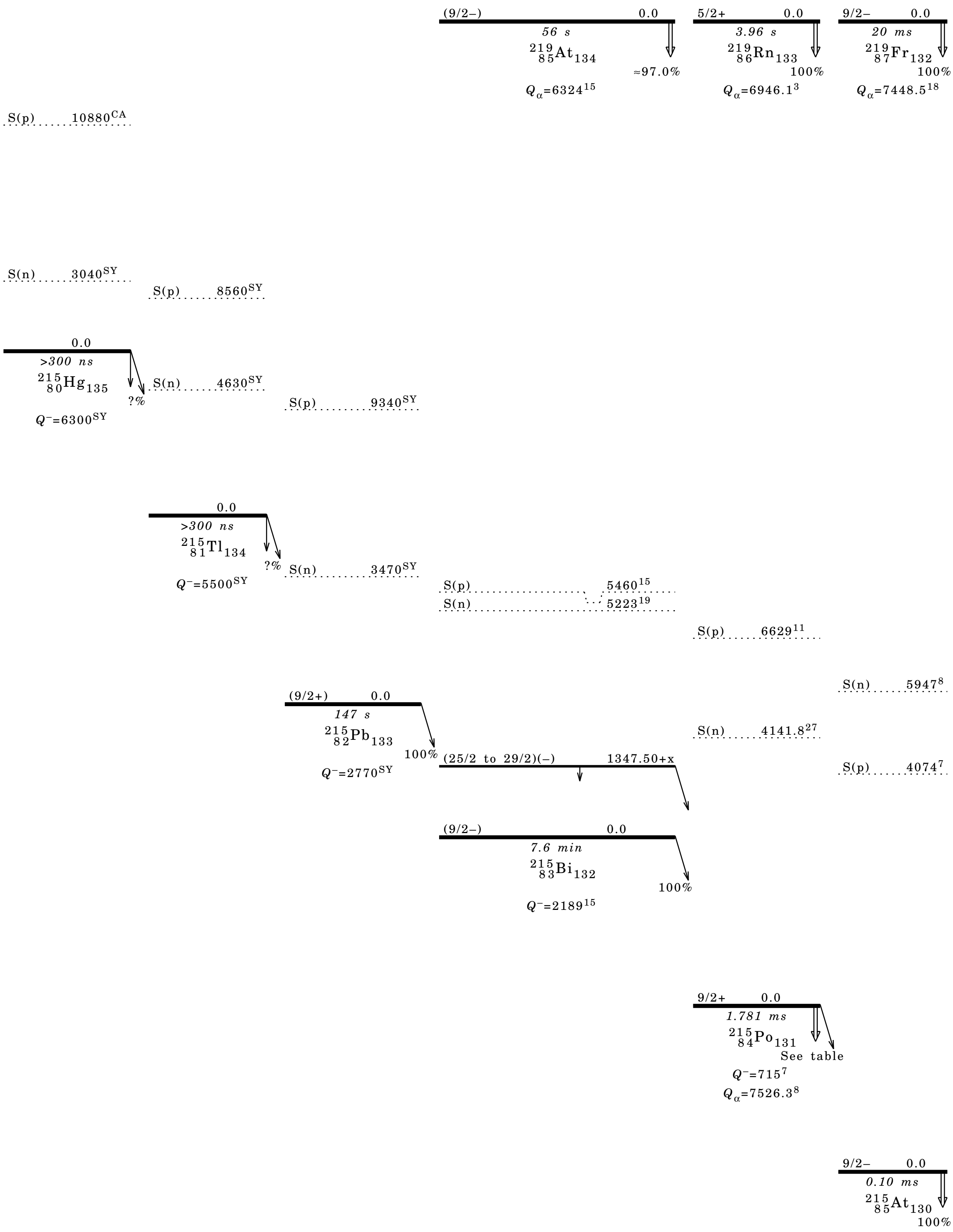

Skeleton Scheme for A=215 (continued)

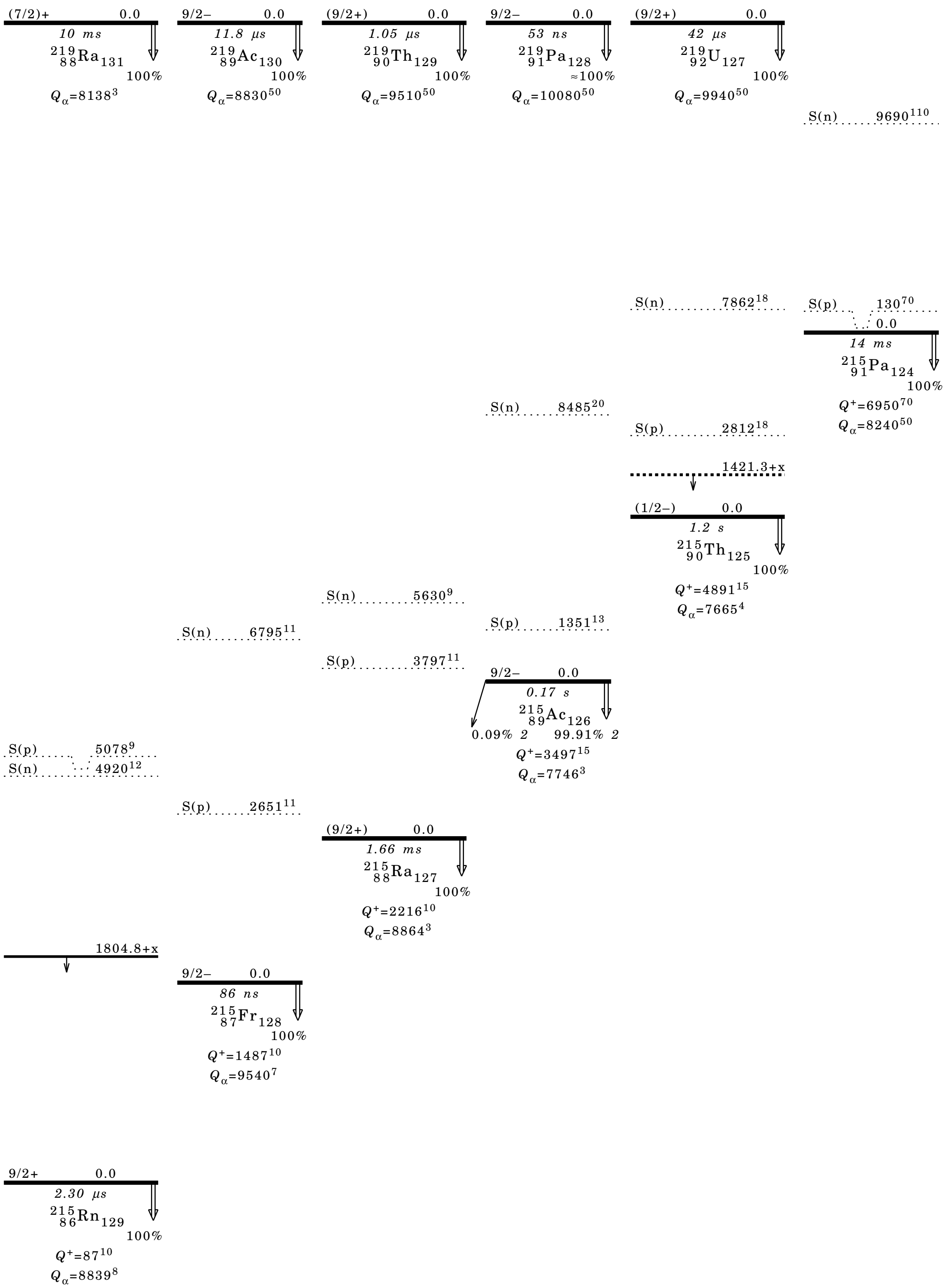

Ground–State and Isomeric–Level Properties for A=215

Nuclide	Level	Jπ	$T_{1/2}$	Decay Modes
^{215}Hg	0.0		>300 ns	%β^-=?; %β^-n=?
^{215}Tl	0.0		>300 ns	%β^-=?; %β^-n=?
^{215}Pb	0.0	(9/2+)	147 s *12*	%β^-=100
^{215}Bi	0.0	(9/2−)	7.6 min *2*	%β^-=100
	1347.50+x	(25/2:29/2)(−)	36.9 s *6*	%IT=76.9 *5*; %β^-=23.1 *5*
^{215}Po	0.0	9/2+	1.781 ms *5*	%α=99.99977 *2*; %β^-=2.3×10^{-4} *2*
^{215}At	0.0	9/2−	0.10 ms *2*	%α=100
^{215}Rn	0.0	9/2+	2.30 µs *10*	%α=100
	1804.8+x		57 ns *+21−12*	%IT=100
^{215}Fr	0.0	9/2−	86 ns *5*	%α=100
^{215}Ra	0.0	(9/2+)	1.66 ms *2*	%α=100
^{215}Ac	0.0	9/2−	0.17 s *1*	%α=99.91 *2*; %ε+%β^+=0.09 *2*
^{215}Th	0.0	(1/2−)	1.2 s *2*	%α=100
	1421.3+x		0.77 µs *6*	%IT≈100
^{215}Pa	0.0		14 ms *2*	%α=100
^{219}At	0.0	(9/2−)	56 s *3*	%α≈97.0; ...
^{219}Rn	0.0	5/2+	3.96 s *1*	%α=100
^{219}Fr	0.0	9/2−	20 ms *2*	%α=100
^{219}Ra	0.0	(7/2)+	10 ms *3*	%α=100
^{219}Ac	0.0	9/2−	11.8 µs *15*	%α=100
^{219}Th	0.0	(9/2+)	1.05 µs *3*	%α=100
^{219}Pa	0.0	9/2−	53 ns *10*	%α≈100
^{219}U	0.0	(9/2+)	42 µs *+34−13*	%α=100

Adopted Levels

Q(β⁻)=6300 *SY*; S(n)=3040 *SY*; S(p)=10880 *CA*; Q(α)=990 *CA* 2012Wa38,1997Mo25.
Estimated uncertainties: ΔQ(β⁻)=500, ΔS(n)=570 (2012Wa38).
Q(β⁻) and S(n) from 2012Wa38, S(p) and Q(α) from 1997Mo25.
Q(β⁻n)=1670 *450*, S(2n)=7600 *500* (syst,2012Wa38). S(2p)=20780 (1997Mo25,calculated).

^{215}Hg evaluated by B. Singh.

2010Al24: ^{215}Hg nuclide identified in ^{9}Be(^{238}U,X) reaction with a beam energy of 1 GeV/nucleon produced by the SIS synchrotron at GSI facility. Target=2500 mg/cm^2. The fragment residues were analyzed with the high resolving power magnetic spectrometer– Fragment Recoil Separator (FRS) at GSI. The identification of nuclei was made on the basis of magnetic rigidity, velocity, time–of–flight, energy loss and atomic number of the fragments using two plastic scintillators and two multisampling ionization chambers. The FRS magnet was tuned to center on ^{210}Au, ^{216}Pb, ^{219}Pb, ^{227}At and ^{229}At nuclei along the central trajectory of FRS.

Unambiguous identification of nuclides required the separation of different charge states of the nuclei passing through the FRS. At 1 GeV/nucleon incident energy of ^{238}U, the fraction of fully stripped ^{226}Po nuclei was about 89%. Through the measurement of difference in magnetic rigidity in the two sections of the FRS and the difference in energy loss in the two ionization chambers, the charge state of the transmitted nuclei was determined, especially, that of the singly charged (hydrogen–like) nuclei which preserved their charge in the current experimental setup. Measured production cross sections with 10% statistical and 20% systematic uncertainties.

Criteria established in 2010Al24 for acceptance of identification of a new nuclide: 1. number of events should be compatible with the corresponding mass and atomic number located in the expected range of positions at both image planes of the FRS spectrometer; 2. number of events should be compatible with >95% probability that at least one of the counts does not correspond to a charge–state contaminant. Comparisons of measured σ with model predictions using the computer codes COFRA and EPAX.

^{215}Hg Levels

E(level)	$T_{1/2}$	Comments
0.0	>300 ns	%β⁻=? ; %β⁻n=? Production σ=61.8 pb (from e–mail reply of Oct 29, 2010 from H. Alvarez–Pol, which also stated that further analysis was in progress). The β⁻ and delayed neutron decay are the only decay modes expected. Theoretical %β⁻n=4.2 (1997Mo25). E(level): the observed fragments are assumed to be in the ground state of ^{215}Hg nuclei. From A/Z plot (figure 1 in 2010Al24), 4 or 5 events are assigned to ^{215}Hg. $T_{1/2}$: lower limit from time–of–flight as given in 2006Ca30 for a similar setup. Actual half–life is expected to be much longer as suggested by the theoretical value of 0.25 s for β decay and >10^{20} s for α decay (1997Mo25), and systematics value of 1 s for β decay (2012Au07). Jπ: 3/2+ from systematics (2012Au07), and 9/2+ predicted in 1997Mo25 calculations. Production cross section measured in 2010Al24, values are given in figure 2, plot of σ versus mass number of Hg isotopes. Statistical uncertainty=10%, systematic uncertainty=20%.

Adopted Levels

Q(β⁻)=5500 *SY*; S(n)=4630 *SY*; S(p)=8560 *SY*; Q(α)=1810 *CA* 2012Wa38,1997Mo25.
Estimated uncertainties: ΔQ(β⁻)=320, ΔS(n)=360, ΔS(p)=500 (2012Wa38).
Q(β⁻), S(n) and S(p) from 2012Wa38; Q(α) from 1997Mo25.
Q(β⁻n)=2020 *300*, S(2n)=8020 *300* (syst,2012Wa38). S(2p)=19580 (1997Mo25,calculated).

^{215}Tl evaluated by B. Singh.

Continued on next page

Adopted Levels (continued)

2010Al24: ^{215}Tl nuclide identified in ^{9}Be(^{238}U,X) reaction with a beam energy of 1 GeV/nucleon produced by the SIS synchrotron at GSI facility. Target=2500 mg/cm^{2}. The fragment residues were analyzed with the high resolving power magnetic spectrometer– Fragment Recoil Separator (FRS) at GSI. The identification of nuclei was made on the basis of magnetic rigidity, velocity, time–of–flight, energy loss and atomic number of the fragments using two plastic scintillators and two multisampling ionization chambers. The FRS magnet was tuned to center on ^{210}Au, ^{216}Pb, ^{219}Pb, ^{227}At and ^{229}At nuclei along the central trajectory of the FRS.

Unambiguous identification of nuclides required the separation of different charge states of the nuclei passing through the FRS. At 1 GeV/nucleon incident energy of ^{238}U, the fraction of fully stripped ^{226}Po nuclei was about 89%. Through the measurement of difference in magnetic rigidity in the two sections of the FRS and the difference in energy loss in the two ionization chambers, the charge state of the transmitted nuclei was determined, especially, that of the singly charged (hydrogen–like) nuclei which preserved their charge in the current experimental setup. Measured production cross sections with 10% statistical and 20% systematic uncertainties.

Criteria established in 2010Al24 for acceptance of identification of a new nuclide: 1. number of events should be compatible with the corresponding mass and atomic number located in the expected range of positions at both image planes of the FRS spectrometer; 2. number of events should be compatible with >95% probability that at least one of the counts does not correspond to a charge–state contaminant. Comparisons of measured σ with model predictions using the computer codes COFRA and EPAX.

2004DeZV: the authors mention using RILIS ionization source to study the ^{215}Tl activity by βγγ coincidence arrangement, but no resonant γ rays were seen. Most likely, the ^{215}Tl activity was not formed in this study.

^{215}Tl Levels

E(level)	$T_{1/2}$	Comments
0.0	>300 ns	%β^-=? ; %β^-n=? Production σ=0.877 nb (from e–mail reply of Oct 29, 2010 from H. Alvarez–Pol, which also stated that further analysis was in progress). From A/Z plot (figure 1 in 2010Al24), ≈ 35 events are assigned to ^{215}Tl. E(level): the observed fragments are assumed to be in the ground state of ^{215}Tl nuclei. The β^- and delayed neutron decay are the only decay modes expected. Theoretical %β^-n=99 (1997Mo25). $T_{1/2}$: lower limit from time–of–flight as given in 2006Ca30 for a similar setup. Actual half–life is expected to be much larger as suggested by the theoretical value of 20 s for β decay and >10^{20} s for α decay (1997Mo25), and systematic value of 5 s for β decay (2012Au07). Jπ: 1/2+ predicted in 1997Mo25 calculations, and from systematics (2012Au07). Production cross section measured in 2010Al24, values are given in figure 2, plot of σ versus mass number for Tl isotopes. Statistical uncertainty=10%, systematic uncertainty=20%.

$^{215}_{82}Pb_{133}$–1 $^{215}_{82}Pb_{133}$–1

Adopted Levels

Q(β^-)=2770 *SY*; S(n)=3470 *SY*; S(p)=9340 *SY*; Q(α)=2620 *SY* 2012Wa38.
Estimated uncertainties: ΔQ(β^-)=ΔS(n)=100, ΔS(p)=ΔQ(α)=220 (2012Wa38).
S(2n)=8530 *100*, S(2p)=17830 *320* (syst,2012Wa38).

^{215}Pb evaluated by B. Singh.

2010Al24 claim to identify ^{215}Pb for the first time, however as explained below, there have been several previous reports from GSI and ISOLDE, CERN groups where this isotope was identified, produced, and its half–life measured, for example in 1998Pf02 and in the thesis by 2004DeZV.

1998Pf02: GSI group: ^{9}Be(^{238}U,X), E=1 GeV/nucleon. Identification of ^{215}Pb by time–of–flight, energy loss, and Bρ measurements; FRS separator. Measured cross section.

Continued on next page

Adopted Levels (continued)

1998RyZY, 1998Va13, 2003Ku26: ISOLDE, CERN group: 1998RyZY: reported tentative identification of ^{215}Pb with $T_{1/2}$=36.5 s formed in ^{232}Th(p,X) at 1 GeV from the observation of a γ cascade in ^{215}Bi. This was also mentioned briefly in 1998Va13. But later, in 2003Ku26, using RILIS source, this activity was reassigned to a high–spin isomer in ^{215}Bi. However, 2003Ku26 stated that ^{215}Pb isotope had been identified and that its study would be published elsewhere (reference 11 in 2003Ku26). In 2003Ko26, yield in Th(p,X) E=1 GeV reaction and using RILIS source, was reported (in figure 4 of 2003Ko26) as 0.3 μCi. In Fall 2002 Newsletter of ISOLDE, CERN, a short article by S. Franchoo quoted the half–life of ^{215}Pb as 147 s *12*. In 2012Au07 (NUBASE), $T_{1/2}$ is listed as 36 s *1*, a value based on a report by 1998RyZY, which was refuted in 2003Ku26. Confirmatory details of the ISOLDE, CERN group are reported in the thesis by 2004DeZV, where half–life of ^{215}Pb from γ–decay and the decay scheme of ^{215}Pb to ^{215}Bi are presented. This thesis was brought to the evaluator's attention by Professor P. van Duppen in e–mail communications of June 2011.

2004DeZV, 2013De20: ^{215}Pb produced via reaction ^{238}U(p,X) with E(p)=1.4 GeV, ionized by the Resonance ionization laser ion source (RILIS) and separated using the ISOLDE on–line mass separator. Detector system included an Si–detector for α–particles, one low–energy Ge and two HPGe detectors for x rays and γ rays, as well as a plastic scintillator ΔE detector for β–particles. Measured Eγ, Iγ, Iβ, βγ and γγ coincidence. Deduced levels in ^{215}Bi, $T_{1/2}$.

2010Al24: ^{215}Pb nuclide identified in ^{9}Be(^{238}U,X) reaction with a beam energy of 1 GeV/nucleon produced by the SIS synchrotron at GSI facility. Target=2500 mg/cm^2. The fragment residues were analyzed with the high resolving power magnetic spectrometer Fragment separator (FRS). The identification of nuclei was made on the basis of magnetic rigidity, velocity, time–of–flight, energy loss and atomic number of the fragments using two plastic scintillators and two multisampling ionization chambers. The FRS magnet was tuned to center on ^{210}Au, ^{216}Pb, ^{219}Pb, ^{227}At and ^{229}At nuclei along the central trajectory of FRS. See also an earlier report 2009Al32 from the same group as 2010Al24. Unambiguous identification of nuclides required the separation of different charge states of the nuclei passing through the FRS. At 1 GeV/nucleon incident energy of ^{238}U, fraction of fully stripped ^{226}Po nuclei was about 89%. Through the measurement of difference in magnetic rigidity in the two sections of the FRS and the difference in energy loss in the two ionization chambers, the charge state of the transmitted nuclei was determined, especially, that of the singly charged (hydrogen–like) nuclei which preserved their charge in the current experimental setup. Measured production cross sections with 10% statistical and 20% systematic uncertainties. Criterion established in 2010Al24 for acceptance of identification of a new nuclide: 1. number of events should be compatible with the corresponding mass and atomic number located in the expected range of positions at both image planes of the FRS spectrometer; 2. number of events should be compatible with >95% probability that at least one of the counts does not correspond to a charge–state contaminant. Comparisons of measured σ with model predictions using the computer codes COFRA and EPAX.

Nuclear structure calculations:

2012Ko09: calculated rms radii, rms radius of neutron and proton distributions, isovector shift of nuclear rms radii, bulk density, neutron skin.

2008Ma17: HFB calculations of binding energy, two–neutron separation energy, odd–even mass staggering and pairing gaps.

2003Bo06: calculated $T_{1/2}$ using Shell model and quasiparticle RPA.

1987Sa51: calculated isotope shifts, B(E2).

^{215}Pb Levels

E(level)	Jπ	$T_{1/2}$	Comments
0.0	(9/2+)	147 s *12*	%β^-=100. RMS charge radius $\langle r^2\rangle^{1/2}$=5.567 fm *7*; deduced from extrapolation of evaluated rms charge radii of ^{208}Pb to ^{214}Pb (2013An02), with slope k_z=0.36 in formula 9 of 2004An14. E(level): the observed fragments are assumed to be in the ground state of ^{215}Pb nuclei. $T_{1/2}$: from decay curves of γ rays (2013De20,2004DeZV). Other: 36 s *1* reported in 1998RyZY was refuted by 2003Ku26. Jπ: 9/2+ from systematics (2012Au07), and also proposed in 2013De20. 7/2 predicted in 1997Mo25 calculations. From A/Z plot (figure 1 in 2010Al24), a large number (certainly more than few hundreds) of events are assigned to ^{215}Pb. In 1998Pf02, number of events in figure 1 seems about 60. The β^- decay is the only decay mode expected, and observed in 2013De20. Production σ=51.7 nb (from e–mail reply of Oct 29, 2010 from H. Alvarez–Pol, which also stated that further analysis was in progress); 90 nb *20* (1998Pf02). Production cross sections measured in 2010Al24 are given in authors' figure 2, plot of σ versus mass number for Pb isotopes. Statistical uncertainty=10%, systematic uncertainty=20%.

Adopted Levels, Gammas

Q(β⁻)=2189 *15*; S(n)=5223 *19*; S(p)=5460 *15*; Q(α)=5300 *40* 2012Wa38.
S(2n)=9264 *16*, S(2p)=14710 *30* (2012Wa38).

^{215}Bi evaluated by D. Abriola, P. Demetriou, B. Singh, R. Gowrishankar, K. Vijay Sai.

1953Hy83: β⁻ decay inferred by measurements of the α decay of the ^{215}Po daughter nucleus, measured half–life.
1965Nu03: descendant of radioactive source ^{227}Ac. Measured $T_{1/2}$.
1990Ru02: source produced by spallation of 200–MeV protons on targets of ^{232}Th. ^{215}Bi(7.6 min) activity was identified by mass separation and by the observation of known γ rays in the daughter nucleus ^{215}Po. Measured $T_{1/2}$. The β⁻ particles were detected in a 4π plastic scintillator.
2008We02: precise mass measurement using ISOLTRAP Penning–trap mass spectrometer.

^{215}Bi Levels

Cross Reference (XREF) Flags

A ^{215}Pb β⁻ Decay (147 s)
B ^{215}Bi IT Decay (36.9 s)
C ^{219}At α Decay (56 s)

E(level)†	Jπ	XREF	$T_{1/2}$	Comments
0.0	(9/2−)	ABC	7.6 min *2*	%β⁻=100. RMS charge radius $<r^2>^{1/2}$=5.576 fm *9*; deduced from extrapolation of evaluated rms charge radii of ^{209}Bi to ^{213}Bi (2013An02), with slope k_z=0.35 in formula 9 of 2004An14. %β⁻: only β⁻ decay mode observed (1990Ru02,1953Hy83). %α≈8.×10⁻⁵ from systematics of α branching versus Q(α) for ^{212}Bi, ^{213}Bi, and ^{214}Bi. Jπ: analogy to ^{209}Bi, ^{211}Bi, and ^{213}Bi suggests $\pi h_{9/2}$ configuration. Strong β feeding of 293, (11/2+) level in ^{215}Po corroborates this configuration assignment. $T_{1/2}$: weighted average of 7.7 min *2* (1990Ru02), 7.5 min *4* (1989Bu09), and 7.4 min *6* (1965Nu03). Other value: 8 min *2* (1953Hy83). $<r^2>^{1/2}$=5.552 fm *3* (extrapolation from ^{209}Bi value using formula (4) in 2004An14).
183.5 *3*	(7/2−)	A		Jπ: M1 γ to (9/2−); analogy to ^{211}Bi, ^{213}Bi, suggests $\pi h_{7/2}$ configuration. Large HF for α decay parent nuclei to a corresponding 7/2− state observed in ^{211}Bi and ^{213}Bi corroborates this configuration assignment.
746.60?‡ *10*	(13/2−)§	B		
854.5 *10*		A		
1022.5 *10*		A		
1160.70?‡ *14*	(17/2−)§	B		
1168.5 *10*		A		
1199.8 *7*		A		
1347.50 *17*	(21/2−)§	B		
1347.50+x	(25/2 to 29/2)(−)	B	36.9 s *6*	%IT=76.9 *5*; %β⁻=23.1 *5*. %β⁻: deduced by the evaluators from weighted average of gamma transition intensities for five strong γ rays in 2003Ku26. Value of %β⁻=23.8 *4* in 2003Ku26 is slightly different but could not be reproduced by the evaluators. E(level): x=40 +*80*−*40* (2003Ku26, from non–observation of Bi K–x rays in coin with 186.8γ). Other estimate: 20 *20* (2012Au07). $T_{1/2}$: from weighted average (2003Ku26) of 37.1 s *5* and 36.4 s *8* from the decay curves of 187, 414, 747 γ rays in isomer decay and 226, 256, 308, 419 γ rays in β⁻ decay, respectively. Note that reduced χ^2=9 for the second set of γ decay curves. From the same data, evaluators obtain weighted average of 36.7 s *5* with reduced χ^2=5.7. Jπ: possible configuration= $[\pi h_{9/2}\otimes((\nu g_{9/2}{}^5)_{9/2}\otimes\nu i_{11/2})_{10+}]_{(25/2-:29/2-)}$. 2003Ku26 further propose 27/2− from expected M3 transition to 1347, (21/2−) level, based on partial half–life of the isomeric transition of <80 keV.
1959.8 *12*		A		

Footnotes continued on next page

Adopted Levels, Gammas (continued)

^{215}Bi Levels (continued)

† From Eγ data.
‡ The ordering of the 187–414–747 cascade is not established, the one given here is just one of the possibilities. Thus the positions of the intermediate levels at 747 and 1161 could be different.
§ E2 --> (E2) --> (E2) γ cascade feeding (9/2–) g.s. suggests (21/2–) --> (17/2–) --> (13/2–) spin–parity sequence.

γ(^{215}Bi)

E(level)	Eγ	Iγ	Mult.	α	Comments
183.5	183.5 *3*	100	M1	1.82 *3*	Mult.: from measured α(K)exp in ^{215}Pb β^- decay. Some E2 admixture is possible.
746.60?	746.6 *1*	100	(E2)†	0.01258	
854.5	671 *1*	100			
1022.5	839 *1*	100			
1160.70?	414.1 *1*	100	(E2)†	0.0491	
1168.5	985 *1*	100			
1199.8	1016 *1*	82 *30*			
	1200 *1*	100 *65*			
1347.50	186.8 *1*	100	(E2)	0.571	Mult.: from measured α(K)exp in ^{215}Bi IT decay.
1347.50+x	x				Eγ: x=40 *+80–40* (2003Ku26). There may be one or more γ transitions from the isomer, but each should be lower than 80 keV. from non–observation of Bi K–x rays in coin with 186.8γ.
1959.8	760 *1*	100			

† From γ intensity balance in 187–414–747 γ cascade in IT decay. See details in ^{215}Bi IT decay dataset.

^{215}Pb β^- Decay (147 s) 2013De20

Parent ^{215}Pb: E=0; Jπ=(9/2+); $T_{1/2}$=147 s *12*; Q(g.s.)=2770 *100*; %β^- decay=100.
^{215}Pb–J,$T_{1/2}$: From ^{215}Pb Adopted Levels.
^{215}Pb–Q(β^-): 2770 *100* (syst,2012Wa38). Other: 2013De20 used 3.2 MeV in deducing log *ft* values.
^{215}Pb–%β^- decay: %β^-=100.
2013De20 (also 2004DeZV thesis): ^{215}Pb produced via the reaction ^{238}U(p,X) with E(p)=1.4 GeV, ionized by the Resonance Ionization Laser Ion Source (RILIS) and separated using the ISOLDE on–line mass separator. Detector system included an Si–detector for α–particles, one low–energy Ge and two HPGe detectors for x–rays and γ–rays, as well as a plastic scintillator ΔE detector for β–particles. Measured Eγ, Iγ, Iβ, βγ, γγ coincidence. Deduced levels, $T_{1/2}$. Data listed from 2013De20 also contain adjusted β feedings communicated to the evaluators by H. De Witte by an email reply of June 19, 2013.
The decay scheme is considered as incomplete by the evaluators.

^{215}Bi Levels

E(level)†	Jπ‡	$T_{1/2}$‡
0.0	(9/2–)	7.6 min *2*
183.5 *3*	(7/2–)	
854.5 *10*		
1022.5 *10*		
1168.5 *10*		
1199.8 *7*		
1959.8 *12*		

† From Eγ data.
‡ From Adopted Levels.

^{215}Pb β^- Decay (147 s) 2013De20 (continued)

β^- radiations

$E\beta^-$	E(level)	$I\beta^{-\dagger}$	Log *ft*‡	Comments
(810 *100*)	1959.8	1.0 *5*	>6.0	$I\beta^-$: 1.4 *7* (2013De20, adjusted value).
(1570 *100*)	1199.8	1.7 *12*	>6.8	$I\beta^-$: 2.1 *16* (2013De20, adjusted value).
(1600 *100*)	1168.5	2.1 *7*	>6.7	$I\beta^-$: 2.6 *13* (2013De20, adjusted value).
(1750 *100*)	1022.5	1.8 *6*	>6.9	$I\beta^-$: 2.4 *11* (2013De20, adjusted value).
(1920 *100*)	854.5	1.2 *5*	>7.3	$I\beta^-$: 1.6 *8* (2013De20, adjusted value).
(2590 *100*)	183.5	18 *5*	>6.6	$I\beta^-$: 16 *11* (2013De20, adjusted value).
(2770 *100*)	0.0	≤74	≥6.1	$I\beta^-$: original value of ≤81% *4* is adjusted to ≤74% *6* in an email reply from the first author of 2013De20. Value of 81% was based on Iγ(293.5γ)(absolute)=35.2% taken from 2003Ku26, but γ intensities in 2003Ku26 were incorrectly labeled as absolute, these were relative values instead (see ^{215}Bi to ^{215}Po decay dataset). Evaluators deduce absolute Iγ of 293.5γ as 48.9% *15* in ^{215}Bi decay, based on which the first author of 2013De20 has deduced Iβ≤76% *4*. The β feeding to g.s. is deduced from a comparison of the measured intensities of γ and α lines in the decay chain: ^{215}Pb -->^{215}Bi -->^{215}Po -->^{211}Pb. Intensities of the following lines were measured: 183.5γ from decay of ^{215}Pb to ^{215}Bi, 293.5γ from decay of ^{215}Bi to ^{215}Po, and 7386α line from the decay of ^{215}Po to ^{211}Pb. By normalizing to the known absolute intensity of 7386α, absolute intensities of 183.5 and 293.5 gammas were deduced, both assigned mult=M1. From these values, lower limits of β feedings to excited states in ^{215}Bi and ^{215}Po were deduced, which in turn gave upper limits of β feedings to ground states with values of 74% *6* for ^{215}Pb to ^{215}Bi decay. Value in 2004DeZV was ≤67% *5*; and ≤12% *8* for ^{215}Bi to ^{215}Po decay.

† Only the apparent β feedings, deduced by the evaluators from intensity balances, are given, assuming β feeding of 74% *6* to the g.s., since the decay scheme is considered as incomplete in the population of higher energy levels, some of which may decay directly to the g.s.. Adjusted values of β feedings communicated by the first author of 2013De20 are listed under comments.

‡ Values are treated as lower limits due to incomplete level level scheme. Note that log *ft* values listed in figure 3 of 2013De20 are high by 0.3–0.6 due to higher Q(β^-) value of 3.2 MeV used by the authors.

γ(^{215}Bi)

Iγ normalization: I(γ+ce) of 183.5γ and 1200γ≈19, for g.s. β feeding of ≤74% *6* (adjusted value communicated by an email reply of June 19, 2013 from the first author of 2013De20).

Eγ	E(level)	Iγ†	Mult.	α	Comments
183.5 *3*	183.5	100 *19*	M1	1.82 *3*	α(K)exp=1.2 *4* (2013De20). Mult.: measured α(K)exp from K x ray and Iγ gives dominant M1 with δ(E2/M1)<0.7, or much less likely E1+M2 with δ(M2/E1)=0.50 *8*. Some E2 admixture is possible. Also α(K)exp=1.4 *3* from total β-gated K x ray spectrum (2013De20).
671 *1*	854.5	14 *5*			
760 *1*	1959.8	12 *5*			
839 *1*	1022.5	21 *7*			
985 *1*	1168.5	24 *8*			
1016 *1*	1199.8	14 *5*			
1200 *1*	1199.8	17 *11*			

† For absolute intensity per 100 decays, multiply by ≈0.087.

^{215}Pb β^- Decay (147 s) 2013De20 (continued)

Decay Scheme

Intensities: relative Iγ

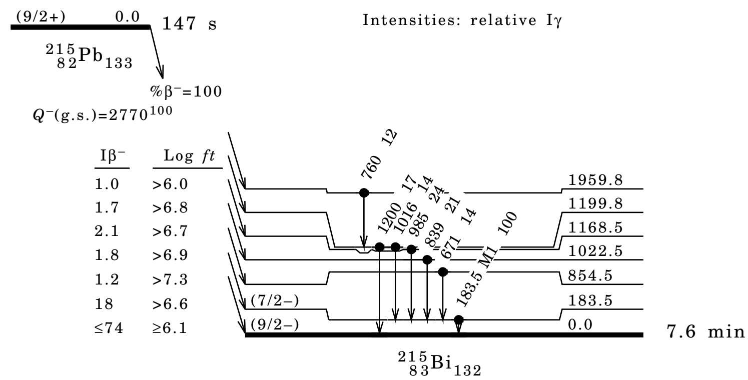

^{215}Bi IT Decay (36.9 s) 2003Ku26

Parent ^{215}Bi: E=1347.50+x; Jπ=(25/2:29/2)(–); $T_{1/2}$=36.9 s *6*; %IT decay=76.9 *5*.

^{215}Bi–%IT decay: From %β⁻=23.1 *5* (from Adopted Levels).

2003Ku26: ^{215}Bi produced by ^{232}Th(p,X) and ^{238}U(p,X) at 1 GeV proton energy, followed by mass separation. Measured Eγ, Iγ, α, γγ, βγ coin, αγ coin, γ(x–ray) coin using large Ge detector for γ, and low energy Ge detector for x rays and low–energy γ rays, plastic scintillator for β.

^{215}Bi Levels

E(level)†	Jπ§	$T_{1/2}$§	Comments
0.0	(9/2–)	7.6 min *2*	
746.60?‡ *10*	(13/2–)		
1160.70?‡ *14*	(17/2–)		
1347.50 *17*	(21/2–)		
1347.50+x	(25/2 to 29/2)(–)	36.9 s *6*	%IT=76.2 *4*; %β⁻=23.8 *4*. %β⁻: from 2003Ku26, comparison of γ intensities in the two cascades: one from IT decay and the other from β⁻ decay of this isomer. $T_{1/2}$: from weighted average of values from decay curves for seven γ rays (2003Ku26). See comment in Adopted Levels. Jπ: possible configuration= $[\pi h_{9/2}\otimes((\nu g_{9/2}{}^5)_{9/2}\otimes\nu i_{11/2})_{10+}]_{(25/2:29/2)(-)}$. E(level): x=40 *+80–40* (2003Ku26).

† From Eγ values.

‡ The ordering of the 187–414–747 cascade is not established, the one given here is just one of the possibilities. Thus the positions of the intermediate levels at 747 and 1161 could be different.

§ From Adopted Levels.

γ(^{215}Bi)

Eγ	E(level)	Iγ‡	Mult.	α	Comments
x	1347.50+x				Eγ: x=40 *+80–40* (2003Ku26).
186.8† *1*	1347.50	52 *2*	(E2)	0.571	α(K)exp=0.24 *3* (2003Ku26). α(K)exp measured from K x ray and Iγ. Mult.: measured α(K)exp gives dominant E2; δ(E2/M1)=5.0 *11*, or unlikely possibility of E1+M2 with δ(M2/E1)=0.165 *15*.
414.1† *1*	1160.70?	76 *3*	(E2)	0.0491	Mult.: α(exp)=0.075 *60* (evaluators) from intensity balance at 1160.7 level is consistent with E2; with δ(E2/M1)=2.2 *12*. Other possibility of E1+M2 with δ(M2/E1)=0.35 *15* is unlikely.
746.6† *1*	746.60?	75 *3*	(E2)	0.01258	Mult.: intensity balance at 746.6 level is consistent with E2 or M1, and marginally with E1 also.

† The ordering of the 187–414–747 cascade is not established.

‡ For absolute intensity per 100 decays, multiply by 1.000 *7*.

^{215}Bi IT Decay (36.9 s) 2003Ku26 (continued)

Decay Scheme

Intensities: I(γ+ce) per 100 parent decays
%IT=76.9 *5*

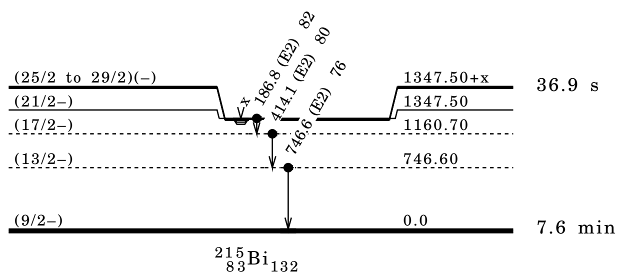

^{219}At α Decay (56 s) 1953Hy83,1989Bu09

Parent ^{219}At: E=0.0; Jπ=(9/2−); $T_{1/2}$=56 s *3*; Q(g.s.)=6324 *15*; %α decay≈97.0.

^{219}At–Q(α): From 2012Wa38.

^{219}At–J: From 2001Li44, based on experimental level scheme study and proposed configuration=$[\pi h_{9/2}{}^{3} \otimes \nu g_{9/2}{}^{-2}]_{9/2-}$. HF=1.1 implying a favored α decay supports (9/2−) for the ground states of ^{219}At and ^{215}Bi.

^{219}At–$T_{1/2}$: From ^{219}At Adopted Levels in ENSDF database.

^{219}At–%α decay: %α≈97 from quoted α/β$^-$ ratio of ≈30, as determined from measurements of the ^{219}At/^{219}Rn peak ratio (1953Hy83).

1953Hy83: ^{227}Ac source. Chemical/physical separation of radioactive target. Detector: ionization chamber. Measured $T_{1/2}$, Eα, α and β$^-$ decay, α/β$^-$ ratio.

1989Bu09: ^{219}At activity was produced by spallation of 600–MeV protons on targets of ^{232}Th. Assignment to ^{219}At is based on mass separation and on identification of the daughter nucleus ^{215}Bi in the source. The disintegration rate was determined by measuring the β$^-$ activity with a 4 π plastic scintillator detector. Measured $T_{1/2}$.

^{215}Bi Levels

E(level)	Jπ	$T_{1/2}$	Comments
0.0	(9/2−)	7.6 min *2*	Jπ,$T_{1/2}$: from Adopted Levels.

α radiations

Eα	E(level)	Iα‡	HF†	Comments
6208 *15*	0.0	100	1.1	Eα: deduced by evaluators from Qα=6324 *15* (2012Wa38). Measured value of Eα=6270 keV *50* (1953Hy83), further adjusted upward by 5 keV (1991Ry01) due to a change in the calibration energy of Eα values from ^{211}Bi decay, is higher than the value deduced from Q(α) value, although, it is within the experimental uncertainty.

† Using $r_0(^{215}Bi)$=1.5467 *4*, interpolated value deduced from $r_0(^{216}Po)$=1.5555 *2* and $r_0(^{214}Pb)$=1.5379 *7* (1998Ak04).

‡ For α intensity per 100 decays, multiply by ≈0.97.

Adopted Levels, Gammas

Q(β⁻)=715 *7*; S(n)=4141.8 *27*; S(p)=6629 *11*; Q(α)=7526.3 *8* 2012Wa38.
S(2n)=10030 *4*, S(2p)=11916 *7* (2012Wa38).

^{215}Po evaluated by J.K. Tuli, B. Singh, Sudeb Bhattacharya, S. Dasgupta, J.Y. Lee.

^{215}Po Levels

Cross Reference (XREF) Flags

A ^{215}Bi β⁻ Decay (7.6 min)
B ^{215}Bi β⁻ Decay (36.9 s)
C ^{219}Rn α Decay (3.96 s)

E(level)†	Jπ	XREF	$T_{1/2}$	Comments
0.0‡	9/2+	ABC	1.781 ms *5*	%α=99.99977 *2*; %β⁻=2.3×10^{-4} *2* (1950Av61). RMS charge radius $<r^2>^{1/2}$=5.627 fm *20*; deduced from interpolation of evaluated rms charge radii of ^{208}Po to ^{216}Po (2013An02), with slope k_z=0.37 in formula 9 of 2004An14. $T_{1/2}$: weighted average of 1.778 ms *5* (1961Vo06), and 1.784 ms *6* (1971Er02). Other value: 1.83 ms *4* (1942Wa04). Jπ: favored α decay (HF=1.4) to ^{211}Pb (Jπ=9/2+). %β⁻: from observation of ≈8 MeV α from ^{215}At decay (1950Av61). Other values: ≈5×10^{-4} (1944Ka01,1944Ka02); ≈4×10^{-4} (1955Ad09).
271.228‡ *10*	7/2+	A C	195 ps *15*	$T_{1/2}$: (α)(ce)(t) coin (1974Bo11). Other value: <250 ps (1969Be67). Jπ: 271.2γ M1+E2 to 9/2+; 130.6γ M1+E2 from 5/2+.
293.56§ *4*	(11/2)+	ABC		Jπ: 293γ M1 to 9/2+.
401.812‡ *10*	5/2+	A C	66 ps *7*	Jπ: favored α decay (HF=3.4) from ^{219}Rn (Jπ=5/2+); 401.8γ E2 to 9/2+. $T_{1/2}$: from $T_{1/2}$(402 level)/$T_{1/2}$(271 level)=0.336 *23* (Doppler shift measurement in ^{219}Rn α decay) and using $T_{1/2}$(271 level)=195 ps *15* (1974Bo11).
517.63§ *6*	7/2+,9/2+	A C		Jπ: 517.6γ M1(+E2) to 9/2+; 224.0γ to (11/2)+. Jπ=7/2+ member of possible configuration=$\pi h_{9/2}{}^2\otimes\nu g_{9/2}{}^4\otimes\nu i_{11/2}$.
608.30‡ *20*	(11/2+,13/2+)	A C		Jπ: 608.3γ to 9/2+; no gamma rays to 7/2+ or 5/2+. Possible Jπ=13/2+ member of configuration=$\pi h_{9/2}{}^2\otimes\nu g_{9/2}{}^5$.
676.64 *7*		A C		
708.1 *5*		C		
712.66?@ *21*	(15/2+)#	B		
732.7 *4*		C		
835.32 *22*		A C		
877.2 *6*		C		
891.1 *3*		C		
930.1 *11*		C		
1021.07?@ *23*	(19/2+)#	B		
1073.7 *4*	(5/2+)	C		Jπ: large α hindrance factor (HF=31 from 5/2+ ^{219}Rn parent). Level belongs to possible ground state configuration=$\pi h_{9/2}{}^2\otimes\nu g_{9/2}{}^5$.
1077.6 *15*		A		
1094.2 *10*		C		
1176.2 *20*		A		
1247.37?@ *25*	(23/2+)#	B		
1294.53 *11*		A		
1398.8 *3*		A		
1503.3?@ *5*	(23/2−)#	B		
1682.1?@ *6*	(25/2−)#	B		
2001.3?@ *5*	(−)	B		Jπ: log *ft*=5.2 from (25:29/2)(−) parent.
2159.5 *6*	(−)	B		Jπ: log *ft*=5.4 from (25:29/2)(−) parent.

† From least–squares fit to Eγ data.
‡ Configuration=$\pi h_{9/2}{}^2\otimes\nu g_{9/2}{}^5$.
§ Configuration=$\pi h_{9/2}{}^2\otimes\nu g_{9/2}{}^4\otimes\nu i_{11/2}$.
# From 2003Ku26 based on assumed ordering of the cascade in ^{215}Po (36.9 s) β⁻ decay.
@ The orderings of the 158–319–179 and 498–256–226–308–419 γ cascades are not established, the ones given here is just one of the possibilities, thus the positions of the intermediate levels may be different.

Adopted Levels, Gammas (continued)

γ(^{215}Po)

E(level)	Eγ†	Iγ†	Mult.‡	δ‡	α	Comments
271.228	271.23 *1*	100	M1+E2	3.6 +*7*−*5*	0.207 *12*	B(M1)(W.u.)=0.00032 *7*; B(E2)(W.u.)=20.0 *16*.
293.56	293.56 *4*	100	M1		0.536	
401.812	130.60 *3*	2 *1*	M1+E2	0.62 +*5*−*4*	4.40 *11*	B(M1)(W.u.)=0.0018 *10*; B(E2)(W.u.)=15 *8*.
	401.81 *1*	100 *3*	E2		0.0555	B(E2)(W.u.)=9.2 *12*.
517.63	224.0@ *7*	3.2 *5*				
	517.63 *6*	100 *5*	M1(+E2)		0.1162	α: for M1.
608.30	608.3 *2*	100				
676.64	383.1 *6*	2.5 *4*				Iγ: 33 implied in β⁻ decay is in severe disagreement.
	405.4 *6*	1.4 *3*				
	676.64 *7*	100 *13*				
708.1	436.9 *6*	93 *7*				
	708.1 *8*	100 *30*				
712.66?	419.1§ *2*	100	(E2)§		0.0497	
732.7	330.8 *4*	100 *11*				
	461.6 *8*	17 *3*				
	732.8 *10*	7 *4*				
835.32	542.7# *25*	30# *10*				γ not reported in ^{219}Rn a decay.
	564.1 *3*	90 *10*				
	835.3 *3*	100 *10*				
877.2	877.2 *6*	100				
891.1	373.5 *6*	33 *4*				
	489.3 *5*	83 *11*				
	619.9 *6*	43 *14*				
	891.1 *4*	100 *29*				
930.1	321.8 *10*	100				
1021.07?	308.4§ *1*	100	(E2)§		0.1161	
1073.7	556.1 *10*	17 *10*				
	671.9 *6*	67 *34*				
	802.5 *6*	100 *33*				
	1073.7 *6*	100 *33*				
1077.6	784# *2*	83# *17*				
	806.5# *22*	100# *17*				
1094.2	576.6 *10*	100				
1176.2	905# *2*	100#				
1247.37?	226.3§ *1*	100	(E2)§		0.308	
1294.53	776.9# *1*	100# *17*				
	1023.1# *12*	75# *8*				
	1294.5# *3*	75# *8*				
1398.8	1104.5# *5*	100# *5*				
	1127.7# *7*	32# *5*				
	1399.2# *4*	55# *5*				
1503.3?	255.9§ *4*	100	(E1)§		0.0454	
1682.1?	178.7§ *4*	100	[M1]§		2.13 *4*	
2001.3?	319.1§ *3*	26 *3*	[M1]§		0.427	
	498.0§ *1*	100 *6*	[E2]§		0.0324	
2159.5	158.2§ *2*	100	[E2]§		1.115	

† From ^{219}Rn α decay, unless otherwise stated.
‡ From ce data in ^{219}Rn α decay, unless otherwise stated.
§ From ^{215}Bi β⁻ decay (36.9 s) decay; but ordering of the 158–319–179 and 256–226–308–419 cascades is not established. The ordering given here is just one of the possibilities.
# From ^{215}Bi β⁻ decay (7.6 min).
@ Placement of transition in the level scheme is uncertain.

^{215}Bi β^- Decay (7.6 min) 2003Ku26

Parent ^{215}Bi: E=0.0; Jπ=(9/2−); $T_{1/2}$=7.6 min *2*; Q(g.s.)=2189 *15*; %β⁻ decay=100.
^{215}Bi–J,$T_{1/2}$: From ^{215}Bi Adopted Levels.
^{215}Bi–Q(β⁻): From 2012Wa38.
2003Ku26: ^{215}Bi produced by ^{232}Th(p,X) and ^{238}U(p,X) at 1 GeV proton energy, followed by mass separation. Measured Eγ, Iγ, α, γγ, βγ coin, αγ coin, γ x ray coin using large Ge detector for γ–rays, low–energy Ge detector for x rays and low–energy γ rays, plastic scintillator for β.
2004DeZV: estimated β feeding to the ground state.
See also evaluation of this decay scheme by the Decay Data Evaluation Project (DDEP on www.nucleide.org); published in M.M. Be et al., Table of Radionuclides, volume 7, BIPM Monographie–5 (2013).
1990Ru02: ^{215}Bi mass-separated source produced by spallation of 200–MeV protons on targets of ^{232}Th. Measured Eγ, Iγ, γγ coin, βγ coin. Detectors: 4π plastic scintillator, Ge(Li).

^{215}Po Levels

E(level)†	Jπ‡
0.0	9/2+
271.11 *10*	7/2+
293.53 *10*	(11/2)+
401.6 *10*	5/2+
517.53 *17*	7/2+,9/2+
609.0 *5*	(11/2+,13/2+)
677.6 *7*	
835.7 *5*	
1077.6 *15*	
1176.1 *20*	
1294.43 *18*	
1398.8 *3*	

† From least–squares fit of Eγ data.
‡ From Adopted Levels.

β⁻ radiations

Eβ⁻	E(level)	Iβ⁻†‡	Log *ft*†	Comments
(790 *15*)	1398.8	5.7	5.7	Iβ⁻: 6.2% (2003Ku26).
(895 *15*)	1294.43	4.2	6.0	Iβ⁻: 4.5% (2003Ku26).
(1013 *16*)	1176.1	0.4	7.2	
(1111 *15*)	1077.6	1.5	6.8	Iβ⁻: 1.7% (2003Ku26).
(1353 *15*)	835.7	3.1	6.8	Iβ⁻: 3.3% (2003Ku26).
(1511 *15*)	677.6	1.1	7.4	
(1580 *15*)	609.0	1.4	7.4	Iβ⁻: 1.5% (2003Ku26).
(1671 *15*)	517.53	0.7	7.8	Iβ⁻: 0.5% (2003Ku26).
(1787 *15*)	401.6	1.0	7.7	
(1895 *15*)	293.53	71 *9*	6.0 *1*	Iβ⁻: 77% (2003Ku26).
(1918§ *15*)	271.11	<0.4	>8.2	Iβ⁻: 2.2% in 2003Ku26 could not be reproduced by the evaluators. Intensity balance gives 0.0% *4*.
(2189§ *15*)	0.0	10 *10*	>6.9	Iβ⁻: from 12% *8* (2004DeZV), and <3% from log *ft*>7.7 in 2003Ku26. In DDEP evaluation, a large feeding of 61% *6* was suggested based on an approach which is "approximate and of highly questionable merit" as stated by the DDEP evaluators.

† Except for the strongly populated level at 293.5 keV, all other values should be considered as limits (upper for Iβ and lower for log *ft* values), since the level scheme is likely incomplete above the excitation energy of 1400 keV. The Iβ feedings given here are deduced from γ–intensity balances based on 10% *10* β feeding to g.s. Values listed in 2003Ku26 are given under comments.
‡ Absolute intensity per 100 decays.
§ Existence of this branch is questionable.

γ(^{215}Po)

Iγ normalization: Based on β feeding of 10% *10* to g.s.; from 12% *8* (2004DeZV) summed gamma–transition intensity=90 *10* to ground state. 2003Ku26 estimated negligible β feeding to the ground state based on measured ratio of ^{215}Bi g.s. and isomer components in Iα in ^{215}Po α decay and in Iγ(294γ).

Eγ	E(level)	Iγ†§	Mult.‡	δ‡	α	Comments
271.1 *1*	271.11	2.9 *1*	M1+E2	3.6 *+7−5*	0.207 *12*	
293.5 *1*	293.53	35.2 *11*	M1		0.537	
384 *1*	677.6	0.2 *1*				Iγ(384)/Iγ(678)=0.33 is in severe disagreement from 0.025 in ^{219}Rn a decay.
401.6 *10*	401.6	0.7 *1*	E2		0.0555	
517.5 *2*	517.53	1.5 *1*	M1(+E2)		0.1162	α: for M1.
542.7 *25*	835.7	0.3 *1*				
564.4 *5*	835.7	1.0 *1*				

Continued on next page (footnotes at end of table)

^{215}Bi β^- Decay (7.6 min) 2003Ku26 (continued)

$\gamma(^{215}$Po) (continued)

Eγ	E(level)	Iγ†§	Eγ	E(level)	Iγ†§	Eγ	E(level)	Iγ†§
609.0 *5*	609.0	1.0 *1*	806.5 *22*	1077.6	0.6 *1*	1104.5 *5*	1398.8	2.2 *1*
677.6 *10*	677.6	0.6 *1*	836.3 *10*	835.7	0.9 *1*	1127.7 *7*	1398.8	0.7 *1*
776.9 *1*	1294.43	1.2 *2*	905 *2*	1176.1	0.3 *1*	1294.5 *3*	1294.43	0.9 *1*
784 *2*	1077.6	0.5 *1*	1023.1 *12*	1294.43	0.9 *1*	1399.2 *4*	1398.8	1.2 *1*

† In table 3 of their paper, 2003Ku26 state that gamma intensities are in percent per decay, but this is inconsistent with their decay scheme in their figure 6. The intensities quoted in table 3 of 2003Ku26 are relative intensities, instead, as communicated in a priv. comm. of April 2011 from J. Kurpeta (first author of 2003Ku26) to evaluator (Filip Kondev, ANL) of Decay Data Evaluation Project (DDEP).

‡ From Adopted Gammas.

§ For absolute intensity per 100 decays, multiply by 1.39 *16*.

Decay Scheme

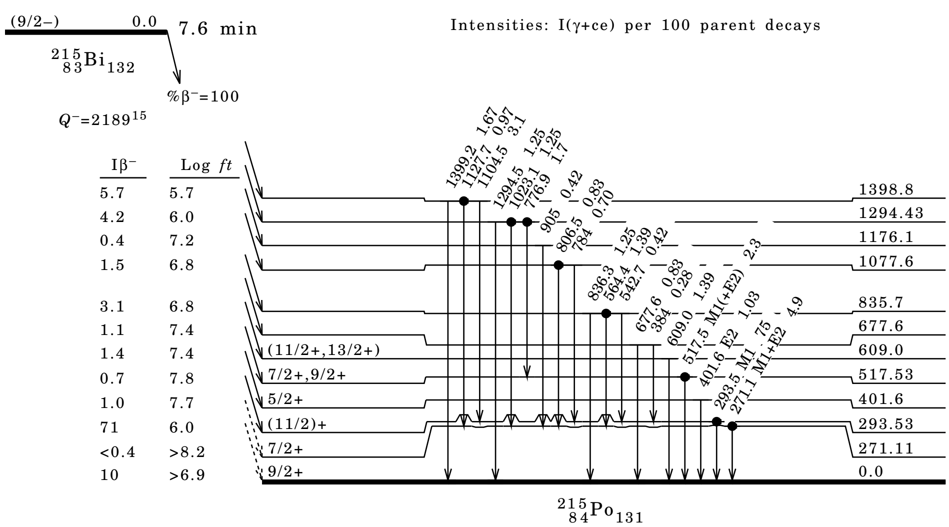

^{215}Bi β^- Decay (36.9 s) 2003Ku26

Parent ^{215}Bi: E=1347.5+x; Jπ=(25/2:29/2)(−); $T_{1/2}$=36.9 s *6*; Q(g.s.)=2189 *15*; %β⁻ decay=23.1 *5*.

^{215}Bi−E,J,$T_{1/2}$: From ^{215}Bi Adopted Levels.

^{215}Bi−Q(β⁻): From 2012Wa38.

^{215}Bi−%β⁻ decay: %β⁻=23.8 *4* (2003Ku26) from weighted average of total intensities of five γ rays (226, 255, 293, 308, 419) in cascade, assuming that each γ ray carries the total cascade intensity (see discussion in section 4 of 2003Ku26). Evaluators obtain 23.1% *5* from the weighted average of the same five γ rays using Iγ data and multipolarities assigned in 2003Ku26. The α values were deduced using the BrIcc computer code.

2003Ku26: ^{215}Bi produced by ^{232}Th(p,X) and ^{238}U(p,X) at 1 GeV proton energy, followed by mass separation. Measured Eγ, Iγ, α, γγ, βγ coin, αγ coin, γ(x ray) coin using large Ge detector for γ, low−energy Ge detector for x rays and low−energy γ rays, plastic scintillator for β.

^{215}Bi β^- Decay (36.9 s) 2003Ku26 (continued)

^{215}Po Levels

E(level)†	Jπ§
0.0	9/2+
293.50 *10*	(11/2)+
712.60?‡ *23*	(15/2+)
1021.00?‡ *25*	(19/2+)
1247.3?‡ *3*	(23/2+)
1503.2?‡ *5*	(23/2−)
1682.0?‡ *6*	(25/2−)
2001.2?‡ *5*	(−)
2159.4 *6*	(−)

† From Eγ data.
‡ The orderings of the 158–319–179 and 498–256–226–308–419 γ cascades are not established, the ones given here is just one of the possibilities, thus the positions of the intermediate levels could be different.
§ From adopted levels.

β^- radiations

Eβ⁻	E(level)	Iβ⁻‡	Log *ft*†
(1377+x *15*)	2159.4	6.8 *9*	5.4
(1535+x *15*)	2001.2?	14.8 *16*	5.2

† Deduced using the LOGFT computer code. 2003Ku26 give 5.18 for 2159 level and 5.48 for 2001 level. These values should be reversed as suggested by γ–ray intensities.
‡ Absolute intensity per 100 decays.

γ(^{215}Po)

Eγ	E(level)	Iγ§	Mult.‡	α	Comments
158.2† *2*	2159.4	3.2 *4*	[E2]	1.115	
178.7† *4*	1682.0?	2.2 *3*	[M1]	2.13 *4*	I(γ+ce): 2003Ku26 list 7.2, evaluators obtain 6.9.
226.3† *1*	1247.3?	18.0 *10*	(E2)	0.308	I(γ+ce): 2003Ku26 list 23.7, evaluators obtain 23.5.
255.9† *4*	1503.2?	21.9 *9*	(E1)	0.0454	
293.5 *1*	293.50	14.7 *5*	M1	0.537	Iγ: from coin data. I(γ+ce): 2003Ku26 list 22.9, evaluators obtain 22.6.
308.4† *1*	1021.00?	22.2 *11*	(E2)	0.1161	I(γ+ce): 2003Ku26 list 24.9, evaluators obtain 24.8.
319.1† *3*	2001.2?	4.0 *4*	[M1]	0.427	
419.1† *2*	712.60?	20 *2*	(E2)	0.0497	I(γ+ce): 2003Ku26 list 24.4, evaluators obtain 21.0. Value in 2003Ku26 corresponds to M1 for 419.1γ.
498.0 *1*	2001.2?	15.4 *10*	[E2]	0.0324	

† The orderings of the 158–319–179 and 498–256–226–308–419 cascades are not established, the one given here is just one of the possibilities.
‡ From adopted gammas or assumed from Jπ assignments.
§ For absolute intensity per 100 decays, multiply by 1.000 *22*.

^{215}Bi β^- Decay (36.9 s) 2003Ku26 (continued)

Decay Scheme

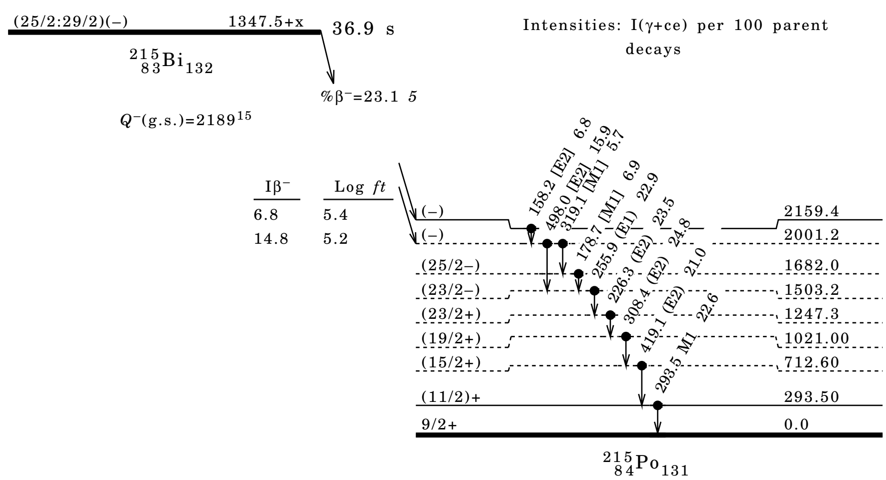

^{219}Rn α Decay (3.96 s) 1999Li05,1976Bl13,1970Kr08

Parent ^{219}Rn: E=0.0; Jπ=5/2+; $T_{1/2}$=3.96 s *1*; Q(g.s.)=6946.1 *3*; %α decay=100.

^{219}Rn–J,$T_{1/2}$: From ^{219}Rn Adopted Levels in ENSDF database.

^{219}Rn–Q(α): From 2012Wa38.

1976Bl13: precise measurement of Eγ, Iγ. Detector: Ge(Li).

1970Kr08: measured Eγ, Iγ, αγ(θ), αγ(lin pol, θ), Ice. Detectors: Ge(Li), magnetic spectrometer.

1970Da09: measured Eγ, Iγ, γγ coin, Ice. Detectors: Ge(Li), scint, magnetic spectrometer.

1968Br17, 1967Da20: measured Eγ, Iγ. Detector: Ge(Li).

1999Li05: measured Eγ, Iγ, Ice, αγ coin, αe coin. Detectors: Ge, Si(Li).

Others: 1972HeYM, 1969Be67, 1966Po02, 1965Va10, 1957Pa07, 1957Pi31.

αγ(θ) measurements: 1972HeYM, 1970Kr08, 1970Da09, 1969Be67, 1967Le05, 1965Cl05, and 1961Br32.

αγ linear polarization correlations and γγ(θ) measurements: 1970Kr08.

^{215}Po Levels

E(level)†	Jπ‡	$T_{1/2}$	Comments
0.0§	9/2+	1.781 ms *4*	$T_{1/2}$: from Adopted Levels.
271.228§ *10*	7/2+	195 ps *15*	$T_{1/2}$: (α)(ce)(t) coin (1974Bo11). Other value: <250 ps (1969Be67).
293.56# *4*	(11/2)+		
401.812§ *10*	5/2+	66 ps *7*	$T_{1/2}$: from $T_{1/2}$(402)/$T_{1/2}$(271)=0.336 *23* (Doppler shift measurement), and $T_{1/2}$(271)=195 ps *15* (1974Bo11).
517.60# *6*	7/2+,9/2+		
608.30§ *20*	(11/2+,13/2+)		
676.66 *7*			
708.1 *5*			
732.7 *4*			
835.32 *22*			
877.2 *6*			
891.1 *3*			
930? *1*			
1073.7 *4*	(5/2+)		
1094.2 *10*			

† From a least–squares fit to Eγ data.

‡ From Adopted Levels.

§ Configuration=$\pi h_{9/2}{}^2 \otimes \nu g_{9/2}{}^5$.

\# Configuration=$\pi h_{9/2}{}^2 \otimes \nu g_{9/2}{}^4 \otimes \nu i_{11/2}$.

^{219}Rn α Decay (3.96 s) 1999Li05,1976Bl13,1970Kr08 (continued)

α radiations

Values of Eα from 1962Wa18 given in comments were measured with a magnetic spectrograph. Original Eα values have been increased by evaluators an average of 1.5 keV because of changes in the calibration energies of ^{215}Po and ^{211}Bi (1977Ma30).

α particle energies of 1957Pi31 presented in comments have been increased by 3 keV because of a change in the calibration energy of ^{242}Cm (1977Ma30). Other: 1992Sc26.

Eα	E(level)	Iα&	HF@	Comments
5744§ *15*	1094.2	0.00009# *5*	270 *150*	Iα: measured value=0.0001 (1999Li05).
5764§ *8*	1073.7	0.00092# *20*	33 *8*	Other value: Eα=5786.5, Iα≈0.001 (1965Va10). Iα: measured value=0.001 (1999Li05).
5900§ *15*	930?	≈0.0001#	≈1426	
5944§ *6*	891.1	0.0020# *3*	107 *17*	Other value: Eα=5947.9, Iα=0.0037, originally assigned by 1962Wa18 to ^{211}Bi α decay. Reassigned by 1965Va10 (on the basis of αγ coin measurements) to ^{219}Rn α decay. Iα: measured value=0.002 (1999Li05).
5958§ *15*	877.2	0.00032# *11*	770 *270*	Iα: measured value=0.0001 (1999Li05).
6000§ *6*	835.32	0.0031# *5*	123 *20*	Eα=6000.8, Iα=0.0044 (1962Wa18). Iα: measured value=0.003 (1999Li05).
6100§ *8*	732.7	0.0012# *2*	900 *150*	Other value: Eα=6102.0, Iα=0.003 (1962Wa18). Iα: measured value=0.001 (1999Li05).
6124§ *8*	708.1	0.00063# *13*	2.2×10^{3} *5*	Iα: measured value=0.001 (1999Li05).
6158§ *4*	676.66	0.018# *2*	105 *12*	Other value: Eα=6158.6, Iα=0.0174 (1962Wa18). Iα: measured value=0.018 (1999Li05).
6223§ *6*	608.30	0.0043# *11*	850 *220*	Other value: Eα=6223.6, Iα=0.0026 (1962Wa18). Iα: measured value=0.004 (1999Li05).
6311§ *3*	517.60	0.051# *4*	172 *14*	Other value: Eα=6311.8, Iα=0.054 (1962Wa18). Iα: measured value=0.054 (1999Li05).
6425.0† *10*	401.812	7.5‡ *6*	3.4 *3*	Other values: Iα=7.5 *5* (1962Gi04). Eα=6423.9 (1961Ry02). Eα=6422, Iα=5 (1957Pi31,1977Ma30). Eα=6425 *1*, Iα=7.5 (1999Li05). Iα: Iα=7.7 *7*, deduced by evaluators from γ–ray transition intensity balance.
6530§ *2*	293.56	0.110# *10*	630 *58*	Other value: Eα=6529, Iα=0.12 (1962Wa18). Iα: measured value=0.12 (1999Li05).
6552.6† *10*	271.228	12.9‡ *6*	6.6 *4*	Other values: Eα=6552.8 (1962Wa18,1977Ma30). Iα=12.9 *6* (1962Gi04). Eα=6550.9 (1961Ry02). Eα=6550, Iα=13 (1957Pi31,1977Ma30). Eα=6553 *1*, Iα=13 (1999Li05). Iα: Iα=12.3 *9*, deduced by evaluators from γ–ray transition intensity balance.
6819.1† *3*	0.0	79.4‡ *10*	11.1 *2*	Other values: Eα=6819.0 (1962Wa18,1977Ma30). Iα=79.6 *10* (1962Gi04). Eα=6817.6 *10* (1961Ry02). Eα=6816 *2*, Iα=82 (1957Pi31,1977Ma30). Eα=6819.1 *3*, Iα=79.3 (1999Li05). Iα: Iα=79.8 *12*, deduced by evaluators from γ–ray transition intensity balance.

† From 1971Gr17, detector: magnetic spectrometer. Adjusted value as recommended by 1991Ry01.
‡ From 1962Wa18, detector: magnetic spectrograph. Adjusted value as recommended by 1991Ry01.
§ From 1999Li05.
# Deduced by evaluators from γ–ray transition intensity balance. Measured value from 1999Li05 is given under comments.
@ Using r_0(^{215}Po)=1.557 *4*, interpolated value from r_0(^{214}Po)=1.559 *8* and r_0(^{216}Po)=1.5555 *2* (1998Ak04).
& Absolute intensity per 100 decays.

γ(^{215}Po)

Iγ normalization: from Iγ(271γ, ^{219}Rn)/Iγ(269γ, ^{223}Ra)=0.786 *42*, measured from a ^{223}Ra source with ^{219}Rn in equilibrium (1976Bl13), and using %Iγ(269γ, ^{223}Ra)=13.7 *2* (see ^{223}Ra α decay). The excellent agreement of the α–particle abundances to the g.s., 271, and 402 levels (deduced from γ–ray transition intensity balances) with values measured directly confirm the quality of the γ–ray data and that of the decay scheme normalization.

Eγ†	E(level)	Iγ†#	Mult.	δ	α	Comments
130.60 *3*	401.812	1.2 *8*	M1+E2	0.62 *+5–4*	4.40 *11*	Others: 1968Br17, 1965Va10. Mult.,δ: from ce(L1)/ce(L2) exp=2.4 *5* and ce(L1)/ce(L3) exp=2.8 *4* (1970Da09). δ=0.58 from ce data (1999Li05) is in agreement, but conversion coefficients or L/M ratio are not

Continued on next page (footnotes at end of table)

^{219}Rn α Decay (3.96 s) 1999Li05,1976Bl13,1970Kr08 (continued)

γ(^{215}Po) (continued)

Eγ†	E(level)	Iγ†#	Mult.	δ	α	Comments
						given in this study.
x221.5‡ *3*		0.28 *4*				This γ ray has been assigned by 1968Br17 and 1970Kr08 to the decay of ^{223}Ra, and by 1970Da09 to the decay of ^{219}Rn (1977Ma30). Not seen by 1999Li05.
224.0 *7*	517.60	0.013 *2*	[M1,E2]		0.7 *4*	
271.23 *1*	271.228	100 *2*	M1+E2	3.6 *+7−5*	0.207 *12*	Mult.,δ: from ce(L1)/ce(L2) exp=0.516 *47*, ce(L1)/ce(L3) exp=1.035 *92* (1970Da09), and ce(K):ce(L1):ce(L2):ce(L3) exp=30.6 *9*:4.5:8.3 *5*:3.6 *9* (1972HeYM). Other values: α(K)exp=0.107 *16*, α(L3)exp=0.016 *5*, ce(L3)/ce(L1)+ce(L2) exp=0.40 *6* (1970Kr08). δ=3.7 *+10−6* if all data are used. δ=4.0 from ce data (1999Li05) is in agreement, but conversion coefficients or K/L/M ratios are not given in this study. Other values: Eγ=271.6, Iγ=87 (1957Pi31), Eγ=268, Iγ=11.0 (1957Pa07). Other: 1966Po02.
293.56 *4*	293.56	0.68 *4*	M1		0.536	Mult.: dominant M1 from α(K)exp (1999Li05), and probably also from K/L/M ratio, but no numerical data are given in this work. M1 from intensity balance arguments in the decay of ^{215}Bi to ^{215}Po (2003Ku26).
321.8& *10*	930?	8×10^{-04} *4*				
x324.9‡ *10*		<0.06				Eγ,Iγ: from 1967Da20. Not seen by 1999Li05.
330.8 *4*	732.7	0.009 *1*				
x337.7‡ *10*		0.08 *2*				Not seen by 1999Li05.
x370.9‡ *15*		<0.1				Eγ,Iγ: from 1967Da20. Other value: Iγ≈0.02 (1965Va10). Not seen by 1999Li05.
373.5 *6*	891.1	0.0023 *3*				
x380‡		≈0.0003				γ ray is uncertain (1965Va10). Not seen by 1999Li05.
383.1 *6*	676.66	0.0040 *6*				
401.81 *1*	401.812	61 *2*	E2		0.0555	Other values: Eγ=401, Iγ=77 (1966Po02); Eγ=400.6, Iγ=48 (1957Pi31). Others: 1965Va10, 1957Pa07. Mult.: from α(K)exp=0.027 *12* and ce(K)/ce(L3) exp=7 *2* (1970Kr08). Other: E2 from ce data (1999Li05), but no coefficients or ratios are given.
405.4 *6*	676.66	0.0023 *4*				
436.9 *6*	708.1	0.0028 *5*				
x438.2‡ *6*		<0.28				Eγ,Iγ: from 1967Da20. Other value: Eγ=438.7 *3*, Iγ=0.48 *5* (1968Br17). 1968Br17 assigned this transition to the decay of ^{215}Po. 1967Da20 suggested (on the basis of αγ-coin results of 1965Va10) that the contribution from ^{215}Po decay is 0.26≤Iγ≤0.44, which establishes an upper limit of Iγ≈0.28 from ^{219}Rn decay (1977Ma30). Not seen by 1999Li05.
461.6 *8*	732.7	0.0015 *3*				
489.3 *5*	891.1	0.0058 *8*				
517.60 *6*	517.60	0.41 *2*	M1(+E2)		0.1162	Mult.: dominant M1 from α(K)exp (1999Li05), but no numerical data are given in this work. α: for M1. Eγ,Iγ: Eγ=516.5 *5*, Iγ=0.22 *5* (1970Da09) were not included in the input for averaging. Other: 1965Va10.
x538.2§ *15*		0.06§ *3*				
556.1 *10*	1073.7	5×10^{-04} *3*				
564.1 *3*	835.32	0.014 *3*				Iγ: other value: Iγ≈0.02 (1965Va10).
576.6 *10*	1094.2	8×10^{-04} *4*				
608.3 *2*	608.30	0.040 *10*				Other value: Iγ≈0.026 (1965Va10).

Continued on next page (footnotes at end of table)

^{219}Rn α Decay (3.96 s) 1999Li05,1976Bl13,1970Kr08 (continued)

γ(^{215}Po) (continued)

Eγ†	E(level)	Iγ†#	Comments
619.9 *6*	891.1	0.003 *1*	
671.9 *6*	1073.7	0.002 *1*	
676.66 *7*	676.66	0.16 *2*	Other value: Iγ≈0.1 (1965Va10).
708.1 *8*	708.1	0.003 *1*	
732.8 *10*	732.7	6×10^{-04} *3*	
802.5 *6*	1073.7	0.003 *1*	
835.3 *3*	835.32	0.015 *3*	Eγ,Iγ: other values: Eγ≈833, Iγ≈0.01 (1965Va10).
877.2 *6*	877.2	0.003 *1*	
891.1 *4*	891.1	0.007 *2*	Eγ,Iγ: other values: Eγ=889.0 *15*, Iγ=0.015 *7* (1967Da20). Iγ≈0.01 (1965Va10).
x1055§ *2*		0.006§ *3*	
1073.7 *6*	1073.7	0.003 *1*	

† Weighted average from 1999Li05, 1976Bl13, 1970Kr08, 1970Da09, 1968Br17, and 1967Da20.
‡ Uncertain γ ray.
§ From 1967Da20. Other value: Iγ≈0.003 (1965Va10). Not seen by 1999Li05.
# For absolute intensity per 100 decays, multiply by 0.108 *6*.
& Placement of transition in the level scheme is uncertain.
x γ ray not placed in level scheme.

Decay Scheme

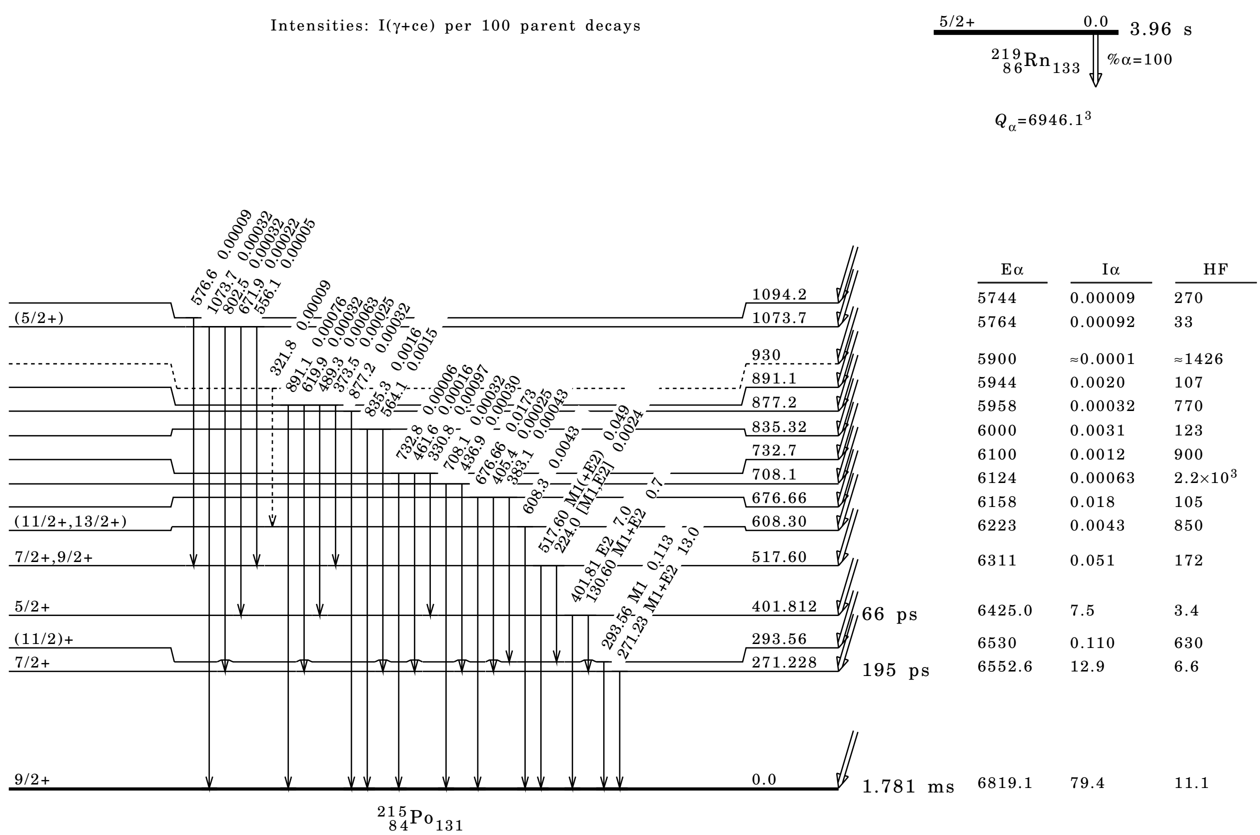

Adopted Levels, Gammas

Q(β⁻)=–87 *10*; S(n)=5947 *8*; S(p)=4074 *7*; Q(α)=8178 *4* 2012Wa38.
S(2n)=10818 *8*, S(2p)=10603 *8* (2012Wa38).

^{215}At evaluated by S.K. Basu, G. Mukherjee, B. Singh, Srijit Bhattacharya, A. De, D. Mondal.

^{215}At Levels

Shell–model configuration assignments are based on predicted level energies, and on those assigned in ^{214}Po and ^{216}Rn (1993Li07).

Cross Reference (XREF) Flags

A ^{215}Po β⁻ Decay (1.781 ms)
B ^{219}Fr α Decay (20 ms)

E(level)†	Jπ	XREF	$T_{1/2}$	Comments
0.0‡	9/2–	AB	0.10 ms *2*	%α=100. $T_{1/2}$: from 1951Me10. Jπ: favored α decay (HF=3.3) to ^{211}Bi g.s. (Jπ=9/2–); consistent with other odd–A isotopes of At.
169.88§ *10*	(7/2)–	B		Jπ: 169.9γ M1+E2 to 9/2–. In analogy with 896 level (Jπ=7/2–) in ^{209}Bi, and to other odd–A isotopes of At. Also shell–model prediction.
352.00‡ *10*	(5/2)–	B		Jπ: 352.0γ E2 to 9/2–. In analogy with 2826 level (Jπ=5/2–) in ^{209}Bi. Also shell–model prediction.
364.0# *10*	(13/2+)	B		Jπ: shell model.
472.29‡ *17*	(7/2–)	B		Jπ: 472.2γ (M1) to 9/2–. Also shell–model prediction.
517.00‡ *20*	(13/2)–	B		Jπ: 517.0γ E2 to 9/2–. 153γ to 363 level (13/2+). Also shell model prediction.
580‡	(3/2–)	B		Jπ: shell–model prediction.

† From least–squares fit to Eγ values.
‡ Member of configuration=$\pi h_{9/2}{}^3 \otimes \nu g_{9/2}{}^4$.
§ Member of configuration=$\pi h_{9/2}{}^2 \otimes \pi f_{7/2} \otimes \nu g_{9/2}{}^4$.
\# Member of configuration=$\pi h_{9/2}{}^2 \otimes \pi i_{13/2} \otimes \nu g_{9/2}{}^4$.

γ(^{215}At)

E(level)	Eγ	Iγ	Mult.†	δ	α
169.88	169.9 *1*	100	M1+E2	0.73 *16*	2.06 *19*
352.00	352.0 *1*	100	E2		0.0830
472.29	302.6 *3*	≈12			
	472.2 *2*	100 *30*	(M1)		0.1613
517.00	153‡	≈3	[E1]		0.1617
	517.0 *2*	100 *21*	E2		0.0310

† From K x ray/Iγ ratios in coincidence with individual α–particle groups (1993Li07).
‡ Placement of transition in the level scheme is uncertain.

^{215}Po β⁻ Decay (1.781 ms) 1950Av61

Parent ^{215}Po: E=0; Jπ=9/2+; $T_{1/2}$=1.781 ms *4*; Q(g.s.)=715 *7*; %β⁻ decay=2.3×10^{-4} *2*.
^{215}Po–J,$T_{1/2}$: From ^{215}Po Adopted Levels.
^{215}Po–Q(β⁻): From 2012Wa38.
^{215}Po–%β⁻ decay: Measured value of %β⁻=0.00023 *2* (1950Av61). Others: ≈0.0004% (1955Ad09), ≈0.0005% (1944Ka01,1944Ka02).
1950Av61: deduced β⁻ decay mode from observation of ≈8.0 MeV α from α decay of ^{215}At.
Others: 1955Ad09, 1944Ka01, 1944Ka02.

^{215}Po β^- Decay (1.781 ms) 1950Av61 (continued)

^{215}At Levels

E(level)	Jπ	Comments
0.0	9/2–	Assumed that g.s. of ^{215}At is populated in this decay. Jπ: from Adopted Levels.

^{219}Fr α Decay (20 ms) 1993Li07,1968Ba73,1966Gr07

Parent ^{219}Fr: E=0.0; Jπ=9/2–; $T_{1/2}$=20 ms *2*; Q(g.s.)=7448.5 *18*; %α decay=100.
^{219}Fr–J,$T_{1/2}$: From ^{219}Fr Adopted Levels in ENSDF database.
^{219}Fr–Q(α): From 2012Wa38.
1993Li07: ^{219}Fr activity was produced as descendant of a mass–separated source of ^{223}Ac. Measured Eα, Iα, Eγ, Iγ, αγ coin. Detectors: Ge(Li) for γ rays, Si(Li) for α particles.
1968Ba73: descendant of ^{227}Pa. Measured Eα, Iα. Detector: magnetic spectrograph.
1966Gr07: descendant of ^{227}Pa. Measured Eα, Iα, Eγ, αγ coin. Detectors: semi, scint.
1982Bo04: ^{219}Fr source produced by spallation of 5–GeV protons on targets of U and Th. Measured Eα, Iα. Detectors: semi.
Other: 1982Bo04.

^{215}At Levels

Shell–model configuration assignments are based on predicted level energies, and on those assigned in ^{214}Po and ^{216}Rn.

E(level)†	Jπ‡	$T_{1/2}$‡
0.0§	9/2–	0.10 ms *2*
169.88# *10*	(7/2)–	
352.00§ *10*	(5/2)–	
364.0@ *10*	(13/2+)	
472.29§ *17*	(7/2–)	
517.00§ *20*	(13/2)–	
580§	(3/2–)	

† Deduced by evaluators from a least–squares fit to γ–ray energies.
‡ From Adopted Levels.
§ Member of configuration=$\pi h_{9/2}{}^{3}\otimes\nu g_{9/2}{}^{4}$.
\# Member of configuration=$\pi h_{9/2}{}^{2}\otimes\pi f_{7/2}\otimes\nu g_{9/2}{}^{4}$.
@ Member of configuration=$\pi h_{9/2}{}^{2}\otimes\pi i_{13/2}\otimes\nu g_{9/2}{}^{4}$.

α radiations

Eα†	E(level)	Iα†§	HF‡	Comments
6744	580	<0.03	>26	Eα,Iα: from 1993Li07.
6802.9 *20*	517.00	0.25	6	Other value: Eα=6780 *10*, value deduced by 1977Ma30 from an α spectrum presented in 1966Gr07. Original Eα=6680 is probably a typographical error. Iα=0.3 *1* (1966Gr07). Eα=6805, Iα=0.25 (1993Li07). Iα: 0.20 *4*, deduced by evaluators from γ–ray transition intensity balance.
6846.2 *25*	472.29	0.05	44	Other value: Eα=6820 *10*; value deduced by 1977Ma30 from an α spectrum presented in 1966Gr07. Original Eα=6720 is probably a typographical error. Iα=0.2 *1* (1966Gr07). Eα=6849, Iα=0.05 (1993Li07). Iα: 0.06 *2*, deduced by evaluators from γ–ray transition intensity balance.
6956.6 *30*	364.0	≈0.02	≈271	Other values: Eα=6958, Iα≈0.02 (1993Li07).
6967.3 *20*	352.00	0.6	10	Other values: Eα=6950 *10*, Iα(6967α + 6957α)=0.8 *1* (1966Gr07); Eα=6968, Iα=0.6 (1993Li07). Iα: 0.61 *5*, deduced by evaluators from γ–ray transition intensity balance.
7145.7 *20*	169.88	0.25 *7*	103 *31*	Iα: weighted average of 0.3 *1* (1966Gr07) and 0.2 *1* (1968Ba73,1977Ma30). Iα: 0.30 *3*, deduced by evaluators from γ–ray transition intensity balance. Other value: 0.2 (1993Li07). Eα: other values: 7140 *10* (1966Gr07), 7148 (1993Li07).

Continued on next page (footnotes at end of table)

^{219}Fr α Decay (20 ms) 1993Li07,1968Ba73,1966Gr07 (continued)

α radiations (continued)

Eα†	E(level)	Iα†§	HF‡	Comments
7312.3 *18*	0.0	98.8 *2*	0.97 *10*	Eα: value adjusted from Eα=7312.2 *20* (1968Ba73) and Eα=7317 *4* (1982Bo04), as recommended by 1991Ry01. Other values: Eα=7300 *10*, Iα=98.4 (1966Gr07); Eα=7307 *20*, energy has been increased by 7 keV to account for changes in calibration energies (1951Me10,1977Ma30); Eα=7313 (1993Li07). Iα: from 1991Ry01.

† From 1968Ba73, unless otherwise specified.
‡ Using $r_0(^{215}At)$=1.5575 *80*, interpolated value deduced from $r_0(^{214}Po)$=1.559 *8*, and $r_0(^{216}Rn)$=1.556 *8* (1998Ak04).
§ Absolute intensity per 100 decays.

γ(^{215}At)

Measured intensity of $K_\alpha+K_\beta$ x rays=0.22 *3*.
Iγ normalization: Measured absolute γ–ray intensities (1993Li07).

Eγ†	E(level)	Iγ†§	Mult.‡	δ	α	Comments
153#	517.00	≈0.006	[E1]		0.1617	
169.9 *1*	169.88	0.10 *1*	M1+E2	0.73 *16*	2.06 *19*	Mult.,δ: from α(K)exp=1.5 *2* (1993Li07).
x225		≈0.01				Eγ: uncertain γ ray.
302.6 *3*	472.29	≈0.006				
352.0 *1*	352.00	0.56 *5*	E2		0.0830	Mult.: from α(K)exp=0.06 *1* (1993Li07).
472.2 *2*	472.29	0.050 *15*	(M1)		0.1613	Mult.: from α(K)exp≈0.1 (1993Li07).
517.0 *2*	517.00	0.19 *4*	E2		0.0310	Mult.: from α(K)exp=0.03 *1* (1993Li07).

† From 1993Li07. Other: 1968Gr07.
‡ From K x ray/Iγ ratios in coincidence with individual α–particle groups (1993Li07).
§ Absolute intensity per 100 decays.
\# Placement of transition in the level scheme is uncertain.
x γ ray not placed in level scheme.

Decay Scheme

Intensities: I(γ+ce) per 100 parent decays

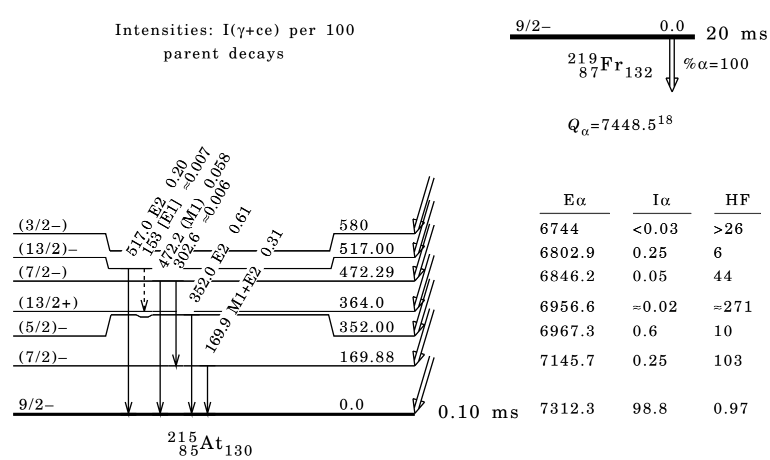

Adopted Levels, Gammas

Q(β⁻)=−1487 *10*; S(n)=4920 *12*; S(p)=5078 *9*; Q(α)=8839 *8* 2012Wa38.
S(2n)=11613 *9*, S(2p)=9093 *8* (2012Wa38).

^{215}Rn evaluated by S.K. Basu, G. Mukherjee, B. Singh, Srijit Bhattacharya, A. De, D. Mondal.

^{215}Rn identified as descendent of ^{227}U (1952Me13,1969Ha32); and descendent of ^{223}Th (1970Va13).

^{215}Rn Levels

Cross Reference (XREF) Flags

A ^{219}Ra α Decay (10 ms)
B ^{207}Pb(^{18}O,2α2nγ)

E(level)[†]	Jπ[‡]	XREF	$T_{1/2}$	Comments
0.0[§]	9/2+	AB	2.30 μs *10*	%α=100. RMS charge radius $<r^2>^{1/2}$=5.620 fm *20*; deduced from interpolation of evaluated rms charge radii of ^{212}Rn to ^{222}Rn (2013An02), with slope k_z=0.39 in formula 9 of 2004An14. $T_{1/2}$: from 1970Va13. Jπ: favored α decay (HF≈1.6) to ^{211}Po (Jπ=9/2+). %ε<1.0×10^{-11} for log *ft*>5.9. %ε+%β⁺<3×10^{-7}, theory (1973Ta30).
213.97 *18*	(7/2,9/2)+	A		Jπ: 592γ M1(+E2) from (7/2)+; uncertain 214.1γ to 9/2+. Possible configuration=$\nu g_{9/2}{}^3$.
290.8 *3*	(7/2,9/2,11/2)−	A		Jπ: 291γ E1 to 9/2+. Possible configuration=$\nu g_{9/2}{}^2 \otimes \nu j_{15/2}$.
315.82[#] *4*	(11/2)+	AB		Jπ: (7/2,11/2)+ from αγ(θ) (1989Ha26); 11/2+ consistent with (E2) 629.8γ from 946.3, (15/2+) level. Based on a comparison of decay schemes of α decays of ^{221}Th to ^{217}Ra and ^{219}Ra to ^{215}Rn, 1994Sh02 assigned 11/2+ to this level.
570.14[§] *17*	(13/2+)	B		
805.7 *3*	(7/2)+	A		Jπ: 805γ M1+E2 to 9/2+; low α hindrance factor (HF=3.3) from ^{219}Ra (Jπ=(7/2)+). Probable configuration=$\nu g_{9/2}{}^2 \otimes \nu i_{11/2}$, same as that of 315.8 level (see discussion in 1994Sh02).
946.33[#] *19*	(15/2+)	B		
1016.49[§] *23*	(17/2+)	B		
1334.28[#] *23*	(19/2+)	B		
1403.8[§] *3*	(21/2+)	B		
1607.8[#] *3*	(23/2+)	B		
1731.1[§] *3*	(25/2+)	B		
1804.8[#] *3*	(27/2+)	B		
1804.8+x		B	57 ns *+21−12*	%IT=100. $T_{1/2}$: from γ(t) in ^{9}Be(^{238}U,X), E=1 GeV/nucleon reaction (2013Bo18,2012BoZU). E(level): may correspond to 1804.8, 27/2+ level, but from available data in 2013Bo18 and 2012BoZU, location of the isomer remains uncertain. Three γ rays of 287, 392 and 656 keV of similar intensities are reported in 2012BoZU, which may be related to the decay of this isomer.
2287.1[#] *4*	(29/2+)	B		
y		B		
383.5+y *20*		B		
542.2+y *3*		B		

† From least squares fit to Adopted gamma-ray energies.
‡ For high-spin (J>11/2) levels, assignments are based on γ(θ) data, multipolarity assignments, band structures, and systematics of similar bands in ^{213}Rn, ^{217}Rn and ^{219}Th. These assignments are the same as the ones in 2012De11, except that parentheses have been added by the evaluators since strong arguments seem lacking.
§ (A): $\nu g_{9/2}{}^3$ band.
\# (B): $\nu g_{9/2}{}^2 \otimes \nu i_{11/2}$ band.

Adopted Levels, Gammas (continued)

γ(^{215}Rn)

E(level)	Eγ†	Iγ†	Mult.†	δ†	α	Comments
213.97	214.1§ *2*	100	(M1+E2)		1.0 *6*	
290.8	290.8 *3*	100	E1		0.0357	
315.82	315.82 *4*	100	M1(+E2)	<0.2	0.503	Eγ: from ^{219}Ra α decay.
570.14	570.2 *2*	100	(E2)		0.0259	
805.7	489§ *1*	≤42				
	592.0 *3*	100 *17*	M1(+E2)	<0.7	0.0721	
	805.2 *4*	58 *17*	M1+E2		0.028‡ *16*	
946.33	376.4 *2*	<7.7				
	629.8 *2*	100 *12*	(E2)		0.0208	
1016.49	446.2 *2*	100	(E2)		0.0464	
1334.28	317.7 *2*	40 *8*	(M1+E2)		0.31‡ *20*	
	388.1 *2*	100 *30*	[E2]		0.0665	
1403.8	387.2 *2*	100	(E2)		0.0670	
1607.8	203.9 *2*	100 *22*	(M1)		1.743	
	273.6 *2*	89 *19*	(E2)		0.183	
1731.1	123.2 *2*	50 *10*	(M1)		7.25	Mult.: from γ–ray intensity balance (2012De11).
	327.4 *2*	100 *20*	[E2]		0.1067	
1804.8	197.0 *2*	100	(E2)		0.552	
2287.1	482.3 *2*	100	[M1+E2]		0.10‡ *7*	
383.5+y	383.5 *2*	100				
542.2+y	158.7 *2*	100				

† From either ^{219}Ra α decay or ^{207}Pb(^{18}O,2α2nγ). Only the 315.8 level is populated in both datasets.
‡ Value overlaps M1 and E2.
§ Placement of transition in the level scheme is uncertain.

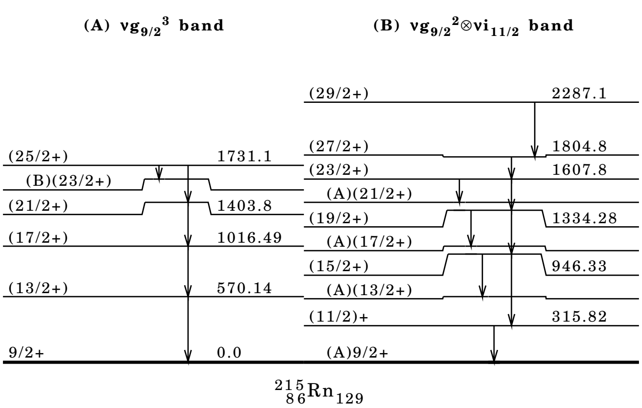

^{219}Ra α Decay (10 ms) 1987El02,1970Va13,1994Sh02

Parent ^{219}Ra: E=0.0; Jπ=(7/2)+; $T_{1/2}$=10 ms *3*; Q(g.s.)=8138 *3*; %α decay=100.
^{219}Ra–J,$T_{1/2}$: From ^{219}Ra Adopted Levels in ENSDF database.
^{219}Ra–Q(α): From 2012Wa38.
1994Sh02: ^{219}Ra activity was produced as the daughter nuclide of ^{223}Th through the ^{208}Pb(^{18}O,3n)^{223}Th reaction. Measured Eα, Iα, αγ coin from a source in equilibrium with ^{223}Th. Detectors: Semiconductor, Ge(Li) detector.
1987El02: ^{219}Ra activity was produced as descendant of ^{223}Th. Measured Eα, Eγ, Iγ, Ice, αγ coin, α–ce coin. Detectors: semi, Ge(Li), Si(Li). Assignment of α–particle groups to ^{219}Ra has been based on the agreement with Eα from 1970Va13, and on the observation of Rn K x ray in coincidence with α particles.
Because of the decay scheme normalization, evaluators interpreted absolute γ–ray transition intensities reported by authors as absolute I(γ+ce) (photons plus conversion electrons) intensities.
1970Va13: ^{219}Ra activity was produced by ^{208}Pb(^{16}O,αn), and identified by excitation functions, cross bombardment, and genetic relationship to its α–decay daughter nucleus ^{215}Rn. Measured Eα, Iα. Semiconductor detector.

Continued on next page (footnotes at end of table)

^{219}Ra α Decay (10 ms) 1987El02,1970Va13,1994Sh02 (continued)

1969Ha32: ^{219}Ra activity was produced as descendant of ^{227}U, ^{223}Th, and identified by its genetic relationship to its α–decay daughter nucleus ^{215}Rn. Measured Eα, Iα. Semiconductor detector.

^{215}Rn Levels

1994Sh02 interpreted the level structure in ^{215}Rn in terms of both the reflection asymmetric model and the shell model.

E(level)@	Jπ#	$T_{1/2}$#
0.0§	9/2+	2.30 μs *10*
213.96§ *18*	(7/2,9/2)+	
290.8‡ *3*	(7/2,9/2,11/2)–	
315.82† *4*	(11/2)+	
805.7† *4*	(7/2)+	

† Member of configuration=$\nu g_{9/2}{}^2 \otimes \nu i_{11/2}$.
‡ Configuration=$\nu g_{9/2}{}^2 \otimes \nu j_{15/2}$.
§ Member of configuration=$\nu g_{9/2}{}^3$.
# From Adopted Levels.
@ From least squares fit to γ–ray energies of 1987El02.

α radiations

Eα	E(level)	Iα§	HF‡	Comments
7198 *6*	805.7	2.4† *3*	3.3 *11*	Eα: weighted average of 7220 *20* (in coin with 592γ), 7250 *40* (in coin with 805γ)(1987El02), and 7196 *5* (1994Sh02).
7678 *3*	315.82	66.2 *15*	4.7 *15*	Eα: weighted average of 7675 *5* (1987El02), 7675 *10* (1970Va13), 7700 (20) 1969Ha32, 7679 *3* (1994Sh02). Iα: Iα=65.7 *15* deduced by evaluators from γ–ray transition intensity balance. Other values: Iα=65 *5* (1970Va13), Iα=70 *10* (1969Ha32), Iα=62 (1994Sh02).
7706 *10*	290.8	0.9† *2*	410 *160*	Eα: weighted average of 7720 *20* (measured in coin with 291γ, 1987El02), and 7703 *10* (1994Sh02).
7780 *10*	213.96	≈0.5	≈1274	Eα,Iα: inferred from αγ coin (1994Sh02).
7988 *3*	0.0	30.5 *15*	90 *28*	Iα: deduced by evaluators using ΣIα=100%. Other values: Iα=30 *10* (1969Ha32), Iα=35 *2* (1970Va13), Iα=34 (1994Sh02). Other: 1952Me13. Iα=30.7 *16* deduced by evaluators from γ–ray transition intensity balance. Eα: weighted average of 7980 *10* (1970Va13), 7990 *20* (1969Ha32), and 7989 *3* (1994Sh02).

† Deduced by evaluators from γ–ray transition intensity balance.
‡ Using $r_0(^{215}Rn)$=1.5595 *60*, interpolated value deduced from $r_0(^{214}Rn)$=1.563 *4*, and $r_0(^{216}Rn)$=1.556 *8* (1998Ak04).
§ Absolute intensity per 100 decays.

γ(^{215}Rn)

See 1989Ha26 for αγ(θ).

Eγ†	E(level)	Mult.	δ	α	I(γ+ce)†‡§	Comments
214.1# *2*	213.96	(M1+E2)		1.0 *6*	1.5 *3*	Mult.: K x ray/γ≈1 (α(K)exp≈0.1) (1994Sh02), α(L)exp=0.14 *3* (1987El02). Assignment to ^{219}Ra α decay is not definite. α: overlaps M1 and E2.
290.8 *3*	290.8	E1		0.0357	0.91 *18*	Eγ: other value: 290.6 (1994Sh02). Mult.: from α(K)exp<0.05 (1987El02).
315.82 *4*	315.82	M1(+E2)	<0.2	0.503	66.2 *15*	I(γ+ce): from a precise measurement of 7675α abundance (1987El02). Mult.: from α(K)exp=0.55 *8*, α(L)exp=0.10 *2*, and α(M)exp=0.020 *3* (1987El02). δ: from ce data.
489# *1*	805.7				≤0.5	
592.0 *3*	805.7	M1(+E2)	<0.7	0.0721	1.2 *2*	Mult.: from α(K)exp=0.07 *2* and α(L)exp=0.03 *1* (1987El02). δ: from ce data.
805.2 *4*	805.7	M1+E2		0.028 *16*	0.7 *2*	Mult.: from α(K)exp=0.03 *2* (1987El02). α: overlaps M1 and E2.

† From 1987El02, unless otherwise specified.
‡ Absolute transition intensity measured relative to %I(γ+ce)=66.2 *15* for 316γ. This value resulted from a precise measurement of the α–particle abundance that populates the 316 level (1987El02).
§ Absolute intensity per 100 decays.
# Placement of transition in the level scheme is uncertain.

^{219}Ra α Decay (10 ms) 1987El02,1970Va13,1994Sh02 (continued)

Decay Scheme

Intensities: I(γ+ce) per 100 parent decays

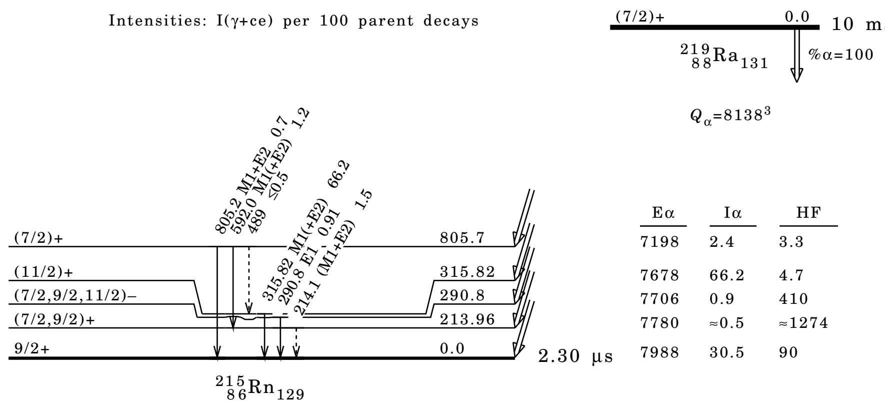

^{207}Pb(^{18}O,2α2nγ) 2012De11

Includes population of a high–spin isomer through fragmentation of ^{238}U beam at 1 GeV/nucleon (2012BoZU,2013Bo18).

2012De11: E(^{18}O)=93 MeV from INFN, Legnaro facility. Measured Eγ, Iγ, γγ–, αγ–, (x ray)γ–coin, γ(θ) using GASP–ISIS spectrometer. Target=2 mg/cm^2 thick backed by a 25 μg/cm^2 carbon foil. Gamma rays were detected by GASP array of 40 Compton–suppressed Ge detectors and multiplicity filter of 80 BGO detectors. The alpha particles from reaction channel were detected by ISIS telescopic array of 40 ΔE–E Si detectors. A total of 350,000 γγα coincidence events were recorded, about 33% of which belonged to 2α2n channel leading to levels in ^{215}Rn, others to 2α1n channel leading to levels in ^{216}Rn. Deduced high–spin levels, J, π in ^{215}Rn.

2013Bo18, 2012BoZU: ^{9}Be(^{238}U,X), E=1 GeV/nucleon; measured Eγ, Iγ, half–life of a high–spin isomer by γ(t) method.

^{215}Rn Levels

E(level)†	Jπ‡	$T_{1/2}$	Comments
0.0§	9/2+		
316.5# *2*	11/2+		
570.1§ *2*	13/2+		
946.3# *2*	15/2+		
1016.5§ *2*	17/2+		
1334.3# *2*	19/2+		
1403.8§ *3*	21/2+		
1607.8# *3*	23/2+		
1731.1§ *3*	(25/2)+		
1804.8# *4*	27/2+		
1804.8+x		57 ns *+21−12*	%IT=100. $T_{1/2}$: from γ(t) in ^{9}Be(^{238}U,X), E=1 GeV/nucleon reaction (2013Bo18,2012BoZU). E(level): may correspond to 1804.8, 27/2+ level, but from available data in 2013Bo18 and 2012BoZU location of the isomer remains uncertain. Three γ rays of 287, 392 and 656 keV of similar intensities are reported in 2012BoZU, which may be related to the decay of this isomer.
2287.1# *4*	(29/2+)		
y			
383.5+y *2*			
542.2+y *3*			

† From least–squares fit to Eγ data.
‡ As assigned by 2012De11 based on multipolarity assignments, band structures, and systematics of similar bands in ^{213}Rn, ^{217}Rn and ^{219}Th. In Adopted Levels, most of these assignments are given in parentheses since strong arguments are lacking.
§ (A): Band built on $νg_{9/2}^3$.
# (B): Band built on $νg_{9/2}^2⊗νi_{11/2}$.

^{207}Pb(^{18}O,2α2nγ) 2012De11 (continued)

γ(^{215}Rn)

R(θ)=angular anisotropy ratio for a set of detectors at 31.7°, 36.0°, 144.0° and 148.3° and the other set at 90° relative to the incident beam direction. Expected ratio is 1 for ΔJ=2, quadrupole (or stretched quadrupole) and 0.57 for ΔJ=1, dipole (or stretched dipole). No gating transitions were used for these measurements.

Eγ	E(level)	Iγ	Mult.†	α	Comments
123.2 *2*	1731.1	5 *1*	(M1)	7.24	Mult.: from γ–ray total intensity balance (2012De11).
158.7 *2*	542.2+y	22 *6*			R(θ)=1.1 *5*.
197.0 *2*	1804.8	9 *2*	(E2)	0.552	R(θ)=0.90 *26*.
203.9 *2*	1607.8	27 *6*	(M1)	1.743	R(θ)=0.5 *2*.
ˣ215.6‡ *2*		4.3 *9*			
ˣ230.9‡ *2*		4.1 *9*			
273.6 *2*	1607.8	24 *5*	(E2)	0.183	R(θ)=0.92 *25*.
ˣ287#					
316.4 *2*	316.5	25 *3*	M1	0.516	R(θ)=0.7 *2*.
317.7§ *2*	1334.3	10§ *2*	(M1+E2)	0.31 *20*	Mult.: I(γ+ce)=15 *5* and Iγ=10 *2* listed in 2012De11 suggest M1. α: value overlaps M1 or E2.
327.4 *2*	1731.1	10 *2*	[E2]	0.1067	
376.4 *2*	946.3	<2			
383.5 *2*	383.5+y	42 *8*			Eγ: from table I of 2012De11. Eγ=383.3 in authors' level–scheme figure 2. Mult.: (E2) deduced by evaluators from I(γ+ce)=45 *9* and Iγ=42 *8* listed in 2012De11, but asymmetry ratio suggests dipole. R(θ)=0.6 *2*.
387.2 *2*	1403.8	78 *14*	(E2)	0.0670	R(θ)=0.9 *2*.
388.1§ *2*	1334.3	25§ *7*	[E2]	0.0665	Mult.: (E2) in 2012De11.
ˣ392#					
446.2 *2*	1016.5	86 *6*	(E2)	0.0464	R(θ)=0.85 *15*.
482.3 *2*	2287.1	13 *1*	[M1+E2]	0.10 *7*	α: value overlaps M1 or E2.
570.2 *2*	570.1	100 *5*	(E2)	0.0259	R(θ)=1.00 *15*.
ˣ572.5‡ *2*		5 *2*			
629.8 *2*	946.3	26 *3*	(E2)	0.0208	R(θ)=0.9 *3*.
ˣ656#					

† Dipole or quadrupole from angular anisotropy ratios; electric or magnetic character from total intensity balance.
‡ This γ ray belongs to ^{215}Rn but is not included in the present level scheme.
§ Contaminated line. Intensity deduced from coincidence spectra.
\# The γ ray reported by 2012BoZU in ^{9}Be(^{238}U,X), E=1 GeV/nucleon reaction, and in coincidence with known transitions in ^{215}Rn from the work of 2012De11, but not placed in level scheme. 2012BoZU state that intensities of 287, 392 and 656 γ rays are similar.
ˣ γ ray not placed in level scheme.

Adopted Levels, Gammas

Q(β⁻)=–2216 *10*; S(n)=6795 *11*; S(p)=2651 *11*; Q(α)=9540 *7* 2012Wa38.
S(2n)=12272 *9*, S(2p)=7680 *8* (2012Wa38).

^{215}Ac evaluated by A.K. Jain, S. Singh, B. Singh, N. Kaur, S. Lakshami, B. Maheshwari.

^{215}Fr identified (1961Gr43) in excitation function measurements in ^{208}Pb(^{11}B,4n)^{215}Fr reaction. 1970Bo13 identified ^{215}Fr as descendent of ^{223}Pa, and estimated its half–life.
All γ–ray and excited–state data are from the ^{208}Pb(^{11}B,4nγ) dataset.

^{215}Fr Levels

The low–lying states of ^{215}Fr result from the coupling of an $h_{9/2}$ proton to the 0+, 2+, 4+, 6+, and 8+ states of the even–even core (^{214}Rn). The energies of these even–spin states are similar to those of the 9/2, and (11/2,13/2), (15/2,17/2), (21/2,19/2) doublets in ^{215}Fr. The long–range α particle groups emitted from these states in ^{215}Fr are analogous to those emitted from the g.s., 4+, 6+, and 8+ states in ^{216}Ra.
First level scheme of ^{215}Fr with four excited states was reported by 1982GoZU (also 1983GoZX). 1984De16 extended the level scheme up to 3068 level with 20 gamma rays. A contemporary study by 1984Sc25 produced a level scheme up to 3462 level with 26 gamma rays; the level scheme up to 3068–keV level almost the same as in 1984De16. 1985Dr04 measured polarization asymmetries for several of the gamma rays, establishing definite multipolarities. They reported 21 gamma rays and essentially confirmed the earlier level schemes of 1984De16 and 1984Sc25. In the opinion of the evaluators, further work is needed to define the ordering of the cascades above 2251 level.

Cross Reference (XREF) Flags

A ^{219}Ac α Decay (11.8 μs)
B ^{208}Pb(^{11}B,4nγ)

E(level)†	Jπ§	XREF	$T_{1/2}$	Comments
0.0	9/2–	AB	86 ns *5*	%α=100. RMS charge radius $<r^2>^{1/2}$=5.620 fm *20*; deduced from interpolation of evaluated rms charge radii of ^{212}Fr to ^{228}Fr (2013An02), with slope k_z=0.36 in formula 9 of 2004An14. Value has been adjusted upward by 0.004 fm to account for slight difference in the systematics trend of deduced rms radii for A=215, and evaluated values in 2013An02 for A=210 isotopes. Jπ: favored α decay (HF≈1) to ^{211}At (Jπ=9/2–). $T_{1/2}$: from slope of α–decay time spectrum fitted to two components: 86 ns and 30 ns (1984De16). Others: 104 ns *16* (1984Sc25, slope of time spectrum); 0.12 μs *2* (1974No02, measured for ≈90 ns only), <0.5 μs (1970Bo13). Weighted average of all results is 89 ns *6*. Configuration=$\pi 1h_{9/2}\otimes$0+. No ε decay. Evaluators calculated %ε+%β⁺=1.0×10⁻⁸ for logft=5.0. %ε+%β⁺<1.0×10⁻⁸, theory (1973Ta30).
670.34 *13*	(13/2)–	B		Jπ: 670γ E2 to 9/2–. Configuration=$\pi 1h_{9/2}\otimes$2+.
699.97 *13*	(11/2)–	B		Jπ: 700γ M1+E2 to 9/2–. Configuration=$\pi 1h_{9/2}\otimes$2+.
835.43 *14*	(13/2)+	B		%α=4.3 *15*. Jπ: 135γ E1 to (11/2)–. %α: deduced by evaluators from Iα(10160)/Iα(total)= 3.8% *15* (1984Sc25), and renormalizing g.s. α branch from 87.7% to 100%.
1121.51 *17*	(17/2)–	B		%α=0.9 *1*. Jπ: 451γ E2 to (13/2)–. Configuration=$\pi 1h_{9/2}\otimes$4+. %α: for 1121 and/or 1149 levels; deduced by evaluators from Iα(10460)/Iα(total)=0.8% *1* (1984Sc25), and renormalizing g.s. α branch from 87.7% to 100%.
1149.04 *14*	(15/2)–	B		%α=0.9 *1*. Jπ: 479γ M1+E2 to (13/2)–. Configuration=$\pi 1h_{9/2}\otimes$4+. %α: for 1121 and/or 1149 levels; deduced by evaluators from Iα(10460)/Iα(total)=0.8% *1* (1984Sc25), and renormalizing g.s. α branch from 87.7% to 100%.
1440.02 *18*	(19/2)–	B	4 ns *2*	μ=3.1 *9* (1984De16). %α=4.7 *4*. Jπ: 318γ M1+E2 to (17/2)–. Configuration=$\pi 1h_{9/2}\otimes$6+. μ: from g factor=0.33 *10*, DPAD of γ rays (1984De16), value is for 1440 and/or 1573 level. %α: deduced by evaluators from Iα(10740)/Iα(total)=4.1% *3* (1984Sc25), and renormalizing g.s. α branch from 87.7% to 100%. $T_{1/2}$: γγ(t) (1984De16), value is for 1440 and/or 1573 level 10789 (1984De16).
1457.36 *21*	(21/2)–	B		Jπ: 336γ E2 to (17/2)–. Configuration=$\pi 1h_{9/2}\otimes$6+.

Continued on next page (footnotes at end of table)

Adopted Levels, Gammas (continued)

^{215}Fr Levels (continued)

E(level)†	Jπ§	XREF	$T_{1/2}$	Comments
1573.10 *21*	(23/2)−	B	3.5 ns *14*	%α=4.1 *4*. μ=3.8 *12* (1984Sc25). Jπ: 115.8γ M1 to (21/2)−. Configuration=$\pi 1h_{9/2}{}^5 \otimes \nu 2g_{9/2}{}^1 \otimes \nu 1i_{11/2}{}^1$. Theoretical g−factor=0.12 (1984Sc25) for the assigned shell−model configuration. μ: from g factor=0.33 *10*, DPAD of γ rays (1984De16), value is for 1440 and/or 1573 level. %α: deduced by evaluators from Iα(10890)/Iα(total)=3.6% *3* (1984Sc25), and renormalizing g.s. α branch from 87.7% to 100%. $T_{1/2}$: γγ(t) centroid shift method (1984Sc25). Other value: 4 ns *2*, γγ(t) centroid shift method (1984De16) for 1440 and/or 1573 level.
1680.6?‡ *3*	(25/2−)	B		Jπ: 107.4γ M1(+E2) to (23/2)−. Configuration=$\pi 1h_{9/2}{}^5 \otimes \nu 2g_{9/2}{}^1 \otimes \nu(1i_{11/2}{}^1)$.
1813.62 *25*	(27/2)−	B	2.1 ns *14*	Jπ: 133γ M1+E2 to (25/2)−; 240.5γ E2 to (23/2)−. Configuration=$\pi(1h_{9/2}{}^4,2f_{7/2}{}^1) \otimes \nu(2g_{9/2}{}^1,1i_{11/2}{}^1)$. Theoretical g−factor=0.35 (1984Sc25) for assigned configuration. $T_{1/2}$: γγ(t), αγ(t) centroid shift method (1984Sc25).
2015.9 *3*	(29/2)+	B	4.7 ns *14*	μ=6.8 *29* (1984De16,1989Ra17,2011StZZ). Jπ: 202γ E1 to (27/2)−. Theoretical g−factor=0.43 (1984Sc25) for configuration=$\pi(1h_{9/2}{}^4,1i_{13/2}{}^1) \otimes \nu(2g_{9/2}{}^1)$ agrees with experimental value. μ: from g factor=0.47 *20*, DPAD of γ rays (1984De16). $T_{1/2}$: γγ(t) and/or αγ(t) with centroid−shift method. Weighted average of 5.5 ns *14* (1984Sc25), and 3 ns *2* (1984De16). Other: 9.8 ns *14* (1982GoZU) tentatively assigned to a 1612 level decaying by 202γ, but this γ now deexcites a level at 2016 keV; also this half−life may have contribution from higher−lying isomers at 3068 and 3462 keV with half−lives of 14.6 ns and 22.9 ns, respectively.
2251.3 *4*	(33/2)+	B	5.3 ns *14*	μ=7.8 *17* (1984De16,1989Ra17,2011StZZ). Jπ: 235.4γ E2 to (29/2)+. Theoretical g−factor=0.49 (1984Sc25) for configuration=$\pi(1h_{9/2}{}^4,1i_{13/2}{}^1) \otimes \nu(2g_{9/2}{}^1,1i_{11/2}{}^1)$ agrees with experimental value. μ: from g factor=0.47 *10*, DPAD of γ rays (1984De16). $T_{1/2}$: γγ(t) and/or αγ(t) with centroid−shift method. Weighted average of 5.5 ns *14* (1984Sc25), and 5 ns *2* (1984De16).
2806.8?‡ *4*	(35/2)−	B		Jπ: 555.5γ E1 to (33/2)+. Configuration=$\pi(1h_{9/2}{}^5) \otimes \nu(2g_{9/2}{}^1,1i_{11/2}{}^1)$.
2900.4?‡ *4*	(35/2−)	B		Jπ: predicted by shell model (1984Sc25) with configuration= $\pi(1h_{9/2}{}^4,2f_{7/2}{}^1) \otimes \nu(2g_{9/2}{}^1,1i_{11/2}{}^1)$. Jπ=33/2(+) proposed in 1985Dr04.
3014.0?‡ *5*	(37/2−)	B		Jπ: 113.7γ to (35/2−). Shell−model configuration=$\pi(1h_{9/2}{}^5) \otimes \nu(2g_{9/2}{}^1,1i_{11/2}{}^1)$.
3068.9 *4*	(39/2)−	B	14.6 ns *14*	μ=9.2 *4* (1984De16,1989Ra17,2011StZZ). Jπ: 818γ E3 to (33/2)+. Theoretical g−factor=0.41 (1984Sc25) for configuration=$\pi(1h_{9/2}{}^4,1i_{13/2}{}^1) \otimes \nu(1i_{11/2}{}^1,1j_{15/2}{}^1)$ agrees with experimental value. μ: from g factor=0.47 *2*, DPAD of γ rays (1984De16, corrected for diamagnetism and Knight shift). Other: g=0.48 *2*, DPAD of α particles (1984De16). $T_{1/2}$: γγ(t) (262γ−555γ time curves fitted to a two−level decay formula) (1984Sc25). Other: 33 ns *5* or 30 ns *5* (1984De16), which may correspond to the half−life of the isomer at 3462 keV.
3207.5 *5*	(41/2−)	B		Jπ: 193.6γ (E2) to (37/2−). Shell−model configuration=$\pi(1h_{9/2}{}^5) \otimes \nu(2g_{9/2}{}^1,1i_{11/2}{}^1)$.
3409.1 *4*	(41/2)	B		Jπ: ΔJ=1, dipole 340γ to (39/2)−.
3417.1?‡ *5*	(45/2−)	B		Jπ: 210γ (E2) to (41/2−).
3462.3 *6*	(47/2+)	B	22.9 ns *21*	Jπ: 45γ (E1) to (45/2−). Configuration= $\pi(1h_{9/2}{}^4,1i_{13/2}{}^1) \otimes \nu(2g_{9/2}{}^1,1i_{11/2}{}^1)$. Theoretical g−factor=0.61 (1984Sc25). $T_{1/2}$: γγ(t) (262γ−555γ time curves fitted to a two−level decay formula), and from 210γ time spectrum (1984Sc25). Other: 33 ns *5*, γγ(t) for all γ rays; 30 ns *5*, time spectrum of g.s. α transition fitted to a two−component decay (1984De16); where this half−life is assigned to 3068 level.

† From a least−squares fit of γ−ray energies.

‡ The orderings of 133−107 cascade from 1813 level; 262−55 cascade from 3069−keV level; 194−114−649 cascade from 3207 level; and 45−210 cascade from 3462 level are not established. The level energies for the intermediate levels can be different for alternate orderings.

§ As proposed in 1985Dr04, 1984Sc25 and 1984De16 based on γ(θ), γ(lin pol), ce, and transition probabilities. Multiple quasi−particle shell model configurations presented here are from 1984Sc25.

Adopted Levels, Gammas (continued)

γ(^{215}Fr)

All data are from ^{208}Pb(^{11}B,4nγ).

E(level)	Eγ	Iγ	Mult.	δ	α	Comments
670.34	670.35 *15*	100	E2		0.0191	
699.97	699.95 *15*	100	M1+E2	−3.8 *5*	0.0206 *10*	
835.43	135.41 *15*	100 *4*	(E1)		0.227	
	164.96 *15*	56.8 *25*	(E1)		0.1402	
1121.51	451.23 *15*	100	E2		0.0473	
1149.04	(27.5 *2*)		(M1)		124 *4*	Eγ: from level–energy difference.
	313.41 *15*	16.7 *7*	E1		0.031	Iγ: from 1984Sc25. Others: 24 *4* (1984De16), 45.4 *17* (1985Dr04); the latter in severe disagreement.
	449.11 *15*	100.0 *24*	E2		0.0479	
	478.80 *15*	76 *5*	M1+E2	−3.8 *+5−4*	0.050 *3*	Iγ: other: 100 *12* (1984De16) is in disagreement.
1440.02	290.93 *15*	100 *3*	E2		0.1590	B(E2)(W.u.)=0.6 *4*.
	318.52 *15*	22 *3*	M1+E2	+10 *+6−2*	0.125 *4*	Iγ: unweighted average of values in 1984Sc25 and 1985Dr04. B(M1)(W.u.)=3.×10^{-7} *+4−3*; B(E2)(W.u.)=0.09 *5*.
1457.36	335.88 *15*	100	E2		0.1039	
1573.10	115.8 *2*	5.3 *6*	[M1]		9.43	B(M1)(W.u.)=5.1×10^{-5} *22*.
	133.05‡ *15*	100‡ *9*	E2		2.67	B(E2)(W.u.)=12 *5*.
1680.6?	107.4† *3*	100	M1(+E2)		11.66 *19*	α: for M1.
1813.62	133.05†‡ *15*	41‡ *11*	M1+E2	+0.50 *+13−18*	5.6 *4*	B(M1)(W.u.)=0.0004 *3*; B(E2)(W.u.)=1.7 *15*.
	240.53 *15*	100 *4*	E2		0.292	B(E2)(W.u.)=1.1 *8*.
2015.9	202.32 *15*	100	E1		0.0858	B(E1)(W.u.)=4.5×10^{-6} *14*.
2251.3	235.39 *15*	100	E2		0.314	B(E2)(W.u.)=1.5 *4*.
2806.8?	555.48† *15*	100	E1		0.00922 *13*	
2900.4?	649.09† *15*	100	D+Q			
3014.0?	113.7† *3*	100	[M1]		9.94 *16*	
3068.9	262.01† *15*	100 *3*	E2		0.220	B(E2)(W.u.)=0.26 *3*.
	817.53 *15*	34.4 *16*	(E3)		0.0331	B(E3)(W.u.)=27 *3*.
3207.5	138.5 *3*	52 *10*	[M1]		5.67	
	193.6† *2*	100 *20*	(E2)		0.622	
3409.1	340.25 *15*	100	D			
3417.1?	209.6† *2*	100	E2		0.468	
3462.3	45.2† *3*	100	(E1)		0.894 *21*	B(E1)(W.u.)=4.7×10^{-5} *5*.

† The orderings of 133–107 cascade from 1813 level; 262–55 cascade from 3069 level; 194–114–649 cascade from 3207 level; and 45–210 cascade from 3462 level are not established.
‡ Multiply placed; intensity suitably divided.

^{219}Ac α Decay (11.8 μs) 1970Bo13,1989Mi17

Parent ^{219}Ac: E=0.0; Jπ=9/2−; $T_{1/2}$=11.8 μs *15*; Q(g.s.)=8830 *50*; %α decay=100.
^{219}Ac–J,$T_{1/2}$: From Adopted Levels of ^{219}Ac in ENSDF database.
^{219}Ac–Q(α): From 2012Wa38.
1970Bo13: ^{219}Ac activity was produced as descendant of ^{223}Pa by following reactions: ^{205}Tl(^{22}Ne,4n), ^{208}Pb(^{19}F,4n), ^{209}Bi(^{20}Ne,α2n), and ^{209}Bi(^{22}Ne,α4n), E=90–135 MeV. The activity was identified by excitation functions, cross bombardments, and by genetic relationships between parent and daughter nuclei. Measured Eα. Detector: semi.
1989Mi17: ^{219}Ac activity was produced by ^{209}Bi(^{16}O,α2n) and ^{205}Tl(^{16}O,2n), E=87.4–101.9 MeV, and identified by mass separation and excitation functions. Measured Eα, half-life. Detector: semi.

^{215}Fr Levels

E(level)	Jπ	$T_{1/2}$	Comments
0.0	9/2−	86 ns *5*	Jπ,$T_{1/2}$: from Adopted Levels.

^{219}Ac α Decay (11.8 μs) 1970Bo13,1989Mi17 (continued)

α radiations

Eα	E(level)	Iα‡	HF†	Comments
8664 *10*	0.0	100	1.2 *2*	Eα: from 1970Bo13. Original energy has been decreased by 1 keV because of a change in the calibration energy of ^{212}Po (1991Ry01).

† r_0(^{215}Fr=1.5645 *65*; interpolated value deduced from r_0(^{214}Rn)=1.563 *4* and r_0(^{216}Ra)=1.566 *9* (1998Ak04).
‡ Absolute intensity per 100 decays.

^{208}Pb(^{11}B,4nγ) 1984Sc25,1984De16,1985Dr04

Includes ^{204}Hg(^{15}N,4nγ),E≈78 MeV; ^{207}Pb(^{11}B,3n).

1984Sc25: target: >99% enriched ^{208}Pb, E(^{11}B)=66 MeV. Measured Eγ, Iγ, γγ coin, αγ coin, γγ(t), αγ(t), γ(θ) for θ=90°, 115°, 127°, 138°, and 149°. Measured level half–lives, α decay from g.s. and excited levels. Deduced γ–ray multipolarities. Detectors: Ge(Li), high–purity germanium, Si surface barrier.

1984De16: ^{208}Pb(^{11}B,4n), target: 98% enriched ^{208}Pb, E(^{11}B)=58, 62 MeV. Measured Eγ, Iγ, γγ coin, αγ coin, ce–ce coin, γγ(t), αγ(t), differential perturbed angular distribution (DPAD) of α particles, α decay from g.s. and excited levels, level half–lives. The ^{207}Pb(^{11}B,3n) reaction was used to confirm the assignment of measured α particles to ^{215}Fr.

1984De16: ^{204}Hg(^{15}N,4nγ), target: 98% enriched ^{204}Hg cooled to −30° C, E(^{15}N)≈78 MeV. Measured differential perturbed angular distribution (DPAD) for γ rays. Deduced γ–ray multipolarities, g–factors, half–lives.

1985Dr04: target: enriched ^{208}Pb, E(^{11}B)=45–66 MeV. Measured Eγ, Iγ, γγ, γ(x ray) coin, γ(θ)(θ=0° to 90° in 15° increments), γ–ray excitation functions, and γ(lin pol). Deduced level scheme, multipolarities, spins and parities.

1982GoZU, 1983GoZX: ^{213}Tl(^{13}C,3nγ), E=65 MeV; measured Eγ, Iγ, Eα, γ(θ), αγ coin, γγ coin; deduced levels, level half–life. Gamma cascade 201.6–290.2–450.5–670.2 from a 1612.5 level of 9.8 ns *14* half–life discovered in this work. For the first time, excited states in ^{215}Fr were identified at 670.2, (13/2−); 1120.7, (17/2−); 1410.9, (21/2−); and isomer at 1612.5 keV. The α decays were observed from g.s., 1410 and 1612 levels.

^{215}Fr Levels

First level scheme of ^{215}Fr with four excited states was reported in 1982GoZU (also 1983GoZX). 1984De16 extended the level scheme up to 3068 level with 20 gamma rays. A contemporary study by 1984Sc25 produced a level scheme up to 3462 level with 26 gamma rays; the level scheme up to 3068 level almost the same as in 1984De16. 1985Dr04 measured polarization asymmetries for several of the gamma rays, establishing definite multipolarities. They reported 21 gamma rays and essentially confirmed the earlier level schemes of 1984De16 and 1984Sc25. In the opinion of the evaluators, further work is needed to define the ordering of the cascades above the 2251 level.

E(level)†	Jπ§	$T_{1/2}$	Comments
0.0	9/2−	86 ns *5*	%α=100. $T_{1/2}$: from Adopted Levels. Measured Eα=9365 (1982GoZU), 9630 (1984Sc25), 9369 (1984De16).
670.34 *13*	(13/2)−		
699.97 *13*	(11/2)−		
835.43 *14*	(13/2)+		%α=4.3 *15*. %α: deduced by evaluators from Iα(10160)/Iα(total)= 3.8% *15* (1984Sc25), and renormalizing g.s. α branch from 87.7% to 100%. It is assumed by the evaluators that 1984Sc25 have corrected for 78% detection of the ground state α branch in αγ–coin spectrum. Measured Eα=10160 *30* (1984Sc25).
1121.51 *17*	(17/2)−		%α=0.9 *1*. %α: for 1121 and/or 1149 levels; deduced by evaluators from Iα(10460)/Iα(total)=0.8% *1* (1984Sc25), and renormalizing g.s. α branch from 87.7% to 100%. It is assumed by the evaluators that 1984Sc25 have corrected for 78% detection of the ground state α branch in αγ–coin spectrum. Measured Eα=10460 *30* (1984Sc25), 10493 (1984De16) from 1121+1149 levels.
1149.04 *14*	(15/2)−		%α=0.9 *1*. %α: for 1121 and/or 1149 levels; deduced by evaluators from Iα(10460)/Iα(total)=0.8% *1* (1984Sc25), and renormalizing g.s. α branch from 87.7% to 100%. It is assumed by the evaluators that 1984Sc25 have corrected for 78% detection of the ground state α branch in αγ–coin spectrum. Measured Eα=10460 *30* (1984Sc25), 10493 (1984De16) from 1121+1149 levels.

Continued on next page (footnotes at end of table)

$^{208}Pb(^{11}B,4n\gamma)$ 1984Sc25,1984De16,1985Dr04 (continued)

^{215}Fr Levels (continued)

E(level)†	Jπ§	$T_{1/2}$	Comments
1440.02 *18*	(19/2)–	4 ns *2*	g=0.33 *10* (1984De16). %α=4.7 *4*. g: DPAD of γ rays (1984De16), value is for 1440 and/or 1573 level. %α: deduced by evaluators from Iα(10740)/Iα(total)=4.1% *3* (1984Sc25), and renormalizing g.s. α branch from 87.7% to 100%. It is assumed by the evaluators that 1984Sc25 have corrected for 78% detection of the ground state α branch in αγ–coin spectrum. $T_{1/2}$: γγ(t) (1984De16), value is for 1440 and/or 1573 level. Measured Eα=10760 (1982GoZU), 10740 *30* (1984Sc25), 10789 (1984De16).
1457.36 *21*	(21/2)–		
1573.10 *21*	(23/2)–	3.5 ns *14*	%α=4.1 *4*. g=–0.33 *10* (1984Sc25). g: from DPAD, g factor=0.33 10 (1984De16) for 1440 and/or 1573 level. %α: deduced by evaluators from Iα(10890)/Iα(total)=3.6% *3* (1984Sc25), and renormalizing g.s. α branch from 87.7% to 100%. It is assumed by the evaluators that 1984Sc25 have corrected for 78% detection of the ground state α branch in αγ–coin spectrum. $T_{1/2}$: γγ(t) centroid shift method (1984Sc25). Other value: 4 ns *2*, γγ(t) centroid shift method (1984De16) for 1440 and/or 1573 level. Measured Eα=10909 (1982GoZU), 10890 *30* (1984Sc25), 10919 (1984De16).
1680.6?‡ *3*	(25/2)–		
1813.62 *25*	(27/2)–	2.1 ns *14*	$T_{1/2}$: γγ(t), αγ(t) centroid shift method (1984Sc25).
2015.9 *3*	(29/2)+	4.7 ns *14*	g=0.47 *20* (1984De16). g: DPAD of γ rays (1984De16). $T_{1/2}$: γγ(t) and/or αγ(t) with centroid–shift method. Weighted average of 5.5 ns *14* (1984Sc25), and 3 ns *2* (1984De16). Other: 9.8 ns *14* (1982GoZU) tentatively assigned to a 1612 level decaying by 202γ, but this γ now deexcites a level at 2016 keV; also this half–life may have contribution from higher–lying isomers at 3068 and 3462 keV with half–lives of 14.6 ns and 22.9 ns, respectively.
2251.3 *4*	(33/2)+	5.3 ns *14*	g=0.47 *10* (1984De16). g: DPAD of γ rays (1984De16). $T_{1/2}$: γγ(t) and/or αγ(t) with centroid–shift method. Weighted average of 5.5 ns *14* (1984Sc25), and 5 ns *2* (1984De16).
2806.8?‡ *4*	(35/2)–		
2900.4?‡ *4*	(35/2–)		Jπ: from 1984Sc25. 33/2(+) proposed in 1985Dr04.
3014.0?‡ *5*	(37/2–)		
3068.9 *4*	(39/2)–	14.6 ns *14*	g=0.47 *2* (1984De16). g: from DPAD of γ rays (1984De16, corrected for diamagnetism and Knight shift). Other: 0.48 *2*, DPAD of α particles (1984De16). $T_{1/2}$: γγ(t) (262γ–555γ time curves fitted to a two–level decay formula) (1984Sc25). Other: 33 ns *5* or 30 ns *5* (1984De16), which may correspond to the half–life of the isomer at 3462 keV.
3207.5 *5*	(41/2–)		
3409.1 *4*	(41/2)		
3417.1?‡ *5*	(45/2–)		
3419.4? *5*			Tentative level in 1985Dr04 not included in Adopted Levels.
3462.3 *6*	(47/2+)	22.9 ns *21*	$T_{1/2}$: γγ(t) (262γ–555γ time curves fitted to a two–level decay formula), and from 210γ time spectrum (1984Sc25). Other: 33 ns *5*, γγ(t) for all γ rays; 30 ns *5*, time spectrum of g.s. α transition fitted to a two–component decay (1984De16); where this half–life is assigned to 3068 level.

† From a least–squares fit of γ–ray energies.

‡ The orderings of 133–107 cascade from 1813 level; 262–55 cascade from 3069 level; 194–114–649 cascade from 3207 level; and 45–210 cascade from 3462 level are not established. The level energies for the intermediate levels can be different for alternate orderings.

§ As proposed in 1985Dr04, 1984Sc25 and 1984De16 based on γ(θ), γ(lin pol), ce, and transition probabilities.

$^{208}Pb(^{11}B,4n\gamma)$ 1984Sc25,1984De16,1985Dr04 (continued)

$\gamma(^{215}Fr)$

Eγ[†]	E(level)	Iγ[‡]	Mult.[c]	δ	α	Comments
(27.5[#] *2*)	1149.04	[#]	(M1)		124 *4*	Eγ: from level–energy difference. Mult.: not E1 since this line is not observed in γ spectrum.
45.2[#b] *3*	3462.3	17[#@] *2*	(E1)		0.894 *21*	Mult.: from intensity balance at 3417 level.
107.4[b] *3*	1680.6?	8[@] *1*	M1(+E2)		11.66 *19*	Mult.: from 1984De16, based on K and L lines. α: for M1.
[x]112[§]						
113.7[#b] *3*	3014.0?	0.4[#@] *1*	[M1]		9.94 *16*	
115.8 *2*	1573.10	1.7[@] *2*	[M1]		9.43	
133.05[e] *15*	1573.10	32[&e] *3*	E2		2.67	A_2=+0.23 *4*, A_4=−0.07 *7* (1985Dr04). A_2=+0.24 *5*, A_4=−0.06 *5* for doublet (1984Sc25).
	1813.62	11[&e] *3*	M1+E2	+0.50 *+13−18*	5.6 *4*	δ: from γ(θ) (1984De16).
135.41 *15*	835.43	7.1 *3*	(E1)		0.227	A_2=−0.09 *4*, A_4=−0.01 *7* (1985Dr04). Non–observation in ce spectrum of 1984De16 suggests E1.
138.5[#] *3*	3207.5	2.6[#@] *5*	[M1]		5.67	
164.96[a] *15*	835.43	4.03 *23*	(E1)		0.1402	A_2=+0.37 *5*, A_4=−0.04 *7* (1985Dr04); ΔJ=0 transition. Iγ: from Iγ(165)/Iγ(135)=0.568 *32* (1985Dr04).
193.6[#b] *2*	3207.5	5[#] *1*	(E2)		0.622	A_2=+0.37 *9*, A_4=0.00 *10* (1984Sc25).
202.32 *15*	2015.9	101 *3*	E1		0.0858	A_2=−0.26 *4*, A_4=−0.03 *6*, POL=+0.53 *17* (1985Dr04). A_2=−0.11 *5*, A_4=+0.02 *5* (1984Sc25). A_2=−0.19 *2*, Iγ(prompt)/Iγ(delayed)=0.23 *4* (1984De16). K/L ratio overlaps E1 or M1 (1984De16).
209.6[#b] *2*	3417.1?	26[#] *1*	E2		0.468	A_2=+0.27 *5*, A_4=−0.07 *5* (1984Sc25).
[x]229[§]						
235.39 *15*	2251.3	79 *3*	E2		0.314	A_2=+0.23 *4*, A_4=−0.09 *6* (1985Dr04). A_2=+0.39 *6*, A_4=−0.06 *5* (1984Sc25). A_2=+0.24 *3*, Iγ(prompt)/Iγ(delayed)=0.22 *4* (1984De16).
[x]239[§]						
240.53 *15*	1813.62	27 *1*	E2[d]		0.292	A_2=+0.29 *4*, A_4=−0.10 *7* (1985Dr04). A_2=+0.35 *6*, A_4=−0.05 *5* (1984Sc25). A_2=+0.20 *5*, Iγ(prompt)/Iγ(delayed)=0.30 *5* (1984De16).
262.01[b] *15*	3068.9	38 *1*	E2[d]		0.220	A_2=+0.35 *4*, A_4=−0.12 *7*, POL=+0.46 *37* (1985Dr04). A_2=+0.35 *6*, A_4=−0.05 *5* (1984Sc25). A_2=+0.25 *5*, Iγ(prompt)/Iγ(delayed)=0.15 *4* (1984De16).
290.93 *15*	1440.02	97 *3*	E2[d]		0.1590	A_2=+0.32 *4*, A_4=−0.11 *6*, POL=+0.55 *9* (1985Dr04). A_2=+0.36 *5*, A_4=−0.05 *5* (1984Sc25). A_2=+0.26 *5*, Iγ(prompt)/Iγ(delayed)=0.35 *6* (1984De16).
313.41 *15*	1149.04	7.0 *3*	E1		0.031	A_2=−0.03 *4*, A_4=−0.06 *6*, POL=+0.30 *18* (1985Dr04). A_2=−0.11 *8*, A_4=−0.03 *10* (1984Sc25). Non–observation in ce spectrum of 1984De16 suggests E1.
318.52 *15*	1440.02	19 *1*	M1+E2	+10 *+6−2*	0.125 *4*	A_2=−0.22 *4*, A_4=+0.22 *6*, POL=+0.49 *21* (1985Dr04). A_2=−0.18 *5*, A_4=+0.14 *7* (1984Sc25). K/L ratio overlaps E2 and E3 (1984De16). δ: from γ(θ) (1985Dr04). Dominant E2 with <10% M1 admixture from ce data in 1984De16.

Continued on next page (footnotes at end of table)

$^{208}Pb(^{11}B,4n\gamma)$ 1984Sc25,1984De16,1985Dr04 (continued)

$\gamma(^{215}Fr)$ (continued)

Eγ†	E(level)	Iγ‡	Mult.[c]	δ	α	Comments
335.88 *15*	1457.36	19 *1*	E2[d]		0.1039	A_2=+0.31 *4*, A_4=−0.09 *7* (1985Dr04). A_2=+0.27 *6*, A_4=−0.12 *5* (1984Sc25). Iγ(prompt)/Iγ(delayed)=0.23 *8* (1984De16).
340.25 *15*	3409.1		D			A_2=−0.14 *7*, A_4=+0.01 *7* (1985Dr04). Eγ: from 1985Dr04. This γ ray was observed by 1984Sc25 in αγ coin, but not placed in the level scheme. Iγ: 7.6 *3* (1985Dr04) relative to 100 for 670γ.
449.11 *15*	1149.04	42 *1*	E2[d]		0.0479	A_2=+0.31 *4*, A_4=−0.09 *7*, POL=+0.50 *14* (1985Dr04). POL for 451+449. A_2=+0.41 *6*, A_4=−0.05 *5* (1984Sc25). A_2=+0.30 *10*, Iγ(prompt)/Iγ(delayed)=0.46 *5* (1984De16).
451.23 *15*	1121.51	57 *2*	E2[d]		0.0473	A_2=+0.30 *4*, A_4=−0.09 *7*, POL=+0.50 *14* (1985Dr04). POL for 451+449. A_2=+0.33 *6*, A_4=−0.03 *5* (1984Sc25). A_2=+0.21 *5*, Iγ(prompt)/Iγ(delayed)=0.45 *5* (1984De16).
478.80 *15*	1149.04	32 *2*	M1+E2	−3.8 *+5−4*	0.050 *3*	A_2=−0.42 *4*, A_4=+0.13 *4*, POL=+0.42 *9* (1985Dr04). A_2=−0.31 *5*, A_4=+0.11 *7* (1984Sc25). A_2=−0.21 *5*, Iγ(prompt)/Iγ(delayed)=0.36 *6* (1984De16). δ: from γ(θ); weighted average of −3.75 *+50−40* (1985Dr04) and −6 *+3−4* (1984De16).
519.0[a f] *3*	3419.4?					
555.48[b] *15*	2806.8?	42 *2*	E1		0.00922 *13*	A_2=−0.25 *4*, A_4=+0.02 *6*, POL=+0.58 *16* (1985Dr04). A_2=−0.21 *5*, A_4=−0.04 *5* (1984Sc25). A_2=−0.20 *6*, Iγ(prompt)/Iγ(delayed)=0.13 *5* (1984De16).
649.09[b] *15*	2900.4?	6 *1*	D+Q			A_2=−0.11 *5*, A_4=−0.26 *6* (1985Dr04). A_2=−0.36 *11*, A_4=−0.21 *14* (1984Sc25). Mult.,δ: from γ(θ) data. δ(E2/M1)=−1.27 $^{18-12}$ (1985Dr04), but (E1) in 1984Sc25. Negative A_4 is inconsistent with pure E1.
670.35 *15*	670.34	98 *4*	E2[d]		0.0191	A_2=+0.27 *4*, A_4=−0.08 *7*, POL=+0.42 *5* (1985Dr04). A_2=+0.31 *5*, A_4=−0.04 *5* (1984Sc25). A_2=+0.20 *5*, Iγ(prompt)/Iγ(delayed)=0.60 *6* (1984De16).
699.95 *15*	699.97	44 *2*	M1+E2	−3.8 *5*	0.0206 *10*	A_2=−0.34 *4*, A_4=+0.16 *6*, POL=+0.39 *6* (1985Dr04). A_2=−0.30 *4*, A_4=−0.11 *5* (1984Sc25). A_2=−0.16 *8*, Iγ(prompt)/Iγ(delayed)=0.65 *6* (1984De16). K/L ratio overlaps E2 and E3 (1984De16). δ: from γ(θ); weighted average of −3.75 *+55−40* (1985Dr04) and −7 *+3−13* (1984De16).
817.53 *15*	3068.9	13 *1*	(E3)		0.0331	A_2=+0.50 *6*, A_4=+0.08 *7* (1985Dr04). A_2=+0.57 *6*, A_4=+0.12 *7* (1984Sc25). K/L ratio agrees better with E3 but also not far from E2 (1984De16).

† Weighted average from 1984Sc25 and 1985Dr04. Values in 1984De16 given to nearest keV with a general uncertainty of 0.5 keV are in agreement with the adopted values here.

Footnotes continued on next page

^{208}Pb(^{11}B,4nγ) 1984Sc25,1984De16,1985Dr04 (continued)

γ(^{215}Fr) (continued)

‡ From 1984Sc25 at E(^{11}B)=66 MeV, unless otherwise specified. Corresponding values from 1984De16 at E(^{11}B)=58 MeV, and from 1985Dr04 at E(^{11}B)=58 MeV are listed under document records. For branching ratios in Adopted dataset, all values are considered. Note that intensities in 1985Dr04 are relative to 100 for 670γ; relative to 101 for 202γ in 1964Sc25, and relative to 100 for 202γ in 1984De16.

§ Seen by 1984Sc25 only in αγ coin spectrum but not placed in level scheme.

γ from 1984Sc25 only.

@ From delayed γ (1984Sc25).

& From γγ coin spectrum (1984Sc25).

a γ from 1985Dr04 only.

b The orderings of 133–107 cascade from 1813 level; 262–55 cascade from 3069 level; 194–114–649 cascade from 3207 level; and 45–210 cascade from 3462 level are not established.

c From γ(θ), γ(lin pol), K/L ratios, transition intensity balances, and RUL (for E2 and M2). The data are from 1984De16, 1984Sc25, and and 1985Dr04, as listed under comments.

d E2 from measured K/L ratios with comparison to theoretical values shown in figure 8 of 1984De16. Numerical K/L values are not given explicitly.

e Multiply placed; intensity suitably divided.

f Placement of transition in the level scheme is uncertain.

x γ ray not placed in level scheme.

Level Scheme

Intensities: relative Iγ

@ Multiply placed; intensity suitably divided

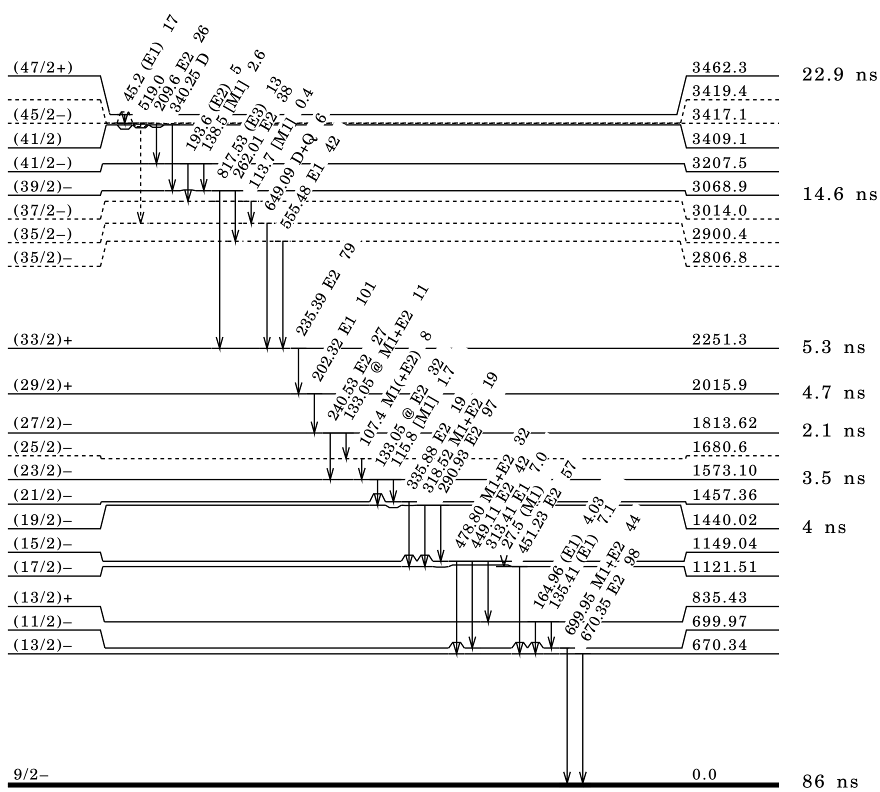

$^{215}_{87}Fr_{128}$

Adopted Levels, Gammas

Q(β⁻)=–3497 *15*; S(n)=5630 *9*; S(p)=3797 *11*; Q(α)=8864 *3* 2012Wa38.
S(2n)=13967 *22*, S(2p)=6346 *9* (2012Wa38).

^{215}Ra evaluated by S. Kumar, B. Singh, K. Rojeeta Devi, A. Rohilla.

^{215}Ra identified (1961Gr43,1962Gr20) in excitation function measurements in ^{209}Bi(^{11}B,5n)^{215}Ra reaction. 1968Va18 identified ^{215}Ra as descendent of ^{219}Th.

2012Co22: ^{207}Pb(^{64}Ni,X), E=5.92 MeV/nucleon; measured lifetime of rotating nuclear molecules or dinuclear system (DNS). Detected reaction products and measured their velocity distribution correlated with α particles from fragments. The ^{64}Ni beam from UNILAC accelerator at GSI facility, reaction products separated by SHIP velocity filter. Target=300 μg/cm^2 thick ^{207}Pb deposited on a 40 μg/cm^2 thick carbon foil and covered by a layer of 10 μg/cm^2 carbon. Isotopes identified by their α decay characteristics. For ^{215}Ra, measured mean lifetime of DNS τ=2.0× 10^{-20} s *3*.

^{215}Ra Levels

The level structure of ^{215}Ra, described by a multiparticle octupole coupling mechanism, leads to configuration mixed isomers with characteristic enhanced E3 transitions. These have been explained by the coupling of octupole vibrations to the shell–model configurations presented here for the six protons and single neutron outside closed shells (1998St24).

The low–lying yrast levels in ^{215}Ra also have been interpreted in terms of the shell model by coupling the odd neutron to experimentally determined energies in ^{214}Ra (1983Lo16). The enhancement of the 773–keV E3 transition in ^{215}Ra is due mostly to the coupling of the particle orbital to the octupole phonon in the ^{208}Pb core. Its B(E3)(W.u.)=37 *2* agrees with the systematics for E3 transitions in the ^{208}Pb region (1983Lo16). See also 1998St24, 1989Dr02, 1985Be05, and 1988Fu10 for further discussions on B(E3) values for this nucleus.

Cross Reference (XREF) Flags

A ^{215}Ac ε Decay (0.17 s)
B ^{219}Th α Decay (1.05 μs)
C ^{206}Pb(^{13}C,4nγ)

E(level)†	Jπ‡	XREF	T$_{1/2}$§	Comments
0.0#	(9/2+)	ABC	1.66 ms *2*	%α=100. RMS charge radius <r^2>$^{1/2}$=5.619 fm *20*; deduced from interpolation of evaluated rms charge radii of ^{214}Ra to ^{232}Ra (2013An02), with slope k$_z$=0.37 in formula 9 of 2004An14. Value has been adjusted upward by 0.004 fm to account for slight difference in the systematics trend of deduced rms radii for A=215, and evaluated values in 2013An02 for A=210 isotopes. No ε, β$^+$ decay observed. Theoretical estimates: %ε+%β$^+$<2×10^{-4} (1973Ta30), <7×10^{-5} (1997Mo25). T$_{1/2}$: weighted average of 1.64 ms *4* (2005Li17), 1.62 ms *+16–13* (2000Ni02), 1.68 ms *2* (2000He17), 1.56 ms *10* (1970To08), 1.7 ms *2* (1968Va18), 1.5 ms *1* (1991An10; also 1.5 ms *3* in 1991An13). Other: 1.6 ms (1961Gr43,1962Gr20). Jπ: analogy to N=127 isotones (for example ^{211}Po and ^{213}Rn) suggest Jπ=(9/2+). Shell model configuration for the odd neutron is expected to be g$_{9/2}$.
773.0@ *2*	(15/2–)	C	67.2 ns *14*	Jπ: 773γ E3 to (9/2+). Analogy with 896–keV state (Jπ=(15/2–)) in ^{213}Rn. T$_{1/2}$: from γγ(t) (1998St24; also 68.6 ns *21* in 1989Dr02). Others: 77 ns *2* (1988Fu10), 67 ns *3* (1987AdZU). Value from 1988Fu10 is considered by the evaluators as discrepant. From pulsed–beam method, values are 110 ns *8* (1989Dr02), 120 ns *10* (1983Lo16). The higher values in pulsed–beam experiments are likely due to much longer half–life (7.3 μs) of the 1877 level, which will affect the observed decay rate of 773γ, thus making it more difficult to measure lifetime in the ns range with this method.
1625.3# *3*	(17/2+)	C		Jπ: 852γ E1 to (15/2–). Analogy with 1529–keV state (Jπ=(17/2+)) in ^{213}Rn.
1821.2# *3*	(21/2+)	C	25.0 ns *14*	Jπ: 196γ E2 to (17/2+), 1048γ E3 to (15/2–). Analogy with 1664–keV state (Jπ=(21/2+)) in ^{213}Rn (1988Fu10). T$_{1/2}$: other: 23 ns *5* (1983Lo16).
1877.8& *3*	(25/2+)	C	7.29 μs *20*	Jπ: analogous state at >1664 keV with T$_{1/2}$≈1 μs has been observed in ^{213}Rn (1988Fu10). T$_{1/2}$: weighted average of 7.6 μs *2* (2004He25), 6.86 μs *28* (1998St24), 7.2 μs *2* (1988Fu10). Other: ≥2 μs (1983Lo16). Mixed with 2053.8 level by particle octupole coupling.
1994.5& *3*	(23/2+)	C		
2053.8# *4*	(25/2+)	C		Mixed with 1877.8 level by particle octupole coupling.
2214.4a *4*	(27/2–)	C		

Continued on next page (footnotes at end of table)

Adopted Levels, Gammas (continued)

^{215}Ra Levels (continued)

E(level)†	Jπ‡	XREF	$T_{1/2}$§	Comments
2246.9[b] *4*	(29/2−)	C	1.39 μs *7*	
2246.9+x[b]	(31/2−)	C		E(level): x ≤35 keV.
3088.8+x[c] *2*	(33/2+)	C		
3143.7+x[d] *3*	(35/2+)	C		
3331.1+x[d] *4*	(37/2+)	C		
3413.4+x[b] *4*	(37/2−)	C		
3415.6+x[d] *4*	(37/2+)	C		
3586.4+x[e] *4*	(37/2+)	C		
3738.6+x[b] *4*	(39/2−)	C		
3756.6+x[b] *4*	(43/2−)	C	555 ns *10*	μ=15.61 *6* (1998St24,2011StZZ). $T_{1/2}$: other: 0.59 μs *18* (1987AdZU). Octupole−mixed state. μ: from g factor=+0.726 *3* (TDPAD method, 1998St24). Other measurement: 15.78 *15* (1987AdZU, from g factor=+0.734 *7*, stroboscopic observation of perturbed angular distribution). Theoretical value=+0.73 (1998St24). Measured isomer yield ratio: R_{exp}=7.9 *8* (2013Ba29) in ^{9}Be(^{238}U,X) reaction at 1 GeV/nucleon, where R_{exp}=Y/(N_{imp}FG), N_{imp} is number of implanted ions, Y is the isomeric yield, F and G are correction factors for in−flight isomer decay losses and the finite detection time of the γ radiation, respectively. Comparison of measured yield ratios with theoretical values calculated by using ABRABLA Monte−Carlo code.
3765.7+x *4*		C		Jπ: 434.6γ to (37/2+) suggests 37/2 to 41/2.
3855.0+x *4*		C		Jπ: 439.4γ to (37/2+) suggests 37/2 to 41/2.
3935.4+x[a] *4*	(43/2−)	C		Octupole−mixed state.
4207.3+x *5*		C		
4366.8+x[c] *4*	(45/2+)	C		
4553.5+x[b] *4*	(47/2−)	C		
4567.0+x[c] *4*	(49/2+)	C	10.47 ns *14*	μ=18.87 *25* (1998St24,2011StZZ). $T_{1/2}$: other: ≈10 ns (1987AdZU). μ: from g factor=+0.77 *1* (TDPAD method, 1998St24). Theoretical value=+0.80 (1998St24).
4686.2+x[a] *5*	(47/2−)	C		
4882.7+x[a] *4*	(51/2−)	C		
5372.7+x[c] *5*	(53/2+)	C		
5608.6+x[f] *5*	(55/2−)	C		
5608.7+x[c] *5*	(57/2+)	C	1.66 ns *14*	
6033.5+x[g] *5*	(57/2+)	C		
6076.4+x[g] *5*	(59/2+)	C		
6283.2+x[g] *6*	(61/2+)	C		

† From a least−squares fit to Eγ values from 1998St24.

‡ As proposed by 1998St24, based on γ−ray multipolarities, angular distributions, transition strengths, and excitation functions. These assignments are placed in parentheses since Jπ assignment for the ground state is still tentative. Shell model configurations from 1998St24 are based on level energies and γ−transition rates.

§ From pulsed beam method (1998St24), unless otherwise stated. Values from previous measurements are given under comments.

Member of configuration=$\pi h_{9/2}{}^{6}\otimes\nu g_{9/2}$.

@ Member of configuration=$\pi h_{9/2}{}^{6}\otimes\nu j_{15/2}$.

& Member of configuration=$\pi h_{9/2}{}^{5}\otimes\pi f_{7/2}\otimes\nu g_{9/2}$.

a Member of configuration=$\pi h_{9/2}{}^{4}\otimes\pi f_{7/2}\otimes\pi i_{13/2}\otimes\ \nu_{9/2}$.

b Member of configuration=$\pi h_{9/2}{}^{5}\otimes\pi i_{13/2}\otimes\nu g_{9/2}$.

c Member of configuration=$\pi h_{9/2}{}^{4}\otimes\pi i_{13/2}{}^{2}\otimes\nu g_{9/2}$.

d Member of configuration=$\pi h_{9/2}{}^{5}\otimes\pi f_{7/2}\otimes\nu g_{9/2}$.

e Member of configuration=$\pi h_{9/2}{}^{4}\otimes\pi f_{7/2}{}^{2}\otimes\nu g_{9/2}$.

f Member of configuration=$\pi h_{9/2}{}^{3}\otimes\pi f_{7/2}{}^{2}\otimes\ \pi i_{13/2}\otimes\nu g_{9/2}$.

g Member of configuration=$\pi h_{9/2}{}^{3}\otimes\pi f_{7/2}\otimes\ \pi i_{13/2}{}^{2}\otimes\nu g_{9/2}$.

Adopted Levels, Gammas (continued)

γ(^{215}Ra)

All γ-ray data are from ^{206}Pb(^{13}C,4nγ).

E(level)	Eγ	Iγ	Mult.	δ	α	Comments
773.0	773.0 *2*	100	E3		0.0404	B(E3)(W.u.)=38.4 *8*.
1625.3	852.3 *2*	100	E1		0.00425	
1821.2	196.0 *2*	100.0 *6*	E2		0.629	B(E2)(W.u.)=0.48 *3*.
	1048.2 *2*	48.6 *4*	E3		0.0195	B(E3)(W.u.)=2.91 *17*.
1877.8	56.5 *2*	100	E2		145 *4*	B(E2)(W.u.)=0.0121 *6*.
1994.5	173.3 *2*	100	M1		3.27	
2053.8	59.3 *2*	16 *2*	M1		14.25 *25*	
	176.0 *2*	100 *2*	M1		3.13	
2214.4	336.6 *2*	100	(E1)		0.0272	
2246.9	(32.5)	0.997 *13*	[M1]		84 *5*	B(M1)(W.u.)=3.4×10^{-7} *5*.
	193.1 *2*	100.0 *17*	M2(+E3)	<0.2	10.99	δ: ce data gives δ(E3/M2)<0.45, but RUL(E3)=100 gives δ<0.2. B(M2)(W.u.)=0.17 *1*; B(E3)(W.u.)<100.
	369.1 *2*	32 *3*	M2+E3	1.07 *+25−20*	0.81 *9*	B(M2)(W.u.)=0.0011 *4*; B(E3)(W.u.)=4.8 *13*.
2246.9+x	x					Eγ: no transition seen, but required for current level scheme. Estimated value of x ≤ 35 keV.
3088.8+x	841.9 *2*	100	E1		0.00435	
3143.7+x	54.9 *2*	100	M1		17.9 *4*	
3331.1+x	187.4 *2*	100	M1		2.63	
3413.4+x	269.7 *2*	100	D			
3415.6+x	271.9 *2*	100	M1		0.930	
3586.4+x	170.8 *2*	19 *4*	M1		3.41	
	255.4 *2*	100 *12*	M1		1.106	
	442.6 *2*	10 *4*				
3738.6+x	152.2 *2*	46.5 *5*	E1		0.1740	
	323.1 *2*	30.7 *10*	E1		0.0298	
	325.3 *2*	4.0 *10*				
	407.4 *2*	100.0 *10*	E1		0.0180	
3756.6+x	(18.0)	0.029 *2*	[E2]		25400	B(E2)(W.u.)=0.24 *7*.
	425.5 *2*	100 *3*	E3		0.240	B(E3)(W.u.)=37 *3*.
3765.7+x	434.6 *2*	100				
3855.0+x	439.4 *2*	100				
3935.4+x	178.6 *2*	100	M1		3.01	
4207.3+x	352.3 *2*	100				
4366.8+x	431.5 *2*	98.8 *25*	E1		0.01597	
	610.2 *2*	100 *5*				
4553.5+x	797.3 *2*	100	(Q)			
4567.0+x	(13.5)	10.5 *5*	[E1]		5.74	B(E1)(W.u.)=0.00026 *6*.
	200.1 *2*	100.0 *19*	(E2)		0.584	B(E2)(W.u.)=0.758 *23*.
	810.2 *2*	59.3 *19*	(E3)		0.0359	B(E3)(W.u.)=37.6 *15*.
4686.2+x	750.7 *2*	100	(Q)			
4882.7+x	196.3 *2*	23 *3*	[E2]		0.626	
	315.6 *2*	100 *4*				
	329.5 *2*	12 *3*				
5372.7+x	490.1 *2*	100 *3*	D			
	805.7 *2*	47.6 *16*	(Q)			
5608.6+x	725.9 *2*	100				
5608.7+x	236.0 *2*	100	E2		0.328	B(E2)(W.u.)=4.6 *4*.
6033.5+x	424.8 *2*	100				
6076.4+x	467.7 *2*	100				
6283.2+x	249.7 *2*	100				

^{215}Ac ε Decay (0.17 s) 1968Va04

Parent ^{215}Ac: E=0.0; Jπ=9/2−; $T_{1/2}$=0.17 s *1*; Q(g.s.)=3497 *15*; %ε+%$β^+$ decay=0.09 *2*.
^{215}Ac–J,$T_{1/2}$: From ^{215}Ac Adopted Levels.
^{215}Ac–Q(ε): From 2012Wa38.
^{215}Ac–%ε+%$β^+$ decay: %ε+%$β^+$=0.09 *2* (1968Va04).
1968Va04: ε+$β^+$ branching ratio obtained by observing the presence of an 8.70 MeV *2* α group assigned to α decay of ^{215}Ra. ^{215}Ra as daughter of ^{215}Ac formed in ^{203}Tl(^{16}O,4n)^{215}Ac reaction.

^{215}Ra Levels

E(level)	Jπ	Comments
0.0	(9/2+)	Assumed that g.s. is populated in ε decay of ^{215}Ac.

^{219}Th α Decay (1.05 μs) 1973Ha32

Parent ^{219}Th: E=0.0; Jπ=(9/2+); $T_{1/2}$=1.05 μs *3*; Q(g.s.)=9510 *50*; %α decay=100.
^{219}Th–J,$T_{1/2}$: From Adopted Levels of ^{219}Th in ENSDF database.
^{219}Th–Q(α): From 2012Wa38.
^{219}Th activity was produced by ^{206}Pb(^{16}O,3n), E=80–90 MeV. Isotopic assignment is based on its genetic relationship to ^{215}Ra, and on measured excitation functions. Measured Eα. Detector: semi.

^{215}Ra Levels

E(level)	Jπ	$T_{1/2}$	Comments
0.0	(9/2+)	1.66 ms *2*	Jπ,$T_{1/2}$: from Adopted Levels.

α radiations

Eα	E(level)	Iα‡	HF†
9340 *20*	0.0	100	2.0 *2*

† Using r_0(^{215}Ra)=1.560 *9*, interpolated value deduced from r_0(^{214}Ra)=1.554 *9* and r_0(^{216}Ra)=1.566 *9* (1998Ak04).
‡ Absolute intensity per 100 decays.

^{206}Pb(^{13}C,4nγ) 1998St24

Includes reactions: ^{206}Pb(^{12}C,3nγ); ^{208}Pb(^{12}C,5nγ); and ^{208}Pb(^{13}C,6nγ).
1998St24: target: 92% enriched ^{206}Pb. E=78 MeV. Measured Eγ, Iγ, γγ coin, γγ(t), γγ(θ), ce, differential perturbed angular distributions, excitation functions for E=66–84 MeV. Deduced γ–ray multipolarities, angular distribution coefficients, levels half–life (pulsed–beam measurements), gyromagnetic factors, detectors: hyperpure Ge, superconducting solenoidal electron spectrometer with a cooled Si(Li) detector (1998St24). See 1989Dr02 from the same group for measurement of lifetime of 773–keV level and E3 multipolarity of 773γ by ce measurements using ^{208}Pb(^{12}C,5nγ), E=80 MeV; and ^{206}Pb(^{13}C, 4nγ), E=78 MeV reactions.
2004He25: ^{208}Pb(^{12}C,5nγ): measured Eγ, half–life of 1878–keV isomer.
1988Fu10: ^{206}Pb(^{12}C,3nγ), E=67 MeV, ≥90% enriched ^{206}Pb target. Measured Eγ, Iγ, γγ coin, γ(θ) for 9 angles between θ=80° and 160°, γ–ray linear polarization, γγ(t). Deduced transition multipolarities. Measured levels half–life using a pulsed beam method, and also γγ(t). Eγ, Iγ data reported for eight γ rays; γ(θ) and γ(lin pol) for four of these.
1987AdZU: ^{206}Pb(^{13}C,4nγ), E=80 MeV. Measured Eγ, γγ coin, γγ(t). Measured levels half–life, Measured g–factor by stroboscopic observation of γ–ray perturbed angular distributions. A detailed level scheme reported with 24 γ transitions and 20 excited states.
1983Lo16: ^{208}Pb(^{13}C,6nγ), E=95 MeV, 99% enriched ^{208}Pb target. Measured Eγ, Iγ, γ(θ) for 8 angles between 60° and 158°, γγ coin, γ(θ), γγ(t). Deduced transition multipolarities. Measured level half–life using a pulsed beam method. Data reported for three γ rays in a cascade: 196, 772 and 850 keV.
The nucleus of ^{215}Ra has six valence protons and a single valence neutron outside the Z=82, N=126 closed shells. Most of the states up to about 6 MeV have configurations involving four to six protons in the $h_{9/2}$ orbital, for which E2 decays are retarded or forbidden, and dipole and octupole transitions are prominent. The authors have explained the strength of E3 transitions as well as the measured gyromagnetic factors in terms of the multi–particle octupole coupling mechanism (1998St24).

Continued on next page (footnotes at end of table)

^{206}Pb(^{13}C,4nγ) 1998St24 (continued)

2013Ba29: measured experimental isomer production ratio in ^{9}Be(^{238}U,X) reaction at E=1 GeV/nucleon (2013Ba29) using the FRS, RISING gamma detector array, and TOF arrangement at GSI facility.

^{215}Ra Levels

The level scheme presented here is from 1998St24. First level scheme for ^{215}Ra was proposed by 1983Lo16 with four excited states and 195–851–772 γ cascade depopulated from a (25/2), μs isomer at an unknown energy slightly above this cascade. 1988Fu10 confirmed this cascade and an isomer of 7.2 μs above this cascade, they added another transition in the level scheme at 1048 keV parallel to 195-keV transition. Four weaker γ rays were unplaced in this work. A more extensive level scheme was proposed in annual laboratory reports (1987AdZU,1986AdZV) with 20 levels up to 5.6 MeV and 24 gamma rays. However, no other details were provided in this study. Except for some differences in placement of γ rays, most features of the level scheme and gamma-ray energies in 1987AdZU have been confirmed by 1998St24.

E(level)[†]	Jπ[‡]	$T_{1/2}$[§]	Comments
0.0[#]	9/2+	1.66 ms *2*	$T_{1/2}$: from Adopted Levels.
773.0[@] *2*	15/2−	67.2 ns *14*	$T_{1/2}$: from γγ(t) (1998St24; also 68.6 ns *21* in 1989Dr02). Others: 77 ns *2* (1988Fu10), 67 ns *3* (1987AdZU). Value from 1988Fu10 is considered by the evaluators as discrepant. From pulsed-beam method, values are 110 ns *8* (1989Dr02), 120 ns *10* (1983Lo16). The higher values in pulsed-beam experiments are likely due to much longer half-life (7.3 μs) of the 1877 level, which will affect the observed decay rate of 773γ, thus making it more difficult to measure lifetime in the ns range with this method.
1625.3[#] *3*	17/2+		
1821.2[#] *3*	21/2+	25.0 ns *14*	$T_{1/2}$: other: 23 ns *5* (1983Lo16).
1877.8[&] *3*	25/2+	7.29 μs *20*	$T_{1/2}$: weighted average of 7.6 μs *2* (2004He25), 6.86 μs *28* (1998St24), 7.2 μs *2* (1988Fu10). Other: ≥2 μs (1983Lo16). Mixed with 2053.8 level by particle octupole coupling.
1994.5[&] *3*	23/2+		
2053.8[#] *4*	25/2+		Mixed with 1877.8 level by particle octupole coupling.
2214.4[a] *4*	27/2(−)		
2246.9[b] *4*	29/2−	1.39 μs *7*	
2246.9+x[b]	31/2−		E(level): x ≤35 keV.
3088.8+x[c] *2*	33/2+		
3143.7+x[d] *3*	35/2+		
3331.1+x[d] *4*	37/2+		
3413.4+x[b] *4*	37/2−		
3415.6+x[d] *4*	37/2+		
3586.4+x[e] *4*	37/2+		
3738.6+x[b] *4*	39/2−		
3756.6+x[b] *4*	43/2−	555 ns *10*	g=+0.726 *3* (1998St24). $T_{1/2}$: other: 0.59 μs *18* (1987AdZU). Octupole-mixed state. g: TDPAD method (1998St24). Other measurement: +0.734 *7* (1987AdZU, stroboscopic observation of perturbed angular distribution). Theoretical value=+0.73 (1998St24). Measured isomer yield ratio: R_{exp}=7.9 *8* (2013Ba29) in ^{9}Be(^{238}U,X) reaction at 1 GeV/nucleon, where $R_{exp}=Y/(N_{imp}FG)$, N_{imp} is number of implanted ions, Y is the isomeric yield, F and G are correction factors for in-flight isomer decay losses and the finite detection time of the γ radiation, respectively. Comparison of measured yield ratios with theoretical values calculated by using ABRABLA Monte-Carlo code.
3765.7+x *4*			
3855.0+x *4*			
3935.4+x[a] *4*	43/2−		Octupole-mixed state.
4207.3+x *5*			
4366.8+x[c] *4*	45/2+		
4553.5+x[b] *4*	47/2−		
4567.0+x[c] *4*	49/2+	10.47 ns *14*	g=+0.77 *1* (1998St24). $T_{1/2}$: other: ≈10 ns (1987AdZU). g: TDPAD method. Theoretical value=+0.80 (1998St24).
4686.2+x[a] *5*	47/2−		
4882.7+x[a] *4*	51/2−		
5372.7+x[c] *5*	53/2+		
5608.6+x[f] *5*	55/2−		
5608.7+x[c] *5*	57/2+	1.66 ns *14*	
6033.5+x[g] *5*	(57/2+)		
6076.4+x[g] *5*	(59/2+)		

Continued on next page (footnotes at end of table)

^{206}Pb(^{13}C,4nγ) 1998St24 (continued)

^{215}Ra Levels (continued)

E(level)[†]	Jπ[‡]
6283.2+x[g] *6*	(61/2+)

[†] From a least–squares fit to Eγ values from 1998St24.
[‡] As proposed by 1998St24, based on γ–ray multipolarities, angular distributions, transition strengths, and excitation functions. These assignments are the same in Adopted Levels, except that all are placed in parentheses since Jπ assignment for the ground state is still tentative. Shell model configurations (1998St24) are based on level energies and γ–transition rates.
[§] From pulsed beam method (1998St24), unless otherwise stated. Values from previous measurements are given under comments.
[#] Member of configuration=$\pi h_{9/2}{}^{6}\otimes\nu g_{9/2}$.
[@] Member of configuration=$\pi h_{9/2}{}^{6}\otimes\nu j_{15/2}$.
[&] Member of configuration=$\pi h_{9/2}{}^{5}\otimes\pi f_{7/2}\otimes\nu g_{9/2}$.
[a] Member of configuration=$\pi h_{9/2}{}^{4}\otimes\pi f_{7/2}\otimes\pi i_{13/2}\otimes\ \nu_{9/2}$.
[b] Member of configuration=$\pi h_{9/2}{}^{5}\otimes\pi i_{13/2}\otimes\nu g_{9/2}$.
[c] Member of configuration=$\pi h_{9/2}{}^{4}\otimes\pi i_{13/2}{}^{2}\otimes\nu g_{9/2}$.
[d] Member of configuration=$\pi h_{9/2}{}^{5}\otimes\pi f_{7/2}\otimes\nu g_{9/2}$.
[e] Member of configuration=$\pi h_{9/2}{}^{4}\otimes\pi f_{7/2}{}^{2}\otimes\nu g_{9/2}$.
[f] Member of configuration=$\pi h_{9/2}{}^{3}\otimes\pi f_{7/2}{}^{2}\otimes\ \pi i_{13/2}\otimes\nu g_{9/2}$.
[g] Member of configuration=$\pi h_{9/2}{}^{3}\otimes\pi f_{7/2}\otimes\ \pi i_{13/2}{}^{2}\otimes\nu g_{9/2}$.

γ(^{215}Ra)

All γ–ray data are from 1998St24, unless otherwise stated.

Eγ[†]	E(level)	Iγ[†]	Mult.[#]	δ[@]	α	Comments
x	2246.9+x					Eγ: no transition seen, but required for current level scheme. Estimated value of x ≤ 35 keV.
(13.5[§])	4567.0+x	0.57 *3*	[E1]		5.74	Iγ: from Iγ(13.5)/Iγ(200)=6.4 *3*/61 *1* (1998St24).
(18.0[§])	3756.6+x	0.0020 *2*	[E2]		25400	Iγ: from Iγ(18.0)/Iγ(425)=0.029 *2*/99.97 (1998St24).
(32.5[§] *6*)	2246.9	0.059 *1*	[M1]		84 *5*	Iγ: from Iγ(32.5)/Iγ(193)=0.79 *1*/79.2 *2* (1998St24).
54.9 *2*	3143.7+x	2.1 *2*	M1		17.9 *4*	α(exp)=11 *4*.
56.5 *2*	1877.8	0.8[‡] *1*	E2		145 *4*	α(exp)=94 *40*.
59.3 *2*	2053.8	1.6 *2*	M1		14.25 *25*	α(exp)=15 *7*.
152.2 *2*	3738.6+x	9.4 *1*	E1		0.1740	α(exp)<0.42; A_2=–0.12 *4*.
170.8 *2*	3586.4+x	1.0 *2*	M1		3.41	α(exp)=5.2 *33*.
173.3 *2*	1994.5	3.9 *1*	M1		3.27	Iγ: 2 *1* (1988Fu10) in ^{206}Pb(^{12}C,3nγ), E=67 MeV. α(exp)=3.6 *14*; A_2=+0.03 *6*.
176.0 *2*	2053.8	9.9 *2*	M1		3.13	Iγ: 5 *2* (1988Fu10) in ^{206}Pb(^{12}C,3nγ), E=67 MeV. α(exp)=5.0 *5*; α(L)exp=0.40 *3*; A_2=+0.16 *4*.
178.6 *2*	3935.4+x	1.6 *2*	M1		3.01	α(exp)=3.6 *3*; A_2=+0.38 *34*.
187.4 *2*	3331.1+x	9.8 *2*	M1		2.63	α(exp)=2.7 *7*.
193.1 *2*	2246.9	5.9 *1*	M2(+E3)	<0.2	10.99	δ: ce data gives δ(E3/M2)<0.45, but RUL(E3)=100 gives δ<0.2. α(exp)=9.1 *6*; α(L)exp=3 *1*; α(M)exp=0.63 *6*; A_2=+0.13 *6*.
196.0 *2*	1821.2	46.7[‡] *3*	E2		0.629	Iγ: 42 *12* (1988Fu10) in ^{206}Pb(^{12}C,3nγ), E=67 MeV; 30 *3* (1983Lo16) in ^{208}Pb(^{13}C,6nγ), E=95 MeV. α(exp)=0.56 *3*; α(L)exp=0.201 *11*; α(M)exp=0.084 *5*; A_2=+0.09 *1*. A_2=+0.070 *13*; A_4=–0.002 *21* (1988Fu10). POL=–0.08 *7* (1988Fu10). A_2=+0.22 *6*; A_4=–0.12 *5* (1983Lo16).
196.3 *2*	4882.7+x	2.8[‡] *4*	[E2]		0.626	
200.1 *2*	4567.0+x	5.4 *1*	(E2)		0.584	A_2=+0.29 *4*.
236.0 *2*	5608.7+x	5.5 *1*	E2		0.328	α(exp)<0.70; A_2=+0.36 *6*.
249.7 *2*	6283.2+x	1.3 *4*				
255.4 *2*	3586.4+x	5.2[‡] *6*	M1		1.106	α(exp)=1.6 *7*; A_2=+0.33 *12*.

Continued on next page (footnotes at end of table)

$^{206}Pb(^{13}C,4n\gamma)$ 1998St24 (continued)

$\gamma(^{215}Ra)$ (continued)

Eγ†	E(level)	Iγ†	Mult.#	δ@	α	Comments
269.7 *2*	3413.4+x	9.8 *1*	D			Iγ: 5 *2* (1988Fu10) in $^{206}Pb(^{12}C,3n\gamma)$, E=67 MeV. A_2=−0.20 *3*.
271.9 *2*	3415.6+x	4.2 *2*	M1		0.930	α(exp)=1.4 *4*; A_2=−0.06 *5*.
315.6 *2*	4882.7+x	12.0‡ *5*				
323.1 *2*	3738.6+x	6.2 *2*	E1		0.0298	α(exp)<0.48; A_2=−0.15 *9*.
325.3 *2*	3738.6+x	0.8 *2*				
329.5 *2*	4882.7+x	1.4 *3*				
336.6 *2*	2214.4	4.2 *2*	(E1)		0.0272	α(K)exp<0.27.
352.3 *2*	4207.3+x	1.0‡ *2*				
369.1 *2*	2246.9	1.9 *2*	M2+E3	1.07 *+25−20*	0.81 *9*	α(K)exp=0.51 *6*; α(L)exp=0.19 *3*; α(M)exp=0.08 *2*.
407.4 *2*	3738.6+x	20.2 *2*	E1		0.0180	α(K)exp=0.024 *5*; A_2=−0.11 *2*.
424.8 *2*	6033.5+x	1.8‡ *4*				
425.5 *2*	3756.6+x	6.9 *2*	E3		0.240	α(K)exp=0.126 *14*; α(L)exp=0.08 *1*; α(M)exp=0.04 *1*; A_2=+0.20 *8*.
431.5 *2*	4366.8+x	7.9 *2*	E1		0.01597	α(exp)<0.07; A_2=−0.20 *5*.
434.6 *2*	3765.7+x	1.3‡ *2*				
439.4 *2*	3855.0+x	1.4‡ *2*				
442.6 *2*	3586.4+x	0.5‡ *2*				
467.7 *2*	6076.4+x	1.0 *2*				
490.1 *2*	5372.7+x	6.3 *2*	D			A_2=−0.30 *6*.
610.2 *2*	4366.8+x	8.0 *4*				
725.9 *2*	5608.6+x	2.3‡ *4*				
750.7 *2*	4686.2+x	2.2 *1*	(Q)			A_2=+0.25 *12*.
773.0 *2*	773.0	100.0	E3		0.0404	α(K)exp=0.0239 *7*; α(L)exp=0.0091 *3*; α(M)exp=0.0028 *2*; A_2=+0.12 *2*. A_2=+0.227 *10*; A_4=+0.002 *16* (1988Fu10). POL=−0.13 *1* (1988Fu10). A_2=+0.35 *13*; A_4=−0.26 *22* (1983Lo16).
797.3 *2*	4553.5+x	8.3 *2*	(Q)			A_2=+0.39 *6*.
805.7 *2*	5372.7+x	3.0 *1*	(Q)			A_2=+0.20 *10*.
810.2 *2*	4567.0+x	3.2 *1*	(E3)		0.0359	A_2=+0.74 *9*.
841.9 *2*	3088.8+x	55.4 *4*	E1		0.00435	Iγ: 18 *2* (1988Fu10) in $^{206}Pb(^{12}C,3n\gamma)$, E=67 MeV. α(K)exp<0.013; A_2=−0.21 *1*.
852.3 *2*	1625.3	74.2 *5*	E1		0.00425	Iγ: 64 *3* (1988Fu10) in $^{206}Pb(^{12}C,3n\gamma)$, E=67 MeV; 86 *9* (1983Lo16) in $^{208}Pb(^{13}C,6n\gamma)$, E=95 MeV. α(K)exp=0.0046 *4*; α(L)exp=0.0010 *2*; α(M)exp=0.00016 *11*; A_2=−0.09 *1*. A_2=−0.092 *13*; A_4=+0.001 *21* (1988Fu10). A_2=−0.18 *2*; A_4=−0.05 *3* (1983Lo16). POL=−0.04 *2* (1988Fu10).
1048.2 *2*	1821.2	22.7 *2*	E3		0.0195	Iγ: 18 *2* (1988Fu10) in $^{206}Pb(^{12}C,3n\gamma)$, E=67 MeV. α(K)exp=0.0127 *7*; α(L)exp=0.0059 *5*; α(M)exp=0.0037 *10*; A_2=+0.06 *2*. A_2=+0.13 *4*; A_4=+0.05 *7* (1988Fu10). POL=−0.04 *5* (1988Fu10).

† From $^{206}Pb(^{13}C,4n\gamma)$ (1998St24). Energy uncertainty of 0.2 keV is assigned based on e-mail reply of Nov. 22, 2012 from T. Kibedi (in consultation with A.E. Stuchbery).
‡ From γγ coin data. Transition is weak or contaminated in singles data (1998St24).
§ Transition implied by γγ coin data (1998St24). The transition energy is from level-energy difference.
# From ce, γ(θ) and linear polarization data.
@ Deduced by the evaluators from ce data in 1998St24.

$^{206}Pb(^{13}C,4n\gamma)$ 1998St24 (continued)

Level Scheme

Intensities: relative Iγ

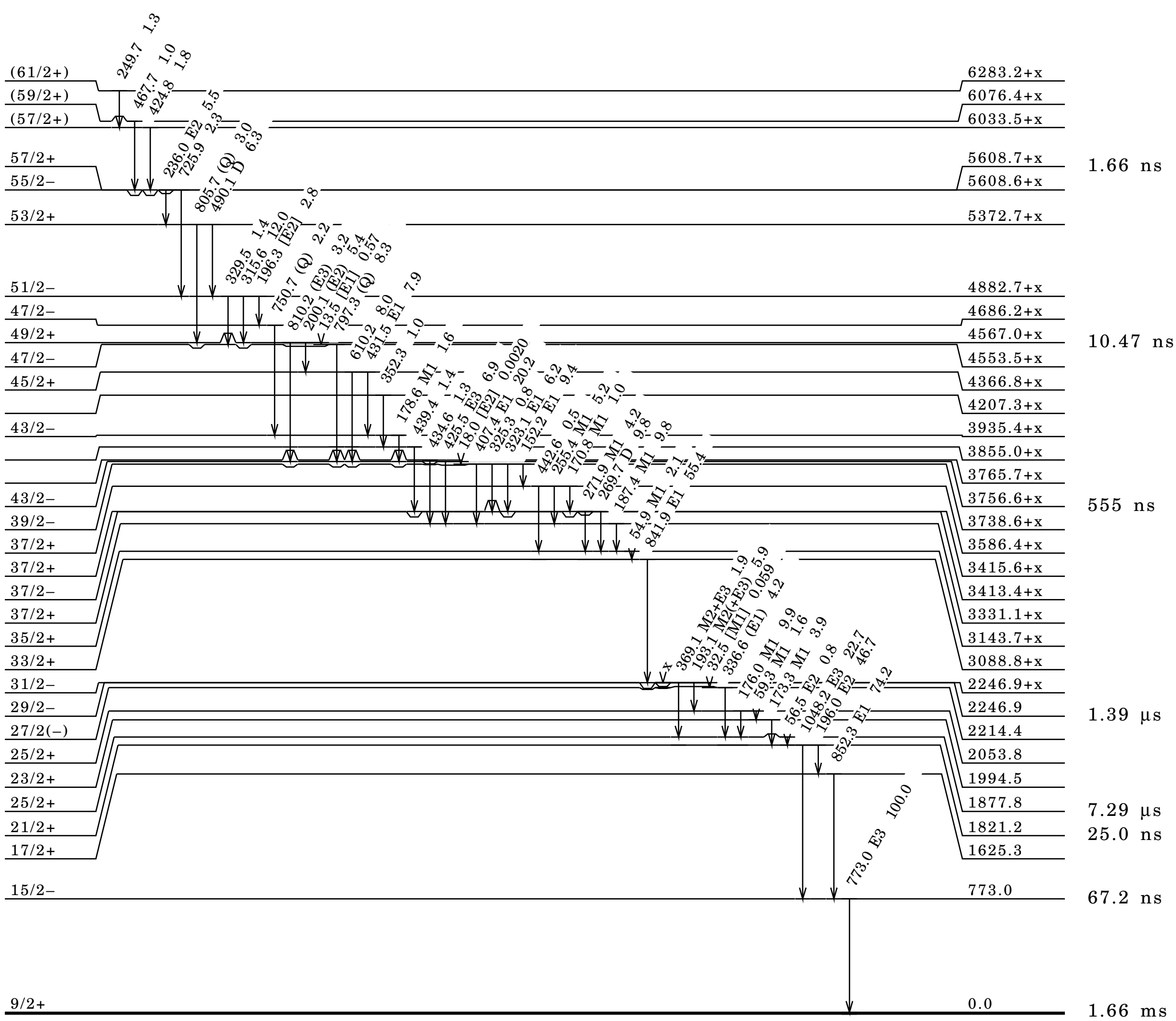

$^{215}_{88}Ra_{127}$

Adopted Levels, Gammas

Q(β⁻)=–4891 *15*; S(n)=8485 *20*; S(p)=1351 *13*; Q(α)=7746 *3* 2012Wa38.
S(2n)=16270 *50*, S(2p)=4994 *13* (2012Wa38).

^{215}Ac evaluated by A.K. Jain, S. Singh, B. Singh, N. Kaur, S. Lakshami, B. Maheshwari.

States in ^{215}Ac have been interpreted in terms of the shell model configurations $h_{9/2}$, $f_{7/2}$, and $i_{13/2}$ available for the seven protons beyond closed shell (Z=82) (1983De08).

2003Ca21: large–scale shell model calculations were performed for ^{215}Ac employing the computer code NATHAN with using modified Kuo–Herling interaction. Additional low–lying levels are predicted in these calculations which have not been observed experimentally.

2013Ba29: measured experimental isomer production ratio in ^{9}Be(^{238}U,X) reaction at E=1 GeV/nucleon (2013Ba29) using the FRS, RISING gamma detector array, and TOF arrangement at GSI facility.

^{215}Ac Levels

Cross Reference (XREF) Flags

A ^{219}Pa α Decay (53 ns)
B ^{204}Pb(^{15}N,4nγ)

E(level)†	Jπ‡	XREF	$T_{1/2}$§	Comments
0.0	9/2–	AB	0.17 s *1*	%α=99.91 *2*; %ε+%β⁺=0.09 *2* (1968Va04). %ε+%β⁺: from observation of an 8.70 MeV *2* α group assigned to ^{215}Ra (1968Va04). $T_{1/2}$: from 1968Va04. Jπ: favored α decay (HF=1.3) to ^{211}Fr (Jπ=9/2–).
1317.0 *5*	(13/2–)	B		Configuration=$\pi 1h_{9/2}{}^{7}$.
1621.0 *7*	(17/2–)	B	30 ns *10*	μ=7.82 *16* (1983De08,1989Ra17). μ: 7.74 *9* from g factor=0.910 *10* (TDPAD,1983De08). 1989Ra17 (also 2011StZZ) compilation lists 7.82 *16*. It appears that 1989Ra17 applied upward correction of 1% and doubled the uncertainty, probably based on estimated diamagnetism and Knight shift of 0±1% by 1983De08. Configuration=$\pi 1h_{9/2}{}^{7}$.
1796.0# *9*	(21/2–)	B	185 ns *30*	μ=9.66 *20* (1983De08,1989Ra17). Configuration=$\pi 1h_{9/2}{}^{7}$. μ: 9.56 *11* from g factor=0.910 *10* (TDPAD,1983De08). 1989Ra17 (also 2011StZZ) compilation lists 9.66 *20*. It appears that 1989Ra17 applied upward correction of 1% and doubled the uncertainty, probably based on estimated diamagnetism and Knight shift of 0±1% by 1983De08.
1796.0+x	(23/2–)	B		E(level): x=50 *50*, extrapolated from Eγ=511 keV in ^{211}At, and Eγ=265 keV in ^{213}Fr. Configuration=$\pi 1h_{9/2}{}^{6}\otimes\pi 2f_{7/2}{}^{1}$.
2438+x#	(29/2+)	B	335 ns *10*	μ=15.13 *30* (1983De08,1989Ra17). Jπ: B(E3)(W.u.)=24.7 *9* is similar to that of the corresponding E3 transition in ^{213}Fr, and typical of fast E3 transitions in this region. The strength enhancement of such transitions is due to the coupling with octupole vibrations in the even core nucleus. μ: 14.98 *15* from g factor=1.033 *10* (TDPAD,1983De08). 1989Ra17 (also 2011StZZ) compilation lists 15.13 *30*. It appears that 1989Ra17 applied upward correction of 1% and doubled the uncertainty, probably based on estimated diamagnetism and Knight shift of 0±1% by 1983De08. Configuration=$\pi 1h_{9/2}{}^{6}\otimes\pi 1i_{13/2}{}^{1}$.

† From γ–ray energies.
‡ Assignments are based on γ(θ) data, the analogy with the corresponding levels in the N=126 isotones ^{211}At and ^{213}Fr, and also on the agreement of experimental g–factors with shell–model predictions (*i.e.* constant values for $h_{9/2}$ states).
§ From γ(t) in ^{204}Pb(^{15}N,4nγ).
\# Measured isomer yield ratio: R_{exp}=20 *4* for 1796, 21/2– level and 20 *5* for 2438+x, (29/2+) level (2013Ba29) in ^{9}Be(^{238}U,X) reaction at 1 GeV/nucleon, where $R_{exp}=Y/(N_{imp}FG)$, N_{imp} is number of implanted ions, Y is the isomeric yield, F and G are correction factors for in–flight isomer decay losses and the finite detection time of the γ radiation, respectively. Comparison of measured yield ratios with theoretical values calculated by using ABRABLA Monte–Carlo code.

Adopted Levels, Gammas (continued)

γ(^{215}Ac)

E(level)	Eγ†	Iγ†	Mult.‡	α	Comments
1317.0	1317.0 *5*	100	(E2)	0.00567	
1621.0	304.0 *5*	100	(E2)	0.1538	B(E2)(W.u.)=0.08 *3*.
1796.0	175.0 *5*	100	(E2)	1.021 *19*	B(E2)(W.u.)=0.119 *20*.
1796.0+x	x				Eγ: x=50 *50* (1983De08).
2438+x	642.0 *5*	100	(E3)	0.0702	B(E3)(W.u.)=27.4 *9*.

† From ^{204}Pb(^{15}N,4nγ).
‡ From γ(θ), and comparison with the corresponding transitions in N=126 isotones ^{211}At and ^{213}Fr. All multipolarities are assumed as stretched.

^{219}Pa α Decay (53 ns) 1987FaZS

Parent ^{219}Pa: E=0.0; Jπ=9/2–; $T_{1/2}$=53 ns *10*; Q(g.s.)=10080 *50*; %α decay≈100.
^{219}Pa–J,$T_{1/2}$: From ^{219}Pa Adopted Levels in ENSDF database.
^{219}Pa–E: Assumed as the g.s. In ^{219}Pa Adopted Levels in ENSDF database, value is listed as 0+x.
^{219}Pa–Q(α): From 2012Wa38.
1987FaZS: ^{219}Pa was produced by ^{204}Pb(^{19}F,4n), E=100 MeV. Assignment of this activity to ^{219}Pa is based on excitation functions, and on the systematics of α–particle energies and half–lives for other protactinium isotopes. Measured Eα. Detector: annular system of gas detectors.
2001Ni06: production of ^{219}Pa in Ce(^{82}Se,X), E(c.m.)=215–253 MeV; measured cross section.
2005Li17: production of ^{219}Pa in Be(^{238}U,X), E=1 GeV/nucleon; measured cross section.

^{215}Ac Levels

E(level)	Jπ	$T_{1/2}$	Comments
0.0	9/2–	0.17 s *1*	Jπ,$T_{1/2}$: From Adopted Levels.

α radiations

Eα	E(level)	Iα‡	HF†
9900 *50*	0.0	100	≈1.0

† Using r_0(^{215}Ac)≈1.54, interpolated value from r_0(^{214}Ra)=1.554 *9*, and r_0(^{216}Th)≈1.52 (1998Ak04).
‡ For α intensity per 100 decays, multiply by ≈1.00.

^{204}Pb(^{15}N,4nγ) 1983De08

1983De08: target: 99.7% enriched ^{204}Pb, E(^{15}N)=84 MeV. Measured Eγ, Iγ, γγ coin. Measured γ–ray differential perturbed angular distributions (TDPAD), level half–lives, and g–factors. Measured γ rays in coincidence with delayed α particles. Deduced transition multipolarities.
Others:
2006Po01: measured yield of 330–ns isomer of ^{215}Ac in ^{9}Be(^{238}U,X) reaction at E=900 MeV/nucleon. Experiment performed at GSI facility using the FRS fragment separator. Measured experimental ratio (R_{exp})=4.8 *12*, where R_{exp}=Y/(N_{imp}FG), where N_{imp} is number of implanted ions, Y is the isomeric yield, F and G are correction factors for in–flight isomer decay losses and the finite detection time of the γ radiation, respectively. Comparison of measured yields with theoretical yields calculated by ABRABLA Monte–Carlo code. Using similar experimental arrangement, 2013Ba29 measured R_{exp})=20 *4* for (29/2+) isomer at 2438+x, and 20 *5* for 21/2– isomer at 1796 keV.
2005Li17: measured yield of ^{215}Ac in ^{9}Be(^{238}U,X) reaction at E=1 GeV/nucleon. Experiment performed at GSI facility using the FRS fragment separator.
2000He17: observed γα coincidences from ^{215}Ac at GSI facility by using UNILAC accelerator beams of ^{51}V, ^{50}Ti, ^{22}Ne, and ^{12}C with targets of ^{170}Er, ^{208}Pb, and ^{209}Bi.

^{204}Pb(^{15}N,4nγ) 1983De08 (continued)

^{215}Ac Levels

The g–factors given from 1983De08 are uncorrected for diamagnetism and Knight shift. From similar systems, the authors estimate this correction as 0±1%.

E(level)†	Jπ‡	$T_{1/2}$§	Comments
0.0	9/2–		
1317.0 *5*	13/2–		
1621.0 *7*	17/2–	30 ns *10*	g=0.910 *10* (1983De08).
1796.0# *9*	21/2–	185 ns *30*	g=0.910 *10* (1983De08).
1796.0+x	(23/2–)		E(level): x=50 *50*, extrapolated from Eγ=511 keV in ^{211}At, and Eγ=265 keV in ^{213}Fr.
2438+x#	(29/2+)	335 ns *10*	g=1.033 *10* (1983De08).

† From γ-ray energies; x=50 keV *50*, extrapolated from Eγ=511 keV in ^{211}At, and Eγ=265 keV in ^{213}Fr.
‡ From 1983De08.
§ From γ(t) (1983De08) unless otherwise noted.
\# Measured isomer yield ratio: R_{exp}=20 *4* for 1796, 21/2– level and 20 *5* for 2438+x, (29/2+) level (2013Ba29) in ^{9}Be(^{238}U,X) reaction at 1 GeV/nucleon, where R_{exp}=Y/(N_{imp}FG), N_{imp} is number of implanted ions, Y is the isomeric yield, F and G are correction factors for in–flight isomer decay losses and the finite detection time of the γ radiation, respectively. Comparison of measured yield ratios with theoretical values calculated by using ABRABLA Monte–Carlo code.

γ(^{215}Ac)

The assignment of γ rays to ^{215}Ac was based on the measurement of coincident Ac x rays, of delayed α particles (from ^{215}Ac and ^{216}Ac, with a ratio of 2:1), and on the level systematics of analogous levels in the lighter isotones ^{211}At and ^{213}Fr.

Eγ	E(level)	Mult.†	α	Comments
x	1796.0+x			Eγ: x=50 *50* (1983De08).
175.0 *5*	1796.0	(E2)	1.021 *19*	A_2=+0.31 *10*.
304.0 *5*	1621.0	(E2)	0.1538	A_2=+0.33 *10*.
642.0 *5*	2438+x	(E3)	0.0702	A_2=+0.52 *3*.
1317.0 *5*	1317.0	(E2)	0.00567	A_2=+0.31 *10*.

† From γ(θ), and comparison with the corresponding transitions in ^{211}At and ^{213}Fr. All multipolarities are assumed as stretched.

Level Scheme

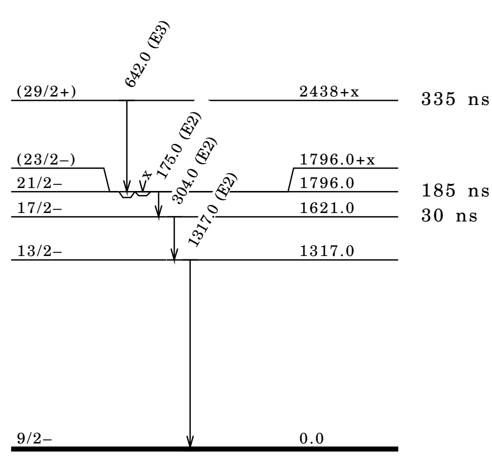

$^{215}_{89}Ac_{126}$

Adopted Levels, Gammas

Q(β⁻)=−6950 *70*; S(n)=7862 *18*; S(p)=2812 *18*; Q(α)=7665 *4* 2012Wa38.
S(2n)=17340 *70*, S(2p)=4014 *22*, Q(εp)=3540 *10* (2012Wa38).

^{215}Th evaluated by B. Singh.

1968Va18: activity was produced by ^{206}Pb(^{16}O,7n), E=90–160 MeV, and identified by excitation functions, genetic relationship to daughter nuclei, and agreement with α–particle energy decay systematics.
2000He17: activity was produced by ^{170}Er(^{51}V,p5n), E=214–286 MeV, and separated from the beam with a velocity filter. The activity was identified by excitation functions, and by its genetic relationship to daughter nuclei. Measured Eα, αγ coin. Detectors: Ge, Si.
2007Le14: ^{215}Th produced in ^{182}W(^{40}Ar,X), E=191,197 MeV at JYFL, Jyvaskyla facility, RITU separator, GREAT spectrometer for particle detection. Measured α–particle spectrum and half–life.

^{215}Th Levels

Cross Reference (XREF) Flags

A ^{219}U α Decay (42 μs)
B ^{170}Er(^{50}Ti,5nγ)

E(level)	Jπ	XREF	$T_{1/2}$	Comments
0.0	(1/2−)	AB	1.2 s *2*	%α=100. No ε decay observed (<1.5% in 1968Va18). $T_{1/2}$: from 1968Va18. Other: 0.63 s *+126−21* (2007Le14). Jπ: from α–decay systematics of N=125, Jπ=1/2− isotones ^{209}Po, ^{211}Rn, and ^{213}Ra. These nuclei strongly populate a 5/2− g.s., and, 1/2− and 3/2− excited states. The hindrance factors for ^{215}Th α decay are: 7.0 (5/2−), 2.0 (1/2−), and 7.8 (3/2−), using r_0(^{211}Ra)=1.479, from adjacent even–even nuclei. Expected shell–model configuration=$\pi p_{1/2}$.
560.8 *2*	(5/2−)	B		Jπ: from systematics of neighboring nuclides (2005Ku31).
1421.3† *3*	†	B		
1421.3+x?†	†	B	0.77 μs *6*	%IT≈100. $T_{1/2}$: from γ(t) (2005Ku31) in ^{170}Er(^{50}Ti,5nγ).

† From comparison of energies and half–lives of 9/2− isomers in neighboring nuclei, 9/2− is ruled out. Two possibilities have been discussed by 2005Ku31: 860.5γ may be E3 transition from 11/2+ to 1/2−, which gives half–life consistent with Weisskopf estimates; or there is a level above 1421.3 keV from which a low–energy highly converted transition is omitted. 2005Ku31 could not rule out any of these two possibilities.

γ(^{215}Th)

E(level)	Eγ
560.8	560.8 *2*
1421.3	860.5 *2*
1421.3+x?	x

^{219}U α Decay (42 μs) 1993An07,1994Ye08

Parent ^{219}U: E=0.0; Jπ=(9/2+); $T_{1/2}$=42 μs *+34−13*; Q(g.s.)=9940 *50*; %α decay=100.
^{219}U–$T_{1/2}$: From ^{219}U Adopted Levels. Other: 0.08 s *10−3* (2007Le14).
^{219}U–J: Proposed by 2007Le14 based on hindered α decays in N=127 isotones.
^{219}U–Q(α): From 2012Wa38.
1993An07: ^{219}U produced and identified in ^{197}Au(^{27}Al,X), reaction at E=5.5 MeV/nucleon; measured Eα, Iα, αα–correlation; deduced half–life, Q value for α decay.
2007Le14 (also 2005Le42): ^{219}U produced in ^{182}W(^{40}Ar,X), E=191,197 MeV at JYFL, Jyvaskyla facility, RITU separator, GREAT spectrometer for particle detection. Measured α–particle spectrum and half–life.
No HF deduced since r_0 parameter for ^{216}Th is not known.

^{219}U α Decay (42 μs) 1993An07,1994Ye08 (continued)

^{215}Th Levels

E(level)	Jπ	$T_{1/2}$	Comments
0.0	(1/2−)	1.2 s *2*	Jπ,$T_{1/2}$: from Adopted levels.

α radiations

Eα	E(level)	Iα†	Comments
9774 *18*	0.0	100	Eα: from 2007Le14. Other: 9680 *40* (1993An07).

† Absolute intensity per 100 decays.

^{170}Er(^{50}Ti,5nγ) 2005Ku31

2005Ku31: E=4.35 MeV/nucleon. ^{215}Th recoils were separated from the beam using a velocity filter SHIP at GSI facility and implanted into a position–sensitive 16–strip PIPS semiconductor detector. Measured Eγ, Iγ, (recoil)–γ–α–γ correlations and coincidences using Clover Ge detector for γ rays.

^{215}Th Levels

E(level)	Jπ	$T_{1/2}$	Comments
0.0	(1/2−)		
560.8 *2*	(5/2−)		Jπ: from systematics of neighboring nuclides.
1421.3† *3*	†		
1421.3+x?†	†	0.77 μs *6*	$T_{1/2}$: from γ(t) (2005Ku31).

† From comparison of energies and half–lives of 9/2− isomers in neighboring nuclei, 9/2− is ruled out. Two possibilities have been discussed by 2005Ku31: 860.5γ may be E3 transition from 11/2+ to 1/2−, which gives half–life consistent with Weisskopf estimates; or there is a level above 1421.3 keV from which a low–energy highly converted transition is omitted. 2005Ku31 could not rule out any of these two possibilities.

γ(^{215}Th)

Delayed γ rays of 560.8 and 860.5 keV seen in γγ coin and in (recoil)(γ)(α from ^{215}Th decay) coin.

Eγ	E(level)
x	1421.3+x?
560.8 *2*	560.8
860.5 *2*	1421.3

Adopted Levels

S(n)=9690 *110*; S(p)=130 *70*; Q(α)=8240 *50* 2012Wa38.
S(2n)=17940 *100*, S(2p)=2870 *90*, Q(εp)=4140 *70* (2012Wa38).

^{215}Pa evaluated by B. Singh.

1979Sc09: ^{215}Pa activity was produced by ^{181}Ta(^{40}Ar,6n), E=165–202 MeV, and separated from the beam with a velocity filter. The activity was identified by excitation functions, and by its genetic relationship to daughter nuclei. Measured Eα. Detector: semi.
1999Bo52: yield of ^{215}Pa measured in ^{197}Au(^{24}Mg,X), E<176 MeV.
2000He17 (also 1996An21): ^{215}Pa activity was produced by ^{170}Er(^{51}V,6n), E=214–286 MeV, separated from the beam with a velocity filter, and implanted into a 16–strip semiconductor detector. The activity was identified by its genetic relationship to daughter nuclei. Measured Eα, half–life.

^{215}Pa Levels

E(level)	$T_{1/2}$	Comments
0.0	14 ms *2*	%α=100. %ε+%β^+<6% (theoretical,1997Mo25). $T_{1/2}$: from 2000He17. Other value: 14 ms *+20–3* (1979Sc09) is in agreement but less precise. Jπ: 9/2– from systematics (2012Au07), 13/2+ from theoretical prediction (1997Mo25).

REFERENCES FOR A=215

1942Wa04 A.G.Ward – Proc.Roy.Soc.(London) 181A, 183 (1942)
1944Ka01 B.Karlik, T.Bernert – Z.Physik 123, 51 (1944)
1944Ka02 B.Karlik, T.Bernert – Naturwissenschaften 32, 44 (1944)
1950Av61 P.Avignon – J.Phys.Radium 11, 521 (1950)
1951Me10 W.W.Meinke, A.Ghiorso, G.T.Seaborg – Phys.Rev. 81, 782 (1951)
1952Me13 W.W.Meinke, A.Ghiorso, G.T.Seaborg – Phys.Rev. 85, 429 (1952)
1953Hy83 E.K.Hyde, A.Ghiorso – Phys.Rev. 90, 267 (1953)
1955Ad09 M.Ader – Compt.Rend. 240, 2138 (1955)
1957Pa07 H.Paul, H.Warhanek – Helv.Phys.Acta 30, 272 (1957)
1957Pi31 R.C.Pilger, Jr. – Thesis, Univ.California (1957); UCRL–3877 (1957)
1961Br32 F.Braganca Gil, G.Y.Petit – J.Phys.Radium 22, 680 (1961)
1961Gr43 R.D.Griffioen, R.D.Macfarlane – UCRL–10023, p.50 (1961)
1961Ry02 A.Rytz – Helv.Phys.Acta 34, 240 (1961)
1961Vo06 Yu.M.Volkov, A.P.Komar, G.A.Korolev, G.E.Kocharov – Izvest.Akad.Nauk SSSR, Ser.Fiz. 25, 1188 (1961); Columbia Tech.Transl. 25, 1193 (1962)
1962Gi04 M.Giannini, D.Prosperi, S.Sciuti – Nuovo Cimento 25, 1314 (1962)
1962Gr20 R.D.Griffioen, R.D.Macfarlane – Bull.Am.Phys.Soc. 7, No.8, 541, K5 (1962)
1962Wa18 R.J.Walen, V.Nedovesov, G.Bastin–Scoffier – Nuclear Phys. 35, 232 (1962)
1964Sc25 O.W.B.Schult, U.Gruber, B.P.Maier, F.W.Stanek – Z.Physik 180, 298 (1964)
1965Cl05 S.Cluzeau – Thesis, University of Bordeaux (1965)
1965Nu03 M.Nurmia, D.Giessing, W.Sievers, L.Varga – Ann.Acad.Sci.Fennicae, Ser.A VI, No.167 (1965)
1965Va10 K.Valli, J.Aaltonen, G.Graeffe, M.Nurmia – Ann.Acad.Sci.Fenn., Ser.A VI, No.184 (1965)
1966Gr07 G.Graeffe, P.Kauranen – J.Inorg.Nucl.Chem. 28, 933 (1966)
1966Po02 P.Polak, A.H.Wapstra, C.Ythier – Priv.Comm. (1966)
1967Da20 J.Dalmasso, H.Maria – Compt.Rend. 265B, 822 (1967)
1967Le05 J.Letessier, D.Bertault, S.Cluzeau, G.Y.Petit – Nucl.Phys. A96, 689(1967)
1968Ba73 G.Bastin, C.F.Leang, R.J.Walen – J.Phys.(Paris), Suppl.No.1, Colloq.C1–181 (1968)
1968Br17 C.Briancon, C.F.Leang, R.Walen – Compt.Rend. 266B, 1533 (1968)
1968Gr07 J.Graff, G.Chouraqui, M.Port, J.M.Thirion, S.Jang, T.Muller – J.Phys.(Paris) 29, 141 (1968)
1968Va04 K.Valli, W.J.Treytl, E.K.Hyde – Phys.Rev. 167, 1094 (1968)
1968Va18 K.Valli, E.K.Hyde – Phys.Rev. 176, 1377 (1968)
1969Be67 D.Bertault, M.Vidal, G.Y.Petit – J.Phys.(Paris) 30, 909 (1969)
1969Ha32 R.L.Hahn, M.F.Roche, K.S.Toth – Phys.Rev. 182, 1329 (1969)
1970Bo13 J.Borggreen, K.Valli, E.K.Hyde – Phys.Rev. C2, 1841 (1970)
1970Da09 W.F.Davidson, R.D.Connor – Nucl.Phys. A149, 385 (1970)
1970Kr08 K.Krien, M.J.Canty, P.Herzog – Nucl.Phys. A157, 456 (1970)
1970To08 H.Ton, W.Beens, S.Roodbergen, J.Blok – Nucl.Phys. A155, 235 (1970)
1970Va13 K.Valli, E.K.Hyde, J.Borggreen – Phys.Rev. C1, 2115 (1970)
1971Er02 A.Erlik, J.Felsteiner, H.Lindeman, M.Tatcher – Nucl.Instrum.Methods 92, 45 (1971)
1971Gr17 B.Grennberg, A.Rytz – Metrologia 7, 65 (1971)
1972HeYM W.H.A.Hesselink – NP–19781 (1972)
1973Ha32 O.Hausser, W.Witthuhn, T.K.Alexander, A.B.McDonald, J.C.D.Milton, A.Olin – Phys.Rev.Lett. 31, 323 (1973)
1973Ta30 K.Takahashi, M.Yamada, T.Kondoh – At.Data Nucl.Data Tables 12, 101 (1973)
1974Bo11 J.D.Bowman, L.Ley, B.Richter – Nucl.Phys. A220, 367 (1974)
1974No02 T.Nomura, K.Hiruta, M.Yoshie, O.Hashimoto – Phys.Rev. C9, 1168 (1974)
1976Bl13 K.Blaton–Albicka, B.Kotlinska–Filipek, M.Matul, K.Stryczniewicz, M.Nowicki, E.Ruchowska–Lukasiak – Nukleonika 21, 935 (1976)
1977Ma30 C.Maples – Nucl.Data Sheets 22, 223 (1977)
1979Sc09 K.–H.Schmidt, W.Faust, G.Munzenberg, H.–G.Clerc, W.Lang, K.Pielenz, D.Vermeulen, H.Wohlfarth, H.Ewald, K.Guttner – Nucl.Phys. A318, 253 (1979)
1982Bo04 J.D.Bowman, R.E.Eppley, E.K.Hyde – Phys.Rev. C25, 941 (1982)
1982GoZU Y.Gono, Y.Itoh, S.Sasagase, M.Sugawara, T.Kubo, T.Nomura, S.Hayashibe, K.Hiruta – Proc.Intern.Symp. Dynamics of Nuclear Collective Motion – High Spin States and Transitional Nuclei – , Yamanishi, Japan, p.283 (1982)
1983De08 D.J.Decman, H.Grawe, H.Kluge, K.H.Maier – Z.Phys. A310, 55 (1983)
1983GoZX Y.Gono, Y.Itoh, M.Sasagase, M.Sugawara, T.Kubo, T.Nomura, S.Hayashibe, K.Hiruta – RIKEN–82, p.51 (1983)
1983Lo16 T.Lonnroth, C.Baktash – Phys.Scr. 28, 459 (1983)
1984De16 D.J.Decman, H.Grawe, H.Kluge, K.H.Maier, A.Maj, M.Menningen, N.Roy, W.Wiegner – Nucl.Phys. A419, 163 (1984)
1984Sc25 N.Schulz, S.Khazrouni, A.Chevallier, J.Chevallier, L.Kraus, I.Linck, D.C.Radford, J.Dudek, W.Nazarewicz – J.Phys.(London) G10, 1201 (1984)
1985Be05 I.Bergstrom, B.Fant – Phys.Scr. 31, 26 (1985)
1985Dr04 M.W.Drigert, J.A.Cizewski, M.S.Rosenthal – Phys.Rev. C32, 136 (1985)
1986AdZV M.Adachi, M.Fukuda, M.Taya, T.Furusawa, M.Iwasaki, H.Taketani – Inst.Nucl.Study, Univ.Tokyo, Ann.Rept., 1985, p.53 (1986)
1987AdZU M.Adachi, T.Furusawa, M.Fukuda, M.Taya, F.Nakabeppu, H.Taketani – Inst.Nucl.Study, Univ.Tokyo, Ann.Rept., 1986, p.35 (1987)
1987El02 A.M.Y.El–Lawindy, J.D.Burrows, P.A.Butler, J.R.Cresswell, V.Holliday, G.D.Jones, R.Tanner, R.Wadsworth, D.L.Watson, K.A.Connell, J.Simpson, C.Lauterbach, J.R.Mines – J.Phys.(London) G13, 93 (1987)

REFERENCES FOR A=215 (CONTINUED)

1987FaZS T.Faestermann, A.Gillitzer, K.Hartel, W.Henning, P.Kienle – Contrib.Proc. 5th Int.Conf.Nuclei Far from Stability, Rosseau Lake, Canada, K12 (1987)

1987Sa51 H.Sagawa, A.Arima, O.Scholten – Nucl.Phys. A474, 155 (1987)

1988Fu10 Y.Fukuchi, T.Komatsubara, H.Sakamoto, T.Aoki, K.Furuno – J.Phys.Soc.Jpn. 57, 2976 (1988)

1989Bu09 D.G.Burke, H.Folger, H.Gabelmann, E.Hagebo, P.Hill, P.Hoff, O.Jonsson, N.Kaffrell, W.Kurcewicz, G.Lovhoiden, K.Nybo, G.Nyman, H.Ravn, K.Riisager, J.Rogowski, K.Steffensen, T.F.Thorsteinsen, and the ISOLDE Collaboration – Z.Phys. A333, 131 (1989)

1989Dr02 G.D.Dracoulis, F.Riess, A.E.Stuchbery, R.A.Bark, S.L.Gupta, A.M.Baxter, M.Kruse – Nucl.Phys. A493, 145 (1989)

1989Ha26 E.D.Hackett, J.A.Kuehner, J.C.Waddington, G.D.Jones – Phys.Rev. C40, 1234 (1989)

1989Mi17 H.Miyatake, T.Nomura, S.Kubono, J.Tanaka, M.Oyaizu, H.Okawa, N.Ikeda, K.Sueki, H.Kudo, K.Morita, T.Shinozuka – Nucl.Phys. A501, 557 (1989)

1989Ra17 P.Raghavan – At.Data Nucl.Data Tables 42, 189 (1989)

1990Ru02 E.Ruchowska, J.Zylicz, C.F.Liang, P.Paris, Ch.Briancon – J.Phys.(London) G16, 255 (1990)

1991An10 A.N.Andreev, D.D.Bogdanov, V.I.Chepigin, A.P.Kabachenko, O.N.Malyshev, G.M.Ter–Akopian, A.V.Yeremin – Z.Phys. A338, 363 (1991)

1991An13 A.N.Andreev, D.D.Bogdanov, A.V.Eremin, A.P.Kabachenko, O.N.Malyshev, G.M.Ter–Akopyan, V.I.Chepigin – Yad.Fiz. 53, 895 (1991); Sov.J.Nucl.Phys. 53, 554 (1991)

1991Ry01 A.Rytz – At.Data Nucl.Data Tables 47, 205 (1991)

1992Sc26 P.Schuurmans, J.Wouters, P.De Moor, N.Severijns, W.Vanderpoorten, J.Vanhaverbeke, L.Vanneste – Hyperfine Interactions 75, 423 (1992)

1993An07 A.N.Andreyev, D.D.Bogdanov, V.I.Chepigin, A.P.Kabachenko, O.N.Malyshev, R.N.Sagaidak, G.M.Ter–Akopian, M.Veselsky, A.V.Yeremin – Z.Phys. A345, 247 (1993)

1993Li07 C.F.Liang, P.Paris, R.K.Sheline – Phys.Rev. C47, 1801 (1993)

1994Sh02 R.K.Sheline, C.F.Liang, P.Paris, A.Gizon, V.Barci – Phys.Rev. C49, 725 (1994)

1994Ye08 A.V.Yeremin, A.N.Andreyev, D.D.Bogdanov, G.M.Ter–Akopian, V.I.Chepigin, V.A.Gorshkov, A.P.Kabachenko, O.N.Malyshev, A.G.Popeko, R.N.Sagaidak, S.Sharo, E.N.Voronkov, A.V.Taranenko, A.Yu.Lavrentjev – Nucl.Instrum.Methods Phys.Res. A350, 608 (1994)

1996An21 A.N.Andreev, A.G.Popeko, A.V.Eremin, S.Hofmann, F.Hessberger, H.Folger, V.Ninov, S.Saro – Bull.Rus.Acad.Sci.Phys. 60, 119 (1996)

1997Mo25 P.Moller, J.R.Nix, K.–L.Kratz – At.Data Nucl.Data Tables 66, 131 (1997)

1998Ak04 Y.A.Akovali – Nucl.Data Sheets 84, 1 (1998)

1998Pf02 M.Pfutzner, P.Armbruster, T.Baumann, J.Benlliure, M.Bernas, W.N.Catford, D.Cortina–Gil, J.M.Daugas, H.Geissel, M.Gorska, H.Grawe, R.Grzywacz, M.Hellstrom, N.Iwasa, Z.Janas, A.R.Junghans, M.Karny, S.Leenhardt, M.Lewitowicz, A.C.Mueller, F.de Oliviera, P.H.Regan, M.Rejmund, K.Rykaczewski, K.Summerer – Phys.Lett. 444B, 32 (1998)

1998RyZY K.Rykaczewski, J.Kurpeta, A.Plochocki, M.Karny, J.Szerypo, A.–H.Evensen, E.Kugler, J.Lettry, H.Ravn, P.Van Duppen, A.Andreyev, M.Huyse, A.Wohr, A.Jokinen, J.Aysto, A.Nieminen, M.Huhta, M.Ramdhane, G.Walter, P.Hoff, and the ISOLDE Collaboration – Proc.Conf on Exotic Nuclei and Atomic Masses, Bellaire, Michigan, June 23–27, 1998, p.581 (1998); AIP Conf.Proc. 455 (1998)

1998St24 A.E.Stuchbery, G.D.Dracoulis, T.Kibedi, A.P.Byrne, B.Fabricius, A.R.Poletti, G.J.Lane, A.M.Baxter – Nucl.Phys. A641, 401 (1998)

1998Va13 P.Van Duppen, and the ISOLDE Collaboration – Nucl.Instrum.Methods Phys.Res. B134, 267 (1998)

1999Bo52 D.D.Bogdanov, M.Veselsky, A.V.Yeremin, A.P.Kabachenko, O.N.Malyshev, Yu.A.Muzychka, B.I.Pustylnik, A.G.Popeko, R.N.Sagaidak, G.M.Ter–Akopian, V.I.Chepigin – Yad.Fiz. 62, No 11, 1931 (1999); Phys.Atomic Nuclei 62, 1794 (1999)

1999Li05 C.F.Liang, P.Paris, R.K.Sheline – Phys.Rev. C59, 648 (1999)

2000He17 F.P.Hessberger, S.Hofmann, D.Ackermann, V.Ninov, M.Leino, S.Saro, A.Andreyev, A.Lavrentev, A.G.Popeko, A.V.Yeremin – Eur.Phys.J. A 8, 521 (2000); Erratum Eur.Phys.J. A 9, 433 (2000)

2000Ni02 K.Nishio, H.Ikezoe, S.Mitsuoka, J.Lu – Phys.Rev. C61, 034309 (2000)

2001Br31 E.Browne – Nucl.Data Sheets 93, 763 (2001); Erratum Nucl.Data Sheets 96, 391 (2002)

2001Li44 C.F.Liang, P.Paris, R.K.Sheline – Phys.Rev. C64, 034310 (2001)

2001Ni06 K.Nishio, H.Ikezoe, S.Mitsuoka, K.Satou, S.C.Jeong – Phys.Rev. C63, 044610 (2001)

2003Bo06 I.N.Borzov – Phys.Rev. C 67, 025802 (2003)

2003Ca21 E.Caurier, M.Rejmund, H.Grawe – Phys.Rev. C 67, 054310 (2003)

2003Ko26 U.Koster, V.N.Fedoseyev, A.N.Andreyev, U.C.Bergmann, R.Catherall, J.Cederkall, M.Dietrich, H.De Witte, D.V.Fedorov, L.Fraile, S.Franchoo, H.Fynbo, U.Georg, T.Giles, M.Gorska, M.Hannawald, M.Huyse, A.Joinet, O.C.Jonsson, K.L.Kratz, K.Kruglov, Ch.Lau, J.Lettry, V.I.Mishin, M.Oinonen, K.Partes, K.Perajarvi, B.Pfeiffer, H.L.Ravn, M.D.Seliverstov, P.Thirolf, K.Van de Vel, P.Van Duppen, J.Van Roosbroeck, L.Weissman, and the IS365/IS387/IS393/ISOLDE Collaborations – Nucl.Instrum.Methods Phys.Res. B204, 347 (2003)

2003Ku26 J.Kurpeta, A.Plochocki, A.N.Andreyev, J.Aysto, A.De Smet, H.De Witte, A.–H.Evensen, V.Fedoseyev, S.Franchoo, M.Gorska, H.Grawe, M.Huhta, M.Huyse, Z.Janas, A.Jokinen, M.Karny, E.Kugler, W.Kurcewicz, U.Koster, J.Lettry, A.Nieminen, K.Partes, M.Ramdhane, H.L.Ravn, K.Rykaczewski, J.Szerypo, K.Van de Vel, P.Van Duppen, L.Weissman, G.Walter, A.Wohr, and the IS387 and ISOLDE Collaborations – Eur.Phys.J. A 18, 31 (2003)

2004An14 I.Angeli – At.Data Nucl.Data Tables 87, 185 (2004)

2004DeZV H.De Witte – Thesis, Leuven Univ. Belgium (2004)

2004He25 F.P.Hessberger, S.Hofmann, I.Kojouharov, D.Ackermann – Eur.Phys.J. A 22, 253 (2004)

2005Ku31 P.Kuusiniemi, F.P.Hessberger, D.Ackermann, S.Hofmann, B.Sulignano, I.Kojouharov, R.Mann – Eur.Phys.J. A 25, 397 (2005)

REFERENCES FOR A=215 (CONTINUED)

2005Le42 A.–P.Leppanen, J.Uusitalo, S.Eeckhaudt, T.Enqvist, K.Eskola, T.Grahn, F.P.Hessberger, P.T.Greenlees, P.Jones, R.Julin, S.Juutinen, H.Kettunen, P.Kuusiniemi, M.Leino, P.Nieminen, J.Pakarinen, J.Perkowski, P.Rahkila, C.Scholey, G.Sletten – Eur.Phys.J. A 25, Supplement 1, 183 (2005)

2005Li17 Z.Liu, J.Kurcewicz, P.J.Woods, C.Mazzocchi, F.Attallah, E.Badura, C.N.Davids, T.Davinson, J.Doring, H.Geissel, M.Gorska, R.Grzywacz, M.Hellstrom, Z.Janas, M.Karny, A.Korgul, I.Mukha, M.Pfutzner, C.Plettner, A.Robinson, E.Roeckl, K.Rykaczewski, K.Schmidt, D.Seweryniak, H.Weick – Nucl.Instrum.Methods Phys.Res. A543, 591 (2005)

2006Ca30 E.Casarejos, J.Benlliure, J.Pereira, P.Armbruster, M.Bernas, A.Boudard, S.Czajkowski, T.Enqvist, R.Legrain, S.Leray, B.Mustapha, M.Pravikoff, F.Rejmund, K.–H.Schmidt, C.Stephan, J.Taieb, L.Tassan–Got, C.Volant, W.Wlazlo – Phys.Rev. C 74, 044612 (2006)

2006Po01 Zs.Podolyak, J.Gerl, M.Hellstrom, F.Becker, K.A.Gladnishki, M.Gorska, A.Kelic, Y.Kopatch, S.Mandal, P.H.Regan, K.–H.Schmidt, P.M.Walker, H.J.Wollersheim, A.Banu, G.Benzoni, H.Boardman, E.Casarejos, J.Ekman, H.Geissel, H.Grawe, D.Hohn, I.Kojouharov, J.Leske, R.Lozeva, M.N.Mineva, G.Neyens, R.D.Page, C.J.Pearson, M.Portillo, D.Rudolph, N.Saito, H.Schaffner, D.Sohler, K.Summerer, J.J.Valiente–Dobon, C.Wheldon, H.Weick, M.Winkler – Phys.Lett. B 632, 203 (2006)

2007Le14 A.P.Leppanen, J.Uusitalo, M.Leino, S.Eeckhaudt, T.Grahn, P.T.Greenlees, P.Jones, R.Julin, S.Juutinen, H.Kettunen, P.Kuusiniemi, P.Nieminen, J.Pakarinen, P.Rahkila, C.Scholey, G.Sletten – Phys.Rev. C 75, 054307 (2007)

2008Ki07 T.Kibedi, T.W.Burrows, M.B.Trzhaskovskaya, P.M.Davidson, C.W.Nestor, Jr. – Nucl.Instrum.Methods Phys.Res. A589, 202 (2008)

2008Ma17 J.Margueron, H.Sagawa, K.Hagino – Phys.Rev. C 77, 054309 (2008)

2008We02 C.Weber, G.Audi, D.Beck, K.Blaum, G.Bollen, F.Herfurth, A.Kellerbauer, H.–J.Kluge, D.Lunney, S.Schwarz – Nucl.Phys. A803, 1 (2008)

2009Al32 H.Alvarez–Pol, J.Benlliure, E.Casarejos, L.Audouin, D.Cortina–Gil, T.Enqvist, B.Fernandez, A.R.Junghans, B.Jurado, P.Napolitani, J.Pereira, F.Rejmund, K.–H.Schmidt, O.Yordanov – Eur.Phys.J. A 42, 485 (2009)

2010Al24 H.Alvarez–Pol, J.Benlliure, E.Casarejos, L.Audouin, D.Cortina–Gil, T.Enqvist, B.Fernandez–Dominguez, A.R.Junghans, B.Jurado, P.Napolitani, J.Pereira, F.Rejmund, K.–H.Schmidt, O.Yordanov – Phys.Rev. C 82, 041602 (2010)

2011Pr03 B.Pritychenko, E.Betak, M.A.Kellett, B.Singh, J.Totans – Nucl.Instrum.Methods Phys.Res. A640, 213 (2011)

2011StZZ N.J.Stone – INDC(NDS)–0594 (2011)

2012Au07 G.Audi, F.G.Kondev, M.Wang, B.Pfeiffer, X.Sun, J.Blachot, M.MacCormick – Chin.Phys.C 36, 1157 (2012)

2012BoZU M.Bowry, Zs.Podolyak, J.Kurcewicz, S.Pietri, M.Bunce, P.H.Regan, F.Farinon, H.Geissel, C.Nociforo, A.Prochazka, H.Weick, P.Allegro, J.Benlliure, G.Benzoni, P.Boutachkov, J.Gerl, M.Gorska, A.Gottardo, N.Gregor, R.Janik, R.Knobel, I.Kojouharov, T.Kubo, Yu.A.Litvinov, E.Merchan, I.Mukha, F.Naqvi, B.Pfeiffer, M.Pfutzner, W.Plass, M.Pomorski, B.Riese, M.V.Ricciardi, K.–H.Schmidt, H.Schaffner,N.Kurz, A.M.D.Bacelar, A.M.Bruce, G.F.Farrelly, N.Alkhomashi, N.Al–Dahan, C.Scheidenberger, B.Sitar, P.Spiller, J.Stadlmann, P.Strmen, B.Sun, H.Takeda, I.Tanihata, S.Terashima, J.J.Valiente Dobon, J.S.Winfield, H.–J.Wollersheim, P.J.Woods – Proc.Intern.Conf.on Nuclear Structure and Dynamics, 12, Opatija, Croatia, 9–13 July, 2012, T.Niksic, M.Milin, D.Vretenar, S.Szilner, Eds., p.317 (2012); AIP Conf.Proc.1491 (2012)

2012Co22 V.Comas, S.Heinz, S.Hofmann, D.Ackermann, J.Heredia, F.P.Hessberger, J.Khuyagbaatar, B.Kindler, B.Lommel, R.Mann – Eur.Phys.J. A 48, 180 (2012)

2012De11 M.E.Debray, M.Davidson, J.Davidson, A.J.Kreiner, M.A.Cardona, D.Hojman, D.R.Napoli, S.Lenzi, G.de Angelis, M.De Poli, A.Gadea, D.Bazzacco, C.Rossi–Alvarez, N.Medina, C.A.Ur – Phys.Rev. C 86, 014326 (2012)

2012Ko09 V.M.Kolomietz, S.V.Lukyanov, A.I.Sanzhur – Phys.Rev. C 85, 034309 (2012)

2012Wa38 M.Wang, G.Audi, A.H.Wapstra, F.G.Kondev, M.MacCormick, X.Xu, B.Pfeiffer – Chin.Phys.C 36, 1603 (2012)

2013An02 I.Angeli, K.P.Marinova – At.Data Nucl.Data Tables 99, 69 (2013)

2013Ba29 A.M.D.Bacelar, A.M.Bruce, Zs.Podolyak, N.Al–Dahan, M.Gorska, S.Lalkovski, S.Pietri, M.V.Ricciardi, A.Algora, N.Alkhomashi, J.Benlliure, P.Boutachkov, A.Bracco, E.Calore, E.Casarejos, I.J.Cullen, A.Y.Deo, P.Detistov, Zs.Dombradi, C.Domingo–Pardo, M.Doncel, F.Farinon, G.F.Farrelly, H.Geissel, W.Gelletly, J.Gerl, N.Goel, J.Grebosz, R.Hoischen, I.Kojouharov, N.Kurz, S.Leoni, F.Molina, D.Montanari, A.I.Morales, A.Musumarra, D.R.Napoli, R.Nicolini, C.Nociforo, A.Prochazka, W.Prokopowicz, P.H.Regan, B.Rubio, D.Rudolph, K.–H.Schmidt, H.Schaffner, S.J.Steer, K.Steiger, P.Strmen, T.P.D.Swan, I.Szarka, J.J.Valiente–Dobon, S.Verma, P.M.Walker, H.Weick, H.J.Wollersheim – Phys.Lett. B 723, 302 (2013)

2013Bo18 M.Bowry, Zs.Podolyak, S.Pietri, J.Kurcewicz, M.Bunce, P.H.Regan, F.Farinon, H.Geissel, C.Nociforo, A.Prochazka, H.Weick, N.Al–Dahan, N.Alkhomashi, P.R.P.Allegro, J.Benlliure, G.Benzoni, P.Boutachkov, A.M.Bruce, A.M.D.Bacelar, G.F.Farrelly, J.Gerl, M.Gorska, A.Gottardo, J.Grebosz, N.Gregor, R.Janik, R.Knobel, I.Kojouharov, T.Kubo, N.Kurz, Yu.A.Litvinov, E.Merchan, I.Mukha, F.Naqvi, B.Pfeiffer, M.Pfutzner, W.Plass, M.Pomorski, B.Riese, M.V.Ricciardi, K.–H.Schmidt, H.Schaffner, C.Scheidenberger, E.C.Simpson, B.Sitar, P.Spiller, J.Stadlmann, P.Strmen, B.Sun, I.Tanihata, S.Terashima, J.J.Valiente Dobon, J.S.Winfield, H.–J.Wollersheim, P.J.Woods – Phys.Rev. C 88, 024611 (2013)

2013De20 H.De Witte, S.Eeckhaudt, A.N.Andreyev, I.N.Borzov, J.Cederkall, A.De Smet, D.V.Fedorov, V.N.Fedoseyev, S.Franchoo, M.Gorska, H.Grawe, G.Huber, M.Huyse, Z.Janas, U.Koester, W.Kurcewicz, J.Kurpeta, A.Plochocki, K.Van de Vel, P.Van Duppen, L.Weissman – Phys.Rev. C 87, 067303 (2013)

The Long-Baseline Neutrino Experiment

Exploring Fundamental Symmetries of the Universe

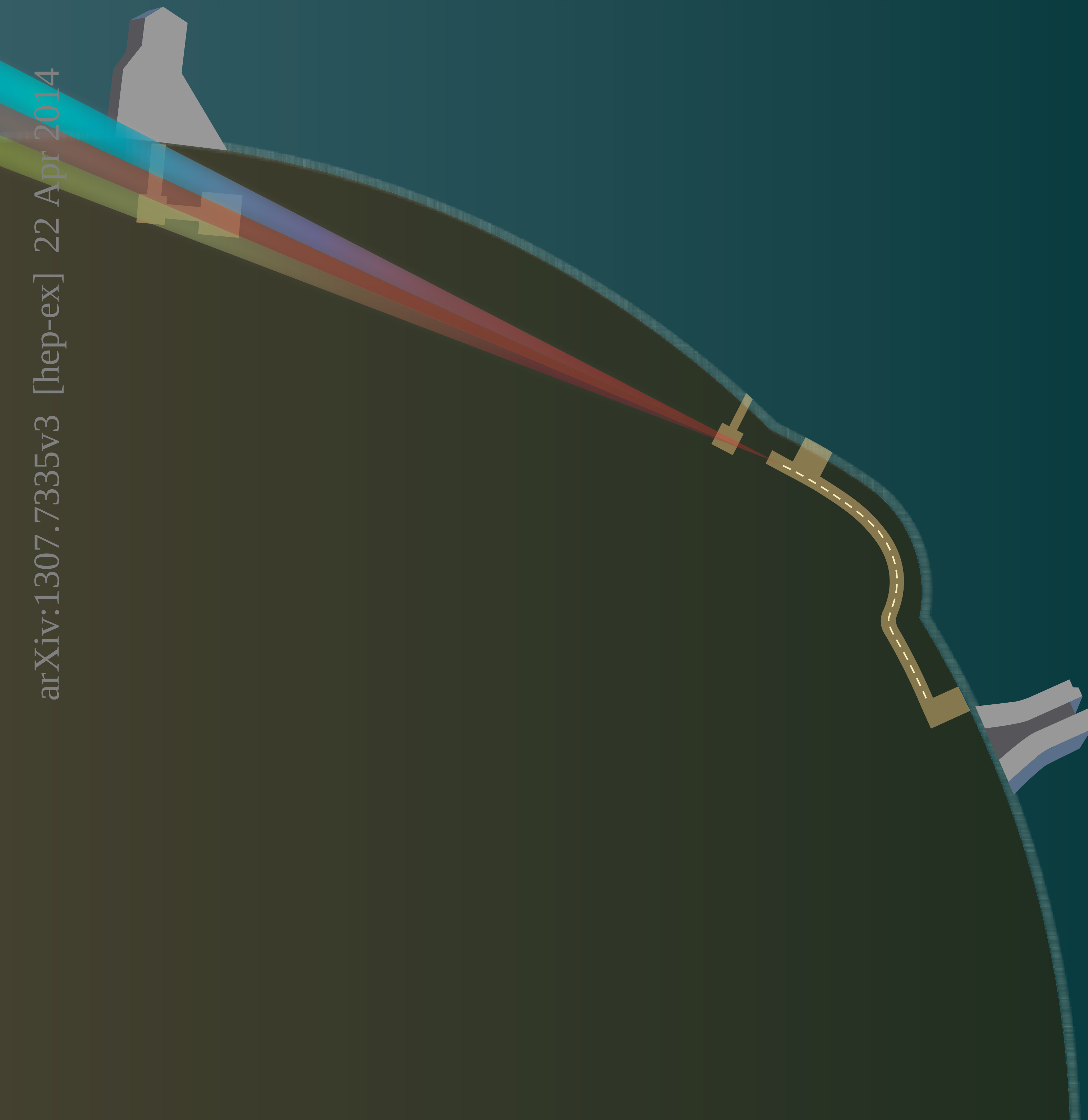

BNL-101354-2014-JA
FERMILAB-PUB-14-022
LA-UR-14-20881
arXiv:1307.7335

The Long-Baseline Neutrino Experiment

Exploring Fundamental Symmetries of the Universe

April 15, 2014

Cover design by Diana Brandonisio, Fermilab Visual Media Services

Typeset in LaTeX

The LBNE Collaboration

C. Adams[85], D. Adams[7], T. Akiri[23], T. Alion[67], K. Anderson[25], C. Andreopoulos[40], M. Andrews[25], I. Anghel[33], J. C. C. d. Anjos[14], M. Antonello[36], E. Arrieta-Diaz[46], M. Artuso[74], J. Asaadi[74], X. Bai[69], B. Baibussinov[56], M. Baird[32], B. Balantekin[84], B. Baller[25], B. Baptista[32], D. Barker[68], G. Barker[81], W. A. Barletta[45], G. Barr[55], L. Bartoszek[41], A. Bashyal[76], M. Bass[18], V. Bellini[13], P. A. Benetti[58], B. E. Berger[18], M. Bergevin[8], E. Berman[25], H. Berns[8], A. Bernstein[39], R. Bernstein[25], B. Bhandari[30], V. Bhatnagar[57], B. Bhuyan[31], J. Bian[49], M. Bishai[7], A. Blake[11], F. Blaszczyk[42], E. Blaufuss[44], B. Bleakley[71], E. Blucher[15], S. Blusk[74], V. Bocean[25], F. Boffelli[58], J. Boissevain[41], T. Bolton[35], M. Bonesini[48], S. Boyd[81], A. Brandt[76], R. Breedon[8], C. Bromberg[46], R. Brown[7], G. Brunetti[25], N. Buchanan[18], B. Bugg[75], J. Busenitz[2], E. Calligarich[58], L. Camilleri[19], G. Carminati[9], R. Carr[19], C. Castromonte[27], F. Cavanna[85], S. Centro[56], A. Chen[25], H. Chen[7], K. Chen[7], D. Cherdack[18], C. Chi[19], S. Childress[25], B. C. Choudhary[21], G. Christodoulou[40], C. Christofferson[69], E. Church[85], D. Cline[10], T. Coan[72], A. Cocco[51], J. Coelho[78], S. Coleman[17], J. M. Conrad[45], M. Convery[64], R. Corey[69], L. Corwin[69], J. Cranshaw[4], D. Cronin-Hennessy[49], A. Curioni[48], H. da Motta[14], T. Davenne[65], G. S. Davies[33], S. Dazeley[39], K. De[76], A. de Gouvea[53], J. K. de Jong[55], D. Demuth[49], C. Densham[65], M. Diwan[7], Z. Djurcic[4], R. Dolfini[58], J. Dolph[7], G. Drake[4], S. Dye[29], H. Dyuang[67], D. Edmunds[46], S. Elliott[41], M. Elnimr[2], S. Eno[44], S. Enomoto[82], C. O. Escobar[25], J. Evans[43], A. Falcone[58], L. Falk[73], A. Farbin[76], C. Farnese[56], A. Fava[56], J. Felde[44], S. Fernandes[2], F. Ferroni[58], F. Feyzi[84], L. Fields[53], A. Finch[37], M. Fitton[65], B. Fleming[85], J. Fowler[23], W. Fox[32], A. Friedland[41], S. Fuess[25], B. Fujikawa[38], H. Gallagher[78], R. Gandhi[28], G. Garvey[41], V. M. Gehman[38], G. d. Geronimo[7], D. Gibin[56], R. Gill[7], R. A. Gomes[27], M. C. Goodman[4], J. Goon[68], N. Graf[60], M. Graham[64], R. Gran[50], C. Grant[8], N. Grant[37], H. Greenlee[25], L. Greenler[84], S. Grullon[59], E. Guardincerri[41], V. Guarino[4], E. Guarnaccia[80], G. Guedes[24], R. Guenette[85], A. Guglielmi[56], M. M. Guzzo[12], A. T. Habig[50], R. W. Hackenburg[7], H. Hadavand[76], A. Hahn[25], M. Haigh[81], T. Haines[41], T. Handler[75], S. Hans[7], J. Hartnell[73], J. Harton[18], R. Hatcher[25], A. Hatzikoutelis[75], S. Hays[25], E. Hazen[6], M. Headley[70], A. Heavey[25], K. Heeger[85], J. Heise[70], R. Hellauer[44], J. Hewes[43], A. Himmel[23], M. Hogan[18], P. Holanda[12], A. Holin[79], G. Horton-Smith[35], J. Howell[25], P. Hurh[25], J. Huston[46], J. Hylen[25], R. Imlay[42], J. Insler[42], G. Introzzi[58], Z. Isvan[7], C. Jackson[76], J. Jacobsen[44], D. E. Jaffe[7], C. James[25], C. Jen[80], M. Johnson[25], R. Johnson[16], R. Johnson[17], S. Johnson[17], W. Johnston[18], J. Johnstone[25], B. J. Jones[45], H. Jostlein[25], T. Junk[25], R. Kadel[38], K. Kaess[50], G. Karagiorgi[19], J. Kaspar[82], T. Katori[45], B. Kayser[25], E. Kearns[6], P. Keener[59], E. Kemp[12], S. H. Kettell[7], M. Kirby[25], J. Klein[59], G. Koizumi[25], S. Kopp[77], L. Kormos[37], W. Kropp[9], V. A. Kudryavtsev[66], A. Kumar[57], J. Kumar[29], T. Kutter[42], F. La Zia[13], K. Lande[59], C. Lane[22], K. Lang[77], F. Lanni[7], R. Lanza[45], T. Latorre[59], J. Learned[29], D. Lee[41], K. Lee[10], Q. Li[25], S. Li[7], Y. Li[7], Z. Li[23], J. Libo[67], S. Linden[6], J. Ling[7], J. Link[80], L. Littenberg[7], H. Liu[30], Q. Liu[41], T. Liu[72], J. Losecco[54], W. Louis[41], B. Lundberg[25], T. Lundin[25], J. Lundy[76], A. A. Machado[26], C. Maesano[8], S. Magill[4], G. Mahler[7], D. Malon[4], S. Malys[52], F. Mammoliti[13], S. K. Mandal[21], A. Mann[78], P. Mantsch[25],

A. Marchionni[25], W. Marciano[7], C. Mariani[80], J. Maricic[29], A. Marino[17], M. Marshak[49], J. Marshall[11], S. Matsuno[29], C. Mauger[41], K. Mavrokoridis[40], N. Mayer[78], N. McCauley[40], E. McCluskey[25], K. McDonald[61], K. McFarland[63], D. McKee[35], R. McKeown[83], R. McTaggart[71], R. Mehdiyev[77], D. Mei[68], A. Menegolli[58], G. Meng[56], Y. Meng[10], D. Mertins[2], M. Messier[32], W. Metcalf[42], R. Milincic[29], W. Miller[49], G. Mills[41], S. R. Mishra[67], N. Mokhov[25], C. Montanari[58], D. Montanari[25], C. Moore[25], J. Morfin[25], B. Morgan[81], W. Morse[7], Z. Moss[45], C. A. Moura[1], S. Mufson[32], D. Muller[64], J. Musser[32], D. Naples[60], J. Napolitano[62], M. Newcomer[59], R. Nichol[79], T. Nicholls[65], E. Niner[32], B. Norris[25], J. Nowak[37], H. O'Keeffe[37], R. Oliveira[12], T. Olson[78], B. Page[46], S. Pakvasa[29], O. Palamara[85], J. Paley[4], V. Paolone[60], V. Papadimitriou[25], S. Park[76], Z. Parsa[7], K. Partyka[85], B. Paulos[84], Z. Pavlovic[41], S. Peeters[73], A. Perch[79], G. Perdue[63], J. D. Perkin[66], R. Petti[67], A. Petukhov[69], F. Pietropaolo[56], R. Plunkett[25], C. Polly[25], S. Pordes[25], M. Potekhin[7], R. Potenza[13], A. Prakash[45], O. Prokofiev[25], X. Qian[7], J. L. Raaf[25], V. Radeka[7], I. Rakhno[25], Y. Ramachers[81], R. Rameika[25], J. Ramsey[41], A. Rappoldi[58], G. Raselli[58], P. Ratoff[37], S. Ravindra[76], B. Rebel[25], J. Reichenbacher[2], D. Reitzner[25], S. Rescia[7], M. Richardson[66], K. Rielage[41], K. Riesselmann[25], M. Robinson[66], L. Rochester[64], M. Ronquest[41], M. Rosen[29], M. Rossella[58], C. Rubbia[26], R. Rucinski[25], S. Sahijpal[57], H. Sahoo[4], P. Sala[47], D. Salmiera[58], N. Samios[7], M. Sanchez[33], A. Scaramelli[47], H. Schellman[53], R. Schmitt[25], D. Schmitz[15], J. Schneps[78], K. Scholberg[23], E. Segreto[36], S. Seibert[59], L. Sexton-Kennedy[25], M. Shaevitz[19], P. Shanahan[25], R. Sharma[7], T. Shaw[25], N. Simos[7], V. Singh[5], G. Sinnis[41], W. Sippach[19], T. Skwarnicki[74], M. Smy[9], H. Sobel[9], M. Soderberg[74], J. Sondericker[7], W. Sondheim[41], A. Sousa[16], N. J. Spooner[66], M. Stancari[25], I. Stancu[2], D. Stefan[36], A. Stefanik[25], J. Stewart[7], S. Stone[74], J. Strait[25], M. Strait[15], S. Striganov[25], G. Sullivan[44], Y. Sun[29], L. Suter[4], A. Svenson[67], R. Svoboda[8], B. Szczerbinska[20], A. Szelc[85], M. Szydagis[8], S. Söldner-Rembold[43], R. Talaga[4], M. Tamsett[73], S. Tariq[25], R. Tayloe[32], C. Taylor[41], D. Taylor[70], A. Teymourian[10], H. Themann[7], M. Thiesse[66], J. Thomas[79], L. F. Thompson[66], M. Thomson[11], C. Thorn[7], M. Thorpe[65], X. Tian[67], D. Tiedt[69], W. Toki[18], N. Tolich[82], M. Torti[58], M. Toups[45], C. Touramanis[40], M. Tripathi[8], I. Tropin[25], Y. Tsai[64], C. Tull[38], M. Tzanov[42], J. Urheim[32], S. Usman[52], M. Vagins[34], G. A. Valdiviesso[3], R. Van Berg[59], R. Van de Water[41], P. Van Gemmeren[4], F. Varanini[56], G. Varner[29], K. Vaziri[25], G. Velev[25], S. Ventura[56], C. Vignoli[36], B. Viren[7], D. Wahl[84], A. Waldron[73], C. W. Walter[23], H. Wang[10], W. Wang[83], T.K. Warburton[66], D. Warner[18], R. Wasserman[18], B. Watson[76], A. Weber[55], W. Wei[68], D. Wells[69], M. Wetstein[15], A. White[76], H. White[41], L. Whitehead[30], D. Whittington[32], J. Willhite[70], R. J. Wilson[18], L. Winslow[10], K. Wood[67], E. Worcester[7], M. Worcester[7], T. Xin[33], K. Yarritu[41], J. Ye[72], M. Yeh[7], B. Yu[7], J. Yu[76], T. Yuan[17], A. Zani[58], G. P. Zeller[25], C. Zhang[7], C. Zhang[68], E. D. Zimmerman[17], and R. Zwaska[25]

[1]ABC Federal University, Santo André –SP, 09210-580, Brazil
[2]Univ. of Alabama (Tuscaloosa), Tuscaloosa, AL 35487-0324, USA
[3]Univ. Federal de Alfenas em Poços de Caldas, 11999, CEP 37715-900 Poços de Caldas-MG, Brazil
[4]Argonne National Lab., Argonne, IL 60439, USA
[5]Banaras Hindu University, Dept. of Physics, Varanasi UP 221005, India

[6]Boston University, Boston, MA 02215, USA
[7]Brookhaven National Lab., Upton, NY 11973-5000, USA
[8]Univ. of California (Davis), Davis, CA 95616, USA
[9]Univ. of California (Irvine), Irvine, CA 92697-4575, USA
[10]Univ. of California (Los Angeles), Los Angeles, CA 90095-1547, USA
[11]Univ. of Cambridge, JJ Thomson Avenue, Cambridge CB3 0HE, UK
[12]Univ. de Campinas, Av. Sérgio Buarque de Holanda, 777 CEP 13083-859 Campinas-SP, Brazil
[13]Univ. di Catania, Corso Italia, I-95129 Catania, Italy
[14]Centro Brasileiro de Pesquisas Físicas, Rio de Janeiro, BR-22290-180, Brazil
[15]Univ. of Chicago, Chicago, IL 60637-1434, USA
[16]Univ. of Cincinnati, Cincinnati, OH 45221-0011, USA
[17]Univ. of Colorado, Boulder, CO 80309, USA
[18]Colorado State University, Fort Collins, CO 80523, USA
[19]Columbia University, New York, NY 10027, USA
[20]Dakota State University, Madison, SD 57042, USA
[21]Univ. of Delhi, Department of Physics and Astrophysics, Delhi 110007, India
[22]Drexel University, Philadelphia, PA 19104, USA
[23]Duke University, Durham, NC 27706, USA
[24]Univ. Estadual de Feira de Santana, 44036-900, Feira de Santana-BA, Brazil
[25]Fermi National Accelerator Lab, Batavia, IL 60510-0500, USA
[26]INFN, Laboratori Nazionali del Gran Sasso, I-67010 Assergi, AQ, Italy
[27]Univ. Federal de Goias, Goiania, Goias, Brazil
[28]Harish-Chandra Research Institute, Jhunsi, Allahabad 211 019, India
[29]Univ. of Hawaii, Honolulu, HI 96822-2219, USA
[30]Univ. of Houston, Houston, TX 77204, USA
[31]Indian Institute of Technology Guwahati, Guwahati, 781 039, India
[32]Indiana University, Bloomington, IN 47405-7105, USA
[33]Iowa State University, Ames, IO 50011, USA
[34]Kavli IPMU, Univ. of Tokyo, Kashiwa Shi, Chiba 277-8568, Japan
[35]Kansas State University, Manhattan, KS 66506, USA
[36]Laboratori Nazionali del Gran Sasso, I-67010 Assergi, AQ, Italy
[37]Lancaster University, Bailrigg, Lancaster LA1 4YB, UK
[38]Lawrence Berkeley National Lab., Berkeley, CA 94720-8153, USA
[39]Lawrence Livermore National Lab., Livermore, CA 94551, USA
[40]Univ. of Liverpool, L69 7ZE, Liverpool, UK
[41]Los Alamos National Laboratory, Los Alamos, NM 87545, USA
[42]Louisiana State University, Baton Rouge, LA 70803-4001, USA
[43]Univ. of Manchester, Oxford Road, Manchester M13 9PL, UK
[44]Univ. of Maryland, College Park, MD 20742-4111, USA

[45]Massachusetts Institute of Technology, Cambridge, MA 02139-4307, USA
[46]Michigan State University, East Lansing, MI 48824, USA
[47]Univ. di Milano, INFN Sezione di Milano, I-20133 Milano, Italy
[48]Univ. of Milano and INFN Sezione di Milano Bicocca, Piazza della Scienza 3, 20126 Milano, Italy
[49]Univ. of Minnesota, Minneapolis, MN 55455, USA
[50]Univ. of Minnesota (Duluth), Duluth, MN 55812, USA
[51]Univ. di Napoli, Complesso Universitario di Monte S. Angelo, I-80126 Napoli, Italy
[52]National Geospatial-Intelligence Agency, Reston, VA 20191, USA
[53]Northwestern University, Evanston, Il 60208, USA
[54]Univ. of Notre Dame, Notre Dame, IN 46556-5670, USA
[55]Univ. of Oxford, Oxford, OX1 3RH, UK
[56]Univ. of Padova, Dip. Fisica e Astronomia G. Galilei and INFN Sezione di Padova, I-35131 Padova, Italy
[57]Panjab University, Chandigarh, 160014 U.T., India
[58]Univ. of Pavia, INFN Sezione di Pavia, I-27100 Pavia, Italy
[59]Univ. of Pennsylvania, Philadelphia, PA 19104-6396, USA
[60]Univ. of Pittsburgh, Pittsburgh, PA 15260, USA
[61]Princeton University, Princeton, New Jersey 08544-0708, USA
[62]Rensselaer Polytechnic Inst., Troy, NY 12180-3590, USA
[63]Univ. of Rochester, Rochester, NY 14627-0171, USA
[64]SLAC National Acceleratory Laboratory, Menlo Park, CA 94025, USA
[65]STFC Rutherford Appleton Laboratory, Harwell Oxford, Didcot OX11 0QX, UK
[66]Univ. of Sheffield, Sheffield, S3 7RH, UK
[67]Univ. of South Carolina, Columbia, SC 29208, USA
[68]Univ. of South Dakota, Vermillion, SD 57069, USA
[69]South Dakota School of Mines and Technology, Lead, SD 57754, USA
[70]South Dakota Science And Technology Authority, Lead, SD 57754, USA
[71]South Dakota State University, Brookings, SD 57007, USA
[72]Southern Methodist University, Dallas, TX 75275, USA
[73]Univ. of Sussex, Brighton, BN1 9RH, UK
[74]Syracuse University, Syracuse, NY 13244-1130, USA
[75]Univ. of Tennessee, Knoxville, TN, USA
[76]Univ. of Texas (Arlington), Arlington, TX 76019, USA
[77]Univ. of Texas (Austin), Austin, TX 78712-0264, USA
[78]Tufts University, Medford, MA 02155, USA
[79]University College London, London, WC1E 6BT, UK
[80]Virginia Tech., Blacksburg, VA 24061-0435, USA
[81]Univ. of Warwick, Coventry CV4 7AL, UK
[82]Univ. of Washington, Seattle, WA 98195-1560, USA
[83]College of William and Mary, Williamsburg, VA 23187-8795, USA

[84]Univ. of Wisconsin, Madison, WI 53706, USA
[85]Yale University, New Haven, CT 06520, USA

Abstract

The preponderance of matter over antimatter in the early Universe, the dynamics of the supernova bursts that produced the heavy elements necessary for life and whether protons eventually decay — these mysteries at the forefront of particle physics and astrophysics are key to understanding the early evolution of our Universe, its current state and its eventual fate. The Long-Baseline Neutrino Experiment (LBNE) represents an extensively developed plan for a world-class experiment dedicated to addressing these questions.

Experiments carried out over the past half century have revealed that neutrinos are found in three states, or *flavors*, and can transform from one flavor into another. These results indicate that each neutrino flavor state is a mixture of three different nonzero mass states, and to date offer the most compelling evidence for physics beyond the Standard Model. In a single experiment, LBNE will enable a broad exploration of the three-flavor model of neutrino physics with unprecedented detail. Chief among its potential discoveries is that of matter-antimatter asymmetries (through the mechanism of charge-parity violation) in neutrino flavor mixing — a step toward unraveling the mystery of matter generation in the early Universe. Independently, determination of the unknown neutrino mass ordering and precise measurement of neutrino mixing parameters by LBNE may reveal new fundamental symmetries of Nature.

Grand Unified Theories, which attempt to describe the unification of the known forces, predict rates for proton decay that cover a range directly accessible with the next generation of large underground detectors such as LBNE's. The experiment's sensitivity to key proton decay channels will offer unique opportunities for the ground-breaking discovery of this phenomenon.

Neutrinos emitted in the first few seconds of a core-collapse supernova carry with them the potential for great insight into the evolution of the Universe. LBNE's capability to collect and analyze this high-statistics neutrino signal from a supernova within our galaxy would provide a rare opportunity to peer inside a newly-formed neutron star and potentially witness the birth of a black hole.

To achieve its goals, LBNE is conceived around three central components: (1) a new, high-intensity neutrino source generated from a megawatt-class proton accelerator at Fermi National Accelerator Laboratory, (2) a fine-grained near neutrino detector installed just downstream of the source, and (3) a massive liquid argon time-projection chamber deployed as a far detector deep underground at the Sanford Underground Research Facility. This facility, located at the site of the former Homestake Mine in Lead, South Dakota, is $\sim$1,300 km from the neutrino source at Fermilab — a distance (baseline) that delivers optimal sensitivity to neutrino charge-parity symmetry violation and mass ordering effects. This ambitious yet cost-effective design incorporates scalability and flexibility and can accommodate a variety of upgrades and contributions.

With its exceptional combination of experimental configuration, technical capabilities, and potential for transformative discoveries, LBNE promises to be a vital facility for the field of particle physics worldwide, providing physicists from institutions around the globe with opportunities to collaborate in a twenty to thirty year program of exciting science.

Contents

List of Figures

List of Tables

How to Read this Document

The LBNE science document is intended to inform a diverse readership about the goals and capabilities of the LBNE experiment. Your approach to reading this document will depend upon your purpose as well as your level of knowledge about high energy and neutrino physics.

The colored boxes distributed throughout the document highlight the important take-away points. They are integral to the document, but to the extent possible, are written in language accessible to the nonscientist.

The three chapters Chapter 1 *Introduction and Executive Summary*, Chapter 3 *Project and Design* and Chapter 9 *Summary and Conclusion* together provide a comprehensive overview of LBNE's scientific objectives, its place in the landscape of neutrino physics experiments worldwide, the technologies it will incorporate and the capabilities it will possess. Much of the information in these chapters is accessible to the lay reader, but of course, the scientific concepts, goals and methods around which LBNE is designed are by their nature highly specialized, and the text in certain sections is correspondingly technical.

In Chapter 2 *The Science of LBNE*, the initial paragraphs in each section provide some introductory information, but in general this chapter assumes a working knowledge of high energy physics and, ideally, familiarity with neutrino physics.

The three chapters that delve into the areas corresponding to the scientific objectives of LBNE: Chapter 4 *Neutrino Mixing, Mass Hierarchy and CP Violation*, Chapter 5 *Nucleon Decay Motivated by Grand Unified Theories* and Chapter 6 *Core-Collapse Supernova Neutrinos*, assume a working knowledge of high energy physics and particle astrophysics. This is also true of Chapter 7 *Precision Measurements with a High-Intensity Neutrino Beam* and Chapter 8 *Additional Far Detector Physics Opportunities*, as well as the appendices.

Chapter 1 Introduction and Executive Summary

The Long-Baseline Neutrino Experiment (LBNE) will provide a unique, world-leading program for the exploration of key questions at the forefront of particle physics and astrophysics.

Chief among its potential discoveries is that of matter-antimatter symmetry violation in neutrino flavor mixing — a step toward unraveling the mystery of matter generation in the early Universe. Independently, determination of the neutrino mass ordering and precise measurement of neutrino mixing parameters by LBNE may reveal new fundamental symmetries of Nature.

To achieve its ambitious physics objectives as a world-class facility, LBNE has been conceived around three central components:

1. an intense, wide-band neutrino beam
2. a fine-grained *near* neutrino detector just downstream of the neutrino source
3. a massive liquid argon time-projection chamber (LArTPC) deployed as a *far* neutrino detector deep underground, 1,300 km downstream; this distance between the neutrino source and far detector — the *baseline* — is measured along the line of travel through the Earth

The neutrino beam and near detector will be installed at the Fermi National Accelerator Laboratory (Fermilab), in Batavia, Illinois. The far detector will be installed at the Sanford Underground Research Facility in Lead, South Dakota.

The location of its massive high-resolution far detector deep underground will enable LBNE to significantly expand the search for proton decay as predicted by Grand Unified Theories, as well as study the dynamics of core-collapse supernovae through observation of their neutrino bursts, should any occur in our galaxy during LBNE's operating lifetime.

The near neutrino detector will enable high-precision measurements of neutrino oscillations, thereby enhancing the sensitivity to matter-antimatter symmetry violations and will exploit the potential of high-intensity neutrino beams as probes of new physics.

With its extensively developed design and flexible configuration, LBNE provides a blueprint for an experimental program made even more relevant by recent neutrino mixing parameter measurements.

1.1 Overview

Although neutrinos are the most abundant of known matter particles (fermions) in the Universe, their properties are the least well understood. The very existence of neutrino mass constitutes evidence of physics beyond the Standard Model. Understanding the nature of neutrinos has consequently become an essential goal for particle physics.

Observations of oscillations of neutrinos from one type (flavor) to another in numerous recent experiments have provided evidence for neutrino flavor mixing and for small, but nonzero, neutrino masses. The framework characterizing these observations is similar to that describing corresponding phenomena in the quark sector, but with a very different pattern of mixing angle values. As in the quark case, this framework involves a phase parameter, $\delta_{\rm CP}$, that changes sign under combined charge conjugation and parity (CP) reversal operations and thus would lead to CP symmetry-violating asymmetries between the pattern of oscillations for neutrinos and antineutrinos. While groundbreaking on its own, the observation of such asymmetries would also provide an experimental underpinning for the basic idea of leptogenesis* as an explanation for the Baryon Asymmetry of the Universe (BAU).

Neutrino oscillation data so far tell us about differences in the squared masses of the neutrino mass states, and about the sign of the mass-squared difference between two of the states, but not about the difference of those with respect to the third, which may be heavier (*normal* ordering) or lighter (*inverted* ordering) than the other two. Resolving this neutrino mass hierarchy ambiguity, along with precise measurements of neutrino mixing angles, would have significant theoretical, cosmological and experimental implications. One important consequence of mass hierarchy determination, in particular, would be the impact on future experiments designed to determine whether — uniquely among the fundamental fermions — neutrinos are their own antiparticles, so-called *Majorana* particles. Though long suspected, this hypothesis that neutrinos are Majorana particles has yet to be either established or ruled out. Strong evidence for the *inverted* hierarchy would establish conditions required by the next generation of neutrinoless double-beta decay searches to settle this question even with a null result (no observation). Because the forward scattering of neutrinos in matter alters the oscillation pattern in a hierarchy-dependent way, the long baseline of LBNE — with the neutrinos traveling through the Earth's mantle — enables a decisive determination of the hierarchy, independent of the value of $\delta_{\rm CP}$.

Additionally, the high-precision determination of oscillation parameters such as mixing angles and squared-mass differences will provide insight into the differences between the quark and lepton mixing patterns, which is necessary for deciphering the flavor structure of physics in the Standard Model. Taken together, the above suite of measurements will thoroughly test the standard three-neutrino flavor paradigm that guides our current understanding, and will provide greatly extended

*Leptogenesis refers to the mechanisms that generated an asymmetry between leptons and antileptons in the early Universe, described in Section 2.2.1.

sensitivity to signatures for nonstandard neutrino interactions in matter.

The arena of non-accelerator physics using massive underground detectors such as the LBNE far detector is also ripe with discovery potential. The observation of nucleon decay would be a watershed event for the understanding of physics at high energy scales. Neutrinos from supernovae are expected to provide key insights into the physics of gravitational collapse, and may also reveal fundamental properties of the neutrino.

Among massive detectors designed for neutrino and nucleon decay physics, the LArTPC technology offers unmatched capabilities for position and energy resolution and for high-precision reconstruction of complex interaction topologies over a broad energy range. It also provides a compact, scalable approach for achieving the required sensitivity to the primary physics signatures to be explored by LBNE. As these capabilities are also important for non-accelerator neutrino physics, LBNE will complement the large, underground water Cherenkov and/or scintillator-based detectors that may be operating in parallel. LArTPC detectors are especially well-suited to proton decay modes such as the supersymmetry-favored $p \rightarrow K^+\overline{\nu}$ mode, uniquely providing detection efficiency and background rejection sufficient to enable a discovery with a single well-reconstructed event. With regard to supernova-neutrino detection, liquid argon detectors are primarily sensitive to the ν_e component of the flux, while $\overline{\nu}_e$ interactions dominate for water and scintillator-based detectors. Thus, LBNE will be sensitive to different features of the supernova-neutrino production process. Finally, the LArTPC technology opens up an avenue for precision studies of oscillation physics with atmospheric neutrinos, thereby augmenting the results of the beam-based measurements at the core of the experiment.

The highly capable near detector will measure the absolute flux and energy scales of all four neutrino species in the LBNE beam, as well as neutrino cross sections on argon, water, and other nuclear targets in the beam's energy range. These measurements are needed to attain the ultimately desired precision of the oscillation parameter measurements. Additionally, the near detector will enable a broad range of precision neutrino-interaction measurements, thereby adding a compelling scientific program of its own.

The unique combination in LBNE of a 1,300−km baseline, exceptional resolution, large target mass and deep underground location offers opportunity for discovery of entirely unanticipated phenomena. History shows that ambitious scientific endeavors with leading-edge instruments have often been rewarded with unexpected signatures of new physics.

LBNE is an extensively developed experiment whose execution will have substantial impact on the overall direction of high energy physics (HEP) in the U.S. The U.S. Department of Energy (DOE) has endorsed the science objectives of LBNE, envisioning the experiment as a phased program, and has given first stage (CD-1) approval with a budget of $867M toward the initial phase. The science scope of this and subsequent phases will depend on the level of investment by additional national and international partners.

This document outlines the LBNE physics program and how it may evolve in the context of long-term planning studies [1]. The physics reach of this program is summarized under scenarios that are consistent with short-, medium- and long-term considerations. The general conclusions regarding the scientific capabilities of LBNE in a phased program are twofold:

1. A full-scope LBNE will provide an exciting broad-based physics program with exceptional capabilities for all of the identified core physics objectives, and many additional ones.
2. A first phase with a LArTPC far detector of fiducial[†] mass 10 kt[‡] or greater will substantially advance the field of neutrino oscillation physics while laying the foundations for a broader physics program in a later phase.

Section 1.2 provides the context for development of LBNE as a phased program that maintains flexibility for enhancements in each of its stages through the contributions of additional partners. The physics reach of LBNE at various stages is summarized in Section 1.3.

[†]In neutrino experiments, not all neutrino interactions in the instrumented (active) volume of a detector are used for physics studies. Only interactions that are well contained within the instrumented volume are used. The smaller volume of detector that encompasses the neutrino interactions is known as the *fiducial volume* and the target mass contained within it is known as the *fiducial mass*. Unless otherwise noted, this document will use fiducial mass to characterize the far detector size.

[‡]The *kt* refers to a metric kiloton, equivalent to 1,000 kg.

1.2 Development of a World-Class Experiment

To achieve the transformative physics goals of LBNE in an era of highly constrained funding for basic research in the U.S., the conceptual design has evolved so as to provide a scalable, phased and global approach, while maintaining a U.S. leadership role as the host for a global facility. International partnerships are being actively pursued to both enhance and accelerate the LBNE Project.

LBNE's primary beamline is designed to operate initially with a beam power of 1.2 MW, upgradable to 2.3 MW. This beamline extracts protons with energies from 60 to 120 GeV from the Fermilab Main Injector. The protons collide with a target to generate a secondary beam of charged particles, which in turn decay to generate the neutrino beam.

The liquid argon TPC far detector technology combines fine-grained tracking with total absorption calorimetry. Installed 4,850 ft underground to minimize backgrounds, this detector will be a powerful tool for long-baseline neutrino oscillation physics and underground physics such as proton decay, supernova neutrinos and atmospheric neutrinos. The far detector design is scalable and flexible, allowing for a phased approach, with an initial fiducial mass of at least 10 kt and a final configuration of at least 34 kt.

A high-precision near detector is planned as a separate facility allowing maximal flexibility in phasing and deployment.

The concept of a high-intensity neutrino beam directed toward a distant, massive underground detector to simultaneously investigate the nature of the neutrino, proton decay and astrophysical sources of neutrinos has been under serious investigation since the late 1990s [2,3,4,5,6,7,8,9]. Since that time both the science goals and concepts for implementation have been the subject of intense study and review by distinguished panels. These panels include the National Academies Neutrino Facilities Assessment Committee in 2003 [10], the National Science and Technology Council Committee on Science in 2004 [11], the National Academies EPP2010 panel in 2006 [12], the HEPAP/NSAC Neutrino Scientific Assessment Group in 2007 [13], the HEPAP Particle Physics Project Prioritization Panel (P5) in 2008 [14], the National Academies ad hoc Committee to Assess the Science Proposed for DUSEL in 2011 [15], and most recently the HEPAP Facilities Subpanel in 2013 [16]. High-level studies performed in Europe and Asia have come to similar conclusions (e.g., [17]) about the merits and feasibility of such a program.

1.2.1 Long-Term Vision

LBNE as described in this document has been developed by a collaboration formally established in 2009, which currently comprises over 475 collaborators from over 80 institutions in six countries. In January 2010 the DOE formally recognized the LBNE science objectives with approval of the mission need statement (CD-0) [18]. This action established LBNE as a DOE project. Fermilab has recognized LBNE as a central component of its long-term future program.

The central role of LBNE within the U.S. particle physics program has been acknowledged in other documents prepared for the 2013 particle physics community planning exercise [1], including the Project X Physics Book [19] and the reports from Intensity Frontier working groups on neutrino physics [20] and baryon number violation [21].

The LBNE conceptual design reflects a flexible and cost-effective approach to next-generation neutrino physics experiments that maintains a world-leadership role for the U.S. over the long term. The full-scope LBNE includes a 34−kt fiducial mass (50−kt total) far detector located in a new experimental area to be excavated at the 4,850-ft level of the Sanford Underground Research Facility[§] in the former Homestake Mine, and a fine-grained near neutrino detector located on the Fermilab site. Simultaneous construction of a new neutrino beamline at Fermilab would permit operation with an initial beam power of 1.2 MW, enabled by upgrades to the front end of the accelerator complex carried out within the Proton Improvement Plan-II (PIP-II) program [22]. In anticipation of potential enhancements beyond PIP-II [23], the beamline is designed to support upgrades to accommodate a beam power of 2.3 MW. The 1,300−km baseline is in the optimal range for the neutrino oscillation program. The cosmic ray shielding provided by the deep underground site for the far detector enables the non-accelerator portion of the physics program, including proton decay searches, detailed studies of neutrino bursts from galactic supernovae, and precision analyses of atmospheric-neutrino samples.

The overall physics reach of LBNE is predominantly limited by detector mass. From the outset, a guiding principle of the far detector design has been scalability. The conceptual design for the full-scope detector, consisting of two identical 17−kt (25−kt total) TPC modules housed within separate vessels (cryostats), employs technology developed by the liquefied natural gas (LNG) storage and transport industry. The TPC modules themselves consist of arrays of modular anode and cathode plane assemblies (APAs and CPAs) that are suspended from rails affixed to the top of the cryostats. The APA/CPA dimensions are chosen for ease of transportation and installation. The modularity of the detectors allows flexibility in the geometry and phased construction of the LBNE far detector complex. Cost-effective designs for larger detector masses are readily obtained by increasing the vessel size and simply adding APA/CPA units, thereby also exploiting economies of scale and benefiting from an increased ratio of volume to surface area. Detector mass may also be increased through the addition of distinct detectors of the same or a different technology, either

[§]Much larger detectors could also be accommodated at this facility.

during initial construction or in a later phase.

1.2.2 Present Status of the LBNE Project

Since DOE CD-0 approval, a compete conceptual design for the full-scope LBNE has been developed, consisting of a 34−kt LArTPC far detector located 4,850 feet underground, a 1,300−km baseline, a highly capable near neutrino detector, and a multi-megawatt-capable neutrino beamline. This design has been thoroughly reviewed, and found to be sound, most recently at a Fermilab Director's CD-1 Readiness Review in March 2012 [24]. Since then, considerable effort has been devoted to understanding how the LBNE Project can be staged so as to accommodate anticipated budget conditions while maintaining compelling physics output at each stage [25]. This process led to a first-phase configuration that was reviewed by the DOE in October [26] and November 2012 [27], and that received CD-1 approval [28] in December 2012. This configuration [29,30,31,32,33,34] maintained the most important aspects of LBNE: the 1,300−km baseline to the Sanford Underground Research Facility, a large — of order tens of kilotons in fiducial mass — LArTPC far detector design, and a multi-megawatt-capable, wide-band neutrino/antineutrino beam. However, the far detector size was limited at CD-1 to 10 kt and placed at the surface under minimal overburden, and the near detector was deferred to a later phase.

The DOE CD-1 approval document [28] explicitly allows adjustment of the scope of the first phase of LBNE in advance of CD-2 if additional partners bring significant contributions to LBNE. *Using the CD-1 DOE funding as the foundation, the goal for the first phase of LBNE is a deep underground far detector of at least 10 kt, placed in a cavern that will accommodate up to a 34−kt detector, coupled with a 1.2−MW neutrino beamline, and a highly capable near detector.* This goal has been endorsed by the LBNE Collaboration, the LBNE Project, the Fermilab directorate, and the DOE Office of High Energy Physics. Since a large portion of the LBNE Project cost is in civil infrastructure, funding contributions from new partners could have considerable impact on the experimental facilities, and therefore the physics scope, in the first phase.

1.2.3 Global Partnerships

Global conditions are favorable for significant international partnerships in developing and building LBNE. As an example, the 2013 update [17] of the European Strategy for Particle Physics document places long-baseline neutrino physics among the highest-priority large-scale activities for Europe, recognizing that it requires "significant resources, sizeable collaborations and sustained commitment." It includes the primary recommendation of exploring "the possibility of major participation in leading long-baseline neutrino projects in the U.S. and Japan." As of March 2014 the LBNE Collaboration includes institutions from the U.S., Brazil, India, Italy, Japan and the United Kingdom. Discussions with a number of potential international partners are underway — some already at an advanced stage. A summary of recent progress in these discussions can be found in the presentation of LBNE status to the U.S. Particle Physics Projects Prioritization Panel in November 2013 [35].

1.2.4 Context for Discussion of Physics Sensitivities

To reflect the physics reach of various phasing scenarios, this document presents many of the parameter sensitivities for the accelerator-based neutrino topics as functions of exposure, defined as the product of detector fiducial mass, beam power and run time. As needed, the capabilities of both a 10−kt first-phase configuration and the full 34−kt configuration are explicitly highlighted, each benchmarked for six to ten years of operations with a 1.2−MW beam power from the PIP-II accelerator upgrades at Fermilab. Since the U.S. program planning exercises currently under way look beyond the present decade, this document also presents the long-term physics impact of the full-scope LBNE operating with the 2.3−MW beam power available with further anticipated upgrades to the Fermilab accelerator complex.

1.3 The LBNE Physics Program

The technologies and configuration of the planned LBNE facilities offer excellent sensitivity to a range of physics processes:

- The muon-neutrino (ν_μ) beam produced at Fermilab with a peak flux at 2.5 GeV, coupled to the baseline of 1,300 km, will present near-optimal sensitivity to neutrino/antineutrino charge-parity (CP) symmetry violation effects.
- The long baseline of LBNE will ensure a large matter-induced asymmetry in the oscillations of neutrinos and antineutrinos, thus providing a clear, unambiguous determination of the mass ordering of the neutrino states.
- The near detector located just downstream of the neutrino beamline at Fermilab will enable high-precision long-baseline oscillation measurements as well as precise measurements and searches for new phenomena on its own using the high-intensity neutrino beam.
- The deep-underground LArTPC far detector will provide superior sensitivities to proton decay modes with kaons in the final states, modes that are favored by many Grand Unified and supersymmetric theoretical models.
- Liquid argon as a target material will provide unique sensitivity to the electron-neutrino (ν_e) component of the initial burst of neutrinos from a core-collapse supernova.
- The excellent energy and directional resolution of the LArTPC will allow novel physics studies with atmospheric neutrinos.

This section summarizes LBNE's potential for achieving its core physics objectives based on the current experimental landscape, scenarios for staging LBNE, and the technical capabilities of LBNE at each stage.

LBNE's capability to achieve the physics objectives described in this document has been subject to extensive review over a number of years. In addition to the various reviews of the LBNE Project described in Section 1.2, reviews that focused strongly on LBNE's science program include the DOE Office of Science Independent Review of Options for Underground Science in the spring of 2011 [36], the LBNE Science Capabilities Review (by an external panel commissioned by LBNE) [37] in the fall of 2011, and the LBNE Reconfiguration Review [25] in the summer of 2012.

1.3.1 Neutrino Mixing, Mass Hierarchy and CP Violation

Neutrino Mass Hierarchy: The 1,300−km baseline establishes one of LBNE's key strengths: sensitivity to the matter effect. This effect leads to a large discrete asymmetry in the $\nu_\mu \to \nu_e$ versus $\overline{\nu}_\mu \to \overline{\nu}_e$ oscillation probabilities, the sign of which depends on the mass hierarchy (MH). At 1,300 km this asymmetry is approximately $\pm 40\%$ in the region of the peak flux; this is larger than the maximal possible CP-violating asymmetry associated with $\delta_{\rm CP}$, meaning that both the MH and $\delta_{\rm CP}$ can be determined unambiguously with high confidence within the same experiment using the beam neutrinos.

In detail, the sensitivity of LBNE depends on the actual values of poorly known mixing parameters (mainly $\delta_{\rm CP}$ and $\sin^2\theta_{23}$), as well as the true value of the MH itself. The discrimination between the two MH hypotheses is characterized as a function of the *a priori* unknown true value of $\delta_{\rm CP}$ by considering the difference, denoted $\Delta\chi^2$, between the $-2\log\mathcal{L}$ values calculated for a data set with respect to these hypotheses, considering all possible values of $\delta_{\rm CP}$¶. In terms of this test statistic, the MH sensitivity of LBNE with 34 kt, and running three years each in ν and $\overline{\nu}$ modes in a 1.2−MW beam is illustrated in Figure 1.1 for the case of normal hierarchy for two different values of $\sin^2\theta_{23}$. Across the overwhelming majority of the parameter space for the mixing parameters that are not well known (mainly $\delta_{\rm CP}$ and $\sin^2\theta_{23}$), LBNE's determination of the MH will be definitive, but even for unfavorable combinations of the parameter values, a statistically ambiguous outcome is highly unlikely.

The least favorable scenario corresponds to a true value of $\delta_{\rm CP}$ in which the MH asymmetry is maximally offset by the leptonic CP asymmetry, and where, independently, $\sin^2\theta_{23}$ takes on a value at the low end of its experimentally allowed range. For this scenario, studies indicate that with a 34−kt LArTPC operating for six years in a 1.2−MW beam, LBNE on its own can (in a typical data set) distinguish between normal and inverted hierarchy with $|\Delta\chi^2| = \overline{|\Delta\chi^2|} = 25$. This corresponds to a $\geq 99.9996\%$ probability of determining the correct hierarchy. In $> 97.5\%$ of data sets, LBNE will measure $|\Delta\chi^2| > 9$ in this scenario, where measuring $|\Delta\chi^2| = 9$ with an expected value of 25 corresponds to a significance in excess of three Gaussian standard deviations.

Concurrent analysis of the corresponding atmospheric-neutrino samples in an underground detector will improve the precision with which the MH is resolved. It is important to note that for the initial stages of LBNE, a greatly improved level of precision in the determination of the MH can be achieved by incorporating constraints from NOνA and T2K data. With an initial 10−kt detector, for half the range of possible $\delta_{\rm CP}$ values, the expected significance exceeds $\overline{\Delta\chi^2} = 25$; again this corresponds to a $\geq 99.9996\%$ probability of determining the correct hierarchy. To put this in context, it is notable that even an extended NOνA program [38] at four times its nominal exposure

¶For the case of the MH determination, the usual association of this test statistic with a χ^2 distribution for one degree of freedom is incorrect; additionally the assumption of a Gaussian probability density implicit in this notation is not exact. The discussion in Chapter 4 provides a brief description of the statistical considerations.

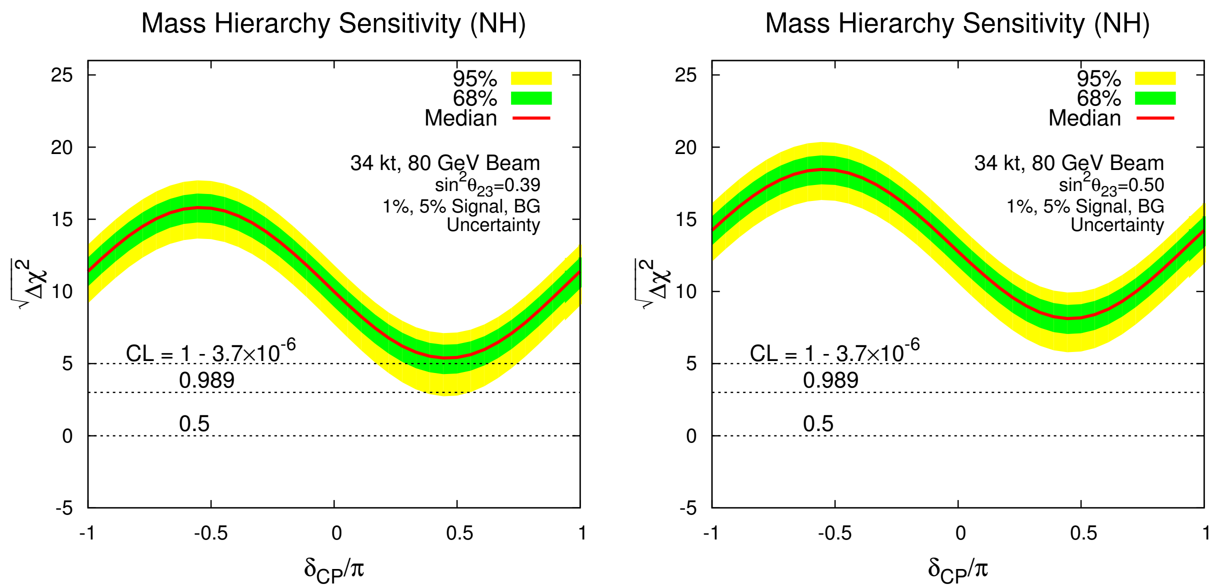

Figure 1.1: The square root of the mass hierarchy discrimination metric $\Delta\chi^2$ is plotted as a function of the unknown value of $\delta_{\rm CP}$ for the full-scope LBNE with 34 kt, 3+3 ($\nu + \overline{\nu}$) years of running in a 1.2−MW beam, assuming normal hierarchy. The plot on the left is for an assumed value of $\sin^2\theta_{23} = 0.39$ (based on global fits and assuming worst-case θ_{23} octant), while that on the right is for $\sin^2\theta_{23} = 0.5$ (maximal mixing). In each plot, the red curve represents the median experimental value expected ($\sqrt{\overline{\Delta\chi^2}}$), estimated using a data set absent statistical fluctuations, while the green and yellow bands represent the range of $\Delta\chi^2$ values expected in 68% and 95% of all possible experimental instances, respectively. For certain values of $\sqrt{\Delta\chi^2}$, horizontal lines are shown, indicating the corresponding confidence levels ($1-\alpha$ in the language of hypothesis testing) with which a typical experiment ($\beta = 0.5$) correctly determines the MH, computed according to a Bayesian statistical formulation (Section 4.3.1 for further discussion).

(of six years of operation at 700 kW), would have coverage at the $\overline{\Delta\chi^2} = 9$ level or better for only 40% of the $\delta_{\rm CP}$ range.

CP Violation and the Measurement of $\boldsymbol{\delta_{\rm CP}}$: The LBNE program has two somewhat distinct objectives with regard to CP symmetry violation in the $\nu_\mu \to \nu_e$ oscillation channel. First, LBNE aims to make a precise determination of the value of $\delta_{\rm CP}$ within the context of the standard three-flavor mixing scenario described by the PMNS matrix (discussed in Section 2.2). Second, and perhaps more significantly, LBNE aims to observe a signal for leptonic CP violation, independent of the underlying nature of neutrino oscillation phenomenology. Within the standard three-flavor mixing scenario, such a signal will be observable, provided $\delta_{\rm CP}$ is not too close to either of the values for which there is no CP violation (zero and π). Together, the pursuit of these two goals provides a thorough test of the standard three-flavor scenario.

Figure 1.2 shows the expected 1σ resolution for $\delta_{\rm CP}$ as a function of exposure for a proton beam power of 1.2 MW. At this beam power, in a six-year run, a 10−kt far detector will be able to measure $\delta_{\rm CP}$ to $\pm\ 20^\circ - 30^\circ$ (depending on its value), independent of other experiments. A full-scope LBNE operating with multi-megawatt beam power in a later phase, will achieve a precision better than $\pm 10°$, comparable to the current precision on the CP phase in the CKM matrix in the quark sector.

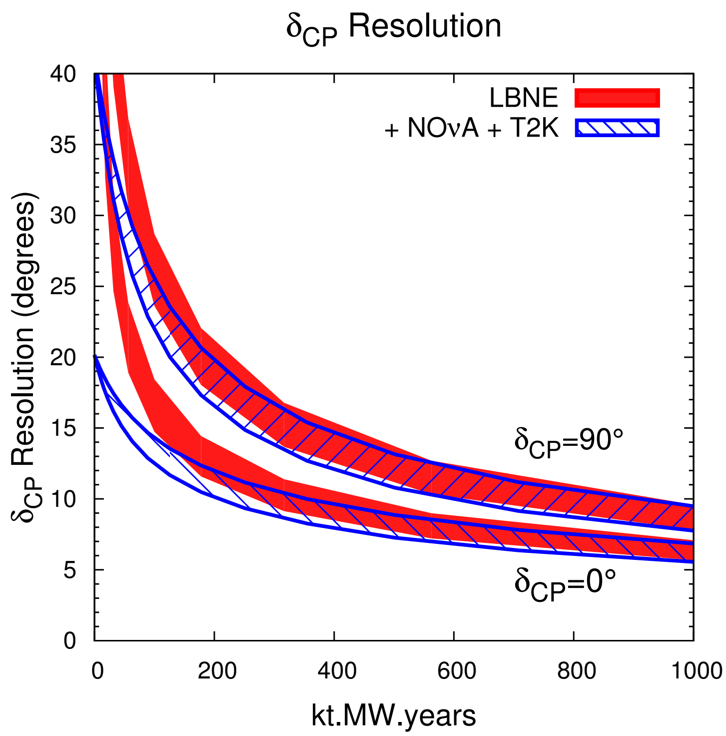

Figure 1.2: The expected 1σ resolution for $\delta_{\rm CP}$ as a function of exposure in detector mass (kiloton) $\times$ beam power (MW) $\times$ time (years). The red curve is the precision that could be obtained from LBNE alone, while the blue curve represents the combined precision from LBNE plus the T2K and NOνA experiments. The width of the bands represents variation with the range of beamline design parameters and proton energy values being considered.

LBNE with a $10-$kt detector, in combination with T2K and NOνA, will determine leptonic CP violation with a precision of 3σ or greater for $\approx 40\%$ of $\delta_{\rm CP}$ values in a six-year run with $1.2-$MW beam power. It is important to note that LBNE alone dominates the combined sensitivity and that T2K and NOνA have very limited sensitivity to CP violation on their own. To reach 5σ for an appreciable fraction of the range of $\delta_{\rm CP}$, the full-scope LBNE will be needed to control systematic errors while accumulating large enough samples in the far detector to reach this level of sensitivity. No experiment can provide coverage at 100%, since CP violation effects vanish as $\delta_{\rm CP} \to 0$ or π.

Determination of $\sin^2 2\theta_{23}$ and Octant Resolution: In long-baseline experiments with ν_μ beams, the magnitude of ν_μ disappearance and ν_e appearance signals is proportional to $\sin^2 2\theta_{23}$ and $\sin^2 \theta_{23}$, respectively, in the standard three-flavor mixing scenario. Current ν_μ disappearance data are consistent with maximal mixing, $\theta_{23} = 45°$. To obtain the best sensitivity to both the magnitude of its deviation from $45°$ as well as its sign (θ_{23} octant), a combined analysis of the two channels is needed [39]. As demonstrated in Chapter 4, a 10−kt LBNE detector will be able to resolve the θ_{23} octant at the 3σ level or better for θ_{23} values less than 40° or greater than 50°, provided $\delta_{\rm CP}$ is not too close to zero or π. A full-scope LBNE will measure θ_{23} with a precision of 1° or less, even for values within a few degrees of 45°.

1.3.2 Nucleon Decay Physics Motivated by Grand Unified Theories

The LBNE far detector will significantly extend lifetime sensitivity for specific nucleon decay modes by virtue of its high detection efficiency relative to water Cherenkov detectors and its low background rates. As an example, LBNE has enhanced capability for detecting the $p \to K^+\overline{\nu}$ channel, where lifetime predictions from supersymmetric models extend beyond, but remain close to, the current (preliminary) Super-Kamiokande limit of $\tau/B > 5.9 \times 10^{33}$ year (90% CL) from a 260−kt · year exposure [40][‖]. The signature for an isolated semi-monochromatic charged kaon in a LArTPC is distinctive, with multiple levels of redundancy. A 34−kt LBNE far detector deep underground will reach a limit of 3×10^{34} year after ten years of operation (Figure 1.3), and would see nine events with a background of 0.3 should τ/B be 1×10^{34} year, just beyond the current limit. Even a 10−kt detector (placed underground) would yield an intriguing signal of a few events after a ten-year exposure in this scenario.

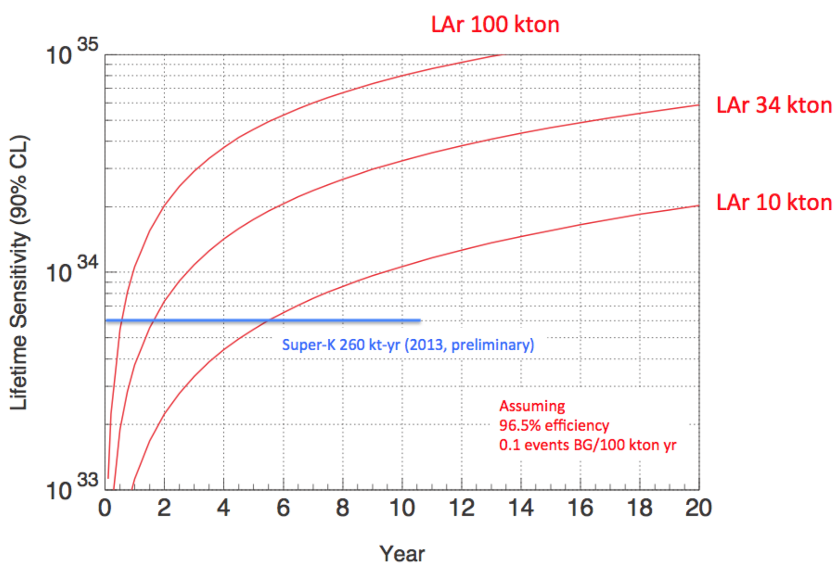

Figure 1.3: Sensitivity to the decay $p \to K^+\overline{\nu}$ as a function of time for underground liquid argon detectors with different masses.

‖The lifetime shown here is divided by the branching fraction for this decay mode, τ/B, and as such is a *partial lifetime*.

1.3.3 Supernova-Neutrino Physics and Astrophysics

The neutrinos from a core-collapse supernova are emitted in a burst of a few tens of seconds duration, with about half in the first second. Energies are in the range of a few tens of MeV, and the luminosity is divided roughly equally between the three known neutrino flavors. Currently, experiments worldwide are sensitive primarily to electron antineutrinos ($\overline{\nu}_e$), with detection through the inverse-beta decay process on free protons**, which dominates the interaction rate in water and liquid-scintillator detectors. Liquid argon has a unique sensitivity to the electron-neutrino (ν_e) component of the flux, via the absorption interaction on ^{40}Ar as follows:

$$\nu_e + {}^{40}\text{Ar} \quad\rightarrow\quad e^- + {}^{40}\text{K}^*$$

This interaction can be tagged via the coincidence of the emitted electron and the accompanying photon cascade from the $^{40}\text{K}^*$ de-excitation. About 900 events would be expected in a 10−kt fiducial mass liquid argon detector for a supernova at a distance of 10 kpc. In the neutrino channel the oscillation features are in general more pronounced, since the ν_e spectrum is always significantly different from the ν_μ (ν_τ) spectra in the initial core-collapse stages, to a larger degree than is the case for the corresponding $\overline{\nu}_e$ spectrum. Detection of a large neutrino signal in LBNE would help provide critical information on key astrophysical phenomena such as

1. the neutronization burst
2. formation of a black hole
3. shock wave effects
4. shock instability oscillations
5. turbulence effects

1.3.4 Precision Measurements with a High-Intensity Neutrino Source and High-Resolution Near Detector

The near neutrino detector will provide precision measurements of neutrino interactions, which in the medium to long term are essential for controlling the systematic uncertainties in the long-baseline oscillation physics program. The near detector, which will include argon targets, will measure the absolute flux and energy-dependent shape of all four neutrino species, ν_μ, $\overline{\nu}_\mu$, ν_e and $\overline{\nu}_e$ to accurately predict for each species the far/near flux ratio as a function of energy. It will also measure the four-momenta of secondary hadrons, such as charged and neutral mesons, produced

**This refers to neutrino interactions with the nucleus of a hydrogen atom in H_2O in water detectors or in hydrocarbon chains in liquid scintillator detectors.

in the neutral and charged current interactions that constitute the dominant backgrounds to the oscillation signals.

With 240,000 (85,000) ν_μ ($\overline{\nu}_\mu$) charged current and 90,000 (35,000) neutral current interactions per ton per 1×10^{20} protons-on-target at 120 GeV in the ν ($\overline{\nu}$) beam, the near detector will also be the source of data for a rich program of neutrino-interaction physics in its own right. These numbers correspond to 10^7 neutrino interactions per year for the range of beam configurations and near detector designs under consideration. Measurement of fluxes, cross sections and particle production over a large energy range of 0.5 GeV to 50 GeV (which can also help constrain backgrounds to proton decay signals from atmospheric neutrinos) are the key elements of this program. Furthermore, since the near detector data will feature very large samples of events that are amenable to precision reconstruction and analysis, they can be exploited for sensitive studies of electroweak physics and nucleon structure, as well as for searches for new physics in unexplored regions (heavy sterile neutrinos, high-Δm^2 oscillations, light Dark Matter particles, and so on).

1.4 Summary

The LBNE physics program has been identified as a priority of the global HEP community for the coming decades. The facilities available in the U.S. are the best suited internationally to carry out this program and the substantially developed LBNE design is at the forefront of technical innovations in the field. Timely implementation of LBNE will significantly advance the global HEP program and assure continued intellectual leadership for the U.S. within this community.

This chapter has touched only briefly on the most prominent portion of the full suite of physics opportunities enabled by LBNE. The following chapters cover these in detail, as well as topics that were omitted here in the interest of brevity and focus. In Chapter 9 progress toward LBNE physics milestones is addressed, based on one potential scenario for the operation of successive stages of LBNE detector and PIP-II implementations, and the broad role of LBNE is discussed in the context of such scenarios. The present chapter concludes with a summary of its key points.

The primary science goals of LBNE are drivers for the advancement of particle physics. The questions being addressed are of wide-ranging consequence: the origin of flavor and the generation structure of the fermions (i.e., the existence of three families of quark and lepton flavors), the physical mechanism that provides the CP violation needed to generate the Baryon Asymmetry of the Universe, and the high energy physics that would lead to the instability of matter. Achieving these goals requires a dedicated, ambitious and long-term program. No other proposed long-baseline neutrino oscillation program with the scientific scope and sensitivity of LBNE is as advanced in terms of engineering development and project planning. A phased program with a far detector of even modest size in the initial stage (e.g., 10 kt) will enable exciting physics in the intermediate term, including a definitive mass hierarchy determination and a measurement of the CP phase without ambiguities, while providing the fastest route toward achieving the full range of LBNE's science objectives. Should LBNE find that the CP phase is not zero or π, it will have found strong indications ($> 3\sigma$) of leptonic CP violation. Global interest is favorable for contributions from international partners to accelerate and enhance this program, including the LBNE first-phase scope.

Implementing the vision that has brought LBNE to this point will allow the U.S. to host this world-leading program, bringing together the world's neutrino community to explore key questions at the forefront of particle physics and astrophysics. Moreover, the excitement generated by both the technical challenges of mounting LBNE and the potential physics payoffs are widely shared — among the generation of scientists who have been paving the way for these innovations, as well as the young scientists for whom LBNE will provide numerous research opportunities over the next two decades.

Chapter 2 The Science of LBNE

The Standard Model of particle physics describes all of the known fundamental particles and the electroweak and strong forces that, in combination with gravity, govern today's Universe. The observation that neutrinos have mass is one demonstration that the Standard Model is incomplete. By exploring physics beyond the Standard Model, LBNE will address fundamental questions about the Universe:

What is the origin of the matter-antimatter asymmetry in the Universe? Immediately after the Big Bang, matter and antimatter were created equally, yet matter now dominates. By studying the properties of neutrino and antineutrino oscillations, LBNE is pursuing the most promising avenue for understanding this asymmetry.

What are the fundamental underlying symmetries of the Universe? Resolution by LBNE of the detailed mixing patterns and ordering of neutrino mass states, and comparisons to the corresponding phenomena in the quark sector, could reveal underlying symmetries that are as yet unknown.

Is there a Grand Unified Theory of the Universe? Experimental evidence hints that the physical forces observed today were unified into one force at the birth of the Universe. Grand Unified Theories (GUTs), which attempt to describe the unification of forces, predict that protons should decay, a process that has never been observed. LBNE will probe proton lifetimes predicted by a wide range of GUT models.

How do supernovae explode? The heavy elements that are the key components of life — such as carbon — were created in the super-hot cores of collapsing stars. LBNE's design will enable it to detect the neutrino burst from core-collapse supernovae. By measuring the time structure and energy spectrum of a neutrino burst, LBNE will be able to elucidate critical information about the dynamics of this special astrophysical phenomenon.

What more can LBNE discover about the Standard Model? The high intensity of the LBNE neutrino beam will provide a unique probe for precision tests of Standard Model processes as well as searches for new physics in unexplored regions.

LBNE has been designed to address a wide range of scientific topics using well-characterized, high-intensity, accelerator-based neutrino beams, a long baseline for neutrino oscillations, and a very large, deep-underground detector with excellent particle identification capabilities over a large range of energies. While maximizing the reach for a core set of scientific objectives, its design — described in Chapter 3 — accommodates the flexibility to extend the scope of measurements as additional resources become available.

2.1 Scientific Objectives of LBNE

The scientific objectives of LBNE have been categorized into primary, secondary, and additional secondary objectives according to priorities developed and agreed upon by the LBNE community and accepted as part of the CD-0 (Mission Need) approval by the U.S. Department of Energy [41].

Primary objectives of LBNE, in priority order, are the following measurements:

1. precision measurements of the parameters that govern $\nu_\mu \to \nu_e$ oscillations; this includes precision measurement of the third mixing angle θ_{13}, measurement of the charge-parity (CP) violating phase $\delta_{\rm CP}$, and determination of the neutrino mass ordering (the sign of $\Delta m^2_{31} = m^2_3 - m^2_1$), the so-called *mass hierarchy*
2. precision measurements of the mixing angle θ_{23}, including the determination of the octant in which this angle lies, and the value of the mass difference, $|\Delta m^2_{32}|$, in $\nu_\mu \to \nu_{e,\mu}$ oscillations
3. search for proton decay, yielding significant improvement in the current limits on the partial lifetime of the proton (τ/BR) in one or more important candidate decay modes, e.g., $p \to K^+\overline{\nu}$
4. detection and measurement of the neutrino flux from a core-collapse supernova within our galaxy, should one occur during the lifetime of LBNE

In a phased approach to LBNE, the goal of the first phase is to maximize the effectiveness of the facility to achieve the first two objectives, above. The mass hierarchy determination and the precision determination of θ_{23} will most likely be complete in the first phase of LBNE; while the precision determination of CP violation will require the full-scope LBNE, an initial measurement of the CP phase parameter $\delta_{\rm CP}$ will be performed in earlier phases.

Secondary objectives, which may also be enabled by the facility designed to achieve the primary objectives, include:

1. other accelerator-based, neutrino oscillation measurements; these could include further sensitivity to Beyond Standard Model (BSM) physics such as nonstandard interactions
2. measurements of neutrino oscillation phenomena using atmospheric neutrinos
3. measurement of other astrophysical phenomena using medium-energy neutrinos

Additional secondary objectives, the achievement of which may require upgrades to the facility that is designed to achieve the primary physics objectives (e.g., deployment of additional detector mass or alternate detector technologies), include:

1. detection and measurement of the diffuse supernova-neutrino flux
2. measurements of neutrino oscillation phenomena and of solar physics using solar neutrinos
3. measurements of astrophysical and geophysical neutrinos of low energy

In addition, a rich set of science objectives enabled by a sophisticated near neutrino detector have been identified. A primary and a secondary objective, respectively, are:

1. measurements necessary to achieve the primary physics research objectives listed above
2. studies of neutrino interactions that may be enabled either by the facility designed to achieve the primary objectives or by future upgrades to the facility and detectors; these include precision studies of the weak interaction, studies of nuclear and nucleon structure, and searches for new physics

2.2 Neutrino Three-Flavor Mixing, CP Violation and the Mass Hierarchy

The Standard Model of particle physics (Figure 2.1) presents a remarkably accurate description of the elementary particles and their interactions. However, its limitations beg deeper questions about Nature. The unexplained patterns of quarks, leptons, flavors and generations imply that a more fundamental underlying theory must exist. LBNE plans to pursue a detailed study of neutrino mixing, resolve the neutrino mass ordering, and search for CP violation in the lepton sector by studying the oscillation patterns of high-intensity ν_μ and $\overline{\nu}_\mu$ beams measured over a long baseline.

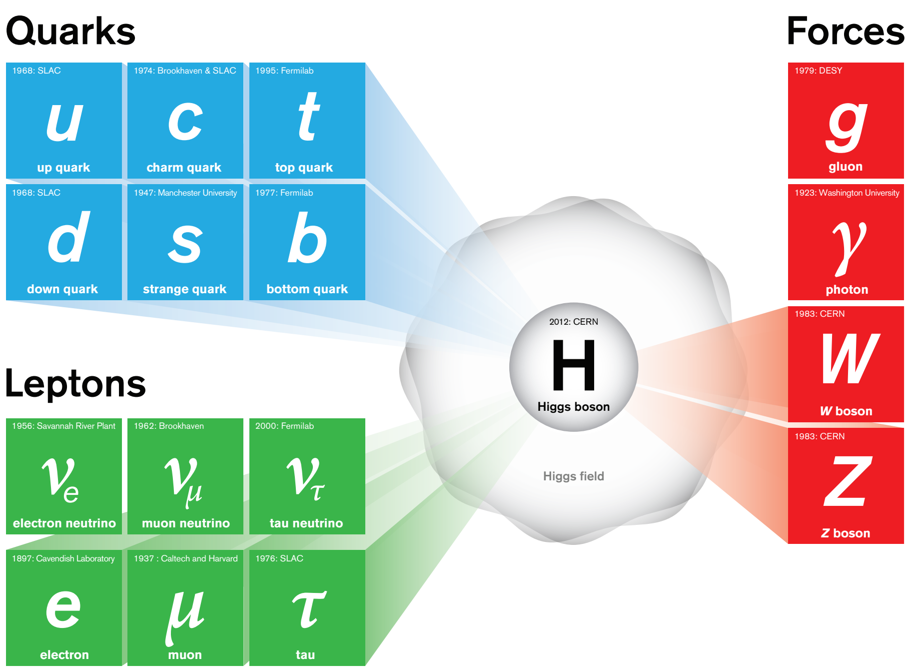

Figure 2.1: Known particles and forces in the Standard Model of particle physics. The quarks and leptons are arranged in pairs into three generations: $(u, d), (c, s), (t, b)$ and $(\nu_e, e), (\nu_\mu, \mu), (\nu_\tau, \tau)$, respectively. There are three known neutrino mass states ν_1, ν_2, ν_3 which are mixtures of the three neutrino flavors ν_e, ν_μ, ν_τ shown in this figure. The Standard Model includes the gluon (g), photon (γ) and $(W^\pm, Z^0)$ bosons that are the mediators of the strong, electromagnetic and weak interactions, respectively. The Higgs boson is a manifestation of the Higgs field that endows all the known particles with mass.

Results from the last decade, indicating that the three known types of neutrinos have nonzero mass, mix with one another and oscillate between generations, imply physics beyond the Standard Model [42]. Each of the three flavors of neutrinos, ν_e, ν_μ and ν_τ (Figure 2.1), is known to be a different mix of three mass eigenstates ν_1, ν_2 and ν_3 (Figure 2.2). In the Standard Model, the simple Higgs mechanism, which has now been confirmed by the observation of the Higgs boson [43,44], is responsible for both quark and lepton masses, mixing and charge-parity (CP) violation (the mechanism responsible for matter-antimatter asymmetries). However, the small size of neutrino masses and their relatively large mixing bears little resemblance to quark masses and mixing, suggesting that different physics — and possibly different mass scales — in the two sectors may be present, and motivating precision study of mixing and CP violation in the lepton sector.

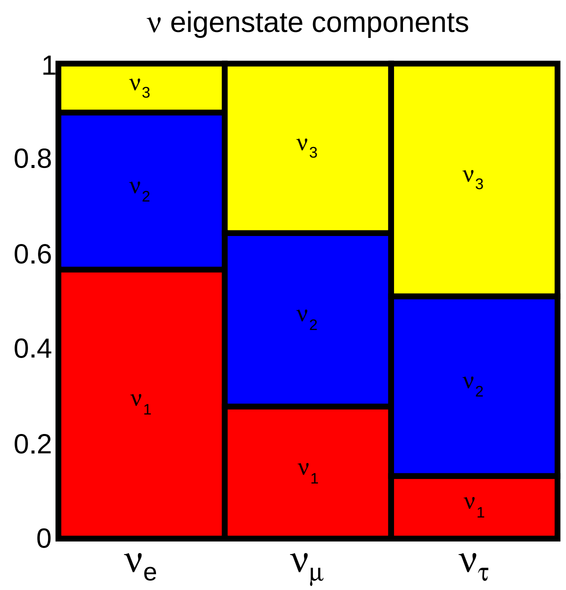

Figure 2.2: The neutrino mass eigenstate components of the known flavor eigenstates.

Neutrino oscillation arises from mixing between the flavor and mass eigenstates of neutrinos, corresponding to the weak and gravitational interactions, respectively. This three-flavor-mixing scenario can be described by a rotation between the weak-interaction eigenstate basis $(\nu_e,\ \nu_\mu,\ \nu_\tau)$ and the basis of states of definite mass $(\nu_1,\ \nu_2,\ \nu_3)$. In direct correspondence with mixing in the quark sector, the transformations between basis states is expressed in the form of a complex unitary matrix, known as the PMNS matrix :

$$\begin{pmatrix} \nu_e \\ \nu_\mu \\ \nu_\tau \end{pmatrix} = \underbrace{\begin{pmatrix} U_{e1} & U_{e2} & U_{e3} \\ U_{\mu 1} & U_{\mu 2} & U_{\mu 3} \\ U_{\tau 1} & U_{\tau 2} & U_{\tau 3} \end{pmatrix}}_{U_{\text{PMNS}}} \begin{pmatrix} \nu_1 \\ \nu_2 \\ \nu_3 \end{pmatrix}. \tag{2.1}$$

The PMNS matrix in full generality depends on just three mixing angles and a CP-violating phase. The mixing angles and phase are designated as $(\theta_{12},\ \theta_{23},\ \theta_{13})$ and $\delta_{\rm CP}$. This matrix can be parameterized as the product of three two-flavor mixing matrices as follows, where $c_{\alpha\beta} = \cos\theta_{\alpha\beta}$ and $s_{\alpha\beta} = \sin\theta_{\alpha\beta}$:

$$U_{\rm PMNS} = \underbrace{\begin{pmatrix} 1 & 0 & 0 \\ 0 & c_{23} & s_{23} \\ 0 & -s_{23} & c_{23} \end{pmatrix}}_{\rm I} \underbrace{\begin{pmatrix} c_{13} & 0 & e^{i\delta_{\rm CP}} s_{13} \\ 0 & 1 & 0 \\ -e^{i\delta_{\rm CP}} s_{13} & 0 & c_{13} \end{pmatrix}}_{\rm II} \underbrace{\begin{pmatrix} c_{12} & s_{12} & 0 \\ -s_{12} & c_{12} & 0 \\ 0 & 0 & 1 \end{pmatrix}}_{\rm III} \tag{2.2}$$

The parameters of the PMNS matrix determine the probability amplitudes of the neutrino oscillation phenomena that arise from mixing.

The relationship between the three mixing angles θ_{12}, θ_{23}, and θ_{13} and the mixing between the neutrino flavor and mass states can be described as follows [45]:

$$\tan^2\theta_{12} \ : \ \frac{\text{amount of } \nu_e \text{ in } \nu_2}{\text{amount of } \nu_e \text{ in } \nu_1} \tag{2.3}$$

$$\tan^2\theta_{23} \ : \ \text{ratio of } \nu_\mu \text{ to } \nu_\tau \text{ in } \nu_3 \tag{2.4}$$

$$\sin^2\theta_{13} \ : \ \text{amount of } \nu_e \text{ in } \nu_3 \tag{2.5}$$

The frequency of neutrino oscillation among the weak-interaction (flavor) eigenstates depends on the difference in the squares of the neutrino masses, $\Delta m^2_{ij} \equiv m^2_i - m^2_j$; a set of three neutrino mass states implies two independent mass-squared differences (Δm^2_{21} and Δm^2_{32}). The ordering of the mass states is known as the *neutrino mass hierarchy*. An ordering of $m_1 < m_2 < m_3$ is known as the *normal hierarchy* since it matches the ordering of the quarks in the Standard Model, whereas an ordering of $m_3 < m_1 < m_2$ is referred to as the *inverted hierarchy*.

Since each flavor eigenstate is a mixture of three mass eigenstates, there can be an overall phase difference between the quantum states, referred to as $\delta_{\rm CP}$. A nonzero value of this phase implies that neutrinos and antineutrinos oscillate differently — a phenomenon known as charge-parity (CP) violation. $\delta_{\rm CP}$ is therefore often referred to as the *CP phase* or the *CP-violating phase*.

The entire complement of neutrino experiments to date has measured five of the mixing parameters: the three angles θ_{12}, θ_{23} and (recently) θ_{13}, and the two mass differences Δm^2_{21} and Δm^2_{32}. The sign of Δm^2_{21} is known, but not that of Δm^2_{32}, which is the crux of the mass hierarchy ambiguity. The values of θ_{12} and θ_{23} are large, while θ_{13} is smaller [46]. The value of $\delta_{\rm CP}$ is unknown. The real values of the entries of the PMNS mixing matrix, which contains information on the strength of flavor-changing weak decays in the lepton sector, can be expressed in approximate form as

$$|U_{\rm PMNS}| \sim \begin{pmatrix} 0.8 & 0.5 & 0.2 \\ 0.5 & 0.6 & 0.6 \\ 0.2 & 0.6 & 0.8 \end{pmatrix}. \tag{2.6}$$

The three-flavor-mixing scenario for neutrinos is now well established. However, the mixing parameters are not known to the same precision as are those in the corresponding quark sector, and several important quantities, including the value of $\delta_{\rm CP}$ and the sign of the large mass splitting, are still undetermined. In addition, several recent anomalous experimental results count among their possible interpretations phenomena that do not fit this model [47,48,49,50].

The relationships between the values of the parameters in the neutrino and quark sectors suggest that mixing in the two sectors is qualitatively different. Illustrating this difference, the value of the entries of the CKM quark-mixing matrix (analogous to the PMNS matrix for neutrinos, and thus indicative of the strength of flavor-changing weak decays in the quark sector) can be expressed in approximate form as

$$|V_{\rm CKM}| \sim \begin{pmatrix} 1 & 0.2 & 0.004 \\ 0.2 & 1 & 0.04 \\ 0.008 & 0.04 & 1 \end{pmatrix} \tag{2.7}$$

and compared to the entries of the PMNS matrix given in Equation 2.6. As discussed in [51], the question of why the quark mixing angles are smaller than the lepton mixing angles is an important part of the "flavor problem."

Quoting the discussion in [20], "while the CKM matrix is almost proportional to the identity matrix plus hierarchically ordered off-diagonal elements, the PMNS matrix is far from diagonal and, with the possible exception of the U_{e3} element, all elements are $\mathcal{O}(1)$." One theoretical method often used to address this question involves the use of non-Abelian discrete subgroups of $SU(3)$ as flavor symmetries; the popularity of this method comes partially from the fact that these symmetries can give rise to the nearly *tri-bi-maximal*[*] structure of the PMNS matrix. Whether employing these flavor symmetries or other methods, any theoretical principle that attempts to describe the fundamental symmetries implied by the observed organization of quark and neutrino mixing — such as those proposed in unification models — leads to testable predictions such as sum rules between CKM and PMNS parameters [20,42,51,53]. Data on the patterns of neutrino mixing are already proving crucial in the quest for a relationship between quarks and leptons and their seemingly arbitrary generation structure. Table 2.1 displays the comparison between quark and lepton mixing

[*]Tri-bi-maximal mixing refers to a form of the neutrino mixing matrix with effective bimaximal mixing of ν_μ and ν_τ at the atmospheric scale ($L/E \sim 500$ km/ GeV) and effective trimaximal mixing for ν_e with ν_μ and ν_τ at the solar scale ($L/E \sim$ 15,000 km/ GeV) [52].

in terms of the fundamental parameters and the precision to which they are known†, highlighting the limited precision of the neutrino-mixing parameter measurements.

Table 2.1: Best-fit values of the neutrino mixing parameters in the PMNS matrix (assumes normal hierarchy) from [54], their 1σ uncertainties and comparison to the analogous values in the CKM matrix [55]. ΔM^2 is defined as $m_3^2 - (m_1^2 + m_2^2)/2$.

Parameter	Value (neutrino PMNS matrix)	Value (quark CKM matrix)
$\boldsymbol{\theta_{12}}$	$34 \pm 1°$	$13.04 \pm 0.05°$
$\boldsymbol{\theta_{23}}$	$38 \pm 1°$	$2.38 \pm 0.06°$
$\boldsymbol{\theta_{13}}$	$8.9 \pm 0.5°$	$0.201 \pm 0.011°$
$\boldsymbol{\Delta m^2_{21}}$	$+(7.54 \pm 0.22) \times 10^{-5}$ eV^2	
$\boldsymbol{\lvert\Delta M^2\rvert}$	$(2.43^{+0.10}_{-0.06}) \times 10^{-3}$ eV^2	$m_3 >> m_2$
$\boldsymbol{\delta_{\mathrm{CP}}}$	$-170 \pm 54°$	$67 \pm 5°$

Clearly much work remains in order to complete the standard three-flavor mixing picture, particularly with regard to θ_{23} (is it less than, greater than, or equal to $45°$?), mass hierarchy (normal or inverted?) and δ_{CP}. Additionally, there is great value in obtaining a set of measurements for multiple parameters *from a single experiment*, so that correlations and systematic uncertainties can be handled properly. Such an experiment would also be well positioned to extensively test the standard picture of three-flavor mixing. LBNE is designed to be this experiment.

2.2.1 CP Violation in the Quark and Lepton Sectors

In the particular parameterization of the PMNS matrix shown in Equation 2.2, the middle factor, labeled 'II', describes the mixing between the ν_1 and ν_3 mass states, and depends on the CP-violating phase δ_{CP}. In the three-flavor model, leptonic CP violation in an oscillation mode occurs due to the interference of contributions from terms in this factor — some of which contain δ_{CP} (i.e., involve the ν_1-ν_3 mixing directly) and some of which do not. The presence of nonzero CP-odd terms, e.g., Equation 2.15, (which requires $\delta_{\mathrm{CP}} \neq 0$ or π) in the interference patterns would result in an asymmetry in neutrino versus antineutrino oscillations. The magnitude of the CP-violating terms in the oscillation depends most directly on the size of the Jarlskog Invariant [56], a function that was introduced to provide a measure of CP violation independent of mixing-matrix parameterization. In terms of the three mixing angles and the (as yet unmeasured) CP-violating phase, the Jarlskog Invariant is:

$$J_{CP}^{\mathrm{PMNS}} \equiv \frac{1}{8} \sin 2\theta_{12} \sin 2\theta_{13} \sin 2\theta_{23} \cos\theta_{13} \sin\delta_{\mathrm{CP}}. \tag{2.8}$$

†A global fit [54] to existing results from current experiments sensitive to neutrino oscillation effects is the source for the PMNS matrix values.

The relatively large values of the mixing angles in the lepton sector imply that leptonic CP-violation effects may be quite large — depending on the value of the phase $\delta_{\rm CP}$, which is currently unknown. Experimentally, it is unconstrained at the 2σ level by the global fit [54]. Many theoretical models, examples of which include [57,58,59,60,61,62], provide predictions for $\delta_{\rm CP}$, but these predictions range over all possible values so do not yet provide any guidance.

Given the current best-fit values of the mixing angles [54] and assuming normal hierarchy,

$$J_{CP}^{\rm PMNS} \approx 0.03 \sin \delta_{\rm CP}. \tag{2.9}$$

This is in sharp contrast to the very small mixing in the quark sector, which leads to a very small value of the corresponding quark-sector Jarlskog Invariant [55],

$$J_{CP}^{\rm CKM} \approx 3 \times 10^{-5}, \tag{2.10}$$

despite the large value of $\delta_{CP}^{\rm CKM} \approx 70^\circ$.

To date, all observed CP-violating effects have occurred in experiments involving systems of quarks, in particular strange and b-mesons [55]. Furthermore, in spite of several decades of experimental searches for other sources of CP violation, all of these effects are explained by the CKM quark-mixing paradigm, and all are functions of the quark-sector CP phase parameter, $\delta_{\rm CP}^{\rm CKM}$. In cosmology, successful synthesis of the light elements after the Big Bang [63,64] (Big Bang Nucleosynthesis) requires that there be an imbalance in the number of baryons and antibaryons to one part in a billion when the Universe is a few minutes old [65]. CP violation in the quark sector has not, however, been able to explain the observed Baryon Asymmetry of the Universe (BAU), due to the small value of J_{CP}^{CKM}.

Baryogenesis [66] is a likely mechanism for generating the observed matter-antimatter asymmetry of our Universe. One way that it is elegantly achieved is by first having *leptogenesis* in the very early Universe. That mechanism can come about from the production and decay of very heavy right-handed neutrinos, if they are Majorana states (i.e. do not conserve lepton number‡), CP symmetry is violated in their decays (thus distinguishing particles and antiparticles) and the Universe is in non-equilibrium. Leptogenesis will lead to an early dominance of antileptons over leptons. When the cooling Universe reaches the electroweak phase transition, $T \sim 250\,\text{GeV}$, a baryon number excess is generated from the lepton asymmetry by a $B - L$‡ conserving mechanism (analogous to proton decay in that it violates B and L separately but conserves $B - L$) already present in the Standard Model.

The heavy Majorana right-handed neutrino states that could give rise to leptogenesis in the very early Universe are also a natural consequence of the GUT-based *seesaw* mechanism [67] — the simplest and most natural explanation of the observed super-light neutrino mass scales. The seesaw

‡In the Standard Model, lepton number (L) and baryon number (B) are conserved quantum numbers. Leptons have $B = 0$ and $L = 1$ and antileptons have $L = -1$. A quark has $L = 0$ and $B = 1/3$ and an antiquark has $B = -1/3$.

mechanism is a theoretical attempt to reconcile the very small masses of neutrinos to the much larger masses of the other elementary particles in the Standard Model. The seesaw mechanism achieves this unification by assuming an unknown new physics scale that connects the observed low-energy neutrino masses with a higher mass scale that involves very heavy sterile neutrino states. The seesaw mechanism as generator of neutrino mass is in addition to the Higgs mechanism that is now known to be responsible for the generation of the quark, charged lepton, and vector boson masses.

The no-equilibrium leptogenesis ingredient is expected in a hot Big Bang scenario, but the Majorana nature of the heavy neutrinos and needed CP violation can only be indirectly inferred from light neutrino experiments by finding lepton number violation (validating their Majorana nature via neutrinoless double-beta decay) and observing CP violation in ordinary neutrino oscillations.

Recent theoretical advances have demonstrated that CP violation, necessary for the generation of the Baryon Asymmetry of the Universe at the GUT scale (baryogenesis), can be directly related to the low-energy CP violation in the lepton sector that could manifest in neutrino oscillations. As an example, the theoretical model described in [68] predicts that leptogenesis, the generation of the analogous lepton asymmetry, can be achieved if

$$|\sin\theta_{13}\sin\delta_{\rm CP}| \gtrsim 0.11 \tag{2.11}$$

This implies $|\sin\delta_{\rm CP}| \gtrsim 0.7$ given the latest global fit value of $|\sin\theta_{13}|$ [69].

The goal of establishing an experimental basis for assessing this possibility should rank very high on the list of programmatic priorities within particle physics, and can be effectively addressed by LBNE.

2.2.2 Observation of CP-Violating Effects in Neutrino Oscillation Experiments

Whereas the Standard Model allows for violation of charge-parity (CP) symmetries in weak interactions, CP transformations followed by time-reversal transformations (CPT) are invariant. Under CPT invariance, the probabilities of neutrino oscillation and antineutrino oscillation are equivalent, i.e., $P(\nu_l \to \nu_l) = P(\overline{\nu}_l \to \overline{\nu}_l)$ where $l = e,\ \mu,\ \tau$. Measurements of $\nu_l \to \nu_l$ oscillations in which the flavor of the neutrino before and after oscillations remains the same are referred to as *disappearance* or *survival* measurements. CPT invariance in neutrino oscillations was recently tested by measurements of $\nu_\mu \to \nu_\mu$ and $\overline{\nu}_\mu \to \overline{\nu}_\mu$ oscillations [70]; no evidence for CPT violation was found. Therefore, asymmetries in neutrino versus antineutrino oscillations arising from CP violation effects can only be accessed in *appearance* experiments, defined as oscillations of $\nu_l \to \nu_{l'}$, in which the flavor of the neutrino after oscillations has changed. Because of the intrinsic challenges of producing and detecting ν_τ's, the oscillation modes $\nu_{\mu,e} \to \nu_{e,\mu}$ provide the most promising experimental signatures of leptonic CP violation.

For $\nu_{\mu,e} \to \nu_{e,\mu}$ oscillations that occur as the neutrinos propagate through matter, as in terrestrial long-baseline experiments, the coherent forward scattering of ν_e's on electrons in matter modifies the energy and path-length dependence of the vacuum oscillation probability in a way that depends on the magnitude *and* sign of Δm^2_{32}. This is the Mikheyev-Smirnov-Wolfenstein (MSW) effect [71,72] that has already been observed in solar-neutrino oscillation (disappearance) experiments [73,74,75,76]. The oscillation probability of $\nu_{\mu,e} \to \nu_{e,\mu}$ through matter, in a constant density approximation, keeping terms up to second order in $\alpha \equiv |\Delta m^2_{21}|/|\Delta m^2_{31}|$ and $\sin^2\theta_{13}$, is [77,55]:

$$P(\nu_\mu \to \nu_e) \cong P(\nu_e \to \nu_\mu) \cong P_0 + \underbrace{P_{\sin\delta}}_{\text{CP violating}} + P_{\cos\delta} + P_3 \tag{2.12}$$

where

$$\begin{aligned}
P_0 &= \sin^2\theta_{23}\frac{\sin^2 2\theta_{13}}{(A-1)^2}\sin^2[(A-1)\Delta], &(2.13)\\
P_3 &= \alpha^2\cos^2\theta_{23}\frac{\sin^2 2\theta_{12}}{A^2}\sin^2(A\Delta), &(2.14)\\
P_{\sin\delta} &= \alpha\frac{8J_{cp}}{A(1-A)}\sin\Delta\sin(A\Delta)\sin[(1-A)\Delta], &(2.15)\\
P_{\cos\delta} &= \alpha\frac{8J_{cp}\cot\delta_{\mathrm{CP}}}{A(1-A)}\cos\Delta\sin(A\Delta)\sin[(1-A)\Delta], &(2.16)
\end{aligned}$$

and where

$$\Delta = \Delta m^2_{31}L/4E,\ and\ A = \sqrt{3}G_F N_e 2E/\Delta m^2_{31}.$$

In the above, the CP phase δ_{CP} appears (via J_{cp}) in the expressions for $P_{\sin\delta}$ (the CP-odd term) which switches sign in going from $\nu_\mu \to \nu_e$ to the $\overline{\nu}_\mu \to \overline{\nu}_e$ channel, and $P_{\cos\delta}$ (the CP-conserving term) which does not. The matter effect also introduces a neutrino-antineutrino asymmetry, the origin of which is simply the presence of electrons and absence of positrons in the Earth.

Recall that in Equation 2.2, the CP phase appears in the PMNS matrix through the mixing of the ν_1 and ν_3 mass states. The physical characteristics of an appearance experiment are therefore determined by the baseline and neutrino energy at which the mixing between the ν_1 and ν_3 states is maximal, as follows:

$$\begin{aligned}
\frac{L(\mathrm{km})}{E_\nu(\mathrm{GeV})} &= (2n-1)\frac{\pi}{2}\frac{1}{1.27\times\Delta m^2_{31}(\mathrm{eV}^2)} &(2.17)\\
&\approx (2n-1)\times 510\ \mathrm{km/GeV} &(2.18)
\end{aligned}$$

where $n = 1, 2, 3...$ denotes the oscillation nodes at which the appearance probability is maximal.

The dependences on E_ν of the oscillation probability for the LBNE baseline of L =1,300 km are plotted on the right in Figures 2.3 and 2.4. The colored curves demonstrate the variation in the ν_e appearance probability as a function of E_ν, for three different values of δ_{CP}.

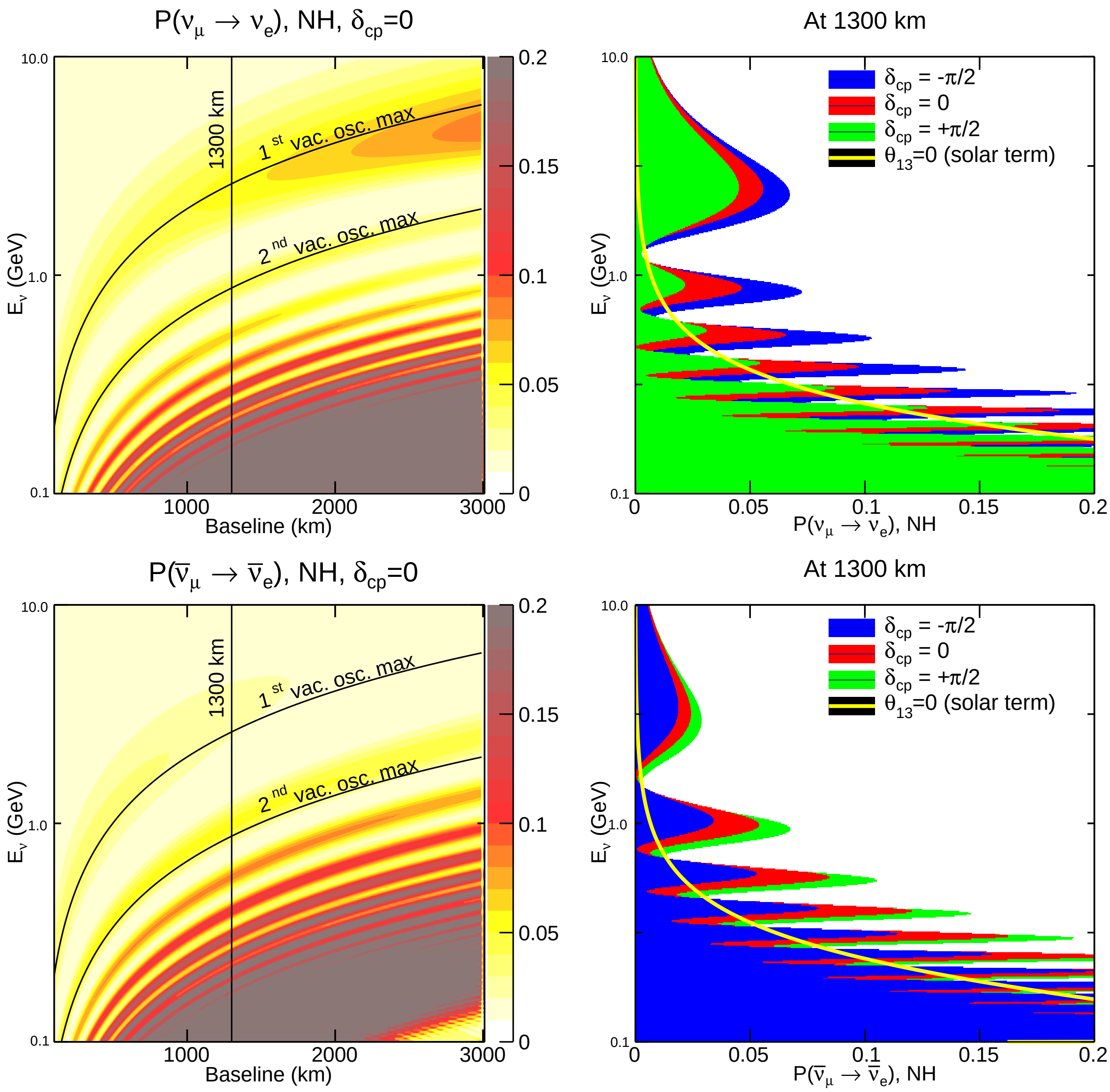

Figure 2.3: Neutrino oscillation probabilities as a function of energy and baseline, for different values of $\delta_{\rm CP}$, *normal hierarchy*. The oscillograms on the left show the $\nu_\mu \to \nu_e$ oscillation probabilities as a function of baseline and energy for *neutrinos* (top left) and *antineutrinos* (bottom left) with $\delta_{\rm CP} = 0$. The figures on the right show the projection of the oscillation probability on the neutrino energy axis at a baseline of 1,300 km for $\delta_{\rm CP} = 0$ (red), $\delta_{\rm CP} = +\pi/2$ (green), and $\delta_{\rm CP} = -\pi/2$ (blue) for neutrinos (top right) and antineutrinos (bottom right). The yellow curve is the ν_e appearance solely from the "solar term" due to ν_1 to ν_2 mixing as given by Equation 2.14.

The variation in the $\nu_\mu \to \nu_e$ oscillation probabilities with the value of $\delta_{\rm CP}$ indicates that it is experimentally possible to measure the value of $\delta_{\rm CP}$ at a fixed baseline using only the observed shape of the $\nu_\mu \to \nu_e$ *or* the $\overline{\nu}_\mu \to \overline{\nu}_e$ appearance signal measured over an energy range that encompasses at least one full oscillation interval. A measurement of the value of $\delta_{\rm CP} \neq 0$ or π, assuming that neutrino mixing follows the three-flavor model, would imply CP violation. The CP

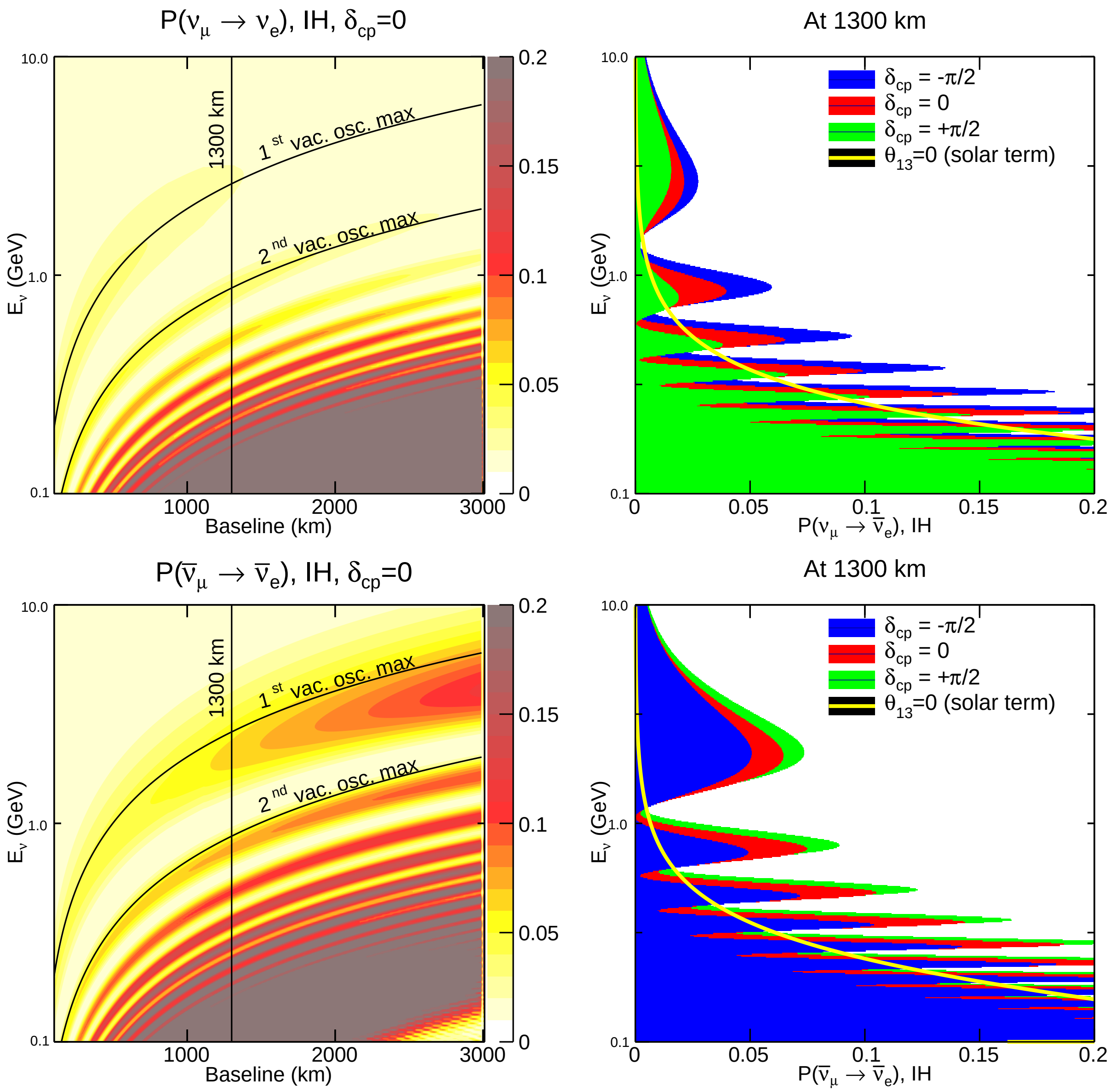

Figure 2.4: Neutrino oscillation probabilities as a function of energy and baseline, for different values of $\delta_{\rm CP}$, *inverted hierarchy*. The oscillograms on the left show the $\nu_\mu \to \nu_e$ oscillation probabilities as a function of baseline and energy for *neutrinos* (top left) and *antineutrinos* (bottom left) with $\delta_{\rm CP} = 0$. The figures on the right show the projection of the oscillation probability on the neutrino energy axis at a baseline of 1,300 km for $\delta_{\rm CP} = 0$ (red), $\delta_{\rm CP} = +\pi/2$ (green), and $\delta_{\rm CP} = -\pi/2$ (blue) for neutrinos (top right) and antineutrinos (bottom right).The yellow curve is the ν_e appearance solely from the "solar term" due to ν_1 to ν_2 mixing as given by Equation 2.14.

asymmetry, $\mathcal{A}_{CP}$, is defined as

$$\mathcal{A}_{CP} = \frac{P(\nu_\mu \to \nu_e) - P(\overline{\nu}_\mu \to \overline{\nu}_e)}{P(\nu_\mu \to \nu_e) + P(\overline{\nu}_\mu \to \overline{\nu}_e)}. \tag{2.19}$$

In the three-flavor model the asymmetry can be approximated to leading order in Δm^2_{21} as [78]:

$$\mathcal{A}_{CP} \sim \frac{\cos\theta_{23}\sin 2\theta_{12}\sin\delta_{\rm CP}}{\sin\theta_{23}\sin\theta_{13}}\left(\frac{\Delta m^2_{21}L}{4E_\nu}\right) + \text{matter effects} \tag{2.20}$$

Regardless of the value obtained for $\delta_{\rm CP}$, it is clear that the explicit observation of an asymmetry between $P(\nu_l \to \nu_{l'})$ and $P(\overline{\nu}_l \to \overline{\nu}_{l'})$ is sought to directly demonstrate the leptonic CP violation effect that a value of $\delta_{\rm CP}$ different from zero or π implies. For long-baseline experiments such as LBNE, where the neutrino beam propagates through the Earth's mantle, the leptonic CP-violation effects must be disentangled from the matter effects.

2.2.3 Probing the Neutrino Mass Hierarchy via the Matter Effect

The asymmetry induced by matter effects as neutrinos pass through the Earth arises from the change in sign of the factors proportional to Δm^2_{31} (namely A, Δ and α; Equations 2.12 to 2.16) in going from the normal to the inverted neutrino mass hierarchy. This sign change provides a means for determining the currently unknown mass hierarchy. The oscillation probabilities given in these approximate equations for $\nu_\mu \to \nu_e$ as a function of baseline in kilometers and energy in GeV are calculated numerically with an exact formalism [79] and shown in the oscillograms of Figure 2.3 and 2.4 for $\delta_{\rm CP} = 0$, for normal and inverted hierarchies, respectively. The oscillograms include the matter effect, assuming an Earth density and electron fraction described by [80]. These values are taken as a constant average over paths through regions of the Earth with continuous density change. Any baseline long enough to pass through a discontinuity is split into three or more segments each of constant average density and electron fraction. The solid black curves in the oscillograms indicate the location of the first and second oscillation maxima as given by Equation 2.18, assuming oscillations in a vacuum; matter effects will change the neutrino energy values at which the mixing between the ν_1 and ν_3 mass states is maximal.

> The significant impact of the matter effect on the $\nu_\mu \to \nu_e$ and $\overline{\nu}_\mu \to \overline{\nu}_e$ oscillation probabilities at longer baselines (Figures 2.3 and 2.4) implies that ν_e appearance measurements over long distances through the Earth provide a powerful probe into the neutrino mass hierarchy question: is $m_1 > m_3$ or vice-versa?

The dependence of the matter effect on the mass hierarchy is illustrated in the oscillograms plotted on the left hand side of Figures 2.3 and 2.4, and can be characterized as follows:

- For normal hierarchy, $P(\nu_\mu \to \nu_e)$ is enhanced and $P(\overline{\nu}_\mu \to \overline{\nu}_e)$ is suppressed. The effect increases with baseline at a fixed L/E.
- For inverted hierarchy, $P(\nu_\mu \to \nu_e)$ is suppressed and $P(\overline{\nu}_\mu \to \overline{\nu}_e)$ is enhanced. The effect increases with baseline at a fixed L/E.

- The matter effect has the largest impact on the probability amplitude at the first oscillation maximum.
- The matter effect introduces a phase shift in the oscillation pattern, shifting it to a lower energy for a given baseline when the hierarchy changes from normal to inverted. The shift is approximately -100 MeV.

2.2.4 Disentangling CP-Violating and Matter Effects

In Figure 2.5, the asymmetries induced by matter and maximal CP violation (at $\delta_{\rm CP} = \pm\pi/2$) are shown separately as 2D oscillograms in baseline and neutrino energy. The matter effect induces an asymmetry in $P(\nu_l \to \nu_{l'})$ and $P(\overline{\nu}_l \to \overline{\nu}_{l'})$ that adds to the CP asymmetry. At longer baselines ($> 1000\,$km), the matter asymmetry in the energy region of the first oscillation node is driven primarily by the change in the ν_e appearance amplitude. At shorter baselines ($\mathcal{O}(100\,\rm km)$) the asymmetry is driven by the phase shift. The dependence of the asymmetry on baseline and energy, where the oscillation probabilities peak and the appearance signals are largest, can be approximated as follows:

$$\mathcal{A}_{cp} \propto L/E, \tag{2.21}$$

$$\mathcal{A}_{matter} \propto L \times E. \tag{2.22}$$

The phenomenology of $\nu_\mu \to \nu_e$ oscillations described in Section 2.2.2 implies that the experimental sensitivity to CP violation and the mass hierarchy from measurements of the total asymmetry between $P(\nu_l \to \nu_{l'})$ and $P(\overline{\nu}_l \to \overline{\nu}_{l'})$ requires the disambiguation of the asymmetry induced by the matter effect and that induced by CP violation. This is particularly true for experiments designed to access mixing between the ν_1 and ν_3 mass states using neutrino beams of $\mathcal{O}(1\,\rm GeV)$. Such beams require baselines of at least several hundred kilometers, at which the matter asymmetries are significant. The currently known values of the oscillation parameters permit calculation of the magnitude of the matter asymmetry within an uncertainty of $< 10\%$; only the sign of the asymmetry, which depends on the sign of Δm^2_{31}, is unknown. Since the magnitude of the matter asymmetry is known, baselines at which the size of the matter asymmetry exceeds that of the maximal possible CP asymmetry are required in order to separate the two effects.

Figure 2.6 illustrates the ambiguities that can arise from the interference of the matter and CP asymmetries. The plots show the total asymmetry as a function of $\delta_{\rm CP}$ at four baseline values (clockwise from top left): 290 km, 810 km, 2,300 km and 1,300 km. The curves in black and red illustrate the asymmetries at the first and second oscillation nodes, respectively. The solid lines represent normal hierarchy, and the dashed lines represent inverted hierarchy. The plots demonstrate that experimental measurements of the asymmetry (Equation 2.19) at the first oscillation node could yield ambiguous results for short baselines if the hierarchy is unknown. This occurs in regions of the $(L, E, \delta_{\rm CP})$ phase space where the matter and CP asymmetries cancel partially or

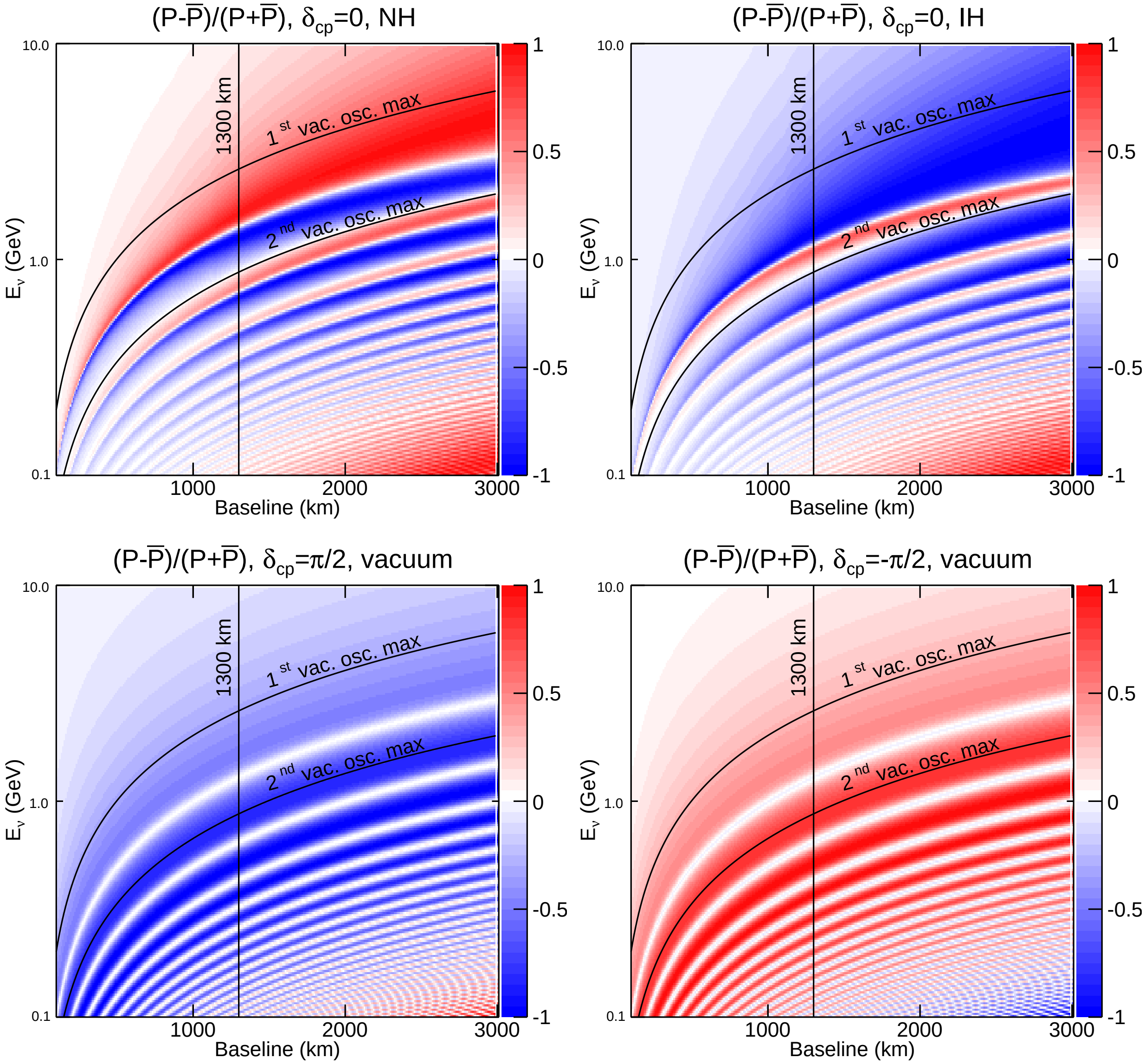

Figure 2.5: The $\nu/\overline{\nu}$ oscillation probability asymmetries as a function of baseline. The top two figures show the asymmetry induced by the matter effect only for normal (top left) and inverted (top right) hierarchies. The bottom figures show the asymmetry induced through the CP-violating phase $\delta_{\rm CP}$ in vacuum, for $\delta_{\rm CP} = +\pi/2$ (bottom left) and $\delta_{\rm CP} = -\pi/2$ (bottom right)

totally. For example, the green lines in Figure 2.6 indicate the asymmetry at the first node for maximal CP violation ($\delta_{\rm CP} = \pi/2$) with an inverted hierarchy. At a baseline of 290 km, the measured asymmetry at $\delta_{\rm CP} = \pi/2$ (inverted hierarchy) is degenerate with that at $\delta_{\rm CP} \sim 0$ (normal hierarchy) at the first node. Measurements of the asymmetry at different L/E or at different baselines can break the degeneracies (Equation 2.22). At very long baselines, for which the matter asymmetry exceeds the maximal CP asymmetry at the first oscillation node, there are no degeneracies and the mass hierarchy and CP asymmetries can be resolved within the same experiment. For the current best-fit values of the oscillation parameters, the matter asymmetry exceeds the maximal possible CP asymmetry at baselines of $\geq$ 1,200 km.

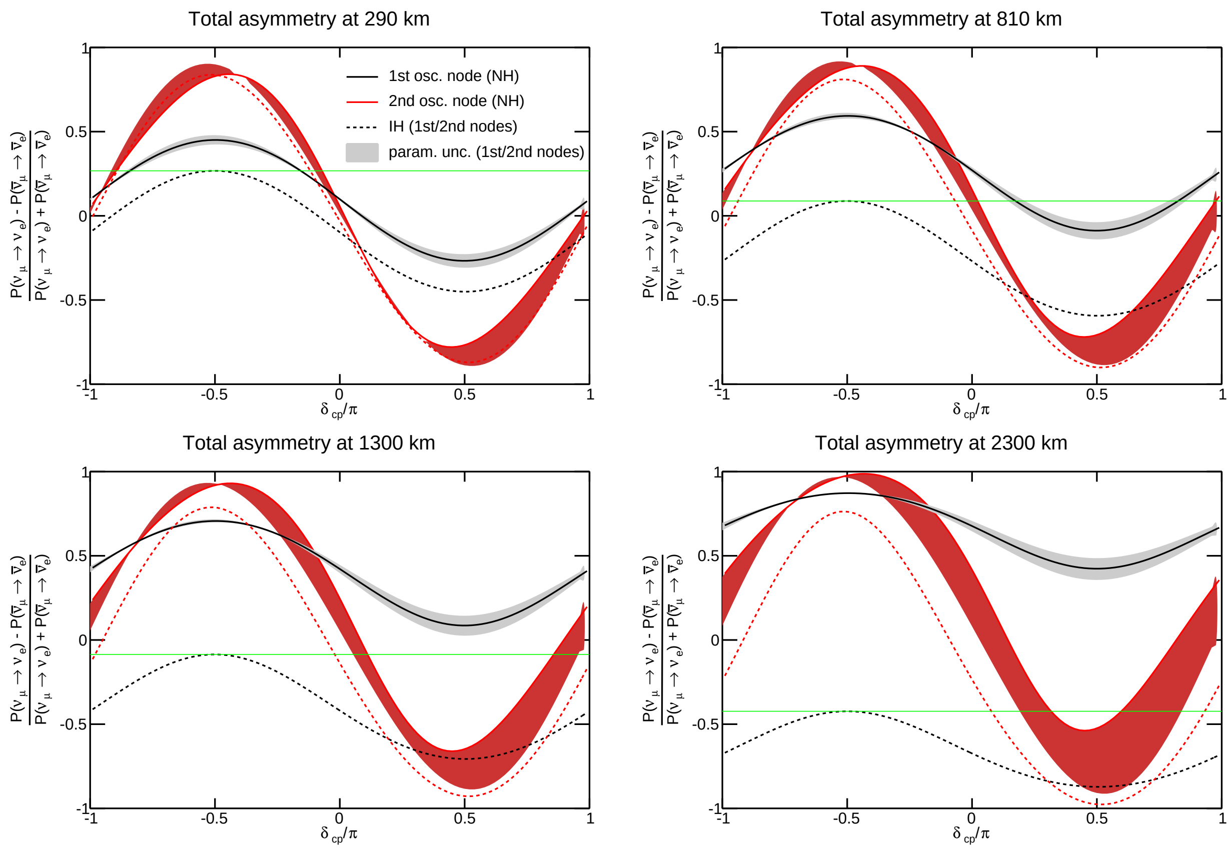

Figure 2.6: The $\nu/\overline{\nu}$ oscillation probability asymmetries versus $\delta_{\rm CP}$ at the first two oscillation nodes. Clockwise from top left: 290 km, 810 km, 2,300 km and 1,300 km. The solid/dashed black line is the total asymmetry at the first oscillation node for normal/inverted hierarchy. The red lines indicate the asymmetries at the second node.

2.2.5 Optimization of the Oscillation Baseline for CPV and Mass Hierarchy

The simple arguments above suggest that a baseline $\geq$ 1,200 km is required to search for CP violation and determine the mass hierarchy simultaneously in a single long-baseline neutrino oscillation experiment. To understand the performance of a long-baseline experiment as a function of baseline using realistic neutrino beamline designs, a study of the sensitivities to CP violation and the mass hierarchy as a function of baseline was carried out using a neutrino beamline design optimized individually for each baseline. A 34−kt LArTPC neutrino detector at the far site was assumed since it has a high ν_e-identification efficiency that is flat over a large range of energies (Chapter 4). The beamline design was based on the NuMI beamline utilizing the 120−GeV, 1.2−MW proton beam from the Fermilab Main Injector and was fully simulated using GEANT3 [82]. Varying

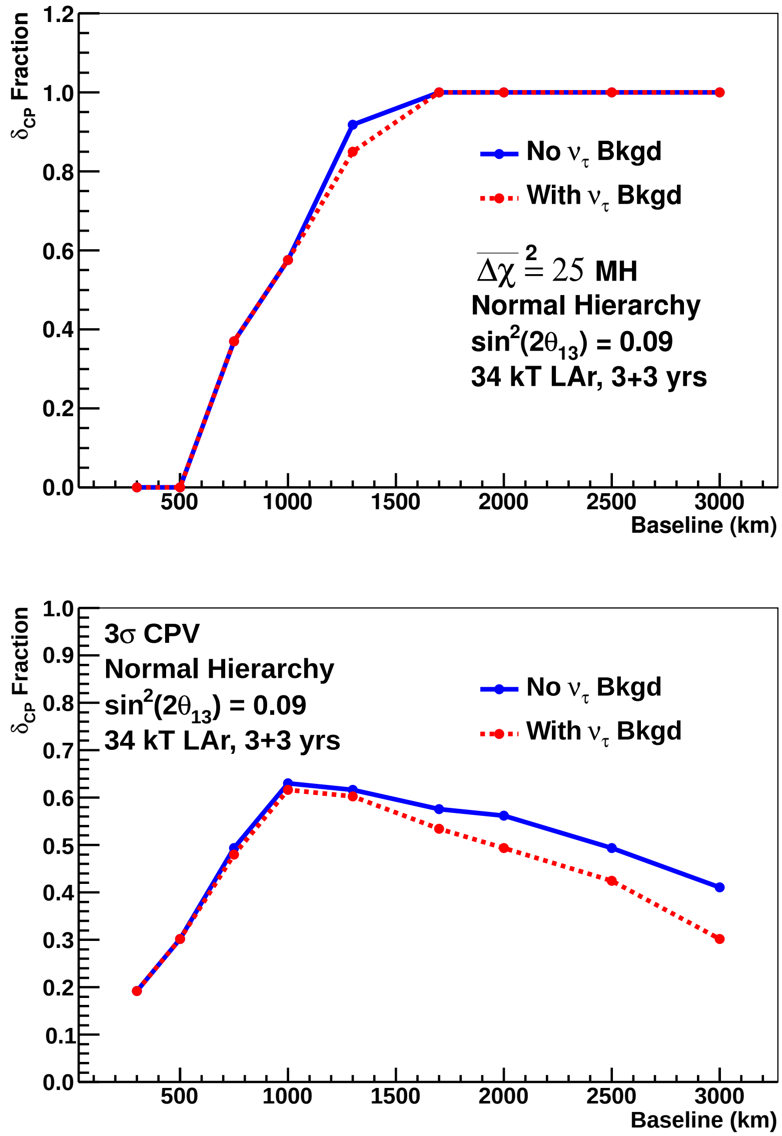

Figure 2.7: The fraction of δ_{CP} values for which the mass hierarchy can be determined with an average $|\overline{\Delta\chi^2}| = 25$ or greater as a function of baseline (top) and the fraction of δ_{CP} values which CP violation can be determined at the 3σ level or greater as a function of baseline (bottom). A NuMI based beam design with a 120−GeV beam was optimized for each baseline. Projections assume $\sin^2 2\theta_{13} = 0.09$ and a 34−kt LArTPC as the far detector [81]. An exposure of 3yrs+3yrs of neutrino+antineutrino running with 1.2−MW beam power is assumed.

the distance between the target and the first horn allowed selection of a beam spectrum that covered the first oscillation node and part of the second. The design incorporated an evacuated decay pipe of 4-m diameter and a length that varied from 280 to 580 m. For baselines less than 1,000 m, the oscillation occurs at neutrino energies where on-axis beams produce too little flux. Therefore, off-axis beams — which produce narrow-band, low-energy neutrino fluxes — were simulated for these baselines, with the off-axis angle chosen to provide the most coverage of the first oscillation node. The results of this study [81] are summarized in Figure 2.7. The sensitivity to CP violation (bottom plot) assumes that the mass hierarchy is unknown. An updated study with more detail is available [83]. The baseline study indicates that with realistic experimental conditions, baselines between 1,000 and 1,300 km are near optimal for determination of CP violation. With baselines $> 1{,}500$ km, the correct mass hierarchy could be determined with a probability greater than 99% for all values of $\delta_{\rm CP}$ with a large LArTPC far detector. However, at very long baselines, in one of the neutrino beam polarities (ν/$\overline{\nu}$ for inverted/normal hierarchy) the event rate suppression due to the matter effect becomes very large, making it difficult to observe an explicit CP-violation asymmetry.

2.2.6 Physics from Precision Measurements of Neutrino Mixing

Precision measurements of the neutrino mixing parameters in long-baseline oscillations not only reveal the neutrino mixing patterns in greater detail, but also serve as probes of new physics that manifests as perturbations in the oscillation patterns driven by three-flavor mixing.

The determination of whether there is maximal mixing between ν_μ and ν_τ — or a measurement of the deviation from maximal — is of great interest theoretically [59,84,85,86,87,88]. Models of quark-lepton universality propose that the quark and lepton mixing matrices (Equations 2.7 and 2.6, respectively) are given by

$$U^{\rm CKM} = 1 + \epsilon_{\rm Cabbibo} \text{ and} \tag{2.23}$$
$$U^{\rm PMNS} = T + \epsilon_{\rm Cabbibo}, \tag{2.24}$$

where T is determined by Majorana physics [89] and $\epsilon_{\rm Cabbibo}$ refers to small terms driven by the Cabbibo weak mixing angle ($\theta_C = \theta_{12}^{\rm CKM}$). In such models $\theta_{23} \sim \pi/4 + \Delta\theta$, where $\Delta\theta$ is of order the Cabbibo angle, θ_C, and $\theta_{13} \sim \theta_C/\sqrt{2}$. It is therefore important to determine experimentally both the value of $\sin^2\theta_{23}$ and the octant of θ_{23} if $\theta_{23} \neq 45°$.

Studying ν_μ disappearance probes $\sin^2 2\theta_{23}$ and $|\Delta m^2_{32}|$ with very high precision. Disappearance measurements can therefore determine whether ν_μ-ν_τ mixing is maximal or near maximal such that $\sin^2 2\theta_{23} = 1$, but they cannot resolve the octant of θ_{23} if ν_μ-ν_τ mixing is less than maximal. Combining the ν_μ disappearance signal with the ν_e appearance signal can help determine the θ_{23} octant and constrain some of the theoretical models of quark-lepton universality.

Direct unitarity tests, in which the individual components of the PMNS matrix are measured separately, are challenging due to limited experimentally available oscillation channels [90,91]. Application of the "proof by contradiction" principle offers another way to perform the unitarity tests. In these tests, the mixing angles are extracted from the data by assuming unitarity in the standard three-flavor framework. If measurements of the same mixing angle by two different processes are inconsistent, then the standard three-flavor framework is insufficient and new physics beyond this framework is required. Observation of unitarity violation will constrain the phase space of possible new physics. In particular, the precision measurement of $\sin^2 2\theta_{13}$ provides the most promising unitarity test [91] for the PMNS matrix. It is important to note that several theoretical models of new physics, such as the existence of sterile neutrinos or nonstandard interactions, could lead to apparent deviations of the $\sin^2 2\theta_{13}$ value measured in ν_e appearance experiments from that measured in reactor ($\overline{\nu}_e$ disappearance) experiments.

Precision measurements of ν_μ and $\overline{\nu}_\mu$ survival over long baselines could reveal nonstandard physics driven by new interactions in matter. Examples of some of these effects and the experimental signatures in long-baseline oscillations are discussed in Chapter 4.

In addition, experiments with long enough baselines and sufficient neutrino flux at $E_\nu > 3$ GeV, coupled with high-resolution tracking detectors, as in the LBNE design, can also probe $\nu_\mu \to \nu_\tau$ appearance with higher precision than is currently possible using ν_τ charged-current interactions. The combination of $\nu_\mu \to \nu_\mu$, $\nu_\mu \to \nu_e$, and $\nu_\mu \to \nu_\tau$ can ultimately over-constrain the three-flavor model of neutrino oscillations both in neutrino and antineutrino modes.

2.2.7 Oscillation Physics with Atmospheric Neutrinos

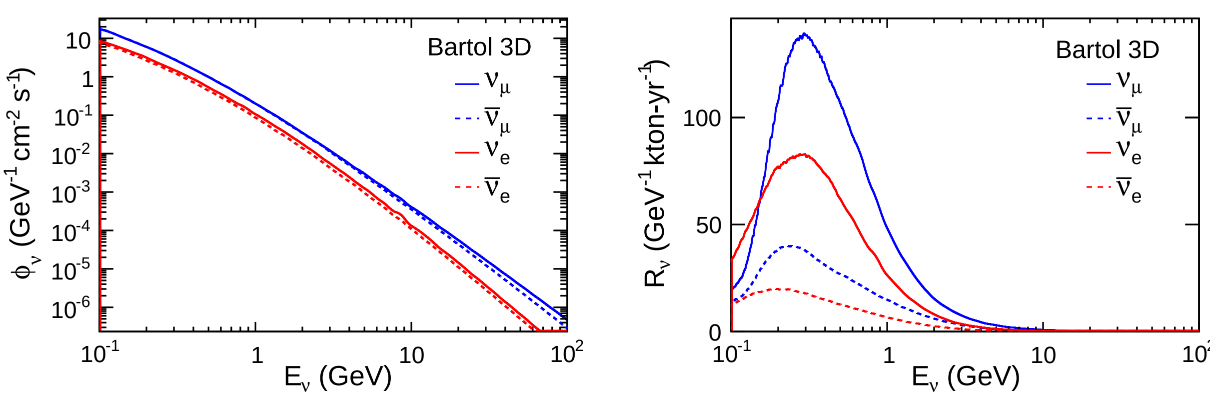

Figure 2.8: The atmospheric neutrino flux in neutrinos per second per square centimeter as a function of neutrino energy for different flavors (left). The atmospheric neutrino spectrum per GeV per kt per year for the different species (right).

Atmospheric neutrinos are unique among sources used to study oscillations; the flux contains neutrinos and antineutrinos of all flavors, matter effects play a significant role, both Δm^2 values contribute to the oscillation patterns, and the oscillation phenomenology occurs over several orders of magnitude in both energy (Figure 2.8) and path length. These characteristics make atmospheric neutrinos ideal for the study of oscillations and provide a laboratory suitable to search for exotic phenomena for which the dependence of the flavor-transition and survival probabilities on energy and path length can be defined. The probabilities of atmospheric $\nu_\mu \to \nu_e$ and $\overline{\nu}_\mu \to \overline{\nu}_e$ oscillations for normal and inverted hierarchies are shown as a function of zenith angle in Figure 2.9.

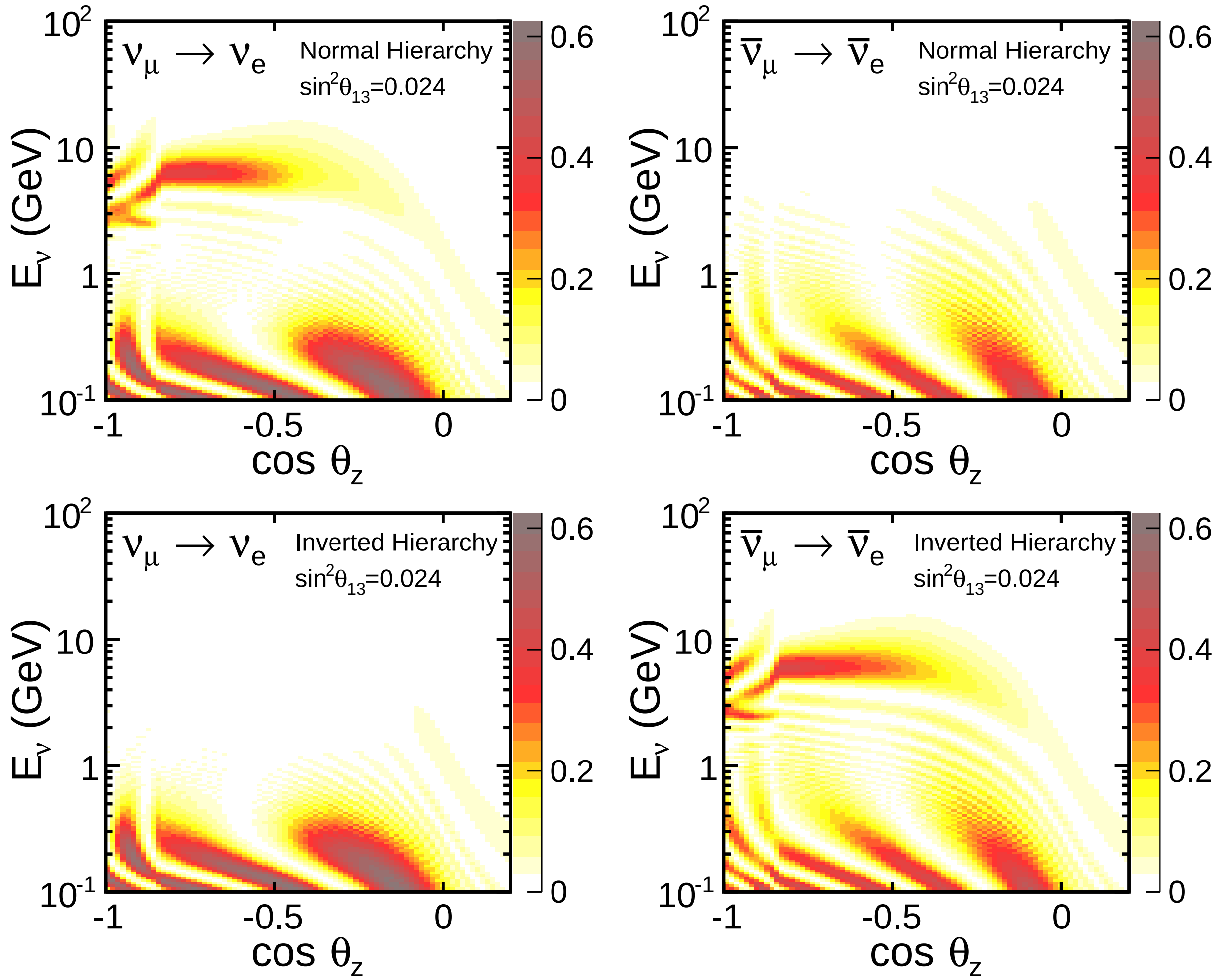

Figure 2.9: The probabilities of atmospheric $\nu_\mu \to \nu_e$ (left) and $\overline{\nu}_\mu \to \overline{\nu}_e$ (right) oscillations for normal (top) and inverted (bottom) hierarchies as a function of zenith angle.

Even with dedicated long-baseline experiments exploring the large mass splitting (Δm^2_{32}) for nearly a decade, atmospheric data continue to contribute substantially to our understanding of the neutrino sector. Broadly speaking:

- The data demonstrate *complementarity* with beam results via two- and three-flavor fits and the measurement of a ν_τ appearance signal consistent with expectations.
- The data serve to increase measurement *precision* through global fits, given that the sensitivity of atmospheric neutrinos to the mass hierarchy is largely independent of $\delta_{\rm CP}$ and the

octant of θ_{23}.

- *New physics* searches with atmospheric neutrinos have placed limits on CPT violation, non-standard interactions, mass-varying neutrinos and Lorentz-invariance violation.

Atmospheric neutrinos can continue to play these roles in the LBNE era given LBNE's deep-underground far detector. In particular, complementarity will be vital in a future where, worldwide, the number of high-precision, long-baseline beam/detector facilities is small. The physics potential of a large underground liquid argon detector for measuring atmospheric neutrinos is discussed in Section 4.6.

2.3 Nucleon Decay Physics Motivated by Grand Unified Theories

Searches for proton decay, bound-neutron decay and similar processes such as di-nucleon decay and neutron-antineutron oscillations test the apparent but unexplained conservation law of baryon number. These decays are already known to be rare based on decades of prior searches, all of which have produced negative results. If measurable event rates or even a single-candidate event were to be found, it would be sensible to presume that they occurred via unknown virtual processes based on physics beyond the Standard Model. The impact of demonstrating the existence of a baryon-number-violating process would be profound.

2.3.1 Theoretical Motivation from GUTs

The class of theories known as Grand Unified Theories (GUTs) make predictions about both baryon number violation and proton lifetime that may be within reach of the full-scope LBNE experiment. The theoretical motivation for the study of proton decay has a long and distinguished history [92,93,94] and has been reviewed many times [95,96,97]. Early GUTs provided the original motivation for proton decay searches in kiloton-scale detectors placed deep underground to limit backgrounds. The 22.5−kt Super–Kamiokande experiment extended the search for proton decay by more than an order of magnitude relative to the previous generation of experiments. Contemporary reviews [98,99,100] discuss the strict limits already set by Super–Kamiokande and the context of the proposed next generation of larger underground experiments such as Hyper-Kamiokande and LBNE.

Although no evidence for proton decay has been detected, the lifetime limits from the current generation of experiments already constrain the construction of many contemporary GUT models.

In some cases, these lifetime limits are approaching the upper limits allowed by GUT models. This situation points naturally toward continuing the search with new, larger detectors. These searches are motivated by a range of scientific issues:

- Conservation laws arise from underlying symmetries in Nature [101]. Conservation of baryon number is therefore unexplained since it corresponds to no known long-range force or symmetry.
- Baryon number non-conservation has cosmological consequences, such as a role in inflation and the matter-antimatter asymmetry of the Universe.
- Proton decay is predicted at some level by almost all GUTs.
- Some GUTs can accommodate neutrinos with nonzero mass and characteristics consistent with experimental observations.
- GUTs incorporate other previously unexplained features of the Standard Model such as the relationship between quark and lepton electric charges.
- The unification scale is suggested both experimentally and theoretically by the apparent convergence of the running coupling constants of the Standard Model. The unification scale is in excess of 10^{15} GeV.
- The unification scale is not accessible by any accelerator experiment; it can only be probed by virtual processes such as with proton decay.
- GUTs usually predict the relative branching fractions of different nucleon decay modes. Testing these predictions would, however, require a sizeable sample of proton decay events.
- The dominant proton decay mode of a GUT is often sufficient to roughly identify the likely characteristics of the GUT, such as gauge mediation or the involvement of supersymmetry.

The observation of even a single unambiguous proton decay event would corroborate the idea of unification and the signature of the decay would give strong guidance as to the nature of the underlying theory.

2.3.2 Proton Decay Modes

From the body of literature, two decay modes (shown in Figure 2.10) emerge that dominate the LBNE experimental design. The more well-known of the two, the decay mode of $p \to e^+\pi^0$, arises from gauge mediation. It is often predicted to have the higher branching fraction and is also

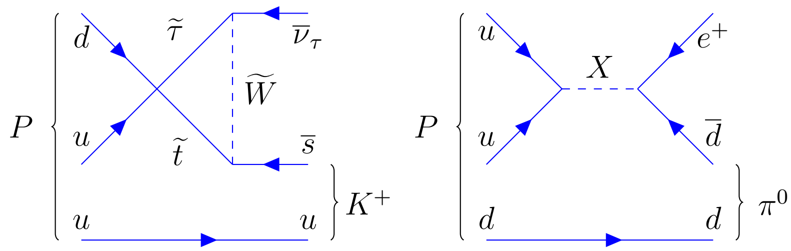

Figure 2.10: Feynman diagrams for proton decay modes from supersymmetric GUT, $p^+ \rightarrow K^+\overline{\nu}$ (left) and gauge-mediation GUT models, $p^+ \rightarrow e^+\pi^0$ (right).

demonstrably the more straightforward experimental signature for a water Cherenkov detector. In this mode, the total mass of the proton is converted into the electromagnetic shower energy of the positron and two photons from π^0 decay, with a net momentum vector near zero.

The second key mode is $p \rightarrow K^+\overline{\nu}$. This mode is dominant in most supersymmetric GUTs, many of which also favor additional modes involving kaons in the final state. This decay mode with a charged kaon is uniquely interesting; since stopping kaons have a higher ionization density than other particles, a LArTPC could detect it with extremely high efficiency, as described in Chapter 5. In addition, many final states of K^+ decay would be fully reconstructable in a LArTPC.

There are many other allowed modes of proton or bound neutron into antilepton plus meson decay that conserve $B - L$[§], but none of these will influence the design of a next-generation experiment. The most stringent limits, besides those on $p \rightarrow e^+\pi^0$, include the lifetime limits on $p \rightarrow \mu^+\pi^0$ and $p \rightarrow e^+\eta$, both of which are greater than 4×10^{33} years [102]. Any experiment that will do well for $p \rightarrow e^+\pi^0$ will also do well for these decay modes. The decays $p \rightarrow \overline{\nu}\pi^+$ or $n \rightarrow \overline{\nu}\pi^0$ may have large theoretically predicted branching fractions, but they are experimentally difficult due to the sizeable backgrounds from atmospheric-neutrino interactions. The decay $p \rightarrow \mu^+K^0$ can be detected relatively efficiently by either water Cherenkov or LArTPC detectors.

A number of other possible modes exist, such as those that conserve $B+L$, that violate only baryon number, or that decay into only leptons. These possibilities are less well-motivated theoretically, as they do not appear in a wide range of models, and are therefore not considered here.

Figure 2.11 shows a comparison of experimental limits, dominated by recent results from Super–Kamiokande to the ranges of lifetimes predicted by an assortment of GUTs. At this time, the theory literature does not attempt to precisely predict lifetimes, concentrating instead on suggesting the dominant decay modes and relative branching ratios. The uncertainty in the lifetime predictions comes from details of the theory, such as masses and coupling constants of unknown heavy particles, as well as poorly known details of matrix elements for quarks within the nucleon.

[§] In these models, the quantum number $B - L$ is expected to be conserved even though B and L are not individually conserved.

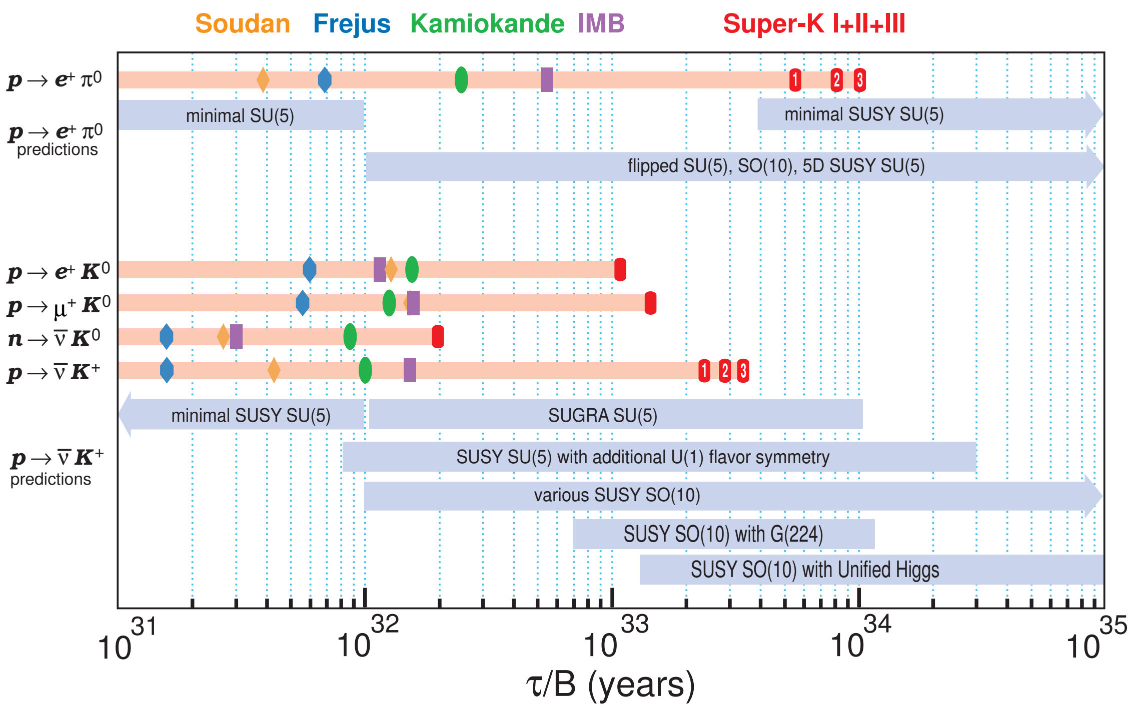

Figure 2.11: Proton decay lifetime limits [55,102] compared to lifetime ranges predicted by Grand Unified Theories. The upper section is for $p \to e^+\pi^0$, most commonly caused by gauge mediation. The lower section is for SUSY-motivated models, which commonly predict decay modes with kaons in the final state. The marker symbols indicate published experimental limits, as indicated by the sequence and colors on top of the figure.

It is apparent from Figure 2.11 that a continued search for proton decay is by no means assured of obtaining a positive result. With that caveat, an experiment with sensitivity to proton lifetimes between 10^{33} and 10^{35} years is searching in the right territory over virtually all GUTs; even if no proton decay is detected, stringent lifetime limits will provide strong constraints on such models. Minimal SU(5) was ruled out by the early work of IMB and Kamiokande and minimal SUSY SU(5) is considered to be ruled out by Super–Kamiokande. In most cases, another order of magnitude in improved limits will not rule out specific models but will constrain their allowed parameters; this could allow identification of models which must be fine-tuned in order to accommodate the data, and are thus less favored.

As Chapter 5 will show, the performance and scalability of the LArTPC technology opens up nucleon decay channels that are not as readily accessible in existing and proposed water Cherenkov detectors, providing LBNE with a unique and compelling opportunity for discovery.

2.4 Supernova-Neutrino Physics and Astrophysics

For over half a century, researchers have been grappling to understand the physics of the neutrino-driven core-collapse supernova. The interest in observing the core-collapse supernova explosion mechanism comes from the key role supernovae of this type have played in the history of the Universe. Without taking supernova feedback into account, for example, modern simulations of galaxy formation cannot reproduce the structure of our galactic disk. More poetically, the heavy elements that are the basis of life on Earth were synthesized inside stars and ejected by supernova explosions.

Neutrinos from a core-collapse supernova are emitted in a burst of a few tens of seconds duration, with about half emitted in the first second. They record the information about the physical processes in the center of the explosion during the first several seconds — as it is happening. Energies are in the few-tens-of-MeV range and luminosity is divided roughly equally between flavors. The basic model of core collapse was confirmed by the observation of neutrino events from SN1987A, a supernova in the Large Magellanic Cloud — outside the Milky Way — 50 kpc (kiloparsecs) away. Nineteen events were detected in two water Cherenkov detectors [103,104] and additional events were reported in a scintillator detector [105]. The neutrino signal from a core-collapse supernova in the Milky Way is expected to generate a high-statistics signal from which LBNE could extract a wealth of information [106,107].

The expected rate of core-collapse supernovae is two to three per century in the Milky Way [108,109]. In a 20-year experimental run, LBNE's probability of observing neutrinos from a core-collapse supernova in the Milky Way is about 40%. The detection of thousands of supernova-burst neutrinos from this event would dramatically expand the science reach of the experiment, allowing observation of the development of the explosion in the star's core and probing the equation-of-state of matter at nuclear densities. In addition, independent measurements of the neutrino mass hierarchy and the θ_{13} mixing angle are possible, as well as additional constraints on physics beyond the Standard Model.

Each of the topics that can be addressed by studying supernova-burst neutrinos represent important outstanding problems in modern physics, each worthy of a separate, dedicated experiment, and the neutrino physics and astrophysics communities would receive payback simultaneously. The opportunity of targeting these topics in a single experiment is very attractive, especially since it may come only at incremental cost to the LBNE Project.

The explosion mechanism is thought to have three distinct stages: the collapse of the iron core, with the formation of the shock and its breakout through the neutrinosphere; the accretion phase, in which the shock temporarily stalls at a radius of about 200 km while the material keeps raining in; and the cooling stage, in which the hot proto-neutron star loses its energy and trapped lepton number, while the re-energized shock expands to push out the rest of the star. Each of these three stages is predicted to have a distinct signature in the neutrino signal. Thus, it should be possible to directly observe, for example, how long the shock is stalled. More exotic features of the collapse may be observable in the neutrino flux as well, such as possible transitions to quark matter or to a black hole. (An observation in conjunction with a gravitational wave detection would be especially interesting; e.g. [110,111].)

Over the last two decades, neutrino flavor oscillations have been firmly established in solar neutrinos and a variety of terrestrial sources. The physics of the oscillations in the supernova environment promises to be much richer than in any of the cases measured to date, for a variety of reasons:

- Neutrinos travel through the changing profile of the explosion with stochastic density fluctuations behind the expanding shock and, due to their coherent scattering off of each other, their flavor states are coupled.
- The oscillation patterns come out very differently for the normal and inverted mass hierarchies.
- The expanding shock and turbulence leave a unique imprint in the neutrino signal.
- Additional information on oscillation parameters, free of supernova model-dependence, will be available if matter effects due to the Earth can be observed in detectors at different locations around the world [112,113].
- The observation of this potentially copious source of neutrinos will also allow limits on coupling to axions, large extra dimensions, and other exotic physics (e.g., [114,115]).
- The oscillations of neutrinos and antineutrinos from a core-collapse supernova manifest very differently. In the neutrino channel, the oscillation features are in general more pronounced, since the initial spectra of ν_e and ν_μ (ν_τ) are always significantly different. It would be extremely valuable to detect both neutrino and antineutrino channels with high statistics.

Only about two dozen neutrinos were observed from SN1987A, which occurred in a nearby galaxy; in contrast, the currently proposed next-generation detectors would register thousands or tens of thousands of interactions from a core-collapse supernova in our galaxy. The type of observed interactions will depend on the detector technology: a water-Cherenkov detector is primarily sensitive to $\overline{\nu}_e$'s, whereas a LArTPC detector has excellent sensitivity to ν_e's. In each case, the high event rate implies that it should be possible to measure not only the time-integrated spectra, but also their second-by-second evolution. This is a key feature of the supernova-burst physics potential of the planned LBNE experiment.

Currently, experiments worldwide are sensitive primarily to $\overline{\nu}_e$'s, via inverse-beta decay on free protons, which dominates the interaction rate in water and liquid-scintillator detectors. Liquid argon exhibits a unique sensitivity to the ν_e component of the flux, via the absorption interaction on

^{40}Ar, $\nu_e + {}^{40}\mathrm{Ar} \rightarrow e^- + {}^{40}\mathrm{K}^*$. In principle, this interaction can be tagged via the coincidence of the electron and the ^{40}K* de-excitation gamma cascade. About 900 events would be expected in a 10−kt fiducial liquid argon detector for a core-collapse supernova at 10 kpc. The number of signal events scales with mass and the inverse square of distance, as shown in Figure 2.12. For a collapse

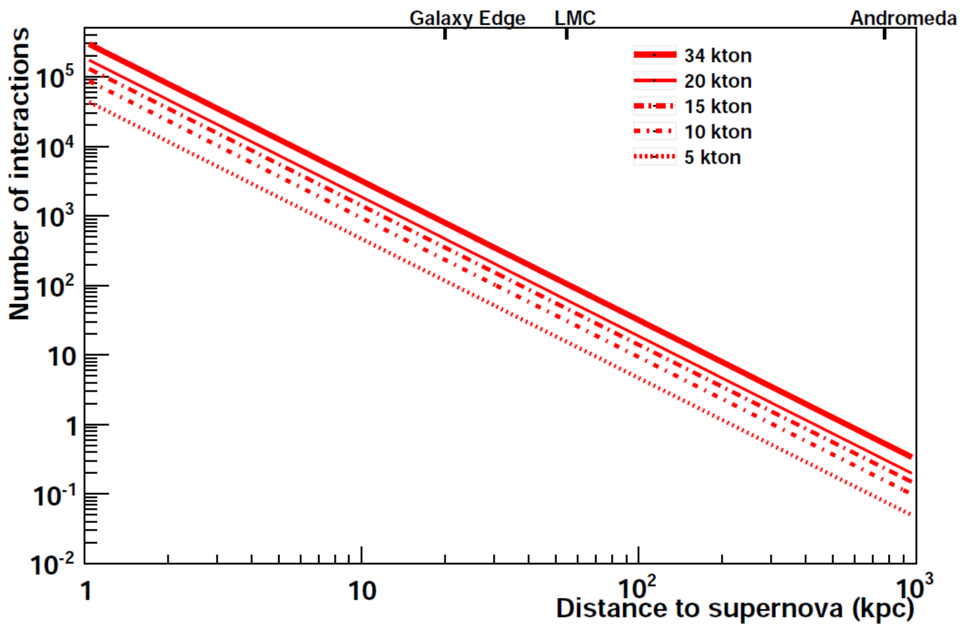

Figure 2.12: Number of supernova neutrino interactions in a liquid argon detector as a function of distance to the supernova for different detector masses. Core collapses are expected to occur a few times per century, at a most-likely distance from 10 kpc to 15 kpc.

in the Andromeda galaxy, massive detectors of hundreds of kilotons would be required to observe a handful of events. However, for supernovae within the Milky Way, even a relatively small 10−kt detector would gather a significant ν_e signal.

Because the neutrinos emerge promptly after core collapse, in contrast to the electromagnetic radiation which must beat its way out of the stellar envelope, an observation could provide a prompt supernova alert [116,117], allowing astronomers to find the supernova in early light turn-on stages, which could yield information about the progenitor (in turn, important for understanding oscillations). Further, observations and measurements by multiple, geographically separated detectors during a core collapse — of which several are expected to be online over the next few decades [106,118] — will enhance the potential science yield from such a rare and spectacular event [112].

Chapter 3 Project and Design

The LBNE Project was formed to design and construct the Long-Baseline Neutrino Experiment. The experiment will comprise a new, high-intensity neutrino source generated from a megawatt-class proton accelerator at Fermi National Accelerator Laboratory (Fermilab) directed at a large far detector at the Sanford Underground Research Facility in Lead, SD. A near detector will be located about 500 m downstream of the neutrino production target. LBNE is currently planned as a phased program, with increased scientific capabilities at each phase.

- The experimental facilities are designed to meet the primary scientific objectives of the experiment: (1) fully characterize neutrino oscillations, including measuring the value of the unknown CP-violating phase, δ_{CP}, and determining the ordering of the neutrino mass states, (2) significantly improve proton decay lifetime limits, and (3) measure the neutrino flux from potential core-collapse supernovae in our galaxy.
- The LBNE beamline, based on the existing *Neutrinos at the Main Injector* (NuMI) beamline design, is designed to deliver a wide-band, high-purity ν_μ beam with a peak flux at 2.5 GeV, which optimizes the oscillation physics potential at the 1,300−km baseline. The beamline will operate initially at 1.2 MW and will be upgradable to 2.3 MW utilizing a proton beam with energy tunable from 60 to 120 GeV.
- The full-scope LBNE far detector is a liquid argon time-projection chamber (LArTPC) of fiducial mass 34 kt.

  The TPC design is modular, allowing flexibility in the choice of initial detector size.
- The LBNE far detector will be located 4,850 feet underground, a depth favorable for LBNE's search for proton decay and detection of the neutrino flux from a core-collapse supernova.
- The high-precision near detector and its conventional facilities can be built as an independent project, at the same time as the far detector and beamline, or later.

3.1 LBNE and the U.S. Neutrino Physics Program

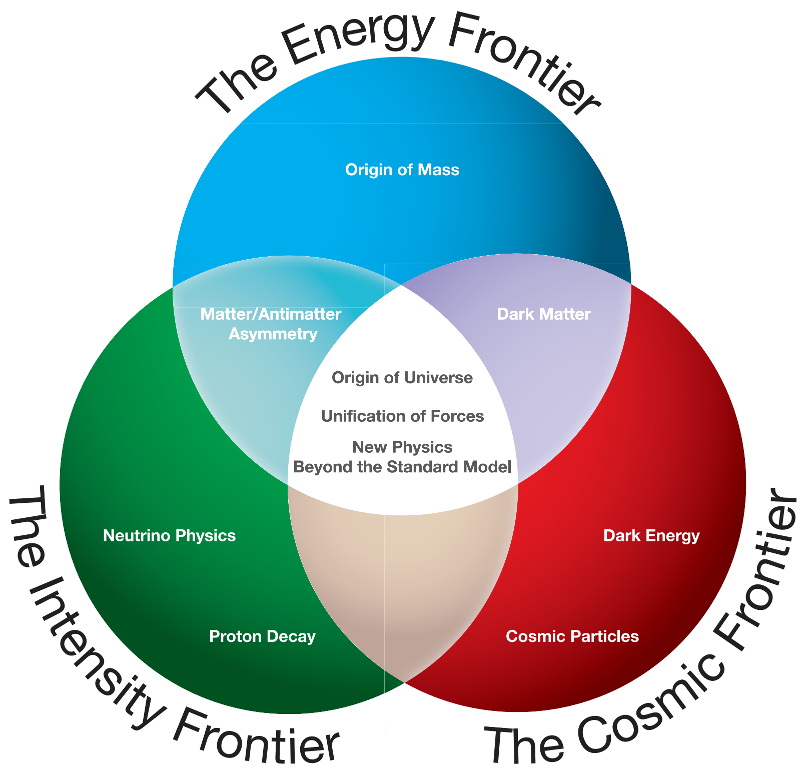

Figure 3.1: Three frontiers of research in particle physics form an interlocking framework that addresses fundamental questions about the laws of Nature and the cosmos. Each frontier, essential to the whole, has a unique approach to making discoveries [14].

In its 2008 report, the U.S. Particle Physics Project Prioritization Panel (P5)* recommended a world-class neutrino physics program as a core component of a U.S. particle physics program [14] that revolves around three research frontiers as shown in Figure 3.1. Included in the report is the long-term vision of a large far detector at the site of the former Homestake Mine in Lead, SD, and a high-intensity, wide-band neutrino source at Fermilab. At the time, the proposed Deep Underground Science and Engineering Laboratory (DUSEL) was planned to occupy the site of the former mine; it is now the Sanford Underground Research Facility.

*P5 is an advisory panel to the two main funding bodies for particle physics in the United States, the Department of Energy (DOE) and the National Science Foundation (NSF).

On January 8, 2010 the DOE approved the Mission Need [18] statement† for a new long-baseline neutrino experiment that would enable this world-class program and firmly establish the U.S. as the leader in neutrino science. The LBNE experiment is designed to meet this Mission Need.

With the facilities provided by the LBNE Project and the unique features of the experiment — in particular the long baseline of 1,300 km, the wide-band beam and the high-resolution, underground far detector — LBNE will conduct a broad scientific program addressing key physics questions concerning the nature of our Universe as described in Chapter 2. The focus of the long-baseline neutrino program will be the explicit demonstration of leptonic CP violation, if it exists, and the determination of the neutrino mass hierarchy.

> The 1,300−km baseline has been determined to provide optimal sensitivity to CP violation and the measurement of $\delta_{\rm CP}$, and is long enough to enable an unambiguous determination of the neutrino mass hierarchy [83].

The focus of the non-beam scientific program will be to search for proton decay, to enable detailed studies of atmospheric neutrinos, and to detect and measure the neutrino flux from a supernova, should one occur within our galaxy.

It is currently planned to implement LBNE as a phased program, with increased scientific capabilities at each phase. The initial phase of LBNE will achieve significant advances with respect to its primary scientific objectives as compared to current experiments. The *goal* for the initial phase of LBNE is:

1. A new neutrino beamline at Fermilab driven by a 60 to 120 GeV proton beam with power of up to 1.2 MW.
2. A liquid argon time-projection chamber (LArTPC) detector of fiducial mass at least 10 kt located at the Sanford Underground Research Facility at a depth of 4,850 feet.
3. A high-precision near neutrino detector on the Fermilab site.

The cost for this initial phase (with a 10−kt far detector) is estimated to be 1.2B U.S.$ according to DOE standard project accounting.

In December of 2012, the DOE issued CD-1 (Conceptual Design phase) approval for a budget of 867M$ U.S. based on a reduced scope that excluded the near neutrino detector and the underground placement of the far detector. Domestic and international partners are being sought to enable construction of the full first-phase scope outlined above. Subsequent phases of LBNE are expected to include additional far detector mass and upgrades of the beam to $\geq$2.3−MW capability.

† A *Mission Need* statement initiates the process and provides initial funding toward developing the conceptual design of a DOE scientific project.

3.2 Near Site: Fermi National Accelerator Laboratory

Fermilab, located 40 miles west of Chicago, Illinois, is a DOE-funded laboratory dedicated to high energy physics. The laboratory builds and operates accelerators, detectors and other facilities that physicists from all over the world use to carry out forefront research.

Dramatic discoveries in high energy physics have revolutionized our understanding of the interactions of the particles and forces that determine the nature of matter in the Universe. Two major components of the Standard Model of Fundamental Particles and Forces were discovered at Fermilab: the bottom quark (May-June 1977) and the top quark (February 1995). In July 2000, Fermilab experimenters announced the first direct observation of the tau neutrino, thus filling the final slot in the lepton sector of the Standard Model. Run II of the Fermilab Tevatron Collider was inaugurated in March 2001. The Tevatron was the world's highest-energy particle accelerator and collider until the Large Hadron Collider at CERN came online in 2011.

While CERN now hosts the world's highest-energy particle collider, the Fermilab accelerator complex is being retooled to produce the world's highest-intensity beams of protons, muons and neutrinos. Scientists from around the world can exploit this capability to pursue cutting-edge research in the lepton sector of the Standard Model where strong hints of new physics have surfaced.

The beamline and near detector for LBNE will be constructed at Fermilab, referred to as the *Near Site*.

Fermi National Accelerator Laboratory, originally named the National Accelerator Laboratory, was commissioned by the U.S. Atomic Energy Commission, under a bill signed by President Lyndon B. Johnson on November 21, 1967. On May 11, 1974, the laboratory was renamed in honor of 1938 Nobel Prize winner Enrico Fermi, one of the preeminent physicists of the atomic age.

Today, the DOE operates national laboratories throughout the United States, including Fermilab. The DOE awarded to Fermi Research Alliance (FRA) the management and operating contract for Fermilab, effective January 1, 2007. The FRA is a tax-exempt, limited liability company (LLC) organized and operated for charitable, scientific and educational purposes under Section 501(c)(3) of the Internal Revenue Code. The two members of FRA are the University of Chicago and the Universities Research Association (URA). FRA has earned extensions to the Fermilab contract through Dec. 31, 2015.

At Fermilab, a robust scientific program pushes forward on the three interrelated scientific frontiers specified by the P5 panel in 2008 [14] and illustrated in Figure 3.1:

1. At the Energy Frontier, Fermilab scientists are significant contributors to the LHC and to the CMS experiment.

2. At the Intensity Frontier, Fermilab operates two neutrino beams that support a number of experiments. In the next few years several new neutrino and muon experiments will be coming online, of which LBNE will be the largest.

3. At the Cosmic Frontier, Fermilab runs and/or participates in several experiments, with instruments installed in North America, South America and Europe.

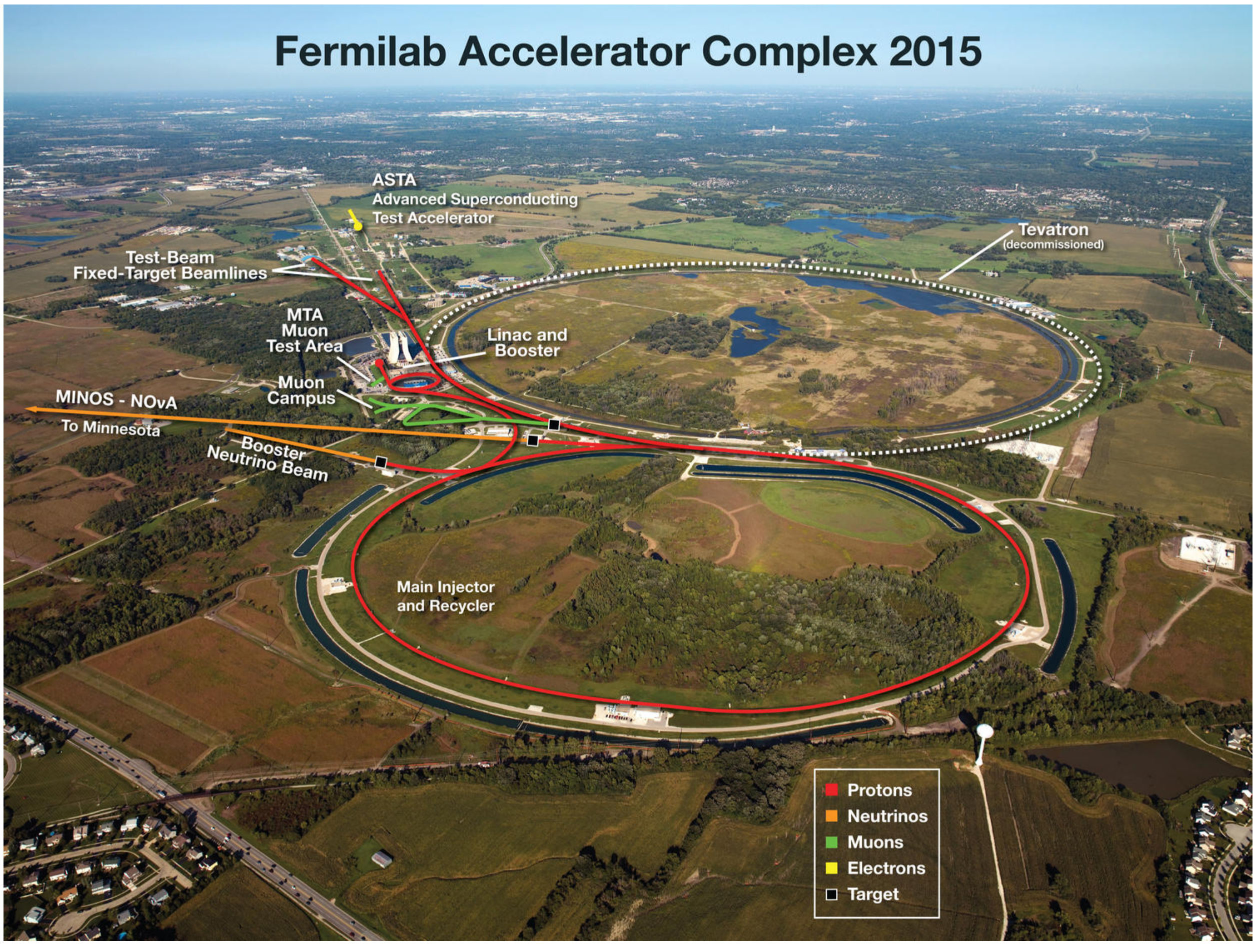

Figure 3.2: The accelerator chain at Fermi National Accelerator Laboratory. A 400−MeV linear accelerator (linac) feeds into the 15-Hz Booster, which produces an 8−GeV beam. The Booster beam is used for the Booster Neutrino Beamline experiments. The Booster feeds into the 120−GeV Main Injector. The Main Injector is the source for the NuMI beamline, which supplies a high-power, high-energy neutrino beam to the MINOS/MINOS+ and NOνA experiments.

The neutrino beams at Fermilab come from two of the lab's proton accelerators (Figure 3.2), the 8−GeV Booster, which feeds the *Booster Neutrino Beamline* (BNB), and the 120−GeV Main Injector (MI), which feeds the NuMI beamline. The LBNE beamline, described in Section 3.4, will utilize the MI beam.

NuMI, on which LBNE's beamline design is based, is a high-energy neutrino beam that has been operating since 2004. It was designed for steady 400−kW operation and achieved that goal by the end of the MINOS experimental run in 2012. As shown in Figure 3.3, the NuMI beamline was running with an average of 9×10^{18} protons per week ($\approx 2.7 \times 10^{20}$ protons-on-target per year) in mid 2012.

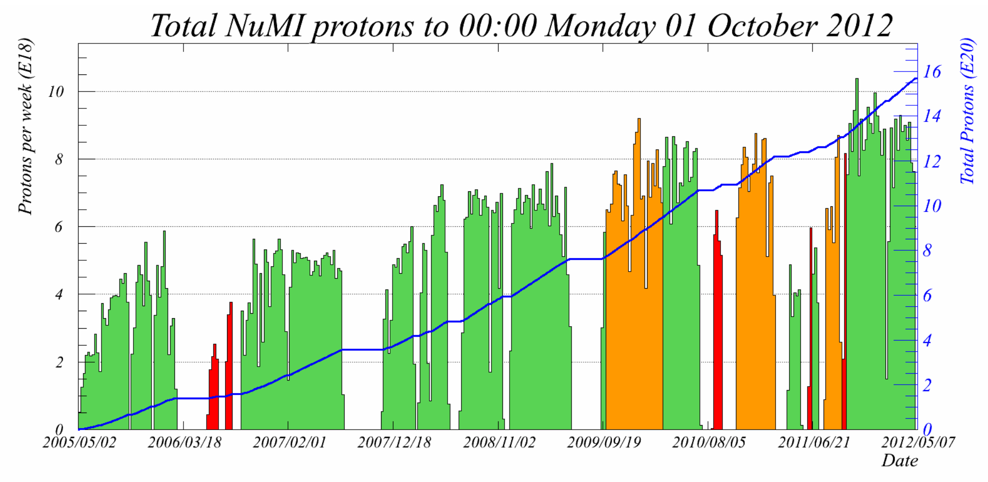

Figure 3.3: The NuMI beamline performance

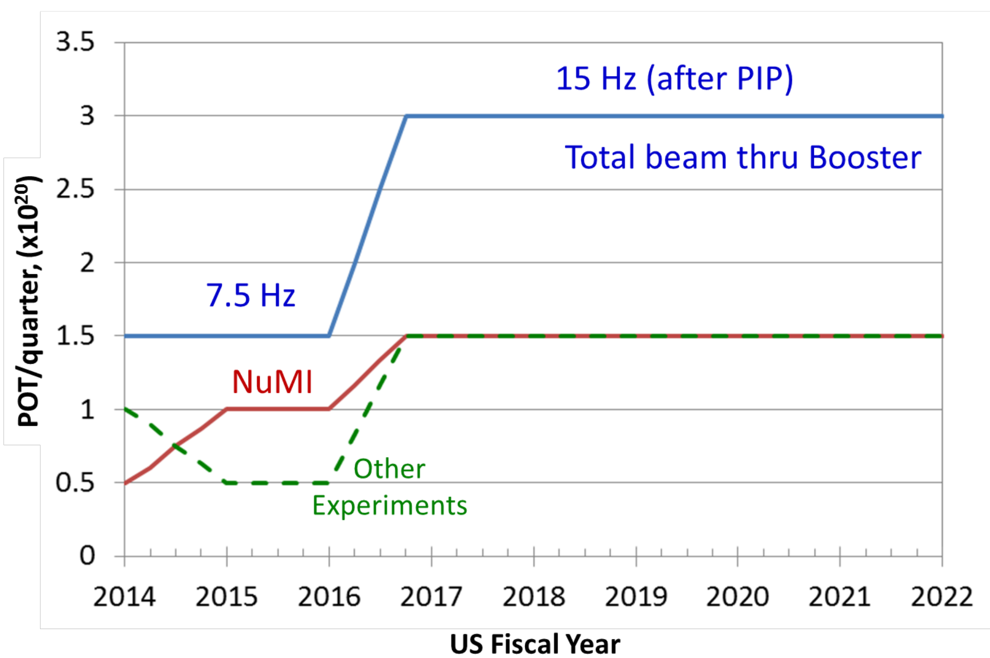

Figure 3.4: A possible ramp-up scenario for proton flux from Fermilab's proton source for the Intensity Frontier experiments.

Upgrades to the Recycler‡ and MI as part of the NOνA Project, as well as the Proton Improvement Plan (PIP) that is currently underway, comprise a set of improvements to the existing Linac, Booster and MI aimed at supporting 15-Hz beam operations from the Booster (Figure 3.4).

In combination, the NOνA upgrades and the PIP create a capability of delivering 700 kW from the MI at 120 GeV ($\approx 6 \times 10^{20}$ proton-on-target per year) by 2016. The proton beam power expected to be available as a function of MI beam energy after completion of the PIP upgrades is shown in Figure 3.5.

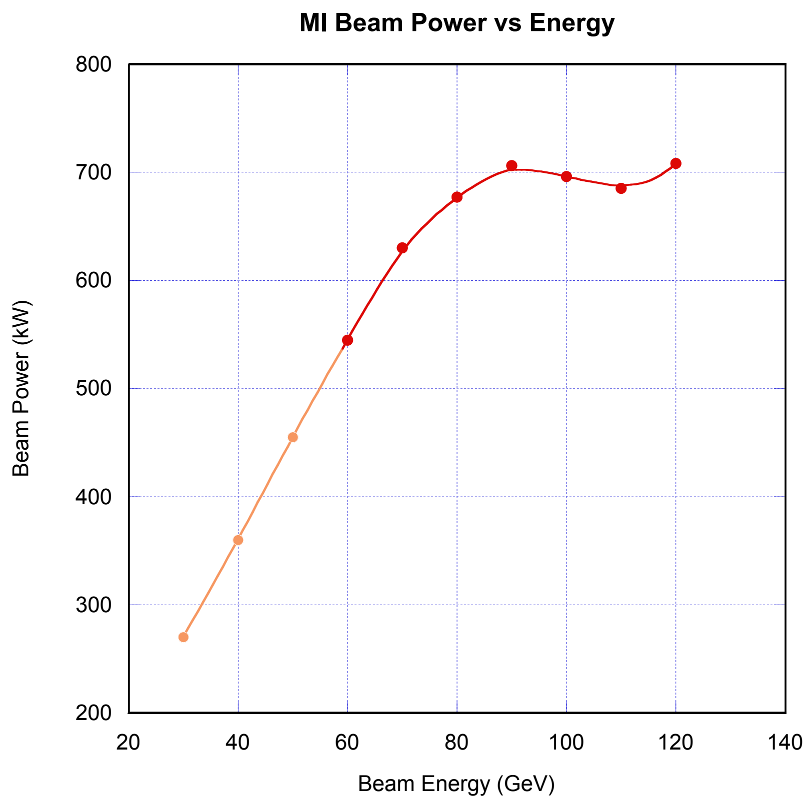

Figure 3.5: Proton beam power expected to be available as a function of MI beam energy after proton-improvement-plan (PIP) upgrades.

A conceptual plan for further upgrades to the Fermilab accelerator complex has been completed. Called the *Proton Improvement Plan-II* (PIP-II) [22], its goal is to increase the capabilities of the existing accelerator complex to support delivery of 1.2 MW of beam power to the LBNE production target at the initiation of operations, while simultaneously providing a platform for subsequent upgrades of the complex to multi-MW capability. The starting point of this plan is the *Project X Reference Design Report* [23].

‡The Recycler, a fixed 8-GeV kinetic energy storage ring located directly above the MI beamline, stores protons from the 8-GeV Booster during MI ramp up.

The primary bottleneck to providing increased beam power at Fermilab is the Fermilab Booster, limited by space-charge forces at injection. In the intermediate term the most cost-effective approach to removing this bottleneck is to increase the injection energy into the Booster. The PIP-II meets this goal via an 800−MeV superconducting linear accelerator (linac), operated at low duty factor, but constructed of accelerating modules that are capable of continuous-wave (CW) operations if provided with sufficient cryogenic cooling and appropriate RF power. This is expected to increase the beam intensity delivered from the Booster by 50% relative to current operations. Shortening the MI cycle time to 1.2 s yields a beam power of 1.2 MW at 120 GeV. The conceptual site layout of PIP-II is shown in Figure 3.6. Further possible upgrades beyond PIP-II would require replacing the 8−GeV Booster with a superconducting linac injecting into the MI at energies between 6 and 8 GeV as shown in Figure 3.6, eventually increasing the power from the MI to 2.0–2.3 MW at 60–120 GeV.

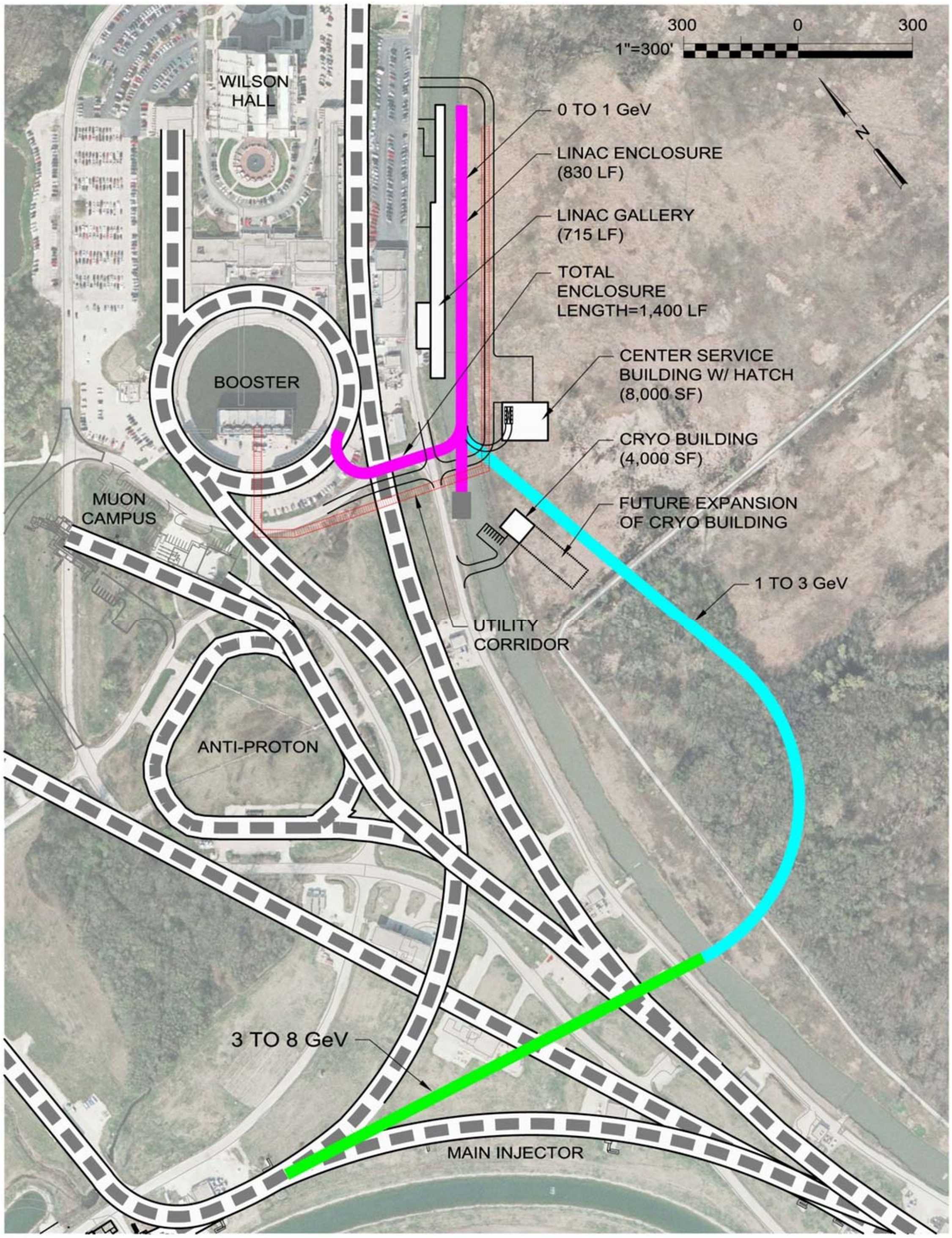

Figure 3.6: Site layout of PIP- II is shown as the magenta line which is the 800 MeV linac enclosure and transfer line. New construction includes the linac enclosure, transfer line enclosure, linac gallery, center service building, utility corridor, and cryo building. Dashed areas represent existing or planned underground enclosures. Further possible upgrades to the Fermilab complex beyond PIP- II are shown in the bottom half of the figure: cyan is a 1-3 GeV CW linac and transfer line, and green is a 3-8 GeV pulsed linac [22].

3.3 Far Site: Sanford Underground Research Facility

The Sanford Underground Research Facility [119] is a laboratory located on the site of the former Homestake gold mine in Lead, SD that is dedicated to underground science. This laboratory has been selected as the location of the far detector for LBNE, and is referred to as the *Far Site*.

Underground neutrino experiments in the former mine date back to 1967 when nuclear chemist Ray Davis installed a solar neutrino experiment 4,850 feet below the surface [120]. Ray Davis earned a share of the Nobel Prize for physics in 2002 for his experiment, which ran until 1993.

LBNE is envisioned as the next-generation, multi-decade neutrino experiment at this site seeking groundbreaking discoveries.

In 2006, Barrick Gold Corporation donated the Homestake Gold Mine site, located in Lead, South Dakota (Figure 3.7) to the State of South Dakota, following over 125 years of mining. Mining operations created over 600 km of tunnels and shafts in the facility, extending from the surface to over 8,000 feet below ground. The mining levels are distributed $\sim$150 feet apart and are referenced by their depth below the facility entrance, e.g., the level 4,850 feet below ground is referred to as the *4850L*. This former mine encompasses the deepest caverns in the western hemisphere, offering extensive drifts both vertically and laterally. A detailed vertical cross section of the 60 underground levels developed for mining is shown in Figure 3.8.

In 2004, the South Dakota state legislature created the South Dakota Science and Technology Authority (SDSTA) to foster scientific and technological investigations, experimentation and development in South Dakota. A six-member board of directors appointed by the governor of South Dakota directs the SDSTA. The SDSTA's first task was to reopen the former Homestake site to the 4,850-foot level for scientific research. At this site, the SDSTA now operates and maintains the Sanford Underground Research Facility through a contract managed and overseen by a dedicated operations office at Lawrence Berkeley National Laboratory as a deep-underground research laboratory. The Sanford Underground Research Facility property comprises 186 acres on the surface and 7,700 acres underground. The surface campus includes approximately 253,000 gross square feet of existing structures. A surface schematic of the campus is shown in Figure 3.9.

The state legislature has since committed more than $40 million in state funds to the development of the Sanford Underground Research Facility, and the state has also obtained a $10 million Community Development Block Grant to help rehabilitate the site. In addition, a $70 million donation from philanthropist T. Denny Sanford has been used to reopen the site for science and to establish the Sanford Center for Science Education. The initial concepts for the facility were developed with

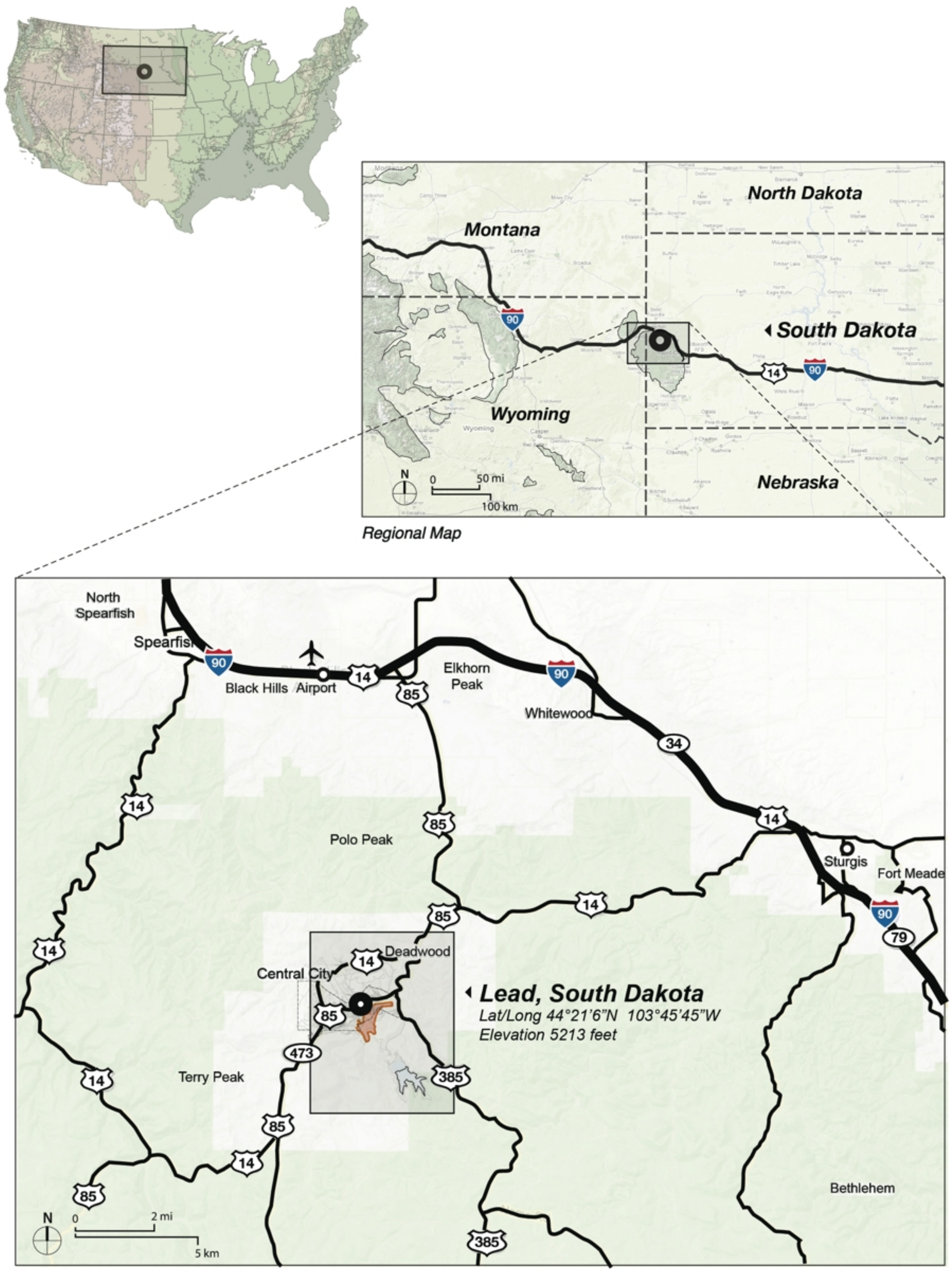

Figure 3.7: Location of the town of Lead, South Dakota - the site of the former Homestake Gold Mine.

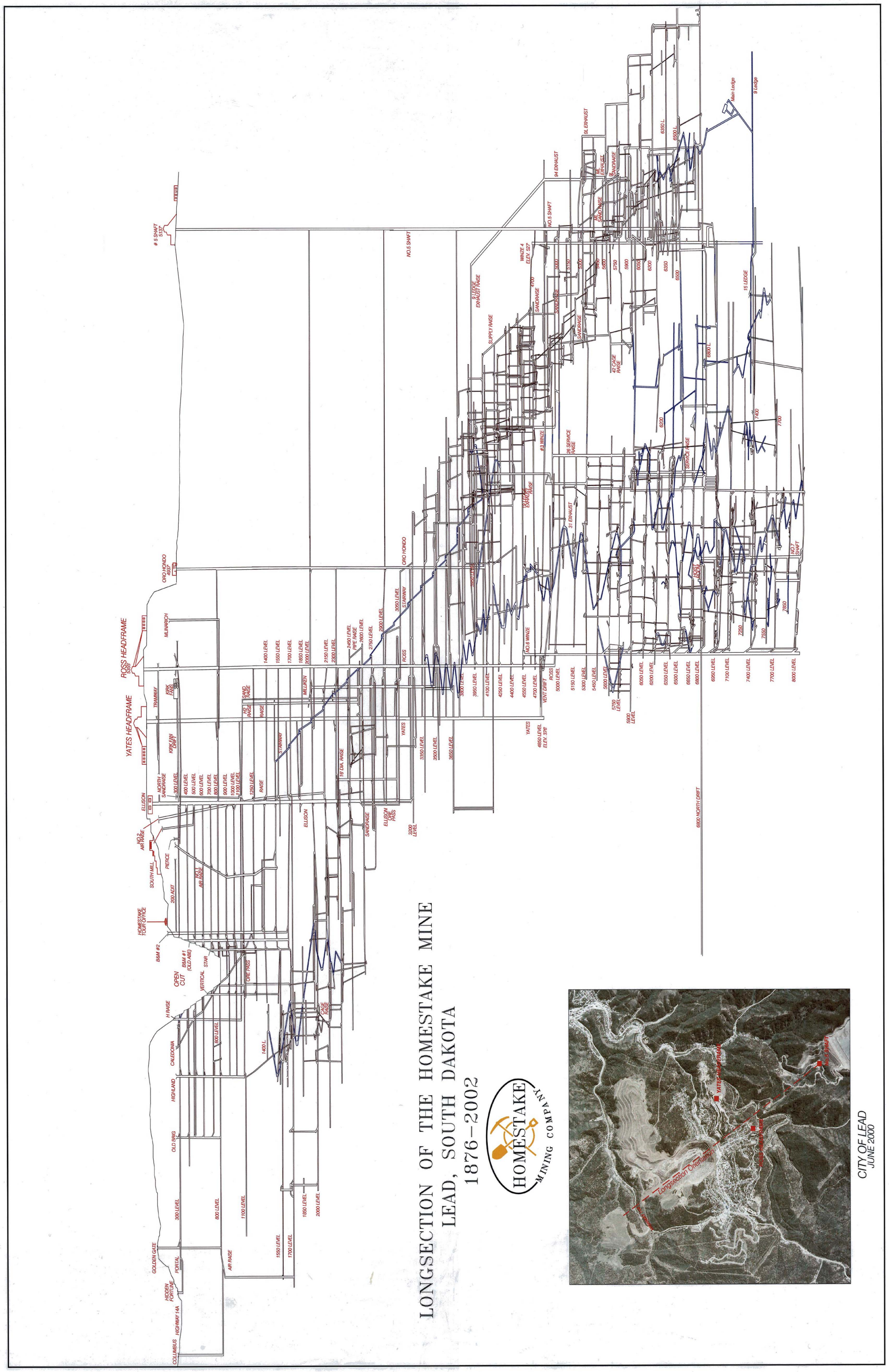

Figure 3.8: The long section of the former Homestake Gold Mine. This figure illustrates the 60 underground levels extending to depths greater than 8,000 feet. The location of cross section is indicated in the inset along a NW to SE plane. The projection extends for 5.2 km along this plane

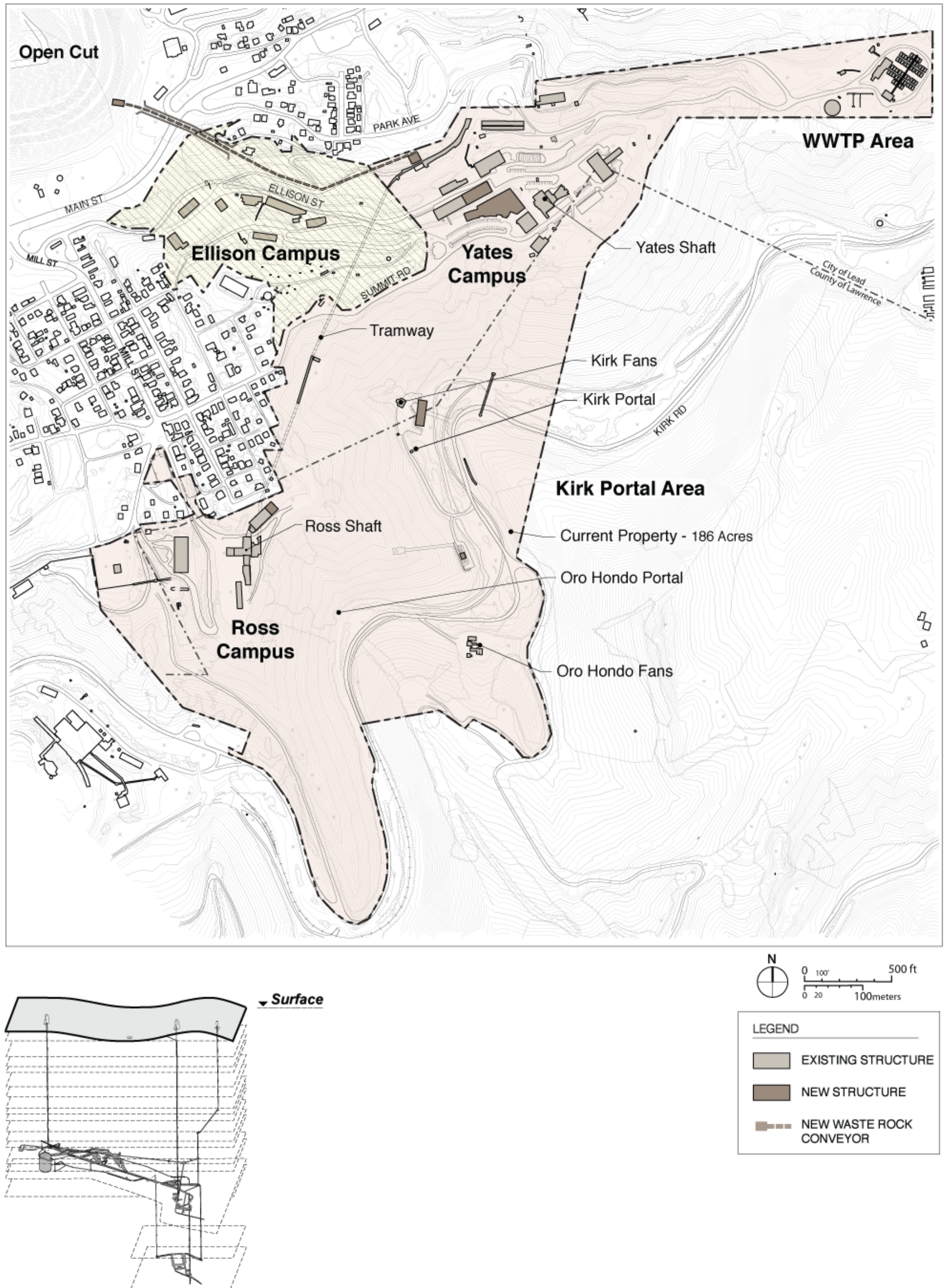

Figure 3.9: The surface and underground campuses of the Sanford Underground Research Facility. The 3D inset image illustrates the plans to develop the 4850L and 7400L. Most current experiments are at the 4850L.

the support of the U.S. National Science Foundation (NSF) as the primary site for the NSF's Deep Underground Science and Engineering Laboratory (DUSEL). With the National Science Board's decision to halt development of the NSF-supported underground laboratory, the DOE now supports the operation of the facility in addition to state and private funding. Both the NSF and the DOE support experiments at the site.

Access to the underground areas has been reestablished and the primary access rehabilitated and improved. The facility has been stabilized and the accumulated underground water has been pumped out below 5,680 ft. The area around the Davis cavern at the 4850L, named for the late Ray Davis, has been enlarged and adapted primarily for current and next-generation dark matter and neutrinoless double-beta decay experiments. This upgraded area of the 4850L is now called the Davis Campus. Additional science efforts are located throughout the facility, including an ultrapure detector development laboratory, geophysics and geological efforts, and a public outreach program. A 3D schematic highlighting the planned development of the 4850L is shown in Figure 3.10. The

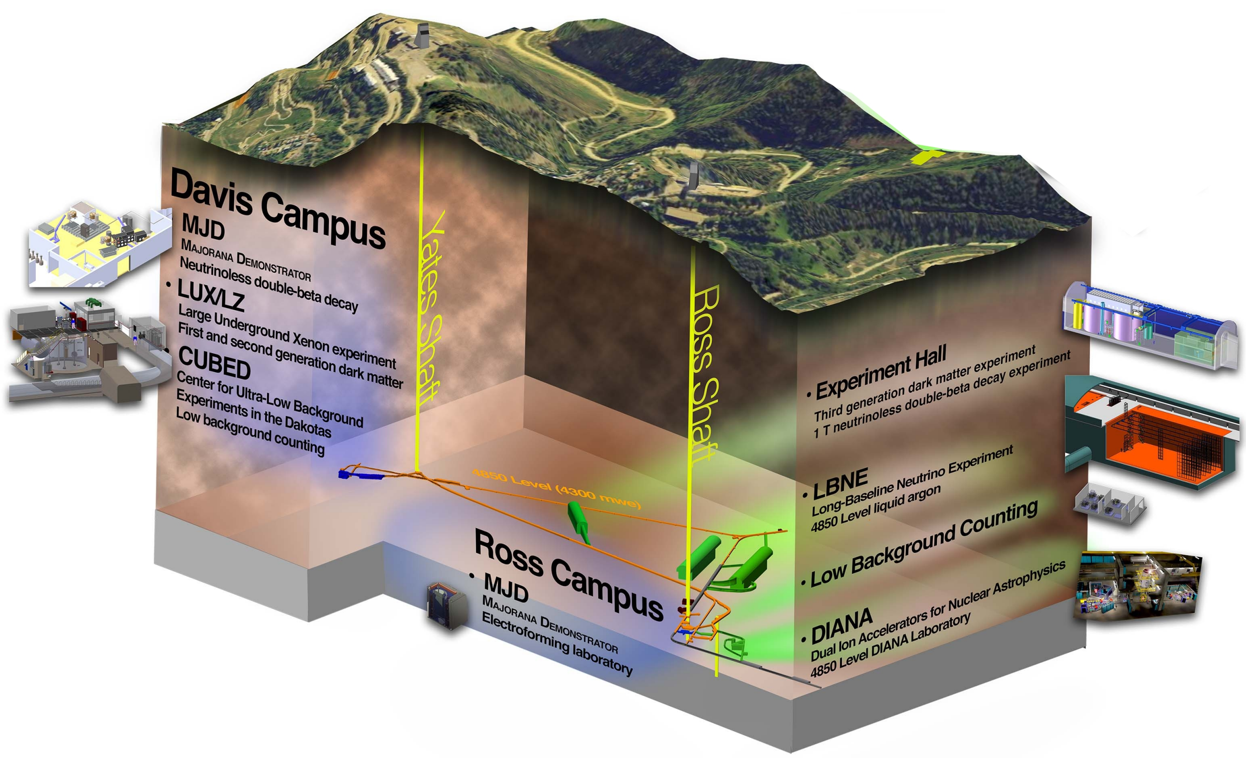

Figure 3.10: Layout of experiments at the 4,850−ft level in the Sanford Underground Research Facility

LBNE far detector will be located in new excavated spaces near the bottom of the Ross Shaft, about 1 km from the Davis Campus. The 4,850−ft depth makes it an extremely competitive location in terms of cosmic-ray background suppression for undertaking the nucleon decay and supernova neutrino studies that LBNE plans to address. Figure 3.11 shows the predicted cosmic-ray flux at this site [121] as compared to other underground laboratories worldwide.

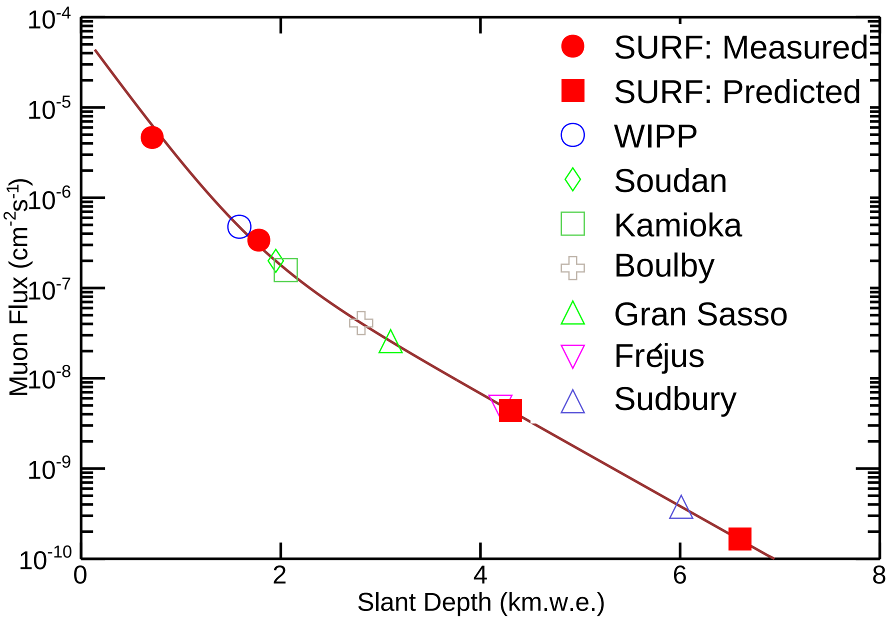

Figure 3.11: Predicted cosmic-ray flux as a function of depth. The predicted muon flux at the 4,850 ft and 8,000 ft levels of the Sanford Underground Research Facility (SURF) are show as red squares. Two measured depths in the facility are shown as red circles. Values for other underground laboratories are also shown [121]. The line shows a parameterized model of the muon flux.

Another advantage of the 4850L Sanford Underground Research Facility site for LBNE is the low level of rock radioactivity that could contribute backgrounds to the supernova burst neutrino signal and other low-energy physics searches. It was found that the U/Th/K radioactivity for the underground bedrocks at Homestake is in general very low when compared to common construction materials such as concrete and shotcrete; some samples are in the sub-ppm levels. However, samples from rhyolite intrusions, *a very small fraction of the total*, show a relatively high content of U, Th, and K more typical of the levels found in other laboratories, in particular those in granitic formations. Regions of potential rhyolite intrusions have been identified and documented as shown in Figure 3.12. In some cases local shielding significantly mitigates the impact of the rhyolite intrusions. Table 3.1 presents some of the assay results, obtained by direct gamma counting for rock samples from the mine, including those collected close to the 4850L [122]. The Large Underground Xenon (LUX) experiment is now operating in the cavern first excavated for Davis in the 1960s. LUX is the most sensitive detector yet to search for dark matter [123]. The Majorana Demonstrator experiment (MJD), also being installed in a newly excavated space adjacent to the original Davis cavern, will search for neutrinoless double-beta decay. Figure 3.13 shows four photographs of facilities and activities at the Sanford Underground Research Facility related to the LUX and MJD at the 4850L. The LBNE far detector will benefit from the common infrastructure being developed to house large experiments underground. The layout of the different proposed experiments at the 4850L, including the LBNE detector, is shown in Figure 3.10.

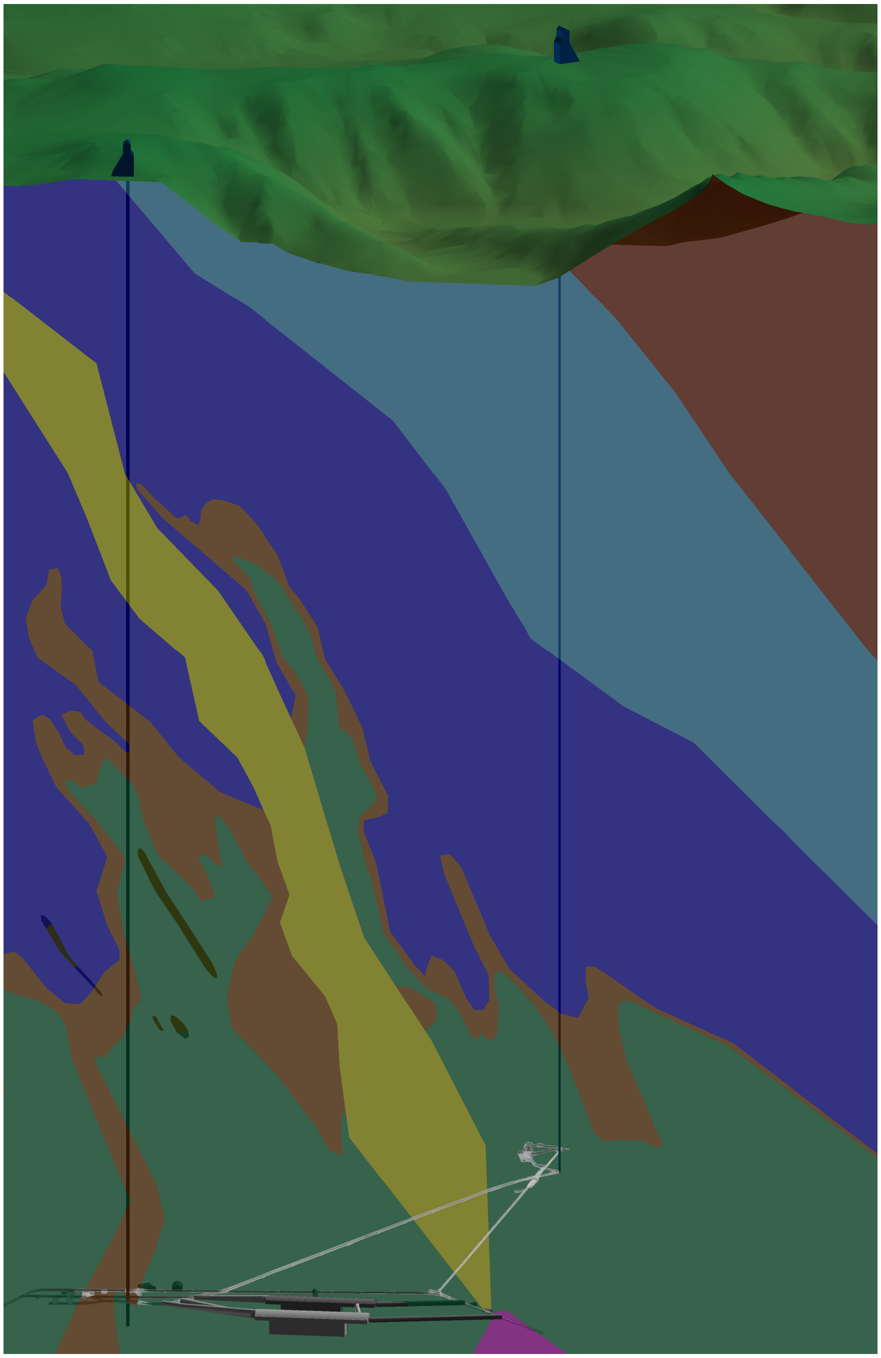

Figure 3.12: Geologic long section of Sanford Underground Research Facility showing the main rock formations. The dark green rock is the Poorman formation, and the yellow areas indicate a projected rhyolite swarm. The proposed location of two LBNE detector caverns are shown in the foreground.

In addition to LBNE, LUX and MJD, the Sanford Underground Research Facility science program for the coming five to ten years (Figure 3.14) consists of the expansion of the LUX dark matter search, the Center for Ultralow Background Experiments at Dakota (CUBED), and the geoscience installations. Long-term plans are being developed to host a nuclear astrophysics program

Table 3.1: Partial U/Th/K assay results for Sanford Underground Research Facility rock samples. Overall errors estimated to be ∼10-20%. Also shown are results for various construction materials (shotcrete/concrete).

	Uranium (ppm) Ave. [Range]	Thorium (ppm) Ave. [Range]	Potassium (%) Ave. [Range]
U/G Country Rock	0.22 [0.06-0.77]	0.33 [0.24-1.59]	0.96 [0.10-1.94]
Shotcrete	1.89 [1.74-2.23]	2.85 [2.00-3.46]	0.88 [0.41-1.27]
Concrete Blocks	2.16 [2.14-2.18]	3.20 [3.08-3.32]	1.23 [1.27-1.19]
Rhyolite Dike	8.75 [8.00-10.90]	10.86 [8.60-12.20]	4.17 [1.69-6.86]

Figure 3.13: Sanford Underground Research Facility: Administration building and Yates shaft headframe (top left); corridor at 4,850 ft (1,480 m) depth leading to clean rooms and experimental halls (top right); billet of radiopure electroformed copper for the MJD experiment being placed on a lathe in a clean room at 4,850 ft depth (bottom left); LUX experiment at 4,850 ft depth (bottom right).

involving underground particle accelerators (CASPAR and DIANA), and second- and third-generation dark matter experiments.

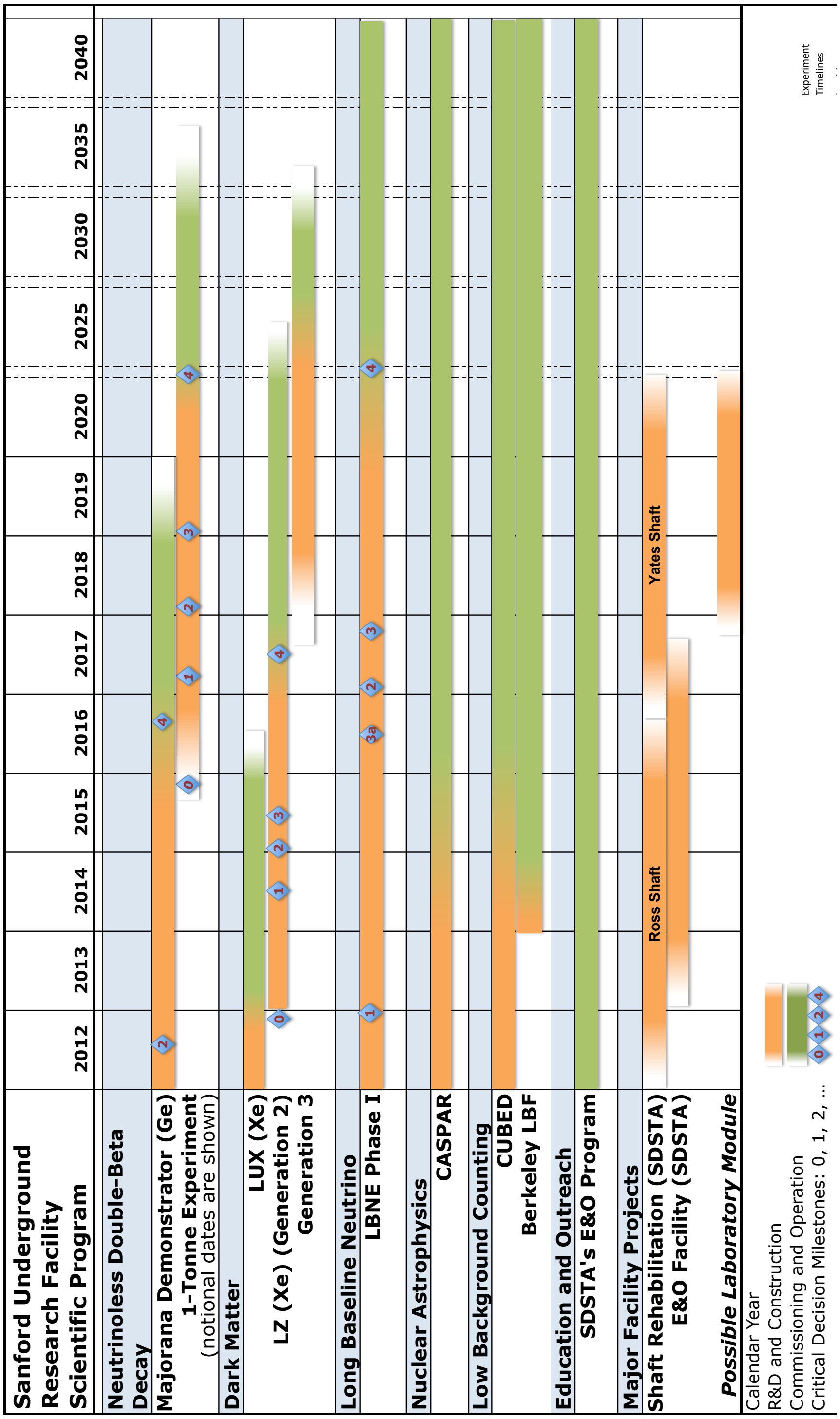

Figure 3.14: Timeline exploring the long-term potential of deep science experiments at the Sanford Underground Research Facility. Figure courtesy of Mike Headley, the Sanford Underground Research Facility.

3.4 Beamline

The LBNE neutrino beamline, located at Fermilab, utilizes a conventional horn-focused neutrino beam produced from pion decay-in-flight, based largely on the highly successful NuMI beamline design:

- The primary beam utilizes 60- to 120−GeV protons from the Main Injector accelerator. The primary beamline is embedded in an engineered earthen embankment — a novel construction concept to reduce costs and improve radiological controls.
- The beamline is designed to operate at 1.2 MW and to support an upgrade to 2.3−MW operation.
- The beamline will generate a wide-band, high-purity beam, selectable for muon neutrinos or muon antineutrinos. Its tunable energies from 60 to 120 GeV will be well matched to the 1,300−km neutrino oscillation baseline.

The LBNE beamline facility will aim a beam of neutrinos toward the LBNE far detector located 1,300 km away at the Sanford Underground Research Facility. The beamline facility, which will be fully contained within Fermilab property, will consist of a primary (proton) beamline, a neutrino beamline, and conventional facilities to support the technical components of the primary and neutrino beamlines [30]. The LBNE beamline reference design parameters approved at CD-1 are summarized in Table 3.2. Improvements to this design that have been made or are being considered are described in this section, including the important change to an initial beam power of 1.2 MW, enabled by the planned PIP-II. The beamline needed for the full-scope LBNE will be realized in the first phase of LBNE and will be upgradable to 2.3 MW.

The primary beam, composed of protons in the energy range of 60-120 GeV, will be extracted from the MI-10 straight section of the Main Injector using single-turn extraction. The beam will then be transported to the target area within a beam enclosure embedded in an engineered earthen embankment (hill). The primary-beam transport section is designed for very low losses. The embankment's dimensions are designed to be commensurate with the bending strength of the required dipole magnets so as to provide a net 5.8° downward vertical bend to the neutrino beam (Figures 3.15 and 3.16). The beamline is then buried by soil shielding that is placed at a stable angle of repose, resulting in the embankment final geometry.

For 120−GeV operation and with the MI upgrades implemented for the NOνA experiment [126], the fast, single-turn extraction will deliver 4.9×10^{13} protons to the LBNE target in a 10−μs pulse. With a 1.33−s cycle time, the beam power for NOνA is 700 kW. Additional accelerator upgrades planned as PIP-II [22] will increase the protons per cycle to 7.5×10^{13} and reduce the

Table 3.2: Partial set of parameters for the elements of the LBNE Beamline reference design at CD-1 from Volume 2 of the CDR [30]. The reference design described a 700 kW beam; it has since been changed to 1.2 MW. For each parameter the third column lists the range that had been studied prior to CD-1. Distances between beam elements are given from the upstream face (the end facing the proton beam) with respect to the upstream (front) face of Horn 1.

Element	Parameter	Range studied	Reference design value (700 kW)
Proton Beam	energy	60 GeV to 120 GeV	120 GeV
	protons per pulse		4.9×10^{13}
	cycle time between pulses		1.33 s
	size at target $\sigma_{x,y}$	1 mm to 2 mm	1.3 mm
	duration		1.0×10^{-5} sec
	POT per year		6.5×10^{20}
Target	material	graphite, beryllium hybrid [124]	graphite
	length	$\geq$ 2 interaction lengths	966 mm
	profile	rectangular, round (r = 5 mm to 16 mm)	rectangular 7.4 mm x 15.4 mm
	dist. from Horn 1 (front)	0 cm to −250 cm	−35 cm to −285 cm
Focusing Horn 1 [125]	shape	cylindrical-parabolic, double-parabolic	double-parabolic (NuMI)
	length (focusing region)	2,500 mm to 3,500 mm	3,000 mm
	current	180 kA to 350 kA	200 kA
	minimum inner radius		9.0 mm
	maximum outer radius		174.6 mm
Focusing Horn 2	shape	double-parabolic	NuMI Horn 2
	length (focusing region)	3,000 mm to 4,000 mm	3,000 mm
	current	180 kA to 350 kA	200 kA
	minimum inner radius		39.0 mm
	maximum outer radius		395.4 mm
	dist. from Horn 1 (front)	4,000 mm to 10,000 mm	6,600 mm
Decay Pipe	length	200 m to 350 m	204 m
	radius	1.0 m to 3.0 m	2 m
	atmosphere	Air, He, vacuum	air at atm. pressure
	dist. from Horn 1 (front)	11 m to 23 m	17.3 m

cycle time to 1.2 s, resulting in an initial beam power for LBNE of 1.2 MW. The LBNE beamline is designed to support additional beam power upgrades beyond PIP-II, discussed in Section 3.2, that can increase the beam power up to 2.3 MW. At 1.2−MW operation the accelerator and primary beamline complex are expected to deliver 11×10^{20} protons per year to the target.

Approximately 85% of the protons interact with the solid target, producing pions and kaons that subsequently get focused by a set of magnetic horns into a decay pipe where they decay into muons and neutrinos (Figure 3.17). The neutrinos form a wide-band, sign-selected neutrino or antineutrino

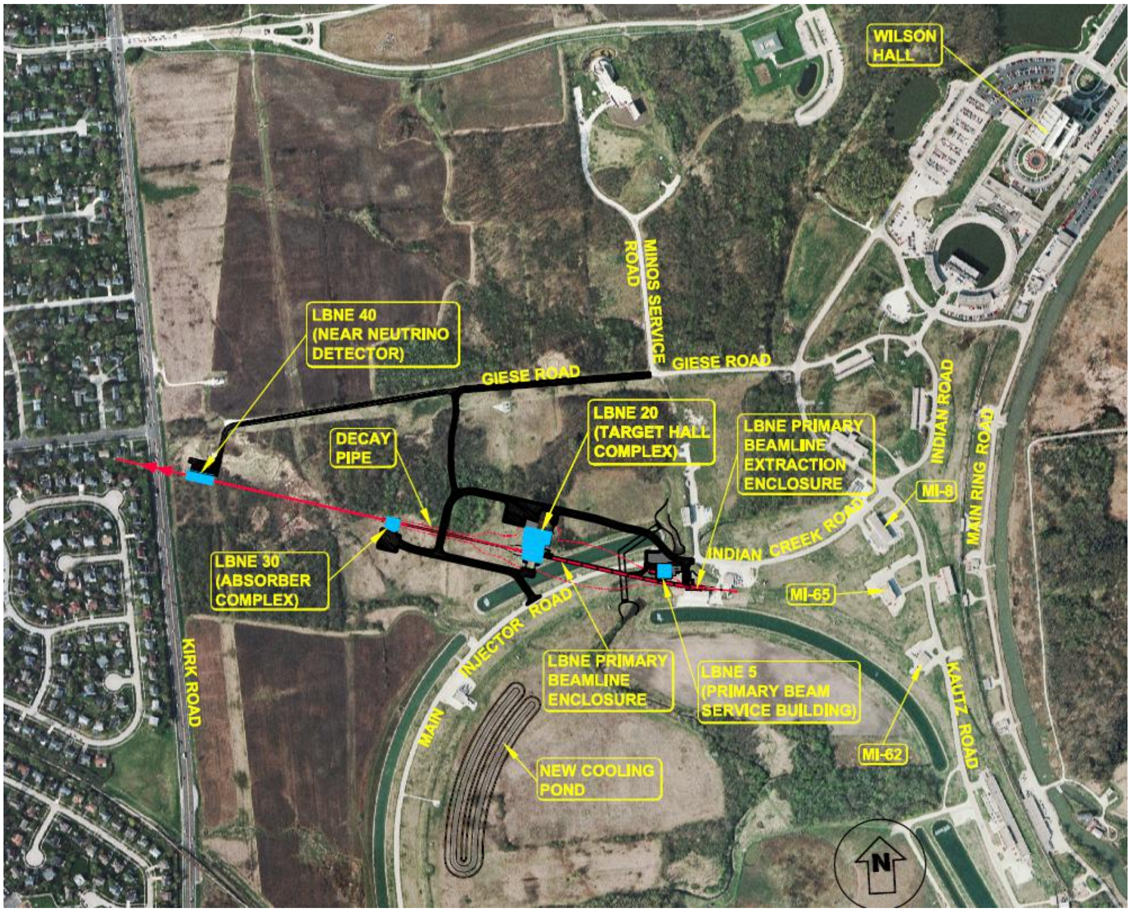

Figure 3.15: Plan view of the overall Near Site project layout showing locations for the LBNE Beamline extraction point from the MI, the primary beamline, target hall, decay pipe, absorber and near neutrino detector.

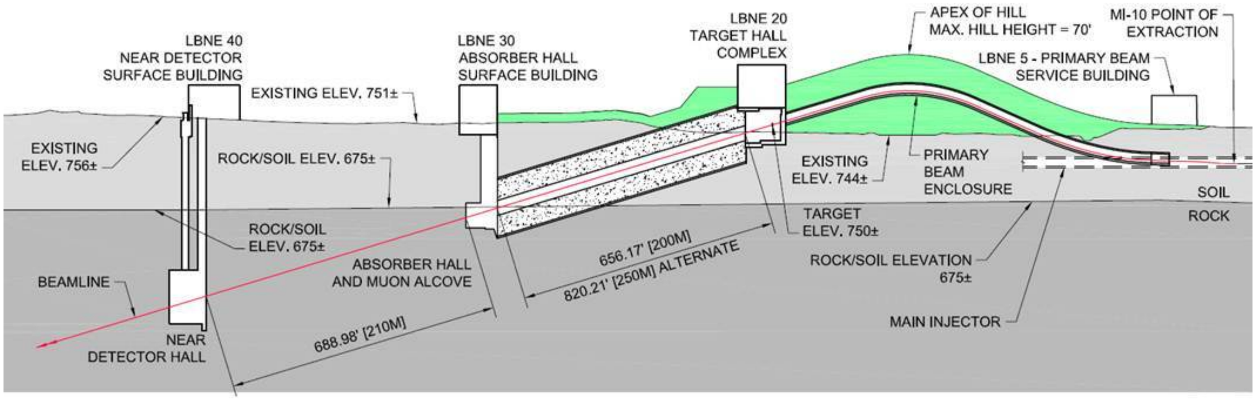

Figure 3.16: Longitudinal section of the LBNE Beamline facility. The beam enters from the right in the figure, the protons being extracted from the MI-10 extraction point at the Main Injector.

beam, designed to provide flux in the energy range of 0.5 to 5 GeV. This energy range will cover the first and second neutrino-oscillation maxima, which for a 1,300−km baseline are at approximately 2.5 and 0.8 GeV, respectively.

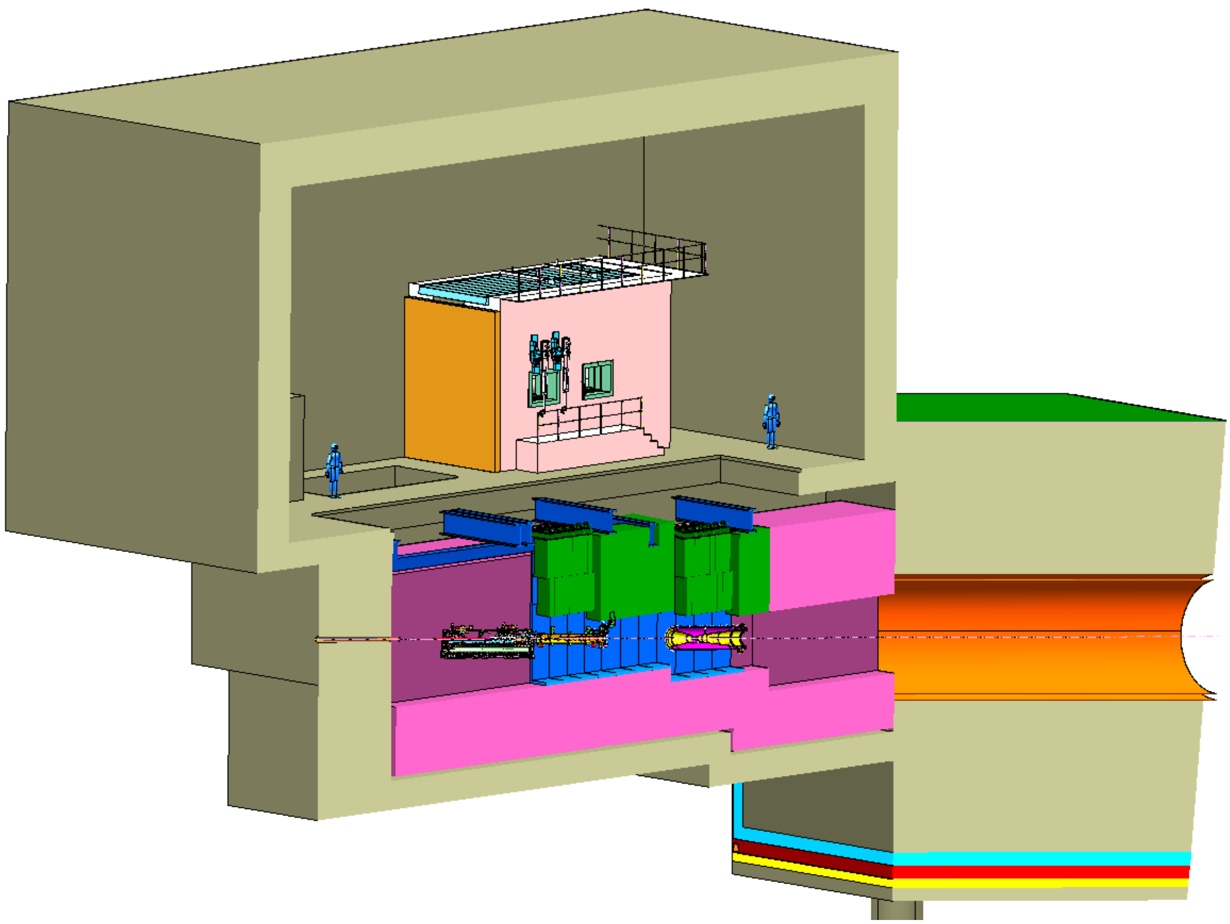

Figure 3.17: Schematic of the upstream portion of the LBNE neutrino beamline showing the major components of the neutrino beam. The target chase bulk steel shielding is shown in magenta. Inside the target chase from left to right (the direction of the beam) pointing downwards: the beam window, horn-protection baffle and target mounted on a carrier, the two toroidal focusing horns (the green custom shielding blocks are part of the horn support modules that are not shown) and the decay pipe (orange). Above the chase and to the right is the work cell for horn and target system repairs. The beige areas indicate concrete shielding.

The reference target design for LBNE is an upgraded version of the NuMI-LE (Low Energy) target that was used for eight years to deliver beam to the MINOS experiment. The target consists of 47 segments, each 2 cm long, of POCO graphite ZXF-5Q. Focusing of charged particles is achieved by two magnetic horns in series, the first of which partially surrounds the target. They are both NuMI/NOνA-design horns with double-paraboloid inner conductor profiles. The NuMI/NOνA-design horns currently operate at 185 kA to 200 kA. The horns have been evaluated and found to be operable with currents up to 230 kA but the striplines that supply the horn currents are still under evaluation. Additional development of the target and horns is required to adapt the existing designs from the 700−kW beam power used by NOνA to 1.2 MW for LBNE. The horn current polarity can be changed to selectively focus positive or negative hadrons, thus producing high purity ($> 90\%$ in oscillation region) ν_μ or $\overline{\nu}_\mu$ beams. Each beam polarity will have a $< 10\%$ contamination of neutrinos of the "wrong sign" in the oscillation energy region ($\overline{\nu}$'s in the ν beam and vice-versa) from decays of wrong-sign hadrons that propagate down the center of the focusing horns — where there is no magnetic field — into the decay volume. In addition, a $\leq 1\%$ contamination of ν_e and $\overline{\nu}_e$ in the ν_e appearance signal region is produced by the decays of tertiary muons from pion decays, and decays of kaons. The neutrino flux components from the LBNE CD-1 beamline design produced using a full Geant4 simulation of both horn polarities are shown in Figure 3.18. The

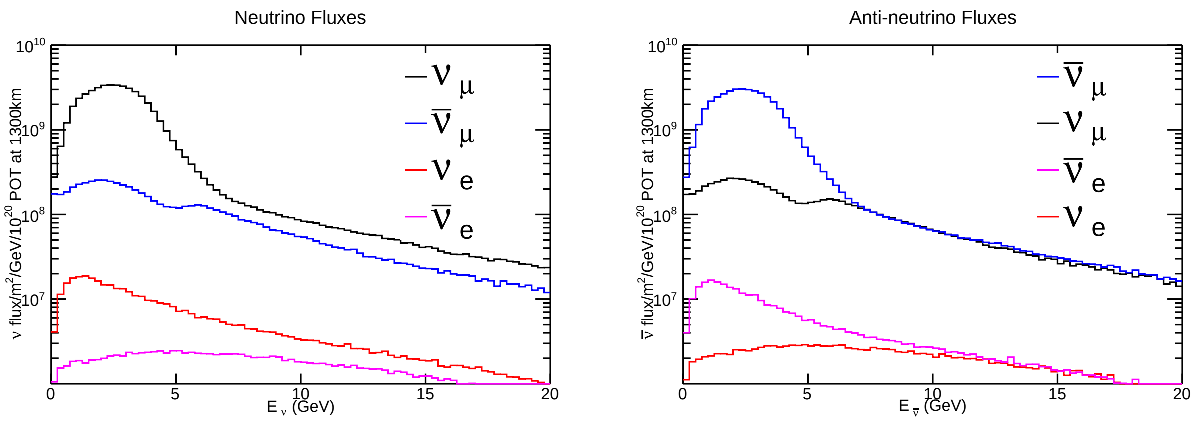

Figure 3.18: The neutrino beam fluxes (left) and antineutrino beam fluxes (right) produced by a Geant4 simulation of the LBNE beamline. The horn current assumed is 200 kA, the target is located 35 cm in front of horn 1, the decay pipe is air-filled, 4 m in diameter and 204 m in length.

beamline design provides a wide-band neutrino beam with a peak flux at 2.5 GeV, which matches the location of the first $\nu_\mu \to \nu_e$ oscillation maximum. The NuMI reference target design used for LBNE allows the target to be moved with respect to Horn 1. The location of the upstream face [§] of the target with respect to the upstream face of Horn 1 can be varied from −35 cm (default location) to −2.85 m, thus the LBNE beamline can produce a wide range of beam spectra. Three possible far-site beam spectra, produced by moving the target from −35 cm (low-energy) to −1.5 m (medium-energy) to −2.5 m (high energy) are shown in Figure 3.19.

The decay volume design for LBNE is a helium-filled, air-cooled pipe of circular cross section with a diameter of 4 m and length from 204 m to 250 m optimized such that decays of the pions and kaons result in neutrinos in the energy range useful for the experiment. A 250−m decay pipe is the maximum length that will allow the near neutrino detector complex to fit within the Fermilab site boundaries. At the end of the decay region, the absorber, a water-cooled structure of aluminum and steel, is designed to remove any residual hadronic particles; it must absorb a large fraction of the incident beam power of up to 2.3 MW. Instrumentation immediately upstream of the absorber

[§] The proton beam direction determines the upstream and downstream conventions. The upstream (front) face of Horn 1 is therefore the Horn 1 face closest to the proton beam window.

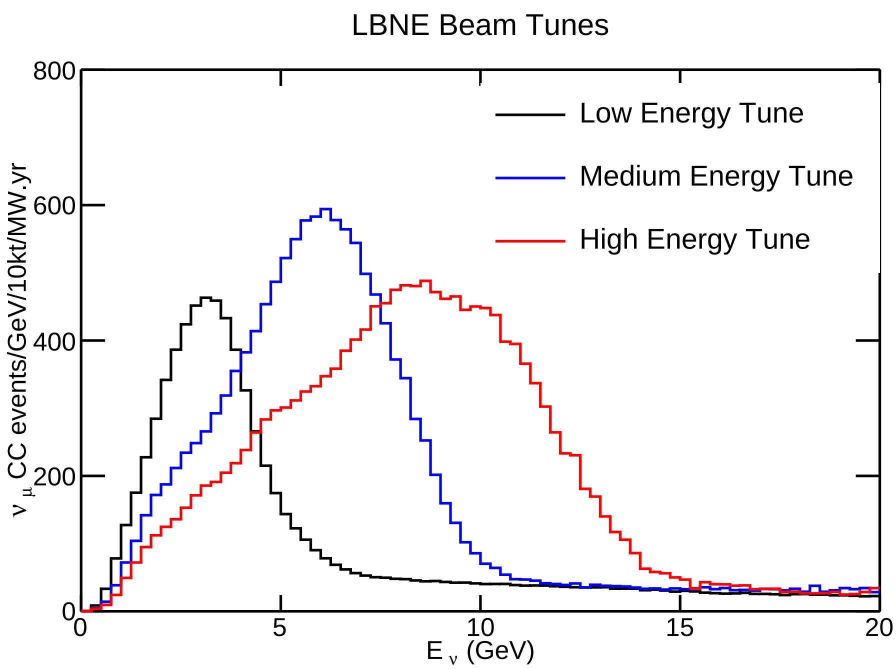

Figure 3.19: Event interaction rates at the LBNE far detector in the absence of oscillations and due to neutrinos produced by a 120 GeV proton beam for several target positions relative to Horn 1. The black curve shows the expected interaction spectrum for the low-energy tune (LE) where the upstream face of the target is located 35 cm upstream of Horn 1, the blue curve is a sample medium-energy (ME) tune with the target located 1.5 m upstream of Horn 1 and the red curve is the high-energy tune (HE) with the target located 2.5 m upstream of Horn 1. The horn current assumed is 200 kA, the decay pipe is air-filled, 4 m in diameter and 204 m in length.

measures the transverse distribution of the resultant hadronic showers to monitor the beam on a pulse-by-pulse basis.

An array of muon detectors in a small alcove immediately downstream of the absorber measures tertiary-beam muons and thereby indirectly provides information on the direction, profile and flux of the neutrino beam. This will be described in Section 3.5.

The beamline conventional facilities include the civil construction required to house the beamline components in their planned layout as shown in Figures 3.15 and 3.16. Following the beam from southeast to northwest, or roughly from right to left in Figure 3.15, the elements include the underground Extraction Enclosure, the Primary Beam Enclosure (inside the embankment) and its accompanying surface-based Service Building (LBNE 5), the Target Complex (LBNE 20) located in the embankment, the Decay Pipe, the underground Absorber Hall with the muon alcove, and its surface-based Service Building (LBNE 30). The embankment will need to be approximately 290 m long and 18 m above grade at its peak. The planned near neutrino detector facility is located as near as is feasible to the west site boundary of Fermilab, along the line-of-sight indicated in red in Figure 3.15.

The parameters of the beamline facility were determined taking into account several factors including the physics goals, the Monte Carlo modeling of the facility, spatial and radiological constraints and the experience gained by operating the NuMI facility at Fermilab. The relevant radiological concerns, prompt dose, residual dose, air activation and tritium production have been extensively modeled and the results implemented in the system design. The beamline facility design described above minimizes expensive underground construction and significantly enhances capability for ground-water radiological protection. In general, components of the LBNE beamline system that cannot be replaced or easily modified after substantial irradiation are being designed for 2.3−MW operation. Examples of such components are the shielding of the target chase and decay pipe, and the absorber with its associated shielding.

The following LBNE beamline design improvements beyond the CD-1 conceptual design are being assessed:

- An increase in the length of the decay pipe up to 250 m (the maximum length allowed by the existing Fermilab site boundaries), and also possibly an increase in its diameter up to 6 m. Increases to the decay pipe size would require additional cost of the order several tens of millions of dollars. Increasing the length of the decay pipe from 200 to 250 m increases the overall event rate in the oscillation region by 12%. Increases in the decay pipe diameter produce a 6% increase in the low-energy neutrino event rate as shown in Table 3.3.
- It has recently been decided to fill the decay pipe with helium instead of air. The total ν_μ event rate increases by about 11%, with a decrease in $\overline{\nu}$ contamination in the neutrino beam. Introducing helium in the decay pipe requires the design and construction of a decay pipe window.
- An increase in the horn current of the horns by a modest amount (from 200 kA to 230 kA); this is expected to increase the neutrino event rates by about 10-12% at the first oscillation maximum [127]. A Finite Element Analysis simulation and a cooling test of the horns are underway to evaluate this option.
- Use of an alternate material to the POCO graphite for the target to increase the target longevity. This would involve additional R&D effort and design work. A beryllium target, for example, could be made shorter, potentially improving the horn focusing.
- Development of more advanced horn designs that could boost the low-energy flux in the region of the second oscillation maximum. It should be noted that the target and horn systems can be modified or replaced even after operations have begun if improved designs enable higher beam flux.

Table 3.3 summarizes the impact of the beam design improvements after CD-1 and the additional costs required. Together, the changes are anticipated to result in an increase of $\sim 50\%$ in the ν_e

appearance signal rate at the far detector. A 30% increase in signal event rate at the far detector can be achieved for $<$ 10 M\$ without changing the CD-1 decay pipe size (4 m diameter $\times$ 204 m length) by changing from an air-filled to a helium-filled decay pipe. Increasing the decay pipe size to 6 m diameter $\times$ 250 m length would result in an additional 15% increase in flux but would cost an additional $\sim$ 47 M\$ — this includes the cost of a redesigned absorber.

Table 3.3: Impact of the beam improvements under study on the neutrino $\nu_\mu \to \nu_e$ CC appearance rates at the far detector in the range of the first and second oscillation maxima, shown as the ratio of appearance rates: the *improved* rate divided by the rate from the beam design described in the Conceptual Design Report.

Changes	0.5 to 2 GeV	2 to 5 GeV	Extra Cost
Horn current 200 kA $\to$ 230 kA	1.00	1.12	none
Proton beam 120 $\to$ 80 GeV at constant power	1.14	1.05	none
Target NuMI-style graphite $\to$ Be cylinder	1.10	1.00	$<$ 1 M\$
Decay pipe Air $\to$ He	1.07	1.11	$\sim$ 8 M\$
Decay pipe diameter 4 m $\to$ 6 m	1.06	1.02	$\sim$ 17 M\$
Decay pipe length 200 m $\to$ 250 m	1.04	1.12	$\sim$ 30 M\$
Total	**1.48**	**1.50**	

3.5 Near Detector

A high-resolution near neutrino detector located approximately 500 m downstream of the LBNE neutrino production target, as shown in Figure 3.16, is a key component of the full LBNE scientific program:

- The near neutrino detector will enable the LBNE experiment to achieve its primary scientific goals — in particular discovery-level sensitivity to CP violation and high-precision measurements of the neutrino oscillation parameters, including the unknown CP-violating phase, $\delta_{\rm CP}$.
- A rich program of LBNE physics measurements at the near detector will exploit the potential of high-intensity neutrino beams as probes of new physics.

To achieve the precision required to make a significant advancement in the measurement of neutrino oscillation parameters over current experiments and to reach the desired 5σ sensitivity to CP violation (discussed in Chapters 4 and 7), LBNE will need to measure the unoscillated flux spectrum, to a few percent, for all neutrino species in the beam: ν_μ, ν_e, $\overline{\nu}_\mu$ and $\overline{\nu}_e$. This requires a high-resolution, magnetized near neutrino detector with high efficiency for identifying and measuring electrons and muons. To measure the small ν_e contamination in the beam with greater precision, the detector would need to be able to distinguish e^+ from e^-; this would require a low-density detector with a commensurately long physical radiation length. In addition, use of an argon target nucleus — similar to the far detector — would allow cancellation of systematic errors. A reference design has been developed for a near neutrino detector that will meet these requirements; in particular it will measure the neutrino event rates and cross sections on argon, water and other nuclear targets for both ν_e and ν_μ charged current (CC) and neutral current (NC) scattering events.

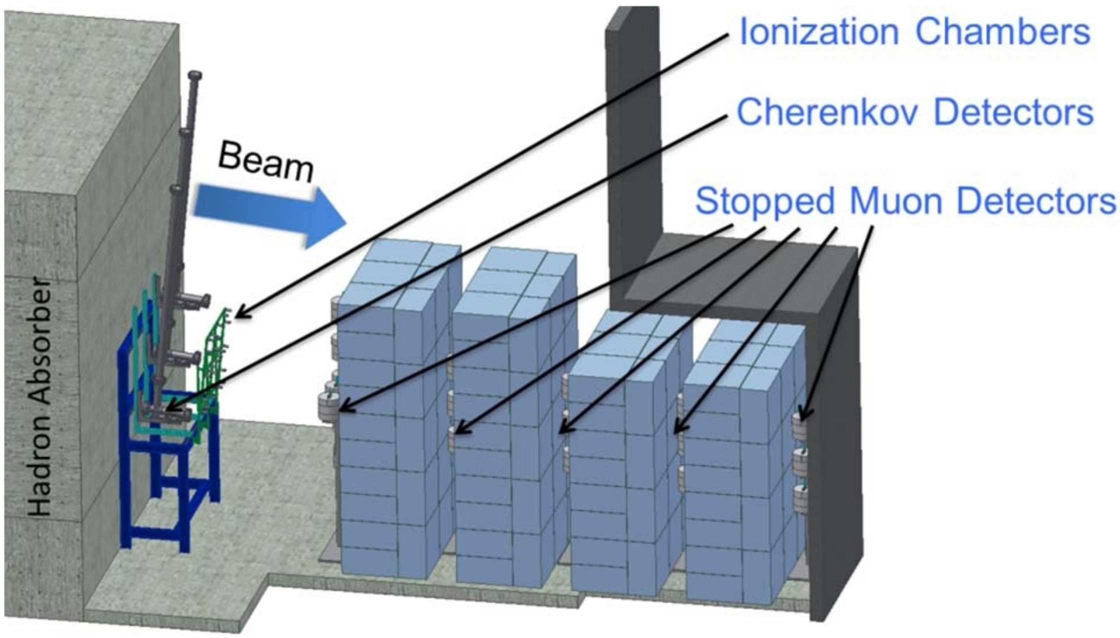

Figure 3.20: System of tertiary-beam muon detectors, located downstream of the LBNE beamline absorber, for monitoring the muon flux from the LBNE beamline.

In addition to the near neutrino detector, a sophisticated array of muon detectors will be placed just downstream of the absorber. The muon detectors, shown in Figure 3.20, detect mostly muons from the two-body decays of $\pi^{+(-)} \to \mu^{+(-)}\nu_\mu(\overline{\nu}_\mu)$ in the beamline, thus the measured muon and ν_μ flux distributions are highly correlated. The ionization chamber array will provide pulse-by-pulse monitoring of the beam profile and direction. The variable-threshold gas Cherenkov detectors will map the energy spectrum of the muons exiting the absorber on an on-going basis. The stopped muon detectors will sample the lowest-energy muons, which are known to correlate with the neutrino flux above 3 GeV — equivalent to about half the neutrino flux near the first oscillation maximum — and a decreasing fraction of it at lower energy. This system, together with the existing level of understanding of the similar NuMI beam and experience in previous neutrino oscillation experiments, will provide additional constraints on the understanding of the neutrino beam, and will thus support and complement the near neutrino detector measurements.

The reference design for the near neutrino detector is a fine-grained tracker [128], illustrated in Figure 3.21. It consists of a $3 \times 3 \times 7.04$ m^3 straw-tube tracking detector (STT) and electromagnetic

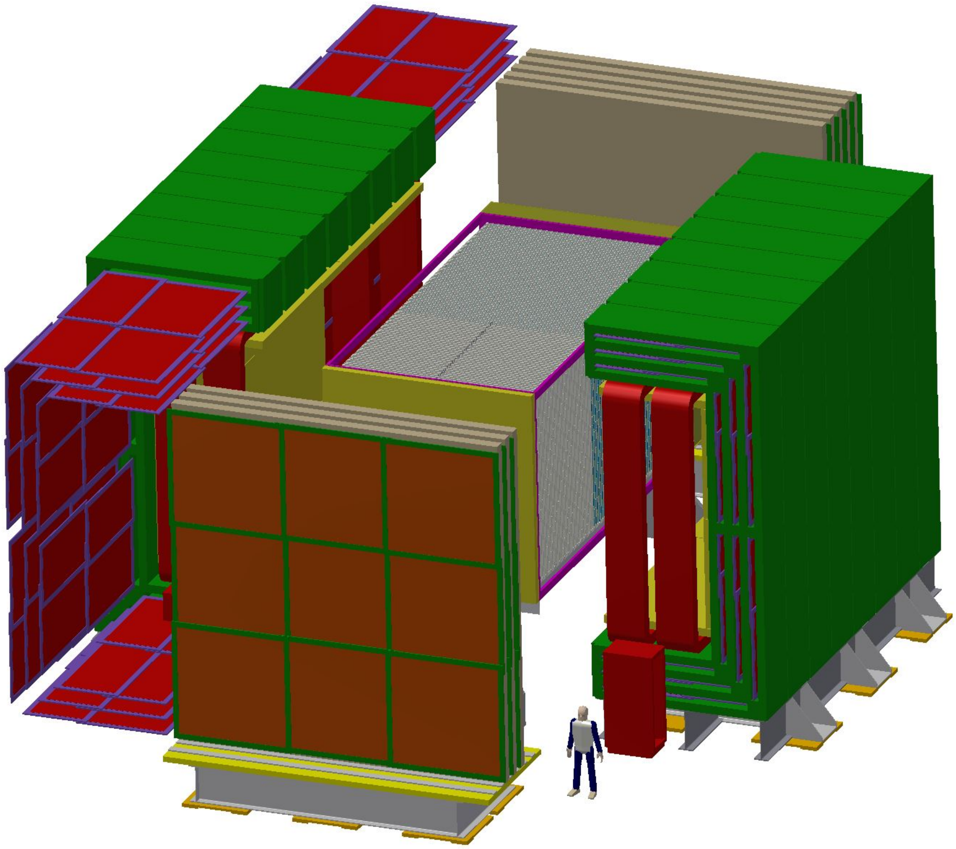

Figure 3.21: The LBNE near neutrino detector reference design with the dipole magnet open to show the straw-tube tracker (grey) and electromagnetic calorimeter (yellow). RPCs for muon identification (red squares) are embedded in the yoke steel and up- and downstream steel walls.

calorimeter inside of a 0.4-T dipole magnet, illustrated in Figure 3.22, and resistive plate chambers for muon identification (MuID) located in the steel of the magnet and also upstream and downstream of the tracker. High-pressure argon gas targets, as well as water and other nuclear targets, are embedded in the upstream part of the tracking volume. The nominal active volume of the STT corresponds to eight tons of mass. The STT is required to contain sufficient mass of argon gas in tubes (Al or composite material) to provide at least a factor of ten more statistics than expected in the far detector. Table 3.4 summarizes the performance for the fine-grained tracker's configuration, and Table 3.5 lists its parameters.

Figure 3.22 shows the locations of the electromagnetic calorimeter and MuID next to the magnet steel and magnet coils. The fine-grained tracker has excellent position and angular resolutions due to its low-density (~ 0.1 g/cm^3), high-precision STT. The low density and magnetic field allow it to distinguish e^+ from e^- on an event-by-event basis. The high resolution is important for determining the neutrino vertex and determining whether the neutrino interaction occurs in a water or argon target. Electrons are distinguished from hadrons using transition radiation.

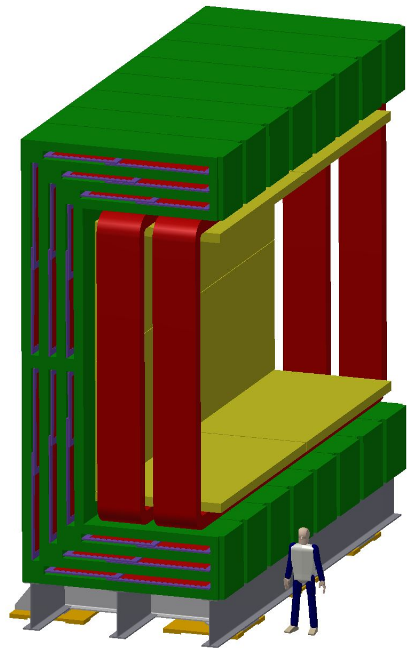

Figure 3.22: A schematic drawing of the ECAL (yellow modules) next to the magnet coils (red) and MuID (blue modules) interspersed in the magnet steel (green).

Table 3.4: Summary of the performance for the fine-grained tracker configuration

Performance Metric	Value
Vertex resolution	0.1 mm
Angular resolution	2 mrad
E_e **resolution**	5%
E_μ **resolution**	5%
$\nu_\mu/\overline{\nu}_\mu$ **ID**	Yes
$\nu_e/\overline{\nu}_e$ **ID**	Yes
NCπ^0**/CC**e **rejection**	0.1%
NCγ**/CC**e **rejection**	0.2%
NCμ**/CC**e **rejection**	0.01%

The design of the near neutrino detector is the subject of study by the LBNE Collaboration, and alternatives such as a magnetized liquid argon TPC will be investigated further. A detailed description of the fine-grained tracker can be found in [129], and descriptions of it and the alternative LArTPC design are presented in the March 2012 LBNE CDR (Volume 3 of [31]).

High-intensity neutrino beams can be used as probes of new physics and given the broad energy range of the LBNE beam, a diverse range of physics measurements is possible in the high-resolution near neutrino detector. These potentially wide-ranging physics measurements would complement other physics programs, such as those at Jefferson Laboratory, that are using proton,

Table 3.5: Parameters for the fine-grained tracker.

Parameter	Value
STT detector volume	$3 \times 3 \times 7.04$ m^3
STT detector mass	8 tons
Number of straws in STT	123,904
Inner magnetic volume	$4.5 \times 4.5 \times 8.0$ m^3
Targets	1.27-cm thick argon (~ 50 kg), water and others
Transition radiation radiators	2.5 cm thick
ECAL X_0	10 barrel, 10 backward, 18 forward
Number of scintillator bars in ECAL	32,320
Dipole magnet	2.4-MW power; 60-cm steel thickness
Magnetic field and uniformity	0.4 T; $< 2\%$ variation over inner volume
MuID configuration	32 RPC planes interspersed between 20-cm thick layers of steel

electron or ion beams from colliders and fixed-target facilities. A detailed discussion of the physics capabilities of a high-resolution near detector is presented in Chapter 7 and in [129].

3.6 Far Detector

The full-scope LBNE far detector is a liquid argon time-projection chamber of fiducial mass 34 kt located at the 4,850−ft level of the Sanford Underground Research Facility. The LArTPC technology allows for high-precision identification of neutrino flavors, offers excellent sensitivity to proton decay modes with kaons in the final state and provides unique sensitivity to electron neutrinos from a core-collapse supernova. The full detector size and its location at a depth of 4,850 feet will enable LBNE to meet the primary scientific goals — in particular, to find evidence for CP violation over a large range of $\delta_{\rm CP}$ values, and to significantly advance proton-decay lifetime limits. Conceptual designs of the 34−kt underground detector are well developed.

The liquid argon TPC technology chosen for LBNE combines fine-grained tracking with total absorption calorimetry to provide a detailed view of particle interactions, making it a powerful tool for neutrino physics and underground physics such as proton decay and supernova-neutrino observation. It provides millimeter-scale resolution in 3D for all charged particles. Particle types can be identified both by their dE/dx and by track patterns, e.g., the decays of stopping particles. The modest radiation length (14 cm) is sufficiently short to identify and contain electromagnetic showers from electrons and photons, but long enough to provide good e/γ separation by dE/dx (one versus two minimum ionizing particles) at the beginning of the shower. In addition, photons can be distinguished from electrons emanating from an event vertex by the flight path before their first interaction. These characteristics allow the LArTPC to identify and reconstruct signal events with high efficiency while rejecting backgrounds to provide a high-purity data sample. The principal design parameters of the full-scope LBNE LArTPC far detector are given in Table 3.6.

Table 3.6: Principal design parameters of the full-scope LBNE LArTPC far detector from [32].

Parameter	Value
Total/Active/Fiducial Mass	50/40/34 kt
Number of Detector Modules (Cryostats)	2
Drift Cell Configuration within Module	3 wide $\times$ 2 high $\times$ 18 long drift cells
Drift Cell Dimensions	2 $\times$ 3.7 m wide (drift) $\times$ 7 m high $\times$ 2.5 m long
Detector Module Dimensions	22.4 m wide $\times$ 14 m high $\times$ 45.6 m long
Anode Wire Spacing	$\sim$5 mm
Wire Planes (Orientation from vertical)	Grid (0°), Induction 1 (45°), Induction 2 (-45°) Collection (0°)
Drift Electric Field	500 V/cm
Maximum Drift Time	2.3 ms

Scalability has been a design consideration of critical importance for the LBNE Project, and for the far detector in particular, since the Project's inception in 2009. A 10−kt LArTPC far detector configuration has been identified as the minimal initial configuration of LBNE that can make significant advances toward the primary scientific goals of LBNE. Because of the scalability built into the LBNE design, other, more capable, configurations could be accomplished either in the initial phase with the identification of additional resources, or at a later stage.

Other important considerations for the construction of LBNE's large LArTPC far detector include:

1. cryogenic safety and the elimination of hazards associated with large cryogenic liquid volumes
2. attainment of stringent argon purity requirements with respect to electronegative contaminants (e.g., < 0.2 ppb O_2 concentration)
3. ease of transport and assembly of TPC mechanical systems
4. efficient deployment of high-sensitivity/low-noise electronics for readout of the ionization signal

The far detector complex for both the first-phase ($\geq$ 10−kt) and full 34−kt options will be outfitted with two separately instrumented detector vessels instead of a single, larger vessel — an approach which has several benefits. First, this design enables each cryostat and TPC to be filled and commissioned while the other remains available for liquid storage, allowing for repairs to be made after the start of commissioning, should that be necessary. Secondly, it allows deployment of TPCs of different designs. This would enable, for example, international partners to contribute a detector of an alternate design, based on their own experience, or one that would emphasize a particular research interest.

The detector vessels will be constructed using technology standards from the liquefied natural gas (LNG) industry. With similar requirements and geometries, adaptation of industrial LNG cryostat design provides a high-performance, extensively tested approach to the challenge of liquid argon containment for LBNE. The cryostats in large LNG tanker ships are constructed using a thin (1–2 mm), polished, stainless steel inner membrane surrounded by thick foam passive insulation. With stainless steel as the only wetted surface, this is an inherently clean design, ideal for liquid argon detectors where high purity is essential.

The underground detector placement at the 4850L of the Sanford Underground Research Facility was studied in detail during the Conceptual Design Phase of LBNE and presented at the Fermilab Director's Independent Conceptual Design Review in March of 2012 [24]. Significant effort has been invested to minimize the (dominant) cost of the far site conventional facilities.

3.6.1 The 10−kt Detector Design

- The far detector for the initial phase of LBNE will have fiducial mass of *at least* 10 kt. This mass allows for high probability determination of the neutrino mass hierarchy and can provide evidence for CP violation, if this effect is large.
- The detector needs to be located deep underground to provide sensitivity for proton decay searches in the kaon modes and for measuring neutrinos from potential supernovae in the galaxy.
- A conceptual design for a 10−kt LArTPC has been developed, thoroughly reviewed and found to be sound.
- LBNE is working with international partners in an effort to deploy a more massive far detector in the initial phase.

A conceptual design for the initial 10−kt far detector for the first-phase LBNE Project has been developed that is easily scalable to larger detectors. Many of the detector elements, in particular the modular TPC design and readout electronics, utilize full-scale modules and designs that can easily be replicated in larger numbers to instrument a larger detector. This design consists of two

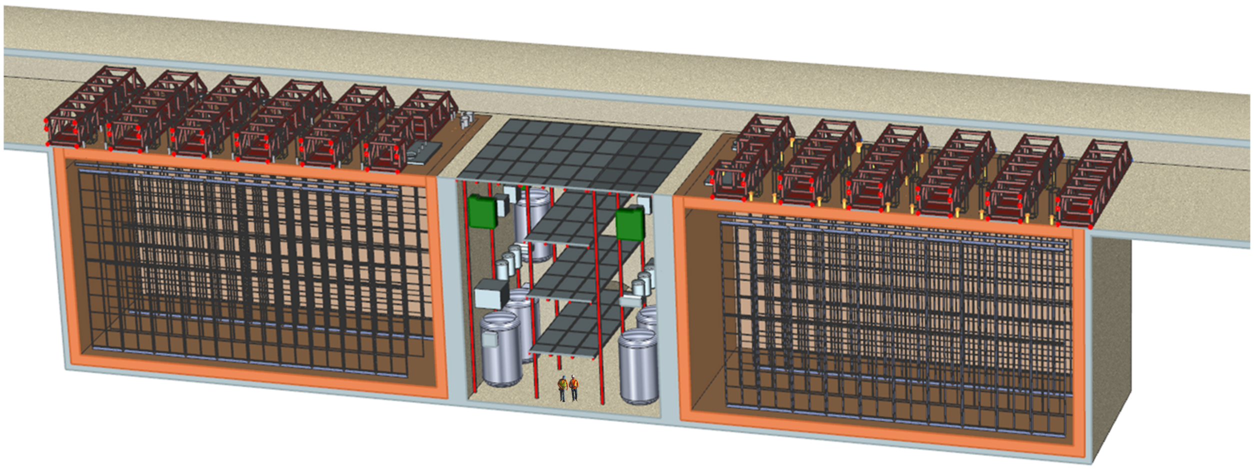

Figure 3.23: 3D view of the 10−kt far detector showing a lateral cross section of the two 5−kt fiducial-mass LArTPC vessels

9.4−kt liquid argon vessels [32], each designed to hold a 5−kt fiducial-mass LArTPC as shown in Figure 3.23.

The cryogenics systems for the 10−kt detector will consist of two 85−kW liquid nitrogen liquefaction plants, a liquid argon receiving station, a liquid argon circulation system with liquid purifiers, and a liquid argon re-condensing system. All the cryogenics systems are similar to large-scale systems found in industrial applications.

The LBNE TPC design for the 10−kt detector consists of three rows of cathode plane assemblies (CPAs) interspersed with two rows of anode plane assemblies (APAs), similar to the layout concept shown in Figure 3.24 bottom right, with readout electronics mounted directly on the APA frames (Figure 3.24, left). These elements run the length of a cryostat module, save for space at one end allocated to the cryogenics systems. A field cage for shaping the electric field covers the top, bottom, and ends of the detector. The spacing between the CPA and APA rows is 3.48 m and the cathode planes will be operated at 173 kV, establishing a drift field of 500 V/cm and a corresponding maximum drift time of 2.16 ms.

The APAs and CPAs are designed in a modular fashion as illustrated in Figure 3.24, top right. Each APA/CPA is constructed with a support frame 2.5 m long and 7 m high; these dimensions are chosen for ease of transportation to the detector site and installation within the cryostat. During installation, two APAs are connected end-to-end to form a 14 m tall, 2.5 m long unit, which is transported to its final position in the detector and suspended there using a rail system at the top of the detector. Pairs of CPAs are installed in a similar fashion. This system of 2.5 m long detector elements is easily scalable to any desired detector size. A total of 40 APAs and 60 CPAs per cryostat are needed for the 10−kt detector design, configured as two rows of APAs, ten APA pairs long.

Three sense wire planes (two *induction* planes and one *collection* plane) with wire pitches of 4.8

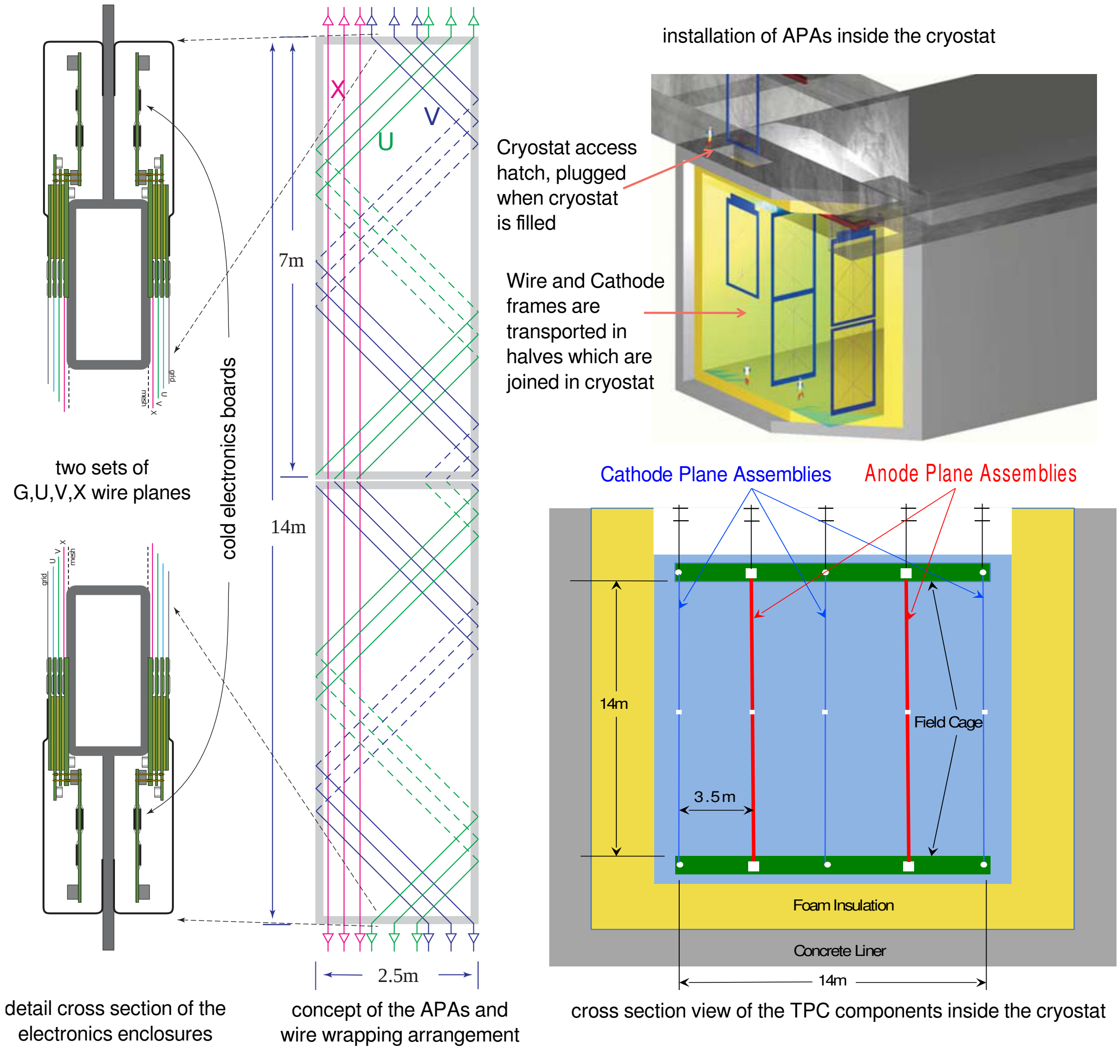

Figure 3.24: The LBNE TPC modular construction concept

mm are mounted on each side of an APA frame, for sensitivity to ionization signals originating within the TPC cell on either side. The wires on these planes are oriented vertically (collection) and at $\pm 45°$ (induction)¶. The induction plane wires are wrapped around the APA frame, and are therefore sensitive to charge arriving from either side of the APA, depending on where the charge arrives along the length of the wires. This configuration allows placement of readout electronics at the top and bottom of each two-APA unit. (Cables from the bottom APA are routed up through the support frame, thereby eliminating any obstruction they would otherwise cause.) In this way, adjacent APA-pairs can be abutted so as to minimize the uninstrumented region in the gaps between them along the length of the detector.

¶The current design uses a $36°$ orientation to remove hit assignment ambiguities.

Low-noise, low-power CMOS (Complementary Metal Oxide Semiconductor) preamplifier and ADC ASICS (Application Specific Integrated Circuit) have been developed for deployment on circuit boards mounted directly on the APA frames. This scheme ensures good signal-to-noise performance, even allowing for some attenuation of long-drift ionization signals due to residual impurities in the argon. It also offers the possibility of digital signal processing, including multiplexing and zero suppression at the front end, thereby limiting the cable plant within the cryostat and the number of penetrations required, while also easing requirements on the downstream read-out/DAQ systems located outside the cryostat. The ASICS have been laid out following design rules developed explicitly for long-term operation at cryogenic temperatures.

In order to separate neutrino beam events from other interactions — particularly for proton decay and supernova neutrino signals — it is necessary to accurately determine the event time relative to the neutrino beam time window or an incoming cosmic muon. If the event time is known at the microsecond level then out-of-time cosmic-ray backgrounds for beam neutrinos can be rejected to the level of 10^{-5} (the beam spill duty factor). The slow ionization-electron drift velocity gives the TPC its 3D imaging capability, but an independent fast signal is required to localize events in time and in space along the drift direction. The excellent scintillation properties of liquid argon ($\mathcal{O}(10^4)$ photons per MeV of energy deposition) are exploited to address this issue. A photon detection system is planned for detection of the 128-nm scintillation light that, in turn, allows determination of the event timing. Several photon detector designs are under study. The most advanced design uses cast acrylic bars coated with wavelength shifter, and SiPMs (silicon photomultipliers) at the ends for read-out. These bars will be assembled into paddles of dimensions 10 cm by 2 m, and mounted on the APA frames, fitting within the 5-cm gap between the sets of wire planes located on both sides of the frames. Initial studies indicate a light yield of 0.1 to 0.5 photoelectrons per MeV.

3.6.2 The 34−kt Detector Design

One possible design of a 34−kt detector is two 17−kt modules placed end-to-end in a common cavern at the 4,850−ft level of the Sanford Underground Research Facility, as shown in Figure 3.25. This design was reviewed at the Fermilab Director's Independent Conceptual Design Review in March of 2012 [24].

Alternatively, the 34−kt detector can be realized by adding a roughly 24−kt detector of essentially the same design as the 10−kt detector, housed in a set of two cryostats, each holding 12 kt (20 kt total) of liquid argon. In this configuration the additional cryostats each have three APA rows (total 84 APAs) and four CPA rows (total 112 CPAs), making them wider than the 10−kt design described in Section 3.6.1. The APA-to-CPA row spacing is expanded to 3.77 m and the length of each is increased to 14 APA units long.The cryogenics system installed for the 10−kt design will simply be expanded from two to four 85−kW refrigerators to service both the 10−kt and the 24−kt detector. The 24−kt detector hall will be excavated parallel to the 10−kt detector hall as shown in Figure 3.26.

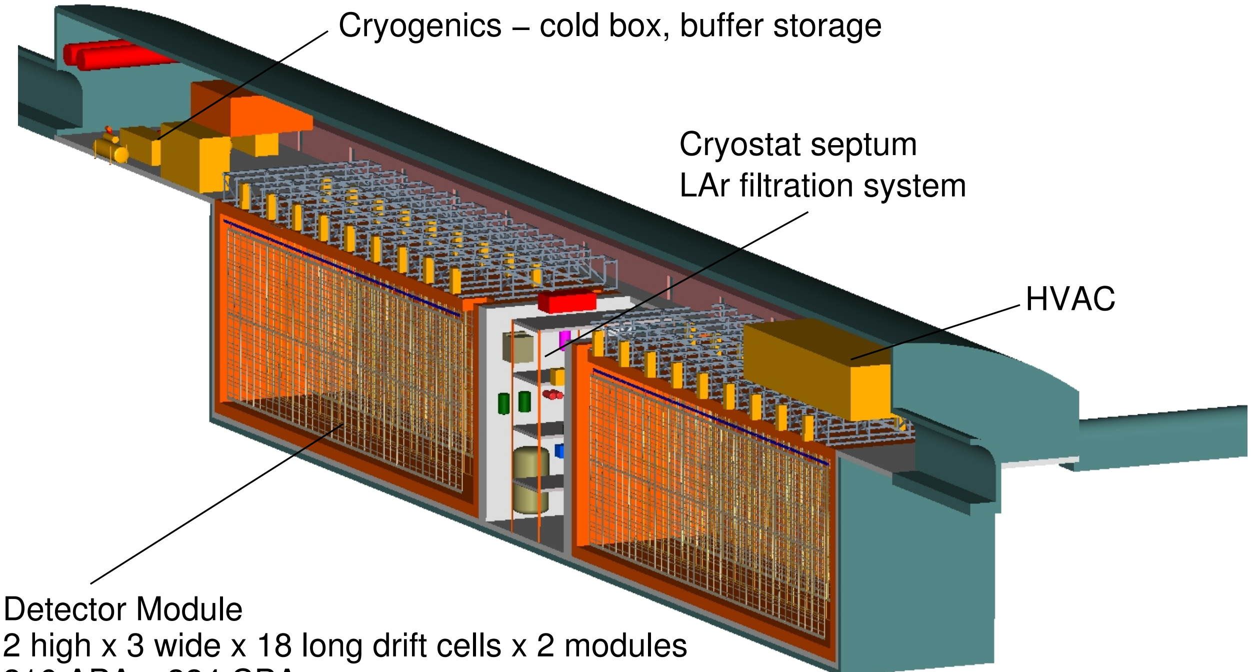

Figure 3.25: Schematic of a 34−kt LArTPC design. The detector comprises two 17−kt LArTPC vessels.

Given the modular design of the detector and the use of industrial technologies in the cryogenics system, there is a great deal of flexibility in possible contributions from new partners to expand the size of the detector. The details of any scope change would depend on the interests, capabilities and resources of the new partners.

A full geotechnical site investigation is underway to characterize the rock mass in which it is planned to site the LBNE far detector. Mapping of existing drifts in the vicinity of the proposed detector location has been completed and a core boring program was launched in early 2014. This investigation will explore the area with enough breadth to allow flexibility in siting and sizing detector modules in the future before design work begins. The proposed boring layouts are shown in Figure 3.27 overlaid with possible 34−kt and 70−kt modules to demonstrate the large capacity of this location.

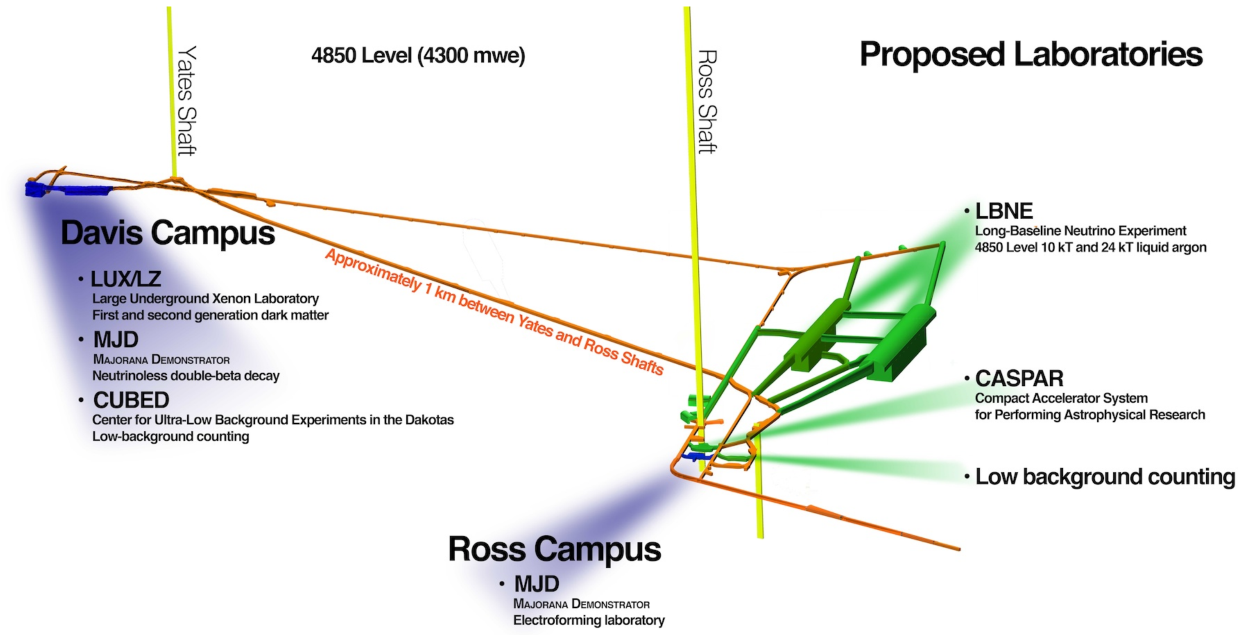

Figure 3.26: Layout of the 10−kt + 24−kt LArTPC detector halls at the 4,850−ft level of the Sanford Underground Research Facility.

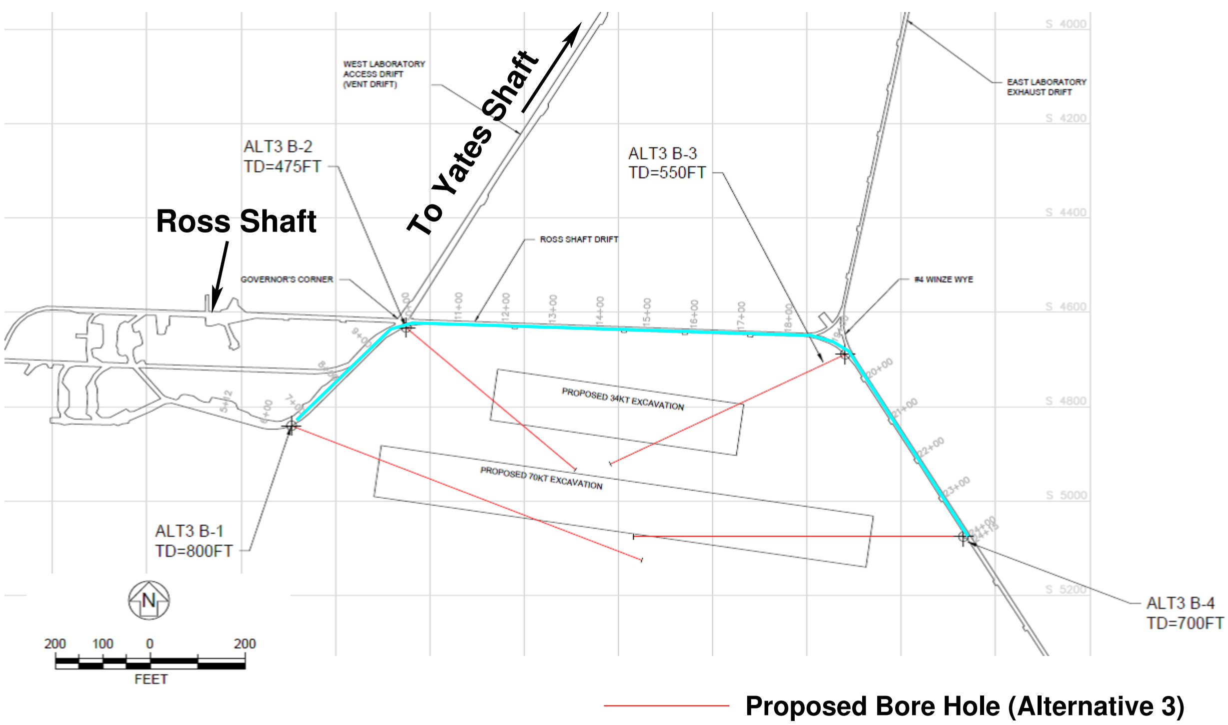

Figure 3.27: Geotechnical site investigation plan, showing the drifts that have been mapped (blue) and the planned core borings (red) overlaid on possible locations of caverns that would accommodate the 34−kt or larger (70−kt shown as an example) LArTPC detectors.

Chapter 4 Neutrino Mixing, Mass Hierarchy and CP Violation

LBNE is designed to address the science of neutrino oscillations with superior sensitivity to many mixing parameters in a single experiment, in particular,

1. precision measurements of the parameters that govern $\nu_\mu \to \nu_e$ and $\overline{\nu}_\mu \to \overline{\nu}_e$ oscillations; this includes precision measurement of the third mixing angle θ_{13}, measurement of the CP-violating phase δ_{CP}, and determination of the mass ordering (the sign of Δm^2_{32})
2. precision measurements of $\sin^2 2\theta_{23}$ and $|\Delta m^2_{32}|$ in the $\nu_\mu/\overline{\nu}_\mu$ disappearance channel
3. determination of the θ_{23} octant using combined precision measurements of the $\nu_e/\overline{\nu}_e$ appearance and $\nu_\mu/\overline{\nu}_\mu$ disappearance channels
4. search for nonstandard physics that can manifest itself as differences in higher-precision measurements of ν_μ and $\overline{\nu}_\mu$ oscillations over long baselines

4.1 Experimental Requirements Based on Oscillation Phenomenology

The experimental requirements for designing a neutrino oscillation experiment to simultaneously address neutrino CP violation and the mass hierarchy (MH) can be extrapolated as follows from the phenomenology summarized in Chapter 2:

1. *Phenomenology: An appearance experiment is necessary to extract the CP-violating effects.*

   Experimental requirements:

   - The experiment will probe oscillations of $\nu_{\mu,e} \to \nu_{e,\mu}$.
   - The experiment will identify ν_e and ν_μ with high efficiency and purity in order to tag (or otherwise know) the flavor of the neutrino before and after flavor transformations.
   - The experiment requires $E_\nu >$100 MeV so that it will be possible to perform flavor-tagging of muon neutrinos using the lepton flavor produced in a charged current (CC) interaction ($\nu_\mu + N \to \mu N' X$).

2. *Phenomenology: In the three-flavor mixing model, the CP-violating Jarlskog invariant arises in the interference term $P_{\sin\delta}$ as given by Equation 2.15; the oscillation scale where the interference term is maximal is that determined by the mixing between the ν_1 and ν_3 states.*

   Experimental requirements:

   ◦ The experimental baseline and corresponding neutrino energy are chosen according to Equation 2.18 such that L/E equals 510 km/GeV to maximize sensitivity to the CP-violating term in the neutrino flavor mixing.

   ◦ Flavor-tagging of muon neutrinos that can be produced either at the source or after flavor-mixing requires $E_\nu > 100$ MeV; therefore, the experimental baselines over which to measure neutrino oscillations are $L > 50$ km*.

3. *Phenomenology: In the three-flavor model $\nu_{\mu,e} \rightarrow \nu_{e,\mu}$ oscillations depend on all parameters in the neutrino mixing matrix as well as on the mass differences, as shown in Equations 2.12 to 2.15.*

   Experimental requirements:

   ◦ The precision with which $\delta_{\rm CP}$ can be determined — and the sensitivity to small CP-violating effects or CP violation outside the three-flavor model — requires precision determination of all the other mixing parameters, preferably in the same experiment. The experiment will be designed so as to minimize dependence on external measurements of the oscillation parameters.

4. *Phenomenology: Observation of CP violation requires the explicit observation of an asymmetry between $P(\nu \rightarrow \nu)$ and $P(\overline{\nu} \rightarrow \overline{\nu})$.*

   Experimental requirements:

   ◦ The experiment will probe the oscillations of both neutrinos and antineutrinos in an unambiguous way.

   ◦ The experiment will be capable of charge tagging in addition to flavor tagging. Charge tagging can be achieved at detection using the lepton charge and/or at production by selecting beams purely of neutrinos or antineutrinos.

   ◦ The experiment will be capable of resolving degeneracies between matter and CP asymmetries in order to determine the MH. This can be achieved by using a baseline greater than 1,000 km or with measurements probing oscillations over a range of L/E values.

*Neutrino experiments using beams from pion decay-at-rest experiments such as DAEδALUS are exceptions since the $\overline{\nu}_\mu$ production spectrum is well known and only the $\overline{\nu}_e$ flavor after oscillations is tagged through inverse-beta decay. The neutrino energies are $\sim$50 MeV below the CC muon-production threshold.

5. *Phenomenology: CP asymmetries are maximal at the secondary oscillation nodes.*

   Experimental requirements:

   - Coverage of the L/E scale of the secondary oscillation nodes improves experimental sensitivity to small values of $\delta_{\rm CP}$ by enabling measurements of the asymmetry at the secondary nodes where the CP asymmetries are much larger and where there is no degeneracy with the matter asymmetries. The experiment will be performed with a wide-band beam to provide sensitivity to the L/E scale of both the first and second oscillation nodes.
   - The experimental baseline will be $>$150 km, given that muon flavor tagging is required at either production or detection. The secondary oscillation nodes are located at scales set by Equation 2.18 where $n > 1$. The second oscillation maximum is located at scales given by L/E $\sim$1,500 km/GeV.

Based on the experimental requirements prescribed by the neutrino oscillation phenomenology detailed above, pursuit of the primary science objectives for LBNE dictates the need for a very large mass (10 kt to 100 kt) neutrino detector located at a distance greater than 1,000 km from the neutrino source. This large mass coupled with a powerful wide-band beam and long exposures is required to accumulate enough neutrino interactions — $\mathcal{O}$(1,000) events — to make precision measurements of the parameters that govern the subdominant $\nu_\mu \to \nu_e$ oscillations. At 1,300 km, the baseline chosen for LBNE, both the first and second oscillation nodes are at neutrino energies $>$ 0.5 GeV, as shown in Figure 4.1. This places both neutrino oscillation nodes in a region that is well matched to the energy spectrum of the high-power conventional neutrino beams that can be obtained using the 60 GeV to 120 GeV Main Injector (MI) proton accelerator at Fermilab.

4.2 Simulation of Neutrino Oscillation Experiments

To evaluate the sensitivity of LBNE and to optimize the experiment design, it is important to accurately predict the neutrino flux produced by the neutrino beamline, the neutrino interaction rate at the far detector, and the far detector performance. This is achieved using Monte Carlo (MC) simulations and the GLoBES [130,131] package. The simulations and experimental assumptions that are used to evaluate the sensitivity of LBNE to neutrino mixing parameters, to the neutrino mass hierarchy (MH) and to CP violation are described in this section.

4.2.1 Expected Signal

The LBNE beamline design, described in Section 3.4, is simulated using Geant4 [132]. The simulated ν_μ spectrum (unoscillated flux $\times$ cross section) at 1,300 km obtained from the LBNE beamline using 80$-$GeV protons from the MI is shown as the black histogram in Figure 4.1. At this baseline, there is no degeneracy between matter and CP asymmetries at the first oscillation node where the LBNE neutrino beam spectrum peaks. The wide coverage of the oscillation patterns enables the search for physics beyond the three-flavor model because new physics effects may interfere with the standard oscillations and induce a distortion in the oscillation patterns. As a next-generation neutrino oscillation experiment, LBNE aims to study in detail the spectral shape of neutrino mixing over the range of energies where the mixing effects are largest. This is crucial for advancing the science beyond the current generation of experiments, which depend primarily on rate asymmetries.

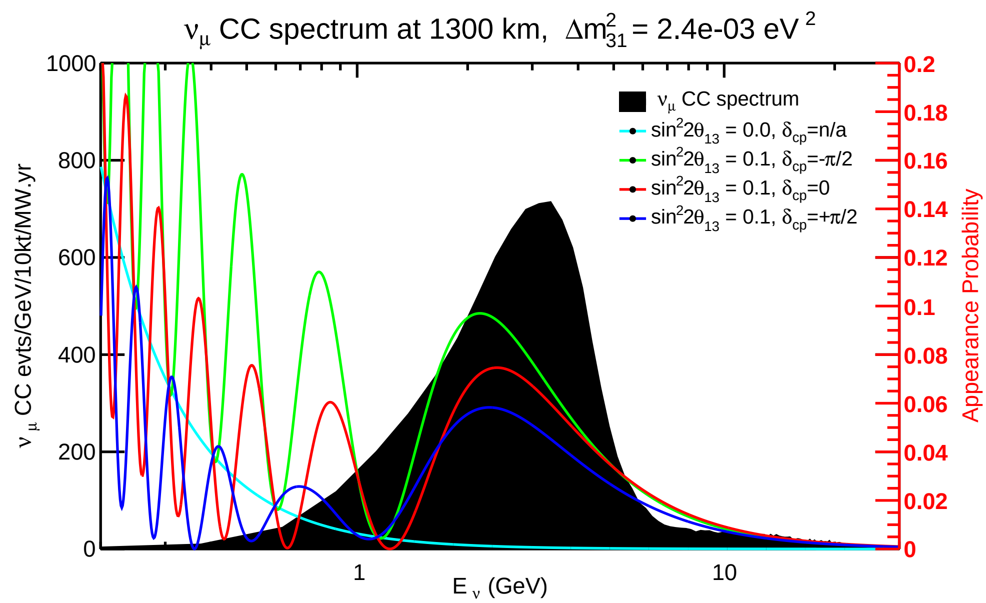

Figure 4.1: The simulated unoscillated spectrum of ν_μ events from the LBNE beam (black histogram) overlaid with the $\nu_\mu \to \nu_e$ oscillation probabilities (colored curves) for different values of $\delta_{\rm CP}$ and normal hierarchy.

The LBNE reconfiguration study [25] determined that the far detector location at the Sanford Underground Research Facility provides an optimal baseline for precision measurement of neutrino oscillations using a conventional neutrino beam from Fermilab. The 1,300−km baseline optimizes sensitivity to CP violation and is long enough to resolve the MH with a high level of confidence, as shown in Figure 2.7.

Table 4.1 lists the beam neutrino interaction rates for all three known species of neutrinos as expected at the LBNE far detector. This table shows only the raw interaction rates using the neutrino flux from the Geant4 simulations of the LBNE beamline and the default interaction cross sections included in the GLoBeS package [130] with *no detector effects included*. A tunable LBNE beam spectrum, obtained by varying the distance between the target and the first focusing horn (Horn 1), is assumed. The higher-energy tunes are chosen to enhance the ν_τ appearance signal and improve the oscillation fits to the three-flavor paradigm. To estimate the NC event rates based on visible

Table 4.1: Raw ν oscillation event rates at the LBNE far site with $E_\nu < 10$ GeV. Assumes 1.8×10^7 seconds/year (Fermilab). *POT* is *protons-on-target*. Oscillation parameters used are: $\theta_{12} = 0.587$, $\theta_{13} = 0.156$, $\theta_{23} = 0.670$, $\Delta m^2_{21} = 7.54 \times 10^{-5}\,\mathrm{eV}^2$, and $\Delta m^2_{31} = +2.47 \times 10^{-3}\,\mathrm{eV}^2$ (normal hierarchy). The NC event rate is for events with visible energy > 0.5 GeV. For comparison, the rates at other neutrino oscillation experiments (current and proposed) are shown for similar exposure in mass and time. No detector effects are included.

Experiment *details*	**Baseline** **km**	ν_μ **unosc.** **CC**	ν_μ **osc.** **CC**	ν_e **beam** **CC**	ν_μ **NC**	$\nu_\mu \to \nu_\tau$ **CC**	$\nu_\mu \to \nu_e$ **CC** $\delta_{\mathrm{CP}} = -\frac{\pi}{2}$,	**0,**	$\frac{\pi}{2}$
LBNE LE	1,300								
80 GeV, 1.2 MW									
1.5 × 10^{21} *POT/year*									
50 kt · year ν		12721	4339	108	3348	156	605	480	350
50 kt · year $\overline{\nu}$		4248	1392	34	1502	48	51	86	106
LBNE ME	1,300								
120 GeV, 1.2 MW									
1 × 10^{21} *POT/year*									
50 kt · year ν		19613	12317	72	5808	686	435	399	293
T2K	295								
30 GeV, 750 kW									
9 × 10^{20} *POT/year*									
50 kt · year ν		2100	898	41	360	< 1	73	58	39
MINOS LE	735								
120 GeV, 700 kW									
6 × 10^{20} *POT/year*									
50 kt · year ν		17574	11223	178	4806	115	345	326	232
50 kt · year $\overline{\nu}$		5607	3350	56	2017	32	58	85	88
NOvA ME	810								
120 GeV, 700 kW									
6 × 10^{20} *POT/year*									
50 kt · year ν		4676	1460	74	1188	10	196	168	116
50 kt · year $\overline{\nu}$		1388	428	19	485	2	22	35	41
LBNO	2,300								
50 GeV ∼ 2 MW									
3 × 10^{21} *POT/year*									
50 kt · year ν		8553	2472	48	2454	570	534	426	336
50 kt · year $\overline{\nu}$		3066	828	15	1140	255	24	45	54
ν**-Factory** *details*		ν_μ **unosc.** **CC**	ν_μ **osc.** **CC**		ν_μ **NC**	$\nu_\mu \to \nu_\tau$ **CC**	$\nu_e \to \nu_\mu$ **CC** $\delta_{\mathrm{CP}} = -\frac{\pi}{2}$,	**0,**	$\frac{\pi}{2}$
NuMAX I	1,300								
3 GeV, 1 MW									
0.94 × 10^{20} μ*/year*									
50 kt · year μ^+		1039	339		484	28	71	97	117
50 kt · year μ^-		2743	904		945	89	24	19	12
NuMAX II	1,300								
3 GeV, 3 MW									
5.6 × 10^{20} μ*/year*									
50 kt · year μ^+		6197	2018		2787	300	420	580	700
50 kt · year μ^-		16349	5390		5635	534	139	115	85

energies above 0.5 GeV, a true-to-visible energy smearing function based on output from the GENIE neutrino MC generator [133] is used. For comparison, the rates at current neutrino oscillation experiments such as T2K [134], MINOS [135] and NOνA [126] are shown for similar exposure in mass and time and using the same interaction cross sections. The raw interaction rates from other proposed neutrino oscillation experiments such as LBNO [136] and the NuMAX neutrino factory designs [137] are also shown†. It is important to note that the duty factors for the JPARC and CERN beams are $\sim 1/3$ and $\sim 1/2$ of NuMI/LBNE respectively. For LBNO, the event rates are obtained using the optimized beam from the HP-PS2 50$-$GeV synchrotron [138] with an exposure of 3×10^{21} POT/year. The LBNO duty cycle is assumed to be $\sim 10^7$ seconds/year, which corresponds to a beam power of 2 MW. Note that for Stage 1 and Stage 2 of the NuMAX neutrino factory proposal [137], Project X beams [23] at 3 GeV with 1 and 3 MW, respectively, are needed‡ It is clear that the LBNE beam design and baseline produce high rates of ν_e appearance coupled with large rate asymmetries when CP-violating effects are included. For example, LBNE has significantly higher appearance rates with a Main Injector 1.2$-$MW beam when compared to Stage 1 of the NuMAX neutrino factory with a 1$-$MW beam from a 3$-$GeV linac. The ν_e appearance rates are very similar in LBNE and LBNO with normal hierarchy (NH), but the $\overline{\nu}_e$ appearance rates (NH) in LBNO are $\approx 1/2$ that of LBNE due to the suppression from the larger matter effect (longer baseline) in LBNO.

4.2.2 Detector Simulation using the GLoBES Package

For the sensitivity studies presented here, the GLoBES package [130,131] was used to simulate the detector response using simple smearing and using detector efficiency values based on results from ICARUS and earlier simulation efforts as documented in [29]. The values used in GLoBES are shown in Table 4.2.

Studies from ICARUS have estimated and measured single-particle energy resolutions in liquid argon. Below 50 MeV, the energy resolution of electrons is $11\%/\sqrt{E[\mathrm{MeV}]} + 2\%$. The energy resolution of an electromagnetic shower with energy in the range (50–5000) MeV is $33\%/\sqrt{E(\mathrm{MeV})}+1\%$ [139] and that of hadronic showers is $\approx 30\%/\sqrt{E(\mathrm{GeV})}$. A significant fraction of the ν_e-CC signal in LBNE in the range of 1 GeV to 6 GeV comes from non-quasi-elastic CC interactions with a large component of the visible energy in the hadronic system. From recent simulations of neutrino interactions in this region it has been determined that $< E_{\mathrm{lepton}}/E_\nu >\approx 0.6$. For this reason, the total ν_e energy resolution for the neutrino oscillation sensitivity calculation is chosen to be $15\%/\sqrt{E(\mathrm{GeV})}$. In a non-magnetized LArTPC, the muon momentum can be obtained from measurements of range and multiple scattering. The muon momentum resolution for partially con-

†T2K uses a JPARC neutrino beam, MINOS and NOνA use the Fermilab NuMI neutrino beam and LBNO uses a CERN neutrino beam.

‡Project X has been superseded by PIP-II as of late 2013; PIP-II is briefly described in Section 3.4.

Table 4.2: Estimated range of the LArTPC detector performance parameters for the primary oscillation physics. Signal efficiencies, background levels, and resolutions are obtained from ICARUS and earlier simulation efforts (middle column) and the value chosen for the baseline LBNE neutrino oscillation sensitivity calculations (right column).

Parameter	Range of Values	Value Used for LBNE Sensitivities
	For ν_e-CC appearance studies	
ν_e-CC efficiency	70-95%	80%
ν_μ-NC misidentification rate	0.4-2.0%	1%
ν_μ-CC misidentification rate	0.5-2.0%	1%
Other background	0%	0%
Signal normalization error	1-5%	1-5%
Background normalization error	2-15%	5-15%
	For ν_μ-CC disappearance studies	
ν_μ-CC efficiency	80-95%	85%
ν_μ-NC misidentification rate	0.5–10%	1%
Other background	0%	0%
Signal normalization error	1-10%	5–10%
Background normalization error	2-20%	10-20%
	For ν-NC disappearance studies	
ν-NC efficiency	70-95%	90%
ν_μ-CC misidentification rate	2-10%	10%
ν_e-CC misidentification rate	1-10%	10%
Other background	0%	0%
Signal normalization error	1-5%	under study
Background normalization error	2-10%	under study
	Neutrino energy resolutions	
ν_e-CC energy resolution	$15\%/\sqrt{E(GeV)}$	$15\%/\sqrt{E(GeV)}$
ν_μ-CC energy resolution	$20\%/\sqrt{E(GeV)}$	$20\%/\sqrt{E(GeV)}$
E_{ν_e} scale uncertainty	under study	under study
E_{ν_μ} scale uncertainty	1-5%	2%

tained muons is found to be in the range $10-15\%$ [140,141] for muons in the 0.5 GeV to 3 GeV range. The ν_μ total energy resolution in LBNE is, therefore, assumed to be $20\%/\sqrt{E(\mathrm{GeV})}$; the resolution will be significantly better than this for the small subsample of events in which muons are fully contained by the detector.

Figures 4.2 and 4.3 show the predicted spectra of observed signal and background events in LBNE produced from the GLoBES implementation, including the effects of neutrino oscillation. Figure 4.2 shows the ν_μ and $\overline{\nu}_\mu$-CC sample and Figure 4.3 shows the ν_e and $\overline{\nu}_e$-CC appearance sample. Table 4.3 shows the expected LBNE signal and background event rates in ν_μ disappearance and ν_e

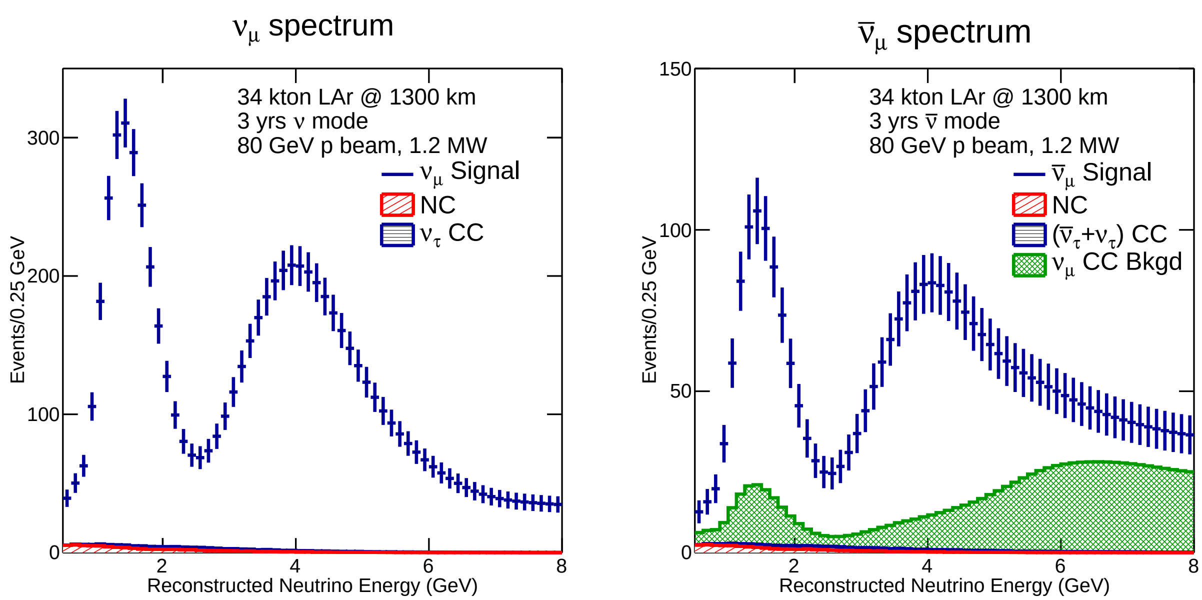

Figure 4.2: The expected reconstructed neutrino energy spectrum of ν_μ or $\overline{\nu}_\mu$ events in a 34−kt LArTPC for three years of neutrino (left) and antineutrino (right) running with a 1.2−MW beam.

Table 4.3: Expected number of neutrino oscillation signal and background events in the energy range 0.5 GeV to 8.0 GeV at the far detector after detector smearing and event selection. The calculation assumes $\sin^2(2\theta_{13}) = 0.09$ and $\delta_{CP} = 0$. The event rates are given per 10−kt LArTPC and three years of running with the improved 80−GeV LBNE beam at 1.2 MW. For signal, the number of ν and $\overline{\nu}$ events are shown separately, while for the background estimates ν and $\overline{\nu}$ events are combined. The MH has negligible impact on ν_μ disappearance signals.

Beam	Hierarchy	Signal Events	Background Events				
		$\nu_x/\overline{\nu}_x$ CC	ν_μ NC	ν_μ CC	ν_e Beam	ν_τ CC	Total
			$\nu_\mu \to \nu_{x=\mu}$ (disappearance)				
Neutrino	-	2056/96	23	N/A	-	18	41
Antineutrino	-	280/655	10	N/A	-	10	20
			$\nu_\mu \to \nu_{x=e}$ (appearance)				
Neutrino	Normal	229/3	21	25	47	14	107
Neutrino	Inverted	101/5	21	25	49	17	112
Antineutrino	Normal	15/41	11	11	24	9	55
Antineutrino	Inverted	7/75	11	11	24	9	55

appearance modes for neutrinos and antineutrinos, for normal (NH) and inverted (IH) hierarchy. The rates are given per 10 kt of fiducial LArTPC mass.

The GLoBES implementation used in the sensitivity studies presented here appears to be in good agreement with more recent results from the Fast MC, described in Section A.3. Updated sensitivity and systematics studies are currently underway using the Fast MC for detector simulation, and customized GLoBES-based software for the oscillation fits and propagation of systematics. A full

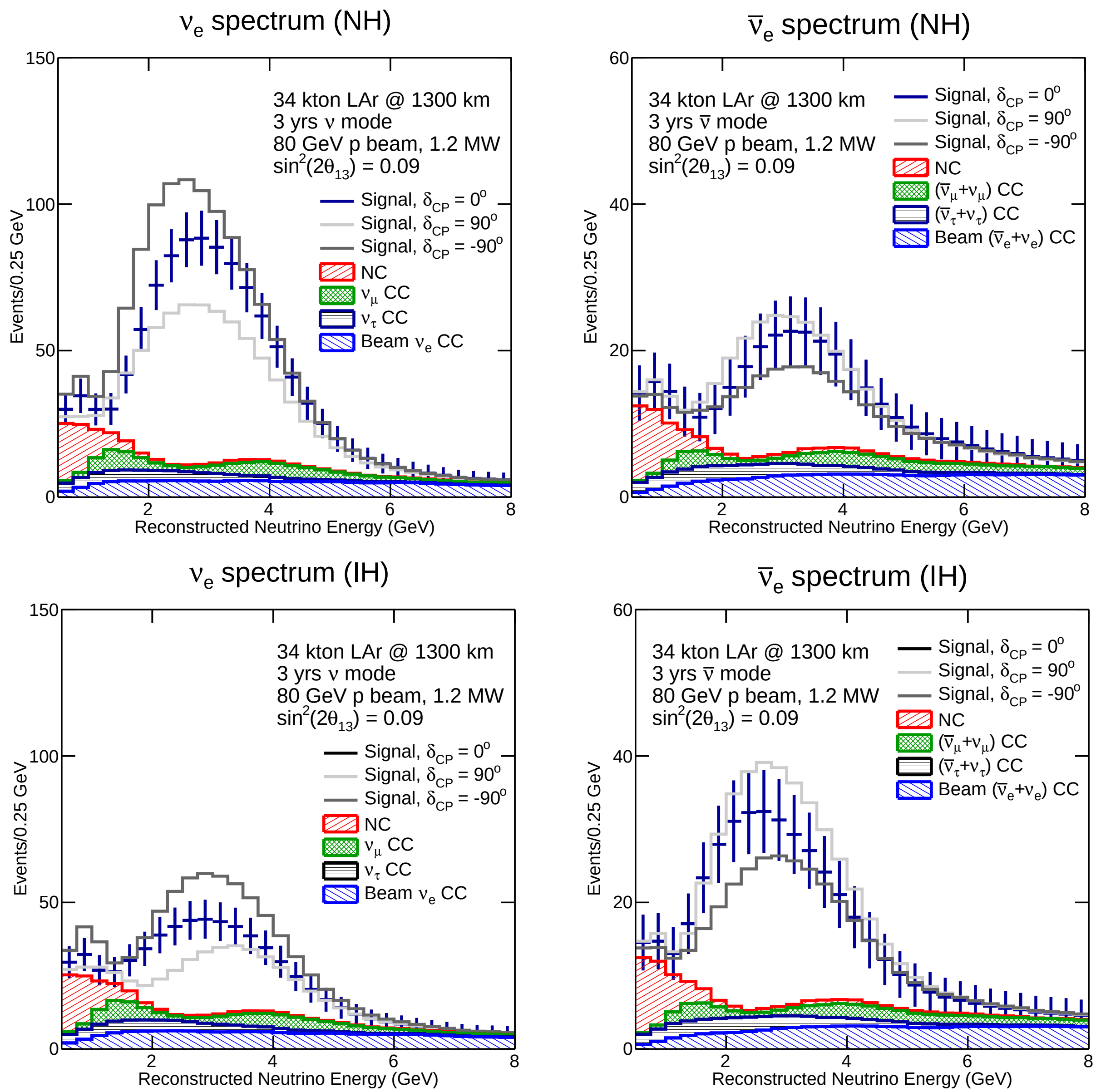

Figure 4.3: The expected reconstructed neutrino energy spectrum of ν_e or $\overline{\nu}_e$ oscillation events in a 34−kt LArTPC for three years of neutrino (left) and antineutrino (right) running with a 1.2−MW, 80−GeV beam assuming $\sin^2(2\theta_{13}) = 0.09$. The plots on the top are for normal hierarchy and the plots on the bottom are for inverted hierarchy.

MC simulation of the far detector and automated event reconstruction is being developed; this is also described in Appendix A.

4.3 Measurements of Mass Hierarchy and the CP-Violating Phase

The neutrino mass hierarchy (MH) and the value of the CP-violating phase, δ_{CP}, are currently unknown. Knowledge of the MH has significant theoretical, cosmological and experimental implications. A determination of the δ_{CP} value to be neither zero (0) nor π would constitute the first observation of CP violation in the lepton sector.

The expected performance of a 10−kt LArTPC far detector 1,300 km downstream from a neutrino source is detailed in the LBNE Conceptual Design Report Volume 1 [29]. Estimated sensitivities to the determination of the MH and discovery of CP violation, presented both here and in the CDR, are calculated using the GLoBES package. The detector response assumed in these calculations is summarized in Table 4.2. The sensitivities are obtained by simultaneously fitting the $\nu_\mu \to \nu_\mu$, $\overline{\nu}_\mu \to \overline{\nu}_\mu$, $\nu_\mu \to \nu_e$, and $\overline{\nu}_\mu \to \overline{\nu}_e$ oscillated spectra, examples of which are shown in Figures 4.2 and 4.3. The ν_τ background is not used in the sensitivity calculations since it is expected that further analysis will reduce this background to negligible levels.

In these calculations, experimental sensitivity is quantified using $\Delta\chi^2$ parameters, which are determined by comparing the predicted spectra for various scenarios. These quantities are defined, differently for neutrino MH and CP-violation sensitivity, to be:

$$\begin{aligned}
\Delta\chi^2_{MH} &= |\chi^2_{MH^{test}=IH} - \chi^2_{MH^{test}=NH}|, && (4.1)\\
\Delta\chi^2_{CPV} &= \min\left(\Delta\chi^2_{CP}(\delta_{\mathrm{CP}}^{test}=0), \Delta\chi^2_{CP}(\delta_{\mathrm{CP}}^{test}=\pi)\right), \text{ where} && (4.2)\\
\Delta\chi^2_{CP} &= \chi^2_{\delta_{\mathrm{CP}}^{test}} - \chi^2_{\delta_{\mathrm{CP}}^{true}}. && (4.3)
\end{aligned}$$

These sensitivities are evaluated separately for true NH and IH. Since the true value of δ_{CP} is unknown, a scan is performed over all possible values of $\delta_{\mathrm{CP}}^{true}$. The individual χ^2 values are calculated using

$$\chi^2(\mathbf{n}^{true}, \mathbf{n}^{test}, f) = 2\sum_i^{N_{reco}} (n_i^{true} ln \frac{n_i^{true}}{n_i^{test}(f)} + n_i^{test}(f) - n_i^{true}) + f^2, \tag{4.4}$$

where $\mathbf{n}$ are event rate vectors in N_{reco} bins of reconstructed energy and f represents a nuisance parameter to be profiled. Nuisance parameters include the values of mixing angles, mass splittings, and signal and background normalization. The nuisance parameters are constrained by Gaussian priors; in the case of the oscillation parameters, the Gaussian prior has standard deviation determined by taking 1/6 of the 3σ range allowed by the global fit [54].

With the exception of results reported in Section 4.3.1, where more information on the statistical interpretation of MH sensitivity is provided, the sensitivities presented here are for the *typical experiment* with no statistical fluctuations considered. In the absence of statistical fluctuations, the χ^2 value for the *true* spectra is identically zero. Statistical fluctuations are incorporated by repeatedly varying the contents of each energy bin in each sample by drawing from a Poisson distribution with the expected number of events in that bin as the mean.

This section presents the sensitivities of various LBNE configurations to determination of the MH and CP violation. In particular, a 10−kt far detector and the full-scope 34−kt far detector are considered. In each case, the performance of LBNE with both the 120−GeV beamline design presented in the CDR [30] as well as the upgraded 80−GeV beam described in Section 3.4 is studied. In addition, the sensitivities at different possible stages of LBNE with increases to far detector mass and Main Injector beam upgrades are estimated.

Figure 4.4 summarizes the sensitivities for determining the MH and CP violation ($\delta_{\rm CP} \neq 0$ or π) as a function of the true value of $\delta_{\rm CP}$ with a 10−kt LArTPC. The red band shows the sensitivity that is achieved with an exposure of six years with equal exposures in ν and $\overline{\nu}$ mode in a 1.2−MW beam. The cyan band shows the sensitivity obtained by combining the 10−kt LBNE with T2K and NOνA, where the T2K exposure is 7.8 $\times$ 10^{21} POT in ν mode only and the NOνA exposure is six years (assuming 6 $\times$ 10^{20} POT per year) with equal exposures in ν and $\overline{\nu}$ mode. The bands indicate the sensitivity range corresponding to different levels of signal and background normalization uncertainties and different possible beam designs. The gray curves are the expected sensitivities for the combination of NOνA and T2K. The known mixing parameters are allowed to float in the fit, but are constrained (using a Gaussian prior) by the uncertainties from the 2012 global best fit [54]. The reactor mixing angle, $\sin^2 2\theta_{13}$, is constrained to be 0.094 ± 0.005. The uncertainty is equal to the size of the current systematic uncertainty from the Daya Bay Experiment [142] and is used as a conservative estimate of the precision that will be achieved by the current generation of reactor experiments. Figure 4.5 shows the sensitivities for determining the MH and CP violation as a function of the true value of $\delta_{\rm CP}$ after six years of running in the LBNE 34−kt configuration under the same assumptions.

The sensitivity bands in Figures 4.4 and 4.5 represent the variation in sensitivity as a function of the beam design and normalization uncertainties on the signal and background. The solid curve at the lower end of the red band represents the beamline design described in the LBNE CDR Volume 2 [30] for which there is no near detector. The dashed line above the solid curve represents the sensitivity with the beam design improvements currently under study as described in Section 3.4, still without a near detector. The dashed line at the upper end of the red band represents the case in which both the beam design improvements and a high-resolution, highly capable near detector are implemented. The key design goal of the LBNE near detector and beamline simulation software is to enable a prediction of the far detector unoscillated flux with a precision of $\leq 2\%$. Therefore, the total signal and background normalization uncertainties on the ν_μ disappearance signal are assumed to be 5% and 10%, respectively. The default ν_e appearance signal *uncorrelated* normalization uncertainties for the full-scope LBNE presented in this chapter are assumed to be 1%. The ν_e appearance background uncertainty is expected to be at least as good as the $\sim 5\%$ [143] achieved by the ν_e appearance search in the MINOS experiment.

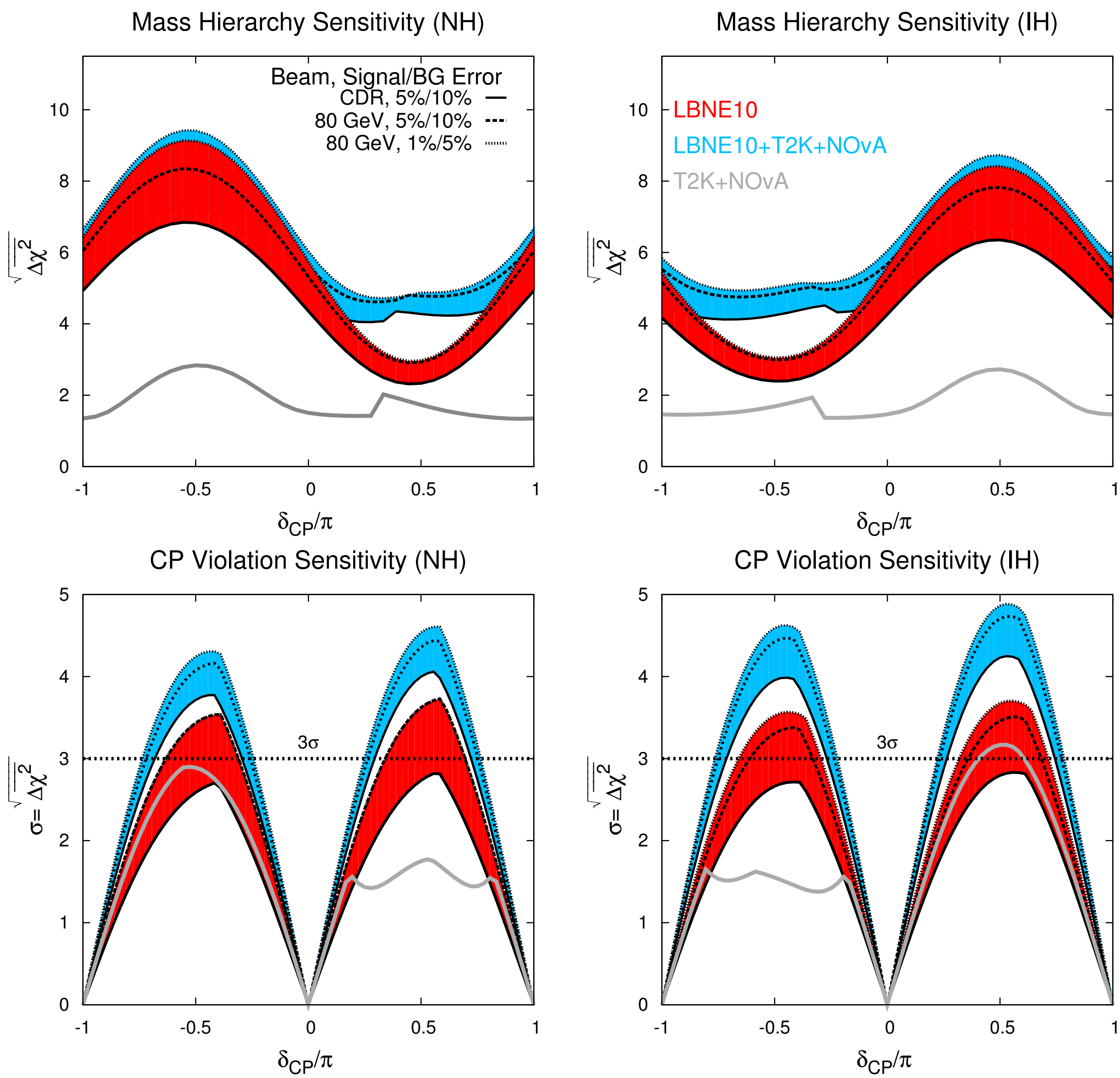

Figure 4.4: The significance with which the mass hierarchy (top) and CP violation ($\delta_{\rm CP} \neq 0$ or π, bottom) can be determined as a function of the value of $\delta_{\rm CP}$. The plots on the left are for normal hierarchy and the plots on the right are for inverted hierarchy. The red band shows the sensitivity that is achieved by a typical experiment with the LBNE 10−kt configuration alone, where the width of the band shows the range of sensitivities obtained by varying the beam design and the signal and background uncertainties as described in the text. The cyan band shows the sensitivity obtained by combining the 10−kt LBNE with T2K and NOνA, and the gray curves are the expected sensitivities for the combination of NOνA and T2K; the assumed exposures for each experiment are described in the text. For the CP-violation sensitivities, the MH is assumed to be unknown.

A detailed discussion of the systematics assumptions for LBNE is presented in Section 4.3.2. In the case that LBNE has no near neutrino detector, the uncertainties on signal and background are expected to be 5% and 10%, respectively, extrapolating from the performance and detailed knowledge of the NuMI beam on which the LBNE beamline is modeled, in situ measurements of

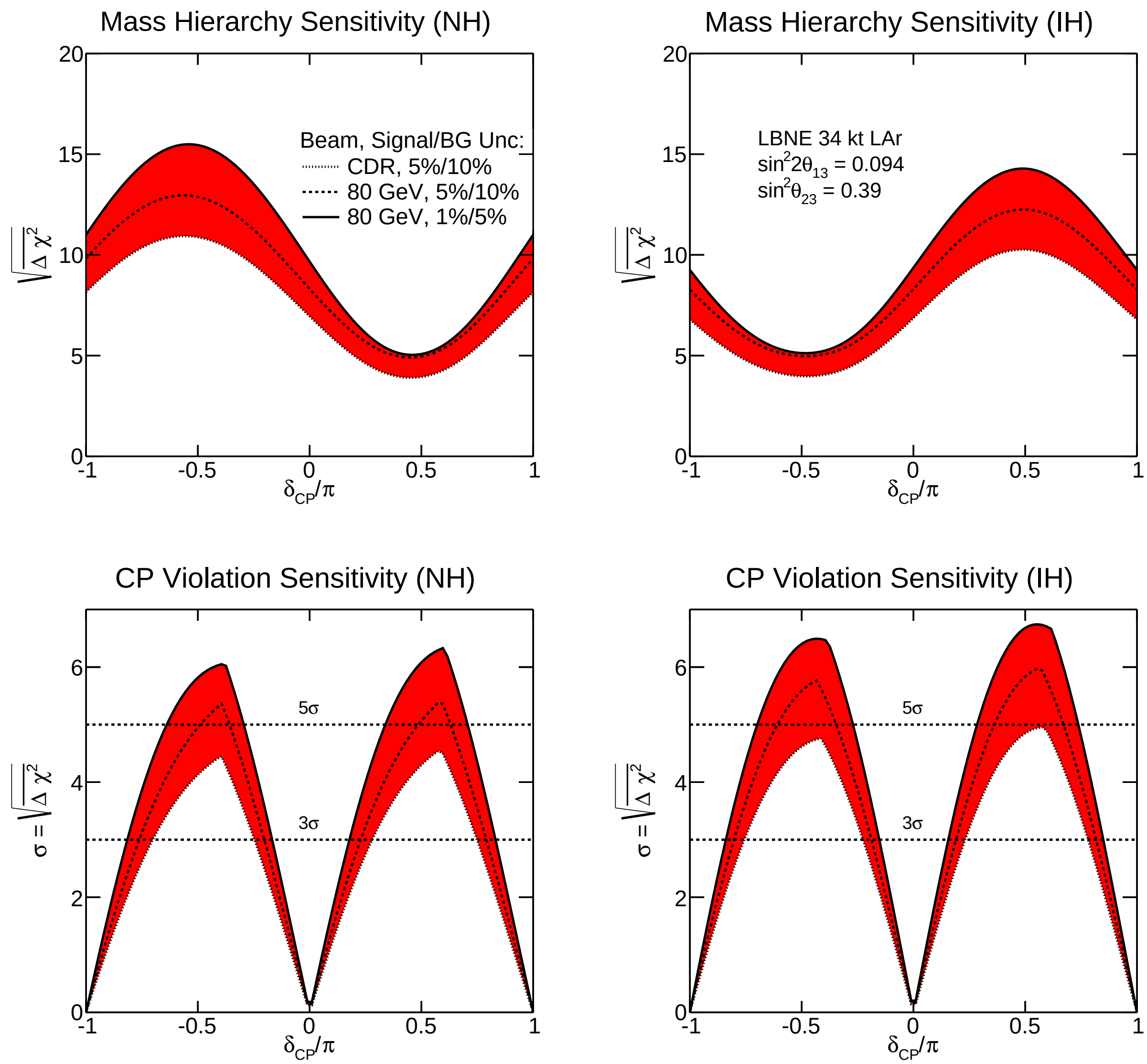

Figure 4.5: The significance with which the mass hierarchy (top) and CP violation ($\delta_{\rm CP} \neq 0$ or π, bottom) can be determined by a typical LBNE experiment with a 34−kt far detector as a function of the value of $\delta_{\rm CP}$. The plots on the left are for normal hierarchy and the plots on the right are for inverted hierarchy. The width of the red band shows the range of sensitivities that can be achieved by LBNE when varying the beam design and the signal and background uncertainties as described in the text.

the muon flux at the near site as described in [29], the expectation of improved hadron production measurements with the NA61 and MIPP experiments, and the experience of previous ν_e appearance experiments as summarized in Table 4.4.

Table 4.4: Summary of achieved systematic error performance in several select prior $\nu_\mu \to \nu_e$ oscillation experiments. These numbers were extracted from publications and may not correspond exactly to the description in the text. NBB/WBB indicates a narrow/wide band beam. *No ND* indicates there was no near detector, and *ND-FD* indicates a two (near-far) detector experiment with extrapolation of the expected background and signal from the near to the far detector. In the case of T2K, the quoted systematic (*) is actually the total uncertainty on the observed events, which are predominately signal.

Experiment	Year	ν_μ-NC/CC Events	ν_e-CC Events	Background Syst.Error	Comment
BNL E734 [144]	1985	235	418	20%	No ND
BNL E776(NBB) [145]	1989	10	9	20%	No ND
BNL E776 (WBB) [146]	1992	95	40	14%	No ND
NOMAD [147]	2003	<300	5500	$< 5\%$	No ND
MiniBooNE [148]	2008	460	380	9%	No ND
MiniBooNE [49]	2013	536	782	5%	SciBooNE
MINOS [143]	2013	111	36	4%	ND–FD
T2K [149]	2013	1.1	26	9%*	ND–FD

4.3.1 Interpretation of Mass Hierarchy Sensitivities

LBNE will be definitive in its ability to discriminate between normal and inverted mass hierarchy for the allowed range of unknown parameters such as $\delta_{\rm CP}$ and $\sin^2\theta_{23}$. To assess the sensitivity of LBNE to this physics, particularly for the case of less favorable parameter values, detailed understanding of statistical significance is essential.

At the true values of $\delta_{\rm CP}$ for which the mass hierarchy asymmetry is maximally offset by the leptonic CP asymmetry, LBNE's sensitivity to the mass hierarchy is at its minimum. Even in this case, with a 34−kt LArTPC operating for six years in a 1.2−MW beam, the $|\Delta\chi^2|$ value obtained in a typical data set will exceed 25, allowing LBNE on its own to rule out the incorrect mass ordering at a confidence level above $1-3.7\times10^{-6}$. Considering fluctuations, LBNE will measure, in $\geq 97.5\%$ of all possible data sets for this least favorable scenario, a value of $|\Delta\chi^2|$ equal to 9 or higher, which corresponds to a $\geq 99\%$ probability of ruling out the incorrect hierarchy hypothesis.

In the mass hierarchy (MH) determination, only two possible results are considered, as the true MH is either normal (NH) or inverted (IH). Reference [150] presents the statistical considerations of determining the sensitivity of an experiment to the MH, framed partly in the context of two separate but related questions:

1. *Given real experimental data, with what significance can the MH be determined?*
2. *When evaluating future experimental sensitivities, what is the probability that a particular experimental design will be able to determine the MH with a given significance?*

Once data are in hand, a number of techniques based either within Bayesian or frequentist statistics make it possible to determine the level of confidence at which one MH hypothesis or the other can be ruled out. In assessing the sensitivity of future experiments, it is common practice to generate a simulated data set (for an assumed true MH) that does not include statistical fluctuations. The expected sensitivity can be reported as $\overline{\Delta\chi^2}$, representative of the mean or the most likely value of $\Delta\chi^2$ that would be obtained in an ensemble of experiments for a particular true MH. With the exception of Figure 4.7, the sensitivity plots in this document have been generated using this method.

However, addressing the expected sensitivity of an experiment per the second question above requires consideration of the effect of statistical fluctuations and variations in systematics. If the experiment is repeated many times, a distribution of $\Delta\chi^2$ values will appear. Studies in [150] and elsewhere (e.g., [151]) show that the $\Delta\chi^2$ metric employed here *does not* follow the commonly expected χ^2 function for one degree of freedom, which has a mean of $\overline{\Delta\chi^2}$ and can be interpreted using a Gaussian distribution with a standard deviation of $\sqrt{|\overline{\Delta\chi^2}|}$. Rather, these studies show that when the observed counts in the experiment are large enough, the distribution of $\Delta\chi^2$ used here approximately follows a Gaussian distribution with a mean and standard deviation of $\overline{\Delta\chi^2}$ and $2\sqrt{|\overline{\Delta\chi^2}|}$, respectively [150].

Figure 4.6 shows the expected distribution of $\Delta\chi^2$ values in LBNE from toy Monte Carlo studies. The interpretation of pairs of distributions, such as those in the various panels of this figure, depends on the information being sought. For example, one is not necessarily interested simply in the fraction of experiments where $\Delta\chi^2$ has the "right" sign. (An experiment that obtains a small value of $\Delta\chi^2$, even with the "right" sign, would not be particularly constraining since there is no way *a priori* to know which is the right sign — this is what the experiment is attempting to measure.) It should also be noted that in general $|\overline{\Delta\chi^2_{\mathrm{MH=NH}}}|$, i.e., true NH, is not necessarily equal to $|\overline{\Delta\chi^2_{\mathrm{MH=IH}}}|$, i.e., true IH, nor do the corresponding distributions necessarily have the same shape. For some ranges in δ_{CP}, for example, the event rate in LBNE is sufficiently different for the two MH hypotheses that the corresponding distributions in $\Delta\chi^2$ are quite distinct.

The plots shown on the left in Figure 4.6 illustrate the case for a true value of $\delta_{\mathrm{CP}} = 0°$, where the $\Delta\chi^2$ distributions for NH and IH scenarios are similar. Shown on the right are the corresponding distributions for the case of $\delta_{\mathrm{CP}} = 90°$, where for NH the matter asymmetry is maximally offset by the CP asymmetry, leading to poorer MH discrimination. For the IH case, these effects go in the same direction, leading to better MH discrimination. The converse is the case for $\delta_{\mathrm{CP}} = -90°$. Since the true value of δ_{CP} is unknown (although a best-fit value and confidence interval

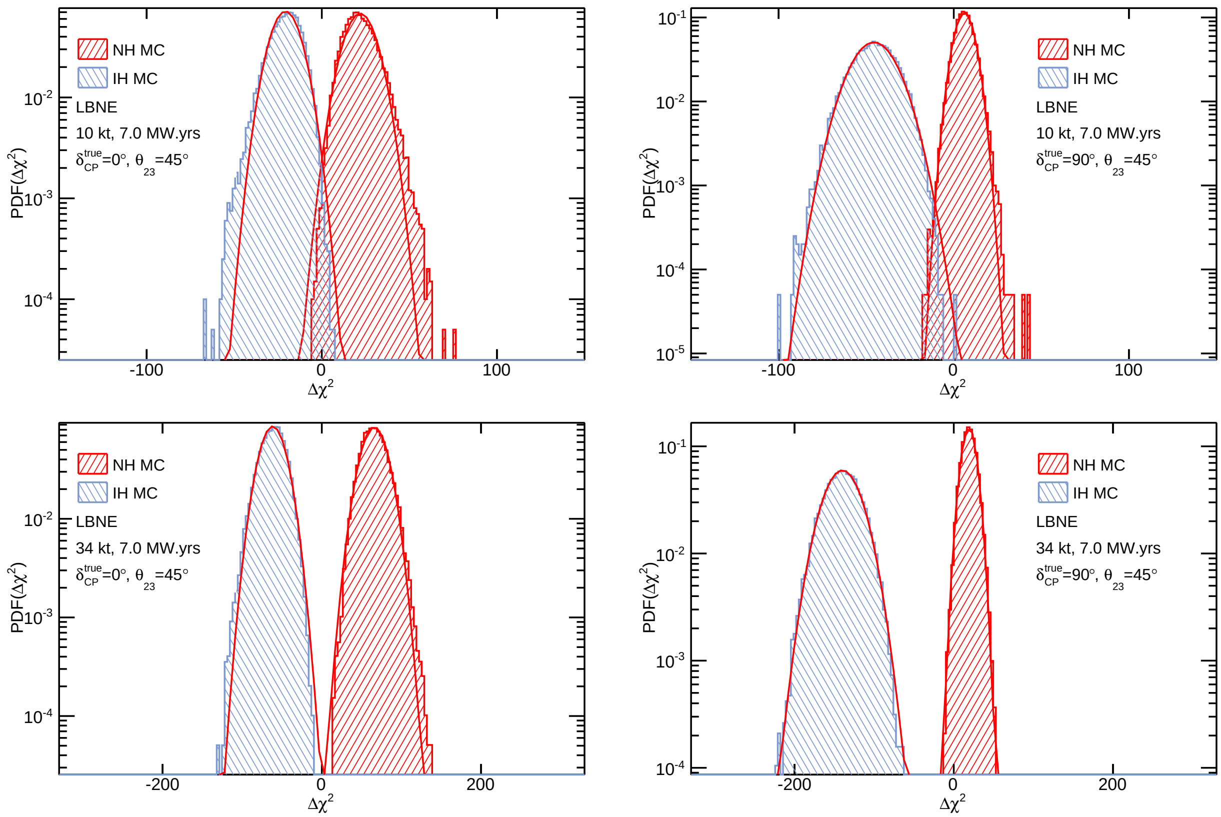

Figure 4.6: $\Delta\chi^2_{\mathrm{MH=NH}}$ (red) and $\Delta\chi^2_{\mathrm{MH=IH}}$ (blue) distributions for LBNE from Toy MC studies. The top set of figures are for a 10−kt detector operating six years in a 1.2−MW beam. The bottom set is for a 34−kt detector operating six years in a 1.2−MW beam. The figures on the left are for $\delta_{cp}^{true} = 0$ and the figures on the right are for $\delta_{cp}^{true} = 90°$. The value of δ_{CP} is unconstrained in the fit.

will emerge from the analysis of the data collected), comparison of a given value of $\Delta\chi^2$ with expected distributions for NH and IH cases for the *same* value of δ_{CP} does not in general provide the appropriate test. For simplicity, following [151], the discussion below focuses on the respective values of δ_{CP} for which the experiment will have poorest sensitivity for NH ($+90°$) and IH ($-90°$) scenarios.

Given the above introduction to the statistical fluctuation issues, it is natural to employ the statistical language of hypothesis testing in projecting LBNE's MH sensitivity. Specifically, α is defined as the desired Type-I error rate — that is, the probability of rejecting a particular hypothesis, e.g., NH, in the case where this is the true hypothesis. One can then ask what the corresponding Type-II error rate β would be, defined as the probability of accepting the hypothesis being tested (NH in this example), when in fact the alternate hypothesis (IH) is true. The pair of α and β would correspond to a particular value of $\overline{\Delta\chi^2}$ chosen (in advance of the experiment) as a criterion for deciding whether to rule out the NH (or IH). Historically, many experiments have characterized their anticipated sensitivity by reporting α for the case of $\beta = 0.5$, which is nothing more than that given by the median value of the test statistic (in this case, $\Delta\chi^2 = \overline{\Delta\chi^2}$) as described above.

Sometimes, the sensitivity is also reported as the square root of $\overline{\Delta\chi^2}$.

Due to the approximate symmetry of the MH ambiguity as a function of δ_{CP} for the two MH scenarios and the desire to be able to reject exactly one of the two possible mass orderings [151], it is also natural to report a value of α for an experiment such that $\alpha = \beta$ [152,153,151]. In this way, it is possible to express just how *unlucky* an experiment can be while maintaining a corresponding sensitivity α. In the case of LBNE, a reasonable benchmark for comparison corresponds to $\overline{\Delta\chi^2} = 36$. For this case, specifying $\alpha = \beta$ yields $\alpha = 0.0013$, which means that the experiment will have a 0.13% probability of ruling out the true MH hypothesis and of accepting the wrong MH hypothesis.

As described above, and as is evident in the plots presented, such as those in Figures 4.4 and 4.5, the sensitivity of LBNE is strongly dependent on the true value of δ_{CP}; Figure 4.7 shows that it also depends on the true value of $\sin^2\theta_{23}$. While plotting the value of α (for some choice of β, such as $\beta = 0.5$ or $\beta = \alpha$) as a function of these parameters encapsulates the sensitivity, a visually helpful presentation is obtained by plotting the expected mean value, $\overline{\Delta\chi^2}$, as well as ranges of possible values corresponding to the expected distribution in $\Delta\chi^2$. Thus, Figure 4.7 shows the dependence of $\sqrt{|\overline{\Delta\chi^2}|}$ on the true value of δ_{CP} for the typical LBNE data set, for two possible values of $\sin^2\theta_{23}$, as well as the corresponding expectation bands within which 68% (green) and 95% (yellow) of LBNE sensitivities will fall. These expectation bands give a semi-quantitative picture of the likely range of outcomes for the experiment.

The horizontal dashed lines on Figure 4.7 specify the confidence level of an experiment with a particular value of $\Delta\chi^2$ such that:

$$\mathrm{CL} = P(\text{favored MH}|\text{data}\,x)/(P(\text{favored MH}|\text{data}\,x) + P(\text{unfavored MH}|\text{data}\,x)), \quad (4.5)$$

following the convention in [150], where the notation $P(\mathrm{A}|\mathrm{B})$ represents the probability of A given condition B, and these probabilities are inferred from the corresponding likelihoods via Bayes' Theorem. Alternatively, the $\Delta\chi^2$ values shown in these plots can be approximately translated to sensitivities in terms of α, for whatever choice of β is desired, following, for example, the prescription described in [151].

As seen in Figure 4.7, a typical LBNE data set with a 34−kt detector can determine the MH with $|\overline{\Delta\chi^2}| \geq 25$ for all values of δ_{CP} (for the left plot, where $\sin^2\theta_{23} = 0.39$). From a Bayesian analysis, the probability that an experiment measuring $|\Delta\chi^2| = 25$ has ruled out the true MH hypothesis is 3.7×10^{-6}, as indicated for the corresponding horizontal dashed line in the plots in this figure. When considering the effect of statistical fluctuations, for the same value of θ_{23}, about 97.5% of experiments will determine the MH with $|\Delta\chi^2| > 9$ for the least favorable value of δ_{CP}, where $|\Delta\chi^2| = 9$ corresponds to a CL of 98.9%.

For the bulk of the range of δ_{CP}, the sensitivity of LBNE is vastly better than for the least favorable value described above. Furthermore, newer data prefer values of θ_{23} closer to maximal [69], which

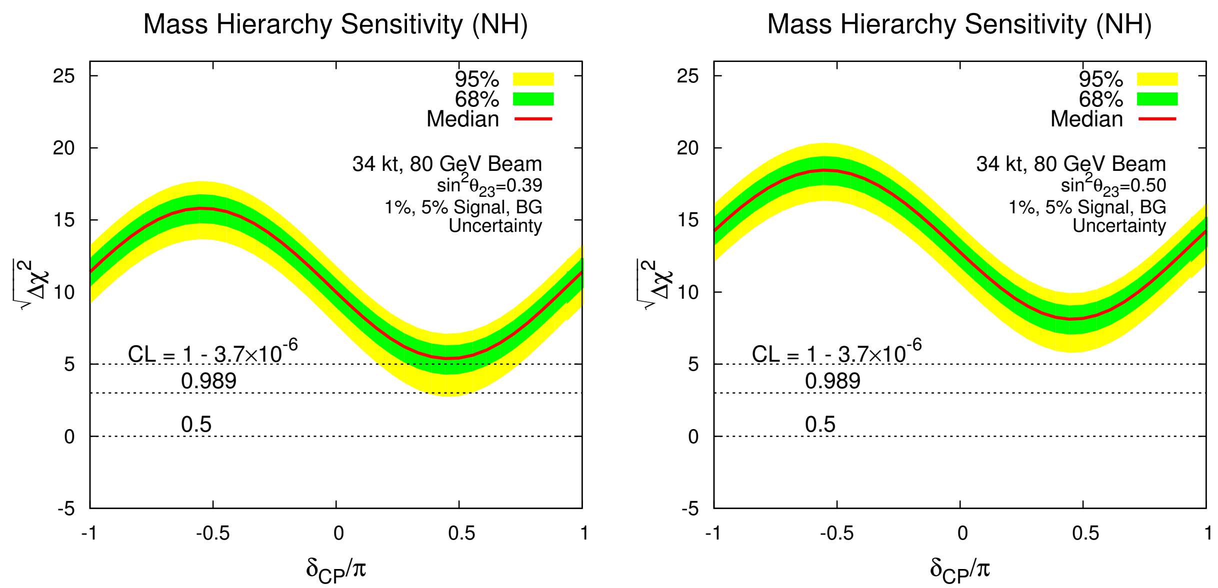

Figure 4.7: The square root of the mass hierarchy discrimination metric $\Delta\chi^2$ is plotted as a function of the unknown value of $\delta_{\rm CP}$ for the full-scope LBNE with 34 kt, 3+3 ($\nu + \overline{\nu}$) years of running in a 1.2−MW beam, for true NH. The red curve represents the most likely experimental value obtained, estimated using a data set absent statistical fluctuations, while the green and yellow bands represent the range of $\Delta\chi^2$ values expected in 68% and 95% of all possible experimental cases, respectively. The horizontal lines indicate the probability that an experiment with that value of $\Delta\chi^2$ correctly determines the MH, computed according to a Bayesian statistical formulation. The plot on the left assumes a value of $\sin^2\theta_{23} = 0.39$ [54], while that on the right assumes $\sin^2\theta_{23} = 0.5$ (maximal ν_μ-ν_τ mixing).

results in significantly enhanced LBNE MH sensitivity. As shown in the right-hand plot of Figure 4.7, if $\sin^2\theta_{23} = 0.5$, the expected MH sensitivity for the typical LBNE experiment at the least favorable $\delta_{\rm CP}$ point is $|\overline{\Delta\chi^2}| \approx 64$, which is significantly larger than the sensitivity of $|\overline{\Delta\chi^2}| \approx 25$ expected for the same value of $\delta_{\rm CP}$ if $\sin^2\theta_{23} = 0.39$. This suggests that a typical LBNE data set will determine the MH with $|\Delta\chi^2|$ well above the benchmark value of 36 mentioned above for even the least favorable values of $\delta_{\rm CP}$.

In addition to detailed LBNE-specific frequentist studies reported in [151], an LBNE-specific update (using both Bayesian and frequentist approaches) to the general statistical studies reported in [150] is in preparation.

4.3.2 Sensitivities and Systematics

The main systematic uncertainties in any experiment are determined by the analysis strategy employed and the performance of the detector. Figure 4.8 outlines the analysis strategy commonly employed to extract oscillation parameters in two-detector long-baseline neutrino oscillation experiments. The measured spectrum of ν_μ events in the near detector, $N_{\rm ND}^{data}(\nu_\mu)$ is extrapolated to the far detector and is used to predict both the ν_μ and ν_e appearance signals in the far detector, $N_{\rm FD}^{expected}(\nu_\mu)$ and $N_{\rm FD}^{expected}(\nu_e)$ respectively. The measured spectrum of ν_e candidates in the near

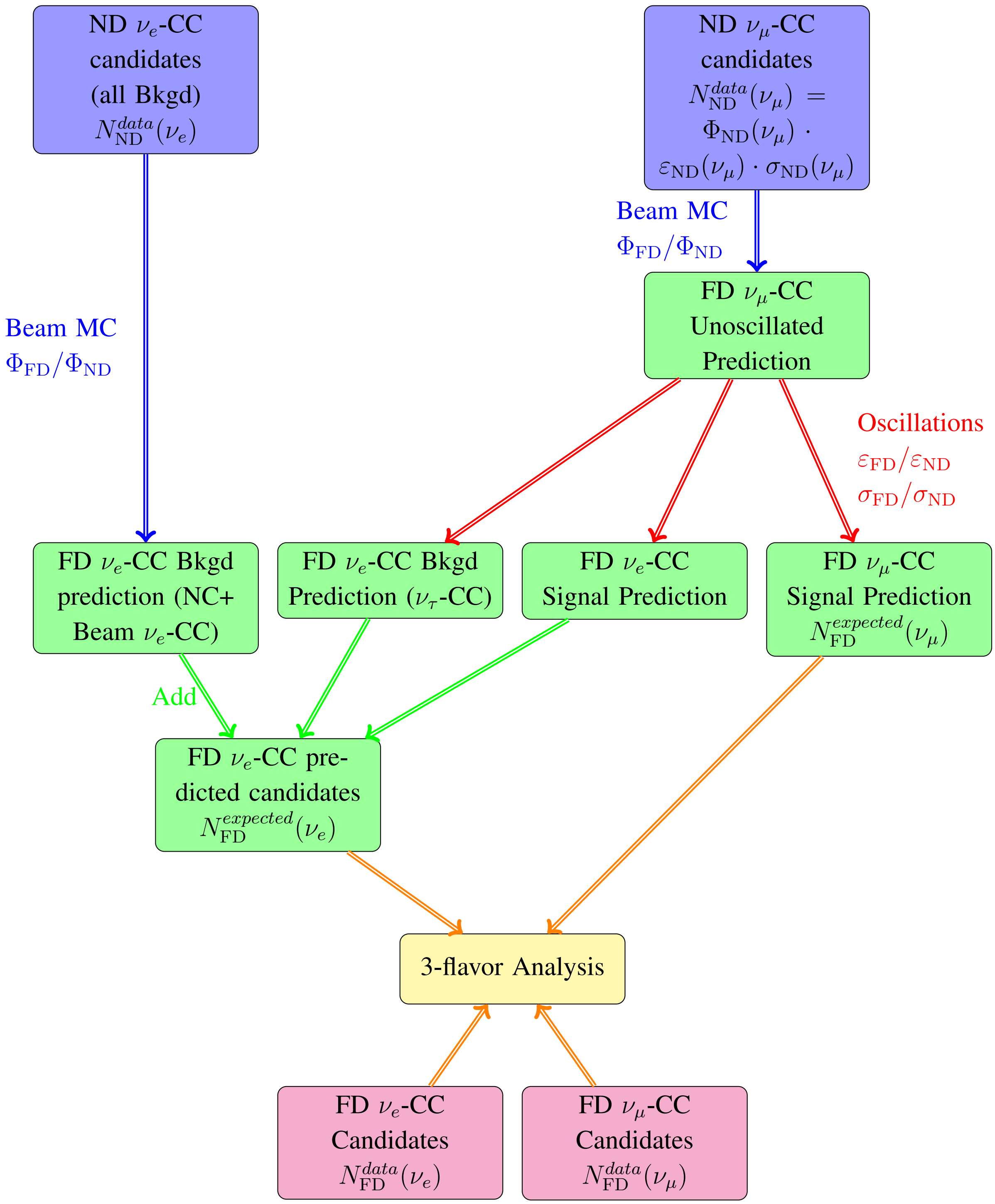

Figure 4.8: Flow chart of the ν_e appearance analysis method in a two-detector long-baseline experiment. Φ refers to the beam flux, ε refers to detector efficiencies and smearing, and σ refers to neutrino interaction modeling. The terms ND and FD refer to the near and far detector, respectively.

detector, $N_{\mathrm{ND}}^{data}(\nu_e)$, which comprises mostly the beam ν_e events and NC π^0 misidentified events, is used to predict the background to the ν_e appearance signal in the far detector. In LBNE, neutrino oscillation parameters will be extracted using a fit to four far detector data samples: ν_e, $\overline{\nu}_e$, ν_μ, and $\overline{\nu}_\mu$, which will allow for partial cancellation of uncertainties.

In the current generation of experiments, the measured spectrum of neutrino events in the near detector is a product of beam flux (Φ), detector efficiency and smearing (ε), and neutrino interaction dynamics (σ). To extrapolate the observed spectra in the near detector to the far detector, corrections have to be made for:

1. Differences in the beam flux in the near and far detectors, $\Phi_{\mathrm{FD}}/\Phi_{\mathrm{ND}}$: The near detector is much closer to the neutrino beamline and sees an extended source of neutrinos from the decay pipe as compared to the far detector, which observes a point source. A beam MC is used to correct for these differences. Uncertainties arise from inaccuracies in the simulation of the hadron production from the target, the focusing of the horns, the material in the beamline (which absorbs hadrons before they can decay), and the decay channel geometry.

2. Differences in near and far detector smearing and efficiencies, $\varepsilon_{\mathrm{FD}}/\varepsilon_{\mathrm{ND}}$: The largest uncertainties arise from the different event selection efficiencies in the near and far detectors and, in particular, the imperfect modeling of the energy scales of the near and far detectors. Identical near and far detectors allow most of these uncertainties to cancel in the extrapolation in the case of the ν_μ signal prediction. The ν_e signal prediction is extrapolated from $N_{\mathrm{ND}}^{data}(\nu_\mu)$; thus there are irreducible residual uncertainties arising from different criteria used to select ν_e and ν_μ candidate events and different detector response functions.

3. Differences in the interactions of neutrinos in the near and far detector, $\sigma_{\mathrm{FD}}/\sigma_{\mathrm{ND}}$: In the case in which both near and far detectors use the same target nucleus, the differences cancel for extrapolation of the ν_μ signal from the near to the far detector. When using the ν_μ signal in the near detector to predict the ν_e (and ν_τ) signals in the far detector, uncertainties arising from differences in ν_e (ν_τ) and ν_μ interactions, $\sigma_{\mathrm{FD}}(\nu_e)/\sigma_{\mathrm{ND}}(\nu_\mu)$, dominate. These uncertainties are limited by theoretical uncertainties and are typically smaller at higher energies.

The estimation of the expected signals at the far detector can be summarized thus:

$$N_{\mathrm{ND}}^{data}(\nu_\mu) = \Phi_{\mathrm{ND}}(\nu_\mu) \otimes \varepsilon_{\mathrm{ND}}(\nu_\mu) \otimes \sigma_{\mathrm{ND}}(\nu_\mu) \tag{4.6}$$

$$N_{\mathrm{FD}}^{expected}(\nu_\mu) = N_{\mathrm{ND}}^{data}(\nu_\mu) \otimes \frac{\Phi_{\mathrm{FD}}(\nu_\mu)}{\Phi_{\mathrm{ND}}(\nu_\mu)} \otimes P(\nu_\mu \to \nu_\mu) \otimes \frac{\varepsilon_{\mathrm{FD}}(\nu_\mu)}{\varepsilon_{\mathrm{ND}}(\nu_\mu)} \otimes \frac{\sigma_{\mathrm{FD}}(\nu_\mu)}{\sigma_{\mathrm{ND}}(\nu_\mu)} \tag{4.7}$$

$$
\begin{aligned}
N_{\mathrm{FD}}^{expected}(\nu_e) \quad = \quad & \underbrace{N_{\mathrm{ND}}^{data}(\nu_\mu) \otimes \frac{\Phi_{\mathrm{FD}}(\nu_\mu)}{\Phi_{\mathrm{ND}}(\nu_\mu)} \otimes P(\nu_\mu \to \nu_e) \otimes \frac{\varepsilon_{\mathrm{FD}}(\nu_e)}{\varepsilon_{\mathrm{ND}}(\nu_\mu)} \otimes \frac{\sigma_{\mathrm{FD}}(\nu_e)}{\sigma_{\mathrm{ND}}(\nu_\mu)}}_{\text{Expected signal events}} \\
& + \underbrace{N_{\mathrm{ND}}^{data}(\nu_e) \otimes \frac{\Phi_{\mathrm{FD}}(\nu_e)}{\Phi_{\mathrm{ND}}(\nu_e)} \otimes P(\nu_e \to \nu_e) \otimes \frac{\varepsilon_{\mathrm{FD}}(\nu_e)}{\varepsilon_{\mathrm{ND}}(\nu_e)} \otimes \frac{\sigma_{\mathrm{FD}}(\nu_e)}{\sigma_{\mathrm{ND}}(\nu_e)}}_{\text{Beam } \nu_e \text{ events}} \\
& + \text{NC background extrapolated from } N_{\mathrm{ND}}^{data}(\nu_e) \\
& + \nu_\tau \text{ background extrapolated from } N_{\mathrm{ND}}^{data}(\nu_\mu) \qquad (4.8)
\end{aligned}
$$

Expected systematic uncertainties on the LBNE ν_e appearance and ν_μ signal samples in the three-flavor fit for LBNE (Table 4.2) are extrapolated from the current performance of the MINOS [143,154] and T2K [149] experiments. The dominant uncertainties on the current ν_e appearance analysis from MINOS and T2K and the expected corresponding uncertainties in LBNE are shown in Table 4.5. The categorization of the dominant experimental uncertainties in Table 4.5 are not always in exact correspondence since T2K and MINOS are very different experiments and deploy different analysis techniques. A detailed description of the expected LBNE performance on each of the dominant uncertainties follows.

Beam flux uncertainties: The LBNE high-resolution near detector is being designed with the goal of accurately measuring the unoscillated beam flux at the near site with a precision $\leq 2\%$ for both shape and absolute normalization. Table 4.6 summarizes the precision that can be achieved using different near detector analysis techniques, described in detail in Section 7.1, to measure the absolute normalization and shape of the different components of this flux. It is important to note that several of these techniques have already been used and *proven to work* in neutrino experiments such as MINOS [155] and NOMAD [156,157]. In particular, the inclusive neutrino charged current (CC) cross-section measurement in the MINOS near detector reported in [155] has already achieved a normalization uncertainty of $\sim 2\%$ in the range of $3 < E_\nu < 9$ GeV using the low-ν_0 method described in Section 7.1. The total systematic uncertainty on the NuMI neutrino flux determination by the MINOS near detector reported in [155] was $\sim 6\%$ and was limited by the detector performance. Recent independent studies on extraction of the neutrino flux using the low-ν_0 method [158] indicate that the technique can be reliably extended down to 1 GeV.

The LBNE near detector is being designed to significantly improve performance relative to the current generation of high-intensity neutrino detectors. A detailed beamline simulation will enable the extrapolation of the LBNE near detector flux measurements to the unoscillated far detector spectrum with high precision using techniques similar to those used by MINOS [159]. The near-to-far ν_μ unoscillated-spectrum extrapolation uncertainties already achieved by MINOS are $< 3\%$ in the MINOS (and also in the LBNE) appearance signal range of $1 < E_\nu < 8$GeV [160,159]. The MINOS extrapolation does not include any independent constraints on the hadron production spectrum from the proton target or information on the horn focusing performance from the muon flux measurements at the near site. The NuMI beamline — the design of which is very similar to

Table 4.5: The dominant systematic uncertainties on the ν_e appearance signal prediction in MINOS and T2K and a projection of the expected uncertainties in LBNE. For the MINOS uncertainties *absolute* refers to the total uncertainty and ν_e is the effect on the ν_e appearance signal only. The LBNE uncertainties are the total *expected* uncertainties on the ν_e appearance signal which include both correlated and uncorrelated uncertainties in the three-flavor fit.

Source of Uncertainty	MINOS Absolute/ν_e	T2K ν_e	LBNE ν_e	Comments
Beam Flux after N/F extrapolation	3%/0.3%	2.9%	2%	MINOS is normalization only. LBNE normalization and shape highly correlated between ν_μ/ν_e.
		Detector effects		
Energy scale (ν_μ)	7%/3.5%	included above	(2%)	Included in LBNE ν_μ sample uncertainty only in three-flavor fit. MINOS dominated by hadronic scale.
Absolute energy scale (ν_e)	5.7%/2.7%	3.4% includes all FD effects	2%	Totally active LArTPC with calibration and test beam data lowers uncertainty.
Fiducial volume	2.4%/2.4%	1%	1%	Larger detectors = smaller uncertainty.
		Neutrino interaction modeling		
Simulation includes: hadronization cross sections nuclear models	2.7%/2.7%	7.5%	$\sim 2\%$	Hadronization models are better constrained in the LBNE LArTPC. N/F cancellation larger in MINOS/LBNE. X-section uncertainties larger at T2K energies. Spectral analysis in LBNE provides extra constraint.
Total	**5.7%**	**8.8%**	**3.6 %**	**Uncorrelated ν_e uncertainty in full LBNE three-flavor fit = 1-2%.**

LBNE's — is expected to operate for more than a decade with improved flux measurements using the much more capable MINERνA detector [161] in both the low-energy and high-energy tunes. MINERνA is designed to measure the absolute NuMI flux with a precision of $\sim 5\%$ or better; data from MINERνA will be used to further improve the accuracy of the LBNE beamline simulation, reducing the uncertainties on the extrapolation of the flux. A new program of hadron production measurements at the NA61/SHINE [162] experiment will also reduce the near-to-far extrapolation uncertainties from the LBNE beamline simulation. The combination of LBNE near detector flux measurements and improved beamline simulation is expected to enable a prediction of the far detector ν_e appearance signal with a precision of $< 2\%$ total normalization and shape uncertainty. Since this uncertainty is highly correlated among the four data samples in the three-flavor fit, the final uncorrelated uncertainty on the ν_e signal sample will be significantly smaller.

Table 4.6: Precisions achievable from in situ ν_μ and ν_e flux measurements in the fine-grained, high-resolution ND with different techniques.

Technique	Flavor	Absolute normalization	Relative flux $\Phi(E_\nu)$	Near Detector requirements
NC Scattering $\boldsymbol{\nu_\mu e^- \to \nu_\mu e^-}$	ν_μ	2.5%	$\sim 5\%$	e ID θ_e Resolution e^-/e^+ Separation
Inverse muon decay $\boldsymbol{\nu_\mu e^- \to \mu^- \nu_e}$	ν_μ	3%		μ ID θ_μ Resolution 2-Track (μ+X) Resolution μ energy scale
CC QE $\boldsymbol{\nu_\mu n \to \mu^- p}$ $\boldsymbol{Q^2 \to 0}$	ν_μ	$3-5\%$	$5-10\%$	D target p Angular resolution p energy resolution Back-Subtraction
CC QE $\boldsymbol{\overline{\nu}_\mu p \to \mu^+ n}$ $\boldsymbol{Q^2 \to 0}$	$\overline{\nu}_\mu$	5%	10%	H target Back-Subtraction
Low-$\boldsymbol{\nu_0}$	ν_μ		2.0%	μ^- vs μ^+ E_μ-Scale Low-E_{Had} Resolution
Low-$\boldsymbol{\nu_0}$	$\overline{\nu}_\mu$		2.0%	μ^- vs μ^+ E_μ-Scale Low-E_{Had} Resolution
Low-$\boldsymbol{\nu_0}$	$\nu_e/\overline{\nu}_e$	1-3%	2.0%	e^-/e^+ Separation (K^0_L)
CC	ν_e/ν_μ	<1%	~2%	e^- ID & μ^- ID p_e/p_μ Resolution
CC	$\overline{\nu}_e/\overline{\nu}_\mu$	<1%	~2%	e^+ ID & μ^+ ID p_e/p_μ Resolution
Low-$\boldsymbol{\nu_0}$/CohPi	$\overline{\nu}_\mu/\nu_\mu$	~2%	~2%	μ^+ ID & μ^- ID p_μ Resolution E_{Had} Resolution

ν_μ **energy-scale uncertainty:** Both T2K and MINOS use the reconstructed ν_μ event spectrum in the near detector to predict the ν_e appearance signal at the far detector. Therefore the ν_μ energy-scale uncertainty in the near detector is propagated as an uncertainty on the ν_e appearance signal at the far detector. In MINOS — which has a high proportion of non-QE events — the ν_μ energy-scale uncertainty is dominated by uncertainty in the hadronic energy scale (7% for $E_\nu < 3$ GeV) [163] and the muon energy scale (2.5%). Utilization of the low-ν_0 method for energies less than 3 GeV in LBNE reduces the hadronic energy-scale contribution to the uncertainty in the ν_μ energy scale in the near detector. As discussed in Chapter 7, it is expected that both the muon and hadronic energy-scale uncertainties in the near detector will be $<1\%$, so far detector energy-scale uncertainties will dominate the uncertainty in the ν_μ signal prediction. The high-resolution LArTPC far detector and an active program of hadron test-beam experiments planned for LBNE will reduce far detector hadronic energy-scale uncertainties, which also contribute to uncertainty in the energy scale of the far detector ν_μ signal used in the three-flavor analysis. Extrapolating from MINOS, the LBNE ν_μ energy-scale uncertainty is thus estimated to be $\sim 2\%$.

In MINOS, the 7% ν_μ energy-scale uncertainty resulted in a residual uncertainty of 3.5% on the ν_e signal prediction. In the LBNE full three-flavor analysis, this uncertainty is 100% correlated between the predicted ν_μ and ν_e signal samples; therefore a E_{ν_μ} energy-scale uncertainty of 2% is assigned to the ν_μ signal prediction in LBNE. The residual uncorrelated uncertainty on the ν_e signal prediction is considered to be negligible.

Absolute ν_e energy-scale uncertainties: In Figure 4.9, the MH and CP-violation sensitivity obtained using a rate-only, a shape-only and a rate+shape analysis of ν_e appearance is shown. This study demonstrates that a critical component of LBNE's oscillation sensitivity is an accurate measurement of the shape of the ν_e appearance signal. This measurement depends on the precision

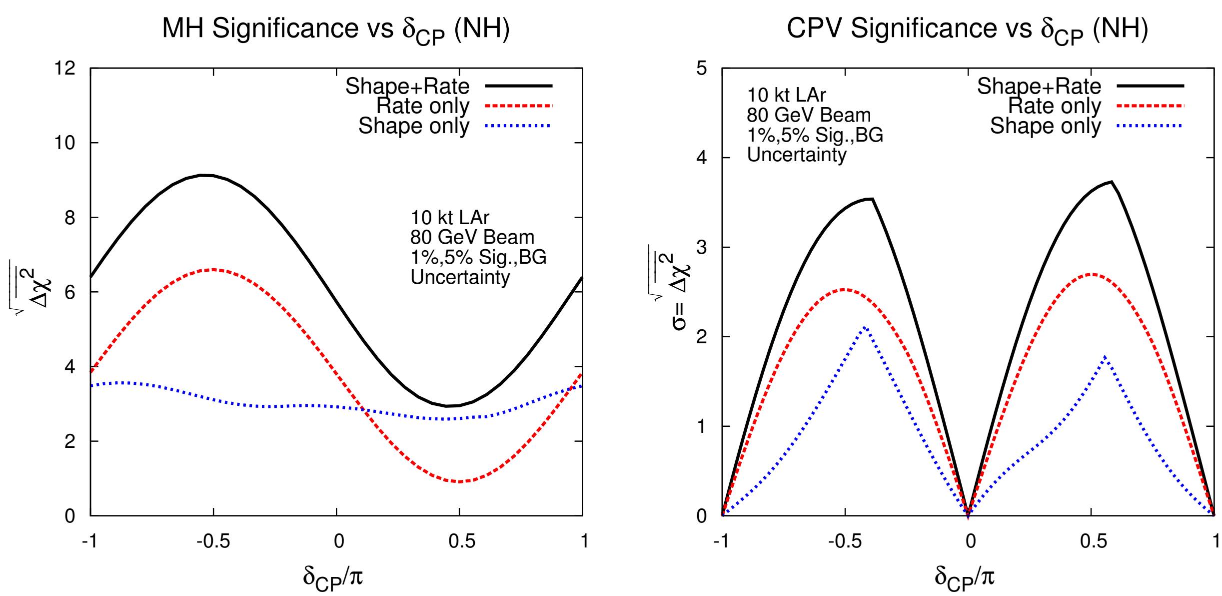

Figure 4.9: The mass hierarchy (left) and CP violation (right) sensitivities from shape, rate, and shape+rate. The sensitivity is for a 10−kt detector, 1.2−MW beam, 3+3 ($\nu + \overline{\nu}$) years, for true normal hierarchy.

with which the detector response to ν_e interactions is understood. The ν_e energy-scale uncertainty, which is not yet included in the current sensitivity calculation with the GLoBES framework, is therefore expected to be an important systematic uncertainty in the LBNE oscillation analysis.

The effect of ν_e energy-scale uncertainty on the ν_e signal normalization, determined by the precision of detector calibration, was 2.7% in MINOS and 3.4% in T2K, where the T2K uncertainty actually includes most far detector effects. LBNE's LArTPC detector technology is expected to outperform both the MINOS sampling calorimeter and the T2K water Cherenkov detector in reconstruction of the ν_e interaction. For example, the proton produced from the ν_e-QE interaction — the interaction with potentially the best ν_e energy resolution — is clearly visible in a LArTPC [164], whereas it is often below Cherenkov threshold in T2K. An active program of test beam experiments with LArTPCs is currently being planned to address the detector response to electrons and hadrons. Results from the test beam experiments and the projected performance of the in situ calibration will enable LBNE to limit the detector energy-scale uncertainties below the level achieved by the current generation of experiments.

Hadronic energy is expected to contribute more than half of the total energy deposit for many ν_e and ν_μ interactions in LBNE. The hadronic energy scale does not depend on neutrino flavor; since it should be identical for ν_e and ν_μ interactions, this portion of the absolute energy-scale uncertainty is expected to largely cancel in the LBNE three-flavor analysis. This cancellation may be reduced to the extent that event-selection criteria vary the hadronic energy fraction among the samples.

Simulation uncertainties: The simulation uncertainties listed in Table 4.5 refer primarily to uncertainties in modeling neutrino interactions with the target nucleus in the near and far detectors. These uncertainties include ν_e and ν_μ cross-section uncertainties, uncertainties arising from the modeling of the structure of the target nucleus, modeling of final-state interactions within the nucleus, and hadronization model uncertainties arising from the break up of the target nucleus in higher-energy inelastic interactions. The deployment of identical nuclear targets in the MINOS (iron) and LBNE (argon) near and far detectors allows for a larger cancellation of the simulation uncertainties as compared to T2K, which used dissimilar target nuclei in its near detector (carbon) and far detector (oxygen). A high-resolution near detector such as that being designed for LBNE will enable further constraints on the hadronization models by resolving many of the individual particles produced in resonance and deep inelastic interactions, which represent $\sim$75% of LBNE neutrino interactions.

The MINOS ν_e appearance analysis achieved a 2.7% residual uncertainty from simulation after the near-to-far extrapolation. The MINOS simulation uncertainty is dominated by hadronization uncertainties, because cross-section uncertainties largely cancel between the identical nuclei in the near and far detectors. The T2K residual uncertainty after near-to-far extrapolation is 7%. Additionally, the T2K analysis includes more sources of cross-section uncertainties than MINOS and, at the lower T2K energies, larger differences in ν_μ/ν_e cross sections (2.9 %) persist after extrapolating the ν_μ spectrum in the near detector to the ν_e signal prediction in the far.

The LBNE near detector design is required to achieve a cancellation of near-to-far cross-section and hadronization-model uncertainties at the same level as MINOS or better. The ν_e appearance signal in LBNE peaks at 2.5 GeV; these higher energies will result in lower uncertainties from the cross-section effects considered by T2K. In addition, since cross-section variations impact the observed ν_e and ν_μ spectra differently when compared to oscillation effects, the fit to the wide-band spectrum in LBNE could constrain some of these uncertainties further. Therefore, it is expected that

LBNE could reduce the total ν_e appearance simulation uncertainties to a level of 2%. Preliminary results from the LBNE Fast MC simulation (described in Section A.3) indicate that many cross-section uncertainties cancel out when combining the ν_μ disappearance and ν_e appearance signal samples in a three-flavor fit, resulting in a much smaller uncorrelated uncertainty on the ν_e signal sample.

It is important to note that some $\nu/\overline{\nu}$ simulation uncertainties may not cancel out in the near-to-far extrapolation or in the combined fit; in particular, uncertainties due to nuclear models and intra-nuclear effects are different for $\nu/\overline{\nu}$ interactions. New models of intra-nuclear effects are being evaluated to determine the size of these irreducible residual uncertainties. Additionally, there are uncertainties at the level of 1-2% in the cross sections that will not cancel between ν_e and ν_μ [165]. In the absence of theoretical progress, these should also be considered irreducible.

Fiducial volume uncertainties: One of the dominant uncertainties in the MINOS ν_μ disappearance analysis — a high-precision oscillation analysis based on a detailed spectral shape — was the fiducial-volume uncertainty, which included near and far detector reconstruction uncertainties. The uncertainty on the fiducial volume of the MINOS far detector alone was 2.4%. T2K, with a much larger far detector (22.5 kt fiducial), was able to reduce this uncertainty to the 1% level. It is expected that LBNE will be able to achieve this level of uncertainty on the ν_e appearance signal. With the combination of all four signal samples ($\nu_\mu, \overline{\nu}_\mu, \nu_e, \overline{\nu}_e$) in a three-flavor fit, the ν_e uncorrelated portion of this uncertainty is expected to be smaller than 1%.

ν_e **appearance background systematic uncertainties:** The ν_e appearance normalization uncertainty is expected to be at least as good as the $\sim 5\%$ [143] achieved by the ν_e appearance search in the MINOS experiment, using the technique of predicting intrinsic-beam and neutral current (NC) background levels from near detector measurements. The LBNE far detector should be able to provide additional constraints on the background level by independently measuring NC and ν_τ background.

In Figure 4.10, the MH and CP-violation sensitivities as a function of exposure are evaluated using three different sets of assumptions regarding the uncorrelated ν_e signal/background normalization uncertainties: 1%/5% (the goal of the LBNE scientific program), 2%/5% and 5%/10%. The last is a conservative estimate of the uncertainties that can be achieved in LBNE without unoscillated neutrino beam measurements at the near site. The impact of signal and background normalization uncertainties on the MH sensitivity is small even at high exposures given the large $\nu/\overline{\nu}$ asymmetry at 1,300 km and the fact that much of the sensitivity to the MH comes from analysis of the spectral shapes (Figure 4.9). For CP violation, however, the impact of normalization uncertainties is significant at exposures $\geq 100\,\text{kt} \cdot \text{MW} \cdot \text{years}$.

Table 4.7 summarizes the LBNE exposures required to reach 3σ and 5σ sensitivity to CP violation for at least 50% of all possible values of δ_{CP}. The exposures vary depending on the assumptions made about the normalization uncertainties that can be achieved in LBNE. The normalization un-

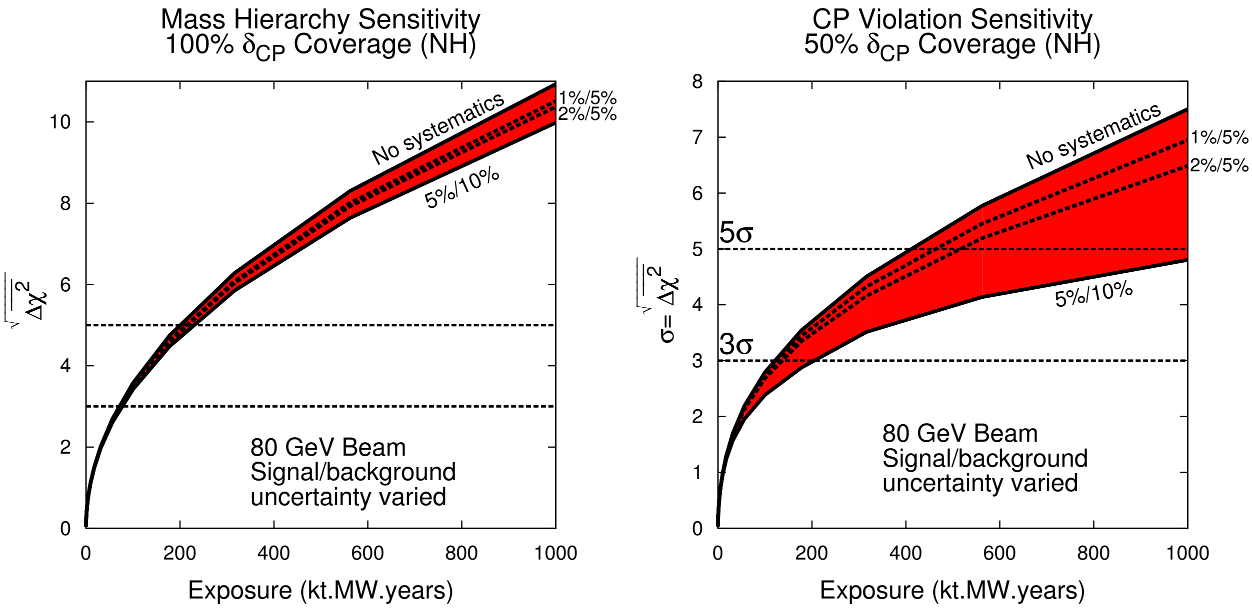

Figure 4.10: The mass hierarchy (left) and CP violation (right) sensitivities as a function of exposure in kt · year, for true normal hierarchy. The band represents the range of signal and background normalization errors.

Table 4.7: The exposures required to reach 3σ and 5σ sensitivity to CP violation for at least 50% of all possible values of $\delta_{\rm CP}$ as a function of systematic uncertainties assumed on the ν_e appearance signal. The uncertainties varied are the uncorrelated signal normalization uncertainty (Sig) and the background normalization uncertainty (Bkgd).

Systematic uncertainty	CPV Sensitivity		Required Exposure
	$\delta_{\rm CP}$ Fraction	$(\sqrt{\Delta\chi^2})$	
0 (statistical only)	50% $\delta_{\rm CP}$	3 σ	100 kt · MW · year
	50% $\delta_{\rm CP}$	5 σ	400 kt · MW · year
1%/5% (Sig/bkgd)	50% $\delta_{\rm CP}$	3 σ	100 kt · MW · year
	50% $\delta_{\rm CP}$	5 σ	450 kt · MW · year
2%/5% (Sig/bkgd)	50% $\delta_{\rm CP}$	3 σ	120 kt · MW · year
	50% $\delta_{\rm CP}$	5 σ	500 kt · MW · year
5%/10% (no near ν det.)	50% $\delta_{\rm CP}$	3 σ	200 kt · MW · year

certainty assumptions range from 1-2%/5% on signal/background to 5%/10%. The uncertainties listed in Table 4.7 and shown in the sensitivity figures pertain to the ν_e appearance signal and background normalization. In Figure 4.9 the sensitivities obtained from the rate only, shape only and rate+shape of the appearance spectrum are shown for a 10−kt detector with an 80−GeV beam. For CP violation (right), the rate information dominates the sensitivity, but the shape information enables the detector to exceed 3σ sensitivity for large CP violation. For the MH sensitivity, Figure 4.9 (left) demonstrates that the sensitivity in the least favorable range of $\delta_{\rm CP}$ values is dominated by the shape information. Further analysis has shown that it is the region of the second oscillation node that is responsible for this effect. The shape of the signal in this region will enable LBNE to determine the sign of $\delta_{\rm CP}$, which is sufficient to break the degeneracy with MH effects and determine the correct sign of the mass ordering.

Figures 4.11, 4.12, and 4.13 show the variation in sensitivity to CP violation and MH when the true value of the oscillation parameters θ_{13}, θ_{23} and Δm^2_{31} are varied within the 3σ range allowed by the 2012 3ν global fit [54]. These sensitivities are calculated for six years with equal exposures in ν and $\overline{\nu}$ mode in a $1.2-$MW beam for the case in which an upgraded $80-$GeV beam and a near detector have both been implemented.

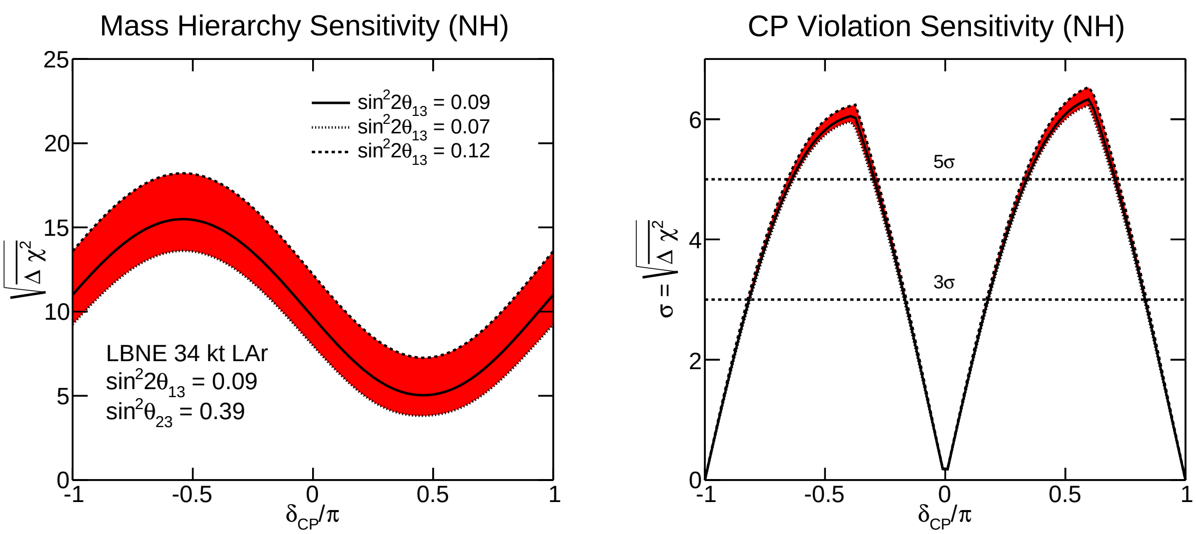

Figure 4.11: The significance with which the mass hierarchy (left) and CP violation, i.e., $\delta_{\rm CP} \neq 0$ or π, (right) can be determined by a typical LBNE experiment as a function of the value of $\delta_{\rm CP}$ for an allowed range of θ_{13} values and for normal hierarchy; assumes a $34-$kt far detector.

In comparing Figures 4.11, 4.12 and 4.13, the dependence on the true value of θ_{23} is particularly striking. As $\sin^2\theta_{23}$ increases, the sensitivity to CP violation decreases because the CP asymmetry that LBNE measures is inversely proportional to $|\sin\theta_{23}|$ as demonstrated in Equation 2.20. For the same reason, as θ_{23} increases, the degeneracy between the CP and matter asymmetries is broken, which increases the LBNE sensitivity to neutrino MH. The explicit dependence of MH sensitivity on the value of $\sin^2\theta_{23}$ is shown in Figure 4.14. As this plot makes clear, LBNE resolves the MH with a significance of $\sqrt{\Delta\chi^2} > 6$ for nearly all allowed values of $sin^2\theta_{23}$ and $\delta_{\rm CP}$.

4.3.3 Summary of CP-Violation and Mass Hierarchy Sensitivities

For the $10-$kt LBNE, the statistical uncertainties are much larger than the systematic uncertainties. Combining the sensitivity from the $10-$kt LBNE with expected knowledge from the NOνA and T2K experiments would allow LBNE to achieve a $\geq 4\sigma$ sensitivity for detecting CP violation for 30% of the allowed values of $\delta_{\rm CP}$ and a $\geq 3\sigma$ sensitivity for 50% of these values. It is clear that

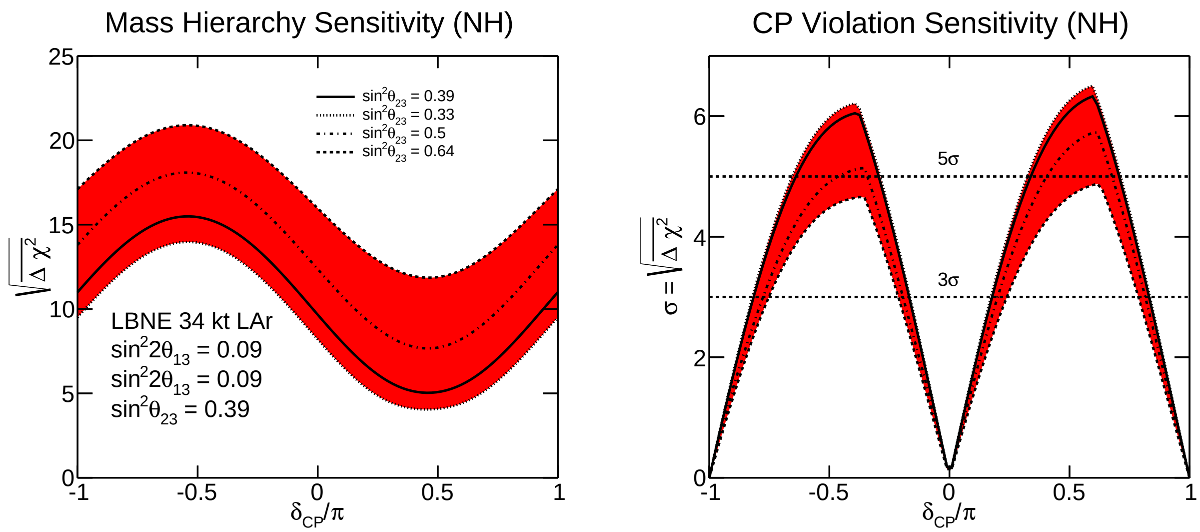

Figure 4.12: The significance with which the mass hierarchy (left) and CP violation, i.e., $\delta_{\rm CP} \neq 0$ or π, (right) can be determined by a typical LBNE experiment as a function of the value of $\delta_{\rm CP}$ for an allowed range of θ_{23} values and for normal hierarchy; assumes a 34−kt far detector.

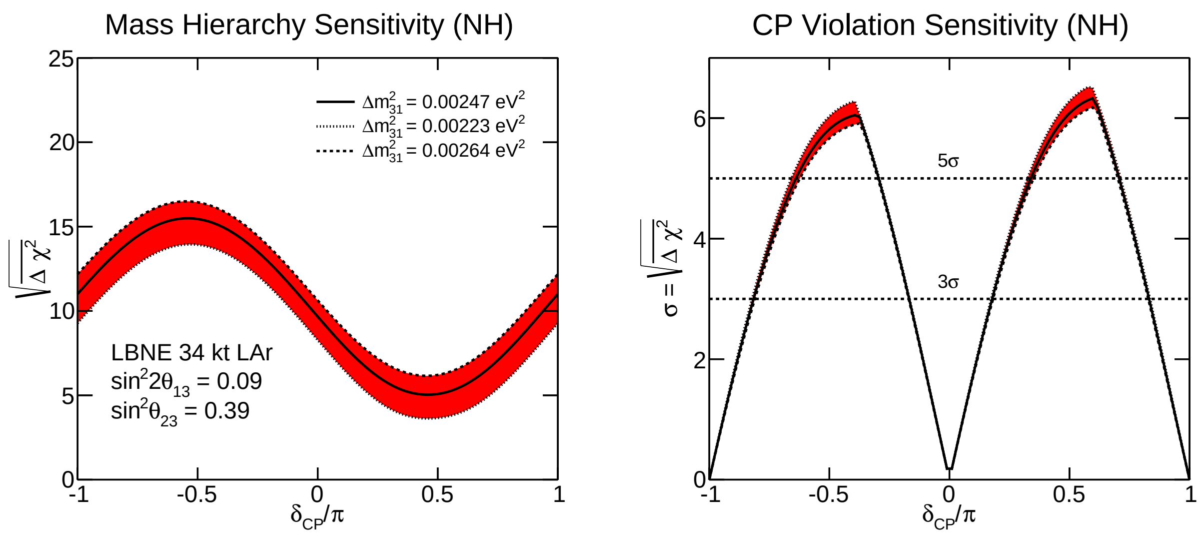

Figure 4.13: The significance with which the mass hierarchy (left) and CP violation, i.e., $\delta_{\rm CP} \neq 0$ or π, (right) can be determined by a typical LBNE experiment as a function of the value of $\delta_{\rm CP}$ for an allowed range of Δm^2_{31} values and for normal hierarchy; assumes a 34−kt far detector.

the 10−kt LBNE sensitivity would be the dominant contribution in the combined sensitivities and would therefore represent a significant advance in the search for leptonic CP violation over the current generation of experiments, particularly in the region where the CP and matter effects are degenerate.

The combination with T2K and NOνA would allow the MH to be determined with a *minimum* precision of $|\overline{\Delta\chi^2}| \geq 25$ over 60% $\delta_{\rm CP}$ values and $|\overline{\Delta\chi^2}| \geq 16$ for all possible values of $\delta_{\rm CP}$. Due to the low event statistics in these experiments, the combination with NOνA and T2K only helps

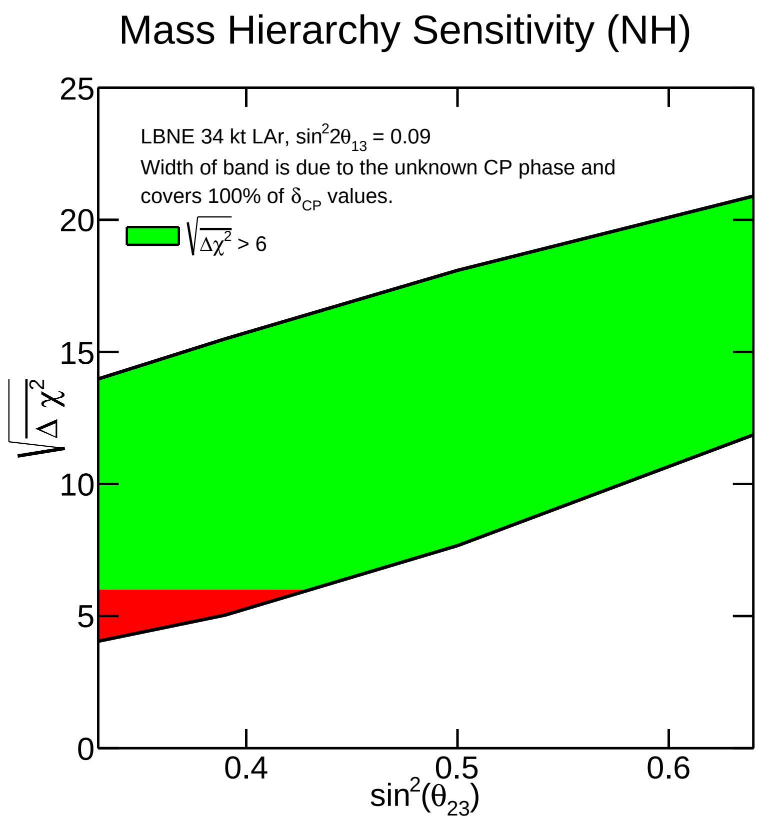

Figure 4.14: The significance with which the MH can be determined by a typical LBNE experiment as a function of the value of $\sin^2\theta_{23}$, for the 3σ allowed range of $\sin^2\theta_{23}$, for true normal hierarchy. The width of the band is due to the unknown value of $\delta_{\rm CP}$ and covers all possible values of $\delta_{\rm CP}$. The green region shows the parameter space for which $\sqrt{\Delta\chi^2} > 6$. Assumes a 34−kt far detector with 6 years of running in a 1.2 MW beam.

the sensitivity in the region of $\delta_{\rm CP} > 0$ (NH) or $\delta_{\rm CP} < 0$ (IH) where there are residual degeneracies between matter and CP-violating effects. As will be discussed in Section 4.6, the combination with atmospheric neutrino oscillation studies can also be used to improve the MH sensitivity in this region for the LBNE 10−kt configuration.

Assuming the normal hierarchy, the most recent global fit of experimental data for the three-neutrino paradigm favors a value of $\delta_{\rm CP}$ close to $-\pi/2$ with $\sin\delta_{\rm CP} < 0$ at a confidence level of $\sim 90\%$ [69] (Figure 4.15). LBNE alone with a 10−kt detector and six years of running would resolve with $\geq 3\sigma$ precision the question of whether CP is violated for the currently favored value of $\delta_{\rm CP}$. With a 34−kt detector running for six years, LBNE, alone will achieve a precision approaching 6σ.

Table 4.8 summarizes the MH and CP sensitivities that can be reached by a typical experiment with the LBNE 10−kt and 34−kt configurations assuming a running time of 3+3 ($\nu + \overline{\nu}$) years with a 1.2−MW beam under a variety of scenarios.

Table 4.8: The mass hierarchy and CP violation sensitivities that can be reached with a typical data set from the LBNE 10−kt and 34−kt configurations with a 1.2 MW beam, no near neutrino detector (ND) unless otherwise stated, and a run time of 3+3 $\nu + \overline{\nu}$ years under a variety of beam and systematic scenarios, for normal hierarchy. Note that the sensitivities for inverted hierarchy are similar but not identical. As discussed in the text, the significance of the MH determination should not be interpreted using Gaussian probabilities.

Scenario ($\sin^2\theta_{23} = 0.39$)	**MH sensitivity**		**CPV sensitivity**	
	$\delta_{\rm CP}$ Fraction	**($\sqrt{\Delta\chi^2}$)**	**$\delta_{\rm CP}$ Fraction**	**($\sqrt{\Delta\chi^2}$)**
LBNE 10 kt, CDR beam	50%	≥ 4	40%	$\geq 2\sigma$
	100%	≥ 2	-	-
LBNE 10 kt, 80−GeV upgraded beam	50%	≥ 5	23%	$\geq 3\sigma$
	100%	≥ 3	55%	$\geq 2\sigma$
LBNE 10 kt, 80−GeV beam, with ν ND	50%	≥ 5	33%	$\geq 3\sigma$
	100%	≥ 3	60%	$\geq 2\sigma$
+ NOνA (6 yrs), T2K (7.8 $\times$ 10^{21} POT)	75%	≥ 5	30%	$\geq 4\sigma$
	100%	≥ 4	50%	$\geq 3\sigma$
LBNE 34 kt , CDR beam	50%	≥ 7	20%	$\geq 4\sigma$
	100%	≥ 4	50%	$\geq 3\sigma$
LBNE 34 kt, 80−GeV upgraded beam	50%	≥ 8	15%	$\geq 5\sigma$
	100%	≥ 5	35%	$\geq 4\sigma$
LBNE 34 kt, 80−GeV beam, with ν ND	50%	≥ 9	35%	$\geq 5\sigma$
	100%	≥ 5	50%	$\geq 4\sigma$

4.3.4 CP-Violating and Mass Hierarchy Sensitivities with Increased Exposures

Figure 4.16 shows the minimum significance with which the MH can be resolved and CP violation determined by LBNE as a function of increased exposure in units of mass $\times$ beam power $\times$ time[§]. For this study, the LBNE beamline improvements discussed in Section 3.4 are used with E_p = 80 GeV, and the signal and background normalization uncertainties are assumed to be 1% and 5%, respectively. Both ν_e and ν_μ appearance signals are used in a combined analysis. Due to the long baseline, the determination of the MH in LBNE to high precision does not require a large exposure; a sensitivity of $\sqrt{\Delta\chi^2} = 5$ for the worst case (NH, $\delta_{\rm CP} = \pi/2$ or IH, $\delta_{\rm CP} = -\pi/2$) requires an exposure of ~ 200 kt $\cdot$ MW $\cdot$ years, but $\sqrt{\Delta\chi^2} = 5$ sensitivity can be reached for 50% of the allowed values of $\delta_{\rm CP}$ with an exposure of less than 100 kt $\cdot$ MW $\cdot$ years. On the other hand, reaching discovery-level sensitivity ($\geq 5\sigma$) to leptonic CP violation for at least 50% of the possible values of $\delta_{\rm CP}$ will require large exposures of ≈ 450 kt $\cdot$ MW $\cdot$ years. Figure 4.17 demonstrates the

[§]Time is denoted in years of running at Fermilab. One year of running at Fermilab corresponds to $\approx 1.7 \times 10^7$ seconds.

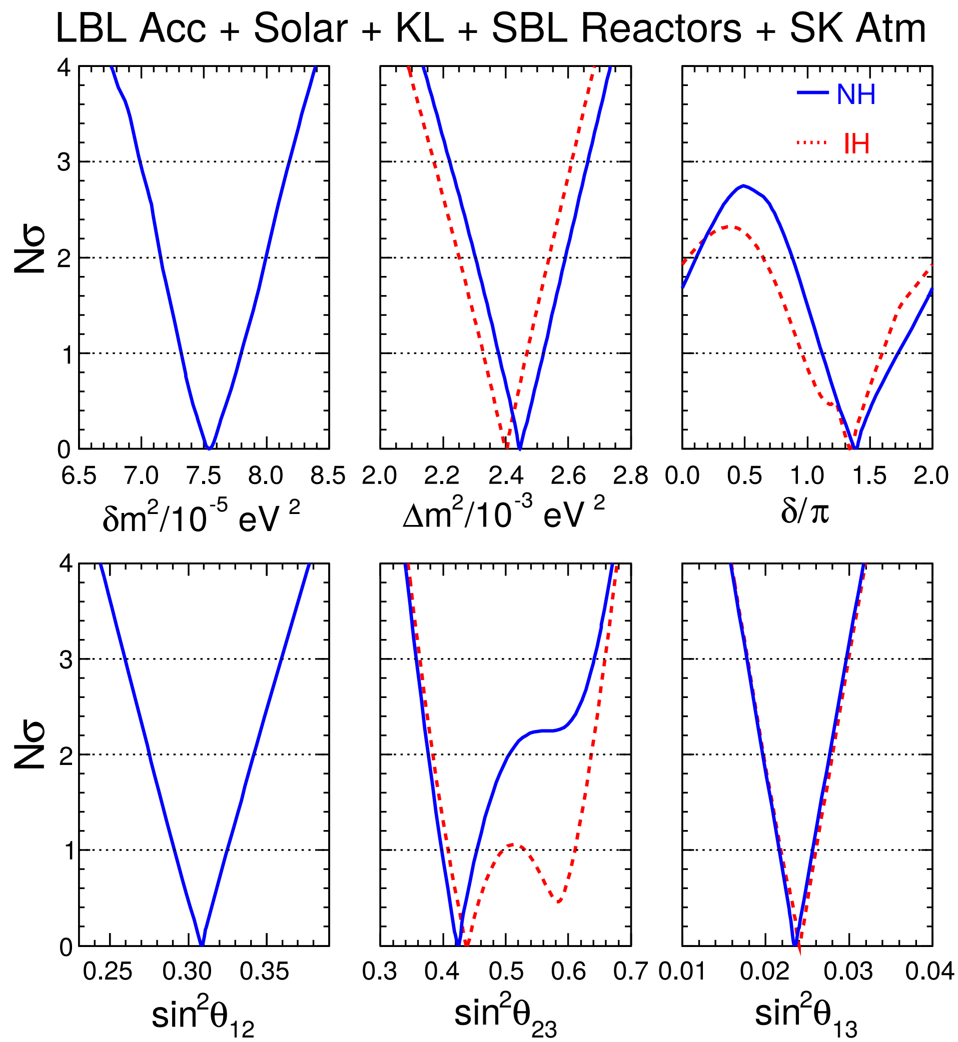

Figure 4.15: Results of the 2013 global analysis from Capozzi *et al.* shown as Nσ bounds on the six parameters governing three ν flavor oscillations. Blue (solid) and red (dashed) curves refer to NH and IH, respectively. Figure is from [69].

sensitivity to CP violation as a function of $\delta_{\rm CP}$ and exposure that can be achieved with various stages of the Fermilab Proton-Improvement-Plan (PIP-II and upgrades to PIP-II). In this study, the PIP-II upgrades are assumed to provide LBNE with 1.2 MW¶ at 80 GeV, followed by further upgrades in which the booster is replaced with a linac that will provide 2.3 MW from the Main Injector (MI), also at 80 GeV. The study demonstrates that it is possible to reach 5σ sensitivity to CP violation over at least 40% of $\delta_{\rm CP}$ values running for a little over 10 years, starting with the PIP-II MI power and a LArTPC greater than 10 kt, and phasing in more detector mass. Other possible staging scenarios of detector mass and beam power are discussed in Chapter 9.

¶The assumed exposures are only accurate to the level of 15% due to incomplete knowledge of the PIP-II final design parameters and running conditions.

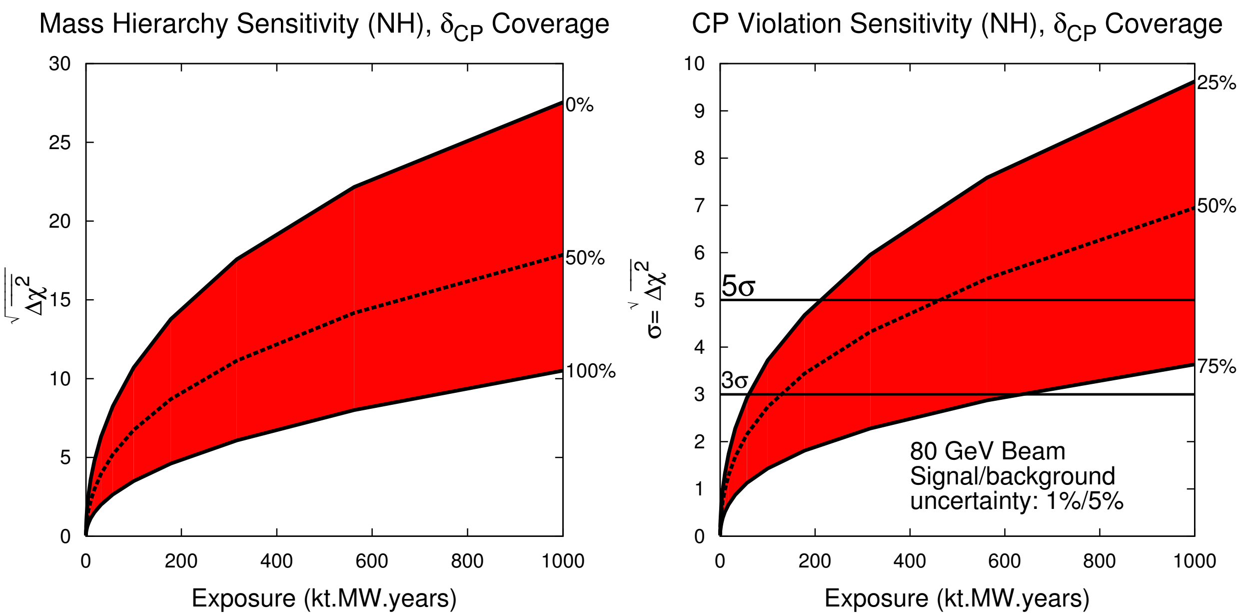

Figure 4.16: The minimum significance with which the mass hierarchy (left) and CP violation (right) can be resolved as a function of exposure in detector mass (kiloton) $\times$ beam power (MW) $\times$ time (years), for true NH. The red band represents the fraction of $\delta_{\rm CP}$ values for which the sensitivity can be achieved with at least the minimal significance on the y-axis.

Table 4.9: The CP violation sensitivities that can be reached by LBNE alone starting with the LBNE 10−kt configuration with a 1.2−MW beam and a run time of 3+3 ($\nu+\overline{\nu}$) years and phasing in additional far detector mass and beam power upgrades beyond the current PIP-II. In all cases, the sensitivities are calculated using the 80 GeV upgraded beam and 1%/5% signal/background normalization uncertainties, for true normal hierarchy. The sensitivity for each stage includes exposure from the previous stage(s) of the experiment.

Exposure	Possible Scenario	CPV sensitivity	
		$\delta_{\rm CP}$ Fraction	$(\sqrt{\Delta\chi^2})$
60 kt · years 1.2 MW beam	PIP-II, 10 kt, 6 years	60% $\delta_{\rm CP}$	$\geq 2\sigma$
		33% $\delta_{\rm CP}$	$\geq 3\sigma$
+ 200 kt · years 1.2 MW beam	PIP-II, 34 kt, 6 years	40% $\delta_{\rm CP}$	$\geq 5\sigma$
+ 200 kt · years 2.3 MW beam	Booster replaced, 34 kt, 6 years	60% $\delta_{\rm CP}$	$\geq 5\sigma$

4.4 Measurement of θ_{23} and Determination of the Octant

The value of $\sin^2 2\theta_{23}$ is measured to be > 0.95 at 90% CL using atmospheric neutrino oscillations [166]. This corresponds to a value of θ_{23} near 45°, but leaves an ambiguity as to whether the value of θ_{23} is in the lower octant (less than 45°), the upper octant (greater than 45°) or exactly 45°. The value of $\sin^2\theta_{23}$ from the 2013 global fit reported by [69] is $\sin^2\theta_{23} = 0.425^{+0.029}_{-0.027}(1\sigma)$ for normal hierarchy (NH), but as shown in Figure 4.15, the distribution of the χ^2 from the global fit has another local minimum — particularly if the MH is inverted — at $\sin^2\theta_{23} \approx 0.59$. A *maximal* mixing value of $\sin^2\theta_{23} = 0.5$ is therefore still allowed by the data and the octant is still largely

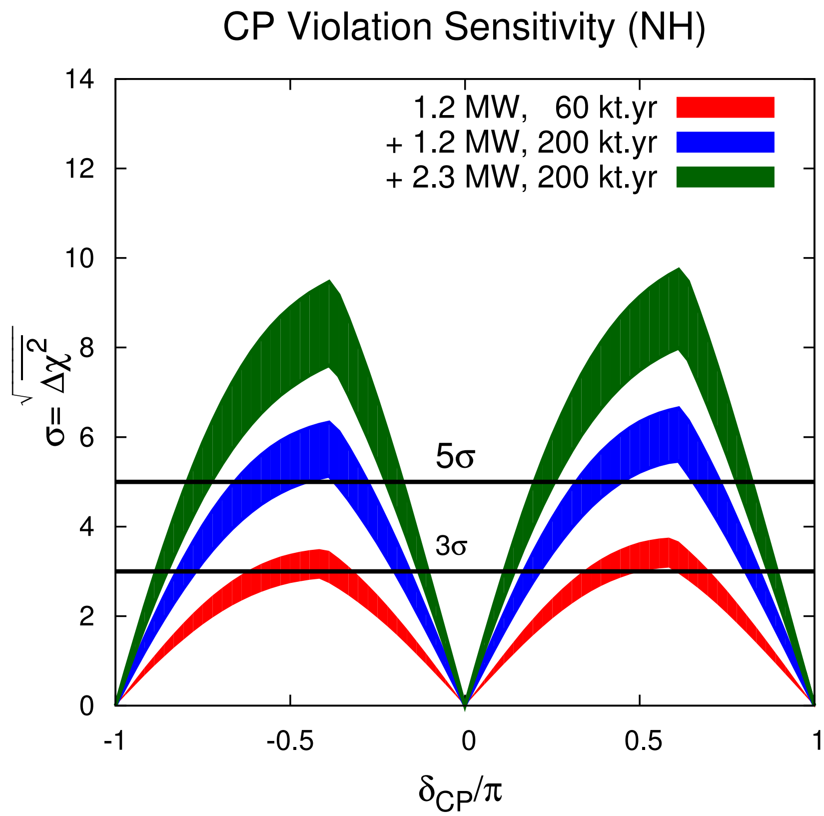

Figure 4.17: The significance with which CP violation — $\delta_{\rm CP} \neq 0$ or π — can be determined as a function of $\delta_{\rm CP}$. The different color curves represent possible exposures from different stages of PIP and detector mass upgrades as follows: 1.2 MW, 60 kt·years (red) + 1.2 MW, 200 kt·years (blue) + 2.3 MW, 200 kt·years (green). The sensitivity for each higher exposure is in addition to that from all lower exposures. The bands represent the range of sensitivities obtained from the improvements to the CDR beamline design.

undetermined. As discussed in Chapter 2, a value of θ_{23} exactly equal to 45° would indicate that ν_μ and ν_τ have equal contributions from ν_3, which could be evidence for a previously unknown symmetry. It is therefore important experimentally to determine the value of $\sin^2\theta_{23}$ with sufficient precision to determine the octant of θ_{23}.

The measurement of $\nu_\mu \to \nu_\mu$ oscillations is sensitive to $\sin^2 2\theta_{23}$, whereas the measurement of $\nu_\mu \to \nu_e$ oscillations is sensitive to $\sin^2\theta_{23}$. A combination of both ν_e appearance and ν_μ disappearance measurements can probe both maximal mixing and the θ_{23} octant. With the large statistics and rich spectral structure in a wide-band, long-baseline experiment such as LBNE (Figure 4.2), precision measurements of $\sin^2\theta_{23}$ can be significantly improved compared to existing experiments, particularly for values of θ_{23} near $45°$. Figure 4.18 demonstrates the measurement precision of θ_{23} and Δm^2_{31} that can be achieved for different true values of these parameters by a 10−kt LBNE detector. The subdominant $\nu_\mu \to \nu_e$ appearance signal in a 10−kt detector is limited by statistical uncertainties.

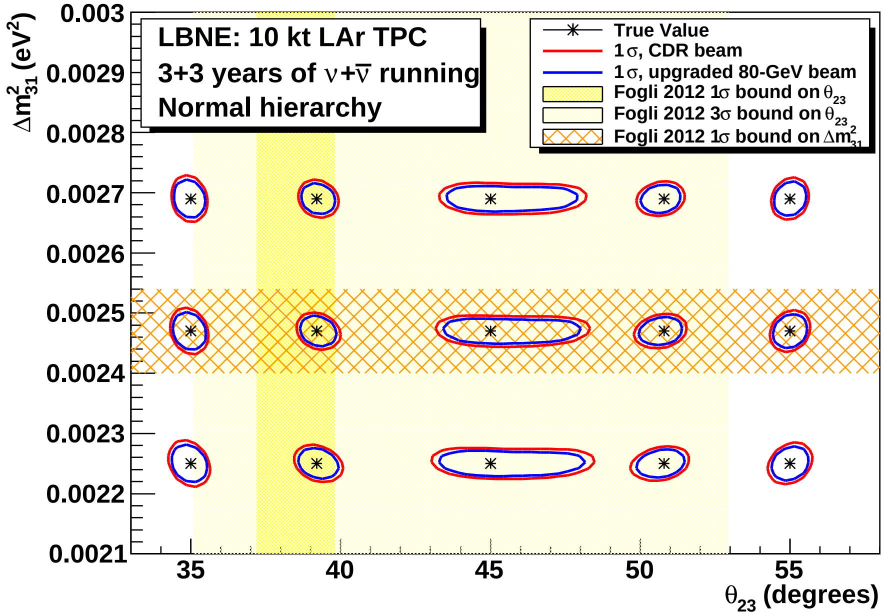

Figure 4.18: The precision with which a simultaneous measurement of θ_{23} and Δm^2_{31} can be determined with 10 kt and 3+3 years of $\nu + \overline{\nu}$ running in a 1.2−MW beam. The yellow bands represent the 1σ and 3σ allowed ranges of θ_{23} and the orange hatched region represents the 1σ allowed range of Δm^2_{31} from [54].

The significance with which a 10−kt LBNE detector can determine the θ_{23} octant is shown in the top plot of Figure 4.19. The $\Delta\chi^2$ metric is defined as:

$$\Delta\chi^2_{octant} \quad = \quad |\chi^2_{\theta_{23}^{test}>45^\circ} - \chi^2_{\theta_{23}^{test}<45^\circ}|, \tag{4.9}$$

where the value of θ_{23} in the *wrong* octant is constrained only to have a value within the *wrong* octant (i.e., it is not required to have the same value of $\sin^2 2\theta_{23}$ as the true value). The individual χ^2 values are given by Equation 4.4. As in the $\Delta\chi^2$ metrics for MH and CP violation, the χ^2 value for the *true* octant is identically zero in the absence of statistical fluctuations. If θ_{23} is within the 1σ bound of the global fit [54], an LBNE 10−kt detector alone will determine the octant with $> 3\sigma$ significance for all values of $\delta_{\rm CP}$. Figure 4.19 (bottom) demonstrates the increasing sensitivity to the θ_{23} octant for values closer to maximal ν_μ-ν_τ mixing that can be achieved with subsequent phases of LBNE coupled with upgrades in beam power from the Main Injector.

With sufficient exposure, LBNE can resolve the θ_{23} octant with $> 3\sigma$ significance even if θ_{23} is within a few degrees of 45°, the value at which the mixing between the ν_μ and ν_τ neutrino states is maximal.

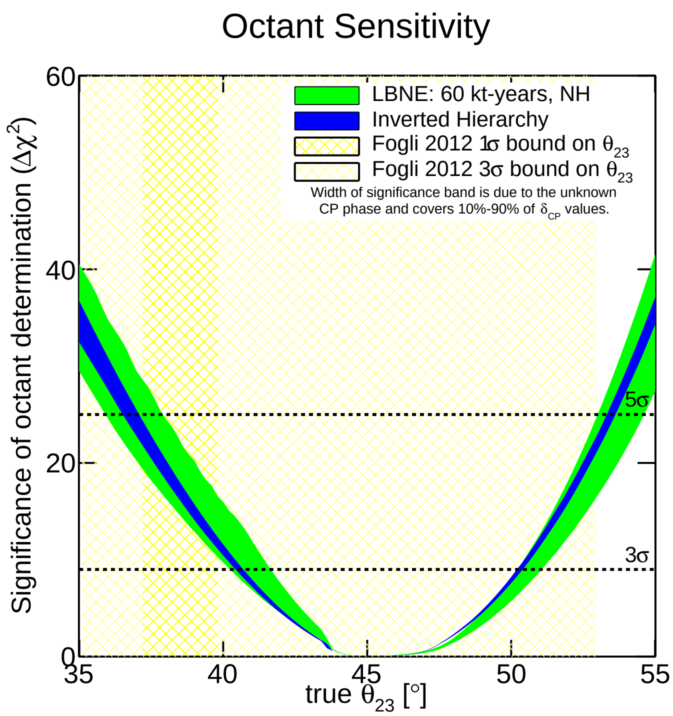

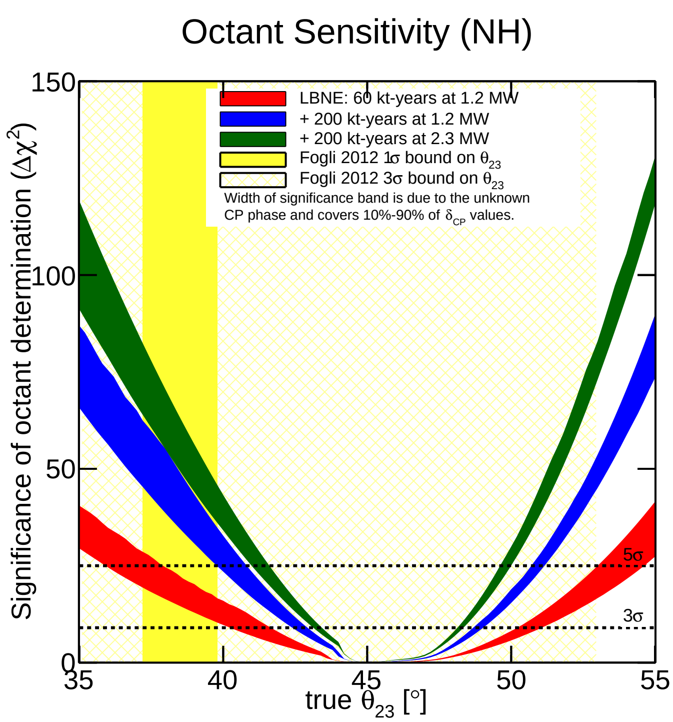

Figure 4.19: Top: significance with which LBNE can resolve the θ_{23} octant degeneracy for 3+3 years of ν+$\overline{\nu}$ running at 1.2 MW with a 10−kt detector. The bands are for normal (green) and inverted (blue) hierarchy. The widths of the bands correspond to the fraction of $\delta_{\rm CP}$ values covered at this significance or higher, ranging from 10% to 90%. The yellow bands represent the 1σ and 3σ allowed ranges of θ_{23} from [54]. Bottom: significance with which LBNE can resolve the θ_{23} octant degeneracy (normal hierarchy) for equal ν+$\overline{\nu}$ running with increased exposure. The colored bands represent increasing exposures as follows: 1.2 MW, 60 kt·year (red) + 1.2 MW, 200 kt·years (blue) + 2.3 MW, 200 kt·years (green). The sensitivity for each higher exposure is in addition to that from all lower exposures.

4.5 Precision Measurements of the Oscillation Parameters in the Three-Flavor Model

The rich oscillation structure that can be observed by LBNE and the excellent particle identification capability of the detector will enable precision measurement in a single experiment of all the mixing parameters governing ν_1-ν_3 and ν_2-ν_3 mixing. As discussed in Chapter 2, theoretical models probing quark-lepton universality predict specific values of the mixing angles and the relations between them. The mixing angle θ_{13} is expected to be measured accurately in reactor experiments by the end of the decade with a precision that will be limited by systematics. The systematic uncertainty on the value of $\sin^2 2\theta_{13}$ from the Daya Bay reactor neutrino experiment, which has the lowest systematics, is currently $\sim 4\%$ [142].

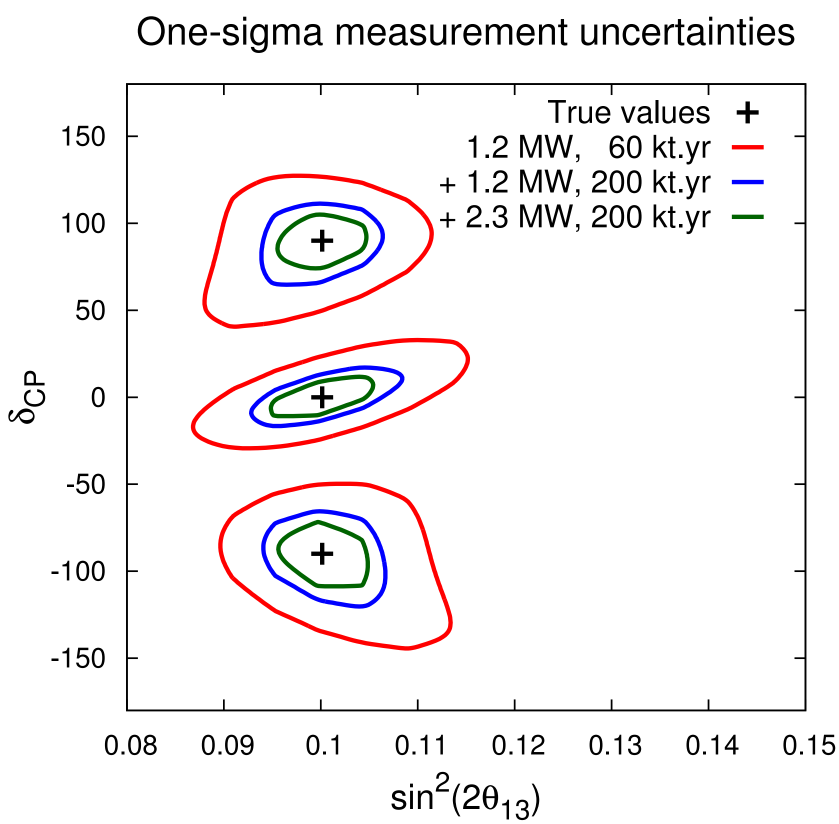

Figure 4.20: Measurement of δ_{CP} and θ_{13} in LBNE with different exposures, for true normal hierarchy (NH). The different color curves represent one-sigma contours for three possible exposures from different stages of PIP and detector mass upgrades as follows: 1.2 MW, 60 kt·year (red), 1.2 MW, 200 kt·years (blue) + 2.3 MW, 200 kt·years (green). The sensitivity for each higher exposure is in addition to that from all lower exposures.

While the constraint on θ_{13} from the reactor experiments will be important in the early stages of LBNE for determining CP violation, measuring δ_{CP} and determining the θ_{23} octant, LBNE itself will eventually be able to measure θ_{13} independently with a precision on par with the final precision expected from the reactor experiments. Whereas the reactor experiments measure θ_{13} using $\overline{\nu}_e$ disappearance, LBNE will measure it through ν_e and $\overline{\nu}_e$ appearance, thus providing an independent constraint on the three-flavor mixing matrix. Figure 4.20 demonstrates the precision with which LBNE can measure $\delta_{\rm CP}$ and θ_{13} simultaneously, with no external constraints on θ_{13}, as a function of increased exposure, for three different exposures. Both appearance and disappearance modes are included in the fit using the upgraded $80-$GeV beam. Signal/background normalization uncertainties of 1%/5% are assumed.

Figure 4.21 shows the expected 1σ resolution on different three-flavor oscillation parameters as a function of exposure in kt $\cdot$ year in a $1.2-$MW beam with LBNE alone and LBNE in combination with the expected performance from T2K and NOνA. It should be noted that LBNE alone could reach a precision on $\sin^2 2\theta_{13}$ of 0.005 with an exposure of $\sim$300 kt $\cdot$ MW $\cdot$ years. LBNE can also significantly improve the resolution on Δm^2_{32} beyond what the combination of NOνA and T2K can achieve, reaching a precision of $1 \times 10^{-5}\,\mathrm{eV}^2$ with an exposure of $\sim$300 kt $\cdot$ MW $\cdot$ years. The precision on Δm^2_{32} will ultimately depend on tight control of energy-scale systematics. Initial studies of the systematics reveal that the measurement of ν_μ disappearance in LBNE over a full oscillation interval, with two oscillation peaks and two valleys (Figure 4.2), reduces the dependency of the Δm^2_{23} measurement on the energy-scale systematics, which limited the measurement precision in MINOS [163].

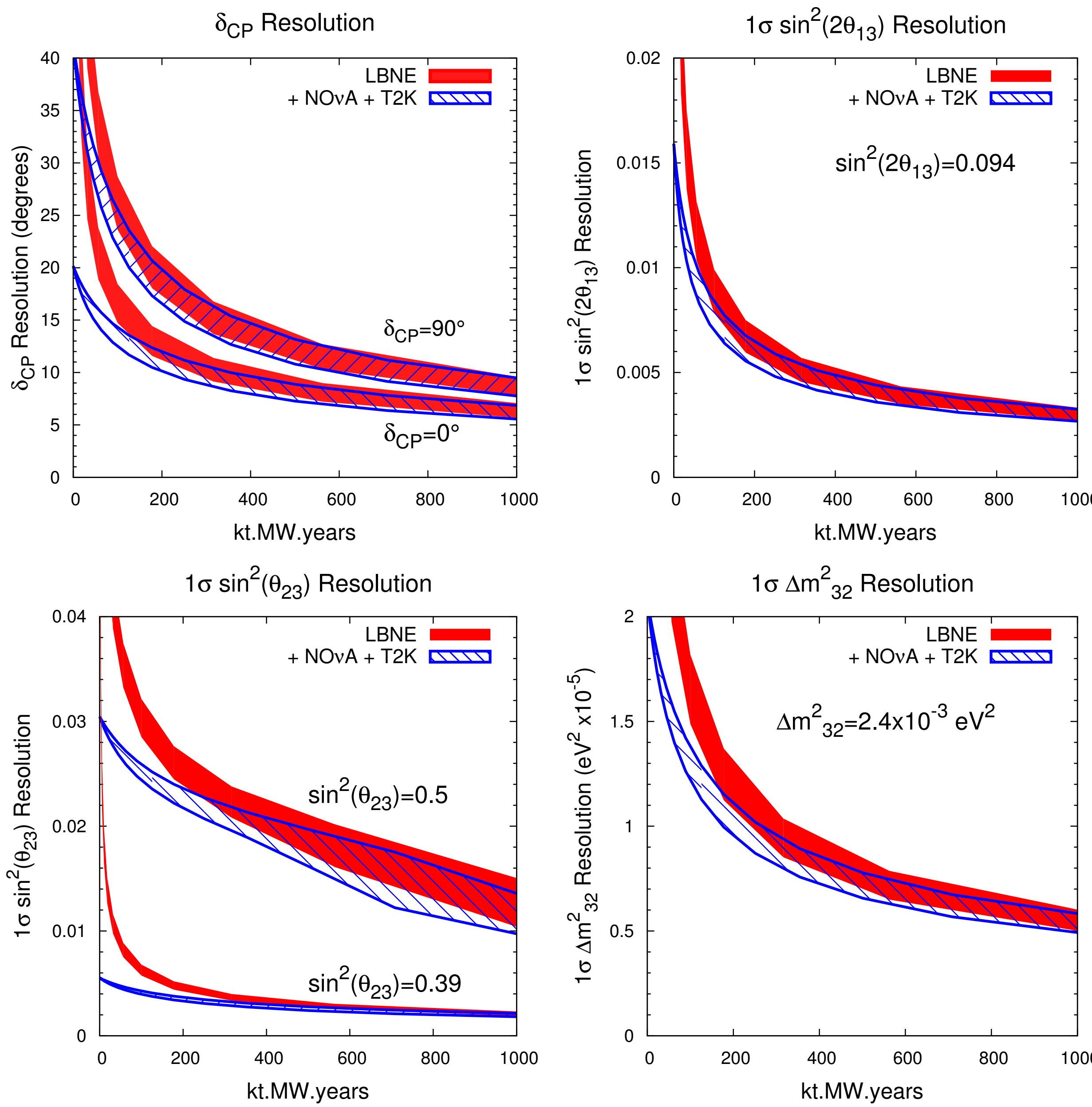

Figure 4.21: The expected 1σ resolution on different three-flavor oscillation parameters as a function of exposure in kt · MW · years, for true NH. The red curve indicates the precision that could be obtained from LBNE alone, and the blue curve represents the combined precision from LBNE and the T2K and NOνA experiments. The width of the bands represents the range of performance with the beam improvements under consideration.

4.6 Oscillation Studies Using Atmospheric Neutrinos

Atmospheric neutrinos are unique among sources used to study oscillations: the flux contains neutrinos and antineutrinos of all flavors, matter effects play a significant role, both Δm^2 values contribute, and the oscillation phenomenology occurs over several orders of magnitude each in energy (Figure 2.8) and path length. These characteristics make atmospheric neutrinos ideal for the study of oscillations (in principle sensitive to all of the remaining unmeasured quantities in the PMNS matrix) and provide a laboratory in which to search for exotic phenomena for which the dependence of the flavor-transition and survival probabilities on energy and path length can be defined. The large LBNE LArTPC far detector, placed at sufficient depth to shield against cosmic-ray background, provides a unique opportunity to study atmospheric neutrino interactions with excellent energy and path-length resolutions.

LBNE has obtained far detector physics sensitivities based on information from atmospheric neutrinos by using a Fast MC and a three-flavor analysis framework developed for the MINOS experiment [167]. Four-vector-level events are generated using the GENIE neutrino event generator [133]. For atmospheric neutrinos the Bartol [168] flux calculation for the Soudan, MN site was used, and for beam neutrinos the 80−GeV, 1.2−MW beamline design described in Section 3.4 was used. In this section, unless otherwise specified, the oscillation parameters are as specified in Table 4.10.

Table 4.10: Oscillation parameters used in the atmospheric-neutrino analysis.

Parameter	Value
$\Delta m^2 = 1/2(\Delta m^2_{32} + \Delta m^2_{31})$ (NH)	$+2.40 \times 10^{-3}$ eV^2
$\sin^2\theta_{23}$	0.40
Δm^2_{21}	7.54×10^{-5} eV^2
$\sin^2\theta_{12}$	0.307
$\sin^2\theta_{13}$	0.0242
δ_{CP}	0

The expected interaction rates in 100 kt · year are shown in Table 4.11. All interactions occur on argon and are distributed uniformly throughout a toy detector geometry consisting of two modules, each 14.0 m high, 23.3 m wide, and 45.4 m long. For this study, events with interaction vertices outside the detector volume (e.g., events that produce upward-going stopping or through-going muons) have not been considered. Cosmogenic background has not been studied in detail, but since atmospheric neutrinos are somewhat more tolerant of background than proton decay, a depth that is sufficient for a proton decay search is expected to also be suitable for studies of atmospheric neutrinos. Given the detector's 4,850−ft depth, a veto should not be necessary and the full fiducial mass of the detector should be usable.

Table 4.11: Expected atmospheric ν interaction rates in a LArTPC with an exposure of 100 kt · years for the Bartol flux and GENIE argon cross sections (no oscillations).

Flavor	CC	NC	Total
ν_μ	10,069	4,240	14,309
$\overline{\nu}_\mu$	2,701	1,895	4,596
ν_e	5,754	2,098	7,852
$\overline{\nu}_e$	1,230	782	2,012
Total:	**19,754**	**9,015**	**28,769**

A Fast MC runs on the produced four-vectors, placing events into containment and flavor categories. Containment is evaluated by tracking leptons through the liquid argon detector box geometry and classifying events as either fully contained (FC) or partially contained (PC). A detection threshold of 50 MeV is assumed for all particles. Flavor determination, in which events are placed into electron-like or muon-like categories, is based on properties of the primary and secondary particles above detection threshold. Electrons are assumed to be correctly identified with 90% probability and other electromagnetic particles (e.g., π^0, γ) are misidentified as electrons 5% of the time. Muons are identified with 100% probability and charged pions are misidentified as muons 1% of the time. Events in which neither of the two leading particles is identified as a muon or electron are placed into an *NC-like* category. With these assumptions, the purities of the flavor-tagged samples are 97.8% for the FC electron-like sample, 99.7% for the FC muon-like sample, and 99.6% for the PC muon-like sample. The NC-like category is not used in this analysis, but would be useful for ν_τ appearance studies. The energy and direction of the event are then assigned by separately smearing these quantities of the leptonic and hadronic systems, where the width of the Gaussian

Table 4.12: Detector performance assumptions for the atmospheric neutrino and the combined atmospheric+beam neutrino analyses.

Particle	Resolution
Angular Resolutions	
Electron	1°
Muon	1°
Hadronic System	10°
Energy Resolutions	
Stopping Muon	3%
Exiting Muon	15%
Electron	$1\%/\sqrt{E(GeV)} \oplus 1\%$
Hadronic System	$30\%/\sqrt{E(GeV)}$

resolution functions for each flavor/containment category are given in Table 4.12. Detector performance assumptions are taken both from the LBNE CDR [29] and from published results from the ICARUS experiment [139,169,170,171]. Including oscillations, the expected number of events in 100 kt · year is summarized in Table 4.13.

Table 4.13: Atmospheric-neutrino event rates including oscillations in 100 kt · year with a LArTPC, fully or partially contained in the detector fiducial volume.

Sample	Event rate
fully contained electron-like sample	4,015
fully contained muon-like sample	5,958
partially contained muon-like sample	1,963

Figure 4.22 shows the expected L/E distribution for *high-resolution* muon-like events from a 350 kt · year exposure; the latest data from Super-Kamiokande are shown for comparison. LBNE defines high-resolution events similarly to Super-Kamiokande, i.e., either by excluding a region of low-energy events or events pointing toward the horizon where the baseline resolution is poor. The data provide excellent resolution of the first two oscillation nodes, even when taking into account the expected statistical uncertainty.

In performing oscillation fits, the data in each flavor/containment category are binned in energy and zenith angle. Figure 4.23 shows the zenith angle distributions for several ranges of reconstructed energy, where oscillation features are clearly evident.

The power to resolve the mass hierarchy (MH) with atmospheric neutrinos comes primarily from the MSW enhancement of few-GeV neutrinos at large zenith angles. This enhancement occurs for neutrinos in the normal hierarchy and antineutrinos in the inverted hierarchy. Figure 4.24 shows zenith angle distributions of events in the relevant energy range for each of the three flavor/containment categories. Small differences are evident in comparing the NH and IH predictions.

Since the resonance peak occurs for neutrinos in the NH and antineutrinos in the IH, the MH sensitivity can be greatly enhanced if neutrino and antineutrino events can be separated. The LBNE detector will not be magnetized; however, its high-resolution imaging offers possibilities for tagging features of events that provide statistical discrimination between neutrinos and antineutrinos. For the sensitivity calculations that follow, two such tags are included: a proton tag and a decay-electron tag. For low-multiplicity events, protons occur preferentially in neutrino interactions; protons are tagged with 100% efficiency if their kinetic energy is greater than 50 MeV. Decay electrons are assumed to be 100% identifiable and are assumed to occur 100% of the time for μ^+ and 25% of the time for μ^-, based on the $\mu^\pm$ capture probability on ^{40}Ar.

In the oscillation analysis, 18 nuisance parameters are included, with detector performance parameters correlated between beam and atmospheric data. In all cases, $\sin^2\theta_{12}$, $\Delta m^2 = 1/2(\Delta m^2_{32} + \Delta m^2_{31})$, and Δm^2_{21} are taken to be fixed at the values given in Table 4.10. The fits then range over

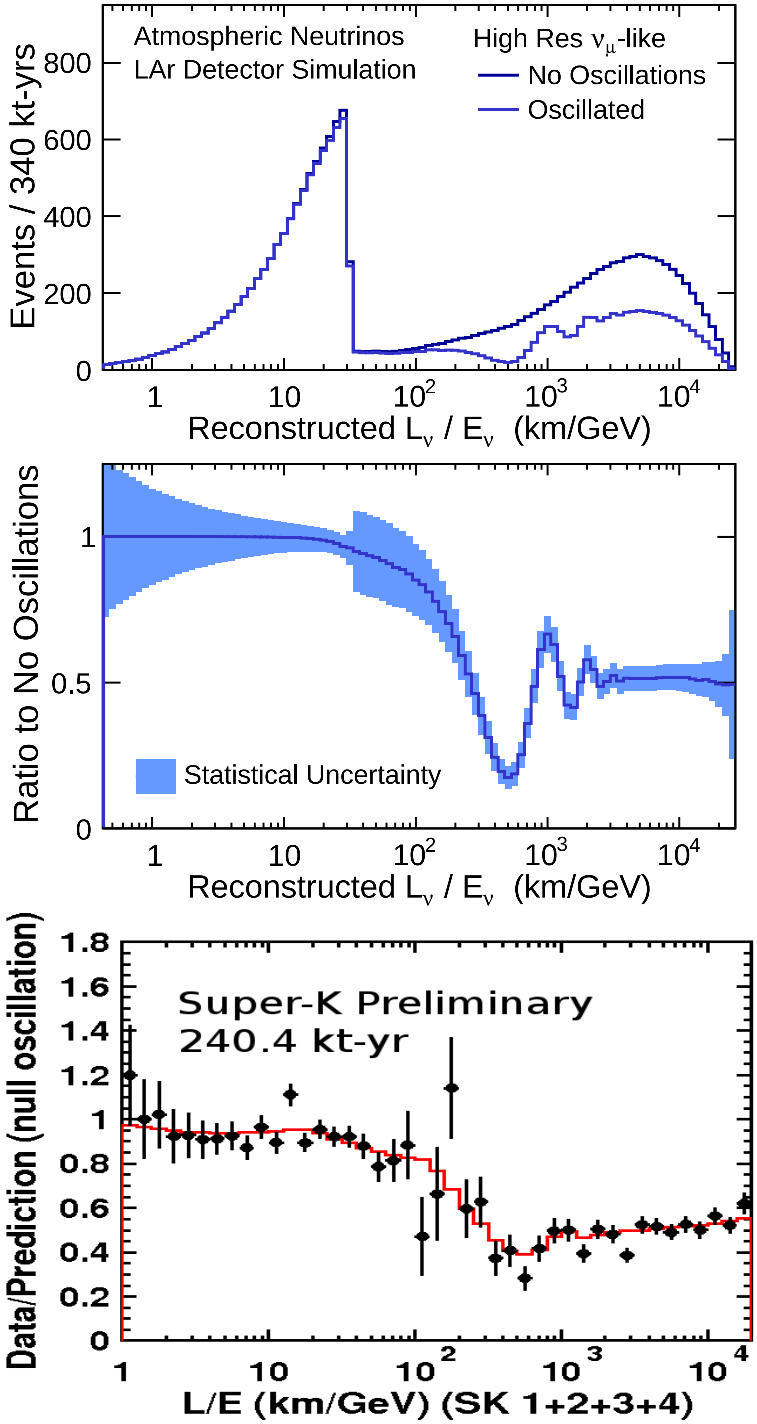

Figure 4.22: Reconstructed L/E distribution of *high-resolution* μ-like atmospheric neutrino events in LBNE with a 340 kt·MW·year exposure with and without oscillations (top); the ratio of the two, with the shaded band indicating the size of the statistical uncertainty (center); the ratio of observed data over the null oscillation prediction from the Super-Kamiokande detector with 240.4 kt · years of exposure (bottom).

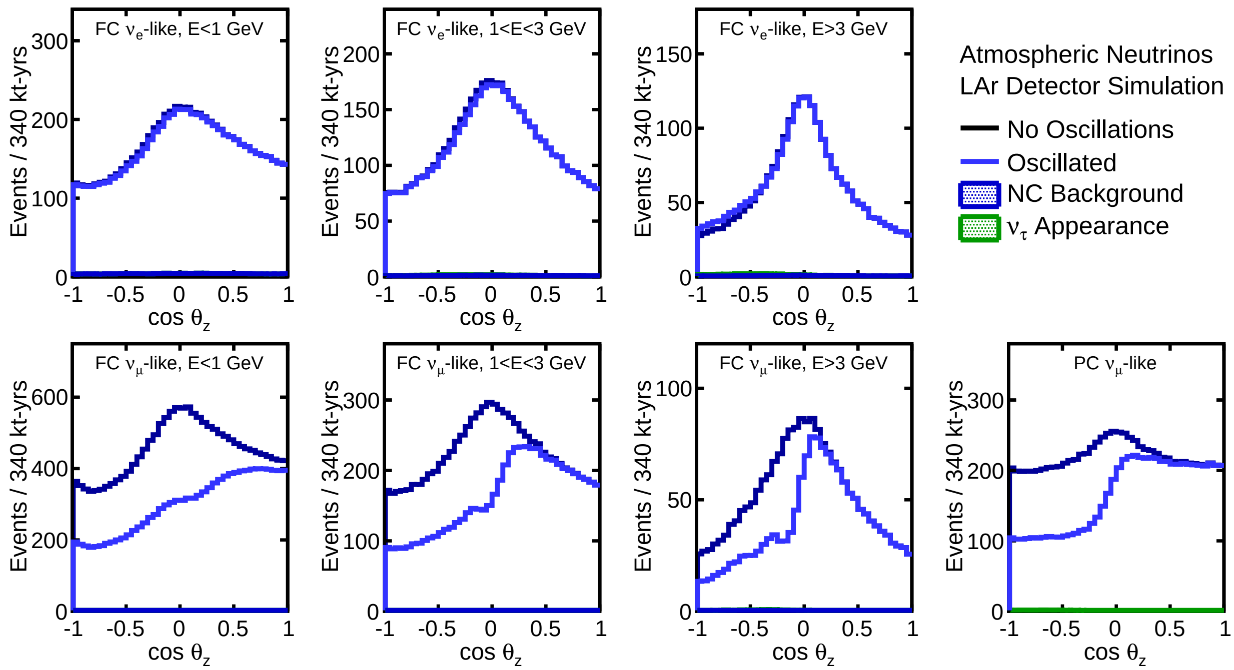

Figure 4.23: Reconstructed zenith angle distributions in several ranges of energy for the FC e-like, FC μ-like, and PC μ-like samples. The small contributions from NC background and ν_τ are also shown.

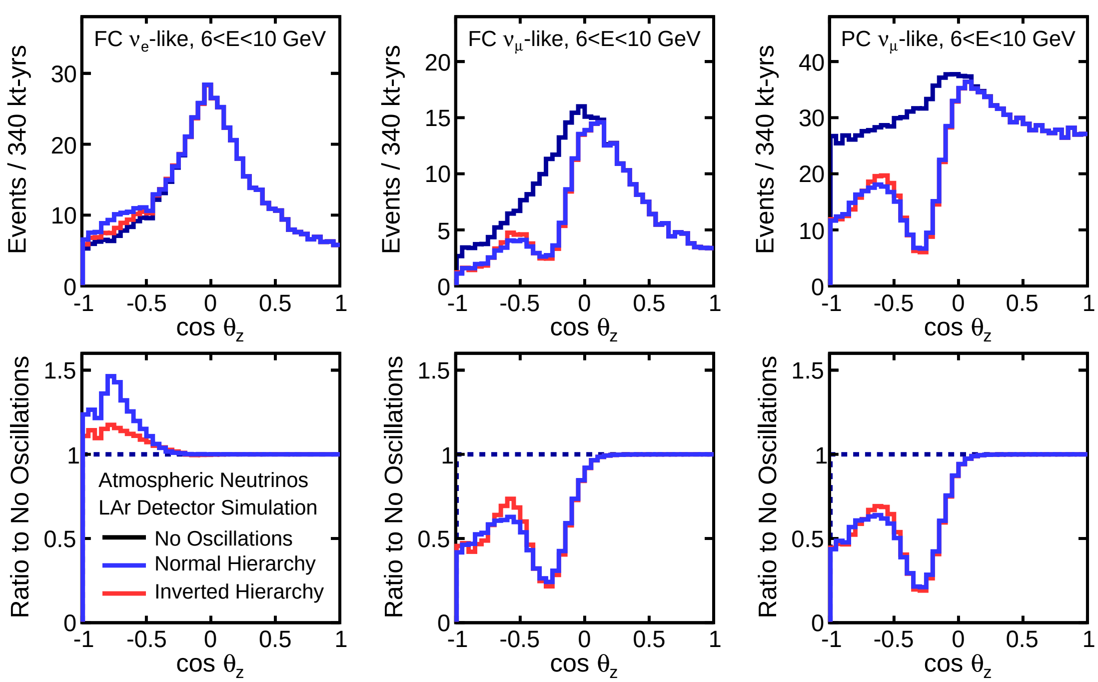

Figure 4.24: Reconstructed zenith angle distributions for 6 to 10−GeV events in the different FC and PC samples. Top plots show the expected distributions for no oscillations (black), oscillations with normal (blue), and inverted (red) hierarchy. Bottom plots show the ratio of the normal and inverted expectations to the no-oscillation distributions for each category.

θ_{23}, θ_{13}, δ_{CP}, and the MH. A 2% constraint is assumed on the value of θ_{13}; this value is chosen to reflect the expected ultimate precision of the current generation of reactor-neutrino experiments. The systematic errors included in this analysis are given in Table 4.14.

Table 4.14: Systematic errors included in the atmospheric and beam+atmospheric neutrino analysis. The beam values assume the existence of a near detector (ND). Atmospheric spectrum ratios include the combined effect of flux and detector uncertainties (e.g., the up/down flux uncertainty as well as the uncertainty on the detector performance for the up/down ratio). The atmospheric spectrum shape uncertainty functions are applied separately for $\nu_\mu, \nu_e, \overline{\nu}_\mu, \overline{\nu}_e$.

	Atmospheric	Beam (Assumes ND)
Normalization	Overall (15%)	μ-like (5%) e-like (1%)
NC Background	e-like (10%)	μ-like (10%) e-like (5%)
Spectrum Ratios	up/down (2%) ν_e/ν_μ (2%) $\overline{\nu}_\mu/\nu_\mu$ (5%) $\overline{\nu}_e/\nu_e$ (5%)	
Spectrum Shape	$f(E < E_0) = 1 + \alpha(E - E_0)/E_0$ $f(E > E_0) = 1 + \alpha \log(E/E_0)$ where σ_α=5%	
Energy Scales (Correlated)	Muons (stopping 1%, exiting 5%) Electrons (1%) Hadronic System (5%)	

For the determination of the MH, the $\overline{\Delta\chi^2}$ value is calculated between the best-fit points in the NH and IH where, at each, the nuisance parameters have been marginalized. The sensitivity in the plots that follow is given as $\sqrt{\overline{\Delta\chi^2}}$. Figure 4.25 shows the MH sensitivity from a 340-kt $\cdot$ year exposure of atmospheric neutrino data alone. For all values of the MH and δ_{CP}, the MH can be determined at $\sqrt{\overline{\Delta\chi^2}} > 3$. The resolution depends significantly on the true value of θ_{23}; the sensitivity for three θ_{23} values is shown. The sensitivity depends relatively weakly on the true hierarchy and the true value of δ_{CP}. This is in sharp contrast to the MH sensitivity of the beam, which has a strong dependence on the true value of δ_{CP}. Figure 4.26 shows the MH sensitivity as a function of the fiducial exposure. Over this range of fiducial exposures, the sensitivity goes essentially as the square root of the exposure, indicating that the measurement is not systematics-limited. Figure 4.27 shows the octant and CPV sensitivity from a 340-kt $\cdot$ year exposure of atmospheric neutrino data alone. For the determination of the octant of θ_{23}, the $\overline{\Delta\chi^2}$ value is calculated between the best-fit points in the lower ($\theta_{23} < 45°$) and higher ($\theta_{23} > 45°$) octants, where at each, the nuisance parameters have been marginalized. The discontinuities in the slopes of the octant sensitivity plot are real features, indicating points at which the best fit moves from one hierarchy to the other. For the detection of CP violation, the $\overline{\Delta\chi^2}$ exclusion is similarly computed for $\delta_{\mathrm{CP}} = (0, \pi)$.

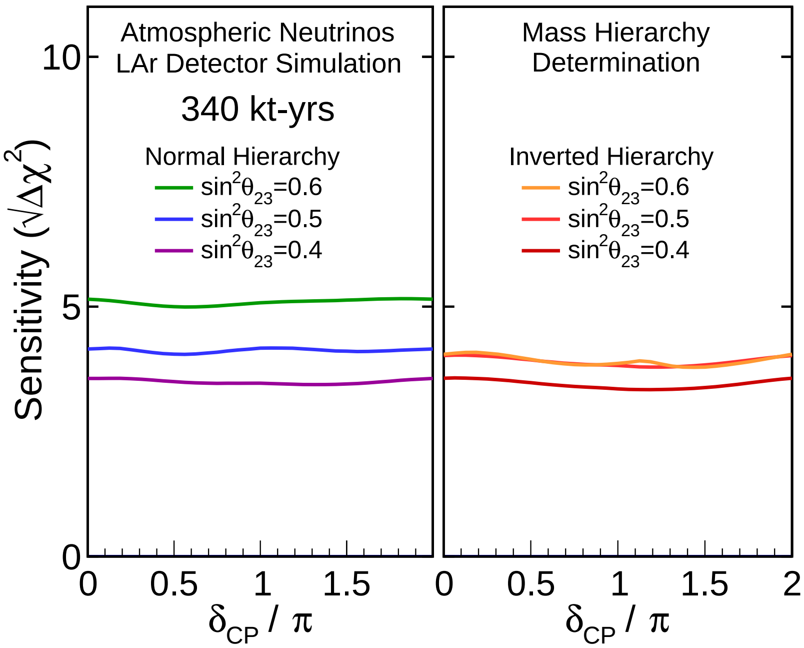

Figure 4.25: Sensitivity of 340 kt · years of atmospheric neutrino data to MH as a function of $\delta_{\rm CP}$ for true normal (left) and inverted (right) hierarchy and different assumed values of $\sin^2\theta_{23}$.

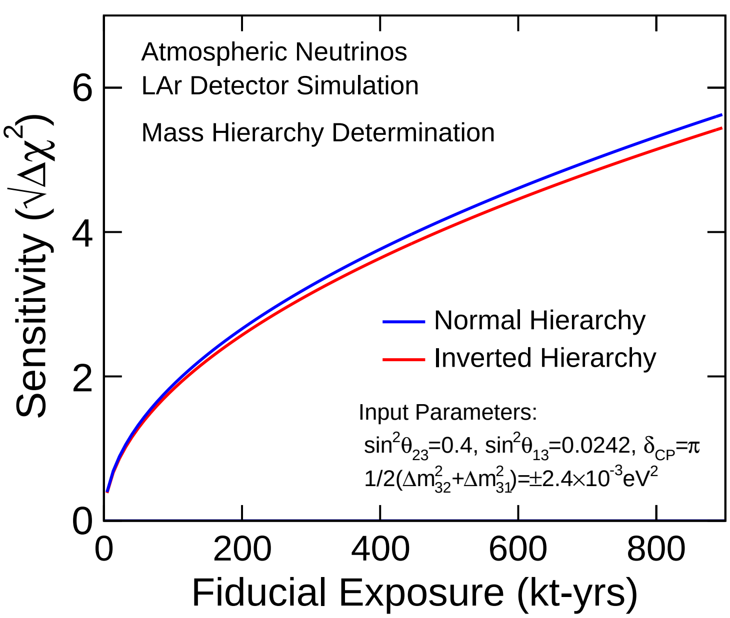

Figure 4.26: Sensitivity to mass hierarchy using atmospheric neutrinos as a function of fiducial exposure in a liquid argon detector.

Figure 4.28 shows the combined sensitivity to beam and atmospheric neutrinos for determination of the MH. This assumes a 10-year run with equal amounts of neutrino and antineutrino running in a 1.2−MW beam.

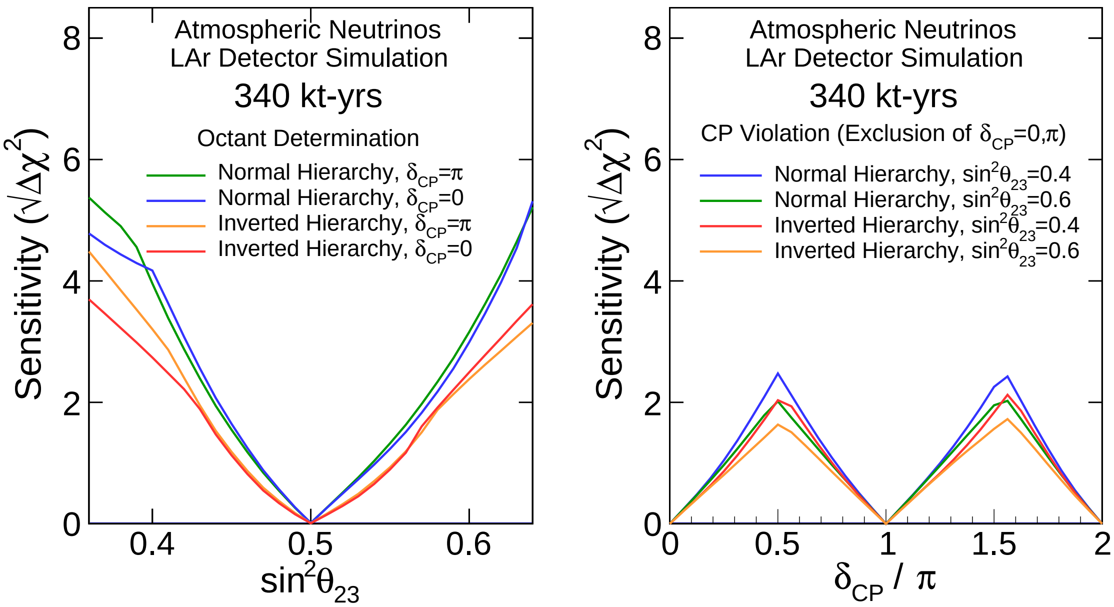

Figure 4.27: Sensitivity to θ_{23} octant (left) and CPV (right) using atmospheric neutrinos.

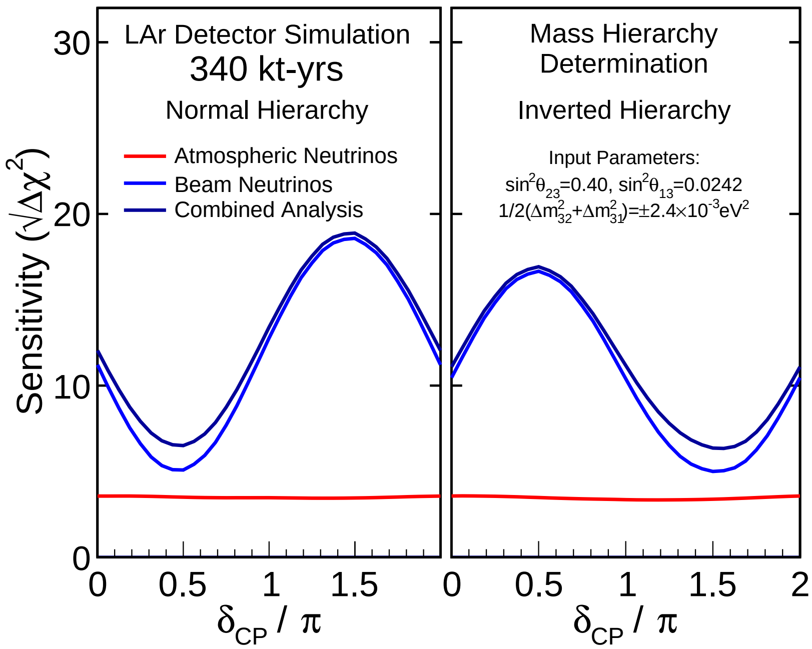

Figure 4.28: Sensitivity to mass hierarchy using atmospheric neutrinos combined with beam neutrinos with an exposure of 340 kt · year in a 1.2−MW beam for normal (left) and inverted (right) hierarchy.

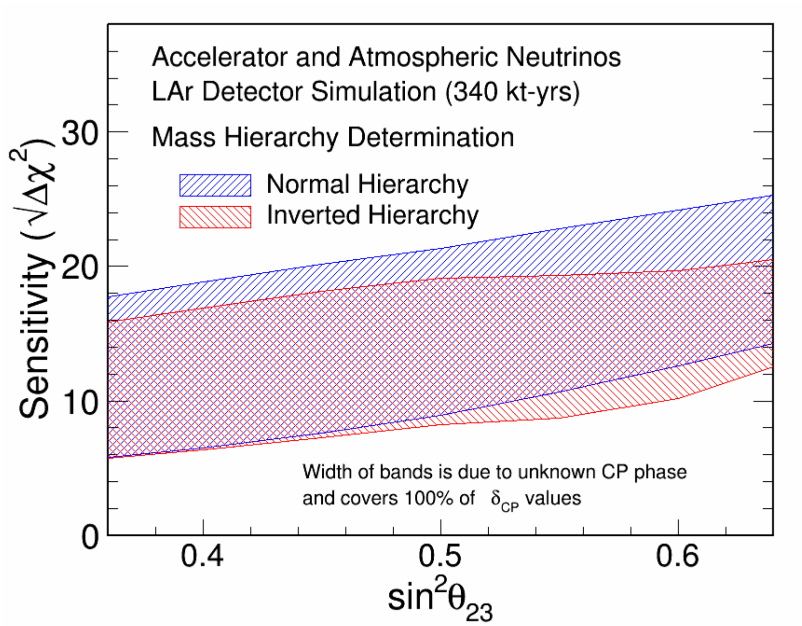

Figure 4.29: Sensitivity to mass hierarchy using atmospheric neutrinos combined with beam neutrinos as a function of the true value of $\sin^2\theta_{23}$, for true normal (blue) and inverted (red) hierarchy. The width of the band is due to the unknown value of $\delta_{\rm CP}$ and covers all possible values of $\delta_{\rm CP}$. Assumes an exposure of 340 kt · year in a 1.2−MW beam.

In the region of $\delta_{\rm CP}$ where the LBNE neutrino-beam-only analysis is least sensitive to the mass hierarchy, atmospheric neutrinos measured in the same experiment offer comparable sensitivity. The combined beam and atmospheric neutrino sensitivity to the mass hierarchy is $|\sqrt{\Delta\chi^2}| > 6$ for all values of $\delta_{\rm CP}$ ($\sin^2\theta_{23} = 0.4$) in a 34−kt detector, assuming a 1.2−MW beam running for ten years. It is important to note that the combined sensitivity is better than the sum of the separate $\Delta\chi^2$ values, as the atmospheric data help to remove degeneracies in the beam data.

Figure 4.29 shows the combined sensitivity to beam and atmospheric neutrinos for determination of MH as a function of the true value of $\sin^2\theta_{23}$, for the same 340-kt · year exposure in a 1.2−MW beam. This can be compared to Figure 4.14 in Section 4.3.3, which shows the same sensitivity using only beam neutrinos.

Figure 4.30 shows the combined sensitivity to beam and atmospheric neutrinos for the θ_{23} octant determination and CPV. The role played by atmospheric data in resolving beam-neutrino degeneracies is also clear from considering the combined and beam-only sensitivities in these plots.

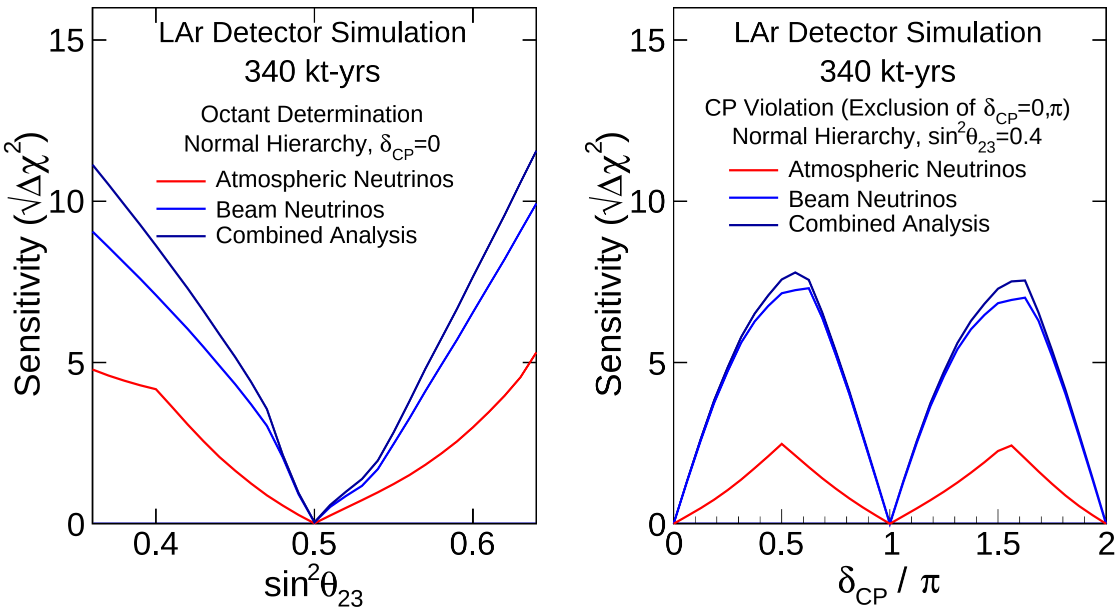

Figure 4.30: Sensitivity to θ_{23} octant (left) and CPV (right) using atmospheric neutrinos combined with beam neutrinos with an exposure of 340 kt · year in a 1.2−MW beam.

4.7 Searches for Physics Beyond the Standard Three-Flavor Neutrino Oscillation Model

Due to the very small masses and large mixing of neutrinos, their oscillations over a long distance act as an exquisitely precise interferometer with high sensitivity to very small perturbations caused by new physics phenomena, such as:

- nonstandard interactions in matter that manifest in long-baseline oscillations as deviations from the three-flavor mixing model
- new long-distance potentials arising from discrete symmetries that manifest as small perturbations on neutrino and antineutrino oscillations over a long baseline
- sterile neutrino states that mix with the three known active neutrino states
- large compactified extra dimensions from String Theory models that manifest through mixing between the Kaluza-Klein states and the three active neutrino states

Full exploitation of LBNE's sensitivity to such new phenomena will require higher-precision predictions of the unoscillated neutrino flux at the far detector and large exposures.

This section explores the potential of the full-scope LBNE design to pursue physics beyond the three-flavor neutrino oscillation model.

4.7.1 Search for Nonstandard Interactions

Neutral current (NC) nonstandard interactions (NSI) can be understood as nonstandard matter effects that are visible only in a far detector at a sufficiently long baseline. They can be parameterized as new contributions to the MSW matrix in the neutrino-propagation Hamiltonian:

$$H = U \begin{pmatrix} 0 & & \\ & \Delta m^2_{21}/2E & \\ & & \Delta m^2_{31}/2E \end{pmatrix} U^\dagger + \tilde{V}_{\mathrm{MSW}} \, , \tag{4.10}$$

with

$$\tilde{V}_{\mathrm{MSW}} = \sqrt{2} G_F N_e \begin{pmatrix} 1 + \epsilon^m_{ee} & \epsilon^m_{e\mu} & \epsilon^m_{e\tau} \\ \epsilon^{m*}_{e\mu} & \epsilon^m_{\mu\mu} & \epsilon^m_{\mu\tau} \\ \epsilon^{m*}_{e\tau} & \epsilon^{m*}_{\mu\tau} & \epsilon^m_{\tau\tau} \end{pmatrix} \tag{4.11}$$

Here, U is the leptonic mixing matrix, and the ϵ-parameters give the magnitude of the NSI relative to standard weak interactions. For new physics scales of a few hundred GeV, a value of $|\epsilon| \lesssim 0.01$ is expected [172,173,174]. LBNE's 1,300−km baseline provides an advantage in the detection of NSI relative to existing beam-based experiments with shorter baselines. Only atmospheric-neutrino experiments have longer baselines, but the sensitivity of these experiments to NSI is limited by systematic effects.

To assess the sensitivity of LBNE to NC NSI, the NSI discovery reach is defined in the following way: the expected event spectra are simulated using GLoBeS, assuming *true* values for the NSI parameters, and a fit is then attempted assuming no NSI. If the fit is incompatible with the simulated data at a given confidence level, the chosen *true* values of the NSI parameters are considered to be within the experimental discovery reach. In Figure 4.31, the NSI discovery reach of LBNE is shown; only one of the $\epsilon^m_{\alpha\beta}$ parameters at a time is taken to be non-negligible.

4.7.2 Search for Long-Range Interactions

The small scale of neutrino-mass differences implies that minute differences in the interactions of neutrinos and antineutrinos with currently unknown particles or forces may be detected through perturbations to the time evolution of the flavor eigenstates. The longer the experimental baseline, the higher the sensitivity to a new long-distance potential acting on neutrinos. For example, some of the models for such long-range interactions (LRI) as described in [175] (Figure 4.32) could contain discrete symmetries that stabilize the proton and give rise to a dark-matter candidate particle, thus providing new connections between neutrino, proton decay and dark matter experiments. The

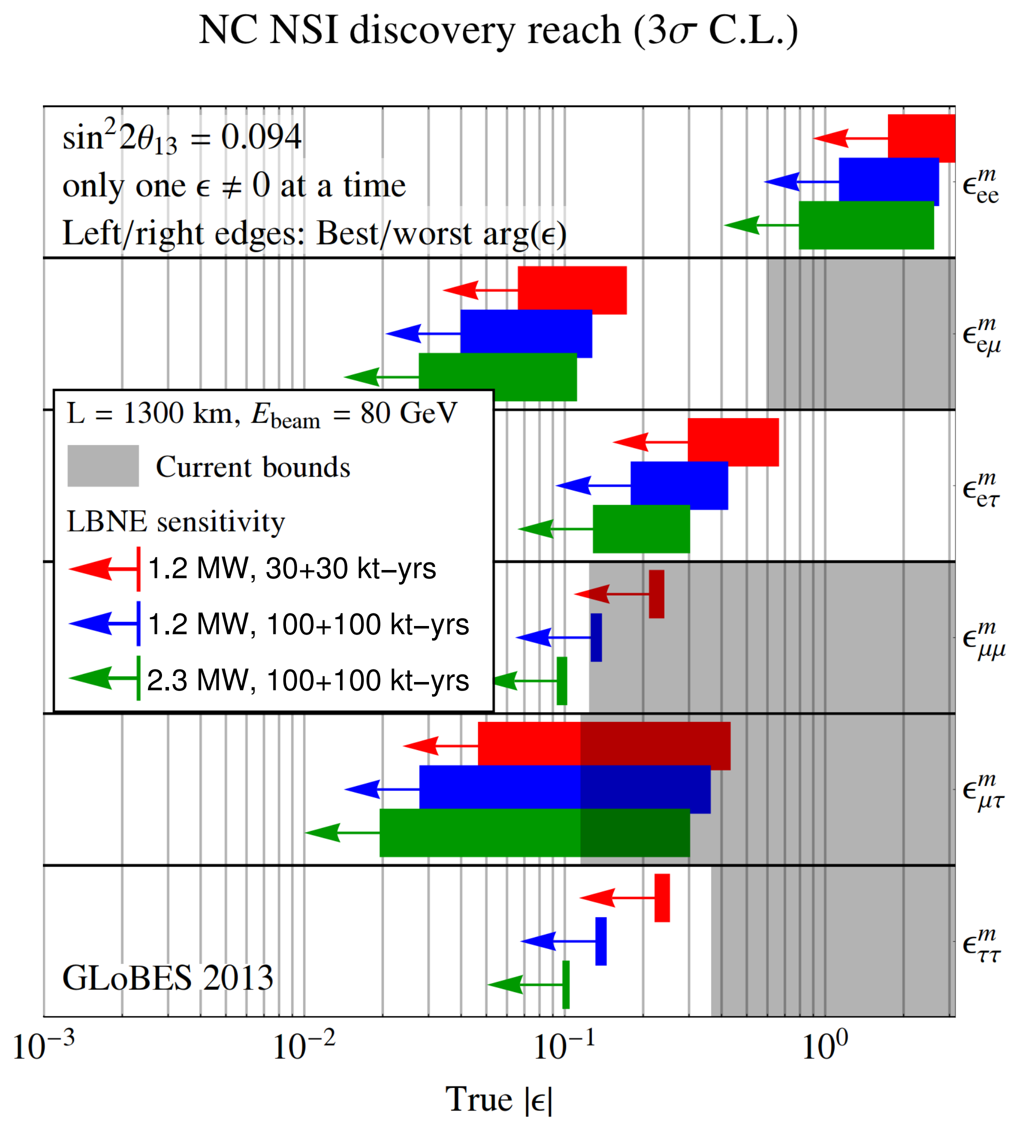

Figure 4.31: Nonstandard interaction discovery reach in LBNE with increasing exposure: 1.2 MW, 60 kt·years (red) + 1.2 MW, 200 kt · year (blue) + 2.3 MW, 200 kt · year (green). The left and right edges of the error bars correspond to the most favorable and the most unfavorable values for the complex phase of the respective NSI parameters. The gray shaded regions indicate the current model-independent limits on the different parameters at 3σ [172,173]. For this study the value of $\sin^2 2\theta_{13}$ was assumed to be 0.09. Figure courtesy of Joachim Kopp.

longer baseline of LBNE improves the sensitivity to LRI beyond that possible with the current generation of long-baseline neutrino experiments. The sensitivity will be determined by the amount of $\nu_\mu/\overline{\nu}_\mu$-CC statistics accumulated and the accuracy with which the unoscillated and oscillated ν_μ spectra can be determined.

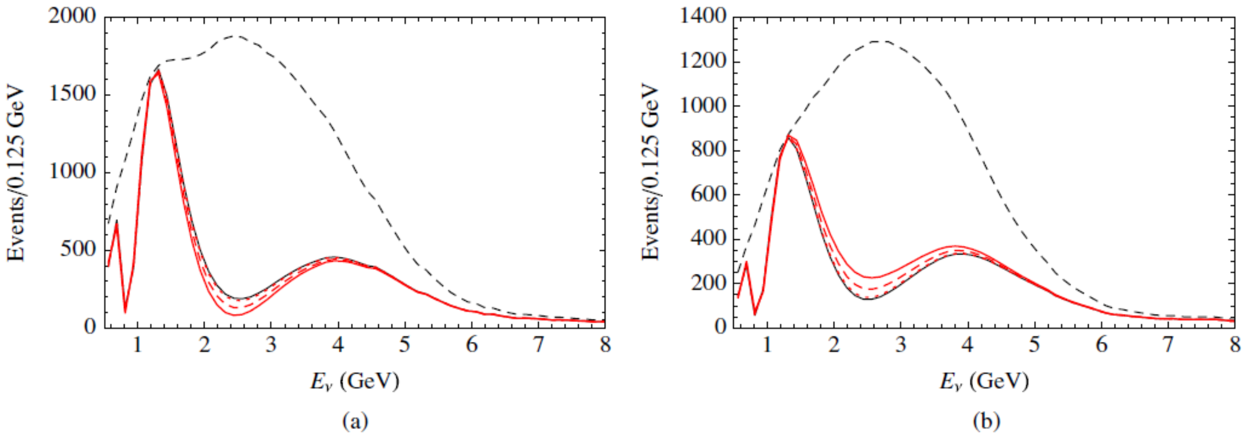

Figure 4.32: Long-range interactions in LBNE. The number of (a) neutrino and (b) antineutrino events versus E_ν, in a long-baseline experiment with a 1,300−km baseline. The unoscillated case (top black dashed curves) and the case of no new physics (thin black solid curves) are displayed, as well as the cases with $\alpha' = (1.0, 0.5, \text{and } 0.1) \times 10^{-52}$, corresponding to red solid, dashed, and dotted curves, respectively. α' is the *fine structure constant* of such interactions, which is constrained to be $\alpha' \leq 10^{-47}$ [175].

4.7.3 Search for Mixing between Active and Sterile Neutrinos

Searches for evidence of active-sterile neutrino mixing at LBNE can be conducted by examining the NC event rate at the far detector and comparing it to a precise estimate of the expected rate extrapolated from ν_μ flux measurements from the near detector and from beam and detector simulations. Observed deficits in the NC rate could be evidence for mixing between the active neutrino states and unknown sterile neutrino states. The most recent such search in a long-baseline experiment was conducted by the MINOS experiment [176].

LBNE will provide a unique opportunity to revisit this search with higher precision over a large range of neutrino energies and a longer baseline. The expected rate of NC interactions with visible energy $>$ 0.5 GeV in a 10−kt detector over three years is approximately 2,000 events (Table 4.1) in the low-energy beam tune and 3,000 events in the medium-energy beam tune. The NC identification efficiency is high, with a low rate of ν_μ-CC background misidentification as shown in Table 4.2. The high-resolution LArTPC far detector will enable a coarse measurement of the incoming neutrino energy in a NC interaction by using the event topology and correcting for the missing energy of the invisible neutrino. This will greatly improve the sensitivity of LBNE to active-sterile mixing as compared to current long-baseline experiments such as MINOS+ since both the energy spectrum and the rate of NC interactions can be measured at both near and far detectors. Studies are currently underway to quantify LBNE's sensitivity to active-sterile mixing.

4.7.4 Search for Large Extra Dimensions

Several theoretical models propose that right-handed neutrinos propagate in large compactified extra dimensions, whereas the standard left-handed neutrinos are confined to the four-dimensional brane [177]. Mixing between the right-handed *Kaluza-Klein* modes and the standard neutrinos would change the mixing patterns predicted by the three-flavor model. The effects could manifest, for example, as distortions in the disappearance spectrum of ν_μ. The rich oscillation structure visible in LBNE, measured with its high-resolution detector using both beam and atmospheric oscillations, could provide further opportunities to probe for this type of new physics. Studies are underway to understand the limits that LBNE could impose relative to current limits and those expected from other experiments.

4.8 Comparison of LBNE Sensitivities to other Proposed Experiments

With tight control of systematics, LBNE will reach 5σ sensitivity to CP violation for a large fraction of $\delta_{\rm CP}$ values. LBNE delivers the best resolution of the value of $\delta_{\rm CP}$ with the lowest combination of power-on-target and far detector mass when compared to other future proposed neutrino oscillation experiments (Figure 4.33).

In Figure 4.33, the CP-violation sensitivity of LBNE is compared to that of other proposed neutrino oscillation experiments from an *independent study* with updated LBNE input based on [178]. The dashed black curve labeled “2020” is the expected sensitivity from the current generation of experiments that could be achieved by 2020. “LBNE-Full” represents a 34−kt LArTPC running in a 1.2−MW beam for 3 (ν) +3 ($\overline{\nu}$) years. “LBNE-PX” is LBNE staged with PIP-II and further upgraded beams with power up to 2.0 MW as shown in Figure 4.17. “T2HK” is a 560−kt (fiducial mass) water Cherenkov detector running in a 1.66−MW beam for 1.5 (ν) + 3.5 ($\overline{\nu}$) years [179]. “LBNO$_{100}$” is a 100−kt LArTPC at a baseline of 2,300 km running in a 0.8−MW beam from CERN for 5 (ν) + 5 ($\overline{\nu}$) years [180]. “IDS-NF” is the Neutrino Factory with a neutrino beam generated from muon decays in a 10−GeV muon storage ring produced from a 4−MW, 8−GeV Project X proton beam coupled with 100−kt magnetized iron detectors at a baseline of 2,000 km for 10 ($\nu + \overline{\nu}$) simultaneously) [181]. LBNE can reach 5σ sensitivity to CP violation for a large fraction of $\delta_{\rm CP}$ values with the lowest combination of power-on-target and far detector mass when compared to current and future proposed neutrino oscillation experiments.

Alone, LBNE can potentially reach a precision on $\delta_{\rm CP}$ between roughly 6° and 10°, i.e., close to the 4° CKM precision on $\delta_{\rm CP}^{\rm CKM}$ — but an exposure of $\sim$700 kt · MW · years is needed. Nevertheless, as shown in Figure 4.34, wide-band, long-baseline experiments such as LBNE (and LBNO) can

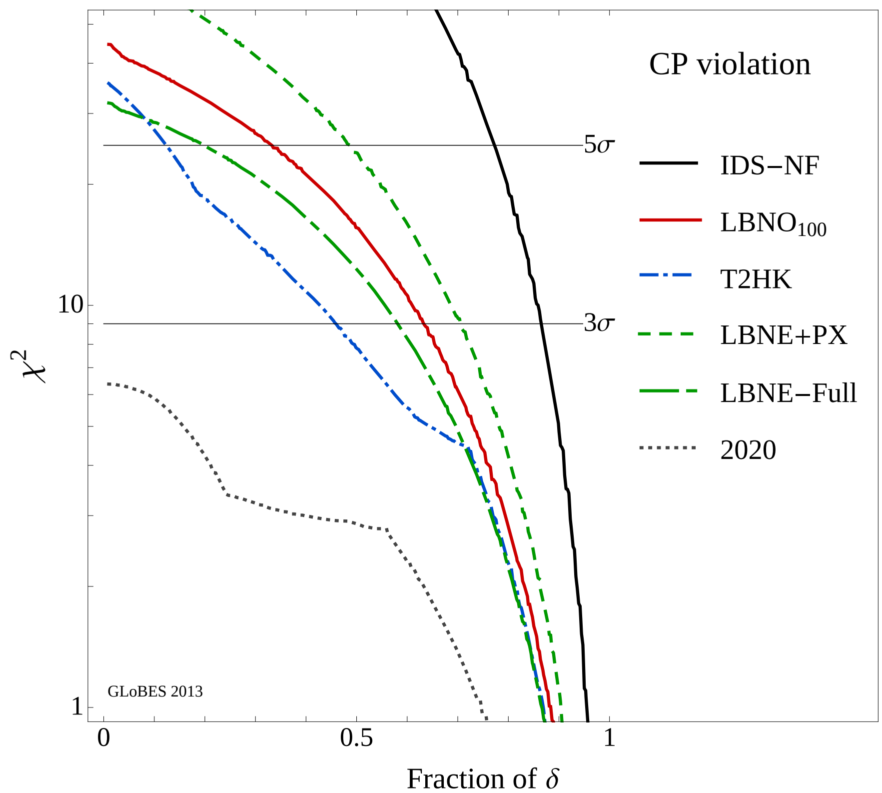

Figure 4.33: The minimal CP-violation sensitivity for a given fraction of $\delta_{\rm CP}$ values for different proposed neutrino oscillation experiments. The exposure and baseline of each experiment is described in the text. Figure is based on the studies detailed in [178].

achieve nearly CKM precision on $\delta_{\rm CP}$ with much less exposure than is required for existing experiments such as NOνA, T2K and proposed short-baseline, off-axis experiments such as T2HK. With the exception of the NuMAX sensitivity, which is taken from [182], the resolutions in the colored bands in Figure 4.34 are calculated independently by LBNE using GLoBES and found to be in good agreement with the values reported by the experiments themselves (T2HK [183], NOνA [38], LBNO [184]).

It is important to note that the precision on $\delta_{\rm CP}$ in the off-axis experiments shown in Figure 4.34 assumes the mass hierarchy (MH) is resolved. If the MH is unknown, the resolution of T2K, NOνA and T2HK will be much poorer than indicated. LBNE does not require external information on the MH to reach the precisions described in this section. Only a neutrino factory can possibly outperform a wide-band, long-baseline experiment — but not by much — for equivalent power, target mass and years of running. To achieve this precision, however, LBNE will need to tightly control the systematic uncertainties on the ν_e appearance signal. Its high-resolution near detector will enable it to reach this level of precision, as described in Section 3.5.

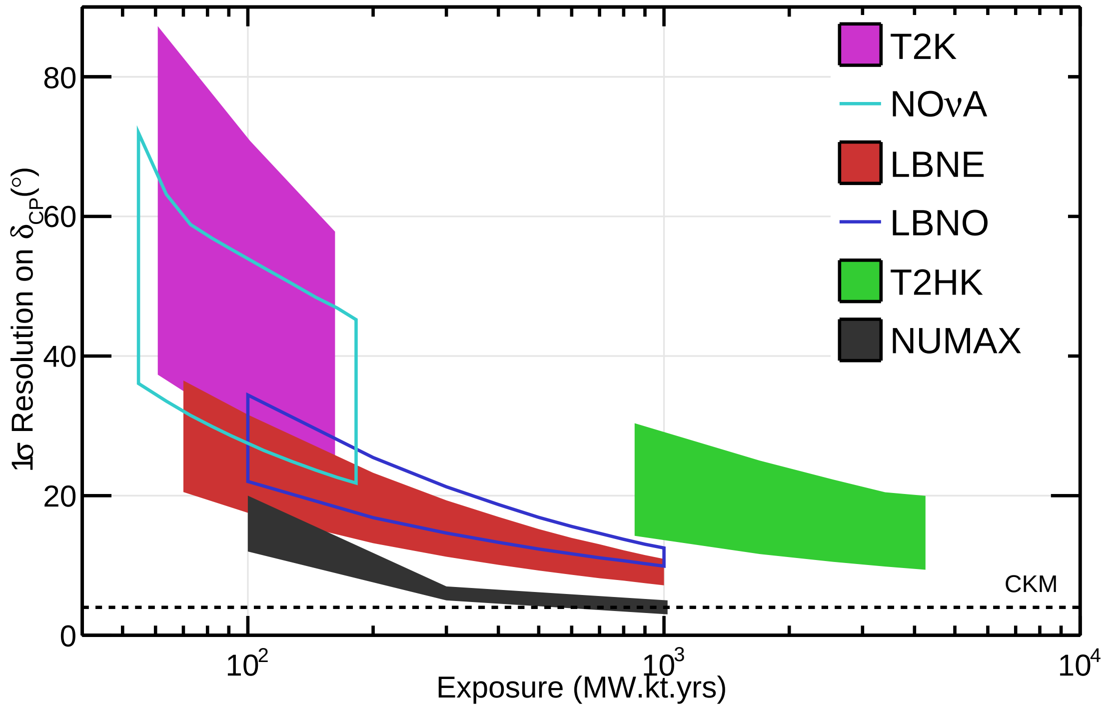

Figure 4.34: The 1σ resolution on $\delta_{\rm CP}$ that can be achieved by existing and proposed beamline neutrino oscillation experiments as a function of exposure in terms of mass $\times$ beam power $\times$ years of running. The band represents the variation in the resolution as a function of $\delta_{\rm CP}$ with the lower edge representing the best resolution and the upper edge the worst. The bands start and stop at particular milestones. For example, the LBNE band starts with the resolutions achieved by the 10−kt LBNE and ends with the full-scope LBNE running with the 2.3−MW upgrades beyond PIP-II. With the exception of the NuMAX sensitivity, which is taken from [182], the resolutions in the colored bands are calculated independently by LBNE using GLoBES. The dashed line denotes the 4° resolution point which is the resolution of $\delta_{\rm CP}^{\rm CKM}$ from the 2011 global fits.

An independent study comparing LBNE's sensitivity to the mass ordering to that of current and future proposed experiments highlights its potential [151]. The study uses frequentist methods of hypothesis testing to define sensitivities. The validity of the approach is tested using toy MC simulations of the various experiments. The comparison of expected MH sensitivities for a variety of current and proposed experiments using different approaches with reasonable estimates as to the start time of the different experiments is summarized in Figure 4.35.

Future upgrades to the Fermilab accelerator complex — in particular the prospect of high-power, low-energy proton beams such as the 3−MW, 8−GeV beam originally proposed as Stage 4 of Project X — could open up further unique opportunities for LBNE to probe CP violation using on-axis, low-energy beams specifically directed at the second oscillation maximum where CP effects dominate the asymmetries [185]. Such high-power, low-energy beams could even enable studies in ν_1-ν_2 mixing in very long-baseline experiments.

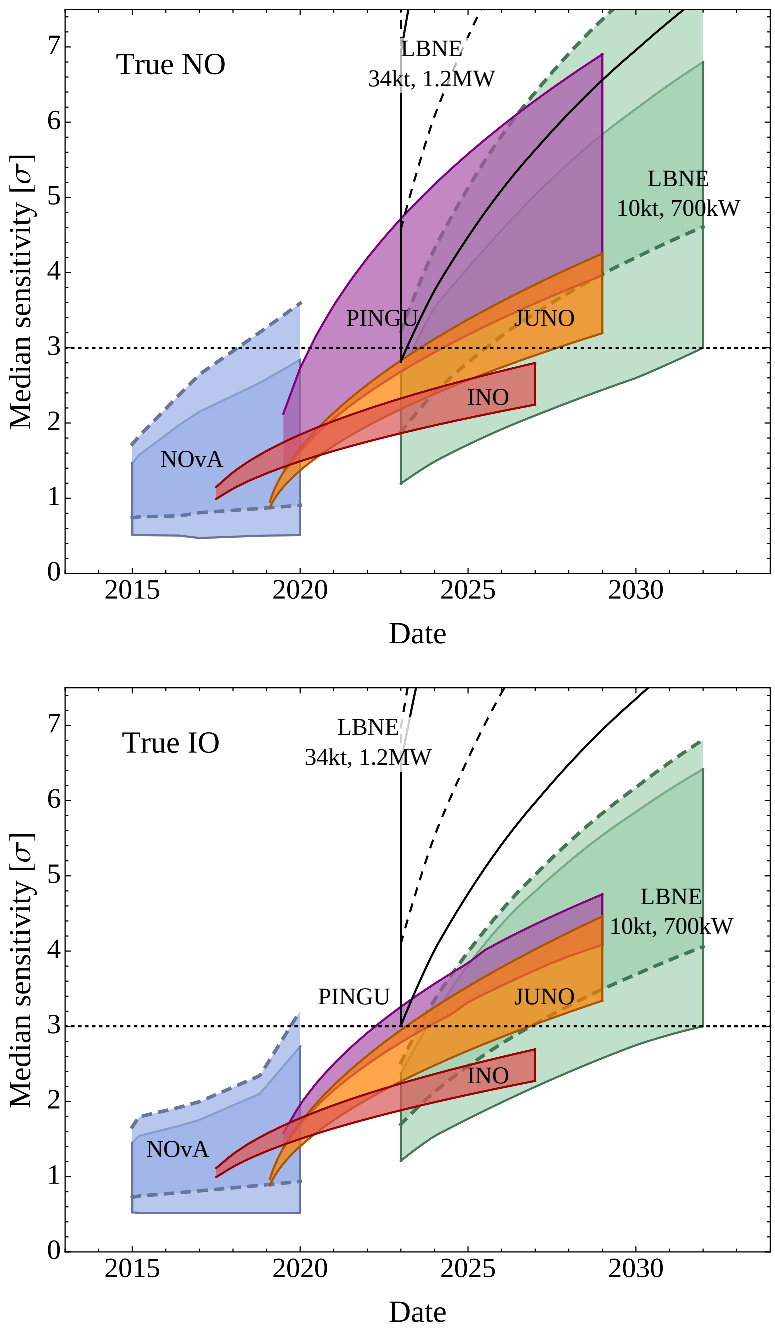

Figure 4.35: The top (bottom) figure shows the median sensitivity in number of sigmas for rejecting the inverted (normal) hierarchy if the normal (inverted) hierarchy is true for different facilities as a function of the date. The width of the bands corresponds to different true values of the CP phase δ_{CP} for NOνA and LBNE, different true values of θ_{23} between 40° and 50° for INO and PINGU, and energy resolution between $3\%/\sqrt{E\ (\mathrm{MeV})}$ and $3.5\%/\sqrt{E\ (\mathrm{MeV})}$ for JUNO. For the long-baseline experiments, the bands with solid (dashed) contours correspond to a true value for θ_{23} of 40° (50°). In all cases, octant degeneracies are fully considered. This figure is from the analysis presented in [151], however, for the plots shown here, the beam power for the full-scope, 34−kt LBNE has been changed to 1.2 MW to reflect the Fermilab PIP-II upgrade plan.

Chapter 5 Nucleon Decay Motivated by Grand Unified Theories

Baryon number conservation is an unexplained symmetry in the Universe with deep connections to both cosmology and particle physics. As one of the conditions underlying the observed matter-antimatter asymmetry of the Universe, baryon number *should* be violated. Nucleon decay, which is a manifestation of baryon number violation, is a hallmark of many Grand Unified Theories (GUTs), theories that connect quarks and leptons in ways not envisioned by the Standard Model. Observation of proton or bound-neutron decay would provide a clear experimental signature of baryon number violation.

Predicted rates for nucleon decay based on GUTs are uncertain but cover a range directly accessible with the next generation of large underground detectors. LBNE, configured with its massive, deep-underground LArTPC far detector, offers unique opportunities for the discovery of nucleon decay, with sensitivity to key decay channels an order of magnitude beyond that of the current generation of experiments.

5.1 LBNE and the Current Experimental Context

Current limits on nucleon decay via numerous channels are dominated by Super–Kamiokande (SK) [186], for which the most recently reported preliminary results are based on an overall exposure of 260 kt · year. Although the SK search has so far not observed nucleon decay, it has established strict limits (90% CL) on the partial lifetimes for decay modes of particular interest to GUT models such as $\tau/B(p \to e^+\pi^0) > 1.3 \times 10^{34}$ year and $\tau/B(p \to K^+\overline{\nu}) > 0.59 \times 10^{34}$ year [40]. These are significant limits on theoretical models that constrain model builders and set a high threshold for the next-generation detectors such as LBNE and Hyper-Kamiokande (Hyper-K). After more than ten years of exposure, the SK limits will improve only slowly. A much more massive detector such as Hyper-K — which will have a $560-$kt fiducial mass — is required to make a significant (order-of-magnitude) improvement using the water Cherenkov technique.

The uniqueness of proton decay signatures in a LArTPC and the potential for reconstructing them with redundant information has long been recognized as a key strength of this technology. A LArTPC can reconstruct all final-state charged particles and make an accurate assessment of particle type, distinguishing between muons, pions, kaons and protons. Electromagnetic showers are readily measured, and those that originate from photons generated by π^0 decay can be distinguished to a significant degree from those that originate from ν_e charged-current (CC) interactions. Kiloton-per-kiloton, LArTPC technology is expected to outperform water Cherenkov in both detection efficiency and atmospheric-neutrino background rejection for most nucleon decay modes, although intranuclear effects, which can smear out some of the proton decay signal, are smaller for oxygen and nonexistent for hydrogen.

When mass and cost are taken into account, water Cherenkov technology is optimum for the $p \to e^+\pi^0$ final-state topology, where the signal efficiency is roughly 40% and the background rate is two events per Mt $\cdot$ year. The efficiency estimate for this mode [187] for a LArTPC is 45% with one event per Mt $\cdot$ year — not a significant enough improvement in efficiency to overcome the penalty of the higher cost per kiloton for liquid argon.

For the $p \to K^+\overline{\nu}$ channel, on the other hand, the LArTPC technology is superior based on the same criteria. In a LArTPC, the K^+ track is reconstructed and identified as a charged kaon. The efficiency for the $K^+\overline{\nu}$ mode in a LArTPC is estimated to be as high as 97.5% with a background rate of one event per Mt $\cdot$ year. In water Cherenkov detectors the efficiency for this mode is roughly 19% for a low-background search, with a background rate of four events per Mt $\cdot$ year. Based on these numbers and a ten-year exposure, LBNE's 34$-$kt LArTPC and the 560$-$kt Hyper-K WCD have comparable sensitivity (at 90% CL), but the estimated LArTPC background of 0.3 events is dramatically better than the 22 estimated for Hyper-K (assuming no further improvement in analysis technique past that currently executed for SK [40]).

5.2 Signatures for Nucleon Decay in Liquid Argon

The LBNE LArTPC's superior detection efficiencies for decay modes that produce kaons will outweigh its relatively low mass compared with multi-hundred-kiloton water Cherenkov detectors. Because the LArTPC can reconstruct protons that are below Cherenkov threshold, it can reject many atmospheric-neutrino background topologies by vetoing on the presence of a recoil proton. Due to its excellent spatial resolution, it also performs better for event topologies with displaced vertices, such as $p \to K^+\overline{\nu}$ (for multi-particle K^+ decay topologies) and $p \to K^0\mu^+$. The latter mode is preferred in some SUSY GUTs.

For modes with no electron in the final state, the same displaced vertex performance that underpins long-baseline neutrino oscillation measurements allows the rejection of CC interactions of atmospheric ν_e's. As will be stressed for the key mode of $p \to K^+\overline{\nu}$ described in detail below, the capability to reconstruct the charged kaon with the proper range and dE/dx profile allows for a high-efficiency, background-free analysis. In general, these criteria favor all modes with a kaon, charged or neutral, in the final state. Conversely, the efficiency for decay modes to a lepton plus light meson will be limited by intranuclear reactions that plague liquid argon to a greater extent than they do ^{16}O in a water Cherenkov detector.

An extensive survey [187] of nucleon decay efficiency and background rates for large LArTPCs with various depth/overburden conditions, published in 2007, provides the starting point for the assessment of LBNE's capabilities. Table 5.1 lists selected modes where LArTPC technology exhibits a significant performance advantage (per kiloton) over the water Cherenkov technology. The remainder of this chapter focuses on the capabilities of LBNE for the $p \to K^+\overline{\nu}$ channel, as the most promising from theoretical and experimental considerations. Much of the discussion that follows can be applied to cover the other channels with kaons listed in the table.

Table 5.1: Efficiencies and background rates (events per Mt · year) for nucleon decay channels of interest for a large underground LArTPC [187], and comparison with water Cherenkov detector capabilities. The entries for the water Cherenkov capabilities are based on experience with the Super–Kamiokande detector [40].

Decay Mode	Water Cherenkov		Liquid Argon TPC	
	Efficiency	Background	Efficiency	Background
$p \to K^+\overline{\nu}$	19%	4	97%	1
$p \to K^0\mu^+$	10%	8	47%	< 2
$p \to K^+\mu^-\pi^+$			97%	1
$n \to K^+e^-$	10%	3	96%	< 2
$n \to e^+\pi^-$	19%	2	44%	0.8

The key signature for $p \to K^+\overline{\nu}$ is the presence of an isolated charged kaon (which would also be monochromatic for the case of free protons, with p =340 MeV). Unlike the case of $p \to e^+\pi^0$, where the maximum detection efficiency is limited to 40–45% because of inelastic intranuclear scattering of the π^0, the kaon in $p \to K^+\overline{\nu}$ emerges intact (because the kaon momentum is below threshold for inelastic reactions) from the nuclear environment of the decaying proton $\sim 97\%$ of the time. Nuclear effects come into play in other ways, however: the kaon momentum is smeared by the proton's Fermi motion and shifted downward by re-scattering [188]. The kaon emerging from this process is below Cherenkov threshold, therefore a water detector would need to detect it after it stops, via its decay products. Not all K decay modes are reconstructable, however, and even for those that are, insufficient information exists to determine the initial K momentum. Still, water detectors can reconstruct significant hadronic channels such as $K^+ \to \pi^+\pi^0$ decay, and the $6-$MeV gamma from de-excitation of O^{16} provides an added signature to help with the $K^+ \to \mu^+\nu$ channel. The overall detection efficiency in SK [40] thus approaches 20%.

In LArTPC detectors, the K^+ can be tracked, its momentum measured by range, and its identity positively resolved via detailed analysis of its energy-loss profile. Additionally, all decay modes can be cleanly reconstructed and identified, including those with neutrinos, since the decaying proton is essentially at rest. With this level of detail, it is possible for a single event to provide overwhelming evidence for the appearance of an isolated kaon of the right momentum originating from a point within the fiducial volume. The strength of this signature is clear from cosmogenic-induced kaons observed by the ICARUS Collaboration in the cosmic-ray (CR) test run of half of the T600 detector, performed at a surface installation in Pavia [189] and in high-energy neutrino interactions with the full T600 in the recent CNGS (CERN Neutrinos to Gran Sasso) run [190]. Figure 5.1 shows a sample event from the CNGS run in which the kaon is observed as a progressively heavily-ionizing track that crosses into the active liquid argon volume, stops, and decays to $\mu\nu$, producing a muon track that also stops and decays such that the Michel-electron track is also visible. The 3D reconstruction of the event is shown in Figure 5.2.

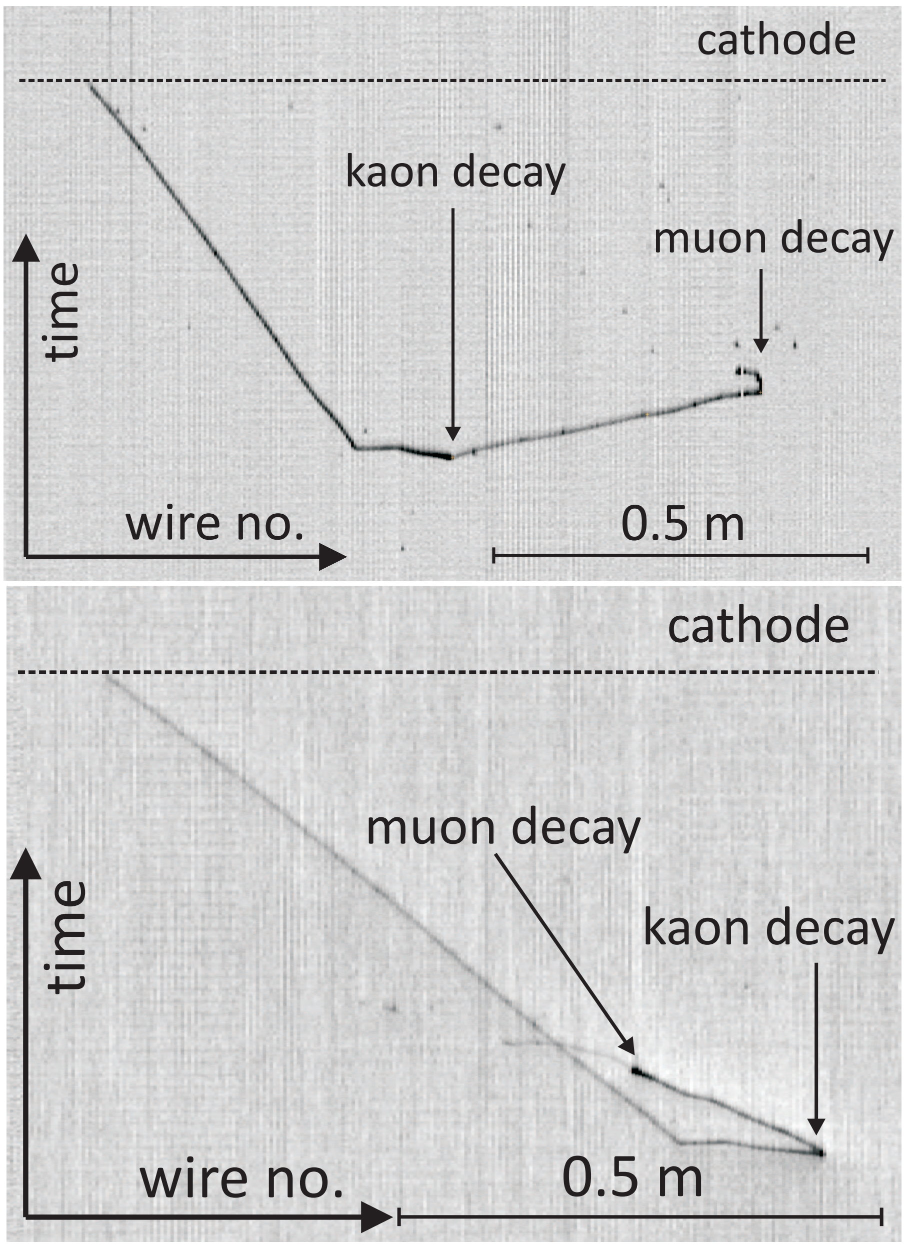

Figure 5.1: Event display for a decaying kaon candidate $K \to \mu\nu_\mu$ $\mu \to e\nu_e\nu_\mu$ in the ICARUS T600 detector observed in the CNGS data (K: 90 cm, 325 MeV; μ : 54 cm, 147 MeV; e : 13 cm, 27 MeV). The top figure shows the signal on the collection plane, and the bottom figure shows the signal on the second induction plane [190].

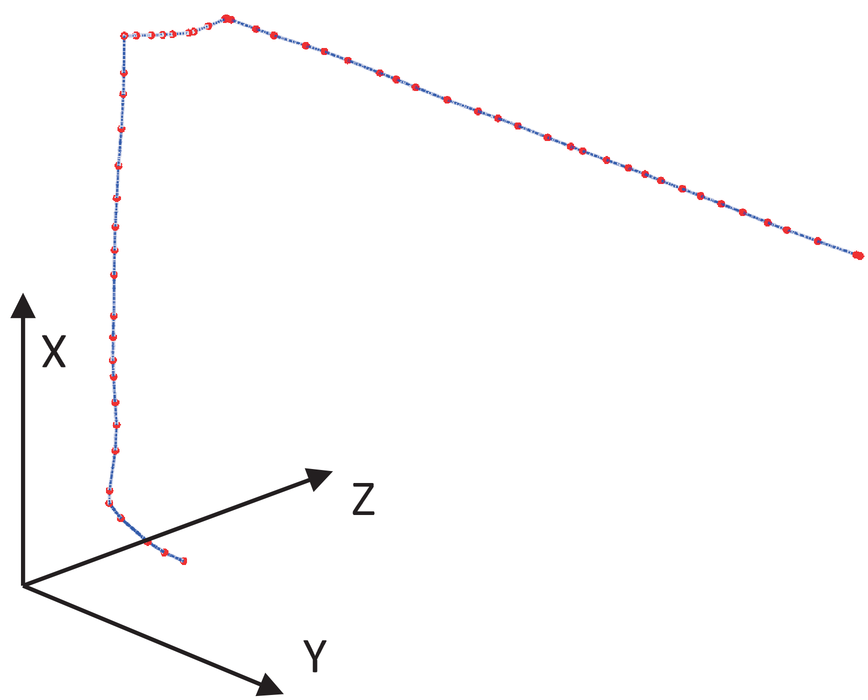

Figure 5.2: 3D reconstruction of the decaying kaon event observed in the ICARUS T600 detector and shown in Figure 5.1.

If it can be demonstrated that background processes mimicking this signature can be rejected at the appropriate level, a single $p \to K^+\overline{\nu}$ candidate could constitute evidence for proton decay.

5.3 Background Levels and Rejection Capabilities

This section discusses the key background processes and their signatures, focusing on the $p \to K^+\overline{\nu}$ channel as the benchmark mode*. The two potential sources of background are cosmic-ray muons and atmospheric neutrinos, described separately below.

5.3.1 Cosmic-Ray Muon Backgrounds

Cosmic-ray (CR) muons contribute background signals when they penetrate the detector. Hence, the self-shielding feature of the LArTPC and the depth of the site are important assets for controlling the rate of signals that can mimic a proton decay event. Additionally, the energy deposition associated with spallation products is well below the hundreds-of-MeV range for depositions from proton decay final-state particles.

The most pernicious CR-muon background in liquid argon for proton decay with kaon final states

*Much of this discussion applies equally well to other nucleon decay modes involving charged or neutral kaons.

thus comes from particular pathological processes. Specifically, CR muons that produce kaons via photonuclear interactions in the rock near the detector or in the liquid argon itself but outside the active volume are capable of producing signatures that mimic $p \to K^+\overline{\nu}$ and other modes with kaons. CR-induced kaon backgrounds as a function of depth have been studied for liquid argon [187,191,192].

In particular, at the 4,850-ft level, the vertical rock overburden will be approximately 4-km water equivalent, at which depth the muon rate through a 34−kt LArTPC will be approximately $0.1\,\mathrm{s}^{-1}$. This is low enough that a veto on the detection of a muon in the liquid argon volume can be applied with negligible loss of live-time. Specifically, assuming a maximum drift time of 2 ms, the probability of a muon passing through the detector in time with any candidate event (i.e., a candidate for proton decay or other signal of interest) will be 2×10^{-4}. Thus, any candidate event that coincides in time with a large energy deposition from a muon or muon-induced cascade can be rejected with a negligible signal efficiency loss of 0.02%. Only background from events associated with CR muons in which the muon itself does not cross the active region of the detector remain to be considered.

One class of such backgrounds involves production of a charged kaon outside the active volume, which then enters the active region. Assuming unambiguous determination of the drift time (via the scintillation-photon detection system and other cues such as detailed analysis of the dE/dx profile of the kaon candidate), it will be possible to identify and reject such entering kaons with high efficiency. It should be noted that, through studies of CR muons that interact within the active volume of the detector, backgrounds of this type can be well characterized with data from the detector itself.

A potentially less tractable background for the decay mode $p^+ \to K^+\overline{\nu}$ occurs when a neutral particle (e.g., a K^0_L) originating in a muon-induced cascade outside the detector propagates into the detector volume and undergoes a charge-exchange reaction in the fiducial volume. To further understand the possible rate for this background at LBNE, simulations of CR muons and their secondaries at depth have been run. The rate of positive kaons produced inside the 34−kt detector by a neutral particle entering from outside (and with no muon inside) has been found to be 0.9 events per year before any other selection criteria are applied. Further studies included the following additional selection criteria:

1. No muon is in the detector active volume.
2. The K^+ candidate is produced inside the liquid argon active volume at a distance from the wall greater than 10 cm.
3. The energy deposition from the K^+ and its descendants (excluding decay products) is less than 150 MeV.

4. The total energy deposition from the K^+, its descendants and decay products is less than 1 GeV.

5. Energy deposition from other particles in the muon-induced cascade (i.e., excluding the energy deposition from the positive kaon, its descendants and decay products) is less than 100 MeV.

No event survived the additional selection criteria, resulting in an upper bound on the rate of this type of background event of 0.07 events per year in a 34−kt LArTPC, equivalent to two events per Mt $\cdot$ year. A key factor contributing to the rejection of CR backgrounds to this level is that although a large number of K^+'s generated by cosmic rays deposit an energy similar to that expected from proton decay, the energy depositions from K^+'s are not the only ones recorded for these events. Other particles from the CR-muon interaction tend also to enter the detector and deposit additional visible energy, making the rejection of background events simpler than would be expected assuming only the appearance of a kaon in the detector.

In addition to the impact of an active veto system for detectors at various depths, the studies of [187] also consider impacts of progressively restrictive fiducial volume cuts. Together, these and the above studies demonstrate that proton decay searches in the LBNE LArTPC at the 4,850-ft level can be made immune to CR-muon backgrounds, without the requirement of an external active veto system. To the extent that there are uncertainties on the rate of kaon production in CR-muon interactions, one has flexibility to suppress background from this source further by application of modest fiducial volume cuts.

5.3.2 Background from Atmospheric-Neutrino Interactions

Unlike the case of CR-muon backgrounds, the contamination of a nucleon decay candidate set due to interactions of atmospheric neutrinos cannot be directly controlled by changing the depth or fiducial volume definition of the LBNE detector. Furthermore the atmospheric-neutrino flux is naturally concentrated around the energy range relevant for proton decay. In the analysis of [187], a single simulated neutral-current (NC) event survived the requirement of having an isolated single kaon with no additional tracks or π^0's, and total deposited energy below 800 MeV. This event is responsible for the estimated background rate of 1.0 per Mt $\cdot$ year.

While this rate is acceptable for LBNE, it is natural to ask to what extent simulations are capable of providing reliable estimates for such rare processes. What if the actual rate for single-kaon atmospheric-neutrino events is higher by a factor of ten or more? Is that even conceivable? To set the scale, it is useful to recall that the atmospheric-neutrino sample size in LBNE is expected to be of order 10^5 per Mt $\cdot$ year of exposure (Table 4.11). Hence, “rare-but-not-negligible” in this context denotes a process that occurs at a level of no less than 10^{-6}.

Super–Kamiokande has given considerable attention to atmospheric-neutrino backgrounds in its nucleon decay searches (e.g., [193]). In the SK analyses, data obtained with relaxed cuts have been studied to validate the atmospheric-neutrino flux and interaction models employed. Consequently, the atmospheric-neutrino backgrounds for nucleon decay searches are well established at the level required for the water Cherenkov detector approach to this physics.

For the case of LBNE, however, with a different detector technology, and with a goal of being sufficiently background-free to enable a discovery based on observation of a single candidate event, one would like to go further to understand at a detailed level what the rates for the specific background processes are. The first question to ask is what are the physical processes that could produce the exact signature of a $p \to K^+\overline{\nu}$ event? Some possibilities are discussed below.

Strange particle production in $\Delta S = 0$ processes: An identified source of background events for SK [193] involves associated production of a pair of strange hadrons, nominally in the strong decay of a nucleonic resonance excited via an inelastic NC neutrino-nucleon interaction. This could be in the form of a kaon accompanying a Λ baryon. Again, conservation of strangeness holds that the baryon cannot be absorbed, and thus a weak decay of the strange quark is guaranteed. For water Cherenkov detectors the strange baryon is produced with a small enough momentum that its decay products are typically below Cherenkov threshold. For a liquid argon detector, these final state particles should be detectable, leaving distinctive signatures that can be reconstructed. Thus in principle, this source of background can be suppressed with appropriate event reconstruction and analysis tools. To understand this prospect in quantitative terms, the range of kinematic distributions are currently under investigation.

It is possible to imagine yet more contrived scenarios, for example where the meson produced is a K^0_L that escapes detection, while a charged kaon (K^- in this case) results from the decay of an excited Λ or Σ baryon produced in association. However, one would expect such processes to be even more rare than those described above. Thus if the rates for (say) the $K^+\Lambda$ production channel described above can be constrained as being sufficiently small, it can be argued that the more contrived scenarios can be ignored.

Strange particle production in $\Delta S = 1$ processes: A potentially challenging source of background is production of a single charged kaon (in this case a K^-) in a $\Delta S = 1$ process. In the simplest case, one could think of it as the Cabibbo-suppressed version of single π production in a CC antineutrino interaction. In contrast to the $\Delta S = 0$ processes described above, no strange baryon is produced in association, and so there are no other hadrons to detect. (Similarly, one could imagine the kaon originating in the decay of a strange baryon resonance produced in a Cabibbo-suppressed neutrino interaction, accompanied by a neutron that goes undetected.) On the other hand, such processes can only occur in CC interactions, and thus a charged lepton will accompany the kaon. This therefore constitutes a background only for cases where the charged lepton is missed, which should be rare. The combination of probabilities associated with (1) Cabibbo-suppression, (2) single hadron production, and (3) circumstances causing the charged lepton to be missed, lead to an overall suppression of this source of background. Thus it should be possible to rule it out as a source of concern for LBNE on the basis of these features alone.

Misidentification of pions in atmospheric neutrino events: While misidentification of leading pions as kaons in atmospheric-neutrino scattering events is a potential problem, it can be argued that the rate for such misidentification events can be controlled. Key signatures for the kaon are found in the distinctive residual-range dependence of its energy deposition near the end of its trajectory (nominally 14 cm) as well as in the explicit reconstruction of its decay products. Similarly, tails in the measurement of dE/dx would be a concern if they led a pion track to mimic a kaon, however the momentum (30 MeV) and hence range of the muon produced in the decay of a stopping pion would not match that of the corresponding muon (236 MeV) in a $K^+ \to \mu^+\nu$ decay. Thus, it should be possible to control this background experimentally.

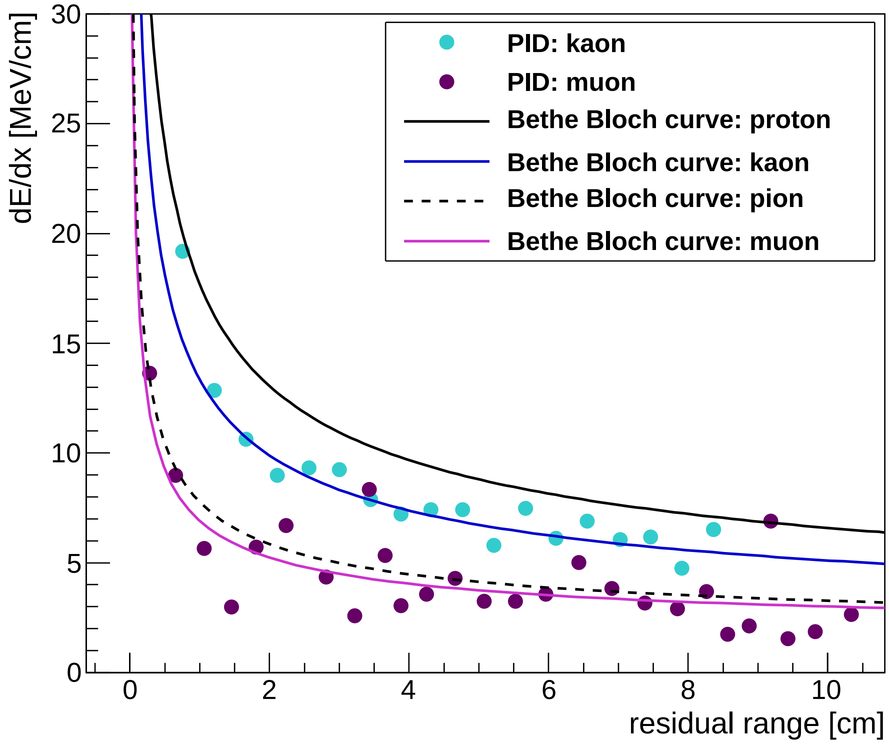

Figure 5.3: Measurements of dE/dx versus residual range for signals associated with the kaon track in Figure 5.1 (cyan points) and the decay muon (magenta points). Overlaid are the expected dE/dx profiles for the two particle identities [190].

One variant of this background source occurs for the case where the pion decays in flight. Two experimental handles on this background can be immediately identified. First is the deviation from the expected dE/dx profile for a kaon, which will be more dramatic than in the case of the stopping pion. Second is the correlation of the direction of the decay muon with that of the pion, which is absent in the decay of a particle at rest. Assessment of the cumulative impact of event rejection based on these features is under study. However, the decaying kaon observed in the ICARUS CNGS run displayed in Figure 5.1 can be used to give a sense of the π/K discrimination possible in a LArTPC via dE/dx. In Figure 5.3, the measurements of dE/dx versus residual range for the anode wires registering signals from the kaon and muon tracks in this event are plotted against the expected dE/dx profiles [190]. The data from the kaon track (cyan points) agree very well with the expected dE/dx profile (blue curve) and are quite distinguishable from the expected pion profile (dashed curve).

Event reconstruction pathologies: While consideration of rare event topologies in atmospheric-neutrino interactions is important, it will be equally important to understand ways in which more typical events might be misreconstructed so as to mimic nucleon decay processes. For example, a quasi-elastic ν_μ-CC interaction will produce a muon and a recoil proton from a common vertex. However, it may be possible to interpret the vertex as the kink associated with the decay of a stopping kaon, where the proton track is confused with a kaon traveling in the opposite direction. Tools are still under development to be able to understand the degree to which this possibility poses a potential background. Naively, the dE/dx profile of the proton as a function of residual range will not match the time-reversed version of this for a kaon, and distributions of kinematic quantities will be distinct. Additionally, such a background will only affect the portion of the $p \to K^+\overline{\nu}$ analysis focused on $K^+ \to \mu^+\nu$; other K^+ decays will be immune to this pathology.

The point of this example is to illustrate that although the exquisite performance characteristics of the LArTPC technique enables unambiguous identification of nucleon decay signatures, an extensive program of detailed analysis will be required to fully exploit these capabilities.

Conclusions on atmospheric-neutrino backgrounds: The above examples suggest that it will be possible to demonstrate the desired level of suppression of atmospheric-neutrino background without undue reliance on simulations via a combination of arguments based on existing experimental data (from SK proton decay searches, as well as data from various sources on exclusive and inclusive neutrino-interaction processes that yield rare topologies), physics considerations, and detailed analysis of anticipated detector response. For the latter, ongoing LBNE event-reconstruction efforts will play a role with simulated atmospheric-neutrino samples. Additionally, useful input is expected to come in over the short/intermediate term from analyses of LArTPC data from ArgoNeuT, MicroBooNE and the proposed LArIAT. Finally, while the state of neutrino flux and interaction models is already quite advanced, vigorous theoretical work is ongoing to improve these further, exploiting existing data from neutrino and electron-scattering experiments. In particular, kaon production in neutrino interactions in relevant energy ranges is receiving renewed attention [194].

5.4 Summary of Expected Sensitivity to Key Nucleon Decay Modes

Based on the expected signal efficiency and the upper limit on the background rates estimated in Section 5.3, the expected limit on the proton lifetime as a function of running time in LBNE for $p \to K^+\overline{\nu}$ is shown in Figure 5.4.

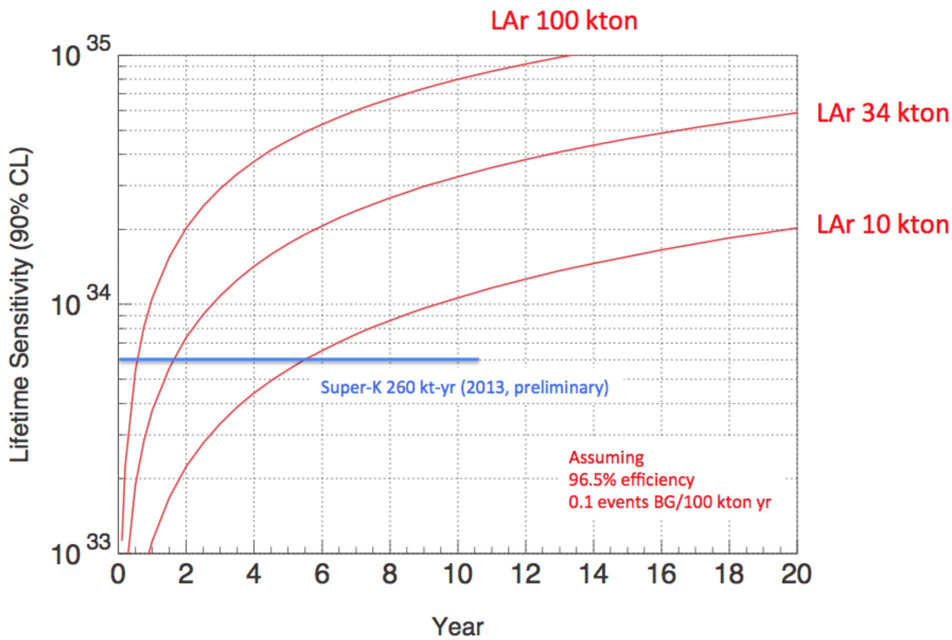

Figure 5.4: Proton decay lifetime limit for $p \to K^+\overline{\nu}$ as a function of time for underground LArTPCs of fiducial masses 10, 34 and 100 kt. For comparison, the current limit from SK is also shown. The limits are at 90% C.L., calculated for a Poisson process including background, assuming that the detected events equal the expected background.

Figure 5.4 demonstrates that to improve the current limits on the $p \to \overline{\nu}K^+$, set by Super–Kamiokande, significantly beyond that experiment's sensitivity, a LArTPC detector of at least 10 kt, installed deep underground, is needed. A 34−kt detector will improve the current limits by an order of magnitude after running for two decades. Clearly a larger detector mass would improve the limits even more in that span of time.

While the background rates are thought to be no higher than those assumed in generating the above sensitivity projections, it is possible to estimate the impact of higher rates. For $p \to K^+\overline{\nu}$, Table 5.2 shows a comparison of the 90% CL lower bounds on proton lifetime for an exposure of 340 kt · year assuming the nominal 1.0 per Mt · year background rate with the corresponding bounds for a rate that is ten times higher, as well as for a fully background-free experiment. While a factor of ten increase in the background would hurt the sensitivity, useful limits can still be obtained. As stated above, however, there is good reason to believe such a case is highly unlikely.

Table 5.2: The impact of different assumed background rates on the expected 90% CL lower bound for the partial proton lifetime for the $p \to K^+\overline{\nu}$ channel, for a 34−kt detector operating for ten years. The expected background rate is one event per Mt · year. Systematic uncertainties are not included in these evaluations.

Background Rate	Expected Partial Lifetime Limit
0 events/Mt · year	3.8×10^{34} years
1 events/Mt · year	3.3×10^{34} years
10 events/Mt · year	2.0×10^{34} years

Sensitivities have been computed for some of the other decay channels listed in Table 5.1. The limits that could be obtained from an LBNE 34−kt detector in ten years of running as compared to other proposed future experiments and theoretical expectations are shown in Figure 5.5.

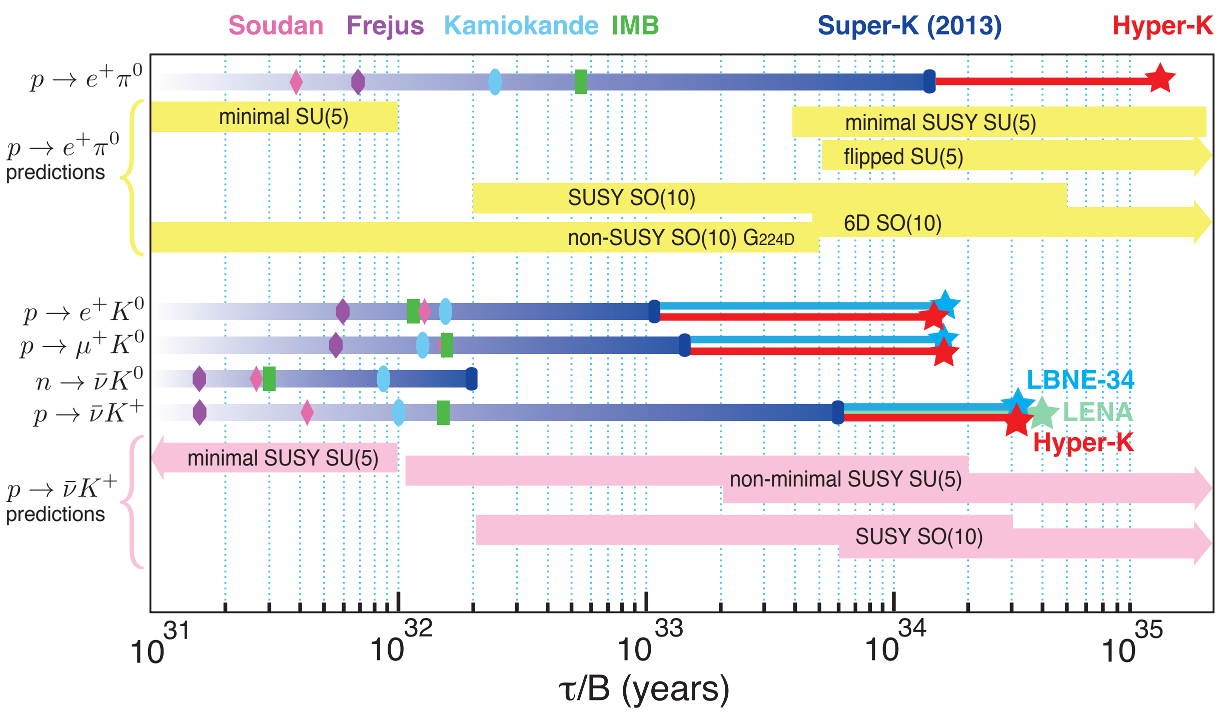

Figure 5.5: Proton decay lifetime limits that can be achieved by the LBNE 34−kt detector compared to other proposed future experiments. The limits are at 90% C.L., calculated for a Poisson process including background, assuming that the detected events equal the expected background.

Chapter 6 Core-Collapse Supernova Neutrinos

Neutrinos emitted in the first few seconds of a core-collapse supernova carry with them the potential for great insight into the mechanisms behind some of the most spectacular events that have played key roles in the evolution of the Universe. Collection and analysis of this high-statistics neutrino signal from a supernova within our galaxy would provide a rare opportunity to witness the energy and flavor development of the burst as a function of time. This would in turn shed light on the astrophysics of the collapse as well as on neutrino properties.

6.1 The Neutrino Signal and Astrophysical Phenomena

A core-collapse supernova* occurs when a massive star reaches the end of its life, and stellar burning can no longer support the star's weight. This catastrophic collapse results in a compact remnant such as a neutron star, or possibly a black hole, depending on the mass of the progenitor. The infall is followed by a *bounce* when sufficiently high core density is reached, and in some unknown (but nonzero) fraction of cases, the shock wave formed after the bounce results in a bright explosion [195]. The explosion energy represents only a small fraction of the enormous total gravitational binding energy of the resulting compact remnant, however — thanks to the neutrinos' weak coupling, which allows them to escape — within a few tens of seconds almost all of the energy is emitted in the form of neutrinos in the tens-of-MeV range. In spite of their weak coupling, the neutrinos are copious enough to (very likely) play a significant role in the explosion.

Neutrinos from the celebrated SN1987A core collapse [103,104] in the Large Magellanic Cloud outside the Milky Way were observed; however, the statistics were sparse and a great many questions remain. A high-statistics observation of a neutrino burst from a nearby supernova would be possible with the current generation of detectors. Such an observation would shed light on the nature of the astrophysical event, as well as on the nature of neutrinos themselves. Sensitivity to the different flavor components of the flux is highly desirable.

The core-collapse neutrino signal starts with a short, sharp *neutronization* burst primarily composed of ν_e (originating from $p + e^- \to n + \nu_e$, as protons and electrons get squeezed together), and is followed by an *accretion* phase lasting some hundreds of milliseconds, as matter falls onto the collapsed core. The later *cooling* phase over $\sim$10 seconds represents the main part of the signal, over which the proto-neutron star sheds its gravitational binding energy. The neutrino flavor con-

**Supernova* always refers to a *core-collapse supernova* in this chapter unless stated otherwise.

tent and spectra change throughout these phases, and the supernova's temperature evolution can be followed with the neutrino signal. Some fairly generic supernova signal features are illustrated in Figure 6.1, based on [196] and reproduced from [197].

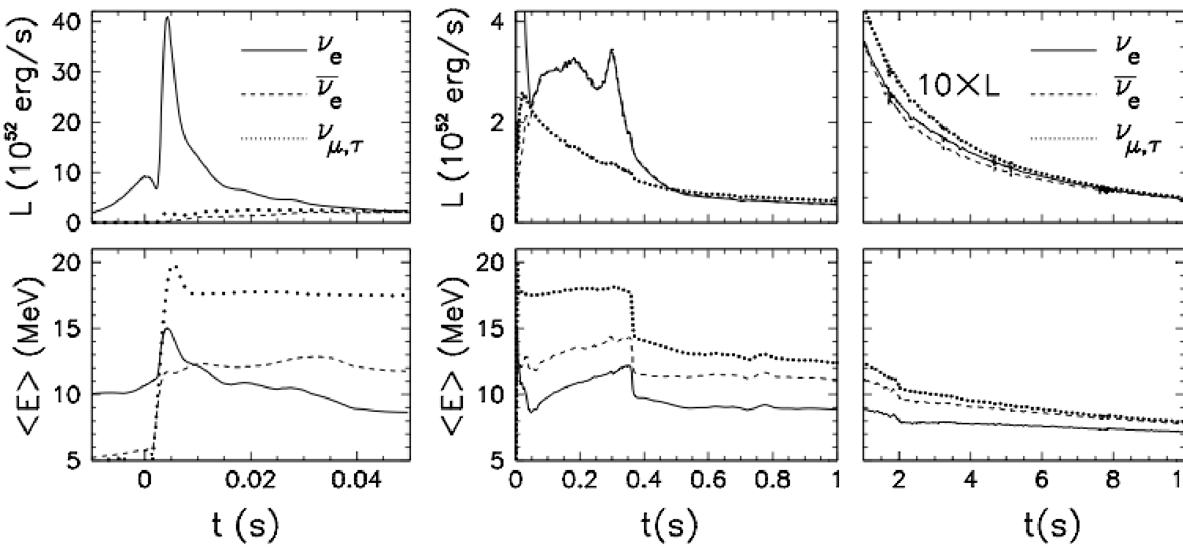

Figure 6.1: Expected core-collapse neutrino signal from the *Basel* model [196], for a 10.8 $M_\odot$ progenitor. The left plots show the very early signal, including the neutronization burst; the middle plots show the accretion phase, and the right plots show the cooling phase. Luminosities as a function of time are shown across the top plots. The bottom plots show average energy as a function of time for the ν_e, $\overline{\nu}_e$ and $\nu_{\mu,\tau}$ flavor components of the flux (fluxes for ν_μ, $\overline{\nu}_\mu$, ν_τ, and $\overline{\nu}_\tau$ should be identical). Figure courtesy of [197].

The supernova-neutrino spectrum at a given moment in time is expected to be well described by a parameterization [198,199] given by:

$$\phi(E_\nu) = \mathcal{N} \left(\frac{E_\nu}{\langle E_\nu \rangle} \right)^\alpha \exp \left[-\,(\alpha+1)\,\frac{E_\nu}{\langle E_\nu \rangle} \right] , \tag{6.1}$$

where E_ν is the neutrino energy, $\langle E_\nu \rangle$ is the mean neutrino energy, α is a *pinching parameter*, and $\mathcal{N}$ is a normalization constant. Large α corresponds to a more pinched spectrum (suppressed high-energy tail). This parameterization is referred to as a *pinched-thermal* form. The different ν_e, $\overline{\nu}_e$ and ν_x, $x = \mu, \tau$ flavors are expected to have different average energy and α parameters and to evolve differently in time.

A wide variety of astrophysical phenomena affect the flavor-energy-time evolution of the spectrum, including neutrino oscillation effects that are determined by the mass hierarchy (MH) and *collective* effects due to neutrino-neutrino interactions. A voluminous literature exists exploring these collective phenomena, e.g., [200,201,202,203,204,205,206,207,208].

A number of astrophysical phenomena associated with supernovae are expected to be observable in the supernova-neutrino signal, providing a remarkable window into the event, for example:

- The initial burst, primarily composed of ν_e and called the *neutronization* or *breakout* burst, represents only a small component of the total signal. However, oscillation effects can manifest in an observable manner in this burst, and flavor transformations can be modified by the *halo* of neutrinos generated in the supernova envelope by scattering [209].
- The formation of a black hole would cause a sharp signal cutoff (e.g., [210,211]).
- Shock wave effects (e.g., [212]) would cause a time-dependent change in flavor and spectral composition as the shock wave propagates.
- The standing accretion shock instability (SASI) [213,214], a *sloshing* mode predicted by 3D neutrino-hydrodynamics simulations of supernova cores, would give an oscillatory flavor-dependent modulation of the flux.
- Turbulence effects [215,216] would also cause flavor-dependent spectral modification as a function of time.

This list is far from comprehensive. Furthermore, signatures of *collective* effects and signatures that depend on the MH will make an impact on many of the above signals (examples will be presented in Section 6.2). Certain phenomena are even postulated to indicate beyond-the-Standard-Model physics [217] such as axions, extra dimensions and an anomalous neutrino magnetic moment; non-observation of these effects, conversely, would enable constraints on these phenomena.

The supernova-neutrino burst signal is prompt with respect to the electromagnetic signal and therefore can be exploited to provide an early warning to astronomers [116,117]. Additionally, a LArTPC signal [218] is expected to provide some pointing information, primarily from elastic scattering on electrons.

Even non-observation of a burst, or non-observation of a ν_e component of a burst in the presence of supernovae (or other astrophysical events) observed in electromagnetic or gravitational wave channels, would still provide valuable information about the nature of the sources. Moreover, a long-timescale, sensitive search yielding no bursts will also provide limits on the rate of core-collapse supernovae.

6.2 Expected Signal and Detection in Liquid Argon

As discussed in Section 2.4, liquid argon is known to exhibit a singular sensitivity to the ν_e component of a supernova-neutrino burst. This feature is especially important, as it will make LBNE a unique source in the global effort to combine data from a variety of detectors with different flavor sensitivities to obtain a complete picture of the physics of the burst.

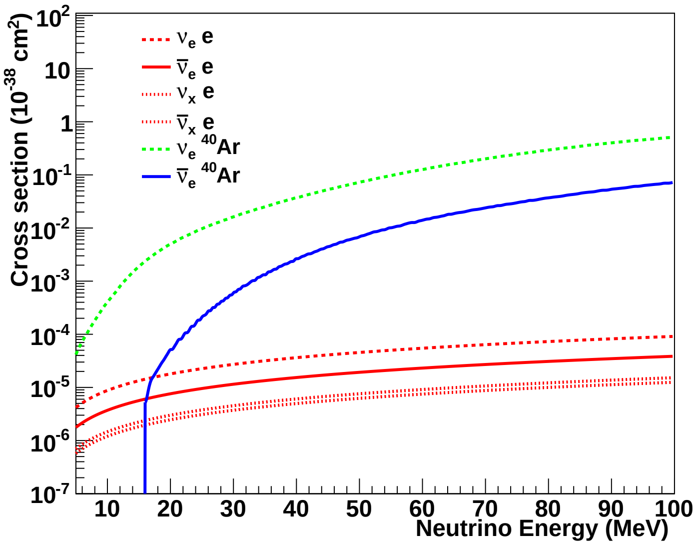

Figure 6.2: Cross sections for supernova-relevant interactions in argon.

The predicted event rate from a supernova-neutrino burst may be calculated by folding expected neutrino differential energy spectra in with cross sections for the relevant channels, and with detector response. For event rate estimates in liquid argon, a detection threshold of 5 MeV is assumed. The photon-detection system of the LBNE far detector, coupled with charge collection and simple pattern recognition, is expected to provide a highly efficient trigger. Most LBNE supernova physics sensitivity studies so far have been done using parameterized detector responses from [139] implemented in the SNOwGLoBES software package [219]. SNOwGLoBES takes as input fluxes, cross sections (Figure 6.2), *smearing matrices* (that incorporate both interaction product spectra and detector response) and post-smearing efficiencies. The energy resolution used is

$$\frac{\sigma}{E\ (\mathrm{MeV})} = \frac{11\%}{\sqrt{E\ \mathrm{MeV}}} + 2\% \qquad (6.2)$$

Work is currently underway using the full Geant4 simulation [132] framework and the LArSoft software package [220] to characterize low-energy response for realistic LBNE detector configurations. Preliminary studies of the detector response with the full simulation are summarized in Section A.1.2 and are found to be consistent with the parameterized response implemented in SNOwGLoBES.

Table 6.1 shows rates calculated with SNOwGLoBES for the dominant interactions in argon for the *Livermore* model [221], and the *GKVM* model [222]. Figure 6.3 shows the expected observed differential event spectra for these fluxes. Clearly, the ν_e flavor dominates.

Table 6.1: Event rates for different supernova models in 34 kt of liquid argon for a core collapse at 10 kpc, for ν_e and $\overline{\nu}_e$ charged-current channels and elastic scattering (ES) on electrons. Event rates will simply scale by active detector mass and inverse square of supernova distance.

Channel	Events *Livermore* model	Events *GKVM* model
$\nu_e + ^{40}\mathrm{Ar} \rightarrow e^- + ^{40}\mathrm{K}^*$	2308	2848
$\overline{\nu}_e + ^{40}\mathrm{Ar} \rightarrow e^+ + ^{40}\mathrm{Cl}^*$	194	134
$\nu_x + e^- \rightarrow \nu_x + e^-$	296	178
Total	**2794**	**3160**

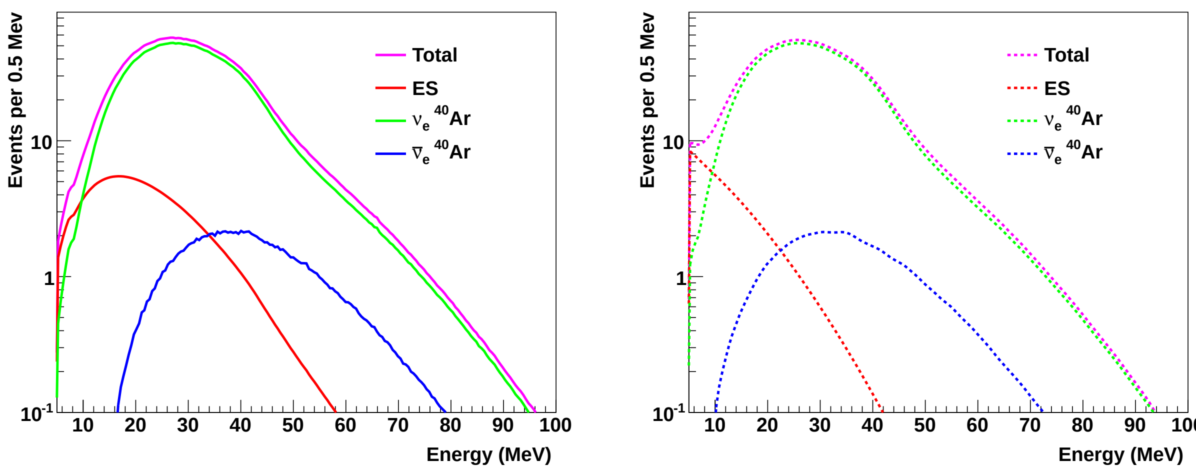

Figure 6.3: Supernova-neutrino event rates in 34 kt of argon for a core collapse at 10 kpc, for the GKVM model [222] (events per 0.5 MeV), showing three relevant interaction channels. Left: interaction rates as a function of true neutrino energy. Right: *smeared* rates as a function of detected energy, assuming resolution from [139].

Figure 6.4 gives another example of an expected burst signal, for which a calculation with detailed time dependence of the spectra is available [223] out to nine seconds post-bounce. This model has relatively low luminosity but a robust neutronization burst. Note that the relative fraction of neutronization-burst events is quite high.

In Figure 6.5, different oscillation hypotheses have been applied to *Duan* fluxes [208]. The Duan flux represents only a single late time slice of the supernova-neutrino burst and not the full flux; MH information will be encoded in the time evolution of the signal, as well. The figure illustrates, if only anecdotally, potential MH signatures.

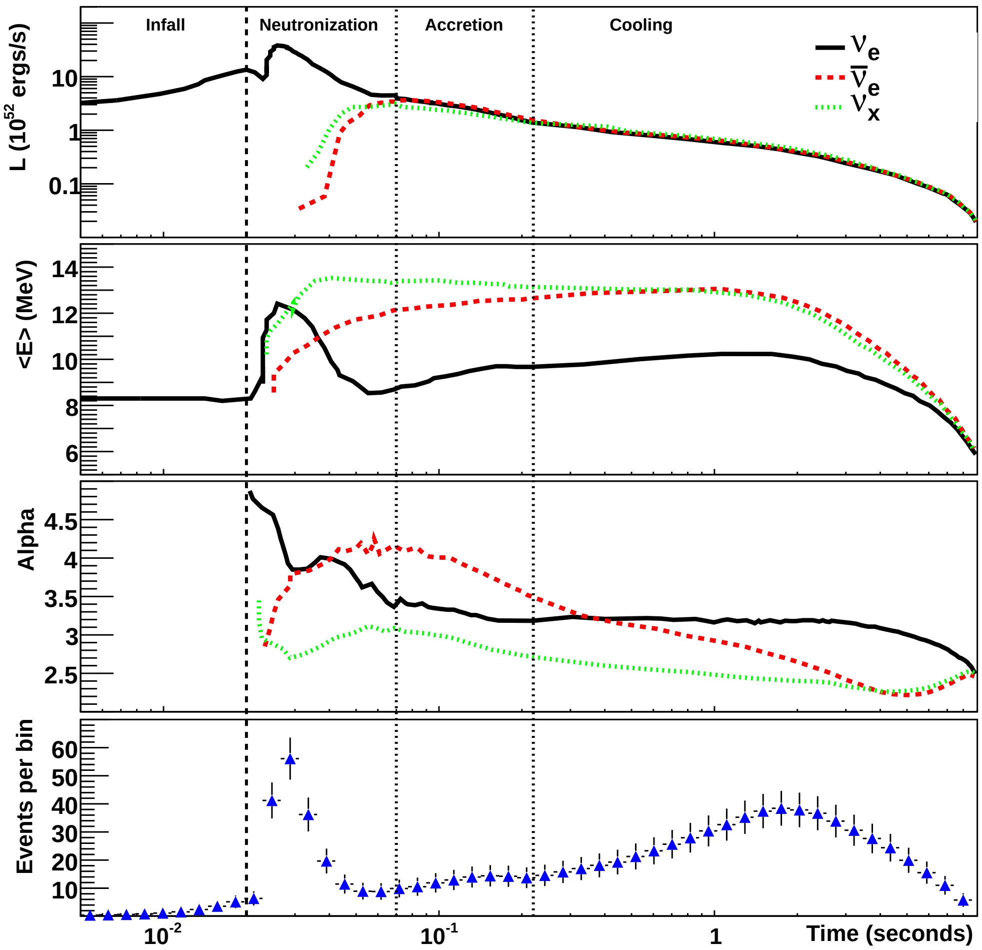

Figure 6.4: Expected time-dependent signal for a specific flux model for an electron-capture supernova [223] at 10 kpc. The top plot shows the luminosity, the second plot shows average neutrino energy, and the third plot shows the α (pinching) parameter. The fourth (bottom) plot shows the total number of events (mostly ν_e) expected in 34 kt of liquid argon, calculated using SNoWGLoBES. Note the logarithmic binning in time; the plot shows the number of events expected in the given bin and the error bars are statistical. The vertical dashed line at 0.02 seconds indicates the time of core bounce, and the vertical lines indicate different eras in the supernova evolution. The leftmost time interval indicates the infall period. The next interval, from core bounce to 50 ms, is the neutronization burst era, in which the flux is composed primarily of ν_e. The next period, from 50 to 200 ms, is the accretion period. The final era, from 0.2 to 9 seconds, is the proto-neutron-star cooling period.

Another potential MH signature is shown in Figure 6.6, for which a clear time-dependent shock-wave-related feature is visible for the normal MH case.

Figure 6.7 shows yet another example of a preliminary study showing how one might track supernova temperature as a function of time with the ν_e signal in liquid argon. Here, a fit is made to the pinched-thermal form of Equation 6.1. Not only can the internal temperature of the supernova be effectively measured, but the time evolution is observably different for the different hierarchies.

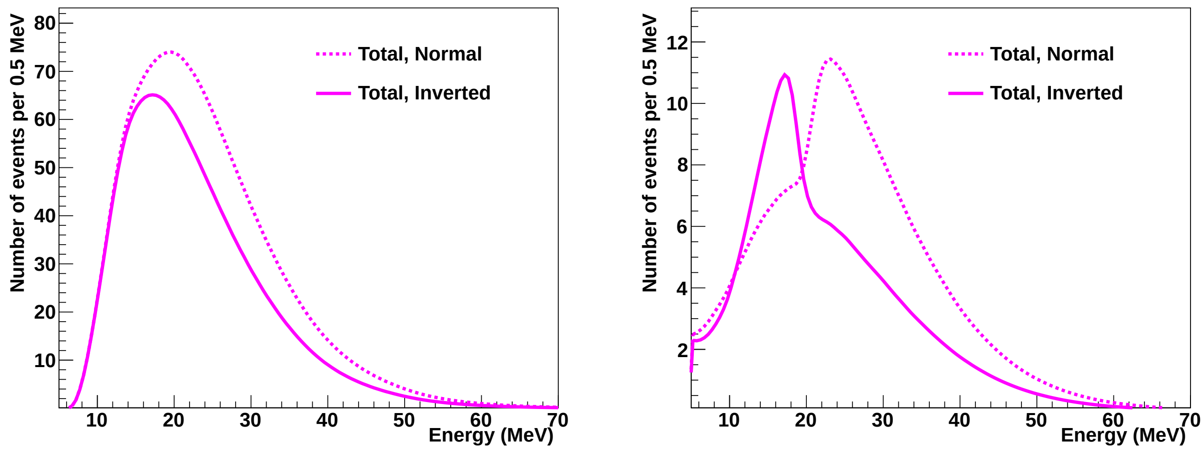

Figure 6.5: Comparison of total event rates for normal and inverted MH, for a specific flux example, for a 100−kt water Cherenkov detector (left) and for a 34−kt LArTPC (right) configuration, in events per 0.5 MeV. There are distinctive features in liquid argon for different neutrino mass hierarchies for this supernova model [224].

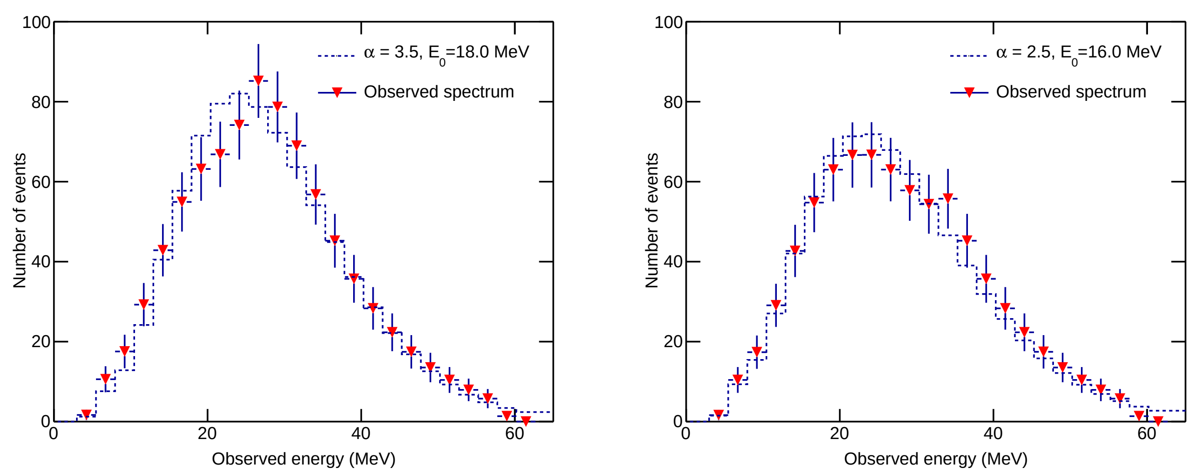

Figure 6.6: Observed ν_e spectra in 34 kt of liquid argon for a 10-kpc core collapse, representing about one second of integration time each at one-second intervals during the supernova cooling phase. The dashed line represents the best fit to a parameterized pinched-thermal spectrum. Clear *non-thermal* features in the spectrum that change with time are visible, on the left at around 20 MeV and on the right at around 35 MeV. Error bars are statistical. These features are present *only* for the normal MH.

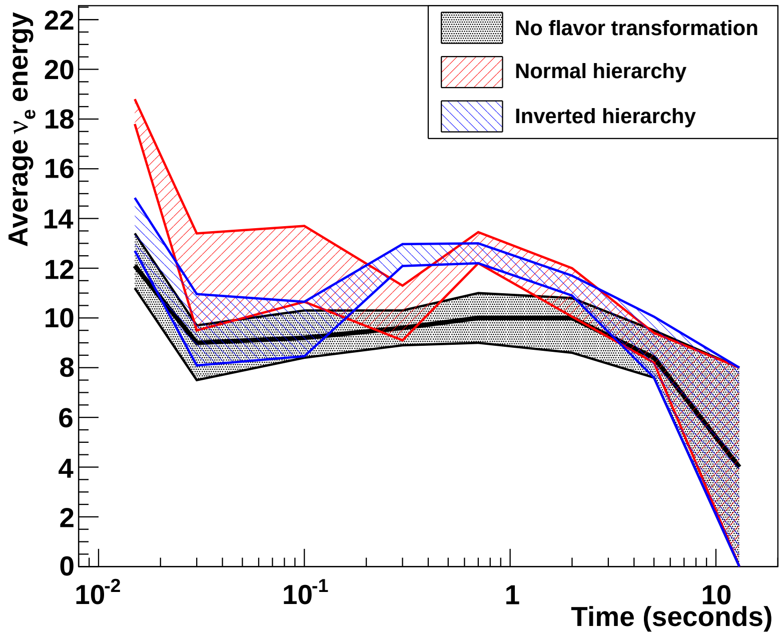

Figure 6.7: Average ν_e energy from fit to SNOwGLoBES-smeared, pinched-thermal spectrum as a function of time (34 kt at 10 kpc), for a flux model based on [225] and including collective oscillations, for two different MH assumptions. The bands represent 1σ error bars from the fit. The solid black line is the truth $\langle E_\nu \rangle$ for the unoscillated spectrum. Clearly, meaningful information can be gleaned by tracking ν_e spectra as a function of time.

6.3 Low-Energy Backgrounds

6.3.1 Cosmic Rays

Due to their low energy, supernova-neutrino events are subject to background from cosmic rays, although the nature of the signal — a short-timescale burst — is such that the background from these muons and their associated Michel electrons can in principle be well known, easily distinguished and subtracted. Preliminary studies [226] suggest that the shielding provided by the 4,850−ft depth available at the Sanford Underground Research Facility is acceptable.

6.3.2 Local Radiation Sources

It is possible that radioactive decays will directly overlap with the energy spectrum created by supernova-neutrino events in LBNE. It is also possible for an ensemble of radioactive-decay events in and around higher-energy particle interactions (e.g., from beam neutrinos) to obscure the edges of electromagnetic showers from highly scattering particles such as electrons and pions; this would appear as the radiological equivalent of dark noise in a digital image, and could potentially introduce a systematic uncertainty in the energy calculated for events, even at much higher energy than the decays themselves. It is therefore very important to calculate the radioactive-decay backgrounds in the LBNE far detector with sufficient accuracy to properly account for their presence, either as direct backgrounds or as systematic effects in energy calculations. To this end, LBNE collaborators are in the process of creating a physics-driven, radioactive-background budget and associated event generator for low-energy background events in the far detector.

The radioactive-background budget will have many components, each of which will fall into one of two categories:

1. intrinsic radioactive contamination in the argon or support materials, or
2. cosmogenic radioactivity produced in situ from cosmic-ray showers interacting with the argon or the support materials.

The former is dependent on the detector materials, and is therefore independent of far detector depth. The latter is strongly coupled to the cosmic-ray flux and spectrum. A preliminary estimate [227] of the cosmogenic radioactivity from beta emitters produced from cosmic-ray interactions with argon in the LBNE far detector at the 4,850 ft level of the Sanford Underground Research Facility is shown in Figure 6.8. Both of these background categories add to the direct energy depositions from cosmic rays themselves and associated showers.

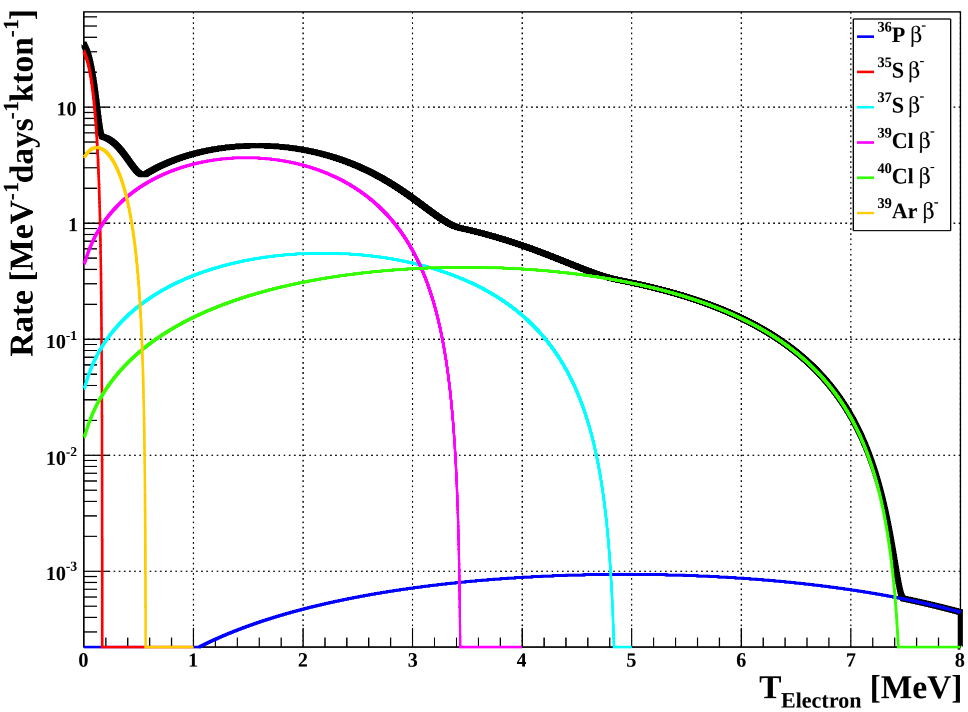

Figure 6.8: Cosmogenic background rates in the LBNE LArTPC as a function of the decay beta kinetic energy calculated at the 4,850−ft level of the Sanford Underground Research Facility.

6.3.3 Intrinsic Radioactive Background Mitigation

Intrinsic backgrounds in the far detector come from the radioactive material that is prevalent in the detector materials (both active and instrumentation/support materials and the cryostat itself), in the cavern walls and in the dust [228]. The isotopes of primary interest are "the usual suspects" in experiments where radioactive backgrounds must be controlled: ^{232}Th and ^{238}U (and their associated decay chains), ^{40}K, and ^{60}Co. In addition, ^{39}Ar will contribute a significant component, since it is present in natural argon harvested from the atmosphere at the level of approximately 1 Bq/kg. In consequence, a 10−kt far detector filled with $^{\mathrm{nat.}}$Ar will experience a rate from ^{39}Ar of approximately 10 MHz across the whole detector. The beta decay spectrum from ^{39}Ar is thankfully quite low in energy (Q_β = 0.565 MeV), so it will not interfere directly with the supernova signal, but it may contribute to the *dark noise* effect. Furthermore, the product of the average beta energy with this rate indicates the level at which the background due to introduction of power into the detector becomes a problem. This radioactive power from ^{39}Ar is approximately:

$$P_{Rad} \sim 0.25 \text{ MeV} \times 10 \text{ MHz} = 2.5 \times 10^6 \text{ MeV/s}. \tag{6.3}$$

Because this category of background can come from the cavern walls, the concrete cavern lining, the cryostat materials or the materials that compose the submersed instrumentation, it is important to know which type of radioactive decay is produced by each isotope as well as the total energy it releases. For instance, an alpha decay from an isotope in the U or Th decay chain will deposit its full energy into the detector if it occurs in the active region of the detector, but will deposit no energy if it occurs inside of some macroscopically thick piece of support material because of its very short range ($\lesssim$1 µm) in most solids. This requires different accounting for energy depositions from intrinsic radioactive contamination measured in different locations (or groups of locations). This is clearly a tractable problem, but one which must be handled with care and forethought.

Since a large body of work has been compiled on the control of radiological background in previous experiments that have encountered similar conditions, much of the work in this area will be cited from these experiments (e.g., DARKSIDE [229], EXO [230], ICARUS, BOREXINO, KamLAND and Super–Kamiokande). Work remains, however, on understanding the background particular to the LBNE far detector location/depth (e.g., radon levels and dust activity, for instance), and on integrating existing and new work into the LBNE simulation, reconstruction and analysis framework.

6.4 Summary of Core-Collapse Supernova Sensitivities

LBNE, with its high-resolution LArTPC far detector, is uniquely sensitive to the ν_e component of the neutrino flux from a core-collapse supernova within our galaxy. The ν_e component of the neutrino flux dominates the initial neutronization burst of the supernova. Preliminary studies indicate that such a supernova at a distance of 10 kpc would produce ∼3,000 events in a 34−kt LArTPC. The time dependence of the signal will allow differentiation between different neutrino-driven core-collapse dynamical models, and will exhibit a discernible dependence on the neutrino mass hierarchy.

A low energy threshold of $\sim 5\,\mathrm{MeV}$ will enable the detector to extract the rich information available from the ν_e supernova flux. LBNE's photon detection system is being designed to provide a high-efficiency trigger for supernova events. Careful design and quality control of the detector materials will minimize low-energy background from radiological contaminants.

Chapter 7 Precision Measurements with a High-Intensity Neutrino Beam

The LBNE near neutrino detector provides scientific value beyond its essential role of calibrating beam and neutrino interaction properties for the long-baseline physics program described in Chapter 4. By virtue of the theoretically clean, purely weak leptonic processes involved, neutrino beams have historically served as unique probes for new physics in their interactions with matter. The high intensity and broad energy range of the LBNE beam will open the door for a highly capable near detector to perform its own diverse program of incisive investigations.

The reduction of systematic uncertainties for the neutrino oscillation program requires excellent resolution in the reconstruction of neutrino events. Combined with the unprecedented neutrino fluxes available — which will allow the collection of $\mathcal{O}(10^8)$ inclusive neutrino charged current (CC) interactions for 10^{22} protons-on-target (POT) just downstream of the beamline — the near detector (ND) will significantly enhance the LBNE long-baseline oscillation program and produce a range of short-baseline neutrino scattering physics measurements. The combined statistics and resolution expected in the ND will allow precise tests of fundamental interactions resulting in a better understanding of the structure of matter.

Table 7.1 lists the expected number of beam-neutrino interactions per ton of detector at the LBNE ND site, located 459 m downstream from the target.

This chapter presents a short description of some of the studies that can be performed with LBNE's fine-grained near neutrino detector and gives a flavor of the outstanding physics potential. A more detailed and complete discussion of the ND physics potential can be found in [129].

Appendix B describes neutrino scattering kinematics and includes definitions of the kinematic variables used in this chapter.

7.1 Precision Measurements with Long-Baseline Oscillations

From the studies of uncertainties and the impact of the spectral shape presented in Section 4.3.2, it is evident that to fully realize the goals of the full LBNE scientific program — in particular, sensitivity to CP violation and the precision measurement of the three-flavor oscillation parameters — it is necessary to characterize the expected unoscillated neutrino flux with high precision. In addition to the precise determination of the neutrino flux, shape and flavor composition, the char-

Table 7.1: Estimated interaction rates in the neutrino (second column) and antineutrino (third column) beams per ton of detector (water) for 1×10^{20} POT at 459 m assuming neutrino cross-section predictions from NUANCE [231] and a 120−GeV proton beam using the CDR reference design. Processes are defined at the initial neutrino interaction vertex and thus do not include final-state effects. These estimates do not include detector efficiencies or acceptance [232,233].

Production mode	ν_μ Events	$\overline{\nu}_\mu$ Events
CC QE ($\nu_\mu n \to \mu^- p$)	50,100	26,300
NC elastic ($\nu_\mu N \to \nu_\mu N$)	18,800	8,980
CC resonant π^+ ($\nu_\mu N \to \mu^- N \pi^+$)	67,800	0
CC resonant π^- ($\overline{\nu}_\mu N \to \mu^+ N \pi^-$)	0	20,760
CC resonant π^0 ($\nu_\mu n \to \mu^- \, p \, \pi^0$)	16,200	6,700
NC resonant π^0 ($\nu_\mu N \to \nu_\mu \, N \, \pi^0$)	16,300	7,130
NC resonant π^+ ($\nu_\mu p \to \nu_\mu \, n \, \pi^+$)	6,930	3,200
NC resonant π^- ($\nu_\mu n \to \nu_\mu \, p \, \pi^-$)	5,980	2,570
CC DIS ($\nu_\mu N \to \mu^- X$ or $\overline{\nu}_\mu N \to \mu^+ X, W > 2$)	66,800	13,470
NC DIS ($\nu_\mu N \to \nu_\mu X$ or $\overline{\nu}_\mu N \to \overline{\nu}_\mu X, W > 2$)	24,100	5,560
NC coherent π^0 ($\nu_\mu A \to \nu_\mu A \pi^0$ or $\overline{\nu}_\mu A \to \overline{\nu}_\mu A \pi^0$)	2,040	1,530
CC coherent π^+ ($\nu_\mu A \to \mu^- A \pi^+$)	3,920	0
CC coherent π^- ($\overline{\nu}_\mu A \to \mu^+ A \pi^-$)	0	2,900
NC resonant radiative decay ($N^* \to N\gamma$)	110	50
NC elastic electron ($\nu_\mu e^- \to \nu_\mu e^-$ or $\overline{\nu}_\mu e^- \to \overline{\nu_\mu} e^-$)	30	17
Inverse Muon Decay ($\nu_\mu e \to \mu^- \nu_e$)	12	0
Other	42,600	15,800
Total CC (rounded)	**236,000**	**81,000**
Total NC+CC (rounded)	**322,000**	**115,000**

acterization of different neutrino interactions and interaction cross sections on a liquid argon target is necessary to estimate physics backgrounds to the oscillation measurements. The high-resolution near tracking detector described in Section 3.5 can measure the unoscillated flux normalization, shape and flavor to a few percent using systematically independent techniques that are discussed in the following sections.

7.1.1 Determination of the Relative Neutrino and Antineutrino Flux

The most promising method of determining the shape of the ν_μ and $\overline{\nu}_\mu$ flux is by measuring CC events with low hadronic-energy deposition (low-ν) where ν is the total energy of the hadrons that are produced after a neutrino interaction, $E_\nu - E_\mu$. It is important to note that not all the hadrons escape the remnant nucleus, and intranuclear effects will smear the visible energy of the hadronic system. A method of relative flux determination known as low-ν_0 — where ν_0 is a given value of visible hadronic energy in the interaction that is selected to minimize the fraction of the total interaction energy carried by the hadronic system — is well developed [234]. The method follows from the general expression of the ν-nucleon differential cross section:

$$\mathcal{N}(\nu < \nu_0) \simeq C\Phi(E_\nu)\nu_0 \left[\mathcal{A} + \left(\frac{\nu_0}{E_\nu}\right)\mathcal{B} + \left(\frac{\nu_0}{E_\nu}\right)^2 \mathcal{C} + \mathcal{O}\left(\frac{\nu_0}{E_\nu}\right)^3\right], \tag{7.1}$$

where the coefficients are $\mathcal{A} = \mathcal{F}_2, \mathcal{B} = (\mathcal{F}_2 \pm \mathcal{F}_3)/2, \mathcal{C} = (\mathcal{F}_2 \mp \mathcal{F}_3)/6$, and $\mathcal{F}_i = \int_0^1 \int_0^{\nu_0} F_i(x) dx d\nu$ is the integral of structure function $F_i(x)$. The dynamics of neutrino-nucleon scattering implies that the number of events in a given energy bin with hadronic energy $E_{\text{had}} < \nu_0$ is proportional to the (anti)neutrino flux in that energy bin up to corrections $\mathcal{O}(\nu_0/E_\nu)$ and $\mathcal{O}(\nu_0/E_\nu)^2$. The number $\mathcal{N}(\nu < \nu_0)$ is therefore proportional to the flux up to correction factors of the order $\mathcal{O}(\nu_0/E_\nu)$ or smaller, which are not significant for small values of ν_0 at energies $\geq \nu_0$. The coefficients $\mathcal{A}$, $\mathcal{B}$ and $\mathcal{C}$ are determined for each energy bin and neutrino flavor within the ND data.

LBNE's primary interest is the relative flux determination, i.e., the neutrino flux in one energy bin relative to that in another; variations in the coefficients do not affect the relative flux. The prescription for the relative flux determination is simple: count the number of neutrino CC events below a certain small value of hadronic energy (ν_0). The observed number of events, up to the correction of the order $\mathcal{O}(\nu_0/E_\nu)$ due to the finite ν_0 in each total visible energy bin, is proportional to the relative flux. The smaller the factor ν_0/E_ν is, the smaller is the correction. Furthermore, the energy of events passing the low-ν_0 cut is dominated by the corresponding lepton energy.

It is apparent from the above discussion that this method of relative flux determination is not very sensitive to nucleon structure, QCD corrections or types of neutrino interactions such as scaling or nonscaling. With the excellent granularity and resolution foreseen in the low-density magnetized tracker, it will be possible to use a value of ν_0 ~0.5 GeV or lower, thus allowing flux predictions down to E_ν ~0.5 GeV. A preliminary analysis with the high-resolution tracker achieved a precision $\leq 2\%$ on the relative ν_μ flux with the low-ν_0 method in the energy region $1 \leq E_\nu \leq 30$ GeV in the fit with $\nu_0 < 0.5$ GeV. Similar uncertainties are expected for the $\overline{\nu}_\mu$ component (the dominant one) in the antineutrino beam mode (negative focusing).

7.1.2 Determination of the Flavor Content of the Beam: $\nu_\mu, \overline{\nu}_\mu, \nu_e, \overline{\nu}_e$

The empirical parameterization of the pion and kaon neutrino parents produced from the proton target, determined from the low-ν_0 flux at the ND, allows prediction of the ν_μ and $\overline{\nu}_\mu$ flux at the far detector location. This parameterization provides a measure of the $\pi^+/K^+/\mu^+(\pi^-/K^-/\mu^-)$ distributions of neutrino parents of the beam observed in the ND. Additionally, with the capability to identify $\overline{\nu}_e$ CC interactions, it is possible to directly extract the elusive K_L^0 content of the beam. Therefore, an accurate measurement of the $\nu_\mu, \overline{\nu}_\mu$ and $\overline{\nu}_e$ CC interactions provides a prediction of the ν_e content of the beam, which is an irreducible background for the ν_e appearance search in the far detector:

$$\nu_e \equiv \mu^+(\pi^+ \to \nu_\mu) \oplus K^+(K^+ \to \nu_\mu) \oplus K^0_L \tag{7.2}$$
$$\overline{\nu}_e \equiv \mu^-(\pi^- \to \overline{\nu}_\mu) \oplus K^-(K^- \to \overline{\nu}_\mu) \oplus K^0_L \tag{7.3}$$

The μ component is well constrained from $\nu_\mu(\overline{\nu}_\mu)$ CC data at low energy, while the $K^\pm$ component is only partially constrained by the $\nu_\mu(\overline{\nu}_\mu)$ CC data at high energy and requires external hadro-production measurements of $K^\pm/\pi^\pm$ ratios at low energy from hadro-production experiments such as MIPP [235] and NA61 [162]. Finally, the K^0_L component can be constrained by the $\overline{\nu}_e$ CC data and by external dedicated measurements at hadron-production experiments. In the energy range $1(5) \leq E_\nu \leq 5(15)$ GeV, the approximate relative contributions to the ν_e spectrum are 85% (55%) from μ^+, 10% (30%) from K^+ and 3% (15%) from K^0_L.

Based on the NOMAD experience, a precision of $\leq 0.1\%$ on the flux ratio ν_e/ν_μ is expected at high energies. Taking into account the projected precision of the ν_μ flux discussed in Section 7.1.1, this translates into an absolute prediction for the ν_e flux at the level of 2%.

Finally, the fine-grained ND can directly identify ν_e CC interactions from the LBNE beam. The relevance of this measurement is twofold:

1. It provides an independent validation for the flux predictions obtained from the low-ν_0 method.

2. It can further constrain the uncertainty on the knowledge of the absolute ν_e flux.

7.1.3 Constraining the Unoscillated ν Spectral Shape with the QE Interaction

In any long-baseline neutrino oscillation program, including LBNE, the quasi-elastic (QE) interactions are special. First, the QE cross section is substantial at lower energies [236]. Second, because of the simple topology (a μ^- and a proton), the visible interaction energy provides, to first order, a close approximation to the neutrino energy (E_ν). In the context of a fine-grained tracker, a precise measurement of QE will impose direct constraints on nuclear effects related to both the primary and final-state interaction (FSI) dynamics (Section 7.6), which can affect the overall neutrino energy scale and, thus, the entire oscillation program. To this end, the key to reconstructing a high-quality sample of ν_μ QE interactions is the two-track topology where both final-state particles are visible: μ^- and p. A high-resolution ND can efficiently identify the recoil proton and measure its momentum vector as well as dE/dx. Preliminary studies indicate that in a fine-grained tracking detector the efficiency (purity) for the proton reconstruction in QE events is 52% (82%). A comparison between the neutrino energy reconstructed from the muon momentum through the QE kinematics (assuming a free target nucleon) with the visible neutrino energy measured as the sum of μ and p energies is sensitive to both nuclear effects and FSI. Furthermore, comparing the two-track sample

(μ and p) with the single-track sample (in which only μ is reconstructed) empirically constrains the rate of FSI.

7.1.4 Low-Energy Absolute Flux: Neutrino-Electron NC Scattering

Neutrino neutral current (NC) interaction with the atomic electron in the target, $\nu_\mu e^- \to \nu_\mu e^-$, provides an elegant measure of the absolute flux. The total cross section for NC elastic scattering off electrons is given by [237]:

$$\sigma(\nu_l e \to \nu_l e) = \frac{G_\mu^2 m_e E_\nu}{2\pi}\left[1 - 4\sin^2\theta_W + \frac{16}{3}\sin^4\theta_W\right], \tag{7.4}$$

$$\sigma(\overline{\nu}_l e \to \overline{\nu}_l e) = \frac{G_\mu^2 m_e E_\nu}{2\pi}\left[\frac{1}{3} - \frac{4}{3}\sin^2\theta_W + \frac{16}{3}\sin^4\theta_W\right], \tag{7.5}$$

where θ_W is the weak mixing angle (WMA). For the currently known value of $\sin^2\theta_W \simeq 0.23$, the above cross sections are very small: $\sim 10^{-42}(E_\nu/\mathrm{GeV})$ cm^2. The NC elastic scattering off electrons can be used to determine the absolute flux normalization since the cross section only depends on the knowledge of $\sin^2\theta_W$. Within the Standard Model, the value of $\sin^2\theta_W$ at the average momentum transfer expected at LBNE, $Q \sim 0.07$ GeV, can be extrapolated down from the LEP/SLC* measurements with a precision of $\leq 1\%$. The $\nu_\mu e^- \to \nu_\mu e^-$ will produce a single e^- collinear with the ν-beam (≤ 40 mrad). The background, dominated by the asymmetric conversion of a photon in an ordinary ν-nucleon NC event, will produce e^- and e^+ in equal measure with much broader angular distribution. A preliminary analysis of the expected elastic scattering signal in the high-resolution tracking ND shows that the scattering signal can be selected with an efficiency of about 60% with a small background contaminant. The measurement will be dominated by the statistical error. The determination of the absolute flux of the LBNE neutrinos is estimated to reach a precision of $\simeq 2.5\%$ for $E_\nu \leq 10$ GeV. The measurement of NC elastic scattering off electrons can only provide the integral of all neutrino flavors.

7.1.5 High-Energy Absolute Flux: Neutrino-Electron CC Scattering

The ν_μ-e^- CC interaction, $\nu_\mu + e^- \to \mu^- + \nu_e$ (*inverse muon decay* or *IMD*), offers an elegant way to determine the absolute flux. Given the energy threshold needed for this process, IMD requires $E_\nu \geq 10.8$ GeV. The high-resolution ND in the LBNE neutrino beam will observe $\geq$ 2,000 IMD events in three years. The reconstruction efficiency of the single, energetic forward μ^- will be $\geq$ 98%; the angular resolution of the IMD μ is ≤ 1 mrad. The background, primarily from the ν_μ-QE interactions, can be precisely constrained using control samples. In particular, the systematic limitations of the CCFR ([238,239]) and the CHARM-II [240] IMD measurements can be

*LEP was the Large Electron-Positron Collider at CERN that operated from 1989 to 2000 and provided a detailed study of the electroweak interaction.

substantially alleviated in LBNE with the proposed ND design. A preliminary analysis indicates that the absolute flux can be determined with an accuracy of $\approx 3\%$ for $E_\nu \geq 11\,\text{GeV}$ (average $E_\nu \approx 25\,\text{GeV}$).

7.1.6 Low-Energy Absolute Flux: QE in Water and Heavy-Water Targets

Another independent method to extract the absolute flux is through the QE-CC scattering ($\nu_\mu n(p) \to \mu^- p(n)$) on deuterium at low Q^2. Neglecting terms in $(m_\mu/M_n)^2$ at $Q^2 = 0$, the QE cross section is independent of neutrino energy for $(2E_\nu M_n)^{1/2} > m_\mu$:

$$\frac{d\sigma}{dQ^2} \mid Q^2 = 0 \mid = \frac{G_\mu^2 \cos^2\theta_c}{2\pi} \left[F_1^2(0) + G_A^2(0) \right] = 2.08 \times 10^{-38}\ \text{cm}^2\text{GeV}^{-2}, \tag{7.6}$$

which is determined by neutron β decay and has a theoretical uncertainty $< 1\%$. The flux can be extracted experimentally by measuring low Q^2 QE interactions (≤ 0.05 GeV) and extrapolating the result to the limit of $Q^2 = 0$. The measurement requires a deuterium (or hydrogen for antineutrino) target to minimize the smearing due to Fermi motion and other nuclear effects. This requirement can only be achieved by using both H_2O and D_2O targets embedded in the fine-grained tracker and extracting the events produced in deuterium by statistical subtraction of the larger oxygen component. The experimental resolution on the muon and proton momentum and angle is crucial. Dominant uncertainties of the method are related to the extrapolation to $Q^2 = 0$, to the theoretical cross section on deuterium, to the experimental resolution and to the statistical subtraction. Sensitivity studies and the experimental requirements are under study.

7.1.7 Neutral Pions, Photons and $\pi^\pm$ in NC and CC Events

The principal background to the ν_e and $\overline{\nu}_e$ appearance comes from the NC events where a photon from the π^0 decay produces a signature similar to that produced by ν_e-induced electron; the second source of background is due to π^0's from ν_μ CC where the μ^- evades identification — typically at high y_{Bj}. Since the energy spectra of NC and CC interactions are different, it is critical for the ND to measure π^0's in NC and CC interactions in the full kinematic phase space.

The proposed ND is designed to measure π^0's with high accuracy in three topologies:

1. Both photons convert in the tracker ($\simeq$25%).
2. One photon converts in the tracker and the other in the calorimeter ($\simeq$50%).
3. Both photons convert in the calorimeter; the first two topologies afford the best resolution because the tracker provides precise γ-direction measurement.

The π^0 reconstruction efficiency in the proposed fine-grained tracker is expected to be $\geq 75\%$ if photons that reach the ECAL are included. By contrasting the π^0 mass in the tracker versus in the calorimeter, the relative efficiencies of photon reconstruction will be well constrained.

Finally, the $\pi^{\pm}$ track momentum and dE/dx information will be measured by the tracker. An in situ determination of the charged pions in the $\nu_\mu/\overline{\nu}_\mu$ CC events — with μID and without μID — and in the ν NC events is crucial to constrain the systematic error associated with the $\nu_\mu(\,\overline{\nu}_\mu)$ disappearance, especially at low E_ν.

7.1.8 Signal and Background Predictions for the Far Detector

In order to achieve reliable predictions for signal and backgrounds in the far detector, near detector measurements — including (anti)neutrino fluxes, nuclear cross sections and detector smearing — must be unfolded and extrapolated to the far detector location. The geometry of the beam and detectors (point source versus extended source) as well as the expected neutrino oscillations imply differences in the (anti)neutrino fluxes in the near and far detectors. These differences, in turn, will result in increased sensitivity of the long-baseline analysis to cross-section uncertainties, in particular between neutrinos and antineutrinos and for exclusive background topologies. Furthermore, the much higher event rates at the near site and the smaller detector size (i.e., reduced containment) make it virtually impossible to achieve identical measurement conditions in both the near and far detectors. However, as discussed in Sections 7.1.1 to 7.1.7, the energy, angular and space resolution of the low-density ND are key factors in reducing the systematic uncertainties achievable on the event predictions for the far detector; the ND can offer a precise *in situ* measurement of the absolute flux of all flavor components of the beam, $\nu_\mu, \nu_e, \bar{\nu}_\mu, \bar{\nu}_e$, resulting in constraints on the parent $\pi^{\pm}/K^{\pm}/\mu^{\pm}$ distributions. In addition, measurements of momenta and energies of final-state particles produced in (anti)neutrino interactions will allow a detailed study of exclusive topologies affecting the signal and background rates in the far detector. All of these measurements will be used to cross-check and fine-tune the simulation programs needed for the actual extrapolation from the near to the far detector.

It is important to note that several of these techniques have already been used and *proven to work* in neutrino experiments such as MINOS [155] and NOMAD [156,157,241]. The higher segmentation and resolution in the LBNE ND with respect to past experiments will increase the available information about the (anti)neutrino event topologies, allowing further reduction of systematic uncertainties both in the ND measurements and in the Monte Carlo extrapolation.

For a more detailed discussion of the impact of ND measurements on the long-baseline oscillation analysis see Section 4.3.2.

7.2 Electroweak Precision Measurements

Neutrinos and antineutrinos are the most effective probes for investigating electroweak physics. Interest in a precise determination of the weak mixing angle ($\sin^2\theta_W$) at LBNE energies via neutrino scattering is twofold: (1) it provides a direct measurement of neutrino couplings to the Z boson and (2) it probes a different scale of momentum transfer than LEP did by virtue of not being at the Z boson mass peak.

The weak mixing angle can be extracted experimentally from three main NC physics processes:

1. deep inelastic scattering off quarks inside nucleons: $\nu N \to \nu X$
2. elastic scattering off electrons: $\nu e^- \to \nu e^-$
3. elastic scattering off protons: $\nu p \to \nu p$

Figure 7.1 shows the Feynman diagrams corresponding to the three processes.

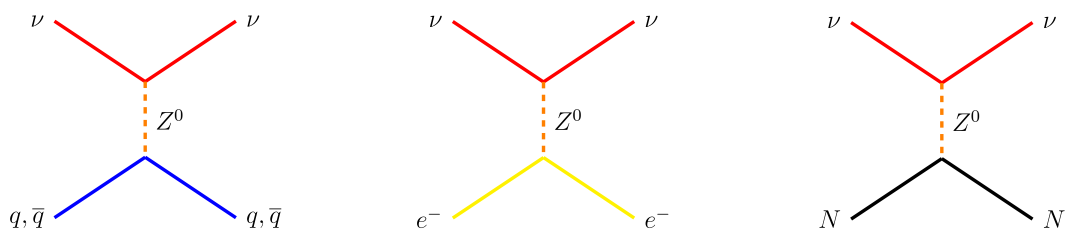

Figure 7.1: Feynman diagrams for the three main neutral current processes that can be used to extract $\sin^2\theta_W$ with the LBNE near detector. From left, deep inelastic scattering off quarks, elastic scattering off electrons and elastic scattering off nucleons.

7.2.1 Deep Inelastic Scattering

The most precise measurement of $\sin^2\theta_W$ in neutrino deep inelastic scattering (DIS) comes from the NuTeV experiment, which reported a value that is 3σ from the Standard Model [242]. The LBNE ND can perform a similar analysis in the DIS channel by measuring the ratio of NC and CC interactions induced by neutrinos:

$$\mathcal{R}^\nu \equiv \frac{\sigma^\nu_{\rm NC}}{\sigma^\nu_{\rm CC}} \simeq \rho^2 \left(\frac{1}{2} - \sin^2\theta_W + \frac{5}{9}(1+r)\sin^4\theta_W \right). \tag{7.7}$$

Here ρ is the relative coupling strength of the neutral-to-charged current interactions ($\rho = 1$ at tree-level in the Standard Model) and r is the ratio of antineutrino to neutrino cross section ($r \sim 0.5$).

The absolute sensitivity of $\mathcal{R}^\nu$ to $\sin^2\theta_W$ is 0.7, which implies that a measurement of $\mathcal{R}^\nu$ to 1% precision would in turn provide a 1.4% precision on $\sin^2\theta_W$. This technique was used by the CDHS [243], CHARM [244] and CCFR [245] experiments. In contrast to the NuTeV experiment, the antineutrino interactions cannot be used for this analysis at LBNE due to the large number of ν_μ DIS interactions in the $\overline{\nu}_\mu$ beam compared to the $\overline{\nu}_\mu$ DIS interactions.

The measurement of $\sin^2\theta_W$ from DIS interactions can only be performed with a low-density magnetized tracker since an accurate reconstruction of the NC event kinematics and of the ν CC interactions are crucial for keeping the systematic uncertainties on the event selection under control. The analysis selects events in the ND after imposing a cut on the visible hadronic energy of $E_{\rm had} > 5\,\text{GeV}$ (the CHARM analysis had $E_{\rm had} > 4\,\text{GeV}$). With an exposure of 5×10^{21} POT in the 120$-$GeV beam using the CDR reference design, about 7.7×10^6 CC events and 2.4×10^6 NC events are expected, giving a statistical precision of 0.074% on $\mathcal{R}^\nu$ and 0.1% on $\sin^2\theta_W$ (Table 7.2).

The use of a low-density magnetized tracker can substantially reduce systematic uncertainties compared to a massive calorimeter. Table 7.2 shows a comparison of the different uncertainties on the measured $\mathcal{R}^\nu$ between NuTeV and LBNE. While NuTeV measured both $\mathcal{R}^\nu$ and $\mathcal{R}^{\overline{\nu}}$, the largest experimental uncertainty in the measurement of $\mathcal{R}^\nu$ is related to the subtraction of the ν_e CC contamination from the NC sample. Since the low-density tracker at LBNE can efficiently reconstruct the electron tracks, the ν_e CC interactions can be identified on an event-by-event basis, reducing the corresponding uncertainty to a negligible level. Similarly, uncertainties related to the location of the interaction vertex, noise, counter efficiency and so on are removed by the higher resolution and by changing the analysis selection. The experimental selection at LBNE will be dominated by two uncertainties: the knowledge of the $\overline{\nu}_\mu$ flux and the kinematic selection of NC interactions. The former is relevant due to the larger NC/CC ratio for antineutrinos. The total experimental systematic uncertainty on $\sin^2\theta_W$ is expected to be about 0.14%.

The measurement of $\mathcal{R}^\nu$ will be dominated by theoretical systematic uncertainties on the structure functions of the target nucleons. The estimate of these uncertainties for LBNE is based upon the extensive work performed for the NOMAD analysis and includes a Next-to-Next-Leading-Order (NNLO) QCD calculation of structure functions (NLO for charm production) [246,247,248], parton distribution functions (PDFs) extracted from dedicated low-Q global fits, high-twist contributions [246], electroweak corrections [249] and nuclear corrections [250,251,252]. The charm quark production in CC, which has been the dominant source of uncertainty in all past determinations of $\sin^2\theta_W$ from νN DIS, is reduced to about 4% of the total ν_μ CC DIS for $E_{\rm had} > 5$ GeV with the low-energy beam spectrum at LBNE. This number translates into a systematic uncertainty of 0.14% on $\mathcal{R}^\nu$ (Table 7.2), assuming the current knowledge of the charm production cross section. It is worth noting that the recent measurement of charm dimuon production by the NOMAD experiment allowed a reduction of the uncertainty on the strange sea distribution to $\sim 3\%$ and on the charm quark mass m_c to ~ 75 MeV [241]. The lower neutrino energies available at LBNE reduce

Table 7.2: Comparison of uncertainties on the $\mathcal{R}^{\nu}$ measurement between NuTeV and LBNE with a 5 t fiducial mass after an exposure of 5×10^{21} POT (5 year) with the CDR reference 120−GeV beam. The corresponding relative uncertainties on $\sin^2\theta_W$ must be multiplied by a factor of 1.4, giving for LBNE a projected overall precision of 0.35%.

Source of uncertainty	$\delta R^{\nu}/R^{\nu}$ NuTeV	$\delta R^{\nu}/R^{\nu}$ LBNE	Comments
Data statistics	0.00176	0.00074	
Monte Carlo statistics	0.00015		
Total Statistics	*0.00176*	*0.00074*	
$\nu_e, \overline{\nu}_e$ **flux** ($\sim$ **1.7%**)	0.00064	0.00010	e^-/e^+ identification
Energy measurement	0.00038	0.00040	
Shower length model	0.00054	n.a.	
Counter efficiency, noise	0.00036	n.a.	
Interaction vertex	0.00056	n.a.	
$\overline{\nu}_\mu$ **flux**	n.a.	0.00070	Large $\bar{\nu}$ contamination
Kinematic selection	n.a.	0.00060	Kinematic identification of NC
Experimental systematics	*0.00112*	*0.00102*	
d,s→c, s-sea	0.00227	0.00140	Based on existing knowledge
Charm sea	0.00013	n.a.	
$r = \sigma^{\overline{\nu}}/\sigma^{\nu}$	0.00018	n.a.	
Radiative corrections	0.00013	0.00013	
Non-isoscalar target	0.00010	N.A.	
Higher twists	0.00031	0.00070	Lower Q^2 values
R_L (F_2, F_T, xF_3)	0.00115	0.00140	Lower Q^2 values
Nuclear correction		0.00020	
Model systematics	*0.00258*	*0.00212*	
Total	**0.00332**	**0.00247**	

the accessible Q^2 values with respect to NuTeV, increasing in turn the effect of non-perturbative contributions (high twists) and R_L. The corresponding uncertainties are reduced by the recent studies of low-Q structure functions and by improved modeling with respect to the NuTeV analysis (NNLO vs. LO). The total model systematic uncertainty on $\sin^2\theta_W$ is expected to be about 0.21% with the reference beam configuration. The corresponding total uncertainty on the value of $\sin^2\theta_W$ extracted from νN DIS is 0.35%.

Most of the model uncertainties will be constrained by dedicated in situ measurements using the large CC samples and employing improvements in theory that will have evolved over the course of the experiment. The low-density tracker will collect about 350,000 neutrino-induced inclusive charm events in a five-year run with the 120−GeV 1.2−MW beam. The precise reconstruction of charged tracks will allow measurement of exclusive decay modes of charmed hadrons (e.g., D^{*+}) and measurement of charm fragmentation and production parameters. The average semileptonic branching ratio B_μ is of order 5% with the low-energy LBNE beam, and the low-density ND will be able to reconstruct both the $\mu\mu$ and μe decay channels. Currently, the most precise sample of 15,400 dimuon events has been collected by the NOMAD experiment. Finally, precision measurements of CC structure functions in the LBNE ND would further reduce the uncertainties on PDFs and on high-twist contributions.

The precision that can be achieved from νN DIS interactions is limited by both the event rates and the energy spectrum of the standard beam configuration. The high-statistics beam exposure with the low-energy default beam-running configuration (described in Chapter 3) combined with a dedicated run with the high-energy beam option would increase the statistics by more than a factor of ten. This major step forward would not only reduce the statistical uncertainty to a negligible level, but would provide large control samples and precision auxiliary measurements to reduce the systematic uncertainties on structure functions. The two dominant systematic uncertainties, charm production in CC interactions and low Q^2 structure functions, are essentially defined by the available data at present. Overall, the use of a high-energy beam with upgraded intensity can potentially improve the precision achievable on $\sin^2\theta_W$ from νN DIS to better than 0.2%.

7.2.2 Elastic Scattering

A second independent measurement of $\sin^2\theta_W$ can be obtained from NC $\nu_\mu e$ elastic scattering. This channel has lower systematic uncertainties since it does not depend on knowledge of the structure of nuclei, but it has limited statistics due to its very low cross section. The value of $\sin^2\theta_W$ can be extracted from the ratio of interactions [237] as follows:

$$\mathcal{R}_{\nu e}(Q^2) \equiv \frac{\sigma(\overline{\nu}_\mu e \to \overline{\nu}_\mu e)}{\sigma(\nu_\mu e \to \nu_\mu e)}(Q^2) \simeq \frac{1 - 4\sin^2\theta_W + 16\sin^4\theta_W}{3 - 12\sin^2\theta_W + 16\sin^4\theta_W}, \tag{7.8}$$

in which systematic uncertainties related to the selection and the electron identification cancel out. The absolute sensitivity of this ratio to $\sin^2\theta_W$ is 1.79, which implies that a measurement of $\mathcal{R}_{\nu e}$ to 1% precision would provide a measurement of $\sin^2\theta_W$ to 0.65% precision.

The best measurement of NC elastic scattering off electrons was performed by CHARM II, which observed $2677{\pm}82$ ν and $2752{\pm}88$ $\overline{\nu}$ events [253]. The CHARM II analysis was characterized by a sizable uncertainty related to the extrapolation of the background into the signal region.

The event selection for NC elastic scattering is described in Section 7.1.4. Since the NC elastic scattering off electrons is also used for the absolute flux normalization, the WMA analysis can be performed only with the low-density, magnetized tracker in conjunction with a large liquid argon detector. In the case of the flux normalization measurement, the total reconstructed statistics is limited to about 4,500 (2,800) $\nu(\bar{\nu})$ events. These numbers do not allow a competitive determination of $\sin^2\theta_W$ by using the magnetized tracker alone. However, a 100$-$t liquid argon detector in the ND would be expected to collect about 90,000 (60,000) reconstructed $\nu(\overline{\nu})$ events with the standard beam, and an additional factor of two with an upgraded 2.3$-$MW beam.

A combined analysis of both detectors can achieve the optimal sensitivity: the fine-grained tracker is used to reduce systematic uncertainties (measurement of backgrounds and calibration), while the liquid argon detector provides the statistics required for a competitive measurement. Overall, the use of the complementary liquid argon detector can provide a statistical accuracy on $\sin^2\theta_W$ of about 0.3%. However, the extraction of the WMA is dominated by the systematic uncertainty on the $\overline{\nu}_\mu/\nu_\mu$ flux ratio in Equation (7.8). This uncertainty has been evaluated with the low-ν_0 method for the flux extraction and a systematic uncertainty of about 1% was obtained on the ratio of the $\overline{\nu}_\mu/\nu_\mu$ flux integrals. An improved precision on this quantity could be achieved from a measurement of the ratios π^-/π^+ and ρ^-/ρ^+ from coherent production in the fine-grained tracker. Due to the excellent angular and momentum resolution and to large cancellations of systematic uncertainties, preliminary studies indicate that an overall precision of about 0.3% can be achieved on the $\overline{\nu}_\mu/\nu_\mu$ flux ratio using coherent production.

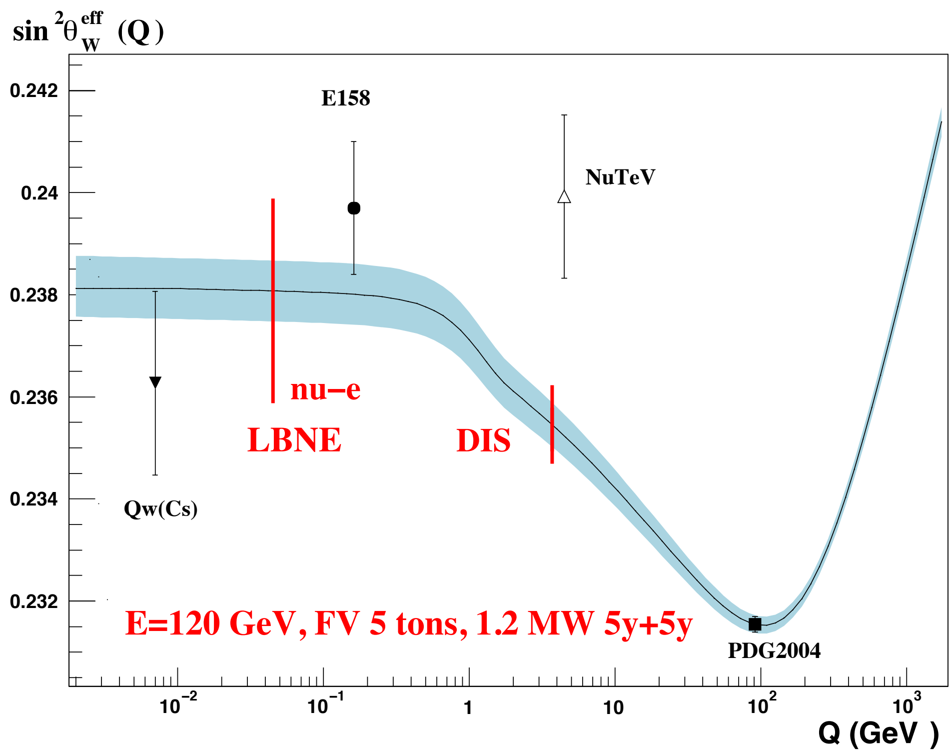

Figure 7.2: Expected sensitivity to the measurement of $\sin^2\theta_W$ from the LBNE ND with the reference 1.2−MW beam and an exposure of 5×10^{21} POT with a neutrino beam (five years) and 5×10^{21} POT with an antineutrino beam (five years). The curve shows the Standard Model prediction as a function of the momentum scale [254]. Previous measurements from Atomic Parity Violation [255,256], Moeller scattering (E158 [257]), ν DIS (NuTeV [242]) and the combined Z pole measurements (LEP/SLC) [256] are also shown for comparison. The use of a high-energy beam tune can reduce the LBNE uncertainties by almost a factor of two.

Together, the DIS and the NC elastic scattering channels involve substantially different scales of momentum transfer, providing a tool to test the running of $\sin^2\theta_W$ in a single experiment. To this end, the study of NC elastic scattering off protons can provide additional information since it occurs at a momentum scale that is intermediate between the two other processes. Figure 7.2 summarizes the target sensitivity from the LBNE ND, compared with existing measurements as a function of the momentum scale.

In the near future, another precision measurement of $\sin^2\theta_W$ is expected from the $Q_{\rm weak}$ experiment [258] at Jefferson Laboratory. From the measurement of parity-violating asymmetry in elastic electron-proton scattering, the $Q_{\rm weak}$ experiment should achieve a precision of 0.3% on $\sin^2\theta_W$ at $Q^2 = 0.026$ GeV^2. It should be noted that the $Q_{\rm weak}$ measurement is complementary to those from neutrino scattering given the different scale of momentum transfer and the fact that neutrino measurements are the only direct probe of the Z coupling to neutrinos. With the 12$-$GeV upgrade of Jefferson Laboratory, the Q_{weak} experiment [259] could potentially reach precisions on the order of 0.2-0.1 %.

7.3 Observation of the Nucleon's Strangeness Content

The strange-quark content of the proton and its contribution to the proton spin remain enigmatic [260]. The question is whether the strange quarks contribute substantially to the vector and axial-vector currents of the nucleon. A large observed value of the strange-quark contribution to the nucleon spin (axial current), Δs, would enhance our understanding of the proton structure.

The spin structure of the nucleon also affects the couplings of axions and supersymmetric particles to dark matter.

7.3.1 Strange Form Factors of Nucleons

The strange quark *vector* elastic form factors[†] of the nucleon have been measured to high precision in parity-violating electron scattering (PVES) at Jefferson Lab, Mainz and elsewhere. A recent global analysis [261] of PVES data finds a strange magnetic moment $\mu_s = 0.37 \pm 0.79$ (in units of the nucleon magneton), so that the strange quark contribution to proton magnetic moment is less than 10%. For the strange electric charge radius parameter, ρ_s, one finds a very small value, $\rho_s = -0.03 \pm 0.63$ GeV^{-2}, consistent with zero. Both results are consistent with theoretical expectations based on lattice QCD and phenomenology [262].

[†]Nucleon form factors describe the scattering amplitudes off different partons in a nucleon. They are usually given as a function of Q^2 the momentum transfer to the nucleon from the scattering lepton (since the structure of the nucleon looks different depending on the energy of the probe).

In contrast, the strange *axial vector* form factors are poorly determined. A global study of PVES data [261] finds $\widetilde{G}_A^N(Q^2) = \widetilde{g}_A^N \left(1 + Q^2/M_A^2\right)^2$, where $M_A = 1.026$ GeV is the axial dipole mass, with the effective proton and neutron axial charges $\widetilde{g}_A^p = -0.80 \pm 1.68$ and $\widetilde{g}_A^n = 1.65 \pm 2.62$.

The strange quark axial form factor at $Q^2 = 0$ is related to the *spin* carried by strange quarks, Δs. Currently the world data on the spin-dependent g_1 structure function constrain Δs to be ≈ -0.055 at a scale $Q^2 = 1$ GeV^2, with a significant fraction coming from the region $x < 0.001$.

An independent extraction of Δs, which does not rely on the difficult measurements of the g_1 structure function at very small values of the Bjorken variable x, can be obtained from (anti)neutrino NC elastic scattering off protons (Figure 7.3). Indeed, this process provides the most direct measurement of Δs. The differential cross section for NC-elastic and CC-QE scattering of (anti)neutrinos from protons can be written as:

$$\frac{d\sigma}{dQ^2} = \frac{G_\mu^2}{2\pi}\frac{Q^2}{E_\nu^2}\left(A \pm BW + CW^2\right); \quad W = 4E_\nu/M_p - Q^2/M_p^2, \tag{7.9}$$

where the positive (negative) sign is for neutrino (antineutrino) scattering and the coefficients A, B, and C contain the vector and axial form factors as follows:

$$\begin{aligned} A &= \frac{1}{4}\left[G_1^2(1+\tau) - \left(F_1^2 - \tau F_2^2\right)(1-\tau) + 4\tau F_1 F_2\right] \\ B &= -\frac{1}{4}G_1\left(F_1 + F_2\right) \\ C &= \frac{1}{16}\frac{M_p^2}{Q^2}\left(G_1^2 + F_1^2 + \tau F_2^2\right) \end{aligned}$$

The axial-vector form factor, G_1, for NC scattering can be written as the sum of the known axial form factor G_A plus a strange form factor G_A^s:

$$G_1 = \left[-\frac{G_A}{2} + \frac{G_A^s}{2}\right], \tag{7.10}$$

while the NC vector form factors can be written as:

$$F_{1,2} = \left[\left(\frac{1}{2} - \sin^2\theta_W\right)\left(F_{1,2}^p - F_{1,2}^n\right) - \sin^2\theta_W\left(F_{1,2}^p + F_{1,2}^n\right) - \frac{1}{2}F_{1,2}^s\right], \tag{7.11}$$

where $F_1^{p(n)}$ is the Dirac form factor of the proton (neutron), $F_2^{p(n)}$ is the corresponding Pauli form factor, and $F_{1,2}^s$ are the strange-vector form factors. These latter form factors are expected to be small from the PVES measurements summarized above. In the limit $Q^2 \to 0$, the differential cross section is proportional to the square of the axial-vector form factor $d\sigma/dQ^2 \propto G_1^2$ and $G_A^s \to \Delta s$. The value of Δs can therefore be extracted experimentally by extrapolating the NC differential cross section to $Q^2 = 0$.

7.3.2 Extraction of the Strange Form Factors

Previous neutrino scattering experiments have been limited by the statistics and by the systematic uncertainties on background subtraction. One of the earliest measurements available comes from the analysis of 951 NC νp and 776 NC $\overline{\nu} p$ collected by the experiment BNL E734 [263,264,265]. There are also more recent results with high statistics from MiniBooNE where a measurement of Δs was carried out using neutrino NC elastic scattering with 94,531 νN events [266]. The MiniBooNE measurement was limited by the inability to distinguish the proton and neutron from νN scattering. The LBNE neutrino beam will be sufficiently intense that a measurement of NC elastic scattering on protons in the fine-grained ND can provide a definitive statement on the contribution of the strange sea to either the axial or vector form factor.

Systematic uncertainties can be reduced by measuring the NC/CC ratios for both neutrinos and antineutrinos as a function of Q^2:

$$\mathcal{R}_{\nu p}(Q^2) \equiv \frac{\sigma(\nu_\mu p \to \nu_\mu p)}{\sigma(\nu_\mu n \to \mu^- p)}(Q^2); \qquad \mathcal{R}_{\overline{\nu} p}(Q^2) \equiv \frac{\sigma(\overline{\nu}_\mu p \to \overline{\nu}_\mu p)}{\sigma(\overline{\nu}_\mu p \to \mu^+ n)}(Q^2), \tag{7.12}$$

Figure 7.3 shows the absolute sensitivity of both ratios to Δs for different values of Q^2. The sensitivity for $Q^2 \sim 0.25$ GeV^2 is about 1.2 for neutrinos and 1.9 for antineutrinos, which implies that a measurement of $\mathcal{R}_{\nu p}$ and $\mathcal{R}_{\overline{\nu} p}$ of 1% precision would enable the extraction of Δs with an uncertainty of 0.8% and 0.5%, respectively.

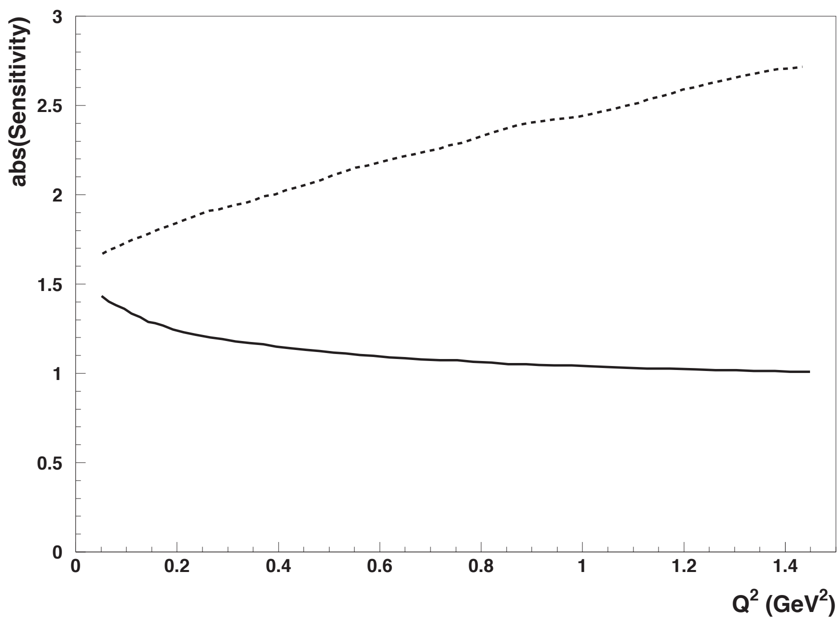

Figure 7.3: Sensitivity (magnitude) of the ratios $\mathcal{R}_{\nu p}$ (solid) and $\mathcal{R}_{\overline{\nu} p}$ (dashed) to a variation of the strange contribution to the spin of the nucleon, Δs, as a function of Q^2. Values greater than one imply that the relative uncertainty on Δs is smaller than that of the corresponding ratio (see text).

The design of the tracker includes several different nuclear targets. Therefore, most of the neutrino scattering is from nucleons embedded in a nucleus, requiring nuclear effects to be taken into account. Fortunately, in the ratio of NC/CC, the nuclear corrections are expected to largely cancel out. The Δs analysis requires a good proton reconstruction efficiency as well as high resolution on both the proton angle and energy. To this end, the low-density tracker can increase the range of the protons inside the ND, allowing the reconstruction of proton tracks down to $Q^2 \sim 0.07\,\text{GeV}^2$. This capability will reduce the uncertainties in the extrapolation of the form factors to the limit $Q^2 \to 0$.

Table 7.3 summarizes the expected proton range for the low-density ($\rho \sim 0.1\,\text{g}\,\text{cm}^{-3}$) straw-tube tracker (STT) in the ND tracking detector design described in Section 3.5. About $2.0(1.2) \times 10^6$ $\nu p(\overline{\nu} p)$ events are expected after the selection cuts in the low-density tracker, yielding a statistical precision on the order of 0.1%.

Table 7.3: Expected proton range for the low-density (ρ $\sim$0.1 g cm^{-3}) tracker. The first column gives the proton kinetic energy and the last column the proton momentum. The Q^2 value producing T_p is calculated assuming the struck nucleon is initially at rest.

T_p MeV	Q^2 GeV$^2/c^2$	Range STT cm	P_p GeV$/c$
20	0.038	4.2	0.195
40	0.075	14.5	0.277
60	0.113	30.3	0.341
80	0.150	50.8	0.395
100	0.188	75.7	0.445

The determination of Δs in the STT utilizes analysis techniques performed by the FINeSSE Collaboration [267] and used by the SciBooNE experiment. In particular, based on the latter, LBNE expects a purity of about 50%, with background contributions of 20% from neutrons produced outside of the detector, 10% νn events and 10% NC pion backgrounds. The dominant systematic uncertainty will be related to the background subtraction. The low-energy beam spectrum at LBNE provides the best sensitivity for this measurement since the external background from neutron-induced proton recoils will be reduced by the strongly suppressed high-energy tail. The low-density magnetized tracker is expected to increase the purity by reducing the neutron background and the NC pion background. The outside neutron background, it should be noted, can be determined using the $n \to p + \pi^-$ process in the STT. The sensitivity analysis is still in progress, however LBNE is confident of achieving a precision on Δs of about 0.02–0.03.

7.4 Nucleon Structure and QCD Studies

Precision measurements of (anti)neutrino differential cross sections in the LBNE near detector will provide additional constraints on several key nucleon structure functions that are complementary to results from electron scattering experiments.

In addition, these measurements would directly improve LBNE's oscillation measurements by providing accurate simulation of neutrino interactions in the far detector and offer an estimate of all background processes that are dependent upon the angular distribution of the outgoing particles in the far detector. Furthermore, certain QCD analyses — i.e., global fits used for extraction of parton distribution functions (PDFs) via the differential cross sections measured in ND data — would constrain the systematic error in precision electroweak measurements. This would apply not only in neutrino physics but also in hadron collider measurements.

7.4.1 Determination of the F_3 Structure Function and GLS Sum Rule

For quantitative studies of inclusive deep-inelastic lepton-nucleon scattering, it is vital to have precise measurements of the F_3 structure functions as input into global PDF fits. Because it depends on weak axial quark charges, the F_3 structure function can only be measured with neutrino and antineutrino beams and is unique in its ability to differentiate between the quark and antiquark content of the nucleon. On a proton target, for instance, the neutrino and antineutrino F_3 structure functions (at leading order in α_s) are given by

$$xF_3^{\nu p}(x) = 2x\left(d(x) - \overline{u}(x) + s(x) + \cdots\right), \tag{7.13}$$

$$xF_3^{\overline{\nu}p}(x) = 2x\left(u(x) - \overline{d}(x) - \overline{s}(x) + \cdots\right), \tag{7.14}$$

$$xF_3^{\nu n}(x) = 2x\left(u(x) - \overline{d}(x) + s(x) + \cdots\right), \tag{7.15}$$

$$xF_3^{\overline{\nu}n}(x) = 2x\left(d(x) - \overline{u}(x) - \overline{s}(x) + \cdots\right). \tag{7.16}$$

where $u_v = u - \bar{u}$ and $d_v = d - \bar{d}$ are the valence sea quark distributions. Under the assumption of a symmetric strange sea, i.e., $s(x) = \bar{s}(x)$, the above expressions show that a measurement of the average $xF_3 = (xF_3^{\nu N} + xF_3^{\bar{\nu}N})/2$ for neutrino and antineutrino interactions on isoscalar targets provides a direct determination of the valence quark distributions in the proton. This measurement is complementary to the measurement of Drell-Yan production at colliders, which is essentially proportional to the sea quark distributions.

The first step in the structure function analysis is the measurement of the differential cross section:

$$\frac{1}{E_\nu}\frac{d\sigma^2}{dxdQ^2} = \frac{N(x,Q^2,E_\nu)}{N(E_\nu)}\frac{\sigma_{\rm tot}/E_\nu}{dxdQ^2} \tag{7.17}$$

where $N(x, Q^2, E_\nu)$ is the number of events in each (x, Q^2, E_ν) bin and $N(E_\nu)$ is the number of events in each E_ν bin integrated over x and Q^2. The average xF_3 structure function can be extracted by taking the difference between neutrino and antineutrino differential cross sections:

$$\frac{1}{E_\nu}\frac{d^2\sigma^\nu}{dxdQ^2} - \frac{1}{E_\nu}\frac{d^2\sigma^{\bar\nu}}{dxdQ^2} = 2\left[y\left(1-\frac{y}{2}\right)\frac{y}{Q^2}\right]xF_3 \tag{7.18}$$

where xF_3 denotes the sum for neutrino and antineutrino interactions.

The determination of the xF_3 structure functions will, in turn, allow a precision measurement of the Gross-Llewellyn-Smith (GLS) QCD sum rule:

$$\begin{aligned} S_{\rm GLS}(Q^2) &= \frac{1}{2}\int_0^1 \frac{1}{x}\left[xF_3^{\nu N} + xF_3^{\bar\nu N}\right]dx \\ &= 3\left[1 - \frac{\alpha_s(Q^2)}{\pi} - a(n_f)\left(\frac{\alpha_s(Q^2)}{\pi}\right)^2 - b(n_f)\left(\frac{\alpha_s(Q^2)}{\pi}\right)^3\right] + \Delta\mathrm{HT} \end{aligned} \tag{7.19}$$

where α_s is the strong coupling constant, n_f is the number of quark flavors, a and b are known functions of n_f, and the quantity ΔHT represents higher-twist contributions. The equation above can be inverted to determine $\alpha_s(Q^2)$ from the GLS sum rule. The most precise determination of the GLS sum rule was obtained by the CCFR experiment on an iron target [268] $S_{\rm GLS}(Q^2 = 3\ GeV^2) = 2.50 \pm 0.018 \pm 0.078$. The high-resolution ND combined with the unprecedented statistics would substantially reduce the systematic uncertainty on the low-x extrapolation of the xF_3 structure functions entering the GLS integral. In addition, the presence of different nuclear targets, as well as the availability of a target with free protons will allow investigation of isovector and nuclear corrections, and adding a tool to test isospin (charge) symmetry (Section 7.5).

7.4.2 Determination of the Longitudinal Structure Function $F_L(x, Q^2)$

The structure function F_L is directly related to the gluon distribution $G(x, Q^2)$ of the nucleon, as can be seen from the Altarelli-Martinelli relation:

$$F_L(x,Q^2) = \frac{\alpha_s(Q^2)}{\pi}\left[\frac{4}{3}\int_x^1 \frac{dy}{y}\left(\frac{x}{y}\right)^2 F_2(x,Q^2) + n_f\int_x^1\frac{dy}{y}\left(\frac{x}{y}\right)^2\left(1-\frac{x}{y}\right)G(y,Q^2)\right] \tag{7.20}$$

where n_f is the number of parton flavors. In the leading order approximation the longitudinal structure function F_L is zero, while at higher orders a nonzero $F_L(x, Q^2)$ is originated as a consequence of the violation of the Callan-Gross relation:

$$F_L(x,Q^2) = \left(1+\frac{4M^2x^2}{Q^2}\right)F_2(x,Q^2) - 2xF_1(x,Q^2) \tag{7.21}$$

where $2xF_1 = F_T$ is the transverse structure function. A measurement of $R = F_L/F_T$ is therefore both a test of perturbative QCD at large x and a clean probe of the gluon density at small x where the quark contribution is small. A poor knowledge of R, especially at small x, results in uncertainties in the structure functions extracted from deep inelastic scattering cross sections, and in turn, in electroweak measurements. It is instructive to compare the low-Q^2 behavior of R for charged-lepton versus neutrino scattering. In both cases CVC implies that $F_T \propto Q^2$ as $Q^2 \to 0$. However, while $F_L \propto Q^4$ for the electromagnetic current, for the weak current F_L is dominated by the finite PCAC (partial conservation of the axial current) contribution [251]. The behavior of R at $Q^2 \ll 1$ GeV^2 is therefore very different for charged-lepton and neutrino scattering. A new precision measurement of the Q^2 dependence of R with (anti)neutrino data would also clarify the size of the high-twist contributions to F_L and R, which reflect the strength of multi-parton correlations (qq and qg).

The ratio of longitudinal to transverse structure functions can be measured from the y dependence of the deep inelastic scattering data. Fits to the following function:

$$F(x, Q^2, \epsilon) = \frac{\pi(1-\epsilon)}{y^2 G_F^2 M E_\nu} \left[\frac{d^2\sigma^\nu}{dxdy} + \frac{d^2\sigma^{\bar{\nu}}}{dxdy} \right] = 2xF_1(x, Q^2) \left[1 + \epsilon R(x, Q^2) \right] \tag{7.22}$$

have been used by CCFR and NuTeV to determine $R = \sigma_L/\sigma_T$. In this equation $\epsilon \simeq 2(1-y)/(1+(1-y)^2)$ is the polarization of the virtual W boson. This equation assumes $xF_3^\nu = xF_3^{\bar{\nu}}$, and a correction must be applied if this is not the case. The values of R are extracted from linear fits to F versus ϵ at fixed x and Q^2 bins.

7.4.3 Determination of F_2^n and the d/u Ratio of Quark Distribution Functions

Because of the larger electric charge on the u quark than on the d, the electromagnetic proton F_2 structure function data provide strong constraints on the u-quark distribution, but are relatively insensitive to the d-quark distribution. To constrain the d-quark distribution a precise knowledge of the corresponding F_2^n structure functions of free neutrons is required, which in current practice is extracted from inclusive deuterium F_2 data. At large values of x ($x > 0.5$) the nuclear corrections in deuterium become large and, more importantly, strongly model-dependent, leading to large uncertainties on the resulting d-quark distribution. Using the isospin relation $F_2^{\bar{\nu}p} = F_2^{\nu n}$ and $F_2^{\nu p} = F_2^{\bar{\nu}n}$ it is possible to obtain a direct determination of $F_2^{\nu n}$ and $F_2^{\bar{\nu}n}$ with neutrino and antineutrino scattering off a target with free protons. This determination is free from model uncertainties related to nuclear targets. The extraction of $F_2^{\nu n}$ and $F_2^{\bar{\nu}n}$ will allow a precise extraction on the d-quark distribution at large x. Existing neutrino data on hydrogen have relatively large errors and do not extend beyond $x \sim 0.5$ [269,270].

The $F_2^{\bar{\nu}p}$ and $F_2^{\nu p}$ structure functions can be obtained from interactions on a target with free protons after subtracting the contributions from xF_3 and R. These latter can either be modeled within global PDF fits or taken from the other two measurements described above. As discussed in Section 7.5

the LBNE ND can achieve competitive measurements of $F_2^{\bar{\nu}p}$ and $F_2^{\nu p}$ with an increase of statistics of three orders of magnitude with respect to the existing hydrogen data [269,270].

7.4.4 Measurement of Nucleon Structure Functions

At present neutrino scattering measurements of cross sections have considerably larger uncertainties than those of the electromagnetic inclusive cross sections. The measurement of the differential cross sections [236] is dominated by three uncertainties: (1) muon energy scale, (2) hadron energy scale, and (3) knowledge of the input (anti)neutrino flux. Table 7.4 shows a comparison of past and present experiments and the corresponding uncertainties on the energy scales. The most precise measurements are from the CCFR, NuTeV and NOMAD experiments, which are limited to a statistics of about 10^6 neutrino events.

Table 7.4: Summary of past experiments performing structure function measurements. The expected numbers in the LBNE near detector for a five-year run with the 1.2−MW 120−GeV reference beam (5×10^{21} POT) are also given for comparison.

Experiment	Mass	ν_μ CC Stat.	Target	E_ν (GeV)	ΔE_μ	$\Delta E_{\rm H}$
CDHS [271]	750 t	10^7	p,Fe	20-200	2.0%	2.5%
BEBC [272,273]	various	5.7×10^4	p,D,Ne	10-200		
CCFR [274,275]	690 t	1.0×10^6	Fe	30-360	1.0%	1.0%
NuTeV [276]	690 t	1.3×10^6	Fe	30-360	0.7%	0.43%
CHORUS [277]	100 t	3.6×10^6	Pb	10-200	2.5%	5.0%
NOMAD [156]	2.7 t	1.3×10^6	C	5-200	0.2%	0.5%
[241]	18 t	1.2×10^7	Fe	5-200	0.2%	0.6%
MINOS ND [155]	980 t	3.6×10^6	Fe	3-50	2-4%	5.6%
LBNE ND	5 t	5.9×10^7	$(C_3H_6)_n$	0.5-30	$< 0.2\%$	$< 0.5\%$

The MINERνA [161] experiment is expected to provide new structure function measurements on a number of nuclear targets including He, C, Fe and Pb in the near future. Since the structure function measurement mainly involves DIS events, the MINERνA measurement will achieve a competitive statistics after the completion of the new run with the medium-energy beam. MINERνA will focus on a measurement of the ratio of different nuclear targets to measure nuclear corrections in (anti)neutrino interactions. It must be noted that the MINERνA experiment relies on the MINOS ND for muon identification. The corresponding uncertainty on the muon-energy scale (Table 7.4) is substantially larger than that in other modern experiments, e.g., NuTeV and NOMAD, thus limiting the potential of absolute structure function measurements. Furthermore, the muon-energy scale is also the dominant source of uncertainty in the determination of the (anti)neutrino fluxes with the low-ν method. Therefore, the flux uncertainties in MINERνA are expected to be larger than in NOMAD and NuTeV.

Given its reference beam design and 1.2−MW proton-beam power, LBNE expects to collect about 2.3×10^7 neutrino DIS events and about 4.4×10^6 antineutrino DIS events in the ND. These numbers correspond to an improvement by more than one order of magnitude with respect to the most precise past experiments, e.g., NuTeV [276] and NOMAD [156,241]. With these high-statistics samples, LBNE will be able to significantly reduce the gap between the uncertainties on the weak and electromagnetic structure functions. A possible high-energy run with the upgraded 2.3−MW beam would offer a further increase by more than a factor of ten in statistics.

In addition to the large data samples, the use of a high-resolution, low-density spectrometer allows LBNE to reduce systematic uncertainties with respect to previous measurements. The LBNE ND is expected to achieve precisions better than 0.2% and 0.5% on the muon- and hadron-energy scales, respectively. These numbers are based on the results achieved by the NOMAD experiment (Table 7.4), which had much lower statistics and poorer resolution than is expected in the LBNE ND. The calibration of the momentum and energy scales will be performed with the large sample of reconstructed $K^0_S \to \pi\pi$, $\Lambda \to p\pi$, and $\pi^0 \to \gamma\gamma$ decays. In addition, the overall hadronic energy scale can be calibrated by exploiting the well-known structure of the Bjorken y distribution in (anti)neutrino DIS interactions [156,278]. The relative fluxes as a function of energy can be extracted to a precision of about 2% with the low-ν method, due to the small uncertainty on the muon-energy scale. The world average absolute normalization of the differential cross sections $\sigma_{\rm tot}/E$, is known to 2.1% precision [55]. However, with the 1.2−MW beam available from the PIP-II upgrades, it will be possible to improve the absolute normalization using ν-e NC elastic scattering events, coherent meson production, etc. An overall precision of 1-2% would make (anti)neutrino measurements comparable to or better than the complementary measurements from charged-lepton DIS.

On the time scale of LBNE, comparable measurements from (anti)neutrino experiments are not expected, primarily due to the low energy of competing beamlines (J-PARC neutrino beamline in Japan [279]) or to the poorer resolution of the detectors used (MINERνA [161] , T2K [134], NOνA [126]). The experimental program most likely to compete with the LBNE ND measurements is the 12−GeV upgrade at Jefferson Laboratory (JLab) [280]. However, it must be emphasized that the use of electron beams at JLab makes this program *complementary* to LBNE's. In particular, the three topics discussed above are specific to the (anti)neutrino interactions.

Several planned experiments at JLab with the energy-upgraded 12−GeV beam will measure the d/u ratio from D targets up to $x \sim 0.85$, using different methods to minimize the nuclear corrections. The LBNE measurement will be competitive with the proposed JLab 12−GeV experiments, since the large statistics expected will allow a precise determination of $F_2^{\nu n}$ and $F_2^{\bar{\nu} n}$ up to $x \sim 0.85$. Furthermore, the use of a weak probe coupled with a wide-band beam will provide a broader Q^2 range than in JLab experiments, thus allowing a separation of higher twist and other sub-leading effects in $1/Q^2$.

7.5 Tests of Isospin Physics and Sum-Rules

One of the most compelling physics topics accessible to LBNE's high-resolution near detector is the isospin physics using neutrino and antineutrino interactions. This physics involves the Adler sum rule and tests isospin (charge) symmetry in nucleons and nuclei.

The Adler sum rule relates the integrated difference of the antineutrino and neutrino F_2 structure functions to the isospin of the target:

$$\mathcal{S}_A(Q^2) = \int_0^1 dx \, \left[F_2^{\overline{\nu}}(x,Q^2) - F_2^{\nu}(x,Q^2)\right]/(2x) = 2\, I_z, \tag{7.23}$$

where the integration is performed over the entire kinematic range of the Bjorken variable x and I_z is the projection of the target isospin vector on the quantization axis (z axis). For the proton $\mathcal{S}_A^p = 1$ and for the neutron $\mathcal{S}_A^n = -1$.

In the quark-parton model the Adler sum is the difference between the number of valence u and d quarks of the target. The Adler sum rule survives the strong-interaction effects because of the conserved vector current (CVC) and provides an exact relation to test the local current commutator algebra of the weak hadronic current. In the derivation of the Adler sum rule the effects of both non-conservation of the axial current and heavy-quark production are neglected.

Experimental tests of the Adler sum rule require the use of a hydrogen target to avoid nuclear corrections to the bound nucleons inside the nuclei. The structure functions $F_2^{\overline{\nu}}$ and F_2^{ν} have to be determined from the corresponding differential cross sections and must be extrapolated to small x values in order to evaluate the integral. The test performed in bubble chambers by the BEBC Collaboration — the only test available — is limited by the modest statistics; it used about 9,000 $\overline{\nu}$ and 5,000 ν events collected on hydrogen [273].

The LBNE program can provide the first high-precision test of the Adler sum rule. To this end, the use of the high-energy beam tune shown in Figure 3.19, although not essential, would increase the sensitivity, allowing attainment of higher Q^2 values. Since the use of a liquid H_2 bubble chamber is excluded in the ND hall due to safety concerns, the (anti)neutrino interactions off a hydrogen target can only be extracted with a subtraction method from the composite materials of the ND targets. Using this technique to determine the position resolution in the location of the primary vertex is crucial to reducing systematic uncertainties. For this reason, a precision test of the Adler sum rule is best performed with the low-density magnetized ND.

A combination of two different targets — the polypropylene $(C_3H_6)_n$ foils placed in front of the STT modules and pure carbon foils — are used in the low-density, magnetized ND to provide a fiducial hydrogen mass of about 1 t. With the LBNE fluxes from the standard exposure, $5.0(1.5) \times 10^6 \pm 13(6.6) \times 10^3(sub.)$ $\nu(\overline{\nu})$ CC events (where the quoted uncertainty is dominated by the statistical subtraction procedure) would be collected on the hydrogen target. The level of precision that can be achieved is sufficient to open up the possibility of making new discoveries in the quark and hadron structure of the proton. No other comparable measurement is expected on the timescale of LBNE.

7.6 Studies of (Anti)Neutrino-Nucleus Interactions

An integral part of the physics program envisioned for the LBNE ND involves detailed measurements of (anti)neutrino interactions in a variety of nuclear targets. The LBNE ND offers substantially larger statistics coupled with a much higher resolution and, in turn, lower systematic uncertainties with respect to past experiments (Table 7.4) or ongoing and future ones (MINERνA [161], T2K [134], NOνA [126]). The most important nuclear target is of course the argon target, which matches the LBNE far detector. The ND standard target is polypropylene $(C_3H_6)_n$, largely provided by the mass of the STT radiators. An additional proposed ND target is argon gas in pressurized aluminum tubes with sufficient mass to provide $\simeq$10 times the ν_μCC and NC statistics as expected in the LBNE far detector. Equally important nuclear targets are carbon (graphite), which is essential in order to get (anti)neutrino interactions on free protons through a statistical subtraction procedure from the main polypropylene target (Section 7.5), and calcium. In particular, this latter target has the same atomic weight ($A = 40$) as argon but is isoscalar. One additional nuclear target is iron, which is used in the proposed India-based Neutrino Observatory (INO) [281]. The modularity of the STT provides for successive measurements using thin nuclear targets (thickness $< 0.1X_0$), while the excellent angular and space resolution allows a clean separation of events originating in different target materials. Placing an arrangement of different nuclear targets upstream of the detector provides the desired nuclear samples in (anti)neutrino interactions. For example, a single 7$-$mm-thick calcium layer at the upstream end of the detector will provide about 3.1×10^5 ν_μCC interactions in one year.

Potential ND studies in nuclear effects include the following:

- nuclear modifications of form factors
- nuclear modifications of structure functions
- mechanisms for nuclear effects in coherent and incoherent regimes
- a dependence of exclusive and semi-exclusive processes
- effect of final-state interactions
- effect of short-range correlations
- two-body currents

The study of nuclear effects in (anti)neutrino interactions off nuclei is directly relevant for the long-baseline oscillation studies. The use of heavy nuclei like argon in the LBNE far detector requires a measurement of nuclear cross sections on the same targets in the ND in order to reduce signal and background uncertainties in the oscillation analyses. Cross-section measurements obtained from other experiments using different nuclei are not optimal; in addition to the different p/n ratio in argon compared to iron or carbon where measurements from other experiments exist, nuclear modifications of cross sections can differ from 5% to 15% between carbon and argon for example, while the difference in the final-state interactions could be larger. Additionally, nuclear modifications can introduce a substantial smearing of the kinematic variables reconstructed from the observed final-state particles. Detailed measurements of the dependence on the atomic number A of different exclusive processes are then required in order to understand the absolute energy scale of neutrino event interactions and to reduce the corresponding systematic uncertainties on the oscillation parameters.

It is worth noting that the availability of a free-proton target through statistical subtraction of the $(C_3H_6)_n$ and carbon targets (Section 7.5) will allow for the first time a direct model-independent measurement of nuclear effects — including both the primary and final-state interactions — on the argon target relevant for the far detector oscillation analysis.

Furthermore, an important question in nuclear physics is how the structure of a nucleon is modified when said nucleon is inside the medium of a heavy nucleus as compared to a free nucleon like the proton in a hydrogen nucleus. Studies of the ratio of structure functions of nuclei to those of free nucleons (or in practice, the deuteron) reveal nontrivial deviations from unity as a function of x and Q^2. These have been well explored in charged-lepton scattering experiments, but little empirical information exists from neutrino scattering. Measurements of structure using neutrino scattering are complementary to those in charged-lepton scattering.

Another reason to investigate the nuclear-medium modifications of neutrino structure functions is that most neutrino scattering experiments are performed on nuclear targets, from which information on the free nucleon is inferred by performing a correction for the nuclear effects. In practice this often means applying the same nuclear correction as for the electromagnetic structure functions, which introduces an inherent model-dependence in the result. In particular, significant differences between photon-induced and weak-boson-induced nuclear structure functions are predicted, especially at low Q^2 and low x, which have not been tested. A striking example is offered by the ratio R of the longitudinal-to-transverse structure functions [251]. While the electromagnetic ratio tends to zero in the photoproduction limit, $Q^2 \to 0$, by current conservation, the ratio for neutrino structure functions is predicted to be *finite* in this limit. Thus, significant discovery potential exists in the study of neutrino scattering from nuclei.

The comparison of argon and calcium targets ($^{40}_{18}$Ar and $^{40}_{20}$Ca) in the LBNE ND would be particularly interesting. Since most nuclear effects depend on the atomic weight A, inclusive properties of (anti)neutrino interactions are expected to be the same for these two targets [251,282,283,284].

This fact would allow the use of both targets to model signal and backgrounds in the LBNE far detector (argon target), as well as to compare LBNE results for nuclear effects on argon with the extensive data on calcium from charged lepton DIS. In addition, a high-precision measurement of (anti)neutrino interactions in both argon and calcium opens the possibility for studying a potential flavor and isovector dependence of nuclear effects and to further test the isospin (charge symmetry) in nuclei (Section 7.5). Evidence for any of these effects would constitute important discoveries.

Finally, the extraction of (anti)neutrino interactions on deuterium from the statistical subtraction of H_2O from D_2O, which is required to measure the fluxes (Section 7.1), would allow the first direct measurement of nuclear effects in deuterium. This measurement can be achieved since the structure function of a free isoscalar nucleon is given by the average of neutrino and antineutrino structure functions on hydrogen ($F_2^{\nu n} = F_2^{\bar{\nu} p}$). A precise determination of nuclear modifications of structure functions in deuterium would play a crucial role in reducing systematic uncertainties from the global PDF fits.

7.7 Search for Heavy Neutrinos

The most economical way to handle the problems of neutrino masses, dark matter and the Baryon Asymmetry of the Universe in a unified way may be to add to the Standard Model (SM) three Majorana singlet fermions with masses roughly on the order of the masses of known quarks and leptons using the seesaw mechanism [67]. The appealing feature of this theory (called the νMSM for *Neutrino Minimal SM*) [285] is that every left-handed fermion has a right-handed counterpart, leading to a consistent way of treating quarks and leptons.

The most efficient mechanism proposed for producing these heavy sterile singlet states experimentally is through weak decays of heavy mesons and baryons, as can be seen from the left-hand diagram in Figure 7.4, showing some examples of relevant two- and three-body decays [286]. These heavy mesons can be produced by energetic protons scattering off the LBNE neutrino production target and the heavy singlet neutrinos from their decays detected in the near detector.

The lightest of the three new singlet fermions in the νMSM, is expected to have a mass from 1 keV to 50 keV [287] and could play the role of the dark matter particle [288]. The two other neutral fermions are responsible for giving mass to ordinary neutrinos via the seesaw mechanism at the *electroweak scale* and for creation of the Baryon Asymmetry of the Universe (BAU; for a review see [287]). The masses of these particles and their coupling to ordinary leptons are constrained by particle physics experiments and cosmology [286,289]. They should be almost degenerate, thus nearly forming Dirac fermions (this is dictated by the requirement of successful baryogenesis). Different considerations indicate that their mass should be in the region of $\mathcal{O}(1)$ GeV [290].

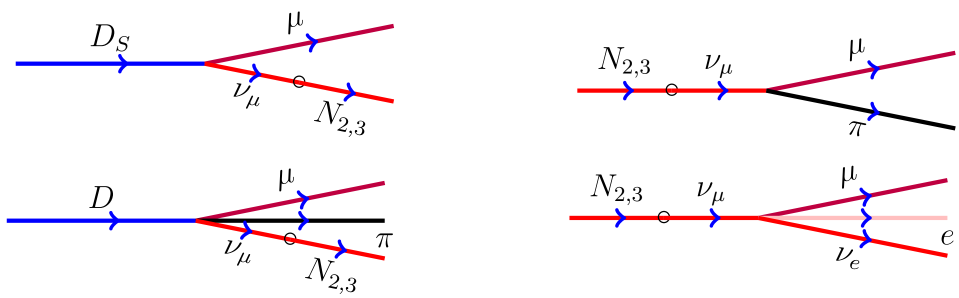

Figure 7.4: Left: Feynman diagrams of meson decays producing heavy sterile neutrinos. Right: Feynman diagrams of sterile-neutrino decays.

The mixing angle, U^2, between the singlet fermions and the three active-neutrino states must be small [285,291] — otherwise the large mixing would have led to equilibration of these particles in the early Universe above the electroweak temperatures, and, therefore, to erasing of the BAU — explaining why these new particles have not been seen previously.

Several experiments have conducted searches for heavy neutrinos, for example BEBC [292], CHARM [293], NuTeV [294] and the CERN PS191 experiment [295,296] (see also a discussion of different experiments in [289]). In the search for heavy neutrinos, the strength of the LBNE ND, compared to earlier experiments, lies in reconstructing the exclusive decay modes, including electronic, hadronic and muonic. Furthermore, the detector offers a means to constrain and measure the backgrounds using control samples.

In case of the LBNE experiment the relevant heavy mesons are charmed. With a typical lifetime (in the rest frame) of about 10^{-10} s, these mesons mostly decay before further interaction, yielding the sterile-neutrino flux. Since these sterile neutrinos are very weakly interacting they can cover quite a large distance before decay, significantly exceeding the distance of roughly 500 m from the target to the ND. The ND can search for decays of neutrinos into SM particles due to mixing with active neutrinos, provided a sufficiently long instrumented decay region is available. Two examples of the interesting decay modes are presented on the right panel of Figure 7.4. More examples can be found in [286].

An estimate of sterile-neutrino events that can be observed in the LBNE ND, N^{LBNE}_{signal}, is obtained by comparing the relevant parameters of the LBNE and CHARM experiments. The number of events grows linearly with the number of protons on target, the number of produced charmed mesons, the detector length (decay region) and the detector area. In particular, this latter linear increase is valid if the angular spread of the neutrino flux, which is on the order of $N_m M_D/E_{beam}$, is larger than the angle at which the ND is seen from the target. Here N_m is the multiplicity of the produced hadrons, and the above condition is valid for both LBNE and CHARM. The number of events decreases linearly when the energy increases, since this increases the lifetime, reducing the decay probability within the detector. Finally, the number of mesons decreases quadratically with the distance between the target and the detector.

The considerations above imply that a search for νMSM sterile neutrinos in the LBNE ND can be competitive after only five years of running with the reference beam, corresponding to an overall integrated exposure of about 5×10^{21} POT with a proton energy of 120 GeV. The use of a low-density, high-resolution spectrometer in the ND substantially reduces backgrounds and allows the detection of both leptonic and hadronic decay modes. Assuming a fiducial length of the magnetized tracker of 7 m as decay region, the ratio between the signal event to be observed in the LBNE ND and those in the CHARM experiment can be estimated to be more than a factor of 50 after only four years of running. Since both production and decay rates are proportional to the square of the neutrino mixing angles, the corresponding improvement in the square of the neutrino mixing angle U^2 will be about a factor of seven with respect to the CHARM experiment. Figure 7.5 shows the projected LBNE sensitivity in the (U^2, M) plane. At lower values of the mass of the heavy neutrinos, additional constraints can be obtained for kaons by comparing the LBNE and PS191 experiments, as shown in Figure 7.5.

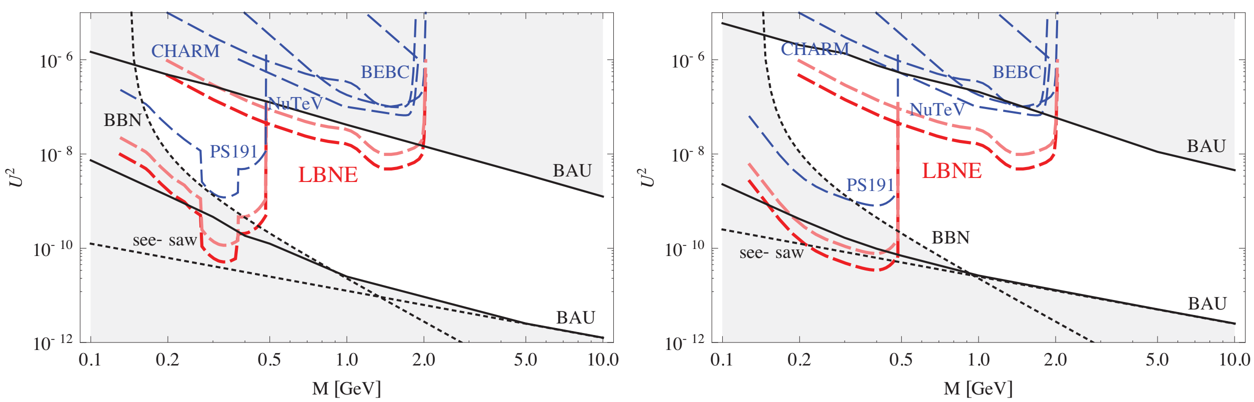

Figure 7.5: Upper limits on U^2, the mixing angle between heavy sterile neutrinos and the light active states, coming from the Baryon Asymmetry of the Universe (solid lines), from the seesaw mechanism (dotted line) and from the Big Bang nucleosynthesis (dotted line). The regions corresponding to different experimental searches are outlined by blue dashed lines. Left panel: normal hierarchy; right panel: inverted hierarchy (adopted from [297]). Pink and red curves indicate the expected sensitivity of the LBNE near detector with an exposure of 5×10^{21} POT ($\sim$ 5 years) with the 1.2−MW reference beam at 120 GeV for detector lengths of 7 m and 30 m , respectively (see text for details).

It must be noted that exploitation of the complete 5 + 5 years ($\nu + \overline{\nu}$) years of data taking would further improve the number of expected events by a factor of two, since it scales linearly with the number of protons on target. With the beam upgrade to 2.3−MW, this improvement would become a factor of four with respect to the initial five year run and the 1.2 MW beam.

A better sensitivity to νMSM can be achieved by instrumenting the upstream region of the ND hall (e.g., with the liquid argon detector and some minimal tracking device upstream). The fiducial volume of the new detector will need to be empty (material-free) or fully sensitive in order to suppress background events. The geometry of the ND hall would allow a maximal decay length of about 30 m. The sensitivity of this configuration can be estimated by rescaling the expected limits on the neutrino mixing angle U^2. The expected number of signal events with a total decay length of $\sim$ 30 m exceeds by about 200 (800) times the number of events in CHARM after a five (5 +5) year run with the standard (upgraded) beam. In turn, this implies an improvement by a factor of 15 (28) in the sensitivity to U^2 with respect to the CHARM experiment.

If the magnetic moment of the sterile neutrinos is sizeable, the dominant decay channel would be a radiative electromagnetic decay into $\gamma\nu$, which has also been proposed as a possible explanation for the observed MiniBooNE low-energy excess [148]. This possibility, in turn, requires a detector capable of identifying and reconstructing single photon events. The low-density ND in LBNE can achieve an excellent sensitivity to this type of search as demonstrated by a similar analysis in NOMAD [298].

7.8 Search for High Δm^2 Neutrino Oscillations

The evidence for neutrino oscillations obtained from atmospheric, long-baseline accelerator, solar and long-baseline reactor data from different experiments consistently indicates two different scales, with Δm^2_{32} $\sim$2.4 $\times$ 10^{-3} eV^2 defining the atmospheric oscillations (also long-baseline accelerator and short-baseline reactor scales) and Δm^2_{21} $\sim$7.9 $\times$ 10^{-5} eV^2 defining the solar oscillations (and long-baseline reactor oscillations). The only way to accommodate oscillations with relatively high Δm^2 at the eV^2 scale as suggested by the results from the LSND experiment [299] is therefore to add one or more sterile neutrinos to the conventional three light neutrinos.

Recently, the MiniBooNE experiment reported that its antineutrino data might be consistent with the LSND $\overline{\nu}_\mu \to \overline{\nu}_e$ oscillation with $\Delta m^2 \sim$ eV^2 [300]. Contrary to the antineutrino data, the neutrino data seem to exclude high Δm^2 oscillations, possibly indicating a different behavior between neutrinos and antineutrinos.

Models with five (3+2) or six (3+3) neutrinos can potentially explain the MiniBooNE results. In addition to the cluster of the three neutrino mass states (accounting for *solar* and *atmospheric* mass splitting), two (or three) states at the eV scale are added, with a small admixture of ν_e and ν_μ to account for the LSND signal. One distinct prediction from such models is a significant probability for $\overline{\nu}_\mu$ disappearance into sterile neutrinos, on the order of 10%, in addition to the small probability for $\overline{\nu}_e$ appearance.

Given a roughly 500−m baseline and a low-energy beam, the LBNE ND can reach the same value $L/E_\nu \sim 1$ as MiniBooNE and LSND. The large fluxes and the availability of fine-grained detectors make the LBNE program well suited to search for active-sterile neutrino oscillations beyond the three-flavor model with Δm^2 at the eV^2 scale.

Due to the potential differences between neutrinos and antineutrinos, four possibilities have to be considered in the analysis: ν_μ disappearance, $\overline{\nu}_\mu$ disappearance, ν_e appearance and $\overline{\nu}_e$ appearance. As discussed in Section 7.1, the search for high Δm^2 oscillations has to be performed simultaneously with the in situ determination of the fluxes.

To this end, an independent prediction of the ν_e and $\overline{\nu}_e$ fluxes starting from the measured ν_μ and $\overline{\nu}_\mu$ CC distributions are required since the ν_e and $\overline{\nu}_e$ CC distributions could be distorted by the appearance signal. The low-ν_0 method can provide such predictions if external measurements for the K_L^0 component are available from hadro-production experiments (Section 7.1).

The study will implement an iterative procedure:

1. extraction of the fluxes from ν_μ and $\overline{\nu}_\mu$ CC distributions assuming no oscillations are present
2. comparison with data and determination of oscillation parameters (if any)
3. new flux extraction after subtraction of the oscillation effect
4. iteration until convergence

The analysis has to be performed separately for neutrinos and antineutrinos due to potential CP or CPT violation, according to MiniBooNE/LSND data. The ratio of ν_e CC events to ν_μ CC events will be measured:

$$\mathcal{R}_{e\mu}(L/E) \equiv \frac{\#\, of\ \nu_e N \to e^- X}{\#\, of\ \nu_\mu N \to \mu^- X}(L/E); \qquad \overline{\mathcal{R}}_{e\mu}(L/E) \equiv \frac{\#\, of\ \overline{\nu}_e N \to e^+ X}{\#\, of\ \overline{\nu}_\mu N \to \mu^+ X}(L/E) \quad (7.24)$$

This is then compared with the predictions obtained from the low-ν_0 method. Deviations of $\mathcal{R}_{e\mu}$ or $\overline{\mathcal{R}}_{e\mu}$ from the expectations as a function of L/E would provide evidence for oscillations. This procedure only provides a relative measurement of $\nu_e(\overline{\nu}_e)$ versus $\nu_\mu(\overline{\nu}_\mu)$; since the fluxes are extracted from the observed ν_μ and $\overline{\nu}_\mu$ CC distributions, an analysis of the $\mathcal{R}_{e\mu}(\overline{\mathcal{R}}_{e\mu})$ ratio cannot distinguish between $\nu_\mu(\overline{\nu}_\mu)$ disappearance and $\nu_e(\overline{\nu}_e)$ appearance.

The process of NC elastic scattering off protons (Section 7.3) can provide the complementary measurement needed to disentangle the two hypotheses of $\nu_\mu(\overline{\nu}_\mu)$ disappearance into sterile neutrinos and $\nu_e(\overline{\nu}_e)$ appearance. In order to cancel systematic uncertainties, the NC/CC ratio with respect to QE scattering will be measured:

$$\mathcal{R}_{NC}(L/E) \equiv \frac{\#\, of\ \nu p \to \nu p}{\#\, of\ \nu_\mu n \to \mu^- p}(L/E); \qquad \overline{\mathcal{R}}_{NC}(L/E) \equiv \frac{\#\, of\ \overline{\nu} p \to \overline{\nu} p}{\#\, of\ \overline{\nu}_\mu p \to \mu^+ n}(L/E) \quad (7.25)$$

It is possible to reconstruct the neutrino energy from the proton angle and momentum under the assumption that the nuclear smearing effects are small enough to neglect (the same for the neutrino CC sample). In the oscillation analysis, only the *relative* distortions of the ratio $\mathcal{R}_{NC}(\overline{\mathcal{R}}_{NC})$ as a function of L/E are of interest, not their absolute values. For $Q^2 > 0.2$ GeV^2 the relative shape of the total cross sections is not very sensitive to the details of the form factors. To improve the energy resolution, it is possible to use neutrino interaction events originating from the deuterium inside the D_2O target embedded into the fine-grained tracker. These events have better energy resolution due to the smaller nuclear smearing effects in D_2O.

An improved oscillation analysis is based on a simultaneous fit to both $\mathcal{R}_{e\mu}(\overline{\mathcal{R}}_{e\mu})$ and $\mathcal{R}_{NC}(\overline{\mathcal{R}}_{NC})$. The first ratio provides a measurement of the oscillation parameters while the latter constrains the $\nu_e(\overline{\nu}_e)$ appearance versus the $\nu_\mu(\overline{\nu}_\mu)$ disappearance. This analysis imposes two main requirements on the ND:

- e^+/e^- separation to provide an unambiguous check of the different behavior between neutrinos and antineutrinos suggested by MiniBooNE
- accurate reconstruction of proton momentum and angle

Validation of the unfolding of the high Δm^2 oscillations from the in situ extraction of the $\nu(\overline{\nu})$ flux would also require changes to the beam conditions, since the ND cannot be easily moved. This would require a short run with a high-energy beam and the capability to change or switch off the beam focusing system.

7.9 Light (sub-GeV) Dark Matter Searches

According to the latest cosmological and astrophysical measurements, nearly eighty percent of the matter in the Universe is in the form of cold, non-baryonic dark matter (DM) [301,302]. The search to find evidence of the particle (or particles) that make up DM, however, has so far turned up empty. Direct detection experiments and indirect measurements at the LHC, however, are starting to severely constrain the parameter space of Weakly-Interacting Massive Particles (WIMPs), one of the leading candidates for DM. The lack of evidence for WIMPs at these experiments has forced many in the theory community to reconsider.

Some theories consider an alternative possibility to the WIMP paradigm in which the DM mass is much lighter than the electroweak scale (e.g., below the GeV level). In order to satisfy constraints on the relic density of DM, these theories require that DM particles be accompanied by light *mediator* particles that would have allowed for efficient DM annihilation in the early Universe. In the simplest form of these theories an extra U(1) gauge field mixes with the SM U(1) gauge field, but with an additional kinetic term. This mixing term provides a *portal* from the dark sector to the charged particles of the SM. In this model, the mediators are called *dark photons* and are denoted by V.

Recently, a great deal of interest has been paid to the possibility of studying models of light (sub-GeV) Dark Matter at low-energy, fixed-target experiments [303,304,305,306]. High-flux neutrino beam experiments — such as LBNE — have been shown to potentially provide coverage of DM+mediator parameter space that cannot be covered by either direct detection or collider experiments.

Upon striking the target, the proton beam can produce the dark photons either directly through $pp(pn) \to V$ as in the left-hand diagram of Figure 7.6 or indirectly through the production of a π^0 or a η meson which then promptly decays into a SM photon and a dark photon as in the center diagram in the figure. For the case where $m_V > 2m_{DM}$, the dark photons will quickly decay into a pair of DM particles.

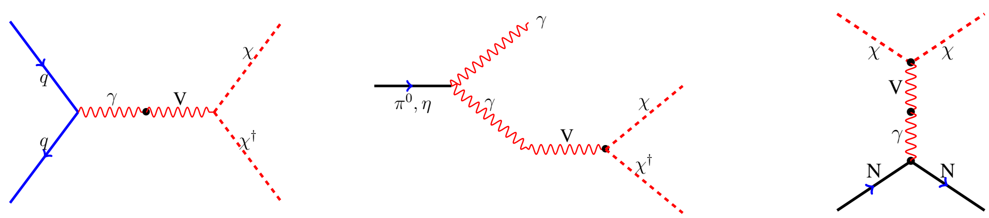

Figure 7.6: On the left is shown the direct production of a dark photon, while, in the center, the dark photon is produced via the decay of a neutral pion or eta meson. In both cases, the dark photon promptly decays into a pair of DM particles. Right: Tree-level scattering of a DM particle off of nuclei. Analogous interactions with electrons in the detector are also possible.

The LBNE ND together with the high-intensity beam will provide an excellent setup for making this measurement. The relativistic DM particles from the beam will travel along with the neutrinos to the detector where they can be detected through NC-like interactions either with electrons or nucleons, as shown in the right-hand diagram of Figure 7.6. Since the signature of a DM event looks similar to that of a neutrino event, the neutrino beam provides the major source of background for the DM signal.

Several ways have been proposed to suppress neutrino backgrounds using the unique characteristics of the DM beam. Since DM will travel much more slowly than the much lighter neutrinos, DM events in the ND will arrive out of time with the beam pulse. In addition, since the electrons struck by DM will be in a much more forward direction compared to neutrino interactions, the angle of these electrons may be used to reduce backgrounds, taking advantage of the ND's fine angular resolution.

Finally, a special run can be devised to turn off the focusing horn to significantly reduce the charged particle flux that will produce neutrinos. Figure 7.7 shows the expected sensitivity of the MiniBooNE DM search using this technique [306]. With a wider-band, higher-energy, more intense

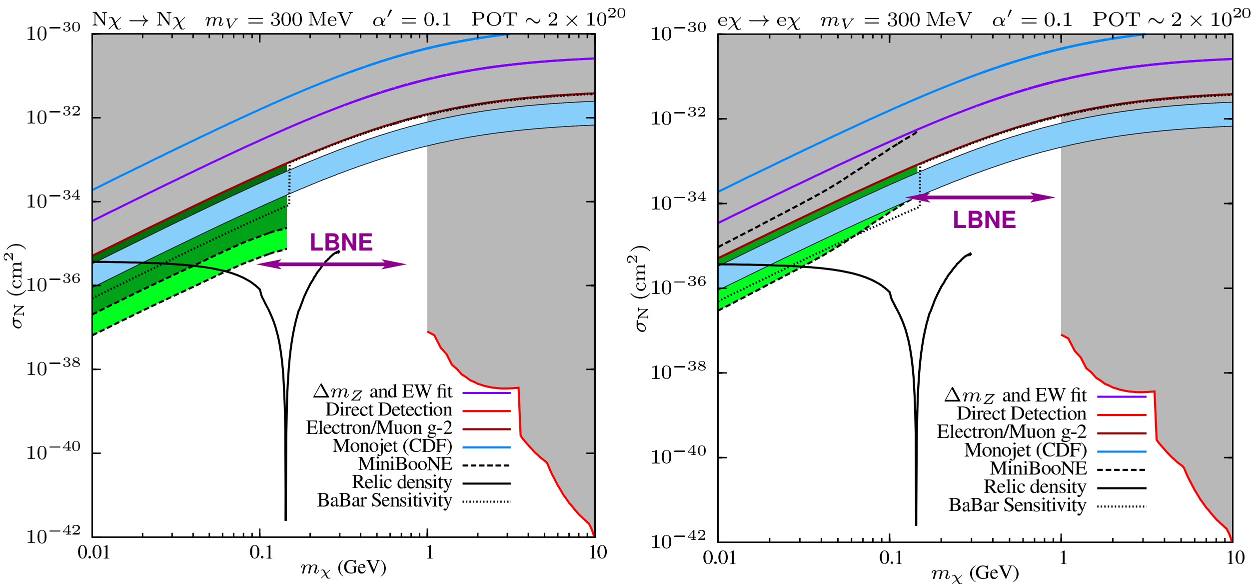

Figure 7.7: Regions of nucleon-WIMP scattering cross section (corresponding to dark matter in the lab moving with $v = 10^{-3}c$). The plot uses $m_V = 300$ MeV and $\alpha' = 0.1$. Constraints are shown from different experiments. The left plot shows the exclusion regions expected from MiniBooNE given 1-10 (light green), 10-1000 (green), and more than 1000 (dark green) elastic scattering events off nucleons. The right panel shows the same for elastic scattering off electrons. The magenta arrows indicate the region where LBNE can extend the MiniBooNE sensitivity. Figure is based on studies in [306].

beam, LBNE is expected to not only cover the MiniBooNE sensitivity region with higher statistics, but will also extend the sensitivity to cover the region between MiniBooNE and the direct DM searches. If the LBNE ND were a LArTPC and the entire detector volume active, the effective number of DM events detected would be much higher when compared to a MINOS-like detector of the same mass. Much more thorough studies must be conducted to obtain reliable sensitivities. This requires an integration of theoretical predictions into a simulation package for the detector.

Chapter 8 Additional Far Detector Physics Opportunities

The deep underground location of LBNE's LArTPC far detector will expand the range of science opportunities it can pursue to potentially include observation of solar and other low-energy neutrinos, dark matter, magnetic monopoles and nucleon-antinucleon transitions.

8.1 Solar Neutrinos

In the early 20^{th} century, Arthur Stanley Eddington suggested that nuclear reactions of protons fuel energy production in the Sun. After the discovery of the neutron, Hans Bethe [307] proposed that the first stage of these nuclear reactions involves the weak interaction: a β decay of a proton into a neutron, a positron and a neutrino accompanied by the fusion of that neutron with another proton to form deuterium. This proton-proton (pp) reaction $p+p \to ^1_1\text{H}+e^+ + \nu_e$ is the origin of most solar neutrinos (called pp neutrinos). In 0.2% of the cases deuterium is produced by the corresponding three-body reaction $p+e^-+p \to ^1_1\text{H}+\nu_e$ (called pep) which produces monoenergetic solar neutrinos at 1.4 MeV. The pp reaction is the starting point of a chain of nuclear reactions which converts four protons into a $^4_2$He nucleus, two positrons and two neutrinos. This reaction chain, shown in Figure 8.1, produces 98% of the energy from the Sun. In addition to pp and pep, neutrinos are produced by the reactions $^7_4\text{Be}+e^- \to ^7_3\text{Li}+\nu_e$ (^{7}Be neutrinos) and $^3_2\text{He}+p \to ^4_2\text{He}+e^+ + \nu_e$ (*hep* neutrinos) as well as the β decay $^8_5\text{B}\to ^8_4\text{Be}+e^+ + \nu_e \to ^4_2\text{He}+^4_2\text{He}+e^+ + \nu_e$ (^{8}B neutrinos). Carl-Friedrich von Weizsäcker [308] complemented the pp-chain with a cyclical reaction chain dubbed *CNO cycle* after the principal elements involved (shown in the top right illustration of Figure 8.1). Although theorized to be responsible for only 2% of energy production in the Sun, the CNO cycle plays the dominant role in the energy production of stars heavier than 1.3 solar masses.

The expected spectra of neutrinos from the pp reaction chain [309] are shown as solid curves in the bottom diagram of Figure 8.1. Neutrinos from the CNO cycle are shown as dashed blue curves.

The chief motivation of Raymond Davis to build his pioneering solar-neutrino detector in the Homestake mine was the experimental verification of stellar energy production by the observation of the neutrinos from these nuclear processes. While he succeeded in carrying out the first measurements of solar neutrinos — and shared the 2002 Nobel Prize in physics for the results — the measured flux [120] fell short of solar model calculations: the *solar-neutrino problem*. Data from the Super–Kamiokande (SK) and SNO [310,311] experiments eventually explained this mystery 30 years later as due to flavor transformation. However, intriguing questions in solar-neutrino physics remain. Some unknowns, such as the fraction of energy production via the CNO cycle in

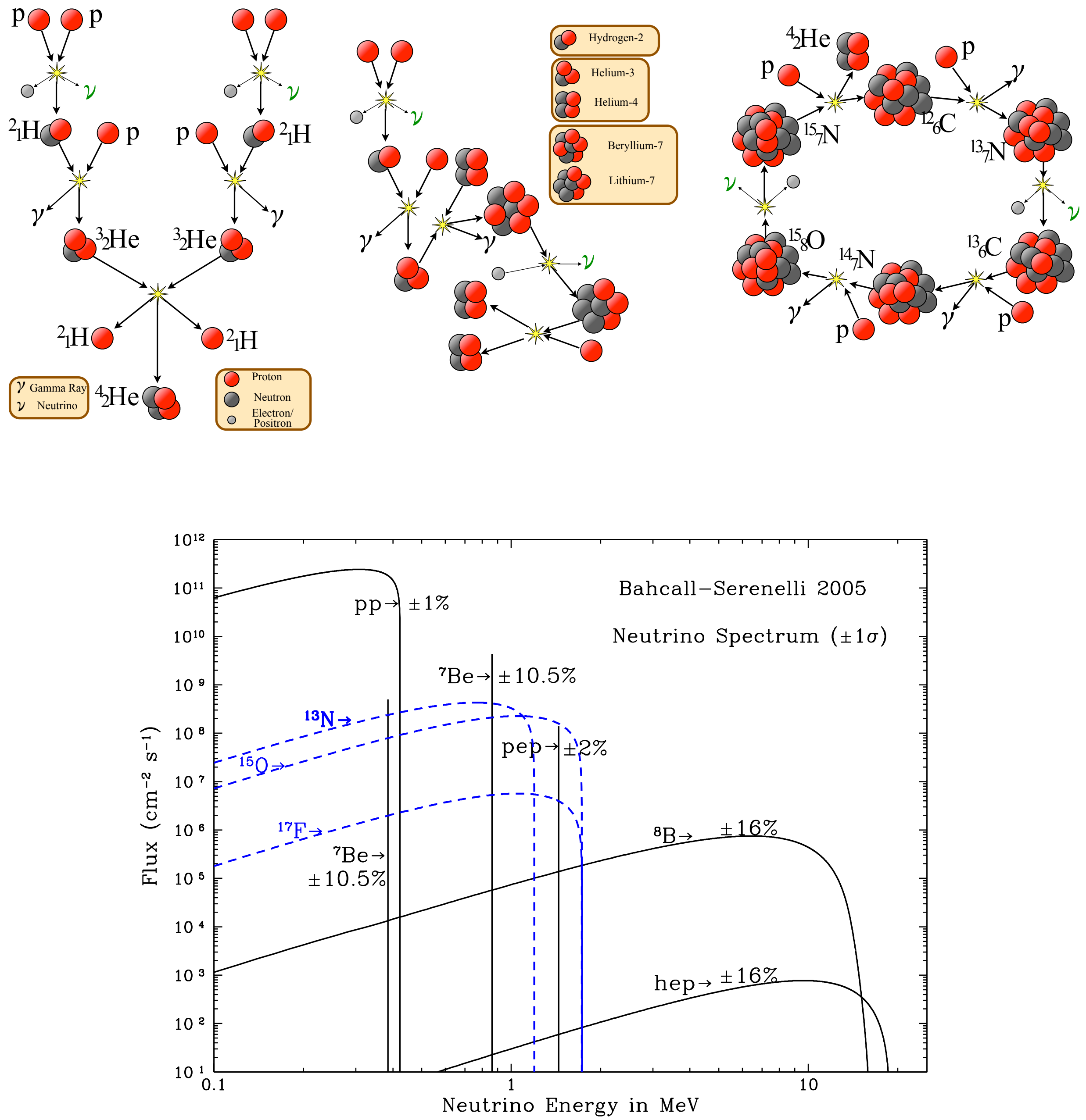

Figure 8.1: Top: the proton-proton and CNO reaction chain in the Sun. Bottom: solar-neutrino fluxes from [309].

the Sun, flux variation due to helio-seismological modes that reach the solar core, or long-term stability of the solar core temperature, are astrophysical in nature. Others directly impact particle physics. Can the MSW model explain the amount of flavor transformation as a function of energy, or are nonstandard neutrino interactions required? Do solar neutrinos and reactor antineutrinos oscillate with the same parameters? Experimental data expected in the immediate future (e.g., further data from Borexino [312] and SK as well as SNO+ [313]) will address some questions, but the high-statistics measurements necessary to further constrain alternatives to the standard oscillation scenario may need to wait for a more capable experiment such as LBNE.

Detection of solar and other low-energy neutrinos is challenging in a LArTPC because of high intrinsic detection energy thresholds for the charged-current (CC) interaction on argon ($>$5 MeV). To be competitive, this physics requires either a very low visible-energy threshold ($\sim$1 MeV) or a very large mass (50 kt). However, compared with other technologies, a LArTPC offers a large cross section and unique signatures from de-excitation photons. Aggressive R&D efforts in low-energy triggering and control of background from radioactive elements may make detection in LBNE possible, and a large detector mass would make the pursuit of these measurements worthwhile.

The solar-neutrino physics potential of a large LArTPC depends primarily on its energy threshold and depth. The energy threshold is not only determined by the ability to pick up a low-energy electron, but also by the light collection of the photon-triggering system as well as background suppression. Only at a deep underground location will it have a reasonable chance of detecting solar neutrinos. In any detector of this kind, the decay of the naturally occurring ^{39}Ar produces β's with a 567$-$keV endpoint and an expected rate of 10 MHz per 10 kt of liquid argon. This limits the fundamental reach of LBNE to neutrino interactions with visible energies above 1 MeV. Possible signatures of solar neutrinos in LBNE are:

Elastic scattering of ^{8}B neutrinos with electrons: This signature would only reproduce the SK data; SK has already accumulated large statistics (>60,000 solar-neutrino events). An energy threshold of about 1 MeV (lower than the SK threshold which is currently 3.5 MeV [314]) would be required for a more interesting measurement of *pep* (defined in Figure 8.1) and CNO fluxes. Such solar-neutrino interactions are difficult to detect, as only low-energy single electrons (and neutrinos) are produced.

Charged-current interactions with argon: The signature for this interaction is:

$$\nu_e + {}^{40}\mathrm{Ar} \rightarrow {}^{40}\mathrm{K}^* + e^- \tag{8.1}$$

This signal is more interesting experimentally, as there is a signature of de-excitation photons and the visible energy is directly correlated with the neutrino energy; however, the reaction has an energy threshold of 5 MeV.

Cosmic-muon and fast-neutrino interactions with the ^{40}Ar nucleus (which are rather complex compared to interactions on ^{16}O or ^{12}C) are likely to generate many long-lived spallation products that could limit the detection threshold for low-energy neutrinos. Studies of the spallation background in the LBNE LArTPC are underway. The production rate of ^{40}Cl, a beta emitter with an endpoint of 7.48 MeV that is a dominant source of background at energies above 5 MeV, is shown in Figure 8.2 as a function of depth. The cosmogenic background rates as a function of beta kinetic energy from several other beta emitters at the 4,850−ft level of Sanford Underground Research Facility are shown in Figure 6.8.

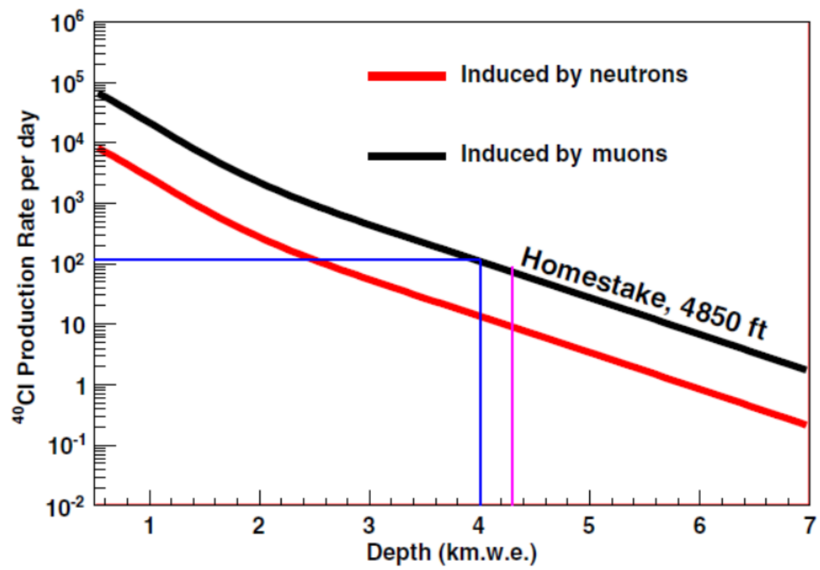

Figure 8.2: ^{40}Cl production rates in a 10−kt detector produced by (n,p) reaction as a function of depth.

In Table 8.1 the solar-neutrino event rate in a 34−kt LArTPC is shown, assuming a 4.5−MeV neutrino energy threshold and 31% ν_e.

Table 8.1: Solar-neutrino event rates in a 34−kt LArTPC assuming a 4.5−MeV neutrino energy threshold and an electron-flavor survival probability $P_{ee} = 31\%$.

Transition	Rate (evts/day)
Fermi	31
Gamow-Teller	88

The ICARUS Collaboration has reported a 10−MeV threshold [315]. Assuming the detector itself has low enough radioactivity levels, this threshold level would enable a large enough detector to measure the electron flavor component of the solar ^{8}B neutrino flux with high statistical accuracy. It could thereby further test the MSW flavor transformation curve (Figure 8.3) with higher statistical precision and potentially better energy resolution.

In addition to these solar matter effects, solar neutrinos also probe terrestrial matter effects with the variation of the ν_e flavor observed with solar zenith angle while the Sun is below the horizon — the *day/night effect*. A sizable effect is predicted only for the highest solar-neutrino energies, so while

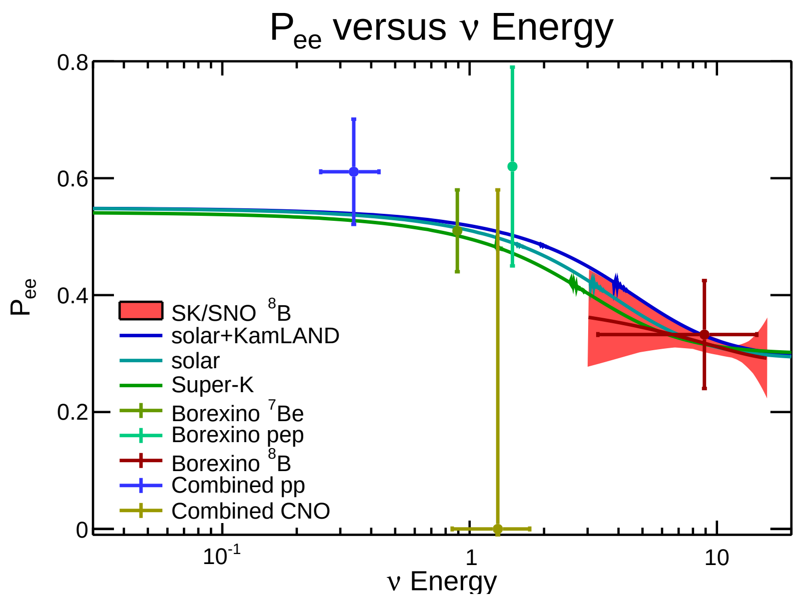

Figure 8.3: Measurements of the solar MSW transition. The red band combines SK and SNO ^{8}B data [75], the green measurements of ^{7}Be and pep are from Borexino [312,316] and the red error bar is Borexino's ^{8}B measurement [317]. The blue pp point and the yellow error bar (CNO) combine all solar data. MSW resonance curves for three different parameters are overlaid.

the comparatively high energy threshold is a handicap for testing the solar MSW resonance curve, it has a smaller impact on the high-statistics test of terrestrial matter effects. Recently, indication of the existence of the terrestrial matter effects were reported [76]. Measurements of this effect currently give the best constraints on the solar mass (Δm^2_{21}) splitting (Figure 8.4) using neutrinos rather than antineutrinos [318].

The comparison of ν disappearance to $\overline{\nu}$ disappearance tests CPT invariance. For good sensitivity to either solar-neutrino measurement, a liquid argon far detector of at least 34 kt is required.

8.2 Indirect Searches for WIMP Dark Matter

If the true nature of Dark Matter (DM) involves a weakly-interacting massive particle (WIMP) with a mass on the order of 1 GeV, an experiment could look for anomalous signals in astrophysical data from the annihilation (or decay) of DM into Standard Model particles, e.g., neutrinos [319]. Neutrinos produced by DM decay are expected to come from such distant objects as the galactic center, the center of the Sun or even from the Earth.

As our solar system moves through the DM halo, WIMPs interact with the nuclei of celestial bodies and become trapped in a body's gravitational well. Over time, the WIMPs accumulate near the core of the body, enhancing the possibility of annihilation. The high-energy neutrinos ($E \sim m_{\mathrm{WIMP}}$) from these annihilations can free-stream through the astrophysical body and emerge

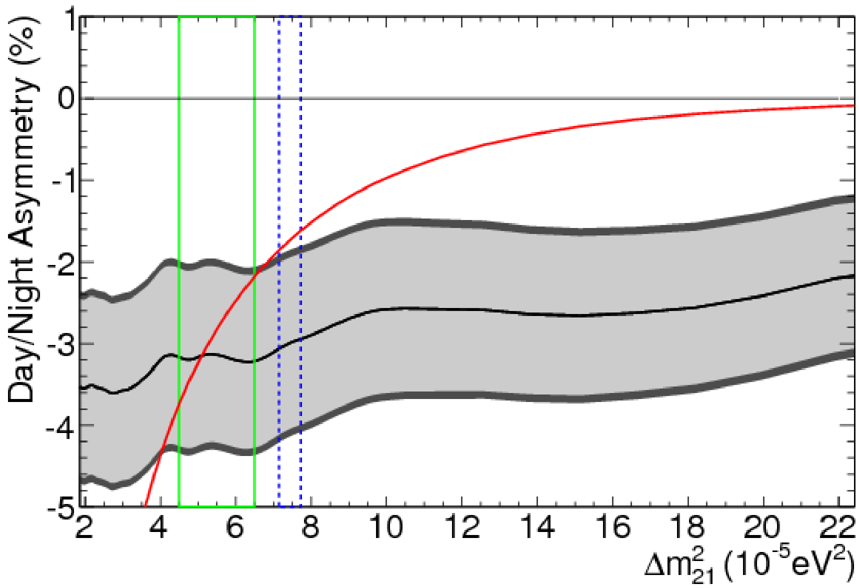

Figure 8.4: Dependence of the measured day/night asymmetry (fitted day/night amplitude times the expected day/night asymmetry in red) on Δm^2_{21}, for $\sin^2\theta_{12} = 0.314$ and $\sin^2\theta_{13} = 0.025$. The 1σ statistical uncertainties from the recent measurements by SK are given by the light grey band. The additional dark grey width to the band shows the inclusion of the systematic uncertainties. Overlaid are the 1σ allowed ranges from the solar global fit (solid green) and the KamLAND experiment (dashed blue). Figure is from [76].

roughly unaffected, although oscillation and matter effects can slightly alter the energy spectrum. Neutrinos produced via the nuclear-fusion processes in the Sun have energies close to 1 MeV, much lower than likely DM-decay neutrino energies.

The LBNE far detector's large mass and directional tracking capabilities will enable it to act as a *neutrino telescope* and search for neutrino signals produced by annihilations of dark matter particles in the Sun and/or the core of the Earth. Detection of high-energy neutrinos coming exclusively from the Sun's direction, for example, would provide clear evidence of dark matter annihilation [320].

IMB [321], IceCube [322] and SK, all water Cherenkov-based detectors, have searched for signals of DM annihilations coming from these sources, so far with negative results. A LArTPC can provide much better angular resolution than can water Cherenkov detectors, therefore providing better separation of the directional solar WIMP signal from the atmospheric-neutrino background. More thorough studies [323] are needed to determine whether LBNE could provide a competitive detection of dark matter.

8.3 Supernova Relic Neutrinos

Galactic supernovae are relatively rare, occurring somewhere between one and four times a century (Chapter 6). In the Universe at large, however, thousands of neutrino-producing explosions occur every hour. The resulting neutrinos — in fact most of the neutrinos emitted by all the supernovae since the onset of stellar formation — suffuse the Universe. Known both as *supernova relic neutrinos (SRN)* and as the *diffuse supernova-neutrino background (DSNB)*, their energies are in the few-to-30−MeV range. SRN have not yet been observed, but an observation would greatly enhance our understanding of supernova-neutrino emission and the overall core-collapse rate.

A liquid argon detector such as LBNE's far detector is sensitive to the ν_e component of the diffuse relic supernova-neutrino flux, whereas water Cherenkov and scintillator detectors are sensitive to the $\overline{\nu}_e$ component. However, backgrounds in liquid argon are as yet unknown, and a huge exposure ($>$500 kt · years) would likely be required for observation. Given a detector of the scale required to achieve these exposures (50 kt to 100 kt) together with tight control of backgrounds, LBNE — in the long term — could play a unique and complementary role in the physics of relic neutrinos.

In the current LBNE design, the irreducible background from solar neutrinos will limit the search for these relic neutrinos to an energy threshold greater than 18 MeV. Similarly, a search for relic antineutrinos is limited by the reactor-antineutrino background to a threshold greater than $\sim$10 MeV. The lower threshold and the smaller average ν_e energy relative to that for $\overline{\nu}_e$ (Figure 8.5) leads to the need for a larger detector mass.

A small but dedicated industry devotes itself to trying to predict the flux of these relic supernova neutrinos here on Earth [324,325,326,327,328,329,330,331]. Examples of two different predicted SRN spectra are shown in Figure 8.5, along with some of the key physics backgrounds from other neutrino sources.

In the LBNE LArTPC, relic supernova electron neutrinos would be detected primarily via the CC process as described by Equation 8.1. The electron track should be accompanied by evidence of ionization from the de-excitation of the potassium, e.g., shorter tracks sharing a common vertex; this is expected to help reduce backgrounds, but a detailed study has not yet been undertaken. In water Cherenkov and scintillator detectors, it is the $\overline{\nu}_e$ SRN flux that is detected through the process of inverse-beta decay. Unlike inverse-beta decay, for which the cross section is known to the several-percent level in the energy range of interest [332,333], the cross section for neutrino interactions on argon is uncertain at the 20% level [334,335,336]. Another limitation is that the solar *hep* neutrinos (defined in Figure 8.1), which have an endpoint at 18.8 MeV, will determine the lower bound of the SRN search window ($\sim$ 16 MeV). The upper bound is determined by the atmospheric ν_e flux as shown in Figure 8.5 and is around 40 MeV. Although the LArTPC provides

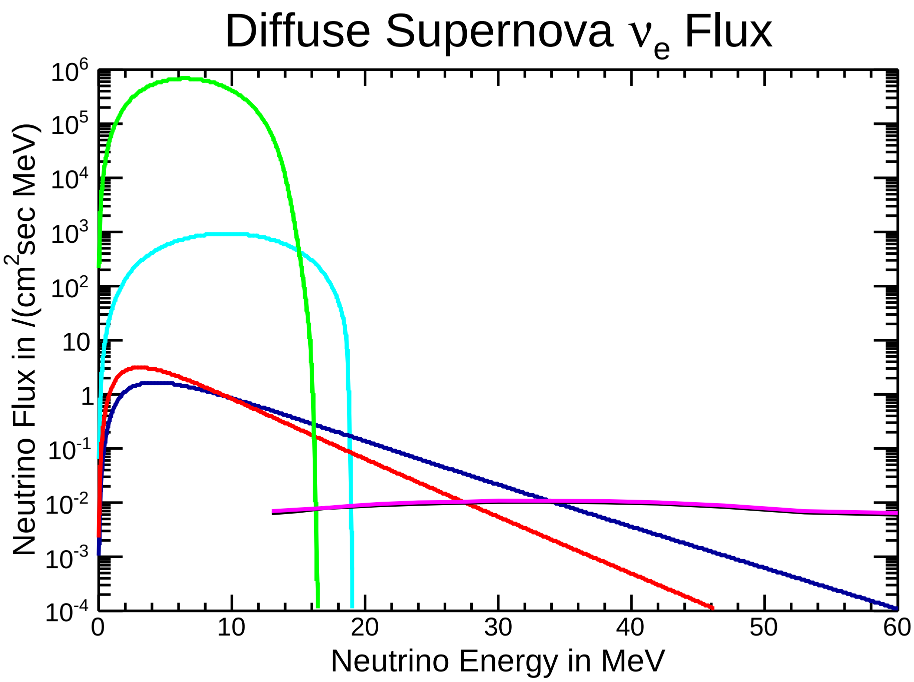

Figure 8.5: Predicted relic supernova ν_e spectra from two different models (red and blue) and some key neutrino backgrounds: ^{8}B solar ν_e (green), hep solar ν_e (cyan) and atmospheric ν_e (magenta).

a unique sensitivity to the ν_e component of the SRN flux, early studies indicate that due to this lower bound of ~16 MeV, LBNE would need a huge mass of liquid argon — of order 100 kt — to get more than 4σ evidence for the diffuse supernova flux in five years [337]. The expected number of relic supernova neutrinos, $N_{\rm SRN}$, that could be observed in a 100−kt LArTPC detector in five years [337] assuming normal hierarchy is:

$$N_{\rm SRN} = 57 \pm 12, \quad 16\,\mathrm{MeV} \le E_e \le 40\,\mathrm{MeV}, \tag{8.2}$$

where E_e is the energy of the electron from the CC interaction as shown in Equation 8.1. The estimate of the SRN rate in Equation 8.2 has a weak dependence on the value of $\sin^2\theta_{13}$. The above calculation is valid for values of $\sin^2\theta_{13} > 10^{-3}$. The main challenge for detection of such a low rate of relic neutrinos in a LArTPC is understanding how much of the large spallation background from cosmic-ray interactions with the heavy argon nucleus (some of which are shown in Figure 6.8) leaks into the SRN search window.

8.4 GUT Monopoles

Searches for massive, slow-moving magnetic monopoles produced in the early Universe continue to be of pressing interest. Magnetic monopoles left over from the Big Bang are predicted by Grand Unified Theories, but to date have not been observed. Because of the very large masses set by the

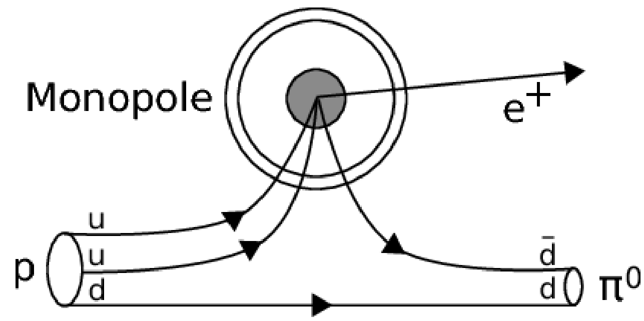

Figure 8.6: Illustration of a proton decay into a positron and a neutral pion catalyzed by a GUT monopole from [341].

GUT scale, these monopoles are normally non-relativistic, however searches for relativistic and ultra-relativistic monopoles are also of interest.

Relativistic monopoles are expected to be heavily ionizing, and hence best suited for detection in the large-area, neutrino-telescope Cherenkov detectors deployed in natural bodies of water or ice (e.g., [338,339]). With its much smaller active area, LBNE will most likely not be competitive in searches for fast monopoles.

Massive GUT monopoles are postulated to catalyze nucleon decay (Figure 8.6). It is possible that large underground detectors could detect this type of signal from transiting monopoles [340,341] via a signature consisting of multiple proton decays concurrent with the monopole's passage through the detector. Proton decay catalyzed by magnetic monopoles may be easier to observe in a LArTPC due to its superior imaging capability as compared to Cherenkov detectors, namely its high detection efficiency for a wider variety of proton decay modes, and its low energy thresholds. Whether these features are sufficient to overcome the limitation of smaller detector area relative to the very large neutrino telescopes has yet to be studied.

It should also be possible for LBNE to detect slow-moving monopoles via time-of-flight measurements, thereby eliminating reliance on the assumption of a proton-decay catalysis signature. The most stringent limits from direct searches for GUT monopoles with velocities in the range $4 \times 10^{-5} < \beta < 1$ have been obtained by the MACRO experiment [342], which has excluded fluxes at the level of $1.4 \times 10^{-16}\,\mathrm{cm}^{-2}\,\mathrm{s}^{-1}\,\mathrm{sr}^{-1}$. These limits probe the flux region just beyond that excluded by the existence of the galactic magnetic field (as characterized in variants of the Parker Bound).

The LBNE LArTPC far detector provides an opportunity to extend the reach of direct searches for slow monopoles, thanks to excellent timing and ionization measurement capabilities. Quantitative studies of sensitivity have yet to be carried out, but it is likely that the full-scope LBNE far detector will exceed the $10{,}000\,\mathrm{m} \cdot \mathrm{sr}$ isotropic-flux acceptance of MACRO.

8.5 Neutron-Antineutron Oscillations ($\Delta B = 2$)

Some Grand Unified Theories suggest the existence of double baryon-number-violating transitions that change nucleons into antinucleons [343]. The nucleon-antinucleon annihilation resulting from such a transition would provide an unmistakable signal in the LBNE LArTPC.

The imaging properties of the detector — superior to those of water detectors — would enable observation of nucleon annihilation final states in which the signal is broadened by the mix of charged and neutral hadrons. This signal could, however, be suppressed in a LArTPC if the neutron-to-antineutron transition rate is suppressed for bound neutrons due to interactions with the other nucleons.

8.6 Geo and Reactor $\overline{\nu}_e$'s

Electron antineutrinos ($\overline{\nu}_e$'s) produced by radioactive decays of the uranium, thorium and potassium present in the Earth are referred to as *geo-antineutrinos*. Decays of these three elements are currently understood to be the dominant source of the heat that causes mantle convection, the fundamental geological process that regulates the thermal evolution of the planet and shapes its surface. Detection of these geo-antineutrinos near the Earth's surface can provide direct information about the deep-Earth uranium and thorium content.

Geo-antineutrino energies are typically below 3.5 MeV. Reactor antineutrinos are somewhat more energetic, up to 8 MeV.

In a LArTPC, electron antineutrinos can in principle be detected by argon inverse-beta decay, represented by

$$\overline{\nu}_e + {}^{40}\mathrm{Ar} \rightarrow {}^{40}\mathrm{Cl}^* + e^+. \tag{8.3}$$

However, the threshold for this reaction is about 8.5 MeV, leading to the conclusion that an ^{40}Ar detector cannot use this method to detect either geo-antineutrinos or reactor antineutrinos.

Interaction via elastic scattering with electrons, another potential avenue, presents other obstacles. Not only are the recoil electrons from this interaction produced at very low energies, but solar neutrinos scatter off electrons and form an irreducible background roughly a thousand times larger than the geo-antineutrino signal. Although LBNE's location far away from any nuclear reactors leaves only a small reactor-antineutrino background and is thus favorable for geo-antineutrino detection, another detector technology (e.g., liquid scintillator) would be required to do so.

Chapter 9 Summary and Conclusion

The preceding chapters of this document describe the design of the Long-Baseline Neutrino Experiment, its technical capabilities, and the breadth of physics topics at the forefront of particle and astrophysics the experiment can address. This chapter concludes the document with several discussions that look forward in time, specifically:

- a consideration of how the design and construction of the LBNE experiment might unfold from this point on for a general class of staging scenarios,
- a summary of the grand vision for the science of LBNE and its potential for transformative discovery,
- a summary of the compelling reasons — such as LBNE's current advanced state of technical development and planning, and its alignment with the national High Energy Physics (HEP) program — for which *LBNE represents the world's best chance for addressing this science on a reasonable timescale*,
- comments on the broader impacts of LBNE, including the overarching benefits to the field of HEP, both within and beyond the U.S. program.

9.1 LBNE Staging Scenarios and Timeline

> With DOE CD-1 ("Alternate Selection and Cost Range") approval in hand, the LBNE Project is working toward its technical design specifications, including detailed costs and schedule, in preparation for CD-2 ("Performance Baseline"). It should be noted that the Project already has fully developed schedules for both the CD-1 scope (10−kt far detector on the surface at the Sanford Underground Research Facility, no near neutrino detector), and for the full-scope (34−kt far detector located deep underground and near neutrino detector) for the scenario of funding solely from DOE. Partnerships with non-DOE groups are being sought to enable the construction of LBNE with a near neutrino detector and an underground far detector mass greater than 10 kt in the first phase.

Section 1.2.3 described the substantial progress that has been achieved so far toward making LBNE a fully international project. While the specific form and timing of contributions from new partners are not yet known, there are several plausible scenarios in which the Project can be implemented to accommodate non-DOE contributions. A review of the DOE project milestones, indicating where flexibility and potential for incorporating non-DOE contributions exist, provides a starting point.

DOE-funded projects are subject to several *critical decision (CD)* milestones as shown in Figure 9.1 and explained in DOE Order O 413.3B [344]. At CD-2 the first-phase LBNE Project will

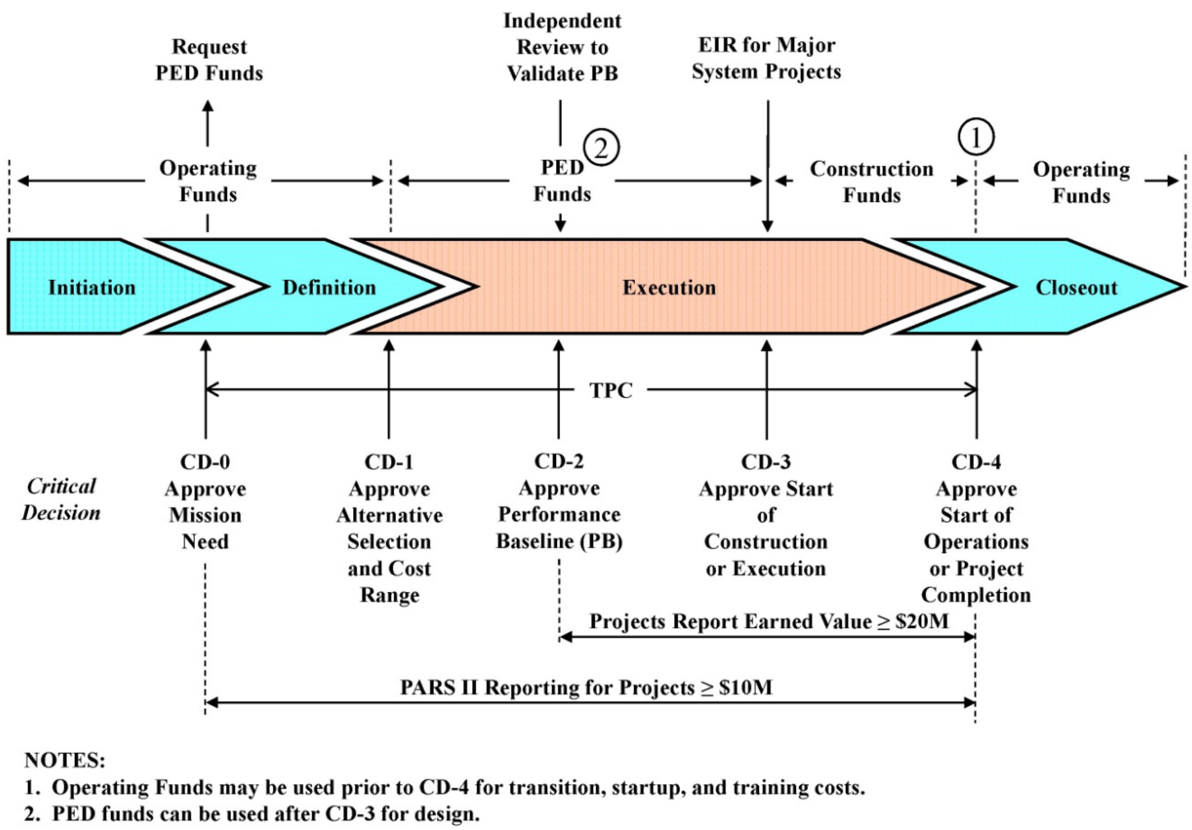

Figure 9.1: Typical DOE Acquisition Management System for line item capital asset projects [344].

be baselined. Currently, the timescale for CD-2 is projected to be toward the end of FY 2016, although the DOE has indicated flexibility in the project approval process specifically to allow for incorporation of scope changes enabled by additional partners. For example, it has been suggested that the design and construction approval for different portions of the Project can be approved at different times to facilitate proper integration of international partners. It is also expected that CD-3a approval (start of construction/execution) may take place for some parts of the Project before CD-2, thereby authorizing expenditures for long-leadtime components and construction activities, such as the advanced site preparation at Fermilab for the new beamline. The CD-4 milestone (completion of the construction project and transition to experiment operations) is currently projected for 2025. However, it is expected that commissioning and operations for LBNE will have started approximately a year before CD-4, which is considered the formal termination of the construction project.

The actual timeframe for achieving LBNE science goals will depend on the manner in which a complex sequence of developments takes place, including the actions of partners as well as implementation of the milestones above for the DOE-funded elements of the Project. Various scenarios for incorporating contributions from new partners/sources of funding have been identified [345].

Using the current understanding of DOE funding profiles, we outline one plausible long-term timeline that integrates evolution of LBNE detector mass with development of the Fermilab accelerator complex (i.e., PIP-II) and contributions from non-DOE partners. Implicit in this timeline is an assumption that agreements with new partners be put in place on a timescale of three years (by 2017). In this scenario, the milestones that bear on the physics are as follows:

1. LBNE begins operation in 2025 with a 1.2−MW beam and a 15−kt far detector. (In such a scenario, a significant fraction of the far detector mass might be provided in the form of a standalone LArTPC module developed, funded, and constructed by international partners.)
2. Data are recorded for five years, for a net exposure of 90 kt · MW · year.
3. In 2030, the LBNE far detector mass is increased to 34 kt, and proton beam power is increased to 2.3 MW.
4. By 2035, after five years of additional running, a net exposure of 490 kt · MW · year is attained.

Physics considerations will dictate the desired extent of operation of LBNE beyond 2035.

This very coarse timeline is indicative of the degree of flexibility available for the staging of various elements of LBNE. For example, near detector construction (and the corresponding funding) could be undertaken by partners outside the U.S., on a timescale driven by the constraints they face, and could be completed somewhat earlier or later than the far detector or beamline.

With this timeline as a guide, the discussion of LBNE physics milestones can be anchored by plausible construction scenarios.

9.2 Science Impact

While considering the practical challenges implicit in the discussion in Section 9.1 for the realization of LBNE, it is important to reiterate the compelling science motivation in broad terms.

The discovery that neutrinos have mass constitutes the only palpable evidence *within the body of particle physics data* that the Standard Model of electroweak and strong interactions does not describe all observed phenomena. In the Standard Model, the simple Higgs mechanism — now confirmed with the observation of the Higgs boson — is responsible for quark as well as lepton masses, mixing and CP violation. Puzzling features such as the extremely small masses of neutrinos compared to other fermions and the large extent of mixing in the lepton sector relative to the quark sector, suggest that new physics not included in the current Standard Model is needed to connect the two sectors. These discoveries have moved the study of neutrino properties to the forefront of experimental and theoretical particle physics as a crucial tool for understanding the fundamental nature and underlying symmetries of the physical world.

The measurement of the neutrino mass hierarchy and search for CP violation in LBNE will further clarify the pattern of mixing and mass ordering in the lepton sector and its relation to the patterns in the quark sector. The impact of exposures of 90 kt · MW · year (2030) and 490 kt · MW · year (2035) for Mass Hierarchy and CP-violation signatures is easily extracted from Figure 4.16. Should CP be violated through neutrino mixing effects, the typical signal in LBNE establishing this would have a significance of at least three (2030) and five standard deviations (2035), respectively for 50% of $\delta_{\rm CP}$ values (and greater than three standard deviations for nearly 75% of $\delta_{\rm CP}$ by 2035). In such a scenario, the mass hierarchy can be resolved with a sensitivity for a typical experiment of $\sqrt{\Delta\chi^2} \geq 6$ for 50% (100%) of $\delta_{\rm CP}$ by 2030 (2035).

If CP is violated maximally with a CP phase of $\delta_{\rm CP} \sim -\pi/2$ as hinted at by global analyses of recent data [69], the significance would be in excess of 7σ. This opportunity to establish the paradigm of leptonic CP violation is highly compelling, particularly in light of the implications for leptogenesis as an explanation for the Baryon Asymmetry of the Universe (BAU). With tight control of systematic uncertainties, additional data taking beyond 2035 would provide an opportunity to strengthen a marginally significant signal should $\delta_{\rm CP}$ take a less favorable value.

Similarly, the typical LBNE data set will provide evidence for a particular mass ordering by 2030 in the scenario described in Section 9.1, and will exclude the incorrect hypothesis at a high degree of confidence by 2035, over the full range of possible values for $\delta_{\rm CP}$, θ_{23} and the mass ordering itself. In addition to the implications for models of neutrino mass and mixing directly following from this measurement, such a result could take on even greater importance. Should LBNE exclude the normal hierarchy hypothesis, the predicted rate for neutrinoless double-beta decay would then be high enough so as to be accessible to the next generation of experiments [346]. A positive result from these experiments would provide unambiguous — and exciting — evidence that neutrinos are Majorana particles*, and that the empirical law of lepton number conservation — a law lacking deeper theoretical explanation — is not exact. Such a discovery would indicate that there may be heavier sterile right-handed neutrinos that mix with ordinary neutrinos, giving rise to the tiny observed neutrino masses as proposed by the seesaw mechanism [67]. On the other hand, a rejection of the normal neutrino mass hierarchy by LBNE coupled with a null result from the next generation of neutrinoless double-beta decay experiments would lead to the conclusion that neutrinos are purely Dirac particles. This would be a profound and astonishing realization, since it is extremely difficult theoretically to explain the tiny masses of Dirac neutrinos. High-precision neutrino oscillation measurements carried out by LBNE beyond 2035 may provide evidence for Majorana neutrino mass effects that are outside of the ordinary Higgs mechanism or for new interactions that differentiate the various neutrino species.

Within the program of underground physics, LBNE's most exciting milestones would correspond to observations of rare events. By 2035, LBNE will have been live for galactic supernova neutrino bursts for ten years in the above scenario. Such an event would provide a spectacular data set that would likely be studied for years and even decades to follow.

For proton decay, the net exposure obtained by 2035 in the above scenario also provides a compelling opportunity. A partial lifetime for $p \to K^+\overline{\nu}$ of 1×10^{34} years, beyond the current limit from Super-Kamiokande by roughly a factor of two, would correspond to six candidate events in LBNE by 2035, with 0.25 background events expected. Running for seven more years would double this sample. (Similarly, one should not ignore the corresponding value of an LBNE construction scenario that has a larger detector mass operating from the start, in 2025). With careful study of backgrounds, it may also be possible to suppress them further and/or relax fiducial cuts to gain further in sensitivity.

Finally, the proposed high-resolution near detector, operating in the high-intensity LBNE neutrino beam, will not only constrain the systematic errors that affect the oscillation physics but will also conduct precise and comprehensive measurements of neutrino interactions — from cross sections to electroweak constants.

9.3 Uniqueness of Opportunity

Considering the time and overall effort taken to reach the current state of development of LBNE, it will be challenging for alternative programs of similarly ambitious scope to begin operation before 2025, particularly in light of the current constrained budget conditions in HEP. It should be noted that similar-cost alternatives for the first phase of LBNE utilizing the existing NuMI beam

*A Majorana particle is an elementary particle that is also its own antiparticle were considered during the reconfiguration exercise in 2012 [25]. The panel concluded that none of these alternatives presented a path toward an experiment capable of a CP-violation signal of 5σ. Furthermore, a large water Cherenkov far detector option for LBNE was carefully considered prior to selection of the LArTPC technology [347]. While both detector options are capable of satisfying the scientific requirements, the LArTPC was judged to have a better potential for scientific performance while also presenting the attraction of an advanced technological approach.

In the broader context of planned experimental programs with overlapping aims for portions of the LBNE science scope, it must be recognized that progress will be made toward some of these during the period before LBNE operations commence. For example, indications for a preferred neutrino mass ordering may emerge from currently running experiments and/or from dedicated initiatives that can be realized on a shorter timescale. Global fits will continue to be done to capitalize, to the extent possible, on the rich phenomenology of neutrino oscillation physics where disparate effects are intertwined. At the same time, each experimental arena will be subject to its own set of systematic uncertainties and limitations.

It is in this sense that the power of LBNE is especially compelling. LBNE will on its own be able to measure the full suite of neutrino mixing parameters, and with redundancy in some cases. To use the MH example just given, it is notable that LBNE will have sensitivity both with beam and atmospheric neutrinos. Control of the relative $\nu_\mu/\overline{\nu}_\mu$ content of the beam as well as the neutrino energy spectrum itself, provides additional handles and cross-checks absent in other approaches.

9.4 Broader Impacts

9.4.1 Intensity Frontier Leadership

The U.S. HEP community faces serious challenges to maintain its vibrancy in the coming decades. As is currently the case with the LHC, the next-generation energy frontier facility is likely to be sited outside the U.S. It is critical that the U.S. host facilities aimed at pursuing science at the HEP scientific frontiers (Figure 3.1), the lack of which could result in erosion of expertise in key technical and scientific sectors (such as accelerator and beam physics).

LBNE represents a world-class U.S.-based effort to address the science of neutrinos with technologically advanced experimental techniques. By anchoring the U.S. Intensity Frontier program [348], LBNE provides a platform around which to grow and sustain core infrastructure for the community. Development of the Fermilab accelerator systems, in particular, will not only advance progress toward achieving the science goals of LBNE, it will also greatly expand the capability of Fermilab to host other key experimental programs at the Intensity Frontier.

9.4.2 Inspirational Project for a New Generation

Attracting young scientists to the field demands a future that is rich with ground-breaking scientific opportunities. LBNE provides such a future, both in the technical development efforts required and its physics reach. The unparalleled potential of LBNE to address fundamental questions about the nature of our Universe by making high-precision, unambiguous measurements with the ambitious technologies it incorporates will attract the best and brightest scientists of the next generation to the U.S. HEP effort.

A young scientist excited by these prospects can already participate in current experiments — some of which use medium-scale LArTPCs — and make contributions to leading-edge R&D activities that provide important preparation for LBNE, both scientifically and technically.

9.5 Concluding Remarks

Understanding the fundamental nature of fermion flavor, the existence of CP violation in the lepton sector and how this relates to the Baryon Asymmetry of the Universe; knowing whether proton decay occurs and how; and elucidating the dynamics of supernova explosions all stand among the grand scientific questions of our times. The bold approach adopted for LBNE provides the most rapid and cost-effective means of addressing these questions. With the support of the global HEP community, the vision articulated in this document can be realized in a way that maintains the level of excitement for particle physics and the inspirational impact it has in the U.S. and worldwide.

Appendix A LBNE Detector Simulation and Reconstruction

A 10−kt or larger LArTPC far detector fulfills the high-mass requirement for LBNE and provides excellent particle identification with high signal-selection efficiency ($\geq 80\%$) over a wide range of energies. The far detector is described in detail in the LBNE Conceptual Design Report Volume 1 [29] and briefly in Section 3.6 of this document. This appendix summarizes the status of the LBNE LArTPC simulation and reconstruction efforts and their expected performance.

A.1 Far Detector Simulation

A.1.1 Tools and Methods

In the full simulation of the far detector, neutrino interactions are simulated with Geant4 [132] using the LArSoft [220] package. LArSoft is being developed to provide an integrated, experiment-agnostic set of software tools to perform simulation, data reconstruction and analysis for LArTPC neutrino experiments. Individual experiments provide experiment-specific components including a detector geometry description and analysis code, and they contribute to the LArSoft software development itself.

LArSoft is based on *art* [349], an event-processing framework developed and supported by the Fermilab Scientific Computing Division. *Art* is designed to be shared by multiple experiments and is currently used by several intensity frontier experiments, including NOνA, Mu2e, MicroBooNE [350] and ArgoNeuT [351]. The last two have liquid argon TPC-based detectors and thus share many simulation and reconstruction requirements with LBNE. Reconstruction algorithms developed in LArSoft for the ArgoNeuT and MicroBooNE experiments can readily benefit LBNE. Examples of neutrino beam interactions in a LArTPC obtained from the LArSoft package using the MicroBooNE detector geometry are shown in Figure A.1.

The LBNE far detector geometries currently available in LArSoft are the LBNE 10−kt surface detector and the 34−kt underground detector. Also included is geometry for a 35−t prototype that LBNE has constructed at Fermilab*. The LBNE far detector geometry description is generated in a flexible way that allows the simulation of various detector design parameters such as the wire spacing and angles, drift distances, and materials. The photon-detector models are based on the design that uses acrylic bars coated with wavelength-shifting tetraphenyl butadiene (TPB), read out with silicon photomultiplier tubes (SiPMs).

Geant4 is used to simulate particles traveling through the active and inactive detector volumes

*One of the goals of the 35−t prototype is to test key elements of the TPC module design for the 10−kt and 34−kt detectors including the wrapped wire planes and drift distances.

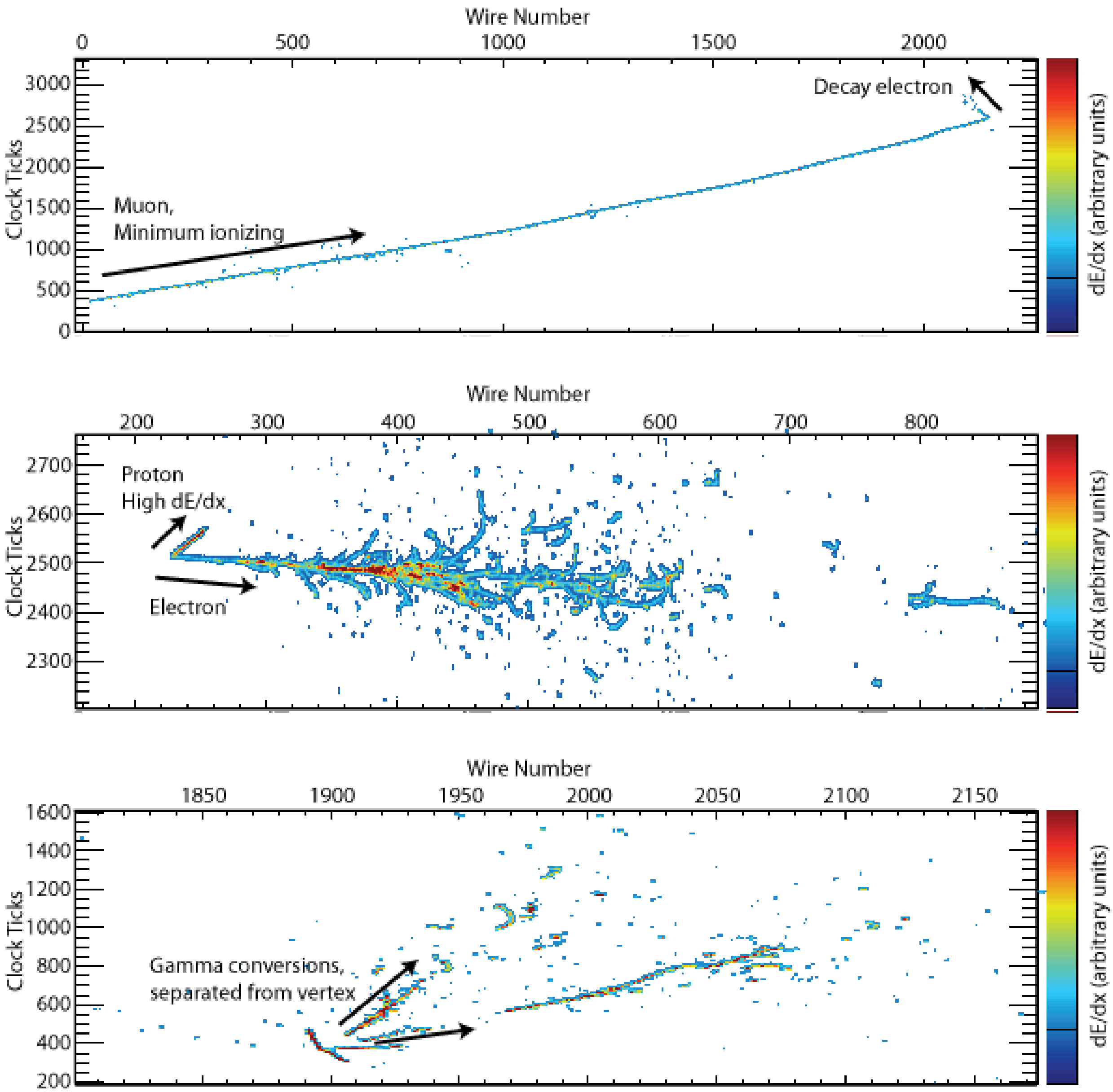

Figure A.1: Examples of neutrino beam interactions in a LArTPC obtained from a Geant4 simulation [220]. A ν_μ-CC interaction with a stopped μ followed by a decay Michel electron (top), a ν_e-CCQE interaction with a single electron and a proton (middle), and an NC interaction which produced a π^0 that then decayed into two γ's with separate conversion vertices (bottom).

and the surrounding materials such as the cryostat and rock. The tens of thousands of photons and electrons produced (by the ionization of the argon) per MeV deposited are simulated using a parameterization rather than a full Geant4 Monte Carlo, as tracking them individually would be prohibitive. The drifting electrons are modeled as many small clouds of charge that diffuse as they travel toward the collection wires. The response of the channels to the drifting electrons is parameterized as a function of drift time, with a separate response function for collection and induction wires. The signals on the induction-plane wires result from induced currents and are thus bipolar as a function of time as charge drifts past the wires, while the signals on the collection-plane wires are unipolar. The response functions include the expected response of the electronics. Noise is simulated using a spectrum measured in the ArgoNeuT detector. The decays of ^{39}Ar are included, but some work is required to make them more realistic.

For the 10−kt far detector, a 1.5-ms readout of the TPC signals at 2 MHz gives a simulated data volume of just under 2 GB per event. If the readout is extended to include the beam window, then in order to collect charge deposited by cosmic rays (which would otherwise be partially contained), a greater data volume will be required. To reduce the data volume and speed up the calculation, long strings of consecutive ADC counts below a settable threshold are suppressed in the readout. Huffman coding of the remaining data is included in the digitization [352].

The photon-detection system likewise requires a full Monte Carlo simulation. Photons propagating from the TPC to the acrylic bars have been fully simulated using Geant4, and their probabilities of striking each bar (as a function of the emission location and the position along the bar at which the photon strikes) have been computed. Smooth parameterizations of these functions are currently used in the simulation to compute the average number of photons expected to strike a bar (as a function of position along it). Given the current design of the optical detectors, approximately 2-3% of VUV (vacuum ultraviolet) photons produced uniformly in the fiducial detector volume strike the bars. This low number is largely due to the small fraction of the total area in contact with the argon that is represented by the bars, and the low reflectivity of the stainless steel cathode planes, the field cage and the CuBe wires.

A second function is used to parameterize the attenuation of light within the bar as a function of position along the bar. The total response of a SiPM to light produced in the detector is the product of the number of photons produced, the probability of the photons to survive propagation, the interaction with the wavelength shifter (commonly called *downconversion*), the attenuation in the bar, and the detection efficiency of the SiPM. This product is used as the mean of a Poisson distribution from which the number of photoelectrons is randomly drawn to simulate the measurement of the SiPM. Measured waveforms for cold SiPMs are used in simulating the digitized response. Measurements in prototype dewars will be used to normalize the yield for signals in the SiPMs as a function of the incident location of the VUV photon on the bar. The NEST [353] model, which describes the conversion of ionization energy into both electrons and photons in an anticorrelated manner, and which has been shown to model a large range of data from noble liquid detectors, is currently being incorporated into the LBNE detector simulation.

A variety of event generators are available for use in the simulation. Neutrino hard-scattering interactions and subsequent nuclear breakup are simulated using GENIE [133], though the use of other generators is possible. Cosmic rays are simulated with CRY [354]. Single particles can be generated one at a time, and general text-file interfaces are available allowing arbitrary generators to be used without linking them with LArSoft.

Currently, samples of single electrons, muons, charged and neutral pions, protons and tau leptons have been generated and simulated using the 10−kt surface geometry and the 35-ton geometry, though without photon-detector simulation. These samples are being used to develop reconstruction algorithms.

Planned improvements to the simulation include creating an interface to a calibration database, updating the response functions with measured responses from MicroBooNE, which uses an electronics design very similar to that of LBNE, simulating the effects of space-charge buildup in the drift volume, and creating more detailed maps of the drift in the gaps between the APAs and the charge that is deposited between the wire planes.

A.1.2 Low-Energy Neutrino-Response Studies with LArSoft

Work is currently underway using the LArSoft simulation package to characterize low-energy response for realistic LBNE detector configurations. Figure A.2 shows a sample 20−MeV event in the LBNE 35−t prototype geometry simulated with LArSoft. So far, most studies have been done with the MicroBooNE geometry, with the results expected to be generally applicable to the larger LBNE detector. For a preliminary understanding of achievable energy resolution, isotropic and uniform monoenergetic electrons with energies of 5-50 MeV (which should approximate the ν_e-CC electron products) were simulated and reconstructed with the LArSoft package. The charge of reconstructed hits on the collection plane was used to reconstruct the energy of the primary electrons. (Induction-plane charge as well as track-length-based reconstruction were also considered, but with inferior results). Figure A.3 shows the results. A correction to compensate for loss of electrons during drift, $Q_{collection} = Q_{production} \times e^{-T_{\rm drift}/T_{\rm electron}}$ (where T_{drift} is the drift time of the ionization electrons, and $T_{electron}$ is the electron lifetime), using Monte Carlo truth to evaluate $T_{\rm drift}$, improved resolution significantly. This study indicated that photon time information will be valuable for low-energy event reconstruction. Some of the resolution was determined to be due to imperfect hit-finding by the nominal reconstruction software. A tuned hit-finding algorithm did somewhat better (Figure A.3), and further improvements for reconstruction algorithms optimized for low-energy events are expected.

Also under study is the potential for tagging ν_e-CC absorption events ($\nu_e + {}^{40}\mathrm{Ar} \rightarrow e^- + {}^{40}\mathrm{K}^*$) using the cascade of de-excitation γ rays, which should serve the dual purposes of rejecting background and isolating the CC component of the signal.

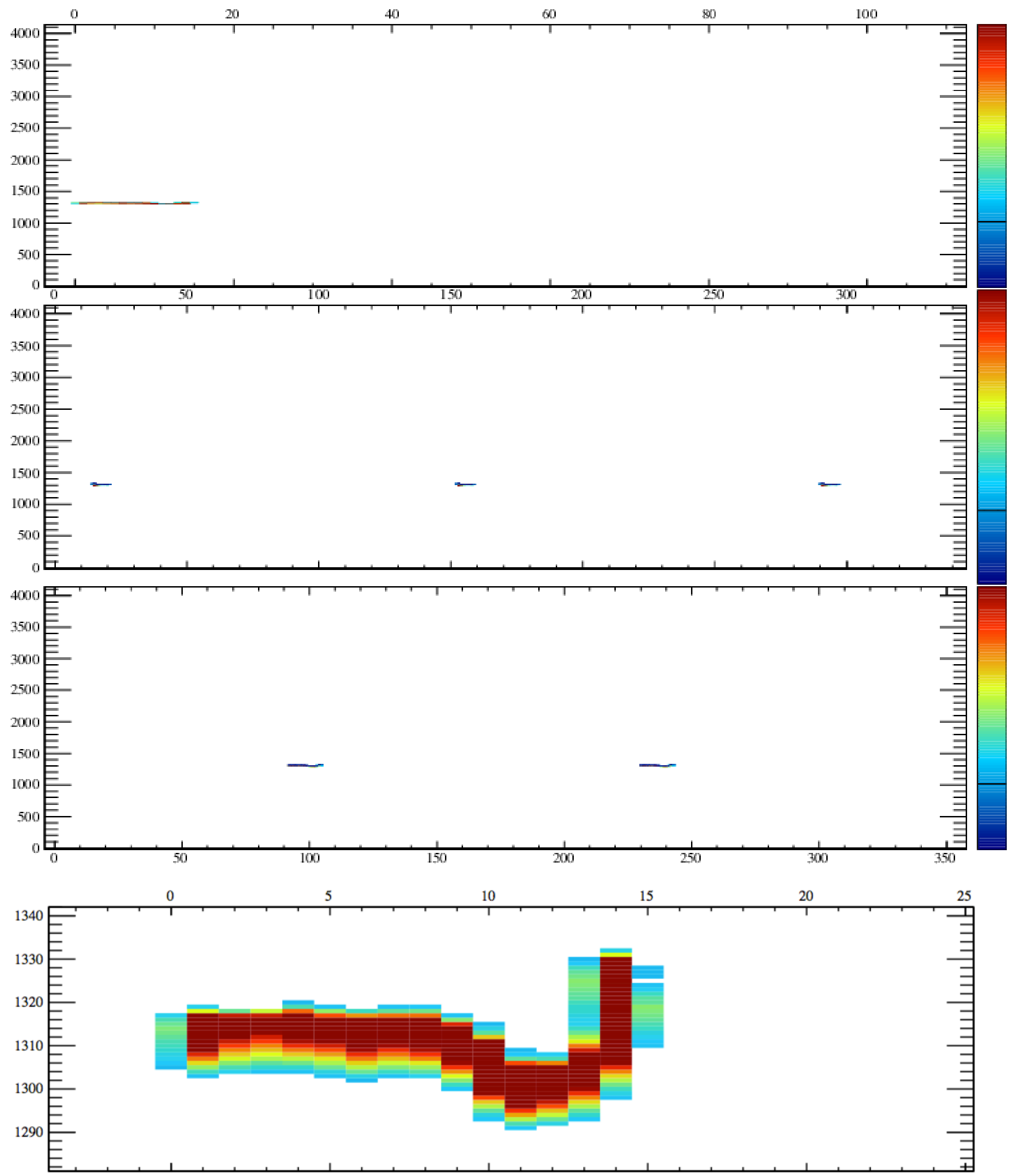

Figure A.2: Raw event display of a simulated 20−MeV event in the LBNE 35−t prototype; the top panel shows the collection plane, and the lower two panels show the induction planes (with multiple images due to wire wrapping). The bottom panel shows a zoom of the collection plane image.

A.2 Far Detector Reconstruction

The first stage of reconstruction of TPC data is unpacking and deconvoluting the electronics and field response of the wire planes. The deconvolution function includes a noise filter that currently is parameterized with ArgoNeuT's noise, but will be tuned for the eventual noise observed in the

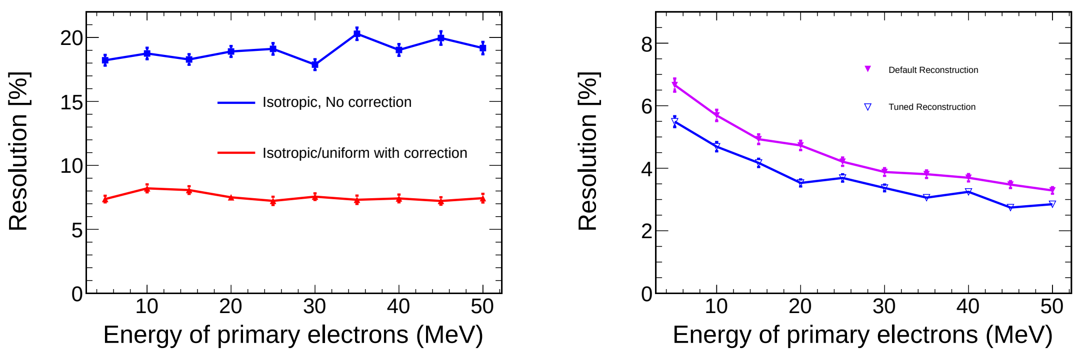

Figure A.3: Left: Comparison of energy resolution (defined as σ/E, where σ is the spread of the collection-plane-charge-based event energy E for a monoenergetic electron), with and without electron-lifetime correction, as a function of electron energy. The blue curve is the energy resolution of isotropic and uniform electrons without electron-lifetime correction. The red curve is the energy resolution with electron-lifetime correction based on MC truth. Right: Comparison of energy resolution before and after tuning the reconstruction algorithm (for fixed position/direction electron events).

LBNE detector. The deconvolution makes sharp, unipolar pulses from the bipolar induction-plane signals and also sharpens the response to collection-plane signals. Hits are then identified in the deconvoluted signals by fitting Gaussian functions, allowing for sums of several overlapping hits in each cluster. In LBNE, because of the large quantity of channels in the far detector, any inefficiency in CPU and memory is magnified. Improvements in the memory-usage efficiency relative to the ArgoNeuT and MicroBooNE implementations have been realized by rearrangement of the processing order and limiting the storage of the intermediate uncompressed raw data and the deconvoluted waveforms.

After signal deconvolution, line-finding and clustering based on a Hough transform in two dimensions is done using an algorithm called *fuzzy clustering* [355]. This clustering is performed separately on data from each induction plane. Since the hit data on LArTPCs are inherently 2D — wire number and arrival time of the charge — the location of the initial ionization point has a 2D ambiguity if the deposition time is unknown. For beam events, the t_0 is known, and thus only a 1D ambiguity remains; this 1D ambiguity is broken by angling the induction-plane wires relative to the collection-plane wires, in order to measure the y location of the hits for which t (thus x) and z are known. For (non-beam) cosmic-ray signals which arrive uniformly in time, the photon system provides t_0. After clustering, 3D track-fitting is performed using a Kalman filter [356]. Dedicated algorithms have been developed to optimize electromagnetic shower reconstruction and energy resolution.

LBNE poses a unique challenge for reconstruction because the induction-plane wires wrap around the edges of the APA frames. This introduces discrete ambiguities that are not present in other LArTPC designs. Whereas a hit on a collection-plane wire identifies uniquely the side of the APA from which it came, this is not known for a hit on an induction-plane wire. The angles between the U and V plane wires are slightly different from 45° and from each other in order to break the ambiguities. A combinatoric issue arises, however, if many hits arrive on different wires at nearly the same time, for instance when a track, or even a track segment, propagates in a plane parallel to the wire planes (i.e., at constant drift distance). Showers will also contain many hits on different wires that arrive at similar times. Hits that arrive at different times can be clustered separately in the Z, U, and V views without ambiguity, while hits that arrive at similar times must be associated using a topological pattern-recognition technique. LBNE is developing a version of the fuzzy clustering tool for use as a pattern-recognition step to allow association of Z, U and V hits, a step that is needed to assign the correct y position to a track segment or portion of a cluster. This process is called *disambiguation* of the induction hits. Misassignment can affect particle-ID performance and reconstructed-energy resolution because fully contained tracks may appear partially contained and vice versa. After disambiguation has been performed, standard track, vertex and cluster reconstruction algorithms are applied.

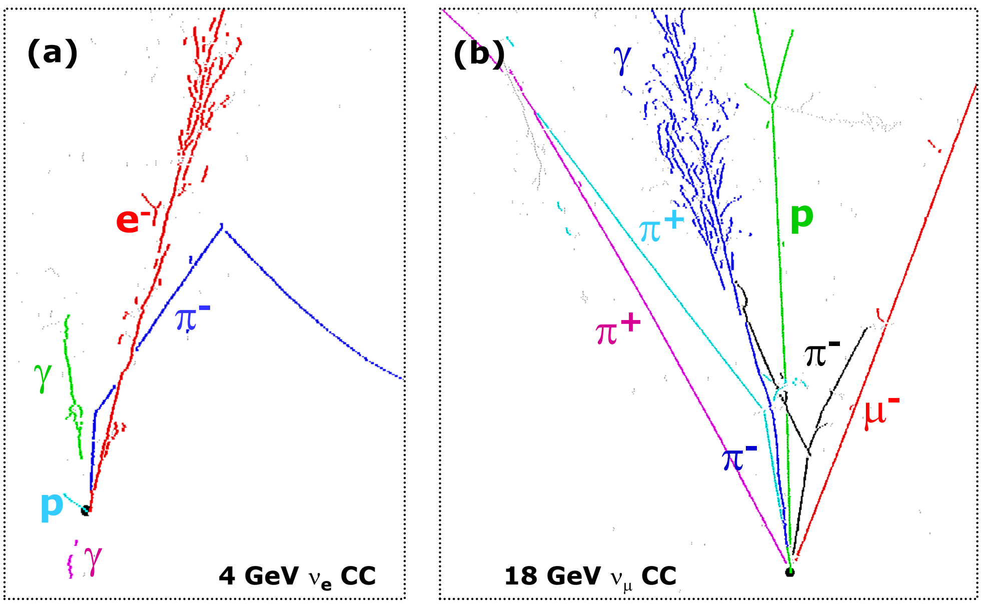

Figure A.4: PANDORA's 2D clusterings of hits created by the particles in two CC neutrino interactions in liquid argon. Panel (a) shows a 4−GeV ν_e interaction, and panel (b) shows an 18−GeV ν_μ interaction. The colors indicate the clusters into which PANDORA has divided the hits, and the particle labels are from the MC truth.

A promising suite of algorithms for event reconstruction is provided by the PANDORA toolkit [357], which provides a framework for reconstruction algorithms and visualization tools. Currently it is being used to develop pattern-recognition algorithms and to reconstruct primary vertices. PANDORA's pattern-recognition algorithm merges hits based on proximity and pointing to form 2D clusters. Vertices are then identified from the clusters that best connect to the same event. Clusters that best correspond to particles emitted from the primary vertex are identified in 2D. These particle candidates are then used to seed 3D reconstructed particles, and a 3D primary vertex is identified. Examples of PANDORA's 2D clustering are shown in Figure A.4 for two simulated CC neutrino-scattering events. Figure A.5 shows the primary vertex spatial resolution in 3D with well-contained simulated beam-neutrino events, using the nominal LBNE spectrum and MicroBooNE geometry.

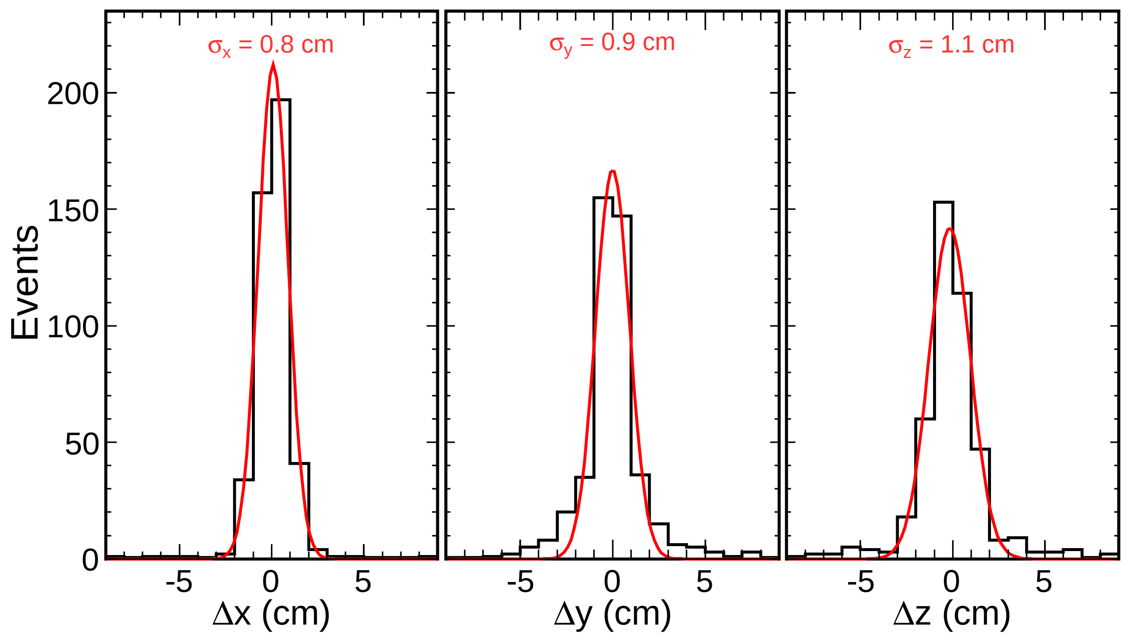

Figure A.5: Distributions of the residuals between the reconstructed and the Monte Carlo true locations of primary vertices in neutrino interactions in the MicroBooNE geometry using the LBNE beam spectrum. The x axis is oriented along the drift field, the y axis is parallel to the collection-plane wires, and the z axis points along the beam direction.

A.3 Fast Monte Carlo

The LBNE full Monte Carlo (MC) simulation will use a Geant4 simulation of the beamline to estimate the neutrino flux, a neutrino interaction generator (e.g., GENIE), and detailed detector simulation that mimics the real detector output for data events. Both data and MC will have the same reconstruction algorithms applied to produce quantities that will be used to analyze the data. The full MC detector simulation and reconstruction algorithms are still under development. Due to their detailed nature, these algorithms are CPU-intensive and time-consuming to run.

In parallel, a Fast Monte Carlo simulation has been developed and is available for use in place of the full MC to explore long-baseline physics analysis topics. A preliminary version of the Fast MC is currently available. Results from the latest detector simulations and advancements in reconstruction algorithms are actively being incorporated to improve the physics models and detector parameterization. Because the Fast MC replaces CPU-intensive portions of the full MC simulation with a fast parameterized model, it offers a quick, dynamic alternative which is useful for trying out new ideas before implementing them in the full MC. This usefulness is expected to remain even after the full MC simulation is mature.

To accurately approximate a full MC simulation, the Fast MC combines the Geant4 LBNE beamline flux predictions, the GENIE event interaction generator, and a parameterized detector response that is used to simulate the measured (reconstructed) energy and momentum of each final-state particle. The simulated energy deposition of the particles in each interaction is then used to calculate reconstructed kinematic quantities (e.g., the neutrino energy), and classify the type of neutrino interaction, including backgrounds and misidentified interactions.

The Fast MC is designed primarily to perform detailed sensitivity studies that allow for the propagation of realistic systematic uncertainties. It incorporates effects due to choices of models and their uncertainties and design decisions and tolerances. The neutrino flux predictions, the neutrino-interaction cross-section models, and the uncertainties related to these are also incorporated. The parameterized detector response is informed by Geant4 simulations of particle trajectories in liquid argon, by studies of detector response simulation in MicroBooNE [350], results reported by the ICARUS Collaboration, and by the expected LBNE detector geometry. The realistic parameterization of reconstructed energy and angle resolution, missing energy, and detector and particle identification acceptances provide a simulation that respects the physics and kinematics of the interaction and allows for propagation of model changes to final-state reconstructed quantities.

Future efforts will allow for propagation of uncertainties in detector effects and of detector design choices. It should be noted that the same GENIE files generated for the Fast MC can be used as inputs for the full detector simulation and the results of the two simulations can be compared both on an event-by-event basis and in aggregate. Studies of this nature can be used to tune the Fast MC and to cross-check the full simulations.

In the current configuration of the Fast MC, GENIE generates interactions on ^{40}Ar nuclei with neutrinos selected from the energy spectra predicted by the Collaboration's Geant4 flux simulations (described in Section 3.4). For each interaction simulated in GENIE, a record of the interaction process, its initial kinematics, and the identity and four-momenta of the final-state particles is produced. The parameterized detector response applies spatial and energy/momentum smearing to each of the final-state particles based on the particle properties and encoded detector-response parameters. Detection thresholds are applied to determine if a final-state particle will deposit energy in the detector and if that energy deposition will allow for particle identification. The detector responses for neutrons and charged pions account for a variety of possible outcomes that describe the way these particles deposit energy in the detector. Neutral pions are decayed into two photons. Their conversion distance from the point of decay determines the starting position of the resulting electromagnetic showers. This distance is chosen from an exponential distribution with a characteristic length based on the radiation length of photons in liquid argon. Tau leptons are also decayed by the Fast MC and their decay products are dealt with appropriately. The spatial extent of tracks and showers in liquid argon is simulated in Geant4 and encoded as a probability distribution function (PDF) or parameterization. Combined with vertex placement in a fiducial volume, the fraction of particle energy and/or track length visible in the detector is determined.

Once the Fast MC reconstructs the kinematics of the event (E_ν, E_{had}, Q^2, x, y, and so on), based on the smeared four-vectors of particles that are above detection threshold, it searches interaction final-state particle lists for lepton candidates to be used in event classification algorithms. The resulting classifications are used to isolate samples for the ν_e appearance and the ν_μ disappearance analyses which are in turn used to build energy spectra on an event-by-event basis.

Currently the classification algorithm categorizes each event as either ν_e-CC, ν_μ-CC, or NC. Events with a candidate muon are classified as ν_μ-CC. Events without a candidate muon, but with a candidate electron/positron are classified as ν_e-CC. Events without a candidate muon or a candidate electron/positron are classified as NC. A ν_τ-CC classification, which would identify ν_τ candidates is under development.

A muon candidate is defined as a MIP-like track that is greater than 2.0 m long, and is not consistent with the behavior of a charged pion. Charged pions will often *shower*, depositing a relatively large amount of energy in the detector at the end of its track, as compared to a muon. There are several situations in which a pion topology will be indistinguishable from a muon: (1) the pion stops at the end of its range without interacting, (2) the kinetic energy of the pion is sufficiently small when is showers, (3) the pion is absorbed cleanly by a nucleus with no hadronic debris, (4) the pion decays in flight, and (5) the track exists the detector. The $2.0-$m cut was chosen because the probability of (1) or (2) is very small for pion tracks above this threshold.

An additional selection probability is enforced for low-energy tracks to simulate acceptance losses due to increased difficulty in particle identification for short tracks, especially in high-multiplicity events. (The falling edge of the selection probability is well below the energy required to generate a $2.0-$m track, minimizing the effect of this criterion.)

An electron candidate is defined as the highest-momentum electromagnetic (EM) shower in an event that is not consistent with a photon. An EM shower is identified as a photon (1) if it converts 2.0 cm or more from the event vertex, (2) if it can be matched with another EM shower in the events to reconstruct the π^0 mass (135 ± 40 MeV), or (3) if dE/dx information from the first several planes of the track is more photon-like than e$\pm$-like. The latter is determined on a probabilistic basis as a function of EM-shower energy and hadronic-shower multiplicity. Signal and background efficiencies from the dE/dx e/γ discriminant are based on MicroBooNE simulations. Cut values are tuned to preserve 95% of the signal across all neutrino energies. As with muon candidates a low-energy selection probability is enforced to account for acceptance losses at low EM-shower energies, especially in high-multiplicity events. For the electron candidates this selection probability is tuned to agree with hand scan studies.

An event with no muon candidate and no electron candidate is assumed to be an NC interaction. Preliminary studies evaluating the use of transverse-momentum imbalance to identify ν_τ-CC interaction candidates have shown promising results for identifying NC candidates as well, and are likely to be included in the near future.

Currently no attempt is made to identify tau lepton candidates in order to isolate a ν_τ-CC sample. A preliminary algorithm to remove $\tau \to \mu + \nu + \nu$ and $\tau \to e + \nu + \nu$ backgrounds has recently been incorporated in the Fast MC. This algorithm may also prove useful for isolating a sample of ν_τ-CC interactions, in which the tau decays to a lepton. Development of an algorithm to identify taus that decay to hadrons is under discussion.

All of the selection criteria can easily be updated to reflect improved simulations or new understanding of particle-identification capabilities and analysis sample acceptances. Changes can also be made to investigate alternate analysis techniques, or more conservative or optimistic assumptions on signal acceptance and/or background-rejection rates. Furthermore, the information required to simulate effects related to particle identification is available in the Fast MC files and users are encouraged to construct and evaluate their own selection criteria.

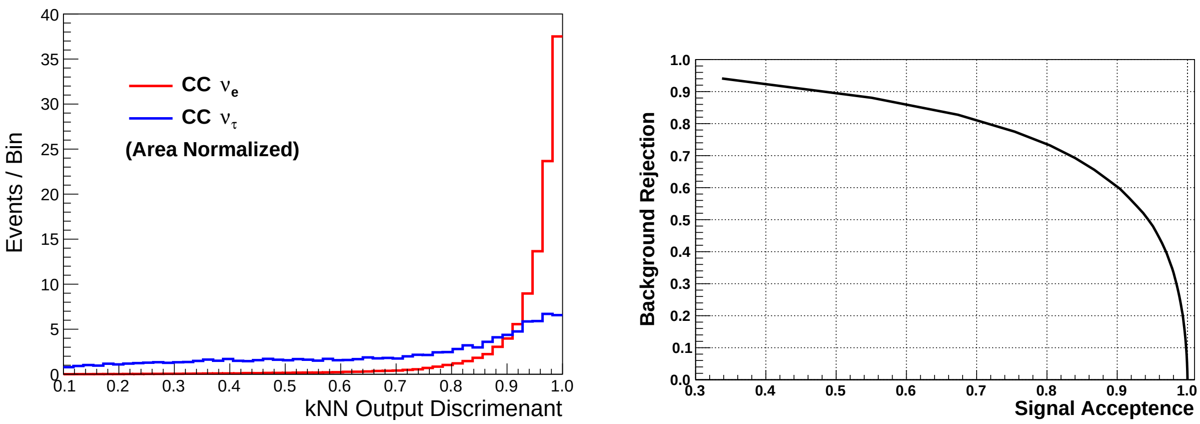

Figure A.6: The output discriminant of a kNN (left) created to remove ν_τ-CC-induced backgrounds from the $\nu_\mu \to \nu_e$ oscillation analysis sample. Signal events (red) tend toward high values, while the ν_τ-CC-induced background events (blue) are more evenly distributed. The fraction of ν_τ-CC-induced backgrounds removed from the $\nu_\mu \to \nu_e$ appearance candidate sample as a function of the corresponding signal efficiency (right). The curve is generated by varying the cut value on the kNN discriminant.

A preliminary algorithm for removing ν_τ-CC-induced backgrounds from from the ν_μ-CC and the ν_e-CC samples has been developed. It employs a k-Nearest Neighbor (kNN) machine-learning technique as implemented in the ROOT TMVA package. The inputs to the kNN are (1) the sum of the transverse momentum with respect to the incoming neutrino direction, (2) the reconstructed energy of the incoming neutrino, and (3) the reconstructed energy of the resulting hadronic shower. Figure A.6 (right) shows the distribution of the output discriminant for true ν_e-CC signal events, and for true ν_τ-CC-induced backgrounds. The algorithm is still being optimized but initial results are promising.

As can be seen in Figure A.6 (left), cuts on the discriminant that preserve 90% of the signal remove roughly 60% of the ν_τ-CC-induced background in the ν_e-CC sample. Similar results are expected for the ν_τ-CC-induced background in the ν_μ-CC sample.

A similar approach is being studied to isolate the ν_τ-CC sample for the ν_τ-CC appearance analysis. Current efforts are focused on identifying a set of reconstructed quantities that separate ν_τ-CC interactions from potential backgrounds. For leptonic decay channels the quantities used in the above kNN are prime candidates. Attempts to reconstruct a ρ mass from tracks originating at the vertex are expected to help to isolate hadronic τ decays. The parameterized pion response will allow for selection of high-energy charged pions produced in hadronic τ decays.

Figures A.7 and A.8 show the Fast MC reconstructed energy spectra of the signal and background for the ν_e appearance and the ν_μ disappearance samples, respectively. As an example of the cross-section and nuclear-effect systematics that can be studied, the black histograms and the bottom insert in each plot show the variation of the spectrum for each event type induced by changing the value of CC M_A^{res} by +1σ (+15%, 2014 GENIE official uncertainty). CC M_A^{res} is the axial mass parameter appearing in the axial form factor describing resonance production interactions in GENIE. This particular example demonstrates a spectral distortion that is not a simple normalization and is different for signal and for background. The effect of varying CC M_A^{res} on the $\nu_\mu \to \nu_e$ analysis sample exhibits a strong correlation with the changes induced in the $\nu_\mu \to \nu_\mu$ analysis sample.

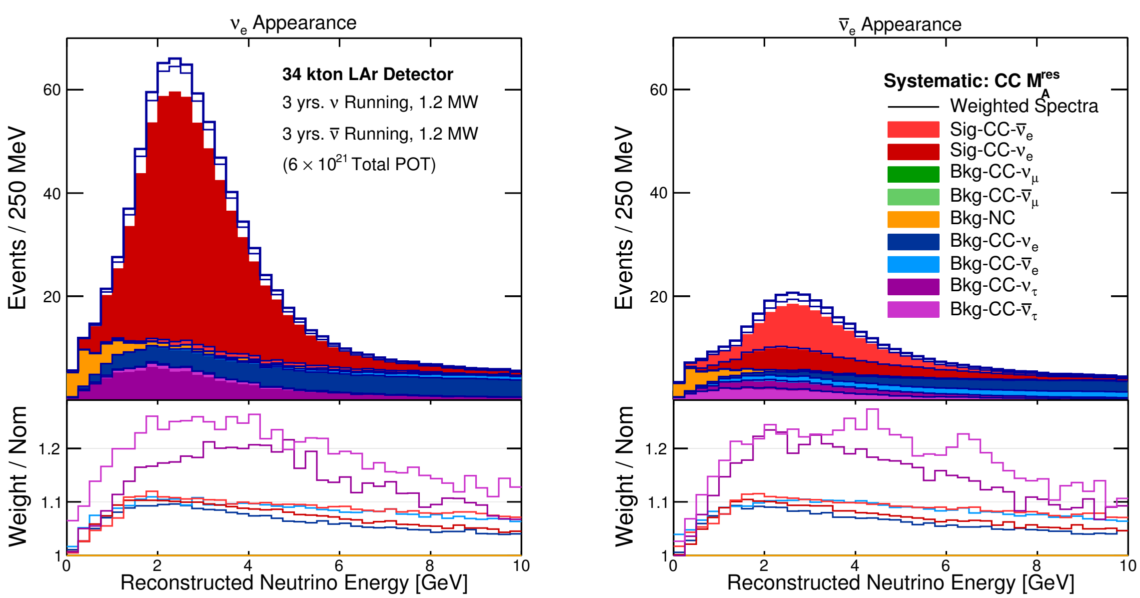

Figure A.7: The reconstructed energy distributions for the signals and backgrounds in the ν_e- (left) and $\overline{\nu}_e$ appearance (right) samples, as predicted by the Fast MC. The black histograms and bottom insert in each plot shows, for each event type, the variation in the spectrum that is induced by changing the value of CC M_A^{res} by +15%.

The left-hand plots of Figures A.9 and A.10 show the acceptance (efficiency) of the signal and the background for the Fast MC ν_e appearance and ν_μ disappearance selections, respectively. The

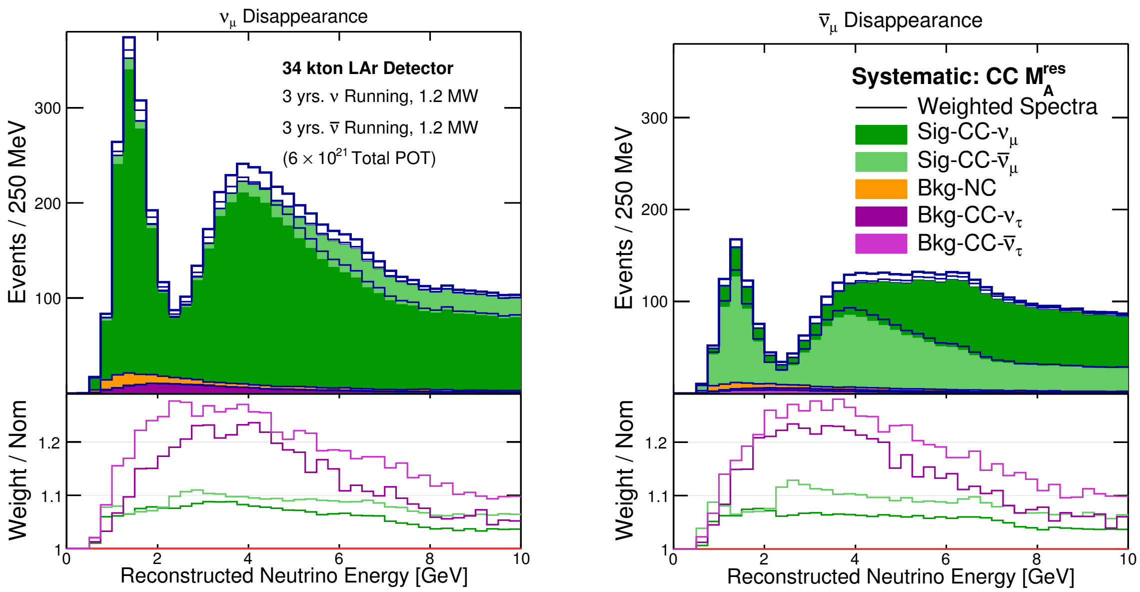

Figure A.8: The reconstructed energy distributions for the signals and backgrounds in the ν_μ (left) and $\overline{\nu}_\mu$ disappearance (right) samples, as predicted by the Fast MC. The black histograms and bottom insert in each plot shows, for each event type, the variation in the spectrum that is induced by changing the value of CC M_A^{res} by +15%.

effects of the low-energy selection probabilities induce the observed low-energy fall off in the ν_e appearance sample. On the other hand, the 2.0−m track length requirement is mainly responsible for the low-energy behavior in the ν_μ disappearance sample. The corresponding plots on the right-hand side show the relative fraction (purity) of the signal and each background sample for the Fast MC ν_e appearance and ν_μ disappearance selections. The increased wrong-sign contamination is evident in the $\overline{\nu}$ beam samples as compared to the ν beam samples. No attempt has been made to reduce the ν_τ background in these plots.

The output of the Fast MC is a file containing the information one would expect from a full MC simulation. There are truth level quantities that describe the generated event, and reconstructed quantities that are calculated from simulated observables. The latter mimic the information that is expected to be available from reconstructing data or full simulation and can be used in designing analyses aimed at measuring physics parameters. Analyses based on the simulated reconstruction produce event samples that can be used to estimate the sensitivity of LBNE to physics model parameters, specifically the parameters of the PMNS matrix, as a function of a variety of input parameters. Currently these studies are done using the GLoBES [130] software package. However, instead of constructing the event-rate spectra as a function of true neutrino energy from predictions of the flux and neutrino-interaction cross sections, they are built event-by-event from the Fast MC. Similarly, smearing functions that give the distribution of measured (reconstructed) neutrino energies as a function of the true neutrino energy are built event-by-event from the Fast MC, rather than estimated from external sources.

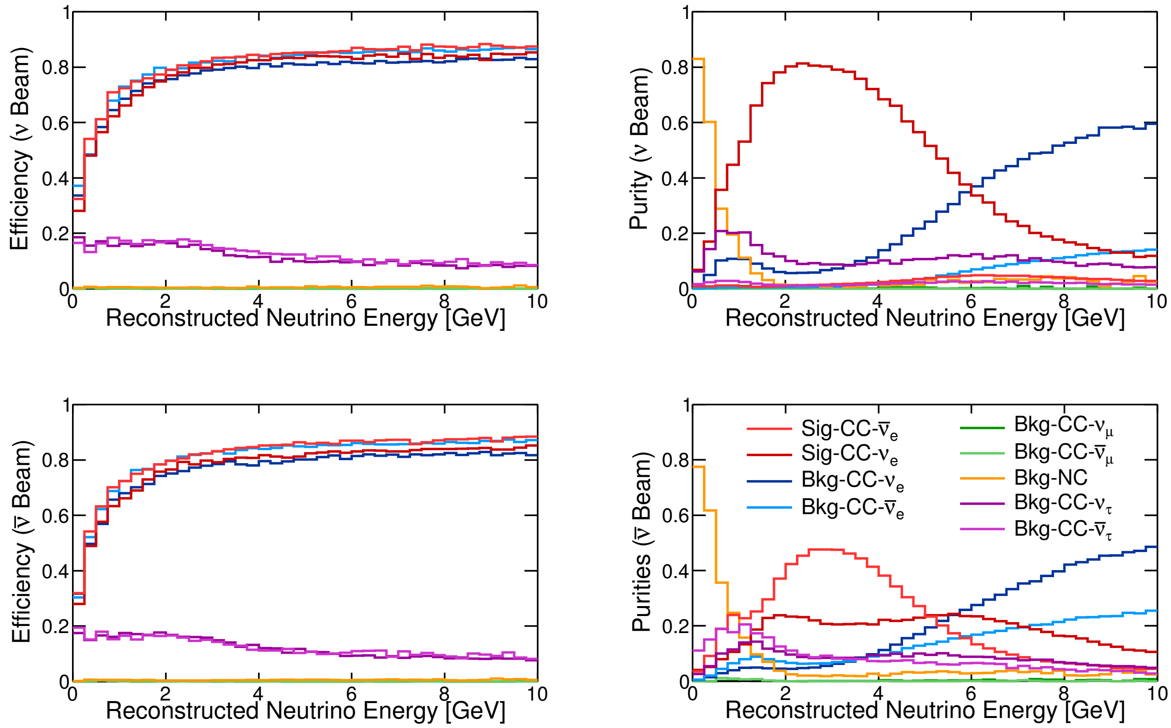

Figure A.9: The expected efficiencies and purities of selecting ν_e appearance events in a LArTPC, obtained from the Fast MC.

In addition to the usual GLoBES inputs the Fast MC can provide systematic uncertainty response functions, which encode the expected changes to the energy spectra when input model parameters are varied within their uncertainties. These response functions, along with an augmented version of GLoBES, can be used to propagate realistic systematic uncertainties in sensitivity studies.

The systematic uncertainty response functions are calculated from weights stored in the Fast MC output files. Each weight corresponds to the probability of producing the event with an alternate physics model relative to the model used. Currently the Fast MC generates weights for parameters in interaction models that can be reweighted in GENIE as well as a variety of parameters related to the neutrino flux. The flux parameters come in three varieties related to: changes to the beamline design, tolerances in the beamline design, and uncertainties in the physics models used in the simulations. The latter two contribute to systematic uncertainties while the first can be used to evaluate the impact of design optimizations.

Propagation of systematic uncertainties through LBNE sensitivity studies using the Fast MC will require inclusion of new algorithms and improvements to existing reweighting algorithms. This includes (1) the introduction of new models into GENIE, (2) adding to and improving the reweighting functions currently in GENIE, (3) constructing flux files that correspond to the changes in the three aforementioned categories, (4) implementing a system for reweighting individual events based on

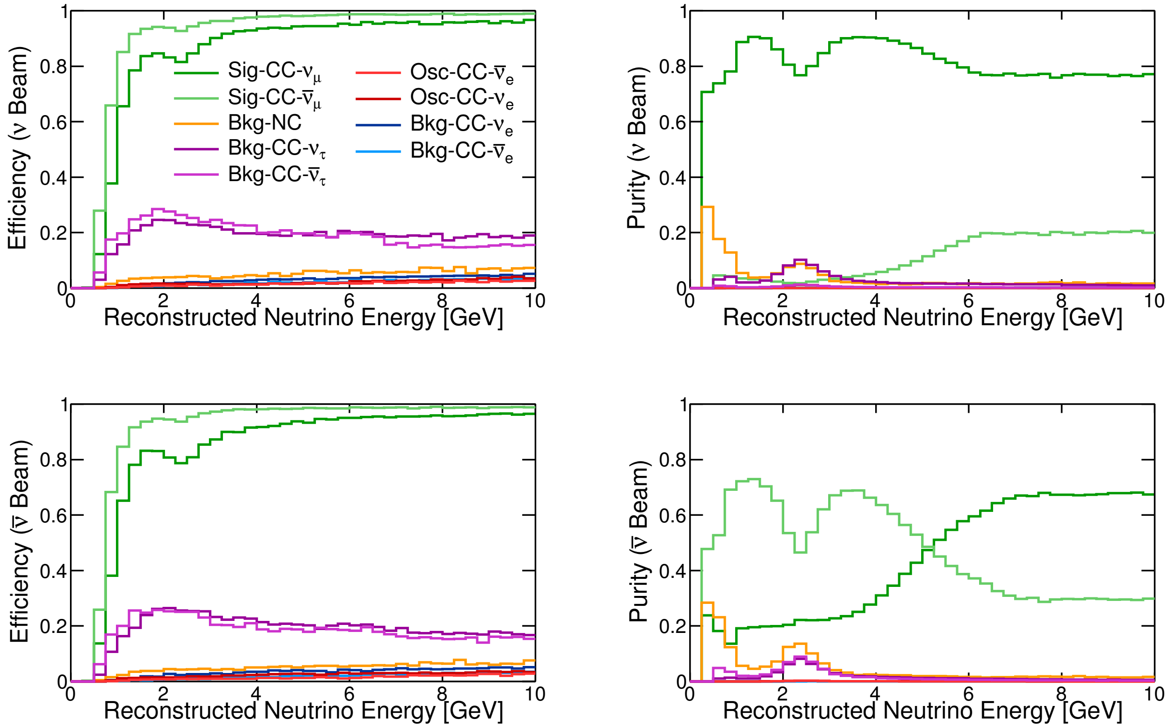

Figure A.10: The expected efficiencies and purities of selecting ν_μ disappearance events in a LArTPC obtained from the Fast MC.

changes to the models of hadronization from proton-target interactions, and (5) introducing detector parameterizations representing alternate detector designs, detector design tolerances, and model choices used in detector simulations.

The current focus of Fast MC studies is estimation of the effect of model uncertainties on sensitivity projections. This includes several steps, the first of which is to look at the changes in the analysis sample spectra induced by propagating individual systematic uncertainties. These studies are benchmarked by calculating the χ^2 between the nominal and altered spectra. In the second step, sensitivities are calculated for combined fits of the four main analysis samples ($\nu_\mu/\overline{\nu}_\mu$ disappearance, $\nu_e/\overline{\nu}_e$ appearance). These studies must be done carefully to allow for realistic constraints of systematic uncertainties across analysis samples within GLoBES. Input covariance matrices can also be used to enforce external constraints on the relations between sources of systematic uncertainty. The results of these studies will inform the investigators as to which model uncertainties cause significant degradation of the sensitivities and therefore must be constrained by other methods. Methods to constrain these parameters will be sought from currently running experiments, proposed intermediate experiments, and from the LBNE beam monitoring and the LBNE near detector. Estimates of these constraints can then be propagated to sensitivity calculations to estimate the degree to which they mitigate the decline in sensitivity.

Current studies focus on propagating uncertainties in flux and GENIE model parameters via reweighting techniques. A example study shown in Figure A.11 illustrates the effect of including the uncertainty on CC M_A^{res} in the calculation of sensitivity to CP violation. The sensitivity studies are performed for (1) a fit to the ν_e appearance sample (three years of ν-beam running), (2) a combined fit of the ν_e appearance sample and the $\overline{\nu}_e$ appearance sample (three years of ν-beam plus three years of $\overline{\nu}$-beam running), and (3) a combined fit of the $\nu_e/\overline{\nu}_e$ appearance samples along with the corresponding $\nu_\mu/\overline{\nu}_\mu$ disappearance samples. All three studies are done in two ways: with no allowance for non-oscillation parameter systematic variation, and with allowed 15% (width gaussian PDF) variations in CC M_A^{res}.

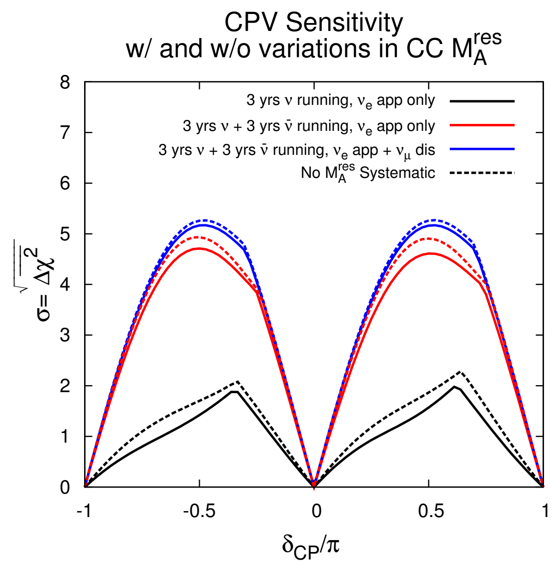

Figure A.11: The sensitivity to CP violation calculated using the energy spectra generated by the Fast MC. The sensitivities were generated with (solid) and without (dashed) allowed variations in the CC M_A^{res} resonance production model parameter in GENIE. The allowed variation degrades the sensitivity, however combined fits of multiple analysis samples provide additional constraints and reduce the impact.

As Figure A.11 shows, the inclusion of allowed variations in CC M_A^{res} degrades the sensitivity. However, combined fits of multiple analysis samples provide additional constraints and reduce the impact. The effect of these sample-to-sample constraints is dependent on the sample statistics, and the curves in Figure A.11 include the statistical limitations on sample-to-sample constraints from a six-year (three years ν + three years $\overline{\nu}$ running) exposure. However, the software also allows for the inclusion of other possible limitations on sample-to-sample constraints related to the relative lack of experimental constraints on cross-section ratios (i.e., $\sigma_{\nu_e}/\sigma_{\nu_\mu}$, $\sigma_{\nu_\tau}/\sigma_{\nu_\mu}$, and $\sigma_{\overline{\nu}}/\sigma_\nu$), as well as theoretical considerations.

The preliminary Fast MC spectra shown in Figures A.7 and A.8 were generated with a different beam configuration than the ones shown in Figures 4.2 and 4.3. Consequently, the sensitivities to CPV shown in Figure A.11 cannot be directly compared to the corresponding figures in Section 4.2.

However, both the Fast MC and the methods discussed in Section 4.2 have been used to generate comparable spectra and to perform a series of sensitivity studies. The two methods are consistent, except regarding known differences between the two simulations, e.g., the inclusion of ν_τ-CC-induced backgrounds. These differences are well understood, as are their impact on oscillation parameter sensitivities.

Eventually the Fast MC seeks to incorporate near detector and atmospheric-neutrino analyses and directly perform combined fits with the long-baseline neutrino analysis samples. These studies will provide the most accurate estimate of the ultimate sensitivity of LBNE, and provide a template for future data analysis procedures.

A.4 Simulation of Cosmic-Ray Background for a 10−kt Surface Detector

A preliminary study of the background events expected from cosmic rays in the 10−kt far detector installed near the surface at the Sanford Underground Research Facility is detailed in [226]. The study simulated cosmic-ray interactions in the far detector and focused on cosmic-ray induced events from neutrons and muons that mimic electron-neutrino interactions in the detector. These include electromagnetic cascades from knock-on electrons, muon bremsstrahlung, and hadronic cascades with electromagnetic components from photons and π^0's. The background from decays of neutral hadrons into electrons such as $K^0_L \rightarrow \pi e \nu$ were also studied. The energy of the cascades was required to be > 0.1 GeV.

These initial studies indicate that a combination of simple kinematic and beam timing cuts will help to significantly reduce the cosmic-ray background event rate in this far detector configuration. In particular:

1. Only electromagnetic cascades with energies greater than 0.25 GeV are considered background. For the neutrino oscillation sensitivity calculations, only neutrino energies ≥ 0.5 GeV are considered.

2. $e^\pm$ background candidates are tracked back to the parent muon; the distance between the muon track and the point-of-closest-approach (PoCA) to the muon track is required to be > 10 cm.

3. The vertex of the $e^\pm$ shower is required to be within the fiducial volume of the detector (defined as 30 cm from the edge of the active detector volume).

4. The $e^\pm$ cascade is required to be within a cone around the beam direction (determined from the angular distribution of the beam signal $e^\pm$ and the incoming neutrino beam).

5. It is assumed that EM showers initiated by γ's and $\pi^0 \to \gamma\gamma$ can be effectively distinguished from primary electron interactions using particle ID techniques such as dE/dX.

6. Events are timed with a precision of ≤1 µs using the photon-detection system, which limits background to events occurring within the 10 µs of the beam spill.

The result of applying these selection criteria to the electromagnetic showers initiated by cosmic rays is summarized in Table A.1 and Figure A.12. The background rates given in Table A.1 include the recalculation for the cosmic flux at 1,500 m above sea level, which was not included in the previous study [226] (and is not included in Figure A.12). In the table, the initial background event rate is calculated for one calendar year assuming a 1.4−ms drift time per beam pulse, a beam pulse every 1.33 seconds and 2×10^7 s/year of running. The expected event rate/yr after various selection criteria is applied from left to right in the table. The rates in all columns except the last are given for a time window of 1.4 ms, corresponding to the maximum electron drift time. The last column shows the rate reduction assuming an efficient photon-detection system. The first three rows show events with a muon in the detector where a PoCA cut (column 3) can be applied. The row labeled 'Missing μ' shows events without a muon in the detector; as there is no muon track, a PoCA cut can not be applied. The detector is assumed to be on the surface with three meters of rock overburden.

Table A.1: Cosmic-ray-induced background (at 1,500 m above sea level) to the beam ν_e-CC signal in the 10−kt detector.

Processes	$E_e >$ **0.25 GeV**	**PoCA > 10 cm and D > 30 cm**	**Beam angle**	**e/γ PID**	**Beam timing**
$\pi^0 \to \gamma \to e^\pm$	2.2×10^6	9.7×10^4	4.8×10^4	1.7×10^3	12
$\mu \to \gamma \to e^\pm$	7.1×10^6	12	0	0	< 0.003
Ext $\gamma \to e^\pm$	1.9×10^6	660	340	13	0.1
$\pi^0, K^0 \to e^\pm$	1.4×10^6	810	240	240	1.7
Missing μ	1.3×10^6	1.8×10^3	580	20	0.1
Atm n	2.9×10^6	1.6×10^4	6.5×10^2	240	1.7
Total	$\mathbf{1.1 \times 10^7}$	$\mathbf{1.2 \times 10^5}$	$\mathbf{5.6 \times 10^4}$	$\mathbf{2.2 \times 10^3}$	**16**

The dominant background is from $\pi^0 \to \gamma \to e^\pm$, which contributes 12 out of the 16 total events per year and comes from π^0's originating in cosmic showers. The study does not yet include specific π^0 reconstruction, only individual e/γ separation. More sophisticated reconstruction techniques should further reduce the π^0 background. The studies indicate that application of these selection criteria coupled with a more detailed background event reconstruction can potentially reduce the background from cosmic rays to a few events per year — mostly in the energy region < 1 GeV.

In Figure A.12, black-filled circles show events before any cuts are applied. The other point icons represent successively applied cuts in the order listed below and in the figure's legend:

1. Blue squares: PoCA to the muon track greater than 30 cm
2. Red triangles: angle with respect to the beam such that 99% of signal events are retained
3. Green triangles: application of energy-dependent e/γ discrimination
4. Magenta open circles: application of efficient photon detection, this allows the reduction of the time window from a maximum drift time of 1.4 ms down to a beam spill of 10 μs

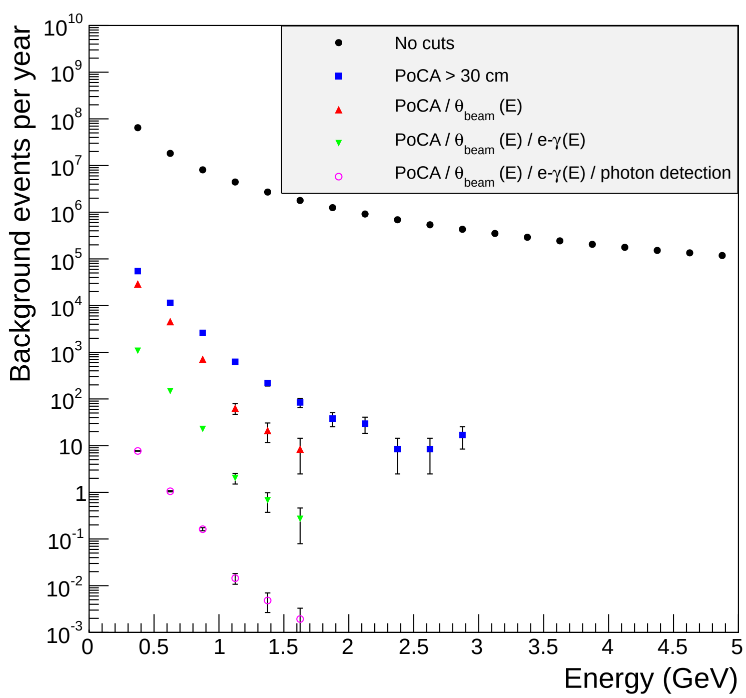

Figure A.12: Energy spectra of muon-induced background events for successively applied background rejection cuts. Simulations have been done for a muon spectrum at sea level. Correction for an altitude of 1,500 m above sea level has not been applied to the data.

Appendix B Neutrino-Nucleon Scattering Kinematics

The following explanation of neutrino-nucleon scattering kinematics is adapted from [358]:

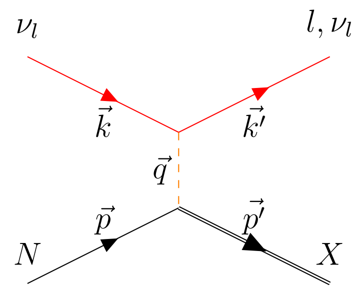

Figure B.1: A schematic diagram of a neutrino-nucleon scattering process

The expression $\nu_l + N \longrightarrow l, \nu_l + X$ describes the scattering of a neutrino, ν_l off a nucleon, N as shown in Figure B.1. This interaction proceeds through the exchange of a $W^{\pm}$ or Z^0 boson, depending on whether it is a CC or NC interaction, respectively. For the case of neutrino scattering, the incoming lepton is a neutrino and the outgoing lepton is either a neutrino (NC) or a charged lepton, l (CC). X denotes the resultant hadronic system.

The nucleon mass, M, is neglected where appropriate; the lepton mass is neglected throughout. The following kinematic variables describe the momenta and energies involved in the scattering process:

- $\vec{k}, \vec{k}'$ are the four-momenta of the incoming and outgoing lepton.
- $\vec{p}$ is the initial four-momentum of the nucleon.
- E_ν is the energy of the incoming neutrino.
- E_N is the energy of the nucleon.

The Lorentz invariants are the following:

- The squared ν+N collision energy is $s = (|\vec{p} + \vec{k}|)^2 = 4E_N E_\nu$.
- The squared momentum transfer to the lepton $Q^2 = -q^2 = -(|\vec{k} - \vec{k}'|)^2$ is equal to the virtuality of the exchanged boson. Large values of Q^2 provide a hard scale to the process, which allows resolution of quarks and gluons in the nucleon.

- The Bjorken variable $x_{Bj} = Q^2/(2\vec{p}\cdot\vec{q})$ is often simply denoted by x. It determines the momentum fraction of the parton (quark or gluon) on which the boson scatters. Note that $0 < x < 1$ for ν+N collisions.
- The inelasticity $y = (\vec{q}\cdot\vec{p})/(\vec{k}\cdot\vec{p})$ is limited to values $0 < y < 1$ and determines in particular the polarization of the virtual boson. In the lab frame, the energy of the scattered lepton is $E_l = E_\nu(1-y) + Q^2/(4E_\nu)$; detection of the scattered lepton thus typically requires a cut on $y < y_{max}$.

These invariants are related by $Q^2 = xys$. The available phase space is often represented in the plane of x and Q^2. For a given ν+N collision energy, lines of constant y are then lines with a slope of 45 degrees in a double logarithmic $x - Q^2$ plot.

Two additional important variables are:

- The squared invariant mass of the produced hadronic system (X) is denoted by $W^2 = (|\vec{p}+\vec{q}|)^2 = Q^2(1-1/x)$. Deep-inelastic scattering (DIS) is characterized by the Bjorken limit, where Q^2 and W^2 become large at a fixed value of x. Note: for a given Q^2, small x corresponds to a high W, Z - N collision energy.
- The energy lost by the lepton (i.e., the energy carried away by the virtual boson) in the nucleon rest frame, is denoted $\nu = \vec{q}\cdot\vec{p}/M = ys/(2M)$.

For scattering on a nucleus of atomic number A, the nucleon momentum $\vec{p}$ would be replaced by $\vec{P}/A$ in the definitions, where $\vec{P}$ is the momentum of the nucleus. Note that the Bjorken variable is then in the range $0 < x < A$.

Acknowledgments

This report is the result of an initial collaboration-wide effort to prepare a whitepaper for the APS Division of Particles and Fields Community Summer Study 2013 [1]. The paper has evolved into LBNE's formal science document due to the hard work of many LBNE Collaboration and Project members. We thank those colleagues who made significant contributions and provided excellent feedback on drafts of this document. The following is a nonexhaustive list of LBNE collaborators who made major contributions to this document. A major contribution is defined as $\geq$ a section and/or a study reported in a figure prepared for this document.

Contribution	LBNE Collaborator(s)
Overall editing	***Anne Heavey, Mary Bishai, Jon Urheim, Brett Viren, Maury Goodman***
Technical/Figures	Brett Viren
Original content	*Bob Wilson (Editor of the 2010 Interim Physics Report)*
General Guidance	Milind Diwan, Bob Wilson, Jim Strait, Sam Zeller, Bill Louis, Hank Sobel, Josh Klein, Nick Samios
Major Contributors by Chapter. A * indicates the chapter editor(s)	
Chapter 1	Jon Urheim*, Jim Strait, Bob Wilson
Chapter 2	Mary Bishai*, Elizabeth Worcester*, Jon Urheim, Kate Scholberg, Ed Kearns, Bill Marciano, Xin Qian.
Chapter 3	Mary Bishai*, Jim Strait, Elaine McCluskey, Kevin Lesko, Jim Stewart, Vaia Papadimitriou, Kevin Yarritu, Bill Louis
Chapter 4	Elizabeth Worcester*, Mary Bishai*, Matt Bass, Andy Blake, Xin Qian, Jon Urheim, Lisa Whitehead
Chapter 5	Ed Kearns*, Jon Urheim*, Vitaly Kudryavtsev
Chapter 6	Kate Scholberg*, Vic Gehman, Alex Friedland
Chapter 7	Roberto Petti*, Sanjib Mishra, Jaehoon Yu, Richard Van de Water
Chapter 8	Michael Smy*, Mary Bishai*, Jaehoon Yu
Chapter 9	Jon Urheim*, Jim Strait
Appendix A	Dan Cherdack*, Tom Junk*, Andy Blake, Vitaly Kudryavtsev, Zepeng Li, Kate Scholberg
Appendix B	Mary Bishai*, Roberto Petti

We would also like to express our gratitude to the following non-LBNE collaborators who supplied us with invaluable information: **Elke Aschenauer (Brookhaven Lab)**, the main editor of the Electron Ion Collider (EIC) whitepaper [358] which inspired the look and style of this document; **Joachim Kopp (Max-Planck Institute, Heidelberg)** for his study of LBNE's sensitivity to Non-Standard Interactions summarized in Section 4.7.1; **Pilar Coloma (Virginia Tech)** for her studies comparing LBNE's sensitivities to other proposed neutrino experiments shown in Figures 4.33 and 4.35; **Patrick Huber (Virginia Tech)** for a long and fruitful collaborative effort, and his critical role in developing the case for a very long-baseline neutrino oscillation experiment over the past decade; **JJ Cherry (LANL)** and **Huaiyu Duan (U. of New Mexico)** for major input on the supernova studies shown in Chapter 6; **Dmitry Gorbunov (Institute for Nuclear Research, Moscow)** for his studies on LBNE sensitivities to νMSM heavy neutrinos shown in Figure 7.5; **Diana Brandonisio (Fermilab VMS)**, our graphic designer for her gorgeous cover design and invaluable design advice.

And last, but most importantly, our effusive thanks to **Anne Heavey** (AKA the **FIXME** monster) — our devoted general editor — for her dogged insistence on clarity and quality, her hard work well above and beyond the call of duty, and for being such an absolute pleasure to work with.

This work was supported in part by the U.S. Department of Energy (DOE), the National Science Foundation (NSF), the Sanford Underground Research Facility and the South Dakota Science and Technology Authority (SDSTA); the Brazilian Federal Agency for the Support and Evaluation of Graduate Education (CAPES), the Sao Paulo Research Foundation (FAPESP) and the National Council for Scientific and Technological Development (CNPq); the UK Science and Technology Facilities Council (STFC); the Italian government's Istituto Nazionale di Fisica Nucleare (INFN); the Indian Department of Atomic Energy (DAE) and the Department of Science and Technology (DST), Ministry of Science and Technology.

References

1. "APS Division of Particles and Fields Community Summer Study 2013," 2013. `http://www.snowmass2013.org`. Cited in Sections 1.1 (pg.4), 1.2.1 (pg.6), and B (pg.235).
2. M. Diwan and C. Jung, "Next generation nucleon decay and neutrino detector. Proceedings, Workshop, NNN99, Stony Brook, USA, September 23-25, 1999," 2000. Cited in Section 1.2 (pg.5).
3. W. J. Marciano, "Extra long baseline neutrino oscillations and CP violation," BNL-HET-01-31, `arXiv:hep-ph/0108181 [hep-ph]`, 2001. Cited in Section 1.2 (pg.5).
4. R. Shrock, "Neutrinos and implications for physics beyond the standard model. Proceedings, Conference, Stony Brook, USA, October 11-13, 2002," 2003. Cited in Section 1.2 (pg.5).
5. M. Diwan, W. Marciano, W. Weng, D. Beavis, M. Brennan, *et al.*, "Report of the BNL neutrino working group: Very long baseline neutrino oscillation experiment for precise determination of oscillation parameters and search for nu mu –> nu e appearance and CP violation," BNL-69395, `arXiv:hep-ex/0211001 [hep-ex]`, 2002. Cited in Section 1.2 (pg.5).
6. M. Diwan, D. Beavis, M.-C. Chen, J. Gallardo, S. Kahn, *et al.*, "Very long baseline neutrino oscillation experiments for precise measurements of mixing parameters and CP violating effects," *Phys.Rev.* **D68** (2003) 012002, `arXiv:hep-ph/0303081 [hep-ph]`. Cited in Section 1.2 (pg.5).
7. W. Weng, M. Diwan, D. Raparia, J. Alessi, D. Barton, *et al.*, "The AGS-Based Super Neutrino Beam Facility Conceptual Design Report," BNL-73210-2004-IR, 2004. Cited in Section 1.2 (pg.5).
8. M. Diwan, S. H. Kettell, L. Littenberg, W. Marciano, Z. Parsa, *et al.*, "Proposal for an Experimental Program in Neutrino Physics and Proton Decay in the Homestake Laboratory," BNL-76798-2006-IR, `arXiv:hep-ex/0608023 [hep-ex]`, 2006. Cited in Section 1.2 (pg.5).
9. V. Barger, M. Bishai, D. Bogert, C. Bromberg, A. Curioni, *et al.*, "Report of the US long baseline neutrino experiment study," FERMILAB-0801-AD-E, BNL-77973-2007-IR, `arXiv:0705.4396 [hep-ph]`, 2007. Cited in Section 1.2 (pg.5).
10. N. R. C. Neutrino Facilities Assessment Committee, *Neutrinos and Beyond: New Windows on Nature*. The National Academies Press, 2003. ISBN 0-309-08716-3. Cited in Section 1.2 (pg.5).
11. Interagency Working Group on the Physics of the Universe. National Science and Technology Council Committee on Science, "A 21st Century Frontier of Discovery: The Physics of the Universe, a Strategic Plan for Federal Research at the Intersection of Physics

and Astronomy.”. February, 2004.
http://pcos.gsfc.nasa.gov/docs/Physics_of_the_Universe.pdf. Cited in Section 1.2 (pg.5).

12. N. R. C. Committee on Elementary Particle Physics in the 21st Century, *Revealing the Hidden Nature of Space and Time: Charting the Course for Elementary Particle Physics*. The National Academies Press, 2006. ISBN 0-309-66039-4. Cited in Section 1.2 (pg.5).
13. Neutrino Scientific Assessment Group, “Recommendations to the Department of Energy and the National Science Foundation on a Future U.S. Program in Neutrino Oscillations. Report to the Nuclear Science Advisory Committee and the High Energy Physics Advisory Board.”. July, 2007. http://science.energy.gov/~/media/hep/pdf/files/pdfs/nusagfinalreportjuly13_2007.pdf. Cited in Section 1.2 (pg.5).
14. Particle Physics Project Prioritization Panel, “U.S. Particle Physics: Scientific opportunities, a plan for the next ten years.”. May, 2008. http://science.energy.gov/~/media/hep/pdf/files/pdfs/p5_report_06022008.pdf. Cited in Sections 1.2 (pg.5), 3.1 (pg.46), and 3.2 (pg.48).
15. Ad Hoc Committee to Assess the Science Proposed for a Deep Underground Science and Engineering Laboratory (DUSEL); National Research Council, *An Assessment of the Deep Underground Science and Engineering Laboratory*. The National Academies Press, 2012. ISBN 978-0-309-21723-1. Cited in Section 1.2 (pg.5).
16. HEPAP Facilities Subpanel, “Major High Energy Physics Facilities 2014-2024. Input to the prioritization of proposed scientific user facilities for the Office of Science.”. March, 2013. http://science.energy.gov/~/media/hep/hepap/pdf/Reports/HEPAP_facilities_letter_report.pdf. Cited in Section 1.2 (pg.5).
17. CERN Council, “The European Strategy for Particle Physics, Update 2013.”. CERN-Council-S/106, May, 2013. http://council.web.cern.ch/council/en/EuropeanStrategy/esc-e-106.pdf. Cited in Sections 1.2 (pg.5) and 1.2.3 (pg.7).
18. DOE Office of Science, Office of High Energy Physics, “Mission Need Statement for a Long-Baseline Neutrino Experiment (LBNE),” DOE, LBNE-doc-6259, 2009. Cited in Sections 1.2.1 (pg.6) and 3.1 (pg.47).
19. A. S. Kronfeld, R. S. Tschirhart, U. Al-Binni, W. Altmannshofer, C. Ankenbrandt, *et al.*, “Project X: Physics Opportunities,” FERMILAB-TM-2557, BNL-101116-2013-BC-81834, JLAB-ACP-13-1725, UASLP-IF-13-001, SLAC-R-1029, ANL-PHY-13-2, PNNL-22523, LBNL-6334E, arXiv:1306.5009 [hep-ex], 2013. Cited in Section 1.2.1 (pg.6).
20. A. de Gouvea *et al.*, **Intensity Frontier Neutrino Working Group** , “Neutrinos,” FERMILAB-CONF-13-479-E, arXiv:1310.4340 [hep-ex], 2013. Cited in Sections 1.2.1 (pg.6) and 2.2 (pg.23).
21. K. Babu, E. Kearns, U. Al-Binni, S. Banerjee, D. Baxter, *et al.*, “Baryon Number Violation,” arXiv:1311.5285 [hep-ph], 2013. Cited in Section 1.2.1 (pg.6).
22. Derwent, P. and others, “Proton Improvement Plan II,” Project X-doc-1232, November, 2013. Cited in Sections 1.2.1 (pg.6), 3.2 (pg.51), and 3.4 (pg.63).

23. S. Holmes, R. Alber, B. Chase, K. Gollwitzer, D. Johnson, *et al.*, “Project X: Accelerator Reference Design,” FERMILAB-TM-2557, BNL-101116-2013-BC-81834, JLAB-ACP-13-1725, PNNL-22523, SLAC-R-1020, UASLP-IF-13-001, `arXiv:1306.5022 [physics.acc-ph]`, 2013. Cited in Sections 1.2.1 (pg.6), 3.2 (pg.51), and 4.2.1 (pg.88).
24. “Final Report, Director’s Independent Conceptual Design and CD-1 Readiness Review of the LBNE Project,” `LBNE-doc-5788`, March, 2012. Cited in Sections 1.2.2 (pg.7), 3.6 (pg.76), and 3.6.2 (pg.79).
25. Y. K. Kim *et al.*, “LBNE Reconfiguration: Steering Committee Report,” 2012. `http://www.fnal.gov/directorate/lbne_reconfiguration/index.shtml`. Cited in Sections 1.2.2 (pg.7), 1.3 (pg.9), 4.2.1 (pg.86), and 9.3 (pg.210).
26. “Department of Energy Review Committee Report on the Technical, Cost, Schedule, and Management Review of the Long Baseline Neutrino Experiment (LBNE),” October, 2012. `http://www.fnal.gov/directorate/OPMO/Projects/LBNE/DOERev/2012/10_30/1210_LBNE_rpt.pdf`. Cited in Section 1.2.2 (pg.7).
27. “Independent Cost Review Closeout for the Long Baseline Neutrino Experiment (LBNE) Project,” `LBNE-doc-6522`, November, 2012. Cited in Section 1.2.2 (pg.7).
28. “Critical Decision 1 Approve Alternative Selection and Cost Range of the Long Baseline Neutrino Experiment (LBNE) Project,” `LBNE-doc-6681`, December, 2012. Cited in Section 1.2.2 (pg.7).
29. **LBNE Project Management Team** , “LBNE Conceptual Design Report, Volume 1: The LBNE Project,” `LBNE-doc-5235`, 2012. Cited in Sections 1.2.2 (pg.7), 4.2.2 (pg.88), 4.3 (pg.92), 4.3 (pg.95), 4.6 (pg.124), and A (pg.213).
30. **LBNE Project Management Team** , “LBNE Conceptual Design Report, Volume 2: The Beamline at the Near Site,” `LBNE-doc-4317`, 2012. Cited in Sections 1.2.2 (pg.7), 3.4 (pg.63), and 4.3 (pg.93).
31. **LBNE Project Management Team** , “LBNE Conceptual Design Report, Volume 3: Detectors at the Near Site,” `LBNE-doc-4724`, 2012. Cited in Sections 1.2.2 (pg.7) and 3.5 (pg.73).
32. **LBNE Project Management Team** , “LBNE Conceptual Design Report, Volume 4: The Liquid Argon Detector at the Far Site,” `LBNE-doc-4892`, 2012. Cited in Sections 1.2.2 (pg.7) and 3.6.1 (pg.77).
33. **LBNE Project Management Team** , “LBNE Conceptual Design Report, Volume 5: Conventional Facilities at the Near Site (MI-10 Shallow),” `LBNE-doc-4623`, 2012. Cited in Section 1.2.2 (pg.7).
34. **LBNE Project Management Team** , “LBNE Conceptual Design Report, Volume 6: Conventional Facilities at the Far Site,” `LBNE-doc-5017`, 2012. Cited in Section 1.2.2 (pg.7).
35. R. J. Wilson, “Long-Baseline Neutrino Experiment, presentation, November 2013,” 2013. `https://indico.fnal.gov/getFile.py/access?contribId=25&sessionId=7&resId=0&materialId=slides&confId=7485`. Cited in Section 1.2.3 (pg.8).

36. Marx-Reichanadter Committee, "Department of Energy Office of Science Review of Options for Underground Science.". June, 2011. `http://science.energy.gov/~/media/np/pdf/review_of_underground_science_report_final.pdf`. Cited in Section 1.3 (pg.9).
37. Grannis, P. and Green, D. and Nishikawa, K. and Robertson, H. and Sadoulet, B. and Wark, D., "The LBNE Science Capability Review," `LBNE-doc-5333`, December, 2011. Cited in Section 1.3 (pg.9).
38. M. Messier, **NOvA Collaboration** , "Extending the NOvA Physics Program," FERMILAB-CONF-13-308-E, `arXiv:1308.0106 [hep-ex]`, 2013. Cited in Sections 1.3.1 (pg.10) and 4.8 (pg.136).
39. P. Huber and J. Kopp, "Two experiments for the price of one? – The role of the second oscillation maximum in long baseline neutrino experiments," *JHEP* **1103** (2011) 013, `arXiv:1010.3706 [hep-ph]`. Cited in Section 1.3.1 (pg.13).
40. E. Kearns, "Future Experiments for Proton Decay. Presentation at ISOUPS (International Symposium: Opportunities in Underground Physics for Snowmass), Asilomar, May 2013," 2013. Cited in Sections 1.3.2 (pg.13), 5.1 (pg.139), 5.1 (pg.140), and 5.2 (pg.141).
41. J. Strait, "Physics Research Goals After Reconfiguration," `LBNE-doc-3056`, 2011. Cited in Section 2.1 (pg.18).
42. R. Mohapatra, S. Antusch, K. Babu, G. Barenboim, M.-C. Chen, *et al.*, "Theory of neutrinos: A White paper," *Rept.Prog.Phys.* **70** (2007) 1757–1867, `arXiv:hep-ph/0510213 [hep-ph]`. Cited in Sections 2.2 (pg.21) and 2.2 (pg.23).
43. G. Aad *et al.*, **ATLAS Collaboration** , "Observation of a new particle in the search for the Standard Model Higgs boson with the ATLAS detector at the LHC," *Phys.Lett.* **B716** (2012) 1–29, `arXiv:1207.7214 [hep-ex]`. Cited in Section 2.2 (pg.21).
44. S. Chatrchyan *et al.*, **CMS Collaboration** , "Observation of a new boson at a mass of 125 GeV with the CMS experiment at the LHC," *Phys.Lett.* **B716** (2012) 30–61, `arXiv:1207.7235 [hep-ex]`. Cited in Section 2.2 (pg.21).
45. DNP/DPF/DAP/DPB Joint Study on the Future of Neutrino Physics, "The Neutrino Matrix.". November, 2004. `http://www.aps.org/policy/reports/multidivisional/neutrino/upload/main.pdf`. Cited in Section 2.2 (pg.22).
46. F. An *et al.*, **Daya Bay Collaboration** , "Improved Measurement of Electron Antineutrino Disappearance at Daya Bay," *Chin. Phys.* **C37** (2013) 011001, `arXiv:1210.6327 [hep-ex]`. Cited in Section 2.2 (pg.22).
47. A. Aguilar-Arevalo *et al.*, **LSND Collaboration** , "Evidence for neutrino oscillations from the observation of anti-neutrino(electron) appearance in a anti-neutrino(muon) beam," *Phys.Rev.* **D64** (2001) 112007, `arXiv:hep-ex/0104049 [hep-ex]`. Cited in Section 2.2 (pg.23).
48. A. Aguilar-Arevalo *et al.*, **MiniBooNE Collaboration** , "A Search for electron neutrino appearance at the $\Delta m^2 \sim 1\mathrm{eV}^2$ scale," *Phys.Rev.Lett.* **98** (2007) 231801, `arXiv:0704.1500 [hep-ex]`. Cited in Section 2.2 (pg.23).

49. A. Aguilar-Arevalo *et al.*, **MiniBooNE Collaboration** , "Improved Search for $\overline{\nu_\mu} \to \overline{\nu_e}$ Oscillations in the MiniBooNE Experiment," *Phys.Rev.Lett.* **110** no. 16, (2013) 161801, `arXiv:1207.4809 [hep-ex]`. Cited in Section 2.2 (pg.23).
50. G. Mention, M. Fechner, T. Lasserre, T. Mueller, D. Lhuillier, *et al.*, "The Reactor Antineutrino Anomaly," *Phys.Rev.* **D83** (2011) 073006, `arXiv:1101.2755 [hep-ex]`. Cited in Section 2.2 (pg.23).
51. S. F. King, A. Merle, S. Morisi, Y. Shimizu, and M. Tanimoto, "Neutrino Mass and Mixing: from Theory to Experiment," `arXiv:1402.4271 [hep-ph]`, 2014. Cited in Section 2.2 (pg.23).
52. P. Harrison, D. Perkins, and W. Scott, "Tri-bimaximal mixing and the neutrino oscillation data," *Phys.Lett.* **B530** (2002) 167, `arXiv:hep-ph/0202074 [hep-ph]`. Cited in Section $*$ (pg.23).
53. C. H. Albright and M.-C. Chen, "Model Predictions for Neutrino Oscillation Parameters," *Phys.Rev.* **D74** (2006) 113006, `arXiv:hep-ph/0608137 [hep-ph]`. Cited in Section 2.2 (pg.23).
54. G. Fogli, E. Lisi, A. Marrone, D. Montanino, A. Palazzo, *et al.*, "Global analysis of neutrino masses, mixings and phases: entering the era of leptonic CP violation searches," *Phys.Rev.* **D86** (2012) 013012, `arXiv:1205.5254 [hep-ph]`. Cited in Sections † (pg.24), 2.2.1 (pg.25), 4.3 (pg.92), 4.3 (pg.93), 4.3.2 (pg.110), and 4.4 (pg.117).
55. J. Beringer *et al.*, **Particle Data Group** , "Review of Particle Physics (RPP)," *Phys.Rev.* **D86** (2012) 010001. Cited in Sections 2.2.1 (pg.25), 2.2.2 (pg.27), and 7.4.4 (pg.183).
56. C. Jarlskog, "A Basis Independent Formulation of the Connection Between Quark Mass Matrices, CP Violation and Experiment," *Z.Phys.* **C29** (1985) 491–497. Cited in Section 2.2.1 (pg.24).
57. A. Meroni, S. Petcov, and M. Spinrath, "A SUSY SU(5)xT' Unified Model of Flavour with large θ_{13}," *Phys.Rev.* **D86** (2012) 113003, `arXiv:1205.5241 [hep-ph]`. Cited in Section 2.2.1 (pg.25).
58. G.-J. Ding, S. F. King, and A. J. Stuart, "Generalised CP and A_4 Family Symmetry," *JHEP* **1312** (2013) 006, `arXiv:1307.4212`. Cited in Section 2.2.1 (pg.25).
59. C. Luhn, "Trimaximal TM_1 neutrino mixing in S_4 with spontaneous CP violation," *Nucl.Phys.* **B875** (2013) 80–100, `arXiv:1306.2358 [hep-ph]`. Cited in Sections 2.2.1 (pg.25) and 2.2.6 (pg.35).
60. G.-J. Ding and Y.-L. Zhou, "Predicting Lepton Flavor Mixing from $\Delta(48)$ and Generalized CP Symmetries," `arXiv:1312.5222 [hep-ph]`, 2013. Cited in Section 2.2.1 (pg.25).
61. S. Antusch, S. F. King, and M. Spinrath, "Spontaneous CP violation in $A_4 \times SU(5)$ with Constrained Sequential Dominance 2," *Phys.Rev.* **D87** no. 9, (2013) 096018, `arXiv:1301.6764 [hep-ph]`. Cited in Section 2.2.1 (pg.25).
62. S. F. King, "A model of quark and lepton mixing," *JHEP* **1401** (2014) 119, `arXiv:1311.3295 [hep-ph]`. Cited in Section 2.2.1 (pg.25).
63. E. Kolb and M. Turner, *The Early Universe*. Westview Press, 1994. ISBN 978-0201626742. Cited in Section 2.2.1 (pg.25).

64. S. Weinberg, *Cosmology*. Oxford University Press, USA, first ed., April, 2008. ISBN 978-0198526827. Cited in Section 2.2.1 (pg.25).
65. G. Steigman, "Primordial Nucleosynthesis in the Precision Cosmology Era," *Ann.Rev.Nucl.Part.Sci.* **57** (2007) 463–491, `arXiv:0712.1100 [astro-ph]`. Cited in Section 2.2.1 (pg.25).
66. M. Fukugita and T. Yanagida, "Baryogenesis Without Grand Unification," *Phys.Lett.* **B174** (1986) 45. Cited in Section 2.2.1 (pg.25).
67. T. Yanagida, "Horizontal Symmetry and Masses of Neutrinos," *Prog.Theor.Phys.* **64** (1980) 1103. Cited in Sections 2.2.1 (pg.25), 7.7 (pg.187), and 9.2 (pg.209).
68. S. Pascoli, S. Petcov, and A. Riotto, "Leptogenesis and Low Energy CP Violation in Neutrino Physics," *Nucl.Phys.* **B774** (2007) 1–52, `arXiv:hep-ph/0611338 [hep-ph]`. Cited in Section 2.2.1 (pg.26).
69. F. Capozzi, G. Fogli, E. Lisi, A. Marrone, D. Montanino, *et al.*, "Status of three-neutrino oscillation parameters, circa 2013," `arXiv:1312.2878 [hep-ph]`, 2013. Cited in Sections 2.2.1 (pg.26), 4.3.1 (pg.99), 4.3.3 (pg.112), 4.4 (pg.115), and 9.2 (pg.208).
70. P. Adamson *et al.*, **MINOS Collaboration** , "Search for the disappearance of muon antineutrinos in the NuMI neutrino beam," *Phys.Rev.* **D84** (2011) 071103, `arXiv:1108.1509 [hep-ex]`. Cited in Section 2.2.2 (pg.26).
71. S. Mikheev and A. Y. Smirnov, "Resonance Amplification of Oscillations in Matter and Spectroscopy of Solar Neutrinos," *Sov.J.Nucl.Phys.* **42** (1985) 913–917. Cited in Section 2.2.2 (pg.27).
72. L. Wolfenstein, "Neutrino Oscillations in Matter," *Phys.Rev.* **D17** (1978) 2369–2374. Cited in Section 2.2.2 (pg.27).
73. G. Bellini *et al.*, **Borexino Collaboration** , "Measurement of the solar 8B neutrino rate with a liquid scintillator target and 3 MeV energy threshold in the Borexino detector," *Phys.Rev.* **D82** (2010) 033006, `arXiv:0808.2868 [astro-ph]`. Cited in Section 2.2.2 (pg.27).
74. G. Bellini, J. Benziger, D. Bick, S. Bonetti, G. Bonfini, *et al.*, "Precision measurement of the 7Be solar neutrino interaction rate in Borexino," *Phys.Rev.Lett.* **107** (2011) 141302, `arXiv:1104.1816 [hep-ex]`. Cited in Section 2.2.2 (pg.27).
75. B. Aharmim *et al.*, **SNO Collaboration** , "Combined Analysis of all Three Phases of Solar Neutrino Data from the Sudbury Neutrino Observatory," *Phys.Rev.* **C88** (2013) 025501, `arXiv:1109.0763 [nucl-ex]`. Cited in Section 2.2.2 (pg.27).
76. A. Renshaw *et al.*, **Super-Kamiokande Collaboration** , "First Indication of Terrestrial Matter Effects on Solar Neutrino Oscillation," `arXiv:1312.5176 [hep-ex]`, 2013. Cited in Sections 2.2.2 (pg.27) and 8.1 (pg.199).
77. M. Freund, "Analytic approximations for three neutrino oscillation parameters and probabilities in matter," *Phys.Rev.* **D64** (2001) 053003, `arXiv:hep-ph/0103300 [hep-ph]`. Cited in Section 2.2.2 (pg.27).

78. W. Marciano and Z. Parsa, "Intense neutrino beams and leptonic CP violation," *Nucl.Phys.Proc.Suppl.* **221** (2011) 166–172, `arXiv:hep-ph/0610258 [hep-ph]`. Cited in Section 2.2.2 (pg.30).
79. B. Viren, "libnuosc++ - A library for calculating 3 neutrino oscillation probabilities.." `https://github.com/brettviren/nuosc`. Cited in Section 2.2.3 (pg.30).
80. A. M. Dziewonski and D. L. Anderson, "Preliminary reference Earth model," *Phys. Earth Plan. Int.* **25** (1981) 297. Cited in Section 2.2.3 (pg.30).
81. J. Appel *et al.*, "Physics Working Group Report to the LBNE Reconfiguration Steering Committee," 2012. `http://www.fnal.gov/directorate/lbne_reconfiguration/files/LBNE-Reconfiguration-PhysicsWG-Report-August2012.pdf`. Cited in Section 2.2.5 (pg.35).
82. R. Brun, F. Bruyant, M. Maire, A. McPherson, and P. Zanarini, "GEANT3," CERN-DD-EE-84-1, 1987. Cited in Section 2.2.5 (pg.33).
83. M. Bass *et al.*, **LBNE Collaboration** , "Baseline optimization for the measurement of CP violation and mass hierarchy in a long-baseline neutrino oscillation experiment," FERMILAB-PUB-13-506-E, `arXiv:1311.0212 [hep-ex]`, 2013. Cited in Sections 2.2.5 (pg.35) and 3.1 (pg.47).
84. M. Raidal, "Relation between the neutrino and quark mixing angles and grand unification," *Phys.Rev.Lett.* **93** (2004) 161801, `arXiv:hep-ph/0404046 [hep-ph]`. Cited in Section 2.2.6 (pg.35).
85. H. Minakata and A. Y. Smirnov, "Neutrino mixing and quark-lepton complementarity," *Phys.Rev.* **D70** (2004) 073009, `arXiv:hep-ph/0405088 [hep-ph]`. Cited in Section 2.2.6 (pg.35).
86. A. Y. Smirnov, "Neutrino mass, mixing and discrete symmetries," *J.Phys.Conf.Ser.* **447** (2013) 012004, `arXiv:1305.4827 [hep-ph]`. Cited in Section 2.2.6 (pg.35).
87. J. Harada, "Non-maximal θ_{23}, large θ_{13} and tri-bimaximal θ_{12} via quark-lepton complementarity at next-to-leading order," *Europhys.Lett.* **103** (2013) 21001, `arXiv:1304.4526 [hep-ph]`. Cited in Section 2.2.6 (pg.35).
88. B. Hu, "Trimaximal-Cabibbo neutrino mixing: A parametrization in terms of deviations from tribimaximal mixing," *Phys.Rev.* **D87** no. 5, (2013) 053011, `arXiv:1212.4079 [hep-ph]`. Cited in Section 2.2.6 (pg.35).
89. P. Ramond, "Fundamental Physics Underground. Presentation at ISOUPS (International Symposium: Opportunities in Underground Physics for Snowmass), Asilomar, May 2013," 2013. Cited in Section 2.2.6 (pg.35).
90. S. Antusch, C. Biggio, E. Fernandez-Martinez, M. Gavela, and J. Lopez-Pavon, "Unitarity of the Leptonic Mixing Matrix," *JHEP* **0610** (2006) 084, `arXiv:hep-ph/0607020 [hep-ph]`. Cited in Section 2.2.6 (pg.35).
91. X. Qian, C. Zhang, M. Diwan, and P. Vogel, "Unitarity Tests of the Neutrino Mixing Matrix," `arXiv:1308.5700 [hep-ex]`, 2013. Cited in Sections 2.2.6 (pg.35) and 2.2.6 (pg.36).

92. J. C. Pati and A. Salam, "Is Baryon Number Conserved?," *Phys.Rev.Lett.* **31** (1973) 661–664. Cited in Section 2.3.1 (pg.38).
93. H. Georgi and S. Glashow, "Unity of All Elementary Particle Forces," *Phys.Rev.Lett.* **32** (1974) 438–441. Cited in Section 2.3.1 (pg.38).
94. S. Dimopoulos, S. Raby, and F. Wilczek, "Proton Decay in Supersymmetric Models," *Phys.Lett.* **B112** (1982) 133. Cited in Section 2.3.1 (pg.38).
95. P. Langacker, "Grand Unified Theories and Proton Decay," *Phys.Rept.* **72** (1981) 185. Cited in Section 2.3.1 (pg.38).
96. W. de Boer, "Grand unified theories and supersymmetry in particle physics and cosmology," *Prog.Part.Nucl.Phys.* **33** (1994) 201–302, `arXiv:hep-ph/9402266 [hep-ph]`. Cited in Section 2.3.1 (pg.38).
97. P. Nath and P. Fileviez Perez, "Proton stability in grand unified theories, in strings and in branes," *Phys.Rept.* **441** (2007) 191–317, `arXiv:hep-ph/0601023 [hep-ph]`. Cited in Section 2.3.1 (pg.38).
98. S. Raby, T. Walker, K. Babu, H. Baer, A. Balantekin, *et al.*, "DUSEL Theory White Paper," SLAC-PUB-14734, FERMILAB-PUB-08-680-T, `arXiv:0810.4551 [hep-ph]`, 2008. Cited in Section 2.3.1 (pg.38).
99. G. Senjanovic, "Proton decay and grand unification," *AIP Conf.Proc.* **1200** (2010) 131–141, `arXiv:0912.5375 [hep-ph]`. Cited in Section 2.3.1 (pg.38).
100. T. Li, D. V. Nanopoulos, and J. W. Walker, "Elements of F-ast Proton Decay," *Nucl.Phys.* **B846** (2011) 43–99, `arXiv:1003.2570 [hep-ph]`. Cited in Section 2.3.1 (pg.38).
101. E. Noether, "Invariant Variation Problems," *Gott.Nachr.* **1918** (1918) 235–257, `arXiv:physics/0503066 [physics]`. Cited in Section 2.3.1 (pg.39).
102. H. Nishino *et al.*, **Super-Kamiokande Collaboration** , "Search for Nucleon Decay into Charged Anti-lepton plus Meson in Super-Kamiokande I and II," *Phys.Rev.* **D85** (2012) 112001, `arXiv:1203.4030 [hep-ex]`. Cited in Section 2.3.2 (pg.40).
103. R. Bionta, G. Blewitt, C. Bratton, D. Casper, A. Ciocio, *et al.*, "Observation of a Neutrino Burst in Coincidence with Supernova SN 1987a in the Large Magellanic Cloud," *Phys.Rev.Lett.* **58** (1987) 1494. Cited in Sections 2.4 (pg.42) and 6.1 (pg.151).
104. K. Hirata *et al.*, **KAMIOKANDE-II Collaboration** , "Observation of a Neutrino Burst from the Supernova SN 1987a," *Phys.Rev.Lett.* **58** (1987) 1490–1493. Cited in Sections 2.4 (pg.42) and 6.1 (pg.151).
105. E. Alekseev, L. Alekseeva, V. Volchenko, and I. Krivosheina, "Possible Detection of a Neutrino Signal on 23 February 1987 at the Baksan Underground Scintillation Telescope of the Institute of Nuclear Research," *JETP Lett.* **45** (1987) 589–592. Cited in Section 2.4 (pg.42).
106. K. Scholberg, "Supernova neutrino detection," *Nucl.Phys.Proc.Suppl.* **221** (2011) 248–253, `arXiv:astro-ph/0701081 [astro-ph]`. Cited in Sections 2.4 (pg.42) and 2.4 (pg.44).
107. A. Dighe, "Physics potential of future supernova neutrino observations," *J.Phys.Conf.Ser.* **136** (2008) 022041, `arXiv:0809.2977 [hep-ph]`. Cited in Section 2.4 (pg.42).

108. G. A. Tammann, W. Loeffler, and A. Schroder, "The Galactic supernova rate," *Astrophys. J. Suppl.* **92** (1994) 487–493. Cited in Section 2.4 (pg.42).
109. E. Cappellaro, R. Evans, and M. Turatto, "A new determination of supernova rates and a comparison with indicators for galactic star formation," *Astron.Astrophys.* **351** (1999) 459, `arXiv:astro-ph/9904225 [astro-ph]`. Cited in Section 2.4 (pg.42).
110. G. Pagliaroli, F. Vissani, E. Coccia, and W. Fulgione, "Neutrinos from Supernovae as a Trigger for Gravitational Wave Search," *Phys. Rev. Lett.* **103** (2009) 031102, `arXiv:0903.1191 [hep-ph]`. Cited in Section 2.4 (pg.43).
111. C. Ott, E. O'Connor, S. Gossan, E. Abdikamalov, U. Gamma, *et al.*, "Core-Collapse Supernovae, Neutrinos, and Gravitational Waves," *Nucl.Phys.Proc.Suppl.* **235-236** (2013) 381–387, `arXiv:1212.4250 [astro-ph.HE]`. Cited in Section 2.4 (pg.43).
112. A. Mirizzi, G. Raffelt, and P. Serpico, "Earth matter effects in supernova neutrinos: Optimal detector locations," *JCAP* **0605** (2006) 012, `arXiv:astro-ph/0604300 [astro-ph]`. Cited in Sections 2.4 (pg.43) and 2.4 (pg.44).
113. S. Choubey, B. Dasgupta, A. Dighe, and A. Mirizzi, "Signatures of collective and matter effects on supernova neutrinos at large detectors," `arXiv:1008.0308 [hep-ph]`, 2010. Cited in Section 2.4 (pg.43).
114. G. G. Raffelt, "Astrophysical axion bounds: An Update," `arXiv:astro-ph/9707268 [astro-ph]`, 1997. Cited in Section 2.4 (pg.43).
115. S. Hannestad and G. Raffelt, "New supernova limit on large extra dimensions," *Phys.Rev.Lett.* **87** (2001) 051301, `arXiv:hep-ph/0103201 [hep-ph]`. Cited in Section 2.4 (pg.43).
116. P. Antonioli *et al.*, "Snews: The supernova early warning system," *New J. Phys.* **6** (2004) 114, `astro-ph/0406214`. Cited in Sections 2.4 (pg.44) and 6.1 (pg.153).
117. K. Scholberg, "The SuperNova Early Warning System," *Astron. Nachr.* **329** (2008) 337–339, `arXiv:0803.0531 [astro-ph]`. Cited in Sections 2.4 (pg.44) and 6.1 (pg.153).
118. K. Scholberg, "Future supernova neutrino detectors," *J.Phys.Conf.Ser.* **203** (2010) 012079. Cited in Section 2.4 (pg.44).
119. "Sanford Underground Research Facility." `http://www.sanfordlab.org`. Cited in Section 3.3 (pg.54).
120. B. Cleveland, T. Daily, R. Davis Jr., J. R. Distel, K. Lande, *et al.*, "Measurement of the solar electron neutrino flux with the Homestake chlorine detector," *Astrophys.J.* **496** (1998) 505–526. Cited in Sections 3.3 (pg.54) and 8.1 (pg.195).
121. F. Gray, C. Ruybal, J. Totushek, D.-M. Mei, K. Thomas, *et al.*, "Cosmic Ray Muon Flux at the Sanford Underground Laboratory at Homestake," *Nucl.Instrum.Meth.* **A638** (2011) 63–66, `arXiv:1007.1921 [nucl-ex]`. Cited in Section 3.3 (pg.58).
122. W. Roggenthen and A. Smith, "U, Th, K contents of materials associated with the Homestake DUSEL site, Lead, South Dakota," *Private Communication* . Cited in Section 3.3 (pg.59).

123. D. Akerib *et al.*, **LUX Collaboration** , "First results from the LUX dark matter experiment at the Sanford Underground Research Facility," `arXiv:1310.8214 [astro-ph.CO]`, 2013. Cited in Section 3.3 (pg.59).
124. M. Bishai and Y. Lu, "Conceptual Designs for a Wide-Band Low-Energy Neutrino Beam Target," `LBNE-doc-3151`, November, 2010.
125. B. Lundberg, "A beginner guide to horn design and history of LBNE horn design," `LBNE-doc-8398`, November, 2014.
126. D. Ayres *et al.*, **NOvA Collaboration** , "The NOvA Technical Design Report," FERMILAB-DESIGN-2007-01, 2007. `http://lss.fnal.gov/archive/design/fermilab-design-2007-01.pdf`. Cited in Sections 3.4 (pg.63), 4.2.1 (pg.88), 7.4.4 (pg.183), and 7.6 (pg.185).
127. E. Worcester, "Potential Sensitivity Improvements with 10 kT LBNE," `LBNE-doc-6599`, 2012. Cited in Section 3.4 (pg.69).
128. S. Mishra, R. Petti, and C. Rosenfeld, "A High Resolution Neutrino Experiment in a Magnetic Field for Project-X at Fermilab," *PoS* **NUFACT08** (2008) 069, `arXiv:0812.4527 [hep-ex]`. Cited in Section 3.5 (pg.71).
129. B. Choudhary *et al.*, **Indian Institutions and Fermilab Collaboration** , "LBNE-India Detailed Project Report (DPR) submitted to DAE, India," `LBNE-doc-6704`, 2012. Cited in Sections 3.5 (pg.73), 3.5 (pg.74), and 7 (pg.163).
130. P. Huber, M. Lindner, and W. Winter, "Simulation of long-baseline neutrino oscillation experiments with GLoBES (General Long Baseline Experiment Simulator)," *Comput.Phys.Commun.* **167** (2005) 195, `arXiv:hep-ph/0407333 [hep-ph]`. Cited in Sections 4.2 (pg.85), 4.2.1 (pg.86), 4.2.2 (pg.88), and A.3 (pg.225).
131. P. Huber, J. Kopp, M. Lindner, M. Rolinec, and W. Winter, "New features in the simulation of neutrino oscillation experiments with GLoBES 3.0: General Long Baseline Experiment Simulator," *Comput.Phys.Commun.* **177** (2007) 432–438, `arXiv:hep-ph/0701187 [hep-ph]`. Cited in Sections 4.2 (pg.85) and 4.2.2 (pg.88).
132. S. Agostinelli *et al.*, **GEANT4** , "GEANT4: A simulation toolkit," *Nucl. Instrum. Meth.* **A506** (2003) 250–303. Cited in Sections 4.2.1 (pg.85), 6.2 (pg.154), and A.1.1 (pg.213).
133. C. Andreopoulos, **GENIE Collaboration** , "The GENIE neutrino Monte Carlo generator," *Acta Phys.Polon.* **B40** (2009) 2461–2475. Cited in Sections 4.2.1 (pg.88), 4.6 (pg.122), and A.1.1 (pg.216).
134. K. Abe *et al.*, **T2K Collaboration** , "The T2K Experiment," *Nucl.Instrum.Meth.* **A659** (2011) 106–135, `arXiv:1106.1238 [physics.ins-det]`. Cited in Sections 4.2.1 (pg.88), 7.4.4 (pg.183), and 7.6 (pg.185).
135. **NuMI-MINOS** . `http://www-numi.fnal.gov/`. Cited in Section 4.2.1 (pg.88).
136. A. Rubbia, "LAGUNA-LBNO: Design of an underground neutrino observatory coupled to long baseline neutrino beams from CERN," *J.Phys.Conf.Ser.* **408** (2013) 012006. Cited in Section 4.2.1 (pg.88).

137. J.-P. Delahaye, C. Ankenbrandt, A. Bogacz, S. Brice, A. Bross, *et al.*, "Enabling Intensity and Energy Frontier Science with a Muon Accelerator Facility in the U.S.: A White Paper Submitted to the 2013 U.S. Community Summer Study of the Division of Particles and Fields of the American Physical Society," FERMILAB-CONF-13-307-APC, `arXiv:1308.0494 [physics.acc-ph]`, 2013. Cited in Section 4.2.1 (pg.88).
138. A. Longhin, "Optimization of neutrino beams for underground sites in Europe," `arXiv:1206.4294 [physics.ins-det]`, 2012. Cited in Section 4.2.1 (pg.88).
139. S. Amoruso *et al.*, **ICARUS Collaboration** , "Measurement of the mu decay spectrum with the ICARUS liquid argon TPC," *Eur.Phys.J.* **C33** (2004) 233–241, `arXiv:hep-ex/0311040 [hep-ex]`. Cited in Sections 4.2.2 (pg.88), 4.6 (pg.124), and 6.2 (pg.154).
140. T2K Collaboration, "A Proposal for a Detector 2km Away from the T2K Neutrino Source.". 2005. `http://www.phy.duke.edu/~cwalter/nusag-members/2km-proposal-05-05-30.pdf`. Cited in Section 4.2.2 (pg.89).
141. A. Ankowski *et al.*, **ICARUS Collaboration** , "Measurement of through-going particle momentum by means of multiple scattering with the ICARUS T600 TPC," *Eur.Phys.J.* **C48** (2006) 667–676, `arXiv:hep-ex/0606006 [hep-ex]`. Cited in Section 4.2.2 (pg.89).
142. F. An *et al.*, **Daya Bay Collaboration** , "Spectral measurement of electron antineutrino oscillation amplitude and frequency at Daya Bay," `arXiv:1310.6732 [hep-ex]`, 2013. Cited in Sections 4.3 (pg.93) and 4.5 (pg.119).
143. P. Adamson *et al.*, **MINOS Collaboration** , "Electron neutrino and antineutrino appearance in the full MINOS data sample," *Phys.Rev.Lett.* **110** no. 17, (2013) 171801, `arXiv:1301.4581 [hep-ex]`. Cited in Sections 4.3 (pg.93), 4.3.2 (pg.103), and 4.3.2 (pg.108).
144. M. J. Murtagh, **E734 Collaboration** , "A Search for muon-neutrino to electron-neutrino oscillations using the E734 detector," BNL-39667, 1987.
145. R. Seto, "BNL E776: A Search for neutrino oscillations," *AIP Conf.Proc.* **176** (1988) 957–963.
146. L. Borodovsky, C. Chi, Y. Ho, N. Kondakis, W.-Y. Lee, *et al.*, "Search for muon-neutrino oscillations muon-neutrino to electron-neutrino (anti-muon-neutrino to anti-electron-neutrino in a wide band neutrino beam," *Phys.Rev.Lett.* **68** (1992) 274–277.
147. P. Astier *et al.*, **NOMAD Collaboration** , "Search for nu(mu) –> nu(e) oscillations in the NOMAD experiment," *Phys.Lett.* **B570** (2003) 19–31, `arXiv:hep-ex/0306037 [hep-ex]`.
148. A. Aguilar-Arevalo *et al.*, **MiniBooNE Collaboration** , "Unexplained Excess of Electron-Like Events From a 1-GeV Neutrino Beam," *Phys.Rev.Lett.* **102** (2009) 101802, `arXiv:0812.2243 [hep-ex]`. Cited in Section 7.7 (pg.190).
149. K. Abe *et al.*, **T2K Collaboration** , "Observation of Electron Neutrino Appearance in a Muon Neutrino Beam," `arXiv:1311.4750 [hep-ex]`, 2013. Cited in Section 4.3.2 (pg.103).

150. X. Qian, A. Tan, W. Wang, J. Ling, R. McKeown, *et al.*, “Statistical Evaluation of Experimental Determinations of Neutrino Mass Hierarchy,” *Phys.Rev.* **D86** (2012) 113011, `arXiv:1210.3651 [hep-ph]`. Cited in Sections 4.3.1 (pg.96), 4.3.1 (pg.97), 4.3.1 (pg.99), and 4.3.1 (pg.100).
151. M. Blennow, P. Coloma, P. Huber, and T. Schwetz, “Quantifying the sensitivity of oscillation experiments to the neutrino mass ordering,” `arXiv:1311.1822 [hep-ph]`, 2013. Cited in Sections 4.3.1 (pg.97), 4.3.1 (pg.98), 4.3.1 (pg.99), 4.3.1 (pg.100), and 4.8 (pg.137).
152. R. Cousins, “Private communication,” 2013. Cited in Section 4.3.1 (pg.99).
153. R. Cousins, J. Mumford, J. Tucker, and V. Valuev, “Spin discrimination of new heavy resonances at the LHC,” *JHEP* **0511** (2005) 046. Cited in Section 4.3.1 (pg.99).
154. P. Adamson *et al.*, **MINOS Collaboration** , “Improved search for muon-neutrino to electron-neutrino oscillations in MINOS,” *Phys.Rev.Lett.* **107** (2011) 181802, `arXiv:1108.0015 [hep-ex]`. Cited in Section 4.3.2 (pg.103).
155. P. Adamson *et al.*, **MINOS Collaboration** , “Neutrino and Antineutrino Inclusive Charged-current Cross Section Measurements with the MINOS Near Detector,” *Phys.Rev.* **D81** (2010) 072002, `arXiv:0910.2201 [hep-ex]`. Cited in Sections 4.3.2 (pg.103) and 7.1.8 (pg.169).
156. Q. Wu *et al.*, **NOMAD Collaboration** , “A Precise measurement of the muon neutrino-nucleon inclusive charged current cross-section off an isoscalar target in the energy range 2.5 < E(nu) < 40-GeV by NOMAD,” *Phys.Lett.* **B660** (2008) 19–25, `arXiv:0711.1183 [hep-ex]`. Cited in Sections 4.3.2 (pg.103), 7.1.8 (pg.169), and 7.4.4 (pg.183).
157. V. Lyubushkin *et al.*, **NOMAD Collaboration** , “A Study of quasi-elastic muon neutrino and antineutrino scattering in the NOMAD experiment,” *Eur.Phys.J.* **C63** (2009) 355–381, `arXiv:0812.4543 [hep-ex]`. Cited in Sections 4.3.2 (pg.103) and 7.1.8 (pg.169).
158. A. Bodek, U. Sarica, K. Kuzmin, and V. Naumov, “Extraction of Neutrino Flux with the Low ν Method at MiniBooNE Energies,” *AIP Conf.Proc.* **1560** (2013) 193–197, `arXiv:1207.1247 [hep-ex]`. Cited in Section 4.3.2 (pg.103).
159. P. Adamson *et al.*, **MINOS Collaboration** , “A Study of Muon Neutrino Disappearance Using the Fermilab Main Injector Neutrino Beam,” *Phys.Rev.* **D77** (2008) 072002, `arXiv:0711.0769 [hep-ex]`. Cited in Section 4.3.2 (pg.103).
160. M. Bishai, “Determining the Neutrino Flux from Accelerator Neutrino Beams,” *Nucl.Phys.Proc.Suppl.* **229-232** (2012) 210–214. Cited in Section 4.3.2 (pg.103).
161. B. Osmanov, **MINERvA Collaboration** , “MINERvA Detector: Description and Performance,” `arXiv:1109.2855 [physics.ins-det]`, 2011. Cited in Sections 4.3.2 (pg.104), 7.4.4 (pg.182), 7.4.4 (pg.183), and 7.6 (pg.185).
162. A. Korzenev, **NA61/SHINE** , “Hadron production measurement from NA61/SHINE,” `arXiv:1311.5719 [nucl-ex]`, 2013. Cited in Sections 4.3.2 (pg.104) and 7.1.2 (pg.166).

163. P. Adamson *et al.*, **MINOS Collaboration** , "Measurement of the neutrino mass splitting and flavor mixing by MINOS," *Phys.Rev.Lett.* **106** (2011) 181801, `arXiv:1103.0340 [hep-ex]`. Cited in Sections 4.3.2 (pg.105) and 4.5 (pg.120).
164. T. Yang, **ArgoNeuT Collaboration** , "New Results from ArgoNeuT," FERMILAB-CONF-13-510-E, `arXiv:1311.2096 [hep-ex]`, 2013. Cited in Section 4.3.2 (pg.107).
165. M. Day and K. S. McFarland, "Differences in Quasi-Elastic Cross-Sections of Muon and Electron Neutrinos," *Phys.Rev.* **D86** (2012) 053003, `arXiv:1206.6745 [hep-ph]`. Cited in Section 4.3.2 (pg.108).
166. K. Abe *et al.*, **Super-Kamiokande Collaboration** , "Search for Differences in Oscillation Parameters for Atmospheric Neutrinos and Antineutrinos at Super-Kamiokande," *Phys.Rev.Lett.* **107** (2011) 241801, `arXiv:1109.1621 [hep-ex]`. Cited in Section 4.4 (pg.115).
167. P. Adamson *et al.*, **MINOS Collaboration** , "Measurement of Neutrino and Antineutrino Oscillations Using Beam and Atmospheric Data in MINOS," *Phys.Rev.Lett.* **110** (2013) 251801, `arXiv:1304.6335 [hep-ex]`. Cited in Section 4.6 (pg.122).
168. V. Agrawal, T. Gaisser, P. Lipari, and T. Stanev, "Atmospheric neutrino flux above 1-GeV," *Phys.Rev.* **D53** (1996) 1314–1323, `arXiv:hep-ph/9509423 [hep-ph]`. Cited in Section 4.6 (pg.122).
169. A. Ankowski *et al.*, "Energy reconstruction of electromagnetic showers from pi0 decays with the icarus t600 liquid argon tpc," *Acta Physica Polonica B* **41** no. 1, (2010) 103, `arXiv:0812.2373 [hep-ex]`. Cited in Section 4.6 (pg.124).
170. F. Arneodo *et al.*, **The ICARUS-Milano Collaboration** , "Performance of a liquid argon time projection chamber exposed to the cern west area neutrino facility neutrino beam," *Phys. Rev. D* **74** (Dec, 2006) 112001. `http://link.aps.org/doi/10.1103/PhysRevD.74.112001`. Cited in Section 4.6 (pg.124).
171. C. Rubbia *et al.*, "Underground operation of the ICARUS T600 LAr-TPC: first results," *JINST* **6** (2011) P07011, `arXiv:1106.0975 [hep-ex]`. Cited in Section 4.6 (pg.124).
172. S. Davidson, C. Pena-Garay, N. Rius, and A. Santamaria, "Present and future bounds on nonstandard neutrino interactions," *JHEP* **0303** (2003) 011, `arXiv:hep-ph/0302093 [hep-ph]`. Cited in Section 4.7.1 (pg.132).
173. M. Gonzalez-Garcia and M. Maltoni, "Phenomenology with Massive Neutrinos," *Phys.Rept.* **460** (2008) 1–129, `arXiv:0704.1800 [hep-ph]`. Cited in Section 4.7.1 (pg.132).
174. C. Biggio, M. Blennow, and E. Fernandez-Martinez, "General bounds on non-standard neutrino interactions," *JHEP* **0908** (2009) 090, `arXiv:0907.0097 [hep-ph]`. Cited in Section 4.7.1 (pg.132).
175. H. Davoudiasl, H.-S. Lee, and W. J. Marciano, "Long-Range Lepton Flavor Interactions and Neutrino Oscillations," *Phys.Rev.* **D84** (2011) 013009, `arXiv:1102.5352 [hep-ph]`. Cited in Section 4.7.2 (pg.132).

176. P. Adamson *et al.*, **MINOS Collaboration** , "Search for sterile neutrino mixing in the MINOS long baseline experiment," *Phys.Rev.* **D81** (2010) 052004, `arXiv:1001.0336 [hep-ex]`. Cited in Section 4.7.3 (pg.134).
177. P. Machado, H. Nunokawa, F. P. d. Santos, and R. Z. Funchal, "Large Extra Dimensions and Neutrino Oscillations," `arXiv:1110.1465 [hep-ph]`, 2011. Cited in Section 4.7.4 (pg.135).
178. P. Coloma, P. Huber, J. Kopp, and W. Winter, "Systematic uncertainties in long-baseline neutrino oscillations for large θ_{13}," *Phys.Rev.* **D87** no. 3, (2013) 033004, `arXiv:1209.5973 [hep-ph]`. Cited in Section 4.8 (pg.135).
179. K. Abe, T. Abe, H. Aihara, Y. Fukuda, Y. Hayato, *et al.*, "Letter of Intent: The Hyper-Kamiokande Experiment — Detector Design and Physics Potential —," `arXiv:1109.3262 [hep-ex]`, 2011. Cited in Section 4.8 (pg.135).
180. A. Stahl, C. Wiebusch, A. Guler, M. Kamiscioglu, R. Sever, *et al.*, "Expression of Interest for a very long baseline neutrino oscillation experiment (LBNO)," CERN-SPSC-2012-021, SPSC-EOI-007, 2012. Cited in Section 4.8 (pg.135).
181. M. Apollonio, A. Bross, J. Kopp, and K. Long, **IDS-NF Collaboration** , "The International Design Study for the Neutrino Factory," *Nucl.Phys.Proc.Suppl.* **229-232** (2012) 515. Cited in Section 4.8 (pg.135).
182. E. Christensen, P. Coloma, and P. Huber, "Physics Performance of a Low-Luminosity Low Energy Neutrino Factory," `arXiv:1301.7727 [hep-ph]`, 2013. Cited in Section 4.8 (pg.136).
183. E. Kearns *et al.*, **Hyper-Kamiokande Working Group** , "Hyper-Kamiokande Physics Opportunities," `arXiv:1309.0184 [hep-ex]`, 2013. Cited in Section 4.8 (pg.136).
184. S. Agarwalla *et al.*, **LAGUNA-LBNO Collaboration** , "The mass-hierarchy and CP-violation discovery reach of the LBNO long-baseline neutrino experiment," `arXiv:1312.6520 [hep-ph]`, 2013. Cited in Section 4.8 (pg.136).
185. M. Bishai, M. Diwan, S. Kettell, J. Stewart, B. Viren, *et al.*, "Precision Neutrino Oscillation Measurements using Simultaneous High-Power, Low-Energy Project-X Beams," BNL-101234-2013-CP, FERMILAB-FN-0962, `arXiv:1307.0807 [hep-ex]`, 2013. Cited in Section 4.8 (pg.137).
186. J. L. Raaf, **Super-Kamiokande Collaboration** , "Recent Nucleon Decay Results from Super-Kamiokande," *Nucl.Phys.Proc.Suppl.* **229-232** (2012) 559. Cited in Section 5.1 (pg.139).
187. A. Bueno, Z. Dai, Y. Ge, M. Laffranchi, A. Melgarejo, *et al.*, "Nucleon decay searches with large liquid argon TPC detectors at shallow depths: Atmospheric neutrinos and cosmogenic backgrounds," *JHEP* **0704** (2007) 041, `arXiv:hep-ph/0701101 [hep-ph]`. Cited in Sections 5.1 (pg.140), 5.2 (pg.140), 5.3.1 (pg.144), 5.3.1 (pg.145), and 5.3.2 (pg.145).
188. D. Stefan and A. M. Ankowski, "Nuclear effects in proton decay," *Acta Phys.Polon.* **B40** (2009) 671–674, `arXiv:0811.1892 [nucl-th]`. Cited in Section 5.2 (pg.141).
189. S. Amerio *et al.*, **ICARUS Collaboration** , "Design, construction and tests of the ICARUS T600 detector," *Nucl.Instrum.Meth.* **A527** (2004) 329–410. Cited in Section 5.2 (pg.141).

190. M. Antonello, B. Baibussinov, P. Benetti, E. Calligarich, N. Canci, *et al.*, "Precise 3D track reconstruction algorithm for the ICARUS T600 liquid argon time projection chamber detector," *Adv.High Energy Phys.* **2013** (2013) 260820, `arXiv:1210.5089 [physics.ins-det]`. Cited in Sections 5.2 (pg.142) and 5.3.2 (pg.148).
191. A. Bernstein, M. Bishai, E. Blucher, D. B. Cline, M. V. Diwan, *et al.*, "Report on the Depth Requirements for a Massive Detector at Homestake," FERMILAB-TM-2424-E, BNL-81896-2008-IR, LBNL-1348E, `arXiv:0907.4183 [hep-ex]`, 2009. Cited in Section 5.3.1 (pg.144).
192. V. Kudryavtsev *et al.*, "Cosmic rays and cosmogenics. report to the lbne collaboration.," `LBNE-doc-5904`, 2012. Cited in Section 5.3.1 (pg.144).
193. K. Kobayashi *et al.*, **Super-Kamiokande Collaboration** , "Search for nucleon decay via modes favored by supersymmetric grand unification models in Super-Kamiokande-I," *Phys.Rev.* **D72** (2005) 052007, `arXiv:hep-ex/0502026 [hep-ex]`. Cited in Section 5.3.2 (pg.146).
194. H. Gallagher, "Private communication.". Cited in Section 5.3.2 (pg.148).
195. H.-T. Janka, "Explosion Mechanisms of Core-Collapse Supernovae," *Ann.Rev.Nucl.Part.Sci.* **62** (2012) 407–451, `arXiv:1206.2503 [astro-ph.SR]`. Cited in Section 6.1 (pg.151).
196. T. Fischer, S. Whitehouse, A. Mezzacappa, F.-K. Thielemann, and M. Liebendorfer, "Protoneutron star evolution and the neutrino driven wind in general relativistic neutrino radiation hydrodynamics simulations," *Astron.Astrophys.* **517** (2010) A80, `arXiv:0908.1871 [astro-ph.HE]`. Cited in Section 6.1 (pg.152).
197. M. Wurm *et al.*, **LENA Collaboration** , "The next-generation liquid-scintillator neutrino observatory LENA," *Astropart.Phys.* **35** (2012) 685–732, `arXiv:1104.5620 [astro-ph.IM]`. Cited in Section 6.1 (pg.152).
198. H. Minakata, H. Nunokawa, R. Tomas, and J. W. Valle, "Parameter Degeneracy in Flavor-Dependent Reconstruction of Supernova Neutrino Fluxes," *JCAP* **0812** (2008) 006, `arXiv:0802.1489 [hep-ph]`. Cited in Section 6.1 (pg.152).
199. I. Tamborra, B. Muller, L. Hudepohl, H.-T. Janka, and G. Raffelt, "High-resolution supernova neutrino spectra represented by a simple fit," *Phys.Rev.* **D86** (2012) 125031, `arXiv:1211.3920 [astro-ph.SR]`. Cited in Section 6.1 (pg.152).
200. H. Duan, G. M. Fuller, and Y.-Z. Qian, "Collective neutrino flavor transformation in supernovae," *Phys.Rev.* **D74** (2006) 123004, `arXiv:astro-ph/0511275 [astro-ph]`. Cited in Section 6.1 (pg.152).
201. G. L. Fogli, E. Lisi, A. Marrone, and A. Mirizzi, "Collective neutrino flavor transitions in supernovae and the role of trajectory averaging," *JCAP* **0712** (2007) 010, `arXiv:0707.1998 [hep-ph]`. Cited in Section 6.1 (pg.152).
202. G. G. Raffelt and A. Y. Smirnov, "Self-induced spectral splits in supernova neutrino fluxes," *Phys.Rev.* **D76** (2007) 081301, `arXiv:0705.1830 [hep-ph]`. Cited in Section 6.1 (pg.152).

203. G. G. Raffelt and A. Y. Smirnov, "Adiabaticity and spectral splits in collective neutrino transformations," *Phys.Rev.* **D76** (2007) 125008, `arXiv:0709.4641 [hep-ph]`. Cited in Section 6.1 (pg.152).
204. A. Esteban-Pretel, A. Mirizzi, S. Pastor, R. Tomas, G. Raffelt, *et al.*, "Role of dense matter in collective supernova neutrino transformations," *Phys.Rev.* **D78** (2008) 085012, `arXiv:0807.0659 [astro-ph]`. Cited in Section 6.1 (pg.152).
205. H. Duan and J. P. Kneller, "Neutrino flavour transformation in supernovae," *J.Phys.G* **G36** (2009) 113201, `arXiv:0904.0974 [astro-ph.HE]`. Cited in Section 6.1 (pg.152).
206. B. Dasgupta, A. Dighe, G. G. Raffelt, and A. Y. Smirnov, "Multiple Spectral Splits of Supernova Neutrinos," *Phys.Rev.Lett.* **103** (2009) 051105, `arXiv:0904.3542 [hep-ph]`. Cited in Section 6.1 (pg.152).
207. H. Duan, G. M. Fuller, and Y.-Z. Qian, "Collective Neutrino Oscillations," *Ann.Rev.Nucl.Part.Sci.* **60** (2010) 569–594, `arXiv:1001.2799 [hep-ph]`. Cited in Section 6.1 (pg.152).
208. H. Duan and A. Friedland, "Self-induced suppression of collective neutrino oscillations in a supernova," *Phys.Rev.Lett.* **106** (2011) 091101, `arXiv:1006.2359 [hep-ph]`. Cited in Sections 6.1 (pg.152) and 6.2 (pg.155).
209. J. F. Cherry, J. Carlson, A. Friedland, G. M. Fuller, and A. Vlasenko, "Halo Modification of a Supernova Neutronization Neutrino Burst," *Phys.Rev.* **D87** (2013) 085037, `arXiv:1302.1159 [astro-ph.HE]`. Cited in Section 6.1 (pg.153).
210. J. F. Beacom, R. Boyd, and A. Mezzacappa, "Black hole formation in core collapse supernovae and time-of-flight measurements of the neutrino masses," *Phys.Rev.* **D63** (2001) 073011, `arXiv:astro-ph/0010398 [astro-ph]`. Cited in Section 6.1 (pg.153).
211. T. Fischer, S. C. Whitehouse, A. Mezzacappa, F. K. Thielemann, and M. Liebendorfer, "The neutrino signal from protoneutron star accretion and black hole formation," `arXiv:0809.5129 [astro-ph]`, 2008. Cited in Section 6.1 (pg.153).
212. R. C. Schirato and G. M. Fuller, "Connection between supernova shocks, flavor transformation, and the neutrino signal," LA-UR-02-3068, `arXiv:astro-ph/0205390 [astro-ph]`, 2002. Cited in Section 6.1 (pg.153).
213. F. Hanke, A. Marek, B. Muller, and H.-T. Janka, "Is Strong SASI Activity the Key to Successful Neutrino-Driven Supernova Explosions?," *Astrophys.J.* **755** (2012) 138, `arXiv:1108.4355 [astro-ph.SR]`. Cited in Section 6.1 (pg.153).
214. F. Hanke, B. Mueller, A. Wongwathanarat, A. Marek, and H.-T. Janka, "SASI Activity in Three-Dimensional Neutrino-Hydrodynamics Simulations of Supernova Cores," *Astrophys.J.* **770** (2013) 66, `arXiv:1303.6269 [astro-ph.SR]`. Cited in Section 6.1 (pg.153).
215. A. Friedland and A. Gruzinov, "Neutrino signatures of supernova turbulence," LA-UR-06-2202, `arXiv:astro-ph/0607244 [astro-ph]`, 2006. Cited in Section 6.1 (pg.153).

216. T. Lund and J. P. Kneller, “Combining collective, MSW, and turbulence effects in supernova neutrino flavor evolution,” arXiv:1304.6372 [astro-ph.HE], 2013. Cited in Section 6.1 (pg.153).
217. G. G. Raffelt, “Particle Physics from Stars,” *Ann. Rev. Nucl. Part. Sci.* **49** (1999) 163–216, arXiv:hep-ph/9903472. Cited in Section 6.1 (pg.153).
218. A. Bueno, I. Gil Botella, and A. Rubbia, “Supernova neutrino detection in a liquid argon TPC,” ICARUS-TM-03-02, arXiv:hep-ph/0307222 [hep-ph], 2003. Cited in Section 6.1 (pg.153).
219. K. Scholberg *et al.*, “SNOwGLoBES: SuperNova Observatories with GLoBES.” http://www.phy.duke.edu/~schol/snowglobes. Cited in Section 6.2 (pg.154).
220. E. D. Church, “LArSoft: A Software Package for Liquid Argon Time Projection Drift Chambers,” arXiv:1311.6774 [physics.ins-det], 2013. Cited in Sections 6.2 (pg.154) and A.1.1 (pg.213).
221. T. Totani, K. Sato, H. E. Dalhed, and J. R. Wilson, “Future detection of supernova neutrino burst and explosion mechanism,” *Astrophys. J.* **496** (1998) 216–225, arXiv:astro-ph/9710203. Cited in Section 6.2 (pg.155).
222. J. Gava, J. Kneller, C. Volpe, and G. C. McLaughlin, “A dynamical collective calculation of supernova neutrino signals,” *Phys. Rev. Lett.* **103** (2009) 071101, arXiv:0902.0317 [hep-ph]. Cited in Section 6.2 (pg.155).
223. L. Hudepohl, B. Muller, H.-T. Janka, A. Marek, and G. Raffelt, “Neutrino Signal of Electron-Capture Supernovae from Core Collapse to Cooling,” *Phys.Rev.Lett.* **104** (2010) 251101, arXiv:0912.0260 [astro-ph.SR]. Cited in Section 6.2 (pg.155).
224. A. Cherry, A. Friedland, and H. Duan, “Private communication.”.
225. M. T. Keil, G. G. Raffelt, and H.-T. Janka, “Monte Carlo study of supernova neutrino spectra formation,” *Astrophys.J.* **590** (2003) 971–991, arXiv:astro-ph/0208035 [astro-ph].
226. E. Church *et al.*, “Muon-induced background for beam neutrinos at the surface,” LBNE-doc-6232, October, 2012. Cited in Sections 6.3.1 (pg.158), A.4 (pg.229), and A.4 (pg.230).
227. Gehman, V. and Kadel, R, “Calculation of intrinsic and cosmogenic backgrounds in the LBNE far detector for use in detection of supernova neutrinos,” LBNE-doc-8419, January, 2014. Cited in Section 6.3.2 (pg.159).
228. J. H. Harley *et al.*, “Report No. 094 - Exposure of the Population in the United States and Canada from Natural Background Radiation,” *National Council on Radiation Protection and Measurements* (2014) . http://www.ncrppublications.org/Reports/094. Cited in Section 6.3.3 (pg.160).
229. L. Grandi, “Darkside-50: performance and results from the first atmospheric argon run,” February, 2014. UCLA’s 11th Symposium on Sources and Detection of Dark Matter and Dark Energy in the Universe. Cited in Section 6.3.3 (pg.160).

230. D. Leonard, P. Grinberg, P. Weber, E. Baussan, Z. Djurcic, *et al.*, "Systematic study of trace radioactive impurities in candidate construction materials for EXO-200," *Nucl.Instrum.Meth.* **A591** (2008) 490–509, `arXiv:0709.4524 [physics.ins-det]`. Cited in Section 6.3.3 (pg.160).
231. D. Casper, "The Nuance neutrino physics simulation, and the future," *Nucl.Phys.Proc.Suppl.* **112** (2002) 161–170, `arXiv:hep-ph/0208030 [hep-ph]`.
232. G. Zeller, "Nuclear Effects in Water vs. Argon," `LBNE-doc-740`, 2010.
233. G. Zeller, "Expected Event Rates in the LBNE Near Detector," `LBNE-doc-783`, 2010.
234. S.R.Mishra, Apr, 1990. Review talk presented at Workshop on Hadron Structure Functions and Parton Distributions, Fermilab. Cited in Section 7.1.1 (pg.164).
235. R. Raja, "The Main injector particle production experiment (MIPP) at Fermilab," *Nucl.Instrum.Meth.* **A553** (2005) 225–230, `arXiv:hep-ex/0501005 [hep-ex]`. Cited in Section 7.1.2 (pg.166).
236. J. Formaggio and G. Zeller, "From eV to EeV: Neutrino Cross Sections Across Energy Scales," *Rev.Mod.Phys.* **84** (2012) 1307, `arXiv:1305.7513 [hep-ex]`. Cited in Sections 7.1.3 (pg.166) and 7.4.4 (pg.182).
237. W. J. Marciano and Z. Parsa, "Neutrino-Electron Scattering Theory," *J. Phys.* **G29** (2003) 2629–2645, `arXiv:hep-ph/0403168`. Cited in Sections 7.1.4 (pg.167) and 7.2.2 (pg.173).
238. S. Mishra, K. Bachmann, R. Bernstein, R. Blair, C. Foudas, *et al.*, "Measurement of Inverse Muon Decay $\nu_\mu + e \to \mu^- + \nu_e$ at Fermilab Tevatron Energies 15-GeV - 600-GeV," *Phys.Rev.Lett.* **63** (1989) 132–135. Cited in Section 7.1.5 (pg.167).
239. S. Mishra, K. Bachmann, R. Blair, C. Foudas, B. King, *et al.*, "Inverse Muon Decay, $\nu_\mu e \to \mu^- \nu_e$, at the Fermilab Tevatron," *Phys.Lett.* **B252** (1990) 170–176. Cited in Section 7.1.5 (pg.167).
240. P. Vilain *et al.*, **CHARM-II Collaboration** , "A Precise measurement of the cross-section of the inverse muon decay muon-neutrino + e- –> mu- + electron-neutrino," *Phys.Lett.* **B364** (1995) 121–126. Cited in Section 7.1.5 (pg.167).
241. O. Samoylov *et al.*, **NOMAD** , "A Precision Measurement of Charm Dimuon Production in Neutrino Interactions from the NOMAD Experiment," *Nucl.Phys.* **B876** (2013) 339–375, `arXiv:1308.4750 [hep-ex]`. Cited in Sections 7.1.8 (pg.169), 7.2.1 (pg.171), and 7.4.4 (pg.183).
242. G. Zeller *et al.*, **NuTeV Collaboration** , "A Precise determination of electroweak parameters in neutrino nucleon scattering," *Phys.Rev.Lett.* **88** (2002) 091802, `arXiv:hep-ex/0110059 [hep-ex]`. Cited in Section 7.2.1 (pg.170).
243. H. Abramowicz, R. Belusevic, A. Blondel, H. Blumer, P. Bockmann, *et al.*, **CDHS Collaboration** , "A Precision Measurement of sin**2theta(W) from Semileptonic Neutrino Scattering," *Phys.Rev.Lett.* **57** (1986) 298. Cited in Section 7.2.1 (pg.171).
244. J. Allaby *et al.*, **CHARM Collaboration** , "A Precise Determination of the Electroweak Mixing Angle from Semileptonic Neutrino Scattering," *Z.Phys.* **C36** (1987) 611. Cited in Section 7.2.1 (pg.171).

245. P. Reutens, F. Merritt, D. MacFarlane, R. Messner, D. Novikoff, *et al.*, **CCFR Collaboration** , "Measurement of $\sin^2 \theta_W$ and ρ in Deep Inelastic Neutrino - Nucleon Scattering," *Phys.Lett.* **B152** (1985) 404–410. Cited in Section 7.2.1 (pg.171).
246. S. Alekhin, S. A. Kulagin, and R. Petti, "Modeling lepton-nucleon inelastic scattering from high to low momentum transfer," *AIP Conf.Proc.* **967** (2007) 215–224, `arXiv:0710.0124 [hep-ph]`. Cited in Section 7.2.1 (pg.171).
247. S. Alekhin, S. A. Kulagin, and R. Petti, "Update of the global fit of PDFs including the low-Q DIS data," `arXiv:0810.4893 [hep-ph]`, 2008. Cited in Section 7.2.1 (pg.171).
248. S. Alekhin, S. A. Kulagin, and R. Petti, "Determination of Strange Sea Distributions from Neutrino-Nucleon Deep Inelastic Scattering," *Phys.Lett.* **B675** (2009) 433–440, `arXiv:0812.4448 [hep-ph]`. Cited in Section 7.2.1 (pg.171).
249. A. Arbuzov, D. Y. Bardin, and L. Kalinovskaya, "Radiative corrections to neutrino deep inelastic scattering revisited," *JHEP* **0506** (2005) 078, `arXiv:hep-ph/0407203 [hep-ph]`. Cited in Section 7.2.1 (pg.171).
250. S. A. Kulagin and R. Petti, "Global study of nuclear structure functions," *Nucl.Phys.* **A765** (2006) 126–187, `arXiv:hep-ph/0412425 [hep-ph]`. Cited in Section 7.2.1 (pg.171).
251. S. A. Kulagin and R. Petti, "Neutrino inelastic scattering off nuclei," *Phys.Rev.* **D76** (2007) 094023, `arXiv:hep-ph/0703033 [HEP-PH]`. Cited in Sections 7.2.1 (pg.171), 7.4.2 (pg.181), and 7.6 (pg.186).
252. S. Kulagin and R. Petti, "Structure functions for light nuclei," *Phys.Rev.* **C82** (2010) 054614, `arXiv:1004.3062 [hep-ph]`. Cited in Section 7.2.1 (pg.171).
253. P. Vilain *et al.*, **CHARM-II Collaboration** , "Precision measurement of electroweak parameters from the scattering of muon-neutrinos on electrons," *Phys.Lett.* **B335** (1994) 246–252. Cited in Section 7.2.2 (pg.173).
254. A. Czarnecki and W. J. Marciano, "Polarized Moller scattering asymmetries," *Int.J.Mod.Phys.* **A15** (2000) 2365–2376, `arXiv:hep-ph/0003049 [hep-ph]`.
255. S. Bennett and C. Wieman, "Erratum: Measurement of the 6s –> 7s Transition Polarizability in Atomic Cesium and an Improved Test of the Standard Model [Phys. Rev. Lett. 82, 2484 (1999)]," *Phys.Rev.Lett.* **82** (1999) 4153–4153.
256. W. Yao *et al.*, **Particle Data Group** , "Review of Particle Physics," *J.Phys.* **G33** (2006) 1–1232.
257. P. Anthony *et al.*, **SLAC E158 Collaboration** , "Precision measurement of the weak mixing angle in Moller scattering," *Phys.Rev.Lett.* **95** (2005) 081601, `arXiv:hep-ex/0504049 [hep-ex]`.
258. J. H. Lee, "The Qweak: Precision measurement of the proton's weak charge by parity violating experiment," *Few Body Syst.* **54** (2013) 129–134. Cited in Section 7.2.2 (pg.175).
259. Nuruzzaman, "Q-weak: First Direct Measurement of the Weak Charge of the Proton," `arXiv:1312.6009 [nucl-ex]`, 2013. Cited in Section 7.2.2 (pg.175).
260. R. Jaffe and A. Manohar, "The G(1) Problem: Fact and Fantasy on the Spin of the Proton," *Nucl.Phys.* **B337** (1990) 509–546. Cited in Section 7.3 (pg.175).

261. R. D. Young, J. Roche, R. D. Carlini, and A. W. Thomas, "Extracting nucleon strange and anapole form factors from world data," *Phys.Rev.Lett.* **97** (2006) 102002, `arXiv:nucl-ex/0604010 [nucl-ex]`. Cited in Sections 7.3.1 (pg.175) and 7.3.1 (pg.176).
262. D. B. Leinweber, S. Boinepalli, I. Cloet, A. W. Thomas, A. G. Williams, *et al.*, "Precise determination of the strangeness magnetic moment of the nucleon," *Phys.Rev.Lett.* **94** (2005) 212001, `arXiv:hep-lat/0406002 [hep-lat]`. Cited in Section 7.3.1 (pg.175).
263. L. Ahrens, S. Aronson, P. Connolly, B. Gibbard, M. Murtagh, *et al.*, "Measurement of Neutrino - Proton and anti-neutrino - Proton Elastic Scattering," *Phys.Rev.* **D35** (1987) 785. Cited in Section 7.3.2 (pg.177).
264. G. Garvey, W. Louis, and D. White, "Determination of proton strange form-factors from neutrino p elastic scattering," *Phys.Rev.* **C48** (1993) 761–765. Cited in Section 7.3.2 (pg.177).
265. W. Alberico, M. Barbaro, S. M. Bilenky, J. Caballero, C. Giunti, *et al.*, "Strange form-factors of the proton: A New analysis of the neutrino (anti-neutrino) data of the BNL-734 experiment," *Nucl.Phys.* **A651** (1999) 277–286, `arXiv:hep-ph/9812388 [hep-ph]`. Cited in Section 7.3.2 (pg.177).
266. A. Aguilar-Arevalo *et al.*, **MiniBooNE Collaboration** , "Measurement of the Neutrino Neutral-Current Elastic Differential Cross Section on Mineral Oil at $E_\nu \sim 1$ GeV," *Phys.Rev.* **D82** (2010) 092005, `arXiv:1007.4730 [hep-ex]`. Cited in Section 7.3.2 (pg.177).
267. L. Bugel *et al.*, **FINeSSE Collaboration** , "A Proposal for a near detector experiment on the booster neutrino beamline: FINeSSE: Fermilab intense neutrino scattering scintillator experiment," FERMILAB-PROPOSAL-0937, `arXiv:hep-ex/0402007 [hep-ex]`, 2004. Cited in Section 7.3.2 (pg.178).
268. W. Leung, P. Quintas, S. Mishra, F. Sciulli, C. Arroyo, *et al.*, "A Measurement of the Gross-Llewellyn-Smith sum rule from the CCFR x(F3) structure function," *Phys.Lett.* **B317** (1993) 655–659. Cited in Section 7.4.1 (pg.180).
269. A. Bodek and A. Simon, "What Do Electron and Neutrino Experiments Tell Us About Nuclear Effects in the Deuteron," *Z.Phys.* **C29** (1985) 231. Cited in Sections 7.4.3 (pg.181) and 7.4.3 (pg.182).
270. G. Jones *et al.*, **Birmingham-CERN-Imperial Coll.-MPI(Munich)-Oxford-University Coll. Collaboration** , "A Measurement of the Proton Structure Functions From Neutrino Hydrogen and Anti-neutrino Hydrogen Charged Current Interactions," *Z.Phys.* **C44** (1989) 379–384. Cited in Sections 7.4.3 (pg.181) and 7.4.3 (pg.182).
271. J. Berge, H. Burkhardt, F. Dydak, R. Hagelberg, M. Krasny, *et al.*, "A Measurement of Differential Cross-Sections and Nucleon Structure Functions in Charged Current Neutrino Interactions on Iron," *Z.Phys.* **C49** (1991) 187–224.
272. D. Allasia *et al.*, **WA25 Collaboration** , "Measurement of the Neutron and Proton Structure Functions From Neutrino and Anti-neutrinos Scattering in Deuterium," *Phys.Lett.* **B135** (1984) 231.

273. D. Allasia, C. Angelini, A. Baldini, L. Bertanza, A. Bigi, *et al.*, "Q**2 Dependence of the Proton and Neutron Structure Functions from Neutrino and anti-neutrinos Scattering in Deuterium," *Z.Phys.* **C28** (1985) 321. Cited in Section 7.5 (pg.184).

274. U.-K. Yang *et al.*, **CCFR/NuTeV Collaboration** , "Measurements of F_2 and $xF_3^{\nu} - xF_3^{\bar{\nu}}$ from CCFR ν_{μ}−Fe and $\bar{\nu}_{\mu}$−Fe data in a physics model independent way," *Phys.Rev.Lett.* **86** (2001) 2742–2745, `arXiv:hep-ex/0009041 [hep-ex]`.

275. U.-K. Yang *et al.*, **CCFR/NuTeV Collaboration** , "Extraction of R = sigma(L) / sigma(T) from CCFR Fe-neutrino(muon) and Fe-anti-neutrino(muon) differential cross-sections," *Phys.Rev.Lett.* **87** (2001) 251802, `arXiv:hep-ex/0104040 [hep-ex]`.

276. M. Tzanov *et al.*, **NuTeV Collaboration** , "Precise measurement of neutrino and anti-neutrino differential cross sections," *Phys.Rev.* **D74** (2006) 012008, `arXiv:hep-ex/0509010 [hep-ex]`. Cited in Section 7.4.4 (pg.183).

277. G. Onengut *et al.*, **CHORUS Collaboration** , "Measurement of nucleon structure functions in neutrino scattering," *Phys.Lett.* **B632** (2006) 65–75.

278. R. Petti and O. Samoylov, "Charm dimuon production in neutrino-nucleon interactions in the NOMAD experiment," *Phys.Part.Nucl.Lett.* **8** (2011) 755–761. Cited in Section 7.4.4 (pg.183).

279. T. Sekiguchi, "Neutrino facility and neutrino physics in J-PARC," *PTEP* **2012** (2012) 02B005. Cited in Section 7.4.4 (pg.183).

280. J. Dudek, R. Ent, R. Essig, K. Kumar, C. Meyer, *et al.*, "Physics Opportunities with the 12 GeV Upgrade at Jefferson Lab," *Eur.Phys.J.* **A48** (2012) 187, `arXiv:1208.1244 [hep-ex]`. Cited in Section 7.4.4 (pg.183).

281. N. Mondal, "India-Based Neutrino Observatory (INO)," *Eur.Phys.J.Plus* **127** (2012) 106. Cited in Section 7.6 (pg.185).

282. A. Butkevich, "Quasi-elastic neutrino charged-current scattering off medium-heavy nuclei: 40Ca and 40Ar," *Phys.Rev.* **C85** (2012) 065501, `arXiv:1204.3160 [nucl-th]`. Cited in Section 7.6 (pg.186).

283. A. Butkevich and S. A. Kulagin, "Quasi-elastic neutrino charged-current scattering cross sections on oxygen," *Phys.Rev.* **C76** (2007) 045502, `arXiv:0705.1051 [nucl-th]`. Cited in Section 7.6 (pg.186).

284. A. M. Ankowski and J. T. Sobczyk, "Construction of spectral functions for medium-mass nuclei," *Phys.Rev.* **C77** (2008) 044311, `arXiv:0711.2031 [nucl-th]`. Cited in Section 7.6 (pg.186).

285. T. Asaka and M. Shaposhnikov, "The nuMSM, dark matter and baryon asymmetry of the universe," *Phys.Lett.* **B620** (2005) 17–26, `arXiv:hep-ph/0505013 [hep-ph]`. Cited in Sections 7.7 (pg.187) and 7.7 (pg.188).

286. D. Gorbunov and M. Shaposhnikov, "How to find neutral leptons of the νMSM?," *JHEP* **0710** (2007) 015, `arXiv:0705.1729 [hep-ph]`. Cited in Sections 7.7 (pg.187) and 7.7 (pg.188).

287. A. Boyarsky, O. Ruchayskiy, and M. Shaposhnikov, "The Role of sterile neutrinos in cosmology and astrophysics," *Ann.Rev.Nucl.Part.Sci.* **59** (2009) 191–214, arXiv:0901.0011 [hep-ph]. Cited in Section 7.7 (pg.187).
288. S. Dodelson and L. M. Widrow, "Sterile-neutrinos as dark matter," *Phys.Rev.Lett.* **72** (1994) 17–20, arXiv:hep-ph/9303287 [hep-ph]. Cited in Section 7.7 (pg.187).
289. A. Atre, T. Han, S. Pascoli, and B. Zhang, "The Search for Heavy Majorana Neutrinos," *JHEP* **0905** (2009) 030, arXiv:0901.3589 [hep-ph]. Cited in Sections 7.7 (pg.187) and 7.7 (pg.188).
290. M. Shaposhnikov, "The nuMSM, leptonic asymmetries, and properties of singlet fermions," *JHEP* **0808** (2008) 008, arXiv:0804.4542 [hep-ph]. Cited in Section 7.7 (pg.187).
291. E. K. Akhmedov, V. Rubakov, and A. Y. Smirnov, "Baryogenesis via neutrino oscillations," *Phys.Rev.Lett.* **81** (1998) 1359–1362, arXiv:hep-ph/9803255 [hep-ph]. Cited in Section 7.7 (pg.188).
292. A. M. Cooper-Sarkar *et al.*, **WA66 Collaboration** , "Search for Heavy Neutrino Decays in the BEBC Beam Dump Experiment," *Phys.Lett.* **B160** (1985) 207. Cited in Section 7.7 (pg.188).
293. F. Bergsma *et al.*, **CHARM Collaboration** , "A Search for Decays of Heavy Neutrinos in the Mass Range 0.5-GeV to 2.8-GeV," *Phys.Lett.* **B166** (1986) 473. Cited in Section 7.7 (pg.188).
294. A. Vaitaitis *et al.*, **NuTeV Collaboration, E815 Collaboration** , "Search for Neutral Heavy Leptons in a High-Energy Neutrino Beam," *Phys.Rev.Lett.* **83** (1999) 4943–4946, arXiv:hep-ex/9908011 [hep-ex]. Cited in Section 7.7 (pg.188).
295. G. Bernardi, G. Carugno, J. Chauveau, F. Dicarlo, M. Dris, *et al.*, "Search for Neutrino Decay," *Phys.Lett.* **B166** (1986) 479. Cited in Section 7.7 (pg.188).
296. G. Bernardi, G. Carugno, J. Chauveau, F. Dicarlo, M. Dris, *et al.*, "Further Limits on Heavy Neutrino Couplings," *Phys.Lett.* **B203** (1988) 332. Cited in Section 7.7 (pg.188).
297. L. Canetti and M. Shaposhnikov, "Baryon Asymmetry of the Universe in the NuMSM," *JCAP* **1009** (2010) 001, arXiv:1006.0133 [hep-ph].
298. C. Kullenberg *et al.*, **NOMAD Collaboration** , "A Search for Single Photon Events in Neutrino Interactions in NOMAD," *Phys.Lett.* **B706** (2012) 268–275, arXiv:1111.3713 [hep-ex]. Cited in Section 7.7 (pg.190).
299. C. Volpe, N. Auerbach, G. Colo, T. Suzuki, and N. Van Giai, "Neutrino C-12 reactions and the LSND and KARMEN experiments on neutrino oscillations," *Phys. Atom. Nucl.* **64** (2001) 1165–1168. Cited in Section 7.8 (pg.190).
300. M. Maltoni and T. Schwetz, "Sterile neutrino oscillations after first MiniBooNE results," *Phys.Rev.* **D76** (2007) 093005, arXiv:0705.0107 [hep-ph]. Cited in Section 7.8 (pg.190).
301. P. Ade *et al.*, **Planck Collaboration** , "Planck 2013 results. XVI. Cosmological parameters," arXiv:1303.5076 [astro-ph.CO], 2013. Cited in Section 7.9 (pg.192).

302. C. Bennett *et al.*, **WMAP** , "Nine-Year Wilkinson Microwave Anisotropy Probe (WMAP) Observations: Final Maps and Results," *Astrophys.J.Suppl.* **208** (2013) 20, arXiv:1212.5225 [astro-ph.CO]. Cited in Section 7.9 (pg.192).
303. B. Batell, M. Pospelov, and A. Ritz, "Exploring Portals to a Hidden Sector Through Fixed Targets," *Phys.Rev.* **D80** (2009) 095024, arXiv:0906.5614 [hep-ph]. Cited in Section 7.9 (pg.193).
304. P. deNiverville, M. Pospelov, and A. Ritz, "Observing a light dark matter beam with neutrino experiments," *Phys.Rev.* **D84** (2011) 075020, arXiv:1107.4580 [hep-ph]. Cited in Section 7.9 (pg.193).
305. P. deNiverville, D. McKeen, and A. Ritz, "Signatures of sub-GeV dark matter beams at neutrino experiments," *Phys.Rev.* **D86** (2012) 035022, arXiv:1205.3499 [hep-ph]. Cited in Section 7.9 (pg.193).
306. R. Dharmapalan *et al.*, **MiniBooNE Collaboration** , "Low Mass WIMP Searches with a Neutrino Experiment: A Proposal for Further MiniBooNE Running," FERMILAB-PROPOSAL-1032, arXiv:1211.2258 [hep-ex], 2012. Cited in Section 7.9 (pg.193).
307. H. Bethe, "Energy production in stars," *Phys.Rev.* **55** (1939) 434–456. Cited in Section 8.1 (pg.195).
308. C. Weizsäcker, "Über Elementumwandlungen im Innern der Sterne II," *Physik.Z.* **39** (1938) 633–646. Cited in Section 8.1 (pg.195).
309. J. N. Bahcall, A. M. Serenelli, and S. Basu, "New solar opacities, abundances, helioseismology, and neutrino fluxes," *Astrophys.J.* **621** (2005) L85–L88, arXiv:astro-ph/0412440 [astro-ph]. Cited in Section 8.1 (pg.195).
310. S. Fukuda *et al.*, **Super-Kamiokande Collaboration** , "Solar B-8 and hep neutrino measurements from 1258 days of Super-Kamiokande data," *Phys.Rev.Lett.* **86** (2001) 5651–5655, arXiv:hep-ex/0103032 [hep-ex]. Cited in Section 8.1 (pg.195).
311. Q. Ahmad *et al.*, **SNO Collaboration** , "Measurement of the rate of nu/e + d -> p + p + e- interactions produced by B-8 solar neutrinos at the Sudbury Neutrino Observatory," *Phys.Rev.Lett.* **87** (2001) 071301, arXiv:nucl-ex/0106015 [nucl-ex]. Cited in Section 8.1 (pg.195).
312. G. Bellini, J. Benziger, D. Bick, S. Bonetti, G. Bonfini, *et al.*, "Precision measurement of the 7Be solar neutrino interaction rate in Borexino," *Phys.Rev.Lett.* **107** (2011) 141302, arXiv:1104.1816 [hep-ex]. Cited in Section 8.1 (pg.197).
313. C. Kraus, **SNO+ Collaboration** , "SNO with liquid scintillator: SNO+," *Prog. Part. Nucl. Phys.* **57** (2006) 150–152. Cited in Section 8.1 (pg.197).
314. H. Sekiya, **Super-Kamiokande Collaboration** , "Solar neutrino analysis of Super-Kamiokande," arXiv:1307.3686, 2013. Cited in Section 8.1 (pg.197).
315. A. Guglielmi, **ICARUS Collaboration** , "Status and early events from ICARUS T600," *Nucl.Phys* **B (Proc. Suppl.) 229-232** (2012) 342–346. Cited in Section 8.1 (pg.198).
316. G. Bellini *et al.*, **Borexino Collaboration** , "First evidence of pep solar neutrinos by direct detection in Borexino," *Phys.Rev.Lett.* **108** (2012) 051302, arXiv:1110.3230 [hep-ex].

317. G. Bellini *et al.*, **Borexino Collaboration** , "Measurement of the solar 8B neutrino rate with a liquid scintillator target and 3 MeV energy threshold in the Borexino detector," *Phys.Rev.* **D82** (2010) 033006, `arXiv:0808.2868 [astro-ph]`.
318. A. Gando *et al.*, **KamLAND Collaboration** , "Reactor On-Off Antineutrino Measurement with KamLAND," `arXiv:1303.4667 [hep-ex]`, 2013. Cited in Section 8.1 (pg.199).
319. J. Silk, K. A. Olive, and M. Srednicki, "The Photino, the Sun and High-Energy Neutrinos," *Phys.Rev.Lett.* **55** (1985) 257–259. Cited in Section 8.2 (pg.199).
320. M. Cirelli, N. Fornengo, T. Montaruli, I. A. Sokalski, A. Strumia, *et al.*, "Spectra of neutrinos from dark matter annihilations," *Nucl.Phys.* **B727** (2005) 99–138, `arXiv:hep-ph/0506298 [hep-ph]`. Cited in Section 8.2 (pg.200).
321. J. LoSecco, J. Van der Velde, R. Bionta, G. Blewitt, C. Bratton, *et al.*, "Limits on the Flux of Energetic Neutrinos from the Sun," *Phys.Lett.* **B188** (1987) 388. Cited in Section 8.2 (pg.200).
322. M. Aartsen *et al.*, **IceCube Collaboration** , "Search for dark matter annihilations in the Sun with the 79-string IceCube detector," *Phys.Rev.Lett.* **110** (2013) 131302, `arXiv:1212.4097 [astro-ph.HE]`. Cited in Section 8.2 (pg.200).
323. M. Blennow, M. Carrigan, and E. F. Martinez, "Probing the Dark Matter mass and nature with neutrinos," *JCAP* **1306** (2013) 038, `arXiv:1303.4530 [hep-ph]`. Cited in Section 8.2 (pg.200).
324. T. Totani, K. Sato, and Y. Yoshii, "Spectrum of the supernova relic neutrino background and evolution of galaxies," *Astrophys.J.* **460** (1996) 303–312, `arXiv:astro-ph/9509130 [astro-ph]`. Cited in Section 8.3 (pg.201).
325. K. Sato, T. Totani, and Y. Yoshii, "Spectrum of the supernova relic neutrino background and evolution of galaxies," 1997. Cited in Section 8.3 (pg.201).
326. D. Hartmann and S. Woosley, "The cosmic supernova neutrino background," *Astropart.Phys.* **7** (1997) 137–146. Cited in Section 8.3 (pg.201).
327. R. Malaney, "Evolution of the cosmic gas and the relic supernova neutrino background," *Astropart.Phys.* **7** (1997) 125–136, `arXiv:astro-ph/9612012 [astro-ph]`. Cited in Section 8.3 (pg.201).
328. M. Kaplinghat, G. Steigman, and T. Walker, "The Supernova relic neutrino background," *Phys.Rev.* **D62** (2000) 043001, `arXiv:astro-ph/9912391 [astro-ph]`. Cited in Section 8.3 (pg.201).
329. S. Ando, J. F. Beacom, and H. Yuksel, "Detection of neutrinos from supernovae in nearby galaxies," *Phys.Rev.Lett.* **95** (2005) 171101, `arXiv:astro-ph/0503321 [astro-ph]`. Cited in Section 8.3 (pg.201).
330. C. Lunardini, "Testing neutrino spectra formation in collapsing stars with the diffuse supernova neutrino flux," *Phys.Rev.* **D75** (2007) 073022, `arXiv:astro-ph/0612701 [astro-ph]`. Cited in Section 8.3 (pg.201).
331. M. Fukugita and M. Kawasaki, "Constraints on the star formation rate from supernova relic neutrino observations," *Mon.Not.Roy.Astron.Soc.* **340** (2003) L7, `arXiv:astro-ph/0204376 [astro-ph]`. Cited in Section 8.3 (pg.201).

332. P. Vogel and J. F. Beacom, "Angular distribution of neutron inverse beta decay, anti-neutrino(e) + p —> e+ + n," *Phys.Rev.* **D60** (1999) 053003, `arXiv:hep-ph/9903554 [hep-ph]`. Cited in Section 8.3 (pg.201).
333. A. Strumia and F. Vissani, "Precise quasielastic neutrino nucleon cross section," *Phys. Lett.* **B564** (2003) 42–54, `arXiv:astro-ph/0302055`. Cited in Section 8.3 (pg.201).
334. W. E. Ormand, P. M. Pizzochero, P. F. Bortignon, and R. A. Broglia, "Neutrino capture cross-sections for Ar-40 and Beta decay of Ti-40," *Phys. Lett.* **B345** (1995) 343–350, `arXiv:nucl-th/9405007`. Cited in Section 8.3 (pg.201).
335. E. Kolbe, K. Langanke, G. Martinez-Pinedo, and P. Vogel, "Neutrino nucleus reactions and nuclear structure," *J. Phys.* **G29** (2003) 2569–2596, `arXiv:nucl-th/0311022`. Cited in Section 8.3 (pg.201).
336. M. Sajjad Athar and S. K. Singh, "nu/e (anti-nu/e) - Ar-40 absorption cross sections for supernova neutrinos," *Phys. Lett.* **B591** (2004) 69–75. Cited in Section 8.3 (pg.201).
337. A. Cocco, A. Ereditato, G. Fiorillo, G. Mangano, and V. Pettorino, "Supernova relic neutrinos in liquid argon detectors," *JCAP* **0412** (2004) 002, `arXiv:hep-ph/0408031 [hep-ph]`. Cited in Section 8.3 (pg.202).
338. R. Abbasi *et al.*, **IceCube Collaboration** , "Search for Relativistic Magnetic Monopoles with IceCube," *Phys.Rev.* **D87** (2013) 022001, `arXiv:1208.4861 [astro-ph.HE]`. Cited in Section 8.4 (pg.203).
339. M. Aartsen *et al.*, **IceCube Collaboration** , "The IceCube Neutrino Observatory Part IV: Searches for Dark Matter and Exotic Particles," `arXiv:1309.7007 [astro-ph.HE]`, 2013. Cited in Section 8.4 (pg.203).
340. K. Ueno *et al.*, **Super-Kamiokande Collaboration** , "Search for GUT Monopoles at Super-Kamiokande," *Astropart.Phys.* **36** (2012) 131–136, `arXiv:1203.0940 [hep-ex]`. Cited in Section 8.4 (pg.203).
341. M. Aartsen *et al.*, **IceCube Collaboration** , "Search for non-relativistic Magnetic Monopoles with IceCube," `arXiv:1402.3460 [astro-ph.CO]`, 2014. Cited in Section 8.4 (pg.203).
342. M. Ambrosio *et al.*, **MACRO Collaboration** , "Final results of magnetic monopole searches with the MACRO experiment," *Eur.Phys.J.* **C25** (2002) 511–522, `arXiv:hep-ex/0207020 [hep-ex]`. Cited in Section 8.4 (pg.203).
343. R. Mohapatra, "Neutron-Anti-Neutron Oscillation: Theory and Phenomenology," *J.Phys.* **G36** (2009) 104006, `arXiv:0902.0834 [hep-ph]`. Cited in Section 8.5 (pg.204).
344. The United States Department of Energy, "Program and Project Management for the Acquisition of Capital Assets," DOE, DOE O 413.3B, November, 2010. Cited in Section 9.1 (pg.206).
345. J. Strait, R. Wilson, and V. Papadimitriou, "LBNE Presentations to P5," `LBNE-doc-8694`, November, 2013. Cited in Section 9.1 (pg.207).
346. S. Bilenky and C. Giunti, "Neutrinoless double-beta decay: A brief review," *Mod.Phys.Lett.* **A27** (2012) 1230015, `arXiv:1203.5250 [hep-ph]`. Cited in Section 9.2 (pg.209).

347. **LBNE Project Management Team** , "LBNE Conceptual Design Report: The LBNE Water Cherenkov Detector," LBNE-doc-5118, 2012. Cited in Section 9.3 (pg.210).
348. J. Hewett, H. Weerts, K. Babu, J. Butler, B. Casey, *et al.*, "Planning the Future of U.S. Particle Physics (Snowmass 2013): Chapter 2: Intensity Frontier," FERMILAB-CONF-14-019-CH02, arXiv:1401.6077 [hep-ex], 2014. Cited in Section 9.4.1 (pg.210).
349. C. Green, J. Kowalkowski, M. Paterno, M. Fischler, L. Garren, *et al.*, "The art framework," *J.Phys.Conf.Ser.* **396** (2012) 022020. Cited in Section A.1.1 (pg.213).
350. T. Katori, **MicroBooNE Collaboration** , "MicroBooNE, A Liquid Argon Time Projection Chamber (LArTPC) Neutrino Experiment," *AIP Conf.Proc.* **1405** (2011) 250–255, arXiv:1107.5112 [hep-ex]. Cited in Sections A.1.1 (pg.213) and A.3 (pg.221).
351. M. Soderberg, **ArgoNeuT Collaboration** , "ArgoNeuT: A Liquid Argon Time Projection Chamber Test in the NuMI Beamline," FERMILAB-CONF-09-516-E, arXiv:0910.3433 [physics.ins-det], 2009. Cited in Section A.1.1 (pg.213).
352. D.Huffman, "A Method for the Construction of Minimum-Redundancy Codes," in *Proceedings of the IRE*. 1952. Cited in Section A.1.1 (pg.215).
353. M. Szydagis, N. Barry, K. Kazkaz, J. Mock, D. Stolp, *et al.*, "NEST: A Comprehensive Model for Scintillation Yield in Liquid Xenon," *JINST* **6** (2011) P10002, arXiv:1106.1613 [physics.ins-det]. Cited in Section A.1.1 (pg.215).
354. C. Hagman, D. Lange, J. Verbeke, and D. Wright, "Cosmic-ray Shower Library (CRY)," Lawrence Livermore National Laboratory, UCRL-TM-229453, March, 2012. http://nuclear.llnl.gov/simulation/doc_cry_v1.7/cry.pdf. Cited in Section A.1.1 (pg.216).
355. R. P. Sandhir, S. Muhuri, and T. Nayak, "Dynamic Fuzzy c-Means (dFCM) Clustering and its Application to Calorimetric Data Reconstruction in High Energy Physics," *Nucl.Instrum.Meth.* **A681** (2012) 34–43, arXiv:1204.3459 [nucl-ex]. Cited in Section A.2 (pg.218).
356. R. E. Kalman, "A new approach to linear filtering and prediction problems," *Transactions of the ASME–Journal of Basic Engineering* **82** no. Series D, (1960) 35–45. Cited in Section A.2 (pg.218).
357. J. Marshall and M. Thomson, "The Pandora software development kit for particle flow calorimetry," *J.Phys.Conf.Ser.* **396** (2012) 022034. Cited in Section A.2 (pg.219).
358. A. Accardi, J. Albacete, M. Anselmino, N. Armesto, E. Aschenauer, *et al.*, "Electron Ion Collider: The Next QCD Frontier - Understanding the glue that binds us all," BNL-98815-2012-JA, JLAB-PHY-12-1652, arXiv:1212.1701 [nucl-ex], 2012. Cited in Sections B (pg.233) and B (pg.235).

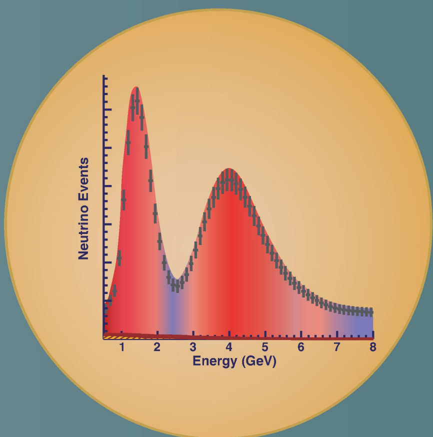

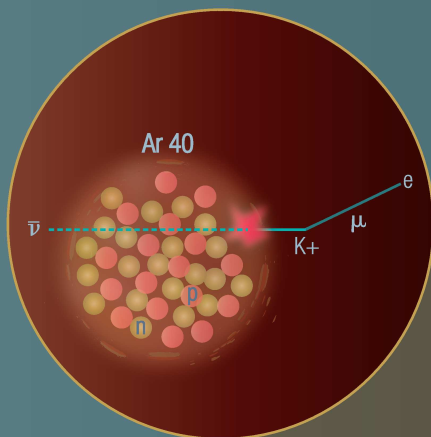

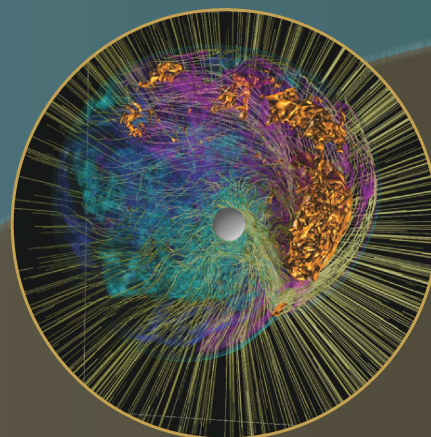

Through precise studies of neutrino flavor oscillations enabled by an intense, optimized beam and advanced detectors, LBNE aims to shed light on the mystery of the matter-antimatter asymmetry in the Universe.

With the world's largest cryogenic particle detector deep underground, LBNE will probe the stability of matter and its relation to the Grand Unification of forces.

LBNE's observation of thousands of neutrinos from a core-collapse supernova in the Milky Way would allow us to peer inside a newly-formed neutron star and potentially witness the birth of a black hole.

U.S. DEPARTMENT OF ENERGY | Office of Science

Sanford Underground Research Facility

Fermilab

Eur. Phys. J. C (2014) 74:2951
DOI 10.1140/epjc/s10052-014-2951-y

THE EUROPEAN
PHYSICAL JOURNAL C

Regular Article - Experimental Physics

Studies of dijet transverse momentum balance and pseudorapidity distributions in pPb collisions at $\sqrt{s_{NN}} = 5.02$ TeV

The CMS Collaboration*

CERN, Geneva, Switzerland

Received: 18 January 2014 / Accepted: 23 June 2014 / Published online: 23 July 2014

Abstract Dijet production has been measured in pPb collisions at a nucleon–nucleon centre-of-mass energy of 5.02 TeV. A data sample corresponding to an integrated luminosity of 35 nb^{-1} was collected using the Compact Muon Solenoid detector at the Large Hadron Collider. The dijet transverse momentum balance, azimuthal angle correlations, and pseudorapidity distributions are studied as a function of the transverse energy in the forward calorimeters ($E_T^{4<|\eta|<5.2}$). For pPb collisions, the dijet transverse momentum ratio and the width of the distribution of dijet azimuthal angle difference are comparable to the same quantities obtained from a simulated pp reference and insensitive to $E_T^{4<|\eta|<5.2}$. In contrast, the mean value of the dijet pseudorapidity is found to change monotonically with increasing $E_T^{4<|\eta|<5.2}$, indicating a correlation between the energy emitted at large pseudorapidity and the longitudinal motion of the dijet frame. The pseudorapidity distribution of the dijet system in minimum bias pPb collisions is compared with next-to-leading-order perturbative QCD predictions obtained from both nucleon and nuclear parton distribution functions, and the data more closely match the latter.

1 Introduction

Relativistic heavy ion collisions allow to study the fundamental theory of strong interactions—quantum chromodynamics (QCD)—under extreme conditions of temperature and energy density. Lattice QCD calculations [1] predict a new chirally-symmetric form of matter that consists of an extended volume of deconfined quarks and gluons above the critical energy density of the phase transition, about 1 GeV/fm^3 [2–5]. One of the most interesting experimental signatures of the formation of this novel matter, the quark-gluon plasma (QGP), is "jet-quenching" resulting from the energy loss of hard-scattered partons passing through the medium. Back-to-back dijets have long been proposed as a particularly useful tool for studying the QGP properties [6,7]. In PbPb collisions at the Large Hadron Collider (LHC), the effects of this medium were observed in the first jet measurements as a dijet transverse momentum imbalance [8,9].

Recent data at the LHC for jets [8–12], correlations between jets and single particles [13–15], and charged-particle measurements [16,17], provide unprecedented information about the jet-quenching phenomenon. For head-on collisions, a large broadening of the dijet transverse momentum ratio ($p_{T,2}/p_{T,1}$) and a decrease in its mean is observed where, as is the case for all the dijet observables in the following discussion, the subscripts 1 and 2 in the kinematical quantities refer to the leading and subleading jets (the two highest-p_T jets), respectively. This observation is consistent with theoretical calculations that involve differential energy loss of back-to-back hard-scattered partons as they traverse the medium [18–20]. At leading order (LO) and in the absence of parton energy loss in the QGP, the two jets have equal transverse momenta (p_T) with respect to the beam axis and are back-to-back in azimuth (e.g. with the relative azimuthal angle $\Delta\phi_{1,2} = |\varphi_1 - \varphi_2| \approx \pi$). However, medium-induced gluon emission in the final state can significantly unbalance the energy of leading and subleading jets and decorrelate the jets in azimuth.

Studies of dijet properties in pPb collisions are of great importance to establish a QCD baseline for hadronic interactions with cold nuclear matter [21,22]. This is crucial for the interpretation of the PbPb results, which could include the effects of both cold nuclear matter and a hot partonic medium. The dijet production rates as a function of jet pseudorapidity (η) have also been proposed as a tool to probe the nuclear modifications of the parton distribution functions (PDFs) [23–28]. Pseudorapidity η is defined as $-\ln[\tan(\theta/2)]$, where θ is the polar angle with respect to the proton beam direction.

In this paper, the first dijet transverse momentum balance and pseudorapidity distribution measurements in pPb colli-

* e-mail: cms-publication-committee-chair@cern.ch

sions are presented as a function of the transverse energy in the forward calorimeters ($E_T^{4<|\eta|<5.2}$). This analysis uses pPb data recorded with the Compact Muon Solenoid (CMS) detector in 2013, corresponding to an integrated luminosity of $35 \pm 1\,\text{nb}^{-1}$. The lead nuclei and protons had beam energies of 1.58 TeV per nucleon and 4 TeV, respectively, corresponding to a nucleon–nucleon centre-of-mass energy of $\sqrt{s_{NN}} = 5.02$ TeV. Jets are reconstructed within $|\eta| < 3$ using the anti-k_T sequential recombination algorithm [29,30] with a distance parameter of 0.3. This analysis is performed using events required to have a dijet with a leading jet $p_{T,1} > 120$ GeV/c, a subleading jet $p_{T,2} > 30$ GeV/c, and $\Delta\phi_{1,2} > 2\pi/3$.

2 The CMS detector

A detailed description of the CMS experiment can be found in Ref. [31]. The silicon tracker, located in the 3.8 T magnetic field of the superconducting solenoid is used to measure charged particles within the pseudorapidity range $|\eta| < 2.5$. It provides an impact parameter resolution of $\approx 15\,\mu$m and a p_T resolution of about 1.5 % for particles with $p_T = 100$ GeV/c. Also located inside the solenoid are an electromagnetic calorimeter (ECAL) and a hadron calorimeter (HCAL). The ECAL consists of more than 75 000 lead tungstate crystals, arranged in a quasi-projective geometry, and distributed in a barrel region ($|\eta| < 1.48$) and in two endcaps that extend up to $|\eta| = 3.0$. The HCAL barrel and endcaps are sampling calorimeters composed of brass and scintillator plates, covering $|\eta| < 3.0$. Iron hadron-forward (HF) calorimeters, with quartz fibers read out by photomultipliers, extend the calorimeter coverage up to $|\eta| = 5.2$ and are used to differentiate between central and peripheral pPb collisions. Calorimeter cells are grouped in projective towers of granularity in pseudorapidity and azimuthal angle given by $\Delta\eta \times \Delta\phi = 0.087 \times 0.087$ close to midrapidity, having a coarser segmentation at large rapidities. An efficient muon system is deployed for the reconstruction and identification of muons up to $|\eta| = 2.4$. The detailed Monte Carlo (MC) simulation of the CMS detector response is based on GEANT4 [32].

Because of the different energies of the two beams, the nucleon–nucleon centre-of-mass frame in pPb collisions is not at rest in the detector frame. Results are presented in the laboratory frame, where the higher energy proton beam is defined to travel in the positive η direction ($\theta = 0$). Therefore, a massless particle emitted at $\eta_{cm} = 0$ in the nucleon–nucleon centre-of-mass frame will be detected at $\eta_{lab} = +0.465$ in the laboratory frame. During part of the data taking period, the directions of the proton and lead beams were reversed. For the dataset taken with the opposite direction proton beam, the standard CMS definition of η was flipped so that the proton always moves towards positive η.

3 Jet reconstruction

Offline jet reconstruction is performed using the CMS "particle-flow" algorithm [33,34]. By combining information from all sub-detector systems, the particle-flow algorithm attempts to identify all stable particles in an event, classifying them as electrons, muons, photons, charged and neutral hadrons. These particle-flow objects are first grouped into "pseudo-towers" according to the CMS HCAL granularity. The transverse-energy of the pseudo-towers is calculated from the scalar sum of the transverse-energy of the particle-flow objects, assuming zero mass. Then, jets are reconstructed based on the pseudo-towers, using the anti-k_T sequential recombination algorithm provided in the FASTJET framework [29,30] with a distance parameter of 0.3.

To subtract the underlying event (UE) background in pPb collisions, an iterative algorithm described in Ref. [35] is employed, using the same implementation as in the PbPb analysis [8]. The energies of the particle-flow candidates are mapped onto projective towers with the same segmentation as the HCAL, and the mean and the dispersion of the energies detected in rings of constant η are subtracted from the jet energy. Jets reconstructed without UE subtraction are used to estimate the systematic uncertainty associated with the subtraction algorithm.

The measured jet energies are then corrected to the energies of the corresponding true particle jets using a factorized multi-step approach [36]. The MC jet energy corrections which remove the non-linearity of the detector response are derived using simulated PYTHIA events [37] (tune D6T with PDFs CTEQ6L1 used for 2.76 TeV, tune Z2 for pp 7 TeV). The residual corrections, accounting for the small differences between data and simulation, are obtained from dijet and photon+jet data and simulated events.

4 The Monte Carlo simulation

In order to study the jet reconstruction performance in pPb collisions, dijet events in pp collisions are first simulated with the PYTHIA MC generator (version 6.423, tune Z2) [38] and later embedded in the simulated pPb underlying events. A minimum hard-interaction scale ($\hat{p}_T$) selection of 30 GeV/c is used to increase the number of dijet events produced in the momentum range studied. To model the pPb underlying event, minimum bias pPb events are simulated with the HIJING event generator [39], version 1.383 [40]. The HIJING simulation with an effective total nucleon–nucleon cross-section of 84 mb is tuned to reproduce the total particle multiplicities and charged-hadron spectra, and to approximate the underlying event fluctuations seen in data.

The complete detector simulation and analysis chain is used to process PYTHIA dijet events and these events are then embedded into HIJING events (denoted as PYTHIA + HIJING). The effects of the pPb underlying event on the jet position resolution, jet energy scale, and jet finding efficiency are studied as a function of the total transverse energy detected by the HF calorimeter, jet pseudorapidity and transverse momentum. These effects are small and do not require specific corrections to the measurements, but they are considered as systematic uncertainties.

5 Event selection

The CMS online event selection employs a hardware-based Level-1 trigger and a software-based high-level trigger (HLT). Events are selected using an inclusive single-jet trigger in the HLT, requiring a calorimeter-based jet with transverse momentum $p_T > 100\,\mathrm{GeV/c}$. The trigger becomes fully efficient for events with a leading jet with $p_T > 120\,\mathrm{GeV/c}$. In addition to the jet data sample, a minimum bias event sample is selected by requiring at least one track with $p_T > 0.4\,\mathrm{GeV/c}$ to be found in the pixel tracker coincident with the pPb bunch crossing.

In the offline analysis, an additional selection of hadronic collisions is applied by requiring a coincidence of at least one of the HF calorimeter towers, with more than 3 GeV of total energy, from the HF detectors on both sides of the interaction point. Events are required to have at least one reconstructed primary vertex. The primary vertex is formed by two or more associated tracks and is required to have a distance from the nominal interaction region of less than 15 cm along the beam axis and less than 0.15 cm in the transverse plane. If there are more than 10 tracks in the event, the fraction of good-quality tracks originating from the primary vertex is required to be larger than 20 % in order to suppress beam backgrounds [41].

In addition to the selection of inelastic hadronic collisions, the analysis has extra requirements on the leading and subleading jet, which are the jets with the largest and the second largest p_T in the $|\eta| < 3$ interval, respectively. These requirements are $p_{T,1} > 120\,\mathrm{GeV/c}$, $p_{T,2} > 30\,\mathrm{GeV/c}$, and $\Delta\phi_{1,2} > 2\pi/3$. Only offline reconstructed jets within $|\eta| < 3$ in the lab frame are considered in this analysis. In order to remove events with residual HCAL noise that are missed by the calorimeter noise rejection algorithms [42,43], either the leading or subleading jet is required to have at least one track with $p_T > 4\,\mathrm{GeV/c}$. This selection does not introduce a bias of the dijet kinematic distributions based on studies using PYTHIA+HIJING MC simulation.

The selected minimum bias and dijet events are divided into HF activity classes according to the raw transverse energy measured in the HF detectors within the pseudorapidity interval $4.0 < |\eta| < 5.2$, denoted as $E_T^{4<|\eta|<5.2}$. This pseudorapidity interval is chosen in order to separate the transverse energy and dijet measurements by a pseudorapidity gap of at least one unit ($3.0 < |\eta| < 4.0$). The HF transverse energy distribution for the selected dijet events in comparison to that for minimum bias events is shown in Fig. 1a. It can be seen that the selection of a high-p_T dijet leads to a bias in the $E_T^{4<|\eta|<5.2}$ distributions toward higher values. The correlation between $E_T^{4<|\eta|<5.2}$ and the raw number of tracks originating from the primary vertex ($N_{trk}^{offline}$) with $|\eta| < 2.4$ and $p_T > 0.4\,\mathrm{GeV/c}$ (before the tracking efficiency correction) is shown in Fig. 1b. A broad correlation between the two quantities is observed in the inclusive

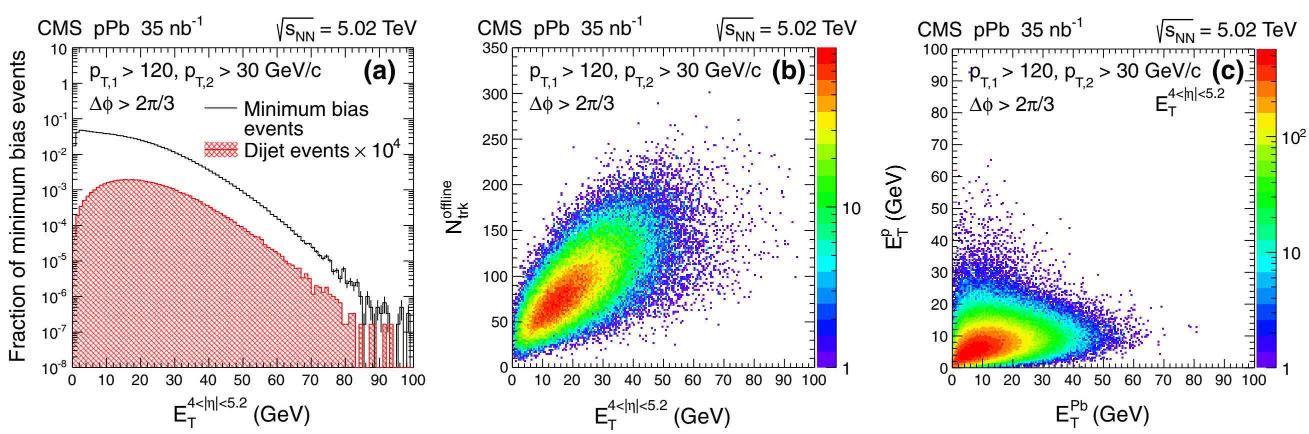

Fig. 1 **a** Raw transverse energy measured by the HF detector in the pseudorapidity interval $4.0 < |\eta| < 5.2$ for minimum bias collisions (*black open histogram*) and dijet events passing the dijet selection defined in this analysis (*red hatched histogram*). **b** Correlation between the raw number of reconstructed tracks from the primary vertex ($N_{trk}^{offline}$) with $|\eta| < 2.4$ and $p_T > 0.4$ GeV/c and raw transverse energy measured by the HF detector in the pseudorapidity interval $4.0 < |\eta| < 5.2$ ($E_T^{4<|\eta|<5.2}$). **c** Correlation between the raw transverse energy measured by the HF in proton (E_T^{p}, measured in the pseudorapidity interval $4.0 < \eta < 5.2$) and lead (E_T^{Pb}, measured in the pseudorapidity interval $-5.2 < \eta < -4.0$) directions

Table 1 Fractions of the data sample for each HF activity class calculated for the minimum bias data passing DS selection and for the jet-triggered data passing dijet selection. The fourth column shows the average multiplicity of reconstructed charged particles per bin with $|\eta| < 2.4$ and $p_T > 0.4\,\text{GeV/c}$ ($N_{\text{trk}}^{\text{corrected}}$). The fifth column gives the mean HF activity in each class calculated from DS events

$E_T^{4<\|\eta\|<5.2}$ range (GeV)	Fraction of DS data (%)	Fraction of dijet data (%)	$\langle N_{\text{trk}}^{\text{corrected}}\rangle$ in DS data	$\langle E_T^{4<\|\eta\|<5.2}\rangle$(GeV) in DS data
<20	73.1	52.6	33 ± 2	9.4
20–25	10.5	16.8	75 ± 3	22.4
25–30	7.1	12.7	89 ± 4	27.3
30–40	6.8	13.0	108 ± 5	34.1
>40	2.5	4.9	140 ± 6	46.3

pPb collisions. The correlation between the raw transverse energy measured by the HF detector in the pseudorapidity interval $4.0 < \eta < 5.2$ (in the proton direction, E_T^{p}) and in the pseudorapidity interval $-5.2 < \eta < -4.0$ (in the lead direction, E_T^{Pb}) is also shown in Fig. 1(c). It can be seen that E_T^{p} and E_T^{Pb} are only loosely correlated. In the sample of selected dijet events, 2 % contain at least one additional jet with $p_T > 20\,\text{GeV/c}$ and $4.0 < |\eta| < 5.2$. The potential bias due to the presence of forward jets is found to be negligible and is included in the systematic uncertainty estimation.

The analysis is performed in five $E_T^{4<|\eta|<5.2}$ bins, separated by the boundaries 20, 25, 30 and 40 GeV. The same analysis is also performed with inclusive data without $E_T^{4<|\eta|<5.2}$ selection, where the mean value of $E_T^{4<|\eta|<5.2}$ is 14.7 GeV. The total number of selected events in data is corrected for the difference between the double-sided (DS) selections using particle- and detector-level information in inelastic hadronic HIJING MC simulation [44]. The DS correction in HIJING is found to be 0.98 ± 0.01. The particle-level selection is very similar to the actual selection described above: at least one particle (proper life time $\tau > 10^{-18}$ s) with $E > 3$ GeV in the pseudorapidity range $-5 < \eta < -3$ and one in the range $3 < \eta < 5$ [44]. The efficiency-corrected fractions of minimum bias events with DS selection [44], as well as the selected dijet events from the jet-triggered sample falling into each HF activity class are provided in Table 1. The average multiplicity of reconstructed charged particles per bin with $|\eta| < 2.4$ and $p_T > 0.4\,\text{GeV/c}$ ($N_{\text{trk}}^{\text{corrected}}$) after efficiency, acceptance, and misreconstruction corrections as described in Ref. [44] is also included in this table. In order to study the correlation between the collision geometry and forward calorimeter energy, the distributions of number of participating nucleons (N_{part}) in the HIJING Monte Carlo simulation in the five $E_T^{4<|\eta|<5.2}$ bins are shown in Fig. 2. While the mean of the N_{part} distribution is found to be increasing monotonically as a function of $E_T^{4<|\eta|<5.2}$, the fluctuation of N_{part} is found to be large in each HF activity class.

The instantaneous luminosity of the pPb run in 2013 resulted in a ~3 % probability of at least one additional interaction occurring in the same bunch crossing. Events with more than one interaction are referred to as "pileup events".

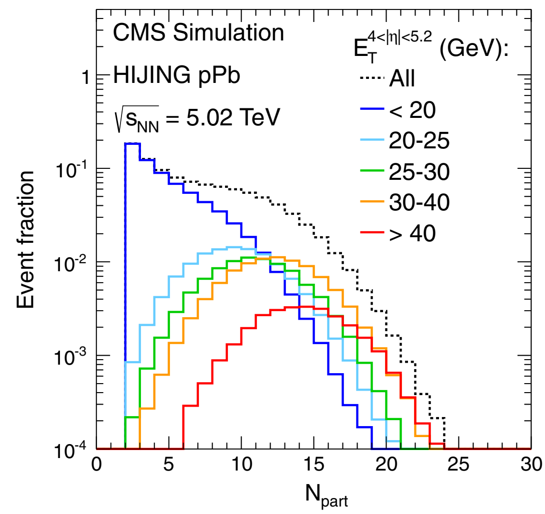

Fig. 2 Number of participating nucleons (N_{part}) in the HIJING MC simulations for five different $E_T^{4<|\eta|<5.2}$ bins and the cumulative distribution without any requirement on $E_T^{4<|\eta|<5.2}$

Since the event classes are typically determined from the forward calorimeter information, the energy deposits from each collision in a given pileup event cannot be separated. Therefore, a pileup rejection algorithm developed in Ref. [45] is employed to select a clean single-collision sample. The pileup rejection efficiency of this filter is greater than 90 % in minimum bias events and it removes a very small fraction (0.01 %) of the events without pileup. The fraction of pileup events after pileup rejection is increasing as a function of $E_T^{4<|\eta|<5.2}$. This fraction is found to be smaller than 2 % in the highest $E_T^{4<|\eta|<5.2}$ bins.

6 Results and discussion

This analysis, motivated by the observation of transverse momentum imbalance in PbPb collisions [8], aims at measuring the dijet transverse momentum ratio and the azimuthal angle correlation in pPb collisions. The dijet pseudorapidity distributions in pPb collisions, which are sensitive to a possible modification of the parton distribution function of the

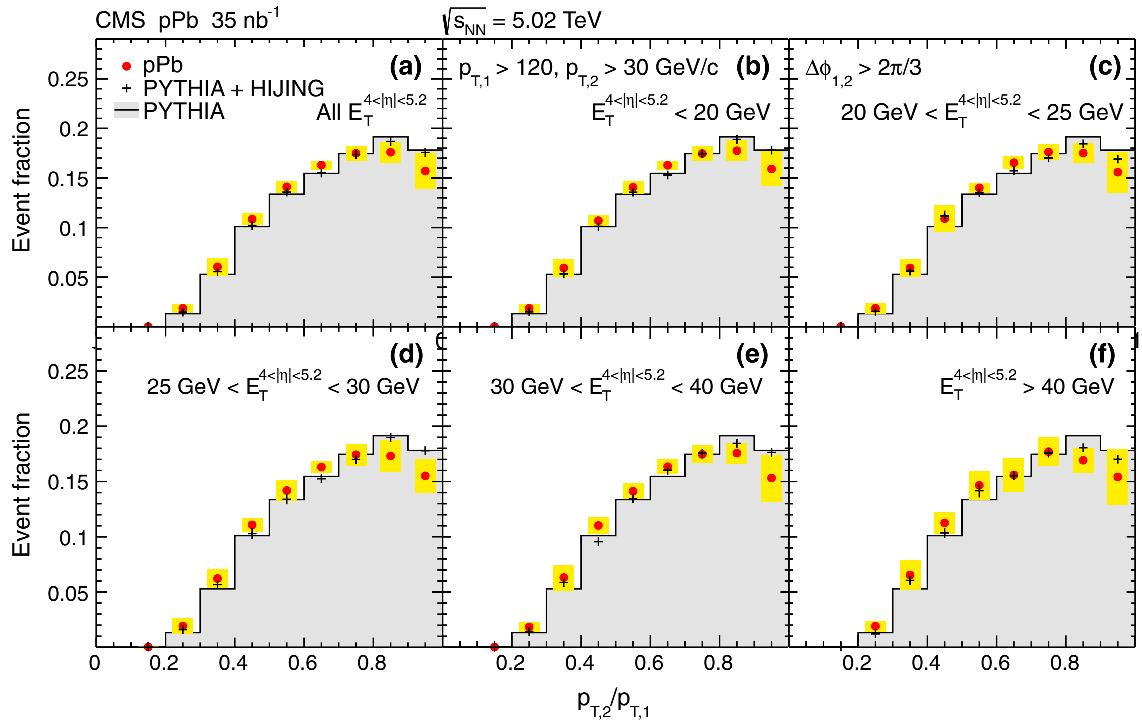

Fig. 3 Dijet transverse momentum ratio ($p_{T,2}/p_{T,1}$) distributions for leading jets with $p_{T,1} > 120$ GeV/c, subleading jets with $p_{T,2} >$ 30 GeV/c, and $\Delta\phi_{1,2} > 2\pi/3$ are shown (**a**) without any selection on the HF transverse energy $E_T^{4<|\eta|<5.2}$, and **b–f** for different $E_T^{4<|\eta|<5.2}$ classes. Results for pPb events are shown as the *red solid circles*, while the *crosses* show the results for PYTHIA + HIJING simulated events. Results for the simulated PYTHIA events are shown as the *grey* histogram which is replicated in all the *panels*. The *error bars* for the statistical uncertainties are smaller than the marker size and the total systematic uncertainties are shown as *yellow boxes*

nuclei (nPDF) with respect to that of the nucleons, are also studied.

6.1 Dijet transverse momentum balance

As a function of collision centrality (i.e. the degree of overlap of the two colliding nuclei), dijet events in PbPb collisions were found to have an increasing transverse momentum imbalance for more central events compared to a pp reference [8–10]. The same analysis is performed in pPb collisions. To characterize the dijet transverse momentum balance (or imbalance) quantitatively, the dijet transverse momentum ratio $p_{T,2}/p_{T,1}$ is used. As shown in Fig. 3, $p_{T,2}/p_{T,1}$ distributions measured in pPb data, PYTHIA and PYTHIA + HIJING agree within the systematic uncertainty in different $E_T^{4<|\eta|<5.2}$ intervals, including the event class with the largest forward calorimeter activity. The residual difference in the dijet transverse momentum ratio between data and MC simulation can be attributed to a difference in the jet energy resolution, which is better in the MC simulation by about ∼1–2 % compared to the data [36].

In order to compare results from pPb and PbPb data, PbPb events which pass the same dijet criteria are selected for further analysis with an additional requirement on the forward activity $E_T^{4<|\eta|<5.2} < 60$ GeV, since the bulk of the pPb events satisfy this condition, as can be seen in Fig. 1b. The measured mean value of $p_{T,2}/p_{T,1}$ from these PbPb data is 0.711 ± 0.007 (stat.) ± 0.014 (syst.), which is slightly higher than that in inclusive pPb collisions (0.689 ± 0.014 (syst.), with a negligible statistical uncertainty). The difference between the $E_T^{4<|\eta|<5.2}$ distributions for pPb and PbPb data, which results in a higher mean $E_T^{4<|\eta|<5.2}$ value for PbPb events (35 GeV), as well as the difference in centre-of-mass energy, should be taken into account in this comparison. The predicted $\langle p_{T,2}/p_{T,1}\rangle$ is 6 % higher at $\sqrt{s_{NN}} = 2.76$ than that at 5.02 TeV in PYTHIA MC simulations.

The main contributions to the systematic uncertainties of $\langle p_{T,2}/p_{T,1}\rangle$ include the uncertainties in the jet energy scale, the jet reconstruction efficiency and the effects of the UE subtraction. The uncertainty in the subtraction procedure is estimated by considering the difference between the p_T ratio results from reconstructed jets with and without UE subtraction, which is close to 1 %. The residual jet energy scale uncertainty is estimated by varying the transverse momentum of the leading and subleading jets independently and is found to be at the 1–2 % level. Uncertainties associated with

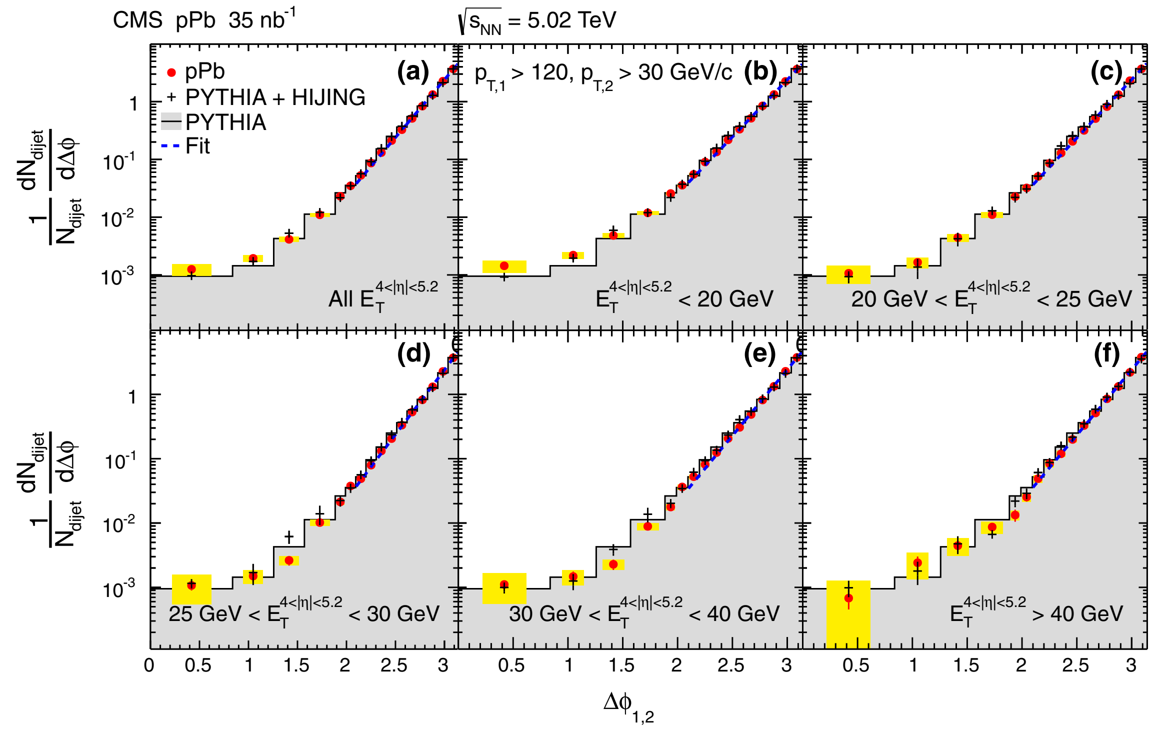

Fig. 4 Distributions of the azimuthal angle difference $\Delta\phi_{1,2}$ between the leading and subleading jets for leading jets with $p_{T,1} > 120$ GeV/c and subleading jets with $p_{T,2} > 30$ GeV/c are shown (**a**) without any selection on the HF transverse energy $E_T^{4<|\eta|<5.2}$, and **b**–**f** for different $E_T^{4<|\eta|<5.2}$ classes. The range for $\Delta\phi$ in this figure extends below the lower bound of $2\pi/3$, which is used in the selection of the dijets for the other observables. Results for pPb events are shown as the *red solid circles*, while the *crosses* show the results for PYTHIA + HIJING simulated events. Results for the simulated PYTHIA events are shown as the *grey histogram* which is replicated in all the *panels*. The *error bars* for the statistical uncertainties are smaller than the marker size and the total systematic uncertainties are shown as *yellow boxes*

jet reconstruction efficiency are found to be at the 0.1 % level based on Monte Carlo simulation.

6.2 Dijet azimuthal correlations

Earlier studies of the dijet and photon-jet events in heavy-ion collisions [8–11] have shown very small modifications of dijet azimuthal correlations despite the large changes seen in the dijet transverse momentum balance. This is an important aspect of the interpretation of energy loss observations [46].

The distributions of the relative azimuthal angle $\Delta\phi_{1,2}$ between the leading and subleading jets that pass the respective p_T selections in six HF activity classes, compared to PYTHIA and PYTHIA + HIJING simulations, are shown in Figure 4. The distributions from pPb data are in good agreement with the PYTHIA reference. To study the evolution of the shape, the distributions are fitted to a normalized exponential function:

$$\frac{1}{N_{\text{dijet}}}\frac{dN_{\text{dijet}}}{d\Delta\phi_{1,2}} = \frac{e^{(\Delta\phi-\pi)/\sigma}}{(1-e^{-\pi/\sigma})\,\sigma} \quad (1)$$

The fit is restricted to the region $\Delta\phi_{1,2} > 2\pi/3$. In the data, the width of the azimuthal angle difference distribution (σ in Eq. (1)) is 0.217 ± 0.0004, and its variation as a function of $E_T^{4<|\eta|<5.2}$ is smaller than the systematic uncertainty, which is 3–4 %. The width in the data is also found to be 4–7 % narrower than that in the PYTHIA simulation.

6.3 Dijet pseudorapidity

The normalized distributions of dijet pseudorapidity η_{dijet}, defined as $(\eta_1 + \eta_2)/2$, are studied in bins of $E_T^{4<|\eta|<5.2}$. Since η_{dijet} and the longitudinal-momentum fraction x of the hard-scattered parton from the Pb ion are highly correlated, these distributions are sensitive to possible modifications of the PDF for nucleons in the lead nucleus when comparing η_{dijet} distributions in pp and pPb collisions. As discussed previously, the asymmetry in energy of the pPb collisions at the LHC causes the mean of the *unmodified* dijet pseudorapidity distribution to be centred around a positive value. However, due to the limited jet acceptance (jet $|\eta| < 3$) it is not centred around $\eta = 0.465$, but at $\eta \sim 0.4$. The major systematic uncertainty for the $\langle\eta_{\text{dijet}}\rangle$ measurement comes

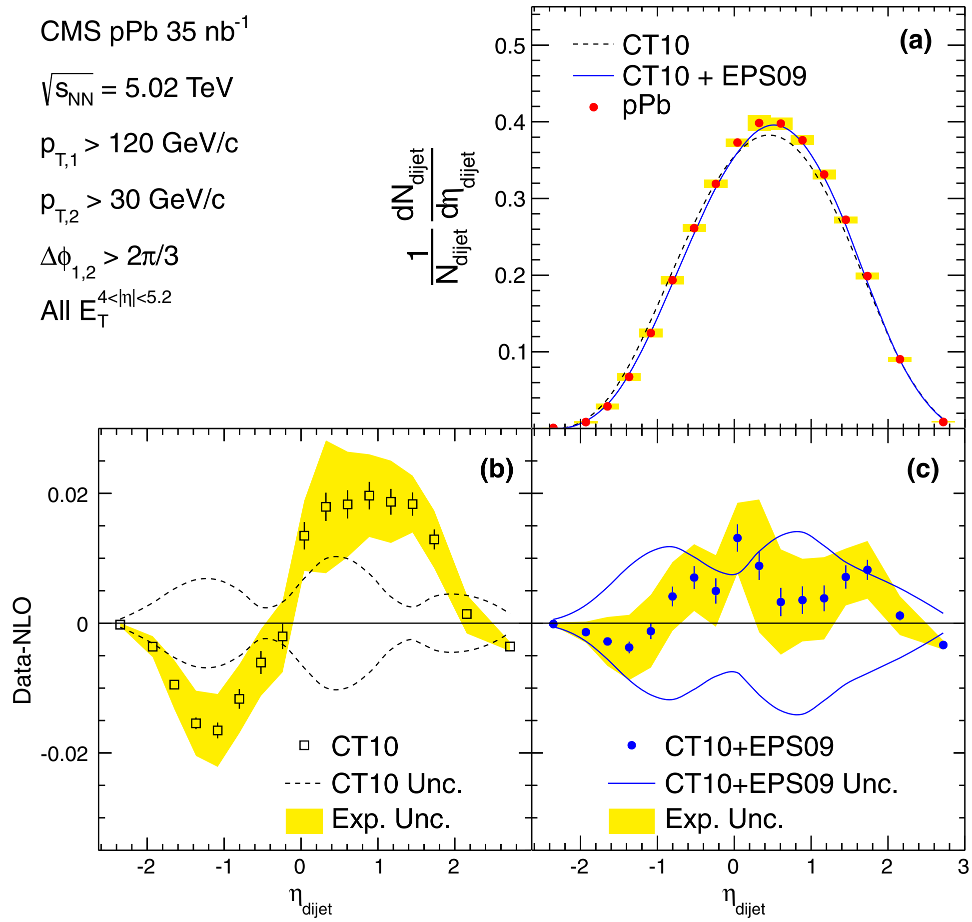

Fig. 5 **a** Distribution of dijet pseudorapidity ($\eta_{dijet} = [\eta_1 + \eta_2]/2$) is shown for pPb dijet events with $p_{T,1} > 120$ GeV/c, $p_{T,2} > 30$ GeV/c, and $\Delta\phi_{1,2} > 2\pi/3$ as the *red solid circles*. The results are compared to NLO calculations using CT10 (*black dashed curve*) and CT10 + EPS09 (*blue solid curve*) PDFs. **b** The difference between η_{dijet} in data and the one calculated with CT10 proton PDF. The *black squares* represent the data points, and the theoretical uncertainty is shown with the *black dashed line*. **c** The difference between η_{dijet} in data and the one calculated with CT10+EPS09 nPDF. The *blue solid circles* show the data points and *blue solid curve* the theoretical uncertainty. The *yellow bands* in **b** and **c** represent experimental uncertainties. The experimental and theoretical uncertainties at different η_{dijet} values are correlated due to normalization to unit area

from the uncertainty in the jet energy correction. Varying the transverse momentum of the jets by <2 % up (down) for the jet at positive (negative) η results in a shift of the $\langle\eta_{dijet}\rangle$ value by ±0.03. The uncertainty associated with the HF activity selection bias is estimated from the difference between PYTHIA without HF activity selection and PYTHIA + HIJING with HF activity selection. The uncertainty is found to be in the range 0.002–0.020. The uncertainty associated with the UE subtraction is studied by comparing the results with and without subtraction, which causes a shift of 0.01 in the two highest HF activity classes. Due to the normalisation to unity, a change in one data point moves the other points in the opposite direction on average, which results in a correlation of the systematic uncertainties at different η_{dijet} values.

The normalized η_{dijet} distribution measured in inclusive pPb collisions, which is compared to next-to-leading-order (NLO) perturbative QCD predictions [47] using the CT10 [48] and EPS09 [24] PDFs, is shown in Fig. 5. The measurement and the NLO calculation based on CT10 + EPS09 PDFs are consistent within the quoted experimental and theoretical uncertainties in the whole η_{dijet} range. On the other hand, the calculation using CT10 alone, which does not account for possible nuclear modifications of the PDFs, gives a poorer description of the observed distribution. This also shows that η_{dijet} in pPb collisions could be used to better constrain the nPDFs by including the measurement in standard global fits of parton densities.

The η_{dijet} distributions are also studied in different HF activity classes, as shown in Fig. 6. The pPb data are compared to PYTHIA and PYTHIA + HIJING simulations. Deviations of the η_{dijet} distributions in each class are observed with respect to the PYTHIA reference without HF activity selection. The analysis was also performed using the PYTHIA + HIJING simulation in the same HF activity classes and no sizable deviation was observed with respect to the PYTHIA reference. This shows that the PYTHIA+HIJING embedded sample, which assumes that hard and soft scatterings are independent, does not describe the correlation between the dijet pseudorapidity distribution and forward calorimeter energy. To illustrate the observed deviation in each HF activity class with respect to that in the inclusive pPb collisions, the ratio of the dijet pseudorapidity distribution from each $E_T^{4<|\eta|<5.2}$ class to the distribution without HF requirements is presented in Fig. 7. A reduction of the fraction of dijets in the $\eta_{dijet} > 1$ region is observed in events with large activity measured by the forward calorimeter. The magnitude of the observed modifi-

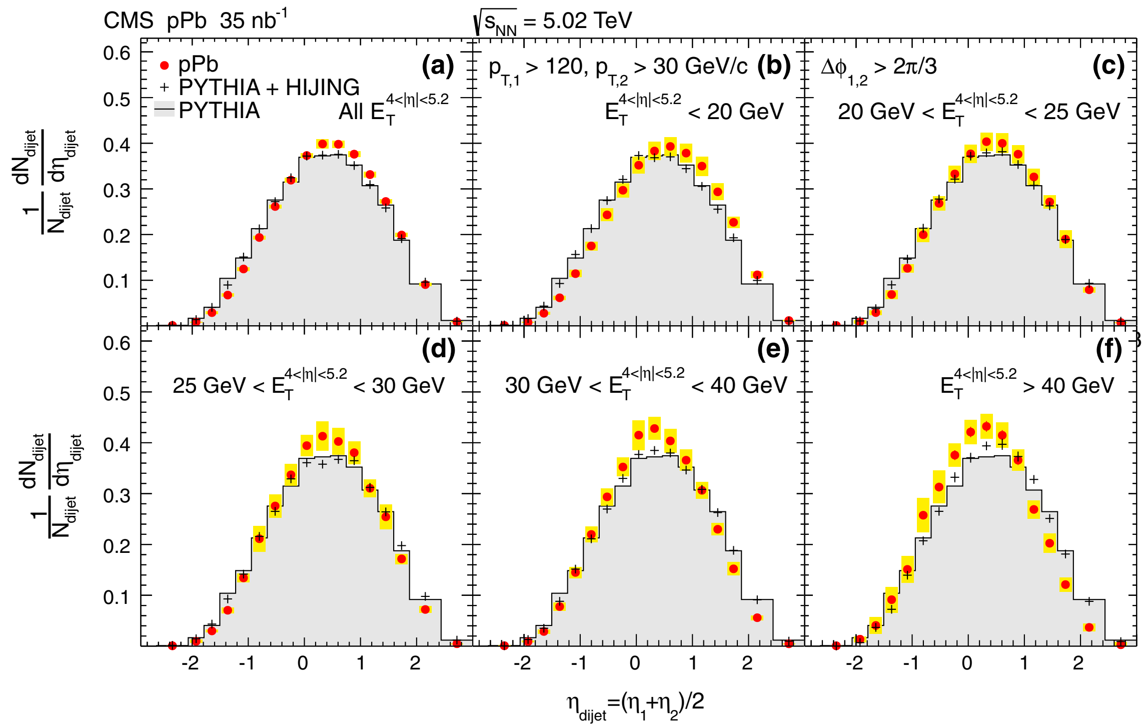

Fig. 6 Distributions of the dijet pseudorapidity (η_{dijet}) for leading jets with $p_{T,1} > 120$ GeV/c and subleading jets with $p_{T,2} > 30$ GeV/c are shown (**a**) without any selection on the HF transverse energy $E_T^{4<|\eta|<5.2}$, and **b**–**f** for different $E_T^{4<|\eta|<5.2}$ classes. Results for pPb events are shown as the *red solid circles*, while the *crosses* show the results for PYTHIA + HIJING simulated events. Results for the simulated PYTHIA events are shown as the *grey histogram* which is replicated in all the *panels*. The *error bars* for the statistical uncertainties are smaller than the marker size and the total systematic uncertainties are shown as *yellow boxes*

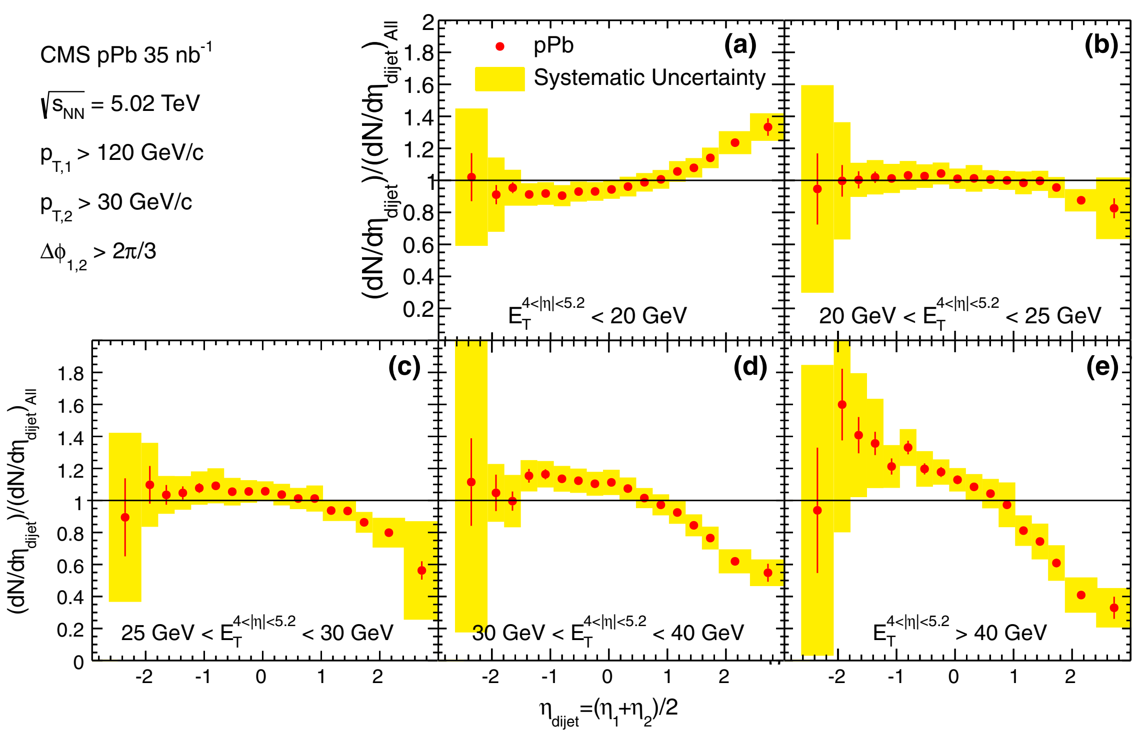

Fig. 7 Ratio of the dijet pseudorapidity distribution from each $E_T^{4<|\eta|<5.2}$ class shown in **b**–**f** of Fig. 6 to the spectrum from the inclusive $E_T^{4<|\eta|<5.2}$ bin shown in **a**. The *error bars* represent the statistical uncertainties and the total systematic uncertainties are shown as *yellow boxes*

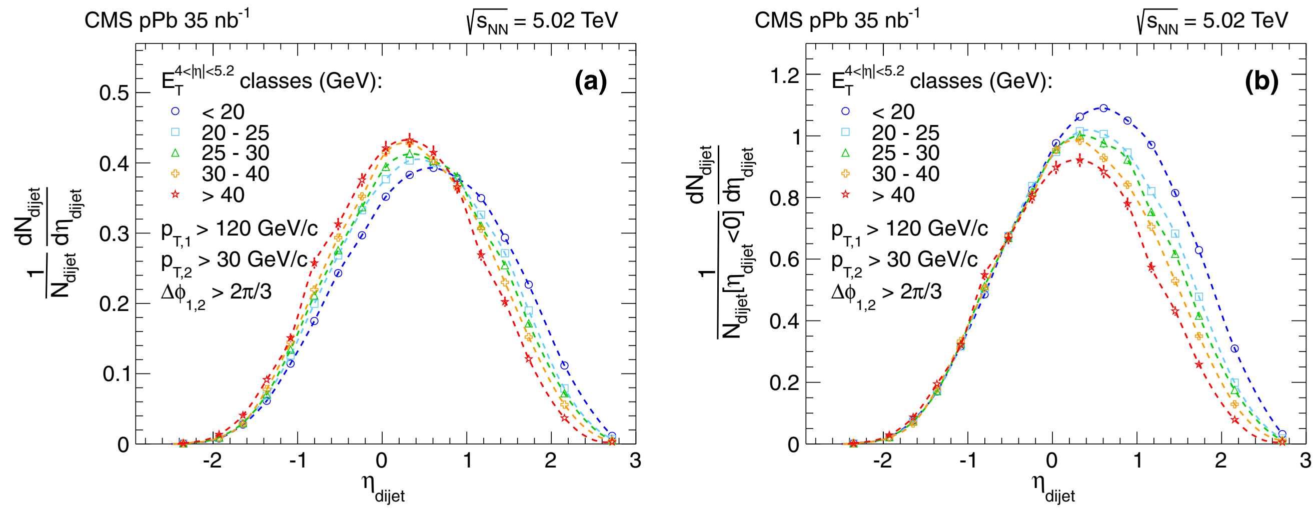

Fig. 8 Dijet pseudorapidity distributions in the five HF activity classes. **a** The distributions are normalized by the number of selected dijet events. **b** The distributions are normalized by the number of dijet events with $\eta_{\text{dijet}} < 0$. The *error bars* represent the statistical uncertainties and the *dashed lines* connecting the data points are drawn to guide the eye

cation is much larger than the predictions from the NLO calculations based on impact-parameter dependent nPDFs [49] in the region $x < 0.1$ for partons in lead nuclei. Note that theory calculations are based on impact parameter, which can take a large range of values in each HF activity class.

The pPb distributions for different HF activity classes, from panels (b)–(f) of Fig. 6, are overlaid in Fig. 8. As shown in Fig. 8a, a systematic monotonic decrease of the average η_{dijet} as a function of the HF transverse energy $E_T^{4<|\eta|<5.2}$ is observed. A decrease in the longitudinal momentum carried by partons that participate in hard scattering coming from the proton, or an increase in the longitudinal momentum of partons from the lead nucleus, with increasing HF transverse energy $E_T^{4<|\eta|<5.2}$ would result in a shift in this direction. In order to compare the shape of the η_{dijet} distributions in the interval $\eta_{\text{dijet}} < 0$ the spectra from pPb data are normalized by the number of dijet events with $\eta_{\text{dijet}} < 0$ in the corresponding HF activity class. In inclusive pPb collisions, this interval roughly corresponds to $x > 0.1$ for partons in lead, a region where the measurement is sensitive to the nuclear EMC effect [50]. Using this normalization, the shapes of the η_{dijet} distributions in the region $\eta_{\text{dijet}} < 0$ are found to be similar, as is shown in Fig. 8b.

Figure 9 summarizes all of the $E_T^{4<|\eta|<5.2}$ dependent dijet results obtained with pPb collisions. A nearly constant width in the dijet azimuthal angle difference distributions and transverse momentum ratio of the dijets as a function of $E_T^{4<|\eta|<5.2}$ is observed. The lower panels show the mean and standard deviation of the dijet pseudorapidity distribution, measured using jets in the pseudorapidity interval $|\eta| < 3$ in the laboratory frame, as a function of the HF transverse energy. Those quantities change significantly with increasing forward calorimeter transverse energy, while the simulated pp dijets embedded in HIJING MC, representing pPb collisions, show no noticeable changes.

One possible mechanism which could lead to the observed modification of the η_{dijet} distribution in events with large forward activity is the kinematical constraint imposed by the selection. Jets with a given transverse momentum at larger pseudorapidity will have a larger energy ($E = \cosh(\eta)\, p_T$). If a large part of the available energy in the collision is observed in the forward calorimeter region, jets above a certain transverse momentum threshold are restricted to be in mid-rapidity, which leads to a narrower dijet pseudorapidity distribution. Moreover, the modification of the PDFs due to the fluctuating size of the proton, as well as the impact parameter dependence of the nuclear PDFs, may further contribute to the observed phenomenon. Therefore, the $\langle\eta_{\text{dijet}}\rangle$ is also studied as a function of the forward calorimeter activity in the lead direction (E_T^{Pb}) at fixed values of forward activity in the proton direction (E_T^{p}).

The correlation between $\langle\eta_{\text{dijet}}\rangle$ and E_T^{Pb} in different E_T^{p} intervals is shown in Fig. 10. With low forward activity in the proton direction ($E_T^{\text{p}} < 5$ GeV, blue circles and solid lines near the top of the figure), the $\langle\eta_{\text{dijet}}\rangle$ is around 0.6 and only weakly dependent on the forward activity in the lead direction. The observed high $\langle\eta_{\text{dijet}}\rangle$ indicates that the mean x of the parton from the proton in the low E_T^{p} events is larger than that in inclusive pPb collisions. With high forward activity in the proton direction ($E_T^{\text{p}} > 11$ GeV, red stars and solid lines near the bottom of the figure), the $\langle\eta_{\text{dijet}}\rangle$ is found to be decreasing as a function of E_T^{Pb}, from 0.37 to 0.17. These results indicate that the degree of modification of the η_{dijet} distribution is highly dependent on the amount of forward activity in the proton direction.

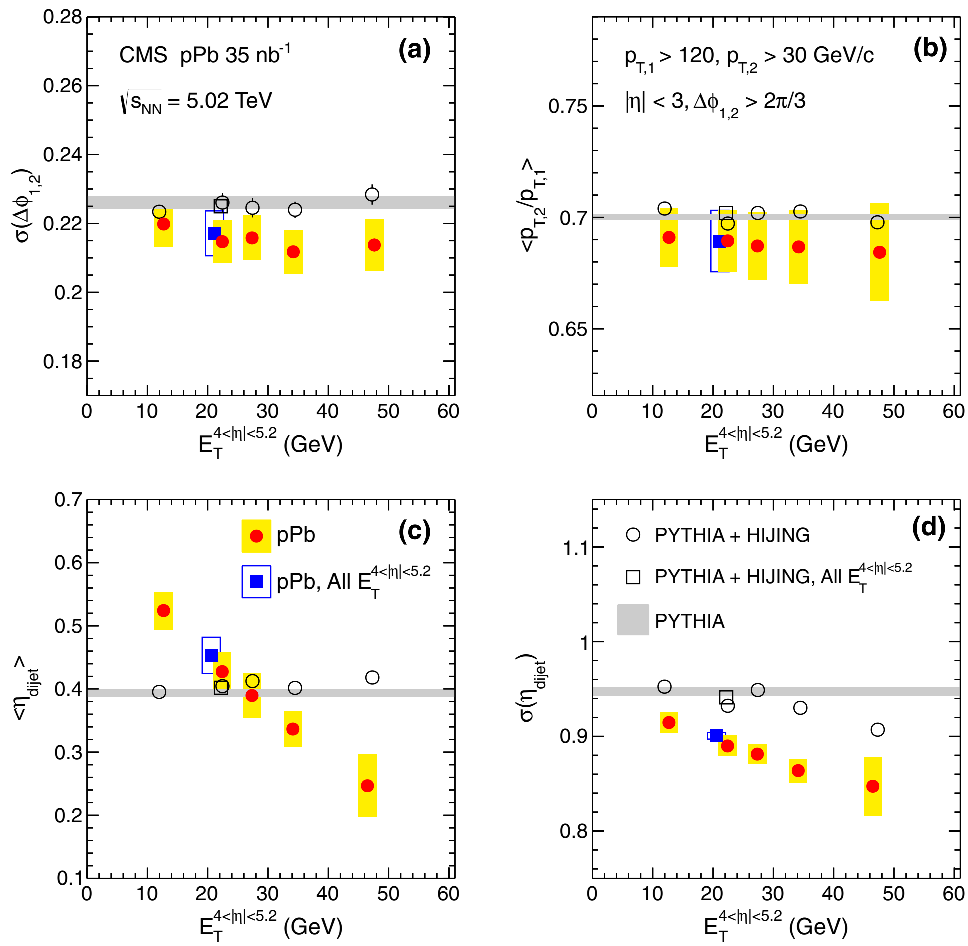

Fig. 9 Summary of the dijet measurements as a function of $E_T^{4<|\eta|<5.2}$. **a** Fitted $\Delta\phi_{1,2}$ width (σ in Eq. (1)). **b** Average ratio of dijet transverse momentum. **c** Mean of the η_{dijet} distribution. **d** Standard deviation of the η_{dijet} distribution. *All panels* show pPb data (*red solid circles*) compared to the PYTHIA + HIJING (*black open circles*) and PYTHIA (*light grey band*, where the band width indicates statistical uncertainty) simulations. The inclusive HF activity results for pPb and PYTHIA + HIJING are shown as *blue solid* and *black empty squares*, respectively. The *yellow*, *grey* and *blue boxes* indicate the systematic uncertainties and the *error bars* denote the statistical uncertainties. Note that the legend is spread over the four subfigures

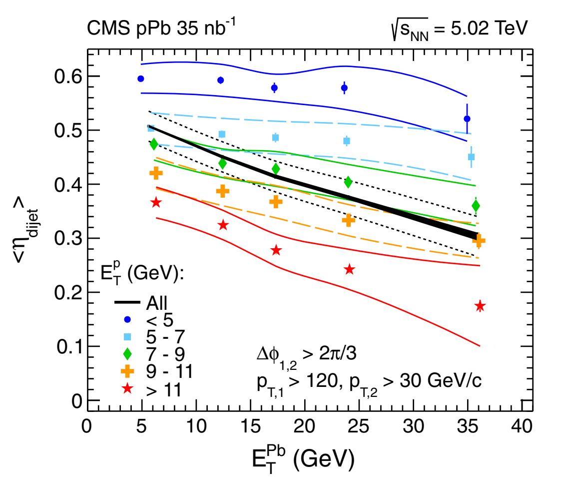

Fig. 10 Mean of η_{dijet} distribution as a function of the raw transverse energy measured in the HF calorimeter in the lead direction (E_T^{Pb}) in bins of forward transverse energy in the proton direction (E_T^{p}). The *lines* indicate the systematic uncertainty on the points with matching color, and the *error bars* denote the statistical uncertainties. The results without selection on (E_T^{p}) are also shown as a *solid black line* with statistical uncertainties represented by the line width. The *dashed black lines* indicate the systematic uncertainty on the *solid black line*

7 Summary

The CMS detector has been used to study dijet production in pPb collisions at $\sqrt{s_{\text{NN}}} = 5.02$ TeV. The anti-k_T algorithm with a distance parameter of 0.3 was used to reconstruct jets based on the combined tracker and calorimeter information. Events containing a leading jet with $p_{T,1} > 120$ GeV/c and a subleading jet with $p_{T,2} > 30$ GeV/c in the pseudorapidity range $|\eta| < 3$ were analyzed. Data were compared to PYTHIA as well as PYTHIA + HIJING dijet simulations. In contrast to what is seen in head-on PbPb collisions, no significant dijet transverse momentum imbalance is observed in pPb data with respect to the simulated distributions. These pPb dijet transverse momentum ratios confirm that the observed dijet transverse momentum imbalance in PbPb collisions is not originating from initial-state effects.

The dijet pseudorapidity distributions in inclusive pPb collisions are compared to NLO calculations using CT10 and CT10 + EPS09 PDFs, and the data more closely match the latter. A strong modification of the dijet pseudorapidity distribution is observed as a function of forward activity. The mean of the distribution shifts monotonically as a function of $E_{\mathrm{T}}^{4<|\eta|<5.2}$. This indicates a strong correlation between the energy emitted at large pseudorapidity and the longitudinal motion of the dijet frame.

Acknowledgments We would like to thank Jose Guilherme Milhano and Nestor Armesto for their suggestion to study the dijet pseudorapidity shift as a function of HF transverse energy in the proton and lead directions, which extended the scope of this analysis. We congratulate our colleagues in the CERN accelerator departments for the excellent performance of the LHC and thank the technical and administrative staffs at CERN and at other CMS institutes for their contributions to the success of the CMS effort. In addition, we gratefully acknowledge the computing centres and personnel of the Worldwide LHC Computing Grid for delivering so effectively the computing infrastructure essential to our analyses. Finally, we acknowledge the enduring support for the construction and operation of the LHC and the CMS detector provided by the following funding agencies: the Austrian Federal Ministry of Science and Research and the Austrian Science Fund; the Belgian Fonds de la Recherche Scientifique, and Fonds voor Wetenschappelijk Onderzoek; the Brazilian Funding Agencies (CNPq, CAPES, FAPERJ, and FAPESP); the Bulgarian Ministry of Education and Science; CERN; the Chinese Academy of Sciences, Ministry of Science and Technology, and National Natural Science Foundation of China; the Colombian Funding Agency (COLCIENCIAS); the Croatian Ministry of Science, Education and Sport, and the Croatian Science Foundation; the Research Promotion Foundation, Cyprus; the Ministry of Education and Research, Recurrent financing contract SF0690030s09 and European Regional Development Fund, Estonia; the Academy of Finland, Finnish Ministry of Education and Culture, and Helsinki Institute of Physics; the Institut National de Physique Nucléaire et de Physique des Particules / CNRS, and Commissariat à l'Énergie Atomique et aux Énergies Alternatives / CEA, France; the Bundesministerium für Bildung und Forschung, Deutsche Forschungsgemeinschaft, and Helmholtz-Gemeinschaft Deutscher Forschungszentren, Germany; the General Secretariat for Research and Technology, Greece; the National Scientific Research Foundation, and National Innovation Office, Hungary; the Department of Atomic Energy and the Department of Science and Technology, India; the Institute for Studies in Theoretical Physics and Mathematics, Iran; the Science Foundation, Ireland; the Istituto Nazionale di Fisica Nucleare, Italy; the Korean Ministry of Education, Science and Technology and the World Class University program of NRF, Republic of Korea; the Lithuanian Academy of Sciences; the Ministry of Education, and University of Malaya (Malaysia); the Mexican Funding Agencies (CINVESTAV, CONACYT, SEP, and UASLP-FAI); the Ministry of Business, Innovation and Employment, New Zealand; the Pakistan Atomic Energy Commission; the Ministry of Science and Higher Education and the National Science Centre, Poland; the Fundação para a Ciência e a Tecnologia, Portugal; JINR, Dubna; the Ministry of Education and Science of the Russian Federation, the Federal Agency of Atomic Energy of the Russian Federation, Russian Academy of Sciences, and the Russian Foundation for Basic Research; the Ministry of Education, Science and Technological Development of Serbia; the Secretaría de Estado de Investigación, Desarrollo e Innovación and Programa Consolider-Ingenio 2010, Spain; the Swiss Funding Agencies (ETH Board, ETH Zurich, PSI, SNF, UniZH, Canton Zurich, and SER); the National Science Council, Taipei; the Thailand Center of Excellence in Physics, the Institute for the Promotion of Teaching Science and Technology of Thailand, Special Task Force for Activating Research and the National Science and Technology Development Agency of Thailand; the Scientific and Technical Research Council of Turkey, and Turkish Atomic Energy Authority; the Science and Technology Facilities Council, UK; the US Department of Energy, and the US National Science Foundation. Individuals have received support from the Marie-Curie programme and the European Research Council and EPLANET (European Union); the Leventis Foundation; the A. P. Sloan Foundation; the Alexander von Humboldt Foundation; the Belgian Federal Science Policy Office; the Fonds pour la Formation à la Recherche dans l'Industrie et dans l'Agriculture (FRIA-Belgium); the Agentschap voor Innovatie door Wetenschap en Technologie (IWT-Belgium); the Ministry of Education, Youth and Sports (MEYS) of Czech Republic; the Council of Science and Industrial Research, India; the Compagnia di San Paolo (Torino); the HOMING PLUS programme of Foundation for Polish Science, cofinanced by EU, Regional Development Fund; and the Thalis and Aristeia programmes cofinanced by EU-ESF and the Greek NSRF.

References

1. F. Karsch, E. Laermann, Thermodynamics and in-medium hadron properties from lattice QCD, in *Quark–Gluon Plasma III*, ed by R. Hwa, p. 1. (Hackensack, USA, 2003). arXiv:hep-lat/0305025
2. J.C. Collins, M.J. Perry, Superdense matter: neutrons or asymptotically free quarks? Phys. Rev. Lett. **34**, 1353 (1975). doi:10.1103/PhysRevLett.34.1353
3. N. Cabibbo, G. Parisi, Exponential hadronic spectrum and quark liberation. Phys. Lett. B **59**, 67 (1975). doi:10.1016/0370-2693(75)90158-6
4. B.A. Freedman, L.D. McLerran, Fermions and gauge vector mesons at finite temperature and density. III. The ground-state energy of a relativistic quark gas. Phys. Rev. D **16**, 1169 (1977). doi:10.1103/PhysRevD.16.1169
5. E.V. Shuryak, Theory of hadronic plasma. Sov. Phys. JETP **47**, 212 (1978)
6. D.A. Appel, Jets as a probe of quark–gluon plasmas. Phys. Rev. D **33**, 717 (1986). doi:10.1103/PhysRevD.33.717
7. J.P. Blaizot, L.D. McLerran, Jets in expanding quark–gluon plasmas. Phys. Rev. D **34**, 2739 (1986). doi:10.1103/PhysRevD.34.2739
8. C.M.S. Collaboration, Observation and studies of jet quenching in PbPb collisions at nucleon–nucleon center-of-mass energy = 2.76 TeV. Phys. Rev. C **84**, 024906 (2011). doi:10.1103/PhysRevC.84.024906, arXiv:1102.1957
9. ATLAS Collaboration, Observation of a centrality-dependent Dijet asymmetry in lead–lead collisions at $\sqrt{s_{\mathrm{NN}}}$ = 2.76 TeV with the ATLAS detector at the LHC, Phys. Rev. Lett. **105**, 252303 (2010). doi:10.1103/PhysRevLett.105.252303, arXiv:1011.6182
10. C.M.S. Collaboration, Jet momentum dependence of jet quenching in PbPb collisions at $\sqrt{s_{\mathrm{NN}}} = 2.76$ TeV. Phys. Lett. B **712**, 176 (2012). doi:10.1016/j.physletb.2012.04.058, arXiv:1202.5022
11. C.M.S. Collaboration, Studies of jet quenching using isolated-photon+jet correlations in PbPb and *pp* collisions at $\sqrt{s_{NN}} = 2.76$ TeV. Phys. Lett. B **718**, 773 (2013). doi:10.1016/j.physletb.2012.11.003, arXiv:1205.0206
12. ATLAS Collaboration, Measurement of the jet radius and transverse momentum dependence of inclusive jet suppression in lead–lead collisions at $\sqrt{s_{NN}}$= 2.76 TeV with the ATLAS detector, Phys. Lett. B **719**, 220 (2013). doi:10.1016/j.physletb.2013.01.024, arXiv:1208.1967
13. CMS Collaboration, Measurement of jet fragmentation into charged particles in pp and PbPb collisions at $\sqrt{s_{\mathrm{NN}}} = 2.76$ TeV, JHEP **1210**, 087 (2012). doi:10.1007/JHEP10, arXiv:1205.5872

14. ALICE Collaboration, Particle-yield modification in jet-like azimuthal di-hadron correlations in Pb–Pb collisions at $\sqrt{s_{NN}} = 2.76$ TeV", Phys. Rev. Lett. **108**, 092301 (2012). doi:10.1103/PhysRevLett.108.092301, arXiv:1110.0121
15. C.M.S. Collaboration, Modification of jet shapes in PbPb collisions at $\sqrt{s_{NN}} = 2.76$ TeV. Phys. Lett. B **730**, 243–263 (2014) doi:10.1016/j.physletb.2014.01.042, arXiv:1310.0878
16. C.M.S. Collaboration, Study of high-p_T charged particle suppression in PbPb compared to pp collisions at $\sqrt{s_{NN}} = 2.76$ TeV. Eur. Phys. J. C **72**, 1945 (2012). doi:10.1140/epjc/s10052-012-1945-x. arXiv:1202.2554
17. ALICE Collaboration, Suppression of charged particle production at large transverse momentum in central Pb–Pb collisions at $\sqrt{s_{NN}} = 2.76$ TeV", Phys. Lett. B **696**, 30 (2011). doi:10.1016/j.physletb.2010.12.020, arXiv:1012.1004
18. Y. He, I. Vitev, B.-W. Zhang, $\mathcal{O}(\alpha_s^3)$ Analysis of inclusive jet and di-jet production in heavy ion reactions at the Large Hadron Collider. Phys. Lett. B **713**, 224 (2012). doi:10.1016/j.physletb.2012.05.054. arXiv:1105.2566
19. C. Young, B. Schenke, S. Jeon, C. Gale, Dijet asymmetry at the energies available at the CERN Large Hadron Collider. Phys. Rev. C **84**, 024907 (2011). doi:10.1103/PhysRevC.84.024907. arXiv:1103.5769
20. G.-Y. Qin, B. Muller, Explanation of Dijet asymmetry in Pb–Pb collisions at the Large Hadron Collider. Phys. Rev. Lett. **106**, 162302 (2011). doi:10.1103/PhysRevLett.106.162302. arXiv:1012.5280. Erratum at doi:10.1103/PhysRevLett.108.189904
21. C.A. Salgado et al., Proton–nucleus collisions at the LHC: scientific opportunities and requirements. J. Phys. G **39**, 015010 (2012). doi:10.1088/0954-3899/39/1/015010. arXiv:1105.3919
22. J.L. Albacete et al., Predictions for p+Pb Collisions at $\sqrt{s_{NN}} = 5$ TeV. Int. J. Mod. Phys. E **22**, 1330007 (2013). doi:10.1142/S0218301313300075. arXiv:1301.3395
23. K.J. Eskola, V.J. Kolhinen, P.V. Ruuskanen, Scale evolution of nuclear parton distributions. Nucl. Phys. B **535**, 351 (1998). doi:10.1016/S0550-3213(98)00589-6. arXiv:hep-ph/9802350
24. K.J. Eskola, H. Paukkunen, C.A. Salgado, EPS09—a new generation of NLO and LO nuclear parton distribution functions. JHEP **04**, 065 (2009). doi:10.1088/1126-6708/2009/04/065, arXiv:0902.4154
25. M. Hirai, S. Kumano, T.-H. Nagai, Nuclear parton distribution functions and their uncertainties. Phys. Rev. C **70**, 044905 (2004). doi:10.1103/PhysRevC.70.044905. arXiv:hep-ph/0404093
26. I. Schienbein et al., Parton distribution function nuclear corrections for charged lepton and neutrino deep inelastic scattering processes. Phys. Rev. D **80**, 094004 (2009). doi:10.1103/PhysRevD.80.094004. arXiv:0907.2357
27. D. de Florian, R. Sassot, Nuclear parton distributions at next-to-leading order. Phys. Rev. D **69**, 074028 (2004). doi:10.1103/PhysRevD.69.074028. arXiv:hep-ph/0311227
28. L. Frankfurt, V. Guzey, M. Strikman, Leading twist nuclear shadowing phenomena in hard processes with nuclei. Phys. Rept. **512**, 255 (2012). doi:10.1016/j.physrep.2011.12.002. arXiv:1106.2091
29. M. Cacciari, G.P. Salam, G. Soyez, The anti-k_t jet clustering algorithm. JHEP **04**, 063 (2008). doi:10.1088/1126-6708/2008/04/063, arXiv:0802.1189
30. M. Cacciari, G.P. Salam, G. Soyez, FastJet user manual. Eur. Phys. J. C **72**, 1896 (2012). doi:10.1140/epjc/s10052-012-1896-2. arXiv:1111.6097
31. CMS Collaboration, The CMS experiment at the CERN LHC. JINST **3**, S08004 (2008). doi:10.1088/1748-0221/3/08/S08004
32. Nucl. Instrum. Meth. GEANT4—a simulation toolkit. **506**, 250 (2003). doi:10.1016/S0168-9002(03)01368-8
33. CMS Collaboration, Particle-flow event reconstruction in CMS and performance for jets, Taus, and E_T^{miss}", CMS Physics Analysis Summary CMS-PAS-PFT-09-001 (2009)
34. CMS Collaboration, Commissioning of the particle-flow event reconstruction with the first LHC collisions recorded in the CMS detector, CMS Physics Analysis Summary CMS-PAS-PFT-10-001 (2010)
35. O. Kodolova, I. Vardanian, A. Nikitenko, A. Oulianov, The performance of the jet identification and reconstruction in heavy ions collisions with CMS detector. Eur. Phys. J. C **50**, 117 (2007). doi:10.1140/epjc/s10052-007-0223-9
36. CMS Collaboration, Determination of jet energy calibration and transverse momentum resolution in CMS, JINST **6**, P11002 (2011). doi:10.1088/1748-0221/6/11/P11002, arXiv:1107.4277
37. T. Sjöstrand, S. Mrenna, P. Skands, PYTHIA 6.4 physics and manual, JHEP **05**, 026 (2006). doi:10.1088/1126-6708/2006/05/026, arXiv:hep-ph/0603175
38. R. Field, Early LHC, (Underlying Event Data—Findings and Surprises) (2010). arXiv:1010.3558
39. X.-N. Wang, M. Gyulassy, HIJING: A Monte Carlo model for multiple jet production in pp, pA, and AA collisions. Phys. Rev. D **44**, 3501 (1991). doi:10.1103/PhysRevD.44.3501
40. M. Gyulassy, X.-N. Wang, HIJING 1.0: A Monte Carlo program for parton and particle production in high-energy hadronic and nuclear collisions. Comput. Phys. Commun. **83**, 307 (1994). doi:10.1016/0010-4655(94)90057-4. arXiv:nucl-th/9502021
41. C.M.S. Collaboration, CMS tracking performance results from early LHC operation. Eur. Phys. J. C **70**, 1165 (2010). doi:10.1140/epjc/s10052-010-1491-3. arXiv:1007.1988
42. CMS Collaboration, Electromagnetic calorimeter commissioning and first results with 7TeV data, CMS Note CMS-NOTE-2010-012 (2010)
43. CMS Collaboration, Identification and filtering of uncharacteristic noise in the CMS hadron calorimeter, JINST **5**, T03014 (2010). doi:10.1088/1748-0221/5/03/T03014, arXiv:0911.4881
44. CMS Collaboration, Study of the production of charged pions, kaons, and protons in pPb collisions at $\sqrt{s_{NN}} = 5.02$ TeV (2013). arXiv:1307.3442 (Submitted to EPJC)
45. C.M.S. Collaboration, Multiplicity and transverse momentum dependence of two- and four-particle correlations in pPb and PbPb collisions. Phys. Lett. B **724**, 213 (2013). doi:10.1016/j.physletb.2013.06.028. arXiv:1305.0609
46. J. Casalderrey-Solana, J.G. Milhano, U.A. Wiedemann, Jet quenching via jet collimation. J. Phys. G **38**, 035006 (2011). doi:10.1088/0954-3899/38/3/035006. arXiv:1012.0745
47. K. Eskola, H. Paukkunen, C. Salgado, A perturbative QCD study of dijets in p+Pb collisions at the LHC, JHEP **10**, 213 (2013). doi:10.1007/JHEP10(2013)213
48. H.-L. Lai et al., New parton distributions for collider physics. Phys. Rev. D **82**, 074024 (2010). doi:10.1103/PhysRevD.82.074024. arXiv:1007.2241
49. I. Helenius, K. J. Eskola, H. Honkanen, C.A. Salgado, Impact-parameter dependent nuclear parton distribution functions: EPS09s and EKS98s and their applications in nuclear hard processes. JHEP **1207**, 073 (2012). doi:10.1007/JHEP07(2012)073, arXiv:1205.5359
50. P.R. Norton, The EMC effect. Rept. Prog. Phys. **66**, 1253 (2003). doi:10.1088/0034-4885/66/8/201

The CMS Collaboration

Yerevan Physics Institute, Yerevan, Armenia
S. Chatrchyan, V. Khachatryan, A. M. Sirunyan, A. Tumasyan

Institut für Hochenergiephysik der OeAW, Wien, Austria
W. Adam, T. Bergauer, M. Dragicevic, J. Erö, C. Fabjan[1], M. Friedl, R. Frühwirth[1], V. M. Ghete, C. Hartl, N. Hörmann, J. Hrubec, M. Jeitler[1], W. Kiesenhofer, V. Knünz, M. Krammer[1], I. Krätschmer, D. Liko, I. Mikulec, D. Rabady[2], B. Rahbaran, H. Rohringer, R. Schöfbeck, J. Strauss, A. Taurok, W. Treberer-Treberspurg, W. Waltenberger, C.-E. Wulz[1]

National Centre for Particle and High Energy Physics, Minsk, Belarus
V. Mossolov, N. Shumeiko, J. Suarez Gonzalez

Universiteit Antwerpen, Antwerpen, Belgium
S. Alderweireldt, M. Bansal, S. Bansal, T. Cornelis, E. A. De Wolf, X. Janssen, A. Knutsson, S. Luyckx, L. Mucibello, S. Ochesanu, B. Roland, R. Rougny, H. Van Haevermaet, P. Van Mechelen, N. Van Remortel, A. Van Spilbeeck

Vrije Universiteit Brussel, Brussel, Belgium
F. Blekman, S. Blyweert, J. D'Hondt, N. Heracleous, A. Kalogeropoulos, J. Keaveney, T. J. Kim, S. Lowette, M. Maes, A. Olbrechts, D. Strom, S. Tavernier, W. Van Doninck, P. Van Mulders, G. P. Van Onsem, I. Villella

Université Libre de Bruxelles, Bruxelles, Belgium
C. Caillol, B. Clerbaux, G. De Lentdecker, L. Favart, A. P. R. Gay, A. Léonard, P. E. Marage, A. Mohammadi, L. Perniè, T. Reis, T. Seva, L. Thomas, C. Vander Velde, P. Vanlaer, J. Wang

Ghent University, Ghent, Belgium
V. Adler, K. Beernaert, L. Benucci, A. Cimmino, S. Costantini, S. Dildick, G. Garcia, B. Klein, J. Lellouch, J. Mccartin, A. A. Ocampo Rios, D. Ryckbosch, S. Salva Diblen, M. Sigamani, N. Strobbe, F. Thyssen, M. Tytgat, S. Walsh, E. Yazgan, N. Zaganidis

Université Catholique de Louvain, Louvain-la-Neuve, Belgium
S. Basegmez, C. Beluffi[3], G. Bruno, R. Castello, A. Caudron, L. Ceard, G. G. Da Silveira, C. Delaere, T. du Pree, D. Favart, L. Forthomme, A. Giammanco[4], J. Hollar, P. Jez, M. Komm, V. Lemaitre, J. Liao, O. Militaru, C. Nuttens, D. Pagano, A. Pin, K. Piotrzkowski, A. Popov[5], L. Quertenmont, M. Selvaggi, M. Vidal Marono, J. M. Vizan Garcia

Université de Mons, Mons, Belgium
N. Beliy, T. Caebergs, E. Daubie, G. H. Hammad

Centro Brasileiro de Pesquisas Fisicas, Rio de Janeiro, Brazil
G. A. Alves, M. Correa Martins Junior, T. Martins, M. E. Pol, M. H. G. Souza

Universidade do Estado do Rio de Janeiro, Rio de Janeiro, Brazil
W. L. Aldá Júnior, W. Carvalho, J. Chinellato[6], A. Custódio, E. M. Da Costa, D. De Jesus Damiao, C. De Oliveira Martins, S. Fonseca De Souza, H. Malbouisson, M. Malek, D. Matos Figueiredo, L. Mundim, H. Nogima, W. L. Prado Da Silva, J. Santaolalla, A. Santoro, A. Sznajder, E. J. Tonelli Manganote[6], A. Vilela Pereira

Universidade Estadual Paulista, São Paulo, Brazil
F. A. Dias[7], T. R. Fernandez Perez Tomei, C. Lagana, S. F. Novaes, Sandra S. Padula

Universidade Federal do ABC, São Paulo, Brazil
C. A. Bernardes, E. M. Gregores, P. G. Mercadante

Institute for Nuclear Research and Nuclear Energy, Sofia, Bulgaria
V. Genchev[2], P. Iaydjiev[2], A. Marinov, S. Piperov, M. Rodozov, G. Sultanov, M. Vutova

University of Sofia, Sofia, Bulgaria
A. Dimitrov, I. Glushkov, R. Hadjiiska, V. Kozhuharov, L. Litov, B. Pavlov, P. Petkov

Institute of High Energy Physics, Beijing, China
J. G. Bian, G. M. Chen, H. S. Chen, M. Chen, R. Du, C. H. Jiang, D. Liang, S. Liang, X. Meng, R. Plestina[8], J. Tao, X. Wang, Z. Wang

State Key Laboratory of Nuclear Physics and Technology, Peking University, Beijing, China
C. Asawatangtrakuldee, Y. Ban, Y. Guo, Q. Li, W. Li, S. Liu, Y. Mao, S. J. Qian, D. Wang, L. Zhang, W. Zou

Universidad de Los Andes, Bogota, Colombia
C. Avila, C. A. Carrillo Montoya, L. F. Chaparro Sierra, C. Florez, J. P. Gomez, B. Gomez Moreno, J. C. Sanabria

Technical University of Split, Split, Croatia
N. Godinovic, D. Lelas, D. Polic, I. Puljak

University of Split, Split, Croatia
Z. Antunovic, M. Kovac

Institute Rudjer Boskovic, Zagreb, Croatia
V. Brigljevic, K. Kadija, J. Luetic, D. Mekterovic, S. Morovic, L. Tikvica

University of Cyprus, Nicosia, Cyprus
A. Attikis, G. Mavromanolakis, J. Mousa, C. Nicolaou, F. Ptochos, P. A. Razis

Charles University, Prague, Czech Republic
M. Finger, M. Finger Jr.

Academy of Scientific Research and Technology of the Arab Republic of Egypt, Egyptian Network of High Energy Physics, Cairo, Egypt
A. A. Abdelalim[9], Y. Assran[10], S. Elgammal[9], A. Ellithi Kamel[11], M. A. Mahmoud[12], A. Radi[13,14]

National Institute of Chemical Physics and Biophysics, Tallinn, Estonia
M. Kadastik, M. Müntel, M. Murumaa, M. Raidal, L. Rebane, A. Tiko

Department of Physics, University of Helsinki, Helsinki, Finland
P. Eerola, G. Fedi, M. Voutilainen

Helsinki Institute of Physics, Helsinki, Finland
J. Härkönen, V. Karimäki, R. Kinnunen, M. J. Kortelainen, T. Lampén, K. Lassila-Perini, S. Lehti, T. Lindén, P. Luukka, T. Mäenpää, T. Peltola, E. Tuominen, J. Tuominiemi, E. Tuovinen, L. Wendland

Lappeenranta University of Technology, Lappeenranta, Finland
T. Tuuva

DSM/IRFU, CEA/Saclay, Gif-sur-Yvette, France
M. Besancon, F. Couderc, M. Dejardin, D. Denegri, B. Fabbro, J. L. Faure, F. Ferri, S. Ganjour, A. Givernaud, P. Gras, G. Hamel de Monchenault, P. Jarry, E. Locci, J. Malcles, A. Nayak, J. Rander, A. Rosowsky, M. Titov

Laboratoire Leprince-Ringuet, Ecole Polytechnique, IN2P3-CNRS, Palaiseau, France
S. Baffioni, F. Beaudette, P. Busson, C. Charlot, N. Daci, T. Dahms, M. Dalchenko, L. Dobrzynski, A. Florent, R. Granier de Cassagnac, P. Miné, C. Mironov, I. N. Naranjo, M. Nguyen, C. Ochando, P. Paganini, D. Sabes, R. Salerno, Y. Sirois, C. Veelken, Y. Yilmaz, A. Zabi

Institut Pluridisciplinaire Hubert Curien, Université de Strasbourg, Université de Haute Alsace Mulhouse, CNRS/IN2P3, Strasbourg, France
J.-L. Agram[15], J. Andrea, D. Bloch, J.-M. Brom, E. C. Chabert, C. Collard, E. Conte[15], F. Drouhin[15], J.-C. Fontaine[15], D. Gelé, U. Goerlach, C. Goetzmann, P. Juillot, A.-C. Le Bihan, P. Van Hove

Centre de Calcul de l'Institut National de Physique Nucleaire et de Physique des Particules, CNRS/IN2P3, Villeurbanne, France
S. Gadrat

Institut de Physique Nucléaire de Lyon, Université de Lyon, Université Claude Bernard Lyon 1, CNRS-IN2P3, Villeurbanne, France
S. Beauceron, N. Beaupere, G. Boudoul, S. Brochet, J. Chasserat, R. Chierici, D. Contardo, P. Depasse, H. El Mamouni, J. Fan, J. Fay, S. Gascon, M. Gouzevitch, B. Ille, T. Kurca, M. Lethuillier, L. Mirabito, S. Perries, J. D. Ruiz Alvarez, L. Sgandurra, V. Sordini, M. Vander Donckt, P. Verdier, S. Viret, H. Xiao

Institute of High Energy Physics and Informatization, Tbilisi State University, Tbilisi, Georgia
Z. Tsamalaidze[16]

RWTH Aachen University, I. Physikalisches Institut, Aachen, Germany
C. Autermann, S. Beranek, M. Bontenackels, B. Calpas, M. Edelhoff, L. Feld, O. Hindrichs, K. Klein, A. Ostapchuk, A. Perieanu, F. Raupach, J. Sammet, S. Schael, D. Sprenger, H. Weber, B. Wittmer, V. Zhukov[5]

RWTH Aachen University, III. Physikalisches Institut A, Aachen, Germany
M. Ata, J. Caudron, E. Dietz-Laursonn, D. Duchardt, M. Erdmann, R. Fischer, A. Güth, T. Hebbeker, C. Heidemann, K. Hoepfner, D. Klingebiel, S. Knutzen, P. Kreuzer, M. Merschmeyer, A. Meyer, M. Olschewski, K. Padeken, P. Papacz, H. Reithler, S. A. Schmitz, L. Sonnenschein, D. Teyssier, S. Thüer, M. Weber

RWTH Aachen University, III. Physikalisches Institut B, Aachen, Germany
V. Cherepanov, Y. Erdogan, G. Flügge, H. Geenen, M. Geisler, W. Haj Ahmad, F. Hoehle, B. Kargoll, T. Kress, Y. Kuessel, J. Lingemann[2], A. Nowack, I. M. Nugent, L. Perchalla, O. Pooth, A. Stahl

Deutsches Elektronen-Synchrotron, Hamburg, Germany
I. Asin, N. Bartosik, J. Behr, W. Behrenhoff, U. Behrens, A. J. Bell, M. Bergholz[17], A. Bethani, K. Borras, A. Burgmeier, A. Cakir, L. Calligaris, A. Campbell, S. Choudhury, F. Costanza, C. Diez Pardos, S. Dooling, T. Dorland, G. Eckerlin, D. Eckstein, T. Eichhorn, G. Flucke, A. Geiser, A. Grebenyuk, P. Gunnellini, S. Habib, J. Hauk, G. Hellwig, M. Hempel, D. Horton, H. Jung, M. Kasemann, P. Katsas, J. Kieseler, C. Kleinwort, M. Krämer, D. Krücker, W. Lange, J. Leonard, K. Lipka, W. Lohmann[17], B. Lutz, R. Mankel, I. Marfin, I.-A. Melzer-Pellmann, A. B. Meyer, J. Mnich, A. Mussgiller, S. Naumann-Emme, O. Novgorodova, F. Nowak, H. Perrey, A. Petrukhin, D. Pitzl, R. Placakyte, A. Raspereza, P. M. Ribeiro Cipriano, C. Riedl, E. Ron, M. Ö. Sahin, J. Salfeld-Nebgen, P. Saxena, R. Schmidt[17], T. Schoerner-Sadenius, M. Schröder, M. Stein, A. D. R. Vargas Trevino, R. Walsh, C. Wissing

University of Hamburg, Hamburg, Germany
M. Aldaya Martin, V. Blobel, H. Enderle, J. Erfle, E. Garutti, K. Goebel, M. Görner, M. Gosselink, J. Haller, R. S. Höing, H. Kirschenmann, R. Klanner, R. Kogler, J. Lange, I. Marchesini, J. Ott, T. Peiffer, N. Pietsch, D. Rathjens, C. Sander, H. Schettler, P. Schleper, E. Schlieckau, A. Schmidt, M. Seidel, J. Sibille[18], V. Sola, H. Stadie, G. Steinbrück, D. Troendle, E. Usai, L. Vanelderen

Institut für Experimentelle Kernphysik, Karlsruhe, Germany
C. Barth, C. Baus, J. Berger, C. Böser, E. Butz, T. Chwalek, W. De Boer, A. Descroix, A. Dierlamm, M. Feindt, M. Guthoff[2], F. Hartmann[2], T. Hauth[2], H. Held, K. H. Hoffmann, U. Husemann, I. Katkov[5], A. Kornmayer[2], E. Kuznetsova, P. Lobelle Pardo, D. Martschei, M. U. Mozer, Th. Müller, M. Niegel, A. Nürnberg, O. Oberst, G. Quast, K. Rabbertz, F. Ratnikov, S. Röcker, F.-P. Schilling, G. Schott, H. J. Simonis, F. M. Stober, R. Ulrich, J. Wagner-Kuhr, S. Wayand, T. Weiler, R. Wolf, M. Zeise

Institute of Nuclear and Particle Physics (INPP), NCSR Demokritos, Aghia Paraskevi, Greece
G. Anagnostou, G. Daskalakis, T. Geralis, S. Kesisoglou, A. Kyriakis, D. Loukas, A. Markou, C. Markou, E. Ntomari, A. Psallidas, I. Topsis-giotis

University of Athens, Athens, Greece
L. Gouskos, A. Panagiotou, N. Saoulidou, E. Stiliaris

University of Ioánnina, Ioánnina, Greece
X. Aslanoglou, I. Evangelou, G. Flouris, C. Foudas, P. Kokkas, N. Manthos, I. Papadopoulos, E. Paradas

Wigner Research Centre for Physics, Budapest, Hungary
G. Bencze, C. Hajdu, P. Hidas, D. Horvath[19], F. Sikler, V. Veszpremi, G. Vesztergombi[20], A. J. Zsigmond

Institute of Nuclear Research ATOMKI, Debrecen, Hungary
N. Beni, S. Czellar, J. Molnar, J. Palinkas, Z. Szillasi

University of Debrecen, Debrecen, Hungary
J. Karancsi, P. Raics, Z. L. Trocsanyi, B. Ujvari

National Institute of Science Education and Research, Bhubaneswar, India
S. K. Swain

Panjab University, Chandigarh, India
S. B. Beri, V. Bhatnagar, N. Dhingra, R. Gupta, M. Kaur, M. Z. Mehta, M. Mittal, N. Nishu, A. Sharma, J. B. Singh

University of Delhi, Delhi, India
Ashok Kumar, Arun Kumar, S. Ahuja, A. Bhardwaj, B. C. Choudhary, A. Kumar, S. Malhotra, M. Naimuddin, K. Ranjan, V. Sharma, R. K. Shivpuri

Saha Institute of Nuclear Physics, Kolkata, India
S. Banerjee, S. Bhattacharya, K. Chatterjee, S. Dutta, B. Gomber, Sa. Jain, Sh. Jain, R. Khurana, A. Modak, S. Mukherjee, D. Roy, S. Sarkar, M. Sharan, A. P. Singh

Bhabha Atomic Research Centre, Mumbai, India
A. Abdulsalam, D. Dutta, S. Kailas, V. Kumar, A. K. Mohanty[2], L. M. Pant, P. Shukla, A. Topkar

Tata Institute of Fundamental Research-EHEP, Mumbai, India
T. Aziz, R. M. Chatterjee, S. Ganguly, S. Ghosh, M. Guchait[21], A. Gurtu[22], G. Kole, S. Kumar, M. Maity[23], G. Majumder, K. Mazumdar, G. B. Mohanty, B. Parida, K. Sudhakar, N. Wickramage[24]

Tata Institute of Fundamental Research-HECR, Mumbai, India
S. Banerjee, S. Dugad

Institute for Research in Fundamental Sciences (IPM), Tehran, Iran
H. Arfaei, H. Bakhshiansohi, H. Behnamian, S. M. Etesami[25], A. Fahim[26], A. Jafari, M. Khakzad, M. Mohammadi Najafabadi, M. Naseri, S. Paktinat Mehdiabadi, B. Safarzadeh[27], M. Zeinali

University College Dublin, Dublin, Ireland
M. Grunewald

INFN Sezione di Bari, Bari, Italy
M. Abbrescia, L. Barbone, C. Calabria, S. S. Chhibra, A. Colaleo, D. Creanza, N. De Filippis, M. De Palma, L. Fiore, G. Iaselli, G. Maggi, M. Maggi, B. Marangelli, S. My, S. Nuzzo, N. Pacifico, A. Pompili, G. Pugliese, R. Radogna, G. Selvaggi, L. Silvestris, G. Singh, R. Venditti, P. Verwilligen, G. Zito

Università di Bari, Bari, Italy
M. Abbrescia, L. Barbone, C. Calabria, S. S. Chhibra, M. De Palma, B. Marangelli, S. Nuzzo, A. Pompili, R. Radogna, G. Selvaggi, G. Singh, R. Venditti

Politecnico di Bari, Bari, Italy
D. Creanza, N. De Filippis, G. Iaselli, G. Maggi, S. My, G. Pugliese

INFN Sezione di Bologna, Bologna, Italy
G. Abbiendi, A. C. Benvenuti, D. Bonacorsi, S. Braibant-Giacomelli, L. Brigliadori, R. Campanini, P. Capiluppi, A. Castro, F. R. Cavallo, G. Codispoti, M. Cuffiani, G. M. Dallavalle, F. Fabbri, A. Fanfani, D. Fasanella, P. Giacomelli, C. Grandi, L. Guiducci, S. Marcellini, G. Masetti, M. Meneghelli, A. Montanari, F. L. Navarria, F. Odorici, A. Perrotta, F. Primavera, A. M. Rossi, T. Rovelli, G. P. Siroli, N. Tosi, R. Travaglini

Università di Bologna, Bologna, Italy
D. Bonacorsi, S. Braibant-Giacomelli, L. Brigliadori, R. Campanini, P. Capiluppi, A. Castro, G. Codispoti, M. Cuffiani, A. Fanfani, D. Fasanella, L. Guiducci, M. Meneghelli, F. L. Navarria, F. Primavera, A. M. Rossi, T. Rovelli, G. P. Siroli, N. Tosi, R. Travaglini

INFN Sezione di Catania, Catania, Italy
S. Albergo, G. Cappello, M. Chiorboli, S. Costa, F. Giordano[2], R. Potenza, A. Tricomi, C. Tuve

Università di Catania, Catania, Italy
S. Albergo, M. Chiorboli, S. Costa, R. Potenza, A. Tricomi, C. Tuve

INFN Sezione di Firenze, Firenze, Italy
G. Barbagli, V. Ciulli, C. Civinini, R. D'Alessandro, E. Focardi, E. Gallo, S. Gonzi, V. Gori, P. Lenzi, M. Meschini, S. Paoletti, G. Sguazzoni, A. Tropiano

Università di Firenze, Firenze, Italy
V. Ciulli, R. D'Alessandro, E. Focardi, S. Gonzi, V. Gori, P. Lenzi, A. Tropiano

INFN Laboratori Nazionali di Frascati, Frascati, Italy
L. Benussi, S. Bianco, F. Fabbri, D. Piccolo

INFN Sezione di Genova, Genova, Italy
P. Fabbricatore, R. Ferretti, F. Ferro, M. Lo Vetere, R. Musenich, E. Robutti, S. Tosi

Università di Genova, Genova, Italy
R. Ferretti, M. Lo Vetere, S. Tosi

INFN Sezione di Milano-Bicocca, Milan, Italy
A. Benaglia, M. E. Dinardo, S. Fiorendi[2], S. Gennai, A. Ghezzi, P. Govoni, M. T. Lucchini[2], S. Malvezzi, R. A. Manzoni[2], A. Martelli[2], D. Menasce, L. Moroni, M. Paganoni, D. Pedrini, S. Ragazzi, N. Redaelli, T. Tabarelli de Fatis

Università di Milano-Bicocca, Milan, Italy
M. E. Dinardo, S. Fiorendi[2], A. Ghezzi, P. Govoni, M. T. Lucchini[2], R. A. Manzoni[2], A. Martelli[2], M. Paganoni, S. Ragazzi, T. Tabarelli de Fatis

INFN Sezione di Napoli, Naples, Italy
S. Buontempo, N. Cavallo, F. Fabozzi, A. O. M. Iorio, L. Lista, S. Meola[2], M. Merola, P. Paolucci[2]

Università di Napoli 'Federico II', Naples, Italy
A. O. M. Iorio

Università della Basilicata (Potenza), Naples, Italy
N. Cavallo, F. Fabozzi

Università G. Marconi (Roma), Naples, Italy
S. Meola[2]

INFN Sezione di Padova, Padua, Italy
P. Azzi, N. Bacchetta, M. Bellato, D. Bisello, A. Branca, R. Carlin, T. Dorigo, F. Fanzago, M. Galanti[2], F. Gasparini, U. Gasparini, P. Giubilato, F. Gonella, A. Gozzelino, K. Kanishchev, S. Lacaprara, I. Lazzizzera, M. Margoni, A.T. Meneguzzo, J. Pazzini, N. Pozzobon, P. Ronchese, F. Simonetto, E. Torassa, M. Tosi, S. Vanini, P. Zotto, A. Zucchetta, G. Zumerle

Università di Padova, Padua, Italy
D. Bisello, A. Branca, R. Carlin, M. Galanti, F. Gasparini, U. Gasparini, P. Giubilato, M. Margoni, A.T. Meneguzzo, J. Pazzini, N. Pozzobon, P. Ronchese, F. Simonetto, M. Tosi, S. Vanini, P. Zotto, A. Zucchetta, G. Zumerle

Università di Trento (Trento), Padua, Italy
K. Kanishchev, I. Lazzizzera

INFN Sezione di Pavia, Pavia, Italy
M. Gabusi, S. P. Ratti, C. Riccardi, P. Vitulo

Università di Pavia, Pavia, Italy
M. Gabusi, S. P. Ratti, C. Riccardi, P. Vitulo

INFN Sezione di Perugia, Pavia, Italy
M. Biasini, G. M. Bilei, L. Fanò, P. Lariccia, G. Mantovani, M. Menichelli, F. Romeo, A. Saha, A. Santocchia, A. Spiezia

Università di Perugia, Pavia, Italy
M. Biasini, L. Fanò, P. Lariccia, G. Mantovani, F. Romeo, A. Santocchia, A. Spiezia

INFN Sezione di Pisa, Pisa, Italy
K. Androsov[28], P. Azzurri, G. Bagliesi, J. Bernardini, T. Boccali, G. Broccolo, R. Castaldi, M. A. Ciocci[28], R. Dell'Orso, F. Fiori, L. Foà, A. Giassi, M. T. Grippo[28], A. Kraan, F. Ligabue, T. Lomtadze, L. Martini, A. Messineo, C. S. Moon[29], F. Palla, A. Rizzi, A. Savoy-Navarro[30], A. T. Serban, P. Spagnolo, P. Squillacioti[28], R. Tenchini, G. Tonelli, A. Venturi, P. G. Verdini, C. Vernieri

Università di Pisa, Pisa, Italy
L. Martini, A. Messineo, A. Rizzi

Scuola Normale Superiore di Pisa, Pisa, Italy
G. Broccolo, F. Fiori, L. Foà, F. Ligabue, C. Vernieri

INFN Sezione di Roma, Rome, Italy
L. Barone, F. Cavallari, D. Del Re, M. Diemoz, M. Grassi, C. Jorda, E. Longo, F. Margaroli, P. Meridiani, F. Micheli, S. Nourbakhsh, G. Organtini, R. Paramatti, S. Rahatlou, C. Rovelli, L. Soffi, P. Traczyk

Università di Roma, Rome, Italy
L. Barone, D. Del Re, M. Grassi, E. Longo, F. Margaroli, F. Micheli, S. Nourbakhsh, G. Organtini, S. Rahatlou, L. Soffi, P. Traczyk

INFN Sezione di Torino, Turin, Italy
N. Amapane, R. Arcidiacono, S. Argiro, M. Arneodo, R. Bellan, C. Biino, N. Cartiglia, S. Casasso, M. Costa, A. Degano, N. Demaria, C. Mariotti, S. Maselli, E. Migliore, V. Monaco, M. Musich, M. M. Obertino, G. Ortona, L. Pacher, N. Pastrone, M. Pelliccioni[2], A. Potenza, A. Romero, M. Ruspa, R. Sacchi, A. Solano, A. Staiano, U. Tamponi

Università di Torino, Turin, Italy
N. Amapane, S. Argiro, R. Bellan, S. Casasso, M. Costa, A. Degano, E. Migliore, V. Monaco, G. Ortona, L. Pacher, A. Potenza, A. Romero, R. Sacchi, A. Solano

Università del Piemonte Orientale (Novara), Turin, Italy
R. Arcidiacono, M. Arneodo, M. M. Obertino, M. Ruspa

INFN Sezione di Trieste, Trieste, Italy
S. Belforte, V. Candelise, M. Casarsa, F. Cossutti, G. Della Ricca, B. Gobbo, C. La Licata, M. Marone, D. Montanino, A. Penzo, A. Schizzi, T. Umer, A. Zanetti

Università di Trieste, Trieste, Italy
V. Candelise, G. Della Ricca, C. La Licata, M. Marone, D. Montanino, A. Schizzi, T. Umer

Kangwon National University, Chunchon, Korea
S. Chang, T. Y. Kim, S. K. Nam

Kyungpook National University, Taegu, Korea
D. H. Kim, G. N. Kim, J. E. Kim, D. J. Kong, S. Lee, Y. D. Oh, H. Park, D. C. Son

Chonnam National University, Institute for Universe and Elementary Particles, Kwangju, Korea
J. Y. Kim, Zero J. Kim, S. Song

Korea University, Seoul, Korea
S. Choi, D. Gyun, B. Hong, M. Jo, H. Kim, Y. Kim, K. S. Lee, S. K. Park, Y. Roh

University of Seoul, Seoul, Korea
M. Choi, J. H. Kim, C. Park, I. C. Park, S. Park, G. Ryu

Sungkyunkwan University, Suwon, Korea
Y. Choi, Y. K. Choi, J. Goh, M. S. Kim, E. Kwon, B. Lee, J. Lee, S. Lee, H. Seo, I. Yu

Vilnius University, Vilnius, Lithuania
A. Juodagalvis

National Centre for Particle Physics, Universiti Malaya, Kuala Lumpur, Malaysia
J. R. Komaragiri

Centro de Investigacion y de Estudios Avanzados del IPN, Mexico City, Mexico
H. Castilla-Valdez, E. De La Cruz-Burelo, I. Heredia-de La Cruz[31], R. Lopez-Fernandez, J. Martínez-Ortega, A. Sanchez-Hernandez, L. M. Villasenor-Cendejas

Universidad Iberoamericana, Mexico City, Mexico
S. Carrillo Moreno, F. Vazquez Valencia

Benemerita Universidad Autonoma de Puebla, Puebla, Mexico
H. A. Salazar Ibarguen

Universidad Autónoma de San Luis Potosí, San Luis Potosí, Mexico
E. Casimiro Linares, A. Morelos Pineda

University of Auckland, Auckland, New Zealand
D. Krofcheck

University of Canterbury, Christchurch, New Zealand
P. H. Butler, R. Doesburg, S. Reucroft, H. Silverwood

National Centre for Physics, Quaid-I-Azam University, Islamabad, Pakistan
M. Ahmad, M. I. Asghar, J. Butt, H. R. Hoorani, W. A. Khan, T. Khurshid, S. Qazi, M. A. Shah, M. Shoaib

National Centre for Nuclear Research, Swierk, Poland
H. Bialkowska, M. Bluj[32], B. Boimska, T. Frueboes, M. Górski, M. Kazana, K. Nawrocki, K. Romanowska-Rybinska, M. Szleper, G. Wrochna, P. Zalewski

Institute of Experimental Physics, Faculty of Physics, University of Warsaw, Warsaw, Poland
G. Brona, K. Bunkowski, M. Cwiok, W. Dominik, K. Doroba, A. Kalinowski, M. Konecki, J. Krolikowski, M. Misiura, W. Wolszczak

Laboratório de Instrumentação e Física Experimental de Partículas, Lisbon, Portugal
P. Bargassa, C. Beirão Da Cruz E Silva, P. Faccioli, P. G. Ferreira Parracho, M. Gallinaro, F. Nguyen, J. Rodrigues Antunes, J. Seixas[2], J. Varela, P. Vischia

Joint Institute for Nuclear Research, Dubna, Russia
S. Afanasiev, P. Bunin, I. Golutvin, I. Gorbunov, A. Kamenev, V. Karjavin, V. Konoplyanikov, G. Kozlov, A. Lanev, A. Malakhov, V. Matveev[33], P. Moisenz, V. Palichik, V. Perelygin, S. Shmatov, N. Skatchkov, V. Smirnov, A. Zarubin

Petersburg Nuclear Physics Institute, Gatchina (St. Petersburg), Russia
V. Golovtsov, Y. Ivanov, V. Kim, P. Levchenko, V. Murzin, V. Oreshkin, I. Smirnov, V. Sulimov, L. Uvarov, S. Vavilov, A. Vorobyev, An. Vorobyev

Institute for Nuclear Research, Moscow, Russia
Yu. Andreev, A. Dermenev, S. Gninenko, N. Golubev, M. Kirsanov, N. Krasnikov, A. Pashenkov, D. Tlisov, A. Toropin

Institute for Theoretical and Experimental Physics, Moscow, Russia
V. Epshteyn, V. Gavrilov, N. Lychkovskaya, V. Popov, G. Safronov, S. Semenov, A. Spiridonov, V. Stolin, E. Vlasov, A. Zhokin

P.N. Lebedev Physical Institute, Moscow, Russia
V. Andreev, M. Azarkin, I. Dremin, M. Kirakosyan, A. Leonidov, G. Mesyats, S. V. Rusakov, A. Vinogradov

Skobeltsyn Institute of Nuclear Physics, Lomonosov Moscow State University, Moscow, Russia
A. Belyaev, E. Boos, A. Ershov, A. Gribushin, V. Klyukhin, O. Kodolova, V. Korotkikh, I. Lokhtin, S. Obraztsov, S. Petrushanko, V. Savrin, A. Snigirev, I. Vardanyan

State Research Center of Russian Federation, Institute for High Energy Physics, Protvino, Russia
I. Azhgirey, I. Bayshev, S. Bitioukov, V. Kachanov, A. Kalinin, D. Konstantinov, V. Krychkine, V. Petrov, R. Ryutin, A. Sobol, L. Tourtchanovitch, S. Troshin, N. Tyurin, A. Uzunian, A. Volkov

Faculty of Physics and Vinca Institute of Nuclear Sciences, University of Belgrade, Belgrade, Serbia
P. Adzic[34], M. Djordjevic, M. Ekmedzic, J. Milosevic

Centro de Investigaciones Energéticas Medioambientales y Tecnológicas (CIEMAT), Madrid, Spain
M. Aguilar-Benitez, J. Alcaraz Maestre, C. Battilana, E. Calvo, M. Cerrada, M. Chamizo Llatas[2], N. Colino, B. De La Cruz, A. Delgado Peris, D. Domínguez Vázquez, C. Fernandez Bedoya, J. P. Fernández Ramos, A. Ferrando, J. Flix, M. C. Fouz, P. Garcia-Abia, O. Gonzalez Lopez, S. Goy Lopez, J. M. Hernandez, M. I. Josa, G. Merino, E. Navarro De Martino, J. Puerta Pelayo, A. Quintario Olmeda, I. Redondo, L. Romero, M. S. Soares, C. Willmott

Universidad Autónoma de Madrid, Madrid, Spain
C. Albajar, J. F. de Trocóniz

Universidad de Oviedo, Oviedo, Spain
H. Brun, J. Cuevas, J. Fernandez Menendez, S. Folgueras, I. Gonzalez Caballero, L. Lloret Iglesias

Instituto de Física de Cantabria (IFCA), CSIC-Universidad de Cantabria, Santander, Spain
J. A. Brochero Cifuentes, I. J. Cabrillo, A. Calderon, S. H. Chuang, J. Duarte Campderros, M. Fernandez, G. Gomez, J. Gonzalez Sanchez, A. Graziano, A. Lopez Virto, J. Marco, R. Marco, C. Martinez Rivero, F. Matorras, F. J. Munoz Sanchez, J. Piedra Gomez, T. Rodrigo, A. Y. Rodríguez-Marrero, A. Ruiz-Jimeno, L. Scodellaro, I. Vila, R. Vilar Cortabitarte

CERN, European Organization for Nuclear Research, Geneva, Switzerland
D. Abbaneo, E. Auffray, G. Auzinger, M. Bachtis, P. Baillon, A. H. Ball, D. Barney, J. Bendavid, L. Benhabib, J. F. Benitez, C. Bernet[8], G. Bianchi, P. Bloch, A. Bocci, A. Bonato, O. Bondu, C. Botta, H. Breuker, T. Camporesi, G. Cerminara, T. Christiansen, J. A. Coarasa Perez, S. Colafranceschi[35], M. D'Alfonso, D. d'Enterria, A. Dabrowski, A. David, F. De Guio, A. De Roeck, S. De Visscher, S. Di Guida, M. Dobson, N. Dupont-Sagorin, A. Elliott-Peisert, J. Eugster, G. Franzoni, W. Funk, M. Giffels, D. Gigi, K. Gill, M. Girone, M. Giunta, F. Glege, R. Gomez-Reino Garrido, S. Gowdy, R. Guida, J. Hammer, M. Hansen, P. Harris, V. Innocente, P. Janot, E. Karavakis, K. Kousouris, K. Krajczar, P. Lecoq, C. Lourenço, N. Magini, L. Malgeri, M. Mannelli, L. Masetti, F. Meijers, S. Mersi, E. Meschi, F. Moortgat, M. Mulders, P. Musella, L. Orsini, E. Palencia Cortezon, E. Perez, L. Perrozzi, A. Petrilli, G. Petrucciani, A. Pfeiffer, M. Pierini, M. Pimiä, D. Piparo, M. Plagge, A. Racz, W. Reece, G. Rolandi[36], M. Rovere, H. Sakulin, F. Santanastasio, C. Schäfer, C. Schwick, S. Sekmen, A. Sharma, P. Siegrist, P. Silva, M. Simon, P. Sphicas[37], J. Steggemann, B. Stieger, M. Stoye, A. Tsirou, G. I. Veres[20], J. R. Vlimant, H. K. Wöhri, W. D. Zeuner

Paul Scherrer Institut, Villigen, Switzerland
W. Bertl, K. Deiters, W. Erdmann, R. Horisberger, Q. Ingram, H. C. Kaestli, S. König, D. Kotlinski, U. Langenegger, D. Renker, T. Rohe

Institute for Particle Physics, ETH Zurich, Zurich, Switzerland
F. Bachmair, L. Bäni, L. Bianchini, P. Bortignon, M. A. Buchmann, B. Casal, N. Chanon, A. Deisher, G. Dissertori, M. Dittmar, M. Donegà, M. Dünser, P. Eller, C. Grab, D. Hits, W. Lustermann, B. Mangano, A. C. Marini, P. Martinez Ruiz del Arbol, D. Meister, N. Mohr, C. Nägeli[38], P. Nef, F. Nessi-Tedaldi, F. Pandolfi, L. Pape, F. Pauss, M. Peruzzi, M. Quittnat, F. J. Ronga, M. Rossini, A. Starodumov[39], M. Takahashi, L. Tauscher, K. Theofilatos, D. Treille, R. Wallny, H. A. Weber

Universität Zürich, Zurich, Switzerland
C. Amsler[40], V. Chiochia, A. De Cosa, C. Favaro, A. Hinzmann, T. Hreus, M. Ivova Rikova, B. Kilminster, B. Millan Mejias, J. Ngadiuba, P. Robmann, H. Snoek, S. Taroni, M. Verzetti, Y. Yang

National Central University, Chung-Li, Taiwan
M. Cardaci, K. H. Chen, C. Ferro, C. M. Kuo, S. W. Li, W. Lin, Y. J. Lu, R. Volpe, S. S. Yu

National Taiwan University (NTU), Taipei, Taiwan
P. Bartalini, P. Chang, Y. H. Chang, Y. W. Chang, Y. Chao, K. F. Chen, P. H. Chen, C. Dietz, U. Grundler, W.-S. Hou, Y. Hsiung, K. Y. Kao, Y. J. Lei, Y. F. Liu, R.-S. Lu, D. Majumder, E. Petrakou, X. Shi, J. G. Shiu, Y. M. Tzeng, M. Wang, R. Wilken

Chulalongkorn University, Bangkok, Thailand
B. Asavapibhop, N. Suwonjandee

Cukurova University, Adana, Turkey
A. Adiguzel, M. N. Bakirci[41], S. Cerci[42], C. Dozen, I. Dumanoglu, E. Eskut, S. Girgis, G. Gokbulut, E. Gurpinar, I. Hos, E. E. Kangal, A. Kayis Topaksu, G. Onengut[43], K. Ozdemir, S. Ozturk[41], A. Polatoz, K. Sogut[44], D. Sunar Cerci[42], B. Tali[42], H. Topakli[41], M. Vergili

Physics Department, Middle East Technical University, Ankara, Turkey
I. V. Akin, T. Aliev, B. Bilin, S. Bilmis, M. Deniz, H. Gamsizkan, A. M. Guler, G. Karapinar[45], K. Ocalan, A. Ozpineci, M. Serin, R. Sever, U. E. Surat, M. Yalvac, M. Zeyrek

Bogazici University, Istanbul, Turkey
E. Gülmez, B. Isildak[46], M. Kaya[47], O. Kaya[47], S. Ozkorucuklu[48]

Istanbul Technical University, Istanbul, Turkey
H. Bahtiyar[49], E. Barlas, K. Cankocak, Y. O. Günaydin[50], F. I. Vardarlı, M. Yücel

National Scientific Center, Kharkov Institute of Physics and Technology, Kharkov, Ukraine
L. Levchuk, P. Sorokin

University of Bristol, Bristol, UK
J. J. Brooke, E. Clement, D. Cussans, H. Flacher, R. Frazier, J. Goldstein, M. Grimes, G. P. Heath, H. F. Heath, J. Jacob, L. Kreczko, C. Lucas, Z. Meng, D. M. Newbold[51], S. Paramesvaran, A. Poll, S. Senkin, V. J. Smith, T. Williams

Rutherford Appleton Laboratory, Didcot, UK
A. Belyaev[52], C. Brew, R. M. Brown, D. J. A. Cockerill, J. A. Coughlan, K. Harder, S. Harper, J. Ilic, E. Olaiya, D. Petyt, C. H. Shepherd-Themistocleous, A. Thea, I. R. Tomalin, W. J. Womersley, S. D. Worm

Imperial College, London, UK
M. Baber, R. Bainbridge, O. Buchmuller, D. Burton, D. Colling, N. Cripps, M. Cutajar, P. Dauncey, G. Davies, M. Della Negra, W. Ferguson, J. Fulcher, D. Futyan, A. Gilbert, A. Guneratne Bryer, G. Hall, Z. Hatherell, J. Hays, G. Iles, M. Jarvis, G. Karapostoli, M. Kenzie, R. Lane, R. Lucas[51], L. Lyons, A.-M. Magnan, J. Marrouche, B. Mathias, R. Nandi, J. Nash, A. Nikitenko[39], J. Pela, M. K. Petridis, M. Pioppi[53], D. M. Raymond, S. Rogerson, A. Rose, C. Seez, P. Sharp[†], A. Sparrow, A. Tapper, M. Vazquez Acosta, T. Virdee, S. Wakefield, N. Wardle

Brunel University, Uxbridge, UK
J. E. Cole, P. R. Hobson, A. Khan, P. Kyberd, D. Leggat, D. Leslie, W. Martin, I. D. Reid, P. Symonds, L. Teodorescu, M. Turner

Baylor University, Waco, USA
J. Dittmann, K. Hatakeyama, A. Kasmi, H. Liu, T. Scarborough

The University of Alabama, Tuscaloosa, USA
O. Charaf, S. I. Cooper, C. Henderson, P. Rumerio

Boston University, Boston, USA
A. Avetisyan, T. Bose, C. Fantasia, A. Heister, P. Lawson, D. Lazic, J. Rohlf, D. Sperka, J. St. John, L. Sulak

Brown University, Providence, USA
J. Alimena, S. Bhattacharya, G. Christopher, D. Cutts, Z. Demiragli, A. Ferapontov, A. Garabedian, U. Heintz, S. Jabeen, G. Kukartsev, E. Laird, G. Landsberg, M. Luk, M. Narain, M. Segala, T. Sinthuprasith, T. Speer, J. Swanson

University of California, Davis, Davis, USA
R. Breedon, G. Breto, M. Calderon De La Barca Sanchez, S. Chauhan, M. Chertok, J. Conway, R. Conway, P. T. Cox,

R. Erbacher, M. Gardner, W. Ko, A. Kopecky, R. Lander, T. Miceli, D. Pellett, J. Pilot, F. Ricci-Tam, B. Rutherford, M. Searle, S. Shalhout, J. Smith, M. Squires, M. Tripathi, S. Wilbur, R. Yohay

University of California, Los Angeles, USA
V. Andreev, D. Cline, R. Cousins, S. Erhan, P. Everaerts, C. Farrell, M. Felcini, J. Hauser, M. Ignatenko, C. Jarvis, G. Rakness, P. Schlein†, E. Takasugi, V. Valuev, M. Weber

University of California, Riverside, Riverside, USA
J. Babb, R. Clare, J. Ellison, J. W. Gary, G. Hanson, J. Heilman, P. Jandir, F. Lacroix, H. Liu, O. R. Long, A. Luthra, M. Malberti, H. Nguyen, A. Shrinivas, J. Sturdy, S. Sumowidagdo, S. Wimpenny

University of California, San Diego, La Jolla, USA
W. Andrews, J. G. Branson, G. B. Cerati, S. Cittolin, R. T. D'Agnolo, D. Evans, A. Holzner, R. Kelley, D. Kovalskyi, M. Lebourgeois, J. Letts, I. Macneill, S. Padhi, C. Palmer, M. Pieri, M. Sani, V. Sharma, S. Simon, E. Sudano, M. Tadel, Y. Tu, A. Vartak, S. Wasserbaech[54], F. Würthwein, A. Yagil, J. Yoo

University of California, Santa Barbara, Santa Barbara, USA
D. Barge, C. Campagnari, T. Danielson, K. Flowers, P. Geffert, C. George, F. Golf, J. Incandela, C. Justus, R. Magaña Villalba, N. Mccoll, V. Pavlunin, J. Richman, R. Rossin, D. Stuart, W. To, C. West

California Institute of Technology, Pasadena, USA
A. Apresyan, A. Bornheim, J. Bunn, Y. Chen, E. Di Marco, J. Duarte, D. Kcira, A. Mott, H. B. Newman, C. Pena, C. Rogan, M. Spiropulu, V. Timciuc, R. Wilkinson, S. Xie, R. Y. Zhu

Carnegie Mellon University, Pittsburgh, USA
V. Azzolini, A. Calamba, R. Carroll, T. Ferguson, Y. Iiyama, D. W. Jang, M. Paulini, J. Russ, H. Vogel, I. Vorobiev

University of Colorado at Boulder, Boulder, USA
J. P. Cumalat, B. R. Drell, W. T. Ford, A. Gaz, E. Luiggi Lopez, U. Nauenberg, J. G. Smith, K. Stenson, K. A. Ulmer, S. R. Wagner

Cornell University, Ithaca, USA
J. Alexander, A. Chatterjee, N. Eggert, L. K. Gibbons, W. Hopkins, A. Khukhunaishvili, B. Kreis, N. Mirman, G. Nicolas Kaufman, J. R. Patterson, A. Ryd, E. Salvati, W. Sun, W. D. Teo, J. Thom, J. Thompson, J. Tucker, Y. Weng, L. Winstrom, P. Wittich

Fairfield University, Fairfield, USA
D. Winn

Fermi National Accelerator Laboratory, Batavia, USA
S. Abdullin, M. Albrow, J. Anderson, G. Apollinari, L. A. T. Bauerdick, A. Beretvas, J. Berryhill, P. C. Bhat, K. Burkett, J. N. Butler, V. Chetluru, H. W. K. Cheung, F. Chlebana, S. Cihangir, V. D. Elvira, I. Fisk, J. Freeman, Y. Gao, E. Gottschalk, L. Gray, D. Green, S. Grünendahl, O. Gutsche, D. Hare, R. M. Harris, J. Hirschauer, B. Hooberman, S. Jindariani, M. Johnson, U. Joshi, K. Kaadze, B. Klima, S. Kwan, J. Linacre, D. Lincoln, R. Lipton, J. Lykken, K. Maeshima, J. M. Marraffino, V. I. Martinez Outschoorn, S. Maruyama, D. Mason, P. McBride, K. Mishra, S. Mrenna, Y. Musienko[33], S. Nahn, C. Newman-Holmes, V. O'Dell, O. Prokofyev, N. Ratnikova, E. Sexton-Kennedy, S. Sharma, W. J. Spalding, L. Spiegel, L. Taylor, S. Tkaczyk, N. V. Tran, L. Uplegger, E. W. Vaandering, R. Vidal, A. Whitbeck, J. Whitmore, W. Wu, F. Yang, J. C. Yun

University of Florida, Gainesville, USA
D. Acosta, P. Avery, D. Bourilkov, T. Cheng, S. Das, M. De Gruttola, G. P. Di Giovanni, D. Dobur, R. D. Field, M. Fisher, Y. Fu, I. K. Furic, J. Hugon, B. Kim, J. Konigsberg, A. Korytov, A. Kropivnitskaya, T. Kypreos, J. F. Low, K. Matchev, P. Milenovic[55], G. Mitselmakher, L. Muniz, A. Rinkevicius, L. Shchutska, N. Skhirtladze, M. Snowball, J. Yelton, M. Zakaria

Florida International University, Miami, USA
V. Gaultney, S. Hewamanage, S. Linn, P. Markowitz, G. Martinez, J. L. Rodriguez

Florida State University, Tallahassee, USA
T. Adams, A. Askew, J. Bochenek, J. Chen, B. Diamond, J. Haas, S. Hagopian, V. Hagopian, K. F. Johnson, H. Prosper, V. Veeraraghavan, M. Weinberg

Florida Institute of Technology, Melbourne, USA
M. M. Baarmand, B. Dorney, M. Hohlmann, H. Kalakhety, F. Yumiceva

University of Illinois at Chicago (UIC), Chicago, USA
M. R. Adams, L. Apanasevich, V. E. Bazterra, R. R. Betts, I. Bucinskaite, R. Cavanaugh, O. Evdokimov, L. Gauthier, C. E. Gerber, D. J. Hofman, S. Khalatyan, P. Kurt, D. H. Moon, C. O'Brien, C. Silkworth, P. Turner, N. Varelas

The University of Iowa, Iowa, USA
U. Akgun, E. A. Albayrak[49], B. Bilki[56], W. Clarida, K. Dilsiz, F. Duru, M. Haytmyradov, J.-P. Merlo, H. Mermerkaya[57], A. Mestvirishvili, A. Moeller, J. Nachtman, H. Ogul, Y. Onel, F. Ozok[49], S. Sen, P. Tan, E. Tiras, J. Wetzel, T. Yetkin[58], K. Yi

Johns Hopkins University, Baltimore, USA
B. A. Barnett, B. Blumenfeld, S. Bolognesi, D. Fehling, A. V. Gritsan, P. Maksimovic, C. Martin, M. Swartz

The University of Kansas, Lawrence, USA
P. Baringer, A. Bean, G. Benelli, R. P. Kenny III, M. Murray, D. Noonan, S. Sanders, J. Sekaric, R. Stringer, Q. Wang, J. S. Wood

Kansas State University, Manhattan, USA
A. F. Barfuss, I. Chakaberia, A. Ivanov, S. Khalil, M. Makouski, Y. Maravin, L. K. Saini, S. Shrestha, I. Svintradze

Lawrence Livermore National Laboratory, Livermore, USA
J. Gronberg, D. Lange, F. Rebassoo, D. Wright

University of Maryland, College Park, USA
A. Baden, B. Calvert, S. C. Eno, J. A. Gomez, N. J. Hadley, R. G. Kellogg, T. Kolberg, Y. Lu, M. Marionneau, A. C. Mignerey, K. Pedro, A. Skuja, J. Temple, M. B. Tonjes, S. C. Tonwar

Massachusetts Institute of Technology, Cambridge, USA
A. Apyan, R. Barbieri, G. Bauer, W. Busza, I. A. Cali, M. Chan, L. Di Matteo, V. Dutta, G. Gomez Ceballos, M. Goncharov, D. Gulhan, M. Klute, Y. S. Lai, Y.-J. Lee, A. Levin, P. D. Luckey, T. Ma, C. Paus, D. Ralph, C. Roland, G. Roland, G. S. F. Stephans, F. Stöckli, K. Sumorok, D. Velicanu, J. Veverka, B. Wyslouch, M. Yang, A. S. Yoon, M. Zanetti, V. Zhukova

University of Minnesota, Minneapolis, USA
B. Dahmes, A. De Benedetti, A. Gude, S. C. Kao, K. Klapoetke, Y. Kubota, J. Mans, N. Pastika, R. Rusack, A. Singovsky, N. Tambe, J. Turkewitz

University of Mississippi, Oxford, USA
J. G. Acosta, L. M. Cremaldi, R. Kroeger, S. Oliveros, L. Perera, R. Rahmat, D. A. Sanders, D. Summers

University of Nebraska-Lincoln, Lincoln, USA
E. Avdeeva, K. Bloom, S. Bose, D. R. Claes, A. Dominguez, R. Gonzalez Suarez, J. Keller, D. Knowlton, I. Kravchenko, J. Lazo-Flores, S. Malik, F. Meier, G. R. Snow

State University of New York at Buffalo, Buffalo, USA
J. Dolen, A. Godshalk, I. Iashvili, S. Jain, A. Kharchilava, A. Kumar, S. Rappoccio, Z. Wan

Northeastern University, Boston, USA
G. Alverson, E. Barberis, D. Baumgartel, M. Chasco, J. Haley, A. Massironi, D. Nash, T. Orimoto, D. Trocino, D. Wood, J. Zhang

Northwestern University, Evanston, USA
A. Anastassov, K. A. Hahn, A. Kubik, L. Lusito, N. Mucia, N. Odell, B. Pollack, A. Pozdnyakov, M. Schmitt, S. Stoynev, K. Sung, M. Velasco, S. Won

University of Notre Dame, Notre Dame, USA
D. Berry, A. Brinkerhoff, K. M. Chan, A. Drozdetskiy, M. Hildreth, C. Jessop, D. J. Karmgard, N. Kellams, J. Kolb, K. Lannon, W. Luo, S. Lynch, N. Marinelli, D. M. Morse, T. Pearson, M. Planer, R. Ruchti, J. Slaunwhite, N. Valls, M. Wayne, M. Wolf, A. Woodard

The Ohio State University, Columbus, USA
L. Antonelli, B. Bylsma, L. S. Durkin, S. Flowers, C. Hill, R. Hughes, K. Kotov, T. Y. Ling, D. Puigh, M. Rodenburg, G. Smith, C. Vuosalo, B. L. Winer, H. Wolfe, H. W. Wulsin

Princeton University, Princeton, USA
E. Berry, P. Elmer, V. Halyo, P. Hebda, J. Hegeman, A. Hunt, P. Jindal, S. A. Koay, P. Lujan, D. Marlow, T. Medvedeva, M. Mooney, J. Olsen, P. Piroué, X. Quan, A. Raval, H. Saka, D. Stickland, C. Tully, J. S. Werner, S. C. Zenz, A. Zuranski

University of Puerto Rico, Mayaguez, USA
E. Brownson, A. Lopez, H. Mendez, J. E. Ramirez Vargas

Purdue University, West Lafayette, USA
E. Alagoz, D. Benedetti, G. Bolla, D. Bortoletto, M. De Mattia, A. Everett, Z. Hu, M. Jones, K. Jung, M. Kress, N. Leonardo, D. Lopes Pegna, V. Maroussov, P. Merkel, D. H. Miller, N. Neumeister, B. C. Radburn-Smith, I. Shipsey, D. Silvers, A. Svyatkovskiy, F. Wang, W. Xie, L. Xu, H. D. Yoo, J. Zablocki, Y. Zheng

Purdue University Calumet, Hammond, USA
N. Parashar

Rice University, Houston, USA
A. Adair, B. Akgun, K. M. Ecklund, F. J. M. Geurts, W. Li, B. Michlin, B. P. Padley, R. Redjimi, J. Roberts, J. Zabel

University of Rochester, Rochester, USA
B. Betchart, A. Bodek, R. Covarelli, P. de arbaro, R. Demina, Y. Eshaq, T. Ferbel, A. Garcia-Bellido, P. Goldenzweig, J. Han, A. Harel, D. C. Miner, G. Petrillo, D. Vishnevskiy, M. Zielinski

The Rockefeller University, New York, USA
A. Bhatti, R. Ciesielski, L. Demortier, K. Goulianos, G. Lungu, S. Malik, C. Mesropian

Rutgers, The State University of New Jersey, Piscataway, USA
S. Arora, A. Barker, J. P. Chou, C. Contreras-Campana, E. Contreras-Campana, D. Duggan, D. Ferencek, Y. Gershtein, R. Gray, E. Halkiadakis, D. Hidas, A. Lath, S. Panwalkar, M. Park, R. Patel, V. Rekovic, J. Robles, S. Salur, S. Schnetzer, C. Seitz, S. Somalwar, R. Stone, S. Thomas, P. Thomassen, M. Walker

University of Tennessee, Knoxville, USA
K. Rose, S. Spanier, Z. C. Yang, A. York

Texas A&M University, College Station, USA
O. Bouhali[59], R. Eusebi, W. Flanagan, J. Gilmore, T. Kamon[60], V. Khotilovich, V. Krutelyov, R. Montalvo, I. Osipenkov, Y. Pakhotin, A. Perloff, J. Roe, A. Safonov, T. Sakuma, I. Suarez, A. Tatarinov, D. Toback

Texas Tech University, Lubbock, USA
N. Akchurin, C. Cowden, J. Damgov, C. Dragoiu, P. R. Dudero, K. Kovitanggoon, S. Kunori, S. W. Lee, T. Libeiro, I. Volobouev

Vanderbilt University, Nashville, USA
E. Appelt, A. G. Delannoy, S. Greene, A. Gurrola, W. Johns, C. Maguire, Y. Mao, A. Melo, M. Sharma, P. Sheldon, B. Snook, S. Tuo, J. Velkovska

University of Virginia, Charlottesville, USA
M. W. Arenton, S. Boutle, B. Cox, B. Francis, J. Goodell, R. Hirosky, A. Ledovskoy, C. Lin, C. Neu, J. Wood

Wayne State University, Detroit, USA
S. Gollapinni, R. Harr, P. E. Karchin, C. Kottachchi Kankanamge Don, P. Lamichhane

University of Wisconsin, Madison, USA
D. A. Belknap, L. Borrello, D. Carlsmith, M. Cepeda, S. Dasu, S. Duric, E. Friis, M. Grothe, R. Hall-Wilton, M. Herndon, A. Hervé, P. Klabbers, J. Klukas, A. Lanaro, A. Levine, R. Loveless, A. Mohapatra, I. Ojalvo, T. Perry, G. A. Pierro, G. Polese, I. Ross, A. Sakharov, T. Sarangi, A. Savin, W. H. Smith

† **Deceased**

1: Also at Vienna University of Technology, Vienna, Austria
2: Also at CERN, European Organization for Nuclear Research, Geneva, Switzerland
3: Also at Institut Pluridisciplinaire Hubert Curien, Université de Strasbourg, Université de Haute Alsace Mulhouse, CNRS/IN2P3, Strasbourg, France
4: Also at National Institute of Chemical Physics and Biophysics, Tallinn, Estonia
5: Also at Skobeltsyn Institute of Nuclear Physics, Lomonosov Moscow State University, Moscow, Russia
6: Also at Universidade Estadual de Campinas, Campinas, Brazil
7: Also at California Institute of Technology, Pasadena, USA
8: Also at Laboratoire Leprince-Ringuet, Ecole Polytechnique, IN2P3-CNRS, Palaiseau, France
9: Also at Zewail City of Science and Technology, Zewail, Egypt
10: Also at Suez Canal University, Suez, Egypt
11: Also at Cairo University, Cairo, Egypt
12: Also at Fayoum University, El-Fayoum, Egypt
13: Also at British University in Egypt, Cairo, Egypt
14: Now at Ain Shams University, Cairo, Egypt
15: Also at Université de Haute Alsace, Mulhouse, France
16: Also at Joint Institute for Nuclear Research, Dubna, Russia
17: Also at Brandenburg University of Technology, Cottbus, Germany
18: Also at The University of Kansas, Lawrence, USA
19: Also at Institute of Nuclear Research ATOMKI, Debrecen, Hungary
20: Also at Eötvös Loránd University, Budapest, Hungary
21: Also at Tata Institute of Fundamental Research-HECR, Mumbai, India
22: Now at King Abdulaziz University, Jeddah, Saudi Arabia
23: Also at University of Visva-Bharati, Santiniketan, India
24: Also at University of Ruhuna, Matara, Sri Lanka
25: Also at Isfahan University of Technology, Isfahan, Iran
26: Also at Sharif University of Technology, Tehran, Iran
27: Also at Plasma Physics Research Center, Science and Research Branch, Islamic Azad University, Tehran, Iran
28: Also at Università degli Studi di Siena, Siena, Italy
29: Also at Centre National de la Recherche Scientifique (CNRS)-IN2P3, Paris, France
30: Also at Purdue University, West Lafayette, USA
31: Also at Universidad Michoacana de San Nicolas de Hidalgo, Morelia, Mexico
32: Also at National Centre for Nuclear Research, Swierk, Poland
33: Also at Institute for Nuclear Research, Moscow, Russia
34: Also at Faculty of Physics, University of Belgrade, Belgrade, Serbia
35: Also at Facoltà Ingegneria, Università di Roma, Roma, Italy
36: Also at Scuola Normale e Sezione dell'INFN, Pisa, Italy
37: Also at University of Athens, Athens, Greece
38: Also at Paul Scherrer Institut, Villigen, Switzerland
39: Also at Institute for Theoretical and Experimental Physics, Moscow, Russia
40: Also at Albert Einstein Center for Fundamental Physics, Bern, Switzerland
41: Also at Gaziosmanpasa University, Tokat, Turkey
42: Also at Adiyaman University, Adiyaman, Turkey
43: Also at Cag University, Mersin, Turkey
44: Also at Mersin University, Mersin, Turkey
45: Also at Izmir Institute of Technology, Izmir, Turkey
46: Also at Ozyegin University, Istanbul, Turkey

47: Also at Kafkas University, Kars, Turkey
48: Also at Faculty of Science, Istanbul University, Istanbul, Turkey
49: Also at Mimar Sinan University Istanbul, Istanbul, Turkey
50: Also at Kahramanmaras Sütcü Imam University, Kahramanmaras, Turkey
51: Also at Rutherford Appleton Laboratory, Didcot, UK
52: Also at School of Physics and Astronomy, University of Southampton, Southampton, UK
53: Also at INFN Sezione di Perugia; Università di Perugia, Perugia, Italy
54: Also at Utah Valley University, Orem, USA
55: Also at Faculty of Physics and Vinca Institute of Nuclear Sciences, University of Belgrade, Belgrade, Serbia
56: Also at Argonne National Laboratory, Argonne, USA
57: Also at Erzincan University, Erzincan, Turkey
58: Also at Yildiz Technical University, Istanbul, Turkey
59: Also at Texas A&M University at Qatar, Doha, Qatar
60: Also at Kyungpook National University, Daegu, Korea

Isomeric decay spectroscopy of the ^{217}Bi isotope

A. Gottardo,[1,2,*] J. J. Valiente-Dobón,[1] G. Benzoni,[3] S. Lunardi,[2,4] A. Gadea,[5] A. Algora,[5,6] N. Al-Dahan,[7] G. de Angelis,[1] Y. Ayyad,[8] D. Bazzacco,[4] J. Benlliure,[8] P. Boutachkov,[9] M. Bowry,[7] A. Bracco,[3,10] A. M. Bruce,[11] M. Bunce,[11] F. Camera,[3,10] E. Casarejos,[12] M. L. Cortes,[9] F. C. L. Crespi,[3,10] A. Corsi,[3,10] A. M. Denis Bacelar,[11] A. Y. Deo,[7,13] C. Domingo-Pardo,[9] M. Doncel,[14] T. Engert,[9] K. Eppinger,[15] G. F. Farrelly,[7] F. Farinon,[9] E. Farnea,[4] H. Geissel,[9] J. Gerl,[9] N. Goel,[9] M. Górska,[9] J. Grebosz,[16] E. Gregor,[9] T. Habermann,[9] R. Hoischen,[9,17] R. Janik,[18] P. R. John,[2,4] S. Klupp,[15] I. Kojouharov,[9] N. Kurz,[9] S. M. Lenzi,[2,4] S. Leoni,[3,10] S. Mandal,[19] R. Menegazzo,[4] D. Mengoni,[4] B. Million,[3] V. Modamio,[1] A. I. Morales,[3] D. R. Napoli,[1] F. Naqvi,[9,20] R. Nicolini,[3,10] C. Nociforo,[9] M. Pfützner,[21] S. Pietri,[9] Zs. Podolyák,[7] A. Prochazka,[9] W. Prokopowicz,[9] F. Recchia,[4] P. H. Regan,[7] M. W. Reed,[7] D. Rudolph,[17] E. Sahin,[1] H. Schaffner,[9] A. Sharma,[9] B. Sitar,[18] D. Siwal,[19] K. Steiger,[15] P. Strmen,[18] T. P. D. Swan,[7] I. Szarka,[18] C. A. Ur,[4] P. M. Walker,[7] H. Weick,[9] O. Wieland,[3] and H-J. Wollersheim[9]

[1]*Istituto Nazionale di Fisica Nucleare, Laboratori Nazionali di Legnaro, 35020 Legnaro, Italy*
[2]*Dipartimento di Fisica e Astronomia dell'Università degli Studi di Padova, 35131 Padova, Italy*
[3]*Istituto Nazionale di Fisica Nucleare, Sezione di Milano, 20133 Milano, Italy*
[4]*Istituto Nazionale di Fisica Nucleare, Sezione di Padova, 35131 Padova, Italy*
[5]*Instituto de Física Corpuscular, CSIC–Universitat de València, E-46980 València, Spain*
[6]*Institute of Nuclear Research of the Hungarian Academy of Sciences, 4026 Debrecen, Hungary*
[7]*Department of Physics, University of Surrey, Guildford, GU2 7XH, United Kingdom*
[8]*Universidade de Santiago de Compostela, E-175706 Santiago de Compostela, Spain*
[9]*GSI Helmholtzzentrum für Schwerionenforschung, D-64291 Darmstadt, Germany*
[10]*Dipartimento di Fisica dell'Università degli Studi di Milano, 20133 Milano, Italy*
[11]*School of Computing, Engineering and Mathematics, University of Brighton, Brighton, BN2 4GJ, United Kingdom*
[12]*EEI, Universidade de Vigo, E-36310 Vigo, Spain*
[13]*Department of Physics, Indian Institute of Technology Roorkee, Roorkee 247667, India*
[14]*Grupo de Física Nuclear, Universidad de Salamanca, E-37008 Salamanca, Spain*
[15]*Physik Department, Technische Universität München, D-85748 Garching, Germany*
[16]*Niewodniczanski Institute of Nuclear Physics, Polish Academy of Science, PL-31-342 Krakow, Poland*
[17]*Department of Physics, Lund University, S-22100 Lund, Sweden*
[18]*Faculty of Mathematics and Physics, Comenius University, 84215 Bratislava, Slovakia*
[19]*Department of Physics and Astrophysics, University of Delhi, Delhi 110007, India*
[20]*Institut für Kernphysik, Universität zu Köln, D-50937 Köln, Germany*
[21]*Faculty of Physics, University of Warsaw, PL-00681 Warsaw, Poland*

(Received 5 June 2014; revised manuscript received 14 August 2014; published 23 September 2014)

The structure of the neutron-rich bismuth isotope ^{217}Bi has been studied for the first time. The fragmentation of a primary ^{238}U beam at the FRS-RISING setup at GSI was exploited to perform γ-decay spectroscopy, since μs isomeric states were expected in this nucleus. Gamma rays following the decay of a $t_{1/2} = 3\ \mu s$ isomer were observed, allowing one to establish the low-lying structure of ^{217}Bi. The level energies and the reduced electric quadrupole transition probability $B(E2)$ from the isomeric state are compared to large-scale shell-model calculations.

DOI: 10.1103/PhysRevC.90.034317 PACS number(s): 23.35.+g, 21.10.Tg, 23.20.−g, 27.80.+w

I. INTRODUCTION

The study of nuclei far from stability is a major research field in modern nuclear physics, a field that has grown substantially with the advent of radioactive ion beams. Various regions of the nuclide chart have been explored with stable beams using mainly fusion-evaporation, deep-inelastic, or fission reactions. However, the neutron-rich isotopes around lead, $Z = 82$, have always been difficult to populate with the aforementioned reactions. In the last fifteen years their study has been made gradually possible by the use of fragmentation reactions combined with in-flight mass separators and advanced setups for decay spectroscopy. For example, the fragmentation of a uranium beam was used to produce ^{212}Pb and ^{211}Bi and measure their isomeric decay [1]. Similarly, the adjacent elements beyond $N = 126$ and below $Z = 82$, such as thallium and mercury, have been studied [2,3]. For the elements beyond $N = 126$ but well above $Z = 82$ the situation is very different, as they can be populated with comparatively large cross sections with spallation or fragmentation reactions on uranium. The α decay from these heavy isotopes can also populate lighter nuclei toward the lead region, enabling their spectroscopic study. However, the bismuth isotopes, one

*andrea.gottardo@lnl.infn.it; present address: Institut de Physique Nucléaire, CNRS/IN2P3, and Université Paris Sud, Orsay, 91406, France.

proton above lead, are not all reachable via decay of easy-to-produce heavy nuclei. The ^{211}Bi isotope has been studied via transfer and fragmentation reactions [1,4,5] and via the β and α decay of ^{211}Pb and ^{215}At, respectively [6,7], leading to the discovery of two isomeric states in the same decay sequence. The ^{213}Bi nucleus has also been studied by α decay of ^{217}At, and its first excited state, $I^\pi = 13/2^-$, was observed [8]. A long-lived isomer has recently been observed in ^{213}Bi, produced via ^{238}U fragmentation, using the technique of mass measurement in a storage ring [9]. Besides ^{211}Bi, the only other known isomeric state in the neutron-rich odd-even bismuth isotopes is in ^{215}Bi, six neutrons above $N = 126$, which was populated with a spallation reaction at ISOLDE [10]. Such reactions at ISOLDE were also successfully employed for the production of ^{215}Pb [11] and ^{218}Bi [12].

Recent improvements in experimental devices and beam intensities presently allow exploring more extensively the exotic neutron-rich nuclei in this region, via fragmentation reactions from a ^{238}U beam [13]. For example, the neutron-rich lead isotopes were studied, by taking advantage of long-lived (μs range) 8^+ seniority isomers, predicted by theory and indeed identified up to ^{216}Pb [13]. Nearby isotopes were also effectively populated for the first time, up to mass number 219 for the bismuth nuclei and to mass 210 for the mercury isotopes [14–16].

In more detail, in this mass region neutrons are filling the $2g_{9/2}$ shell beyond the $N = 126$ shell closure, and this gives rise in the even-even lead isotopes to a low-lying level structure which agrees with the predictions of the seniority scheme [13]. A very basic expectation is that the level structure of $^{211-217}$Bi follows the same pattern, since the unpaired proton outside the $Z = 82$ shell should couple with the excited levels of the corresponding even-even lead core. The situation can be complicated by the fact that the coupling gives rise to a multiplet of states with different spins, which can allow the decay of the seniority isomer to proceed through several branchings. It is also possible that the high-spin members of a multiplet lower the energy, thus creating spin traps with long half-lives ($t_{1/2} \sim$ ms). Experimentally, the two known nuclei ^{211,215}Bi have basically the same low-spin structure [4,10], apart from a level inversion at high spin that forms the measured yrast trap in ^{215}Bi [10]. The long-lived isomer observed in ^{213}Bi is probably also coming from a level inversion. Knowledge of the ^{217}Bi nucleus, which is the object of the present study, is limited to its ground state, which β^- decays to excited states of ^{217}Po with a half-life of 92(3) s [17]. The spin and parity of the ground state are not known but from systematics one can safely assume that it is $9/2^-$, due to the occupation by the 83rd proton of the $h_{9/2}$ single-particle state.

The present paper, which reports the first spectroscopic study of the neutron-rich nucleus ^{217}Bi, is organized as follows. In the first section the experimental setup is described in detail. The second section provides the results from ion-mass identification and γ spectroscopy. The final section deals with the theoretical interpretation of the observed level scheme, in the framework provided by shell-model calculations and by taking into account the recent results on effective three-body forces in lead nuclei [13].

II. EXPERIMENTAL SETUP

The results of this work have been obtained by exploiting the advanced features of the state-of-the-art FRS-RISING setup [18–21] and the UNILAC-SIS-18 accelerator facilities at GSI by using a 1 GeV/A ^{238}U beam with an intensity of around 1.5×10^9 ions/spill. The ∼1-s spills were separated by a ∼2-s period without a beam. The uranium ions were fragmented on a 2.5 g/cm^2 Be target, followed by a 223 mg/cm^2 Nb stripper. The reaction products were separated and identified in mass and atomic number with the double-stage magnetic spectrometer FRS [18]. This is a mass spectrometer suitable for discriminating the different magnetic rigidities of relativistic beams, from light to heavy ions. The information gathered from its detectors (see later) allows one to unambiguously identify masses in the heavy region of interest ($A \sim 210$–220). The first particle detectors along the spectrometer were located at the second focal plane, where different charge states from the primary beam as well as other heavy ions can arrive, since their magnetic rigidity is similar to one of the isotopes of interest. These detectors cannot sustain the resulting high counting rate (∼10^8 Hz) coming from the aforementioned contaminations. Therefore, a homogenous 2 g/cm^2 Al degrader was placed after the first dipole in order to exclude the heavy fragments above polonium from the acceptance of the FRS. The wedge-shaped Al degrader at the intermediate focal plane, after the second dipole, had a thickness of 758 mg/cm^2, and its angle was set to produce a monochromatic beam.

The identification in magnetic rigidity ($B\rho$) is achieved through focal-plane position measurements with respect to the position of a beam with a well-known $B\rho$. The plastic scintillators at the intermediate and final focal planes allow extracting the time of flight (TOF). The mass-to-charge ratio (A/q) of the fragments is calculated from the TOF and the $B\rho$, measured on an event-by-event basis. The atomic number of the fragments is obtained from two ionization chambers placed in the final focal plane. Finally, the comparison of the $B\rho$ before and after the Al wedge-shaped degrader allows one to discriminate a possible change in the ion charge state. These measurements are sufficient to provide a complete identification of the isotopes event by event. Figure 1 shows a typical identification plot obtained. The different isotopes are clearly separated in both Z and A/q ratio (or better A/Z), since only the fully stripped ions were selected.

At the final focal plane, the ions were slowed down in a thick Al degrader in order to reduce the energy of the fragments of interest before they were implanted in a double-sided silicon-strip (DSSSD) detector system comprising three layers, each with three DSSSD pads [21,22]. The monochromatic beam ensured that the implantation depth in the active stopper was the same for all the fragments of a certain A/q and Z. The DSSSD detector system was surrounded by the RISING γ spectrometer, consisting of 105 germanium crystals arranged in 15 clusters with 7 crystals each [19,20]. The full-energy γ-ray peak detection efficiency of the array was measured to be 15% at 662 keV [19]. In the present experiment, due to the presence of the active stopper with its casing, the absolute efficiency of the array was ∼13% at 662 keV. The time correlation between the γ rays and the ions detected with the

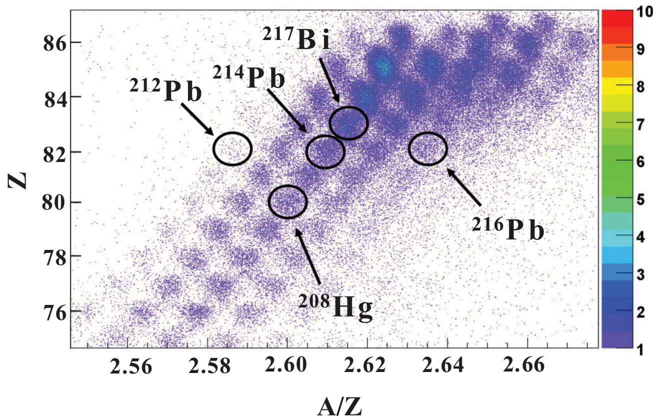

FIG. 1. (Color online) Ion identification plot at the final focal plane of the FRS. The ^{217}Bi products have been circled, as have some neighboring nuclei to provide a reference.

active stopper allowed one to perform at the same time isomer spectroscopy and β-delayed γ-ray spectroscopy [14,15].

III. EXPERIMENTAL RESULTS

Figure 2 shows the γ-ray spectrum following the detected isomeric decay of ^{217}Bi. Four transitions are clearly visible and their intensities are reported in Table I. The peak at 77 keV corresponds to the K_α x rays from bismuth.

Figure 3 presents the results of $\gamma\gamma$ coincidence analysis. The γ rays at 744, 492, and 200 keV are in mutual coincidence, and a coincidence relationship is also evident between the 744- and the 685-keV lines. As already outlined above, one can expect that the structure of bismuth nuclei is determined by the coupling of the single proton outside the $Z = 82$ shell closure to the excited levels in ^{216}Pb. Since the lowest single-proton orbital above $Z = 82$ is $h_{9/2}$, one expects that the low-lying levels in ^{217}Bi have the configuration $\pi h_{9/2} \otimes \nu g_{9/2}^{2}{}^{(0^+\ldots8^+)}$. The isomeric state should have a spin-parity $25/2^-$, with a $\pi h_{9/2} \otimes (\nu 2g_{9/2})^{8^+}$ configuration, corresponding to the 8^+ isomer of lead nuclei. Therefore, following the systematics from lighter odd-even bismuth isotopes, the 200-, 492-, and 744-keV γ rays are assigned to the cascade $21/2^- \rightarrow 17/2^- \rightarrow 13/2^- \rightarrow 9/2^-$. The $25/2^- \rightarrow 21/2^-$ transition is expected to have a low energy (in ^{211}Bi it is only 30 keV), which makes it highly converted and unfeasible to measure with the present experimental setup. The 685-keV γ ray is in coincidence only with the 744-keV transition (see Fig. 3). It is hence assigned to a decay from a state located 685 keV above the $13/2^-$ level and 7 keV lower than the $21/2^-$ state. Figure 4 shows the exponential χ^2 fit to the decay curves of the four transitions. Within errors, the four fits give the same decay constant, which suggests that the four transitions might be following the decay of the same isomer, namely, the expected $25/2^-$ state. Moreover, since one cannot exclude completely that the 685-keV γ ray follows the decay of a second isomer (with a very similar half-life) we have preferred to extract the half-life of the $25/2^-$ isomer from the error-weighted average of the decay constants of the 200- and 492-keV transitions. The isomer half-life deduced in this way is 3.0 ± 0.2 μs.

TABLE I. Areas, intensities corrected for efficiency and internal conversion [23], and $t_{1/2}$ of the isomeric state gated on the different γ-ray transitions measured in ^{217}Bi.

E_γ (keV)	Area	Intensity (%)	$t_{1/2}$ (μs)
200	401 (38)	92 (9)	3.1 (2)
492	331 (32)	87 (8)	2.9 (2)
685	45 (13)	14 (4)	3.3 (7)
744	307 (35)	100 (11)	2.8 (1)

The characteristic K_α x rays from bismuth at 77 keV are observed with an intensity compatible with the internal conversion of the other four γ rays. Given that the binding energy of the K electrons in bismuth is 90.5 keV, this means that the transition directly depopulating the isomer must be below $\sim$90 keV. From systematics in bismuth, lead, and mercury isotopes [2,13], we assume a lower limit

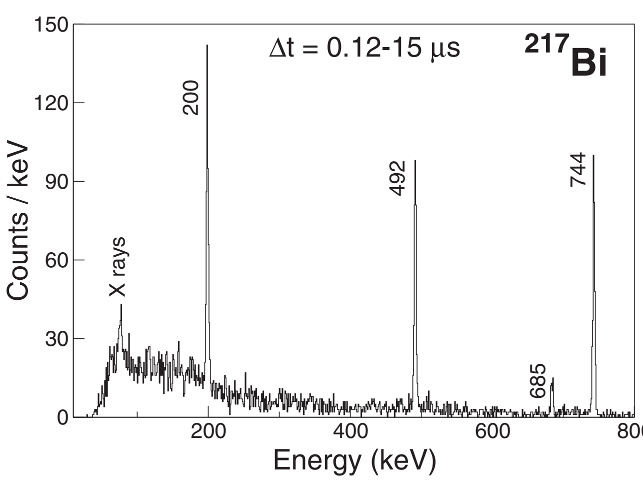

FIG. 2. Gamma-ray spectrum from the decay of the isomeric state in ^{217}Bi. The spectrum has been obtained by gating on the time window 0.12–15 μs.

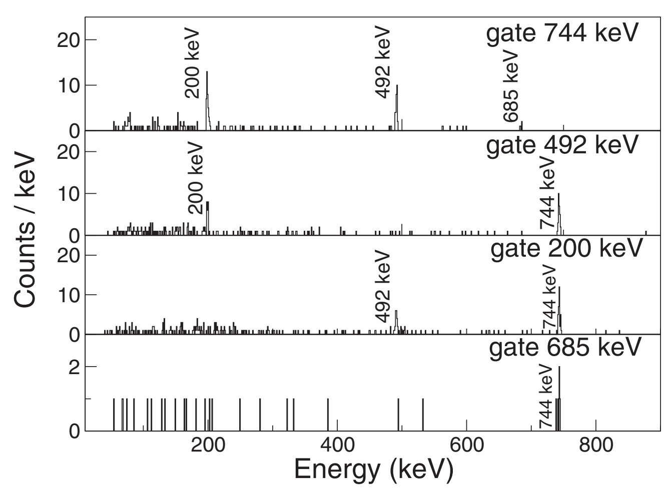

FIG. 3. Gamma-ray prompt coincidence spectra for the decay from the isomeric state in ^{217}Bi, with gates on the four transitions following the isomer.

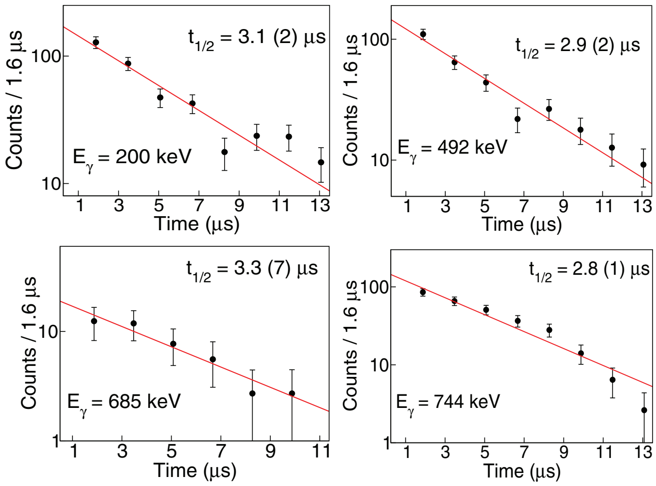

FIG. 4. (Color online) Time distributions and exponential fits (in red) for the 200-, 492-, 685-, and 744-keV transitions assigned to the ^{217}Bi nucleus.

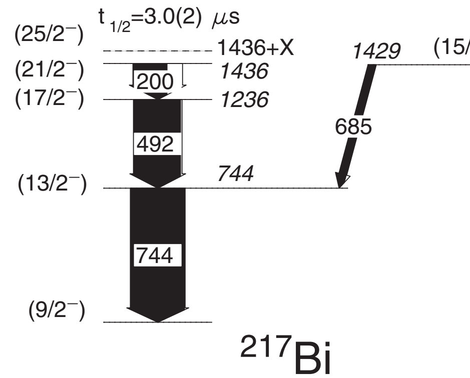

FIG. 5. Level scheme of ^{217}Bi deduced from the present data.

of 20 keV for this transition. Although the energy of the $25/2^- \rightarrow 21/2^-$ transition is not known, the fact that it has to be between 20 and 90 keV implies that it is highly converted, and consequently the energy dependence of the $E2$ transition rate is compensated by the opposite energy dependence of the total $E2$ conversion coefficient [23]. As a result, the $B(E2)$ value from the isomeric state is only weakly dependent on the transition energy, making it possible to have an estimate of the $B(E2)$ strength that ranges from $6.2 \pm 0.3\ e^2\,\mathrm{fm}^4$ for 20 keV to $4.4 \pm 0.2\ e^2\,\mathrm{fm}^4$ for 90 keV.

For the state decaying via the 685-keV γ ray to the $13/2^-$ level in ^{217}Bi, the most straightforward assumption from the measured decay constant is that it belongs to a second decay branch of the same isomer feeding the other states. The γ rays connecting the isomer to this level may not be observed due to their low energy. Given that the x rays observed are compatible with the internal conversion of the four transitions, the energy of these connecting transitions has to be below 90 keV. The most probable scenario is that the 685-keV transition has an $M1$ or $E2$ multipolarity, leading to a $15/2^-$ or $17/2^-$ assignment for the new state at 1429 keV. Such an assignment would imply at least two (or three if the spin is $15/2^-$) transitions connecting the $25/2^-$ isomer to the 1429-keV state. All such transitions will be well below 90 keV, of $E2$ or $M1$ character, and thus almost completely converted. The new states will be isomeric, and the combination of the $25/2^-$ isomer half-life with these intermediate states should lead to the measured half-life of the 1429-keV level. This is compatible only with half-lives of the order of 100 ns or shorter for the intermediate states, which are inside the range expected from systematics in the decay sequence of a seniority isomer of this region [5]. If the 1429-keV state is fed by the $25/2^-$ seniority isomer, this branching ratio of 14(4)% must be considered when estimating $B(E2; 25/2^- \rightarrow 21/2^-)$, resulting in a value which ranges from 5.6 ± 0.3 to $3.6 \pm 0.2\ e^2\,\mathrm{fm}^4$. Nevertheless, one cannot exclude that a second isomer exists in ^{217}Bi and one possibility could be that the 1429-keV state itself is isomeric. An isomeric transition of 685 keV would be well compatible with an $E3$ multipolarity, thus giving a $19/2^+$ isomeric nature for the 1429-keV state. In view of systematics, it is highly unlikely that this state is a second isomer located at such low energy.

Figure 5 shows the level scheme of ^{217}Bi proposed from the present work. Considering the most likely scenario of a second decay branch from the seniority isomer, the two possible spin-parity assignments are indicated for the 1429-keV state, while the $19/2^+$ hypothesis is disregarded.

IV. THEORETICAL DISCUSSION

The new states observed in ^{217}Bi should be formed by coupling a valence proton in the $h_{9/2}$ orbital to the core-excited states in ^{216}Pb. Since the excited states up to 8^+ in ^{216}Pb are understood within the seniority scheme $(2g_{9/2})^2$, the same structure is expected in ^{217}Bi with the yrast states forming the sequence $9/2^-$, $13/2^-$, $17/2^-$, $21/2^-$, and $25/2^-$. Figure 6 shows, for the $^{211-217}$Bi nuclei, the results of shell-model calculations with the Kuo-Herling (KH) interaction [24] compared with the experimentally known level schemes. The valence space to describe these nuclei is constituted by the neutron shells $(g_{9/2}i_{11/2}d_{3/2}d_{5/2}g_{7/2}s_{1/2}j_{15/2})^8$ and by the proton shells $(h_{9/2}f_{7/2}i_{13/2}f_{5/2}p_{3/2}p_{1/2})^1$. A full calculation in this space is feasible, using state-of-the-art large-scale shell-model codes such as ANTOINE or NATHAN [25,26], only up to ^{213}Bi. For ^{215,217}Bi a reduction in the model space is needed. The calculations for these latter two nuclei were performed by restricting the proton valence space to $h_{9/2}f_{7/2}$ and by allowing up to six neutrons in the $i_{11/2}$ shell and up to four neutrons in the $j_{15/2}$ shell, while no restriction is given to the occupancy of the other neutron orbitals $g_{9/2}$, $d_{3/2}$, $d_{5/2}$, $g_{7/2}$, and $s_{1/2}$. The fact that the energy of the first excited state, $13/2^-$, is well reproduced shows that, even with this truncation, the pair scattering from the $\nu g_{9/2}$ orbital to the shells above is properly described.

The agreement between the calculated and experimental level energies is very good, being of the order of 100 keV (see Fig. 6). The analysis of the nuclear wave function confirms the above-mentioned simple scheme where the single proton in the $h_{9/2}$ orbital couples to the excited, seniority-two, neutron states of the corresponding even-even Pb isotopes.

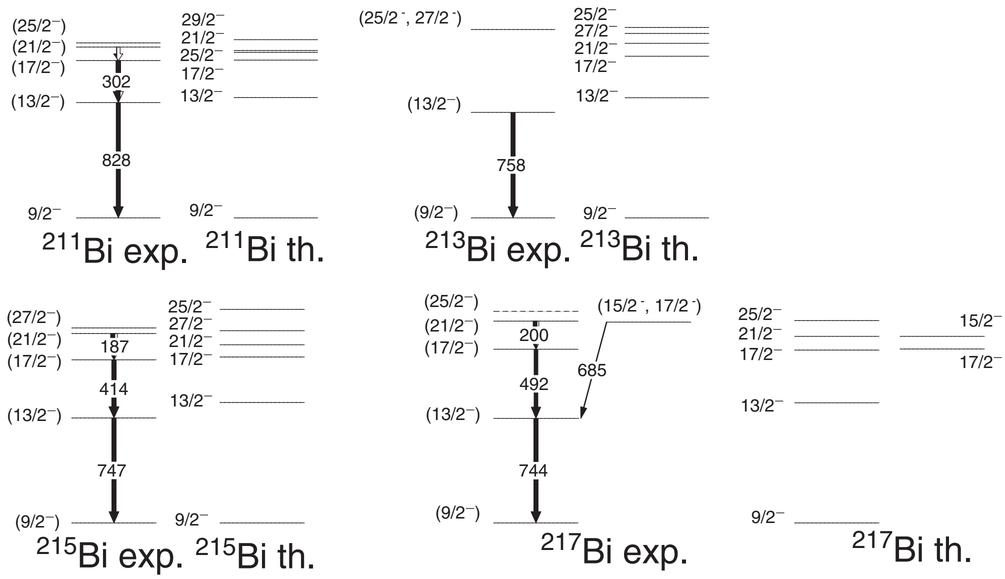

FIG. 6. Experimental and calculated partial level schemes for the odd-mass bismuth isotopes. The calculations were performed using the KH interaction. The ^{217}Bi level scheme results are from the present work. The experimental data are taken from Refs. [4,8–10].

Concerning the 1429-keV level in ^{217}Bi, for which we propose a $15/2^-$ or $17/2^-$ assignment, the shell-model calculations predict both a $15/2^-$ and a $17/2^-$ state close by in energy. A sensitive test of the nuclear wave function is given by the $B(E2)$ values of the transitions depopulating the isomeric states. The half-lives of the $25/2^-$ levels in ^{211}Bi and ^{217}Bi are 1.4 ± 0.3 μs [1] and 3.0 ± 0.2 μs (this work), which yield a reduced transition probability $B(E2)$ of 8(2) $e^2\,\mathrm{fm}^4$ for ^{211}Bi and from 6.2 ± 0.3 to 4.4 ± 0.2 $e^2\,\mathrm{fm}^4$ for ^{217}Bi, as discussed before. The $25/2^-$ seniority isomer is not known in ^{213}Bi, while in ^{215}Bi the presence of the $27/2^-$ spin trap does not allow a seniority isomer. It is worth noting that the spin inversion in ^{215}Bi between $25/2^-$ and $27/2^-$ is well reproduced by shell-model calculations, as shown in Fig. 6. We have calculated the $B(E2)$ values using the same valence space and interaction already employed for the level energies and adopting the standard effective charges for this region: $e_\pi = 1.5e$ and $e_\nu = 0.8e$ [24]. The results are 92 and 1.0 $e^2\,\mathrm{fm}^4$ for ^{211}Bi and ^{217}Bi, respectively. The discrepancy with the experimental results is large. What is most disturbing is that, while the experimental $B(E2)$ values are close to each other, as happens for the corresponding $B(E2)$ values in the core nuclei ^{210}Pb and ^{216}Pb, the theoretical $B(E2)$ values, which for the lead cores were comparable, differ here by a factor of 100. As mentioned above, for the ^{217}Bi calculations a restricted shell-model space had to be used and this could be a possible cause of the large difference in the calculated $B(E2)$ values. With the intent to further understand this behavior, we have applied to the Bi isotopes the same approach successfully adopted in Ref. [13], where effective three-body forces have been included. In the bismuth case, however, since there is a proton in the valence space, it is difficult to perform a diagonalization in a space which includes all the neutron (and proton) shells as in Ref. [13]. On the other hand, it was shown that the relevant renormalization for the quadrupole operator is provided by particle-hole excitations across the $\Delta J = 2, 0\hbar\omega$ shells $\nu i_{13/2}$–$\nu g_{9/2}$ and $\pi h_{11/2}$–$\pi f_{7/2}$, partners in the quasi-SU(3) scheme [13]. They are responsible for quadrupole coherence [27] and their inclusion allows one to evaluate the possible effect of effective three-body forces.

For the bismuth isotopes we have then performed the calculations including only these relevant shells, plus the $\pi h_{9/2}$ orbital occupied by the unpaired proton, where the Kahana-Lee-Scott (KLS) interaction and the effective charges $e_\pi \sim 1.5e$ and $e_\nu \sim 0.5e$ have been used. The calculated level energies are in agreement with the ones obtained with the full space once the paring matrix elements of the $\nu g_{9/2}$ shell are renormalized to reproduce the energy of the $13/2^+$ state. The $B(E2)$ strengths calculated are 38 and 28 $e^2\,\mathrm{fm}^4$ for ^{211}Bi and ^{217}Bi, respectively. The disagreement between the measured and the calculated $B(E2)$ values remains large for both ^{211}Bi and ^{217}Bi. However, with the inclusion of effective three-body forces the calculated $B(E2)$ values for ^{211}Bi and ^{217}Bi become similar, as they are experimentally. The fact that the ratio between the ^{211}Bi and ^{217}Bi$B(E2)$ values is reproduced is significant since it shows that the inclusion of core excitations, equivalent to considering effective three-body forces, is restoring the symmetry in the $B(E2)$ values relatively. What remains to be understood is the discrepancy of the absolute value, which in both nuclei is experimentally lower by a factor of 4–5. Explanations for this behavior are not straightforward and may be found when more refined shell-model calculations in such large spaces become possible or when more dedicated experiments are performed to look into this problem.

V. CONCLUSIONS

The present paper reports on the first results on the excited states in the neutron-rich nucleus ^{217}Bi. The study of this exotic isotope was made possible by the presence of isomeric states, which allowed one to perform decay γ spectroscopy using a radioactive beam produced from the uranium fragmentation. Four transitions were assigned to the decay from an isomeric state with a half-life of 3.0 ± 0.2 μs. The expected decay branch from the seniority isomer was observed, but there is evidence for another decay branch, probably from the same isomer. The derived level scheme was compared with systematics from lighter isotopes, as well as state-of-the-art shell-model calculations. Whereas the level energies of ^{217}Bi as well as of the other lighter odd-even Bi isotopes are well reproduced, the same calculations fail completely to predict the experimental $B(E2)$ values from the $25/2^-$ seniority isomers in ^{211}Bi and ^{217}Bi. When effective three-body forces are included, the correct ratio between the experimental $B(E2)$ values is restored but not the absolute value. These experiments on heavy exotic nuclei are still at the limits in terms of statistics and sensitivity and may gain a lot from the expected improvements of experimental setups and beam intensities. Finally, from the theoretical point in view, in order to overcome the present difficulties, developments of codes able to perform a diagonalization in the full valence space are mandatory.

ACKNOWLEDGMENTS

The work of the GSI accelerator staff is acknowledged. AG, MD, and EF acknowledge the support of Istituto Nazionale di Fisica Nucleare (INFN), Italy, and MICINN, Spain, through the AIC10-D-000568 action. AG has been partially supported by MICINN, Spain, and the Generalitat Valenciana, Spain, under Grants No. FPA2008-06419 and No. PROMETEO/2010/101. The support of the UK STFC and of the DFG(EXC 153) is also acknowledged.

[1] M. Pfützner *et al.*, Phys. Lett. B **444**, 32 (1998).
[2] N. Al-Dahan *et al.*, Phys. Rev. C **80**, 061302(R) (2009).
[3] S. J. Steer *et al.*, Phys. Rev. C **78**, 061302(R) (2008).
[4] G. J. Lane *et al.*, Nucl. Phys. A **682**, 71 (2001).
[5] K. H. Maier *et al.*, Z. Phys. A **332**, 263 (1989).
[6] M. M. Hindi, E. G. Adelberger, S. E. Kellogg, and T. Murakami, Phys. Rev. C **38**, 1370 (1988).
[7] J. D. Bowman, R. E. Eppley, and E. K. Hyde, Phys. Rev. C **25**, 941 (1982).
[8] V. G. Chumin *et al.*, Z. Phys. A **358**, 33 (1997).
[9] L. Chen *et al.*, Nucl. Phys. A **882**, 71 (2012).
[10] J. Kurpeta *et al.*, Eur. Phys. J. A **18**, 31 (2003).
[11] H. DeWitte *et al.*, Phys. Rev. C **87**, 067303 (2013).
[12] H. DeWitte *et al.*, Phys. Rev. C **69**, 044305 (2004).
[13] A. Gottardo *et al.*, Phys. Rev. Lett. **109**, 162502 (2012).
[14] G. Benzoni *et al.*, Phys. Lett. B **715**, 293 (2012).
[15] A. I. Morales *et al.*, Phys. Rev. C **89**, 014324 (2014).
[16] A. Gottardo *et al.*, Phys. Lett. B **725**, 292 (2013).
[17] K. Rykaczewski *et al.*, AIP Conf. Proc. **455**, 581 (1998).
[18] H. Geissel *et al.*, Nucl. Instrum. Methods B **70**, 286 (1992).
[19] S. Pietri *et al.*, Nucl. Instrum. Methods B **261**, 1079 (2007).
[20] P. H. Regan *et al.*, Nucl. Phys. A **787**, 491 (2007).
[21] R. Kumar *et al.*, Nucl. Instrum. Methods A **598**, 754 (2009).
[22] P. H. Regan *et al.*, Int. J. Mod. Phys. E **17**, 8 (2008).
[23] T. Kibédi *et al.*, Nucl. Instrum. Methods A **589**, 202 (2008).
[24] E. K. Warburton and B. A. Brown, Phys. Rev. C **43**, 602 (1991).
[25] E. Caurier and F. Nowacki, Acta Phys. Pol. B **30**, 705 (1999).
[26] E. Caurier, G. Martinez-Pinedo, F. Nowacki, A. Poves, J. Retamosa, and A. P. Zuker, Phys. Rev. C **59**, 2033 (1999).
[27] E. Caurier *et al.*, Rev. Mod Phys. **77**, 427 (2005).

Influence of neutron transfer channels on fusion enhancement in sub-barrier region

Khushboo[1,⋆], *S.* Mandal[1], *N.* Madhavan[2], *S.* Muralithar[2], *J. J.* Das[2,⋆⋆], *S.* Nath[2], *A.* Jhingan[2], *J.* Gehlot[2], *B.* Behera[3], *S.* Verma[1], *H.* Singh[4], *S.* Kalkal[1,⋆⋆⋆], and *R.* Singh[1]

[1]*Department of Physics and Astrophysics, University of Delhi, Delhi-110007, India*
[2]*Inter University Accelerator Centre, Aruna Asaf Ali Marg, New Delhi-110067, India*
[3]*Department of Physics, Panjab University, Chandigarh-160014, India*
[4]*Department of Physics, Kurukshetra University, Kurukshetra-136119, India*

Abstract. Fusion cross-section measurements were performed for system ^{40}Ca + ^{70}Zn around the Coulomb barrier energies using Heavy Ion Reaction Analyzer (HIRA). The observed enhancement in experimental fusion cross-sections was investigated via coupled-channels formalism. The coupling of inelastic excitations alone could not reproduce the experimental data, however, the effect of octupole state of the projectile was observed to be significant. The multi-neutron positive Q-value transfer channels were also included in the calculations using semi-classical model. It was observed that two neutrons pick-up channel gave a major contribution to the fusion enhancement and successfully reproduce the experimental data at above as well as below barrier energies. The coupling of more than two neutrons transfer could not give any significant enhancement to sub-barrier fusion.

1 Introduction

The fusion reaction is an extensively studied phenomenon at and near the Coulomb barrier. A numerous investigations were performed in past years with various systems which showed a large enhancement of fusion cross-sections in comparison with theoretical predictions at sub-barrier energies [1]. It was demonstrated under the framework of coupled-channels (CC) formalism that fusion is influenced by inelastic excitations of colliding nuclei and transfer of neutrons [2]. The effect of inelastic excitations were well understood with the available theoretical models. However, due to the complicated mechanism involved in coupling the transfer channels in theoretical models, the role of multi-neutron transfer on fusion was not explored in detail.

The influence of transfer on fusion was noticed in systems having a positive Q-value for neutron transfer channels [3–9]. However, in few recent work, in spite of positive Q-values, no effect of the transfer channel on fusion enhancement was observed [10–12]. Apart from this, it was demonstrated in a literature that only outermost neutrons (up to two neutrons) of nuclei give a significant contribution to the fusion enhancement [13]. The importance of two neutrons pick-up channel was also highlighted for system ^{40}Ca + ^{64}Ni whose experimental data was well reproduced by coupling with two neutron transfer. This system has positive Q-value for up to six neutrons pick-up channels [14]. Further, the effect of pair transfer on fusion enhancement was reported recently by Stefanini *et al.* [15, 16] for ^{40}Ca + ^{96}Zr system where the fusion cross-sections were measured at deep sub-barrier energies. No fusion hindrance was observed in this system. It was pointed out that strong transfer couplings may be the reason for this observation. Beside these observations, the importance of multi-neutron transfer on sub-barrier fusion was also indicated in an article [5].

Considering all the above observations, in order to explore the effect of transfer channels on fusion enhancement, ^{40}Ca + ^{70}Zn system was selected for the present study. ^{40}Ca is a doubly magic nucleus, however, octupole state was shown to be an important state for ^{40}Ca [17]. The system has positive Q-value for seven neutrons pick-up channels (2n-8n), therefore, importance of multi-neutron transfer on fusion can be examined with this system. The Q-values for 2n to 8n pick-up channels are 4.14, 1.88, 5.96, 2.31, 4.73, 0.14 and 0.98 MeV respectively.

2 Experiment Details

The fusion cross-sections for ^{40}Ca + ^{70}Zn were measured at Inter University Accelerator Centre (IUAC), New Delhi. A pulsed beam of ^{40}Ca was used to bombard a self-supporting ^{70}Zn target (95% isotopic enrichment) of 670 μg/cm^2 thickness. The measurements were carried out using the Heavy Ion Reaction Analyzer (HIRA) [18] which

⋆e-mail: s12khushboo@gmail.com
⋆⋆Present address: National Superconducting Cyclotron Laboratory (NSCL) 640 South Shaw Lane, Michigan State University, East Lansing, Michigan-48824, USA
⋆⋆⋆Present address: School of Physics and Materials Science, Thapar University, Patiala-147004, India

 DOI: 10.1051/epjconf/201716300029

was kept at zero degree with respect to beam direction with 5 mSr of solid angle acceptance. At the focal plane of HIRA, a Multi-Wire proportional Counter (MWPC) of area 15 × 5 cm^2 was placed followed by segmented Ionization Chamber (IC) of 7.0 × 3.5 cm^2 area and active lengths of 3 cm-5.8 cm-13 cm for detection of evaporation residues (ERs) arriving at the focal plane. During the experiment, MWPC and IC were operated at a pressure of 2 mbar and 30 mbar of isobutane gas respectively. In addition to these detectors, two Silicon Surface Barrier Detectors (SSBD) were kept symmetrically at an angle of 25° on both the sides of incoming beam inside the target chamber. These detectors were used to monitor the beam during experiment and for normalization of fusion cross-sections. A carbon foil of thickness 40 μg/cm^2 was placed 10 cm downstream from the target for equilibration of charge states of ERs. For estimation of HIRA transmission efficiency for ERs, a High Purity Germanium (HPGe) detector was mounted on top of the target chamber at 90° to the beam direction.

The cross-section measurements were performed around the Coulomb barrier from laboratory energies 142 to 106 MeV. The fusion cross-sections were calculated using the yield of evaporation residues (ERs) which were separated from the beam-like particles at the focal plane using energy loss in MWPC versus time of flight (TOF) spectrum [5]. For the cross-section calculations, transmission efficiency of HIRA was estimated experimentally by gamma ray coincidence technique [5] and it was found to be 7.8% at 130 MeV laboratory energy. It was also calculated as 7.6% using Monte-Carlo code TERS [19].

3 Results and Discussion

The experimental fusion cross-sections were extracted and compared with the theoretical calculated cross-sections based on coupled-channels formalism as shown in figure 1. The experimental error in fusion cross-sections includes statistics related error and the error in transmission efficiency. The reported energies are corrected for loss in half thickness of the target. For initial estimation of theoretical fusion cross-sections, Akyuz-Winther (AW) parameterization was employed for Woods-Saxon potential. The AW parameters for the ^{40}Ca + ^{70}Zn system were V_0 = 69.87 MeV, r_0 = 1.18 fm and a_0 = 0.67 fm, which gave barrier parameters as V_b = 76.76 MeV, R_b = 10.48 fm and $\hbar\omega$ = 3.70 fm. The calculations were performed using CCFULL code [20] by considering projectile and target nuclei as a vibrator. To begin with, the coupling was switched off and no coupling fusion excitation function was obtained which underpredicted the experimental cross-sections. Therefore, in order to obtain a good fit to the above barrier experimental data, potential parameters were varied. The new set of parameters gave a slightly lower potential barrier as compared to the barrier obtained with AW parameters (V_b). Using these new set of potential parameters, calculations were performed to estimate the fusion cross-sections with state 3$^-$ (E_{3^-} = 3.74 MeV, β_3 = 0.33) of the projectile. Coupling to this state gave a considerable enhancement to the cross-sections in the above barrier region and overpredicted the data in near barrier region. The new set of potential parameters could not give an appropriate fit to the above and near barrier data with projectile coupling hence, it was decided to use AW parameters for further calculations. After including the projectile octupole (3$^-$) state with AW parameters, the cross-sections were enhanced significantly and a reasonable fit to the above and near barrier fusion cross-sections was obtained as can be seen in figure 1. Whereas, the state 2$^+$ (E_{2^+} = 3.90 MeV, β_2 = 0.123) of ^{40}Ca gave a negligible contribution to the fusion cross-sections. In projectile excitations, 3$^-$ state of ^{40}Ca seems to be an important state.

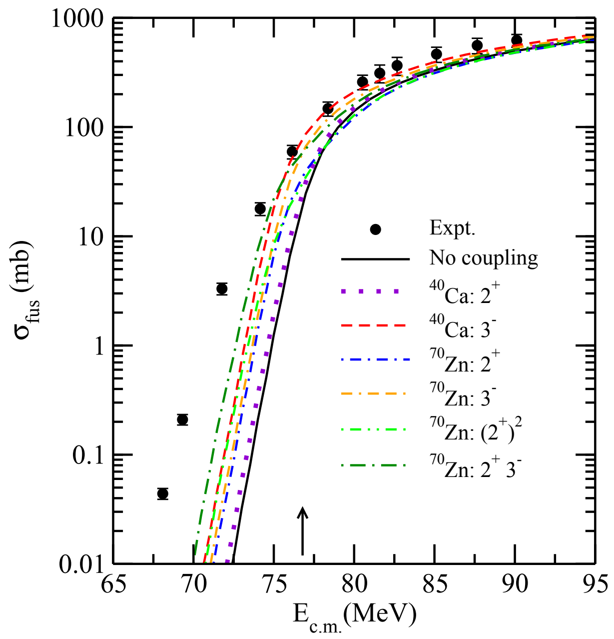

Figure 1. Experimental fusion cross-sections for ^{40}Ca + ^{70}Zn system along with coupled-channels calculations performed with CCFULL code. The arrow at the bottom indicates the position of the barrier.

In case of target excitations, both 2$^+$ (E_{2^+} = 0.88 MeV, β_2 = 0.23) as well as 3$^-$ (E_{3^-} = 2.86 MeV, β_3 = 0.22) states enhanced the cross-sections by a similar amount in below barrier region however, 3$^-$ state gave an additional enhancement in the above barrier region. The multi-phonon and mutual excitations were also taken into consideration in the calculations. The two phonon 2$^+$ state of target further enhanced the cross-sections slightly and the excitation 2$^+$ 3$^-$ gave a considerable enhancement to the cross-sections. When both projectile as well target excitations were considered simultaneously in the calculations, then excitation ^{40}Ca: 3$^-$ and ^{70}Zn: 2$^+$ 3$^-$ overpredicted the data in near barrier region while not explaining the data in sub-barrier region. Whereas, the excitation ^{40}Ca: 3$^-$ and ^{70}Zn: two phonons of 2$^+$ reproduced the data reasonably well in above and near barrier energy region. This is depicted in figure 2.

The inelastic excitations alone could not reproduce the experimental data. This indicates that apart from inelastic excitations, transfer channels may play an important role for ^{40}Ca + ^{70}Zn as Q-value is positive for multi-neutron

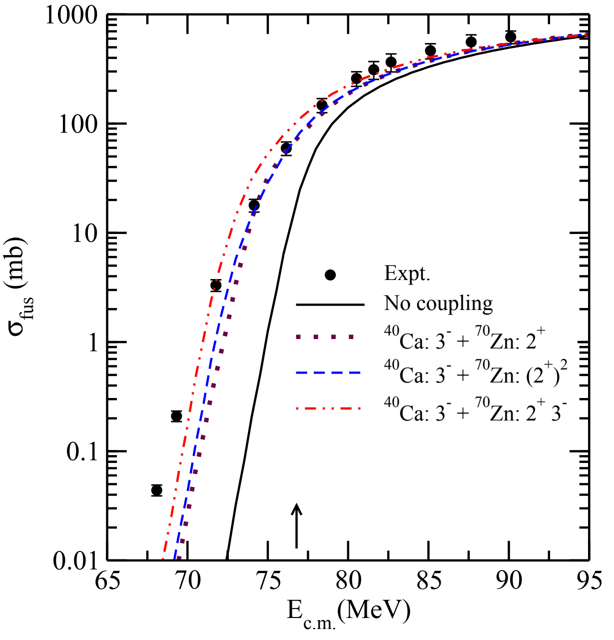

Figure 2. Experimental fusion cross-sections for ^{40}Ca + ^{70}Zn system along with coupled-channels calculations performed with CCFULL code. The combined effect of projectile and target inelastic states are shown with different colored lines (See text). The arrow at the bottom indicates the position of the barrier.

pick-up channels. The code CCFULL considers only one pair of transfer channel between ground states. In order to examine the role of multi-neutron transfer, semi-classical model (empirical coupled-channels, ECC) of Zagrabaev *et al.* [21] was undertaken to perform the calculations through which one can incorporate up to four neutron transfer channels in the calculations on the basis of Q-value. Initially, the fusion excitation function was obtained without coupling of transfer channels as shown in figure 3. After that, neutron pick-up channels were successively added in the calculations. It can be seen that one neutron pick-up channel has negligible effect on fusion enhancement. The two neutron pick-up channel enhanced the sub-barrier cross-sections to a large extent and give an appropriate fit to the entire experimental data. The transfer channels 3n and 4n pick-up could not give any significant enhancement to the cross-sections which implies that the sub-barrier fusion enhancement was mainly due to the two neutron transfer despite the presence of a large number of positive Q-value transfer channels.

A detail investigation is still required to clarify the impact of two or multi-neutron transfer on fusion. The explicit coupling of multi-neutron transfer channels in the theoretical calculations will be advantageous to disentangle the neutron transfer and structure effects on fusion enhancement. The structure of the colliding nuclei may also affect the transfer coupling itself and thereby fusion. The excitation process involved during the re-arrangement of nucleons between colliding partners may influence the dynamics of the sub-barrier fusion process. The presently available exotic ions from radioactive beam facilities opens up a possibility to explore the dynamics of the fusion reactions far away from the stability line where transfer and break up mechanisms may strongly influence the fusion cross-sections around the barrier and in sub-barrier region.

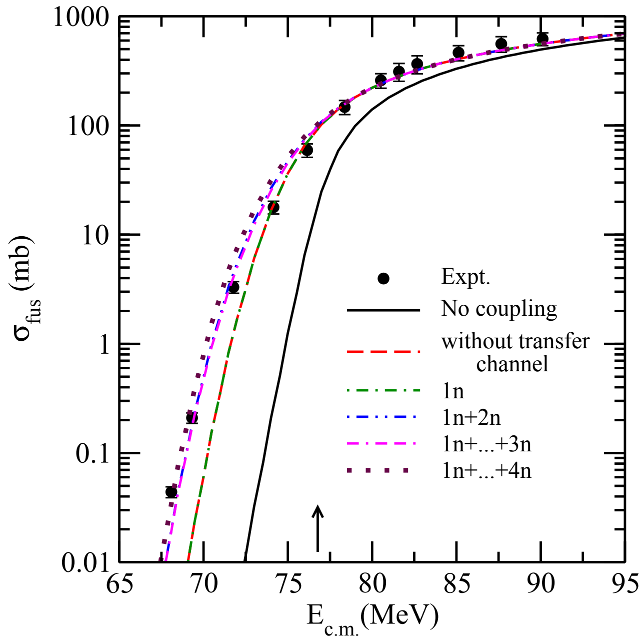

Figure 3. Experimental fusion cross-sections for ^{40}Ca + ^{70}Zn system compared with the theoretical cross-sections obtained using ECC model. The arrow at the bottom indicates the position of the barrier.

4 Summary

Fusion excitation function was measured for the system ^{40}Ca + ^{70}Zn to explore the role of multi-neutron transfer on sub-barrier fusion enhancement. The cross-sections were analyzed within coupled-channels formalism using CCFULL and ECC model. The effect of octupole vibration of ^{40}Ca was found to be major which gave a noticeable enhancement to the cross-sections in the entire energy range. The present results show the importance of transfer channels for explaining the sub-barrier fusion enhancement, however, transfer of only two neutrons was sufficient to reproduce the fusion cross-sections in above and below barrier energy region. It was observed that transfer channels beyond two neutrons have a negligible effect on sub-barrier fusion enhancement indicating the less importance of large number of neutron transfer on sub-barrier fusion.

5 Acknowledgements

We would like to thank Pelletron group of IUAC for providing a good quality of beam throughout the experiment. The authors are extremely thankful to target laboratory of GSI and H. J. Wollersheim for providing the target. We would like to acknowledge the help received from Ranjeet during the experiment. One of the author (Khushboo) would like to thank SERB, Goverment of India for providing international travel grant to attend FUSION17 conference. The financial support of the IUAC research project under UFR-51314 is gratefully acknowledged.

References

[1] M. Dasgupta, D. J. Hinde, N. Rowley, and A. M. Stefanini, Annu. Rev. Nucl. Part. Sci. **48**, 401 (1998)

[2] A. M. Stefanini, D. Ackerman, L. Corradi, J. H. He, G. Montagnoli, S. Beghini, F. Scarlassara, and G. F. Segato, Phys. Rev. C **52**, R1727 (1995)

[3] R. A. Broglia, C. H. Dasso, S. Landowne, and A. Winther, Phys. Rev. C **27**, 2433 (1983)

[4] H. Timmers, D. Ackermann, S. Beghini, L. Corradi, J. He, G. Montagnoli, E. Scarlassara, A. Stefanini, and N. Rowley, Nucl. Phys. A **633**, 421 (1998)

[5] S. Kalkal, S. Mandal, N. Madhavan, E. Prasad, S. Verma, A. Jhingan, R. Sandal, S. Nath, J. Gehlot, B. R. Behera, M. Saxena, S. Goyal, D. Siwal, R. Garg, U. D. Pramanik, S. Kumar, T. Varughese, K. S. Golda, S. Muralithar, A. K. Sinha, and R. Singh, Phys. Rev. C **81**, 044610 (2010)

[6] H. Q. Zhang, C. J. Lin, F. Yang, H. M. Jia, X. X. Xu, Z. D. Wu, F. Jia, S. T. Zhang, Z. H. Liu, A. Richard, and C. Beck, Phys. Rev. C **82**, 054609 (2010)

[7] G. Montagnoli, A. M. Stefanini, H. Esbensen, C. L. Jiang, L. Corradi, S. Courtin, E. Fioretto, A. Goasduff, J. Grebosz, F. Haas, M. Mazzocco, C. Michelagnoli, T. Mijatovic, D. Montanari, C. Parascandolo, K. E. Rehm, F. Scarlassara, S. Szilner, X. D. Tang, and C. A. Ur, Phys. Rev. C **87**, 014611 (2013)

[8] M. Trotta, A. M. Stefanini, L. Corradi, A. Gadea, F. Scarlassara, S. Beghini, and G. Montagnoli, Phys. Rev. C **65**, 011601(R) (2001)

[9] G. Montagnoli, A. M. Stefanini, C. L. Jiang, H. Esbensen, L. Corradi, S. Courtin, E. Fioretto, A. Goasduff, F. Haas, A. F. Kifle, C. Michelagnoli, D. Montanari, T. Mijatovic, K. E. Rehm, R. Silvestri, P. P. Singh, F. Scarlassara, S. Szilner, X. D. Tang, and C. A. Ur, Phys. Rev. C **85**, 024607 (2012)

[10] A. M. Stefanini, G. Montagnoli, F. Scarlassara, C. Jiang, H. Esbensen, E. Fioretto, L. Corradi, B. Back, C. Deibel, B. D. Giovine, J. Greene, H. Henderson, S. Marley, M. Notani, N. Patel, K. Rehm, D. Sewerinyak, X. Tang, C.Ugalde, and S. Zhu, Eur. Phys. J. A **49**, 63 (2013)

[11] Z. Kohley, J. F. Liang, D. Shapira, R. L. Varner, C. J. Gross, J. M. Allmond, A. L. Caraley, E. A. Coello, F. Favela, K. Lagergren, and P. E. Mueller, Phys. Rev. Lett. **107**, 202701 (2011)

[12] H. M. Jia, C. J. Lin, F. Yang, X. X. Xu, H. Q. Zhang, Z. H. Liu, L. Yang, S. T. Zhang, P. F. Bao, and L. J. Sun, Phys. Rev. C **86**, 044621 (2012)

[13] V. A. Rachkov, A. V. Karpov, A. S. Denikin, and V. I. Zagrebaev, Phys. Rev. C **90**, 014614 (2014)

[14] D. Bourgin, S. Courtin, F. Haas, A. M. Stefanini, G. Montagnoli, A. Goasduff, D. Montanari, L. Corradi, E. Fioretto, J. Huiming, F. Scarlassara, N. Rowley, S. Szilner, and T. Mijatovic, Phys. Rev. C **90**, 044610 (2014)

[15] A. M. Stefanini, G. Montagnoli, H. Esbensen, L. Corradi, S. Courtin, E. Fioretto, A. Goasduff, J. Grebosz, F. Haas, M. Mazzocco, C. Michelagnoli, T. Mijatovic, D. Montanari, G. Pasqualato, C. Parascandolo, F. Scarlassara, E. Strano, S. Szilner, D. Torresi, Phys. Lett. B **728**, 639 (2014)

[16] A. M. Stefanini, G. Montagnoli, H. Esbensen, L. Corradi, S. Courtin, E. Fioretto, A. Goasduff, J. Grebosz, F. Haas, M. Mazzocco, C. Michelagnoli, T. Mijatovic, D. Montanari, G. Pasqualato, C. Parascandolo, F. Scarlassara, E. Strano, S. Szilner, N.Toniolo, D. Torresi, EPJ Web of Conferences **86**, 00056 (2015)

[17] J. F. Liang, J. M. Allmond, C. J. Gross, P. E. Mueller, D. Shapira, R. L. Varner, M. Dasgupta, D. J. Hinde, C. Simenel, E. Williams, K. Vo-Phuoc, M. L. Brown, I. P. Carter, M. Evers, D. H. Luong, T. Ebadi, and A. Wakhle, Phys. Rev. C **94**, 024616 (2016)

[18] A. K. Sinha, N. Madhavan, J. . Das, P. Sugathan, D. Kataria, A. Patro, and G. Mehta, Nucl. Inst. Meth. A **339**, 543 (1994)

[19] S. Nath, Comput. Phys. Commun. 180, 2392 (2009)

[20] K. Hagino, N. Rowley, and A. T. Kruppa, Comput. Phys. Commun. **123**, 143 (1999)

[21] V. I. Zagrebaev, A. S. Denikin, A. V. Karpov, A. P. Alekseev, M. A. Naumenko, V. A. Rachkov, V. V. Samarin, V. V. Saiko, NRV web knowledge base on low-energy nuclear physics, http://nrv.jinr.ru/.

The Astrophysical Journal, 834:160 (12pp), 2017 January 10 doi:10.3847/1538-4357/834/2/160

PERIOD–COLOR AND AMPLITUDE–COLOR RELATIONS AT MAXIMUM AND MINIMUM LIGHT FOR RR LYRAE STARS IN THE SDSS STRIPE 82 REGION

Chow-Choong Ngeow[1], Shashi M. Kanbur[2], Anupam Bhardwaj[3,4], Zachariah Schrecengost[2], and Harinder P. Singh[3]
[1] Graduate Institute of Astronomy, National Central University, Jhongli 32001, Taiwan
[2] Department of Physics, SUNY Oswego, Oswego, NY 13126, USA
[3] Department of Physics and Astrophysics, University of Delhi, Delhi 110007, India
[4] European Southern Observatory, Karl-Schwarzschild-Straße 2, Garching D-85748, Germany
Received 2016 October 11; revised 2016 November 3; accepted 2016 November 3; published 2017 January 11

ABSTRACT

Investigation of period–color (PC) and amplitude–color (AC) relations at the maximum and minimum light can be used to probe the interaction of the hydrogen ionization front (HIF) with the photosphere and the radiation hydrodynamics of the outer envelopes of Cepheids and RR Lyraes. For example, theoretical calculations indicated that such interactions would occur at minimum light for RR Lyrae and result in a flatter PC relation. In the past, the PC and AC relations have been investigated by using either the $(V-R)_{\rm MACHO}$ or $(V-I)$ colors. In this work, we extend previous work to other bands by analyzing the RR Lyraes in the Sloan Digital Sky Survey Stripe 82 Region. Multi-epoch data are available for RR Lyraes located within the footprint of the Stripe 82 Region in five (*ugriz*) bands. We present the PC and AC relations at maximum and minimum light in four colors: $(u-g)_0$, $(g-r)_0$, $(r-i)_0$, and $(i-z)_0$, after they are corrected for extinction. We found that the PC and AC relations for this sample of RR Lyraes show a complex nature in the form of flat, linear or quadratic relations. Furthermore, the PC relations at minimum light for fundamental mode RR Lyrae stars are separated according to the Oosterhoff type, especially in the $(g-r)_0$ and $(r-i)_0$ colors. If only considering the results from linear regressions, our results are quantitatively consistent with the theory of HIF-photosphere interaction for both fundamental and first overtone RR Lyraes.

Key words: stars: atmospheres – stars: fundamental parameters – stars: variables: RR Lyrae

Supporting material: machine-readable table

1. INTRODUCTION

It has been well known that the helium II partial ionization zone drives the radial pulsation of Cepheids and RR Lyraes via the κ-mechanism. In between this zone and the photosphere, defined as a layer with an optical depth of $\tau = 2/3$, there exists another partial ionization zone—the hydrogen ionization front (HIF). During the cycle of pulsation, the HIF will move "in-and-out" within the mass distribution. Furthermore, the relative positions of the HIF and stellar photosphere change with the pulsation phase. Hence, it is possible that HIF will interact with the photosphere at certain phases of the pulsation, where the photosphere is located at the base of the HIF. This has been demonstrated with a series of pulsation models constructed, for example, in Simon et al. (1993), Kanbur (1995), Kanbur & Phillips (1996), and Kanbur et al. (2004). Results based on these calculations suggested that this interaction will occur at maximum and and minimum light for Cepheids and RR Lyraes, respectively.

The period–color (hereafter PC) and amplitude–color (hereafter AC) relations at maximum and minimum light can be used as diagnostics of such interactions for Cepheids and RR Lyraes. For instance, the interaction of HIF with the photosphere at certain pulsation phases would imply that the observed PC relation will be flat or very shallow (that is, the slope of the PC relation is close to zero) at these phases (for a thorough discussion on this, see Bhardwaj et al. 2014, and references therein). In the case of Cepheids, the PC and AC relations have been extensively studied in a series of papers (Kanbur & Ngeow 2004; Kanbur et al. 2004, 2007, 2010; Kanbur & Ngeow 2006), as well as in Bhardwaj et al. (2014). For RR Lyraes, Kanbur & Fernando (2005) investigated the PC and AC relations based on 4829 RR Lyraes in Large Magellanic Cloud obtained from the MACHO project, and found that the PC and AC relations at minimum light have a slope close to zero for this set of RR Lyraes. A similar result was also found with the fundamental mode RR Lyraes in the Large and Small Magellanic Cloud using the Optical Gravitational Lensing Experiment III (OGLE-III) data (Bhardwaj et al. 2014). Note that the flatness of the RR Lyraes PC relation at minimum light provides an alternate approach to estimate the reddening (Sturch 1966).[5]

In this paper, we extend the previous work to the RR Lyraes found in the Sloan Digital Sky Survey (SDSS) Stripe 82 region. Kanbur & Fernando (2005) and Bhardwaj et al. (2014) studied the PC and AC relations based on the $(V-R)_{\rm MACHO}$ color and the $(V-I)$ color respectively. In contrast, the SDSS data enables our investigation of PC and AC relations in multi-colors. Preliminary results of this work can be found in Bontorno et al. (2011), and the main purpose of this paper is to present the final results based on the full analysis of the SDSS Stripe 82 RR Lyrae data. We first describe the data and methods used in this paper in Section 2. We then present the analysis of this set of data and the results in Section 3. Finally, a discussion and conclusions of this paper are given in Section 4.

2. DATA AND METHODS

The *ugriz* band photometric light-curve data for RR Lyraes in the SDSS Stripe 82 region was adopted from Sesar et al.

[5] Some examples of using the PC relation at minimum light to estimate reddening can be found in Guldenschuh et al. (2005), Kunder et al. (2010), and Layden et al. (2013). However, detailed investigation of such applications is beyond the scope of this paper.

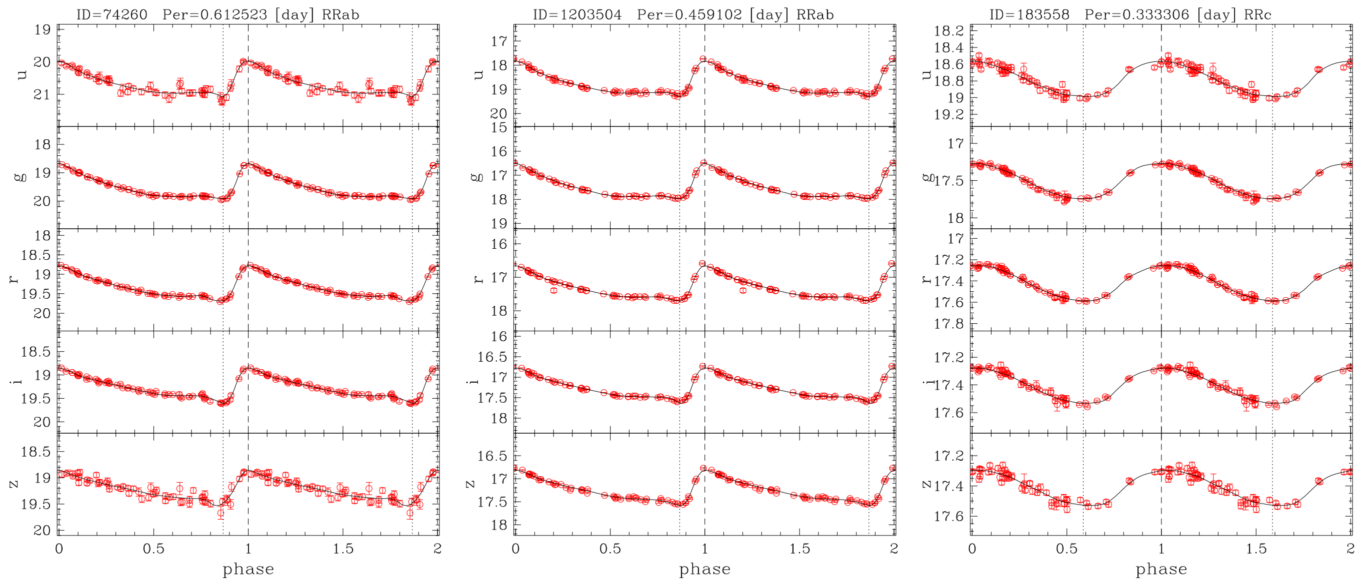

Figure 1. Examples of fitting the *ugriz* template light curves to the light-curve data of RR Lyrae. Both of the light curves' data and the template light curves were taken from Sesar et al. (2010). The dashed and dotted vertical lines represent the phases at *g*-band maximum and minimum light, respectively.

(2010), who found 483 RR Lyrae based on observations that spanned from 1998 September to 2007 November. Median numbers of data points per light curve are 55 and 56 in *uz* bands and *gri* bands, respectively. Further details regarding this data set can be found in Sesar et al. (2010), and will not be repeated here. This set of RR Lyraes includes 379 fundamental mode RRab stars and 104 first overtone RRc stars. In addition to the light-curve data, Sesar et al. (2010) also provided the *ugriz* band template light curves for RR Lyraes. We adopted these template light curves to derive the amplitudes and colors at maximum and minimum light for each RR Lyrae in the sample as described further below.

In the first step, each of the light curves is converted to a phased light curve according to $\phi(t) = t/P - \mathrm{INT}(t/P)$, where P is the pulsation period as given in Sesar et al. (2010) and the function INT takes the integer part of the argument. The template light curves in a given band were then fitted to the phased light curves by determining the mean magnitudes, amplitudes, and the phase difference between the template and phased light curves. The Nelder & Mead (1965) simplex minimization algorithm, implemented within the `GNU Scientific Library`, was employed to perform the fitting.

For a given RR Lyrae, the *g*-band best-fitted template light curve is used to determine the phases of maximum and minimum light, which are needed for constructing the PC and AC relations at these two extreme phases. We use this definition rather than the difference between the brightest and faintest observed points, in order to prevent amplitudes being effected by outliers. In other words, the SDSS colors $(\lambda_1 - \lambda_2)$ at maximum light, where $\lambda_1 < \lambda_2$, were determined from the same phase when the g band is at maximum light. The same procedure was applied to determine the SDSS colors at minimum light. We emphasize that the colors at maximum light and minimum light were not based on the extreme values in a given light curve.[6] The main reason to select the *g*-band light curve as the reference light curve for determining these two extreme phases is because at typical RR Lyrae effective temperatures (around ~6000 K to ~7000 K), Wien's displacement law suggests that the wavelengths at which the blackbody curve peaks will fall within the *g*-band transmission curve. For the same reason amplitudes of these RR Lyraes will be based on the *g*-band fitted template light curves. Taking a reference band in this way and computing the colors at maximum and minimum light with respect to the reference band will preserve the phase differences in light curves at different wavebands.

Figure 1 presents examples of the fitted *ugriz* band template light curves to randomly selected RR Lyraes in our sample. We visually examined all fitted light curves and removed those RR Lyraes that met either one of the following conditions: (a) light curves that show evidence of Blazhko or amplitude modulation[7] and/or (b) light curves that do not exhibit well-defined colors at maximum and minimum light.[8] Our philosophy is governed by selecting a subset of well-fitted light curves, such as those presented in Figure 1, rather than including data that do not have well-determined colors at maximum and minimum light. After visual inspection, 312 and 86 RR Lyraes of *ab*- and *c*-types were left in our sample, respectively. Extinction corrections were determined using the *r*-band extinction values (A_r) given in Sesar et al. (2010); extinctions in other bands were scaled with the following relations:[9] $A_u = 1.873A_r$, $A_g = 1.377A_r$, $A_i = 0.758A_r$, and $A_z = 0.537A_r$.

It is well known that the RRab stars in globular clusters exhibit the so-called Oosterhoff dichotomy (for examples, see Catelan 2009): the Oosterhoff type I and II (hereafter OoI and OoII, respectively) can be distinguished via the period–amplitude (or Bailey) diagram (for examples, see Clement 2000; Smith et al. 2011). Before investigating the PC and AC relations for these RR Lyrae in the next section, we further

[6] That is, the color $(\lambda_1 - \lambda_2)$ at maximum light is not same as $(\lambda_1^{max} - \lambda_2^{max})$, where λ^{max} is the maximum light for light curve in bandpass λ.

[7] Based on visual inspection, we suspect that ~40 RRab and ~11 RRc stars display evidence of Blazhko modulation. This is about 11% of the sample studied here. However, a detailed study to confirm or falsify the Blazhko nature of these RR Lyraes is beyond the scope of this work.

[8] This could be due to, for example, sparse light curves that do not have data points around maximum and/or minimum light, light-curve data points that displayed large scatter, etc.

[9] Adopted from http://www.astro.washington.edu/users/ivezic/sdss/catalogs/stripe82.html.

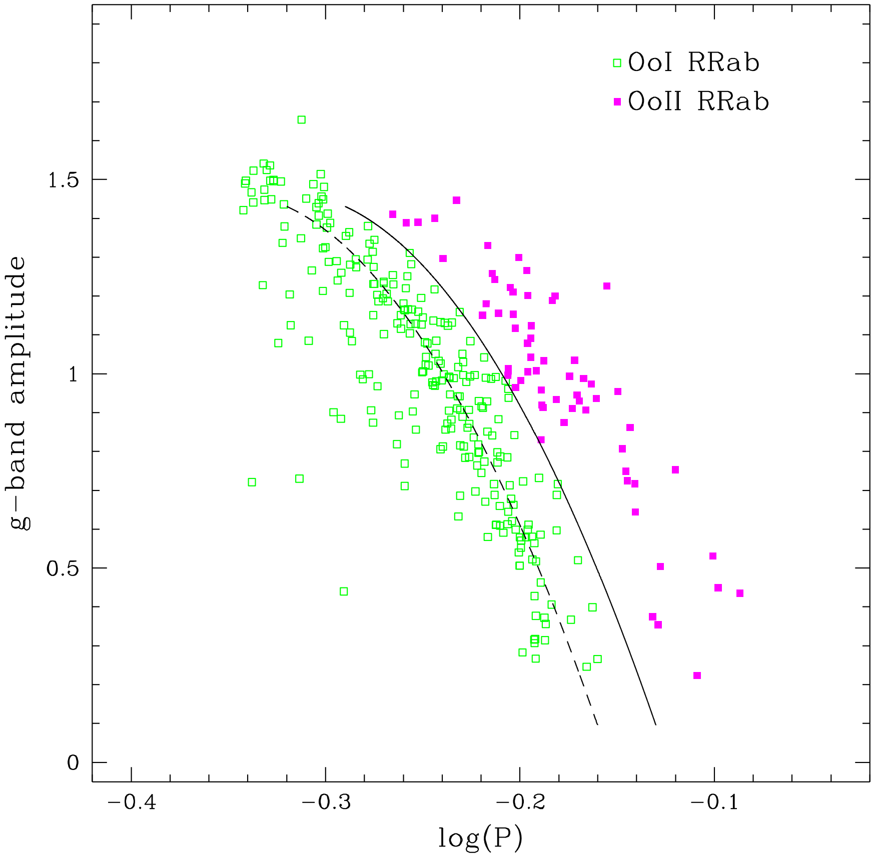

Figure 2. Period–amplitude diagram for RRab stars in our sample. The dashed curve is the quadratic regression fit to the locus of the data, as given in Sesar et al. (2010, their Equation (21)). Shifting this curve to the right by 0.03 in $\log P$ yields the solid curve, which is the criterion given in Sesar et al. (2010) to separate the OoI RRab (open green squares) and OoII RRab (filled magenta squares) stars.

Table 1
Amplitudes and Colors at the Maximum and Minimum Light for RR Lyrae Stars in the Sample

				At Maximum Light				At Minimum Light			
ID[a]	Type	$\log P$	AMP_g[b]	$(u-g)_0$	$(g-r)_0$	$(r-i)_0$	$(i-z)_0$	$(u-g)_0$	$(g-r)_0$	$(r-i)_0$	$(i-z)_0$
4099	ab-OoI	−0.19263	0.564	1.173	0.101	0.020	0.003	1.096	0.266	0.099	0.021
13350	ab-OoI	−0.26123	1.116	1.228	−0.064	−0.082	−0.030	1.127	0.260	0.065	0.038
15927	ab-OoI	−0.21306	0.688	1.256	0.067	−0.004	−0.016	1.229	0.269	0.113	0.014

Notes.
[a] ID from Sesar et al. (2010).
[b] The g-band amplitude.

(This table is available in its entirety in machine-readable form.)

divided our RRab stars into the OoI and OoII types by using the criterion suggested in Sesar et al. (2010). Figure 2 displays the period–amplitude diagram and the classified OoI ($N = 248$) and OoII ($N = 64$) RRab stars.

3. ANALYSIS AND RESULTS

Table 1 presents the g-band amplitudes and the colors at maximum and minimum light for our RR Lyrae sample. The corresponding plots of the PC and AC relations are displayed in Figures 3 and 4, respectively. We discuss our analysis and results on these relations further in the following subsections. The observed PC relations were also compared to the synthetic colors in Figure 5.

3.1. The PC Relations at Maximum Light

Kanbur & Fernando (2005) and Bhardwaj et al. (2014) found a significant non-zero and positive slope for the PC relation at maximum light in the $(V-R)_{\mathrm{MACHO}}$ and $(V-I)$ colors, respectively. In the left panel of Figure 3, we plotted the PC relations at maximum light for RRab and RRc stars: these display a variety of behavior. For example, we found significantly positive slopes for fundamental mode RRab stars for all colors, confirming the results presented in earlier work, except in $(u-g)_0$ color. The $(u-g)_0$ behavior at maximum light is more complicated. The RRab stars appeared to exhibit a flat relation with this becoming negative for the OoII RRab stars. In the case of first overtone RRc stars, shown as red crosses in Figure 3, the $(u-g)_0$ PC slope is negative and a

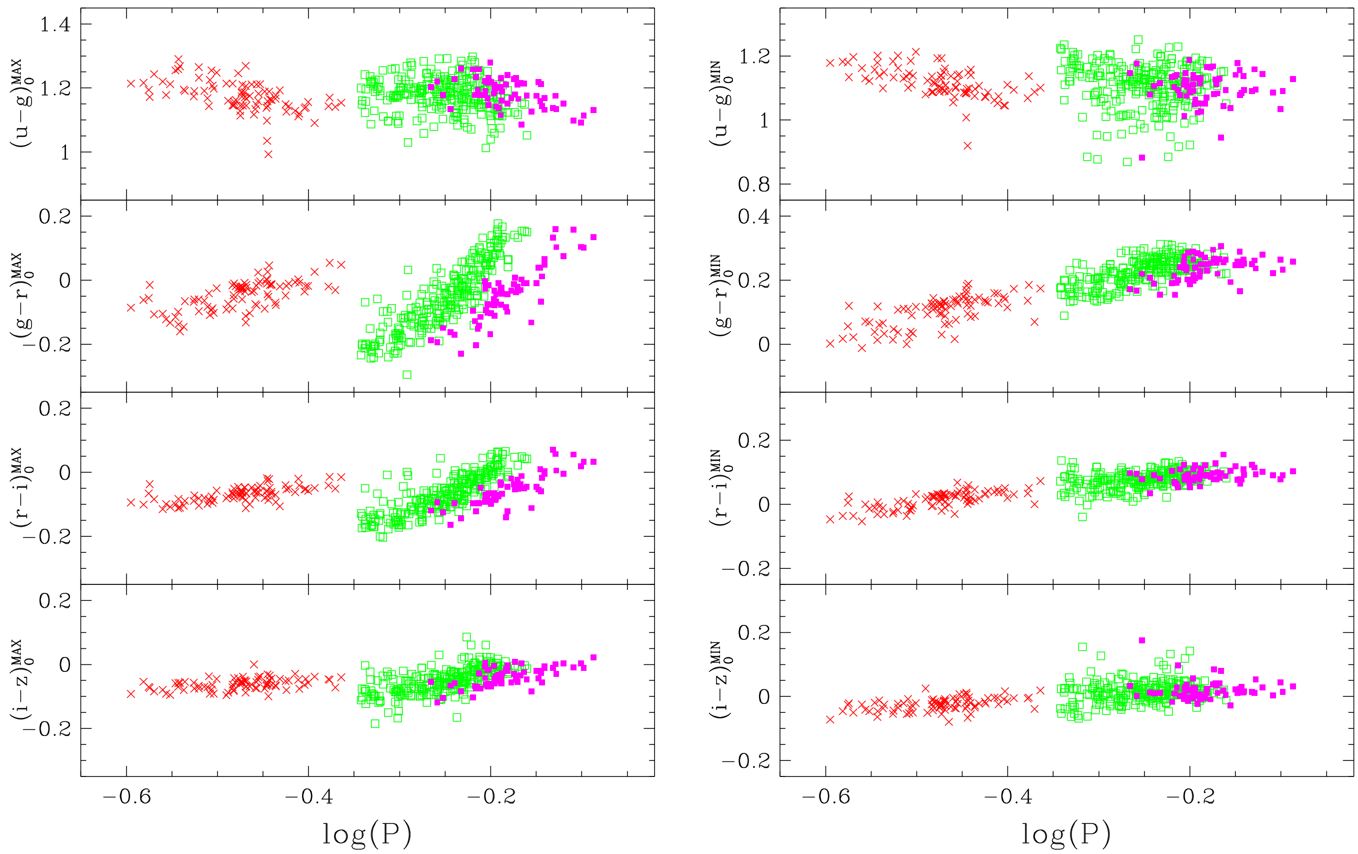

Figure 3. Period–color (PC) relations at (g-band) maximum (left panel) and minimum (right panel) light for the four extinction corrected SDSS colors. Green open squares and magenta filled squares represent the OoI RRab and OoII RRab stars, respectively, while the red crosses are for the RRc stars.

slight positive slope for all other colors. The negative PC slopes in the $(u-g)_0$ color and positive PC slopes in other longer wavelength colors could be understood due to the bolometric corrections when transforming the physical quantities (luminosity and effective temperature), to observable quantities such as magnitudes and colors (Cáceres & Catelan 2008). The left panel of Figure 5 compares the observed colors at maximum light, i.e., those from left panel of Figure 3, to the synthetic colors derived using the relations given in Cáceres & Catelan (2008), which demonstrates that the trends of the PC relations are very similar in both cases.

Figure 3 also reveals that the PC relations at maximum light for RRab stars, especially in the $(g-r)_0$ and $(r-i)_0$ colors, can be split into two sequences that belong to OoI and OoII RRab stars, respectively (note that RRc stars do not split into two sequences in Figure 3). Therefore, regressions on the PC relations were fitted separately to the OoI and OoII RRab stars. We first fit a linear regression to the PC relations at maximum light, and the fitted parameters are listed in columns (2) and (3) in Table 2. We then applied a standard t-test to see if the slope (β_1) from the linear regression is consistent with zero or not, with null and alternate hypotheses as H_0:$\beta_1 = 0$ and H_A: $\beta_1 \neq 0$, respectively. By adopting a confidence level at $\alpha = 0.05$, the null hypothesis can be rejected if the p-value, $p(t)$, is smaller than 0.05. The t-test results given in Table 2 show that $p(t) \sim 0.00$ for all PC relations at maximum light. Hence, these PC relations exhibit a significant slope from the linear regression, regardless of the type of RR Lyrae (OoI RRab, OoII RRab, or RRc). In addition, the linear slopes are different in each SDSS color between the OoI RRab, OoII RRab, and RRc stars.

Inspecting the left panel of Figure 3 suggests that the PC relation at maximum light for RRab stars might not be linear, especially in the $(u-g)_0$, $(g-r)_0$, and $(r-i)_0$ colors. We therefore fitted a quadratic regression to the PC relation at maximum light; the fitted parameters are summarized in columns (7)–(9) in Table 2. Dispersions (σ) from the fitted regressions, listed in columns (4) and (10) of Table 3, might not be a good metric to decide whether linear or quadratic regressions are better fits to the data, as the dispersions show marginal or no improvement when moving from linear to quadratic regressions. Instead, the standard F-test should be applied to evaluate which regression method is better. We calculated the F-value as follows.

$$F = \frac{(\mathrm{RSS}_l - \mathrm{RSS}_q)/[(N-2)-(N-3)]}{\mathrm{RSS}_q/(N-3)},$$

where N is number of data points, and RSS_l and RSS_q are the residual sums of squares for the linear and quadratic regressions, respectively. We also evaluated the p-value under the F-distribution $F_{1,N-3}$ with the null hypothesis that linear regression is sufficient to fit the data. The alternate hypothesis is that the quadratic regression is needed. Results of the F-test are given in columns (11) and (12) of Table 3. As before, we adopted $\alpha = 0.05$ such that the null hypothesis can be rejected if $p(F) < 0.05$.

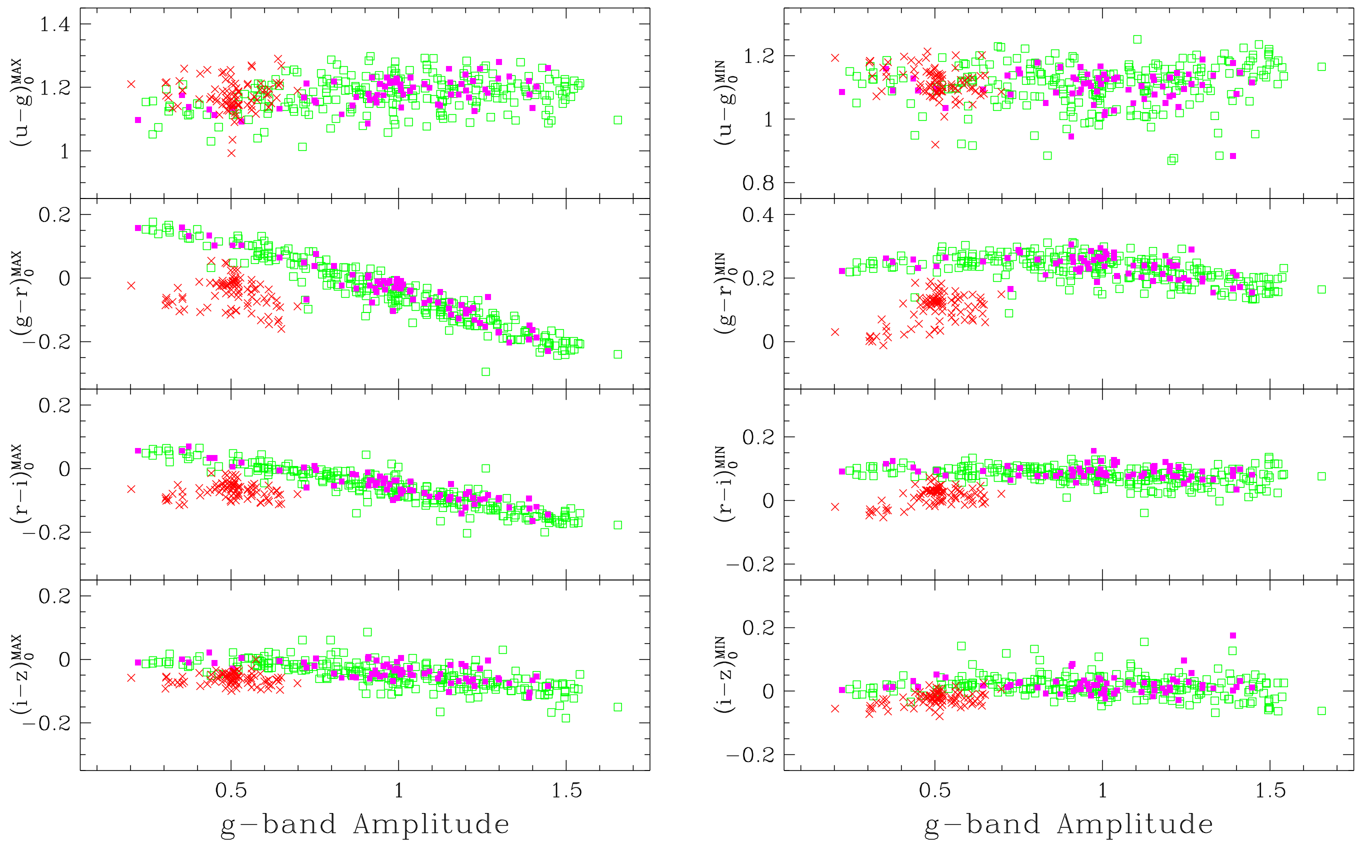

Figure 4. Amplitude–color (AC) relations at (g-band) maximum (left panel) and minimum (right panel) light for the four extinction corrected SDSS colors. Green open squares and magenta filled squares represent the OoI RRab and OoII RRab stars, respectively, while the red crosses are for the RRc stars.

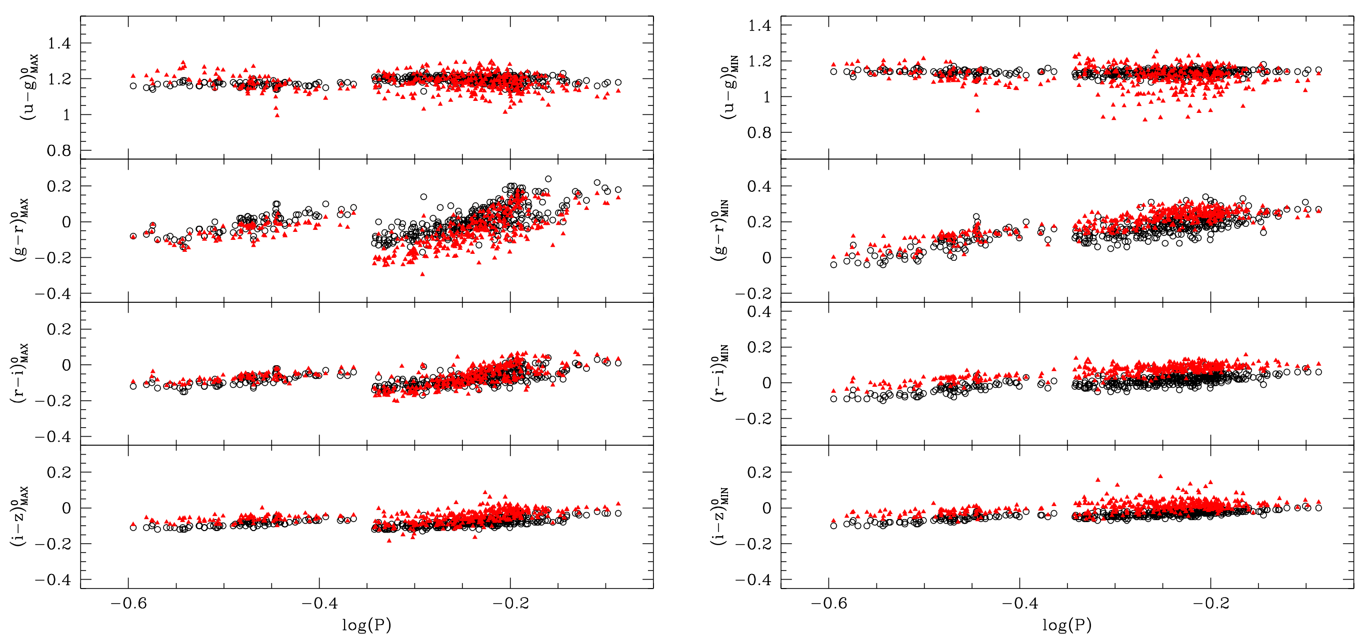

Figure 5. Comparison of the PC relations at (g-band) maximum (left panel) and minimum (right panel) light based on our results given in Table 1 (red filled triangles) and the synthetic colors (black open circles) derived from synthetic magnitudes. The synthetic magnitudes in bandpass λ, M_λ, were calculated based on pseudo-color $C_0 = (u-g)_0 - (g-r)_0$ and the pulsation periods using the relations given in Càceres & Catelan (2008, their Figure 1). The synthetic colors are then derived as $M_{\lambda 1} - M_{\lambda 2}$, where $\lambda 1 < \lambda 2$. For RRc stars, we have fundamentalized the periods (using the relation given in Catelan 2009) before applying the conversion. For clarity, we did not separate the OoI RRab stars, OoII RRab stars, and RRc stars in this figure.

In the case of RRc stars, the F-test provides evidence that a linear regression can be used to fit the PC relation at maximum light in the four SDSS colors. For RRab stars, the F-test suggested that a quadratic regression is a better model for OoI RRab star in the $(u-g)_0$, $(g-r)_0$, and $(r-i)_0$ colors. The $(i-z)_0$ color, on the other hand, shows a marginal F-test result.

Table 2
Period–Color Relations at Maximum and Minimum Light Using Linear and Quadratic Regression

Color	Linear Regression					Quadratic Regression					
	β_0	β_1	σ	t	$p(t)$	β_0	β_1	β_2	σ	F	$p(F)$
(1)	(2)	(3)	(4)	(5)	(6)	(7)	(8)	(9)	(10)	(11)	(12)
At Maximum Light											
OoI RRab											
$(u-g)_0$	1.122 ± 0.019	−0.222 ± 0.076	0.052	2.94	0.00	0.782 ± 0.104	−2.961 ± 0.825	−5.343 ± 1.602	0.051	11.1	0.00
$(g-r)_0$	0.476 ± 0.019	2.106 ± 0.074	0.051	28.5	0.00	0.978 ± 0.099	6.145 ± 0.782	7.878 ± 1.520	0.048	26.9	0.00
$(r-i)_0$	0.232 ± 0.013	1.187 ± 0.050	0.034	23.7	0.00	0.506 ± 0.068	3.395 ± 0.540	4.306 ± 1.048	0.033	16.9	0.00
$(i-z)_0$	0.096 ± 0.012	0.580 ± 0.046	0.032	12.6	0.00	0.207 ± 0.064	1.472 ± 0.509	1.741 ± 0.988	0.031	3.10	0.08
OoII RRab											
$(u-g)_0$	1.076 ± 0.023	−0.596 ± 0.122	0.037	4.87	0.00	0.939 ± 0.070	−2.238 ± 0.806	−4.672 ± 2.269	0.036	4.24	0.04
$(g-r)_0$	0.326 ± 0.027	2.029 ± 0.145	0.044	14.0	0.00	0.355 ± 0.086	2.378 ± 0.989	0.991 ± 2.784	0.045	0.13	0.72
$(r-i)_0$	0.139 ± 0.017	1.081 ± 0.093	0.028	11.6	0.00	0.199 ± 0.055	1.794 ± 0.627	2.029 ± 1.765	0.028	1.32	0.25
$(i-z)_0$	0.054 ± 0.014	0.512 ± 0.075	0.023	6.82	0.00	0.023 ± 0.044	0.142 ± 0.509	−1.052 ± 1.431	0.023	0.54	0.47
RRc											
$(u-g)_0$	0.921 ± 0.042	−0.536 ± 0.087	0.041	6.13	0.00	0.973 ± 0.306	−0.317 ± 1.282	0.228 ± 1.333	0.041	0.03	0.86
$(g-r)_0$	0.229 ± 0.036	0.582 ± 0.075	0.035	7.74	0.00	0.427 ± 0.263	1.414 ± 1.100	0.867 ± 1.143	0.036	0.58	0.45
$(r-i)_0$	0.073 ± 0.019	0.298 ± 0.039	0.019	7.57	0.00	0.258 ± 0.137	1.077 ± 0.572	0.811 ± 0.594	0.018	1.86	0.18
$(i-z)_0$	0.005 ± 0.017	0.139 ± 0.035	0.016	4.01	0.00	−0.053 ± 0.122	−0.102 ± 0.509	−0.252 ± 0.529	0.016	0.23	0.64
At Minimum Light											
OoI RRab											
$(u-g)_0$	1.062 ± 0.025	−0.183 ± 0.099	0.068	1.85	0.07	…	…	…	…	…	…
$(g-r)_0$	0.384 ± 0.012	0.625 ± 0.046	0.031	13.7	0.00	0.155 ± 0.062	−1.220 ± 0.495	−3.598 ± 0.962	0.031	14.0	0.00
$(r-i)_0$	0.140 ± 0.009	0.248 ± 0.035	0.024	7.11	0.00	0.216 ± 0.049	0.858 ± 0.388	1.190 ± 0.754	0.024	2.49	0.12
$(i-z)_0$	0.050 ± 0.012	0.139 ± 0.047	0.032	2.94	0.00	−0.051 ± 0.066	−0.666 ± 0.525	−1.570 ± 1.020	0.032	2.37	0.13
OoII RRab											
$(u-g)_0$	1.108 ± 0.032	0.043 ± 0.175	0.053	0.24	0.81	…	…	…	…	…	…
$(g-r)_0$	0.314 ± 0.020	0.430 ± 0.106	0.032	4.05	0.00	0.147 ± 0.059	−1.573 ± 0.676	−5.701 ± 1.902	0.030	8.99	0.00
$(r-i)_0$	0.116 ± 0.012	0.147 ± 0.066	0.020	2.24	0.03	0.100 ± 0.039	−0.043 ± 0.446	−0.540 ± 1.255	0.020	0.19	0.67
$(i-z)_0$	0.014 ± 0.019	−0.035 ± 0.101	0.031	0.34	0.73	…	…	…	…	…	…
RRc											
$(u-g)_0$	0.866 ± 0.039	−0.528 ± 0.082	0.038	6.46	0.00	1.130 ± 0.285	0.587 ± 1.193	1.162 ± 1.240	0.039	0.88	0.35
$(g-r)_0$	0.408 ± 0.036	0.644 ± 0.076	0.036	8.47	0.00	0.053 ± 0.263	−0.855 ± 1.102	−1.561 ± 1.146	0.036	1.86	0.18
$(r-i)_0$	0.186 ± 0.019	0.364 ± 0.041	0.019	8.96	0.00	0.024 ± 0.141	−0.321 ± 0.591	−0.714 ± 0.614	0.019	1.35	0.25
$(i-z)_0$	0.063 ± 0.018	0.185 ± 0.039	0.018	4.79	0.00	0.107 ± 0.135	0.370 ± 0.567	0.192 ± 0.589	0.018	0.11	0.75

Note. The linear regression takes the form of $C = \beta_0 + \beta_1 \log P$, where C denotes the four (extinction corrected) SDSS colors. Similarly, the quadratic regression takes the form of $C = \beta_0 + \beta_1 \log P + \beta_2 [\log P]^2$. σ is the dispersion from the regression fits. Results from the t-test, the t-values, and the corresponding p-values, $p(t)$, are listed in column (5) and (6). The t-test only tests for the slopes (β_1) in linear regression if they are consistent with zero or not. On the other hand, the F-test was applied to test whether or not quadratic regression is a better model to describe the data. The F-test results are given in columns (11) and (12). The quadratic regression and the F-test were only applied to those relations showing non-zero slopes from the t-test.

This behavior is different from the OoII RRab stars because the PC relation at maximum light in $(u-g)_0$ color is (marginally) nonlinear but linear in the other three colors.

3.2. The PC Relations at Minimum Light

Previous theoretical work, as described in the Introduction, suggested that the PC relation for RR Lyrae is almost independent of pulsation periods at minimum light. In the case of RRab stars, this result was verified from the MACHO data presented in Kanbur & Fernando (2005) and the OGLE-III data as described in Bhardwaj et al. (2014). The RRc stars do not exhibit a flat PC relation at minimum light for the reasons discussed in Bhardwaj et al. (2014). The right panel of Figure 3 presents the PC relations at minimum light in the four SDSS colors. From this figure, clear non-zero slopes of the PC relations at minimum light were found in all four SDSS colors for the RRc stars: this is also seen in the Magellanic Cloud RRc stars in the $(V-I)$ color (Bhardwaj et al. 2014). As in previous subsections, we fitted the linear and quadratic regressions, as well as applied t- and F-tests to these PC relations. Our results presented in Table 2 confirm the existence of a linear PC relation at minimum light for these type of pulsating stars.

In the case of RRab stars, the majority of the PC slopes at minimum light, as presented in Table 2, do not show clear evidence of flatness, which is different to what has been found from previous works. However, we note that in almost all cases except one, the PC slope at minimum light is significantly shallower than the PC slope at maximum light. The exception is the $(u-g)_0$ color for OoI RRab stars. For this data set, combining the t-test and F-test results, the PC relations at minimum light for OoI RRab stars are better described with a quadratic regression in the $(g-r)_0$ color, but linear in the $(r-i)_0$ and $(i-z)_0$ colors. The t-test result of the $(u-g)_0$ PC relation at minimum light of OoI RRab stars suggests a marginal flat relation. The OoII RRab stars, however, display a flat PC relation at minimum light in the $(u-g)_0$ and $(i-z)_0$ colors, but a quadratic and linear relation in the $(g-r)_0$ and $(r-i)_0$ colors, respectively. Finally, we note that trends of the

Table 3
Amplitude–Color Relations at Maximum and Minimum Light Using Linear and Quadratic Regression

Color	Linear Regression					Quadratic Regression					
Color (1)	β_0 (2)	β_1 (3)	σ (4)	t (5)	$p(t)$ (6)	β_0 (7)	β_1 (8)	β_2 (9)	σ (10)	F (11)	$p(F)$ (12)
At Maximum Light											
OoI RRab											
$(u-g)_0$	1.135 ± 0.011	0.043 ± 0.010	0.051	4.25	0.00	1.060 ± 0.024	0.223 ± 0.052	−0.095 ± 0.027	0.050	12.2	0.00
$(g-r)_0$	0.260 ± 0.006	−0.315 ± 0.006	0.031	51.4	0.00	0.241 ± 0.015	−0.270 ± 0.032	−0.024 ± 0.017	0.031	1.97	0.16
$(r-i)_0$	0.112 ± 0.005	−0.180 ± 0.005	0.024	37.6	0.00	0.096 ± 0.011	−0.142 ± 0.025	−0.020 ± 0.013	0.024	2.31	0.13
$(i-z)_0$	0.038 ± 0.006	−0.088 ± 0.006	0.029	15.3	0.00	0.000 ± 0.014	0.002 ± 0.030	−0.048 ± 0.016	0.028	9.39	0.00
OoII RRab											
$(u-g)_0$	1.098 ± 0.017	0.087 ± 0.017	0.037	5.19	0.00	1.072 ± 0.037	0.155 ± 0.084	−0.038 ± 0.046	0.037	0.68	0.41
$(g-r)_0$	0.261 ± 0.014	−0.307 ± 0.013	0.029	22.8	0.00	0.204 ± 0.029	−0.164 ± 0.065	−0.081 ± 0.036	0.029	5.02	0.03
$(r-i)_0$	0.109 ± 0.009	−0.168 ± 0.009	0.019	18.9	0.00	0.106 ± 0.020	−0.159 ± 0.045	−0.005 ± 0.025	0.020	0.04	0.84
$(i-z)_0$	0.030 ± 0.011	−0.070 ± 0.011	0.023	6.57	0.00	−0.003 ± 0.023	0.013 ± 0.052	−0.047 ± 0.029	0.023	2.61	0.11
RRc											
$(u-g)_0$	1.176 ± 0.030	−0.002 ± 0.059	0.050	0.03	0.98	…	…	…	…	…	…
$(g-r)_0$	−0.001 ± 0.027	−0.093 ± 0.054	0.046	1.72	0.09	…	…	…	…	…	…
$(r-i)_0$	−0.066 ± 0.014	−0.006 ± 0.028	0.024	0.22	0.83	…	…	…	…	…	…
$(i-z)_0$	−0.060 ± 0.011	−0.004 ± 0.021	0.018	0.18	0.86	…	…	…	…	…	…
At Minimum Light											
OoI RRab											
$(u-g)_0$	1.086 ± 0.014	0.022 ± 0.014	0.068	1.60	0.11	…	…	…	…	…	…
$(g-r)_0$	0.295 ± 0.007	−0.068 ± 0.007	0.035	9.62	0.00	0.201 ± 0.016	0.158 ± 0.034	−0.119 ± 0.018	0.033	44.8	0.00
$(r-i)_0$	0.107 ± 0.005	−0.029 ± 0.005	0.025	5.94	0.00	0.119 ± 0.012	−0.059 ± 0.026	0.016 ± 0.013	0.025	1.38	0.24
$(i-z)_0$	0.034 ± 0.007	−0.020 ± 0.006	0.032	3.08	0.00	−0.015 ± 0.015	0.099 ± 0.033	−0.063 ± 0.017	0.032	13.2	0.00
OoII RRab											
$(u-g)_0$	1.108 ± 0.025	−0.007 ± 0.024	0.053	0.30	0.76	…	…	…	…	…	…
$(g-r)_0$	0.289 ± 0.016	−0.054 ± 0.015	0.033	3.57	0.00	0.180 ± 0.030	0.223 ± 0.067	−0.156 ± 0.037	0.029	17.6	0.00
$(r-i)_0$	0.108 ± 0.009	−0.018 ± 0.009	0.020	1.97	0.05	…	…	…	…	…	…
$(i-z)_0$	0.012 ± 0.014	0.009 ± 0.014	0.031	0.63	0.53	…	…	…	…	…	…
RRc											
$(u-g)_0$	1.206 ± 0.027	−0.179 ± 0.052	0.044	3.43	0.00	1.314 ± 0.084	−0.657 ± 0.357	0.509 ± 0.377	0.044	1.82	0.18
$(g-r)_0$	−0.032 ± 0.025	0.268 ± 0.050	0.042	5.41	0.00	−0.300 ± 0.074	1.463 ± 0.317	−1.272 ± 0.334	0.039	14.5	0.00
$(r-i)_0$	−0.052 ± 0.014	0.131 ± 0.028	0.024	4.65	0.00	−0.220 ± 0.041	0.879 ± 0.177	−0.797 ± 0.186	0.022	18.3	0.00
$(i-z)_0$	−0.069 ± 0.011	0.087 ± 0.022	0.019	3.88	0.00	−0.119 ± 0.036	0.310 ± 0.153	−0.237 ± 0.161	0.019	2.17	0.14

Note. The linear regression takes the form of $C = \beta_0 + \beta_1 \mathrm{AMP}_g$, where C denotes the four (extinction corrected) SDSS colors and AMP_g is the g-band amplitude. Similarly, the quadratic regression takes the form of $C = \beta_0 + \beta_1 \mathrm{AMP}_g + \beta_2 [\mathrm{AMP}_g]^2$. σ is the dispersion from the regression fits. Results from the t-test, the t-values, and the corresponding p-values, $p(t)$, are listed in columns (5) and (6). The t-test only tests for the slopes (β_1) in linear regression whether or not they are consistent with zero. On the other hand, the F-test was applied to test whether or not quadratic regression is a better model to describe the data. The F-test results are given in columns (11) and (12). The quadratic regressions and the F-test were only applied to those relations showing non-zero slopes from the t-test.

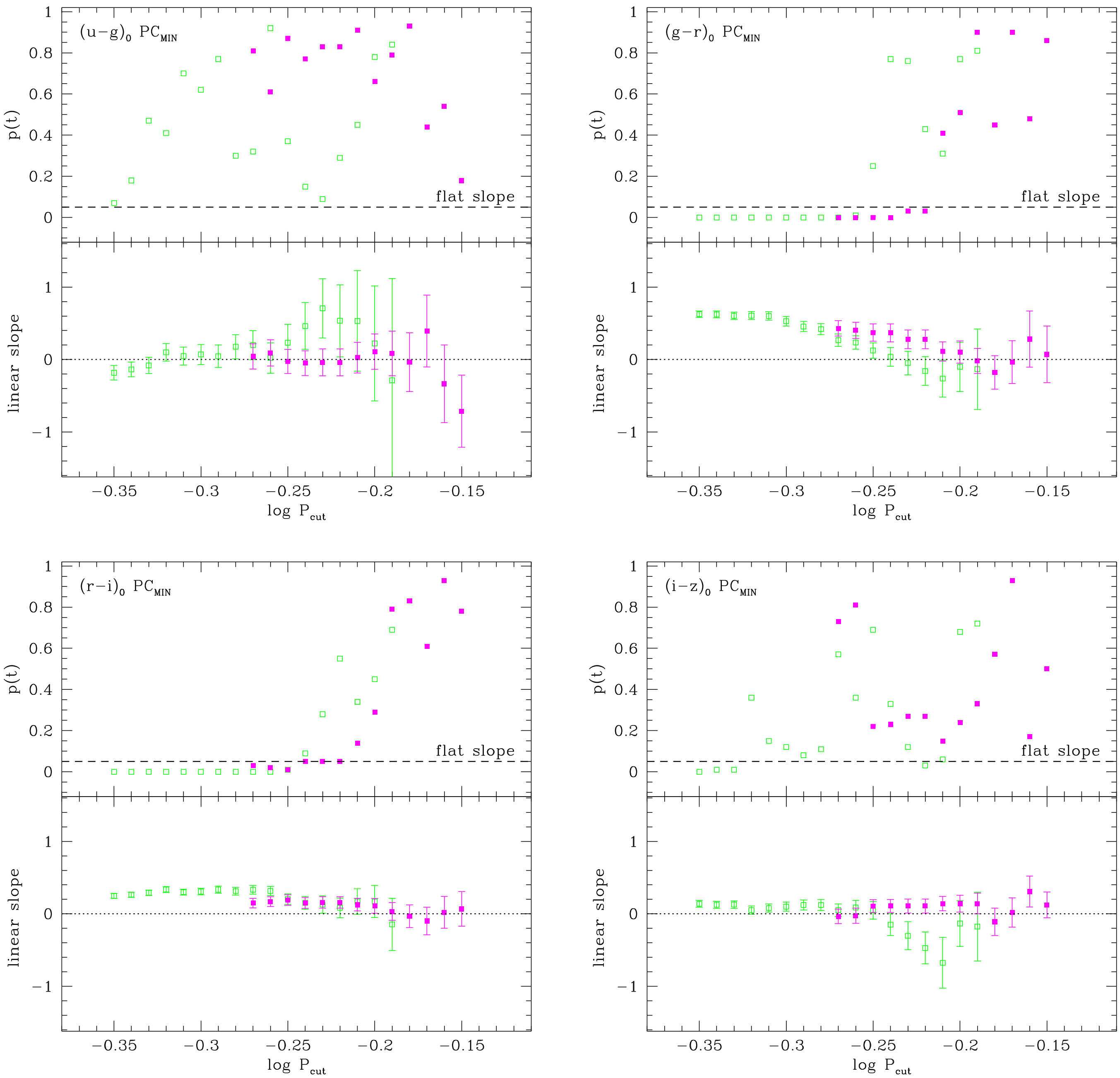

Figure 6. Results of the t-test on PC slopes at minimum light (upper panels in each sub-figures) and the slopes of linear regression (lower panels in each sub-figures) as a function of $\log P_{\rm cut}$, where the linear regressions were fitted to data with $\log P > \log P_{\rm cut}$. We stopped the fitting of linear regression when the number of data is below 10 after removing those RRab stars with $\log P < \log P_{\rm cut}$. The dashed lines represent the adopted confidence level of 0.05: slopes of the regressions are considered flat if $p(t) > 0.05$. The dotted lines indicate the zero slopes, and not the fitting of the data points. Green open squares and magenta filled squares represent the OoI RRab and OoII RRab stars, respectively.

observed PC relations at minimum light are very similar to the PC relation constructed from synthetic colors (right panel of Figure 5).

At first glance, our results on PC relations at minimum light seem to disagree with theoretical expectations (Kanbur & Phillips 1996) and earlier empirical studies (Kanbur & Fernando 2005; Bhardwaj et al. 2014). A careful inspection on the right panel of Figure 3, especially the $(g-r)_0$ PC relation, reveals that a flat PC relation could exist if we consider only RRab stars with $\log P$ greater than approximately -0.2. Therefore, we applied a period cut at $\log P_{\rm cut}$ and fitted a linear regression only for those RRab stars with periods greater than this period cut. This was done separately for OoI and OoII RRab stars. The slopes of the linear regression as a function of the period cut are displayed in lower panels of each sub-panel in Figure 6. We also applied the t-test on these slopes, and the corresponding $p(t)$ values are shown in the upper panels of the sub-figures in the same figure. Our results show that $(u-g)_0$ PC relations at minimum light are always flat regardless of period range and Oosterhoff type. The same result is also found for $(i-z)_0$ OoII PC relations at minimum light. For other PC relations at minimum light, a flat relation exists only if we consider RRab stars with periods greater than a given $\log P_{\rm cut}$. For example, we observed a flat

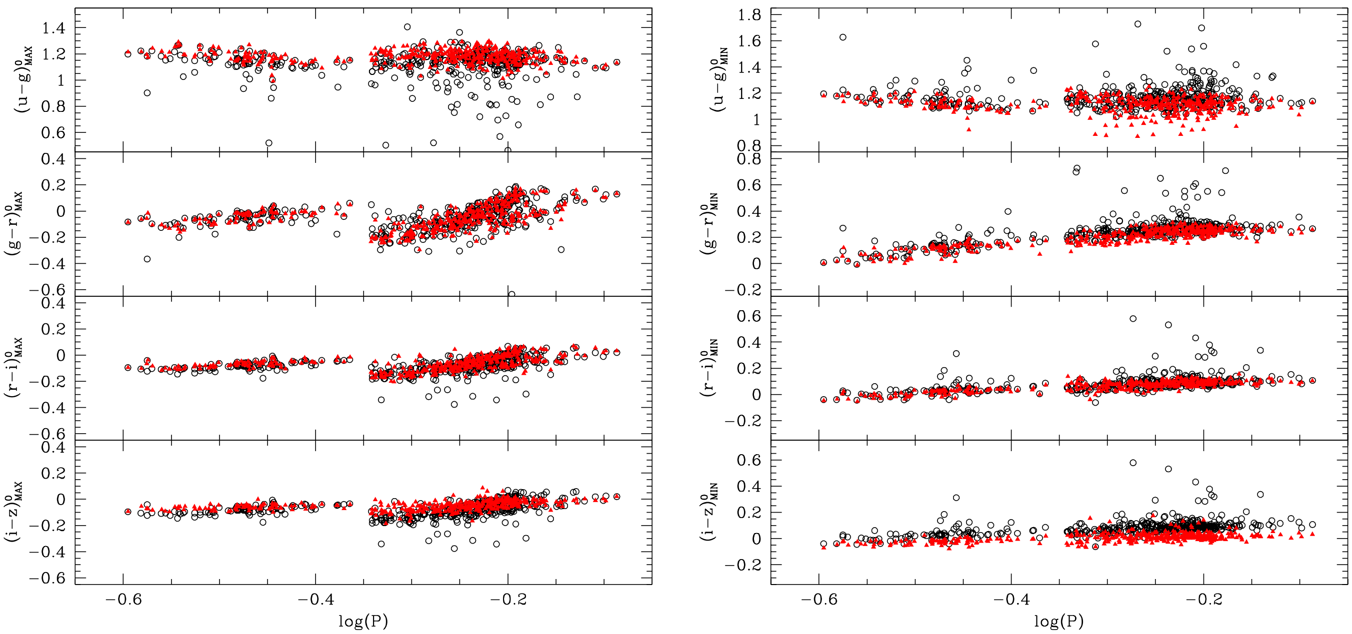

Figure 7. Comparison of the PC relations at (g-band) maximum (left panel) and minimum (right panel) light based on the template light-curve fitting approach (red filled triangles) and Fourier decomposition technique (black open circles) to determine the colors. We used a sixth-order Fourier expansion (an example of such an expression can be found, for example, in Deb & Singh 2009) to fit the *ugriz*-band light-curve data. The problem of larger scatter for the data points based on the Fourier decomposition technique could be potentially remedied using different fitting orders in the Fourier decomposition technique, for example, by applying Baart's condition (Deb & Singh 2009) to provide a better fit to individual light curves. For clarity, we did not separate the OoI RRab stars, OoII RRab stars, and RRc stars in this figure.

$(g-r)_0$ PC relation at minimum light for OoI RRab stars with $\log P > -0.25$.

3.3. The AC Relations at Maximum and Minimum Light

As in the case of PC relations, the AC relations presented in Figure 4 were fitted with linear and quadratic regressions and the results are summarized in Table 3. For RRc stars, flat AC relations are found at maximum light in all four colors, even though the $(g-r)_0$ AC relation shows a marginal result. We note that Bhardwaj et al. (2014) also found a significantly different AC relation at maximum light in the $(V-I)$ color for the LMC and SMC RRc stars. These differences can be attributed to the significantly different sample sizes used in this work and also in the LMC and SMC (Bhardwaj et al. 2014). Furthermore, at $(r-i)_0$ and $(i-z)_0$ colors, temperature fluctuations are expected to have less influence on amplitude variations. Therefore, we do not see a period–amplitude relation for RRc stars in our sample similar to Soszyński et al. (2009) for I-band data. Another possible cause of this difference can be the selection of g-band amplitude as reference for all colors, instead of using amplitude corresponding to the shorter wavelength. For example, we observe that the slope of the $(g-r)_0$ AC relation at maximum light, -0.093 ± 0.054, is almost identical to the $(V-I)$ AC relation based on the Large Magellanic Cloud RRc stars (-0.089 ± 0.014, Bhardwaj et al. 2014). However, it will be interesting to investigate this further with a greater sample in the future, for example, as provided by the Large Synoptic Survey Telescope (LSST). At minimum light, significant non-zero slopes were found for the AC relations as in previous work (Bhardwaj et al. 2014). Further F-test results show that the AC relations at minimum light for RRc stars are linear in the $(u-g)_0$ and $(i-z)_0$ colors, and quadratic in the other two colors.

Both Kanbur & Fernando (2005) and Bhardwaj et al. (2014) found significant and flat (or very shallow) AC relations at maximum light and minimum light, respectively, for the RRab stars. Our t-test results confirm these earlier works that the AC relations at maximum light exhibit a non-vanishing slope in all four SDSS colors. This is a consequence of the relation between PC and AC, originally developed in Simon et al. (1993) and later work (see the Introduction). Some of these relations are better described by a quadratic regression, such as the $(u-g)_0$ and $(i-z)_0$ AC relations for OoI RRab stars and $(g-r)_0$ AC relation for OoII RRab stars. Flat or very shallow AC relations at minimum light are found for OoII RRab stars except the $(g-r)_0$ AC relation. A marginal flat $(u-g)_0$ AC relation at minimum light is also found in OoI RRab stars, but the AC relations in other colors are either linear (for $(r-i)_0$ color) or quadratic (for $(g-r)_0$ and $(i-z)_0$ colors). It is worth mentioning that in $(g-r)_0$ color, the AC relations at minimum light for both OoI and OoII RRab stars are well represented by a quadratic regression, which can also be seen from the right panel in Figure 4.

4. DISCUSSION AND CONCLUSION

The aim of this study is to continue the investigation of empirical PC and AC relations at maximum and minimum light for RR Lyraes in Sloan colors. Such studies can be used to probe the radiation hydrodynamics of the outer envelopes of RR Lyraes (and Cepheids), and potentially be used to estimate the foreground extinction with flat relations. The main differences between this work and previous work, presented in Kanbur & Fernando (2005) and Bhardwaj et al. (2014), include (1) the application of a template light-curve fitting approach to determine the colors at maximum and minimum light instead of using Fourier decomposition technique, (2) separating out the OoI and OoII RRab stars in our sample,

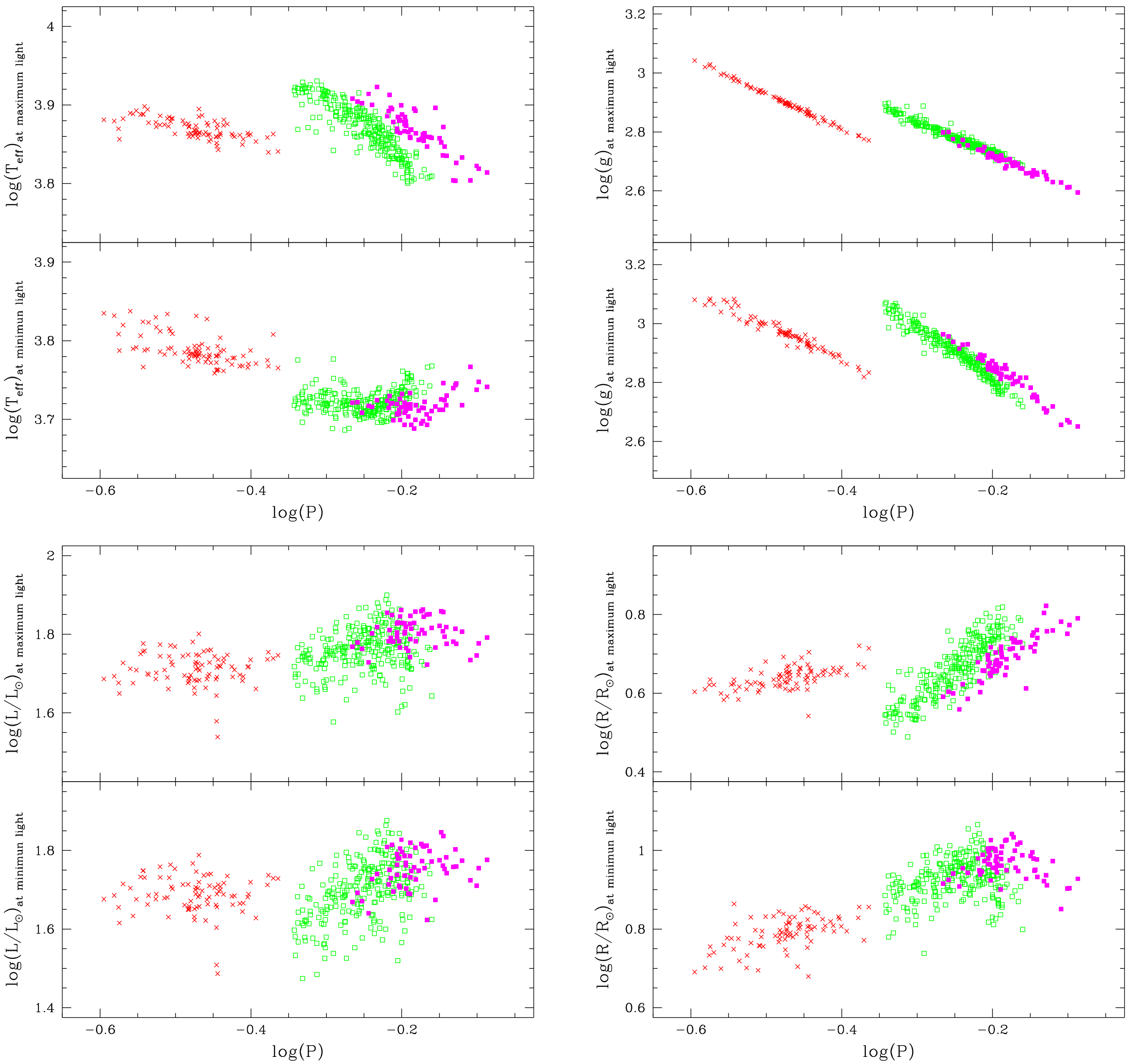

Figure 8. Period–temperature (upper-left panel), period-gravity (upper-right panel), period–luminosity (lower-left panel), and period–radius (lower-right panel) relations at maximum and minimum light for RR Lyrae in our sample. The effective temperature ($\log T_{\mathrm{eff}}$), gravity ($\log[g]$), and the luminosity ($\log[L/L_{\odot}]$) are converted from SDSS colors using the prescription given in Catelan et al. (2013). The adopted conversions involve the pseudo-colors, $C_0 = (u - g)_0 - (g - r)_0$ and/or $m_0 = (g - r)_0 - (r - i)_0$, the $(g - r)_0$ color and $\log P$. Based on the $\log T_{\mathrm{eff}}$ and $\log(L/L_{\odot})$, we calculated the radius, $\log(R/R_{\odot})$, by applying the Stefan–Boltzmann law with $\log T_{\odot} = 5772$ K. For RRc stars, we have fundamentalized the periods (using the relation given in Catelan 2009) before applying the conversion. Green open squares and magenta filled squares represent the OoI RRab and OoII RRab stars, respectively, while the red crosses are for the RRc stars.

which is not done in previous work, and finally (3) the investigation of the relations in four colors based on the SDSS *ugriz* photometry instead of single color in either $(V-R)_{\mathrm{MACHO}}$ or $(V-I)$ color.

Since we applied the template light-curve fitting approach instead of the usual Fourier decomposition technique as was done in the past (Kanbur & Fernando 2005; Bhardwaj et al. 2014), we compare the PC relations at maximum and minimum light based on both methods in Figure 7. This figure reveals that the PC relations obtained from the Fourier decomposition technique, using a fixed fitting order, are very similar to those based on template light-curve fitting, including the separation of OoI and OoII RRab stars in the $(g-r)_0$ PC relations at maximum light. This implies that both methods can deliver similar PC relations, and our results are not affected by the choice of fitting methods. However, Figure 7 also implies that PC relations, especially in the $(u-g)_0$ color, exhibit a larger scatter when using the Fourier decomposition technique.

Our explanation for the PC properties of RR Lyraes relies on the HIF-photosphere interaction (Simon et al. 1993; Kanbur 1995; Kanbur & Phillips 1996; Bhardwaj et al. 2014). As mentioned in the Introduction, the HIF and photosphere are not co-moving during stellar pulsation. Because of this, there are times when the stellar photosphere occurs at the base of the

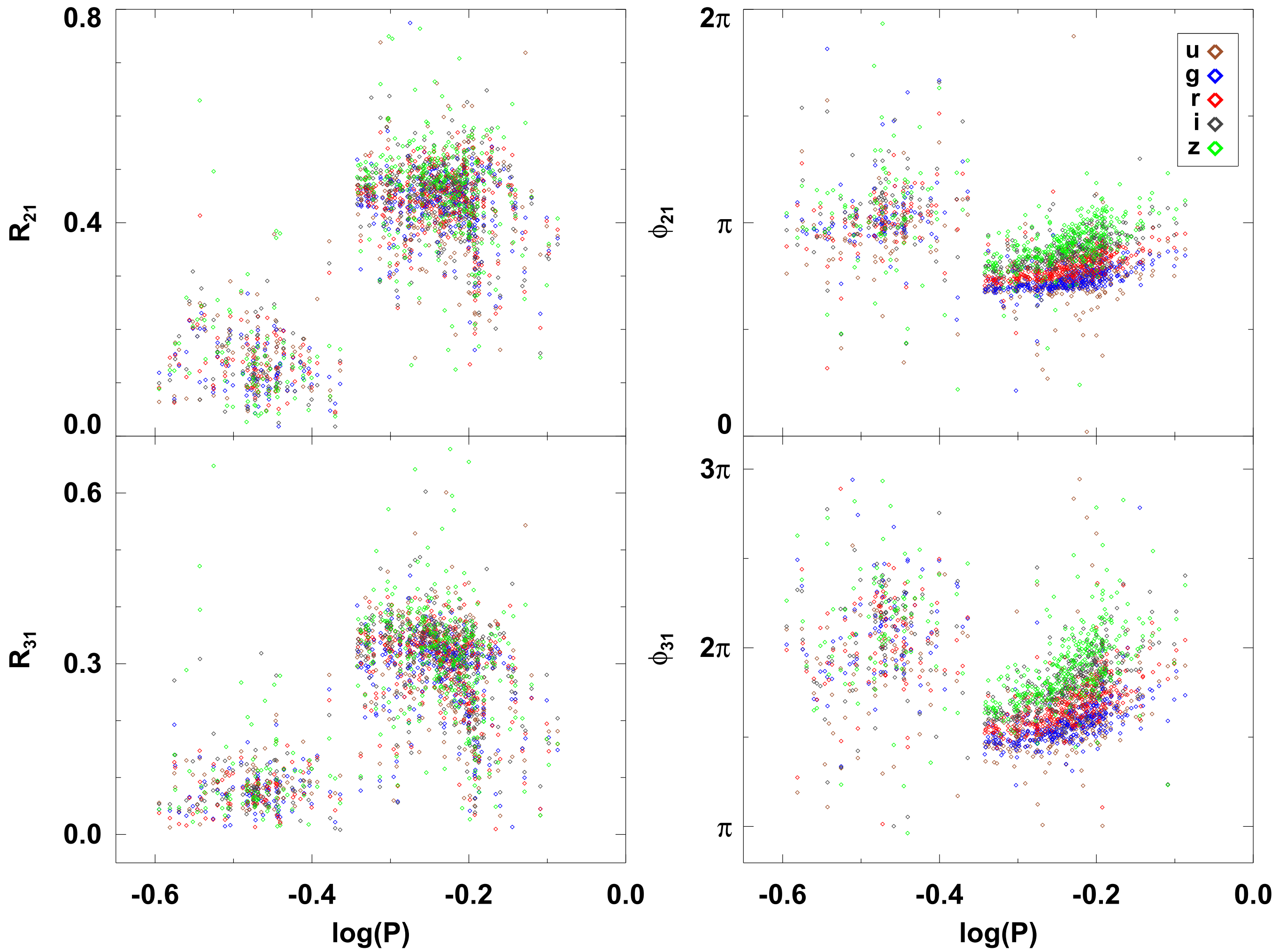

Figure 9. Multi-band lower-order Fourier parameters for the RR Lyrae in our sample. These Fourier parameters are derived from the same Fourier decomposition results as presented in Figure 7. The definition of the Fourier parameters (R_{21}, R_{31}, ϕ_{21}, and ϕ_{31}) can be found, for example, in Deb & Singh (2009) or Bhardwaj et al. (2015). For clarity, we did not separate the OoI RRab stars, OoII RRab stars, and RRc stars in this figure.

HIF. The times when this occurs varies with the type of star (RR Lyrae or Cepheids), period, and pulsation phase. When the two are not engaged in this way, the temperature of the photosphere and hence the color of the star will be related to the period. For RR Lyraes, the HIF and photosphere are always engaged but only at minimum light, the temperature and density are appropriate such that hydrogen reaches significant levels of ionization at temperatures that are increasingly independent of period. As the star brightens from minimum light, the temperatures that are needed to achieve significant levels of hydrogen ionization become increasingly dependent on density and hence a period–color relation develops. This is consistent with the results described here—where the slope of the PC relation at minimum light is not strictly zero but is significantly shallower than the slope at maximum light. The fact that the difference in slopes between the PC relations at maximum and minimum light for RRc stars is considerably smaller than that for fundamental mode RRab stars also provides strong support for the HIF-photosphere theory. These RRc stars are typically hotter than RRab stars, and at these temperatures, Saha ionization equilibrium is much more sensitive to the gas density and hence global stellar parameters.

These remarks also apply to AC relations in the following sense. When there is a difference in PC slopes between minimum and maximum light due to the engagement of the HIF-photosphere mentioned earlier, we expect a corresponding difference in the slope of AC relations at maximum/minimum light. As in Simon et al. (1993), we can apply the Stefan–Boltzmann law at maximum and minimum light such that $M_{\rm min} - M_{\rm max} = 10(\log T_{\rm min} - \log T_{\rm max})$, where $M_{\rm min} - M_{\rm max}$ is the amplitude at a given bandpass. Here we neglect the radius terms assuming that temperature fluctuations are more important than radius variations in changing luminosity. Thus if the slope of the PC relation decreases in going from maximum to minimum light, then the slope in an AC plot should decrease in going from minimum to maximum light. Conversely, if the PC slope increases in going from maximum to minimum, then the AC slope should increase in going from maximum to minimum. Table 3 indeed shows this for $(g-r)_0$ and $(r-i)_0$ colors in the case of RRab stars. The evidence is not quite as strong for the $(i-z)_0$ color but in this case one may argue that this color is very much toward the red part of the spectrum so that flux variations due to temperature variations are considerably reduced. In fact, the RRc stars at $(g-r)_0$ and $(r-i)_0$ colors are also consistent with this.

The behavior of the PC and AC relations for the $(u-g)_0$ color is not consistent with the theory described above, except in the case of OoII RRab stars, which exhibit a shallow PC slope at minimum light, but then the AC relation for these stars has a marginal positive slope. Furthermore, the RRc stars have a negative slope in the PC diagram at maximum light. One possibility is that the u and g bands straddle the peak of the Planck blackbody curve at temperatures relevant to RR Lyraes. This perhaps could lead to the opposite-sign slopes seen in Figure 3 for RRc stars. However, our preliminary calculations suggest that $\log(I_u/I_g)$ does not change slope for a range of temperatures between 5000 and 8000 K. Thus it may be that bolometric corrections, similar to Figure 5, are responsible for this slope change, though we leave a detailed discussion of this for future work.

The SDSS colors of the RR Lyrae in Figure 3 can be converted to effective temperature, logarithmic gravity, and bolometric luminosity using the conversions given in Catelan et al. (2013). Figure 8 presents the converted temperatures, gravities, and luminosities, as well as the radii, as a function of period at maximum and minimum light. For RRab stars at minimum light, we immediately observe that up to $\log P \sim -0.2$, the temperature at the stellar photosphere does not vary much with period,[10] and exhibits a change at $\log P \sim -0.20$ for OoI RRab stars and $\log P \sim -0.18$ for OoII RRab stars. For longer periods, the temperature at minimum light for RRab stars increases as the period increases. Therefore, the HIF-photosphere interaction at minimum light seems to occur at $-0.35 \leqslant \log P \leqslant -0.2$ for OoI RRab stars and at $-0.25 \leqslant \log P \leqslant -0.18$ for the OoII RRab stars. In the case of RRc stars, their effective temperatures are hotter than the RRab stars and hence they do not show a flat relation, in agreement with Bhardwaj et al. (2014). At maximum light, the temperature decreases as pulsation period increases for both RRab and RRc stars. Figure 8 also reveals that the OoI and OoII RRab stars can be well separated in several ways. One example is in the period–temperature and period–radius planes at maximum light.

Figure 9 displays the Fourier parameters for the RR Lyrae light curves in SDSS filters studied here. We see a clear differentiation in the ϕ_{31} and ϕ_{21} phase parameters with wavelength (similar to Cepheids, Bhardwaj et al. 2015) and a clear feature at $\log P \sim -0.2$ in the amplitude parameters R_{21} and R_{31} for RRab stars as reported with OGLE-III data. It is striking that this feature occurs at the same period that changes occur in the plots of $\log(T_{\rm eff})$, $\log(L/L_{\odot})$, $\log(R/R_{\odot})$ against $\log P$ in Figure 8. RRc stars are also clearly differentiated on the Fourier parameter—log P planes. Further data collected from the LSST (for example, see Oluseyi et al. 2012) will be very useful in connecting the change in light-curve structural properties, exemplified by the Fourier parameters, to global stellar properties such as PC and AC relations studied here.

In summary, our study reveals that the structural form of PC and AC relations at maximum and minimum lights for RR Lyraes are much more complicated than previously thought (Kanbur & Fernando 2005; Bhardwaj et al. 2014). They can be expressed as either a flat, a linear, or a quadratic relation in different colors. Furthermore, the PC and AC relations for RRab stars are separated by Oosterhoff types. The empirical results found in this work are certainly worth further theoretical investigations and interpretations, which will be presented in a future paper.

We greatly thank the anonymous referee and M. Catelan for providing valuable comments to improve the manuscript. C.C.N. thanks the funding from the Ministry of Science and Technology (Taiwan) under the contract 104-2112-M-008-012-MY3. A.B. acknowledges the Senior Research Fellowship grant 09/045(1296)/2013-EMR-I from the Human Resource Development Group (HRDG), which is a division of the Council of Scientific and Industrial Research (CSIR), India.

REFERENCES

Bhardwaj, A., Kanbur, S. M., Singh, H. P., Macri, L. M., & Ngeow, C.-C. 2015, MNRAS, 447, 3342
Bhardwaj, A., Kanbur, S. M., Singh, H. P., & Ngeow, C.-C. 2014, MNRAS, 445, 2655
Bontorno, A., Berke, M., Phelps, C., Kanbur, S., & Ngeow, C. 2011, in ASP Conf. Ser. 451, 9th Pacific Rim Conference on Stellar Astrophysics, ed. S. Quain et al. (San Francisco, CA: ASP), 139
Cáceres, C., & Catelan, M. 2008, ApJS, 179, 242
Catelan, M. 2009, Ap&SS, 320, 261
Catelan, M., Torrealba, G. I., Cáceres, C., et al. 2013, in Proc. Int. Astronomical Union, IAU Symp. 289, Advancing the Physics of Cosmic Distances, ed. R. de Grijs & G. Bono (Cambridge: Cambridge Univ. Press), 126
Clement, C. M. 2000, in ASP Conf. Ser. 203, IAU Coll. 176, The Impact of Large-Scale Surveys on Pulsating Star Research, ed. L. Szabados & D. Kurtz (San Francisco, CA: ASP), 266
Deb, S., & Singh, H. P. 2009, A&A, 507, 1729
Guldenschuh, K. A., Layden, A. C., Wan, Y., et al. 2005, PASP, 117, 721
Kanbur, S. M. 1995, A&A, 297, L91
Kanbur, S. M., & Fernando, I. 2005, MNRAS, 359, L15
Kanbur, S. M., Marconi, M., Ngeow, C., et al. 2010, MNRAS, 408, 695
Kanbur, S. M., & Ngeow, C.-C. 2004, MNRAS, 350, 962
Kanbur, S. M., & Ngeow, C.-C. 2006, MNRAS, 369, 705
Kanbur, S. M., Ngeow, C.-C., & Buchler, J. R. 2004, MNRAS, 354, 212
Kanbur, S. M., Ngeow, C.-C., & Feiden, G. 2007, MNRAS, 380, 819
Kanbur, S. M., & Phillips, P. M. 1996, A&A, 314, 514
Kunder, A., Chaboyer, B., & Layden, A. 2010, AJ, 139, 415
Layden, A., Anderson, T., & Husband, P. 2013, arXiv:1310.0549
Nelder, J. A., & Mead, R. 1965, CompJ, 7, 308
Oluseyi, H. M., Becker, A. C., Culliton, C., et al. 2012, AJ, 144, 9
Sesar, B., Ivezić, Ž., Grammer, S. H., et al. 2010, ApJ, 708, 717
Simon, N. R., Kanbur, S. M., & Mihalas, D. 1993, ApJ, 414, 310
Smith, H. A., Catelan, M., & Kuehn, C. 2011, in RR Lyrae Stars, Metal-Poor Stars, and the Galaxy, Astrophysics Series, Vol. 5, ed. A. McWilliam (Pasadena, CA: The Observatories of the Carnegie Institution of Washington), 17
Soszyński, I., Udalski, A., Szymański, M. K., et al. 2009, AcA, 59, 1
Sturch, C. 1966, ApJ, 143, 774

[10] Therefore, the slope seen in the $(u - g)_0$ relations must be due to bolometric corrections as discussed in Section 3.1.

The Astronomical Journal, 151:88 (14pp), 2016 April doi:10.3847/0004-6256/151/4/88

LARGE MAGELLANIC CLOUD NEAR-INFRARED SYNOPTIC SURVEY. II. THE WESENHEIT RELATIONS AND THEIR APPLICATION TO THE DISTANCE SCALE

Anupam Bhardwaj[1], Shashi M. Kanbur[2], Lucas M. Macri[3], Harinder P. Singh[1], Chow-Choong Ngeow[4], R. Wagner-Kaiser[5], and Ata Sarajedini[5]

[1] Department of Physics & Astrophysics, University of Delhi, Delhi 110007, India; anupam.bhardwajj@gmail.com
[2] Department of Physics, The State University of New York at Oswego, Oswego, NY 13126, USA
[3] Mitchell Institute for Fundamental Physics & Astronomy, Department of Physics & Astronomy, Texas A&M University, College Station, TX 77843, USA
[4] Graduate Institute of Astronomy, National Central University, Jhongli 32001, Taiwan
[5] University of Florida, Department of Astronomy, 211 Bryant Space Science Center, Gainesville, FL, 32611, USA
Received 2015 July 9; accepted 2015 October 12; published 2016 March 9

ABSTRACT

We present new near-infrared (NIR) Cepheid period–Wesenheit (P–W) relations in the LMC using time-series observations from the Large Magellanic Cloud NIR Synoptic Survey. We also derive optical+NIR P–W relations using *V* and *I* magnitudes from the Optical Gravitational Lensing Experiment. We employ our new JHK_s data to determine an independent distance to the LMC of $\mu_{\rm LMC} = 18.47 \pm 0.07$*(statistical)* mag, using an absolute calibration of the Galactic relations based on several distance determination methods and accounting for the intrinsic scatter of each technique. We also derive new NIR period–luminosity and Wesenheit relations for Cepheids in M31 using observations from the Panchromatic Hubble Andromeda Treasury survey. We use the absolute calibrations of the Galactic and LMC $W_{J,H}$ relations to determine the distance modulus of M31, $\mu_{\rm M31} = 24.46 \pm 0.20$ mag. We apply a simultaneous fit to Cepheids in several Local Group galaxies covering a range of metallicities ($7.7 < 12 + \log[{\rm O/H}] < 8.6$ dex) to determine a global slope of -3.244 ± 0.016 mag dex^{-1} for the W_{J,K_s} relation and obtain robust distance estimates. Our distances are in good agreement with recent TRGB based distance estimates and we do not find any evidence for a metallicity dependence in the NIR P–W relations.

Key words: Local Group – Magellanic Clouds – stars: variables: Cepheids

Supporting material: machine-readable and VO tables

1. INTRODUCTION

Studies of Cepheid variables are of considerable interest in determining distances to star-forming galaxies out to ~50 Mpc because these pulsating stars obey the well known period–luminosity (P–L) relation or Leavitt Law (Leavitt & Pickering 1912) and hence can be used as standard candles. In the era of precision cosmology, Cepheids play an important role in the cosmic distance scale and are vital in establishing an increasingly more accurate and precise value of the Hubble constant (Riess et al. 2009, 2011). In the recent past, many studies have used classical Cepheids as standard candles for cosmic distance scale work through the P–L and period–luminosity–color relations (Bono et al. 1999; Kanbur et al. 2003; Tammann et al. 2003; Persson et al. 2004; Sandage et al. 2004, 2009; Benedict et al. 2007). Most of these studies involve the calibration of P–L relations for the Galaxy and LMC at optical wavelengths. Some authors assume that the Galactic and LMC P–L relations have similar slopes (Fouqué et al. 2007; Monson et al. 2012). However, the universality of the Cepheid P–L relation is a subject of intense debate, as the metallicity and extinction effects might change the slope as well as the intercept of the P–L relation (Gieren et al. 2006b; Storm et al. 2011) and therefore lead to biases in distance determinations.

Near-infrared (NIR) Cepheid P–L relations acquire a greater significance because these are less susceptible to reddening and metallicity differences between target and calibrating galaxies (Storm et al. 2011; Monson et al. 2012). Another possible reason for discrepancy in Cepheid-based distance estimates is the significant nonlinearities at various periods during the different phases of pulsation at optical wavelengths (Ngeow & Kanbur 2006b; Bhardwaj et al. 2014). These nonlinearities are also observed for mean light P–L relations at optical bands but are expected to be less significant at NIR wavelengths (Bono et al. 1999; Madore & Freedman 2009).

The calibration of Galactic Cepheid P–L relations at optical and NIR bands has been carried out using parallaxes for small samples of variables (Tammann et al. 2003; Ngeow & Kanbur 2004; Benedict et al. 2007; Fouqué et al. 2007; Turner 2010; Storm et al. 2011). For example, Benedict et al. (2007) used highly accurate trigonometric parallaxes from the *Hubble Space Telescope* (*HST*) for 10 Cepheids. The major problem in obtaining solid calibrations within our Galaxy is that accurate distance determinations are only possible for nearby objects ($D \lesssim 500$ pc with *HST*/FGS, recently extended to $D \lesssim 4$ kpc with a "spatial scanning technique" by Riess et al. 2014). The most important fundamental distance measurements come from trigonometric parallaxes. The Hipparcos/Tycho catalogs of parallaxes for classical Cepheids gave a strong impetus to this field (Perryman 1997; Van Leeuwen et al. 2007). Cepheid distances have also been measured to high precision using the Infrared Surface Brightness (IRSB) technique and Baade–Wesselink (BW) methods, where Cepheid pulsation is directly measured with a long-baseline interferometer (Gieren et al. 1998; Storm et al. 2011; Groenewegen 2013).

Recently, a detailed study on period–Wesenheit (P–W) relations in the NIR bands was carried out to determine distances to the Magellanic Clouds by Inno et al. (2013). The reddening-free Wesenheit function (Madore 1982) in the optical bands was also used to derive distances to individual

Galactic Cepheids (Ngeow 2012). The author calibrated the P–L relations at both optical and infrared wavelengths and used these to determine a distance modulus to the LMC. At NIR wavelengths, Persson et al. (2004) derived the P–L relations for Cepheids in the LMC having full phased light curve data and determined the distance modulus to the LMC using Galactic calibrations from the literature.

Determining a robust distance to the LMC is an important step in the cosmic distance scale. Recently, Pietrzyński et al. (2013) used a sample of eight eclipsing binaries to obtain a 2.2% accurate distance to the LMC of $D = 49.97 \pm 1.11$ kpc (equivalent to $\mu_{\rm LMC} = 18.493 \pm 0.048$ mag). One of the motivations for our work is to provide an independent determination of the LMC distance modulus by applying a Galactic calibration to data from the Large Magellanic Cloud NIR Synoptic Survey (LMCNISS; Macri et al. 2015 and erratum, hereafter Paper I). We also extend the distance determination to M31 using recent observations for Cepheids from the Panchromatic Hubble Andromeda Treasury (PHAT) survey (Wagner-Kaiser et al. 2015). Our work also provides a test for the metallicity dependence of Cepheid based distance estimates, considering the fact that Local Group galaxies have a large metallicity range ($7.7 < 12 + \log[\mathrm{O/H}] < 8.6$ dex). Furthermore, this work will be especially important in light of the impending launch of the *James Webb Space Telescope* in a few years, when space-based observations of Cepheids will be exclusively available in the infrared bands. A robust absolute calibration of the NIR P–L relations for Cepheids in the Milky Way and LMC will play an important role in the cosmic distance scale.

This paper, the second in a series, is structured as follows. In Section 2, we present the absolute P–W relations for Cepheids in the LMC using data from Paper I. We determine the robust distance to the LMC using absolute calibration of the Galactic Cepheid P–L and P–W relations (Section 3). We also derive the P–L and P–W relations for M31 using the observations from the PHAT survey (Dalcanton et al. 2012; Williams et al. 2014) in Section 4. Finally, we use Galactic and LMC calibrations to determine metal-independent robust distances to Local Group galaxies (Section 5). Further discussion of the results and important conclusions of our study are presented in Section 6.

2. NIR P–W RELATIONS FOR THE LMC CEPHEIDS

2.1. Photometric Mean Magnitudes

We make use of NIR mean magnitudes for 775 fundamental-mode and 474 first-overtone Cepheids in the LMC from Paper I. These magnitudes are based on observations from a synoptic survey (average of 16 epochs) of the central region of the LMC using the CPAPIR camera at the Cerro Tololo Interamerican Observatory 1.5-m telescope between 2006 and 2007. Most of these Cepheid variables were previously studied in the optical V and I bands by the third phase of the Optical Gravitational Lensing Experiment (OGLE-III) survey (Soszynski et al. 2008; Ulaczyk et al. 2013). The V and I band mean magnitudes are also compiled in Paper I. The calibration into the 2MASS photometric system, extinction corrections, and the adopted reddening law are discussed in detail in Paper I.

2.2. Absolute Calibration of NIR P–W Relations

We derive new NIR and optical+NIR P–W relations for fundamental and first-overtone mode Cepheids using LMCNISS and OGLE data. We note that Paper I presents only the P–L relations; therefore, it is important to derive P–W relations for their application to the distance scale. Moreover, we also emphasize that this large homogeneous data set in the JHK_s bands for Cepheids in the LMC is based on time-series observations as opposed to single-phase observations, as in earlier studies. We modify the definition of the Wesenheit function relative to Inno et al. (2013) as:

$$W^{\lambda_3}_{\lambda_2,\lambda_1} = m_{\lambda_3} - R^{\lambda_2,\lambda_1}_{\lambda_3}(m_{\lambda_2} - m_{\lambda_1}), \tag{1}$$

$$R^{\lambda_2,\lambda_1}_{\lambda_3} = \left[\frac{A_{\lambda_3}}{E(m_{\lambda_2} - m_{\lambda_1})}\right], \tag{2}$$

where m_{λ_i} represents the mean magnitude at wavelength λ_i and $\lambda_1 > \lambda_2$. For simplicity, the superscript λ_3 is dropped from W when $\lambda_1 = \lambda_3$. We adopt the reddening law given in Cardelli et al. (1989) and assume a value of $R_V^{B,V} = 3.23$ to obtain selective absorption ratios $A_I/A_V = 0.610$, $A_J/A_V = 0.292$, $A_H/A_V = 0.181$, and $A_{K_s}/A_V = 0.119$ (Fouqué et al. 2007; Inno et al. 2013). The resulting Wesenheit relations studied in this work are listed in Table 1.

Table 1
Wesenheit Relations

Label	m_{λ_3}	$R^{\lambda_2,\lambda_1}_{\lambda_3}$	m_{λ_2}–m_{λ_1}
$W_{J,H}$	H	1.63	J–H
W_{J,K_s}	K_s	0.69	J–K_s
W_{H,K_s}	K_s	1.92	H–K_s
$W_{V,J}$	J	0.41	V–J
$W_{V,H}$	H	0.22	V–H
W_{V,K_s}	K_s	0.13	V–K_s
$W_{I,J}$	J	0.92	I–J
$W_{I,H}$	H	0.42	I–H
W_{I,K_s}	K_s	0.24	I–K_s
$W^H_{V,I}$	H	0.41	V–I

The Wesenheit magnitudes are given in Table 2, together with their propagated uncertainties. For the NIR relations, we use the final sample of Cepheids from Paper I, since sigma-clipping was already applied in that work. Following Paper I, we calibrate these Wesenheit magnitudes using the highly accurate LMC distance from Pietrzyński et al. (2013). The calibrated Wesenheit magnitudes for fundamental and first-overtone mode Cepheids are plotted separately against $\log(P)$ to fit a P–W relation in the form of $W_{\lambda_2,\lambda_1} = a[\log(P) - 1] + b$. The results for the fundamental and first-overtone mode Cepheids in the LMC are shown in Figures 1 and 2, respectively. In the case of optical+NIR Wesenheit relations, we apply 3σ clipping to the magnitudes before fitting a P–W relation. The optical+NIR P–W relations for fundamental and first-overtone Cepheids are shown in Figure 3, with the derived parameters given in Table 3. We also include a calibration of the $W^H_{V,I}$ relation, which is the primary method used by the SH0ES project (Riess et al. 2009, 2011) to determine Cepheid distances to SNe Ia hosts and ultimately estimate the Hubble constant.

We also provide the P–L relations from Paper I in Table 3 for relative comparison with the P–W relations and the Galactic P–L relations in the next sections. Previously, the largest set of full phased light curve data used in the calibration of the NIR

Table 2
Wesenheit Magnitudes for Cepheids in the LMC

Star ID	Type	log P	$W_{J,H}$ / $\sigma_{W_{J,H}}$	W_{J,K_s} / $\sigma_{W_{J,K_s}}$	W_{H,K_s} / $\sigma_{W_{H,K_s}}$	$W_{V,J}$ / $\sigma_{W_{V,J}}$	$W_{V,H}$ / $\sigma_{W_{V,H}}$	W_{V,K_s} / $\sigma_{W_{V,K_s}}$	$W_{I,J}$ / $\sigma_{W_{I,J}}$	$W_{I,H}$ / $\sigma_{W_{I,H}}$	W_{I,K_s} / $\sigma_{W_{I,K_s}}$	$W^H_{V,I}$ / $\sigma_{W^H_{V,I}}$
0477	FO	0.292	13.922	14.238	14.471	14.732	14.820	14.407	14.853	14.351	14.403	14.397
			0.132	0.085	0.173	0.058	0.053	0.065	0.082	0.062	0.067	0.061
0478	FU	0.442	14.124	14.354	14.523	14.497	14.649	14.408	14.533	14.314	14.404	14.371
			0.167	0.102	0.219	0.064	0.059	0.079	0.089	0.082	0.081	0.079
0482	FU	0.873	12.520	12.820	13.042	13.296	13.494	12.988	13.386	12.921	12.974	13.006
			0.142	0.066	0.088	0.088	0.080	0.031	0.117	0.040	0.033	0.042
0487	FU	0.493	13.930	14.093	14.215	14.528	14.663	14.244	14.590	14.235	14.228	14.305
			0.212	0.139	0.212	0.132	0.122	0.092	0.171	0.049	0.094	0.050
0488	FU	0.562	13.805	14.088	14.296	14.271	14.484	14.158	14.349	14.057	14.160	14.102
			0.104	0.085	0.169	0.044	0.039	0.068	0.067	0.053	0.070	0.054

Note. All 775 fundamental and 474 first-overtone mode Cepheids were used to derive NIR Wesenheit relations, while 3σ clipping was applied for optical+NIR relations. The uncertainties were calculated by propagating the errors in mean magnitudes.

(This table is available in its entirety in machine-readable and Virtual Observatory (VO) forms.)

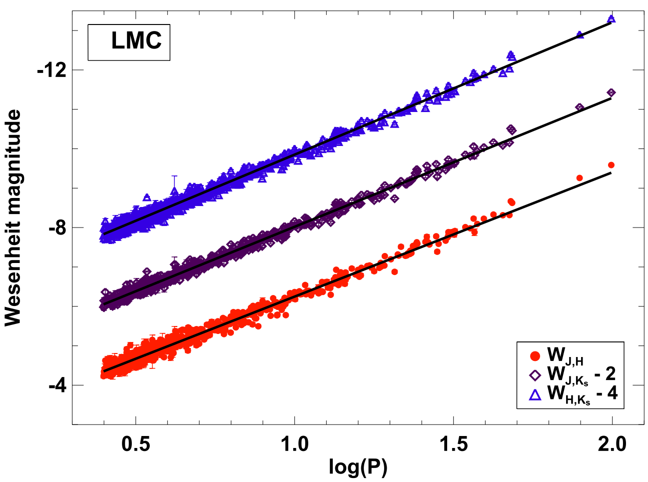

Figure 1. Calibrated NIR P–W relations for fundamental-mode Cepheids in the LMC. The solid line represents the best-fit linear regression to the data points in each band.

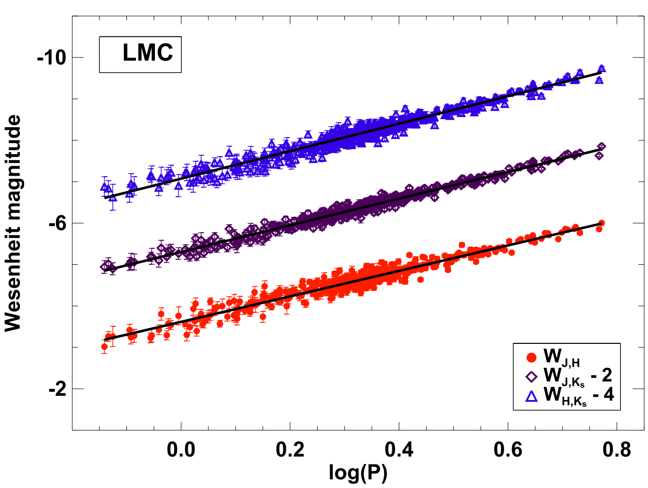

Figure 2. Calibrated NIR P–W relations for first-overtone mode Cepheids in the LMC. The solid line represents the best-fit linear regression to the data points.

P–L and P–W relations consisted of a sample of only 92 stars from Persson et al. (2004). However, this data set includes a larger number of stars with periods between 10 and 100 days which were used in the Paper I and this analysis for the determination of the NIR P–L and P–W relations, respectively. We also list in Table 3 the LMC K_s P–L relation and the W_{V,K_s} P–W relation derived by Ripepi et al. (2012) based on data from the VISTA survey of the Magellanic Clouds System (VMC).

The reddening-free Wesenheit relations are expected to have a smaller dispersion than the corresponding P–L relations. We note from Table 3 that the P–L relations for fundamental-mode Cepheids in J and H show a dispersion (0.120 and 0.101 mag) slightly greater than K_s (0.087 mag). For Wesenheit relations, this dispersion reduces significantly in $W_{J,H}$ and W_{J,K_s} as compared to J and H. In the case of W_{H,K_s}, the dispersion increases relatively as compared to the K_s, presumably due to an insignificant contribution from the color (H–K_s) term. For first-overtone Cepheids, the W_{J,K_s} relation has the smallest dispersion as compared to dispersion in J, H, and K_s (0.131, 0.100, and 0.085) P–L relations. Similarly, the $W_{J,H}$ and W_{H,K_s} Wesenheit also show smaller dispersions similar to fundamental-mode P–L relations. These P–W relations play a vital role in determining reddening-independent accurate distances (Inno et al. 2013).

2.3. Comparison with Published LMC P–L and P–W Relations

We also compare our P–W relations in the LMC with Ripepi et al. (2012) and Inno et al. (2013). We use a standard t-test to check the consistency of the slopes and intercepts of our P–L and P–W relations with published work. Under the null hypothesis that the two slopes are equivalent, the T-values are calculated by incorporating errors on the slopes and the standard deviation. The theoretical $t_{\alpha/2,\nu}$ values are evaluated from the t-distribution, where we adopt the significance level of $\alpha = 0.05$ and $\nu = N_1 + N_2 - 4$, with N_1 and N_2 being the number of Cepheids in the two samples. The probability ($p(t)$) of the observed t-statistic ($|T|$) under the null hypothesis is listed in Table 3. The theoretical t-value, at a fixed α, varies marginally (~1.96–1.98) for a wide range of ν (100–3000) used in our calculations and therefore is not tabulated. The null hypothesis is rejected if $|T| > t$ or $p(t) < 0.05$, i.e., the slopes or zero-points are not equal.

We find that the slope of our K_s-band P–L relation for fundamental and first-overtone mode Cepheids is not consistent with the slope of the P–L relation from the VMC survey

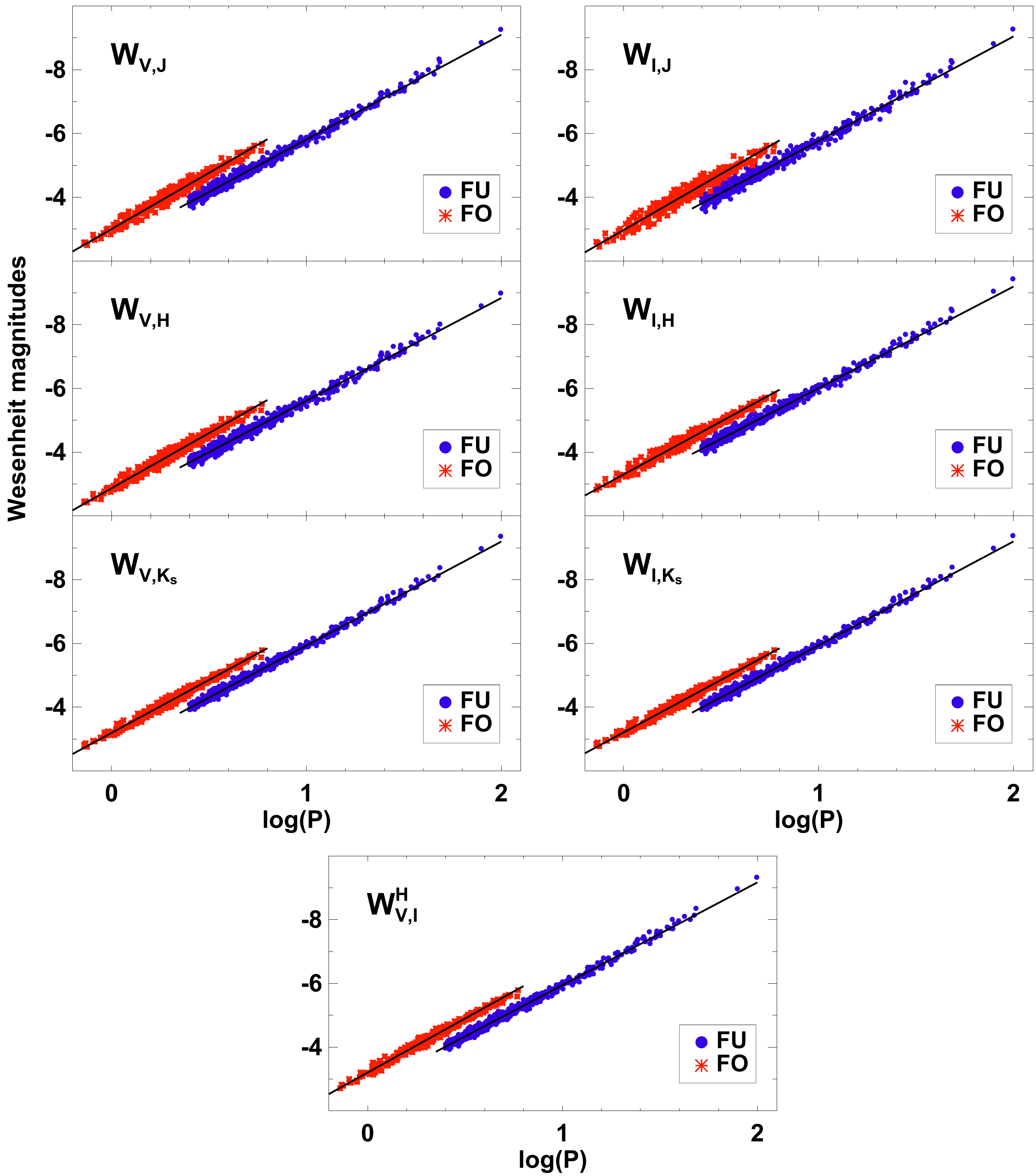

Figure 3. Calibrated optical+NIR P–W relations for fundamental and first-overtone mode Cepheids in the LMC. The solid line represents the best-fit linear regression to the data points.

(Ripepi et al. 2012). However, the intercepts are statistically consistent between these two studies. Our slopes for the fundamental-mode NIR P–W relations are statistically different from those of Inno et al. (2013) in $W_{J,H}$ and W_{J,K_s}, while being consistent in W_{H,K_s}. Similarly, the slopes for all optical+NIR P–W relations are not consistent with the results of Inno et al. (2013). In the case of the first-overtone mode Cepheids, the slopes of the NIR P–W relations from this study are significantly different from the results of Inno et al. (2013), while for the optical+NIR P–W relations, only the $W_{V,J}$ and $W_{I,J}$P–W relations have similar slopes. However, the intercepts of most P–W relations for both fundamental and first-overtone mode Cepheids are in good agreement, given their uncertainties. The t-test also suggests that the zero-points of our relations are statistically consistent with previously published results, except in the case of $W_{V,H}$. A possible reason for the

Table 3
LMC Cepheid NIR P–L and P–W Relations

	Slope	Intercept	σ	N	Src	Slope		Intercept	
						$\|T\|$	$p(t)$	$\|T\|$	$p(t)$
				Fundamental-mode					
J	−3.156 ± 0.004	−5.265 ± 0.049	0.120	775	M15	…	…	…	…
H	−3.187 ± 0.004	−5.646 ± 0.051	0.101	775	M15	…	…	…	…
K_s	−3.247 ± 0.004	−5.717 ± 0.050	0.087	775	M15	…	…	…	…
	−3.295 ± 0.018	−5.718 ± 0.051	0.102	256	R12	2.83	0.00	0.01	0.99
$W_{J,H}$	−3.157 ± 0.014	−6.246 ± 0.049	0.107	775	TW	…	…	…	…
	−3.373 ± 0.008	−6.236 ± 0.048	0.080	1701	I13	14.68	0.00	0.15	0.88
W_{J,K_s}	−3.276 ± 0.010	−6.019 ± 0.049	0.077	775	TW	…	…	…	…
	−3.365 ± 0.008	−5.982 ± 0.048	0.080	1708	I13	6.87	0.00	0.54	0.59
W_{H,K_s}	−3.364 ± 0.013	−5.853 ± 0.049	0.100	775	TW	…	…	…	…
	−3.360 ± 0.010	−5.795 ± 0.048	0.100	1709	I13	0.24	0.81	0.84	0.40
$W_{V,J}$	−3.304 ± 0.012	−5.814 ± 0.049	0.092	698	TW	…	…	…	…
	−3.272 ± 0.009	−5.787 ± 0.048	0.080	1732	I13	2.22	0.03	0.40	0.69
$W_{V,H}$	−3.239 ± 0.013	−5.618 ± 0.049	0.094	700	TW	…	…	…	…
	−3.315 ± 0.008	−5.992 ± 0.048	0.070	1730	I13	5.45	0.00	5.57	0.00
W_{V,K_s}	−3.287 ± 0.010	−5.943 ± 0.049	0.072	699	TW	…	…	…	…
	−3.326 ± 0.008	−5.918 ± 0.048	0.070	1737	I13	3.07	0.00	0.37	0.71
	−3.325 ± 0.014	−5.948 ± 0.050	0.078	256	R12	2.27	0.02	0.07	0.94
$W_{I,J}$	−3.293 ± 0.015	−5.773 ± 0.049	0.114	703	TW	…	…	…	…
	−3.243 ± 0.011	−5.734 ± 0.049	0.100	1735	I13	2.80	0.01	0.57	0.57
$W_{I,H}$	−3.229 ± 0.012	−6.028 ± 0.049	0.088	700	TW	…	…	…	…
	−3.317 ± 0.008	−6.009 ± 0.048	0.080	1734	I13	6.32	0.00	0.28	0.78
W_{I,K_s}	−3.284 ± 0.010	−5.952 ± 0.049	0.076	700	TW	…	…	…	…
	−3.325 ± 0.008	−5.916 ± 0.048	0.070	1737	I13	3.28	0.00	0.53	0.59
$W^{H}_{V,I}$	−3.250 ± 0.010	−5.958 ± 0.048	0.076	700	TW	…	…	…	…
				First-overtone Mode					
J	−3.319 ± 0.020	−5.952 ± 0.050	0.131	474	M15	…	…	…	…
H	−3.227 ± 0.020	−6.231 ± 0.052	0.100	474	M15	…	…	…	…
K_s	−3.257 ± 0.023	−6.292 ± 0.052	0.085	474	M15	…	…	…	…
	−3.471 ± 0.035	−6.384 ± 0.049	0.099	256	R12	5.33	0.00	1.32	0.19
$W_{J,H}$	−3.076 ± 0.035	−6.688 ± 0.050	0.119	474	TW	…	…	…	…
	−3.507 ± 0.015	−6.793 ± 0.048	0.090	1064	I13	12.77	0.00	1.55	0.12
W_{J,K_s}	−3.216 ± 0.024	−6.518 ± 0.049	0.082	474	TW	…	…	…	…
	−3.471 ± 0.013	−6.594 ± 0.048	0.080	1057	I13	9.45	0.00	1.11	0.27
W_{H,K_s}	−3.318 ± 0.035	−6.393 ± 0.050	0.119	474	TW	…	…	…	…
	−3.425 ± 0.017	−6.435 ± 0.049	0.100	1063	I13	2.97	0.00	0.62	0.54
$W_{V,J}$	−3.436 ± 0.029	−6.457 ± 0.049	0.095	422	TW	…	…	…	…
	−3.434 ± 0.014	−6.452 ± 0.048	0.100	1086	I13	0.06	0.95	0.07	0.94
$W_{V,H}$	−3.390 ± 0.028	−6.275 ± 0.049	0.093	421	TW	…	…	…	…
	−3.485 ± 0.011	−6.621 ± 0.048	0.080	1071	I13	3.42	0.00	5.16	0.00
W_{V,K_s}	−3.293 ± 0.021	−6.493 ± 0.049	0.071	421	TW	…	…	…	…
	−3.456 ± 0.013	−6.539 ± 0.048	0.070	1061	I13	6.64	0.00	0.67	0.50
	−3.530 ± 0.025	−6.623 ± 0.049	0.070	256	R12	7.24	0.00	1.89	0.06
$W_{I,J}$	−3.433 ± 0.036	−6.425 ± 0.050	0.118	420	TW	…	…	…	…
	−3.423 ± 0.020	−6.417 ± 0.048	0.130	1100	I13	0.23	0.82	0.11	0.91
$W_{I,H}$	−3.254 ± 0.026	−6.573 ± 0.049	0.086	422	TW	…	…	…	…
	−3.489 ± 0.012	−6.631 ± 0.048	0.080	1072	I13	8.52	0.00	0.86	0.39
W_{I,K_s}	−3.279 ± 0.021	−6.493 ± 0.049	0.074	420	TW	…	…	…	…
	−3.448 ± 0.013	−6.539 ± 0.048	0.080	1059	I13	6.60	0.00	0.66	0.51
$W^{H}_{V,I}$	−3.313 ± 0.021	−6.533 ± 0.050	0.070	421	TW	…	…	…	…

Note. Source: TW—this work; M15—Macri et al. (2015 and erratum), R12—Ripepi et al. (2012), I13—Inno et al. (2013). The intercepts of the P–L and P–W relations from R12 and I13 were transformed to the 2MASS system and recast as $M_\lambda = a_\lambda[\log(P) - 1] + b_\lambda$ for ease of comparison.

inconsistency in slopes may be due to significantly different sample sizes and different photometric calibrations. Moreover, the mean magnitudes in Inno et al. (2013) are obtained from a template fit to single-epoch magnitudes for fundamental-mode Cepheids, while random-phase magnitudes are used for first-overtone Cepheids. Therefore, we emphasize that all our results are based on mean magnitudes from well-sampled light curves.

Table 4
Fourier-fitted Mean Magnitudes

Star	Source	P	Magnitudes (m_0)			σ (m_0)			$E(B-V)$
ID		(days)	J	H	K_s	J	H	K_s	
AK CEP	MP	7.233	8.408	7.888	7.741	0.022	0.024	0.025	0.635
AN AUR	MP	10.291	7.934	7.436	7.275	0.022	0.024	0.026	0.600
AQ PUP	LS	30.104	6.001	5.491	5.308	0.023	0.021	0.022	0.531
AW PER	MP	6.464	5.229	4.822	4.697	0.022	0.024	0.025	0.487
BB SGR	LS	6.637	5.053	4.641	4.512	0.045	0.021	0.022	0.276

Note. Source: MP—Monson & Pierce (2011), BTG—Barnes et al. (1997), LS—Laney & Stobie (1992), W—Welch et al. (1984). The color excess $E(B-V)$ values are taken from Tammann et al. (2003). The error estimate includes the uncertainties from the Fourier fit and the photometry.

(This table is available in its entirety in machine-readable and Virtual Observatory (VO) forms.)

Table 5
Galactic Cepheid Distance Moduli

Star ID	IRSB	σ(IRSB)	MS	σ(MS)	BW	σ(BW)	*HST*-π	σ(*HST*-π)	W.M. (μ)	σ (μ)
AK CEP	…	…	…	…	13.03	0.20	…	…	13.03	0.20
AN AUR	…	…	…	…	13.62	0.22	…	…	13.62	0.22
AQ PUP	12.53	0.04	11.78	0.10	12.38	0.06	…	…	12.40	0.63
AW PER	…	…	…	…	9.94	0.18	…	…	9.94	0.18
BB SGR	9.69	0.03	9.08	0.08	9.55	0.07	…	…	9.58	0.51

Note. The distance determination methods : *Hubble Space Telescope* parallaxes (*HST*-π) (Benedict et al. 2007; Monson et al. 2012; Riess et al. 2014), Infrared Surface Brightness (IRSB) method (Fouqué et al. 2007; Storm et al. 2011), Baade–Wesselink (BW) distances (Groenewegen 2013), main-sequence (MS) fitting to candidate cluster (Turner 2010). We provide the distance moduli compiled from various methods for relative comparison. The adopted distance modulus is the weighted mean (W.M.) of all available distance moduli for each star. The procedure adopted to estimate uncertainties listed in the last column is discussed in the text.

(This table is available in its entirety in machine-readable and Virtual Observatory (VO) forms.)

3. AN INDEPENDENT DISTANCE TO THE LMC USING GALACTIC P–L AND P–W RELATIONS

A precise determination of the distance to the LMC is essential to estimate a value of Hubble constant with a total uncertainty below 2% (Riess et al. 2009, 2011). We aim to determine an independent and robust distance to the LMC using Cepheids as standard candles, following the work of Pietrzyński et al. (2013) based on long-period, late-type eclipsing binaries. The Wesenheit and JHK_s magnitudes from this work and Paper I, respectively, can also be used to obtain an independent estimate of distance to the LMC. An additional feature of this approach is the use of mean magnitudes based on full phased NIR light curves in the target galaxy (the LMC) as opposed to corrected single-epoch observations. However, this requires an absolute calibration of the P–L and P–W relations in the Galaxy. Previous Galactic P–L relations vary significantly in slope and zeropoint, leading to differences of more than ~3% in the inferred LMC distance. A detailed comparison of distance estimates to the LMC using published Galactic P–L relations is provided in the Appendix. Therefore, we re-analyzed the available data in the literature to provide a new robust absolute calibration of the Galactic relations, as explained in the following subsections.

3.1. Absolute Calibration of NIR Galactic Relations

We make use of light curve data for 113 Galactic Cepheids in the JHK_s bands from the literature (Welch et al. 1984; Laney & Stobie 1992; Barnes et al. 1997; Monson & Pierce 2011) for which independent distances are available. The light curve data for these Cepheids, along with their Fourier analysis, are discussed in detail in Bhardwaj et al. (2015). The mean magnitudes obtained using the optimum-order Fourier fit (Baart 1982; Bhardwaj et al. 2015), along with their errors, are listed in Table 4. We compare the Fourier-fitted mean magnitudes with values from the literature and the difference between two sets do not exceed ~0.02 mag. Since the NIR light curve data compiled from various sources are in different photometric systems, we converted these mean magnitudes to the 2MASS photometric system using the standard color transformations.[6] This transformation led to an average change in color of ~0.02 mag. In order to obtain reddening-corrected mean magnitudes in all three bands, color excesses $E(B-V)$ for Galactic Cepheids are adopted from Tammann et al. (2003). We adopt the Cardelli et al. (1989) reddening law as discussed previously and use the absorption ratios to determine $R_J = 0.94$, $R_H = 0.58$, and $R_K = 0.38$. We adopt an uncertainty in the color excess equal to the difference between two independent determinations of $E(B-V)$ for all of these Cepheids, $\Delta E(B-V) \sim 0.03$ mag (Fernie et al. 1995), and propagate this uncertainty into the errors in mean magnitudes using equations given in Tammann et al. (2003).

We compiled distances from various distance determination methods to calibrate the P–L and P–W relations for Galactic Cepheids: *Hubble Space Telescope* parallaxes (*HST*-π), IRSB, BW, and main-sequence (MS) fitting to candidate clusters. Highly accurate *HST* parallaxes for 11 Galactic Cepheids are available in the literature (Benedict et al. 2007; Monson et al. 2012; Riess et al. 2014). We use the updated values of *HST*-π for BETA DOR and W SGR from Table 5 of Monson et al. (2012), which differ slightly from those tabulated in Benedict et al. (2007). The Galactic P–L relations based on IRSB, BW, MS distances are discussed in (Fouqué et al. 2007; Turner 2010; Storm et al. 2011; Monson et al. 2012; Groenewegen

[6] http://www.ipac.caltech.edu/2mass/releases/allsky/doc/sec6_4b.html

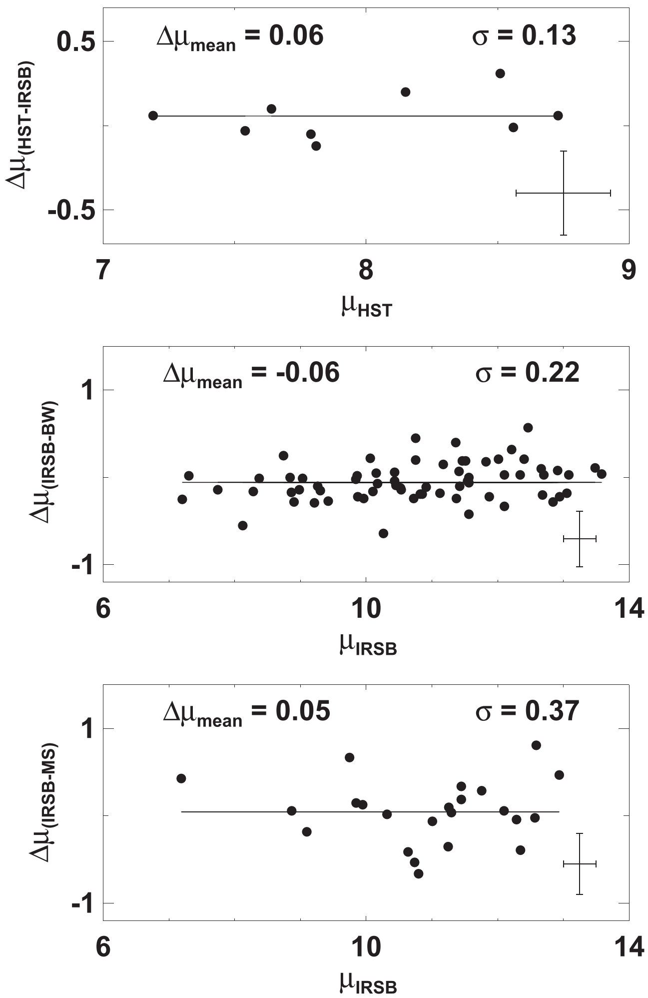

Figure 4. Comparisons of distance moduli obtained using different techniques. The solid lines represent the mean value and representative error bars show the corresponding median uncertainties from Table 5.

2013). We note that the principle of distance determination using IRSB and BW methods is similar but with different treatment of algorithms. Groenewegen (2013) essentially used the same data as Storm et al. (2011) and hence they are not totally independent of each other. Both these studies found a similar dependence of the p-factor on period, but the zero-point implied a shorter distance scale. The LMC distance modulus found by Groenewegen (2013) was shorter as compared to recent studies. Therefore, we only make use of BW distances when the corresponding IRSB distance is not available. The distance moduli from all available methods for a given Cepheid are listed in Table 5.

Figure 4 shows comparisons of distance moduli obtained using different techniques. We consider *HST* parallaxes to be highly precise measurements that include realistic estimates of statistical and systematic sources of uncertainty (median error of 0.14 mag). In contrast, we note that the values listed in Table 5 for the uncertainties in BW, IRSB, and MS distance moduli, as reported in the original publications, are not consistent with the observed dispersions seen in Figure 4. Therefore, we use the latter to estimate a minimum uncertainty for each of these three techniques. Initially, we homogenize the sample by correcting each distance from methods other than *HST*-π for average shifts to match *HST*-π distances. The average shifts between any two methods are (Δ(*HST*-π–IRSB) = 0.06, Δ(*HST*-π–BW) = 0.10, Δ(IRSB–BW) = −0.06, Δ(IRSB–MS) = 0.05). The BW and IRSB methods are very similar and have the highest number of Cepheids in common and also have equal dispersion ($\sigma = 0.13$) with *HST*-π. We consider an equal contribution from each to the variance in the middle panel (Figure 4) and determine their minimum uncertainty as 0.15 mag. We subtract the contribution of IRSB from the observed variance in the bottom panel (Figure 4) to determine a minimum error of 0.33 mag for MS distances. We adopt these values as the minimum allowed uncertainty for a given technique when calculating the mean error-weighted distances and uncertainties listed in the last column of Table 5. For these uncertainties, we adopt a conservative approach and use the greater of the standard deviation of the data and the uncertainty on the mean.

We use extinction-corrected 2MASS mean magnitudes and the adopted mean distance modulus given in Table 5 to calibrate our Galactic P–L and P–W relations. The calculated absolute magnitude for each fundamental mode Cepheid is presented in Table 6. The uncertainty in the absolute magnitude is mostly driven by the large uncertainties on distance and also, to a lesser extent, on reddening correction errors. Since our sample included 10 first-overtone stars (DT CYG, FF AQL, FN AQL, EV SCT, QZ NOR, SU CAS, SZ TAU, V496 AQL, X LAC, Y OPH) as identified from Ngeow (2012), we did not consider these stars in calibrating the P–L relations. We also restricted our sample to include only those stars that have periods greater than 2.5 days. Furthermore, we remove 3σ outliers in each NIR band to fit a P–L relation, for a final sample of 99 stars. Absolute magnitudes are plotted against $\log(P)$ and we fit a P–L relation in the form, $M_\lambda = a_\lambda[\log(P) - 1] + b_\lambda$, where a_λ is the slope and b_λ is the intercept at $\log(P) = 1$. The P–L relations for Galactic Cepheids in each NIR band are shown in Figure 5 and the slopes and intercepts are given in Table 7.

We make use of these calibrated absolute magnitudes to derive P–W relations for the Galaxy. These Wesenheit magnitudes are estimated using Equation (1) and are given in Table 6 together with the absolute magnitudes. We again remove 3σ outliers when fitting each P–W relation. These calibrated P–W relations for the Galaxy are shown in Figure 6 and the results are presented in Table 7. We compare our Galactic NIR P–L relations with those published by Fouqué et al. (2007), Storm et al. (2011) and Ngeow (2012). The results from these studies are also listed in Table 7 and a detailed comparison is discussed in the Appendix.

3.2. Distance to the LMC

Once the Galactic P–L relation is calibrated we can use it to derive the distance moduli of LMC Cepheids. Assuming the JHK_s P–L relations to have universal slopes and intercepts, we calculate the absolute magnitude in all bands for individual LMC Cepheids having period P. We have the mean apparent magnitudes from Paper I for all Cepheids in the LMC, and using the calibrated absolute magnitudes, we estimate individual distance moduli for all LMC Cepheids. We remove the 3σ outliers in the calculated distance moduli and adopt the average value to be the distance modulus in each NIR band. In Section 6, we have provided evidence that the P–L and P–W relations are universal for the Galaxy and the LMC. Hence, we do not observe any significant trend as a function of period in the distance moduli for LMC Cepheids.

Table 6
Calibrated Magnitudes for Fundamental-mode Galactic Cepheids

Star	$\log(P)$	Absolute Magnitudes			σ(Absolute Mag.)			F_1	Wesenheit Magnitudes			σ(Wesenheit Mag.)			F_2
ID		M_J	M_H	M_K	M_J	M_H	M_K		$W_{J,H}$	$W_{J,K}$	$W_{H,K}$	$W_{J,H}$	$W_{J,K}$	$W_{H,K}$	
AK CEP	0.859	−5.223	−5.561	−5.573	0.201	0.201	0.201	Y	−6.112	−5.814	−5.596	0.208	0.202	0.210	Y
AN AUR	1.012	−6.254	−6.529	−6.615	0.221	0.222	0.221	N	−6.978	−6.864	−6.780	0.229	0.222	0.231	N
AQ PUP	1.479	−6.955	−7.201	−7.312	0.630	0.630	0.630	Y	−7.604	−7.558	−7.524	0.631	0.630	0.631	Y
AW PER	0.810	−5.181	−5.452	−5.471	0.181	0.181	0.181	Y	−5.893	−5.671	−5.508	0.189	0.183	0.191	Y
BB SGR	0.822	−4.837	−5.128	−5.190	0.510	0.510	0.510	Y	−5.603	−5.434	−5.310	0.511	0.510	0.512	Y

Note. The uncertainties in absolute magnitudes include the errors in mean magnitudes and distance moduli from Tables 4 and 5, errors from transformations to the 2MASS system, and reddening corrections. These errors are propagated to estimate uncertainty for Wesenheit magnitudes. The flags F_1 and F_2 indicate if the Cepheid is used in final P–L and P–W fits, respectively.

(This table is available in its entirety in machine-readable and Virtual Observatory (VO) forms.)

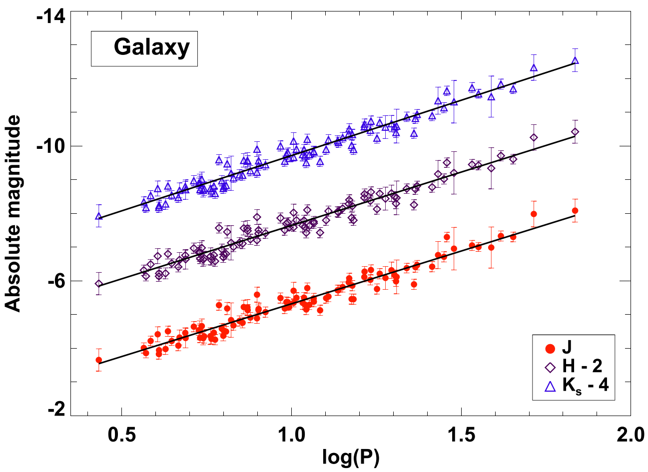

Figure 5. Calibrated NIR P–L relations for fundamental-mode Galactic Cepheids. The solid line represents the best-fit linear regression to the data points in each band.

The values of mean distance moduli for LMC Cepheids are provided in Table 8. These results are in excellent agreement with the result from Pietrzyński et al. (2013), given their uncertainties. This further suggests that the metallicity correction is not needed in H and K_s and the zero-point of the P–L relation in these bands is metallicity independent. The reason for the small variations in these distance moduli could be due to the slight difference in the slopes and intercepts of the two galaxies and also the errors in the transformations of JHK_s Galactic mean magnitudes to the 2MASS system. The LMC distance moduli obtained using the calibration of Galactic P–W relations are also presented in Table 8. Again, these distance moduli are in excellent agreement with the Pietrzyński et al. (2013) result.

The errors in the P–L based distance estimates are only 3%, while those based on P–W are 4%. We expect that with the larger number of Cepheids having high quality light curve data in the LMC OGLE-IV survey, the errors can be reduced further. The Galactic calibrations in our work are based on distances obtained by four independent methods, which have different sources of systematic errors. At present, it is difficult to provide an absolute calibration of Galactic relations with a well-determined systematic uncertainty, which can be propagated to Cepheid based distance estimates. Therefore, we only provide the total statistical uncertainty and the systematic errors are expected to be of the order of, or even larger than the quoted uncertainties. A robust calibration of Galactic relations will only be possible with accurate parallaxes from *GAIA* and then the LMCNISS data can be used to obtain a more precise distance to the LMC. However, our results do provide a useful check on the distance to the LMC, which is consistent and independent to the distance obtained by Pietrzyński et al. (2013).

Alternatively, we also calculate the LMC distance moduli using the slopes and zero-points at $\log(P) = 1.0$ from the LMC P–L relations, given in Table 7. Since the LMC relations exhibit a smaller dispersion, we use these slopes to determine the zero-point of the Galactic relations at $\log(P) = 1.0$. Following Monson et al. (2012), the apparent distance moduli are determined by differencing the LMC and the Galactic zero-points. These distance moduli, presented in Table 8, are found to be consistent with the recent studies on distance determination (Fouqué et al. 2007; Monson et al. 2012; Pietrzyński et al. 2013). All these results provide an average value of the LMC distance modulus $\mu_{\text{LMC}} = 18.47 \pm 0.07$ mag, which is in excellent agreement with the "concordance" distance modulus of $\mu_{\text{LMC}} = 18.49 \pm 0.09$ mag estimated by de Grijs et al. (2014).

We note that the LMC distance moduli estimated using the J-band P–L and the $W_{J,H}$ relations show the largest deviations from the other estimates and the Pietrzyński et al. (2013) value. Since the slope and intercepts are nearly equal for both Galaxy and LMC, we investigate the possible reasons for the difference. We find that the Galactic J-band P–L relation and $W_{J,H}$ Wesenheit show a break around 10 days. We use the F-test (Bhardwaj et al. 2014) to determine the significance of these breaks and find that the $W_{J,H}$ Wesenheit is significantly nonlinear. The LMC P–L and P–W relations were previously found to be nonlinear at 10 days (Sandage et al. 2004; Ngeow et al. 2005; Ngeow & Kanbur 2006a; García-Varela et al. 2013). A detailed statistical analysis of the nonlinearity in our LMC relations and its impact on the distance scale will be presented in a subsequent study.

4. A DISTANCE TO THE ANDROMEDA GALAXY (M31)

We make use of Cepheid observations in M31 from the PHAT survey (Dalcanton et al. 2012; Williams et al. 2014) to estimate the distance to this galaxy. The observations were carried out using the *HST* Advanced Camera for Surveys (*HST*/ACS) and Wide Field Camera 3 (WFC3). There are 477 fundamental-mode Cepheids observed with the *HST* filters F110W and F160W in M31. Since full light curves are not available, random-phase observations must be used. However,

Table 7
Galactic Cepheid NIR P–L and P–W Relations

	Slope	Intercept	σ	N	Src	Slope		Intercept	
						$\|T\|$	$p(t)$	$\|T\|$	$p(t)$
J	−3.127 ± 0.076	−5.320 ± 0.023	0.223	99	TW	…	…	…	…
	−3.194 ± 0.068	−5.258 ± 0.020	0.155	59	F07	0.60	0.55	1.87	0.06
	−3.180 ± 0.090	−5.220 ± 0.030	0.220	70	S11	0.45	0.65	2.64	0.01
	−3.058 ± 0.021	−5.340 ± 0.019	0.073	203	N12	1.11	0.27	0.52	0.61
H	−3.164 ± 0.074	−5.643 ± 0.022	0.219	99	TW	…	…	…	…
	−3.328 ± 0.060	−5.543 ± 0.020	0.146	56	F07	1.57	0.12	3.00	0.00
	−3.300 ± 0.080	−5.590 ± 0.030	0.220	70	S11	1.25	0.21	1.43	0.16
	−3.181 ± 0.022	−5.648 ± 0.020	0.077	203	N12	0.27	0.78	0.13	0.90
K_s	−3.278 ± 0.073	−5.716 ± 0.022	0.219	99	TW	…	…	…	…
	−3.365 ± 0.062	−5.647 ± 0.019	0.144	58	F07	0.82	0.41	2.13	0.03
	−3.330 ± 0.090	−5.660 ± 0.030	0.220	70	S11	0.45	0.65	1.51	0.13
	−3.231 ± 0.021	−5.732 ± 0.020	0.075	203	N12	0.78	0.44	0.40	0.69
$W_{J,H}$	−3.223 ± 0.076	−6.168 ± 0.023	0.228	99	TW	…	…	…	…
W_{J,K_s}	−3.383 ± 0.074	−5.989 ± 0.022	0.223	99	TW	…	…	…	…
	−3.415 ± 0.074	−6.037 ± 0.071	0.230	70	S11	0.31	0.76	0.66	0.51
W_{H,K_s}	−3.499 ± 0.075	−5.856 ± 0.023	0.225	99	TW	…	…	…	…

Note. The P–L relations are taken from the sources : TW—This work, F07—Fouqué et al. (2007), S11—Storm et al. (2011), N12—Ngeow (2012). The P–L and P–W relations from some of these studies are transformed to the notation of $M = a[\log(P) - 1] + b$ for ease of comparison.

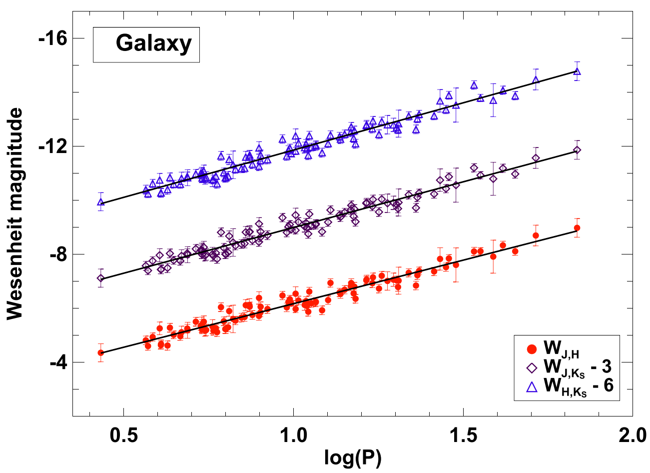

Figure 6. Calibrated NIR P–W relations for fundamental-mode Galactic Cepheids. The solid line represents the best-fit linear regression to the data points in each band.

Table 8
LMC Distance Moduli

	J	H	K_s
$\mu_{\rm LMC}$	18.52 ± 0.06	18.47 ± 0.06	18.47 ± 0.06
	$W_{J,H}$	W_{J,K_s}	W_{H,K_s}
$\mu_{\rm LMC}$	18.40 ± 0.08	18.44 ± 0.09	18.46 ± 0.09
		Fixed Galactic P–L slopes	
$\mu_{\rm LMC}$	18.51 ± 0.06	18.46 ± 0.06	18.48 ± 0.06
		Average value = 18.47 ± 0.07	

the high resolving power of *HST* allows random-phase observations to be comparable to or better than ground-based observations. The improved photometric accuracy reduces the dispersion in P–L relations even with random-phase magnitudes.

4.1. NIR P–L and P–W Relations

We note that no robust observational transformation from *HST* F110W and F160W filters to ground-based J and H is available in the literature. Therefore, we make use of theoretical transformations derived from isochrones (Girardi et al. 2002).[7] We take Girardi isochrones over a range of ages (1–12 Gyr) and metallicities ($Z = 0.0001$–0.03) at $A_V = 0$ and $A_V = 1$ (Bonatto et al. 2004; Girardi et al. 2008). We compare the 2MASS J and H filters to the *HST* WFC3-IR F110W and F160W filters and derive the following transformations over the range of observed F110-F160W colors:

$$J = F110W - 0.038 - 0.270(F110W - F160W) + 0.025(F110W - F160W)^2, \tag{3}$$

$$H = F160W - 0.028 - 0.164(F110W - F160W) - 0.076(F110W - F160W)^2, \tag{4}$$

with rms errors of ∼0.012 mag and ∼0.011 mag in J and H, respectively. We added the rms error in quadrature to the observed photometric error to estimate the associated error for transformed magnitudes. This theoretical transformation led to an average offset of 0.165 mag and 0.073 between J and F110W and H and F160W, respectively.

The random-phase magnitudes are corrected for reddening using the extinction law of Cardelli et al. (1989) using $R_V = 3.1$ and a foreground reddening to M31 of $A_V = 0.17$ mag (Schlafly & Finkbeiner 2011). We derive the P–L relations in J and H and the P–W relation in $W_{J,H}$ using the transformed magnitudes. We calculate Wesenheit magnitudes using Equation (1) and remove 3σ outliers and fit the remaining sample of 440 stars to derive P–L relations and a $W_{J,H}$ P–W relation. These relations are plotted in Figure 7, while their intercepts

[7] http://stev.oapd.inaf.it/cgi-bin/cmd_2.5

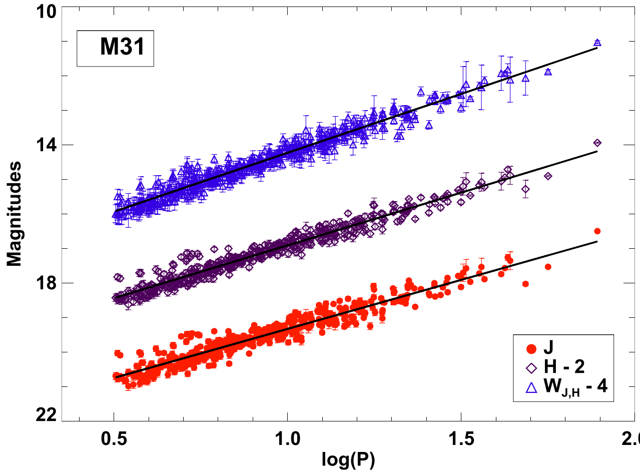

Figure 7. NIR P–L and P–W relations for the M31 Cepheids. The solid line represents the best fit linear regression to the data points.

and slopes are given in Table 9. Our P–L relations in the *J*- and *H*-bands are consistent with P–L relations in *HST* filters derived by Kodric et al. (2015), with slight differences in slopes presumably due to *HST* filters to 2MASS transformations. A more detailed comparison of long period P–L relations in *HST* filters with Kodric et al. (2015) results is provided in Wagner-Kaiser et al. (2015).

We also compare the slope of M31 P–L and P–W relations with the Galaxy and LMC. The results of the t-statistical test are given in Table 10. The slope of the M31 *J*-band P–L relation is statistically different to the Galactic and LMC P–L relations, while the M31 *H*-band P–L relation shows a slope consistent with the Galactic relation (within the large uncertainty in the latter). On the other hand, the M31 $W_{J,H}$ slope is not consistent with our results for the Milky Way or the LMC, yet it is in agreement with the results from Inno et al. (2013). The possible reason for this discrepancy may be the random-phase observations in M31 and Inno et al. (2013) as opposed to magnitudes based on full-phase light curves for our work. Moreover, the derived theoretical transformations may also contribute to the difference in P–W relations.

4.2. The Distance to M31

We use the $W_{J,H}$ magnitudes for the M31 Cepheids to determine the distance to this galaxy. Since we have calibrated P–W relations for Galactic Cepheids, we can calibrate the absolute Wesenheit magnitudes in $W_{J,H}$ for individual M31 Cepheids. We use these calibrated absolute magnitudes together with the Wesenheit magnitudes for M31 to find the distance modulus for each M31 Cepheid independently. We remove the 3σ outliers in the calculated distance moduli and take the mean value to be the distance modulus to M31. However, we note that the P–W relation in $W_{J,H}$ for the Cepheids in M31 is steeper as compared to the Galaxy and the LMC. Therefore, we observe a trend as a function of period in the distance moduli for Cepheids in M31. The mean distance modulus to M31 Cepheids using the Galactic calibration is found to be $\mu_{\rm M31} = 24.42 \pm 0.20$ mag. Similarly, we also make use of the calibrated P–W relation in $W_{J,H}$ for the LMC Cepheids to determine distance moduli of Cepheids in M31. We consider an error-weighted mean to find a true distance modulus to M31 of $\mu_{\rm M31} = 24.50 \pm 0.19$ mag, using the LMC calibration.

Table 9
M31 Cepheid NIR P–L and P–W Relations

Band	Slope	Intercept	σ	N
J	−2.839 ± 0.040	19.331 ± 0.011	0.214	440
H	−3.056 ± 0.033	18.913 ± 0.009	0.173	440
$W_{J,H}$	−3.409 ± 0.035	18.231 ± 0.010	0.183	440

Table 10
Comparison of Slopes of the M31 P–L and P–W Relations with Galaxy and LMC

	Galaxy	Slope	Src	$\|T\|$	$p(t)$
J	M31	−2.839 ± 0.040	TW	…	…
	MW	−3.127 ± 0.076	TW	3.44	0.00
	LMC	−3.156 ± 0.004	M15	10.29	0.00
H	M31	−3.056 ± 0.033	TW	…	…
	MW	−3.164 ± 0.074	TW	1.53	0.13
	LMC	−3.187 ± 0.004	M15	5.08	0.00
$W_{J,H}$	M31	−3.409 ± 0.035	TW	…	…
	MW	−3.223 ± 0.076	TW	2.52	0.01
	LMC	−3.157 ± 0.014	TW	7.64	0.00
	LMC	−3.373 ± 0.008	I13	1.53	0.13

Note. Source: TW—This work, M15—Macri et al. (2015 and erratum), I13—Inno et al. (2013).

Table 11
M31 Distance Moduli

Calibrator	$\mu_{\rm M31}$	Published	Source
Galaxy	24.42 ± 0.20	24.44 ± 0.12	R05
		24.36 ± 0.08	V10
LMC	24.50 ± 0.19	24.38 ± 0.06	R12
		24.46 ± 0.10	D14
Average value = 24.46 ± 0.20			

Note. The values of distance modulus for M31 compiled from literature are taken from the sources : R05—Ribas et al. (2005), V10—Vilardell et al. (2010), R12—Riess et al. (2012), D14—de Grijs & Bono (2014).

These results are again consistent with previous studies (Stanek & Garnavich 1998; Ribas et al. 2005; Vilardell et al. 2006, 2010; Riess et al. 2012; Valls-Gabaud 2013). The values of mean distance modulus for M31 Cepheids obtained using both Galaxy and LMC as calibrators are given in Table 11. The larger error in distance moduli for M31 can be attributed to a greater scatter in the random-phase P–L relation obtained from the single epoch observations from the PHAT survey. However, our results are still in excellent agreement with the "concordance" distance modulus of $\mu_{\rm M31} = 24.46 \pm 0.10$ mag from de Grijs & Bono (2014). We also note that Wagner-Kaiser et al. (2015) determined a distance of 24.51 ± 0.08 mag to M31 using long-period ($P > 10$ days) Cepheids and the P–W relation in *HST* filters.

5. DISTANCES TO LOCAL GROUP GALAXIES

We compiled published NIR mean magnitudes for Cepheids in other Local Group galaxies. Recently, Ngeow et al. (2015) derived the P–L relations for Cepheids in SMC at multiple wavelengths. They used the 2MASS counterparts of OGLE-III

Table 12
The Distance Moduli to Local Group Galaxies Using a Global Fit

	N	Met.	Calibrator			Published			
			Galaxy	LMC	Galaxy+LMC	TRGB	References	Cepheid	References
WLM	29	7.74	24.85 ± 0.11	24.88 ± 0.08	24.92 ± 0.07	25.12 ± 0.15	G11	24.92 ± 0.04	G08
IC 1613	23	7.86	24.20 ± 0.10	24.22 ± 0.07	24.26 ± 0.07	24.24 ± 0.10	G11	24.29 ± 0.04	P06
SMC	602	7.98	18.96 ± 0.08	19.00 ± 0.05	19.03 ± 0.05	18.98	R07	18.96 ± 0.02	D15
NGC 55	36	8.05	26.34 ± 0.09	26.35 ± 0.06	26.37 ± 0.06	…	…	26.43 ± 0.04	GI8
NGC 3109	69	8.06	25.45 ± 0.09	25.47 ± 0.06	25.49 ± 0.06	25.42 ± 0.13	G11	25.57 ± 0.02	S06
NGC 6822	20	8.14	23.39 ± 0.08	23.41 ± 0.06	23.43 ± 0.06	23.26 ± 0.10	G11	24.38 ± 0.02	R14
NGC 300	15	8.35	26.26 ± 0.10	26.28 ± 0.07	26.29 ± 0.07	26.48 ± 0.04	R07	26.37 ± 0.05	G05
NGC 247	10	…	27.57 ± 0.12	27.58 ± 0.09	27.60 ± 0.09	…	…	27.64 ± 0.04	G09
M33	24	8.55	24.60 ± 0.08	24.61 ± 0.06	24.62 ± 0.06	24.71 ± 0.04	R07	24.62 ± 0.07	G13
b_w			−5.980 ± 0.072	−6.009 ± 0.050	−6.010 ± 0.049				
$M_{w,1}$			−3.238 ± 0.027	−3.249 ± 0.019	−3.244 ± 0.016				

Note. The metallicity (12 + log[O/H]) values are taken from Sakai et al. (2004), Bono et al. (2010), and Fiorentino et al. (2012). The published values of distance moduli are taken from the sources : G05—Gieren et al. (2005), G06—Gieren et al. (2006a), S06— Soszyński et al. (2006), P06—Pietrzyński et al. (2006), R07—Rizzi et al. (2007), G08—Gieren et al. (2008b), GI8—Gieren et al. (2008a), G09—Gieren et al. (2009), G11—Górski et al. (2011), F12—Feast et al. (2012), G13—Gieren et al. (2013), R14—Rich et al. (2014), D15—de Grijs & Bono (2015).

SMC fundamental-mode Cepheids and applied random phase corrections to obtain mean JHK_s magnitudes. Also, Rich et al. (2014) determined the distance to NGC 6822 using previously published and newly obtained data in multiple bands. The JHK_s band photometry was calibrated to the 2MASS system. We make use of NIR J and K_s mean magnitudes from these studies in our analysis. The Cepheids in IC 1613 were observed by Scowcroft et al. (2013) using the FourStar NIR camera at Las Campanas and the mean magnitudes are available in JHK_s bands. We also use J and K observations from the Araucaria project for Cepheids in IC 1613, M33, WLM, NGC 3109, NGC 300, NGC 55, NGC 247 (Gieren et al. 2005, 2008a, 2008b, 2013, 2009; Pietrzyński et al. 2006; Soszyński et al. 2006). All these mean magnitudes are transformed to the 2MASS system using color transformations as discussed in previous sections.

We determine the distance moduli to these Local Group galaxies using the W_{J,K_s} P–W relation. We prefer the P–W relations because they are independent of extinction corrections. We use a global fit to all Cepheids in the Local Group galaxies having W_{J,K_s} Wesenheit magnitudes. Therefore, the Wesenheit magnitude $W_{i,j}$ for the jth Cepheid in ith target galaxy is defined as:

$$W_{i,j} = \mu_i + M_{w,1} + b_w \log P_{i,j}, \tag{5}$$

where μ_i is the distance moduli to the target galaxy, and $M_{w,1}$ is the Wesenheit magnitude of a Cepheid with $P = 10$ days in the calibrator galaxy (LMC and/or Milky Way). The parameter b_w is to be determined using the global fit and represents the slope for all Cepheids in the sample. We solve the matrix equation $y = Lq$ using the minimization of χ^2 as discussed in Riess et al. (2009). We use W_{J,K_s} magnitudes for the Galaxy and LMC separately in the above equation to determine distances to other galaxies. We also use a combined calibration based on Galactic and LMC data. The metallicity gradients of Local Group galaxies are based on the T_e scale and adopted from Sakai et al. (2004), Bono et al. (2010), and Fiorentino et al. (2012). We apply the metallicity corrections for calibrations based on the Galaxy and LMC such that $\mu_{i,0} = \mu_i + \gamma(\Delta \log[\mathrm{O/H}])$, where $\Delta \log[\mathrm{O/H}]$ is the difference in mean metallicity between the target and the calibrator galaxy and $\gamma = -0.05 \pm 0.06$ mag dex^{-1} is adopted from Bono et al. (2010) for W_{J,K_s}. The mean metallicity values in this scale for the Galactic and LMC Cepheids are 8.60 and 8.34 dex, respectively. However, we do not apply a metallicity correction when we use the combined Galactic+LMC calibration in the global fit. The estimated values of the distance moduli are presented in Table 12. The uncertainties in the distance moduli obtained from the global fit are only statistical; we also add in quadrature the systematic uncertainty in the zero-point of the calibrator relations to arrive at the final values.

We note that the distance moduli obtained for IC 1613 are in good agreement with the results based on P–L relations by Pietrzyński et al. (2006) and Scowcroft et al. (2013). However, there is a large offset (∼0.2 mag) in the K_s magnitudes for Cepheids in common between these two studies. Using the Pietrzyński et al. (2006) data for our P–W analysis yields a distance modulus consistent with previous work, indicating a problem with the calibration of the Scowcroft et al. (2013) data. We compare our results with recent TRGB and Cepheid distances available in the literature and find good agreement. The difference in Cepheid and TRGB based distance estimates as a function of metallicity is shown in Figure 8. We do not observe any significant trend in estimated distances as a function of metallicity. Furthermore, the metallicity correction leads to a difference of ∼0.06 mag in distance modulus for metal poor galaxies (WLM, IC 1613, SMC), while the mean difference is ∼0.03 mag with or without metallicity correction for other Local Group galaxies. The global fit results in a universal slope of −3.244 ± 0.016 for the W_{J,K_s} Wesenheit relation for Cepheids in Local Group galaxies. We also note that our distance estimates are consistent for a large metallicity range $7.7 < 12 + \log[\mathrm{O/H}] < 8.6$ dex and therefore, our calibrator relations can be applied to future observations of Cepheids in more distant galaxies.

6. CONCLUSIONS

In the present analysis, we analyzed P–L and P–W relations for Cepheids in the LMC, the Galaxy, and M31 at JHK_s wavelengths. We also determine the distances to LMC, M31

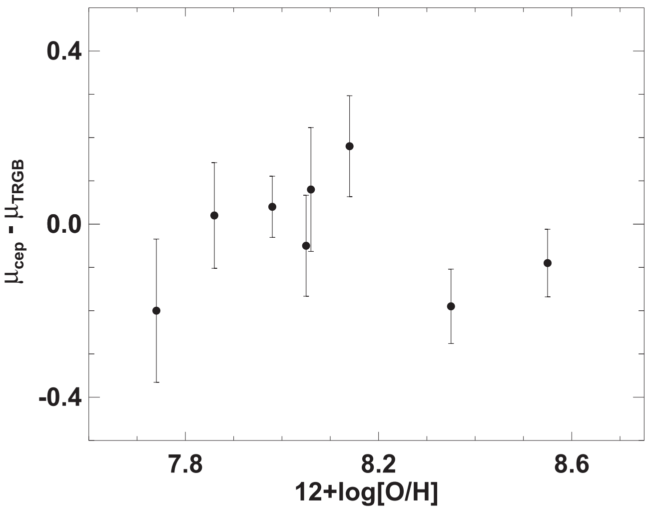

Figure 8. Comparison of Cepheid and TRGB distances to Local Group galaxies as a function of metallicity.

and other Local Group galaxies. We summarize our conclusions arising from this study.

1. We use JHK_s data for Cepheids from LMCNISS (Macri et al. 2015) to derive new P–W relations at these wavelengths. The relations for fundamental-mode Cepheids are based on a sample size nine times larger than the previously published time-series results. The first-overtone P–W relation is calibrated for the first time with phased light curve data, as opposed to random single-phase observations.
2. We obtain a new calibration of Galactic Cepheid P–L and P–W relations based on distances from various methods, taking into account the intrinsic scatter of each technique. Our results bridge the inconsistency between Galactic P–L relations based on independent distances and P–L relations derived using Wesenheit distances. We find our results are consistent with most of the previously published work, considering the large intrinsic scatter in Galactic relations.
3. We use the new LMCNISS data to provide an independent estimate of the distance to the LMC. Using Galactic calibrations, we determine $\mu_{\rm LMC} = 18.47$, with a total statistical uncertainty of ± 0.07 mag, which is in excellent agreement with the value from Pietrzyński et al. (2013) based on late-type eclipsing binaries. However, our error estimates do not include the unknown systematic uncertainties.
4. We derive new P–L and P–W relations for Cepheids in M31, based on the observations from the PHAT survey. We develop theoretical transformations from *HST* filters F110W and F160W to 2MASS *J* and *H*-bands. Although the relations are based on random-phase observations, the highly accurate *HST* observations help to reduce the observed dispersion in P–L and P–W relations.
5. Using Galactic and LMC $W_{J,H}$ Wesenheit relations as references, we estimate a distance modulus for M31 of $\mu_{\rm M31} = 24.46 \pm 0.20$ mag, in excellent agreement with recent determinations (Riess et al. 2012; Valls-Gabaud 2013; de Grijs & Bono 2014).
6. We apply a simultaneous fit to Cepheids in Local Group galaxies, using the Galaxy and LMC as calibrators, to obtain a global slope of -3.244 ± 0.016 mag dex^{-1} in W_{J,K_s} and estimate robust distances, which are found to be consistent with previous results based on TRGB and Cepheids. We do not find a significant metallicity effect at these wavelengths.
7. Our absolute calibration of the Galactic and LMC relations provides accurate distances for Local Group galaxies with a wide metallicity range $(7.7 < 12 + \log[{\rm O/H}] < 8.6)$ dex. In combination with higher-quality NIR light curves for Cepheids at greater distances, they can be used for further improvements in the precision and accuracy of the distance scale.

Table 13
Comparison of LMC Distances Using the Published Galactic P–L Relations

Source	J	H	K_s
F07	18.44 ± 0.05	18.32 ± 0.05	18.37 ± 0.06
S11	18.40 ± 0.06	18.38 ± 0.06	18.40 ± 0.07
N12	18.56 ± 0.05	18.47 ± 0.05	18.50 ± 0.05

Note. The source column represents the calibrator P–L relations from : F07—Fouqué et al. (2007), S11—Storm et al. (2011), N12—Ngeow (2012).

An upcoming study based on LMCNISS data (Bhardwaj et al. in preparation) will include a statistical analysis of nonlinearities in the Leavitt law at $VIJHK_s$ wavelengths and its impact on the distance scale and in constraining theoretical pulsation models.

A.B. acknowledges the Senior Research Fellowship grant 09/045(1296)/2013-EMR-I from the Human Resource Development Group (HRDG), which is a division of the Council of Scientific and Industrial Research (CSIR), India. This work is supported by the grant for the Joint Center for Analysis of Variable Star Data provided by the Indo-U.S. Science and Technology Forum. L.M.M. acknowledges support by the United States National Science Foundation through AST grant number 1211603 and by Texas A&M University through a faculty start-up fund and the Mitchell-Heep-Munnerlyn Endowed Career Enhancement Professorship in Physics or Astronomy. C.C.N. thanks the funding from the Ministry of Science and Technology (Taiwan) under the contract NSC101-2112-M-008-017-MY3. This work also makes use of data products from the 2MASS survey, which is a joint project of the University of Massachusetts and the Infrared Processing and Analysis Center/California Institute of Technology, funded by the National Aeronautics and Space Administration and the National Science Foundation. In addition, this study also makes use of NASA's Astrophysics Data System, the VizieR catalog, and the McMaster Cepheid Photometry database.

APPENDIX
A COMPARISON OF P–L AND P–W RELATIONS

We use our LMCNISS JHK_s mean magnitudes to determine a distance to the LMC with published NIR Galactic P–L relations listed in Table 7. We present the LMC distance moduli obtained using these P–L relations in Table 13. We note that the distances in H and K_s bands are considerably smaller using P–L relations from Fouqué et al. (2007) and Storm et al. (2011). Similarly, the J-band P–L from Ngeow (2012) leads to a relatively greater value of LMC distance as compared to

Table 14
Comparison of Calibrated Galactic and LMC P–L and P–W Relations Derived in the Present Study

		J	H	K_s	$W_{J,H}$	W_{J,K_s}	W_{H,K_s}
Slope	$\|T\|$	0.27	0.12	0.18	1.59	3.03	3.35
	$p(t)$	0.79	0.90	0.86	0.11	0.00	0.00
Intercept	$\|T\|$	0.20	0.49	0.20	1.24	0.44	0.09
	$p(t)$	0.84	0.63	0.84	0.21	0.66	0.92

Pietrzyński et al. (2013). We explore the reasons for possible discrepancy among these relations and compare with our Galactic P–L relations derived in the present study.

Ngeow (2012) used a method involving the Wesenheit function to derive distance moduli for a large number of Galactic Cepheids and found a marginal average difference (−0.061–0.009) with published distances. This method was also calibrated against *HST* parallaxes but the uncertainties listed in that work are only statistical errors. It is important to note that even though the Wesenheit distances are consistent with other methods, there is a significant change in the slope and intercepts of P–L relations from Ngeow (2012) with Fouqué et al. (2007) and Storm et al. (2011). Interestingly, our results based on various distances are very consistent with Ngeow (2012).

We find that our slopes for JHK_s P–L relations are consistent with Fouqué et al. (2007), Storm et al. (2011), and Ngeow (2012) as $p(t) > 0.05$, in all the bands. However, the intercepts of P–L relations show mixed results, with most of them being consistent with published work. The intercepts of JHK_s P–L relations are in excellent agreement with Ngeow (2012) but relatively smaller than Fouqué et al. (2007) and Storm et al. (2011). The t-test suggests that the zero-points of our P–L relations are statistically different from Fouqué et al. (2007) but the zero-point of the H and K_s-band P–L relations are statistically similar to Storm et al. (2011), with the J-band zero-point again being significantly different. We also note that the dispersion in our P–L relations is similar to that of Storm et al. (2011), whereas we have increased the sample size nearly 1.5 times. The discrepancy in results with Fouqué et al. (2007) is mainly due to significantly different sample sizes.

We test the difference in zero-points with Fouqué et al. (2007) and Storm et al. (2011) by comparing the properties of P–L relations derived using only Cepheids common to these samples. We find that the difference in zero-points of the two set of P–L relations is reduced on average by 0.02 mag. Therefore, the slope and intercepts of our P–L relations are not significantly different from published work. A small contribution to this difference in intercepts may be due to the inclusion of few first overtone stars (for example, FN AQL, V496 AQL, and Y OPH) in Fouqué et al. (2007) and Storm et al. (2011). These stars are not considered in our sample, following Ngeow (2012). Our results for the P–W relation in W_{J,K_s} are also consistent with the findings of Storm et al. (2011).

We also compare the slopes and intercepts of Milky Way and LMC Cepheid P–L and P–W relations. From Tables 3 and 7, we find that the intercepts of both P–L and P–W relations for the Galaxy and the LMC are essentially similar in all the bands. The t-test results, given in Table 14, also provide evidence of statistically equal zero-points under a 95% confidence level. Furthermore, the slopes of the P–L and P–W relations for both the Galaxy and LMC are also very similar except in W_{J,K_s} and W_{H,K_s}. This difference in the slopes of the Wesenheit relations is mainly due to the insignificant contribution of color terms in Galactic Wesenheits, which leads to greater dispersion than P–L relations. This provides further empirical evidence that at NIR wavelengths, P–L and P–W relations for Cepheids are universal and the zero-points are independent of metallicity effects (Gieren et al. 2006b; Fouqué et al. 2007; Monson et al. 2012).

REFERENCES

Baart, M. L. 1982, IJNA, 2, 241
Barnes, T. G., III, Fernley, J. A., Frueh, M. L., et al. 1997, PASP, 109, 645
Benedict, G. F., McArthur, B. E., Feast, M. W., et al. 2007, AJ, 133, 1810
Bhardwaj, A., Kanbur, S. M., Singh, H. P., Macri, L. M., & Ngeow, C.-C. 2015, MNRAS, 447, 3342
Bhardwaj, A., Kanbur, S. M., Singh, H. P., & Ngeow, C.-C. 2014, MNRAS, 445, 2655
Bonatto, C., Bica, E., & Girardi, L. 2004, A&A, 415, 571
Bono, G., Caputo, F., Castellani, V., & Marconi, M. 1999, ApJ, 512, 711
Bono, G., Caputo, F., Marconi, M., & Musella, I. 2010, ApJ, 715, 277
Cardelli, J. A., Clayton, G. C., & Mathis, J. S. 1989, ApJ, 345, 245
Dalcanton, J. J., Williams, B. F., Lang, D., et al. 2012, ApJS, 200, 18
de Grijs, R., & Bono, G. 2014, AJ, 148, 17
de Grijs, R., & Bono, G. 2015, AJ, 149, 179
de Grijs, R., Wicker, J. E., & Bono, G. 2014, AJ, 147, 122
Feast, M. W., Whitelock, P. A., Menzies, J. W., & Matsunaga, N. 2012, MNRAS, 421, 2998
Fernie, J. D., Evans, N. R., Beattie, B., & Seager, S. 1995, IBVS, 4148, 1
Fiorentino, G., Clementini, G., Marconi, M., et al. 2012, Ap&SS, 341, 143
Fouqué, P., Arriagada, P., Storm, J., et al. 2007, A&A, 476, 73
García-Varela, A., Sabogal, B. E., & Ramírez-Tannus, M. C. 2013, MNRAS, 431, 2278
Gieren, W., Górski, M., Pietrzyński, G., et al. 2013, ApJ, 773, 69
Gieren, W., Pietrzyński, G., Nalewajko, K., et al. 2006a, ApJ, 647, 1056
Gieren, W., Pietrzyński, G., Soszyński, I., et al. 2005, ApJ, 628, 695
Gieren, W., Pietrzyński, G., Soszyński, I., et al. 2008a, ApJ, 672, 266
Gieren, W., Pietrzyński, G., Soszyński, I., et al. 2009, ApJ, 700, 1141
Gieren, W., Pietrzyński, G., Szewczyk, O., et al. 2008b, ApJ, 683, 611
Gieren, W., Storm, J., Barnes, T. G., III, et al. 2006b, MmSAI, 77, 198
Gieren, W. P., Fouque, P., & Gomez, M. 1998, ApJ, 496, 17
Girardi, L., Bertelli, G., Bressan, A., et al. 2002, A&A, 391, 195
Girardi, L., Dalcanton, J., Williams, B., et al. 2008, PASP, 120, 583
Górski, M., Pietrzyński, G., & Gieren, W. 2011, AJ, 141, 194
Groenewegen, M. A. T. 2013, A&A, 550, A70
Inno, L., Matsunaga, N., Bono, G., et al. 2013, ApJ, 764, 84
Kanbur, S. M., Ngeow, C.-C., Nikolaev, S., Tanvir, N. R., & Hendry, M. A. 2003, A&A, 411, 361
Kodric, M., Riffeser, A., Seitz, S., et al. 2015, ApJ, 799, 144
Laney, C. D., & Stobie, R. S. 1992, A&AS, 93, 93
Leavitt, H. S., & Pickering, E. C. 1912, HarCi, 173, 1
Macri, L. M., Ngeow, C.-C., Kanbur, S. M., Mahzooni, S., & Smitka, M. T. 2015, AJ, 149, 117
Madore, B. F. 1982, ApJ, 253, 575
Madore, B. F., & Freedman, W. L. 2009, ApJ, 696, 1498
Monson, A. J., Freedman, W. L., Madore, B. F., et al. 2012, ApJ, 759, 146
Monson, A. J., & Pierce, M. J. 2011, ApJ, 193, 12
Ngeow, C.-C. 2012, ApJ, 747, 50
Ngeow, C.-C., & Kanbur, S. M. 2004, MNRAS, 349, 1130
Ngeow, C.-C., & Kanbur, S. M. 2006a, ApJ, 650, 180
Ngeow, C.-C., & Kanbur, S. M. 2006b, MNRAS, 369, 723
Ngeow, C.-C., Kanbur, S. M., Bhardwaj, A., & Singh, H. P. 2015, ApJ, 808, 67
Ngeow, C.-C., Kanbur, S. M., Nikolaev, S., et al. 2005, MNRAS, 363, 831
Perryman, M. A. C. 1997, The HIPPARCOS and TYCHO Catalogues Astrometric and Photometric Catalogues Derived from the ESA HIPPARCOS Space Astrometry Mission (ESA SP-402), 1
Persson, S. E., Madore, B. F., Krzemiński, W., et al. 2004, AJ, 128, 2239
Pietrzyński, G., Gieren, W., Soszyński, I., et al. 2006, ApJ, 642, 216
Pietrzyński, G., Graczyk, D., Gieren, W., et al. 2013, Natur, 495, 76
Ribas, I., Jordi, C., Vilardell, F., et al. 2005, ApJL, 635, L37
Rich, J. A., Persson, S. E., Freedman, W. L., et al. 2014, ApJ, 794, 107
Riess, A. G., Casertano, S., Anderson, J., MacKenty, J., & Filippenko, A. V. 2014, ApJ, 785, 161

Riess, A. G., Fliri, J., & Valls-Gabaud, D. 2012, ApJ, 745, 156
Riess, A. G., Macri, L., Casertano, S., et al. 2009, ApJ, 699, 539
Riess, A. G., Macri, L., Casertano, S., et al. 2011, ApJ, 730, 119
Ripepi, V., Moretti, M. I., Marconi, M., et al. 2012, MNRAS, 424, 1807
Rizzi, L., Tully, R. B., Makarov, D., et al. 2007, ApJ, 661, 815
Sakai, S., Ferrarese, L., Kennicutt, R. C., Jr., & Saha, A. 2004, ApJ, 608, 42
Sandage, A., Tammann, G. A., & Reindl, B. 2004, A&A, 424, 43
Sandage, A., Tammann, G. A., & Reindl, B. 2009, A&A, 493, 471
Schlafly, E. F., & Finkbeiner, D. P. 2011, ApJ, 737, 103
Scowcroft, V., Freedman, W. L., Madore, B. F., et al. 2013, ApJ, 773, 106
Soszyński, I., Gieren, W., Pietrzyński, G., et al. 2006, ApJ, 648, 375
Soszynski, I., Poleski, R., Udalski, A., et al. 2008, AcA, 58, 163
Stanek, K. Z., & Garnavich, P. M. 1998, ApJL, 503, L131
Storm, J., Gieren, W., Fouqué, P., et al. 2011, A&A, 534, A95
Tammann, G. A., Sandage, A., & Reindl, B. 2003, A&A, 404, 423
Turner, D. G. 2010, Ap&SS, 326, 219
Ulaczyk, K., Szymański, M. K., Udalski, A., et al. 2013, AcA, 63, 159
Valls-Gabaud, D. 2013, in IAU Symp. 289 Advancing the Physics of Cosmic Distances, ed. R. de Grijs (Cambridge: Cambridge Univ. Press), 235
Van Leeuwen, F., Feast, M. W., Whitelock, P. A., & Laney, C. D. 2007, MNRAS, 379, 723
Vilardell, F., Ribas, I., & Jordi, C. 2006, A&A, 459, 321
Vilardell, F., Ribas, I., Jordi, C., Fitzpatrick, E. L., & Guinan, E. F. 2010, A&A, 509, A70
Wagner-Kaiser, R., Sarajedini, A., Dalcanton, J. J., Williams, B. F., & Dolphin, A. 2015, MNRAS, 451, 5243
Welch, D. L., Wieland, F., McAlary, C. W., et al. 1984, ApJS, 54, 547
Williams, B. F., Lang, D., Dalcanton, J. J., et al. 2014, ApJS, 215, 9